Conference
on Modelling Fluid Flow (CMFF'25)
Radisson Blu Béke Hotel August 26-29, 2025 Budapest / Hungary

Conference on Modelling Fluid Flow CMFF'25
The 19th event of the International Conference Series
on Fluid Flow Technologies held in Budapest since 1959

Conference Proceedings

Edited by J. Vad

Department of Fluid Mechanics / Faculty of Mechanical Engineering
Budapest University of Technology and Economics
2025

Proceedings of the Conference on Modelling Fluid Flow
CMFF'25

Edited by J. Vad

Department of Fluid Mechanics,
Budapest University of Technology and Economics
2025 Budapest, Hungary

ISBN 978-615-112-002-6

Published by the Department of Fluid Mechanics,
Faculty of Mechanical Engineering,
Budapest University of Technology and Economics

Address:
Bertalan Lajos 4-6., H-1111 Budapest, Hungary
www.ara.bme.hu

Conference on Modelling Fluid Flow (CMFF'25)
The 19th International Conference on Fluid Flow Technologies
Budapest, Hungary, August 26 - August 29, 2025

INFLUENCE OF A SCANNING BOX ON THE SETTLING TIME OF MULTI-HOLE PRESSURE PROBES

Johann PUINTNER, Gregor NICHT, Reinhard WILLINGER[1]

[1] Corresponding Author. Institute of Energy Systems and Thermodynamics, TU Wien, Getreidemarkt 9/302, A-1060 Vienna, Austria. Tel.: +43 1 58801 302403, E-mail: reinhard.willinger@tuwien.ac.at

ABSTRACT

The present paper presents an investigation on the settling time of a measurement setup with following components: multi-hole pressure probe, pressure scanning box, connection tubes, piezoresistive pressure transducer. First, an analytical model is presented to calculate the settling time of such a pressure measurement system. The generic model describes the response time of the pressure transducer due to a sudden jump of the pressure at the probe head. Furthermore, the model is extended to take into account the influence of the scanning box. Second, an experimental campaign is performed to verify the analytical model. For this purpose, a three-hole pressure probe is positioned in the open-jet wind tunnel at constant velocity and yaw angle, to generate large pressure differences between the individual sensing holes. Then, the pressure signals are switched by the scanning box in a sequential manner to the single pressure transducer. The results show that the extended analytical model describes the relaxation behaviour and settling time of the measurement system. The obtained time constant can be used to optimize the experimental process to reduce total measurement time. Finally, some conclusions drawn from the investigation of the sensitivity of the time constant on geometrical parameters are presented.

Keywords: experiment, flow model, multi-hole pressure probe, pressure scanning box, pressure transducer, settling time

NOMENCLATURE

a	[m/s]	speed of sound
c	[m/s]	flow velocity
D	[m]	diameter of replacement tube
d	[m]	diameter of tube
l	[m]	length of tube
m	[kg]	mass
$\dot{m}$	[kg/s]	mass flow rate
n	[-]	total number of tube sections
p	[Pa]	static pressure
Δp	[Pa]	static pressure difference
R	[J/kgK]	specific gas constant
Re	[-]	Reynolds number
T	[K]	temperature
t	[s]	time
t_{99}	[s]	settling time
V	[m^3]	volume of plenum
κ	[-]	specific heat ratio
λ	[-]	friction coefficient
ν	[m^2/s]	kinematic viscosity
ρ	[kg/m^3]	density
τ	[s]	time constant

Subscripts

i	number of tube section
A, B, C	index of volume or pressure at plenum
u	ambient conditions
1, 2, 3	probe hole number

1. INTRODUCTION

Multi-hole pressure probes are frequently used measuring instruments in the experimental field of turbomachinery to determine flow characteristics. Three-hole probes are used for two-dimensional flow fields whereas five-hole probes are able to capture three-dimensional flow fields. By measuring the individual hole pressures, it is possible to derive total pressure, static pressure and flow angles and to draw conclusions about the flow field, including total pressure losses. This is an important advantage of pneumatic measurement methods in relation to optical techniques (LDA, PIV) and hot-wire anemometry (CTA). To obtain a comprehensive overview of the flow, the probe is traversed across a measurement plane, comprising of at least one blade pitch and the blade span, resulting in a large number of measurement points. Figure 1 shows a linear cascade of turbine blades in the wind tunnel of the Institute of Energy Systems

and Thermodynamics. Downstream of the cascade, a three-hole pressure probe is arranged to measure the two-dimensional flow field at midspan. The three individual hole pressures are measured by one single pressure transducer. Therefore, a pressure scanning box is arranged between the three-hole probe and the pressure transducer. The purpose of the scanning box is to switch the pressure signals from the multi-hole pressure probe to one single measurement device. Due to the sequential behaviour of the pressure measurement, the whole process is rather time consuming. Another point to take into account is the individual settling time of the pressure probe, the connection tubes and the pressure transducer.

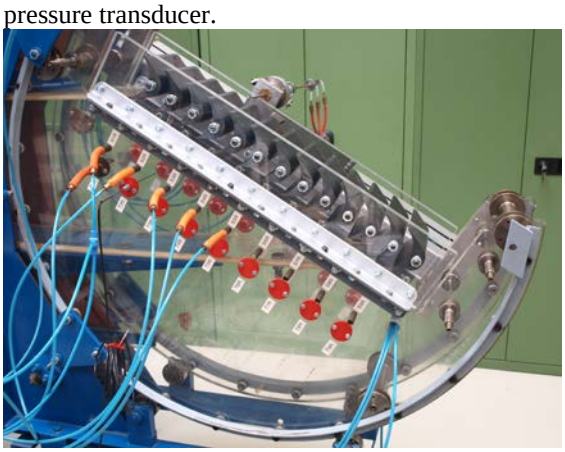

Figure 1. Linear cascade of turbine blades in the wind tunnel

For the planning of the experiment, it is important to know this settling time. On the one hand, the total measurement time should be kept as short as possible. On the other hand, systematic errors will arise, if the waiting time between switching from one pressure channel to the other is too low. This paper presents a combined analytical and experimental investigation on the settling time of multi-hole pressure probes operating with a pressure scanning box.

2. LITERATURE REVIEW

In the open literature, a number of papers can be found which are related to the investigation of the temporal behaviour of pressure measurement systems. From a mathematical point of view, these models can be categorized in first order and second order methods, respectively. If the pressure changes at the probe head appear with high frequency, a second order model is required. This is due to the fact that these models take into account the inertia of the fluid volume in the tubes. As has been pointed out in the introduction, the measurements of interest are steady throughout and a first order model is sufficient. Therefore, the literature review focuses mainly on this kind of models.

An analytical model for the calculation of the response time of gas purged probes connected to a sensitive pressure transducer is presented by Xie and Geldart [1]. The first order model assumes laminar, incompressible flow in the tube and an isothermal change of state in the plenum.

Weidemann [2] gives an analytical and experimental investigation on the inertia of dynamic pressure arrays. The method to calculate a “pneumatic time constant” is based on an electrical analogy.

Sinclar and Robins [3] present an analytical method for the determination of the time lag in pressure measurement systems. The first order model can be categorized into laminar, compressible flow in the tube and an isothermal change of state in the plenum. The main parameters, influencing the response time are analysed. A further objective is to calculate an optimum tube size. Theoretical results are compared with data from systematic experiments.

Lilley and Morton [4] present an analytical method for the calculation of the response time of wind tunnel pressure measurement systems. Additional experiments are performed to validate the analytical model. The detailed model shows that results from simpler methods with concentrated parameters are sufficient to calculate the response time of those systems. However, a prerequisite for sufficient accuracy is to take into account the inlet and exit pressure losses.

A summary of the results from the investigations of [3] and [4] can also be found in the textbook of Wuest [5].

Davis [6] presents a theoretical investigation of the time lag in pressure systems at extremely low pressures. The motivation is that pressure from near vacuum to ambient pressure can appear in transonic and supersonic wind tunnels. Apart from continuous flow, slip flow in the tubes is investigated. This is motivated by the fact that at extremely low pressure, the mean free path is of the same order of magnitude as the diameter of the pressure measuring tube. An experimental check of the validity of the derivation is presented.

Larcombe and Peto [7] provide an analytical method for the calculation of the response time of typical transducer-tube configurations for the measurement of pressure. Since they deal with transonic and supersonic wind tunnels, slip flow as well as continuous flow in the tubes is taken into account. Consideration is given to the special conditions that apply to the case in which the tube systems are connected to a pressure scanning switch.

Bynum et al. [8] provide an overview on wind tunnel pressure measuring techniques. An important aspect is the time response of pressure measuring systems. The report also addresses different options to route tubes from different pressure measurement locations to one single transducer. The authors call this procedure “pneumatic switching”. Many

practical aspects as well as the influence of the pneumatic switching on the total response time are provided.

Recently, the behaviour of pressure measurement systems working together with multi-hole pressure probes is investigated by Grimshaw and Taylor [9] and Brüggemann et al. [10]. To improve the spatial resolution of the flow measurement in a blade wake, multi-hole pressure probes are more and more miniaturized. On the other hand, this increases the response time of the systems and, therefore, the total measurement time. This trade off is discussed and analysed in the papers. The objective is the accurate prediction of the response time and its minimisation. Both papers use the electrical analogy whereas Brüggemann et al. [10] make also a comparison with results from simpler analytical methods.

3. GENERIC FLOW MODEL

The geometry of the generic flow model, consisting of a tube and a plenum, is shown on top of Fig. 2. The rigid tube with length l has a constant circular cross section with diameter $d \ll l$. The volume of the plenum is denoted as V. The pressure measurement device (transducer) is positioned at the end of the plenum. The bottom of Fig. 2 shows spatial and temporal distribution of static pressure p. At time $t \leq 0$, the constant static pressure in the whole system is p_C (blue line). At time $t = 0$, a sudden jump of the pressure from p_C to p_A is assumed at the inlet of the tube. Due to the pressure difference between the inlet of the tube and the plenum, a flow with velocity c is driven in the tube. Due to the mass flow rate into the plenum, the static pressure in the plenum will increase. After an infinite long time ($t = \infty$), the constant static pressure in the whole system will be p_A.

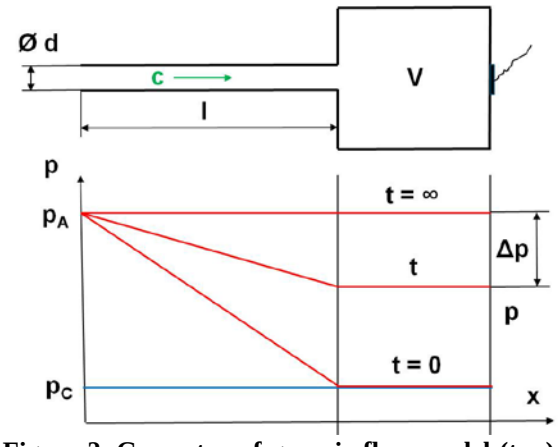

Figure 2. Geometry of generic flow model (top), spatial and temporal pressure distributions (bottom)

Since the pressure difference $p_A - p_C$ is assumed to be small, the density in the tube does not change and the flow can be treated as incompressible. At an arbitrary time t, the pressure loss in the tube is

$$\Delta p = \lambda \frac{l}{d} \rho \frac{c^2}{2}. \tag{1}$$

If the flow is assumed to be laminar, the friction coefficient λ in the tube depends on the Reynolds number according to

$$\lambda = \frac{64}{Re}. \tag{2}$$

As can be seen later, $\lambda l / d \gg 1$. Therefore, the exit loss is neglected in Eq. (1). The mass flow rate driven by the pressure difference Δp is

$$\dot{m} = \rho \frac{d^2 \pi}{4} c = \frac{\pi d^4 \Delta p}{128 l \nu}. \tag{3}$$

A second equation can be derived, if the temporal behaviour of the pressure in the plenum is taken into account. For constant volume V, the change of the fluid mass over time in the plenum is

$$\frac{\mathrm{d}m}{\mathrm{d}t} = \frac{\mathrm{d}(\rho V)}{\mathrm{d}t} = \rho \frac{\mathrm{d}V}{\mathrm{d}t} + V \frac{\mathrm{d}\rho}{\mathrm{d}t} = V \frac{\mathrm{d}\rho}{\mathrm{d}t}. \tag{4}$$

If temperature is assumed as constant in the volume, the change of mass over time is

$$\frac{\mathrm{d}m}{\mathrm{d}t} = \frac{\kappa V}{a^2} \frac{\mathrm{d}p}{\mathrm{d}t}, \tag{5}$$

with the speed of sound for an ideal gas

$$a = \sqrt{\kappa R T} = \sqrt{\kappa \frac{p}{\rho}}. \tag{6}$$

Since the mass flow rate in the tube (Eq. (3)) is equal to the change of mass over time in the plenum (Eq. (5)), it is

$$\frac{\pi d^4 \Delta p}{128 l \nu} = \frac{\kappa V}{a^2} \frac{\mathrm{d}p}{\mathrm{d}t}. \tag{7}$$

According to Fig. 2, the pressure loss in the tube is $\Delta p = p_A - p$ and Eq. (7) can be written as

$$\tau \frac{\mathrm{d}(\Delta p)}{\Delta p} = -\mathrm{d}t, \tag{8}$$

with the time constant

$$\tau = \frac{128}{\pi} \frac{\kappa \nu}{a^2} \frac{l}{d^4} V. \tag{9}$$

This time constant can be found in a similar form in [1]. Equation (8) can be integrated for the initial condition $\Delta p(t{=}0) = p_A - p_C$ and the result is

$$\frac{p - p_C}{p_A - p_C} = 1 - e^{-\frac{t}{\tau}}. \tag{10}$$

The distribution of the nondimensional pressure difference over nondimensional time according to Eq. (10) is plotted in Fig. 3 (red line). The settling time of the system can be defined as the time which is required for the pressure difference to reach 99% of the applied pressure difference (p_A - p_C). This nondimensional settling time

$$\frac{t_{99}}{\tau} = 4.6 \tag{11}$$

is indicated by the blue dot in Fig. 3. The green straight line in Fig. 3 gives an interpretation of the time constant τ, since it is the tangent on the red curve at $t/\tau = 0$.

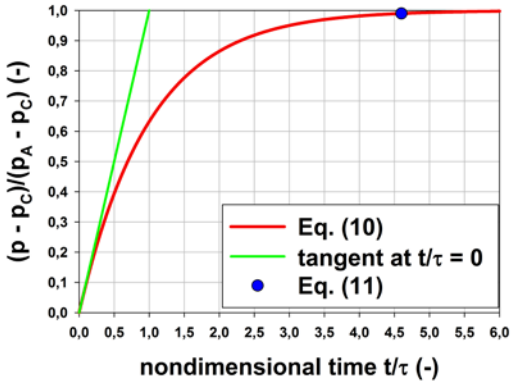

Figure 3. Nondimensional pressure difference versus nondimensional time

According to Fig. 2, the generic flow model is based on one single tube with diameter d and its corresponding length l. In a real measurement setup n tubes with individual diameters d_i and individual lengths l_i are connected in a serial manner. If the first tube with diameter d_1 and length l_1 is defined to set the reference velocity, an equivalent tube length

$$l_e = l_1 + \sum_{i=1}^{n} l_i \left(\frac{d_1}{d_i} \right)^4 \tag{12}$$

can be defined. This equivalent tube length is also introduced in [3]. It can be used for the calculation of the time constant, according to Eq. (9). Another difference between the generic flow model (Fig. 2) and the actual measurement setup is the fact that the pressure scanning box divides the volume V into two separate volumes. These are volume V_A and volume V_B respectively, with

$$V = V_A + V_B. \tag{13}$$

If the valve of the scanning box is closed, both volumes are separated and different pressures will appear in the volumes. Assuming the ideal gas law, it is

$$p_A V_A = m_A R T, \tag{14}$$

$$p_B V_B = m_B R T. \tag{15}$$

A constant temperature T is assumed in both volumes and m_A and m_B are the fluid masses in the individual volumes. If the valve of the scanning box opens very quickly, a mixing process will appear and a pressure p_C will be established in the volume V. If it is assumed that the mixing process is at constant temperature T, the pressure can be calculated according to

$$\frac{p_C - p_B}{p_A - p_B} = \frac{V_A}{V_A + V_B}. \tag{16}$$

4. EXPERIMENTAL APPARATUS AND PROCEDURE

4.1. Open-Jet Wind Tunnel

The open-jet wind tunnel (Fig. 4) consists of a radial blower, a diffuser, a turbulence grid, a settling chamber and a circular cross section nozzle. The radial blower sucks air from the laboratory hall. Therefore, the inlet air temperature is related to the ambient temperature in the laboratory, which is typically about 20 °C. The radial blower is driven by a DC motor with variable rotational speed to set the requested jet velocity at the nozzle. The nozzle with circular cross section (diameter 120 mm) is of Witoszynski type. The contraction ratio between settling chamber and nozzle is about 70:1. The three-hole probe is positioned about one nozzle diameter downstream of the nozzle exit plane. At this section streamwise turbulence intensity in the core of the jet is about 1%.

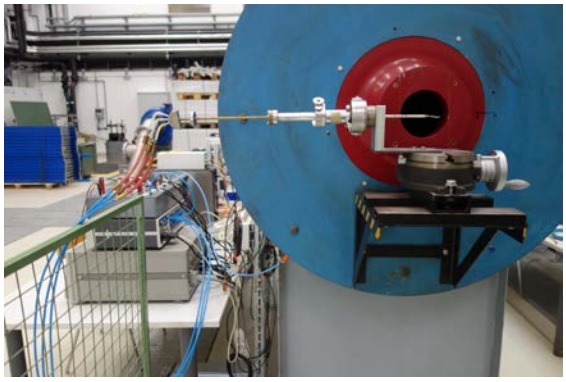

Figure 4. Open-jet wind tunnel with three-hole pressure probe

4.2. Three-Hole Pressure Probe

The present investigation has been performed for a total of five different multi-hole pressure probes. These are three three-hole probes and two five-hole probes, respectively. In this paper, results for one of the three-hole probes are presented. The probe was manufactured in 1994 by SVUSS a.s. [11]. It is a three-hole cobra probe with a characteristic head dimension of 0.8 by 2.4 mm (Fig. 5). The head of the probe consists of three parallel capillary tubes of 0.5 mm inner diameter and 0.8 mm outer diameter, respectively. Hole number "1" is positioned at the centre of the probe head, whereas hole number "2" is on the left hand side and hole number "3" on the right hand side, respectively. A total wedge angle of 60° makes the probe sensitive to variations of the yaw angle in a plane perpendicular to the probe stem. Usually, the probe is operated in the non-nulling mode. The probe stem has a diameter of 6 mm and a total length of 600 mm. Inside of the hollow stem, the capillary tubes of 0.5 mm inner diameter change to capillary tubes of 1.0 mm inner diameter. A stepwise increase of diameters of the capillary tubes inside the probe is a typical provision to reduce their pressure losses. The individual lengths of these capillary tubes are unknown.

Figure 5. Three-hole pressure probe

4.3. Pressure Scanning Box

The pressure scanning box is of type FCO91, manufactured by Furnace Controls Limited [12]. A total of 20 pressure input channels are connected to one single pressure output channel by 20 individual solenoid valves. The solenoid valves can be switched by different operating modes. In the present case, the valves are switched by a current step, produced by the digital output of the data acquisition system. Figure 6 shows a photograph of the scanning box, where the top casing has been dismantled. Inside the casing, the solenoid valves, the internal connection tubes and the electronic equipment can be seen. The internal volumes of the solenoid valves as well as the connection tubes are unknown.

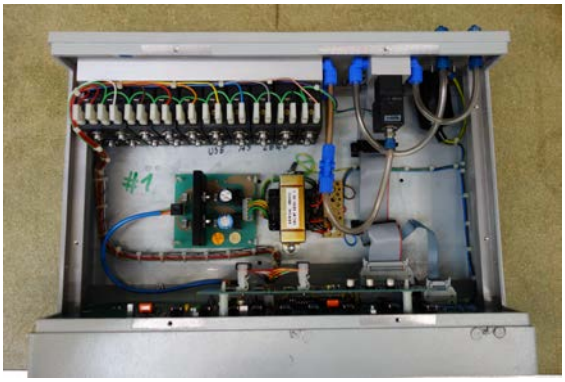

Figure 6. Pressure scanning box (top of the casing dismantled)

4.4. Pressure Transducer

All pressure differences are measured with a HONEYWELL 143PC01D piezoresistive pressure transducer [13]. The operating range of the pressure transducer is ± 69 mbar. One port of the pressure transducer is connected to the output of the pressure scanning box, whereas the other port is open to the atmosphere. Therefore, pressure differences relative to the constant ambient pressure are measured. The pressure transducer is supplied by 8V DC and its output voltage is proportional to the applied pressure difference. A careful inspection of a damaged transducer of the same type has shown that the internal volume of the sensor can be neglected. This means that the transducer does not contribute to the volume V of the plenum.

4.5. Connecting Tubes

Figure 7 shows a schematic representation of the three-hole probe (one capillary tube), the pressure scanning box and the connecting tubes. Inner diameters and tube lengths are summarized in Tab. 1. One single line of the three-hole probe consists of two capillary tubes. Their diameters are 0.5 mm and 1.0 mm, whereas their respective lengths are unknown. The connecting tubes between three-hole probe and pressure scanner, respectively pressure scanner and pressure transducer are of type FESTO. Inner diameter of these plastic tubes is 4.0 mm. The internal volume of the pressure scanning box is approximated by a tube with 4.0 mm inner diameter and length of 0.8 m. On the right hand side, the system is terminated by the pressure transducer. A comparison of the diameters, lengths and volumes of the individual tubes leads to the conclusion that the capillary tubes of the three-hole probe will be responsible for the pressure losses in the system. Therefore, the connecting tubes and the pressure scanning box will contribute to the volume of the plenum. This volume is disconnected by a solenoid valve of the pressure scanning box. To vary the volume of the plenum in a systematic manner, connecting tubes of three different lengths

l_5 have been used between scanning box and pressure transducer (Tab. 1).

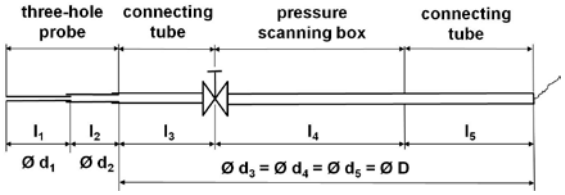

Figure 7. Schematic representation of three-hole probe (one capillary tube), pressure scanning box and connecting tubes

Table 1. Inner diameters and lengths of individual tubes according to Fig. 7

	i	d_i (mm)	l_i (m)
three-hole probe	1	0.5	?
three-hole probe	2	1.0	?
connecting tube	3	4.0	2.0
press. scanning box	4	4.0	0.8
connecting tube	5	4.0	0.5 / 1.0 / 2.0

4.6. Instrumentation

In the settling chamber of the open-jet wind tunnel, total temperature and total pressure are measured my means of a Pt-100 resistor thermometer and wall pressure taps, respectively. The pressure scanning box switches all pressure signals to one single piezoresistive pressure transducer. Control of the scanning box as well as the conversion of the analogue voltages to digital signals is performed by a HP3852A data acquisition system. The system is controlled by a PC, running LabVIEW (National Instruments).

4.7. Measurement Procedure

After the blower of the open-jet wind tunnel has been started, its rotational speed is set to achieve a jet velocity of 48 m/s at the nozzle exit. This corresponds to a probe Reynolds number of about 7500. Then, the three-hole probe is turned by a yaw angle of -30°. At this yaw angle, hole number “2” is at the leeward side and hole number “3” at the windward side, respectively. The objective is to generate large pressure differences between the individual sensing holes. The procedure starts with measurement of total pressure and total temperature in the settling chamber. Then, the pressure signals are switched by the scanning box in a sequential manner to the single pressure transducer, starting with hole number “1”. Sampling rate of the data acquisition system is about 6 Hz. Waiting time between switching is set to about 14 seconds. This time is sufficient for the measured pressure difference to reach the final constant value. The measurement procedure is finished when the pressure scanning box is switched from hole number “3” back to the ambient pressure.

5. EXPERIMENTAL RESULTS

5.1. Temporal Pressure Distribution

As a first experimental result, Fig. 8 shows the distribution of the pressure difference, measured by the piezoresistive pressure transducer over time. The results are valid for a tube length l_5 = 0.5 m. At the beginning of the procedure (t = 0 s), measured pressure difference is zero, since the port of the pressure transducer is connected to the ambient. When the pressure scanning box switches to hole number “1”, the pressure difference increases immediately. This pressure jump can be interpreted as the resulting pressure when the mixing process in the plenum is finished. Then, the pressure difference rises rather slowly. This can be interpreted as the pressure rise in the volume due to the mass flow rate through the connected line of the three-hole probe. Finally, a plateau is reached and the pressure difference stays constant. This behaviour is repeated when the scanning box switches from hole number “1” to hole number “2” and from hole number “2” to hole number “3”, respectively. The only difference is that holes number “1” and “3” see a positive pressure jump whereas hole number “2” experiences a negative pressure jump. The different final pressure levels of the individual holes are a result of the probe yaw angle. Finally, the measured pressure difference jumps to zero, since the port of the pressure transducer is again connected to the ambient.

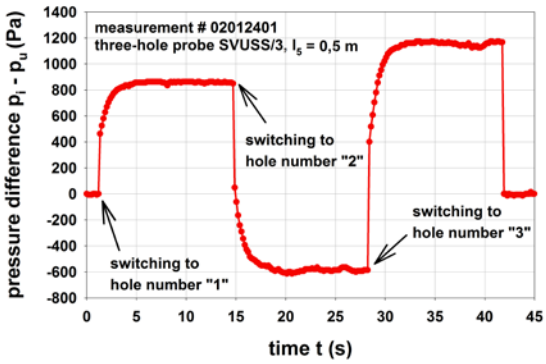

Figure 8. Measured pressure difference ($p_i - p_u$) versus time t (l_5 = 0.5 m)

A detailed pressure distribution for the individual holes and three different lube lengths (l_5 = 0.5 m, 1.0 m and 2.0 m, respectively) is plotted in Figs. 9 to 11. As can be seen, the tube length l_5 has an influence on the mixing pressure. This can be interpreted by Eq. (16), since the Volume V_B is directly linked to the variable tube length l_5, whereas Volume V_A is constant.

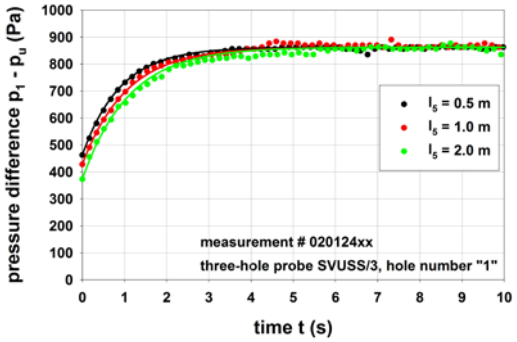

Figure 9. Measured pressure difference ($p_1 - p_u$) for hole number "1" versus time t

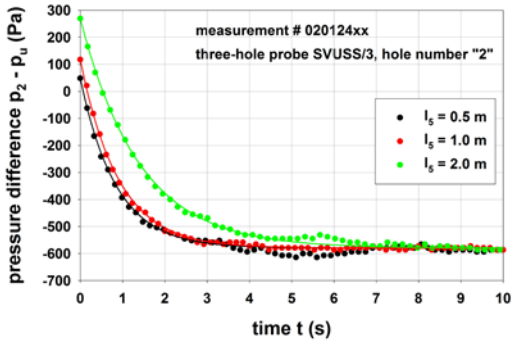

Figure 10. Measured pressure difference ($p_2 - p_u$) for hole number "2" versus time t

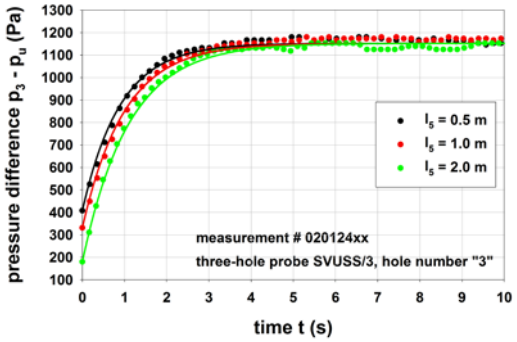

Figure 11. Measured pressure difference ($p_3 - p_u$) for hole number "3" versus time t

Table 2 shows the relative mixing pressure differences $(p_C - p_B)/(p_A - p_B)$ for three different tube lengths l_5. A variation between the individual holes can be seen. Table 2 shows also the arithmetic mean values of the relative mixing pressure differences. As can be seen, the relative mixing pressure differences decrease with increasing tube length l_5. This behaviour can be interpreted using Eq. (16). Since the volumes V_A and V_B are directly related to the tube lengths, it is

$$\frac{p_C - p_B}{p_A - p_B} = \frac{V_A}{V_A + V_B} = \frac{l_3}{l_3 + l_4 + l_5}. \qquad (17)$$

Table 2. Relative mixing pressure difference $(p_C - p_B)/(p_A - p_B)$ from experimental data

	l_5 = 0.5 m	l_5 = 1.0 m	l_5 = 2.0 m
hole "1"	0.536	0.497	0.433
hole "2"	0.564	0.517	0.411
hole "3"	0.570	0.526	0.438
mean value	0.557	0.513	0.427

Results from Eq. (17) are summarized in Tab. 3. For an ideal geometry, there is no influence of individual holes and the relative mixing pressure difference depends on the tube length l_5 only. According to Eq. (17), the relative mixing pressure difference decreases with tube length l_5. A comparison between Tab. 2 and Tab. 3 (grey lines) shows a good agreement between experimental and analytical results. Therefore, the analytical model can be used to describe the mixing process of the pressure measurement setup due to the scanning box.

Table 3. Relative mixing pressure difference $(p_C - p_B)/(p_A - p_B)$ from Eq. (17)

	l_5 = 0.5 m	l_5 = 1.0 m	l_5 = 2.0 m
all holes	0.606	0.526	0.417

5.2. Time Constant and Settling Time

According to the experimental results presented in Figs. 9 to 11, the time constants and the settling time are extracted. In a first step, the temporal behaviour of the pressure difference according to Eq. (10) is fitted to the measurement data. As a result, time constants are extracted for the three different holes related to the tube length l_5. These results are summarized in Tab. 4. As can be seen, there is a variation of the time constants between individual holes. Therefore, arithmetic mean values of the time constant are presented in Tab. 4, too (grey line). As can be seen, time constant increases with increasing tube length l_5. Finally, settling times are calculated according to Eq. (11). For the present measurement setup, settling times are between 4.1 s and 5.5 s, depending on tube length l_5.

Table 4. Time constants τ and settling times t_{99} from experimental data

	l_5 = 0.5 m	l_5 = 1.0 m	l_5 = 2.0 m
τ_1 (s)	0.90	1.05	1.10
τ_2 (s)	0.85	0.90	1.40
τ_3 (s)	0.90	1.00	1.10
τ (s)	0.88	0.98	1.20
t_{99} (s)	4.10	4.50	5.50

According to Eqs. (9) and (12), the time constant of the analytical model is

$$\tau = 32\frac{\kappa\nu}{a^2}\left(\frac{l_1}{d_1^{\,4}} + \frac{l_2}{d_2^{\,4}}\right)D^2(l_3 + l_4 + l_5). \qquad (18)$$

A direct application of Eq. (18) to calculate the time constant is not possible, since lengths l_1 and l_2 of the capillary tubes are unknown. However, since it is known that $l_1 + l_2 = 660$ mm, the time constant can be calculated as a function of tube length l_1. The result can be seen in Fig. 12 (lines). For constant tube length l_5, there is a linear relationship between time constant τ and tube length l_1. Also plotted in Fig. 12 are the experimental values for the time constants according to Tab. 4 (dots). A good correlation between analytical and experimental time constants can be obtained for $l_1 \approx 180$ mm. According to the geometry of the three-hole probe, this is a realistic position for the transition of the capillary tubes from $d_1 = 0.5$ mm to $d_2 = 1.0$ mm.

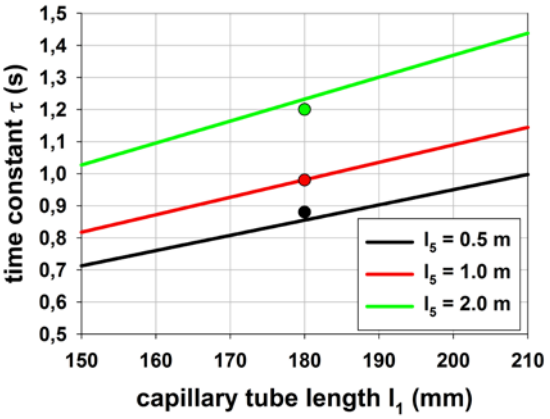

Figure 12. Time constant τ as a function of tube lengths l_1 and l_5

6. FINAL REMARKS

6.1. Reynolds Numbers

The analytical model is based on the assumption that the flow in the capillary tubes is laminar. To justify this assumption, Reynolds numbers which appear in the experiment are calculated. According to Eq. (10), the Reynolds number in the tube with diameter d_1 is

$$Re_1 = \frac{p_A - p_C}{32\rho\nu^2\left(\frac{l_1}{d_1^{\,3}} + \frac{d_1}{d_2}\frac{l_2}{d_2^{\,3}}\right)}\mathrm{e}^{-\frac{t}{\tau}}. \qquad (19)$$

This is the larger Reynolds number in both capillary tubes, since

$$Re_2 = Re_1\frac{d_1}{d_2} < Re_1. \qquad (20)$$

Figure 13 shows the distribution of Reynolds number Re_1 over nondimensional time t/τ for a driving pressure difference $p_A - p_C = 1000$ Pa. This pressure difference is representative for hole number "3" and $l_5 = 2.0$ m (Fig. 11). Reynolds number over time behaves like the mass flow rate or the flow velocity in the capillary tubes. At the beginning of the flow process, Reynolds number shows its maximum value which is still much lower than the critical value $Re_{crit} \approx 2300$. Therefore, the assumption of laminar flow in the analytical model is justified.

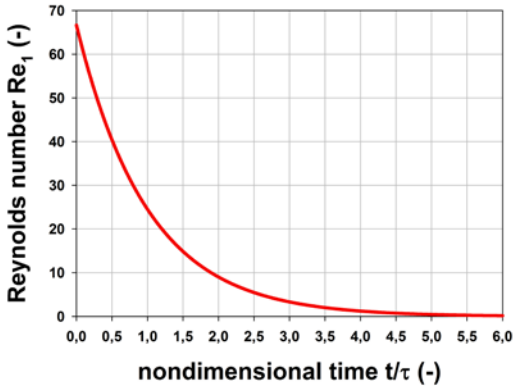

Figure 13. Reynolds number Re_1 versus nondimensional time t/τ

6.2. Uncertainty and Sensitivity

As can be seen from Eqs. (9) or (18), the analytical calculation of the time constant requires the knowledge of the geometry of the pressure measurement system. This means the internal geometry of the multi-hole pressure probe, diameters and lengths of the connecting tubes, the internal volume of the scanning box and, if applicable, the internal volume of the pressure transducer. For a commercial pressure probe, the internal geometry is usually not known. The same is true for a pressure scanning box and a pressure transducer. Therefore, for most practical implementations, it is not possible to calculate the time constant and, therefore, the settling time of the pressure measurement system.

Another aspect is the sensitivity of the time constant on the geometrical parameters of the pressure measurement system. From Eq. (9) it can be derived that the relative sensitivity of the time constant τ to the geometrical parameters l, d and V is

$$\frac{\Delta\tau}{\tau} = \frac{\Delta l}{l} - 4\frac{\Delta d}{d} + \frac{\Delta V}{V}. \qquad (21)$$

This means that the time constant is very sensitive to the inner diameter d of the capillary tube, which is responsible for the pressure loss. Grimshaw and Taylor [9] state that the inner diameters of tubes for pressure probes (hypodermic

tubes) show typical manufacturing variations of ± 15%. According to Eq. (21), this would result in a variation of the time constant of ± 60%. This high sensitivity can explain the variation of the time constants between different holes of the three-hole pressure probe (Tab. 4). Furthermore, the pressure losses in a multi-hole pressure probe can be influenced by fouling or even clogging due to particles in a non-deterministic manner.

7. SUMMARY

Time constants and settling times for a pressure measurement system, consisting of multi-hole pressure probe, pressure scanning box, connection tubes and a piezoresistive pressure transducer have been investigated experimentally. Detailed results are presented for a configuration with a three-hole cobra probe. The temporal behaviour of the system can be explained by an analytical model. It describes the sudden mixing process of two volumes with different pressure but constant temperature and the response of a tube-plenum system to a sudden pressure jump. Due to the lack of detailed geometrical details of the multi-hole pressure probe and the scanning box, it is usually not possible to calculate time constants and settling times with high accuracy. Therefore, it will still be necessary to determine these parameters for an individual configuration by means of experiments.

REFERENCES

[1] Xie, H.-Y. and Geldart, D., 1997, "The response time of pressure probes", *Powder Technology*, Vol. 90, pp. 149-151.

[2] Weidemann, H., 1941, "Inertia of Dynamic Pressure Arrays", *NACA TM 998*.

[3] Sinclair, A.R. and Robins, A.W., 1952, "A Method for the Determination of Time Lag in Pressure Measuring Systems Incorporating Capillaries", *NACA TN 2793*.

[4] Lilley, G.M. and Morton, D., 1960, "The response time of wind tunnel pressure measuring systems", *The College of Aeronautics Cranfield*, Report No. 141.

[5] Wuest, W., 1969, *Strömungsmesstechnik*, Vieweg & Teubner-Verlag.

[6] Davis, W.T., 1958, "Lag in Pressure Systems at Extremely Low Pressures", *NACA TN 4334*.

[7] Larcombe, M.J. and Peto, J.W., 1966, "The Response Times of Typical Transducer-Tube Configurations for the Measurement of Pressures in High-Speed Wind Tunnels", *Aeronautical Research Council*, C.P. No. 913

[8] Bynum, D.S., Ledford, R.L. and Smotherman W.E., 1970, "Wind Tunnel Pressure Measuring Techniques", *AGARDograph No. 145*.

[9] Grimshaw, S.D. and Taylor, J.V., 2016, "Fast Settling Millimetre-Scale Five-Hole Probes", *ASME Paper GT2016-56628*.

[10] Brüggemann, C., Hobel, S., Schatz, M. and Vogt D.M., 2016, "On the Impact of Tube Dimensions of Pneumatic Probes on the Response Time", *XXII Biannual Symposium on Measuring Techniques in Turbomachinery, Transonic and Supersonic Flow in Cascades and Turbomachines*, September 1 – 2, Stuttgart, Germany.

[11] Konecny, G., 1994, "Eichungsprotokoll der Dreilochsonde 0,8 / 600 – 650", SVUSS a.s., Praha, Czech Republic

[12] N.N., 1995, "Instruction manual FCO91 selection box", Furnace Controls Limited, England.

[13] N.N., 1994/95, "Drucksensoren, Luftstrom-, Temperatur und Füllstandssensoren", Katalog E13, Honeywell.

Conference on Modelling Fluid Flow (CMFF'25)
The 19th International Conference on Fluid Flow Technologies
Budapest, Hungary, August 26 - August 29, 2025

HAZARD PREDICTION MODELS FOR BATTERY MODULE AND PACKS: FLAMMABILITY, PARTICLE IGNITED VENT GAS, ARCING WITHOUT AND WITH PARTICLES

Thirumalesha Chittipotula[1], Lucas Eder[2], David Schellander[3]

[1] Corresponding Author. AVL List GmbH, Hans-List-Platz 1, 8020 Graz, Austria, Email: thirumalesha.chittipotula@avl.com
[2] AVL List GmbH, Hans-List-Platz 1, 8020 Graz, Austria, Email: lucas.eder@avl.com
[3] AVL List GmbH, Hans-List-Platz 1, 8020 Graz, Austria, Email: david.schellander@avl.com

ABSTRACT

The safety of the battery cells, module and the pack is very important for the overall safety of an electric vehicle. In this context, "thermal runaway" and "arcing" are two phenomena that require special focus. The current study focuses on predictive modelling of flammability, ignition and arcing in battery module and packs by considering several vent gas species and particles ejected during the battery thermal runaway. Considering the wide range of vent gas species and their compositions, a methodology is developed to incorporate these species in the evaluation of the overall flammability, breakdown voltage and arc-generating capability. Furthermore, a method is presented for modelling the "particle ignited vent gas" and "influence of particles on arcing". The vent gas combustion (with particles as an ignition source) is modelled using two different skeleton mechanisms consisting of various flammable vent gas species. These models are incorporated in a 3D CFD solver (AVL FIRE™ M). The simulations are first performed on simple geometries and later expanded to a full battery pack (consisting of several modules) providing significant insights into the safety of the overall battery system.

Keywords: Arc-generating capability, Breakdown voltage, Hazard prediction, Flammability, Particle ignited vent gas

NOMENCLATURE

A	[1/(Pa m)]	saturation ionization
B	[V/(Pa m)]	ionization energy
D	[m^2/s]	effective diffusivity
E	[V/m]	electrical field strength
F	[*N*]	force
LFL	[-]	lower flammability limit
LOC	[*N*]	limiting oxygen concentration
Q	[C]	electrical charge
UFL	[-]	upper flammability limit
V	[V]	voltage
d	[m]	distance
h	[J]	enthalpy
p	[*Pa*]	pressure
r	[*m*]	radius
t	[*s*]	time
x	[m]	cartesian point
y	[-]	vent gas species mass fraction
γ	[W/(mK)]	thermal conductivity
γ	[-]	emission coef.
ε	[F/m]	dielectric coef.
ρ	[kg/m^3]	density
τ	[N/m^2]	stress tensor
ω	[kg/s]	species source

Subscripts and Superscripts

B	breakdown
i	cartesian coordinate or species
j	cartesian coordinate or species
l	species
mix	mixture
p	particle
se	secondary electron

1. INTRODUCTION AND LITERATURE REVIEW

The safety of the battery module and the battery pack is of utmost importance for the overall safety of an electric vehicle. In this context, "flammability" and "arcing" are two important phenomena that require a special research focus.

The exact determination of the flammability limits in the battery packs is very important in connection with the venting of one or more battery cells, which poses the risk of destruction of the

battery pack and vehicle. In the past, the flammability prediction models are solely based on the pure components of the flammable gases. However, the vent gas from a battery cell consists of a mixture of flammable gases such as CH_4, C_2H_4, CO, and H_2 [1,2]. Depending on the battery material, the molar or the mass fractions of these gases may vary from moderate to high level. Some of these gases have a narrow flammability range, e.g., CH_4, while others have a wide flammability range, e.g., H_2 [2,3]. Therefore, in addition to pure component flammability limits, it is necessary to consider the mixture flammability limits in the battery domain. The mixture based flammable limits change spatially in the battery packs as the gas composition changes. These mixture limits are estimated efficiently in the computational domain while satisfying the thermodynamic principles of mixing [4,5]

Arcing involves the ionization and the electric discharge from the gas medium caused by a high voltage difference between the electrodes where the gas medium acts as the electrical conductor [6][7] . The temperatures in the low-current arcing are around 6500 K and can go up to 20000 K for high-current arcing. Such high temperatures can ignite an ignitable gas mixture and cause damage to battery cells and surrounding materials [8]. In battery packs there are several parts with different electrical potentials. The distances between the parts in modern batteries are very small, down to mm, to get high power density of the battery pack. For modelling the arcing between small gaps Paschen's law is commonly used [9,10], which defines that the gap distance and the pressure in the gap both influence the arcing possibility and must be considered together for getting the breakdown voltage. However, the parameters in the Paschen's law (Townsend constants) depend on the gas medium [10]. The aim of the current work is to accurately model the arc-related properties of battery modules and packs, taking real-world conditions into account (vent gas composition and the real electrode distances). The measured breakdown voltage and critical distances provide the user with the hazard limits to avoid potential arcing in the battery modules and packs. During thermal runaway and destruction of battery, particles can be generated. If particles are emitted into gaps between electrodes, they influence the arc-generating capability. In the gap particles can lead to micro discharge arcs and significantly reduce breakdown voltage [11]. Hence, if particles are in the gap, they should be considered in the computation of the breakdown voltage [12,13].

Furthermore, particles exerted from the venting process often have high temperatures and can ignite the combustible vent gas [14]. In the presence of oxygen and an ignition source this vent gas may ignite and cause rapid fires in the battery pack [15]. Therefore, in this study a model is implemented to incorporate the "particles as ignition source" and subsequent combustion of venting gas is presented.

2. GOVERNING EQUATIONS AND MODEL DESCRIPTION

The governing equations of the 3D CFD and thermal runaway kinetic solvers [16] along with the flammability, breakdown voltage and arcing related models.

3D-CFD Solver governing equations

Continuity, momentum and the enthalpy transport equations which are integral part of the CFD solver are described below.

$$\frac{\partial \rho}{\partial t} + \frac{\partial \rho\, v_j}{\partial x_j} = 0 \tag{1}$$

$$\frac{\partial \rho\, v_i}{\partial t} + \frac{\partial \rho\, v_i\, v_j}{\partial x_j} = -\frac{\partial P}{\partial x_i} + \frac{\partial \tau_{ij}}{\partial x_j} + F \tag{2}$$

$$\frac{\partial h}{\partial t} + \frac{\partial \rho\, v_j\, h}{\partial x_j} = \frac{\partial^2 \gamma\, h}{\partial {x_j}^2} + \dot{q} \tag{3}$$

$$\frac{\partial y_i}{\partial t} + \frac{\partial \rho\, v_j\, y_i}{\partial x_j} = \frac{\partial^2 Đ\, y_i}{\partial {x_j}^2} + \dot{\omega}_\iota \tag{4}$$

Where, ρ is density, v is velocity, P is pressure, τ_{ij} is stress tensor and F is additional forces (e.g., body force). Furthermore, h is the enthalpy of the system, x_j is cartesian component and γ is thermal conductivity. The second term in (3) represents the enthalpy transfer due to convection ($\rho\, v_j$) and is not applicable when applied to the solid domains. y_i is the vent gas species mass fraction in the fluid domain and $\dot{\omega}_\iota$ is the species source generated from the reaction due combustion of vent gas species. Here, Đ is the effective diffusivity of the vent gas species *i* with respect to all other species in the mixture of the venting gas. Effective diffusivity is evaluated as the averaged value based on the molar fractions of the species in the mixture.

The particles are modelled with the Lagrangian approach following [17] and literature cited therein. For particle-wall interaction the solid particle wall contact model including heat-transfer exchange between particles and walls is used.

Flammability

As the vent gas consists of several flammable gases, in this study a mixture flammability index is evaluated based on Le Chatelier's principle and the limiting oxygen concentration (LOC) as shown below [3,4].

$$LFL_{mix} = \frac{\sum y_i}{\sum LFL_i \, y_i} \quad (5)$$

$$UFL_{mix} = \frac{\sum y_i}{\sum UFL_i \, y_i} \quad (6)$$

$$LOC_{mix} = \frac{\sum y_i \, R_i}{\sum LOC_i \, y_i} \quad (7)$$

Where, *i* is flammable gases considered in the evaluation, LFL_i, UFL_i are the lower and upper flammable limits (LFL and UFL) of the pure components. LFL_{mix}, UFL_{mix} are the lower and upper flammability limits of the mixture. LOC_{mix} is the mixture limiting oxygen concentration and Ri is the stoichiometric molar ratio of oxygen to fuel. These flammability limits are determined experimentally for pure component fuels for e.g., Zlochower and Green [3]

The mixture flammability is evaluated in the similar lines as the pure component flammability is evaluated. Where, a parabolic function (flammability) generated from the molar fractions and the flammability limits of the respective components is used to predict the instantaneous values. In case of mixture, the parabolic function is generated based on the mixture molar mass and the mixture flammability limits (low and upper), described from Eqs. (5)-(6). Equation (7) provides an additional condition for the flammability index accounting the minimum oxygen requirement. Below this oxygen available limit the flammability index is set to 0. In the evaluation of the flammability limits several flammable gases produced during the battery thermal runaway such as CH_4, C_2H_4, C_2H_6, C_3H_8, C_4H_{10}, CO, and H_2 are included in this study.

Particle ignited vent gas

Several of FIRE M CFD solver modelling capabilities are combined for this application, such as spray (solid particles) and general gas phase reactions, where particle temperature in a cell acts as an ignition source. This model combination has been proved helpful in understanding the combustion of the vent gas. For modelling the combustion of vent gas mixture, a few reaction mechanisms are reduced from the GRI mechanism [18] by including all the important vent gas species. These reduced skeleton mechanisms (for e.g., consisting of 19 species and 41 reactions or consisting of 25 species and 100 reactions) can predict the initiation and propagation of the combustion in the battery packs in much faster simulation times than compared with the original mechanism. No turbulence chemistry interactions are considered in this study as the effects are not that significant due to the fact that the system is closed, non-moving, and limited in the oxygen concentration. The simulation results provide significant insights into understanding the hazard posed by the vent gas mixture in the presence of hot particles in the battery pack as shown latter in the results and discussion.

Breakdown voltage and Arcing

The prediction of breakdown voltage for pure component gases is straight forward from Paschen's law. The breakdown voltage depends on several factors such as electrode surfaces, terminal voltage, distance and the pressure of the gas medium between the electrodes.

$$V_B = \frac{B \, p \, d}{(\ln(A \, p \, d) - \ln(\ln(1 + \frac{1}{\gamma_{se}})))} \quad (8)$$

Where, V_B is the breakdown voltage p is pressure and d is distance between the electrodes and γ_{se} is the secondary electron emission coefficient and A, B are Townsend's coefficients. A mixture rule based on the molar composition of the species is employed in this work to incorporate the most significant gas components. The parameters A, B and secondary electron emission coefficient ((γ_{se}) are obtained from literature, following [10] [6].

Particularly, in the presence of particles, the breakdown voltage significantly decreases. Therefore, the aim of this modelling study is to evaluate the breakdown voltage of the mixture gas, particles and finally deduce the arc-generating capability criteria. The modelling of particles as arcing source in the battery module or packs is not well researched as of now. Therefore, in this study we extracted the relevant modelling information from gas insulation systems of electronic components. The arcing behaviour in these devises are developed from quite some time. The potential and breakdown voltage of the particles are modelled from [11].

$$V_0 = E_0(d + r) + \frac{Q}{(4 \, \pi \, \varepsilon \, r)} \quad (9)$$

Where, V_0 is the potential of the particle and E_0 is the electrical field strength in the gas field, r is the radius of the particles and d is the distance to the electrode surface (earthed cathode, low voltage side) and Q is the electrical charge of the particle.

The breakdown field strength of the particles (E_{Bp}) is evaluated from experimentally fitted correlation [11].

$$E_{Bp} = 7.38 \, p \left\{1 + \frac{0.952}{\sqrt{p \, r}}\right\} \quad (10)$$

Where, p is the pressure and r is the radius of the particles. As per Eq. (10), as the particle radius increases electrical field strength decreases.

The breakdown voltage of the particle (V_{Bp}) is evaluated from:

$$V_{Bp} = E_{Bp} \, . \, d \qquad (11)$$

To summarise, the breakdown voltage in the gas medium is predicted using Eq. (8) and the breakdown voltage of the particles are predicted using Eq. (11). It is evident from these equations, that the break-down voltage depends on distance between the electrodes and pressure. Since the distance and pressure can change at every computational cell, the breakdown voltage may change accordingly. For e.g., in the case of venting gas ejection temperature and pressure field can be different from one computational cell to other computational cell and therefore breakdown voltage may vary accordingly.

3. RESULTS AND DISCUSSION

The results are first presented for simplified geometries and simplified battery modules as validation studies. Later, the evaluations are made on a real-world battery pack, and the corresponding results are presented at the end of this section. The results are arranged in the following order: flammability index of the gases, breakdown voltage of air, breakdown and arcing index with air and vent gas, breakdown voltage and arcing index with and without particles, particles ignited vent gas and finally the analysis of above models on real world battery pack.

Flammability of the vent gas mixture is simulated first in a simplified model where a vent gas mixture enters a domain filled with air. The vent gas mixture usually consists of some flammable hydrocarbons and inorganic components. Two different variants of the gaseous mixture are considered as the inlet boundary condition. The model conditions of these two simulations are shown in Figure 1.

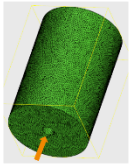

Model Cond.	Value
Velocity	5 m/s
Temperature	900 °C
Inlet species fractions	
CH4	0.33
CO	0.33
H2	0.34
C2H4	0.0

Model Cond.	Value
Velocity	5 m/s
Temperature	900 °C
Inlet species fractions	
CH4	0.25
CO	0.25
H2	0.25
C2H4	0.25

Figure 1: The geometry and the model conditions used for prediction of flammability limits of vent gas mixture.

Figure 2 describes the mixture flammability index and the pure component flammability index (for species CH4) respectively. As seen the flammable region is different for the two scenarios. The mixture flammability index takes into account all the flammable gases in the system according to Le Chatelier's principle as described in the previous Section 3. The flammable region in this case is slightly narrower but much wider making it as the bigger flammable region. In the case of pure component flammability, the fat region where CH_4 cannot burn is shown with 2.0 magnitude in the scale (see Figure 2 (c))

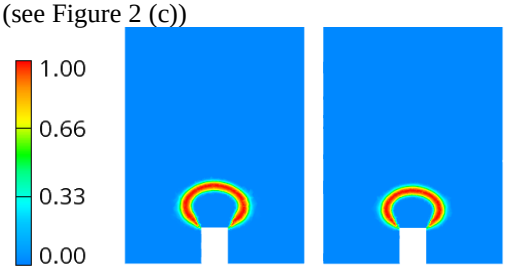

(a) Vent gas mixture flammability

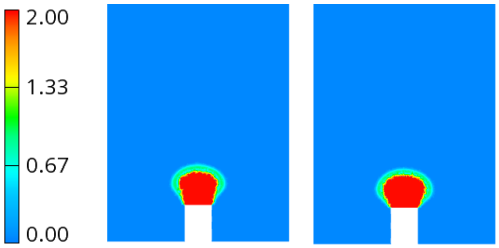

(b) Pure component flammability

Figure 2: Flammability index [-] evaluated based on

(a) mixture composition and

(b) pure component, the magnitude 2 in this case is a fat region representing no flammability.

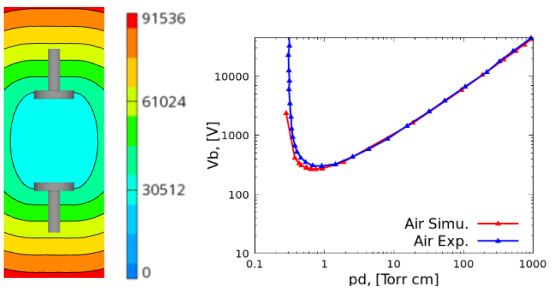

(a) (b)

Figure 3: (a) Breakdown voltage (V) between two parallel plate electrodes and

(b) validation of Paschen's curve for air

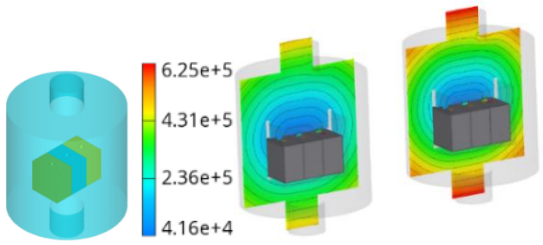

(a) (b) (c)

Figure 4: Breakdown voltage (V) evaluation in

(a) a simplified battery module with 3 prismatic cells (5 cm x 5 cm x 3 cm) placed in a cylindrical box (17 cm x 17 cm) at atmospheric pressure

(b) breakdown voltage venting gas mixture as medium

(c) breakdown voltage with air as medium

The quantitative evaluations are provided for electrode distances, breakdown voltage, critical distances and thus finally estimate the arc-generating capability. The implementation is first validated within a simple geometry where two electrodes are placed 1 cm apart within air medium. The contours of breakdown voltage and the comparisons with the experimental data of the Paschen's curve is shown in Figure 3 (a) and (b) respectively. The simulation data and the published data match well as seen in this figure. The current work also considers the original gas medium with its constituent species surrounding the module and pack instead of assuming air, shown in Figure 4. Considering the wide range of possible vent gases and their compositions, a methodology is developed to incorporate these mixtures in the evaluation of the overall breakdown voltage. This brings a more accurate description of the battery systems as the gas composition changes during a venting event which further brings down the breakdown voltage. Any decision made solely considering air as working medium poses serious consequences on the safety as seen in Figure 4. The breakdown voltage is approximately 30% lower with vent gas composition (see Figure 4 (b)) compared to air (see Figure 4 (c)) as the working medium. The breakdown voltage is lower near to the electrode surfaces (battery module) and increases away from the surfaces.

In addition, the effect of particles on the breakdown voltage is studied first in a simplified model and later in with the complete battery pack. For this purpose, as depicted in Figure 5, a setup with two electrodes separated by few mm of distance and as medium air is used. Conductive particles (copper particles) are introduced in varying size ranges, diameter 10 µm - 1000 µm. The total accumulated mass of the introduced particles is around 10 g. The voltage drop between these two electrodes is fixed for all the simulations at 1500 V. Electrical field strength, potential of the particle (*Vo*), breakdown field strength (*Eb*), breakdown voltage (*Vb*), and the arc generating capability (arc index) is presented in the following paragraph.

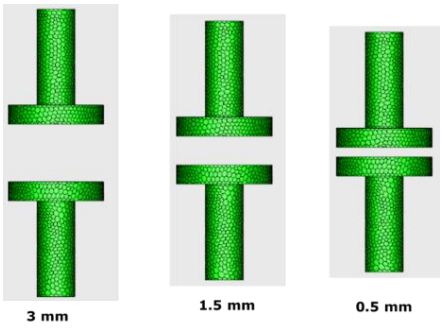

Figure 5: Two parallel electrodes separated by 3mm, 1.5 mm and 0.5 mm

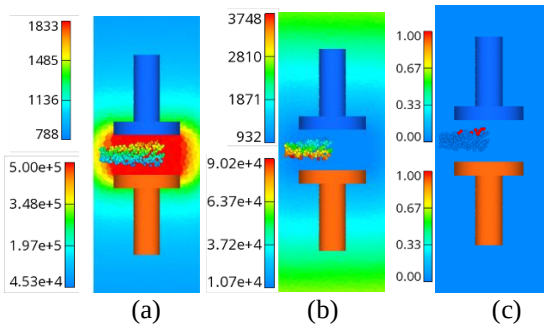

(a) (b) (c)

(i). for 1000 µm Particles & Gap Size 3 mm

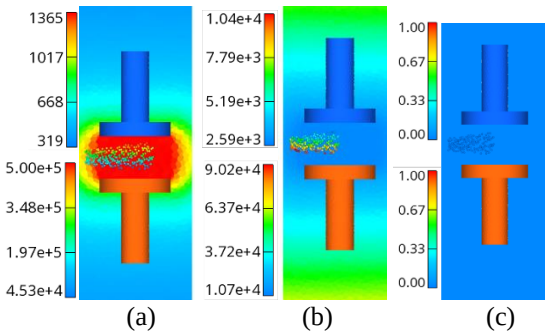

(a) (b) (c)

(ii). for 60 µm Particles & Gap Size 3 mm

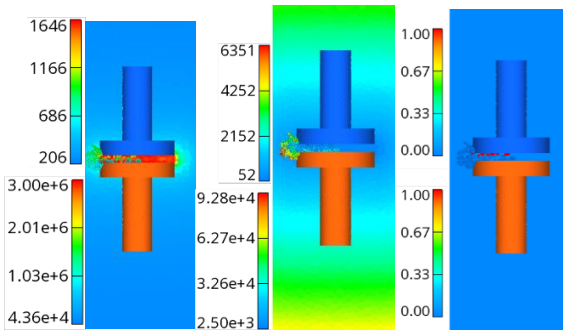

(a) (b) (c)

(iii). for 60 µm Particles & Gap Size 0.5 mm

Figure 6: For three different cases,
(i) Contour plots of potential of particles [V], electrical field strength in the gas medium [V/m],
(ii) Breakdown voltage [V] of both particles and gas medium,
(iii) Arc index [-] in the gas and as well as with the particles

Figure 6 presents the contour plots of potential of the particles (a), electrical field strength in the gas medium (a), breakdown voltage (b), and (c) arc index in gas medium as well as with the particles. The simulations are performed with a wide range of particle diameters and varying distances between the electrodes as depicted in Fig. 5 & 6 (i)-(iii). The results are presented only for the three test cases for the brevity of the manuscript. As seen in this figure, the breakdown voltage is greatly reduced with particles to a few hundred volts from few thousand volts when compared to the vent gas mixture. As depicted, the particle size and the distance between the electrodes greatly influences the breakdown voltage and the arcing probability. At a given distance of 3 mm particles with 1000 μm, few particles are prone to cause arcing (see Figure 6 (i)). Keeping the distance intact at 3 mm particles but reducing the particle diameter to 60 μm does not cause arcing (see Figure 6 (ii)). Keeping the particle diameter intact, i.e., at 60 μm, reducing the distance between the electrodes to 0.5 mm also increased the arc formation risks (see Fig. 6 (iii)). As the distance is reduced to 0.5 mm, the breakdown voltage greatly reduces, and some particles are prone to arcing. In these figures, arc-generating capability is shown in Fig. 6 (c) for cases (i)-(iii). For particles and gas with arc-generating capability one are prone to cause arcing and arc-generating capability zero does not cause arcing.

Particle ignited vent gas models are studied in a simplified battery module as shown in Figure 7. Two prismatic cells are placed in a casing containing air. A methane skeleton mechanism containing 19 species is considered for modelling the combustion in this case. Vent gas with CH4, CO, H2 and CO2 enters the module domain in the molar ratios 0.35, 0.3, 0.2 and 0.1 respectively where pure air is filled. Hot aluminum particles (900°C) ignite the vent gas released from the battery due to the presence of available O2 in the battery module.

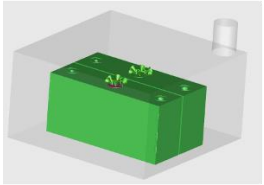

Figure 7: (a) Simplified battery module with two prismatic cells and surrounded by air medium.

The composition of the exerted methane, hot ejected particles, and subsequent ignition of the vent gas in the presence of hot particles is shown in Figure 8 and Figure 9 at two different time steps. The combustion starts at the periphery of the vent gas jet and propagates through the domain as the oxygen availability is present. As seen in Figure 9 (a), as the particles are ejected from the battery cell, the temperature immediately rises due to combustion reaction in the presence of hot particles. These particles act as sparks for starting the combustion process. The combustion further progresses in the domain as seen in Figure 9 (b).

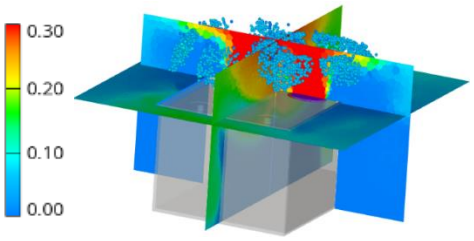

(a) Time = 0.52 s

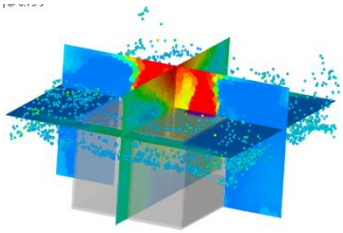

(b) Time = 0.75 s

Figure 8: Mass fraction of methane (-) at two different time steps in the battery module. The ignition starts as soon as the hot particles are ejected from the battery material

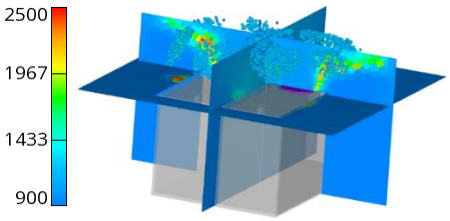

(a) Time = 0.52 s

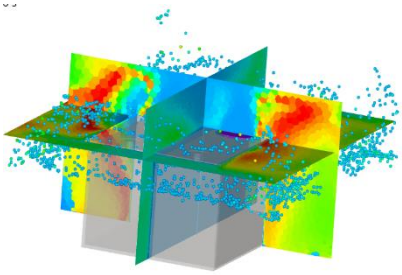

(b) Time = 0.75 s

Figure 9: Temperature (K) contours at two different time steps in the battery module. The ignition starts as soon as the hot particles are ejected from the battery material.

3.1 Description of battery pack under consideration

To evaluate the effects introduced in the previous chapter in a combined manner, a generic battery pack layout was used. The overall dimensions are 170 mm x 1270 mm x 830 mm. Separate details like screws, connector parts, as well as overall irrelevant super components (e.g.: the power converters) have been removed from the CAD model. Usually, battery packs used in the automotive industry do have some sort of liquid cooling. This has also been removed in this specific case.

Figure 10 shows an isometric view of the battery pack to the left and one selected battery module to the right. The whole battery pack consists of 12 battery modules assembled in a double-T-structure. Each battery module consists of 12 prismatic cells connected in series as can be seen in the figure.

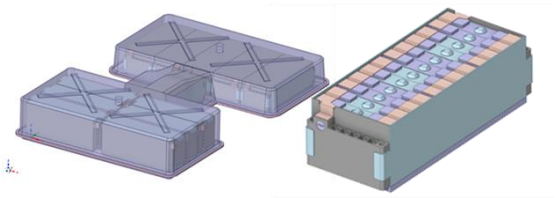

Figure 10: Battery Pack under investigation (left) and one battery module (right)

Components for a conjugate heat transfer simulation that have been retained in the pack are stated in Annex 1. Conductive and Convective heat transfer between all participating domains and media is considered. Radiative heat transfer is not considered. The inner cell material consisting of anode, cathode and electrolyte and the separator has been modelled as a lumped, single material. For thermal runaway considerations this is usually enough. The most important material property when it comes to thermal propagation (the heat spread from battery cell to battery cell in the case of thermal runaway) is the thermal conductivity. For the lumped battery cell, it has been assumed with anisotropic behavior. A list of the material properties can be seen in the table provided in Annex-I.

3.2 Description of thermal runaway modelling

A three-dimensional mesh of roughly 50 million polyhedral cells with sizes between 0.5 and 6 mm is used. The CFD simulation that is carried out is a fully coupled conjugate heat transfer simulation between all the domains mentioned in the previous chapter. Thermal runaway is a multi-phenomenon problem and therefore needs different aspects to be covered. The crucial to be evaluated modelling parts are described in the previous chapters. However, the other important effects are described here therefore the following sectors provide an overview of the model defects during thermal runaway. For the sake of simplicity, the chapters are kept short further information can be found in other papers of the authors [19, 20].

Battery cell heat release

The heat release in the battery cell is mainly characterized by electrochemical reactions, both endothermal (e.g., electrolyte vaporization) and exothermal (decomposition of cathode and anode). It can either be gathered from experiments in ARC reactors, as described by [21], or using chemical modelling, as described in [22–24]. For the sake of simplicity, a curve from AVL's benchmark data, that is appropriate for the battery cells under consideration is taken.

Venting

As the battery active materials undergo physico-chemical transformation (for e.g., SEI decomposition or the hot electrolyte vaporization), the pressure in the battery cell rises and is released either by ripping open the shell (pouch cells), or by exiting through a defined venting port (prismatic and cylindrical cells). The venting mass flow, temperature and species composition can either be gained from testbed data, as described by Golubkov et al. [25], or using a modelling approach like [26]. Within the context of this study, AVL's benchmark data, that is appropriate for the considered cell type, is taken.

Melting

The material properties of meltable parts, as well as the enthalpy of fusion, are taken into consideration for the melting of the material. If the enthalpy of fusion, in combination with start and end temperatures for melting, matches the energy in the meltable part, the solid part is removed, and airflow can pass through.

Burst discs

For the battery module under consideration one burst disc is used. A switchable boundary condition, turning from a wall when the burst disc is closed to a defined outlet pressure when the burst disc is opened, is used. The opening pressure difference is set to 300 mbar.

Particles

Particles are modelled using a Lagrangian description for the particle motion. Coupling of energy, momentum and turbulence exchange with

the surrounding gas phase is considered. Specific submodels are used for the drag law and evaporation. The secondary breakup of particles is not modelled within this study. The initial particle size distribution is constant.

3.3 Description of use case and simulation setup

A certain use case must be chosen to start the thermal runaway and observe its consequences on battery pack level. In this case the back of the pack, where these cells sit upright, has been considered one of the more dangerous use cases. This is due to the fact that the vent gas as well as the subsequent particles directly impinge on the battery pack housing. The following figure shows a top-down view of the battery pack and the initial cell being triggered for thermal runaway. The 12 battery modules are highlighted with respective numbers. This numbering system will be used throughout the paper especially in the interpretation of results.

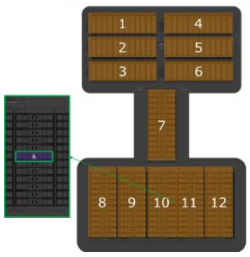

Figure 11: Top down view of the battery pack with triggered battery cell (cell 6 in module 11)

To start the thermal runaway in the simulation cell 6 in battery module 11 is set to an initial temperature of 160 [°C]. All other parts, including the surrounding air are set to 20 [°C]. Based on the cell's local temperature, a certain amount of heat is introduced to heat up the battery cell.

Once the average battery cell temperature reaches the venting temperature, vent gas with a time dependent venting volume, venting temperature and species composition is released in the defined "venting ports". During the venting event, also particles are released at the venting ports. Solid particle matter is ejected together with vent gas at the two venting outlets at the back of the battery pack as indicated in figure 2.

Total mass of solid particles and mass fractions of solid particle material is set to be similar to the results of the measurements from [27], where solid particles were analyzed after thermal runaway of a prismatic cell.

The module covers are treated as meltable solid parts that start to melt at the melting temperature of the applied materials.

Initial time step is set to 0.01 s with an adaptive time step control, adjusting time steps according to critical physical states like predefined critical gas mass flow or burst disc state (f.e. open/closed). Gas species considered for the vent gas are CH_4, H_2 and CO with mole fractions set to 0.3, 0.4, 0.3, respectively. The validity of the modelling approach has been demonstrated in [19] where thermal propagation times and burst disc opening timings have been compared to measurement data. Therefore, the following section will be used to analyze the results with respect to the risk of flammability and arcing. Figure 12 shows the venting of cell 6 in module 11 after about 0.5 s after thermal runaway was triggered in the cell. The image is a zoomed in, isometric view on the battery cell. One can see the battery cells in grey, the busbars in orange. The meltable module covers are only shown in the left part of the image to not obscure the readers view – they are shown as golden, opaque surfaces.

3.4 Evaluation of flammability and particle ignition

The temperature is shown in the first image, the flammability index is shown in the second image. One can see that the gas jet exits with a quite high temperature. It impinges on the meltable covers as they are not molten yet. Due to the fact the vent gas itself has no oxygen in it, the flammability index in the gas jet is zero. Only on the contour of the jet the flammable gases (H2, CH4, CO) mix with oxygen and form a combustible mixture. Here the flammability index has positive values. A correlation could now be made with the solid particles in the vicinity to evaluate possible ignition spots.

3.5 Evaluation of arcing

In the following figure the reader can see the breakdown voltage of the gas mixture – here the view is again an isometric view on battery module 11. The cut-plane shows the breakdown voltage of the gas mixture which is calculated using Paschen's law as described in the earlier chapters. The corresponding values can be seen in the range on the top of the image. The values are still in the range of 10.000 V and more, which is too high for arc formation. This was also observed in the work of [8]. The flammable vent gases reduce the breakdown voltage, but it is still too high to cause arcing in battery packs where voltages of the High Voltage (HV) carriers are at about 800 V. However, in the image also the breakdown voltage of particles can be observed. The range is stated on the lower part of the image. The particles impinged on the meltable module covers and bounced back on the busbars as shown in the image. Here they are now close to the current carrying parts and their breakdown voltage is in the range 100-1000 V, which makes the probability for arcing very high.

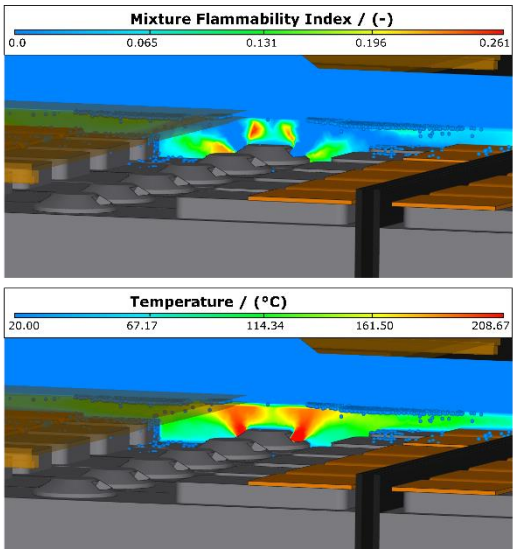

Figure 12: Isometric view of battery cell 6 in module 11 during thermal runaway (top: Temperarture, bottom: Flammability Index)

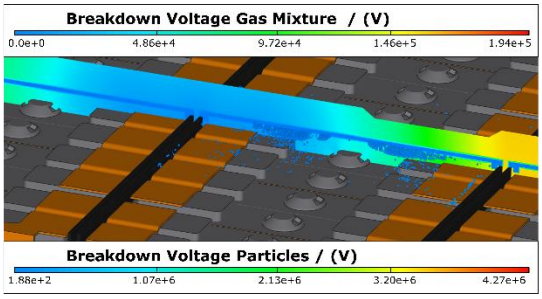

Figure 13: Breakdown Voltage of air (cutplane) and for particles (shown on particle spheres) for the thermal runaway of cell 6

4. SUMMARY

Current study focuses on several predictive models for battery safety and hazard prediction. Flammability, breakdown voltage, arcing are modelled and simulated by considering several possible vent gas species and the solid particles. The developed models are first investigated on simple representative battery module and later, on real life battery pack. The simulation results on the simplified geometries verify the qualitative behaviour of flammability, breakdown voltage and arcing on the system variables. The pack level simulation highlights the applicability of the developed models on complex geometries and provides qualitative and quantitive analysis of the safety operating conditions in the battery packs. Finally, a methodology is presented for particle initiated combustion of the venting gas mixture by considering a reduced skeleton gaseous combustion mechanism (from GRI). The venting gas combustion with particles as ignition source and the flame propagation in the battery packs highlights the modelling capabilities in understanding the possible hazards in the battery packs. The new, advanced features like arcing related quantities for the vent gas and particles can give temporal and spatial view on possible hot spots related to arc formation in the battery pack. Further efforts will focus on correlations between the electrical circuit and breakdown voltage(s) to calculate the full electromagnetics in the battery pack

References

[1] Bugryniec PJ, Resendiz EG, Nwophoke SM, Khanna S, James C, Brown SF. Review of gas emissions from lithium-ion battery thermal runaway failure — Considering toxic and flammable compounds. J Energy Storage 2024;87. https://doi.org/10.1016/j.est.2024.111288.

[2] Baird AR, Archibald EJ, Marr KC, Ezekoye OA. Explosion hazards from lithium-ion battery vent gas. J Power Sources 2020;446. https://doi.org/10.1016/j.jpowsour.2019.227257.

[3] Zlochower IA, Green GM. The limiting oxygen concentration and flammability limits of gases and gas mixtures. J Loss Prev Process Ind 2009;22:499–505. https://doi.org/10.1016/j.jlp.2009.03.006.

[4] Mashuga C V, Crow1 DA. Derivation of Le Chatelier's Mixing Rde for Flammable Limits. n.d.

[5] Kondo S, Takizawa K, Takahashi A, Tokuhashi K, Sekiya A. A study on flammability limits of fuel mixtures. J Hazard Mater 2008;155:440–8. https://doi.org/10.1016/j.jhazmat.2007.11.085.

[6] Marić D, Savić M, Sivoš J, Škoro N, Radmilović-Radjenović M, Malović G, et al. Gas breakdown and secondary electron yields. European Physical Journal D 2014;68. https://doi.org/10.1140/epjd/e2014-50090-x.

[7] Babrauskas V. Arc Breakdown in Air over Very Small Gap Distances. n.d.

[8] Ledinski T, Golubkov AW, Schweighofer O, Erker S. Arcing in Li-Ion Batteries. Batteries 2023;9. https://doi.org/10.3390/batteries9110540.

[9] Massarczyk R, Chu P, Dugger C, Elliott SR, Rielage K, Xu W. Paschen's law studies in cold gases. Journal of Instrumentation 2017;12. https://doi.org/10.1088/1748-0221/12/06/P06019.

[10] Gudmundsson JT, Lundin D. Introduction to magnetron sputtering. High Power Impulse Magnetron Sputtering: Fundamentals, Technologies, Challenges and Applications, Elsevier; 2019, p. 1–48. https://doi.org/10.1016/B978-0-12-812454-3.00006-1.

[11] Hara M, Akazaki M. A method for prediction of gaseous discharge threshold voltage in the presence of a conducting particle. J Electrostat 1976;2:223.
[12] Hara M. Analysis of microdischarge threshold conditions between a conducting sphere and plane. J Electrostat 1982;13:105–18.
[13] Sakai K-I, Abella DL, Suehiro J, Hayashi N, Hara M. Mode of Free-Conducting Particle Motion and Particle-Triggered Breakdown Mechanism in Non-uniform Field Gaps. 2000.
[14] Gongquan Wang, Depeng Kong, Ping Ping, Jennifer Wen, Xiaoqin He, Hengle Zhao, et al. Revealing particle venting of lithium-ion batteries during thermal runaway: A multi-scale model toward multiphase process. ETransportation 2023;16.
[15] Wang Q, Ping P, Zhao X, Chu G, Sun J, Chen C. Thermal runaway caused fire and explosion of lithium ion battery. J Power Sources 2012;208:210–24. https://doi.org/10.1016/j.jpowsour.2012.02.038.
[16] Ferziger JH, Peric M. Computational methods for fluid mechanics. vol. 5. 2002.
[17] Schellander D, Schneiderbauer S, Pirker S. Numerical study of dilute and dense poly-dispersed gas-solid two-phase flows using an Eulerian and Lagrangian hybrid model. Chem Eng Sci 2013.
[18] http://combustion.berkeley.edu/gri-mech/ n.d.
[19] Maier G, Eder L, Schneider J, Suzzi D. Numerische Untersuchung des Thermal Runaway in Lithium-Ionen Batteriesystemen. n.d.
[20] Fritz M, Lucas E, Jürgen S, Thomann M. Modelling and Evaluation of Venting Particles during Battery Thermal Runaway Simulation. KSAE 2022 Annual Autumn Conference & Exhibitio, The Korean Society Of Automotive Engineers; 2022, p. 1684–93.
[21] Essl C, Golubkov AW, Gasser E, Nachtnebel M, Zankel A, Ewert E, et al. Comprehensive hazard analysis of failing automotive lithium-ion batteries in overtemperature experiments. Batteries 2020;6. https://doi.org/10.3390/batteries6020030.
[22] Ren D, Liu X, Feng X, Lu L, Ouyang M, Li J, et al. Model-based thermal runaway prediction of lithium-ion batteries from kinetics analysis of cell components. Appl Energy 2018;228:633–44. https://doi.org/10.1016/j.apenergy.2018.06.126.
[23] García A, Monsalve-Serrano J, Lago Sari R, Fogué Robles Á. Numerical analysis of kinetic mechanisms for battery thermal runaway prediction in lithium-ion batteries. International Journal of Engine Research 2022;23:1691–707. https://doi.org/10.1177/14680874211029902.
[24] Kim GH, Pesaran A, Spotnitz R. A three-dimensional thermal abuse model for lithium-ion cells. J Power Sources 2007;170:476–89. https://doi.org/10.1016/j.jpowsour.2007.04.018.
[25] Golubkov AW, Fuchs D, Wagner J, Wiltsche H, Stangl C, Fauler G, et al. Thermal-runaway experiments on consumer Li-ion batteries with metal-oxide and olivin-type cathodes. RSC Adv 2014;4:3633–42. https://doi.org/10.1039/c3ra45748f.
[26] Coman PT, Rayman S, White RE. A lumped model of venting during thermal runaway in a cylindrical Lithium Cobalt Oxide lithium-ion cell. J Power Sources 2016;307:56–62. https://doi.org/10.1016/j.jpowsour.2015.12.088.
[27] Zhang Y, Wang H, Li W, Li C, Ouyang M. Size distribution and elemental composition of vent particles from abused prismatic Ni-rich automotive lithium-ion batteries. J Energy Storage 2019;26. https://doi.org/10.1016/j.est.2019.100991.

Annex-I

Table 1: Used material properties for the battery pack CFD simulation

Group	Material	Average Density [kg/m³]	Specific heat capacity [J/kgK]	Thermal Conductivity [W/mK]
Inner Cells	Cell Material	2400	1500	33 / 0.7 / 33
Cell Shells	Aluminium	2700	Table	236
Spacer	Plastic	1200	1800	0.3
Endplates	Aluminium	2700	Table	236
Sidplates	Aluminium	2700	Table	236
Baseplates	Aluminium	2700	Table	236
Covers	Plastic	1200	1800	0.3
Busbars	Copper	8960	Table	401
Lower Housing	Steel	7700	Table	Table
Upper Housing	Steel	7700	Table	Table
Sealing Lip	Plastic	1200	1800	0.3
Inner Air	Air (compressible)	Table	Table	Table

Conference on Modelling Fluid Flow (CMFF'25)
The 19th International Conference on Fluid Flow Technologies
Budapest, Hungary, August 26 -August 29, 2025

MULTI-OBJECTIVE DESIGN OPTIMIZATION OF A VARIABLE-PITCH AXIAL FLOW FAN BY USING CFD-BASED META-MODEL

Chan LEE[1], Hyung Jin LEE[2], Sang Yeol LEE[3] , Sang Ho YANG[3]

[1] Corresponding Author. Department of Mechanical Engineering, Faculty of Mechanical Engineering, University of Suwon. Hwaseong, South Korea, Tel.: +82 31 220 2219, E-mail: clee@suwon.ac.kr
[2] PIDOTEC, Beobwon-ro, Songpa-gu, Seoul, South Korea
[3] Research Lab., Samwon E&B, Siheung, South Korea

ABSTRACT

This study defines the design-point efficiency and the standard deviation between the maximum efficiencies under variable-pitch operating conditions as multi-objective functions for a variable-pitch axial flow fan rotor blade. A CFD modeling-based meta-model is developed and used as the simulation engine for this optimization. The CFD model for the variable-pitch fan rotor blade utilizes Reynolds-stress averaged Navier-Stokes equation solver and employed a fine mesh system with $y^+<2$. The meta-model is constructed based on CFD simulation results obtained by changing the pitch angles at the hub, mid-span, and tip of the fan rotor blade, which serve as the design variables. Using the results of the meta-model, a Pareto front is derived, enabling the identification of an optimal design that maximizes design-point efficiency while minimizing the efficiency standard deviation. The CFD-predicted total pressure, efficiency, and power characteristics of the optimally designed variable-pitch fan rotor blade are compared with those of the initial design. From the comparison results, the design-point efficiency of the optimal fan blade rotor is improved by 3.7 percentage points compared to the initial design, and the efficiency standard deviation is reduced to 0.76%.

Keywords: Axial flow fan, CFD, Fan performance, Optimization, Variable-pitch fan operation

NOMENCLATURE

β	[*deg.*]	blade setting angle
θ	[deg.]	tangential coordinate
η	[-]	efficiency
P_T	[*Pa*]	total pressure
Q	[m^3/s]	volume flow rate
y+	[-]	non-dimensional thickness

1. INTRODUCTION

Recent technical challenge for axial flow fans has been to improve fan performance and efficiency in response to global climate change and the trend toward carbon neutrality. Variable pitch axial flow fans offer the advantage of maintaining high efficiency across a wide range of airflow by adjusting the angle of the fan blades, resulting in a 15-20% reduction in power consumption compared to conventional fans[1]. In high-efficiency axial flow fan design, the airflow over the fan blade surface significantly impacts the fan's aerodynamic performance and efficiency, making the optimization of the 3D fan blade geometry a critical task for fan designers[2]. For this reason, there has been extensive research into optimizing fan blade designs for the development of high-efficiency fans[3,4].

Therefore, this paper conducts a new variable pitch axial flow fan design to maximize fan efficiency by applying optimization algorithms to the meta-model based on CFD (Computational Fluid Dynamics) calculation results. In this study, fan design variables are input, and a 3D fan blade shape is constructed through the design program. The designed fan undergoes CFD modelling to calculate key performance indicators such as total pressure, efficiency, and power. This design and analysis process constructs a meta-model which can be combined with the optimization algorithm to obtain the optimal fan design. The optimal fan designed by this method is verified through CFD simulation, and the performance, efficiency, and power characteristics of the fan are predicted based on variable pitch operation to evaluate the energy-saving benefits of this optimal fan.

2. DESIGN AND CFD MODELLING-BASED META-MODEL OF AXIAL FLOW FAN

This study uses the fan blade design program, the FANDAS[5], which was developed and validated in the author's university laboratory. In this study, design variables such as setting angle and camber angle are considered to determine the blade cross-section, as shown in Fig. 1. Once the blade cross-section elements are determined from the camber and setting angles, the blade cross-section elements are stacked along the blade span height from hub to tip to form the 3D fan blade geometry.

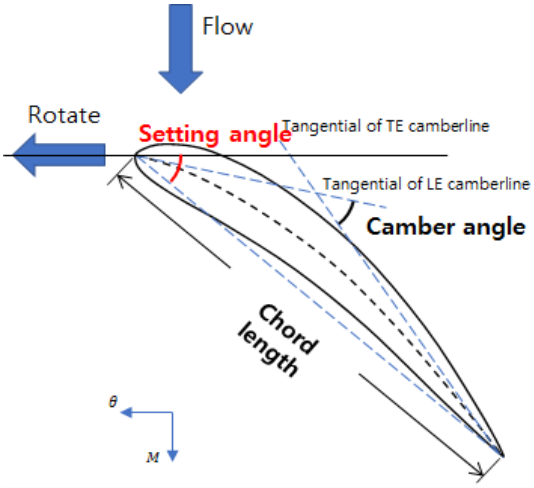

Fig. 1 Camber and setting angles of impeller blade

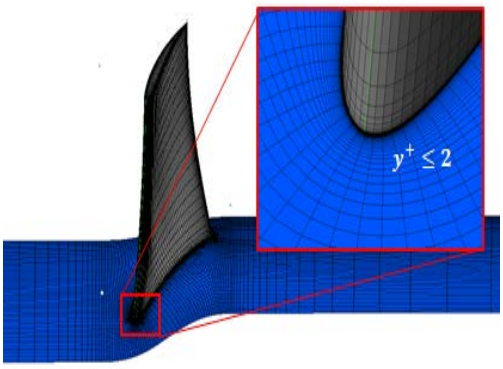

Fig.2 Mesh system on fan impeller blade surface

CFD modeling is performed on fan impeller blades designed by changing the camber angle and setting angle. The ANSYS CFX code[6] is used for the CFD modeling, steady-state RANS (Reynolds-stress Averaged Navier-Stokes equation) solver is used as a numerical analysis method for incompressible and viscous flow, and a k-ω SST model is also used as a turbulence model. For precise calculation of the viscous boundary layer on the impeller blade surface, the wall mesh size is set to y+ < 2 (refer to Fig. 2). The structured mesh is generated using the TurboGrid.The mesh consists of a total of 576,206 cells, with 463,016 cells allocated to the impeller region, where the main viscous flow is generated. The interface between the impeller and stator is treated using the Frozen Rotor approach, aligned with the impeller blade. For the boundary surfaces with repeating conditions, a Rotational Periodic Condition is applied.

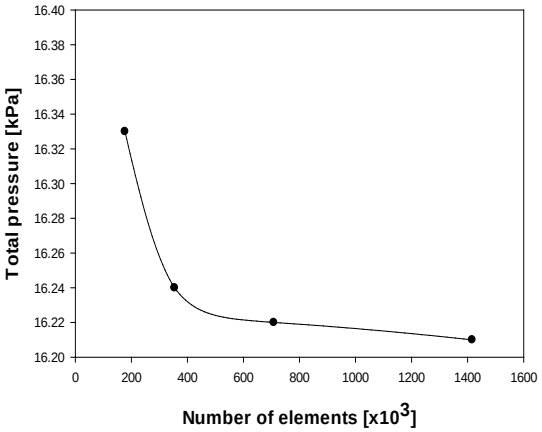

Fig. 3 Grid dependency test of mesh system

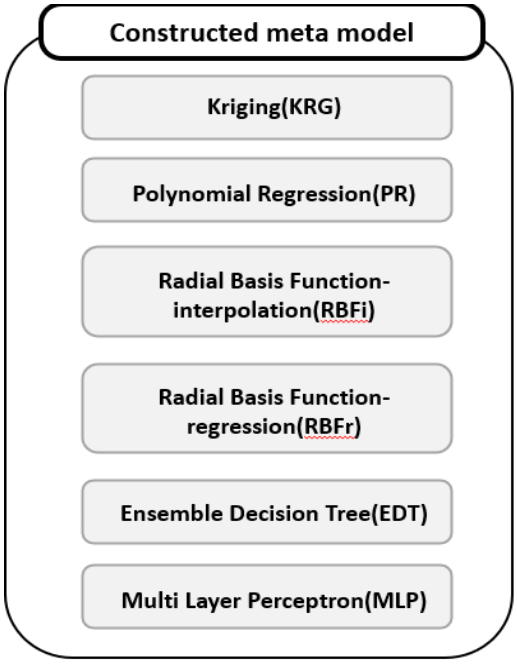

Fig. 4 Meta-model construction processes

In addition, as shown in Fig. 3, the mesh system with the most efficient and highest calculation accuracy is selected through the grid dependency test. Based on the fan performance and efficiency analysis results calculated according to the change in the camber angle and setting angle, a meta-model for fan total pressure, efficiency, and power prediction is constructed. For the meta-model construction, various mathematical techniques [7,8,9] are combined, as shown in Fig. 4. There are two main methods for obtaining data to construct a meta model:

using only pre-existing data and acquiring new data specifically for model construction. The former approach may suffer from data bias or insufficient data volume, but it does not require additional resources, making it a viable option when acquiring new data is difficult. The latter method allows for more balanced data distribution to mitigate potential bias and can produce accurate predictive models even with relatively small datasets; however, it demands additional resources and is typically employed when a new design is introduced or when high prediction accuracy is required. In this study, the former method is chosen due to the substantial resources required for each individual experiment. To mitigate the prediction error caused by the limited amount of available data, six different predictive models are constructed using the same dataset: Kriging (KRG), Radial Basis Function interpolation (RBFi), Polynomial Regression (PR), Radial Basis Function regression (RBFr), Multi-Layer Perceptron (MLP), and Ensemble Decision Tree (EDT). Kriging combines a global model and residuals to accurately pass through the experimental points. RBFi determines performance values by assigning weights to the training data around the prediction point; if the model passes exactly through the experimental points, it is considered RBFi, otherwise it is referred to as RBFr. Polynomial regression is a traditional method that assumes a polynomial form of the data and estimates the coefficients using the least squares method. MLP is a type of artificial neural network with multiple hidden layers that receives inputs through several neurons, applies weights and activation functions, and outputs the prediction result. Lastly, EDT employs a random forest algorithm to train multiple decision trees and combines their outputs for prediction.

Comparing the prediction results by meta-model with the CFD calculation results, the prediction differences are within 0.2%p, indicating that the meta-model shows very accurate prediction results, and furthermore, it is suitable for using the meta-model as a simulation engine for the fan design optimization process for maximizing efficiency.

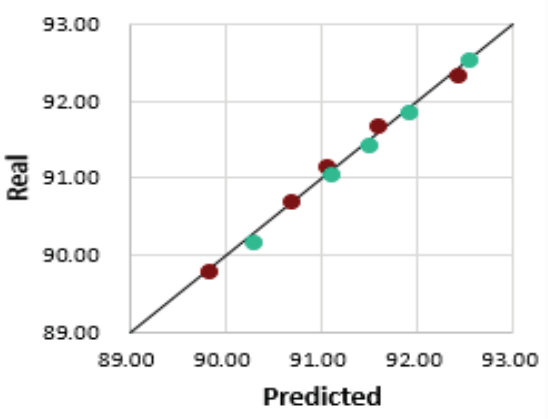

Fig.5 Comparisons between the 3-D CFD simulation (real) and the meta model (predicted)

3. MULTI-OBJECTIVE DESIGN OPTIMIZATION OF A VARIABLE-PITCH FAN

Before performing the optimal design by combining the aforementioned meta-model and an optimization algorithm, it is necessary to define the multi-objective function of the variable-pitch axial fan in this study. Fig. 6 shows the change in the performance and efficiency of the fan under variable-pitch operation conditions. As can be seen in Fig. 6, the variable-pitch axial fan is important in efficiency at the design point, but also requires the characteristic that the efficiency does not decrease rapidly under variable pitch conditions (change in setting angle, β). Therefore, this study defines the efficiency of the design point and the deviation between the maximum efficiencies under different variable pitch conditions as the objective functions of the optimization problem (refer to equations 1 and 2), and optimization (maximization of design point efficiency and minimization of efficiency deviation) of these two objective functions is performed.

$$\eta_{des} = \frac{\Delta P_T Q}{Torque \times Angular\ frequency} \quad (1)$$

$$\Delta\eta = \eta_{peak,\beta} - \eta_{des} \quad (2)$$

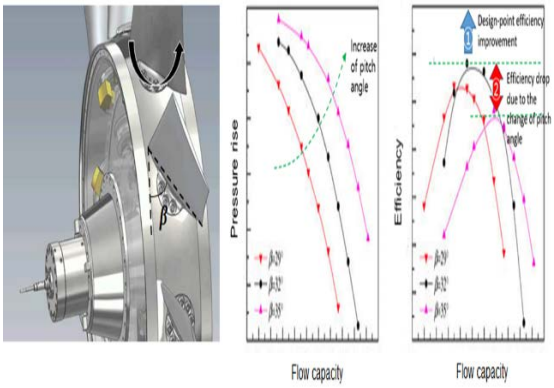

Fig. 6 Performance and efficiency characteristics of variable-pitch axial flow fan

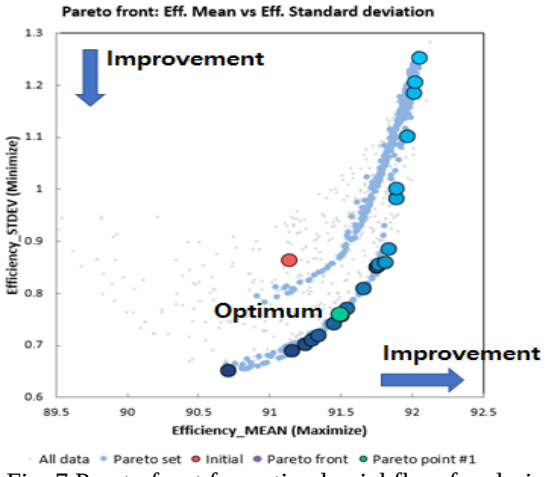

Fig. 7 Pareto front for optimal axial flow fan design

For the design optimization, the camber angles and setting angles are considered as design variables at the impeller blade hub, mid-span and tip locations, so six design variables are dealt with in this study. Table 1 presents the design conditions used in this study, and the variation in blade setting angle (or pitch angle) ranges from -5 degrees to +5 degrees.

Table 1 Design specifications of axial flow fan

Q [m^3/s]	P_T [Pa]	RPM	Power[kW]
90	2000	1200	200

The Pareto front is created by combining the previously constructed meta-model and the optimization algorithm. Fig. 7 shows the Pareto front for the design point efficiency and efficiency deviation, and a region in which the improvement of the design point efficiency and the reduction of the efficiency deviation are satisfied at the same time is found, and the middle point of this region is selected as an optimal point for this optimization.

Regarding the design optimization results, the optimal camber angle of hub and tip is greater than the initial design by free vortex design concept, while the optimal camber angle in mid-span is lower than the initial design. The tip setting angle of the optimal model is slightly larger than the initial design by 2 deg (refer to Figs. 8 and 9).

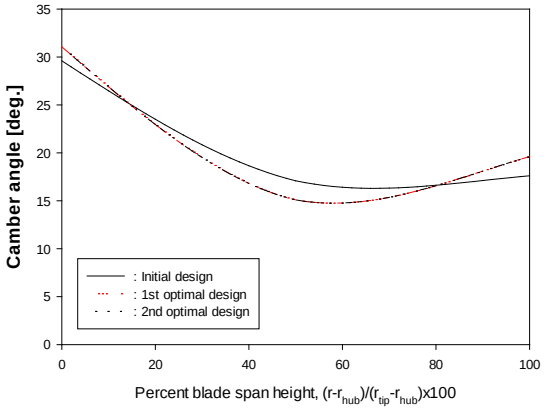

Fig. 8 Spanwise distributions of camber angle

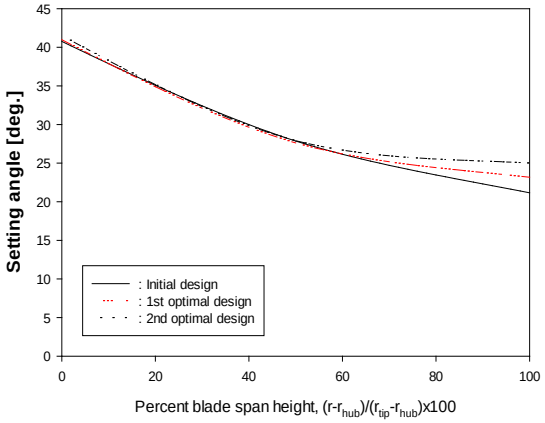

Fig. 9 Spanwise distributions of setting angle

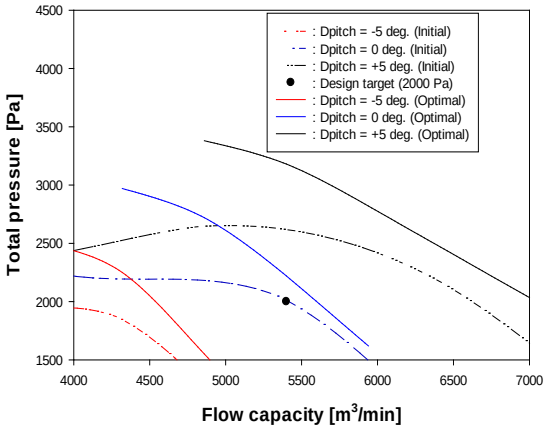

Fig. 10 Total pressure curves of the optimal and the initial fan models

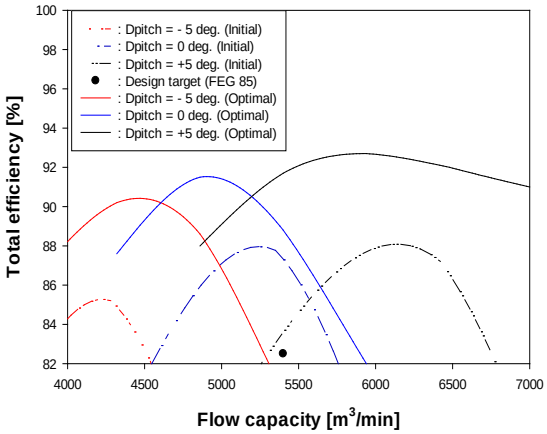

Fig. 11 Efficiency curves of the optimal and the initial fan models

Total pressure curves of the optimal and the initial fan models are predicted by CFD simulations at different variable-pitch conditions and compared in Fig. 10. As shown in Fig. 10, the total pressure curves of the optimal fan model show higher total pressure and more stable performance characteristics without surge up to the low flow rate range when compared with the initial design. . On the other hand, the initial design shows inferior performance characteristics in which the total pressure low compared to the optimal fan model and the pressure decreases rapidly under low flow conditions.

Fig. 11 compares the efficiency characteristics between the optimal design and the initial design. The design point efficiency of the optimal model is 91.5%, which improved by 3.7% compared to the initial design model, 87.8%, Through this design optimization, the deviation of the efficiency change due to variable-pitch operation is reduced from 1.10 % to 0.76%.

4. CONCLUSIONS

The present study proposes an optimization method for the multi-objective design optimization problem of variable-pitch axial flow fan. CFD modelling and simulation are used to construct a meta-model of axial flow fan design, and the meta-model is verified by comparing with precise CFD simulations. The meta-model is used as simulation engine of multi-objective optimization problem. Using the meta-model, a Pareto front is created to maximize design-point fan efficiency as well as to minimize fan efficiency deviation at variable-pitch operation conditions. Through the selection of an optimum design solution from the Pareto front, the optimal fan model shows the design-point efficiency improvement by 3.7% and reduces the efficiency deviation down to 0.76% when compared with the initial design.

ACKNOWLEDGEMENTS

This work was supported by the Korea Institute of Energy Technology Evaluation and Planning (KETEP) grant funded by the Korea government Ministry of Trade, Industry & Energy(MOTIE), Republic of Korea. (No. 2021202080026B)

REFERENCES

[1] Wright, T., and Gerhart, P. M., 2009, *Fluid Machinery: Application, Selection and Design*, 2nd edition, CRC Press.

[2] Angelini, G., Bonanni, T., Corsini, A., Delibra, G., Tieghi, L. and Volponi, D., 2017, *Optimization of an axial fan for air cooled condensers*, Energy Procedia, Vol. 126, pp.754-761

[3] Edward, D.R., Fanny, B.C. and Jean, C.B., 2021. *Optimization of a high pressure industrial fan*, ASME Turbo Expo 2021 proceedings

[4] Kim, S.W., Choi, B.L., Choi, D.H., Lee, C. and Yang, S.H., 2022. *A study on a screening method for dimensionality reduction of large fluid machine optimization problems*, KSFM Journal of Fluid Machinery, Vol.25, pp.48-54

[5] KWT solution. 2023. *FANDAS code user manual*

[6] ANSYS Inc., 2023, *ANSYS CFX manual*, ANSYS

[7] PIDOTEC, 2022, *PIAnO manual*

[8] Lee, H.J., Choi, B.L., Choi, D.H., Lee, C. and Yang, S.H., 2025, *Design Optimization of Axial-flow Fan on Various Operation Conditions*, KSFM Journal of Fluid Machinery, Vol.28, pp.64-74

[9] Lee, C., Kim, S.W., Byun, H.T. and Yang, S.H., 2025, *High-efficiency Axial Flow Fan Design by Combining Through-flow Modeling, Optimization Algorithm and Computational Fluid Dynamics Simulation*, Journal of Applied Fluid mechanics, Vol.18, to be published

Conference on Modelling Fluid Flow (CMFF'25)
The 19th International Conference on Fluid Flow Technologies
Budapest, Hungary, August 26-August 29, 2025

Modelling of Parametric Oscillations in Floating Bodies

Erik SILVA FUJIYAMA[1], Josh DAVIDSON[2], Tamás KALMÁR-NAGY[3]

[1] Department of Fluid Mechanics, Faculty of Mechanical Engineering, Budapest University of Technology and Economics. Bertalan Lajos u. 4 - 6, H-1111 Budapest, Hungary. Corresponding Author. E-mail: erik.fujiyama@edu.bme.hu
[2] Basque Center for Applied Mathematics, Mazarredo 14, 48009 Bilbao, Spain. E-mail: jdavidson@bcamath.org
[3] Department of Fluid Mechanics, Faculty of Mechanical Engineering, Budapest University of Technology and Economics. E-mail: kalmar.nagy.tamas@gpk.bme.hu

ABSTRACT

Parametric resonance is a dynamic instability that causes exponential growth in the amplitude of an oscillating system. This study presents a nonlinear Mathieu-type equation model for floating bodies excited by waves, developed to capture parametric resonance in both the heave and pitch degrees of freedom. The model includes nonlinear hydrostatic restoring forces and incorporates position-dependency of the wave excitation forces. Through a nondimensional analysis, a previous model is simplified. A non-cylindrical axisymmetric spar-buoy was used as a test case. The wave excitation forces were calculated for various heave and pitch positions, and interpolated with a third-order polynomial. Simulations showed parametric resonance when the wave frequency is twice the natural frequency of the structure. The results compared favourably to those from a benchmark model with nonlinear Froude-Krylov forces, but achieving a 1000-fold speed increase. On top of this increased computational efficiency, the presented model facilitates analytical approaches, such as perturbation analysis or harmonic balance.

Keywords: Mathieu equation, nonlinear hydrodynamic modelling, parametric resonance, spar buoy, wave-structure interaction

NOMENCLATURE

F_{hr}	$[N]$	hydrostatic restoring force
H	$[m]$	wave amplitude
I	$[Nm]$	inertia moment
I_a	$[Nm]$	added inertia
M_{hr}	$[Nm]$	hydrostatic restoring momentum
R	$[m]$	buoy radius
T	$[s]$	time scale
V	$[m^3]$	submerged volume
Z	$[m]$	length scale for the heave
g	$[m/s^2]$	gravitational acceleration
$a_{i,j}$	$[-]$	nondimensional coefficient for force amplitude
$b_{i,j}$	$[-]$	nondimensional coefficient for moment amplitude
c_a	$[kg]$	radiation damping
cg	$[m]$	center of gravity
$d_{i,j}$	$[-]$	nondimensional coefficient for heave phase
f_e	$[N]$	excitation force amplitude
$f_{i,j}$	$[-]$	nondimensional coefficient for pitch phase
h_0	$[m]$	height of the truncated cone
h_1	$[m]$	height of the cylinder
m	$[kg]$	mass of the floating body
m_a	$[kg]$	added mass
m_e	$[Nm]$	excitation moment amplitude
x_{cb}	$[m]$	center of buoyancy horizontal position
x_{cg}	$[m]$	center of gravity horizontal position
z	$[m]$	heave position
α	$[m]$	buoy angle
η	$[m]$	wave elevation
ω	$[rad/s]$	wave frequency
ω_0	$[rad/s]$	natural frequency
Φ	$[rad]$	length scale for the pitch
ρ	$[kg^3]$	water density
θ_e	$[rad]$	phase angle
φ	$[rad]$	pitch position
ζ	$[m]$	buoy height position

1. INTRODUCTION

Parametric resonance is a dynamic instability that causes exponential growth in the amplitude of an oscillating system. It occurs in differential equations with time-varying coefficients [1]. The most well-known example of such equations is the Mathieu equation, a second-order ordinary differential equation (ODE) with no external forcing and a harmonically time-varying parameter.

Various phenomena, such as the oscillations of floating vessels [2] are described by the Mathieu equation or variants of it [3]. A floating body excited by waves is often described by a Mathieu equation, with an external excitation and damping added. The

time-varying parameter, normally represents a part of the hydrostatic stiffness, and leads to heave-to-pitch instability.

Heave-to-heave instabilities on the other hand, caused by a non constant cross-sectional area in the body, are rarely found in the literature. This type of instability was studied numerically by Jang and Kim in [4] for the case of an Arctic Spar. Lelkes et al. in [5] developed an analytical model to capture the heave-to-heave parametric instability. In the modelling presented in [5], the occurrence of parametric resonance in the heave was not induced by the nonlinear hydrostatic stiffness term, but rather derived from the wave excitation force being dependent on the heave position. This dependency was obtained through the interpolation of the wave excitation force calculated at various positions. Even though positional dependence of hydrodynamic forces was also considered by Rodriguez and Neves in [6], the approach was different: in [6] a Taylor series expansion was applied to a simplified approximation of the force near the equilibrium point. In [7], the model developed in [5] was expanded to also include the pitch. In this paper, an evaluation of the significance of the parameters by a nondimensionalization will be made in the model presented in [7], and simplifications will be made in the interpolations, making the model simper and faster. A model with nonlinear Froude-Krylov forces [8] will be used as the benchmark.

2. ANALYTICAL MODEL FOR PARAMETRIC RESONANCE

In this Section the same procedure that was used in [5] and [7] to model the movement of a spar-buoy excited by harmonic waves will be applied.

In Figure 1, a floating body is shown along with the world coordinate system $\boldsymbol{ij}$. The origin of this system is horizontally aligned with the body's center of gravity (cg) and vertically at the still water level (SWL), which represents the water surface elevation without wave effects. The motion of the body is constrained to the heave DoF z, i.e vertical motion in the $\boldsymbol{j}$ axis, and the pitch DoF φ, i.e rotation around the cg. The wave elevation η is measured relative to the SWL. By convention, the wave propagation direction follows the direction of the $\boldsymbol{i}$ axis.

Only harmonic wave elevations, defined as

$$\eta(t) = H \cdot \cos(\omega t), \tag{1}$$

where H is the wave amplitude and ω is the wave frequency, are considered.

The model proposed by Lelkes et al. and presented in [5] is

$$\begin{aligned}&(m + m_a(\omega))\,\ddot{z} + c_a(\omega)\dot{z} + F_{hr}(z)\\ &= f_e(z,\omega)H\cos(\omega t - \theta_e(z,\omega)).\end{aligned} \tag{2}$$

where m is the mass of the floating body, m_a is the added mass, c_a is the radiation damping, F_{hr} is the hydrostatic restoring force, f_e and θ_e are the wave excitation amplitude coefficient and the phase angle. By expanding Eq. (2) to also include include the pitch degree of freedom, the following coupled system presented in [7] is obtained

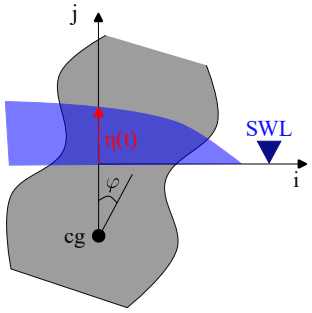

Figure 1. Floating body, wave elevation, and the world coordinate system for two DoFs

$$\begin{aligned}&(m + m_a(\omega))\,\ddot{z} + m_{a2}(\omega)\ddot{\varphi} + c_a(\omega)\dot{z} + c_{a3}(\omega)\dot{\varphi}\\ &+ F_{hr}(z,\varphi) = f_e(z,\varphi,\omega)H\cos(\omega t - \theta_e(z,\varphi,\omega)),\end{aligned} \tag{3}$$

$$\begin{aligned}&(I + I_a(\omega))\,\ddot{\varphi} + I_{a2}(\omega)\ddot{z} + c_{a2}(\omega)\dot{\varphi} + c_{a4}(\omega)\dot{z}\\ &+ M_{hr}(z,\varphi) = m_e(z,\varphi,\omega)H\cos(\omega t - \theta_{e2}(z,\varphi,\omega)),\end{aligned} \tag{4}$$

where I is the rotational inertia, I_a is the added rotational inertia, M_{hr} is the hydrostatic restoring moment, and m_e is the wave excitation amplitude moment coefficient.

3. CASE STUDY

In this Section, a test case is presented to evaluate the performance of the parametric excitation model (Eqs. 3 and 4). The test case is generic, not containing a mooring system, as the primary focus of the model is the wave excitation force. Additionally, conditions of infinite water depth are considered.

3.1. The floating body

The floating body considered in the test case is an axisymmetric spar-buoy, similar to the one examined in [5] and [7]. It consists of a truncated cone and a cylindrical extension, as illustrated in Figure 2. The exact shape of the spar-buoy is defined by:

$$f(\zeta) = \begin{cases} R_1 & \text{if } -\frac{h_0}{2} + h_1 \le \zeta \le \frac{h_0}{2}, \\ R_0 + \zeta\tan(\alpha) & \text{if } -\frac{h_0}{2} \le \zeta \le \frac{h_0}{2}, \\ 0 & \text{otherwise.} \end{cases} \tag{5}$$

The physical parameters of the spar-buoy shown in Fig. 2 and their corresponding values are $\alpha = 0.197\ [rad]$, $R_0 = 3\ [m]$, $h_0 = 10\ [m]$, $h_1 = 15\ [m]$, $R_1 = 2\ [m]$, $z_{cg} = 16\ [m]$, $m = 2.95 \cdot 10^5\ [kg]$, and $I = 1.18 \cdot 10^7\ [kg \cdot m^2]$. The water density is $\rho = 1025\ [kg/m^3]$ and the gravitational acceleration is $g = 9.806\ [m/s^2]$.

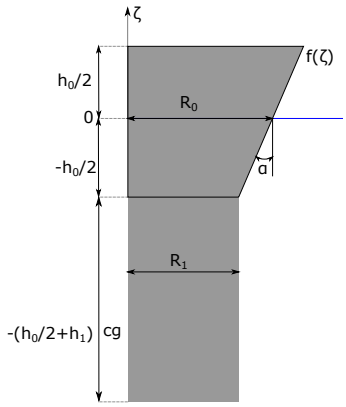

Figure 2. Section of the spar-buoy geometry

3.2. Modelling the test case

With g and ρ given in Subsection 3.1, the hydrostatic restoring terms F_{hr} and M_{hr} are calculated based on the body geometry with

$$F_{hr}(z,\varphi) = \rho_{water} g \Delta V(z,\varphi), \tag{6}$$

where $\Delta V(z) = V(z) - V(0)$, $V(z)$ being the submerged volume, and

$$M_{hr}(z,\varphi) = \rho g \Delta V(z,\varphi) \cdot (x_{cb}(z,\varphi) - x_{cg}), \tag{7}$$

where x_{cb} is the horizontal position of the center of buoyancy, and x_{cg} is the horizontal position of the center of gravity.

In this case $F_{hr}(z,\varphi)$ and $M_{hr}(z,\varphi)$ are calculated numerically with the CAD software FreeCAD [9]. The values for F_{hr} and M_{hr} are determined for a set of discrete pitch angles ranging from -0.21 $[rad]$ to 0.21 $[rad]$, with a step size of 0.07 $[rad]$, and for heave displacements from -4 $[m]$ to 4 $[m]$, with a step size of 1 $[m]$.

An interpolation is then performed on the generated dataset to describe F_{hr} and M_{hr} continuously, employing polynomial functions of the heave z and pitch φ displacement. The resulting polynomial expressions are

$$F_{hr}(z,\varphi) = \rho g \Delta V(z,\varphi) \approx \sum_{1 \le i+j \le 3} r_{i,j} z^i \varphi^j, \tag{8}$$

$$M_{hr}(z,\varphi) = \rho g \Delta V(z,\varphi)(x_{cb}(z,\varphi) - x_{cg}) \approx \sum_{1 \le i+j \le 3} s_{i,j} z^i \varphi^j, \tag{9}$$

where $r_{i,j}$ are the hydrostatic restoring coefficients for the heave obtained from the polynomial interpolation, and $s_{i,j}$ are the hydrostatic restoring coefficients for the pitch obtained from the polynomial interpolation.

The calculation of the wave excitation coefficients f_e, m_e, θ_e, and θ_{e2} is done with the open-source boundary element solver NEMOH [10], which computes first-order hydrodynamic coefficients, such as added mass, radiation and excitation forces in the frequency domain.

A model with nonlinear Froude-Krylov forces that does not consider the diffraction force [8] will be used as the benchmark, so this component will also be neglected in the present study. This approach is common for bodies that are small relative to the wavelength [11], and it can be easily configured with NEMOH.

In this test case, the wave excitation coefficients are computed for the same discrete displacements used in the hydrostatic restoring terms. The wave excitation terms are also interpolated with polynomial functions, yielding the following expressions

$$f_e = \sum_{0 \le i+j \le 3} a_{i,j}(\omega) z^i \varphi^j, \; \theta_e = \sum_{0 \le i+j \le 1} d_{i,j}(\omega) z^i \varphi^j, \tag{10}$$

$$m_e = \sum_{0 \le i+j \le 3} b_{i,j}(\omega) z^i \varphi^j, \; \theta_{e2} = \sum_{0 \le i+j \le 2} f_{i,j}(\omega) z^i \varphi^j \tag{11}$$

where $a_{i,j}$, $d_{i,j}$, $b_{i,j}$, and $f_{i,j}$ are the coefficients obtained from the polynomial interpolation.

The radiation and added mass coefficients m_a, m_{a2}, I_a, I_{a2}, c_a, c_{a2}, c_{a3} and c_{a4}, in Eqs. (3) and (4), are also computed using NEMOH.

The cross terms $m_{a2}(\omega)$, $c_{a3}(\omega)$, $I_{a2}(\omega)$ and $c_{a4}(\omega)$, calculated for NEMOH were negligible, being over four orders of magnitude smaller than the other coefficients. This outcome is expected for an axisymmetric body, so they were neglected from the model in this test case.

The radiation damping coefficients depend on the frequency of the body motion. In a linear model, a body oscillates at the same frequency as the excitation. In a nonlinear model, such as the parametric excitation model, this is not always the case. However, in the present test case, following Lelkes et al. in [5], the radiation damping considered will be with the excitation frequency. Even though this simplification introduces error, the wave excitation forces, which are the primary focus of the model, are not affected. Simplifications of this kind are not uncommon in literature, as seen in works such as [12, 13, 14], where the radiation damping was similarly simplified to focus on other specific aspects of the analysis.

4. NONDIMENSIONALIZATION

In order to better understand the significance of the parameters in the model, and remove terms that do not alter the results, the 2-DoF model is nondimensionalized. The nondimensional variables are defined as follows

$$\tilde{t} = \frac{t}{T}, \tilde{z} = \frac{z}{Z}, \tilde{\varphi} = \frac{\varphi}{\Phi}. \tag{12}$$

The length and angle scales Z and Φ are defined so that $\tilde{z}$ and $\tilde{\varphi}$ have a validity region between -1 and 1. As the validity region of the model is defined as $|z| \leq 4$ $[m]$ and $|\varphi| \leq 0.21$ $[rad]$ (as stated in Section 3),

$$Z = 4\ [m],\ \Phi = 0.21\ [rad]. \tag{13}$$

The time scale T is defined as

$$T = \sqrt{\frac{m + m_a(\omega)}{r_{1,0}}}. \tag{14}$$

The nondimensional equations become

$$\ddot{\tilde{z}} + \alpha_3(\omega)\dot{\tilde{z}} + \sum_{1\leq i+j\leq 3} \gamma_{i,j}(\omega)\tilde{z}^i\tilde{\varphi}^j = \cos\left(\nu\tilde{t} - \sum_{0\leq i+j\leq 1} \xi_{i,j}(\omega)\tilde{z}^i\tilde{\varphi}^j\right) \sum_{0\leq i+j\leq 3} \beta_{i,j}(\omega)\tilde{z}^i\tilde{\varphi}^j, \tag{15}$$

$$\ddot{\tilde{\varphi}} + \alpha_5(\omega)\dot{\tilde{\varphi}} + \sum_{1\leq i+j\leq 3} \zeta_{i,j}(\omega)\tilde{z}^i\tilde{\varphi}^j = \cos\left(\nu\tilde{t} - \sum_{0\leq i+j\leq 2} \chi_{i,j}(\omega)\tilde{z}^i\tilde{\varphi}^j\right) \sum_{0\leq i+j\leq 3} \mu_{i,j}(\omega)\tilde{z}^i\tilde{\varphi}^j, \tag{16}$$

where the nondimensional parameters are

$$\begin{aligned}
&\alpha_3(\omega) = \frac{c_3}{\sqrt{(m + m_a(\omega))r_{1,0}}},\\
&\alpha_5(\omega) = \frac{c_5\sqrt{m + m_a(\omega)}}{(I + I_a(\omega))\sqrt{r_{1,0}}},\\
&\gamma_{i,j}(\omega) = \frac{1}{r_{1,0}} r_{i,j} Z^{i-1}\Phi^i,\ \beta_{i,j}(\omega) = \frac{H}{r_{1,0}} a_{i,j} Z^{i-1}\Phi^i,\\
&\zeta_{i,j}(\omega) = \frac{T^2}{I + I_a(\omega)} s_{i,j} Z^i \Phi^{i-1},\\
&\mu_{i,j}(\omega) = \frac{HT^2}{I + I_a(\omega)} b_{i,j} Z^i \Phi^{i-1},\\
&\nu(\omega) = \omega\sqrt{\frac{m + m_a(\omega)}{r_{1,0}}},\\
&\xi_{i,j} = d_{i,j} Z^i \Phi^j,\ \chi_{i,j} = f_{i,j} Z^i \Phi^j.
\end{aligned} \tag{17}$$

The restoring parameters are now functions of ω. To estimate their orders of magnitude, their values for $\omega = 1.9$ $[rad/s]$ are provided in Eq. 18 and Table 1

$$\alpha_3 = 0.03,\ \alpha_5 = 0.83,\ \nu = 2. \tag{18}$$

The nondimensional coefficients $\gamma_{i,j}$ and $\zeta_{i,j}$ correspond to the hydrostatic restoring coefficients $r_{i,j}$ and $s_{i,j}$. The coefficients $\beta_{i,j}$, $\mu_{i,j}$, $\xi_{i,j}$ and $\chi_{i,j}$ relate to the wave excitation coefficients $a_{i,j}$, $b_{i,j}$, $d_{i,j}$ and $f_{i,j}$, while α_3 and α_5 correspond to the radiation damping terms c_3 and c_5.

i,j	0, 0	1, 0	2, 0	3, 0	1, 0
$\gamma_{i,j}$	0	0.21	-0.012	$2.26 \cdot 10^{-4}$	$4.67 \cdot 10^{-6}$
$\zeta_{i,j}$	0	$-4.42 \cdot 10^{-9}$	$-2.41 \cdot 10^{-9}$	$1.8 \cdot 10^{-10}$	3.61
$\beta_{i,j}$	0.051	-0.02	-0.01	-0.002	$7.93 \cdot 10^{-6}$
$\mu_{i,j}$	0.01	-0.004	-0.002	$-3.84 \cdot 10^{-4}$	$1.56 \cdot 10^{-6}$
$\xi_{i,j}$	$2.6 \cdot 10^{-5}$	$7.06 \cdot 10^{-4}$	0	0	1.84
$\chi_{i,j}$	-1.57	$9.16 \cdot 10^{-5}$	$-1.56 \cdot 10^{-4}$	0	1.05
i,j	0, 2	0, 3	1, 1	2, 1	1, 2
$\gamma_{i,j}$	-2.28	$1.08 \cdot 10^{-5}$	$-8.43 \cdot 10^{-7}$	$4.63 \cdot 10^{-8}$	0.36
$\zeta_{i,j}$	$-8.76 \cdot 10^{-6}$	7.65	-0.77	0.061	$2.21 \cdot 10^{-6}$
$\beta_{i,j}$	0.017	$-8.54 \cdot 10^{-6}$	$6.66 \cdot 10^{-6}$	$-1.23 \cdot 10^{-5}$	-0.001
$\mu_{i,j}$	0.003	$-1.68 \cdot 10^{-6}$	$1.31 \cdot 10^{-6}$	$-2.43 \cdot 10^{-6}$	$-2.38 \cdot 10^{-4}$
$\xi_{i,j}$	0	0	0	0	0
$\chi_{i,j}$	$-1.49 \cdot 10^{-4}$	0	-0.34	0	0

Table 1. Nondimensional polynomial approximation coefficients for hydrostatic restoring terms ($\gamma_{i,j}$ and $\zeta_{i,j}$), and wave excitation terms ($\beta_{i,j}$ and $\mu_{i,j}$)

The nondimensional coefficients $\gamma_{0,1}$, $\gamma_{1,1}$, $\gamma_{2,1}$, $\zeta_{1,0}$, $\zeta_{2,0}$, $\zeta_{3,0}$, $\zeta_{0,2}$, and $\zeta_{1,2}$ in Table 1 have small values. So a polynomial interpolation for the hydrostatic restoring forces was conducted by setting the coefficients corresponding to these small-valued nondimensional coefficients to zero. The threshold for a coefficient to be deemed small was chosen as $2.26 \cdot 10^{-4}$. This choice was made because it was observed that the term $\gamma_{3,0}$ was the smallest coefficient that still significantly affected the interpolation.

With these small terms set to zero, we recalculate the dimensional parameters $r_{i,j}$ and $s_{i,j}$ in this simplified manner. The results are shown in Table 2.

i,j	1, 0	2, 0	3, 0	0, 1
$r_{i,j}$ (SI)	$2.83 \cdot 10^5$	$-1.93 \cdot 10^4$	434	0
$s_{i,j}$ (SI)	0	0	0	$-2.08 \cdot 10^7$
i,j	0, 2	0, 3	1, 1	2, 1
$r_{i,j}$ (SI)	$-2.59 \cdot 10^6$	0	0	0
$s_{i,j}$ (SI)	0	$-4.42 \cdot 10^7$	$5.29 \cdot 10^7$	$-4.97 \cdot 10^5$
i,j	1, 2			
$r_{i,j}$ (SI)	$4.92 \cdot 10^5$			
$s_{i,j}$ (SI)	0			

Table 2. Hydrostatic restoring coefficients obtained from the polynomial interpolation that set small terms to zero

By comparing the results of the interpolation with the values from Table 2 to the one with the original ones, the difference between the two interpolations across the considered range of $|z| \leq 4$ $[m]$ and $|\varphi| \leq 0.21$ $[rad]$ was never bigger than 10^{-10}. This is negligible, considering that $|\bar{F}_{hr}| = 5.9 \cdot 10^5$ $[N]$ and $|\bar{M}_{hr}| = 2.57 \cdot 10^6$ $[Nm]$.

The same procedure was applied to the wave excitation coefficients and led to the values in Table 3.

5. RESULTS

In this Section, the results from the test case detailed in Section 3 with the simplifications from Section 4 are presented and compared to a model with NLFK forces.

The equations for the presented model Eqs. (3) and (4) are solved numerically using the NDSolve function in Wolfram Mathematica 14.1 with its default settings, and the equations for the model with

i,j	0,0	1,0	2,0	3,0
$a_{i,j}$ (SI)	$5.89 \cdot 10^4$	-5897	-722	-34.2
$b_{i,j}$ (SI)	$2.61 \cdot 10^6$	$-519 \cdot 10^5$	$3.23 \cdot 10^4$	1322
i,j	0,2	1,2		
$a_{i,j}$ (SI)	$4.27 \cdot 10^5$	-7481		
$b_{i,j}$ (SI)	$5.84 \cdot 10^6$	$6.15 \cdot 10^5$		
i,j	0,0	0,1	1,1	
$d_{i,j}$ (SI)	$-2.54 \cdot 10^{-5}$	8.7	0	
$f_{i,j}$ (SI)	-1.57	4.94	-0.41	

Table 3. Wave excitation coefficients obtained from the polynomial interpolation that set small terms to zero

NLFK forces, were solved in Matlab R2021a, using the toolbox developed by Giorgi et al. in [8].

The natural frequency ω_0 is also found numerically, by running a simulation without the external excitation. It is critical to note that the validity region of this parametric excitation model is limited to the range over which the excitation and restoring force coefficients were computed, $|z| \leq 4$ $[m]$, and $|\varphi| \leq 0.21$ $[rad]$.

By numerically solving Eqs. (3) and (4) with these simplified interpolations and comparing to their solution with the initial interpolation, the difference was of the order of 10^{-4}. However, with the simplified interpolations, the running time to obtain the interpolation and perform a simulation of 1000 periods went from 1.94 seconds to 0.27 seconds . So neglecting the small terms does not affect the results significantly, while making the code run faster. As for each simulated frequency, a new interpolation for the wave excitation coefficients is necessary, when evaluating multiple frequencies, the difference in time becomes more significant.

The plots in Figures 3 and 4 show the oscillation amplitude in response to a range of input wave frequencies and amplitudes. The RMS of the displacement time series, scaled by the square root of 2 serves as the measure of amplitude for both heave and pitch motions. This RMS is computed over the last 64 wave periods of the simulation to ensure that motions have reached steady-state.

In Fig. 3 these are shown for the region where heave parametric resonance occurs, while in Fig. 4 for the region where the pitch parametric resonance occurs. At a first view, the contour plots indicate a good match between the models.

In Figures 5 and 6, the time series for Point C in Fig. 3 and Point D in Fig. 4 are plotted. For the parametric excitation model, the amplitude grows faster and larger than for the model with NLFK forces, with a difference of around 20% in the amplitudes. The results also appear slightly off-phase. These differences were also noted for the 1-DoF results in [5].

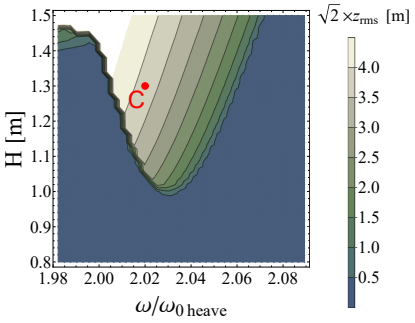

(a) RMS amplitudes for heave from the parametric excitation force model

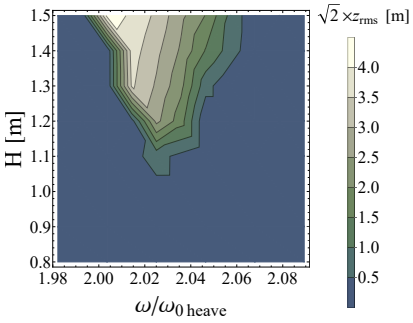

(b) RMS amplitudes for heave from the model with NLFK forces

Figure 3. Contour plots of steady-state amplitudes of the buoy's oscillations in the heave parametric resonance region

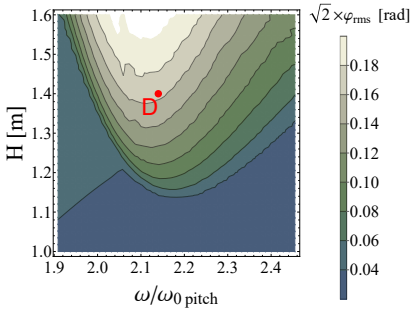

(a) RMS amplitudes for pitch from the parametric excitation force model

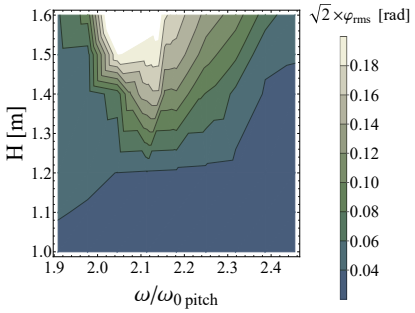

(b) RMS amplitudes for pitch from the model with NLFK forces

Figure 4. Contour plots of steady-state amplitudes of the buoy's oscillations in the pitch parametric resonance region

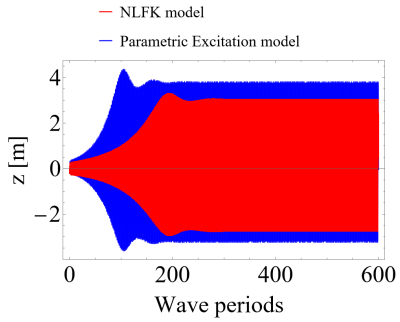

(a) Transient heave oscillations

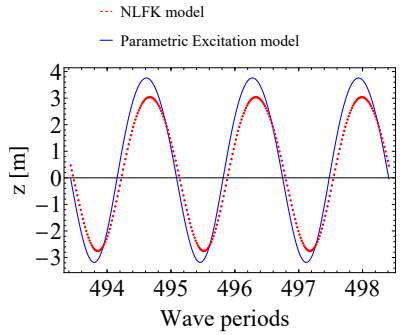

(b) Steady state heave oscillations

Figure 5. Comparison of time series between the parametric excitation model and the model with NLFK forces for the input wave conditions at Point C in Fig. 3: $\frac{\omega}{\omega_{0heave}} = 2.02$ **and** $H = 1.3$ **[**m**]**

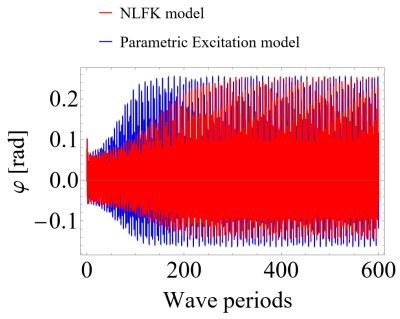

(a) Transient pitch oscillations

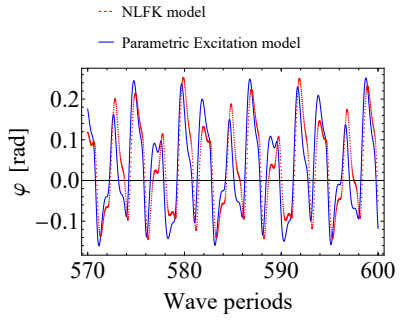

(b) Steady state pitch oscillations

Figure 6. Comparison of time series between the parametric excitation model and the model with NLFK forces for the input wave conditions at Point D in Fig. 4: $\frac{\omega}{\omega_{0pitch}} = 2.14$ **and** $H = 1.4$ **[**m**]**

6. CONCLUSION

In this study, a nondimensional analysis was applied to a previously presented model for a floating body that was able to capture parametric resonance, while being computationally efficient. This modelling approach, with an interpolated parametric excitation is much more computationally efficient than models where the excitation forces are calculated by numerical integration at each step.

By nondimensionalising the system of equations, it was possible to have a better understanding on the significance of the parameters of the model. It was observed that some parameters were negligible, which allowed for the model to be simplified by neglecting them in the interpolation. This simplification did not alter the results, but made the model run much faster.

One important consideration for further studies is that the models presented in this article, calculate the radiation forces as linearly proportional to the body velocity, with the radiation force coefficient derived considering that the body oscillates at the same frequency as the waves. This is a common approach used for single-frequency waves, which is a simplification of the more general convolution integral required in multi-frequency wave spectra [15] [16]. However, as explained in Section 5, in the regions where the parametric resonance occurs, the body oscillates at half of the wave frequency, thus the applied radiation coefficient considers the wrong oscillation frequency. This is something that shall be corrected in an extension of the model to work with polychromatic waves, as the complete convolution integral for the radiation forces must be used for that case.

ACKNOWLEDGEMENTS

The research reported in this paper is part of project no. TKP-6-6/PALY-2021. Project no. TKP-6-6/PALY-2021 has been implemented with the support provided by the Ministry of Culture and Innovation of Hungary from the National Research, Development and Innovation Fund, financed under the TKP2021-NVA funding scheme.

This work has been supported by the Hungarian National Research, Development and Innovation Fund under contract NKFI K 137726. The research reported in this paper and carried out at BME has been supported by the ÚNKP-22-3 New National Excellence Program of the Ministry for Culture and Innovation from the source of the National Research, Development and Innovation Fund.

Erik Silva Fujiyama is funded by the Tempus Public Foundation through the Stipendium Hungaricum Programme.

Josh Davidson is funded by MCIN and by the European Union NextGenerationEU/PRTR-C17.I1, as well as by IKUR Strategy under the collaboration agreement between Ikerbasque Foundation and BCAM on behalf of the Department of Education of the Basque Government.

REFERENCES

[1] Nayfeh, A. H., and Mook, D. T., 2008, *Nonlinear oscillations*, John Wiley & Sons.

[2] Daniel, D. J., 2020, "Exact solutions of Mathieu's equation", *Progress of Theoretical and Experimental Physics*, Vol. 2020 (4), p. 043A01.

[3] Kovacic, I., Rand, R., and Mohamed Sah, S., 2018, "Mathieu's equation and its generalizations: overview of stability charts and their features", *Applied Mechanics Reviews*, Vol. 70 (2).

[4] Jang, H., and Kim, M., 2019, "Mathieu instability of Arctic Spar by nonlinear time-domain simulations", *Ocean Engineering*, Vol. 176, pp. 31–45.

[5] Lelkes, J., Davidson, J., and Kalmár-Nagy, T., 2021, "Modelling of Parametric Resonance for Heaving Buoys With Position-Varying Waterplane Area", *Journal of Marine Science and Engineering*, Vol. 9 (11), p. 1162, URL `https://doi.org/10.3390/jmse9111162`.

[6] Rodríguez, C. A., and Neves, M. A., 2012, "Nonlinear instabilities of spar platforms in waves", *International Conference on Offshore Mechanics and Arctic Engineering*, American Society of Mechanical Engineers, Vol. 44915, pp. 605–614.

[7] Fujiyama, E. S., Lelkes, J., Kalmár-Nagy, T., and Davidson, J., 2025, "A Computationally Efficient Analytical Modelling Approach for Parametric Oscillations in Floating Bodies", *In Review*.

[8] Giorgi, G., Bracco, G., and Mattiazzo, G., 2021, "NLFK4ALL: An open-source demonstration toolbox for computationally efficient nonlinear Froude-Krylov force calculations", *14th WCCM-ECCOMAS Congress*, Vol. 2020, pp. 1–12.

[9] Machado, F., Malpica, N., and Borromeo, S., 2019, "Parametric CAD Modeling for open source scientific Hardware: Comparing Openscad and Freecad Python Scripts", *PLOS ONE*, Vol. 14 (12), p. e0225795, URL `https://doi.org/10.1371/journal.pone.0225795`.

[10] Babarit, A., and Delhommeau, G., 2015, "Theoretical and numerical aspects of the open source BEM solver NEMOH", *11th European Wave and Tidal Energy Conference (EWTEC2015)*, Nantes, France, Proceedings of the 11th European Wave and Tidal Energy Conference, pp. 6–11, URL `https://hal.archives-ouvertes.fr/hal-01198800`.

[11] Folley, M., 2016, *Numerical modelling of wave energy converters: state-of-the-art techniques for single devices and arrays*, Academic Press.

[12] Davidson, J., and Kalmár-Nagy, T., 2020, "A real-time detection system for the onset of parametric resonance in wave energy converters", *Journal of Marine Science and Engineering*, Vol. 8 (10), p. 819.

[13] Gavassoni, E., Gonçalves, P. B., and Roehl, D. M., 2014, "Nonlinear vibration modes and instability of a conceptual model of a spar platform", *Nonlinear Dynamics*, Vol. 76 (1), pp. 809–826.

[14] Hong, Y.-P., Lee, D.-Y., Choi, Y.-H., Hong, S.-K., and Kim, S.-E., 2005, "An experimental study on the extreme motion responses of a spar platform in the heave resonant waves", *Proceedings of the Fifteenth International Offshore and Polar Engineering Conference. Seoul, Korea*, pp. 225–232.

[15] Cummins, W., 1962, "The impulse response function and ship motions", *Tech. rep.*, Department of the Navy, David W. Taylor Model Basin, Hydromechanics Laboratory, Research and Development Report.

[16] Ahmed, A., Yang, L., Huang, J., Shalaby, A., Datla, R., Zuo, L., and Hajj, M., 2024, "Performance characterization and modeling of an oscillating surge wave energy converter", *Nonlinear Dynamics*, pp. 1–19.

Conference on Modelling Fluid Flow (CMFF'25)
The 19th International Conference on Fluid Flow Technologies
Budapest, Hungary, August 26 -August 29, 2025

LAMINAR – TURBULENT TRANSITION IN HELICALLY COILED REACTORS. AN EXPERIMENTAL STUDY WITH HIGH-SPEED PIV

C. Müller[1*], P. Kováts[1], D. Thévenin[1], K. Zähringer[1]

[1] Laboratory of Fluid Dynamics and Technical Flows, Otto-von-Guericke-Universität Magdeburg. Universitätsplatz 2, D-39106 Magdeburg, Germany. Tel.: +49 391 - 67 58654, Fax: +49 391 - 67 52840
*E-mail: conrad.mueller@ovgu.de

ABSTRACT

Helically coiled reactors (HCRs) are widely used in process engineering and biochemistry, especially in micro-reactor applications, to enhance heat and mass transfer. Their design promotes excellent radial mixing with minimal axial back-mixing. At moderate Reynolds numbers, characteristic Dean vortices form within HCRs. Increasing flow velocities lead to more complex vortex structures. The transition from laminar to turbulent flow significantly impacts reactor performance.

Various experimental and numerical studies have attempted to characterize this transition, often using a critical Reynolds number based on the curvature ratio δ = d/D. Although it is generally accepted that HCRs have higher critical Reynolds numbers than straight tubes, reported values differ widely, possibly due to variations in experimental setups and inlet conditions.

We propose a novel experimental setup designed to minimize the influence of inlet and outlet conditions. Reynolds numbers from 460 to 9,650 were examined. Initial Laser Doppler Anemometry (LDA) measurements reveal that velocity fluctuations are weaker near the inner wall and stronger near the outer wall. High-speed Particle Image Velocimetry (PIV) measurements corroborate these findings. Additionally, we demonstrate how inlet conditions influence the transition point and introduce different markers for the laminar-turbulent transition in HCRs through pseudo-3D visualizations, frequency analysis, and qualitative flow analysis.

Keywords: Helically coiled reactor, PIV, spectral entropy, transition, turbulence

NOMENCLATURE

d	[mm]	inner tube diameter
D	[mm]	coil diameter
$\delta = d/D$	[-]	curvature ratio
η	$[\frac{kg}{ms}]$	dyn. viscosity
ρ	[kg/m³]	density
Q	[-]	Q-criterion
$\dot{V}$	[l/min]	volume flow rate
u_r	[m/s]	radial velocity
u_a	[m/s]	axial velocity
f	[s^{-1}]	frequency
f_{rec}	[s^{-1}]	recording frequency
$Re = \rho u d/\eta$	[-]	Reynolds number
FEP	Fluorethylenepropylene	
LDA	Laser Doppler Anemometry	
PIV	Particle Image Velocimetry	
PMMA	Polymethylmethacrylate	

1. INTRODUCTION

The laminar-turbulent transition in helically coiled reactors is widely researched with different approaches since first studies done by Taylor [1] and White [2] in 1927. Figure 1 shows the most important literature findings regarding the transition in HCRs.

The black curves represent studies measuring the pressure drop over HCRs or curved tubes, where the transition is marked by the critical Reynolds number in function of the curvature ratio δ = d/D being the ratio of the inner diameter of the tube and to coiling diameter [3-7]. The red curves represent studies measuring the velocity field in the HCRs by using hot wire anemometry [8], LDA or (stereo-) PIV [9, 10]. The transition in those studies is determined by the velocity fluctuations in function of time with a threshold or qualitative analysis. More modern approaches use the frequency spectrum or energy dissipation rate. Outstanding here is the work of Sreenivasan and Strykowski [8] suggesting a transition region with a low Reynolds number for a first occurrence of fluctuations and a higher boundary where the flow becomes completely turbulent in the whole cross-section of the reactor tube.

As Figure 1 represents, the transition point to turbulence in HCRs is a broad range. The differences between researchers lay in different measurement

techniques and the definition of a turbulent flow itself. Recent numerical studies [11, 12] promote the lower boundary for the transition.

However, all of those studies lack a detailed visualization of the flow structures in the whole tube, often just using single points in the reactors for the analysis. These can most definitely mark a certain state of turbulence, but not the full behaviour of the transition process in HCRs with its more complex vortex structures like Lyne vortices [13] and the geometrical differences of their appearance. Moreover, the deformed pipe flow in HCRs caused by the radial forces leads to an asymmetric problem that seems to be overlooked.

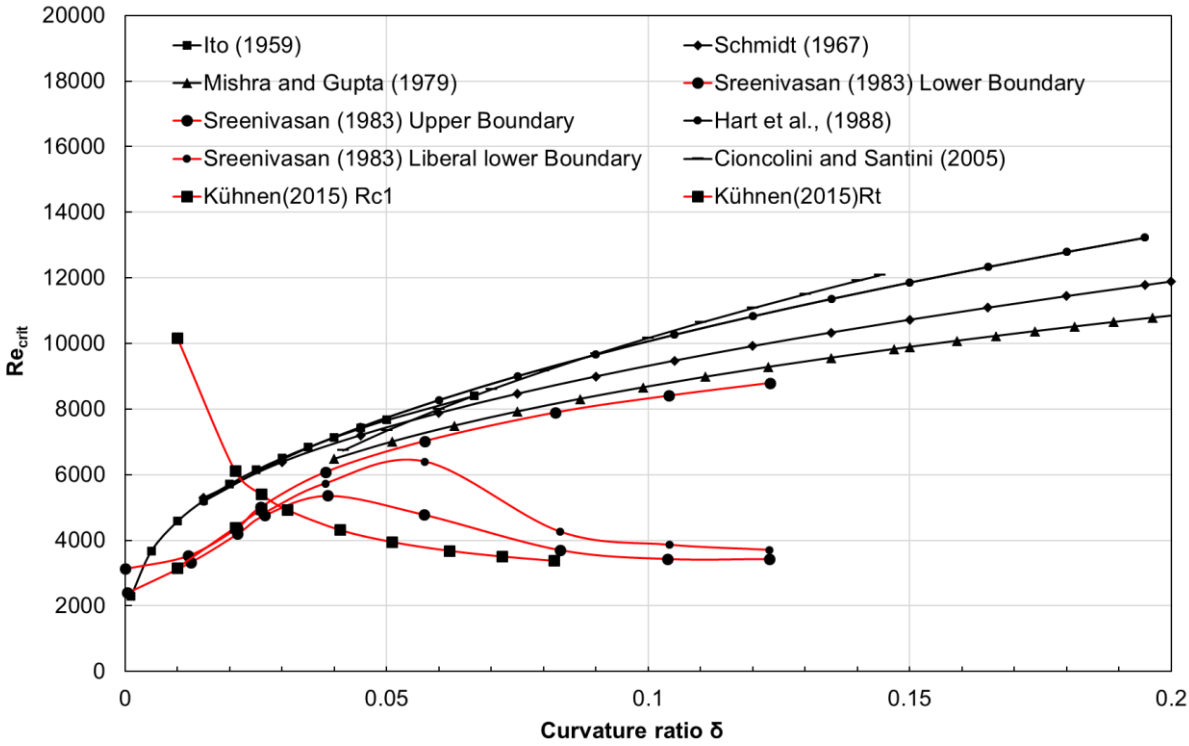

Figure 1. Laminar-turbulent transition in HCRs from literature marked by the critical Reynolds number in function of the curvature ratio δ = d/D.

This work establishes a measuring setup with a very high temporal and spatial resolution, paired with modern visualization approaches and analysis aiming for a highly resulted data base which is used to clarify the transition behaviour and pinpoint the actual transition point. Therefore, the measured Reynolds numbers cover the whole range of possible transitions as suggested by literature (Figure 1).

2. EXPERIMENTAL SETUP

The helix reactor is made of FEP-tube with an inner diameter of 10 mm and a coil diameter of 118 mm resulting in a curvature ratio of δ=0.0848. In total 50 coils are realized resulting in a tube length of 18.53 metres with additional one metre straight inlet and outlet tube. For the high speed PIV setup, the HCR is placed in an acrylic glass tank filled with a 5.25%vol. Glycerol and de-ionised water solution, which is also used as the working fluid. The solution matches the refractive index of the FEP tube (n = 1.3405) [14]. The solution has a density of 1004.045 kg/m³ and a dynamic viscosity of 0.001246 kg m^{-1} s^{-1} (measured with Netzsch Kinexus Pro+). Vestosint PMMA particles with 50 µm diameter are added to the working fluid as tracer particles.

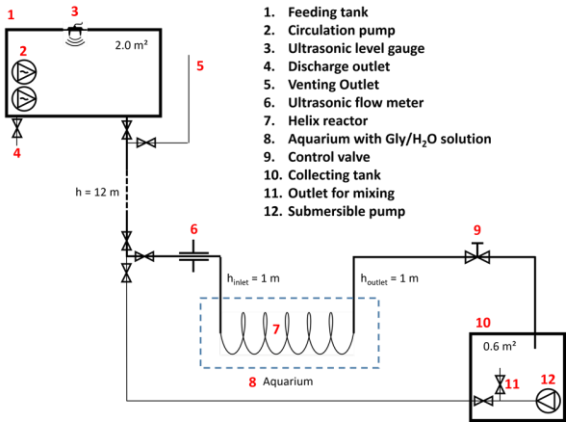

Figure 2. Flow sketch of the experimental setup.

A feeding tank is placed 12 m above the main setup creating a completely gravity driven and so pulsation free flow (Figure 2). The flow rate is measured with an ultrasonic flow metre and controlled with a needle valve at the outlet. Since the

measurements are run as a batch process and the flow rate has to stay stable, the level in the feeding tank has been controlled with a ultrasonic level sensor and a pressure level sensor.

A Phantom VEO L640 high-speed camera (2560x1600 pixels) is set in front of the tank with a 100 mm camera lens (Tokina, AT-X Pro Macro 100 F2.8D) to face the tank as shown in Figure 3 below.

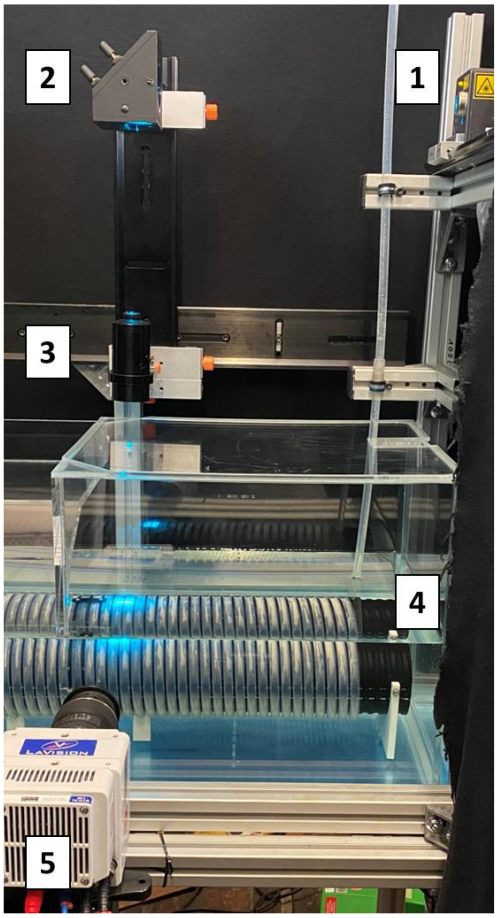

Figure 3. Optical high-speed PIV setup of the cw-laser (1), mirror (2), light sheet optics (3), aquarium with refractive index matched solution, helix reactor (4) and HS-camera (5).

The light source is a continuous-wave laser from Coherent (Model: Genesis MX488-1000 STM) with 488 nm wavelength operated at 120 mW power. The geometrical calibration results in a ~55 pixel/mm resolution. For selected Reynolds numbers in a range of 460 < Re < 9650, flow rates are set and the pixel shift is kept around 2 pixels between snapshots. The relatively small pixel shift is necessary due to the strong out-of-plane movement, since the axial velocity is 10 times higher compared to the radial velocities. For all measurements at least 2 seconds are recorded with different recording frequencies depending on the Reynolds number and listed in Table 1. Also, the axial velocity was measured with PIV, by measuring in the front section of the coil. The light sheet was therefore set in the centre of the tube and the camera was adjusted accordingly. Figure 4 shows a sketch of the setups for the radial measurements in the cross-section of the tube and for the axial measurements in the centre of the front of the coil.

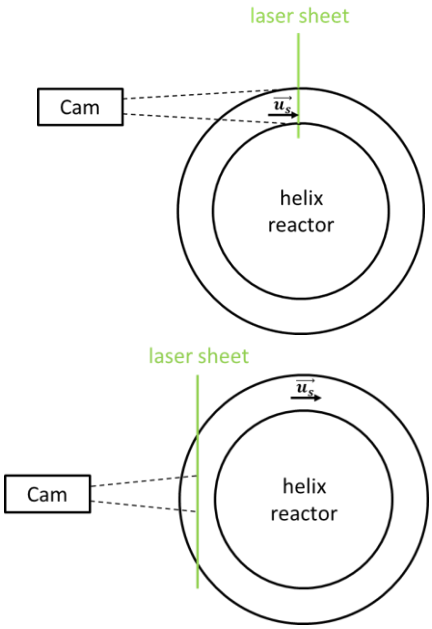

Figure 4. Sketch of the PIV set-ups. Top: radial velocity components. Bottom: axial component is measured in the centre of the tube.

The images are then processed with DaVis 10.2 (LaVision) and visualized with ParaView 5.10.

All measurements are taken at the 40th coil of the HCR where the influence of inlet and outlet vanish. This was proven in previous tests with LDA measurements [15] and will also be validated here with the axial PIV measurements (see Figure 6).

Table 1. Recording parameters of radial and axial PIV measurements

		Radial	Axial
Re	$\dot{V}$	f_{rec}	f_{rec}
$[-]$	$[l/min]$	$[kHz]$	$[kHz]$
460	0.27	0.4	1.0
920	0.54	0.6	2.0
1370	0.80	0.8	3.0
2100	1.23	1.1	4.6
2750	1.61	1.4	6.0
3660	2.14	1.8	8.0
4580	2.68	2.2	10.0
5510	3.22	2.6	12.0
6410	3.75	3.0	12.0
7340	4.29	3.4	12.0
8240	4.82	3.8	12.0
9170	5.36	4.2	12.0
9650	5.64	4.5	12.0

3. POSTPROCESSING

The postprocessing is done in DaVis and consists of an image calibration, a subtraction of a median Gauss filter to enhance the particle images and the PIV processing followed by a vector postprocessing step as clean-up of erroneous vectors. The resulting vector fields are further treated to identify the transition point to turbulence.

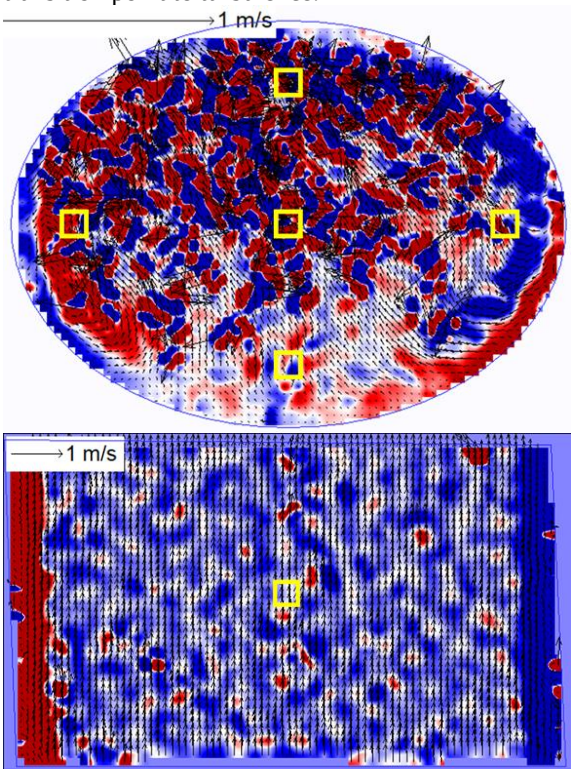

Figure 5. Instantaneous flow fields of the radial velocity (top) and the axial velocity (bottom) with the extraction points of the velocity over time marked in yellow.

First, the local velocity is extracted at 5 points in the cross-section, marked with yellow boxes in Figure 5, and plotted in function of time (Figure 7). In addition, the centre velocity from the axial velocity field (Figure 5 bottom) is extracted and plotted over time to visualise the fluctuations (Figure 8).

Second, the frequency spectrum is analysed from the axial velocity over time plots using FFT (Table 2 and Figure 10).

Third, pseudo-3D vortex structures are reconstructed (Figure 11) from the vector fields. Therefore, the vector fields of the tube cross-section (radial velocity) are stacked in a third plane representing time. This third axis is normalized by dividing the superficial velocity with the recording frequency resulting in the third dimension being in metres. A detailed description of those pseudo 3D-visualizations is found in Müller, Kováts [16]. From these 3D-fields vortices are represented with the Q-Criterion as isosurface coloured by the Z-vorticity for a qualitative analysis.

4. RESULTS

In order to test the independency of the measurement position from the inlet and outlet conditions, the axial velocity was measured in each coil. It is then extracted as velocity over time plot at the centre position (yellow square in Figure 5 bottom image) and its standard deviation normalized by the average velocity is plotted in function of the coil number in Figure 6.

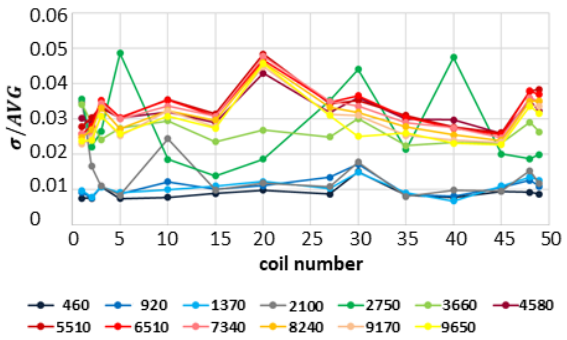

Figure 6. Normalized standard deviation of all Reynolds numbers in function of the coil number.

After the first 3 coils where the initial straight tube flow gets forced into the radial flow structure the standard deviation stabilizes due to the re-laminarizing effects of the coiled flow. However, only after 30-40 coils a full stabilization is realized. Especially at moderate Reynolds numbers (Re = 2100, 2750, 3660) the flow needs at least 30 coils to stabilize. Also noticeable is the impact of the outlet with a sudden increase of the standard deviation for the last 2 coils.

The normalized standard deviation (also known as turbulence intensity) of the axial velocities sorts itself into two regions. Low Reynolds numbers up to Re = 2200 have a σ/AVG of 0.01. Reynolds numbers higher than Re = 3830 have a σ/AVG value of 0.03 to 0.04, so four times higher. Kühnen, Braunshier [9] described that increase in standard deviation also as indicator for the laminar turbulent transition. A transition area can be noticed for Reynolds numbers between $2200 < Re < 3830$ where the curves do not fit to the above mentioned groups.

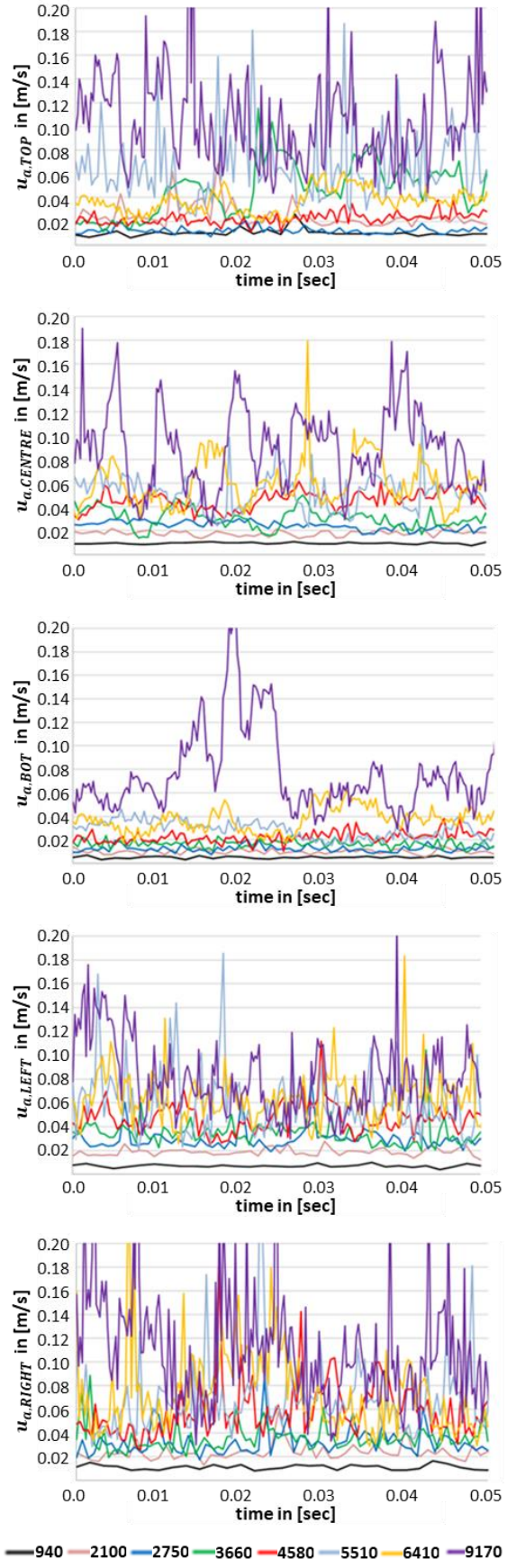

Figure 7. Extracted radial velocity over time of different Reynolds numbers. Locations from top to bottom: Top, Centre, Bottom, Left, Right.

Figure 7 above shows the velocity in function of time from the 5 points shown in Figure 5. From these plots it is obvious, that with rising Reynolds number the fluctuations of the flow become stronger, there are also clear differences depending on the location in the cross-section of the coil. While the fluctuations start to become strong at Re = 4500 in the top, as well as left and right where the Dean vortices are situated, they are much less pronounced in the centre and almost neglectable in the bottom.

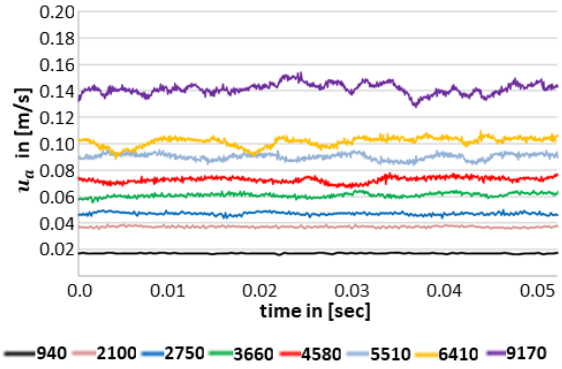

Figure 8. Extracted axial velocity over time of different Reynolds numbers.

The axial velocities over time in Figure 8 have a similar trend with an increase of fluctuations with rising Reynolds number. When taking a look onto a full measurement period (Figure 9) not only high frequency fluctuations but also oscillation waves with lower frequencies become visible.

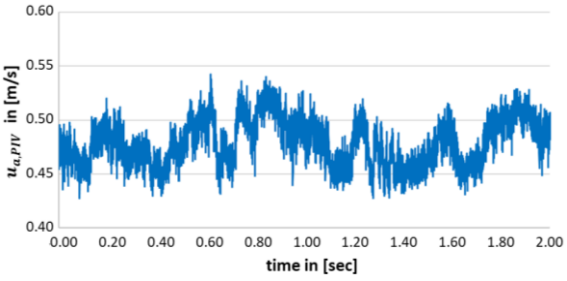

Figure 9. Extracted axial velocity over time of Reynolds number 2880 for the whole measurement time of 2 seconds.

The following Figure 10 shows the frequency spectra of some Reynolds numbers for the axial measurements. As expected, in a completely laminar flow (Re=480) no frequencies could be detected. At medium Reynolds numbers some frequencies are more pronounced. With rising Reynolds number, the frequency spectrum broadens until no frequencies stand out anymore. The two highest detected frequencies are listed in Table 2 below.

Table 2. Highest detected frequencies from FFT for selected Reynolds numbers.

Re	f_1	f_2
460	-	-
2750	1 Hz	3 Hz
3660	6 Hz	36 Hz
5510	7 Hz	22 Hz
9650	Spectrum	

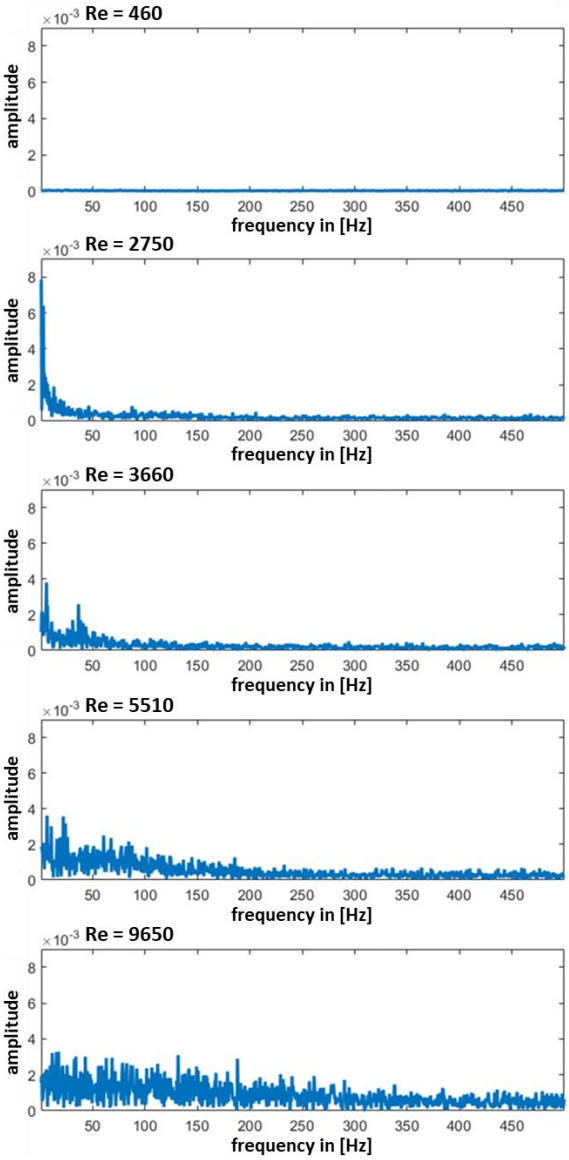

Figure 10. Frequency spectra of selected Reynolds numbers from the FFT analysis of extracted axial velocities.

For a more detailed analysis of the flow it seemed reasonable to visualize the flow as a whole. The instantaneous flow fields are therefore extended to pseudo-3D-visualizations. Figure 11 below shows a selection of Reynolds numbers in an unrolled top-down view of the helix tube. The flow goes from left to right, visualized is the vortex occurrence by the Q-Criterion, coloured with the Z-Vorticity. The represented pseudo distance of 100 mm contains around 500 images depending on the recording frequency and superficial velocity. At low Reynolds number the counter rotating Dean vortices are clearly visible as horizontal stripes near the tube walls indicating a stable and laminar flow. With increasing Reynolds number, Lyne vortices near the centre of the cross-section occur. They merge with the Dean vortices on either side and finally disappear, indicating first instabilities and transition to turbulence (Figure 11, Re = 2750). With even faster flows the Lyne vortices appear with higher frequency and are more unstable (Re=3660). At a certain point the Lyne vortices are no longer distinguishable and the whole flow becomes turbulent. Even the Dean vortices become smeared indicating a completely turbulent flow behaviour (Figure 11, Re = 5510). At the highest measured flow rate with a Reynolds number of Re = 9650, the additional vortex structures have even the same intensity and size as the Dean vortices. It has to be noted, that with increasing Reynolds number the overall vorticity also rises steadily.

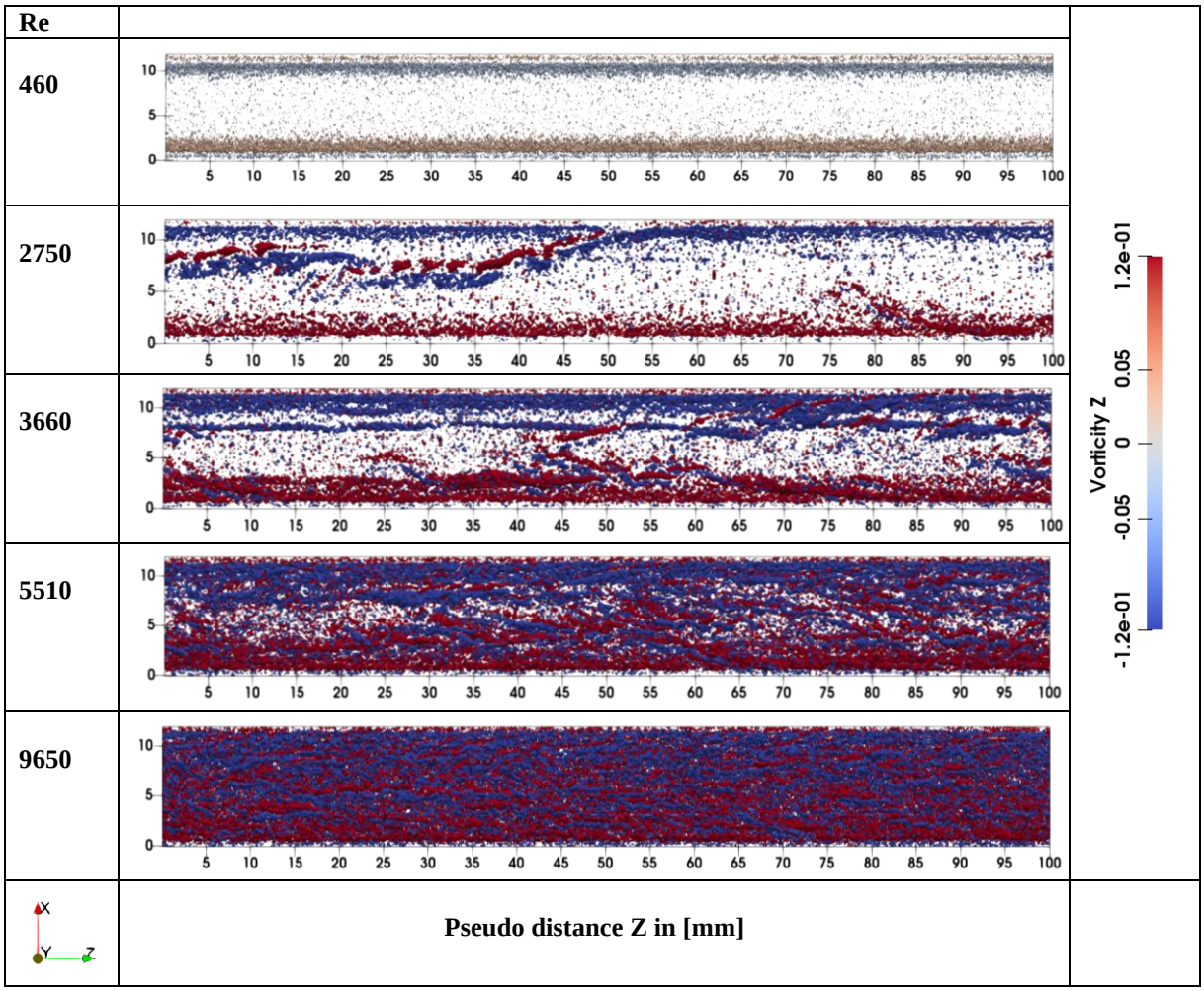

Figure 11. Pseudo-3D-visualizations of the radial velocity fields. Q = 0.0035 to 0.05; Z-Vorticity = - 0.125 to 0.125 (for Re = 460; Q = 0.00035 to 0.05).

5. CONCLUSIONS

In this study, the laminar-turbulent transition of helical coils is examined by LDA and PIV measurements. The independence of inlet and outlet conditions was proven for the set-up with a HCR of 50 coils in a range of coil numbers 30 to 40.

The qualitative analysis of the velocities, measured in the 40th coil, confirms the findings of Sreenivasan and Strykowski [8]. Depending on the location in the cross-section of the helix the flow behaves differently. While in the outer region of the HCR, or here in the top of the cross-section, fluctuations indicate turbulence at lower Reynolds numbers (Re = 5700), the turbulent behaviour in the inner region, here the bottom of the cross-section, is only pronounced at the highest measured Reynolds number of Re = 9650.

The FFT analysis of the axial velocities did not show detectable frequencies for laminar flow conditions. In the transition area some characteristic frequency peaks appear, and a broadening of the frequency spectrum in the completely turbulent region can be recognized.

The pseudo-3D-visualizations of the radial velocities showed the first instabilities as Lyne vortices at Reynolds number Re = 2750 and a fully turbulent flow behaviour at Re = 5510.

OUTLOOK

While searching for the laminar-turbulent transition point in HCRs it becomes clear, that in the asymmetric flow a high dependency on the location is given. The here presented markers for the transition point are either focused on one point in the flow or are just of qualitative nature. For quantitative analysis, measurements of high spatial and temporal resolution are necessary to capture the occurring vortex structures with low experimental noise. A multitude of markers can help to capture all flavours of turbulence making a difference between stable or frequent structures like Lyne vortices and fully turbulent flow with a high vortex dissipation rate. A holistic view of all markers is necessary as validation but also to make a final decision on the transition point.

ACKNOWLEDGMENTS

Funded by the Deutsche Forschungsgemeinschaft (DFG, German Research Foundation) – 444994527. The authors would like to thank their student Justus Herzig for his help and support with carrying out the measurements.

REFERENCES

1. Taylor, G.I., *The criterion for turbulence in curved pipes.* Royal Society Publishing, 1927.
2. White, C.M., *Streamline flow through curved pipes.* Proceedings of the Royal Society of London. Series A, Containing Papers of a Mathematical and Physical Character, 1927. **123**(792): p. 645-663.
3. Itó, H., *Friction Factors for Turbulent Flow in Curved Pipes.* Journal of Basic Engineering, 1959: p. 123-132.
4. Schmidt, E.F., *Warmeubergang und Druckverlust in Rohrschlangen.* Zeitschrift fur Technische Chemie, Verfahrenstechnik und Apparatewesen, 1967. **39**: p. 781-832.
5. Mishra, P. and S.N. Gupta, *Momentum Transfer in Curved Pipes 1. Newtonian Fluids.* Ind. Eng. Chern. Process Des. Dev., 1978. **18**.
6. Hart, J., J. Ellenberger, and P.J. Hamersma, *Single and Two Phase Flow through helically coiled tubes.* Chemical Engineering Science, 1988. **43**: p. 775-783.
7. Cioncolini, A. and L. Santini, *An experimental investigation regarding the laminar to turbulent flow transition in helically coiled pipes.* Experimental Thermal and Fluid Science, 2006. **30**(4): p. 367-380.
8. Sreenivasan, K.R. and P.J. Strykowski, *Stabilization effects in flow through helically coiled pipes.* Experiments in Fluids, 1983. **1**: p. 31-36.
9. Kühnen, J., et al., *Subcritical versus supercritical transition to turbulence in curved pipes.* Journal of Fluid Mechanics, 2015. **770**.
10. Kühnen, J., et al., *Experimental investigation of transitional flow in a toroidal pipe.* Journal of Fluid Mechanics, 2013. **738**: p. 463-491.
11. Gelfgat, A.Y., *A comparative study on instability of steady flows in helical pipes.* Fluid Dynamics Research, 2020. **52**(1).
12. Canton, J., P. Schlatter, and R. Örlü, *Modal instability of the flow in a toroidal pipe.* Journal of Fluid Mechanics, 2016. **792**: p. 894-909.
13. Müller, C., P. Kováts, and K. Zähringer, *On the existence, formation and stabilization of Lyne vortices in helically coiled reactors at moderate Reynolds numbers*, in *20th International Symposium on the Application of Laser and Imaging Techniques to Fluid Mechanics, Lissabon, Portugal*. 2022.
14. Kováts, P., et al., *Mixing characterization in different helically coiled configurations by laser-induced fluorescence.* Experiments in Fluids, 2020. **61**(9).
15. Müller, C., P. Kováts, and K. Zähringer, *Experimental investigation of the laminar-turbulent transition in helically coiled reactors with LDA*, in *Fachtagung "Experimentelle Strömungsmechanik" GALA, München, Deutschland*. 2023.
16. Müller, C., P. Kováts, and K. Zähringer, *Experimental characterization of mixing and flow field in the liquid plugs of gas–liquid flow in a helically coiled reactor.* Experiments in Fluids, 2021. **62**(9).

Conference on Modelling Fluid Flow (CMFF'25)
The 19th International Conference on Fluid Flow Technologies
Budapest, Hungary, August 26 - August 29, 2025

REDESIGNED ADJUSTABLE DIAPHRAGM FOR CONTROLLING AND MITIGATING THE SWIRLING FLOW INSTABILITIES FROM THE CONICAL DIFFUSER OF HYDRAULIC TURBINES

Adrian STUPARU[1], Constantin TANASA[2] and Alin BOSIOC[3]

[2] Corresponding Author. Research Institute for Renewable Energies, "Politehnica" University Timisoara, Victoriei Sq., No.1
E-mail: constantin.tanasa@upt.ro
[1, 3] Department of Hydraulic Machinery, "Politehnica" University Timisoara, Victoriei Sq., No.1, adrian.stuparu@upt.ro, alin.bosioc@upt.ro

ABSTRACT

Currently, the energy market requires the use of renewable energy sources, especially photovoltaic and wind. During the year, these energy sources have large fluctuations. The machines that can compensate for the energy fluctuations given by fluctuating sources are hydraulic turbines. Thus, they end up operating at points other than those for which they were designed, with negative consequences for the operation of the machine. One of the consequences of operating hydraulic turbines at discharges other than the nominal one (for example, the Francis turbine) is the pressure pulsations that appear due to the self-induced instability generated by the swirling flow, in the conical diffuser. One of the modern techniques for mitigating the pressure pulsations that appear at partial discharges in hydraulic turbines (especially those with fixed blades) is the adjustable diaphragm introduced downstream of the conical diffuser. It has previously been shown that this technique can mitigate the swirling flow and the associated pressure fluctuations but can lead to an increase in hydraulic losses. Thus, the present work shows that by redesigning this diaphragm, a compromise can be found between the mitigation of pressure pulsations (dynamic component) and hydraulic losses, respectively the pressure recovery in the conical diffuser (energy component). The results obtained through 3D numerical simulation show that the pressure pulsations have a significant decrease, and the hydraulic losses are minimal when the turbine operates at 70% of the nominal flow.

Keyword: adjustable diaphragm; conical diffuser; hydraulic losses; hydraulic turbine; pressure pulsation; swirling flow

NOMENCLATURE

A_d	$[m^2]$	diaphragm interior area
A_o	$[m^2]$	test section outlet area
D_t	$[m]$	reference diameter from the throat of the test section,
V_t	$[m/s]$	reference velocity from the throat of convergent-divergent test section
d	$[m]$	diaphragm interior diameter
f	$[Hz]$	dominant frequency
ρ	$[kg/m^3]$	density
sh_r	[%]	diaphragm device shutter area
c_p	[-]	pressure recovery coefficient
$\overline{p}_{L0}$	[kPa]	mean pressure from the test section throat
$\overline{p}$	[kPa]	mean pressure
Q	[l/s]	nominal flow
h_p	[m]	hydraulic losses
p_{in}	[kPa]	pressure from the inlet test section
p_{out}	[kPa]	pressure from the outlet of the test section

1. INTRODUCTION

The acute problem faced by hydraulic turbines (especially those with fixed blades such as the Francis turbine), which are imposed by the energy market to operate at operating points far from the optimal one, is due to fluctuating energies such as photovoltaic and wind [1, 2]. This type of operation (at part load) leads to the appearance of the helical vortex or vortex rope phenomenon, in the conical diffuser of the turbine [3]. Vortex rope is the main phenomenon that produces severe pressure fluctuations in the conical diffuser leading over time to cracks or breaks of the runner blades, cracks in the bearings or shaft, tearing of the ogive, etc [4].

To eliminate or to mitigate the instabilities from the conical diffuser, different techniques have been implemented in hydraulic turbines [5-8]. These methods lead to reducing the pressure pulsations over a narrow regime, but they are not effective or even increase the unwanted effects [9-11].

The present paper is focusing on the modern adjustable diaphragm passive control technique, to mitigate the instabilities associated to the vortex rope from the conical diffuser of hydraulic turbines (e.g., Francis turbine), operated at part load conditions. It is mentioned that the proof of concept of the adjustable diaphragm control technique was presented previously [12, 13]. The results obtained previously clearly show that the mitigation of the swirling flow instabilities is directly proportional to the narrowing of the diaphragm surface towards the centre of the conical diffuser axis (the diaphragm is mounted at the outlet of the conical diffuser). Anyway, it is shown that the hydraulic losses have an increase since the shutter area of the diaphragm is close to the diffuser centre and exist a small area where the diaphragm can work without increasing the hydraulic losses but still mitigate the amplitudes associated to the instabilities of the vortex rope.

This paper presents a 3D numerical analysis of pressure filed from dynamic and energetic point of view using a redesigned adjustable diaphragm called IRiS device (Fig. 1). The second section presents the problem setup for numerical analysis, including the computational domain and boundary conditions. Section 3 analyzes the flow field quantifying the hydraulic losses and the unsteady pressure field with and without IRiS device. The conclusions are summarized in last section.

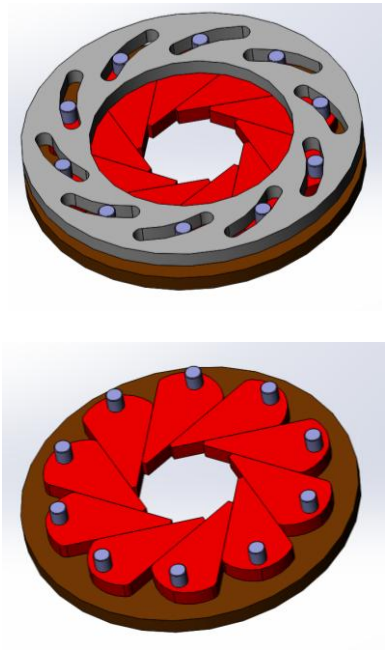

Figure 1. Sketch of the IRiS device.

2. COMPUTATIONAL DOMAIN AND BOUNDARY CONDITIONS

The computational domain corresponds to convergent-divergent part of the swirling flow apparatus developed at Politehnica University Timisoara (UPT) [14]. The convergent section is bordered by the annular inlet section and the throat (Fig. 2). The annular inlet section is considered just downstream to the runner blades. The divergent section includes a discharge cone with semi-angle of 8.5° similar to FLINDT project [15] and a pipe. Three values of the IRiS interior diameter of d = 0.143, 0.134, 0.124 m are considered in this numerical study. According to Figure 2 the IRiS device is located at the outlet of the conical diffuser. Table 1, shows the areas ratio between IRiS interior area and outlet test section area.

Table 1.

IRiS interior diameter d [m]	IRiS interior area A_d [m^2]	Test section outlet area A_o [m^2]	Shutter ratio sh_r [%]
0.143	0.016	0.02	20
0.134	0.014	0.02	30
0.124	0.012	0.02	40

The computational domain previously presented in [12] is presented in Fig. 2. A mixed mesh with approximately 2.8M cells is generated on each computational domain with and without IRiS, Fig. 3. The most distorted element has an Equisize skew value of 0.87.

Boundary conditions imposed for each case uses a velocity profile at the inlet, and the outflow condition on the outlet section. The inflow boundary conditions are obtained computing the flow upstream of the numerical domain in our previous research work. As a result, the inlet velocity profiles (axial, radial and circumferential velocity components) as well as the turbulent quantities (kinetic energy and turbulence dissipation rate) corresponding to a runner speed of 920 rpm are imposed on annular inlet section. Figure 4, shows the velocity profiles from the inlet test section [12]. 3D unsteady numerical simulations with and without IRiS were performed using the Ansys FLUENT 2023 R2 software in order to assess the new approach.

For the numerical setup it was used k-ω GEKO turbulence model. This turbulence model is relatively new introduced to Ansys FLUENT and captures more accurate the flow specifics to hydraulic machines, [17]. The advantage of this turbulence model is that it has enough flexibility to cover a wide range of applications. The model provides free parameters that you can adjust for specific types of applications, without negative impact on the basic calibration of the model.

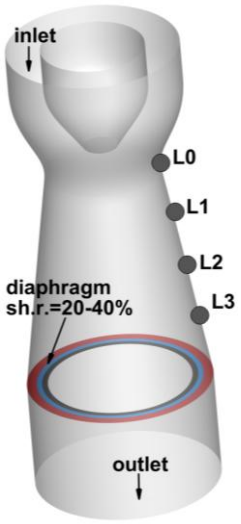

Figure 2. 3D computational domain of the case with diaphragm.

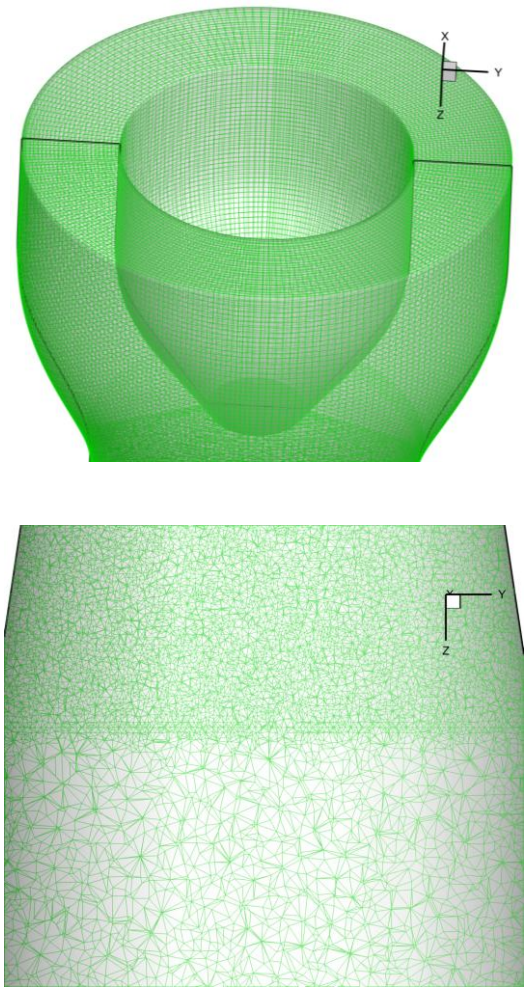

Figure 3. Detail of mesh domain. Inlet of the domain (up) and outlet (down).

This is a tool for model optimization but requires a proper understanding of the impact of these coefficients to avoid mistuning. It is important to emphasize that the model has strong defaults, so one can also apply the model without any fine-tuning, and one should make sure that any tuning is supported by high-quality experimental data.

For this study the default value of the turbulence parameters was applied. The time step applied for the unsteady simulation for all the investigated cases was t = 0.002 s. For our investigation, 5000 time steps were employed for each case, corresponding to a flow time of 10 seconds, for obtaining a stable flow structure. All numerical solutions were converged down to residuals as low as 10^{-4}. Pressure monitors denoted L0…L3 have been placed on 4 levels. The axial distance between two consecutive pressure taps located on the cone wall is 50 mm.

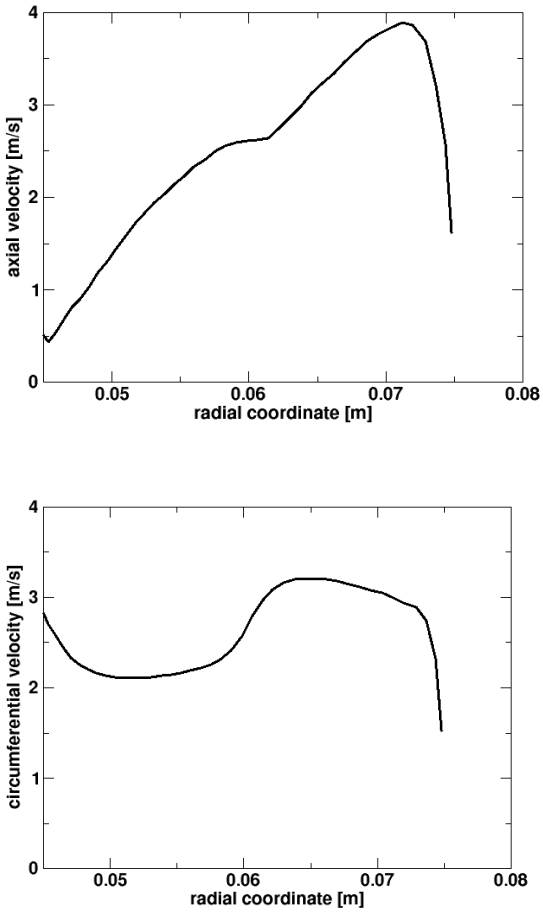

Figure 4. Velocity profiles from the inlet test section [12].

3. NUMERICAL RESULTS

3.1. Unsteady pressure analysis

Numerical simulations for turbulent swirling flow in the test section from UPT, have been

performed for 3 cases of the IRiS device and for the case without IRiS. Figures 5 to 8, shows a first set of numerical results of pressure iso-surface for each case. One can clearly observe that the helical vortex structure still evolves during the IRiS shuttering for all cases, but the corresponding pressure pulsations are mitigated due to the eccentricity is significantly reduced. The above statement is supported by unsteady analysis of pressure signals from the pressure monitors of the domain (Fig. 9).

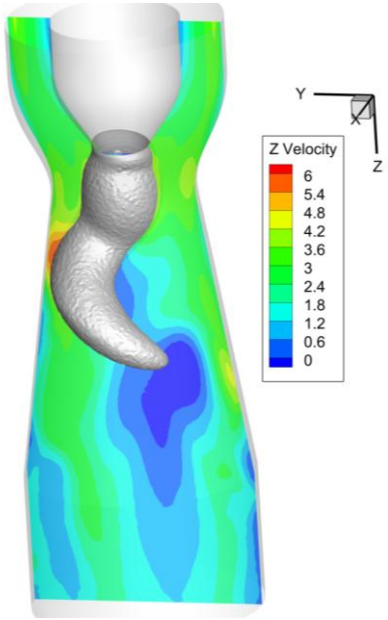

Figure 5. Pressure iso-surface for the case without diaphragm, t=10 s, p=37.700 Pa.

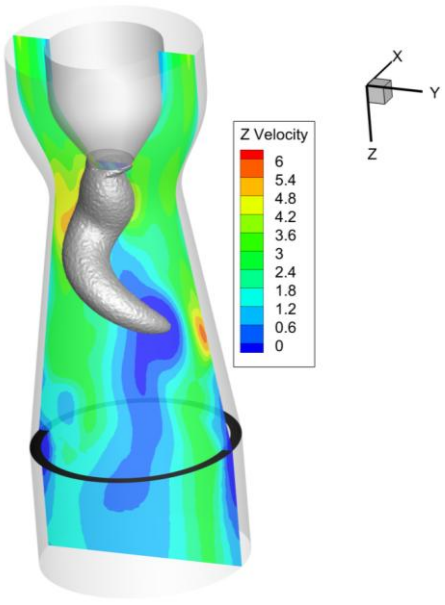

Figure 6. Pressure iso-surface for the case with diaphragm diameter of d = 0. 143 m, t=10 s, p=37.700 Pa.

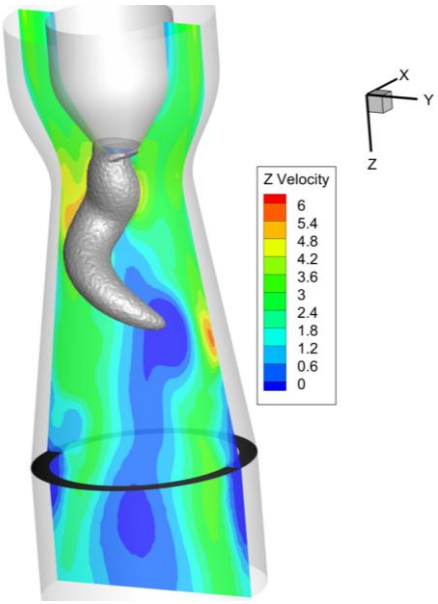

Figure 7. Pressure iso-surface for the case with diaphragm diameter of d = 0.134 m, t=10 s, p=37.700 Pa

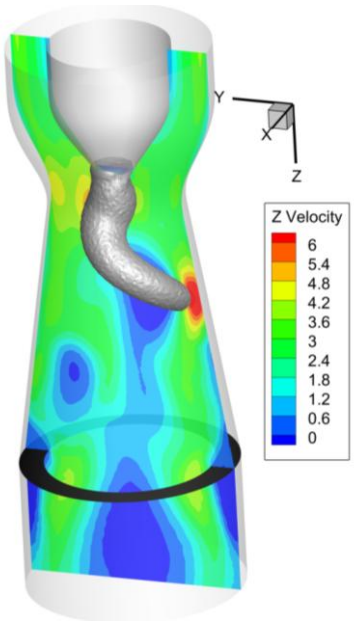

Figure 8. Pressure iso-surface for the case with diaphragm diameter of d = 0.124 m, t=10 s, p=37.700 Pa

For the investigated technique, in this paper, it is obviously that the IRiS device provides a significant drop in amplitude, while the frequency remains constant (f~14 Hz) for all cases. The shutter ratio sh_r = 20% and 40% provides the largest amplitude reduction (up to 60%), compared to the case without IRiS device. The sh_r = 30% has a smaller decrease (up to 32%), because at that configuration the vortex sheet occurs – the flow region formed between stagnant region and the main swirling flow [3].

We conclude that the passive method presented in this paper, has the potential to effectively mitigate the pressure fluctuations in decelerated swirling flow with precessing helical vortex.

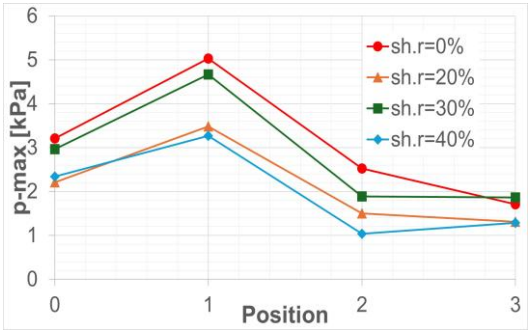

Figure 9. Pressure amplitudes corresponding to pressure taps from the test section domain.

3.2. Mean pressure analysis

The main purpose of the conical diffuser of hydraulic turbines is to convert as much as possible the kinetic energy at the runner outlet into pressure potential energy with minimum hydraulic losses.

This energy conversion is expressed by the wall pressure recovery coefficient c_p, which it is given in dimensionless form by Eq. (2),

$$c_p = \frac{\overline{p} - \overline{p}_{L0}}{\rho \frac{V_t^2}{2}} where V_t = \frac{Q}{\pi \frac{D_t^2}{4}} \qquad (1)$$

where $\overline{p}_{L0}$ is the mean pressure on the wall at L0 level,$\overline{p}$ is the mean pressure measured downstream on the cone wall, $\rho = 998$ kg/m^3 is the water density, V_t is the bulk velocity in the throat and $D_t = 2R_t = 0.1$ [m] is the throat diameter corresponding to L0 level, Q is the nominal flow. The distribution of the pressure coefficient c_p [-] along the cone wall is plotted in Figure 10. The wall pressure recovery in the first part of the cone up to L1 level is negligible if it uses the diaphragm. In contrast, a significant improvement of the wall pressure recovery is obtained downstream to L1 level delaying the separation flow on the wall. For instance, the pressure recovery coefficient (at the wall) is increased up to 30% in the middle of the conical diffuser (on L2 level). For real turbines, this improved pressure recovery in the discharge cone is reflected in an increase of the overall turbine efficiency far from the best efficiency point, especially for low-head hydraulic turbines, since the main fraction of the hydraulic losses at such operating points are associated with the swirl in the draft tube cone. It is expected when the pressure recovery on the cone wall is improved it will have diminished additional hydraulic losses associated to the vortex rope.

However, the hydraulic losses increase on the cone once the diaphragm obstructs the flow more and more. The hydraulic losses cannot be correctly quantified based on experimental data available.

Tănasă et al. [16], reveal that the hydraulic losses are less than half of the value got for the case with vortex rope up to the relative shutter area of 50% and no larger than twice up to the relative shutter area ratio of 70%, respectively.

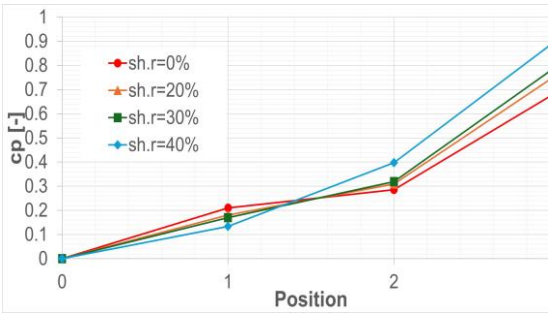

Figure 10. Pressure recovery coefficients vs. axial coordinate.

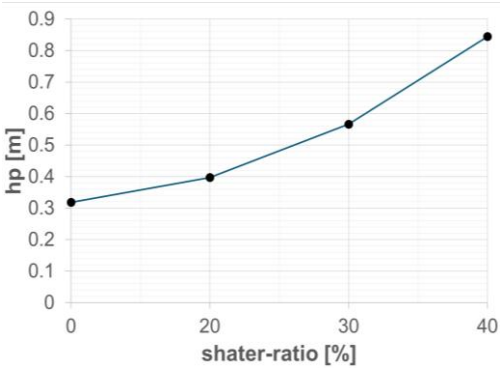

Figure 11. Hydraulic losses versus shutter ratio

Figure 11 shows the loss coefficient defined as:

$$hp = \frac{p_{in} - p_{out}}{\rho g}[m] \qquad (2)$$

We examine the *hydraulic losses* variation with respect to the diaphragm shutter ratio. One can see from Fig. 11 that the hydraulic losses reach the maximum values for the highest shutter ratio of 40%. The evolution of the losses in the cone emphasizes the rapid increase in the hydraulic losses at partial discharge. This is also associated with an increase in the overall performance of the cone as shown in the variation of the pressure recovery coefficient at the wall. It is obvious when throttling the flow at the outlet of the cone, using the IRiS device, the hydraulic losses increase, but also the pressure recovery increase.

4. CONCLUSIONS

The paper reintroduces the concept with adjustable diaphragm (as IRiS device), for mitigating the swirling flow instabilities from the conical diffuser of hydraulic turbines operated at part load conditions. Full 3D unsteady numerical simulations with and without IRiS were performed in order to assess the dynamic and energy recovery performances of the concept. The numerical results clearly show that the helical vortex evolves in a weaker structure when the IRiS is switched on. As a result, the amplitude of the unsteady pressure signals associated to the helical vortex are mitigated up to 60% in the amplitude with constant frequency in all cases. The evolution of the losses in the cone emphasizes the rapid increase in the hydraulic losses at partial discharge. This is also associated with an increase in the overall performance of the cone as shown in the variation of the pressure recovery coefficient at the wall. It is obvious when throttling the flow at the outlet of the cone, using the IRiS device, the hydraulic losses increase but also the pressure recovery increase. It is recommended to operate the IRiS device when the turbine operates over a wide range, far from the best efficiency point (BEP), so that hydraulic losses are minimal with high energy recovery and small pressure pulsations.

Consequently, in our opinion, the above conclusions recommend the IRiS device to be considered for either new or refurbished hydraulic turbines to improve both efficiency and safety of the operation far from the best efficiency point.

ACKNOWLEDGEMENTS

„This work was supported by a grant of the Ministry of Research, Innovation and Digitization, CCCDI - UEFISCDI, project number PN-IV-P7-7.1-PED-2024-1209, within PNCDI IV."

REFERENCES

[1] Renewable Systems Integration, U.S. Department of Energy, https://www.energy.gov/

[2] Rekioua, D., 2023, „Energy Storage Systems for Photovoltaic and Wind Systems: A Review", Energies, **16**, 3893. https://doi.org/10.3390/en16093893

[3] Nishi M, Matsunaga S, Kubota T, Senoo Y, 1982, "Flow regimes in an elbow-type draft tube", Proceedings of 11th IAHR Symposium on Hydraulic Machinery and Systems, Amsterdam p 38.

[4] Baya, A., Muntean, S., Câmpian, V. C., et al., 2010, „Experimental investigations of the unsteady flow in a Francis turbine draft tube cone", 25th IAHR Symposium on Hydraulic Machinery and Systems, Timisoara, Romania, IOP Conf. Series: Earth and Environmental Science **12**, doi:10.1088/1755-1315/12/1/012007

[5] Thike, R.H., 1981, „Practical solutions for draft tube insatbility", *Water Power and Dam Construction*, **33**(2), pp.31-37.

[6] Pappilon, B., Sabourin, M., Couston, M., and Deschenes, C., 2002, "Methods for air admission in hydro turbines", *Proceedings of the 21st IAHR Symposium on Hydraulic Machinery and Systems*, Lausanne, Switzerland, pp. 1-6.

[7] Kjeldsen, M., Olsen, K., Nielsen, T., and Dahlhaug, O., 2006, "Water injection for the mitigation of draft tube pressure pulsations", *IAHR International Meeting of W.G. on Cavitation and Dynamic Problems in Hydraulic Machinery and Systems*, Barcelona, Spain.

[8] Nishi, M., Wang, X. M., Yoshida, K., Takahashi, T., and Tsukamoto, T., 1996, "An Experimental Study on Fins, Their Role in Control of the Draft Tube Surging", *Hydraulic Machinery and Cavitation, in Cabrera, E., et al., eds., Kluwer Academic Publishers*, Dordrecht, The Netherlands, pp. 905-914.

[9] Bosioc, A., Susan-Resiga, R., Muntean, S. and Tanasa, C., 2012, "Unsteady Pressure Analysis of a Swirling Flow with Vortex Rope and Axial Water Injection in a Discharge Cone", *J. Fluids Eng. – Trans. ASME*, **134**(8), 081104, pp. 1-11.

[10] Tanasa, C., Susan-Resiga, R. F., Muntean, S., and Bosioc, A. I., 2013, "Flow-Feedback Method for Mitigating the Vortex Rope in Decelerated Swirling Flows", *J. of Fluids Eng.*, **135**(6).

[11] Tanasa, C., Bosioc, A., Stuparu, et al., 2023, "A Perspective Review of Passive Techniques Applied to Control the Swirling Flow Instabilities From the Conical Diffuser of Hydraulic Turbines." *ASME. Appl. Mech. Rev.* January 2024; **76**(1): https://doi.org/10.1115/1.4056895

[12] Tanasa, C., Susan-Resiga, R. F., Muntean, S., et al., 2015, „Numerical Assessment Of A New Passive Control Method For Mitigating The Precessing Helical Vortex In A Conical Diffuser", *Conference on Modelling Fluid Flow (CMFF'15)*, The 16th International Conference on Fluid Flow Technologies, Budapest, Hungary.

[13] Tanasa, C., Bosioc, A., et al., 2019, „A novel passive method to control the swirling flow with vortex rope from conical diffuser of hydraulic turbines with fixed blades", *Appl. Sci.*, **9**, 4910; doi:10.3390/app9224910

[14] Susan-Resiga, R., Muntean, S., Hasmatuchi, V., Anton, I., and Avellan, F., 2010, "Analysis and Prevention of Vortex Breakdown in the Simplified Discharge Cone of a Francis Turbine", *J. Fluids Eng. – Trans. ASME*, **132**(5), pp. 1-15.

[15] Avellan, F., 2000, "Flow Investigation in a Francis Draft Tube: The FLINDT Project", *Proc. Of the 20th IAHR Symposium on Hydraulic Machinery and Systems*, Charlotte, USA, p. DES-11.

[16] Tănasă, C., Muntean, S., Ciocan, T. and Susan-Resiga, R.F., 2016, "3D Numerical Simulation versus Experimental Assessment of Pressure Pulsations Using a Passive Method for Swirling Flow Control in Conical Diffusers of Hydraulic Turbines", *IOP Conf. Series: Earth Environ. Sci.* **49**(8), 082018, 1-10. doi: 10.1088/1755-1315/49/8/082018.

[17] ANSYS Fluent Help documentation

Conference on Modelling Fluid Flow (CMFF'25)
The 19th International Conference on Fluid Flow Technologies
Budapest, Hungary, August 26 - August 29, 2025

MOBILE SEPARATION OF COMPLEX OIL-WATER MIXTURES WITH AN ADAPTED PITOT PUMP

Jessica DAFIS[1], Xuemei ZHANG[2], Katharina ZÄHRINGER[3]

[1]Corresponding Author. Laboratory of Fluid Dynamics and Technical Flows, Otto von Guericke University Magdeburg, Universitätsplatz 2 39106 Magdeburg, Germany. Tel.: +49 391 67-52539. E-mail: jessica.dafis@ovgu.de
[2] State Key Laboratory of Multiphase Flow in Power Engineering, Xi'an Jiaotong University, Xi'an, China.
[3] Laboratory of Fluid Dynamics and Technical Flows, Otto von Guericke University Magdeburg, Germany. E-mail: zaehringer@ovgu.de

ABSTRACT

Oil-water (o/w) mixtures are found in numerous applications, mainly for processes, chemical and environmental engineering. Whenever oil-containing phases are utilized, the wastewater is often contaminated with oil, and these emulsions can cause significant environmental problems even at low concentrations e.g., polluting water bodies and damaging aquatic ecosystems.

The use of water treatment systems (e.g., the PTJ separating pump described below) is therefore essential in order to reliably remove the oil from the wastewater. In order to improve oil-water separation systems in a reliable manner, concentration measurements must also be accurate. The current study investigates the improvement of accuracy and reliability of o/w concentration measurements. A fluorescence-based imaging method has been developed to quantify the o/w concentration, especially in the relevant, low concentration ranges (5 mg/l to 200 mg/l). This method uses the fluorescent dye *Nile red (CAS-Number: 7385-67-3)*, acquires high-resolution images and analyses the droplet size and fluorescence intensity.

Using these concentration measurements, an existing laboratory test rig is improved in terms of pressure increase, and the control unit is miniaturized in order to convert the lab system into a mobile unit that can be used on-site in case of disasters.

NOMENCLATURE

Latin letters

FS	[-]	flow-split
g	[m s^{-2}]	gravitational acceleration
H_{HPO}	[m]	pressure head
$\dot{m}$	[kg s^{-1}]	mass flow rate
p	[Pa]	static pressure
n	[rpm]	rotational speed
m	[-]	Gradient
k	[-]	Intersection
T	[°C]	Temperature

Greek letters

α	[-]	oil concentration
ρ	[kg m^{-3}]	mixture density

Abbreviations

CF	Coriolis mass flowmeter
HPO	High-Pressure Outlet
LPO	Low-Pressure Outlet
o/w	oil-water
ppm	parts per million (=mg/l)
rpm	revolutions per minute
PTJ	Pitot-Tube Jet (pump)
RoI	Region of Interest

1. ENVIRONMENTAL CHALLENGES OF OIL SPILLS

Water pollution, especially caused by oil spills, remains a significant challenge for society. Given the increasing shortage of drinking water and the rising frequency of environmental disasters, finding effective clean-up solutions is more important than ever [1].

Although the *Deepwater Horizon* spill in 2010, which released 800 million litres of crude oil into the Gulf of Mexico, is the most well-known case, there are numerous other examples of oil pollution in daily life [2,3]. Industrial processes, shipping, and the uncontrolled discharge of bilge oil at ports or through accidents at sea significantly contribute to oil pollution [4]. However, this issue is not limited to oceans — inland waters such as lakes, rivers, and even groundwater can also be polluted. Heavy rain events like floods and high tides destroy houses, vehicles, and machinery containing oils, fuels, and other pollutants, thus threatening groundwater through contamination [4,5].

Standard oil spill control methods, such as barrier systems, chemical dispersants, and

(controlled) burning, often have limited effectiveness and can even worsen environmental damage [6]. Therefore, innovative approaches are urgently needed to quickly and effectively separate oil from contaminated water, enabling the rapid return of cleaned water to water bodies [7].

2. THE LABORATORY PITOT-TUBE JET PUMP FOR OIL-WATER SEPARATION

To deal with environmental problems and remove oil spills quickly and cost-effectively on site the *Chair of Fluid Mechanics and Technical Flows* has developed a mechanical separation method based on a rotating pump system. The modified Pitot-Tube Jet (PTJ) pump is an innovative solution for oil-water separation while simultaneously transporting the two separated phases [8–11]. With the PTJ pump it is possible to achieve significant success in the separation of oil-contaminated water. Laboratory analyses demonstrated a water purity below 2 to 5 ppm, which is a sufficient level to allow the purified water to be discharged directly into the environment.

The name of the Pitot pump comes from Henri Pitot. The Pitot tube extends in radial direction from the rotation axis almost up to the inner wall of the rotor. At this point, the liquid reaches its highest velocity and enters the Pitot tube. As a standard pump system, the Pitot tube has one inlet and one outlet. To adapt the system for separating oil-water mixtures, the Pitot tube was modified to involve one inlet for the oil-water mixture, and two outlets for the separately discharged liquids.

Figure 1 shows the modified Pitot tube inside the small-scale laboratory centrifuge. In first experiments, the system operates without blades and functions purely as a centrifuge. In this setup, the pressure increase results only from rotation and from the pressure build-up inside the Pitot tube, working as a diffusor. Within the Pitot tube, the high kinetic energy of the accelerated fluid is converted into usable pressure energy. In this way, the Pitot tube functions similarly to a volute casing in a classical centrifugal pump.

The incoming o/w mixture is separated in the rotor by centrifugal forces. The heavier phase (water) is pushed towards the outer rotor walls, while the lighter phase (oil) collects in the core, close to the axis of rotation. As a result, the water exits through the head of the Pitot tube, where it experiences a pressure increase before being expelled through the High-Pressure Outlet (HPO), while the oil exits through the second, central outlet, the Low-Pressure Outlet (LPO).

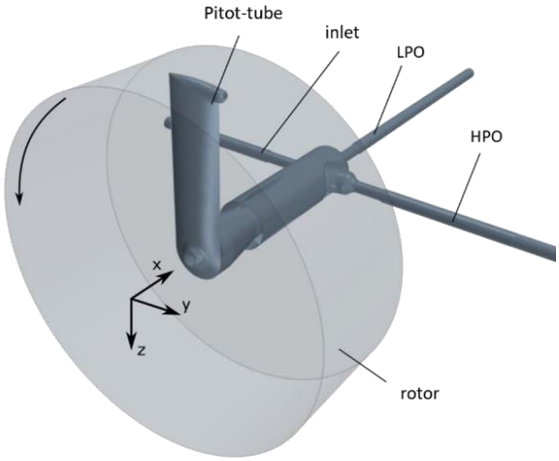

Figure 1: Schematic image of the modified Pitot tube in the lab-scale PTJ.

While combining pumping and separation, the PTJ pump achieves efficient oil-water purification at high flow rates, making it suitable for wastewater treatment in natural environments.

3. EVALUATION OF O/W CONCENTRATION AND PRESSURE

To investigate and optimize the PTJ pump, a laboratory-scale experimental setup was developed and constructed. Connected pipelines and valves ensure that the incoming liquids can be tested under various inflow conditions. The system allows the analysis of different oils and contaminants. For standard tests, sunflower oil is used first for safety reasons. In advanced tests, mineral or synthetic oils and fuels can also be examined. A selection of the tested substances is listed in Table 1. Water is always present as a component, while the oil phases vary.

Table 1: Densities of different fluids tested in the laboratory test rig [12–15]

	Density at ~ 20°C [kg·m^{-3}]
Water	998
Sunflower Oil	918 – 923
Olive Oil	910
Rapeseed Oil	907
Engine Oil	855 – 907
Gasoline	720 – 767
Diesel fuel	802 – 886
Heating Oil	815

Due to differences in density, the separation process varies depending on the type of oil. Mineral and synthetic oils have a greater density difference from water, making them easier to separate. In contrast, vegetable oils such as sunflower oil have a much smaller density difference, which makes their separation more difficult from a physical perspective. While sunflower oil is preferred to limit safety concerns and facilitate handling, it presents a

more challenging separation scenario compared to mineral oils.

Using the schematic experimental setup shown in Figure 2, the key parameters – o/w concentration at the HPO (α_{HPO}) and pressure buildup (H_{HPO}) - can be analysed and evaluated. This allows the identification of relevant parameter ranges and the optimization of the system in order to improve performance.

The *mass flow* ($\dot{m}$), *density* (ρ), and *temperature* (T) are measured during the tests using Coriolis flow meters (CF). The operating principle is based on the controlled generation of Coriolis forces, which occur when translational and rotational movements are superimposed in a system. For pressure measurements, *Cerabar T PMP131* pressure sensors from *Endress & Hauser* are used. The process pressure influences the metal membrane of the sensor. The signal is transmitted to the resistance bridge through a filling liquid. The pressure is determined based on the pressure change, which is proportional to the bridge output voltage. The configuration of the measuring devices is shown in the schematic test setup.

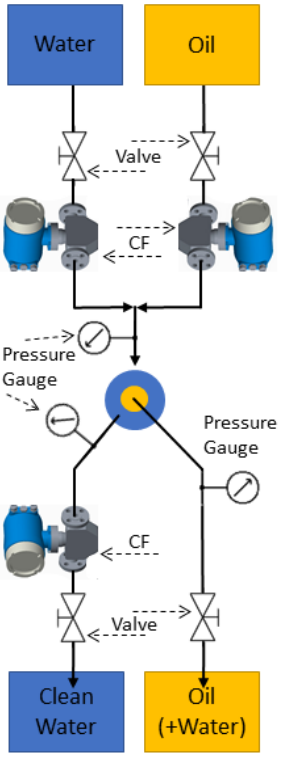

Figure 2: Experimental test setup of the PTJ pump on pilot scale.

The oil concentrations at the HPO and LPO are calculated using the corresponding densities. The correlation can be derived from equations (1a) and (1b). An oil concentration of 0.1 means that oil constitutes 10% of the mass of the mixture.

$$\alpha_{\mathrm{HPO}} = \frac{\rho_{\mathrm{HPO}} - \rho_{\mathrm{Water}}}{\rho_{\mathrm{Oil}} - \rho_{\mathrm{Water}}} \qquad (1a)$$

$$\alpha_{\mathrm{LPO}} = \frac{\rho_{\mathrm{LPO}} - \rho_{\mathrm{Water}}}{\rho_{\mathrm{Oil}} - \rho_{\mathrm{Water}}} \qquad (1b)$$

The measured pressure is converted into the pressure head using equation (2). This represents the height that the pump may have to overcome in order to pump the separated mixture at the accident site if there are barriers to deal with.

$$H_{\mathrm{HPO}} = \frac{\Delta p}{\rho_{\mathrm{HDA}} g} \qquad (2)$$

4. EXPERIMENTAL OPERATION

In previous tests, the operating parameters were adjusted to define the optimum separation ranges. However, due to measurement inaccuracies in the Coriolis flow meters, these parameter limits need further refinement to ensure consistent and optimal separation performance across the full operating range.

The operating parameters include the rotational speed, the mass flow rate at the inlet, the oil concentration at the inlet and the flow split. These parameters define a specific operating point, and variations in these parameters have a direct effect on the two main objectives. Depending on the geometric configuration, the effect of each parameter on these targets varies, resulting in shifts of the operating limits of the system.

In the first tests, a rotor without blades was used, operating as a pure centrifuge, as seen in Figure 3a. Later on, the rotor was modified with a blade geometry that only rotates in the water phase (Figure 3b). This modification was intended to increase the pressure within the system and at the same time prevent the formation of emulsions inside the rotor, which would otherwise affect an efficient separation.

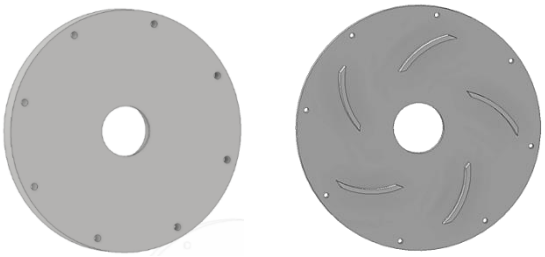

Figure 3: (a) Front of the rotor without blade geometry and (b) with adapted blades that only rotate in the water phase (close to periphery).

A comparison of the pressure increase as a function of the speed shows that a plate with blades generates a higher pressure build-up than the pure centrifuge configuration. As can be seen in Figure 4, the pressure head increases with rotational speed for both geometries. In the configuration with blades, however, the oil concentration, given in the respective boxes in the curves, also increases, which corresponds to a decrease in separation efficiency.

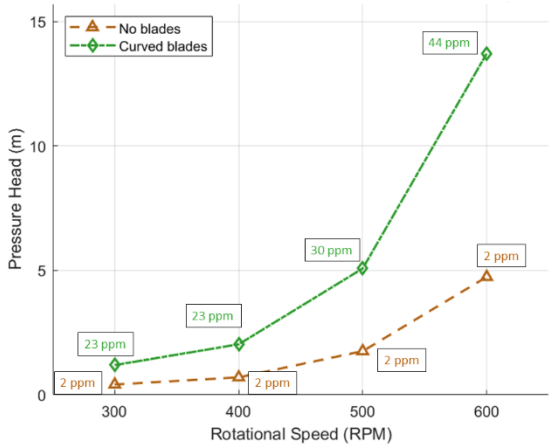

Figure 4: Pressure build-up as a function of rotational speed without blades (orange) and with adapted blades (green). The final oil concentration for each case is given in the respective boxes.

As a result, the parameter limits must be redefined and tightened. Another possibility is that the geometric configuration needs to be further optimized. As the oil concentrations in this system are so low that they cannot be accurately measured by the Coriolis flow meters, samples of the purified water were taken directly from the system and sent to the laboratory for analysis using the TOC (Total Organic Carbon) method.

Although this method is very accurate, it is also very time-consuming. Only a limited number of samples can be analysed, which makes it difficult to vary the parameters and leads to a slow and costly optimization process.

Since the mass balance method is no longer suitable for accurately determining the operating limits and optimizing the system due to the very low permissible oil concentrations in the treated water, a faster and more precise method must be developed to support system optimization.

5. MEASURING THE OIL-WATER CONCENTRATION USING A FLUORESCENT DYE

A better approach for reliably measuring oil concentrations in the range of 5 to 500 ppm has thus been developed. The measurement principle relies on fluorescence imaging of the dyed emulsion.

A requirement for this method is the ability to detect fluorescence signals from the mixture. Aromatic molecules show fluorescent properties. Each substance has a characteristic range of wavelengths at which absorption and fluorescence emission occur.

The oils listed in Table 2 have different fluorescence properties. While vegetable oils generally require excitation in the UV range, mineral oils show an emission peak with excitation in the wavelength range of around 420-490 nm. The sunflower oil used as a standard in the experiments has very weak fluorescence signals. Therefore, the sunflower oil is inoculated with a selective fluorescent dye tracer - *Nile red* (*CAS No. 7385-67-3)* - at a concentration of 1 mg/l in the oil. This tracer is insoluble in water and serves as an effective marker for the oil droplets. The typical absorption and fluorescence spectra of Nile red are shown in Figure 5.

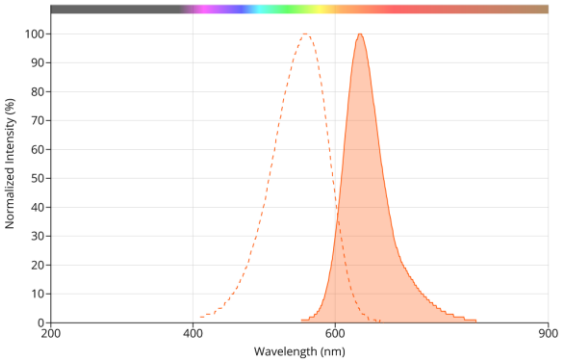

Figure 5: Absorption and fluorescence spectra of Nile red [16]

To simplify further processing, a stock solution of oil and the fluorescent dye Nile red was prepared. For 1 litre of sunflower oil, a mass of 1 mg Nile red was used. The dye, initially in powder form, was thoroughly mixed with the oil until fully dissolved. To ensure a consistent signal, the oil-dye mixture was filtered before being mixed with water to remove any residual solids.

Both, the pure sunflower oil and the oil solution with added *Nile Red* were analysed using a *Horiba Duetta* spectrometer. A 3D fluorescence spectrum was generated, as shown in Figures 6 and 7. The signals from pure sunflower oil are very weak and may not be strong enough for a calibration curve to highlight differences between different concentrations. On the other hand, for the dyed sunflower oil, excitation at a wavelength of 535 nm shows an emission peak at 570 nm.

To set up the experimental system, the excitation wavelength was selected based on the fluorescence spectra, with a green LED chosen as the excitation source. The LED used is a multicolor LED that can emit green, blue, or red light depending on the voltage applied. The blue LED is particularly suitable for further experiments with mineral oils, as these oils do not require the addition of a fluorescent dye. Non-toxic olive oil can also be excited in the red wavelength range and, therefore, can be used for further investigations.

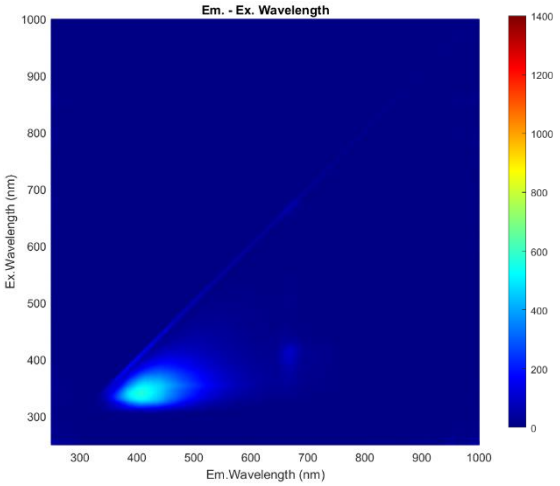

Figure 6: Excitation and emission wavelengths of pure sunflower oil, showing the fluorescence signal.

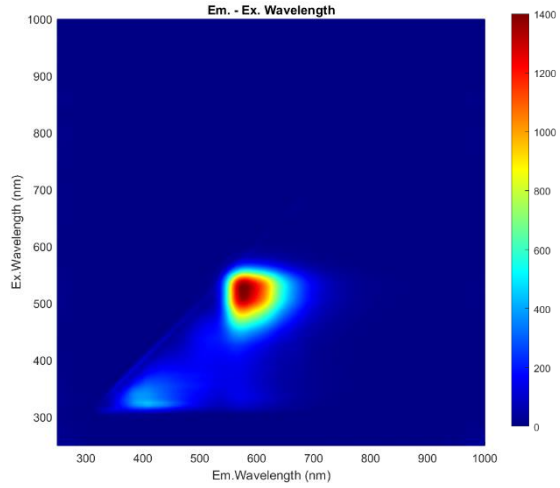

Figure 7: Excitation and emission wavelengths of sunflower oil seeded with 1 mg/l Nile red, showing the fluorescence signal.

6. EXPERIMENTAL SETUP FOR FLUORESCENCE MEASUREMENTS

The fluorescence-based methodology for oil-water (o/w) measurements relies on the presence of a stable and reproducible emulsion.

Generating a stable oil-water mixture without emulsifiers requires high-energy mixing to create fine, dispersed oil droplets. A stable emulsion is essential because fluorescence imaging depends on homogeneously distributed oil droplets for reliable quantification. In this study, a *Polytron PT3100* homogenizer was used, capable of handling up to 2 liters of total volume at a maximum rotational speed of 12,000 rpm. However, even at this speed, the emulsion remained stable for only about three minutes, requiring rapid measurements before phase separation begins. The preparation process was standardized for all experiments.

A volume of 200 ml of deionized water was mixed with a controlled amount of dyed sunflower oil to obtain the desired o/w concentration. The mixtures were dispersed at a rotational speed of 12,000 rpm for 120 seconds.

After the emulsification process, the samples were transferred into disposable cuvettes. These samples were positioned in front of a CMOS camera (*FLIR Blackfly S*, 5 MP), equipped with a *Nikon F60* objective lens (f-number: 2.8, scale factor: 59.7 pixels/mm). All measurements were performed with a constant exposure time of 5000 µs.

For fluorescence excitation, two LEDs (emission peak: 535 nm) were positioned on either side of the cuvette. This setup ensured intense and continuous illumination, crucial for uniform fluorescence excitation. Additionally, black shielding was used to minimize the entry of ambient light, as shown in Figure 8. The images were saved and later used for image processing.

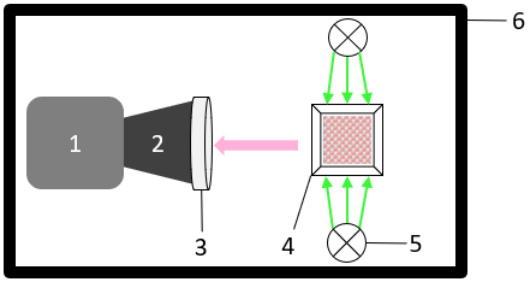

Figure 8: Schematic setup of the fluorescence imaging methodology for o/w concentration measurements [17]

Table 2: Components of experimental setup

1	CMOS camera (Mono, 5MP, 16 bit)
2	Objective lens
3	High-pass filter
4	Cuvette (Oil in water emulsion with Nile red)
5	LED illumination
6	Housing to avoid disturbing light

For image processing, a simple image-analysis algorithm was coded using *Matlab (Version R2019, The MathWorks Inc.)*. The image processing sequence begins by reading the raw images, which are captured as grayscale images (Figure 9).

The grayscale intensity is directly proportional to the fluorescence signal produced by the sample illuminated in the cuvette. Subsequently, a Region of Interest (RoI) is automatically set. This step is necessary to avoid regions with strong optical distortion near the edges of the cuvettes.

Figure 9: Image of the cuvette taken with the *FLIR* camera. RoI marked with a red rectangle.

Since all cuvettes were placed in exactly the same position, the RoI always corresponds to identical pixel regions within the image: 400 pixels in the x-direction (horizontal) and 500 pixels in the y-direction (vertical), resulting in a total of 200,000 pixels. Grayscale intensities (average pixel intensity) and distribution (standard deviation of pixel intensity) were evaluated for this area.

Finally, the resulting intensity value is correlated with the known o/w concentration.

7. RESULTS

A concentration-dependent calibration curve was created based on the measurement setup described in Section 6. Figure 10 shows the correlation between the o/w concentration and the mean fluorescence intensity of the samples.

It can be observed that each oil concentration corresponds to a specific fluorescence intensity value. This relationship allows for the determination of the oil content in the water based on the measured fluorescence intensity, provided that the dye concentration is known (here: 1 mg/l *Nile red* in oil).

This linear correlation enables the fitting of a regression curve through the measured data points and facilitates the quantitative determination of the oil concentration in the water based on the fluorescence intensity. The following equation can be derived from this linear relationship:

$$y = m \cdot x + k \qquad (3)$$

Where y is the fluorescence intensity and x is the oil-water concentration. *Matlab* is used to determine the gradient m and the intersection k on the y-axis. The values obtained for the regression line are:

- Intersection (k) = 403.56
- Gradient (m) = 24.81

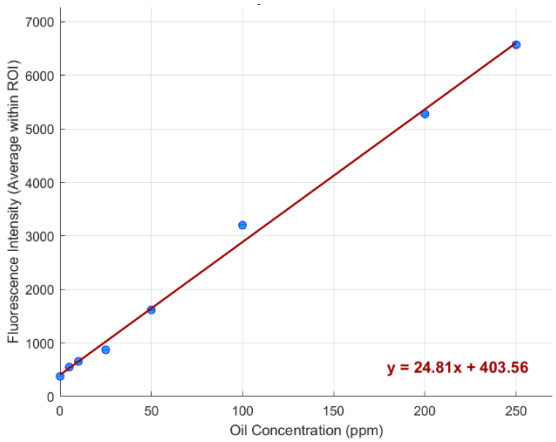

Figure 10: Fluorescence intensity as function of o/w concentration.

This results in the following equation:

$$I = 24.81 \cdot c_{o/w}\,[\text{ppm}] + 403.56 \qquad (4)$$

This equation can be converted to solve c and calculate the oil concentration in the water based on the measured fluorescence intensity. Provided that the dye concentration of 1 mg/l *Nile Red* is known.

$$c_{o/w}[\text{ppm}] = \frac{I - 403.56}{24.81} \qquad (5)$$

8. EXTENSION OF FLUORESCENCE IMAGING WITH MICROSCOPIC ANALYSIS

While a correlation between fluorescence intensity and oil concentration has already been demonstrated, the next step is to investigate the behaviour of the oil droplets in the emulsion as the o/w concentration increases. For this purpose, a second *FLIR* camera was used, and *the Questar QM-1 Long Distance Microscope* (7) was integrated into the experimental setup to investigate the microscopic properties of the emulsion. The extended experimental setup is shown in Figure 11. All other test parameters remained constant.

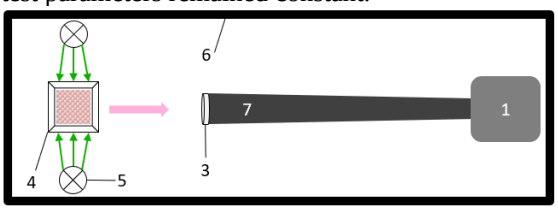

Figure 11: Schematic setup of the fluorescence imaging methodology with microscope analysis

With the long-range microscope, the oil droplets become visible through the fluorescent dye and enable a detailed examination. While the average fluorescence intensity can still be evaluated, the main focus is now on the formation of the droplets and their number as a function of the oil concentration. A

microscope image of the droplets can be seen in Figure 12.

Matlab is used to analyse the number of droplets. A contrast threshold is defined in the script in order to consider only the droplets within a certain focus plane.

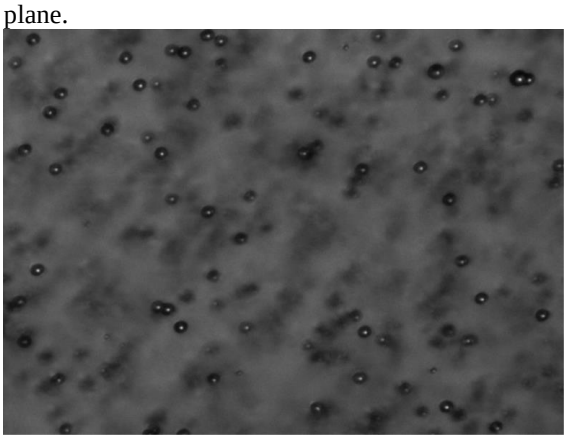

Figure 12: Droplet distribution for 50 ppm o/w

The series of experiments described above was repeated. This time, however, fluorescnence images and microscopic images were taken simultaneously. The analysis of the number of droplets as a function of the oil concentration in water is shown in Figure 13.

While the fluorescence image analysis showed a linear correlation between oil concentration and fluorescence intensity, a correlation between droplet number and oil concentration can also be observed in the microscopic images. However, no linear correlation can yet be derived from the microscopic data. These results clearly show the potential of microscopic studies, but further optimization of both image quality and analysis script are required to accurately count and analyze the droplets. Such improvements could lead to a better understanding of the relationship between oil concentration and droplet behavior.

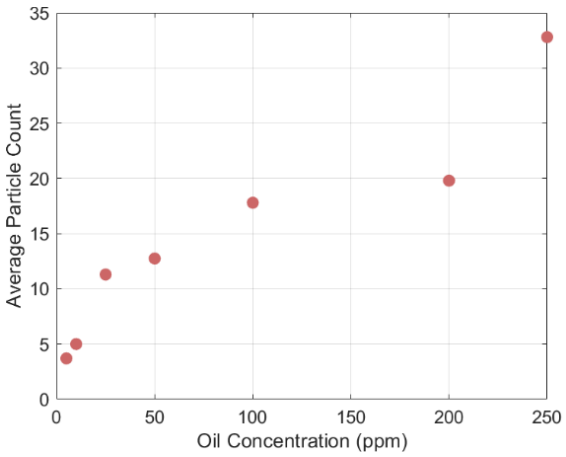

Figure 13: Dependence of the number of particles on the oil concentration.

8. CONCLUSIONS & FUTURE APPLICATIONS

The separation of oil-water mixtures is still a major challenge, especially in environmental protection and industrial applications. The modified PTJ pump presented in this study offers a promising solution by combining centrifugal forces with a pumping mechanism to improve the efficiency of oil-water separation systems. Laboratory tests have shown that this system can achieve a water purity level below 5 ppm, which meets the requirements for the discharge of water in the environment.

One of the biggest challenges in optimizing the PTJ system is the accurate and rapid measurement of the oil-water concentration. While laboratory testing provides highly accurate results, it is time consuming and impractical for real-time testing under field operating conditions, especially given the variability of system parameters. While the in-line method (CF measurement/density mass balance) provides fast results, they lack the accuracy required for precise monitoring below 1000 ppm. Therefore, a fluorescence-based measurement technique using the dye Nile red was introduced in this study as a reliable and fast alternative.

This fluorescence measurement method offers a sample-based evaluation that provides rapid results (a few minutes from sampling to oil concentration determination). A calibration curve for oil concentrations from 5 ppm to 500 ppm has been developed. Good correlations between droplet size and oil concentration have also been demonstrated. Nevertheless, there are still challenges and a need to optimize the microscopic analysis in order to increase accuracy, especially in the lower concentration ranges.

Both methods need also to be further developed to obtain an in-line approach in the future, providing hopefully real-time response times.

According to the results of the present study, it is possible to arrange all components of the set-up in such a way that in-line measurements are possible. However, the calibration function shown in Figure 10 is only valid if all optical and system parameters are kept unchanged. This means that the camera and illumination settings as well as the distances between the individual components in the in-line setup must be identical to the offline setup. In addition, all the oil in the reservoir of the pilot plant must be inoculated at the same *Nile red* concentration (1 mg/l) as before.

In addition, the image processing algorithm, which currently runs in a sequential mode as post-processing after image acquisition, needs to be modified to enable simultaneous image acquisition and processing as a real-time process. This will ultimately enable the development and implementation of a feedback control for the PTJ pump. Such a control is necessary in order to react to

transient process conditions resulting from a fluctuating oil concentration at the inlet, for example.

ACKNOWLEDGEMENT

This project is funded by the (DBU) under the grant number 38123/01 – 23.

We would also like to thank the UFZ Leipzig, in particular Jonas Köhne, for his active support with the sample analyses.

REFERENCES

[1] Sousa, A. M., Pereira, M. J., & Matos, H. A. (2022). *Oil-in-water and water-in-oil emulsions formation and demulsification*. Journal of Petroleum Science and Engineering, **210**, 110041.

[2] Hu, C., Herz, C., & Hartman, R. L. (2013). *Microfluidic dispersion of mineral oil-seawater multiphase flows in the presence of dialkyl sulfonates, polysorbates, and glycols*. Green Processing and Synthesis, **2**(6), 611–623.

[3] Overton, E. B., Adhikari, P. L., Radović, J. R., & Passow, U. (2022). *Fates of petroleum during the Deepwater Horizon oil spill: A chemistry perspective*. Frontiers in Marine Science, **9**.

[4] Singh, B. J., Chakraborty, A., & Sehgal, R. (2023). *A systematic review of industrial wastewater management: Evaluating challenges and enablers*. Journal of Environmental Management, **348**, 119230.

[5] Al-Majed, A. A., Adebayo, A. R., & Hossain, M. E. (2012). A sustainable approach to controlling oil spills. Journal of Environmental Management, **113**, 213–227.

[6] Peterson, C. H., Rice, S. D., Short, J. W., Esler, D., Bodkin, J. L., Ballachey, B. E., & Irons, D. B. (2003). Long-term ecosystem response to the Exxon Valdez oil spill. Science, **302**(5653), 2082–2086.

[7] Kwon, G., Kota, A. K., Li, Y., Sohani, A., Mabry, J. M., & Tuteja, A. (2012). On-demand separation of oil-water mixtures. Advanced Materials, **24**(27), 3666–3671.

[8] Meyer, J. (2019). *Optimierung einer Pitot-Pumpe und deren Adaption zur Öl-Wasser-Trennung* (Ph.D. thesis). University of Magdeburg.

[9] Meyer, J., & Thévenin, D. (2016). *Proceedings of the 9th International Conference on Multiphase Flow*, Firenze, Italy.

[10] Meyer, J., Daróczy, L., & Thévenin, D. (2017). *Shape optimization of the pick-up tube in a Pitot-tube jet pump*. Journal of Fluids Engineering, **139**, 021103/1–11.

[11] von Deylen, J., Köpplin, J., & Thévenin, D. (2022). *Development and validation of a design tool for an improved Pitot-tube jet-pump allowing continuous fluid-fluid separation*. Journal of Fluids Engineering, **144**(7), 071401/1–11.

[12 NIST Standard Reference Database 69. (2008). *Thermophysical properties of fluid systems: Isobaric properties for water*.

[13] Federation of German Heating Industry (BDH). (2021). *Fuel heating oil EL: Information sheet No. 50*. https://www.bdh-industrie.de/downloads#technische-infoblaetter

[14] Park, S. H., Youn, I. M., Lim, Y., & Lee, C. S. (2013). *Influence of the mixture of gasoline and diesel fuels on droplet atomization, combustion, and exhaust emission characteristics in a compression ignition engine*. Fuel Processing Technology, **106**, 392–401.

[15] Ichu, C. B., & N., H. (2019). *Comparative study of the physicochemical characterization and quality of edible vegetable oils*. International Journal of Research in Information Science and Application Technology, **3**(2), 1–9.

[16] AAT Bioquest. (2025). *Spectrum [Nile red]*. Retrieved February 11, 2025, from https://www.aatbio.com/fluorescence-excitation-emission-spectrum-graph-viewer/nile_red

[17] Köpplin, J., Bednarz, L., Hagemeier, T., & Thévenin, D. (2021). *Fluorescence imaging methodology for oil-in-water concentration measurements*. Chemical Engineering & Technology, **44**(7), 1343–1349.

Conference on Modelling Fluid Flow (CMFF'25)
The 19th International Conference on Fluid Flow Technologies
Budapest, Hungary, August 26 - August 29, 2025

PREDICTIONS OF PARTICLE TRAJECTORY RESPONSE TO REYNOLDS NUMBER IN TURBULENT CHANNEL FLOWS USING ARTIFICIAL NEURAL NETWORKS

Lee MORTIMER[1], Michael FAIRWEATHER[2]

[1] Corresponding Author. School of Chemical and Process Engineering, Faculty of Engineering and Physical Sciences, University of Leeds. Leeds LS2 9JT, United Kingdom. E-mail: l.f.mortimer@leeds.ac.uk
[2] School of Chemical and Process Engineering, Faculty of Engineering and Physical Sciences, University of Leeds. Leeds LS2 9JT, United Kingdom. E-mail: m.fairweather@leeds.ac.uk

ABSTRACT

The present work details the development, implementation and performance of a machine-learning (ML) based predictive model for simulating particle-laden wall-bounded turbulent flows. Additionally, the technique is demonstrated with a particular focus on investigating the influence of Reynolds number on particle trajectory responses, comparing with equivalent high-fidelity simulations. Using a hybrid ML algorithm, the model is trained using data from direct numerical simulation (DNS) and Lagrangian particle tracking (LPT) in turbulent channel flows. Training trajectories are obtained from $Re_\tau = 180$ and $Re_\tau = 300$ DNS-LPT predictions across multiple particle Stokes numbers, however, the value of the technique is demonstrated at intermediate Reynolds numbers ($Re_\tau = 240$), which offers strong agreement with DNS-LPT obtained first- and second-order velocity statistics, emphasising the accuracy at predicting particle dynamics at Reynolds numbers the ML model was never trained on. The techniques' effectiveness demonstrates the ability to minimise the need for extensive DNS-LPT particle trajectory data which maintaining high accuracy in predicting dynamic properties and emergent phenomena across different Reynolds numbers. Beyond its immediate scope, this approach has broad applications in industrial and environmental processes where predictive models for turbulent multiphase flows are critical, such as aerosol transport and nuclear waste processing.

Keywords: machine learning, artificial neural networks, direct numerical simulation, Lagrangian particle tracking, turbulent particle-laden channel flows, Reynolds number

NOMENCLATURE

C_D	[-]	drag coefficient
I	[-]	training input vector
N	[-]	spectral element method (SEM) order
N_P	[#]	number of simulated particles
Re_B	[-]	bulk Reynolds number
Re_τ	[-]	shear Reynolds number
U_B	[ms^{-1}]	bulk velocity
d_P^*	[-]	particle diameter
$\boldsymbol{f}^*$	[-]	forcing function
p^*	[-]	pressure field
t^*	[-]	time
u_τ	[ms^{-1}]	fluid shear velocity
$\boldsymbol{u}_F^*$	[-]	fluid velocity vector
u'^*_F	[-]	fluid velocity fluctuation
$\boldsymbol{u}_P^*$	[-]	particle velocity vector
$\boldsymbol{u}_S^*$	[-]	slip velocity vector
$\boldsymbol{x}^*$	[-]	position vector
δ	[m]	channel half-height
ν_F	[m^{2}s^{-1}]	fluid kinematic viscosity
ρ_F	[kgm^{-3}]	fluid density
ρ_P^*	[-]	particle-fluid density ratio
Δt^*	[-]	DNS timestep

Subscripts and Superscripts

P, F	particle, fluid
B, τ	bulk, shear
$*$	bulk non-dimensional units
RMS	root mean square

1. INTRODUCTION

Machine learning (ML) has emerged in recent years as a vital tool in enhancing analysis, research, predictive capabilities and decision-making across countless applications [1]. In essence, the term ML itself encompasses a wide variety of algorithms and

modelling tools used originally for data analysis, but which have been adopted across many scientific disciplines over the last few decades [2]. In such scenarios, ML applications have grown significantly. For instance, in healthcare, ML is capable of diagnosing and predicting diseases through analysis of medical data and imaging [3]. Its scope extends beyond that of scientific purposes into industries such as finance and automation of vehicles where it supports fraud detection [4] and navigation and decision-making in self-driving cars [5]. In such applications, the ability for ML to 'learn' is grounded in being able to obtain training data, from which insights and information can be extracted to develop intelligent models.

Applications of ML further extend into the field of fluid dynamics, facilitated by the existence (and generation) of extensive data from both computational simulations and experiments. ML has been used to address challenges such as turbulence closure models, reduced-order modelling [6] and flow optimisation and control [7, 8]. Jain et al. [9] applied random forest regression in order to predict fluid flow in curved pipes using simulation-generated training data. Aside from mispredictions of vortex positions, the technique was shown to accurately capture important characteristics of turbulent flow in non-trivial geometries. Li et al. [10] used k-nearest neighbour (KNN) techniques to learn the features of mixing tank systems obtained from limited experimental Lagrangian trajectories, demonstrating the effectiveness of ML algorithms applied in the context of experimentally obtained datasets. Yang et al. [11] expanded upon this by introducing the concept of a 'hybrid' ML model which combined preprocessors, noise generators and particle-wall collision algorithms to simulate turbulent single-phase and particle-liquid flows in pipes. This approach was shown to accurately predict local fluid and particle velocities, as well as spatial concentration distributions, having been trained on solely dynamic experimental data.

As the complexity of the fluid dynamic system increases, due to the presence of complex geometries or additional phases, investigation into such scenarios poses greater challenges due to the intricacies of the additional interactions involved. In such systems, the fluid velocity field may fluctuate both due to the existence of turbulent eddies, as well as two-way coupling between particulate phases and the continuous flow field [12] which influences turbulence modulation, and four-way coupling wherein particles may interact with other particles via collision or agglomeration [13]. Being able to capture these phenomena in lower fidelity simulation techniques stands as an ongoing challenge in computational fluid dynamics, which for most purposes one must turn to high fidelity methods such as direct numerical simulation (DNS) and immersed boundary methods to holistically represent the system and extract knowledge from fully resolved simulations. These are often very computationally intensive and require high timeframes to perform the computations. The elucidation of such processes using high fidelity techniques is hence crucial for increasing the accuracy at which these processes are represented in lower order models, which in turn is vital for industrial applications such as the development of digital twins [14].

The present study aims to develop and demonstrate an enhanced predictive model which uses a hybrid ML approach to determine key fluid and particle behaviour in turbulent flows. An artificial neural network (ANN) is trained on dynamic particle databases generated from DNS and Lagrangian particle tracking (LPT) in channel flows. The model seeks to replicate similar trajectories and hence bulk flow observations such as velocity profiles of both phases and concentration profiles of the particulate phase, while reducing the amount of computational resources and time necessary to obtain similar degrees of accuracy. The study further aims to demonstrate the generalisability of the technique, applying the trained algorithm to parameter sets outside those trained upon, in this case considering a Reynolds number previously unseen by the ML algorithm. Finally, the technique builds upon previous attempts [11] by incorporation lagged particle velocities into the training input, manifesting the concept of particle momentum within the model, further generalising the technique to high Stokes number regimes, wherein particle motion is more decorrelated from the local fluid streamlines.

2. METHODOLOGY

2.1. Direct Numerical Simulation

To obtain high accuracy predictions of the continuous flow field capable of capturing all relevant turbulence length and timescales, the DNS code Nek5000 [15] was employed in the context of a turbulent channel flow at various shear Reynolds numbers, $Re_\tau = u_\tau \delta / \nu_F = 180, 240$ and 300. Here, u_τ is the shear velocity, δ is the channel half-height and ν_F is the kinematic viscosity of the fluid phase. Nek5000 uses a spectral element method-based Eulerian solver at high order ($N = 7$) to model the temporal and spatial evolution of the flow field, and is applied on a hexahedral spectral element grid representing a standard channel flow geometry.

The governing equations for the continuous phase are the Navier-Stokes (NS) equations, expressed in non-dimensional form using bulk flow properties to achieve the following:

$$\nabla \cdot \boldsymbol{u}_F^* = 0, \tag{1}$$

$$\frac{D\boldsymbol{u}_F^*}{Dt^*} = -\nabla p^* + \frac{1}{Re_B}\nabla^2 \boldsymbol{u}_F^* + \boldsymbol{f}_{PG}^* + \boldsymbol{f}_{2W}^*. \tag{2}$$

Here, $\boldsymbol{u}_F^*(\boldsymbol{x}^*, t^*)$ represents the fluid velocity vector at position $\boldsymbol{x}^*$ and time t^*, while $p^*(\boldsymbol{x}^*, t^*)$ is the fluid pressure, $Re_B = u_B\delta/\nu_F$ is the bulk Reynolds number, $\boldsymbol{f}_{PG}^*$ is a constant pressure gradient forcing term and $\boldsymbol{f}_{2W}^*$ is an arbitrary cell-dependent forcing term which accounts for two-way momentum exchange between particles and fluid (two-way coupling). In the above and subsequent equations, parameters which are marked with an asterisk $(*)$ imply non-dimensional variables achieved using bulk properties, $(\delta,\ U_B,\ \rho_F)$, with ρ_F the fluid density.

The NS equations are solved numerically on a structured Cartesian grid composed of 27 × 18 × 23 spectral elements of 7th order, amounting to approximately 3.9 million equivalent 'nodes'. The grid is refined in the wall-normal direction to capture near-wall flow structures more accurately, while a uniform distribution of elements is maintained in the streamwise and spanwise directions. The computational domain, defined as $12\delta\times2\delta\times6\delta$, represents a channel geometry. These dimensions are selected to capture all significant vortical structures, and the geometry is illustrated in Fig. 1.

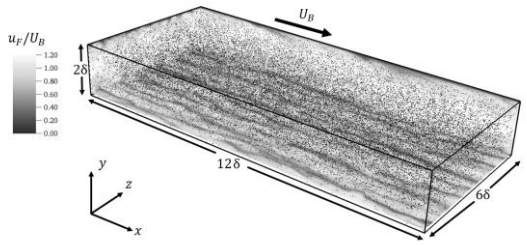

Figure 1: Schematic of the particle-laden turbulent channel flow at Re_τ =180 used in DNS-LPT simulations

The solver uses a constant time step of $\Delta t^* = 0.005$. Periodic conditions are imposed in the streamwise and spanwise directions to ensure that the flow remains cyclic. The extents of the wall-normal direction are located at $y^* = \pm1$ and are subject to no-slip and impermeability conditions. The flow is driven by a constant pressure gradient applied in the streamwise (x^*) direction, with the pressure gradient magnitude specified as follows:

$$\frac{dp^*}{dx^*} = \left(\frac{Re_\tau}{Re_B}\right)^2. \tag{3}$$

2.2. Lagrangian Particle Tracking

To track the trajectories of solid particles within the flow, a Lagrangian particle tracking routine was developed and integrated to run concurrently with the fluid phase solver within Nek5000. Each particle is modelled as a point-like, rigid, impenetrable computational sphere. After each time step of the continuous phase completes, the LPT routine solves the non-dimensional equations of motion for each particle considering a force-balance which acts on the particle's inertia, as described by Maxey [16] and Patterson and Riley [17]. A key objective in developing the hybrid ML algorithm is to generalise the model across a range of Stokes numbers. As a result, forces such as lift, virtual mass, and pressure gradient, in addition to drag, are considered in the calculations since they may be significant under certain conditions, as noted in previous studies [18]. However, the Basset history force is excluded due to its high computational cost and earlier findings suggesting its negligible effect on particle motion [19]. The Newtonian equations governing each particle's motion are as follows:

$$\frac{d\boldsymbol{x}_P^*}{dt^*} = \boldsymbol{u}_P^*, \tag{4}$$

$$\begin{aligned}\mathrm{M_{VM}}\frac{\partial \boldsymbol{u}_P^*}{\partial t^*} = &\underbrace{\frac{3C_D|\boldsymbol{u}_S^*|}{4d_p^*\rho_P^*}\boldsymbol{u}_S^*}_{Drag} + \underbrace{\frac{3}{4}\frac{C_L}{\rho_P^*}(\boldsymbol{u}_S^*\times\boldsymbol{\omega}_F^*)}_{Lift} \\ &+ \underbrace{\frac{1}{2\rho_P^*}\frac{D\boldsymbol{u}_F^*}{Dt^*}}_{Virtual\ Mass} \\ &+ \underbrace{\frac{1}{\rho_P^*}\frac{D\boldsymbol{u}_F^*}{Dt^*}}_{Pressure\ Gradient}.\end{aligned} \tag{5}$$

In Eqs. (4) and (5), $\boldsymbol{x}_P^*$ is the particle position vector, $\boldsymbol{u}_P^*$ the particle velocity vector, $\boldsymbol{u}_F^*$ the fluid velocity vector spectrally interpolated at the position of the particle, $\boldsymbol{u}_S^* = \boldsymbol{u}_F^* - \boldsymbol{u}_P^*$ the slip velocity between the fluid and the particle, d_P^* the particle diameter non-dimensionalised by the channel half-height, ρ_P^* the density ratio between the fluid and the particle and $\boldsymbol{\omega}_F^*$ the vorticity of the fluid interpolated spectrally at the particle position, given by $\boldsymbol{\omega}_F^* = \boldsymbol{\nabla}\times\boldsymbol{u}_F^*$. M_{VM} is the virtual mass modification term given by $M_{VM} = \left(1 + \frac{1}{2\rho_P^*}\right)$. The drag coefficient, C_D, is calculated dynamically using the correlations of Schiller and Naumann [13], where $C_D = 24f_D/Re_P$, with $f_D = (1 + 0.15Re_P^{0.687})$ when $Re_P > 0.5$ and $f_D = 24/Re_P$ otherwise (in the Stokes regime). Here, Re_P is the particle Reynolds number, given by $Re_P = Re_B d_P^*|\boldsymbol{u}_S^*|$. Further details on the calculation and origins of these terms are available in Mortimer et al. [18].

Particle translation during a time step is calculated after each fluid time step has completed. First, spectral interpolation is used to obtain the fluid velocity and its spatial derivatives at the particle positions. Then, Eqs. (4) and (5) are solved using a fourth-order Runge-Kutta scheme, with the time step equivalent to that of the fluid solver.

Collisions between particles and the channel walls are handled as elastic impacts, reversing the wall-normal component of the particle's velocity upon contact. In the periodic directions (streamwise and spanwise), particles exiting the domain on one

side are reintroduced at the corresponding position on the opposite side, maintaining the periodic nature of the channel flow. The training dataset consisted of 18 simulations, across two Reynolds numbers and multiple particle Stokes numbers based on shear scales, St^+, obtained by varying both the particle diameter and the particle-fluid density ratio. The fluid and particle properties used to train and validate are summarised in Table 1.

Table 1. Fluid and particle properties for each simulation considered. Simulation set names ending in T represent those used to train the ML algorithm, whereas V is used to indicate simulations performed for comparison purposes only

Parameter	SIM1T	SIM2V	SIM3T
Re_τ	180	240	300
ρ_P^*	2.5, 1111, 2041		
d_P^*	0.0025, 0.005, 0.0075		
St^+	0.028 → 574.03		
N_P	10,000		

2.3. Hybrid ANN Algorithm

Lagrangian trajectories obtained from the simulation methods described in Sections 2.1 and 2.2 are first pre-processed into a data array containing their vertical positions within the channel and corresponding velocity components, $y^*, u_{x,t}^*, u_{y,t}^*, u_{z,t}^*$. These are then combined with the simulation conditions and the velocities from the previous time step to form the complete input feature set as follows:

$$I = \begin{pmatrix} Re_\tau, \rho_P^*, d_P^*, y^*, \\ u_{x,t-1}^*, u_{y,t-1}^*, u_{y,t-1}^* \end{pmatrix}. \quad (5)$$

An artificial neural network was developed for this study due to its capacity to capture complex, non-linear relationships within the data and its proven accuracy in similar predictive modelling tasks. Previous studies have also demonstrated that ANNs can outperform other methods. The ANN model is configured with four hidden layers containing 256, 128, 64 and 32 configurable neurons and uses the rectified linear unit (*ReLU*) activation function. The number of layers and neurons, as well as the learning rate and batch size, were optimised beforehand through hyperparameter tuning.

Before training, the input features are normalized between 0 and 1 based on the minimum and maximum values of each variable. The training dataset consists of data from $N_P = 10{,}000$ particles with trajectories across 1000 instantaneous time states, sampled at intervals of $t^* = 0.005$. The impact of varying the number of trajectories used for training on the model's performance was evaluated and chosen to ensure optimal training root mean square error. The ANN was trained over 100 epochs and optimised using the adam optimiser, minimising the root-mean-square-error (RMSE) loss function, with a batch size of 32 and a train-test validation split of 0.3.

Once the model was adequately trained, synthetic particle trajectories are generated by first initialising each particle's position within the boundaries of the channel flow domain. The particles are then assigned velocities corresponding to the non-dimensional bulk velocity $U_B^* = 1.0$. During the hybrid ML-informed simulation, the ANN predicts the next particle velocity using the input feature set at the present time, as in Eq. (5). To account for local velocity fluctuations, a Gaussian noise model is also incorporated, defined as:

$$u_F'^* \sim N(\mu, \sigma^2), \quad (6)$$

where the mean, μ, and the standard deviation, σ, were chosen to validate against fluid flow predictions from DNS-LPT simulations and differ for each Reynolds number and parameter set. Furthermore, the wall-normal proximity, $|1 - y^*|$, is taken into account as an additional factor such that μ and σ are both functions of y^*. The predicted subsequent velocity may then be calculated using:

$$u_{p,t}^* = \bar{u}_P^* + u_F'^*, \quad (7)$$

where is $\bar{u}_P^*$ predicted by the trained ANN using the particle/fluid properties, previous velocities, and wall-normal positions within the channel. The particle positions are subsequently updated using a standard Euler time-stepping scheme using a time step identical to that employed in the DNS-LPT.

To handle particle-wall collisions, a collision detection and response mechanism is implemented, identical to that used in the LPT method. Specifically, in the vertical direction, the particle's velocity is reversed upon collision with the channel wall. In the streamwise and spanwise directions, particles exiting one boundary are reintroduced at the corresponding position on the opposite side, preserving the periodic flow characteristics of the channel.

3. RESULTS AND DISCUSSION

Initially, three simulations of unladen turbulent channel flows at SEM order $N = 7$ were conducted, using a constant pressure gradient driving force to establish a statistically stationary turbulence field for $Re_\tau = 180, 240$ and 300. The simulations were initialised with a condition featuring a mean velocity profile containing minor perturbations to promote the transition to turbulence. The simulations ran for $T_S^* = 100$ non-dimensional time units, with statistics collected during the final $50 \leq t^* \leq 100$. Additionally, statistics were measured at $t^* = 10$

intervals to ensure no temporal variations in the results. The $Re_\tau = 180$ and 300 single-phase channel flows have been validated in previous publications [18, 20].

To facilitate the Gaussian noise generation function, velocity fluctuation statistics were collected from the validated channel flows over new simulations with a temporal duration of $t^* = 100$. Figure 2 presents the probability density functions (p.d.f.s) for all three components of the velocity fluctuations, demonstrated in the $Re_\tau = 180$ simulation, and sampled from uniformly distributed locations throughout the channel domain over the entire simulation period. To validate the Gaussian noise model used for predicting local fluctuations on the particles, the sampled velocity fluctuations were compared against the model's predictions. In all three component directions, the noise model is shown to accurately capture the range and distribution of the fluctuating fluid velocities. Similar observations were made for the $Re_\tau = 240$ and 300 flows.

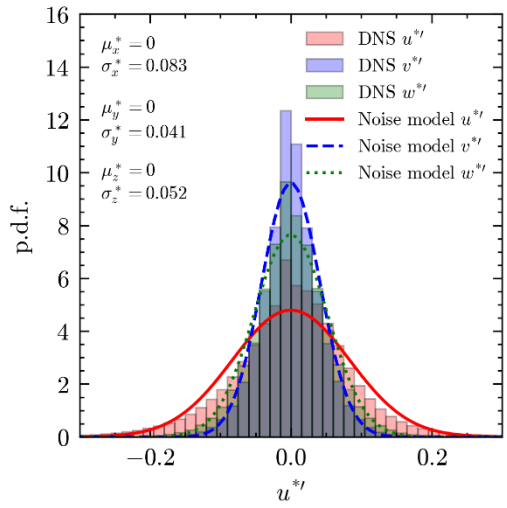

Figure 2: Gaussian noise model validation of velocity fluctuation components for single-phase DNS at $Re_\tau = 180$

In order to improve the accuracy of the Gaussian noise model when representing the true nature of velocity fluctuation distributions, the hybrid ML technique was enhanced to consider a wall proximity based standard deviation for the Gaussian profiles. Figure 3 demonstrates the functional relationship between wall distance and each component of the profile's standard deviation, σ. This was digitised as a look-up table, with points interpolated linearly between each measured region when calculating Eqs. (6) and (7). Because a major focus of the present work is to reduce runtimes while preserving DNS-like accuracy for particle trajectories, the resolution was chosen to resolve the important peaks. However, it should be noted that interpolation of the streamwise component may play a role in reducing accuracy in the hybrid ML model, since the actual peak is fairly sharp, and hence standard deviations are not as likely to be predicted with the same accuracy as in the bulk flow region.

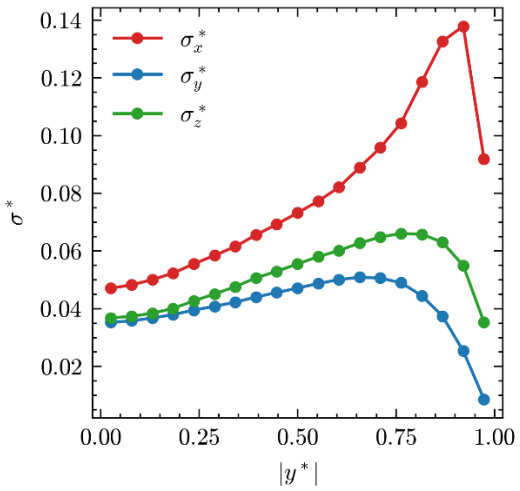

Figure 3: Gaussian noise standard deviation calculation based on velocity fluctuation components for single-phase DNS at $Re_\tau = 180$

The ANN was trained on 10,000 particle trajectories for each simulation dataset over 100 epochs. Training beyond this point led to overfitting, as indicated by an increase in RMSE for the validation dataset compared to the training dataset. After approximately 100 epochs, the validation MSE stabilised at around 4-5%. After training, the model was utilised to simulate particle-laden flows and the results were compared with those from DNS-LPT for corresponding simulations.

Figure 4 compares the predicted mean streamwise velocities of the hybrid ML particles with the DNS-LPT results for $Re_\tau = 180$ and $\rho_P^* = 2.5, d_P^* = 0.0025$. The predictions show excellent agreement across the wall-normal direction of the channel, with some slight overprediction in the bulk flow region. Similar comparisons for the RMS velocity fluctuations and the shear stress are shown in Fig. 5, revealing close alignment of the two predictions close to the wall but noticeable discrepancies in the channel's core. These deviations are more significant for the wall-normal and spanwise components. It is evident that the hybrid ML algorithm tends to overestimate the velocity fluctuations for these two components, likely due to the inability to fully capture emergent behaviour such as particle entrainment in low-speed streaks in the buffer layer, at which the accuracy is weakest. The algorithm also captures the general trends in the shear stress profile, though its accuracy is lower both within the buffer layer region as well as within the bulk flow region.

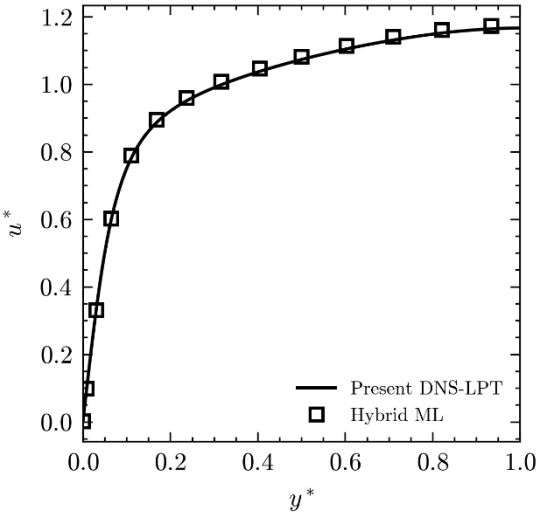

Figure 4: Comparison of mean particle streamwise velocity predictions between the present DNS results and the hybrid ML-predicted trajectories for $Re_\tau = 180$ and $\rho_P^* = 2.5, d_P^* = 0.0025$

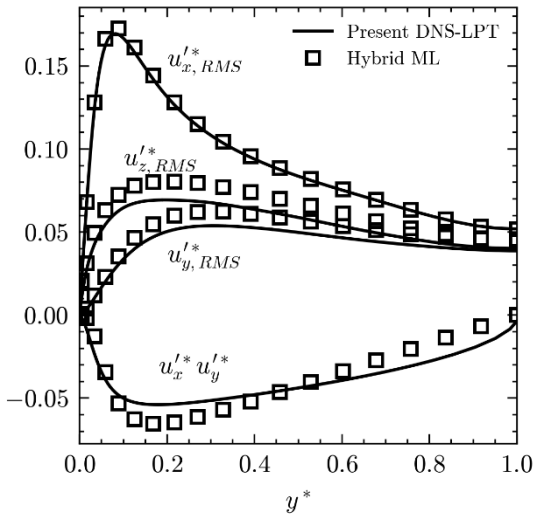

Figure 5: Comparison of and root-mean-square velocity fluctuations and shear stress predictions between the present DNS results and the hybrid ML-predicted trajectories for $Re_\tau = 180$ and $\rho_P^* = 2.5, d_P^* = 0.0025$

To determine the extent to which the hybrid ML algorithm can handle parameter sets outside those originally trained upon, an additional DNS-LPT simulation was performed at $Re_\tau = 240$, which lies halfway between those considered for the training datasets.

Figures 6 and 7 present the comparison of mean streamwise velocities and RMS velocity fluctuations for the untrained parameter set at $Re_\tau = 240$, in order to assess the generalisation capability of the hybrid ML model to conditions outside the training range.

In Figure 6, the predicted mean streamwise velocities show strong agreement with the DNS-LPT results across the wall-normal direction of the channel. Minor discrepancies are observed in the bulk region, where the ML model slightly overestimates the velocities. This overprediction could be attributed to the model's interpolation between the trained datasets at $Re_\tau = 180$ and 300, leading to a slight bias, though slight overprediction was observed in both training datasets. Nevertheless, the model accurately captures the overall trend, demonstrating its ability to generalise the mean particle behaviour to intermediate Reynolds numbers effectively.

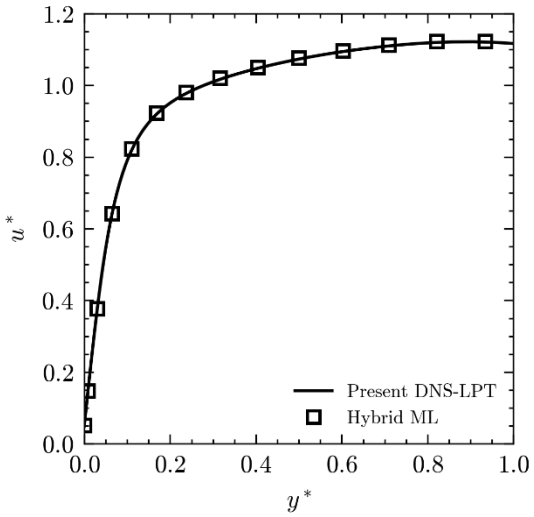

Figure 6: Comparison of mean particle streamwise velocity predictions between the present DNS results and the hybrid ML-predicted trajectories for $Re_\tau = 240$ and $\rho_P^* = 2.5, d_P^* = 0.0025$

Figure 7 compares the RMS velocity fluctuations, exhibiting strong agreement near the channel walls but noticeable deviations in the core region. These discrepancies are more pronounced for the wall-normal and spanwise components, consistent with observations for the other Reynolds numbers. The hybrid ML model tends to this time underpredict the fluctuations, particularly in regions where turbulence modulation is more significant. This is likely due to the model's inability to further fully capture complex emergent behaviours, such as particle clustering and low-speed streak entrainment, which are more prominent at higher Reynolds numbers.

Overall, the hybrid ML model exhibits strong predictive performance for an unseen Reynolds number, validating its generalisability across different flow conditions. However, the overestimation of velocity fluctuations indicates potential areas for improvement, such as incorporating additional physical models or enhancing Gaussian noise modelling techniques to

better inform the model of the presence of turbulent structures and particle-fluid interactions.

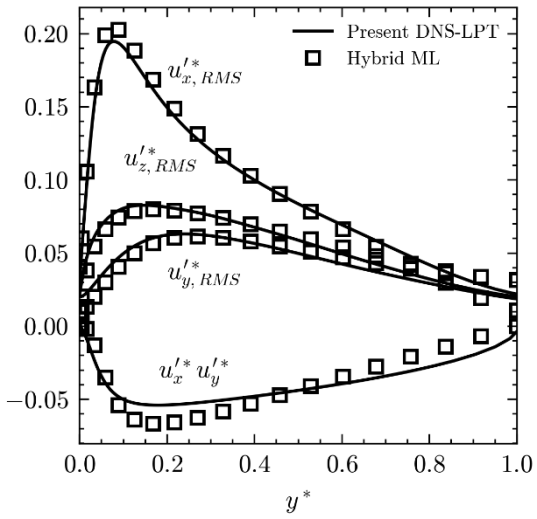

Figure 7: Comparison of and root-mean-square velocity fluctuations and shear stress predictions between the present DNS results and the hybrid ML-predicted trajectories for $Re_\tau = 240$ and $\rho_P^* = 2.5, d_P^* = 0.0025$

4. CONCLUSIONS

This study aimed to develop and validate an enhanced predictive model for simulating particle dispersion, advection, and wall interactions in turbulent channel flows using a hybrid machine learning algorithm. By utilising dynamic databases generated from DNS and LPT, another aim was to reduce the amount of simulation data required to achieve statistically stationary and accurate profiles while maintaining high prediction accuracy. Additionally, the model was tested on an unobserved parameter set at Re_τ=240 to evaluate its generalisability beyond the training parameter sets.

The results demonstrate that the hybrid ML algorithm, which incorporates an ANN model, effectively predicts particle trajectories with a significant reduction in computational cost. The model requires only around 10,000 DNS-LPT trajectories for training (c.f. 300,000 used in comparative studies [20]) and is able to generate additional ML-informed trajectories efficiently, resulting in substantial time and resource savings. This efficiency was particularly evident when generating synthetic trajectories for untrained Reynolds numbers, where the model captured the mean streamwise velocities with high accuracy. Although some discrepancies were noted in the RMS velocity fluctuations, particularly in the wall-normal and spanwise components, the overall agreement with DNS-LPT results was strong, validating the model's predictive capability.

The study demonstrates the potential of the hybrid ML algorithm for efficiently simulating particle dynamics in wall-bounded turbulent flows, making it a critical tool for real-time applications, such as digital twin technology. The model's ability to generalise to an unobserved Reynolds number showcases its robustness and adaptability across different flow conditions. However, the overestimation of velocity fluctuations in the channel core suggests areas for further refinement, such as enhancing the noise model or incorporating additional models (such as physics-informed components to the neural network) to better allow the training to understand interaction with complex flow structures.

Despite these areas for improvement, the reduced computational time and increased efficiency offered by this approach make it a promising alternative to traditional DNS-LPT simulations. Future work will focus on optimising the model architecture, exploring advanced noise modelling techniques, and extending its applicability to more complex flow scenarios and particle behaviours. These advancements will further enhance the model's accuracy and versatility, broadening its utility in both academic research and industrial applications, particularly where real-time analysis and decision-making are critical.

ACKNOWLEDGEMENTS

The authors are grateful to the UK Engineering and Physical Sciences Research Council for funding through the TRANSCEND (Transformative Science and Engineering for Nuclear Decommissioning) project (EP/S01019X/1), and Sellafield Ltd. for funding from the University of Leeds-Sellafield Ltd Centre of Expertise for Sludge (Particulates & Fluids).

REFERENCES

[1] Carleo, G., Cirac, I., Cranmer, K., Daudet, L., Schuld, M., Tishby, N., Vogt-Maranto, L., and Zdeborová, L., 2019, "Machine Learning and the Physical Sciences," *Reviews of Modern Physics*, Vol. 91, 045002.

[2] Mahesh, B., 2020, "Machine Learning Algorithms – A Review," *International Journal of Science and Research (IJSR)*, Vol. 9, pp. 381-386.

[3] Barragán-Montero, A., Javaid, U., Valdés, G., Nguyen, D., Desbordes, P., Macq, B., Willems, S., Vandewinckele, L., Holmström, M., Löfman, F., and Michiels, S., 2021, "Artificial Intelligence and Machine Learning for Medical Imaging: A Technology Review," *Physica Medica*, Vol. 83, pp. 242-256.

[4] Ali, A., Abd Razak, S., Othman, S.H., Eisa, T.A.E., Al-Dhaqm, A., Nasser, M., Elhassan, T., Elshafie, H., and Saif, A., 2012, "Financial Fraud Detection Based on Machine Learning:

A Systematic Literature Review," *Applied Sciences*, Vol. 12, 9637.

[5] Gupta, A., Anpalagan, A., Guan, L., and Khwaja, A.S., 2021, "Deep Learning for Object Detection and Scene Perception in Self-Driving Cars: Survey, Challenges, and Open Issues," *Array*, Vol. 10, 100057.

[6] Wang, Z., Xiao, D., Fang, F., Govindan, R., Pain, C.C., and Guo, Y., 2018, "Model Identification of Reduced Order Fluid Dynamics Systems Using Deep Learning," *International Journal for Numerical Methods in Fluids*, Vol. 86, pp. 255-268.

[7] de Oliveira Maionchi, D., Ainstein, L., dos Santos, F.P., and de Souza Júnior, M.B., 2022, "Computational Fluid Dynamics and Machine Learning as Tools for Optimization of Micromixers Geometry," *International Journal of Heat and Mass Transfer*, Vol. 194, 123110.

[8] Brunton, S.L., Noack, B.R., and Koumoutsakos, P., 2020, "Machine Learning for Fluid Mechanics," *Annual Review of Fluid Mechanics*, Vol. 52, pp. 477-508.

[9] Jain, P., Choudhury, A., Dutta, P., Kalita, K., and Barsocchi, P., 2021, "Random Forest Regression-Based Machine Learning Model for Accurate Estimation of Fluid Flow in Curved Pipes," *Processes*, Vol. 9, 2095.

[10] Li, K., Savari, C., Sheikh, H.A., and Barigou, M., 2023, "A Data-Driven Machine Learning Framework for Modeling of Turbulent Mixing Flows," *Physics of Fluids*, Vol. 35, 015150.

[11] Yang, Z., Li, K., and Barigou, M., 2023, "Experimentally Trained Hybrid Machine Learning Algorithm for Predicting Turbulent Particle-Laden Flows in Pipes," *Physics of Fluids*, Vol. 35, 113309.

[12] Benra, F.K., Dohmen, H.J., Pei, J., Schuster, S., and Wan, B., 2011, "A Comparison of One-Way and Two-Way Coupling Methods for Numerical Analysis of Fluid-Structure Interactions," *Journal of Applied Mathematics*, Vol. 2011, 853560.

[13] Mortimer, L.F., Njobuenwu, D.O., and Fairweather, M., 2020, "Agglomeration Dynamics in Liquid–Solid Particle-Laden Turbulent Channel Flows Using an Energy-Based Deterministic Approach," *Physics of Fluids*, Vol. 32, 043301.

[14] Wagg, D.J., Worden, K., Barthorpe, R.J., and Gardner, P., 2020, "Digital Twins: State-of-the-Art and Future Directions for Modeling and Simulation in Engineering Dynamics Applications," *ASCE-ASME Journal of Risk and Uncertainty in Engineering Systems, Part B: Mechanical Engineering*, Vol. 6, 030901.

[15] Fischer, P.F., Lottes, J.W., and Kerkemeier, S.G., "Nek5000," available at: http://nek5000.mcs.anl.gov/, accessed September 1, 2008.

[16] Maxey, M.R., 1987, "The Gravitational Settling of Aerosol Particles in Homogeneous Turbulence and Random Flow Fields," *Journal of Fluid Mechanics*, Vol. 174, pp. 441-465.

[17] Riley, J.J., and Patterson, J.R.G., 1974, "Diffusion Experiments with Numerically Integrated Isotropic Turbulence," *Physics of Fluids*, Vol. 17, pp. 292-297.

[18] Mortimer, L.F., Njobuenwu, D.O., and Fairweather, M., 2019, "Near-Wall Dynamics of Inertial Particles in Dilute Turbulent Channel Flows," *Physics of Fluids*, Vol. 31, 063302.

[19] Fairweather, M., and Hurn, J.P., 2008, "Validation of an Anisotropic Model of Turbulent Flows Containing Dispersed Solid Particles Applied to Gas-Solid Jets," *Computers and Chemical Engineering*, Vol. 32, pp. 590-599.

[20] Rupp, D.A., Mortimer, L.F., and Fairweather, M., 2023, "Stokes Number and Coupling Effects on Particle Interaction Behavior in Turbulent Channel Flows," *Physics of Fluids*, Vol. 35, 113307.

Conference on Modelling Fluid Flow (CMFF'25)
The 19th International Conference on Fluid Flow Technologies
Budapest, Hungary, August 26 - August 29, 2025

ENHANCING PREDICTIVE ACCURACY OF TURBULENT SUBCOOLED FLOW BOILING USING LES

Hanan ABUREMA[1], Bruce C HANSON[2], Michael FAIRWEATHER[3], Marco COLOMBO[4]

[1] Corresponding Author. School of Chemical & Process Engineering, University of Leeds, Leeds LS2 9JT, UK. E-mail: pmhaa@leeds.ac.uk
[2] School of Chemical & Process Engineering, University of Leeds, Leeds LS2 9JT, UK. E-mail: b.c.hanson@leeds.ac.uk
[3] School of Chemical & Process Engineering, University of Leeds, Leeds LS2 9JT, UK. E-mail: m.fairweather@leeds.ac.uk
[4] School of Mechanical, Aerospace & Civil Engineering, University of Sheffield, Sheffield S10 2TN, UK. E-mail: m.colombo@sheffield.ac.uk

ABSTRACT

The high heat transfer rates required in many cooling systems can often only be achieved through subcooled boiling flows in heated wall regions, with boiling providing the heat transfer rates required to maintain system integrity. Understanding the mechanism of boiling in systems with turbulent subcooled flows is essential for enhancing the predictive capabilities for nuclear thermal hydraulic systems. This study investigates two boiling models coupled with large eddy simulations employing a dynamic subgrid-scale eddy viscosity model. One boiling model utilises a mechanistic force balance approach to predict bubble dynamics: accounting for the bubble growth and detachment processes affected by micro-layer evaporation, heat transfer from the superheated liquid, and condensation on the bubble cap due to the subcooled liquid. The other model employs a reduced correlation-based approach to determine bubble departure diameter and frequency, aiming to improve the applicability of the force balance method while reducing computational and calibration requirements. To evaluate the performance of these models, validation is conducted against experimental data for vertically upward subcooled boiling flows using water and refrigerant R12. These datasets encompass a wide range of operating conditions, ensuring a robust and comprehensive assessment of model accuracy. Results indicate that both models achieve satisfactory predictive accuracy across all tested conditions, demonstrating improvements over equivalent Reynolds-Averaged Navier-Stokes-based approaches. Although the mechanistic model provides superior precision in predicting bubble dynamics, this enhanced accuracy comes at the cost of increased computational demand, making the correlation-based approach a viable alternative for engineering applications requiring reduced computational expense. These findings contribute to the ongoing development of high-fidelity boiling models for nuclear thermal hydraulic simulations, offering valuable insights for future research and industrial applications.

Keywords: subcooled boiling, bubble dynamics, large eddy simulation, force balance model, reduced correlation

NOMENCLATURE

F_b	$[N]$	buoyancy force
F_{cp}	$[N]$	contact pressure force
F_{du}	$[N]$	unsteady drag force
F_p	$[N]$	hydrodynamic force
F_{st}	$[N]$	surface tension force
G_s	[-]	dimensionless shear rate
Ja	[-]	Jacob number
P	$[Pa]$	pressure
R	$[m]$	bubble radius
S	$[1/s]$	rate of strain tensor
d_B	$[m]$	bubble diameter
d_{dep}	$[m]$	bubble departure diameter
d_w	$[m]$	contact diameter
g	$[m/s^2]$	gravitational acceleration
t	$[s]$	time
u	$[m/s]$	velocity
u_τ	$[m/s]$	shear velocity
u^+	[-]	dimensionless velocity
y^+	[-]	dimensionless wall distance
Γ	$[kg/m^3.s]$	mass transfer rate
Δ	$[m]$	filtering width
α	[-]	void fraction
μ	$[kg/m\ .s]$	dynamic viscosity
ν	$[m^2/s]$	kinematic viscosity
ρ	$[kg/m^3]$	density

Subscripts and Superscripts

G	gas
I	Either phase
L	liquid
d	drag
x, *y*	spatial coordinates

1. INTRODUCTION

Boiling phenomena in turbulent subcooled flows are crucial for achieving efficient heat transfer, particularly in thermal hydraulic systems, making it a key focus for researchers in both industry and academia. Subcooled flow boiling plays a critical role in applications requiring effective cooling, such as nuclear reactors, refrigeration systems, and in the chemical processing industries [1]. However, this process is highly complex due to the intricate dynamics of bubble nucleation, growth, detachment, and dispersion near heated surfaces. A comprehensive understanding of these phenomena is crucial for optimising system designs, enhancing performance, and ensuring the reliability and safety of advanced thermal systems.

The transient and complex nature of boiling phenomena makes it difficult to fully understand their underlying physical mechanisms. Experimental studies have primarily aimed at developing empirical correlations based on extensive datasets obtained under diverse geometries, fluid types, and operating conditions [2, 3]. However, these experiments are expensive, and the resulting correlations are often limited to the specific conditions and setups used. To overcome these limitations, computational fluid dynamics (CFD), and particularly Eulerian-Eulerian approaches, have been widely employed to model flow boiling, providing a more adaptable and cost-effective tool for investigating these processes [4].

In this approach, the conservation equations for mass, momentum, and energy are solved separately for each phase. However, this method simplifies the system by averaging the phase occurrence over time and space, which results in the loss of detailed interface structure information. As a result, additional models are required to account for the exchange of mass, momentum, and energy between the phases [5]. The phase change at the heated wall and the distribution of heat flux between the liquid and vapour phases are typically modelled using wall boiling models. One of the most widely used heat flux partitioning models is the Rensselaer Polytechnic Institute (RPI) model [6], in which the external heat flux applied to the heating wall is divided into three primary heat transfer mechanisms: single-phase convection, quenching, and evaporation. These mechanisms depend on several key parameters, including nucleation site density, bubble departure diameter, and bubble departure frequency, with correlations for these quantities initially derived from pool boiling experiments conducted at ambient pressure [7]. A detailed review of the available correlations can be found in [8]. Numerous studies have evaluated the applicability of the RPI model using the standard correlations implemented in most CFD packages. However, these studies have shown that the model often exhibits limited accuracy and generality [4].

Among the key parameters requiring accurate modelling, the bubble departure diameter is particularly important for predicting the void fraction distribution within the flow. Consequently, mechanistic sub-models that explicitly describe bubble dynamics are essential for improving predictive accuracy. Klausner et al. [9] developed a mechanistic model based on a force balance during the bubble's growth phase prior to its departure from a surface. This model demonstrated good predictive performance against their experimental data. Over the years, many researchers have worked on improving the original model to increase its predictive capability across a wider range of experimental conditions [10]. One significant enhancement involved incorporating local condensation effects into the bubble growth rate model, along with modifications to the lift force and surface tension models [11]. Further improvements were made by integrating microlayer evaporation beneath the bubble to enhance model accuracy [12]. Recent research conducted at the Massachusetts Institute of Technology (MIT) has introduced a comprehensive approach to heat flux partitioning by incorporating all essential wall nucleation closures [13]. Using experimental data obtained through advanced measurement techniques, the MIT model provides wall nucleation closures that are applicable across a wide range of pressures and flow conditions. Unlike conventional models, this approach eliminates the need for case-specific calibration, improving its adaptability and reliability [14].

Most existing modelling efforts for subcooled boiling have relied on Reynolds-averaged Navier-Stokes (RANS) approaches due to their relatively low computational cost. However, RANS models tend to over-predict mixing and fail to capture the complex transient dynamics of turbulent flow boiling due to their inherent averaging of turbulent fluctuations. To address these limitations, researchers have increasingly turned to large eddy simulation (LES), which offers a more accurate and robust framework for studying complex boiling phenomena [15]. Although LES requires significantly greater computational resources than RANS-based approaches, continuous advancements in computing power are making it increasingly feasible for high-fidelity analysis and optimisation of boiling flows. In this study, the bubble dynamics model and the reduced-correlation MIT model are implemented in the OpenFOAM code and compared within an LES framework. LES allows a detailed investigation of subcooled boiling flows, offering

improved accuracy in capturing key phenomena. Both models are validated against experimental data for vertically upward boiling flows using water and refrigerant R12 over a wide range of conditions.

2. MATHEMATICAL MODELLING

By spatially filtering the governing equations in the Eulerian-Eulerian two-fluid model in LES, large-scale motions are explicitly resolved, while small subgrid-scale (SGS) fluctuations are modelled:

$$\frac{\partial(\alpha_I \rho_I)}{\partial t} + \nabla.(\alpha_I \rho_I u_I) = \Gamma \tag{1}$$

$$\frac{\partial(\alpha_I \rho_I u_I)}{\partial t} + \nabla.(\alpha_I \rho_I u_I u_I) = \alpha_I \rho_I g - \alpha_I \nabla P + \nabla.(\alpha_I \tau_I) + M_I \tag{2}$$

The influence of the unresolved scales on the resolved scales is represented through the SGS stress tensor, which is modelled as:

$$\tau_i = -\mu_{eff}\left((\nabla u_I) + (\nabla u_I)^T - \frac{2}{3} I(\nabla . u_I)\right) \tag{3}$$

For the liquid phase, the effective viscosity μ_{eff} is determined by considering molecular viscosity, turbulent viscosity, and bubble-induced turbulence, with the latter being modelled using the Sato et al. [16] model, ensuring an accurate representation of the flow dynamics:

$$\mu_{eff} = \mu_{L,L} + \mu_{T,L} + \mu_{BI,L} \tag{4}$$

$$\mu_{BI,L} = \rho_L C_{BI} \alpha_G d_B |u_G - u_L| \tag{5}$$

In this study, the dynamic Smagorinsky SGS model is used to model the unresolved turbulence viscosity, which relies on applying a second filter considering both spatial and temporal variations:

$$\mu_{T,L} = \rho_L (C_s \Delta)^2 \left|\overline{S_{ij}}\right| \tag{6}$$

The precision of the model is improved by accounting for such variations, making it more dependable for capturing flow dynamics. It employs a dynamic procedure to calculate C_s based on the resolved stress tensor L_{ij} and the Germano rate of strain tensor M_{ij} through an iterative process [17]:

$$C_s = \frac{1}{2}\frac{L_{IJ} M_{IJ}}{M_{IJ} M_{IJ}} \tag{7}$$

$$L_{IJ} = \widehat{\bar{u}_\iota \bar{u}_j} - \hat{\bar{u}}_\iota \hat{\bar{u}}_j \tag{8}$$

$$M_{IJ} = \Delta^2 \widehat{\bar{S}_{\iota j} \bar{S}_{\iota j}} - \hat{\bar{S}}_{\iota j} \hat{\bar{S}}_{\iota j} \tag{9}$$

The turbulence kinetic energy is modelled based on the dynamic procedure as:

$$k = C_s . \Delta^2 . |S|^2 \tag{10}$$

For the gas phase, turbulence is not resolved, and the effects of liquid-phase turbulence on the gas phase are neglected. This simplification reduces model complexity and avoids the need for additional equations to account for gas-phase turbulence. The interfacial momentum transfer term M_I introduces the dynamic interaction between the phases in a multiphase flow. This term primarily accounts for contributions from various forces, including drag, lift, wall lubrication, turbulent dispersion, virtual mass, surface tension, and phase change mass transfer forces, particularly in the context of boiling flow. The drag force is the resistance experienced by a bubble as it moves through the liquid, modelled as:

$$F_d = \frac{3}{4}\frac{C_d}{d_B} \alpha_G \rho_L |(u_G - u_L)|(u_G - u_L) \tag{11}$$

The drag coefficient C_d is calculated using the drag model proposed by Tomiyama et al. [18]. The bubbles moving in a shear flow experience a lift force perpendicular to their direction of motion, influencing the radial void distribution in pipes, with small bubbles pushed towards the wall, while larger bubbles tend to move toward the centre after reaching a critical diameter. The wall force, on the other hand, keeps bubbles away from the wall. However, due to the limited understanding of the contributions of lift and wall forces in boiling flows [4], these forces are neglected in this study. The virtual mass force is accounted for using a fixed coefficient of 0.5, and the turbulent dispersion force is modelled following Lopez de Bertodano [19], with a turbulent dispersion coefficient 0.7.

$$F_{vm} = \alpha_G \rho_L C_{vm}\left(\frac{Du_G}{Dt} - \frac{Du_L}{Dt}\right) \tag{12}$$

$$F_{td} = k \nabla \alpha_G \rho_L C_{td} \tag{13}$$

The multiple size group (MUSIG) population balance model is used, which is part of OpenFOAM, with bubble coalescence modelled according to [20] and break-up based on [21].

3. WALL BOILING MODEL

In the mechanistic approach to modelling boiling, the bubble departure diameter is determined by the bubble growth rate, which is predicted through an energy balance. This balance incorporates the heat transfer mechanisms between the bubble, the heated wall, and the surrounding liquid. Recently, Colombo and Fairweather [12] proposed a combined equation that integrates the contributions of superheating and subcooling in predicting the bubble growth rate during flow boiling. These phenomena are crucial as they influence the overall heat transfer efficiency of the system. During the growth process, the forces acting on the bubble can be classified into *x*-direction adhesive forces, which keep the bubble attached to

the nucleation site, and *y*-direction detaching forces which act to separate the bubble from the surface. When the resultant detaching forces exceed the adhesive forces, the bubble departs from the nucleation site. Similarly, for a sliding bubble, if the detaching forces surpass the adhesive forces, the bubble lifts off from the heated surface and moves toward the bulk flow. The various forces influencing bubble growth at the nucleation site are shown in Figure 1, which demonstrates these interactions, with the model summarised in Table 1.

Table 1. Summary of the closures used with the force balance model (FB)

Model	Form
Bubble departure diameter	Klausner et al [9] $\sum F_y = F_{sty} + F_{sl} + F_b \cos\theta + F_{duy} + F_p + F_{cp}$ $\sum F_x = F_{st} + F_{qsd} + F_b \sin\theta + F_{dux}$ $F_{stx} = -1.25 d_w \sigma \frac{\pi(\alpha-\beta)}{\pi^2-(\alpha-\beta)^2}(sin\alpha - sin\beta)$ $F_{sty} = -d_w \sigma \frac{\pi}{(\alpha-\beta)}(cos\beta - cos\alpha)$ $F_{qsd} = 6\pi\rho_l \nu U R \left\{\frac{2}{3} + \left[\left(\frac{12}{Re}\right)^{0.65} + 0.862\right]^{-1.54}\right\}$ $F_{du} = -\rho_l R^2 \left(\frac{2}{3}R^{\cdot 2} + RR^{\cdot 2}\right)$ $F_b = \frac{4}{3}\pi R^3(\rho_l - \rho_g)g$ $F_{sl} = \frac{1}{2}\pi\rho_l U R^2 \left\{3.877 G_s^{0.5}[Re^{-2} + (C_l G_s^{0.5})^4]^{\frac{1}{4}}\right\}$ $F_p = \frac{9}{8}\rho_l U^2 \frac{\pi d_w^2}{4}$ $F_{cp} = \frac{\sigma}{R}\frac{\pi d_w^2}{4}$ Yun et al. [11] $d_w/d_{dep} = 0.067,\ C_l = 0.118$
Bubble growth	Colombo and Fairweather [12] $\frac{dR(t)}{dt} = \frac{1}{C_2} Pr^{-0.5} Ja \left(\frac{k_l}{\rho_l C_{p,l}}\right)^{0.5} t^{-0.5} + \sqrt{\frac{3}{\pi}} Ja \left(\frac{k_l}{\rho_l C_{p,l}}\right)^{0.5} (1-b) t^{-0.5} - \frac{h_c}{\rho_l h_{lg}}(T_{sat} - T_{sub})b$
Nucleation site density	Hibiki and Ishii [22] $N_a` = N_0 \left[1 - exp\left(-\frac{\theta^2}{8\mu^2}\right)\right]\left[exp\left(f` \frac{\lambda`}{R_c}\right) - 1\right]$
Bubble departure frequency	Cole [23] $f = \sqrt{\frac{3}{4}\frac{g(\rho_l - \rho_g)}{d_w \rho_l}}$

In the MIT framework, the departure diameter refers to the bubble size at the moment it detaches from the nucleation site, either by sliding along the heated surface or by moving into the bulk liquid. In contrast, the lift-off diameter describes the size of a sliding bubble at the instant it detaches from the heated surface entirely and moves into the bulk flow. Another essential parameter in the MIT framework is the bubble departure frequency, which is determined by incorporating bubble wait time and an improved representation of bubble growth dynamics, derived from a force balance approach. This methodology captures the interplay between wall superheat and flow subcooling, enabling the accurate prediction of bubble behaviour and detachment trends under various boiling conditions.

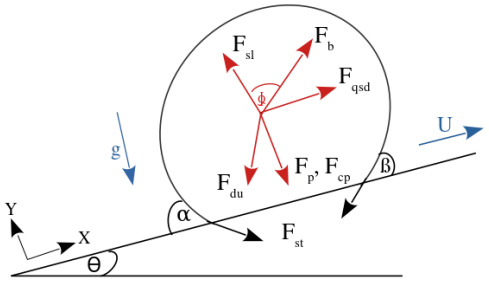

Figure 1. Forces acting on a bubble at the nucleation site

Table 2. Summary of the closures used with the MIT model

Model	Form
Bubble departure diameter	Kommajosyula [13] $18.6\ 10^{-6}\left(\frac{\Delta\rho}{\rho_g}\right)^{0.27} Ja_{sup}^{0.75}(1 + Ja_{sub})^{-0.3} u_l^{-0.26}$
Bubble growth	Kommajosyula [13] $K = \frac{\sqrt{k_l}}{0.804\sqrt{Pr}} Ja_{sup} + \mathcal{X} 1.95 Ja_{sup} k_l$
Nucleation site density	Lemmert and Chawla [24] $N_a = C_n N_{ref}\left(\frac{\Delta T}{dT_{ref}}\right)^{1.805}$
Bubble departure frequency	Kommajosyula [13] $f = \frac{1}{t_{growth}+t_{wait}}$ $t_{growth} = \left(\frac{d_{dep}}{4K}\right)^2$ $t_{wait} = \frac{0.0061\ Ja_{sub}^{0.63}}{\Delta T_{sup}}$

The MIT model represents a robust subcooled flow boiling formulation with new closures applicable over a wide range of flow conditions. In this study, two key closures have been tested: the bubble departure diameter and the bubble departure frequency. By evaluating these closures, the results contribute to a deeper understanding of bubble dynamics in boiling flows and enhance the predictive capabilities of the model. The model parameters and

closures used with the MIT framework are summarised in Table 2.

4. WALL TREATMENT

In LES, the accurate representation of the near-wall region is essential due to the significant velocity gradients near a surface. The standard logarithmic law often fails to capture the complexities of non-equilibrium wall functions and pressure gradient effects, especially in the presence of strong turbulence. To overcome these limitations, Spalding's formula [25] is used, where the turbulence length scale, y^+, is defined as follows:

$$y^+ = u^+ + \frac{1}{E}\left[e^{cu^+} - 1 - cu^+ - \frac{(cu^+)^2}{2} - \frac{(cu^+)^3}{6}\right] \quad (13)$$

where E = 9.025 and c = 0.4, and the dimensionless parameters y^+ and u^+ are defined as:

$$y^+ = \frac{yu_\tau}{\nu} \ , u^+ = \frac{u}{u_\tau} \quad (14)$$

Since Spalding's equation is nonlinear, an iterative procedure, such as the Newton-Raphson method, must be used to solve for u_τ .This method ensures rapid convergence and improves the accuracy of near-wall turbulence modelling by capturing velocity variations more effectively.

5. EXPERIMENTAL AND NUMERICAL SETUP

Two experiments were selected to validate the numerical simulations in this study: the DEBORA experiments [26], and the Bartolomei and Chanturiya [27] experiment. The DEBORA experiments investigated subcooled boiling of Freon-12 in a vertical pipe with an inner diameter of 19.2 mm and a length of 3.5 m, simulating high-pressure water boiling at pressures ranging from 1.46 to 3.01 MPa. In contrast, the Bartolomei and Chanturiya experiment examined subcooled boiling of water in a vertical pipe with a 15.4 mm inner diameter and a heated length of 2 m, operating at pressures up to 15 MPa. Both experiments provided critical data, including area-averaged void fractions, wall temperatures, average bubble diameters, and liquid temperatures. These datasets serve as reliable benchmarks for assessing computational fluid dynamic models as they effectively capture boiling conditions relevant to nuclear reactor systems while remaining experimentally accessible.

The numerical simulations were conducted using a three-dimensional axisymmetric geometry, with the computational domain designed to replicate the experimental setups. To reduce computational cost while maintaining accuracy, a 10° wedge of each pipe was employed as the computational domain. A fully developed velocity profile was specified at the inlet of the domain to ensure representative flow conditions, which is essential for capturing realistic flow behaviour. At the top outlet, a pressure boundary condition was imposed. For the liquid phase, a no-slip boundary condition was applied at the wall, while a free-slip condition was used for the vapour phase to account for the negligible shear stress at the wall for this phase. A central differencing scheme was used for the advection term to minimise numerical diffusion and enhance accuracy. For time discretisation, a second-order backward Euler scheme was selected to improve temporal accuracy and stability. These schemes were chosen to ensure a robust and accurate representation of the complex boiling phenomena under investigation. However, it is important to note that the computational cost varied significantly between the models. The simulation time using the mechanistic model was approximately twice that of the MIT model, primarily due to the detailed treatment of bubble dynamics, which requires additional computational resources to resolve small-scale boiling mechanisms accurately.

6. RESULTS AND DISCUSSION

The results demonstrate the performance of the LES framework when coupled with two distinct boiling models: a mechanistic force balance approach and the reduced, correlation-based MIT model. These models are validated using experimental data for vertically upward subcooled boiling flows. In addition, comparisons are made with previous studies [28] that employed a force balance approach while neglecting subcooling effects, obtained using a RANS-based method. The analysis focuses on key parameters, including void fraction distribution, average bubble diameter, and wall temperature profiles.

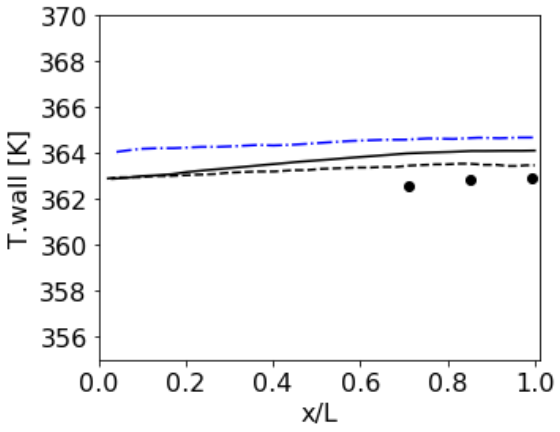

Figure 2. Wall temperature predictions along the heated wall for DEBORA experiment [26]: • data; — FB; --- MIT; - - - Colombo et al. [28]

In Figure 2, which compares predictions with the DEBORA experiment, both the force balance and MIT models tend to over-predict the wall

temperature, with RANS showing the highest over-predictions.

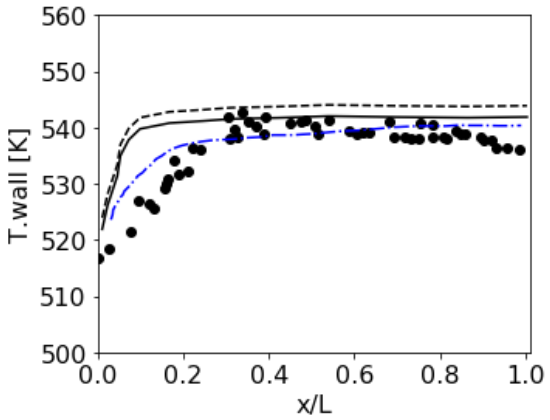

Figure 3. Wall temperature predictions along the heated wall for Bartolomei and Chanturiya experiment [27]: • data; — FB; --- MIT; - · - Colombo et al. [28]

More detailed experimental axial wall temperatures along the pipe length are available for the Bartolomei and Chanturiya [27] case, as shown in Figure 3. Here, the temperature exhibits a rapid increase in the early regions of the pipe, followed by a levelling off and a slight decline towards the outlet. Both the mechanistic and MIT models roughly follow the experimental trend, capturing the rise in wall temperature close to the pipe inlet, although the rate of increase is significantly over-estimated. This increase is primarily influenced by local flow acceleration and changes in heat transfer mechanisms.

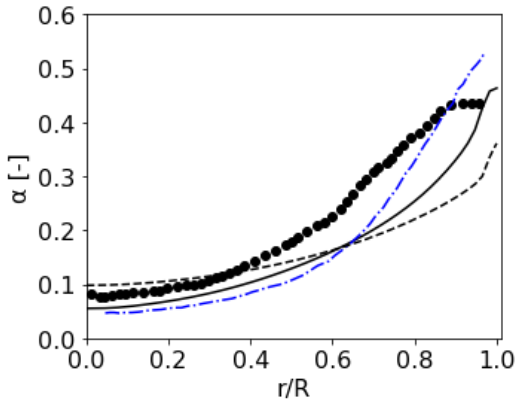

Figure 4. Radial void fraction predictions for DEBORA experiment [26]: • data; — FB; --- MIT; - · - Colombo et al. [28]

Once boiling begins, however, both models show good agreement with the experimental data. The mechanistic model slightly over-predicts the wall temperature, particularly near the pipe end, although less so that the MIT model, most likely due to its detailed treatment of bubble dynamics and heat flux partitioning. Over-prediction by the MIT model can be attributed to its simplified correlation-based approach which does not fully capture the intricate interactions between bubble dynamics and heat transfer, especially under subcooled boiling conditions. In contrast, the predictions from Colombo et al. [28], which rely on a RANS-based approach, show a significant over-prediction of wall temperature for the DEBORA experiment (Figure 2). This discrepancy may stem from the limitations of the RANS framework in resolving complex heat transfer mechanisms and bubble dynamics, particularly in regions where subcooling and phase interactions play a critical role. When comparing similar predictions with the data from Bartolomei and Chanturiya [27], the RANS-based approach, as presented by Colombo et al. [28], shows good agreement with the experimental data in the boiling region but also exhibits a slight overprediction in the non-boiling region.

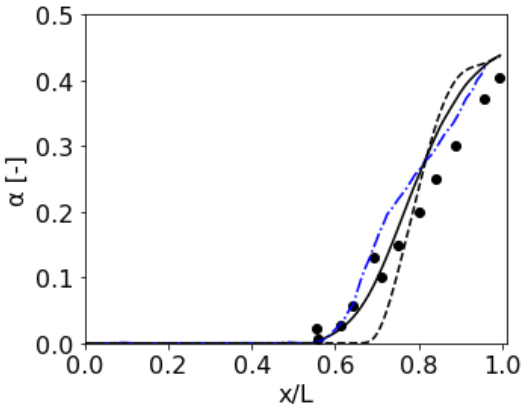

Figure 5. Radial void fraction predictions for Bartolomei and Chanturiya experiment [27]: • data; — FB; --- MIT; - · - Colombo et al. [28]

The predicted radial void fraction profiles, shown in Figures 4 and 5, reveal a wall-peaked distribution, consistent with experimental observations. For the DEBORA experiment, the mechanistic model captures this trend with good agreement to the experimental data, though it slightly over-predicts the void fraction near the wall, similar to the predictions from Colombo et al [28]. This over-prediction highlights the model's detailed resolution of bubble nucleation, growth, and detachment processes. A larger predicted bubble departure diameter results in longer residence times before detachment, leading to a higher evaporative heat flux at the wall. Conversely, smaller bubble departure diameter reduces the evaporative heat flux, causing an increase in wall temperature to maintain a constant flux. The resulting rise in wall temperature may enhance nucleation site density, subsequently increasing the void fraction. In contrast, the MIT model also predicts a wall-peaked profile but shows a lower void fraction near the wall compared to the experimental data. This discrepancy can be attributed to the model's assumption of extended bubble

attachment times, which increases the duration of bubble growth and reduces the frequency of bubble detachment. As a result, fewer bubbles are released into the flow, leading to a lower overall void fraction near the wall. For the Bartolomei and Chanturiya [27] experiment, all the models show a reasonable agreement with the data in Figure 5, although the force balance approach is generally superior. The MIT model indicates later onset boiling, occurring after the pipe's midpoint. This delayed transition to boiling corresponds to the higher predicted wall temperatures (Figure 3), which result from a decreasing local evaporation heat flux at the wall. As more heat is absorbed by the liquid phase prior to bubble lift-off, wall temperatures rise accordingly.

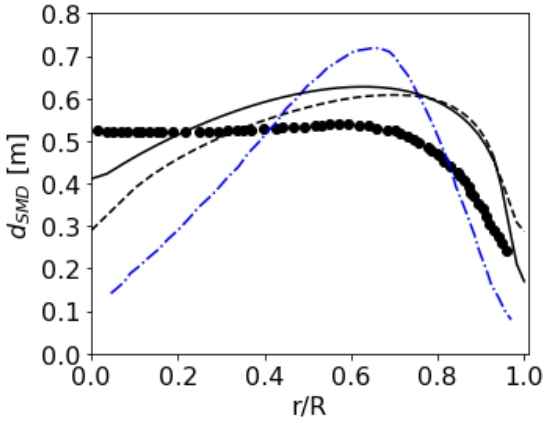

Figure 6. Radial averaged mean diameter predictions for DEBORA experiment [28]: • data; — FB; --- MIT; - - - Colombo et al. [28]

The radial distribution of the average bubble diameter for the DEBORA experiment, as shown in Figure 6, demonstrates that bubble size increases in moving away from the wall, reaching a peak value near the centre of the pipe. The mechanistic model provides the superior prediction of this overall trend but slightly under-predicts the bubble diameter near the pipe centre. This discrepancy is likely due to limitations in the model's treatment of bubble coalescence and interactions within the bulk flow, which would affect the predicted bubble size in the core region. Although both boiling model approaches use the same population balance, the MIT model exhibits a similar trend but predicts smaller bubble sizes compared to the mechanistic model and significantly under-predicts experimental data at the pipe centre. This discrepancy is likely due to the different void profiles between the two models which will affect coalescence and break-up differently. In contrast, the predictions from [28] significantly under-predict the bubble size across the bulk of the radial profile, with the exception of the peak at r/R ≈ 0.65. This under-prediction highlights the need for further development in the population balance model used in [28], which is coupled with the boiling model, to improve the accuracy of bubble size predictions. Notably, the average bubble diameter near the wall differs significantly between the various models, which reflects the initial bubble departure diameter when the bubbles first detach from the wall and move into the bulk of the flow. This variation in departure diameter can negatively affect the prediction of radial void fraction.

7. CONCLUSIONS

This study evaluated the performance of two boiling models, a mechanistic force balance approach and a reduced correlation-based MIT model, coupled with large eddy simulation for predicting turbulent subcooled flow boiling. Validated against data from the DEBORA [26] experiments and those of Bartolomei and Chanturiya [27], the mechanistic model demonstrated superior accuracy in predicting bubble dynamics due to its detailed treatment of heat transfer mechanisms. However, it required greater computational resources compared to the MIT model, which offered a more efficient but less precise alternative.

Although the RANS-based approach relies on an averaging methodology and does not fully resolve turbulence and phase interactions, it provides good predictions of certain parameters. However, RANS models tend to oversimplify the complex, unsteady nature of boiling flows, which reduces their accuracy in predicting key parameters. In contrast, LES offers a more physically realistic representation by resolving large turbulent structures while modelling only the smaller subgrid-scale eddies. This enhanced turbulence resolution improves the accuracy of predictions for bubble departure dynamics, void fraction distribution, and heat transfer mechanisms, particularly in regions dominated by strong phase interactions and subcooling effects. However, LES also exhibits some over-prediction, especially in terms of wall temperature, indicating the need for further refinement to enhance its predictive accuracy.

ACKNOWLEDGEMENTS

This work is supported by the Ministry of Higher Education and Scientific Research of Libya.

REFERENCES

[1] Dhir, V. K., 1998, "Boling Heat Transfer", *Annu. Rev. Fluid Mech.*, Vol. 30, pp. 365-401.

[2] Zhou, K., Coyle, C., Li, J., Buongiorno, J., and Li, W., 2017, "Flow Boiling in Vertical Narrow Microchannels of Different Surface Wettability Characteristics", *Int. J. Heat Mass Transf.*, Vol. 109, pp. 103-114.

[3] Fang, X., Yuan, Y., Xu, A., Tian, L., and Wu, Q., 2017, "Review of Correlations for Subcooled Flow Boiling Heat Transfer and Assessment of their Applicability to Water", *Fusion Eng. Des.*, Vol. 122, pp. 52-63.

[4] Colombo, M., and Fairweather, M., 2016, "Accuracy of Eulerian-Eulerian, Two-Fluid CFD Boiling Models of Subcooled Boiling Flows", *Int. J. Heat Mass Transfer*, Vol. 103, pp. 28-44.

[5] Prosperetti, A., and Tryggvason, G., 2007, "Computational Methods for Multiphase Flow", *Cambridge University Press*.

[6] Kurul, N., and Podowski, M.Z., 1990, "Multidimensional Effects in Forced Convection Subcooled Boiling", *Proc. 9th International Heat Transfer Conference*, Jerusalem, Israel, pp. 21-26.

[7] Tolubinsky, V.I., and Kostanchuk, D.M., 1970, "Vapor Bubbles Growth Rate and Heat Transfer Intensity at Subcooled Water Boiling", *Proc. 4th International Heat Transfer Conference*, Paris, France, B-2.8.

[8] Cheung, S.C.P., Vahaji, S., Yeoh, G.H., and Tu, J.Y., 2014. "Modeling Subcooled Flow Boiling in Vertical Channels at Low Pressures – Part 1: Assessment of Empirical Correlations", *Int. J. Heat Mass Transfer*, Vol. 75, pp. 736-753.

[9] Klausner, J. F., Mei, R., Bernhard, D. M., and Zeng, L. Z., 1993, "Vapor Bubble Departure in Forced Convection Boiling", *Int. J. Heat Mass Transf.*, Vol. 36, pp. 651-662.

[10] Sugrue, R., and Buongiorno, J., 2016. "A Modified Force-Balance Model for Prediction of Bubble Departure Diameter in Subcooled Flow Boiling", *Nucl. Eng. Des.*, Vol. 305, pp. 717-722.

[11] Yun, B.J., Splawski, A., Lo, S., and Song, C.H., 2012, "Prediction of a Subcooled Boiling Flow with Advanced Two-Phase Flow Models", *Nucl. Eng. Des*., Vol. 253, pp. 351-359

[12] Colombo, M., and Fairweather, M., 2015. "Prediction of Bubble Departure in Forced Convection Boiling: A Mechanistic Model", *Int. J. Heat Mass Transfer*, Vol. 85, pp. 135-146.

[13] Kommajosyula, R., 2020, "Development and Assessment of a Physics-Based Model for Subcooled Flow Boiling with Application to CFD", *PhD Thesis, Massachusetts Institute of Technology*.

[14] Pham, M., Bois, G., Francois, F., and Baglietto, E., 2023. "Assessment of State-of-the-art Multiphase CFD Modeling for Subcooled Flow Boiling in Reactor Applications", *Nucl. Eng. Des*., Vol. 411, 112379.

[15] Owoeye, E.J., Schubring, D., 2016. "CFD Analysis of Bubble Microlayer and Growth in Subcooled Flow Boiling", *Nucl. Eng. Des.*, Vol. 304, pp. 151-165.

[16] Sato, Y., Sadatomi, M., and Sekoguchi, K., 1981, "Momentum and Heat Transfer in Two-Phase Bubble Flow – I. Theory", *Int. J. Multiph. Flow*, Vol. 7, pp. 167-177.

[17] Germano, M., Piomelli, U., Moin, P., and Cabot, W.H., 1991, "A Dynamic Subgrid-Scale Eddy Viscosity Model", *Phys. Fluids*, Vol. 3, pp. 1760-1765.

[18] Tomiyama, A., Kataoka, I., Zun, I., and Sakaguchi, T., 1998, "Drag Coefficients of Single Bubbles Under Normal and Micro Gravity Conditions". *JSME Int. J. Ser. B*, Vol. 41, pp. 472-479.

[19] Lopez de Bertodano, M., 1998, "Two Fluid Model for Two-Phase Turbulent Jet", *Nucl. Eng. Des.*, Vol. 179, pp. 65-74.

[20] Prince, M.J., and Blanch, H.W., 1990, "Bubble Coalescence and Break-up in Air-sparged Bubble Columns", *AIChE J*, Vol. 36, pp. 1485-1499.

[21] Lehr, F., Millies, M., and Mewes, D., 2002, "Bubble-size Distributions and Flow Fields in Bubble Columns", *AIChE J*, Vol. 48, pp. 2426-2443.

[22] Hibiki, T., and Ishii, M., 2003, "Active Nucleation Site Density in Boiling Systems", *Int. J. Heat Mass Transfer*, Vol. 46, pp. 2587-2601.

[23] Cole, R., 1960, "A Photographic Study of Pool Boiling in the Region of the Critical Heat Flux", *AIChE J.*, Vol. 6, pp. 533-538.

[24] Lemmert, M., Chawla, J.M., 1977, "Influence of flow velocity on surface boiling heat transfer coefficient", in: E. Hahne, U. Grigull (Eds.), *Heat Transfer in Boiling, Academic Press and Hemisphere*, New York, pp. 237–247.

[25] Spalding, D. B., 1961, "A Single Formula for the Law of the Wall", *J. Appl. Mech. Trans. ASME*, Vol. 28, pp. 455-458.

[26] Garnier, G., Manon, E., and Cubizolles, G., 2001, "Local Measurements of Flow Boiling of Refrigerant 12 in a Vertical Tube", *Multiph. Sci. Technol.*, Vol. 13, pp. 1-111.

[27] Bartolomei, G.G., and Chanturiya, V.M., 1967, "Experimental Study of True Void Fraction when Boiling Subcooled Water in Vertical Tubes", *Therm. Eng*., Vol. 14, pp. 123-128.

[28] Colombo, M., Thakrar, R., Fairweather, M., and Walker, S.P., 2019, "Assessment of Semi-Mechanistic Bubble Departure Diameter Modelling for the CFD Simulation of Boiling Flows", *Nucl. Eng. Des.*, Vol. 344, 15-27.

Conference on Modelling Fluid Flow (CMFF'25)
The 19th International Conference on Fluid Flow Technologies
Budapest, Hungary, August 26 - August 29, 2025

LASER-OPTICAL VALIDATION AND COMPARATIVE ANALYSIS OF NUMERICAL HEAT TRANSFER MODELS FOR SINGLE NOZZLE IMPINGEMENT FLOWS

Eileen Trampe[1], Jan-Henrik Rieger[2], Dominik Büschgens[3], Christian Wuppermann[4]

[1] Corresponding Author. Department for Industrial Furnaces and Heat Engineering, RWTH Aachen University, 52074 Aachen, Germany. Tel.: +49-241-80-26051, E-mail: trampe@iob.rwth-aachen.de
[2] Department for Industrial Furnaces and Heat Engineering, RWTH Aachen University, 52074 Aachen, Germany. E-mail: jan-henrik.rieger@rwth-aachen.de
3 Department for Industrial Furnaces and Heat Engineering, RWTH Aachen University, 52074 Aachen, Germany. E-mail: bueschgens@iob.rwth-aachen.de
4 Department for Industrial Furnaces and Heat Engineering, RWTH Aachen University, 52074 Aachen, Germany. E-mail: wuppermann@iob.rwth-aachen.de

ABSTRACT

A wide variety of heating and cooling applications, including thermal processing, use impingement nozzles for their high heat-transfer coefficients. The resulting thermal loads still require large volume flows and thus process-scale nozzle diameters, resulting in Reynolds numbers of $Re \approx 1 \times 10^4 - 1 \times 10^5$. This work presents a combined thermal- and fluid-dynamic investigation of impingement jets from a single round and a single slot nozzle under these conditions. A central focus is the systematic comparison of the three turbulence models SST *k-ω*, generalized *k-ω* (GEKO) and Reynolds Stress Model (RSM) to identify the option that delivers the most accurate simulation of industrial impingement jets. The validation of the numerical results is based on the experimentally determined heat transfer at a strip and laser-optical Particle Image Velocimetry (PIV) measurements. An optimised set of GEKO parameters further reduces heat-transfer error. The strengths and shortcomings of each model in predicting local velocity, turbulent kinetic energy and heat transfer are revealed by the PIV data.

Keywords:
Computational Fluid Dynamics, Convective Heat Transfer, Impingement Jets, Particle Image Velocimetry, Turbulence Models

NOMENCLATURE

C_{CUR}	[-]	curvature Parameter
C_{MIX}	[-]	mixing Parameter
C_{NW}	[-]	near Wall Parameter
C_{SEP}	[-]	separation Parameter
D	[*mm*]	nozzle diameter
D_h	[*mm*]	hydraulic diameter
H	[*mm*]	strip distance
k	[m^2/s^2]	turbulent kinetic energy (TKE)
μ	[$Pa \cdot s$]	dynamic viscosity
Nu	[-]	Nusselt number
p	[Pa]	pressure
ρ	[kg/m^3]	fluid density
Re	[-]	Reynolds number
SRN	[-]	single round nozzle
SSN	[-]	single slot nozzle
u	[m/s]	fluid velocity
t	[*mm*]	thickness
W	[*mm*]	nozzle width
Φ	[W/m^3]	heat generation
ω	[s^{-1}]	specific turbulence dissipation rate

1. INTRODUCTION

Impingement jets are used in a variety of heating and cooling applications, including thermal processing. Typically, round or slot nozzles are used for the heat treatment of metal strips [1,2]. The first design of these nozzle systems is carried out using empirically derived Nusselt relations, a detailed and sophisticated design makes complex experimental measurements unavoidable [3,4]. Numerical simulation is intended to shorten this development process for new nozzle systems and reduces the number of nozzle system prototypes. However, to this day the prediction accuracy is still insufficient, which is one of the hurdles why numerical modelling is not widely used in industry [5].

The numerical modelling of impingement jets poses a significant challenge due to the substantial variations in flow characteristics along the flow

direction. The flow emerges from the nozzle exit as a free jet, and given the prevailing technical conditions, a turbulent flow structure can be predicted [6]. The subsequent spreading and deceleration of the free jet are a consequence of its interaction with the ambient medium through mixing and momentum exchange. As the distance to the wall surface increases, the free jet transitions into a stagnation point flow, whereby the flow is deflected by the wall. This stagnation zone is characterised by increased turbulence. The subsequent wall jet exhibits flow structures analogous to those of the free jet, widening as the flow velocity increases, while the mean flow velocity decreases. [3,7]

The study aims to investigate whether RANS-based turbulence modelling can predict the flow and heat transfer of industrial-scale impingement nozzles with an accuracy of 5 %, which is required for nozzle-system design. Compared to numerical studies in other application areas, this is an ambitious goal [5,8–11]. In order to expose the limitations of the models and establish a realistic error bound, the simulations are benchmarked against an extensive, high-resolution PIV dataset that resolves the entire impingement region, as well as strip heat-flux measurements. In addition, the potential of the GEKO model, for which there is still little comparative data, is investigated. Optimised GEKO parameters are used for this purpose. The results will be thoroughly compared with data from other publications in the discussion.

2. Problem Description

For the study, a $W = 5$ mm single slot nozzle (SSN) and a $D = 25$ mm single round nozzle (SRN) were used, with a distance of $H = 50$ mm between the nozzle and the strip on which the impingement jet is directed. The test conditions are outlined in Table 1. The Reynolds number for this flow configuration is defined as (1) [7],

$$Re_x = \frac{u\rho x}{\mu} \tag{1}$$

The heat transfer of these nozzles has previously been the subject of an experimental study, thus resulting in the availability of data from these measurements for the purpose of validation. In the experiment, the heat transfer is determined by heating a constantan® strip while it is cooled by the flow. The temperature on the strip is recorded with an infrared camera. The local Nusselt number per pixel can be calculated from the temperature profile, as Trampe et al. [12] explain in their article.

Table 1. Test conditions

Geometry	H/D_h	u	Re
Slot	5	15.8 m/s	11,870
Slot	5	85.0 m/s	54,900
Round	2	19.3 m/s	33,250
Round	2	52.5 m/s	90,000

PIV measurements were conducted in advance to evaluate the simulated flows and quantify the resulting energy. The parameters measured include the flow velocity u and the turbulent kinetic energy (TKE) k, which is a measure of the energy of the vortex movements of a flow. The data was collected on the same test rig that had previously been used to determine the heat transfer. The configuration was expanded to encompass an Nd:YAG laser (wavelength 532 nm, Litron Lasers Ltd) and a camera (CX2-16, LaVision GmbH). The addition of di-ethyl-hexyl sebacate (DEHS) particles to the flow enabled the tracking of particle movement using LaVision's DaVis 11 software.

2.1 Physical modelling and Mesh

The present study investigates the convective heat transfer to a flat strip by an impinging jet, which is the basis of the 3D flow domain, Figure 1. The working medium is air, which is introduced into the flow domain through the nozzles (inlet). The fluid temperature and the fluid velocity are measured beforehand. The heated strip is modelled as a solid body with a thickness of $t = 0.1$ mm and subjected to a constant heat generation related to the experiment. The width of the strip corresponds to 60 times the nozzle width or 30 times the nozzle diameter. The sides of the fluid domain are defined as pressure outlets with a gauge pressure $p = 0$ Pa, while all other walls are assumed to be adiabatic. The fluid domain has a high level of agreement with Shukla's proposals [8].

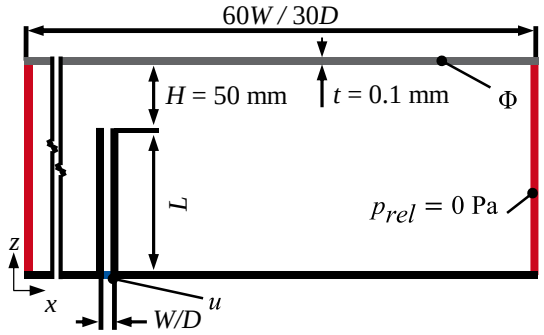

Figure 1. Sketch of the fluid domain for a single nozzle; black/grey: wall, blue: velocity inlet, red: pressure outlet.

In order to analyse the heat transfer on the constantan® strip and compare it with the measured data, a rake is placed over the constantan® strip. The number and spacing of the evaluation points of the rake correspond to the number of the pixels of the temperature measurement, therefore the evaluation points are spaced 1.28 mm apart.

A mesh dependence study was carried out with particular attention to the area near the constantan® strip. The dimensionless wall distance y^+ in this zone must be $y^+ \approx 1$ for high prediction accuracy [13,14]. The grid dependence study was carried out using the

generalized k-ω turbulence model with a nozzle exit velocity of u = 51.2 m/s for a SSN. This corresponds to the average Reynolds number of the studies conducted in this study. The key findings of the mesh dependency study are presented in Table 2.

Table 2. Key figures mesh dependency

Mesh	Cells	y^+_{min}	y^+_{ave}	$\overline{Nu}$	Nu_{Stag}
Coarse	4.3 Mio.	0.9	1.4	446	172
Medium	7.6 Mio.	0.7	1.1	441	171
Fine	15.3 Mio.	0.4	0.7	447	168

It was found that a stable solution was obtained with a mesh of 7.6 million cells. No further improvement was obtained by increasing the number of elements in the mesh. The medium mesh size of 7.6 million cells was selected for further investigation due to it offering the best compromise between computational time and Nusselt number prediction. When analysing the SRN, the same mesh properties are used.

2.2 Turbulence Modelling

A pre-selection of turbulence models was based on previous Reynolds-Averaged Navier-Stokes (RANS) simulations [5], with the k-ω (Shear Stress Transport) SST and generalized k-ω turbulence (GEKO) models chosen due to their low computational cost and good agreement for simulating impingement jets. The k-ω SST model is based on the k-ω standard model in the boundary layer region, and this two-equation model solves one transport equation, each for the TKE k (2) and the vortex frequency ω (3). In these equations, $G_{k,\omega}$ denotes the production of k and ω, respectively. $\Gamma_{k,\omega}$ represents the effective diffusion of k and w, while $Y_{k,\omega}$ represents the dissipation due to turbulence. The generation of turbulence due to the buoyancy effect is denoted by $G_{k,\omega.}$ The source terms, $S_{k,\omega}$, are user-defined.

$$\frac{\partial}{\partial t}(\rho k) + \frac{\partial}{\partial x_i}(\rho k u_i) = \frac{\partial}{\partial x_j}\left(\Gamma_k \frac{\partial k}{\partial x_j}\right) + G_k - Y_k + S_k + G_b \quad (2)$$

$$\frac{\partial}{\partial t}(\rho \omega) + \frac{\partial}{\partial x_i}(\rho \omega u_i) = \frac{\partial}{\partial x_j}\left(\Gamma_\omega \frac{\partial \omega}{\partial x_j}\right) + G_\omega - Y_\omega + S_\omega + G_{\omega b} \quad (3)$$

In the free jet region, the k-ω SST model behaves like the k-ε model, showing good convergence rates. The integration of the standard k-ω and k-ε models offers the benefit of enabling the modelling of both the near wall region and the free jet region in a meaningful manner. The GEKO turbulence model is also founded on the two equations of the k-ω model, but it possesses six additional independent parameters that can be adjusted without compromising the fundamental tenets of the model [15].

The Reynolds Stress Model (RSM) was selected as the third turbulence model. In contrast to the preceding turbulence models, the RSM characterises each respective Reynolds stress using a single equation. This approach abandons the conventional assumption of isotropic turbulence, but also involves a higher computational cost. The RSM stress-ω with shear flow correction was applied in the present work. [16]

3. RESULTS AND DISCUSSION

In the following sections, the local Nusselt number distributions, velocity distributions and the distribution of turbulent kinetic energy are presented for the slot and round nozzle. In each case, a low Reynolds number and a high Reynolds number are analysed.

3.1 Study of various turbulence models

Figure 2 shows the averaged Nusselt number at a Reynolds number of Re = 11,870 above the relative position of a SSN. All turbulence models tend to calculate a lower Nusselt number in the stagnation point than the experimental PIV measurement. The deviation in the stagnation point is 5.5 – 12 %. From the relative position x/D_h = 2, the SST k-ω and GEKO Default model approach the experimental solution but remain below the measured course of the Nusselt number. The RSM delivers consistently lower Nusselt numbers with an average deviation of 36.3 %.

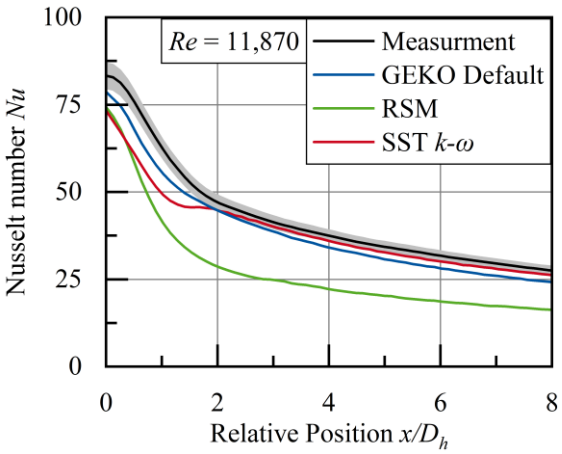

Figure 2. Distribution of *Nu* in cross-section for a SSN *W* = 5 mm, *Re* = 11,870

Figure 3 shows the flow distribution over the relative position x/D_h and the strip distance H. The PIV image corresponds to the experimental measurement. All turbulence models calculate a similar core velocity in the free jet, but a smaller shear layer compared to the PIV measurement. A developed stagnation zone is recognisable in each case. The SST k-ω and GEKO Default model show a local velocity maximum at $x/D_h \approx 1$ in the forming boundary layer zone. The RSM predicts significantly higher velocities in the wall jet than the measurement. The experimental PIV measurement shows a lower velocity and no local maxima.

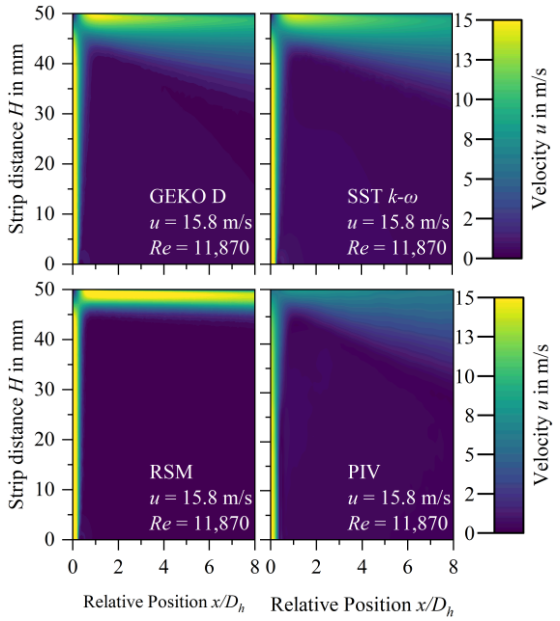

Figure 3. Velocity distribution for a SSN *W* = 5 mm, *Re* = 11,870

Figure 4 shows the turbulent kinetic energy k along the relative position x/D_h and strip distance H. The SST k-ω and GEKO Default model calculate high values of the TKE in the shear flows of the free jet and the wall flow. In contrast, the RSM shows hardly any significant distribution of k over the relative position x/D_h for a given Reynolds number of Re = 11,870.

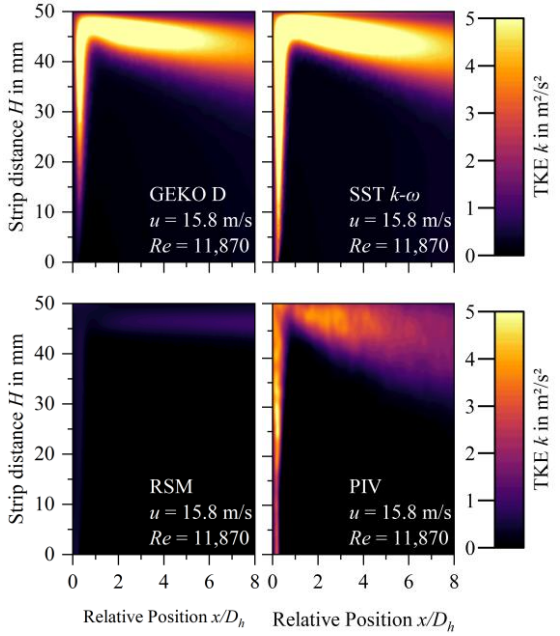

Figure 4. TKE distribution for a SSN *W* = 5 mm, *Re* = 11,870

For a higher flow velocity u = 85 m/s, the Reynolds number for the SSN is Re = 54,900. The corresponding local Nusselt numbers are shown in Figure 5. The experimental Nusselt number in the stagnation point increases by a factor of 2. The SST k-ω and GEKO Default models calculate a Nusselt number that is 9.6 % and 19.7 % higher at the stagnation point. In contrast, the RSM shows good agreement at the stagnation point, with a small deviation of 0.1 %. However, the RSM underestimates the Nusselt number over the full strip length, with an average deviation of 24.3 %.

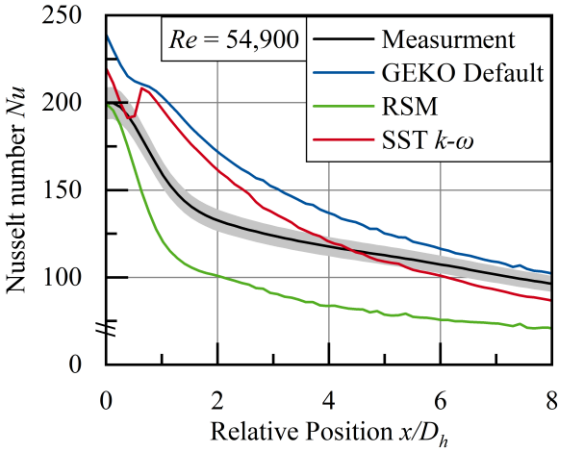

Figure 5. Distribution of *Nu* in cross-section for a SSN *W* = 5 mm, *Re* = 54,900

The SST k-ω model is the only model that calculates a secondary local peak at x/D_h = 1, which is not present in the PIV measurement. The SST k-ω model runs above the measurement up to $x/D_h \approx 4.5$ also intersecting the measurement curve. The GEKO Default model consistently calculates Nusselt numbers that are too high.

The velocity fields for u = 85 m/s of the SST k-ω and GEKO Default models, shown in Figure 6, are similar. A pronounced stagnation zone can be seen at x/D_h = 0, with a local velocity maximum building up due to the pressure gradient at x/D_h = 1. The wall jet widens further along the relative position.

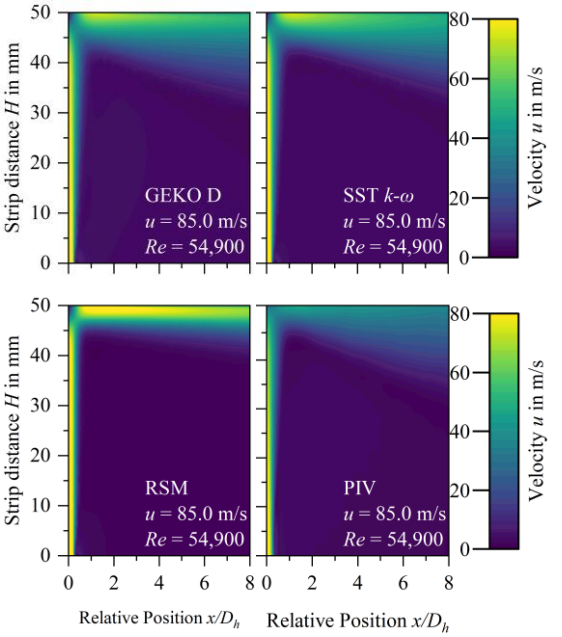

Figure 6. Velocity distribution for a SSN *W* = 5 mm, *Re* = 54,900

The velocity field of the RSM shows a smaller expansion of the wall jet, but a strongly pronounced local maximum and a subsequent high velocity within the wall jet. The PIV measurement shows a similar velocity distribution with a smaller local maximum at $x/D_h \approx 1$ and a larger jet expansion compared to the SST k-ω and GEKO Default results.

For the Reynolds number Re = 54,900 the TKE distribution along the impingement and the wall jet of the SSN is shown in Figure 7. For the SST k-ω and GEKO Default models, the distribution is similar to Figure 4, but with a significantly higher value of k. The RSM calculates significantly lower values compared to the other models and the PIV measurement. Compared to the PIV measurement, the SST k-ω and GEKO Default models calculate overall higher values for k.

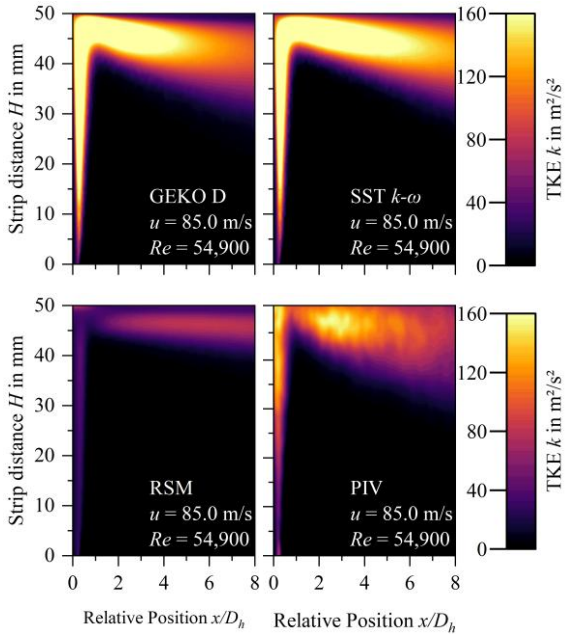

Figure 7. TKE distribution for a SSN W = 5 mm, Re = 54,900

Figure 8 shows the local Nusselt number over the relative position x/D_h of a SRN for a flow velocity at the nozzle outlet of u = 19.3 m/s. For the present boundary conditions this means a Reynolds number of Re = 33,250. All turbulence models calculate an excessive Nusselt number in the stagnation zone compared to the measurement. The local deviation of the turbulence models in the stagnation point is between 26.1 – 45.1 %. In addition, a deviating maximum of Nu is calculated at $x/D_h \approx 1$. This shift of the maximum away from the stagnation point was also observed in [17,18]. The SST k-ω model is closest to the experimental measurement and provides the second local Nu maximum correctly, which results in an average deviation of 24.7 %. The RSM and GEKO Default model have mean deviations of 5.9 % and 29.3 %, respectively, with the second local maximum not being well located. It is evident that the specification of a mean deviation may not always be meaningful, as the SST k-ω model reflects the local Nusselt number more accurately, yet exhibits a higher mean deviation.

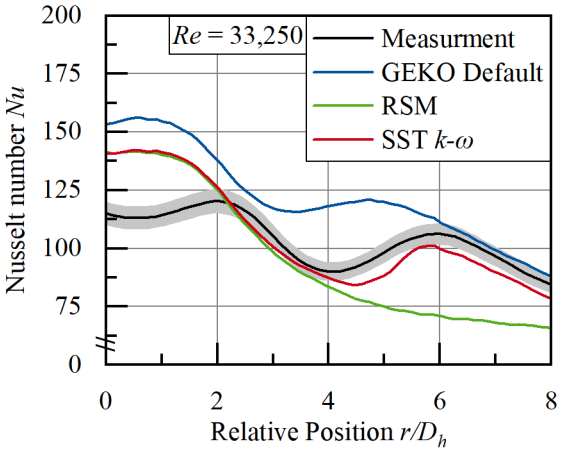

Figure 8. Distribution of Nu in cross-section for a SRN D = 25 mm, Re = 33,250

The velocity distribution of the measured and calculated flow velocity u for the SRN is shown in Figure 9. The turbulence models calculate a significantly larger shear layer of the free jet after the nozzle exit, while the PIV measurement shows a sharper boundary between the jet and the ambient air. All turbulence models show a pronounced stagnation zone as well as a forming and accelerating wall jet. Compared to the velocity profiles of the slot nozzles in Figure 3 and Figure 6, the wall jet of the RSM is in better agreement with the other models and the PIV measurement.

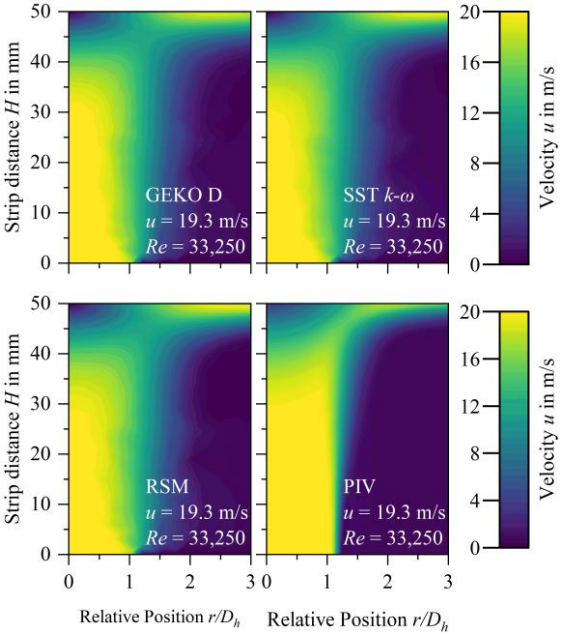

Figure 9. Velocity distribution for a SRN D = 25 mm, Re = 33,250

Figure 10 presents the TKE distribution for the SRN considered at Reynolds number Re = 33,250. As previously observed, the RSM calculates negligible levels of TKE $k \approx 1.5$ m²/s². There is no difference between the values in free jet or wall jet.

The GEKO Default and SST k-ω models calculate a higher k-values than the RSM. Consistent with the broad shear layers in Figure 9, a corresponding TKE distribution is shown over this range. The TKE distribution from the PIV measurement shows a strongly pronounced shear layer where the TKE reaches values up to twice as high as those calculated by the turbulence models.

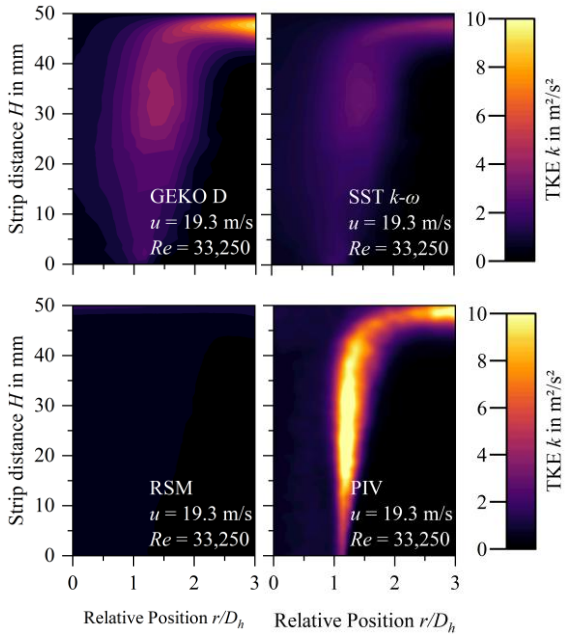

Figure 10. TKE distribution for a SRN D = 25 mm, Re = 33,250

Figure 11 shows the local Nusselt number Nu over the relative position x/D_h for a SRN with a flow velocity of u = 52.5 m/s. At this Reynolds number of Re = 90,000, all turbulence models calculate an excessive Nusselt number in the stagnation zone. The local deviation in the stagnation point is 23 – 33.3 %. It is noticeable that the RSM and GEKO Default model are close for the first local maximum in the range $0 \le x/D_h \le 2.5$. None of the models correctly predicts the second peak.

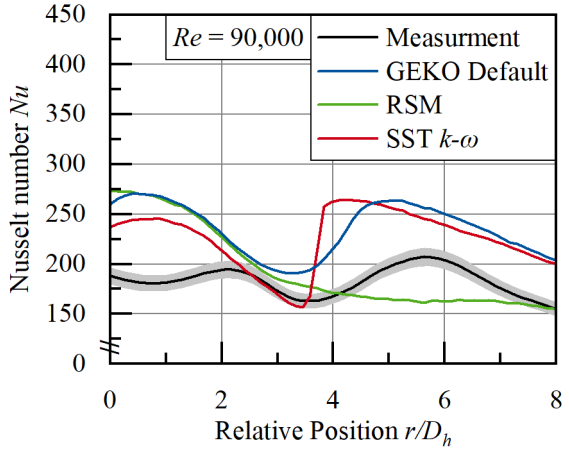

Figure 11. Distribution of Nu in cross-section for a SRN D = 25 mm, Re = 90,000

Figure 12 visualises the velocity distributions for the SRN. Despite the overall higher velocity level, the velocity curves are similar to those in Figure 9. The velocity distributions resulting from the numerical models again show a much more pronounced shear layer between the jet and its surroundings. The inner potential core is clearly visible. The course of the PIV measurement shows a sharp separation between the jet and its environment.

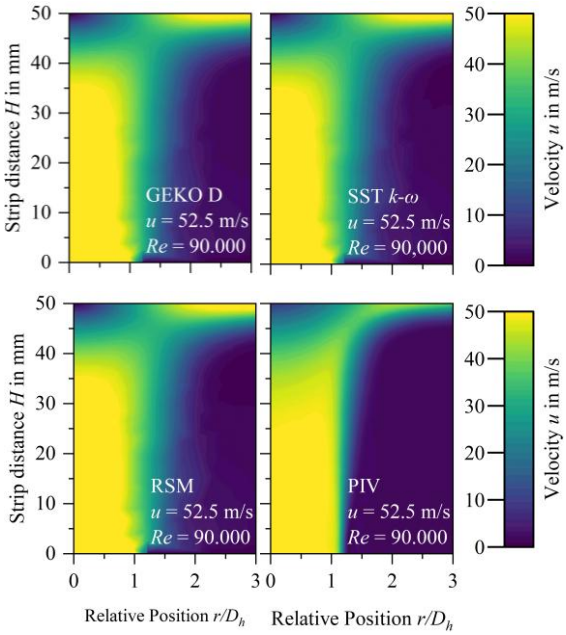

Figure 12. Velocity distribution for a SRN D = 25 mm, Re = 90,000

The TKE distributions for the SRN with Re = 90,000 are shown in Figure 13. The distribution is similar to those for the SRN with the lower flow velocity u in Figure 10, but the level of turbulent kinetic energy k is increased by a factor of 5.

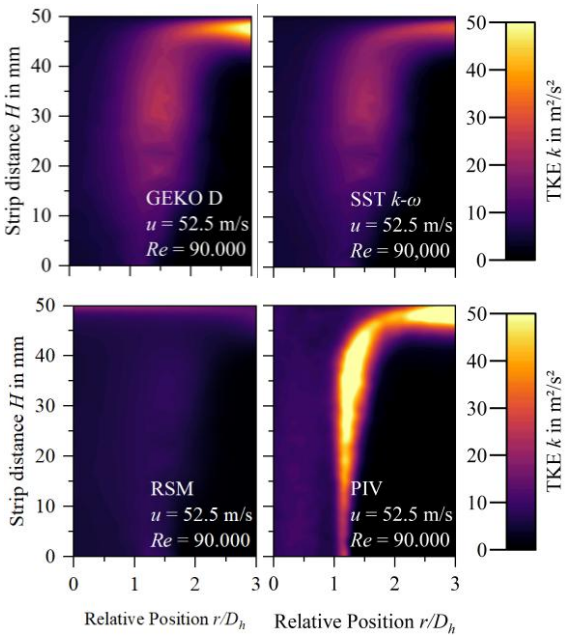

Figure 13. TKE distribution for a SRN D = 25 mm, Re = 90,000

The RSM again calculates very low values for k. In contrast, the GEKO Default and SST k-ω models produce a broader distribution of k with values at intermediate levels. The PIV measurement shows a well-defined shear layer in which the TKE reaches values up to twice as high as in the simulations.

3.2 GEKO parameter study

In the following, the results of the GEKO Default model presented in Section 3.1 are compared with the adjusted parameters of the GEKO model for the SST and SRN. The parameters were set using the method used in Menzler [19]. The algorithm optimises the parameters in such a way that the mean deviation of the Nusselt number is minimised.

The default parameters of the GEKO model and their value ranges, as well as the adjusted GEKO parameters, are shown in Table 3. C_{JET} and C_{CORNER} do not affect the local Nusselt number according to Menzler [19] and are therefore neglected.

Table 3. Investigated GEKO parameters in comparison with the default values

Case	C_{SEP}	C_{NW}	C_{MIX}	C_{CURV}
Default	1.75	0.50	0.30	1.00
Minimum	0.70	2.00	1.00	1.50
Maximum	2.50	0.50	0.30	1.00
SSN; Re = 11,870	4.73	2.98	1.38	1.00
SSN; Re = 58,100	1.75	7.76	21.09	1.00
SRN; Re = 33,250	1.16	-0.69	-1.26	0.03
SRN; Re = 90,000	1.34	-0.31	-0.62	0.85

Figure 14 shows the local Nusselt numbers of the SSN over the relative position for the GEKO default and adjusted parameters. The deviation in the stagnation zone increases with increasing Reynolds number.

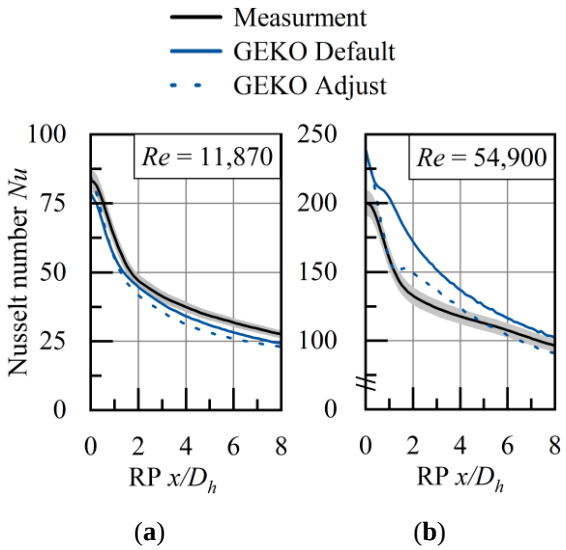

Figure 14. Distribution of *Nu* in cross-section for a SSN *W* = 5 mm (a) *Re* = 11,870 and (b) *Re* = 54,900

At a lower Reynolds number of Re = 11,870 the adjusted parameters lead to a similar deviation from the measurement than the default parameters as of a relative position of $x/D_h \approx 1$. At a higher Reynolds number of Re = 54,900, the adjusted parameters give a more accurate prediction with a mean deviation of only 1.6 %. However, the adjusted parameters lead to a local maximum at $x/D_h \approx 2$, which is not apparent from the measurement. After this local maximum, the Nu distribution runs above the measured values up to $x/D_h \approx 3$. The curve then intersects the measured values and runs below the experimental data, resulting in a smaller deviation on average.

Figure 15 presents the velocity distributions of the default and adjusted parameters for Re = 11,870 in the top two subfigures. The distributions show no qualitative difference. The bottom two subfigures show the TKE distribution. Again, there are no significant differences. This explains the similar Nusselt number curves in Figure 14.

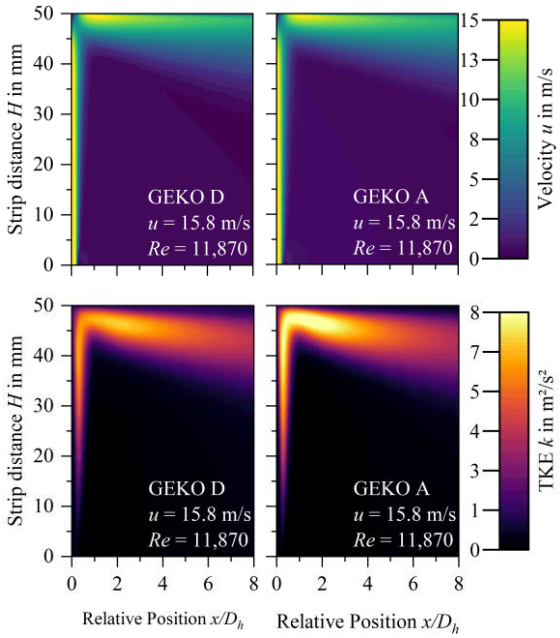

Figure 15. Velocity and TKE distribution for a SSN *W* = 5 mm, *Re* = 11,870

Figure 16 displays the velocity distributions for Re = 54,900 in the upper part of the figure, which are qualitatively similar. The lower part of the figure shows the TKE distribution, which, show significant differences. The adjusted parameters lead to an increased TKE range up to $x/D_h \approx 6$, while this range extends up to $x/D_h \approx 5$ for the default parameters.

Figure 17 shows the comparison of the GEKO default parameters and the adjusted parameters for the SRN. The lower Reynolds number Re = 33,250 and the higher Reynolds number Re = 90,000 are compared. For the lower Reynolds number Re = 33,250 both parameter sets lead to a significant local overestimation of Nu in the stagnation zone with a deviation of about 40 %. The maximum of the Nusselt number is shifted to the relative position $x/D_h \approx 1$. The adjusted parameters result in an

average deviation of *Nu* by 20.4 % compared to 30.3 % deviation for the default parameters.

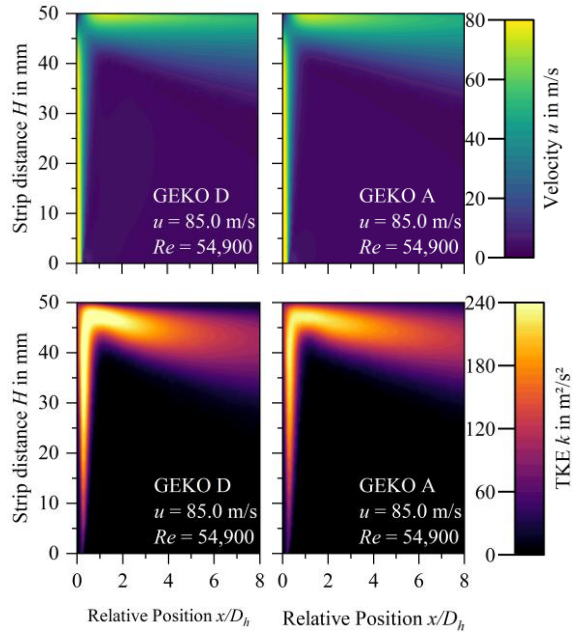

Figure 16. Velocity and TKE distribution for a SSN *W* = 5 mm, *Re* = 54,900

The position of the second local maximum is incorrectly predicted even with the adjust parameters. The local Nusselt numbers of *Re* = 90,000 show a qualitative agreement between measurement and simulation. But the absolute simulated values of *Nu* are significantly increased. The adjusted parameters shift the local minimum further to the measurement result and reduce *Nu* in the second local maximum. This results in an average deviation of 10 % compared to an average deviation of 16.0 % for the default parameters.

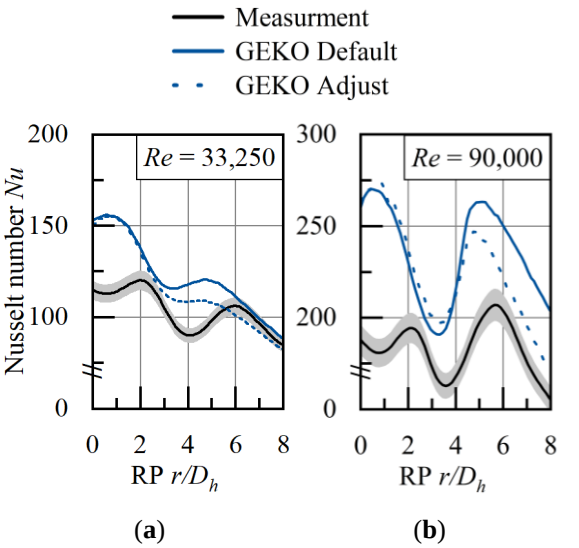

(a) **(b)**

Figure 17. Distribution of *Nu* in cross-section for a SRN *D* = 5 mm (a) *Re* = 33,250 and (b) *Re* = 90,000

Considering the lower Reynolds number of *Re* = 33,250, the velocity and TKE distributions of the default and adjusted parameters are plotted in Figure 18. The velocity distribution appears qualitatively similar. However, the TKE distribution show qualitative differences. With the default parameters, an increased TKE is calculated in the shear layer of the free jet, as well as a stronger local maximum at $x/D_h \approx 3$. With the adjusted parameters, an overall lower value for the TKE is calculated.

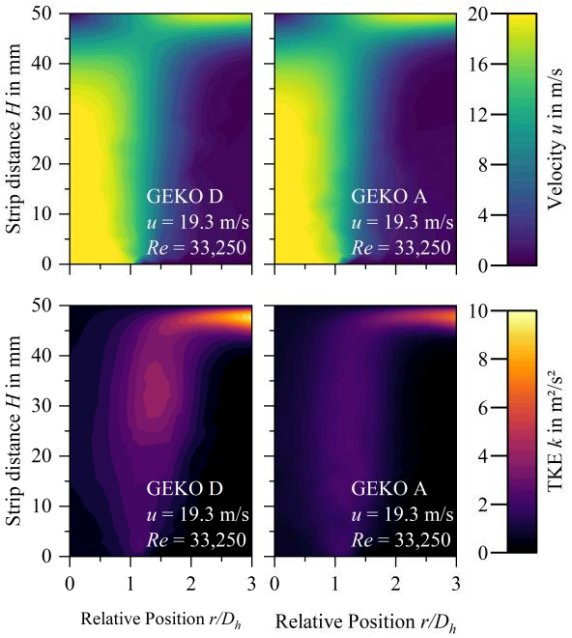

Figure 18. Velocity and TKE distribution for a SRN *D* = 25 mm, *Re* = 33,250

Figure 19 shows the velocity and TKE profiles of the SRN for *Re* = 90,000. The characteristics of the results show a high degree of agreement with the results shown in Figure 17 (SRN with *Re* = 33,250). Notably, these values are locally increased by a factor of 5 due to the increased nozzle exit velocity.

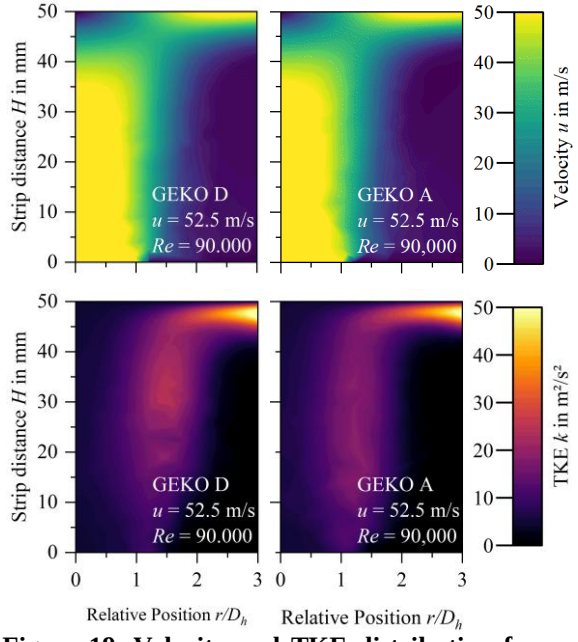

Figure 19. Velocity and TKE distribution for a SRN *D* = 25 mm, *Re* = 90,000

3.3 Discussion

In the following section, the results presented for the impingement jet modelling are discussed and the possible reasons for the insufficient prediction of heat transfer by the turbulence models are presented.

Figure 2 and Figure 5 show that the use of the RSM for the SSN application does not lead to a more accurate prediction of the Nusselt number as the two-equation models. There is no increase in accuracy for this application at the cost of more computation time. The TKE curves of the SSN in Figure 4 and Figure 6 show that the RSM underestimates the intensity of the turbulence, which could contribute to the lower Nusselt number shown in Figure 2 and Figure 5.

For the SRN application, the RSM also does not provide a significant improvement over the two-equation models, characterised by locally high deviations.

The present results of all cases indicate a proportional relationship between the TKE calculated by the turbulence models and the local Nusselt number. The calculated heat transfer rises with increasing TKE. However, the TKE is incorrectly reproduced locally, leading to over- and underestimation of the results. Therefore, it is necessary to adjust the TKE of the respective turbulence models in order to achieve a higher prediction accuracy. The velocities of the impingement jets are correctly represented using the numerical models and therefore do not lead to restrictions in the prediction accuracy.

The achieved prediction accuracy of the local Nusselt number is within the expected range [5]. Without a fundamental modification of the turbulence models, better predictions with RANS-based turbulence models do not seem to be possible. A further possibility is offered by the GEKO model, where the model parameters can be adapted to the specific application.

By optimising the GEKO parameters C_{SEP}, C_{NW}, C_{MIX} and C_{CURV}, an attempt was made to adapt the GEKO model to the considered impingement jets from single slot and round nozzles in order to increase the accuracy of the model. In some cases, values were obtained outside the recommended parameter ranges, the effects of which are not fully understood, see Table 3. For all applications considered, the average deviation for the result based on the adjust GEKO parameters was approximately halved. Even with the optimised parameters, there are still local deviations of up to 39.3 % in the stagnation zone and at the local maxima and minima. Yüksekdağ [17] and Rasheed [20] also optimised the GEKO parameters according to their research question. The investigations were carried out on SRNs with smaller diameters of D = 2.6 mm [17] and D = 15 mm [20] with a Reynolds number of Re = 23,000. Figure 20 compares the simulations carried out with the adjusted GEKO parameters according to Yüksekdağ and Rasheed and the results of this optimisation.

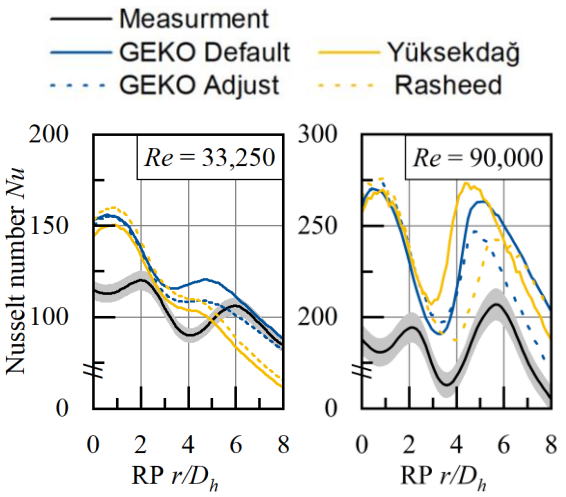

Figure 20. Distribution of *Nu* in cross-section for a SRN *D* = 5 mm (a) *Re* = 33,250 and (b) *Re* = 90,000 GEKO adjustments [17,20]

The comparison shows that the optimised GEKO parameters of Yüksekdağ and Rasheed achieve an improvement of the mean deviation for the SRN to Re = 33,250, but thus incorrectly reflect the local course. The GEKO parameters according to Yüksekdağ achieve a worse prediction accuracy for the SRN with Re = 90,000 than the default settings, while the GEKO parameters according to Rasheed are in the range of the optimisation of this study. This indicates that the optimised GEKO parameters are highly dependent on the geometry and flow conditions, i.e. the Reynolds number, and cannot be transferred without restriction.

Further optimisation potential would lie in a local optimisation of the GEKO parameters, e.g. the course of Nu in Figure 14 (b) could be locally influenced by the parameter C_{NW}. According to Menzler [19], the parameter C_{NW} has an influence on the gradient of Nu after the secondary peak, so that the curve could be further approximated to the experimental curve. Table 2 also shows that the adjusted GEKO parameters depend on the geometry (SSN/SRN) and the flow velocity respectively the Reynolds number. The GEKO model also offers the possibility of fine-tuning the parameters using sub-parameters, which should be investigated in a detailed parameter study.

4. SUMMARY

In this work, the local Nusselt number, velocity and turbulent kinetic energy distribution for impinging jets from single slot and round nozzles were investigated. In each case, a low and a high Reynolds number application have been compared. The main focus is on the comparison and suitability

of the turbulence models, the SST *k-ω* model, the GEKO model with default and adjust parameters and the RSM. The results of the numerical simulations were validated with experimental measurements carried out including heat transfer and PIV measurements. The discussion concluded that the RSM did not bring significant improvements in the prediction of the Nusselt number and underestimated the intensity of the turbulence, resulting in lower Nusselt numbers.

The SST *k-ω* and GEKO Default models performed as expected according to Zuckerman [5]. However, the prediction accuracy is far below the acceptable range for designing nozzle systems based on these simulations. Therefore, a further possibility to increase the prediction accuracy by optimising the GEKO parameters was investigated. The optimisation of the GEKO parameters showed improvements in the mean deviations and a strong dependence on the nozzle geometry respectively the Reynolds number.

For all models it was found that the turbulent kinetic energy is locally inaccurately predicted, while the flow velocities are accurately calculated. This leads to the conclusion that a fundamental modification of the model equations is necessary to increase the prediction accuracy of RANS-based turbulence models for the application of nozzle systems in thermo-process technology. Another possibility is to perform detailed parameter studies on optimised GEKO parameters. In an ideal scenario, superior GEKO parameters will be found that further reduce the discrepancies between simulation and experiment.

REFERENCES

[1] Kramer C, Hansen M, 2006, "Gas jet floatation for the touchless cooling of sensitive stainless steel strips in strip annealing lines", *Heat Processing* 24–26.

[2] Menzler D, 1992, "Konvektionskühlsysteme für Leichtmetallhalbzeuge", *Dissertation RWTH Aachen University, Aachen.*

[3] Martin H, 1977, "Heat and Mass Transfer between Impinging Gas Jets and Solid Surfaces", *Advances in Heat Transfer* Volume 13, Vol 13. Elsevier, pp 1–60.

[4] Hofmann HM,2005. "Wärmeübergang beim pulsierenden Prallstrahl", *Dissertation Universitätsverlag, Karlsruhe.*

[5] VDI e.V., 2013. *VDI-Wärmeatlas*, Springer Berlin Heidelberg, Berlin, Heidelberg.

[6] Bergman TL, Lavine AS, Incropera FP, Dewitt DP, 2011. *Fundamentals of Heat and Mass Transfer*, John Wiley & Sons.

[7] Zuckerman N, Lior N, 2006, "Jet Impingement Heat Transfer: Physics, Correlations, and Numerical Modeling", *Advances in Heat Transfer*, Vol 39. Elsevier, pp 565–631.

[8] Shukla A, Dewan A, 2017, "Flow and thermal characteristics of jet impingement: comprehensive review", *IJHT* 35:153–166.

[9] Barata B, Navalho J, Pereira J, 2023, "RANS simulations of plane impinging jets: On the influence of plate velocity in the Nusselt number secondary peak", *Therm* sci 27:4947–4960.

[10] Alimohammadi S, Murray DB, Persoons T, 2014, "Experimental Validation of a Computational Fluid Dynamics Methodology for Transitional Flow Heat Transfer Characteristics of a Steady Impinging Jet", *Journal of Heat Transfer* 136.

[11] Dutta R, Dewan A, Srinivasan B, 2013, "Comparison of various integration to wall (ITW) RANS models for predicting turbulent slot jet impingement heat transfer", *International Journal of Heat and Mass Transfer* 65:750–764.

[12] Trampe E, Rademacher N, Wulfmeier M, Büschgens D, Pfeifer H, 2024, "A High-Resolution Method for the Experimental Determination of the Heat Transfer Coefficients of Industrial Nozzle Systems in Heat Treatment Plants", *Applied Sciences* 14:3024.

[13] Cebeci, T, ed., 2013. *Analysis of turbulent flows with computer programs*, 3rd edn., Butterworth-Heinemann, Oxford.

[14] Kadivar M, Tormey D, McGranaghan G, 2021, "A review on turbulent flow over rough surfaces: Fundamentals and theories", *International Journal of Thermofluids* 10:100077.

[15] Menter F, Lechner R, Matyushenko A, 2019, "Best Practice: Generalized k-ω Two-Equation Turbulence Model in ANSYS CFD (GEKO) ", *Technical Report* ANSYS Otterfing.

[16] Ansys® F, 2023, "Ansys Fluent Theory Guide".

[17] Yüksekdağ R, Koçak D, Şentürk U, 2024, "Prediction of heat transfer for a single round jet impingement using the GEKO turbulence model", *International Journal of Heat and Fluid Flow* 109:109538.

[18] Sagot B, Antonini G, Christgen A, Buron F, 2008, "Jet impingement heat transfer on a flat plate at a constant wall temperature", *International Journal of Thermal Sciences* 47:1610–1619.

[19] Menzler JE, Klusmann M, Wulfmeier M, Büschgens D, Pfeifer H, 2023, "Simulation of Gas Jet Impingement Cooling in Continuous Heat Treatment Lines with the ANSYS GEKO Turbulence Model", *HTM Journal of Heat Treatment and Materials* 78:91–104.

[20] Rasheed A, Allauddin U, Ali HM, Uzair M, Verdin PG, Siddiqui YH, 2022, "Heat transfer and fluid flow characteristics investigation using detached ribs in an axisymmetric impinging jet flow", *J Therm Anal Calorim* 147:14517–14537.

Conference on Modelling Fluid Flow (CMFF'25)
The 19th International Conference on Fluid Flow Technologies
Budapest, Hungary, August 26 - August 29, 2025

A CFD STUDY ON THE EFFECT OF DEFORMABLE BLADES ON CENTRIFUGAL PUMP PERFORMANCE

Csaba HŐS[1], Balázs ERDŐSI[2]

[1] Corresponding Author. Department of Hydrodynamic Systems, Faculty of Mechanical Engineering, Budapest University of Technology and Economics. Műegyetem rkp. 3., D building, 3rd floor, H-1111 Budapest, Hungary. Tel.: +36 1 463-2216, E-mail: cshos@hds.bme.hu
[2] Department of Hydrodynamic Systems, Faculty of Mechanical Engineering, Budapest University of Technology and Economics. Tel.: +36 70 406-0886, E-mail: erdosi8080@gmail.com

ABSTRACT

This paper uses CFD studies to investigate the effect of passively deforming blades on the flow field, head and efficiency of a centrifugal pump. Impellers with constant blade thickness and width have been considered and mounted to the back shroud with joints at one-third and two-thirds of the blade length. Two different impeller geometries with varying blade thickness and material properties were investigated with two-way coupled numerical fluid-structure-interaction simulation. Not only the standard hydraulic parameters (flow rate, head, input power) were recorded, but the blade deformation was also studied. This paper provides a detailed analysis of the flow field, separation zones and loss mechanism, and the effect of blade deformation. The findings provide headways for further investigations to optimize the impeller's geometry to enhance the turbomachine's operating parameters.

"Keywords: Centrifugal pump, CFD, Flexible blades, Fluid-structure-interaction, Radial flow impeller"

NOMENCLATURE

Latin letters

D	[m]	impeller diameter
H	[m]	head
I	[J/kg]	rothalpy
N_{blade}	[-]	number of blades
P	[kW]	input power
Re	[-]	Reynolds-number
Q	[m^3/s]	flow rate
c	[m/s]	absolute velocity
g	[m/s^2]	gravitational acceleration (9.81)
n_q	[-]	specific speed
r	[m]	impeller radius
u	[m/s]	circumferential velocity
w	[m/s]	relative velocity
y^+	[-]	dimensionless wall distance

Greek symbols

β	[°]	blade angle
δ	[m]	boundary layer thickness
η	[-]	hydraulic efficiency
ρ	[kg/m^3]	density

Subscripts and Superscripts

1	quantities at the leading edge
2	quantities at the trailing edge
m,u	meridional and circumferential component
n	nominal value
ss,ps	suction side and pressure side

1. INTRODUCTION

A significant part of the electricity generated in power plants is used to drive pumps (e.g. drinking water pumps). As a result, it is crucial that these machines can be operated with the highest possible efficiency. The impellers of these machines are usually designed for a single operating point. In real-world conditions, though, operating the machine at other operating points is necessary. In such cases, the increased flow separation on the blades causes the significant growth of the flow losses, which results in a reduction of the efficiency.

In the case of axial flow machines, one possible way to improve efficiency is to change the blade angle. However, this option is not available for radial machines. This paper investigates the viability of a novel approach. The idea is that better efficiency could be achieved at off-design conditions if the blade of the impeller would be passively deformed in a suitable way. Considering that both the pressure difference on the two sides of the blade and centrifugal force act on the blade, the net force causes a passive deformation in the blade shape. The main aim of the investigation is to make this deformation such that it reduces the flow separation.

This may result in an increase in the efficiency of the machine. Research approaches studying the effect of deforming blades can be found in the literature. The previous studies mostly investigate axial-flow machines, especially ones that move air, while the main aim of this actual study is to investigate the use of flexible blades in case of pumps. Such an example of an axial fan with flexible blades can be seen in [1], where piezoelectric ceramic macroscale composite actuators are embedded in the blade of an axial compressor. These actuators are used to achieve deformation and reduce the flow losses. The actuators are used to adjust the twist and the turning of the blade simultaneously. Further approaches are described in [2], that combine the method using piezoelectric actuators in with active flow control. In this case, the flow control means injecting or extracting a flowing medium into or from the boundary layer.

Flexible blades using shape-memory alloys (SMA) were also investigated in different studies, which method allows a greater blade deformation. The more the blade angle at the leading edge can adapt to the actual operating point, the more flow loss emerges due to flow separation. This approach is also found in [3], where an automotive cooling fan is analysed. This describes a method using coupled numerical Fluid-Structure-Interaction (FSI) simulation, like the one used in this actual research. Furthermore, laboratory measurements in a wind tunnel and custom-built measurement equipment were also considered. In the case of study described in [3], however, the changed geometry of the blade resulted in a higher available pressure ratio for the same flow rate but lower efficiency of the ventilator. The effect of the SMA in aerospace applications is investigated in [4], while a study of an expandable-impeller pump is described in [5]. Since the expandable impeller has significant deformation, so the simulation of the fluid-structure interaction had to be made. The structural deformations were time dependent according to [5]. A novel approach can be seen in [6] and [7], that investigates NACA 63-418 profile with flexible trailing edge. The authors of these papers considered both measurement and FSI-simulation and detected significant change in the drag coefficient of the wind turbine. As it can be seen in the literature, the flexible blades of a turbomachine can significantly affect the flow parameters. However, centrifugal pumps were less studied yet.

2. SIMULATION METHODOLOGY

2.1. The hydraulic pre-design of the impellers studied

The geometries of the studied impeller blades were designed with the method of the complex potentials, assuming ideal flow. The blade itself can be considered as a streamline. The design parameters of these impellers are written in Table 1.

Table 1. The design parameters of the studied impellers (with the number of blades)

Geom.	$H\ (m)$	Q (l/s)	n_q (1)	N_{blade}
A	40	30.1	1440	5
B	16	2.833	2345	8

The first one (model *A*) is a larger impeller with also a larger distance between two blades. Therefore, higher deformation could be allowed. The second one (model *B*) is a smaller impeller to be built into a measurement equipment in the future. Besides, its blade number is closer to the ideal (according to empirical formulas) than the first one. A more detailed analysis was done on impeller A, and a less detailed analysis was done on impeller B in this study. However, a half-numeric method was also tested on impeller *B* to reduce the computational cost. The impeller *A* was studied with a blade width 3 mm and is made from steel ($E = 210$ GPa). In the case of the impeller geometry *B*, an impeller made from Aluminium ($E = 68$ GPa) and with 1.5 mm blade width and one made from Acrylonitrile styrene acrylate [ASA], (3D-printed, $E = 1.92$ GPa) and with 2.5 mm blade width were studied. The impeller blades are mounted to the back shroud with joints at one-third and two-thirds of the blade length.

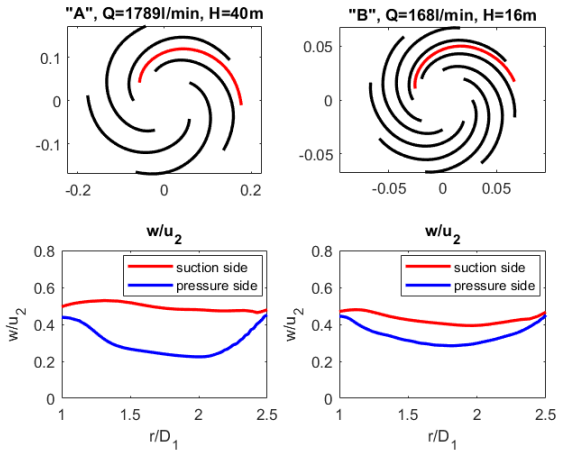

Figure 1. The impeller geometries designed: the A (left) and the B (right) geometries (a streamline in both impellers are marked with red)

It is practical to calculate the relative velocity on the suction and pressure sides of the blade to get the pressure difference between them using Bernoulli's equation. However, according to the previous experiences, these results differ significantly from the results of the simulation the due to the flow separation. So, the study focuses only on the FSI-simulation methods. The pre-design method cannot consider viscous losses too. To calculate the Reynolds number, the flow speed can be evaluated with the relative velocity averaged on the two side of the blade (Figure 1). The relative velocity should be nearly constant along the full length of the blade.

2.2. The pre-processing of the CFD simulation

The main dimensionless parameters describing the turbulence of the flow and the width of the boundary layer are written in Table 2. (Average Reynolds-number of the pump, y^+ on suction and pressure side of the blade, boundary layer thickness.)

Table 2. The main parameters of the three discretized simulation geometries

Geom.	Re (1)	y_{ss}^+ (1)	y_{ps}^+ (1)	δ (mm)
A	7.48*e*5	29.77	53.16	8
B (Alu)	9.52*e*4	39.93	39.93	4.78
B (Asa)	9.52*e*4	16.46	24.69	4.78

The higher Reynolds-number wall turbulence model requires the value of the y^+ between 30 and 300. The mesh of the ASA impeller does not clearly meet this condition; however, it can be allowed for this testing phase of the due to easier meshing. This may lead to imprecise results regarding to flow separation, so further analysis has to be done in the future. The meshes can be qualified with the skewness of their elements (Table 3.). The intolerably deformed elements are usually around the trailing edge of the blade as it can be seen on Figure 2 (bottom-left). This is due to the blade being relatively thin, and the trailing edge being sharp compared to the size of the flow field.

Table 3. The skewness and the average quality of the elements of the simulation geometries

Geom.	min.	max.	avg.	avg. q.
A	$3e-4$	0.94	$7e-2$	0.91
B (Alu)	$6e-4$	0.71	0.11	0.67
B (Asa)	$9e-4$	0.55	$8e-2$	0.9

The simulation was made in *Ansys CFX*. On the sides of the flow field, periodic boundary condition was defined (Figure 2, blue). The blade (Figure 2, yellow) and the boundaries on the top and the bottom of the flow field (Figure 2, grey) can be considered as a no slip wall, resulting in a closed impeller.

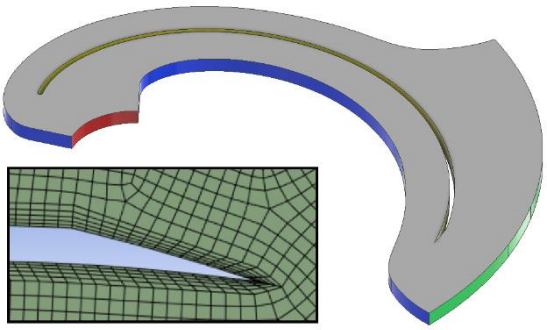

Figure 2. The flow field and the mesh around the trailing edge of the blade (in case of impeller A)

2.3. The FSI simulation

The FSI simulation is a coupled two-way Fluid-structure-action simulation, which is essential for investigating the blade deformation due to the flow and its reaction to the flow region. The mechanical finite-element model of the blade is also discretized (Figure 3). According to Table 3., the minimum, maximum and average value of the skewness and the overall average mesh quality are acceptable in all cases. To run the CFD simulation a rotating flow domain and SST turbulence model was considered.

The mountings can be rigid (like the blade had been welded to the back shroud in two points). This method means the use of cylindrical constraints on the mountings of the blade that restrain all degrees of freedom. The other approach is that the mountings allow rotational movement (like riveted mounting) using cylindrical constraints allowing rotation and adding remote displacement constraint too.

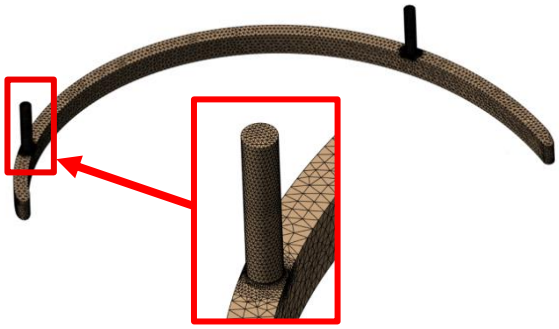

Figure 3. The mechanical model and the place of the mounting

In the case of FSI simulation, only the shape of the blade (Figure 2, yellow) can change; the deformation of every other boundary region of the flow field should be unspecified. Considering the rigid bladed impeller will be important too in the future calculations: it can be managed by running only a CFD simulation on the designed flow field, neglecting the deformation of the blade. The FSI simulation was performed with the help of *Ansys System Coupling* software. Only steady-state simulations were run. Knowing that CFD simulations may be inaccurate in off-design points, the results should be considered carefully, future simulations are recommended. Furthermore, the next phase of this actual research plan is measurement in laboratory, which can give more accurate results in off-design conditions too.

2.4. The Grid sensitivity analysis

Each geometry was investigated with more grids, and the comparison between them was made by the help of the hydraulic parameters of the pump. The sensitivity was studied with only running a CFD simulation on the flow field, without FSI.

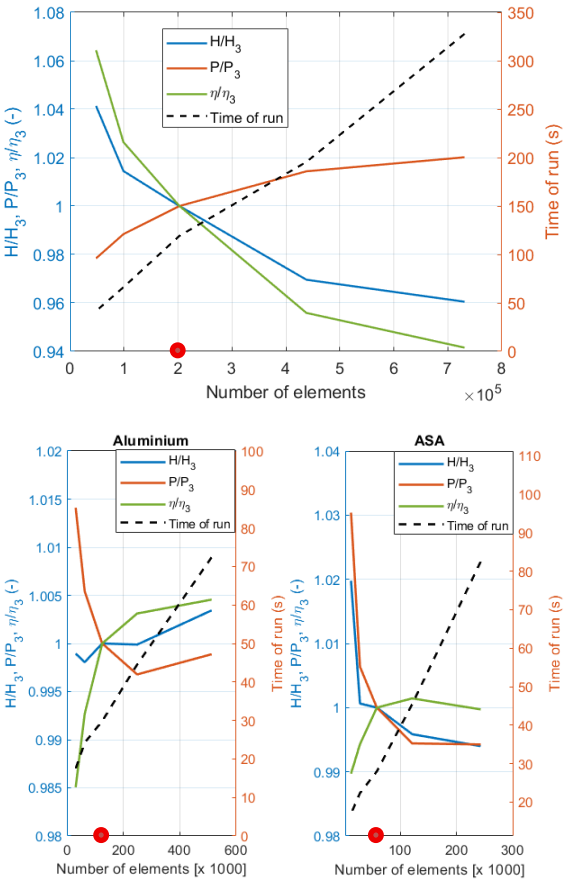

Figure 4. The hydraulic parameters of the impeller *A* (upper) and impeller *B* (lower) got from simulations with different grids

As Figure 4 shows, the hydraulic parameters, such as head, input power and hydraulic efficiency, do not change significantly using different grids. However, the time of a CFD simulation run (or one step of the FSI simulation) is almost directly proportional to the number of elements. As a result, the meshes marked with a red dot (and indexed as the 3rd) on Figure 4 have been chosen for each geometry, which resulted in both satisfactory time of running a simulation and accuracy. (To make visualization easier, the hydraulic parameters were proportioned to the results got with the marked meshes).

3. RESULTS IN CASE OF IMPELLER *A*

3.1. The hydraulic characteristics

As impeller model *A* allowed the largest blade deformation, the difference between the hydraulic parameters of the rigid and the flexible blade was the most significant in this case. (The impeller *B* was made basically to a future measurement equipment.)

The characteristic curves will be usually plotted as function of the relative flow rate: the ratio of the actual and the nominal flow rate. When results are plotted, the continuous lines are trendlines in the following chapters.

Firstly, the head characteristics can give information about the effect of the flexible blade. The numerically calculated head curve of the rigid-bladed impeller should be compared with the theoretical head characteristics.

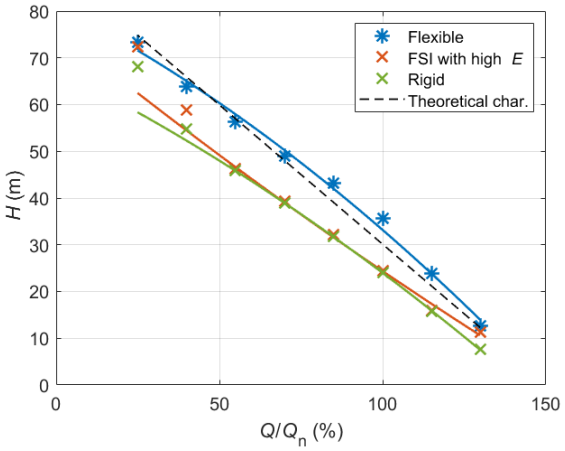

Figure 5. The head characteristics of the rigid and flexible impeller blades and the theoretical head characteristics with a rigid impeller with infinitely many blades

All the impellers investigated was assumed with blades that have constant blade thickness and width. The theoretical head of the studied impeller can be approximated as follows according to empirical equations:

$$H_{t\infty} = -59{,}607\,\frac{Q}{Q_n} + 89{,}717\ (\mathrm{m}) \qquad (1)$$

The head characteristics of the flexible blade run significantly higher than the one of the rigid blades according to Figure 5. The reason of this is the deformation of the impeller circumference (the blade's trailing edge; see section 3.2). The overall deformation of the blade depends on the Young's modulus of the blade material and the geometry of the blade, especially the blade width. In the case of the actual study, linear elastic model can be considered. This means that the deformation is directly proportional to the force applied on the blade and the proportion factor is the Young's modulus

It was also taken to consideration, that the improvement in the pump head is due to the blade deformation and not just numerical error. A simple method was developed: an FSI simulation with the Young's modulus set high (usually over $2 \cdot 10^4$ GPa) that results practically in a rigid blade. If the results of this simulation ran close to the results of the rigid simulation (only CFD simulation without FSI), the change in the hydraulic parameters can be considered as the result of the flexible blades. The overall head has therefore increased. However, this does not necessarily imply an increase in the efficiency and a decrease in flow loss due to flow separation.

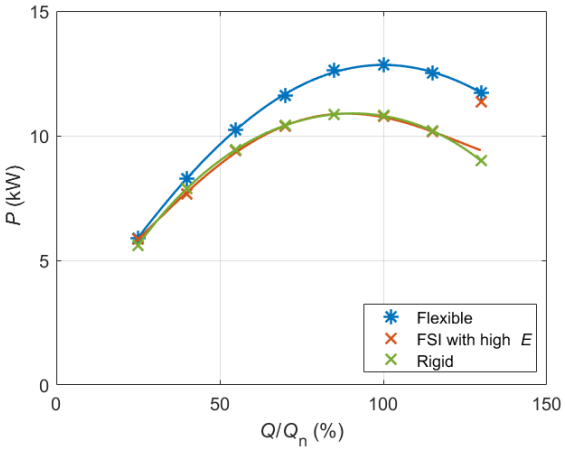

Figure 6. The input power characteristics of the rigid and flexible impeller blades

The input power of the pump should also be taken into consideration, which can be seen on Figure 6. These results are favourable because the input power appears to be higher due to the flexible blading and not a numerical error, as it could be seen in case of the head. It is difficult to calculate the characteristic curves of the recorded power analytically; the hydraulic efficiency curves should be taken into consideration instead (Figure 7).

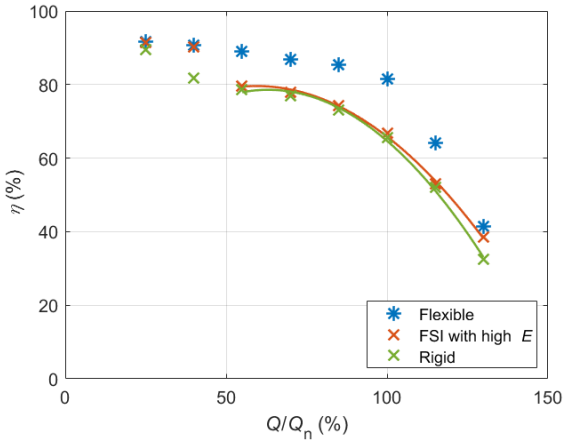

Figure 7. The hydraulic efficiency curves of the rigid and flexible impeller blades

The efficiency of flexible blades is approximately 5-25% better than rigid blades. This was one of the main goals of the research. The efficiency improved mainly for medium flow rates. Since this study investigates only the impeller (the losses of the volute chamber or the mechanical losses were not considered), the efficiency depends only on the friction and the losses due to flow separation. This is, in fact, the hydraulic efficiency of the pump. To investigate these in more detail, and to interpret the improvement in efficiency, it is necessary to carry out a flow chart analysis too, which is discussed in more detail in section 3.3.

3.2. The blade deformation

To analyse the effects of the blade deformation, the velocity triangles at the leading edge and the trailing edge of the blade should be considered. The Figure 8 shows the velocity triangles.

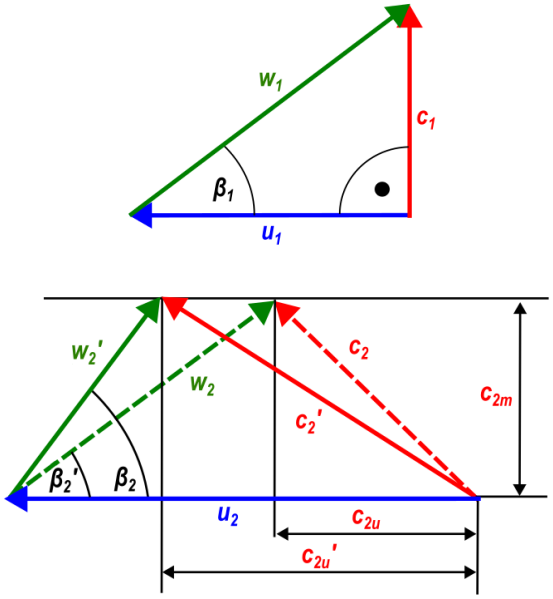

Figure 8. The velocity triangles

Considering Euler's turbine equation:

$$H = \frac{c_{2u}u_2 - c_{1u}u_1}{g} \qquad (2)$$

The value of the head of the pump could be improved in the following cases neglecting the viscous losses and considering only the Equation (2):

- The absolute velocity at the leading edge has less or no circumferential component. The ideal case is that the absolute velocity vector is perpendicular to the circumferential velocity; therefore, the circumferential component of the absolute velocity is zero. This means that the absolute velocity has only a meridional component that can be calculated analytically. Knowing this and the circumferential velocity, the optimal blade angle can be calculated too, as it can be seen on the upper part of the Figure 9 too.
- The circumferential component of the absolute velocity at the trailing edge is higher. This means that the blade angle at the trailing edge should be as high as possible, and as a result, the angle between the circumferential and absolute velocities should be low. This implies that the circumferential component of the absolute velocity is high, next to the same meridional component of the absolute velocity.

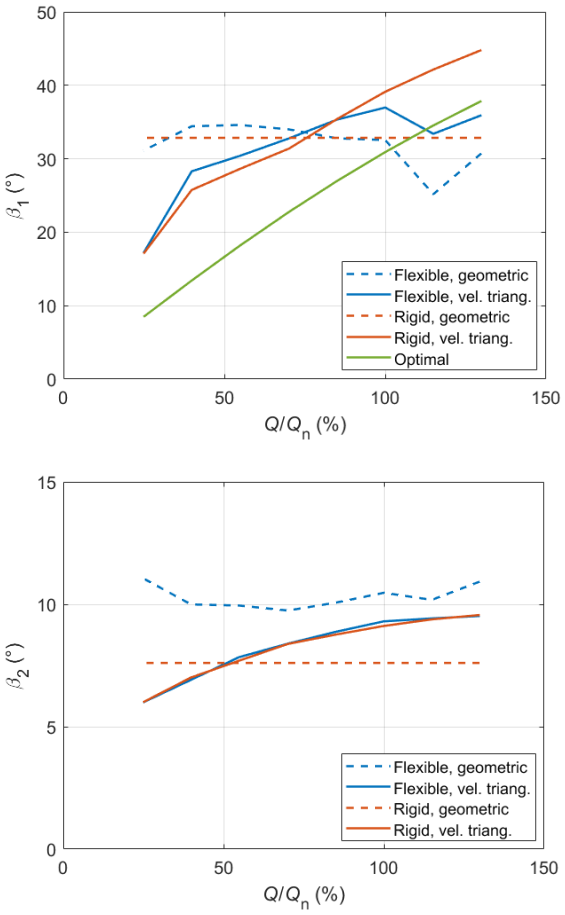

Figure 9. The blade angles at the leading (upper) and the trailing (lower) edge (flexible and rigid blade)

The Ansys CFX post-processor can measure the deformed geometric blade angle. The blade angle can be calculated from the velocity triangle can be known from the simulation results. The upper part of Figure 9 shows that the deformation of the blade angle at the leading edge in the case of flexible blade is opposite to the desired direction. This is due to the flow separation on the leading edge, which results in a suction zone. This zone makes the blade deform opposite to the required direction. The goal would be having the geometric blade angle as close to the optimal as possible and reducing the flow separation.

However, this does not mean that the head achieved get significantly lower as it could be seen in Chapter 3.1. The equation (2) includes the circumferential velocity, which velocity is significantly higher at the trailing edge than at the leading edge. As a result, the deformation of the trailing edge should affect the head of the pump more significantly, because the circumferential velocity is significantly higher at the trailing edge than the leading edge. The characteristics of the deformation and the blade angle are consistent with the head curve, because the higher β_2 angle of the flexible blade resulted in the growth of the pump head.

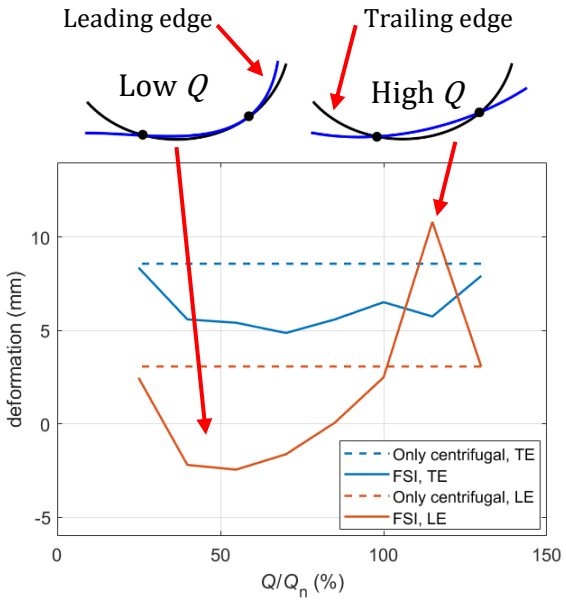

Figure 10. The effect of the centrifugal force and the flow on the deformation of the blade (the deformed blade geometry is blue)

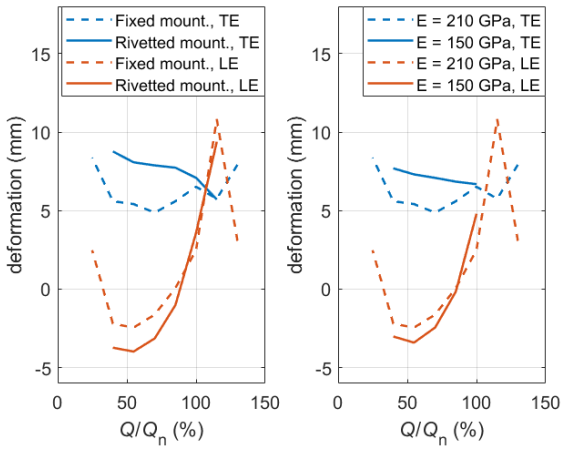

Figure 11. The effect of the mounting (l) and the lower Young's modulus (r) on the deformation

As Figure 11 shows, neither the rivetted mounting nor the more flexible blade material significantly affected the deformation at the blade's edges. This means that the fixed mounting should be preferred to the first testing period of the research: it is easier to manufacture and numerically more stable, too. The more flexible blade material should be investigated with another impeller though, which is written in section 4. It was also studied if the field of the centrifugal force itself can lead to the same amount of deformation as it would be combined with the flow. This would be true, if the FSI simulation gave approximately the same deformation, as the centrifugal force itself. It has been proven to be false, (see Figure 10). As it can be seen, the effect of the flow leads to significantly different deformation.

This is important, because if it was not, an easier simulation without FSI could have been made, reducing computational cost. In the future, a fan impeller should be also taken to consideration, because in this case, the effect of the centrifugal force may be more significant.

3.3. The analysis of the flow field

The blade deformation is a direct answer to the increase in the head of the pump as it could be seen in Chapter 3.1 and 3.2. (therefore, an increase in the input power, too). However, a more detailed study of the impeller flow field is needed to investigate the improved hydraulic efficiency.

The rothalpy, as an energy-dimension quantity, should be taken into consideration. This will be used to investigate the flow losses and, consequently, the efficiency relations for the different simulations. Note that in a stationary coordinate system, the total pressure would be the appropriate variable to study the losses. Neglecting the potential energy and assuming the constant temperature of the fluid, the rothalpy can be written as follows:

$$I = \frac{p}{\rho} + \frac{w^2}{2} - \frac{u^2}{2} \tag{3}$$

In this case, the rothalpy, that describes the losses can decrease due to the work of the shear stresses or dissipation and heat transfer from the flow. The decrease in the rothalpy in the flow field is the following can be seen on Figure 12. This is shown in the case of 85% relative flow rate because this shows the most significant difference between the rigid and the flexible blade.

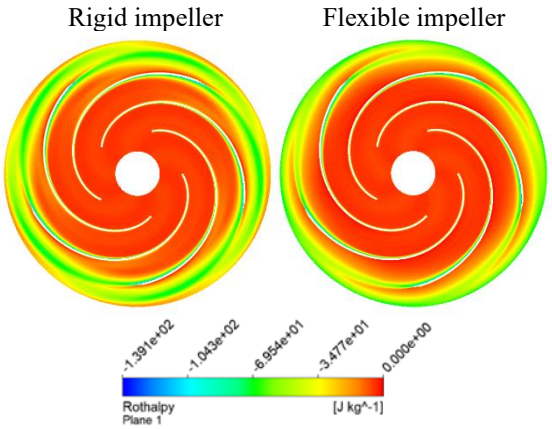

Figure 12. The loss of the rothalpy in the flow field: colour blue means high flow losses

Figure 12. shows that the zones with a higher loss in the rothalpy is wider in case of rigid blade. This implies higher loss due to flow separation, especially around the trailing edge of the blade. The lower this flow separation zones could be, the higher would be.

4. RESULTS IN CASE OF IMPELLER *B*

The impeller geometry *B* was tested with either blade made from Aluminium or 3D-printed ASA for experimental studies to be carried out in the future.

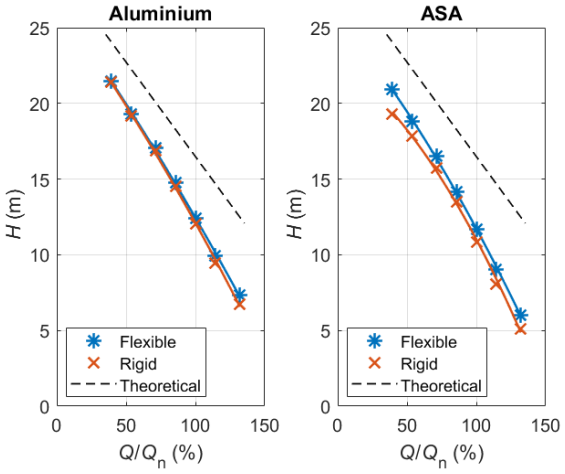

Figure 13. The head characteristics of the Aluminium and ASA-bladed impellers

As Figure 13 shows, the real head characteristics are significantly lower than the theoretical curve compared to the steel impeller. The reason of this is that the blade width of the ASA and the Aluminium blade compared to the impeller diameter is significantly higher than the one made from steel. The trailing edge of these blades is filleted, too, not as sharp as the steel one (see Figure 2). This results in a higher flow separation. Furthermore, the flow separation can affect the characteristics even more due to the higher number of blades.

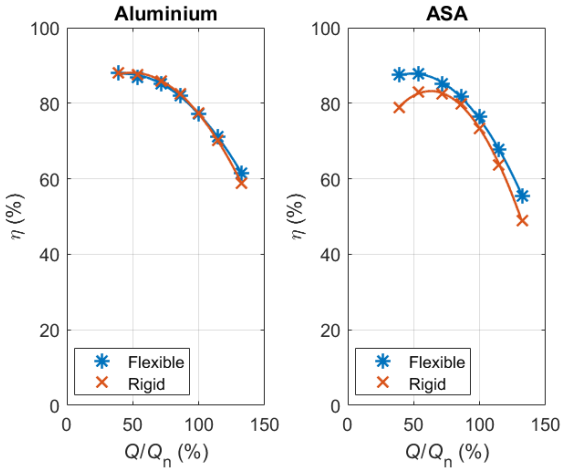

Figure 14. The efficiency characteristics of the Aluminium and ASA-bladed impellers

The ASA blade is more flexible than the Aluminium one. Consequently, bigger improvement can be achieved with it in efficiency. This is even more significant in off-design points (Figure 14).

One of the research goals is exactly this: designing a flexible blade, that improves the hydraulic efficiency in off-design operating points.

The FSI simulation's main disadvantage is its significantly high computational cost, especially with high mesh element numbers. To make the algorithm faster, a half-numeric method was also tested. This means that the net force due to the flow and the centrifugal force field are calculated only in one iteration step. This force is applied to the analytical model of the blade, which means a beam fixed in two points. Solving the differential equation of a flexible beam would be a boundary condition problem that could be solved. However, this method has been proven to resulting in significantly lower deformations than the FSI simulation. The possible cause of this is that the flow separation at the leading edge leads to a pressure drop, and high suction force, as it can be seen in Figure 15. Due to the deformation caused by this force, the higher the deformation at the leading edge is (see section 3.2), the higher the flow separation will be. As a result, this method could not be used to further analysis.

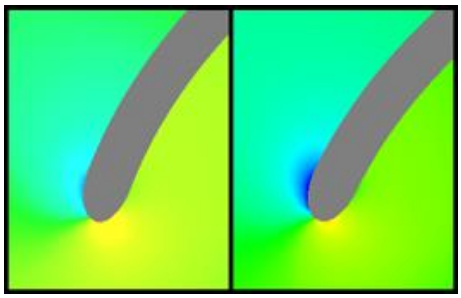

Figure 15. Flow separation zones around the leading edge in the case of rigid blade (left) and deformed flexible blade (right)

5. CONCLUSION

Coupled FSI simulations were used to investigate the effects of rigid and flexible bladed impellers on the hydraulic parameters such as head and efficiency. The flexible impeller increased the efficiency by 10-20% depending on the flow rate, and 15% increment was recorded in case of impeller *A* in the best-efficiency point. In addition, due to the deformation, the head increased. In all cases, the trailing edge of the blade is slightly displaced towards the pressure side, while the leading edge is displaced towards the suction side at lower flow rates and towards the pressure side at higher flow rates. This is quite unfavourable; the blade should deform in such way that the leading edge moves towards the optimal direction. This can be made, for example, by actuators ([1] [3]). However, this method would result in a significantly more difficult and more expensive to manufacture impeller than the passively deformable one. A significant part of the deformation is due to the centrifugal force, but the effect of pressure distribution is also not negligible. It can be stated that the rothalpy remains approximately constant according to the theoretical value between the two blades, but there are separation zones on the blade, too. These depend on the flow rate and the flexibility of the blade. However, the present study of the flow field does not allow a more precise and detailed explanation of the improvement in efficiency, so this requires further analysis such as more accurate simulations and experimental studies. It is also important to make the blade as thin as possible to earn the best efficiency and more streamlined design.

The inaccuracy of the simulation is partly due to the less accurate mesh and numerical scheme. However, a more accurate scheme would made the meshing procedure significantly more difficult. The simulation converges relatively slowly, especially in further distance from the design point, and does not converge at all flow rates. A possible solution to this problem could be a transient simulation, but the computational capacity requirement of this is significantly higher.

REFERENCES

[1] Seidler, M., Bode, C. and Friedric, J., 2024, "Effect of Blade Reference Design Variations on the Morphing Capability of a Shape-Adaptive Fan Rotor" *International Journal of Gas Turbine, Propulsion and Power Systems* Vol. 15., Num. 2.

[2] Seidler, M. et. al., 2024, "Combining shape adaptive blades and active flow control in a multi stage axial compressor: a numerical study" *CEAS Aeronautical Journal*, p. 239–253

[3] A. Suman et. al., 2027, „Analysis of the Aerodynamic and Structural Performance of a Cooling Fan with Morphing Blade" International Journal of Turbomachinery Propulsion and Power (2017,2,7)

[4] Hartl, D. J. and Lagoudas, D. C., 2007, „Aerospace applications of shape memory alloys" *Proc. IMechE* Vol. 221 Part G: J. Aerospace Engineering

[5] Campbell, R. L., Paterson, E. G., 2011, „Fluid–structure interaction analysis of flexible turbomachinery" *Journal of Fluids and Structures 27* (2011) 1376–1391

[6] Daynes, S. and Weaver, P. M., 2012, „A morphing trailing edge device for a wind turbine" *Journal of Intelligent Material Systems and Structures* 23(6) 691–701

[7] Daynes, S. and Weaver, P. M., 2012, „Design and testing of a deformable wind turbine blade control surface" *Smart Materials and Structures* 21 (2012) 105019 (10pp)

Conference on Modelling Fluid Flow (CMFF'25)
The 19th International Conference on Fluid Flow Technologies
Budapest, Hungary, August 26 - August 29, 2025

ASSESSMENT OF RANS TURBULENCE MODELLING APPROACHES FOR POLLUTANT DISPERSION IN VEGETATED STREET CANYONS USING PERIODIC BOUNDARY CONDITIONS

Bálint PAPP [1], Ildikó TROLL [2], Gergely KRISTÓF [3]

[1] Corresponding Author. Department of Fluid Mechanics, Faculty of Mechanical Engineering, Budapest University of Technology and Economics. Address: Műegyetem rkp. 3., H-1111 Budapest, Hungary. E-mail: papp.balint@gpk.bme.hu.
[2] Department of Fluid Mechanics, Faculty of Mechanical Engineering, Budapest University of Technology and Economics. Address: Műegyetem rkp. 3., H-1111 Budapest, Hungary. E-mail: ildikotroll@edu.bme.hu.
[3] Department of Fluid Mechanics, Faculty of Mechanical Engineering, Budapest University of Technology and Economics. Address: Műegyetem rkp. 3., H-1111 Budapest, Hungary. E-mail: kristof.gergely@gpk.bme.hu.

ABSTRACT

Although trees provide shade for pedestrians, enhancing their thermal comfort, dense vegetation can remarkably hinder the ventilation efficiency of an urban area, resulting in greater pedestrian exposure to traffic-related air pollutants. In the present paper, the widely used realizable k-ε and k-ω SST turbulence models, as well as a novel geometry-informed k-ε turbulence model are compared and applied to investigate the impact of tree planting in finite-length street canyons of $H/W = 0.5$ and $L/H = 5$ aspect ratios.

The geometry-informed k-ε model is based on a new eddy viscosity formulation that relies on the same set of physical parameters as the k-ω SST model. The new model constrains the growth of the turbulent length scale by incorporating wall distance, even in flow regions where turbulent kinetic energy dissipation exceeds production (dissipative regime). The geometry-informed (GI) model is implemented in ANSYS Fluent as a user-defined eddy viscosity formulation for the standard k-ε model. The resulting GI k-ε model is parameterized similarly to the standard k-ϵ model, except for the $C_{1\varepsilon}$ constant, which is set to 1.55. The model has previously demonstrated superior accuracy compared to classic eddy viscosity models in some test cases (i.e., channel flow, shear flow, and backward-facing step), though it has not yet been tested in any complex flows.

The present paper proves that the new turbulence model is suitable for the accurate simulation of building-scale transport processes: the validation metrics, characterizing the agreement of the modelled velocity and concentration field with previous measurement data, show similar performance compared to those obtained using the industry standard realizable k-ε and k-ω SST turbulence models.

Keywords: CFD, pollutant dispersion, street canyon, trees, turbulence model, urban air quality.

NOMENCLATURE

Roman symbols

c	kg/m^3	concentration
c^*	1	normalized concentration
$C_{1\varepsilon}$	1	model constant of the k-ε model
c_d	1	drag coefficient
$C_{\varepsilon 4}$	1	model constant of the vegetation model
$C_{\varepsilon 5}$	1	model constant of the vegetation model
D_t	m^2/s	turbulent mass diffusivity
H	m	building height (reference height)
k	m^2/s^2	turbulent kinetic energy (TKE)
K_s	m	equivalent sand-grain roughness (wall roughness)
L	m	canyon length
L_s	m	source length
N	1	number of elements
O	[SI]	reference data observed in the experiments
P	[SI]	model predictions (CFD results)
Q	kg/m^3	total source intensity
Re	1	Reynolds number
Sc_t	1	turbulent Schmidt number
S_k	kg/m/s^3	vegetation source term in the equation for TKE
$S_{u,i}$	N/m^3	vegetation source terms in the momentum equation
S_V	kg/m^3/s	volume source intensity of the passive scalar
S_ε	kg/m/s^4	vegetation source term in the equation for turbulent dissipation
u	m/s	streamwise velocity component

U_∞	m/s	free-stream velocity (reference velocity)
v	m/s	spanwise velocity component
$\mathbf{v}$	m/s	velocity vector
V_s	m^3	volume of the source zone
W	m	canyon width (street width)
w	m/s	vertical velocity component
x	m	streamwise coordinate
y	m	spanwise coordinate
y^+	1	dimensionless wall distance
z	m	vertical coordinate

Greek symbols

β_d	1	model constant of the vegetation model
β_p,	1	model constant of the vegetation model
δ	m	boundary layer depth
Δc^*	%	change of the normalized concentration
Δx	m	mesh resolution
ε	m^2/s^3	dissipation rate of the TKE
ν	m^2/s	kinematic viscosity
ν_t	m^2/s	turbulent viscosity
ρ	kg/m^3	air density
ω	m^2/s^3	specific dissipation rate of TKE

Further notations

$\overline{(X)}$	average of a data set X
σ_X	standard deviation of the data set X
$\lvert\mathbf{x}\rvert$	absolute value of the vector $\mathbf{x}$

1. INTRODUCTION

Air pollution is a significant environmental factor influencing human health, as it presents considerable hazards for pollution-related diseases and premature death. In light of urbanization, it is crucial to gain a comprehensive understanding of the flow dynamics within urban landscapes, as well as the dispersion patterns of pollutants. Moreover, it is essential to analyze the effects of vegetation and various obstructions on pollutant concentration levels, as such insights are vital for the development of reliable methods for urban air quality evaluation.

Urban vegetation, particularly trees, plays a crucial role in the microclimate of municipal areas. Trees mitigate urban heat by providing shade, leading to improved heat comfort and reduced ambient and surface temperatures (Salmond et al., 2016). By reducing runoff, trees help moderate the vulnerability to water flooding. Through intercepting precipitation and facilitating evapotranspiration, vegetation enables better adaptation to the challenges of climate change (Gill et al., 2008). Additionally, tree canopies act as pollutant sinks through dry deposition and absorption (Janhäll, 2015), and can also attenuate traffic noise. Moreover, enhancing urban vegetation supports biodiversity (Gómez-Baggethun et al., 2013) and promotes well-being by encouraging physical activity, stress relief, cognitive restoration, and social interaction (Salmond et al., 2016).

However, trees in street canyons can adversely impact air quality by reducing airflow and trapping pollutants. Over the past two decades, several wind tunnel experiments and computational fluid dynamics (CFD) simulations have examined the aerodynamic effects of urban vegetation, which is reviewed by Janhäll (2015), Gallagher et al. (2015) and Buccolieri et al. (2018). The key findings from the relevant studies are summarized below.

Several researchers have investigated the impact of urban trees at the scale of a single street canyon. Fellini et al. (2022) and Carlo et al. (2024) used wind tunnel measurements, while Buccolieri et al. (2009) combined wind tunnel experiments with numerical simulations to analyze the effects of trees in a street canyon with a height-to-width ratio of 0.5, focusing on perpendicular wind directions. The results obtained by Buccolieri et al. (2009) indicate that trees reduced flow rates by 33% at pedestrian height compared to the empty reference canyon and despite the increased shear within the canyon, caused by the three canopy zones, TKE production remained mostly unchanged. In terms of pollutant concentrations, Fellini et al. (2022) reported an increase of up to 22% for the entire canyon volume. Meanwhile, Buccolieri et al. (2009) found that wall-averaged concentrations increased by 40% on the leeward side but decreased by 25% on the windward side in the presence of trees. Noteworthy results from Fellini et al. (2022) showed that the average pollution level does not correlate with the number of trees, contradicting the belief that an increased vegetation fraction leads to an increased pollutant accumulation. The evaluation of different urban scenarios by Carlo et al. (2024) concluded that cars, boundary walls, and hedges along the pedestrian zones can reduce pollutant exposure by 15%, 23%, and 11%, respectively, while similarly located trees potentially increase exposure by 51% for dense and 17% for sparse tree arrangements.

To achieve more realistic results, some studies have examined either an idealized or an actual urban neighborhood. A study by Gromke and Blocken (2015a, 2015b) analyzed the impact of avenue trees in a simplified urban neighborhood comprising 7×7 building blocks through 3D steady Reynolds-averaged Navier-Stokes (RANS) simulations. It was concluded that a 1% increase in the vegetation coverage in the street canyons corresponded to about a 1% rise in neighborhood-average pollutant concentration, in the 4% to 14% coverage range.

Furthermore, air quality investigations were performed in real urban scenarios in Lisbon and Aveiro, Portugal (Amorim et al., 2013), as well as Pamplona, Spain (Santiago et al., 2017) through similar methods. Both studies revealed significant changes in the flow field due to the presence of trees,

with an average pollutant concentration increase from 7.2% up to 13.2% for perpendicular wind approach and 12% for oblique flows at pedestrian level.

Importantly, the majority of CFD-based research papers model the effects of vegetation via the solution of the Reynolds-averaged Navier-Stokes equation, a turbulence modelling approach frequently used in urban dispersion studies (Toparlar et al., 2017). The RANS approach has a few advantages compared to scale-resolving turbulence models, such as large eddy simulation (LES), namely that (1) its computational demand is significantly smaller than that of LES, and (2) there are numerous best practice guidelines (BPGs) available to support its use (Blocken and Gualtieri, 2012; Blocken, 2015). Therefore, it became common practice in both the industry and in research to employ the available computational power to simulate larger and more complex problems using RANS instead of switching to scale-resolving turbulence models (Blocken, 2018).

On the other hand, RANS results can often be inaccurate, both in urban dispersion studies (see, e.g., Gousseau et al., 2011; and Tominaga and Stathopoulos, 2013), and in other applications as well. It was noted by Kristóf et al. (2025) that in a quasi-stationary free shear flow, various well-known Reynolds-averaged turbulence models lead to qualitatively incorrect results: the velocity magnitude decreases over time, resulting in a decrease in the spatially averaged values of hydraulic power, production, and dissipation. However, when the driving force is maintained, the average value of turbulent kinetic energy remains close to the DNS results, indicating a realistic value. With nearly constant kinetic energy and decreasing dissipation, turbulent viscosity increases, which explains the reduction in velocity amplitude. Throughout this process, the turbulent length scale grows indefinitely. The incorrect asymptotic behavior of these models may also affect the accuracy of the engineering applications of CFD.

To address this issue, Kristóf et al. (2025) introduce a new eddy-viscosity formulation that depends on similar parameters to the k-ω SST model but includes an additional dependence on wall distance in the dissipative regime, proportional to the square root of the wall distance. This slight dependence on wall distance prevents the unlimited growth of the turbulent length scale, which is why we refer to the new formulation as the geometry-informed (GI) model. When incorporated into the standard k-ε model equations, the GI formulation yields a shear stress distribution in equilibrium channel flow that aligns well with known DNS results.

The resulting turbulence model (GI k-ε model) does not require wall function application (it is monotonically integrable from the wall) as long as the numerical grid is sufficiently refined near the solid wall ($y^+ \leq 4$).

The present paper aims to benchmark the new geometry-informed k-ε turbulence model in realistic urban applications, both in the presence of trees and in vegetation-free cases, by comparing the model results to data obtained using the industry standard RANS turbulence models and to the results of wind tunnel experiments.

2. METHODS

2.1. Geometry

A few geometries from the wind tunnel study by Carlo et al. (2024) were replicated using computational fluid dynamics (CFD) simulations. The investigated setup consisted of a regular array of $H = 0.1$ m tall, rectangular building blocks, forming numerous street canyons and intersections. The flow field is characterized by a Reynolds number of $Re = U_\infty H/\nu = 3\times10^7$. The street canyons parallel to the x axis (wind direction) have a height-to-width aspect ratio of $H/W = 1$, and the street canyons perpendicular to the wind direction have an aspect ratio of $H/W = 0.5$. Both types of street canyons are of $L/H = 5$ length. The modelled geometry is shown in Figure 1. The top boundary of the computational

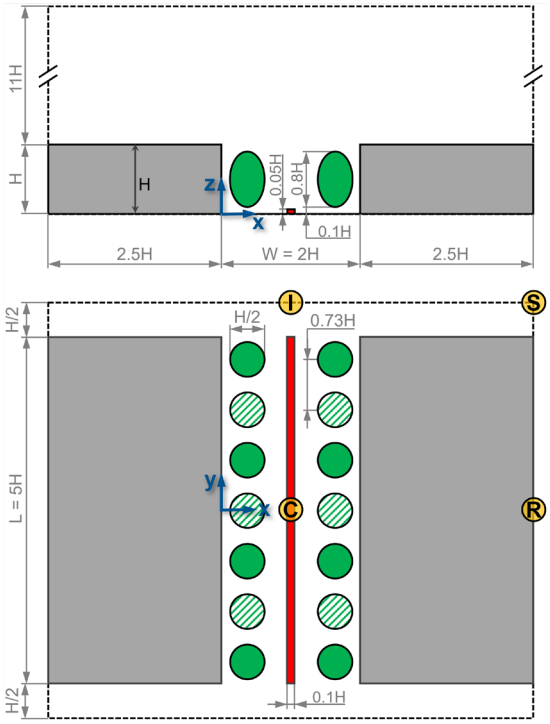

Figure 1. Layout and dimensions of the computational domain. The reference height is $H = 20$ m. In the *sparse trees* scenario (2×4 trees), the vegetation is only considered in the solid green zones, while in the *dense trees* setup (2×7 trees), vegetation is modelled in the zones denoted by both the solid and striped green areas. The yellow markers C (canyon), I (intersection), R (roof), and S (street) denote the location of the velocity profiles shown in Figure 3.

domain was placed $\delta = 11H$ distance above the rooftops, in which δ is the depth of the boundary layer forming above the building, as reported by Carlo et al. (2024) and Fellini et al. (2022).

Carlo et al. (2024) performed concentration measurements in one of the wider, $H/W = 0.5$ street canyons, located perpendicular to the wind direction, which is the critical orientation regarding air quality. In some cases, model trees were installed near the walkways on both sides. The *sparse trees* configuration consisted of four equidistantly placed trees on both sides of the canyon, while the *dense trees* setup had 2×7 trees installed (Figure 1). The wind tunnel experiments employed two parallel line sources in the middle of the canyon, which are modelled as a single combined emission zone in the present model, the length of which is equal to the length of the canyon ($L_s = L = 5H$).

2.2. Meshes and boundary conditions

The computational domain was discretized using polyhedral cells. The target cell size in the focus area, i.e., within the $H/W = 0.5$ canyon, was $H/\Delta x = 33$, with an additional mesh refinement to $H/\Delta x = 66$ near the source zone. The target mesh size was $H/16$ on every solid surface outside the target canyon. Inflation layers with a first layer height of $H/100$ were applied next to all solid boundaries. In the entire mesh, a linear growth rate of a maximum of 1.2 was allowed between adjacent cells, and the largest cells were $H/3$, near the top of the domain. The structure of the mesh is illustrated in Figure 2.

The above meshing parameters correspond to a medium mesh (hereinafter denoted by "M") of 2.04 million elements. Two further meshes were created using a linear refinement ratio, resulting in a coarser 1.01-million-cell and a more refined 5.33-million-cell mesh, hereinafter denoted by "S" and "L", respectively. The orthogonal quality of the cells in each mesh was above 0.17, which is considered adequate.

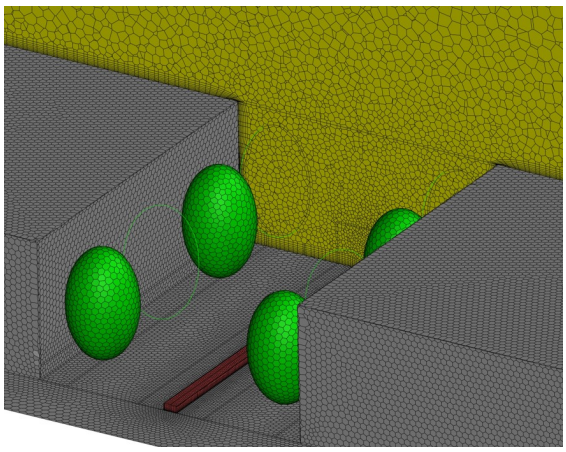

Figure 2. Spatial discretization of the computational domain near the buildings, for the coarsest mesh (S), with a spatial resolution of $H/\Delta x = 22$ within the canyon. The zones representing vegetation are denoted by green color. The pollutant source zone in the middle of the canyon is represented by red color. The yellow plane is an XZ cutplane located in the middle of the canyon ($y = 0$).

To model the repetitive building pattern (see Fellini et al. (2022) and Carlo et al. (2024) for photos of the experimental setup), periodic boundary conditions were applied at the streamwise ends of the computational domain, and symmetry was assumed at the spanwise boundaries and at the top. At the solid boundaries, i.e., at the building walls, at its roof, and on the ground, rough no-slip walls were assumed, in combination with a near-wall treatment using the standard law of the wall. The equivalent sand-grain roughness (K_s) was set uniformly for all walls in each simulation to have a good match with the TKE profile obtained above the buildings in the wind tunnel.

The periodic model was driven by a pressure gradient in the x direction, controlled around the value of –0.08 Pa/m with a prescribed target mass flow rate of air in the x direction of 3.9 kg/s. The mass flow rate was prescribed in order to result in a free-stream velocity of $U_\infty = u(\delta) \approx 5.5$ m/s, in line with the measurements of Carlo et al. (2024).

Importantly, while the flow field is periodic, the concentration field is not: we only want to model the pollutants emitted in the investigated canyon, and no upstream sources are taken into account – similarly to the wind tunnel experiments. Consequently, the flow and concentration fields must be computed separately. After reaching sufficient convergence for the former, the periodic boundaries were decoupled, and the flow field was "frozen", i.e., only the diffusion equation was solved, taking the flow field as an input. For this, a pressure outlet boundary condition is assumed at the downstream boundary (with 0 Pa gauge pressure), allowing the pollutants to leave the simulation domain freely.

2.3. Solver setup

In the majority of the cases presented in this paper, the geometry-informed k-ε model developed by Kristóf et al. (2025) was applied. For comparison, turbulence was also modelled using the realizable k-ε model, which is considered the industry standard approach for steady-state RANS calculations in the field of urban dispersion. Furthermore, the k-ω SST model, widely used in several engineering applications, was also utilized in one simulation.

The dispersion of traffic-related air pollutants was modelled using a passive scalar. The pollutant source was represented by a volume source term, S_V, added to the scalar transport equations. The pollutant emission rate, therefore, can be calculated as $Q = S_V/(\rho V_s)$, in which ρ is the density of air, and V_s is the total volume of the source zones.

Setting an appropriate value for the turbulent Schmidt number, i.e., the ratio of the turbulent viscosity to the turbulent mass diffusivity

($Sc_t = \nu_t/D_t$), can strongly influence the quality of the concentration results calculated based on steady-state RANS models (Gousseau et al., 2011). In the present study, $Sc_t = 0.2$ was chosen for all cases, via optimization over the $Sc_t = 0.04…1.3$ range. According to Tominaga and Stathopoulos (2007), the found optimum value is lower than usually applied in near-field dispersion, but not unprecedented, see e.g., He et al. (1999).

The transport equations were solved using the Coupled solver and second order flux schemes for the spatial discretization of all variables in Ansys Fluent 2023R1. Due to the high characteristic Reynolds number, the limit for the turbulent viscosity ratio was increased to 10^{20}, which is a common practice in building-scale RANS calculations.

2.4. Modelling the effects of vegetation

The effect of vegetation was modelled using the following source terms in the vegetation zones (see Figure 1 and Figure 2) for the flow and turbulence equations, following the model derived by Sanz (2003).

$$S_{u,i} = -\rho c_d u_i |\mathbf{v}| \tag{1}$$

$$S_k = \rho c_d \left(\beta_p |\mathbf{v}|^3 - \beta_d |\mathbf{v}| k\right) \tag{2}$$

$$S_\varepsilon = \rho c_d \frac{\varepsilon}{k} \left(C_{\varepsilon 4} \beta_p |\mathbf{v}|^3 - C_{\varepsilon 5} \beta_d |\mathbf{v}| k\right) \tag{3}$$

In the above equations, $S_{u,i}$, S_k, and S_ε are the source terms appearing in the transport equations for the three velocity components ($u_i = u, v, w$) as well as for the turbulent kinetic energy (k) and its dissipation rate (ε). Furthermore, ρ is the density of air, $c_d = 0.65$ is the drag coefficient of a single tree (Carlo et al., 2024), and $|\mathbf{v}|$ denotes the magnitude of the velocity vector. Finally, $\beta_p = 1$, $\beta_d = 5.1$, $C_{\varepsilon 4} = 0.9$, and $C_{\varepsilon 5} = 0.9$ are model constants.

The source terms in the momentum equation account for the pressure loss caused by the viscous resistance of the tree branches and the leaves. Moreover, the source term in the transport equation of k models the conversion of large-scale TKE into small-scale TKE, as the porous canopy converts the energy of the flow into wake turbulence. Finally, source term for the turbulent dissipation is based on Kolmogorov's relation (Balogh and Kristóf, 2009).

The above formulation is widely used in the literature, such as by Balogh and Kristóf (2009), Balczó et al., (2009), Kenjeres and Ter Kuile (2013), Gromke and Blocken (2015a, 2015b), and Santiago et al. (2019). It is important to note that the values of the parameters (β_p, β_d, $C_{\varepsilon 4}$, and $C_{\varepsilon 5}$) can vary between different studies, and the values used in the present model are taken from Gromke et al. (2015a).

For fellow CFD modelers, we have two practical remarks. Firstly, if the geometry is created in model scale, the full-scale drag coefficient of a single tree must be multiplied by the model scale to yield the same pressure loss – see Balczó et al. (2009) and Gromke (2011). Secondly, for sufficient convergence, the use of an implicit solver is required. Therefore, the derivatives of the above source terms with respect to u_i, k, and ε must be provided – see, e.g., Balczó et al. (2009).

2.5. Performance metrics

To assess the accuracy of the models, the performance metrics proposed by Chang and Hanna (2004) were applied to the concentration results. The full names of the metrics are given in Table 1 later.

$$R = \frac{\overline{(O - \overline{O})(P - \overline{P})}}{\sigma_O \, \sigma_P} \tag{4}$$

$$FAC2 = \frac{1}{N} \sum_{i=1}^{N} f_i, \quad with \quad f_i = \begin{cases} 1 & if \quad 0.5 \le \frac{P_i}{O_i} \le 2 \\ 0 & otherwise \end{cases} \tag{5}$$

$$FB = \frac{\overline{O} - \overline{P}}{0.5\,(\overline{O} + \overline{P})} \tag{6}$$

$$NMSE = \frac{\overline{(O - P)^2}}{\overline{O}\,\overline{P}} \tag{7}$$

$$MG = \exp\left(\overline{\ln O} - \overline{\ln P}\right) \tag{8}$$

$$VG = \exp\left(\overline{(\ln O - \ln P)^2}\right) \tag{9}$$

In addition to the above performance metrics, the average absolute deviation, as defined by Montazeri and Blocken (2013), can be computed as

$$\mathrm{AAD} = \overline{|\mathrm{O} - \mathrm{P}|}\,. \tag{10}$$

In the above formulas, P denotes the model predictions (CFD simulation results), and O denotes the reference data observed in the experiments. Moreover, $\overline{O}$ and $\overline{P}$ stand for the averages over these data sets, σ_O and σ_P represent their standard deviations, and N denotes the number of elements of the data sets. Note that as the absolute measurement uncertainty is unknown, small data are not omitted based on this criterion; hence, the formulas presented in this paper are mathematically simpler than the original ones.

3. RESULTS AND DISCUSSION

This section presents the comparison of the velocity, turbulence, and concentration results obtained throughout seven simulation cases, with combinations of (1) three meshes of different spatial

resolution, (2) three turbulence models and two different wall roughnesses, and (3) three different tree configurations, including the tree-free canyon.

3.1. The impact of the applied turbulence model on the flow and concentration field

Firstly, let us compare the flow fields obtained using different turbulence models. As discussed above, the wall roughness was tuned to achieve a good agreement between the numerical and experimental TKE profiles. As shown in Figure 3, the geometry-informed k-ε model requires around two times higher sand-grain roughness ($K_s/H = 0.15$) to achieve the same turbulence levels compared to the realizable k-ε and the k-ω SST models ($K_s/H = 0.07$). It is also worth noting that the GI k-ε model reproduces the shape of the TKE profile most accurately, especially just above roof height. The agreement of the GI k-ε model results and the experimental data is characterized by NMSE = 6.7×10^{-3} in contrast to 1.1×10^{-2} (realizable k-ε) and 1.8×10^{-2} (k-ω SST). Moreover, despite the fact that the TKE in the bulk flow is set to be similar for all turbulence models, the GI k-ε model yields substantially more turbulence below roof height, which is also visible in Figure 5.

Furthermore, let us assess the shape of the velocity profiles. It can be clearly seen that the GI k-ε model (with $K_s/H = 0.15$) yields the closest match with the experimental results, characterized by NMSE = 5.9×10^{-3} (averaged over the four velocity profiles shown in Figure 3), while the realizable k-ε and the k-ω SST models yield somewhat more modest values (8.3×10^{-3} and 1.7×10^{-2}, respectively). The agreement of the profiles produced by the GI k-ε model is remarkable in the lower part of the "intersection" location, but the three other velocity profiles show similar levels of correspondence, too. Note that all CFD profiles show excellent correlation with the experimental data: the correlation coefficients are over R = 0.98 for each profile.

Secondly, the concentration results presented in Figure 4, obtained using $Sc_t = 0.2$, show a good agreement between the experimental observations and the model predictions in 116 gauging points located within the canyon. It was observed that for higher Sc_t values, the model overpredicts the concentrations for all investigated turbulence models. This draws attention to the fact that the applied periodic modelling approach combined with RANS turbulence models requires setting a lower Sc_t value than usually applied in near-field dispersion studies.

The performance metrics of the concentration results, compiled in Table 1, highlight that although all three models show only acceptable correlation with the experimental data (R = 0.517…0.543), the

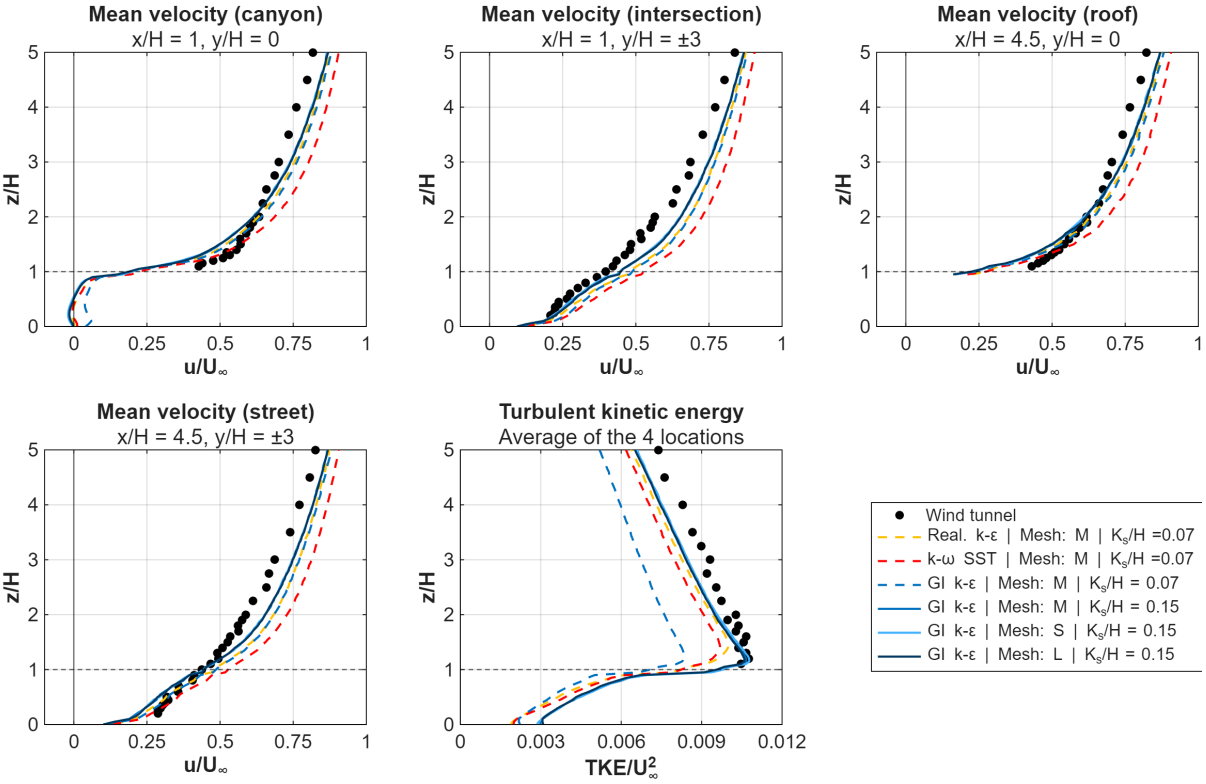

Figure 3. Comparison of the velocity and turbulence profiles obtained in the numerical simulations using turbulence models and meshes and in the wind tunnel experiments by Fellini et al. (2022) and Carlo et al. (2024). The locations of the four vertical profiles are shown in Figure 1. (In this figure, the profiles are only shown up to $z/H = 5$, but they were modelled up to $z/H = 12$.)

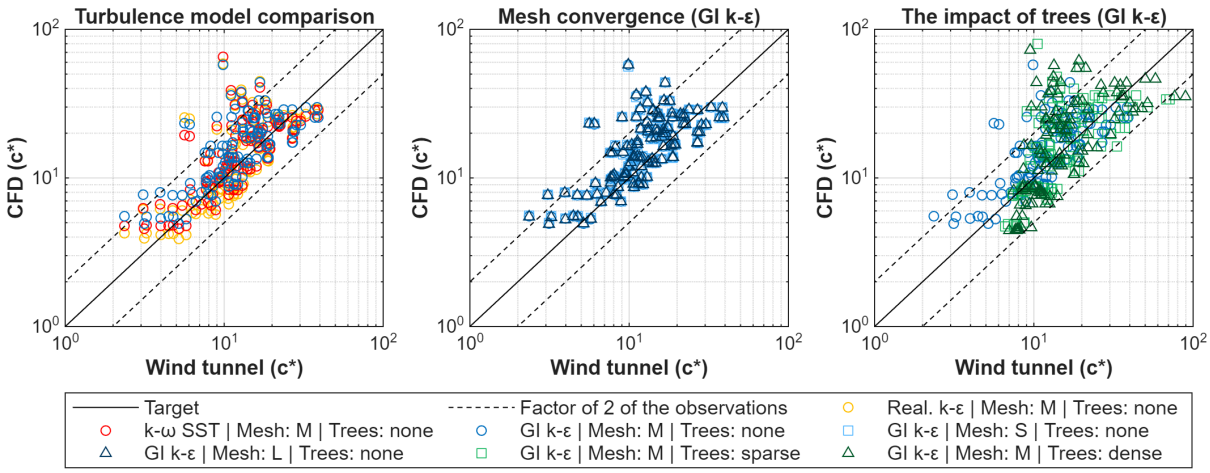

Figure 4. Comparison of the mean normalized concentration ($c^* = cU_\infty L_s H / Q$) obtained in the 116 gauging points of the wind tunnel experiments by Carlo et al. (2024) and the corresponding locations in the CFD simulations of the present study.

systematic error is minor, (FB = 0.171…0.240, MG = 1.137…1.281) and the scatter of the data is also moderate (NMSE = 0.339…0.351, VG = 1.219…1.263). The average absolute deviation of the predicted concentrations from the measured ones is AAD = 5.3…5.9 for the three different turbulence models, which can be considered acceptable, as the range of the experimentally observed concentrations for the empty street canyon was $c^* = 2.4…39.0$.

In conclusion, it can be stated that the geometry-informed k-ε turbulence model is capable of reproducing the flow and concentration field in urban street canyons with similar accuracy as the industry standard realizable k-ε and k-ω SST models.

3.2. Mesh convergence analysis

It can be observed in Figure 3 that the velocity and TKE profiles obtained using different spatial resolutions (within the canyon: $H/22$, $H/33$, $H/50$), shown by the three continuous blue curves, collapse onto one another within a line width. Furthermore, the dispersion results shown in the middle panel of Figure 4 reveal that the concentrations obtained at each gauging point on the different meshes are very close to one another, i.e., the resulting scatter plots show a very good overlap.

The above findings are also reinforced by the performance metrics presented in Table 1: the values of the metrics do not significantly change with the mesh refinement, supporting the conclusion that even a $H/22$ spatial resolution within the canyon is sufficient for steady-state RANS simulations of urban dispersion using the geometry-informed k-ε model.

3.3. The impact of trees on urban air quality

The scatter plots presented in the right-hand panel of Figure 4 reveal that qualitatively, the agreement with the measurement data is similar to that of the treeless case. Moreover, the performance metrics presented in Table 1 show minor improvements in terms of the systematic error (see FB and MG), but the noticeable

Table 1. Performance metrics characterizing the performance of the dispersion model in combination with different meshes, turbulence models and tree configurations. (The formulas for the metrics are given in Eqs. 4-10.)

Tree configuration ▶	none					sparse	dense	**Target**
Turbulence model ▶	real. k-ε	k-ω SST	geometry-informed k-ε					
Metric ▼ **Mesh** ▶	M			S	L	M		
Correlation coefficient (R)	0.543	0.522	0.517	0.523	0.516	0.422	0.456	**1**
Factor of two of observations (FAC2)	0.914	0.888	0.862	0.862	0.862	0.836	0.828	**1**
Fractional bias (FB)	0.171	0.181	0.240	0.235	0.240	0.136	0.163	**0**
Geometric mean bias (MG)	1.137	1.181	1.281	1.277	1.281	1.083	1.093	**1**
Normalized mean square error (NMSE)	0.351	0.345	0.339	0.331	0.341	0.488	0.583	**0**
Geometric variance (VG)	1.237	1.219	1.263	1.259	1.263	1.304	1.391	**1**
Average absolute deviation (AAD)	5.521	5.319	5.941	5.867	5.955	8.286	9.635	**0**

increase of the NMSE, VG, and AAD values suggests that the model predictions of pointwise concentration values are more intensely affected by the random error when vegetation is present. Nevertheless, all metrics can be considered moderate; therefore, the geometry-informed k-ε turbulence model can be viewed as a reasonable alternative for predicting the concentration field in the presence of trees as well.

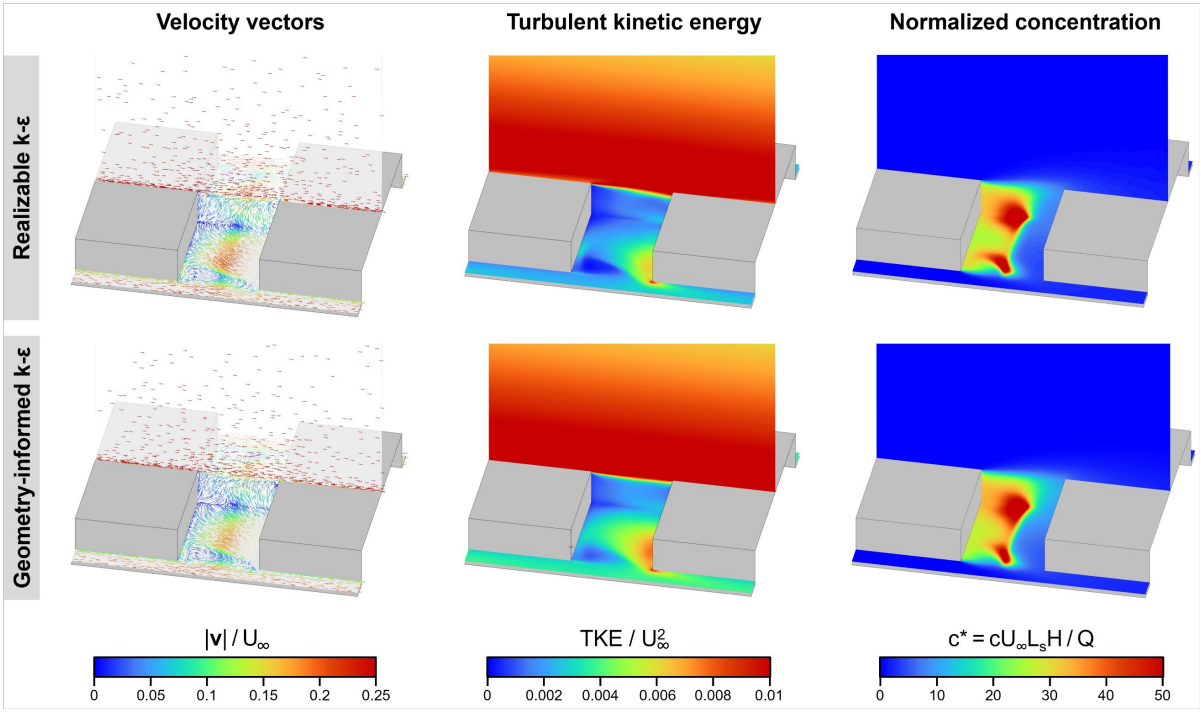

Figure 5. Comparison of the flow and concentration fields obtained using the realizable k-ε model and the geometry-informed k-ε model on the medium-resolution mesh (M). The vertical cut-plane is located at the symmetry plane ($y = 0$), and the horizontal cutplane is located at $z/H = 0.1$.

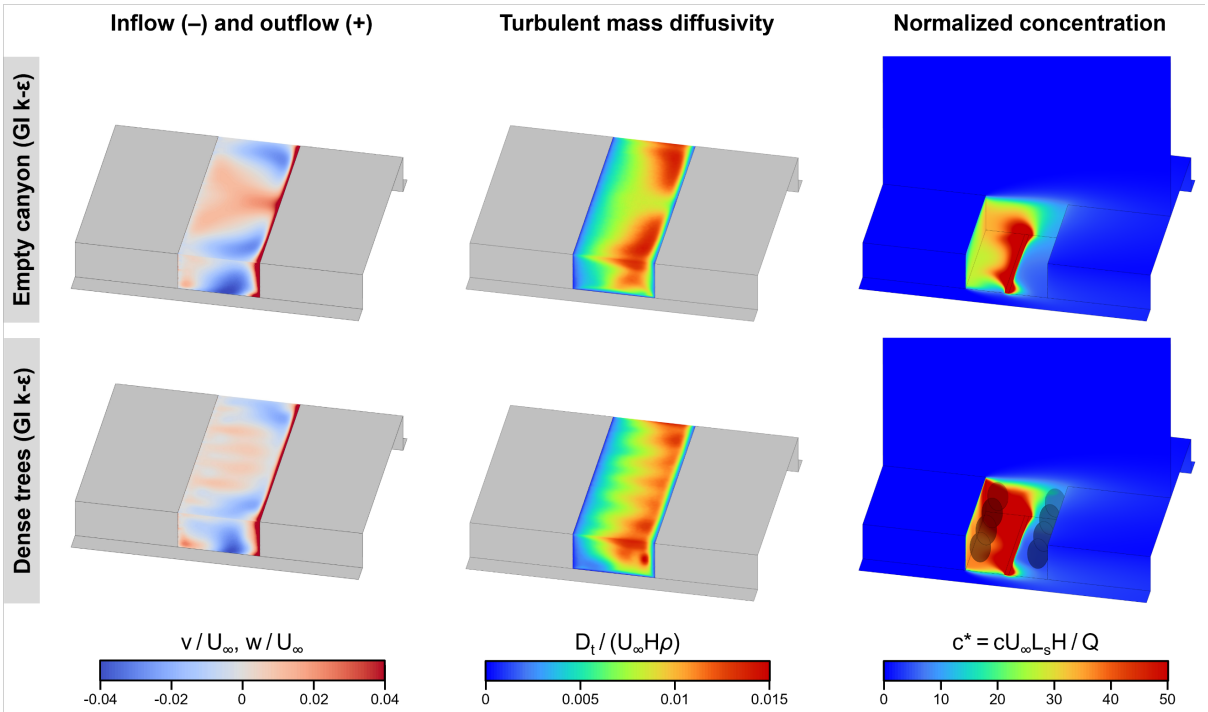

Figure 6. Comparison of the quantities characterizing the transport processes, both for an empty street canyon and one with densely installed trees. The concentration is plotted on the walls and a vertical cut-plane located at the symmetry plane ($y = 0$). All results in this figure were obtained using the geometry-informed k-ε model.

To the best of the Authors' knowledge, no CFD results were previously published for the currently investigated geometry; therefore, a handful of simulation results are hereby presented in order to provide aid in understanding the flow and dispersion processes governing the mass transfer of medium-length street canyons.

The left-hand-side panels of Figure 6 show that the presence of trees substantially decreases the magnitude of the inflow and outflow velocities at the lateral sides of the canyon, and especially at roof level, above both the leeward and the windward walkways. Similarly, the turbulent mass diffusivity at the lateral and vertical boundaries of the canyon, becomes noticeably lower when 2×7 trees are present (i.e., for the dense tree arrangement), resulting in an increase in pedestrian exposure by 31.6% over the leeward (upwind) walkway and a decrease of 9.4%, over the windward (downwind) walkway. Remark: the spatial averages were obtained in $0.1H$ tall and $0.2H$ wide boxes at the feet of the buildings. Although the concentration decrease at the windward pedestrian zone of the vegetated street canyon may sound counterintuitive, Carlo et al. (2024) reported similar findings in the experiments.

The predicted concentration changes in the pedestrian zones and in the entire canyon relative to the tree-free canyon are listed in Table 2 for both tree configurations. The currently presented model results somewhat underestimate the observations of Carlo et al. (2024), who found the canyon-average concentration to increase by 22.3% and 70.5% as the consequence of planting the trees in the sparse and dense configurations, respectively, based on the average of the pointwise measurements.

4. CONCLUSIONS AND OUTLOOK

In this paper, a novel RANS turbulence model, the geometry-informed k-ε (GI k-ε) model developed by Kristóf et al. (2025), was applied to simulate the time-averaged flow and concentration field in a periodic building configuration. The investigated geometry consisted of street canyons of $H/W = 0.5$ and $L/H = 5$, in which the effects of 2×4 and 2×7 trees, installed over the walkways, on urban air quality and pedestrian exposure were also analyzed.

The results underline that the new geometry-informed k-ε turbulence model is a suitable alternative for computing the flow and dispersion field to the industry standard realizable k-ε and k-ω SST turbulence models based on several performance metrics. It was also shown that the GI k-ε model results are of similar accuracy for the two tree arrangements of different density as for an empty street canyon, with the relative concentration increases due to the presence of vegetation also being generally in line with the experimental observations of Carlo et al. (2024) about the same setup.

In its current form, the GI k-ε model differs from the standard k-ε model primarily in the formulation of the eddy viscosity. The optimization of the source terms in the turbulent dissipation (ε) transport equation is the subject of ongoing research. However, even in its present state, the model represents a reasonable alternative approach for simulating urban air pollutant dispersion, and its further development is worth paying attention to.

ACKNOWLEDGEMENTS

The research reported in this paper is part of project no. 146158, implemented with the support provided by the Ministry of Innovation and Technology of Hungary from the National Research, Development and Innovation Fund, financed under the OTKA K 23 funding scheme.

Project no. TKP-6-6/PALY-2021 has been implemented with the support provided by the Ministry of Culture and Innovation of Hungary from the National Research, Development and Innovation Fund, financed under the TKP2021-NVA funding scheme.

The work of Bálint Papp was supported by the EKÖP-24-4-I-BME-357 University Research Scholarship Program of the Ministry for Culture and Innovation from the source of the National Research, Development, and Innovation Fund.

REFERENCES

Amorim, J. H., Rodrigues, V., Tavares, R., Valente, J., & Borrego, C. (2013). CFD modelling of the aerodynamic effect of trees on urban air pollution dispersion. Science of the Total Environment, 461, 541-551. CFD modelling of the aerodynamic effect of trees on urban air pollution dispersion (2013). Sci. Total Environ. 461–462, 541–551. https://doi.org/10.1016/j.scitotenv.2013.05.031

Table 2. The impact of trees on urban air quality: changes in the volume-averaged normalized concentration ($c^* = cU_\infty L_s H / Q$) in both pedestrian zones and in the entire canyon.

	Leeward pedestrian zone		Windward pedestrian zone		Canyon average	
	c^* (–)	Δc^* (%)	c^* (–)	Δc^* (%)	c^* (–)	Δc^* (%)
Empty canyon	28.0	N/A	6.9	N/A	16.9	N/A
Sparse trees	34.9	19.9%	6.5	-6.5%	19.6	14.1%
Dense trees	40.9	31.6%	6.3	-9.4%	21.3	21.0%

Ansys, Inc. (2023). Ansys Fluent User's Guide, release 2023R1. Ansys, Inc., Canonsburg, PA.

Balczó, M., Gromke, C., & Ruck, B. (2009). Numerical modelling of flow and pollutant dispersion in street canyons with tree planting. Meteorologische Zeitschrift, 197–206. https://doi.org/10.1127/0941-2948/2009/0361

Balogh, M., & Kristóf, G. (2009). Fine scale simulation of turbulent flows in urban canopy layers. Időjárás – Quarterly Journal of the Hungarian Meteorological Service. Vol. 114, No. 1–2, pp. 135–148.

Blocken, B. (2015). Computational Fluid Dynamics for urban physics: Importance, scales, possibilities, limitations and ten tips and tricks towards accurate and reliable simulations. Building and Environment, 91, 219–245. https://doi.org/10.1016/j.buildenv.2015.02.015

Blocken, B. (2018). LES over RANS in building simulation for outdoor and indoor applications: A foregone conclusion? Building Simulation, 11(5), 821–870. https://doi.org/10.1007/s12273-018-0459-3

Blocken, B., & Gualtieri, C. (2012). Ten iterative steps for model development and evaluation applied to Computational Fluid Dynamics for Environmental Fluid Mechanics. Environmental Modelling & Software, 33, 1–22. https://doi.org/10.1016/j.envsoft.2012.02.001

Buccolieri, R., Gromke, C., Di Sabatino, S., Ruck, B. (2009). Aerodynamic effects of trees on pollutant concentration in street canyons. Sci. Total Environ. 407(19), 5247–5256. https://doi.org/10.1016/j.scitotenv.2009.06.016

Buccolieri, R., Santiago, J.-L., Rivas, E., Sanchez, B. (2018). Review on urban tree modelling in CFD simulations: Aerodynamic, deposition and thermal effects. Urban For. Urban Green. 31, 212–220. https://doi.org/10.1016/j.ufug.2018.03.003

Carlo, O. S., Fellini, S., Palusci, O., Marro, M., Salizzoni, P., Buccolieri, R. (2024). Influence of obstacles on urban canyon ventilation and air pollutant concentration: An experimental assessment. Build. Environ. 250, 111143. https://doi.org/10.1016/j.buildenv.2023.111143

Chang, J. C., & Hanna, S. R. (2004). Air quality model performance evaluation. Meteorology and Atmospheric Physics, 87(1–3). https://doi.org/10.1007/s00703-003-0070-7

Fellini, S., Marro, M., Del Ponte, A. V., Barulli, M., Soulhac, L., Ridolfi, L., Salizzoni, P. (2022). High resolution wind-tunnel investigation about the effect of street trees on pollutant concentration and street canyon ventilation. Build. Environ. 226, 109763. https://doi.org/10.1016/j.buildenv.2022.109763

Gallagher, J., Baldauf, R., Fuller, C. H., Kumar, P., Gill, L. W., & McNabola, A. (2015). Passive methods for improving air quality in the built environment: A review of porous and solid barriers. Atmospheric environment, 120, 61-70. Passive methods for improving air quality in the built environment: A review of porous and solid barriers (2015). . Atmos. Environ. 120, 61–70. https://doi.org/10.1016/j.atmosenv.2015.08.075

Gill, S. E., Handley, J. F., Ennos, A. R., Pauleit, S., Theuray, N., & Lindley, S. J. (2008). Characterising the urban environment of UK cities and towns: A template for landscape planning. Landscape and urban planning, 87(3), 210-222. Characterising the urban environment of UK cities and towns: A template for landscape planning (2008). Landsc. Urban Plan. 87(3), 210–222. https://doi.org/10.1016/j.landurbplan.2008.06.008

Gómez-Baggethun, E., Gren, Å., Barton, D. N., Langemeyer, J., McPhearson, T., O'Farrell, P., Andersson, E., Hamstead, Z., Kremer, P. (2013). Urban Ecosystem Services, in: Elmqvist, T., Fragkias, M., Goodness, J., Güneralp, B., Marcotullio, P. J., McDonald, R. I., Parnell, S., Schewenius, M., Sendstad, M., Seto, K. C., Wilkinson, C. (Eds.), Urbanization, Biodiversity and Ecosystem Services: Challenges and Opportunities. Springer Netherlands, Dordrecht, 175–251. https://doi.org/10.1007/978-94-007-7088-1_11

Gousseau, P., Blocken, B., Stathopoulos, T., & van Heijst, G. J. F. (2011). CFD simulation of near-field pollutant dispersion on a high-resolution grid: A case study by LES and RANS for a building group in downtown Montreal. Atmospheric Environment, 45(2), 428–438. https://doi.org/10.1016/j.atmosenv.2010.09.065

Gromke, C. (2011). A vegetation modelling concept for Building and Environmental Aerodynamics wind tunnel tests and its application in pollutant dispersion studies. Environmental Pollution, 159(8–9), 2094–2099. https://doi.org/10.1016/j.envpol.2010.11.012

Gromke, C., Blocken, B. (2015a). Influence of avenue-trees on air quality at the urban neighborhood scale. Part I: Quality assurance studies and turbulent Schmidt number analysis

for RANS CFD simulations. Environ. Pollut. 196, 214–223. https://doi.org/10.1016/j.envpol.2014.10.016

Gromke, C., Blocken, B. (2015b). Influence of avenue-trees on air quality at the urban neighborhood scale. Part II: Traffic pollutant concentrations at pedestrian level. Environ. Pollut. 196, 176–184. https://doi.org/10.1016/j.envpol.2014.10.015

He, G., Guo, Y., & Hsu, A. T. (1999). The effect of Schmidt number on turbulent scalar mixing in a jet-in-crossflow. International Journal of Heat and Mass Transfer, 42(20), 3727–3738. https://doi.org/10.1016/S0017-9310(99)00050-2

Janhäll, S. (2015). Review on urban vegetation and particle air pollution – Deposition and dispersion. Atmos. Environ. 105, 130–137. https://doi.org/10.1016/j.atmosenv.2015.01.052

Kenjereš, S., & Ter Kuile, B. (2013). Modelling and simulations of turbulent flows in urban areas with vegetation. Journal of Wind Engineering and Industrial Aerodynamics, 123, 43–55. https://doi.org/10.1016/j.jweia.2013.09.007

Kristóf, G., Kovács, K. A., Kalmár-Nagy, T., and Balogh, M. (2025). A New Viscosity Formulation for Improved Turbulence Modelling in Kolmogorov Flow. Conference on Modelling Fluid Flow (CMFF'25), Budapest, Hungary.

Montazeri, H., & Blocken, B. (2013). CFD simulation of wind-induced pressure coefficients on buildings with and without balconies: Validation and sensitivity analysis. Building and Environment, 60, 137–149. https://doi.org/10.1016/j.buildenv.2012.11.012

Papp, B., Kristóf, G., Istók, B., Koren, M., Balczó, M., & Balogh, M. (2021). Measurement-driven Large Eddy Simulation of dispersion in street canyons of variable building height. Journal of Wind Engineering and Industrial Aerodynamics, 211, 104495. https://doi.org/10.1016/j.jweia.2020.104495

Salmond, J. A., Tadaki, M., Vardoulakis, S., Arbuthnott, K., Coutts, A., Demuzere, M., Dirks, K. N., Heaviside, C., Lim, S., Macintyre, H., McInnes, R. N., Wheeler, B. W. (2016). Health and climate related ecosystem services provided by street trees in the urban environment. Environ. Health 15(1), 95–111. https://doi.org/10.1186/s12940-016-0103-6

Santiago, J.-L., Buccolieri, R., Rivas, E., Calvete-Sogo, H., Sanchez, B., Martilli, A., Alonso, R., Elustondo, D., Santamaría, J. M., & Martin, F. (2019). CFD modelling of vegetation barrier effects on the reduction of traffic-related pollutant concentration in an avenue of Pamplona, Spain. Sustainable Cities and Society, 48, 101559. https://doi.org/10.1016/j.scs.2019.101559

Santiago, J.-L., Rivas, E., Sanchez, B., Buccolieri, R., Martin, F. (2017). The Impact of Planting Trees on NOx Concentrations: The Case of the Plaza de la Cruz Neighborhood in Pamplona (Spain). Atmosphere 8(7), 131. https://doi.org/10.3390/atmos8070131

Sanz, C. (2003). A Note on k—ε Modelling of Vegetation Canopy Air-Flows. Boundary-Layer Meteorology, 108(1), 191–197. https://doi.org/10.1023/A:1023066012766

Tominaga, Y., & Stathopoulos, T. (2007). Turbulent Schmidt numbers for CFD analysis with various types of flowfield. Atmospheric Environment, 41(37), 8091–8099. https://doi.org/10.1016/j.atmosenv.2007.06.054

Tominaga, Y., & Stathopoulos, T. (2013). CFD simulation of near-field pollutant dispersion in the urban environment: A review of current modelling techniques. Atmospheric Environment, 79, 716–730. https://doi.org/10.1016/j.atmosenv.2013.07.028

Toparlar, Y., Blocken, B., Maiheu, B., & van Heijst, G. J. F. (2017). A review on the CFD analysis of urban microclimate. Renewable and Sustainable Energy Reviews, 80, 1613–1640. https://doi.org/10.1016/j.rser.2017.05.248

Conference on Modelling Fluid Flow (CMFF'25)
The 19th International Conference on Fluid Flow Technologies
Budapest, Hungary, August 26 - August 29, 2025

THE EFFECT OF BUBBLE PARAMETERS ON THE MIXING IN A BUBBLE COLUMN WITH COUNTER-CURRENT LIQUID FLOW

Péter KOVÁTS[1], Katharina ZÄHRINGER[2]

[1,2] Laboratory of Fluid Dynamics and Technical Flows, Otto-von-Guericke-Universität Magdeburg. Universitätsplatz 2, D-39106 Magdeburg, Germany. Tel.: +49 391 - 67 58654, Fax: +49 391 - 67 52840 *E-mail: peter.kovats@ovgu.de

ABSTRACT

Bubble columns have been widely studied concentrating mostly on the bubble parameters, and gas/liquid motion. However, bubble generated mixing in the column is rarely analysed, especially with counter-current liquid flow. For this reason, experiments with Laser Induced Fluorescence (LIF) applying Sulforhodamine G as fluorescent tracer dye were performed in a laboratory-scale counter-current flow bubble column. In these experiments the efficiency of the bubble generated mixing was investigated by varying the bubble size, gas and liquid flow rates and the dye inlet position. Additionally, the mixing results were compared to the liquid flow fields obtained from Particle Image Velocimetry (PIV). From the results it is obvious, that bubble induced mixing leads to a good dye distribution inside the column, compared to a single-phase flow without bubbles. It has been found, that the larger the bubbles the higher the bubble induced vorticity, which leads to a better local and therefore global mixing. The highest counter-current liquid flow rate led to a more concentrated dye jet, which was less dispersed than at lower liquid flow rates. As a result, the combination of large bubbles generated with the 3.6 mm capillaries, and a moderate counter-current liquid flow rate (11.1 $l\cdot min^{-1}$) led to the best mixing performance in the investigated bubble column reactor.

Keywords: bubble column reactor, dispersed two-phase flow, counter-current flow, LIF, PIV, mixing

NOMENCLATURE

a	[mm]	major semi-axis
b	[mm]	minor semi-axis
c	[$mg\cdot l^{-1}$]	measured concentration
c_{min}	[$mg\cdot l^{-1}$]	minimum background concentration
c_{max}	[$mg\cdot l^{-1}$]	injected dye concentration
c_n	[$mg\cdot l^{-1}$]	normalized concentration
$c_{n,exp}$	[$mg\cdot l^{-1}$]	experimental normalized concentration
$c_{n,theor}$	[$mg\cdot l^{-1}$]	theoretical normalized concentration
c_{norm}	[$mg\cdot l^{-1}$]	normalized dye concentration ratio, $c_{n,exp}/c_{n,theor}$
d	[m]	column diameter
ESD	[mm]	equivalent sphere diameter
h	[m]	column height
j	[$m\cdot s^{-1}$]	superficial velocity
Q	[$l\cdot h^{-1}$]	volume flow rate
v_b	[$m\cdot s^{-1}$]	bubble velocity
Re_c	[-]	column Reynolds number

Subscripts and Superscripts

g	gas
l	liquid

1. INTRODUCTION

A well-known example of a multiphase flow is gas bubbles in a liquid phase, which occurs in a great variety of natural phenomena, in chemical or biological processes, in waste water treatment, in nuclear engineering or even in everyday life, like in soft drinks. Bubbles are often used for mixing, since they provide favourable mixing and mass transfer properties combined with gentle agitation and low shear stressing of the mixed fluids, compared to other stirring tools. Mixing of liquids is a very energy intensive operation depending on among others the duration of the mixing, the liquid viscosity and reactor geometry. The optimal mixing process would ensure for a minimal power consumption but maximal homogeneity of the mixture. Mixing, induced by the rising bubbles in a bubble column and the resulting interaction between chemical reaction and hydrodynamics in the column is a challenging research field due to its complexity. Traditionally, the mixing time and mixing efficiency is measured in stirred vessels or in bubble columns in an invasive manner with pH

or conductivity probes [1-4]. These measurement techniques are robust, but the probes disturb the flow and the measurement is only point-wise.

For a global mixing characterization different methods are available. One of them is based on acid-base reaction and the colour change of a dye pH-indicator. This method is inexpensive and simple, but it integrates the colour of the whole depth of the investigated volume, which means an averaged mixing characterization in the depth. Therefore, it is efficient for a rough estimation, but ineffective for detailed investigations [2, 5, 6]. Electrical resistance tomography (ERT), which can provide mixing information also in opaque liquids, is also an integrating measurement technique. However, the spatial resolution of these methods are far from common imaging and the correct data reconstruction is very difficult [5, 7, 8]. Besides these techniques, the dye distribution, concentration and mixing homogeneity can be obtained with high temporal and spatial resolution in a 2D plane with planar LIF [5, 9-12]. Because of its accuracy and resolution, this technique was selected for the experiments presented in this paper.

Unfortunately, experimental investigations of bubble-induced mixing and its influence on mass transfer or mixing characterisation and visualisation in bubble columns are rarely found in the literature.

A research group at the IMFT in Toulouse analysed mixing and concentration fluctuations in bubble swarms [13, 14] and investigated mixing in a pseudo-2D bubble column [15]. Also, a group at HZDR in Dresden worked on bubble-induced turbulence and bubble swarms extensively [16-19].

Studies of the mixing behaviour of bubble columns [20-23] or for bubble-induced turbulence [24-28] using simulations can also be found sporadically in the literature.

Unfortunately, experimental studies relating mixing and bubble-induced turbulence in the same bubble column cannot be found.

For this reason, in the present study, an experimental measurement campaign has been performed to obtain the necessary data for a further understanding of mixing processes in bubbly flows with bubble-induced turbulence. Different gas inlet configurations are used to investigate the influence of bubble size and gas and liquid flow rates on mixing in the counter-current model bubble column.

2. EXPERIMENTAL SET-UP

To characterise the liquid flow and mixing in the bubble column, three optical measurement methods have been applied. First, for the liquid phase, Particle Image Velocimetry (PIV) was used to examine the hydrodynamics of the two-phase flow. Then, combined Laser-Induced Fluorescence (LIF) and shadow imaging measurements have been executed in the square laboratory-scale counter-current bubble column, which is made of acrylic glass with an inner side length of d= 0.100 m and a height of h= 2 m (Figure 1, #1). In both experiments, the bubbles were generated with 7 capillaries placed in line in the centre of the bubble column and 500 mm above its bottom (Figure 1, #2). Capillaries with three different sizes, produced air bubbles in a size range of 1 to 9 mm. The bubble column and its peripheral devices have been described in detail in previous papers [29, 30]. The investigated experimental cases are listed in Table 1.

Table 1. Experimental conditions.

Capillary inner diameter/ material	j_g [m· s^{-1}]	Q_g [l· h^{-1}]	j_l [m· s^{-1}]	Q_l (Counter-current) [l· min^{-1}]	Re_c (Column Reynolds number)
0.13 mm/ stainless steel	2.8· 10^{-4}	10	0	0	0
			1· 10^{-3}	0.6	100
			5.2· 10^{-3}	3.1	500
			1.9· 10^{-2}	11.1	1800
			9.3· 10^{-2}	55.5	9000
0.18 mm/ Teflon	2.8· 10^{-4}	10	0	0	0
			1· 10^{-3}	0.6	100
			5.2· 10^{-3}	3.1	500
			1.9· 10^{-2}	11.1	1800
			9.3· 10^{-2}	55.5	9000
3.6 mm/ PEEK	2.7· 10^{-4}	9.7	0	0	0
	1.3· 10^{-3}	48.4	1· 10^{-3}	0.6	100
			5.2· 10^{-3}	3.1	500
			1.9· 10^{-2}	11.1	1800
			9.3· 10^{-2}	55.5	9000

The images have been recorded over the entire measurement section (1 m) of the column with four 5 Mpixel cameras (LaVision Imager sCMOS, Figure 1, #3) equipped with 50 mm Nikon Micro lenses and appropriate filters to record the emitted light of the injected fluorescent dye Sulforhodamine G or the fluorescence signal of the Rhodamine B doped polymethyl methacrylate (PMMA) PIV seeding particles (mean diameter: 1-20 µm). The cameras were focused on the laser light sheet generated by a Nd:YAG double pulse laser (Evergreen PIV, 532 nm) in the centre plane of the column, in line with the bubble injection device. For the LIF experiments, the fluorescent dye was injected into the column with a syringe at 500 mm in the centre plane of the column through a stainless steel capillary with a concentration of c_{max} = 0.1 mg· l^{-1} and 10 ml· min^{-1} flow rate. Simultaneously to the LIF images, shadow images of the bubbles were also recorded, to be able to mask the bubble shapes from the LIF images during image processing and to obtain simultaneously the bubble size distribution of the specific measurement condition. To this end, eight high-power LEDs were used together with a sheet of thin drawing paper, as light diffuser, on the back wall of the column to obtain homogeneous light distribution for the shadow images of the bubbles. The bubble shadow images were acquired on the second frame of the cameras and triggered with an inter-frame time of 40 µs to the LIF images,

which assured that bubbles did not move noticeably in-between both frames.

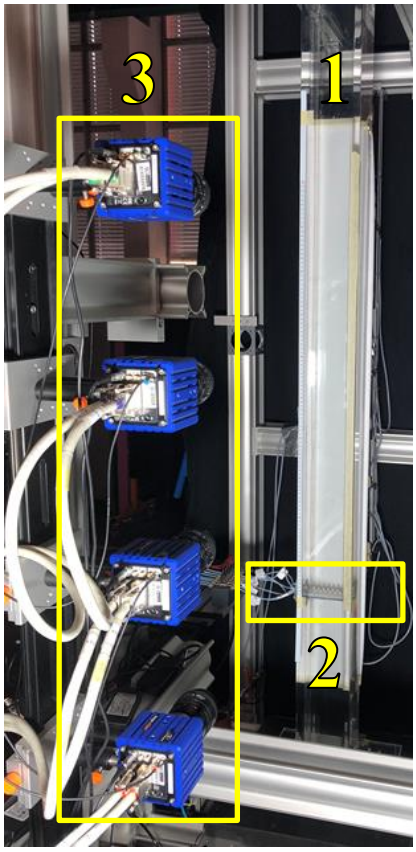

Figure 1. Experimental setup: bubble column (1), gas distributor (2), cameras (3).

The images were calibrated with a 3D calibration target over the whole measurement section for all measurement methods. During the experiments, 3x1500 LIF/Shadow images and overall 4000 PIV images were recorded with 5 Hz recording rate for each investigated case.

3. DATA PROCESSING

All recorded images were processed in DaVis 8.4 (LaVision). In the case of PIV, flow fields were calculated from the recorded double-frame images with a cross-correlation algorithm (multi-pass) with a decreasing interrogation window size from 64x64 pixels to 32x32 pixels, with 50% overlap. To remove false vectors and refine the vector fields, especially in the vicinity and shadows of the bubbles, a median filter was applied. After combining the results of all four measurement windows (obtained simultaneously with the four cameras), a full view of the liquid flow field within the column has been obtained. From these vector fields mean velocity fields were calculated for each investigated case. Moreover, probability density functions were generated to investigate the distributions of the horizontal and vertical velocity components as well as the distribution of the vorticity.

In the case of the LIF images for the mixing analysis, the bubbles were masked with the help of the recorded bubble shadow images (Figure 2). In the next step, the recorded fluorescent light intensities were converted into Sulforhodamine G concentrations with the help of a linear calibration curve, determined before.

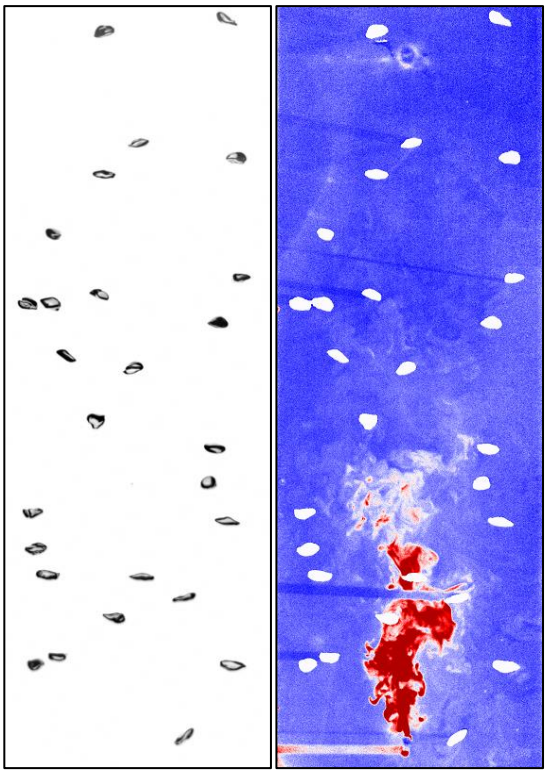

Figure 2. Image processing: shadow image with subtracted background (left), binarised mask from shadow image applied to the LIF image (right).

For the quantification of mixing, a mixing coefficient has been defined:

$$c_n = \frac{c - c_{min}}{c_{max} - c_{min}} \qquad (1)$$

where c_{max} is the injected dye concentration and c_{min} corresponds to a minimum background intensity, which is zero in theory, while for the experiments it is equal to the equivalent intensity of the first recorded image for each run, when no dye is in the system, and therefore it is close to zero. To be able to compare the results from different counter-current liquid flow rates, the experimental normalised concentrations $c_{n,exp}$ have been divided by the normalised theoretical concentration for perfect mixing $c_{n,theor}$ of the respective counter-current liquid flow rate. In the case of perfect

mixing, one obtains $c_{norm} = 1$, in the other cases, c_{norm} is calculated as:

$$c_{norm} = \frac{c_{n,exp}}{c_{n,theor}} \quad (2)$$

To compare the mixing efficiency for different investigated cases the normalised dye concentration ratios at 300 s after injection start will be used in the discussion of the results.

The quantification of the mixing intensity has been described more in detail in a separate paper [29].

4. DISCUSSION

The bubble parameters measured in the bubble column at different flow conditions, and for the flow parameters relevant in the current paper, are listed in Table 2 [30, 31].

Table 2. Global mean results of bubble diameters and velocities.

Capillary diameter [mm]	Q_g [l· h^{-1}]	Q_l [l· min^{-1}]	*ESD* [mm]	v_b [m· s^{-1}]	Aspect ratio
0.13	10	stagnant	2.71	0.31	0.63
0.13	10	0.6	2.7	0.31	0.62
0.13	10	3.1	2.7	0.31	0.62
0.13	10	11.1	2.72	0.30	0.63
0.13	10	55.5	2.91	0.22	0.64
0.18	10	stagnant	3.67	0.30	0.54
0.18	10	0.6	3.47	0.30	0.55
0.18	10	3.1	3.55	0.30	0.55
0.18	10	11.1	3.59	0.28	0.55
0.18	10	55.5	3.75	0.21	0.55
3.6	10	stagnant	6.01	0.28	0.5
3.6	10	0.6	6.03	0.28	0.5
3.6	10	3.1	6.85	0.32	0.53
3.6	10	11.1	6.04	0.27	0.51
3.6	10	55.5	5.9	0.20	0.53
3.6	50	stagnant	6.85	0.32	0.53
3.6	50	0.6	6.89	0.32	0.52
3.6	50	3.1	6.86	0.32	0.53
3.6	50	11.1	6.88	0.30	0.53
3.6	50	55.5	6.6	0.24	0.57

The results show that with increasing gas volume flow rate, the bubble size increases, as well as with an increasing capillary size. The bubble size also increases with increasing counter-current liquid flow rate, except at the largest capillary, where no clear trend can be found. In contrast, the bubble velocity is generally decreasing with an increasing bubble size, and it evidently decreases with an increasing counter-current liquid flow. Also, a slight growth can be found in bubble velocities with increasing gas flow rate. Interestingly, the bubble aspect ratio (*b*/*a*) remains generally the same for one capillary size, independent of the counter-current liquid or gas flow rate, but it decreases with increasing capillary and therefore bubble size. It also has to be mentioned that the shape of the large bubbles generated with the largest capillary is more unstable, than that of the smaller ones. This form-instability is also reflected in the global mean results, mostly in the changing aspect ratios.

All these global parameters (bubble size, velocity, and aspect ratio) have strong influences on mixing in the bubble column. These impacts will be discussed hereafter.

4.1. Mixing results

Figure 3 shows exemplary snapshots of the normalised Sulforhodamine G concentrations 300 seconds after the start of the dye injection. In the cases without bubbles (Figure 3, top row), mixing occurs due to the jet of the dye inlet and due to the counter-current liquid flow. In the stagnant case, the dye accumulates above the inlet, and large-scale, undisturbed dye structures can be found in the column, which is far from perfect mixing. Comparing this case to the cases with counter-current liquid flows, it becomes evident that with increasing counter-current liquid flow rate, the introduced dye heads towards the lower column regions and outlet at the bottom. The dye accumulation over the inlet is also decreased by the increased counter-current liquid flow rate, and the dye is transported downwards in high concentrated pockets.

In the presence of bubbles (Figure 3, bottom row), the large-scale structures vanish due to the bubble-generated upward flow and mixing is strongly enhanced. In the case without counter-current liquid flow and at the lowest counter-current flow rate, the injected dye is almost equally distributed in the whole measurement plane, except the inlet region, where the concentrated dye with higher intensities can be observed. With increasing counter-current flow rate, the low concentration region above the dye inlet spreads downward. At 55.5 l· min^{-1} counter-current liquid flow rate, the dye concentration is low (black regions) in the complete upper half of the column because the injected dye is completely transported downwards.

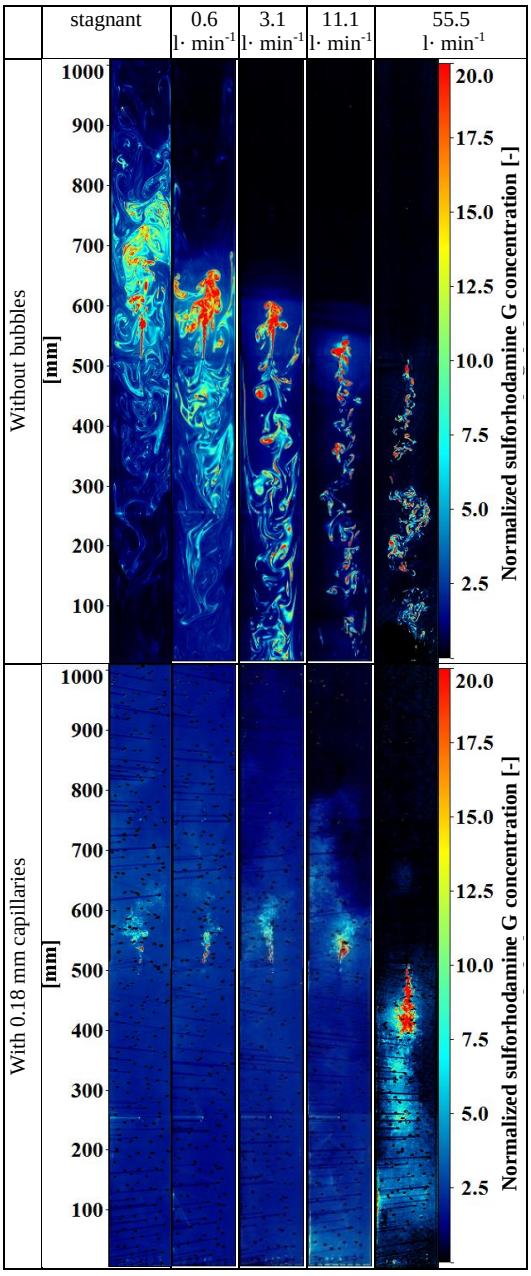

Figure 3. Snapshots of the experiments at t=300 s without (top) and with (bottom) bubbles. Dye inlet at 500 mm, bubbles generated with 0.18 capillaries at 10 l· h^{-1} gas flow rate.

Figure 4 compares the normalised concentration distributions over the column height for the investigated different inlet conditions. On these plots, conspicuous high peak concentrations can be recognised around the dye inlet at 55.5 l· min^{-1} counter-current liquid flow rate. As it was discussed before, the high counter-current liquid flow forces the dye to head downwards, and mixing is poor. Above the inlet, the dye concentration is close to zero in that case.

The stagnant and the two lowest counter-current liquid flow rates perform similar: except in the inlet region, the normalised concentration curves are rather equalised at values between one and two. In all these cases, the mixing efficiency increases with increasing counter-current liquid flow rate in the top half of the column.

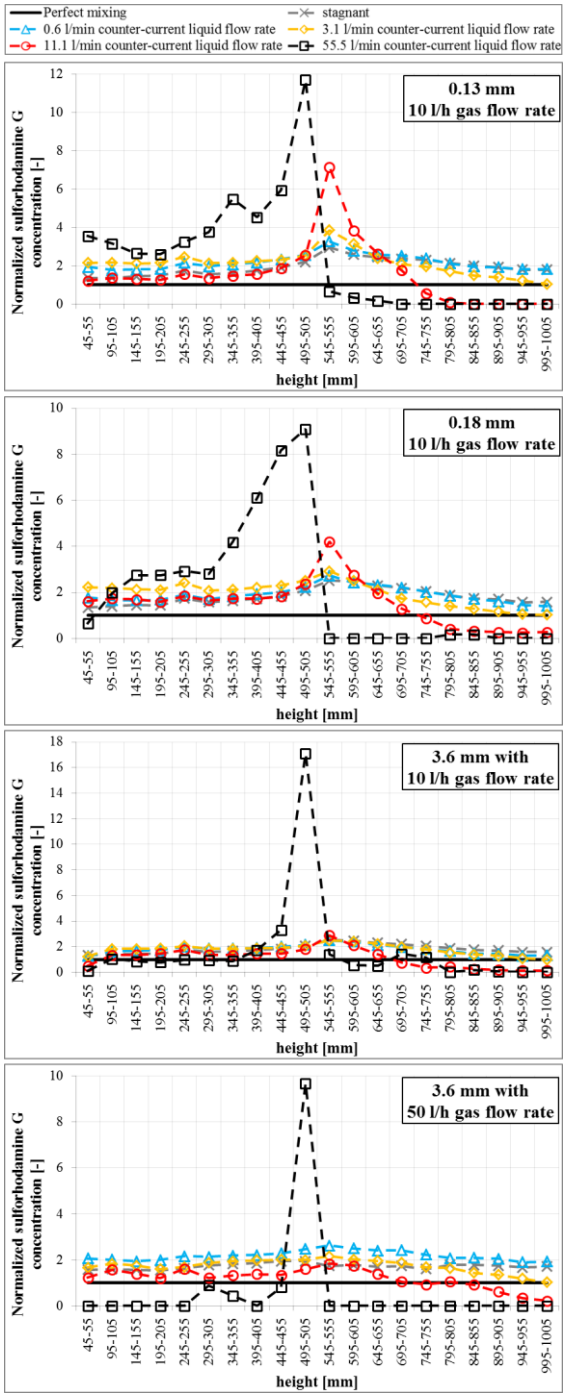

Figure 4. Normalized dye concentration ratios at t=300 s for different counter-current liquid flow rates in function of the column height. Dye inlet at 500 mm, bubbles generated with 0.13, 0.18 and 3.6 mm capillaries at 10 l· h^{-1} and 50 l· h^{-1} gas flow rates.

In the case with the 3.6 mm capillary and 50 $l \cdot h^{-1}$ gas flow rate, this effect is visible over the complete column height. However, in all of the above-mentioned cases, the normalised values lay above perfect mixing. This means that the bubble-generated upward flow is strong enough to transport the dye to the upper half of the column, but mixing is not strong enough to distribute the dye homogeneously in the whole column. In the cases with 11.1 $l \cdot min^{-1}$ counter-current flow rate, a concentration peak also appears at the dye inlet, where the counter-current liquid flow forces the dye to head downwards. But, contrary to the lower counter-current liquid flow rates, just a small amount of dye is transported to the upper half of the column. Here, the bubble-generated upward liquid flow is definitely too weak to transport the dye to the top column section. However, with an increased gas flow rate, at 50 $l \cdot h^{-1}$, the dye concentration gets closer to perfect mixing also in the upper section, due to the stronger upward liquid flow. The best mixing performance has been found with the 3.6 mm capillary at 11.1 $l \cdot min^{-1}$ counter-current liquid and 50 $l \cdot h^{-1}$ gas flow rates, if the inlet is situated at 500 mm, in the middle of the column.

The analysis of the LIF results shows that a large difference exists between the mixing in cases with and without bubbles, but this difference gets less for all the cases with bubbles. For this reason, the vorticity of the liquid flow in the column was investigated, obtained from previous PIV measurements [32]. Vorticity is supposed to have an influence on mixing, since it is supported by the bubble-generated turbulence.

4.2. Bubble-generated turbulence

Figure 5 represents normalised Probability Density Functions (PDF) of the vorticity calculated from the PIV vector fields for the different investigated cases. The top plot shows the PDFs in the counter-current liquid flows, without bubbles. It was expected that with increasing counter-current liquid flow rate, and therefore with increasing Reynolds number from 100 to 9000, the vorticity increases and thus the PDFs get wider. When bubbles are in the flow, they disturb the existing flow pattern and generate additional turbulence. In Figure 5, these cases are shown in the bottom four plots for different capillary diameters, counter-current liquid and gas flow rates. The widths of the PDFs for the two small capillary diameters are comparable to the fully turbulent case (Re=9000, black squares) of the single-phase measurements in the top plot. It has also been found that in the presence of smaller bubbles, generated with the 0.13 and 0.18 mm capillaries, the vorticity distribution is independent of the counter-current liquid flow rate. Since the relative bubble velocity is the same for one given capillary diameter at all counter-current liquid flow rates, this result was expected.

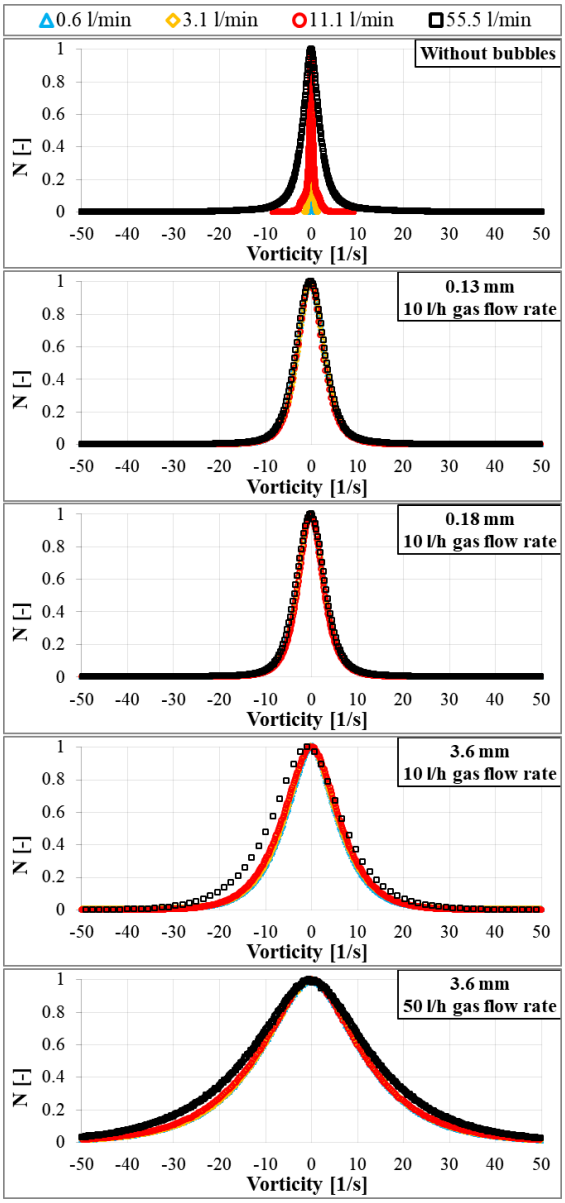

Figure 5. Normalized probability density functions of the vorticity for all investigated cases.

Interestingly, the vorticity distributions for these two inlet sizes are also very similar; however, there is a noticeable difference in bubble sizes as well as in aspect ratios (see in Table 2), and therefore in bubble velocities. This result explains the LIF mixing results on Figure 4, where also very similar dye distributions have been found for these two setups.

In the case of the larger bubbles, produced with the 3.6 mm capillaries, the vorticity distributions get even wider. This effect is further increased with increasing gas flow rate. In these cases, the mean bubble size is almost twice that of the smaller

capillaries. These considerably larger bubbles generate larger and stronger vortex structures, which are reflected in the wider vorticity distributions. On these plots, the curve for 55.5 $l \cdot min^{-1}$ counter-current flow rate clearly separates from the others, while this was not observable on the distributions with smaller capillaries. The reason for that could be the size of the generated vortex structures. At 55.5 $l \cdot min^{-1}$ counter-current flow rate, the vorticity and the vortex structure sizes without bubbles are almost the same as in the cases with the 0.13 and 0.18 mm capillaries bubbles. Therefore, the vorticity distribution for this liquid flow rate remains almost the same with and without bubbles. Contrary to this, the larger bubbles produced with the 3.6 mm capillaries generate larger vortex structures, while the smaller structures from the initially turbulent liquid flow also remain.

The widest vorticity distribution has been found at the largest capillaries and the largest gas flow rate. This explains the mixing results, where the best mixing was also achieved with this setup.

5. CONCLUSIONS

In this paper bubble-induced mixing in a laboratory-scale bubble column has been investigated with LIF measurement technique, applying Sulforhodamine G as tracer dye, combined with shadow imaging. To support the analysis, the results of previous PIV experiments have also been examined. Capillaries with three different diameters were used to generate bubbles in a wide diameter range of 1 to 9 mm. The gas and liquid flow rates have been varied in this study as well.

It has been found that the presence of the bubbles, their size, the gas flow rate and the counter-current liquid flow rate have strong influences on mixing. The results have shown that the larger bubbles induce larger vortex structures, which leads to better mixing. Interestingly, no differences have been found in the vortex distributions between the cases with the two smaller capillaries, despite the noticeable differences in bubble size and aspect ratios.

The highest counter-current liquid flow rate led to a more concentrated dye jet, which was less dispersed than at lower liquid flow rates. The combination of large bubbles generated with the 3.6 mm capillaries and a moderate counter-current liquid flow rate 11.1 $l \cdot min^{-1}$, led to the best mixing performance in the bubble column.

ACKNOWLEDGEMENTS

This work has been carried out in the frame of a joint research project (GZ: RZ 11/3-1 and ZA 527/3-1) funded by the German Research Foundation (DFG). Instrumentation was funded by the Deutsche Forschungsgemeinschaft (DFG, German Research Foundation) – 279416000.

The authors would also like to acknowledge the help of their students Jianye Han, Maximilian Mahler and Steffen Erichson in doing the experiments and parts of the postprocessing. The workshop of LSS is acknowledged for its help in mounting the experimental set-up.

REFERENCES

[1] M. Ravinath, G. R. Kasat, A. B. Pandit, 2008, "Mixing Time in a Short Bubble Column", *The Canadian Journal of Chemical Engineering*, 2008, Vol. 81 (2), pp. 185-195. DOI: 10.1002/cjce.5450810203

[2] Z. Trad, J.-P. Fontaine, C. Larroche, C. Vial, 2017, "Experimental and numerical investigation of hydrodynamics and mixing in a dual-impeller mechanically-stirred digester", *Chem. Eng. J.*, 2017, Vol. 329, pp. 142-155. DOI: 10.1016/j.cej.2017.07.038

[3] F. Wang, N. D. Jin, D. Y. Wang, Y. F. Han, D. Y. Liu, 2017, "Measurement of gas phase characteristics in bubbly oil-gas-water flows using bi-optical fiber and high-resolution conductance probes", *Exp. Therm Fluid Sci.*, 2017, Vol. 88, pp. 361-375. DOI: 10.1016/j.expthermflusci.2017.06.017

[4] J.-L. Muñoz-Cobo, Y. Rivera, C. Berna, A. Escrivá, 2020, "Analysis of Conductance Probes for Two-Phase Flow and Holdup Applications", *Sensors*, 2020, Vol. 20 (24), pp. 7042. DOI: 10.3390/s20247042

[5] S. C. Low, N. Eshtiaghi, L. Shu, R. Parthasarathy, 2017, "Flow patterns in the mixing of sludge simulant with jet recirculation system", *Process Saf. Environ. Prot.*, 2017, Vol. 112, pp. 209-221. DOI: 10.1016/j.psep.2017.08.016

[6] L. A. Melton, C. W. Lipp, R. W. Spradling, K. A. Paulson, 2010, "Dismt - Determination of mixing time through color changes", *Chem. Eng. Commun.*, 2010, Vol. 189 (3), pp. 322-338. DOI: 10.1080/00986440212077

[7] S. A. Hashemi, R. B. Spelay, R. S. Sanders, B. T. Hjertaker, 2021, "A novel method to improve Electrical Resistance Tomography measurements on slurries containing clays", *Flow Measurement and Instrumentation*, 2021, Vol. 80, pp. 101973. DOI: 10.1016/j.flowmeasinst.2021.101973

[8] S. C. Low, D. Allitt, N. Eshtiaghi, R. Parthasarathy, 2018, "Measuring active volume using electrical resistance tomography in a gas-sparged model anaerobic digester", *Chem. Eng. Res. Des.*, 2018, Vol. 130, pp. 42-51. DOI: 10.1016/j.cherd.2017.11.039

[9] J. Coppeta, C. Rogers, 1998, "Dual emission laser induced fluorescence for direct planar scalar behavior measurements", *Exp.*

Fluids, 1998, Vol. 25 (1), pp. 1-15. DOI: 10.1007/s003480050202

[10] X. Wang, R. Wang, S. Du, J. Chen, S. Tan, 2016, "Flow visualization and mixing quantification in a rod bundle using laser induced fluorescence", *Nucl. Eng. Des.*, 2016, Vol. 305, pp. 1-8. DOI: 10.1016/j.nucengdes.2016.01.007

[11] A. Eltayeb, S. Tan, Z. Qi, A. A. Ala, N. M. Ahmed, 2019, "PLIF experimental validation of a FLUENT CFD model of a coolant mixing in reactor vessel down-comer", *Ann. Nucl. Energy*, 2019, Vol. 128, pp. 190-202. DOI: 10.1016/j.anucene.2018.12.051

[12] G. Montante, A. Paglianti, 2015, "Fluid dynamics characterization of a stirred model bio-methanation digester", *Chem. Eng. Res. Des.*, 2015, Vol. 93, pp. 38-47. DOI: 10.1016/j.cherd.2014.05.003

[13] E. Bouche, S. Cazin, V. Roig, F. Risso, 2013, "Mixing in a swarm of bubbles rising in a confined cell measured by mean of PLIF with two different dyes", *Exp. Fluids*, 2013, Vol. 54 (6), pp. DOI: 10.1007/s00348-013-1552-0

[14] E. Alméras, S. Cazin, V. Roig, F. Risso, F. Augier, C. Plais, 2016, "Time-resolved measurement of concentration fluctuations in a confined bubbly flow by LIF", *Int. J. Multiphase Flow*, 2016, Vol. 83, pp. 153-161. DOI: 10.1016/j.ijmultiphaseflow.2016.03.011

[15] E. Alméras, C. Plais, V. Roig, F. Risso, F. Augier, 2018, "Mixing mechanisms in a low-sheared inhomogeneous bubble column", *Chem. Eng. Sci.*, 2018, Vol. 186, pp. 52-61. DOI: https://doi.org/10.1016/j.ces.2018.04.026

[16] T. Ma, H. Hessenkemper, D. Lucas, A. D. Bragg, 2022, "An experimental study on the multiscale properties of turbulence in bubble-laden flows", *J. Fluid Mech.*, 2022, Vol. 936, pp. DOI: 10.1017/jfm.2022.86

[17] T. Ma, H. Hessenkemper, D. Lucas, A. D. Bragg, 2023, "Effects of surfactants on bubble-induced turbulence", *J. Fluid Mech.*, 2023, Vol. 970, pp. DOI: 10.1017/jfm.2023.614

[18] T. Ma, B. Ott, J. Fröhlich, A. D. Bragg, 2021, "Scale-dependent anisotropy, energy transfer and intermittency in bubble-laden turbulent flows", *J. Fluid Mech.*, 2021, Vol. 927, pp. DOI: 10.1017/jfm.2021.760

[19] T. Ma, C. Santarelli, T. Ziegenhein, D. Lucas, J. Fröhlich, 2017, "Direct numerical simulation–based Reynolds-averaged closure for bubble-induced turbulence", *Physical Review Fluids*, 2017, Vol. 2 (3), pp. DOI: 10.1103/PhysRevFluids.2.034301

[20] D. Wiemann, D. Mewes, 2005, "Prediction of Backmixing and Mass Transfer in Bubble Columns Using a Multifluid Model", *Industrial & Engineering Chemistry Research*, 2005, Vol. 44 (14), pp. 4959-4967. DOI: 10.1021/ie049163c

[21] W. Bai, N. G. Deen, J. A. M. Kuipers, 2011, "Numerical Investigation of Gas Holdup and Phase Mixing in Bubble Column Reactors", *Industrial & Engineering Chemistry Research*, 2011, Vol. 51 (4), pp. 1949-1961. DOI: 10.1021/ie102557h

[22] K. Ekambara, J. B. Joshi, 2008, "CFD Simulation of Residence Time Distribution and Mixing in Bubble Column Reactors", *The Canadian Journal of Chemical Engineering*, 2008, Vol. 81 (3-4), pp. 669-676. DOI: 10.1002/cjce.5450810345

[23] D. Bothe, H. Shirzadi, H. J. Warnecke, 2007, "Evaluations of Euler–Euler Simulations of Bubble Columns Based on Numerical Tracer Experiments", *Chem. Eng. Res. Des.*, 2007, Vol. 85 (11), pp. 1491-1496. DOI: 10.1205/cherd06249

[24] Y. Jin, R. F. Cavero, C. Weiland, M. Hoffmann, M. Schlüter, 2023, "Effects of bubble-induced turbulence on interfacial species transport: A direct numerical simulation study", *Chem. Eng. Sci.*, 2023, Vol. 279, pp. 118934. DOI: 10.1016/j.ces.2023.118934

[25] J. B. Joshi, K. Nandakumar, G. M. Evans, V. K. Pareek, M. M. Gumulya, M. J. Sathe, M. A. Khanwale, 2017, "Bubble generated turbulence and direct numerical simulations", *Chem. Eng. Sci.*, 2017, Vol. 157, pp. 26-75. DOI: https://doi.org/10.1016/j.ces.2016.03.041

[26] J. Liu, X. Guan, N. Yang, 2023, "Bubble-induced turbulence in CFD simulation of bubble columns. Part I: Coupling of SIT and BIT", *Chem. Eng. Sci.*, 2023, Vol. 270, pp. 118528. DOI: 10.1016/j.ces.2023.118528

[27] R. Rzehak, E. Krepper, 2013, "CFD modeling of bubble-induced turbulence", *Int. J. Multiphase Flow*, 2013, Vol. 55, pp. 138-155. DOI: 10.1016/j.ijmultiphaseflow.2013.04.007

[28] R. Zamansky, F. Le Roy De Bonneville, F. Risso, 2024, "Turbulence induced by a swarm of rising bubbles from coarse-grained simulations", *J. Fluid Mech.*, 2024, Vol. 984, pp. DOI: 10.1017/jfm.2024.230

[29] P. Kováts, K. Zähringer, Year, "Bubble induced mixing in a bubble column with counter-current liquid flow", Proc. *21st International Symposium on the Application of Laser and Imaging Techniques to Fluid Mechanics*, Lisbon, Portugal, pp. 23/1-19.

[30] H. Khan, P. Kováts, K. Zähringer, R. Rzehak, 2024, "Experimental and numerical investigation of a counter-current flow bubble column", *Chem. Eng. Sci.*, 2024, Vol.

285, pp. 119503. DOI: 10.1016/j.ces.2023.119503
[31] P. Kováts, 2021, "Detailed experimental study of mass transfer and liquid flow in a bubble column with optical measurement techniques", *PhD*, Otto-von-Guericke-Universität Magdeburg (Magdeburg).
[32] P. Kováts, K. Zähringer, 2024, "Statistical Analysis of Bubble Parameters from a Model Bubble Column with and without Counter-Current Flow", *Fluids*, 2024, Vol. 9 (6), pp. 126. DOI: 10.3390/fluids9060126

Conference on Modelling Fluid Flow (CMFF'25)
The 19th International Conference on Fluid Flow Technologies
Budapest, Hungary, August 26-August 29, 2025

MODULATING VORTEX DYNAMICS AROUND CIRCULAR CYLINDER VIA ASYMMETRIC CROSS-SECTIONAL PROFILE MORPHING: A COMPARATIVE STUDY OF CYLINDRICAL AND ELLIPTICAL CONFIGURATIONS

Kamila FETHALLAH[1], Mahmoud MEKADEM[1], Hamid OUALI[1]

[1] Fluid Mechanics Laboratory, Department of Fluid Mechanics and Energy,Ecole Militaire Polytechnique, PB N 17 Bordj El Bahri, Algiers, Algeria. *E-mail: fethallahcamela2@gmail.com

ABSTRACT

This research addresses the critical challenge of finding effective solutions to reduce drag and improve flow control around circular cylinders, which is essential for enhancing the performance and efficiency of various engineering systems. It presents an asymmetric flow control method utilising a crank mechanism to morph the cross-section from circular to elliptical via trailing edge motion. The study examines deformation amplitudes ranging from 10% to 20% and frequencies from 0.97 to 1.09, revealing that a 15% deformation amplitude at a near-natural shedding frequency ($f_d/f_0 = 1.07$) achieves a 44% drag reduction, attributed to reduced velocity deficits and suppressed turbulence intensity. Complementary numerical simulations employing RANS with the Spalart-Allmaras turbulence model at Re = 5600 broaden the analysis to extreme amplitudes (5%–100%) and frequencies ($f_d/f_0 = 0.1$–2.5), indicating that extreme amplitudes (100%) combined with low frequencies ($f_d/f_0 = 0.1$) yield a 42% drag reduction due to reduced recirculation zones. These findings highlight a critical nonlinear dependence of drag reduction on deformation parameters, suggesting asymmetric morphing as an effective strategy for enhancing aerodynamic efficiency in engineering applications.

Keywords: Control frequencies, deformation amplitudes, drag coefficient, elliptical cylindrical deformation, flow dynamics, wake pattern.

1. INTRODUCTION

Active flow control (AFC) dynamically alters fluid behavior with the usage of external energy, solving issues such as drag reduction and boundary layer separation [1, 2]. In contrast to passive control approaches, AFC uses strategies like moving surfaces and synthetic methods to enhance efficiency in aerodynamic and hydrodynamic systems [3]. Boundary layer suppression is a primary goal, which is particularly important for streamlined flow in offshore constructions, turbines, and airfoils [4].

The flow around circular cylinders, a canonical fluid dynamics problem, reveals phenomena like vortex shedding and turbulence transition [5]. Omnipresent in engineering systems like heat exchangers and offshore risers, cylinders require advanced flow control to mitigate drag and vibrations [6], while their environmental impact on sediment transport necessitates optimized designs [7]. Among AFC techniques, movable walls have emerged as a transformative approach, directly modifying near-wall dynamics to delay separation and suppress vortices. These methods energize the boundary layer via surface motion such as rotating cylinders or virtual actuation via dielectric barrier discharge plasma actuators, achieving drag reductions of up to 25% [8, 9].

The effectiveness of movable walls relies on boundary layer manipulation such as high momentum fluid injection to impede adverse pressure gradients [8] to suppress vortex shedding, which is broken up into Von Kármán vortices to damp unsteady forces [4, 9]. Actuation techniques range from active compliant walls with embedded sensors [9], virtual surfaces using plasma actuators [8], to rotating cylinders [10], all validated through numerical and experimental tools. Laminar and Discrete Vortex Methods and Lattice Boltzmann Methods are employed to model hybrid passive-active control [11], while finite element models are used to simulate fluid-structure interaction [12]. Experimentally, wind tunnel tests, particle image velocimetry, and force measurements quantify performance, linking pressure distributions to aerodynamic loads [13, 14].

A modern trend in development integrates machine learning (ML) with active flow control setups, where deep reinforcement learning (DRL) provides

real-time actuation strategies by learning from CFD data [3, 15]. Data-driven approaches propose genetic programming for control-law synthesis [16] and neural ordinary differential equations for fast predictions [17], filling gaps between model- and data-based frameworks. Such ML-based strategies have a profound impact on next-generation flow control systems by enhancing adaptability and computational efficiency.

Building on this interplay between control and fluid dynamics, this paper introduces asymmetric morphing for circular cylinder flow control by means of the periodic motion of the cylinder's trailing edge, as contrasted with traditional methods via radial deformation symmetric with respect to the cylinder axis of oscillation [18, 19, 20] or rotational oscillation of the whole cylinder [21]. Unlike classical momentum injection techniques such as plasma actuators [8] or rotating surfaces [10], the proposed method induces a dynamic transition of the cylinder's cross-section between circular and elliptical configurations using a crank system. The resulting asymmetric, time-varying curvature serves to halt boundary layer separation and vortex coherence.

To quantify the impact of this control technique on flow dynamics, tests were conducted experimentally at Re = 8800, for nine deformation frequencies and three amplitudes, whereas numerical simulations were performed at Re = 5600, for seven frequencies and amplitudes from 5% to 100%. The study endeavors, therefore, through this combined assessment, to work out how the deformation parameters interact with intrinsic flow instabilities in regard to issues where drag proves critical.

NOMENCLATURE

D	[m]	diameter
$\Delta d/d$	[-]	deformation amplitude
f_d	[Hz]	deformation frequency
f_0	[Hz]	natural emission frequency
f_{sh}	[Hz]	vortex emission frequency
R_e	[-]	Reynolds number
S_t	[-]	Strouhal number
U_∞	[m/s]	free flow velocity
U_{mean}	[m/s]	mean speed
U_{RMS}	[m/s]	root mean square speed
C_d	[-]	drag coefficient
C_{d0}	[-]	nominal drag coefficient
C_l	[-]	lift coefficient
R	[-]	drag coefficient reduction rate
T	[N]	drag force
H	[m]	vertical length of measurement
l	[m]	cylinder length
ρ	[kg/m^3]	flow density
$u(t)$	[m/s]	instantaneous velocity signal
$u'(t)$	[m/s]	turbulent velocity fluctuations
x, y	[m]	axial, transversal (coordinate)

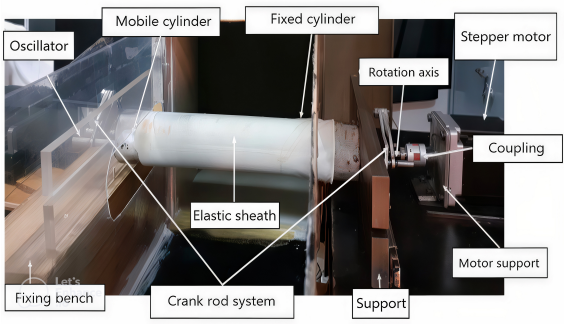

Figure 1. Assembly of mock-up.

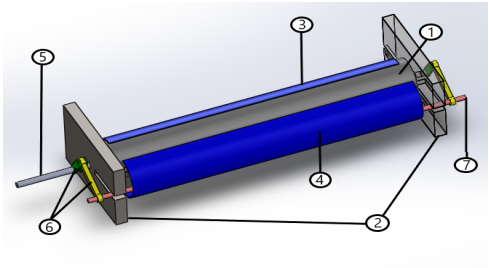

Figure 2. Isometric view of the mock-up.

2. EXPERIMENTAL APPARATUS AND PROCEDURE

2.1. EXPERIMENTAL SETUP

Experiments are performed using the setup illustrated in Fig. 1, which consists of an open-type subsonic wind tunnel (Eiffel HM 170), a hot-wire anemometer, a stepping motor, and a power supply. The wind tunnel features a test section of 292×292 mm^2, a maximum air velocity of 28 m/s, and a turbulence intensity of 1%, allowing for precise flow measurements.

An isometric view of the morphing cylinder assembly is shown in Fig. 2. The model consists of a steel tube (1) flush-mounted to support structures (2) and divided into two aluminum halves: one fixed (3) and the other movable (4), enabling the transition between circular and elliptical cross-sections. The transverse diameter remains constant, while the longitudinal diameter varies through controlled deformation. The assembly is enclosed by an elastic sheath to preserve aerodynamic integrity and maintain consistent surface contact. A stepper motor drives the system via a crank mechanism (6) and an oscillator (7), translating rotary motion into sinusoidal linear displacement of the movable wall. The deformation amplitude and frequency are controlled using an Arduino board, ensuring synchronized actuation without edge misalignment.

2.2. Calibration and procedure

The hot-wire anemometer is calibrated using the Dantec Dynamics StreamLine® Pro Automatic Calibrator, ensuring high precision for velocity calibration within the expected range, not exceeding 5 m/s.

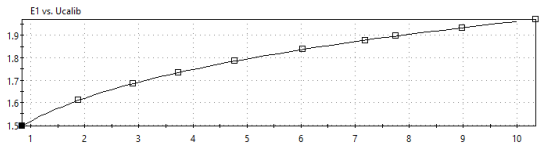

Figure 3. Calibration of the hot-wire sensor.

According to the manufacturer's user manual, the velocity uncertainty at the nozzle outlet during proper calibration is specified as ±1% ±0.02 m/s. The calibration process generates a dataset comprising corrected voltage readings (accounting for temperature fluctuations) and a third-order calibration polynomial. These outputs are illustrated in Fig. 3.

The cylinder is positioned perpendicular to the flow, the hot-wire anemometer taking measurements at a point $3.5D$ downstream from the cylinder's trailing edge ($D = 0.063$ m) and at 0.05 m from the plates. The velocity of the incident flow is 2.5m/s, which corresponds to a Reynolds number based on the initial diameter $Re = 8.8 \times 10^3$. The specific measurement distance was arrived at through an iterative adjustment process intended to properly compensate for inherent physical flow behavior involved in vortex shedding under the natural, uncontrolled condition.

3. NUMERICAL METHOD

The finite-volume method is used to discretize the governing equations, which is employed to perform RANS simulation. The geometric model setup and mesh generation is carried out by GAMBIT, which is the preprocessor of FLUENT.

3.1. Computational setup

The accuracy of computations in fluid dynamics is influenced by grid and computational domain dimensions, particularly when using dynamic meshing to evaluate aerodynamic coefficients. The computational domain [20] (Fig.4) spans $8D$ upstream and $20D$ downstream of the cylinder, with lateral surfaces at $8D$ above/below. For 3D simulations, the domain is extruded along the span (length πD), with $8D$ upstream for flow development and $20D$ downstream for wake analysis. The domain is subdivided into four zones (Fig. 5): Zone 1 (adjacent to the cylinder) uses a refined structured mesh (first grid point at $y^+ = 1$) and is mobile via a User Defined Function (UDF) to model the cylinder's moving wall. This zone undergoes translational motion while maintaining a non-deformable mesh. Zones 2-3 are structured, and Zone 4 is coarsely meshed due to weak physical gradients. Non-conforming interfaces preserve flow accuracy between zones, ensuring fidelity to the experimental geometry.

Table 1. Solver validation.

Author	Re	Method	C_d
Lourenco et Shih [22]	3900	Exp	0.98
Kahil [23]	4020	LES	1.02
Young et Ooi [24]	3900	RANS 2D	1.59
Present work	3470	K-Wsst	0.918
Present work	3470	Spalart-Allmaras	0.974
Present work	3470	K-ω	0.81

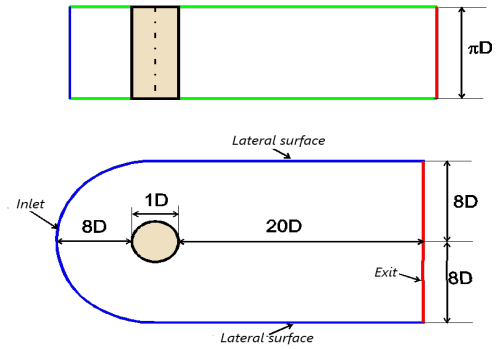

Figure 4. Calculation range and boundary conditions.

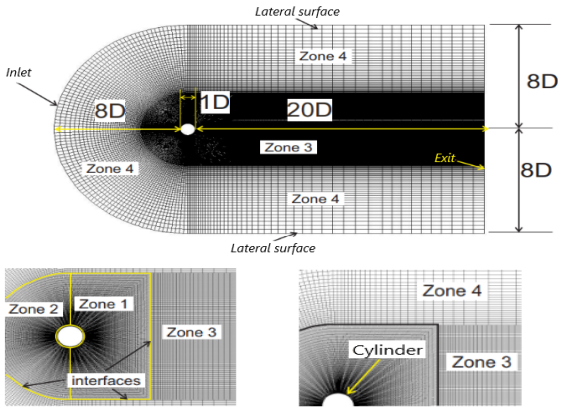

Figure 5. Calculation domain and mesh strategy adopted.

3.2. Solver validation

The drag (C_d) coefficient obtained with different models (Spalart-Allmaras, K-ω SST and K-ω) is compared with those of the experimental work of Lourenco and Shih [22], as reported in Table 1. The results show that the Spalart-Allmaras model gives a good estimate of C_d, with a relative error of 1% compared with the experimental work, while the K-ω SST and K-ω models present relative errors of 6% and 17% respectively, according to the data in Table 1, which leads to the adoption of the Spalart-Allmaras model for simulations with a moving downstream wall.

4. RESULTS AND DISCUSSION

4.1. Experimental results

Instantaneous velocity measurements $u(t)$, obtained by hot-wire anemometry, are used to characterize the vortex dynamics and wake generated by

Table 2. Cases treated with hot wire.

Deformation rate	f_d	f_d/f_0
	data1 : 6.60	0.97
$\Delta d/d = 0.10$	data2 : 6.70	0.98
	data3 : 6.80	1.00
	data4 : 6.90	1.01
$\Delta d/d = 0.15$	data5 : 7.00	1.03
	data6 : 7.10	1.04
	data7 : 7.20	1.06
$\Delta d/d = 0.20$	data8 : 7.30	1.07
	data9 : 7.40	1.09

the cylinder. The $u(t)$ signal is decomposed into a mean component U_{mean} and turbulent fluctuations $u'(t)$, such that:

$$u(t) = U_{\text{mean}} + u'(t), \tag{1}$$

$$\text{with} \quad U_{\text{mean}} = \frac{1}{T}\int_0^T u(t)\,dt, \tag{2}$$

$$\text{and} \quad U_{\text{RMS}} = \sqrt{\frac{1}{T}\int_0^T (u'(t))^2\,dt}. \tag{3}$$

The Fourier transform (FFT) of $u'(t)$ reveals the natural vortex shedding frequency, denoted f_0. The mean velocity U_{mean} not only allows the evaluation of the velocity deficit, which is related to drag, but also enables the indirect estimation of the drag coefficient C_d. The RMS level of $u(t)$, U_{RMS}, reflects the wake thickness and is associated with turbulence intensity. These results show how the elliptical deformation influences these various parameters.

The cases studied experimentally using hot-wire measurements are presented in Table 2.

4.1.1 Vortex-shedding frequency

To study the flow around a cylinder, it is crucial to determine the natural emission frequency of the vortices. The Fourier transform of the instantaneous velocity signal recorded at $x/d = 3.5$, downstream of the vortex formation zone, was used to analyse the frequency content of the fluctuating signal. The frequency detected, $f_0 = 3.401$ Hz (Fig.6), led to a natural emission frequency equivalent to twice this value.

The corresponding Strouhal number, $S_t = 0.21$, calculated using the formula $S_t = 2f_0 d/U_\infty$, aligns perfectly with the Reynolds number considered ($Re = 8800$), in agreement with the results of Norberg et al. [25].

For controlled cases, modulation of the wake frequency by the deformation frequencies imposed on the cylinder was observed. For $\Delta d/d = 10\%$, the vortex emission frequency spectra (Fig.7) show a broad band of peaks around the natural frequency, with a transition to wake synchronization for deformation frequencies around $f_d/f_0 = 1.04$, indicating a complex interaction between cylinder deformation and wake dynamics.

For $\Delta d/d = 15\%$, the variation in deformation frequencies caused the main peaks in the vortex emission frequency spectra to fluctuate around

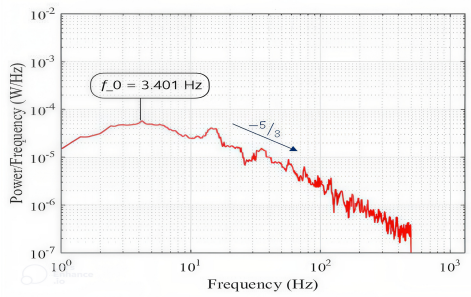

Figure 6. Spectrum of velocity fluctuations at $x/d = 3.5$ on the wake centreline.

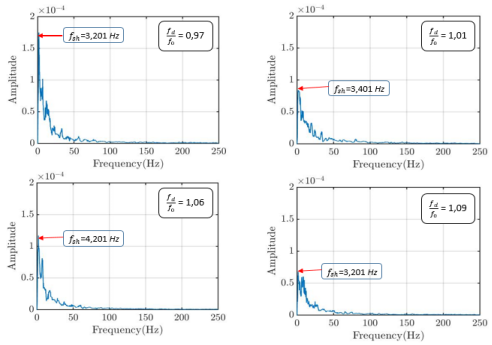

Figure 7. Vortex emission frequency at a point located at x/d 3.5 on the wake centreline for a central line of the wake for a deformation of 10%.

the natural frequency range (Fig.8). The modulation of the vortex emission frequency by the deformation frequencies coincided for $f_d/f_0 = 0.97$. Increasing the deformation frequency caused the peak emission frequency to exceed that of the natural case, likely due to the interaction between the deformation of the cylinder's moving wall and the vibration of the mechanism.

For $\Delta d/d = 20\%$, the emission frequency was practically identical to the natural frequency for $f_d/f_0 = 0.79$. The increase in deformation frequencies led to a considerable amplification of the spectral peak (Fig.9), with an emission frequency exceeding that of the natural case. This is explained by reson-

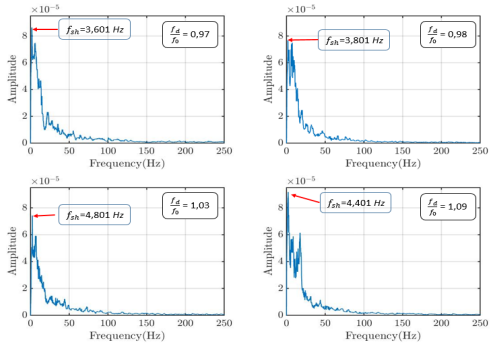

Figure 8. Vortex emission frequency at a point located at x/d 3.5 on the wake centreline for a central line of the wake for a deformation of 15%.

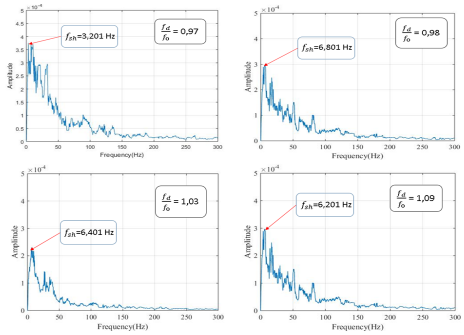

Figure 9. Vortex emission frequency at a point located at x/d 3.5 on the wake centreline for a central line of the wake for a deformation of 20%**.**

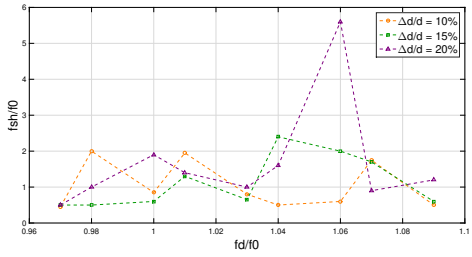

Figure 10. Effect of deformation frequency on vortex emission frequency.

ance when the flow is controlled with a frequency close to its natural frequency, suggesting that cylinder deformation can control and modify wake dynamics.

The effect of the control frequency on the vortex emission frequency varies with deformation amplitude (Fig.10). At 10%, the vortex emission frequency fluctuates around twice the deformation frequency, with a minimum at $f_{\text{sh}}/f_0 = 0.76$. At 15%, it varies around the cylinder's deformation frequency, with extrema at $f_{\text{sh}}/f_0 = 0.5$ and $f_{\text{sh}}/f_0 = 2.4$. At 20%, the vortex emission frequency exceeds five times the deformation frequency, peaking at $f_{\text{sh}}/f_0 = 5.80$ for $f_d/f_0 = 1.06$, showing the influence of deformation amplitude on vortex emission frequency.

4.1.2 Transverse mean velocity

Figures 11, 12, and 13 show the mean transverse velocity profiles normalized by the incident flow velocity, measured at $x/d = 3.5$ from the centre of the cylinder, for different deformation amplitudes ($\Delta d/d = 10\%$, 15%, and 20%) and deformation frequencies.

At 10% amplitude (Fig. 11), the mean velocity remains higher than the nominal case at all frequencies, with a reduction in the velocity deficit associated with a downward deflection of the wake, suggesting a reduction in drag.

At 15% (Fig. 12), the decrease in velocity deficit becomes more pronounced, confirming a more significant reduction in drag while retaining the favorable wake deflection.

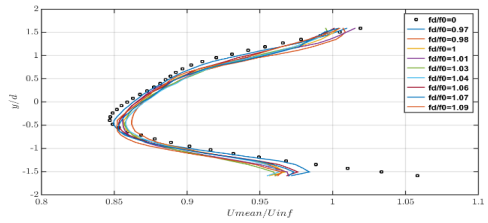

Figure 11. Wake deficit at $x/d = 3.5$ for various strain frequencies at 10% **amplitude.**

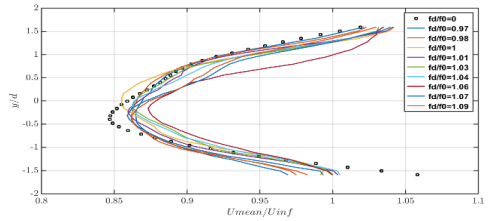

Figure 12. Wake deficit at $x/d = 3.5$ for various strain frequencies at 15% **amplitude.**

However, at 20% (Fig. 13), the behaviour becomes mixed: certain frequencies (0.97, 0.98, 1.00, 1.04) amplify the speed and reduce the deficit, while others (1.01, 1.03, 1.06, 1.07, 1.09) degrade these parameters, increasing the speed deficit.

The optimal state is identified at 15% amplitude with a frequency $fd/f_0 = 1.07$, offering the maximum reduction in velocity deficit and maintaining downward wake deflection, making it the most favourable scenario for drag control.

4.1.3 Root mean square of the transverse velocity fluctuations

The analysis of the distributions of the relative standard deviation (U_{RMS}/U_∞) for different strain amplitudes ($\Delta d/d$) and strain frequencies (f_d/f_0) highlights specific behaviours. For $\Delta d/d = 10\%$ (Fig. 14), the distance between the two peaks is greater than that of the nominal case for all frequencies. For $\Delta d/d = 15\%$ (Fig. 15), the distance between the peaks varies with frequency, increasing for low frequencies and notably decreasing for higher frequencies, resulting in a reduction of the wake thickness and a delay in separation. Finally, for $\Delta d/d = 20\%$ (Fig. 16), the distance between the peaks is minimal for all frequencies, with a near dis-

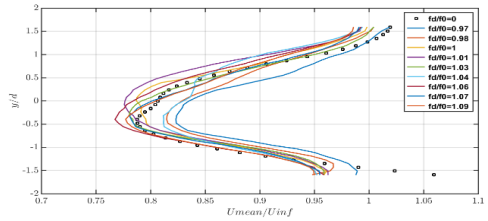

Figure 13. Wake deficit at $x/d = 3.5$ for various strain frequencies at 20% **amplitude.**

appearance of the peaks for $f_d/f_0 = 1.04$, indicating a reduction in the wake thickness and a delayed separation, which suggests that this deformation amplitude is the most favourable for reducing drag.

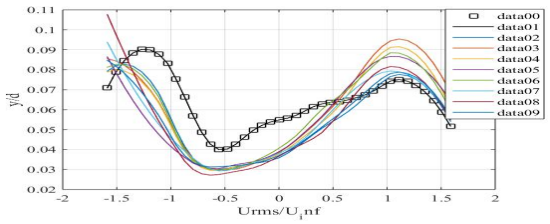

Figure 14. Root-mean-square of velocity fluctuations at $x/d = 3.5$ for a 10% deformation.

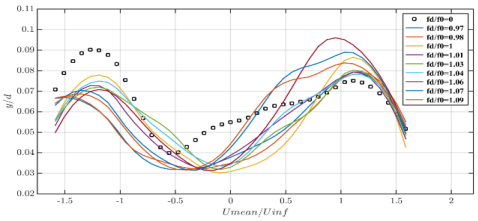

Figure 15. Root-mean-square of velocity fluctuations at $x/d = 3.5$ for a 15% deformation.

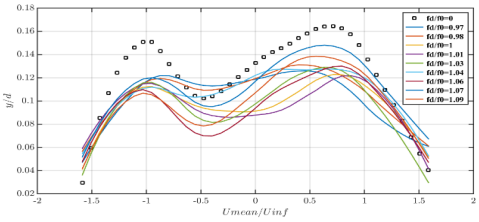

Figure 16. Root-mean-square of velocity fluctuations at $x/d = 3.5$ for a 20% deformation.

4.1.4 Drag coefficient

The drag coefficient is defined as the ratio between the drag force and the dynamic energy of the flow. It is calculated by integrating the velocity profile u/U as a function of y/D, from the drag force equation:

$$T = \int_{-H}^{H} \rho l u (U_\infty - u)\,\mathrm{d}y \tag{4}$$

Where T is the drag force, H is the vertical length of measurement, l is the cylinder length, u is the mean velocity, U_∞ is the incident flow velocity, and ρ is the flow density.
The drag coefficient is defined by:

$$C_d = \frac{T}{\frac{1}{2}\rho U_\infty^2 D l} \Rightarrow C_d = 2\int_{-H}^{H} \frac{u}{U_\infty}\left(1 - \frac{u}{U_\infty}\right)\mathrm{d}\left(\frac{y}{D}\right) \tag{5}$$

This method allows the drag to be evaluated from velocity measurements.

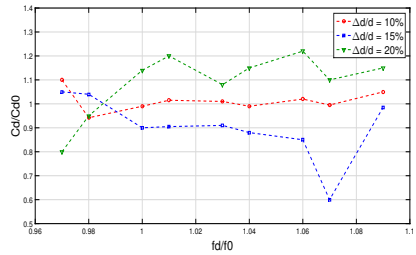

Figure 17. Variation in drag coefficient as a function of control frequency.

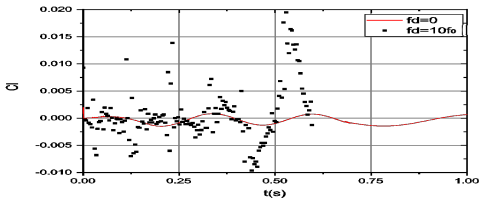

Figure 18. Instantaneous variation in lift coefficient.

Figure 17 highlights how the drag coefficient (C_d) varies as a function of control frequency (f_d/f_0) for different strain amplitudes ($\Delta d/d$). For a strain amplitude of 10%, the reduction in C_d is small (6%) and remains close to the nominal value. On the other hand, for $\Delta d/d = 15\%$, there is a significant reduction in C_d (44%) at $f_d/f_0 = 1.07$, while for $\Delta d/d = 20\%$, the greatest reduction in drag occurs at $f_d/f_0 = 0.97$, with a reduction of 21%. These results indicate that strain amplitude and control frequency strongly influence drag, with greater reductions for higher strain amplitudes and specific control frequencies.

4.2. Numerical results

Given the negligible mean lift coefficient ($C_l \approx 0$) and its minor fluctuations around this value during vortex shedding (Fig.18) consistent with prior findings by Rezaiguia and Ghouali [21] this analysis focuses exclusively on the drag coefficient (C_d). Specifically, the influence of deformation amplitudes ($\Delta d/d$) and frequencies (f_d/f_0) in Table 3 on the mean drag coefficient (C_d) and its root-mean-square (RMS) fluctuations is evaluated. These parameters are detailed in the following sections.

4.2.1 Drag coefficient reduction rate

The results were analyzed in order to obtain average values of drag coefficients and drag gains: $R = (\frac{C_d - C_{d0}}{C_{d0}}) * 100$, by varying the frequency and amplitude of the deformation of the cylinder cross-section. The obtained results show that in all the

Table 3. Cases treated numerically.

f_d/f_0		0.1	0.25	0.5	1.0	1.5	2.0	2.5	
$\Delta d/d$%	5	10	20	30	40	50	60	80	100

Table 4. Drag reduction rates obtained for different frequencies and amplitudes.

$\Delta d/d\%$ \ f_d/f_0	0,1	0,25	0,5	1,0	1,5	2,0	2,5
5	-18,87	-22,18	-23,44	-23,80	-23,51	-23,07	-22,59
10	-20,35	-23,61	-24,21	-24,51	-23,86	-22,39	-22,27
20	-23,42	-25,84	-26,00	-25,83	-24,27	-22,06	-19,90
30	-26,93	-28,46	-28,41	-27,56	-24,84	-21,08	-21,18
40	-30,42	-31,62	-31,29	-29,36	-26,11	-20,55	-20,35
50	-33,29	-34,44	-33,49	-31,34	-27,62	-20,55	-20,45
60	-18,87	-36,50	-35,08	-33,21	-28,33	-20,09	-20,23
80	-39,49	-39,54	-37,23	-37,29	-26,65	-17,54	-16,36
100	-41,92	-41,65	-38,80	-37,40	-23,65	–	-5,391

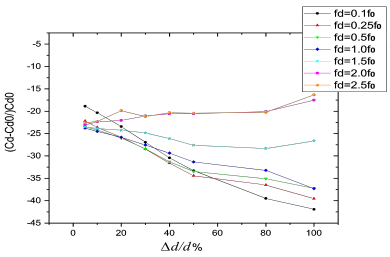

Figure 19. Drag reduction rates as a function of frequency and amplitude.

considered cases, drag reduction rates are negative, hence proving that a reduction in drag has been obtained. These results are summarized in Table 4.

The results obtained in the table are represented graphically in Fig. 19, where it can be noticed that the best reductions (R_{max} = 42%) are obtained for the lowest frequency (f_d/f_0 = 0.1) combined with the highest amplitudes ($\Delta d/d$ = 100%). The minimum drag reduction rates (R_{min} = 5.4%) are obtained with the highest frequencies combined with the highest amplitudes. Thus, the most favourable drag reductions are obtained for the smallest frequencies.

4.2.2 Root Mean Square (RMS) of drag coefficient

Figure 20 shows the evolution of the RMS as a function of the amplitude and frequency of deformation of the cylinder. It shows that the intensity of the turbulence increases proportionally to the frequency and amplitude. As mentioned earlier, this increase is synonymous with an increase in the turbulent kinetic energy in the flow and the energy transported by the vortex structures emitted by the cylinder.

As previously stated, this increase is synonymous with an increase in the turbulent kinetic energy of the flow and the energy transported by the vortex structures emitted by the cylinder. On the other hand, a reduction in turbulent kinetic energy leads to a more stable flow around bluff bodies, which reduces the variability of the drag coefficient, as indicated by a lower RMS.

5. CONCLUSION

This study explores the effectiveness of cylindrical-elliptical deformation of a circular cylinder's cross-section for active flow control, conducted in a subsonic wind tunnel at a Reynolds number of Re = 8800. The experimental results

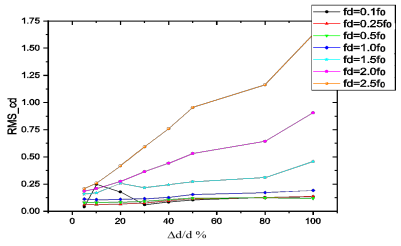

Figure 20. Root-mean-square of fluctuations in drag coefficient.

indicate that deformation significantly influences vortex dynamics, with a maximum drag coefficient reduction of 44% observed at a 15% deformation amplitude and a frequency ratio of f_d/f_0 = 1.07. At a 10% amplitude, the drag reduction is modest at 6%, while at 20% amplitude, a maximum reduction of 21% is achieved at f_d/f_0 = 0.97.

Numerical simulations using the RANS approach with the Spalart-Allmaras model confirm these findings, showing a drag reduction of up to 42% at a 100% deformation amplitude and a low frequency of f_d/f_0 = 0.1. The analysis reveals that lower frequencies and higher amplitudes lead to enhanced flow stability and reduced recirculation zones.

Additionally, the study highlights that the root mean square (RMS) of velocity fluctuations decreases with increased deformation amplitude, indicating reduced wake thickness and delayed flow separation. The modulation of vortex shedding frequency by deformation frequencies demonstrates synchronization effects, particularly at f_d/f_0 ratios near 1, which are crucial for optimizing drag reduction.

REFERENCES

[1] Vakhshouri, M. E., and Çuhadaroğlu, B., 2022, "Effects of uniform injection and suction through perforated pentagonal cylinders on the flow and heat transfer", *International Journal of Numerical Methods for Heat & Fluid Flow*, Vol. 32 (4), pp. 1324–1347.

[2] Ahmad, M., Qayoum, A., Dilawar, M., Bhat, G. S., and Sofi, A. Y., 2025, "Experimental investigation of the effects of cavity design for flow characteristics and heat transfer properties of synthetic jet actuators in quiescent flow", *Journal of Thermal Analysis and Calorimetry*, pp. 1–18.

[3] Jiang-Li, C., Shao-Qiang, C., Feng, R., and Hai-Bao, H., 2022, "Artificially intelligent control of drag reduction around acircular cylinder based on wall pressure feedback br", *ACTA PHYSICA SINICA*, Vol. 71 (8).

[4] Koc, I., 2008, *Experimental investigation of active control of bluff body vortex shedding*, Old Dominion University.

[5] Sarwar, W., 2020, "Active flow control methods for aerodynamic applications", .

[6] Zhao, M., 2023, "A review of recent studies on the control of vortex-induced vibration of circular cylinders", *Ocean Engineering*, Vol. 285, p. 115389.

[7] Choi, S.-D., Eum, T.-S., Shin, E. T., and Song, C. G., 2021, "Numerical investigation of flow around a structure using Navier-slip boundary conditions", *World Journal of Engineering*, Vol. 19 (5), pp. 667–674.

[8] Zhang, X., Choi, K.-S., Huang, Y., and Li, H.-x., 2019, "Flow control over a circular cylinder using virtual moving surface boundary layer control", *Experiments in fluids*, Vol. 60, pp. 1–15.

[9] Pal, D., Sinha, S., Pal, D., and Sinha, S., 1997, "Controlling an unsteady separating boundary layer on a cylinder with an active compliant wall", *35th Aerospace Sciences Meeting and Exhibit*, p. 212.

[10] Bergmann, M., Cordier, L., and Brancher, J.-P., 2005, "Optimal rotary control of the cylinder wake using proper orthogonal decomposition reduced-order model", *Physics of fluids*, Vol. 17 (9).

[11] Oliveira, M. A. d., Moraes, P. G. d., Andrade, C. L. d., Bimbato, A. M., and Alcântara Pereira, L. A., 2020, "Control and suppression of vortex shedding from a slightly rough circular cylinder by a discrete vortex method", *Energies*, Vol. 13 (17), p. 4481.

[12] Chua, M. H., and Liu, B., 2024, "Active Flow Control of Flow Over a Stationary Cylinder Using a Flapping Rod at Low Reynolds Number", *International Conference on Offshore Mechanics and Arctic Engineering*, American Society of Mechanical Engineers, Vol. 87844, p. V006T08A017.

[13] Akbıyık, H., and Akansu, Y., 2021, "Effective flow control around a circular cylinder by using both a splitter plate and plasma actuators as passive and active control methods", *Isı Bilimi ve Tekniği Dergisi*, Vol. 41 (1), pp. 133–140.

[14] Santhanakrishnan, A., Jacob, J., and Suzen, Y., 2006, "Flow control using plasma actuators and linear/annular plasma synthetic jet actuators", *3rd AIAA Flow Control Conference*, p. 3033.

[15] Ren, F., Rabault, J., and Tang, H., 2021, "Applying deep reinforcement learning to active flow control in weakly turbulent conditions", *Physics of Fluids*, Vol. 33 (3).

[16] Ren, F., Wang, C., and Tang, H., 2019, "Active control of vortex-induced vibration of a circular cylinder using machine learning", *Physics of Fluids*, Vol. 31 (9).

[17] Mao, Y., Zhong, S., and Yin, H., 2024, "Model-based deep reinforcement learning for active control of flow around a circular cylinder using action-informed episode-based neural ordinary differential equations", *Physics of Fluids*, Vol. 36 (8).

[18] Oualli, H., 2006, "Influence de la vibration radiale et de la rotation d'un cylindre circulaire sur l'évolution du sillage proche", Ph.D. thesis, Alger.

[19] Menfoukh, L., Hanchi, S., Oualli, H., Bouabdellah, A., and Askovic, R., 2008, "Experimental investigation of a circular radially deforming cylinder near wake using an infrared technique", *International journal of heat and fluid flow*, Vol. 29 (2), pp. 479–494.

[20] Aguedal, L., Semmar, D., Berrouk, A. S., Azzi, A., and Oualli, H., 2018, "3D vortex structure investigation using Large Eddy Simulation of flow around a rotary oscillating circular cylinder", *European Journal of Mechanics-B/Fluids*, Vol. 71, pp. 113–125.

[21] Rezaiguia, H., Ghoualli, M., and Oualli, H., 2021, "Experimental investigation of the flow behind a circular cylinder controlled by combination of a rotary oscillation and a radial deformation", *Journal of the Brazilian Society of Mechanical Sciences and Engineering*, Vol. 43 (5), p. 267.

[22] Lourenco, L., 1993, "Characteristics of the plane turbulent near wake of a circular cylinder", *A particle image velocimetry study*.

[23] Kahil, Y., 2011, "Simulation des grandes échelles d'écoulements turbulents autour de cylindres circulaires à un nombre de Reynolds sous critique", Ph.D. thesis, Paris 6.

[24] Young, M., and Ooi, A., 2007, "Comparative assessment of LES and URANS for flow over a cylinder at a Reynolds number of 3900", .

[25] Norberg, C., 1994, "An experimental investigation of the flow around a circular cylinder: influence of aspect ratio", *Journal of Fluid Mechanics*, Vol. 258, pp. 287–316.

Conference on Modelling Fluid Flow (CMFF'25)
The 19th International Conference on Fluid Flow Technologies
Budapest, Hungary, August 26-August 29, 2025

A CFD STUDY ON DEPOSITION EFFICIENCY IN CASE OF INHALED AEROSOL MEDICATION

Péter SÁFRÁNY[1], Csaba HŐS[2],

[1] Corresponding Author. Department of Hydrodynamic Systems, Faculty of Mechanical Engineering, Budapest University of Technology and Economics. Budapest University of Technology and Economics, Műegyetem rkp. 3., H-1111 Budapest, Hungary. Tel.: +36 30 994 1569, E-mail: psafrany@hds.bme.hu
[2] Department of Hydrodynamic Systems, Faculty of Mechanical Engineering, Budapest University of Technology and Economics. E-mail: hos.csaba@gpk.bme.hu

ABSTRACT

The aim of this study is to examine how the deposition efficiency of inhaled aerosol medications is affected by the varying geometrical characteristics of the extra-thoracic region. To this end, numerical simulations were performed on a realistic geometry, and on a range of simplified and modified versions. The results were compared and evaluated based on several factors, including deposition efficiency, mean velocity, turbulence intensity, overall pressure drop, and velocity profile at the exit plane. The numerical method was validated through 3D printing and measurement of the pressure drop of the realistic geometry and the geometry that performed best among the simplified geometries at the simulated flow rate. These results will facilitate the evaluation of the usability of simplified geometries for flow and particle deposition simulations, thereby enhancing patient-specific simulations where the extra-thoracic region cannot be accurately reconstructed.

Keywords: CFD, CFPD, inhaled medicine, oral airways, particle deposition

NOMENCLATURE

$UMean$	$[m/s]$	time averaged velocity magnitude
k	$[m^2/s^2]$	turbulence kinetic energy

1. INTRODUCTION

Inhaled drug particles are frequently used to treat respiratory diseases such as asthma and chronic obstructive pulmonary disease (COPD). In recent years, inhaled insulin and painkillers have also been developed. However, it is important to note that the main drawback of these devices is the precise dosing. It is evident that the quantity and distribution of the deposited drug particles are crucial for the effectiveness of the therapy. Even when a specific quantity of medication is released into the airways, as in the case of pressurized metered dose inhalers (pMDIs) or dry powder inhalers (DPIs), the deposition of particles is influenced by various factors. These include the inhalation flow rate, the patient's airway geometry, the timing of the actuation, and other variables. Over the years, numerous deposition models have been developed, including the semi-empirical model proposed by the International Commission on Radiological Protection (ICRP), known as the ICRP model [1], the 1D trumpet model, and the stochastic model, where the term 'stochastic' refers to the method of generating paths [2]. However, it is important to note that only computational fluid and particle dynamics (CFPD) simulations can consider the exact patient-specific geometry.

One potential methodology for creating patient-specific three-dimensional geometries and numerical domains involves using computed tomography (CT) or magnetic resonance imaging (MRI) alongside segmentation software capable of determining airway boundaries based on pixel values. Segmentation can be performed effectively on the trachea and the first few bifurcations. However, challenges arise during the reconstruction of the lower airways with reduced diameters and of the mouth-throat region. In the case of the lower airways, the resolution is typically insufficient for reconstruction. In the case of the mouth-throat region, the source of the difficulties lies in the complexity of the geometry [3] and the fact that patients generally keep their mouths closed during medical imaging. This leaves little to no gap for reconstruction. Consequently, reconstruction of the oral cavity and inlet boundary becomes uncertain. The inability to reconstruct the oral cavity significantly restricts research into particle deposition in patient-specific airways, since this region influences the flow properties and particle size distribution beyond the trachea. Without proper geometric modelling of the extra-thoracic region, results regarding deposition in the lower airways cannot be relied upon.

The effect of the geometry of the extra-thoracic region on the flow field and particle deposition has been extensively studied. Heenan et al. [4] demonstrated that local velocity magnitude and flow curvature greatly impact particle deposition. Significant differences occur even in the case of the same patient with different mouth openings. Grgic et al. [5] also showed that the high local velocities and rapid changes in the flow direction are key parameters for local deposition patterns. In their study, Xi et al. [6] investigated the particle deposition and flow field in a realistic oral cavity-throat geometry and its simplified versions. They simplified the overall geometry by replacing the original cross-sections with circular or elliptical ones, and their findings showed that these modifications significantly affected the local deposition patterns. The study concluded that the realistic geometry provided the most accurate deposition predictions at different flow rates. It also identified the glottis and the upper trachea as the geometric features that principally affect deposition, where the so-called laryngeal jet forms. Since the overall geometry was simplified, these features were only included in the realistic model.

Nicolau and Zaki [7] performed direct numerical simulations (DNS) on four realistic extra-thoracic geometries. They found that the flow field and deposition are affected not only by patient-specific geometric differences, but also by the position of the tongue in the case of the same subject.

Xi et al. [8] investigated the effect of total airway volume, oral cavity volume, airway curvature, and glottal area on the transport and deposition of inhaled aerosols in the mouth-throat region. They used and modified the realistic, constant-diameter and elliptical models described in [6] along with the USP IP model described in [9]. They concluded that the glottal area and total airway volume have a greater impact on deposition than curvature and oral cavity volume.

In their study, Feng et al. [10] compared seven different upper airway geometries and identified that the laryngeal jet and the recirculating zone significantly impact particle transport and deposition. Additional studies also revealed that particle deposition in the laryngeal region was enhanced by the formation of the laryngeal jet. [11, 12, 13]. Ma et al. [14] also compared modified, realistic oral cavity–throat models and found that the uvula and epiglottis have the greatest effect on particle deposition, however, the models should also incorporate the soft palate.

It can be concluded that the geometry of the throat plays a key role in the flow characteristics entering the trachea, as well as in particle deposition patterns. Since the throat can be reconstructed from medical images, the aim of this study is to investigate the potential application of a simplified oral cavity in patient-specific particle deposition studies. The main expectation of the simplified geometry is that it should be easily adapted to the reconstructed airways, provide realistic flow characteristics at the tracheal inlet and correctly model the particle filtration properties of the extra-thoracic region. To this end, the flow field and deposition patterns in a realistic extra-thoracic geometry were compared with the results of three simplified oral cavity cases.

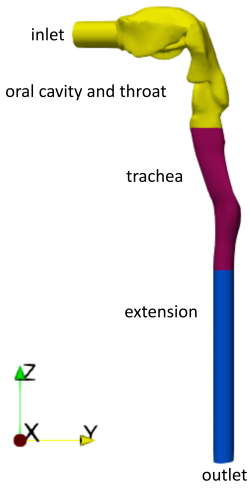

Figure 1. The complete original geometry.

2. NUMERICAL METHODS

2.1. Geometry and the numerical mesh

The geometry of the oral cavity, throat, and trachea is the same as in the SimInhale benchmark case [15]. The trachea was lengthened by 140 mm to minimise the impact of the outlet boundary condition on the flow upstream. The full original geometry (*og*) can be seen in Figure 1. Simplified geometries have been created for our investigation to study the impact of on the simplification of the oral cavity. The inlet of the *og* starts with a 20 mm diameter pipe section, which forms the basis for all the modified geometries. The center line of the *og* was calculated using the VMTK Python package, then the original oral cavity was removed with a plane cut just above the epiglottis. The center line and exact location of the cut are indicated in Figure 2.

The first simplified geometry (*sg1*) was created by extending the inlet, followed by a 90° loft along the center line to the cutoff. In contrast, for the second simplified geometry (*sg2*), involved sweeping the inlet cross-section along the center line and lofting it to the cutoff. The third simplified geometry (*sg3*) featured a swept inlet section and a swept cutoff lofted together. For *sg3*, the sweeps were performed along the lower outline in the YZ section of the original oral cavity rather than along the center line. Side and top views of the simplified geometries can be seen in Figure 3 and 4. As can be seen in Fig 3 and 4, the spaces surrounding the teeth have been completely eliminated, significantly reducing the com-

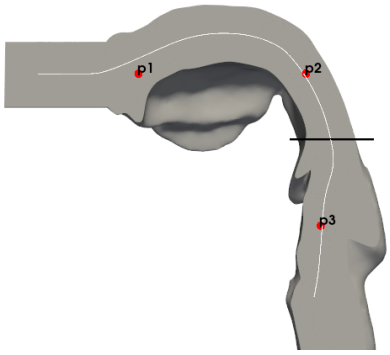

Figure 2. Cross-sectional view of the oral cavity and throat, showing the centerline (white), the location of the plane section cut (black) and the pressure sampling points (red marks).

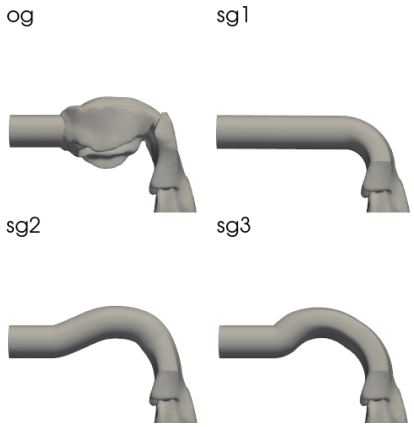

Figure 3. Simplified geometric shapes viewed from the side.

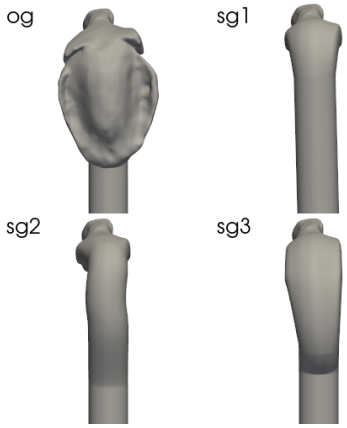

Figure 4. Simplified geometric shapes viewed from the top.

plexity of the domain.

The numerical mesh for the created models was generated using the built-in snappyHexMesh utility in OpenFOAM. Five boundary layer cells were added to the walls, with the height of the first cell set to 60 μm and an expansion ratio of 1.2. Spasov et al. [16] demonstrated that this configuration is adequate for accurately resolving the boundary layer in this geometry.

2.2. Flow field

Numerical simulations were conducted using the OpenFOAM software package. A 60 L/min flow rate and a zero-pressure gradient were set at the inlet for each case, while the outlet boundary conditions were set to zero static pressure and zero velocity gradient. Given that the flow is turbulent at this flow rate, the k-ω SST model was selected for the turbulence modelling. This model performs well in the near wall region but might underestimate the turbulent kinetic energy levels [17]. A commonly applied [16, 18, 17] turbulence intensity of 5% was introduced at the inlet and the omegaWallFunction was applied to the walls to properly model the boundary layer. This wall function calculates the local y+ value and adjusts its parameters accordingly. This is highly beneficial, as both low- and high-velocity zones occur in the geometry.

The used numerical schemes have been adopted from the work of Spasov et al. [16]. The authors demonstrated that the complexity of the geometry prevents achieving a proper steady-state solution, therefore, averaging the flow field from the unsteady solution is the best approach. To achieve this, unsteady simulations lasting 0.5 seconds were conducted using the PIMPLE algorithm, and the flow fields were averaged over all the time steps to obtain mean values.

A grid independence study was conducted on the *og* using three different mesh resolutions. The pressure was monitored in three locations shown in Fig 2. Table 1 presents the results of the grid independence study. The results demonstrate good agreement, with the highest relative deviation between the medium and fine meshes being 3.46% at the third sampling point. Therefore, the medium mesh was accepted for the numerical studies.

Table 1. Mesh independence study results

	Million cells	p1, Pa	p2, Pa	p3, Pa
coarse	3.533	52.51	48.01	27.58
medium	4.686	52.82	48.41	28.03
fine	6.293	53.77	49	29.03

2.3. Particle dynamics

After solving the flow field, the passive transport and deposition of kinematic particles were investigated. The equation of motion for the particles

was solved using the icoUncoupledKinematicParcelFoam solver on the averaged velocity and pressure field. The particles were introduced at the inlet patch with a uniform size distribution. The particle density was set to 1.23 kg/m³, with the smallest diameter set to 1 μm and the largest to 15 μm. The particles had an initial velocity of 40 m/s in the x-direction, with a release duration of 0.1 seconds. These values correspond to the particle size range and velocity released from a pMDI device [19]. A total of 180,000 particles were injected into the domain. Stick interaction was set for the walls, meaning a particle was considered deposited as soon as it hit the wall. The stochasticDispersionRAS model was used to account for turbulence. Each particle was tracked individually and the maximum particle Courant number was set to 5e-3.

3. MESUREMENTS

In order to validate the simulations and determine the effect of simplification on the resistance of the mouth-throat region, the average pressure was measured at the tracheal inlet. Square time-flow curves were generated using a Piston Medical PWG-33 pulmonary waveform generator, and the pressure difference was measured with a Sensirion SDP31 differential pressure sensor. The *og* and *sg2* oral cavity and throat regions were 3D-printed using DLP technology. A short channel with eight pressure sampling ports was added at the exit of the throat to measure the average pressure in the cross-section. The measurement setup is shown below in Fig 5.

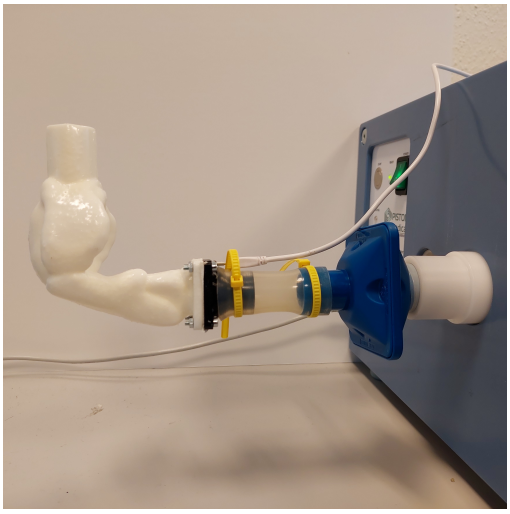

Figure 5. Measurement setup

4. RESULTS

4.1. Velocity field and pressure drop

Simplifying the oral cavity is advantageous from both a reconstruction perspective and because it requires fewer numerical cells, thereby reducing simulation times. The difference in run time was noticeable in particle simulations, where the simplified

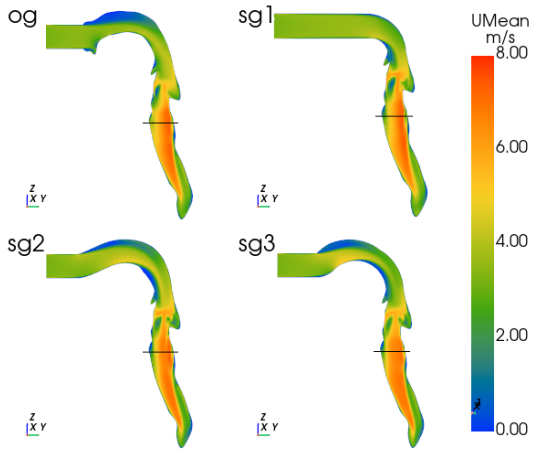

Figure 6. Velocity distribution on the YZ plane

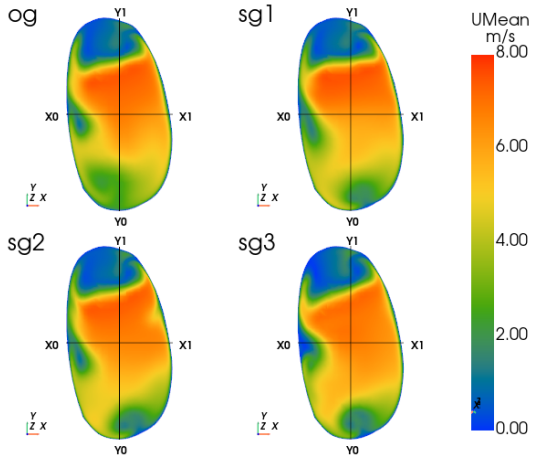

Figure 7. Velocity distribution at the inlet of the trachea.

geometry simulations were, on average, 25% faster.

As emphasized in the introduction, jet formation in the larynx significantly impacts the flow pattern in the trachea and consequently affects flow in the downstream airways. Therefore, a key feature of the simplified geometry should be its ability to produce the same flow pattern at the tracheal inlet.

Figure 6 shows the mean velocity on the YZ plane. The centreline of the original geometry does not fully lie in the YZ plane, which is why the full cross-section has not been included. As can be seen, there is no significant difference in velocity magnitude between the original and simplified cases. The main differences can be observed in the cases of *sg2* and *sg3*, a higher velocity can be seen above the tongue's arc, and the flow separates immediately thereafter. In the case of *sg1*, the separation occurs just before the epiglottis, which reduces its impact on the flow.

Figure 7 and Figure 8 show the mean velocity and turbulence kinetic energy (TKE) distributions at the inlet of the trachea in the latest timestep. The precise location of the sections shown in Fig. 6 is indicated by a black line. The main difference between

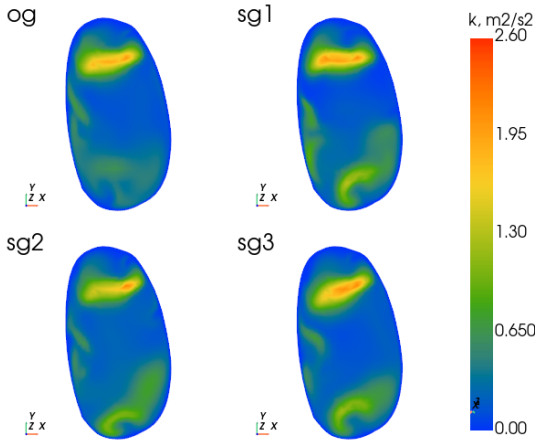

Figure 8. Turbulent kinetic energy distribution at the inlet of the trachea.

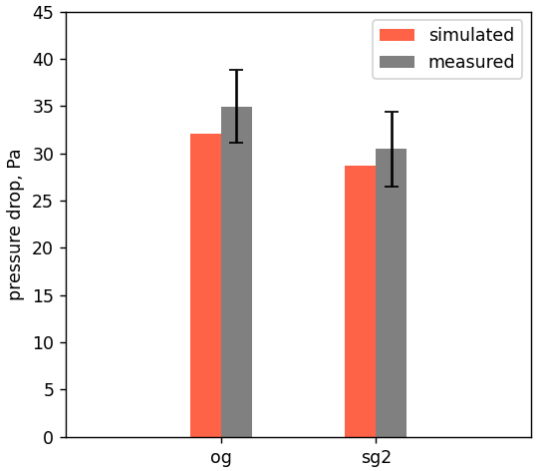

Figure 9. Simulated and measured pressure difference in the *og* and *sg2* oral cavity - throat models

the *og* and the simplified versions can be seen in the shape of the recirculating zones. Other than that, there is no significant difference in the observed velocity distributions. For correct particle deposition results, a proper turbulence kinetic energy distribution is essential [16]. As can be observed in Fig. 8, it is striking that close to the walls on the bottom side, all three simplified geometries generate a much higher local TKE. This is certainly a considerable factor when using simplified geometries.

To gain a more comprehensive understanding of the velocity distribution, the velocity components have been plotted along the X0-X1 and Y0-Y1 lines, as shown in Fig 7. Plots of the velocity components can be seen in Figure 10 and 11. As demonstrated by the velocity magnitude plots, it is not surprising that the z component of the velocity agrees with the original and simplified geometries. Along the X0-X1 line, none of the simplified cases are close to the original geometry with regard to the x component of the velocity. The *sg2*, however, aligns well with the y component. Along the Y0-Y1 line, it is also noteworthy that the x component of all the simplified cases is erroneous in the vicinity of the wall at Y0. Based on the velocity profiles, *sg2* was selected as the most appropriate simplification of the three models investigated.

In the case of the *og*, the simulated and measured pressure differences at 60 L/min between the inlet and the tracheal inlet were 32.06 Pa and 34.97 ±3.86 Pa, respectively. For the *sg2* these values were 28.72 Pa and 30.44 ±3.92 Pa. Considering the unsteadiness of the flow and the uneven pressure distribution in the exit plane, the measured and simulated results are in good agreement. Figure 9 demonstrates the simulated and measured pressure differences for the two models.

4.2. Deposition of particles

The fundamental expectation when employing a simplified oral cavity is that the filtration of particles should be equivalent to that of the original geometry. To investigate this property of simplified geometries, the number of particles deposited in the oral cavity and throat was summed. Histograms of the size distribution of the deposited particles were plotted based on the absolute and normalized particle counts. Normalization was based on particle counts for the *og*. These are shown in Figure 12 and 13.

Using simplified geometries has been shown to significantly reduce particle deposition across all diameters. This finding is somewhat counter-intuitive given the lack of observed differences in the flow field. Relative filtration varies greatly from diameter to diameter, peaking around 5 to 7 μm. Below this, there are large fluctuations, but this is due to the relatively low number of deposited particles. Above 8 μm it remains nearly constant.

Whether simplified geometries can be used will ultimately be determined by whether the same tend-

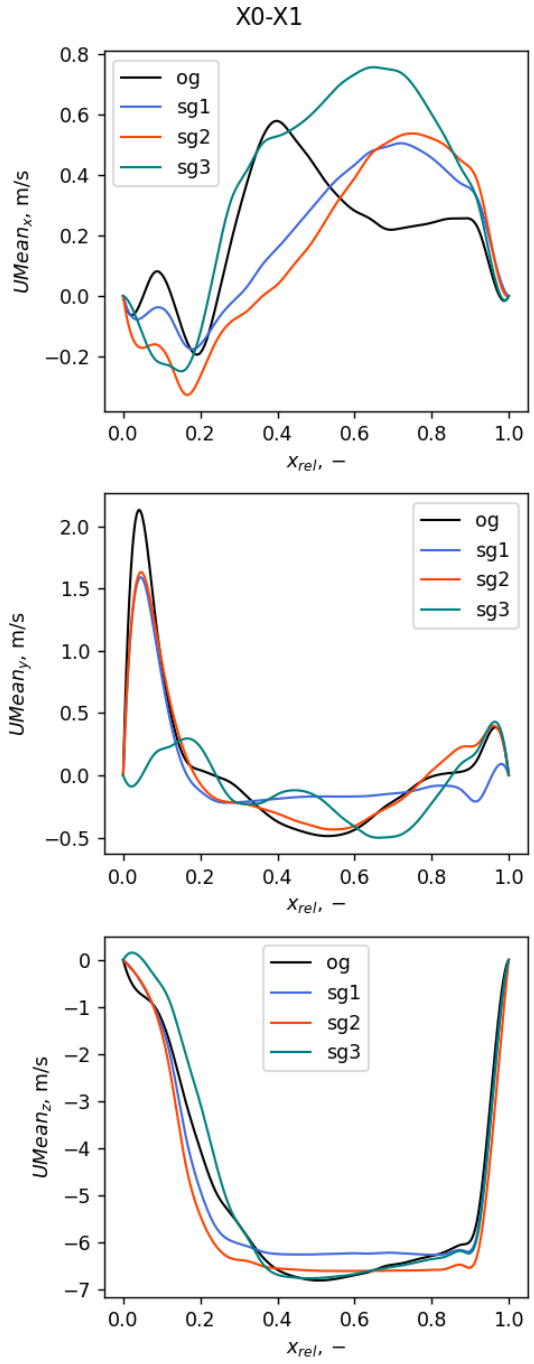

Figure 10. Velocity components along X0-X1

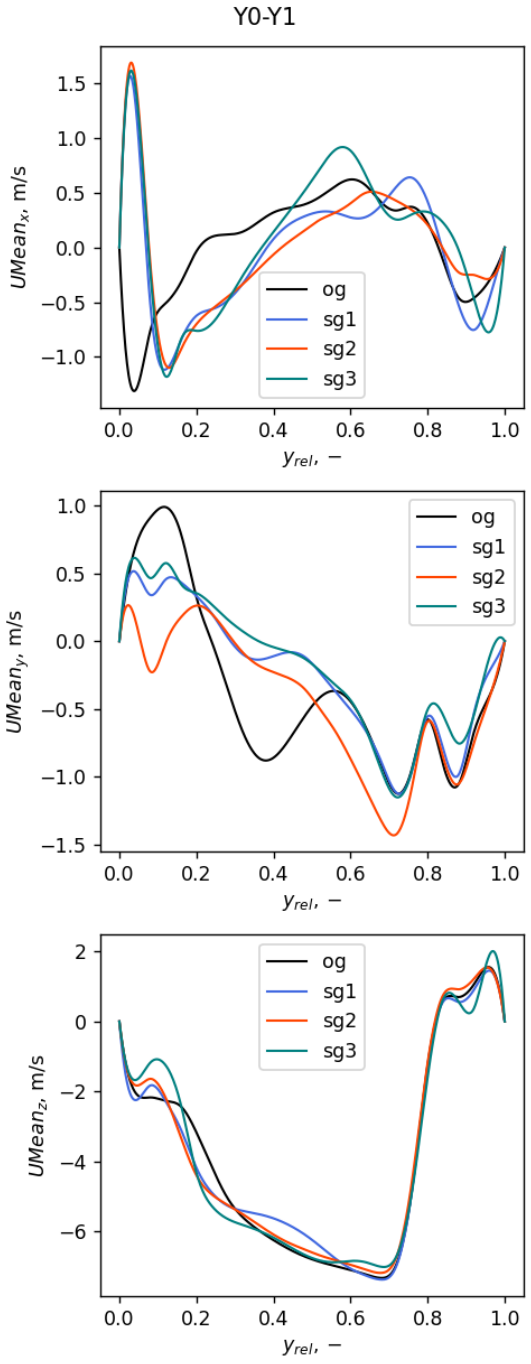

Figure 11. Velocity components along Y0-Y1

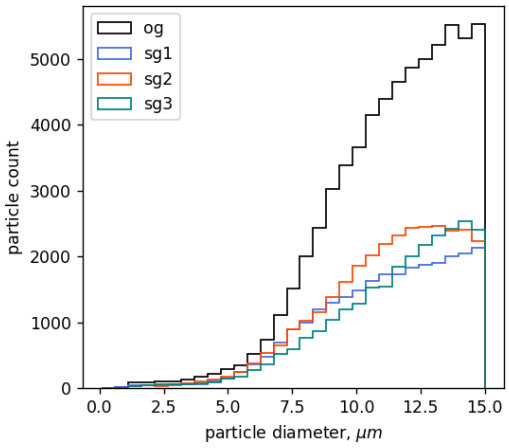

Figure 12. Histogram of the deposited particles in the oral cavity and the throat

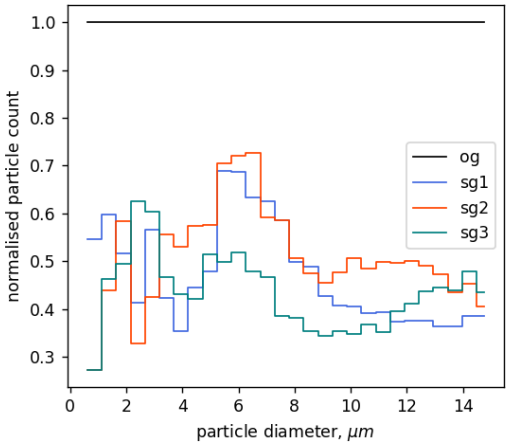

Figure 13. Normalized histogram of the deposited particles in the oral cavity and the throat

ency can be observed for other realistic oral cavity geometries. To enhance the overall performance of the simplification, a more robust and detailed analysis is required. However, it should be noted that such an analysis falls outside the scope of this study.

5. CONCLUSION

In this study, the authors investigated the usability of simplified oral cavity geometries. To this end, numerical unsteady simulations were carried out at a constant flow rate. The study concluded that the geometry of the oral cavity has little to no influence on the velocity field downstream of the throat at the inlet of the trachea. Furthermore, simplification reduced the resistance of the investigated region, which was validated by measurements. These findings are particularly beneficial for flow simulations in the airways, given the significance of the tracheal flow profile for flow distribution and particle deposition in the lower airways.

However, particle deposition simulations revealed limitations of the simplification, as the number of deposited particles was underestimated in the simplified geometries compared to the original geometry.

Further research is necessary to improve the performance of simplified oral cavities. This will involve conducting parameter studies at multiple flow rates and investigating the flow field in greater detail. These investigations will form the basis of future work.

ACKNOWLEDGEMENTS

Project no. kdp-ikt-2023-900-i1-00000957/0000003 has been implemented with the support provided by the Ministry of Culture and Innovation of Hungary from the national research, development and innovation fund, financed under the kdp-2023 funding scheme.

The scientific work/research and/or results publicised in this article were reached with the sponsorship of the Gedeon Richter Talentum Foundation in the framework of the Gedeon Richter Excellence PhD Scholarship of Gedeon Richter.

We acknowledge the Digital Government Development and Project Management Ltd. for awarding us access to the Komondor HPC facility based in Hungary.

REFERENCES

[1] ICRP, 1994, “Human Respiratory Tract Model for Radiological Protection”, *ICRP Publication 66 Ann ICRP 24 (1-3)*.

[2] Hofmann, W., 2011, “Modelling inhaled particle deposition in the human lung—A review”, *Journal of Aerosol Science*, Vol. 42 (10), pp. 693–724.

[3] Koullapis, P., Nicolaou, L., and Kassinos, S., 2018, “In silico assessment of mouth-throat effects on regional deposition in the upper tracheobronchial airways”, *Journal of Aerosol Science*, Vol. 117, pp. 164–188.

[4] Heenan, A. F., Finlay, W. H., Grgic, B., Pollard, A., and Burnell, P. K., 2004, “An investigation of the relationship between the flow field and regional deposition in realistic extra-thoracic airways”, *Journal of Aerosol Science*, Vol. 35, pp. 1013–1023.

[5] Grgic, B., Finlay, W. H., Burnell, P. K., and Heenan, A. F., 2004, “In vitro intersubject and intrasubject deposition measurements in realistic mouth–throat geometries”, *Journal of Aerosol Science*, Vol. 35, pp. 1025–1040.

[6] Xi, J., and Longest, P. W., 2007, “Transport and deposition of micro-aerosols in realistic and simplified models of the oral airway”, *Annals of Biomedical Engineering*, Vol. 35, pp. 560–581.

[7] Nicolaou, L., and Zaki, T. A., 2013, "Direct numerical simulations of flow in realistic mouth–throat geometries", *Journal of Aerosol Science*, Vol. 57, pp. 71–87.

[8] Xi, J., Yuan, J. E., Yang, M., Si, X., Zhou, Y., and Cheng, Y. S., 2016, "Parametric study on mouth–throat geometrical factors on deposition of orally inhaled aerosols", *Journal of Aerosol Science*, Vol. 99, pp. 94–106.

[9] Pharmacopeia, U., 2005, "Physical tests and determinations: Aerosols, nasal sprays, metered-dose inhalers, and dry powder inhalers", *United States Pharmacopeia First Supplement, 28-NF, General Chapter (601)*, p. 3298 – 3316, cited by: 6.

[10] Feng, Y., Zhao, J., Kleinstreuer, C., Wang, Q., Wang, J., Wu, D. H., and Lin, J., 2018, "An in silico inter-subject variability study of extrathoracic morphology effects on inhaled particle transport and deposition", *Journal of Aerosol Science*, Vol. 123, pp. 185–207.

[11] Koullapis, P., Kassinos, S., Bivolarova, M., and Melikov, A., 2016, "Particle deposition in a realistic geometry of the human conducting airways: Effects of inlet velocity profile, inhalation flowrate and electrostatic charge", *Journal of Biomechanics*, Vol. 49 (11), pp. 2201–2212, selected Articles from the International Conference on CFD in Medicine and Biology (Albufeira, Portugal – August 30th - September 4th, 2015).

[12] Atzeni, C., Lesma, G., Dubini, G., Masi, M., Rossi, F., and Bianchi, E., 2021, "Computational fluid dynamic models as tools to predict aerosol distribution in tracheobronchial airways", *Scientific Reports 2021 11:1*, Vol. 11, pp. 1–13.

[13] Worth Longest, P., and Vinchurkar, S., 2007, "Validating CFD predictions of respiratory aerosol deposition: Effects of upstream transition and turbulence", *Journal of Biomechanics*, Vol. 40 (2), pp. 305–316.

[14] Ma, Z., Kourmatzis, A., Milton-McGurk, L., Chan, H.-K., Farina, D., and Cheng, S., 2022, "Simulating the effect of individual upper airway anatomical features on drug deposition", *International Journal of Pharmaceutics*, Vol. 628, p. 122219.

[15] Koullapis, P., Kassinos, S., Muela, J., Perez-Segarra, C., Rigola, J., Lehmkuhl, O., Cui, Y., Sommerfeld, M., Elcner, J., Jicha, M., Saveljic, I., Filipovic, N., Lizal, F., and Nicolaou, L., 2018, "Regional aerosol deposition in the human airways: The SimInhale benchmark case and a critical assessment of in silico methods", *European Journal of Pharmaceutical Sciences*, Vol. 113, pp. 77–94, a special issue dedicated to COST Action SimInhale: cross-disciplinary perspective on the current state of the art and challenges in pulmonary drug delivery.

[16] Spasov, G. H., Rossi, R., Vanossi, A., Cottini, C., and Benassi, A., 2022, "A critical analysis of the CFD-DEM simulation of pharmaceutical aerosols deposition in extra-thoracic airways", *International Journal of Pharmaceutics*, Vol. 629, p. 122331.

[17] Sommerfeld, M., Sgrott, O., Taborda, M., Koullapis, P., Bauer, K., and Kassinos, S., 2021, "Analysis of flow field and turbulence predictions in a lung model applying RANS and implications for particle deposition", *European Journal of Pharmaceutical Sciences*, Vol. 166, p. 105959.

[18] Bass, K., and Worth Longest, P., 2018, "Recommendations for simulating microparticle deposition at conditions similar to the upper airways with two-equation turbulence models", *Journal of Aerosol Science*, Vol. 119, pp. 31–50.

[19] Talaat, M., Si, X., and Xi, J., 2022, "Effect of MDI Actuation Timing on Inhalation Dosimetry in a Human Respiratory Tract Model", *Pharmaceuticals*, Vol. 15 (1).

Conference on Modelling Fluid Flow (CMFF'25)
The 19th International Conference on Fluid Flow Technologies
Budapest, Hungary, August 26-August 29, 2025

Influence Of Cut-Back Leading Edges On Efficiency And Functionality For An Optimized Semi-Open 2-Channel Impeller

David BECK[1], Paul Uwe THAMSEN[2]

[1] Corresponding Author. Chair of Fluid System Dynamics, Institute of Fluid Mechanics and Technical Acoustics, Technische Universität Berlin. Straße des 17. Juni 135, 10623 Berlin, Germany. Tel.: +49 30 314 70941, E-mail: david.beck@tu-berlin.de
[2] Chair of Fluid System Dynamics, Institute of Fluid Mechanics and Technical Acoustics, Technische Universität Berlin. Straße des 17. Juni 135, 10623 Berlin, Germany. E-mail: paul-uwe.thamsen@tu-berlin.de

ABSTRACT

This publication describes the design of a semi-open 2-channel wastewater impeller, that is optimized for its efficiency with the help of response surface optimization. For the optimal design, a prototype is manufactured out of stainless steel that is able to hold different blade leading edge geometries. For the basic modification, the leading edges from the resulting optimal design from the response surface optimization are examined on the test rig with regard to maximum clear water efficiency and functionality. The functionality is tested with the help of two different test procedures: an optical test to investigate the interaction between duster and impeller with the help of a highspeed camera and an endoscope as well as the long-time functional performance test. Different modifications with cut-back leading edges and different hub designs are designed and are also examined in terms of their maximum clear water efficiency and functionality in order to be able to assess the deviation in maximum efficiencies by gaining functionality. The results show that the efficiency-optimized impeller has a high susceptibility to clogging. The modifications of the leading edges show significant improvements on the functionality by slight reduced efficiencies.

Keywords: clogging, functional performance, optical measurements, optimization, test rig, wastewater pump

NOMENCLATURE

D_{LTF}	$[-]$	degree of long-time functional performance
H	$[m]$	head
P	$[kW]$	mechanical power
Q	$[m^3/h]$	flow rate
m_W	$[g]$	mass of duster
n	$[1/min]$	rotational speed
n_q	$[1/min]$	specific speed
u	$[\%]$	position of leading edge
β	$[°]$	blade angle
η	$[-]$	pump efficiency
ϕ	$[°]$	wrap angle

Subscripts and Superscripts

CW	clear water
H	hub
$L25$	low contamination
$L50$	medium contamination
$MOD0$	modification 0
$MOD1$	modification 1
$MOD2$	modification 2
OP	operating point
S	shroud
h	hydraulic
m	mechanic
$0-60$	averaged over 60 minutes
1	position of leading edge
2	position of trailing edge

1. INTRODUCTION

The demands on wastewater pumps are increasing due to the large number of solids in wastewater. Both high energy efficiency and high availability of wastewater pumps are required [1]. The availability of wastewater pumps is particularly challenged by tear-resistant fibrous materials in wastewater, as these are typical for pump failures [2].

In [3] it was already shown that the efficiency of the entire aggregate has no correlation to the susceptibility to clogging. Furthermore, it was shown that neither the impeller type nor the performance class have an influence on the functionality. Moreover, it has already been shown in [4, 5], that geometric modifications of a wastewater impeller can significantly increase the functionality of wastewater pumps. However, in these previous works, the aim was purely to increase functionality without reference to maintaining maximum efficiency. Within the scope of this publication, the functionality is investigated

accordingly, starting from an efficiency-maximized impeller and optimized by geometric steps to improve the clogging behaviour, whereby the focus is on maintaining maximum efficiency.

2. DESIGN OF OPTIMIZED IMPELLER

The impeller for the investigation is designed as a semi-open 2-channel impeller. For this purpose, a basic impeller is designed, which is then optimized by means of response surface optimization (RSO) to obtain a maximum clear water efficiency. For this basic impeller design, the flow rate Q is selected to 400 m^3/h at a head H of 24 m for the design point. With a design speed n of 1487 min^{-1}, the specific speed n_q results in 45.7 min^{-1}.

In order to be able to estimate the attainable target for the efficiency-optimized impeller, the expected maximum efficiency is first considered. Based on [6], a single stage, single-suction volute casing pump achieves a maximum efficiency for a flow rate Q of 360 m^3/h at a specific speed n_q of 45 min^{-1} a clear water efficiency η_{Pump} of approx. 89 %. As this is a wastewater impeller with only two blades, the efficiency factor according to [7] for 2-channel wastewater impellers is used. This factor varies between 0.8 - 0.98. Therefore, the clear water efficiency η_{Pump} results in an expected efficiency range between 71 and 87 %. However, it should be emphasized that this estimate covers both semi-open and closed 2-channel impellers. Since semi-open impellers have lower efficiencies than closed impellers due to the lack of a shroud and the resulting gap between the tips of the impeller blades and housing, efficiencies up to 80 % are assumed on the test rig.

In addition, boundary conditions are defined for the design impeller that remain unchanged during the RSO. The outlet diameter and the outlet width of the impeller are defined and adapted to the existing volute. This volute is used because previous tests have already shown that its design is not susceptible to clogging. The volute casing has a suction side diameter of 200 mm with a discharge side size of 150 mm. In addition, the impeller is required to have three-dimensional blades that can be varied for both the inner and outer streamlines as part of the optimization process. As the bearing housing for the volute casing is already present, the dimensions of the impeller screw are also predetermined. The blade thickness is 10 mm and is also kept constant across all optimization variants. The blade leading edges for the optimization have an elliptical profile in each sample point.

2.1. Impeller Optimization

For the setup of the RSO, the basic impeller is selected. The volute casing used for the simulation is redesigned based on the existing volute casing and contains the same cross-sectional profile.

The simulations of the basic design and the RSO are carried out as stationary simulations using RANS-equations in a coupled solver with the CFX software. The high resolution scheme is used for numerical discretization and turbulence numerics, using second order central differencing. The SST model is used for turbulence modeling in order to achieve good resolution and convergence both in near-wall areas and free streams [8]. The impeller and the volute casing are meshed with unstructured meshes. The blades as well as the hub of the impeller and the volute casing wall are meshed with prism layers. A dimensionsless wall distance between 30 and 50 is used for the impeller and volute casing, whereby logarithmic wall laws are used. The impeller is calculated as a closed impeller, which means that the gap between the tips of the blades and the frontliner used later in the experiment is not calculated. Furthermore, the impeller back shroud cavity is not considered in the simulation as well. In addition, the domain is given an inlet pipe in front of the suction side of the impeller and an extension on the volute casing. Both pipes are treated as frictionless and are unstructured meshes as well. Stationary coupling models between the rotating impeller and the inlet pupe as well as the volute are used in which the flow variables are transferred axially averaged between the domains. For the convergence criterion, the residuals are set to 10^{-5} by using root mean square (RMS).

For the simulation with the basic impeller and the geometrically similar volute casing, a mesh independence analysis is first carried out, which contains a coarse, a medium and a fine mesh for the impeller. The results for the efficiency are shown in Figure 1.

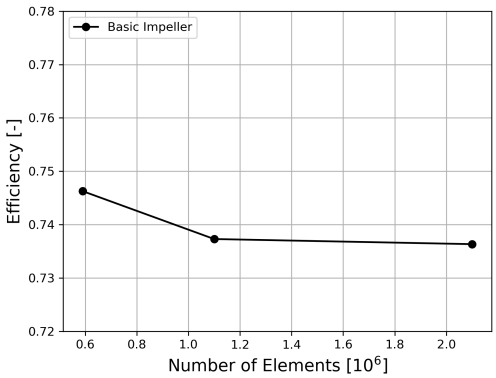

Figure 1. Mesh independence analysis

As can be seen in Figure 1, the deviation between the medium and fine mesh is 0.13 % in efficiency, which is why the medium mesh is used for the RSO. The sample method for the RSO is latin hypercube sampling (LHS). This is due to the fact, that LHS ensures that each parameter is represented in a full manner [9]. For the LHS method, 200 samples are used for the design of experiment (DOE).

A total of ten parameters of the impeller are changed as part of the optimization. Five parameters are selected equally for both the outer (shroud)

and inner (hub) streamline. These include the blade angle of the leading edge β_1 and the blade angle of the trailing edge β_2, the relative starting position of the leading edge u, which influences the diameter of the leading edge accordingly, and, starting from a common baseline, the wrap angle of the leading edge ϕ_1 and the wrap angle of the trailing edge ϕ_2. The parameters vary from the basic design in the direction of both higher and lower values. Figure 2 shows the varied parameters, illustrated using the example of the designed basic impeller for the RSO.

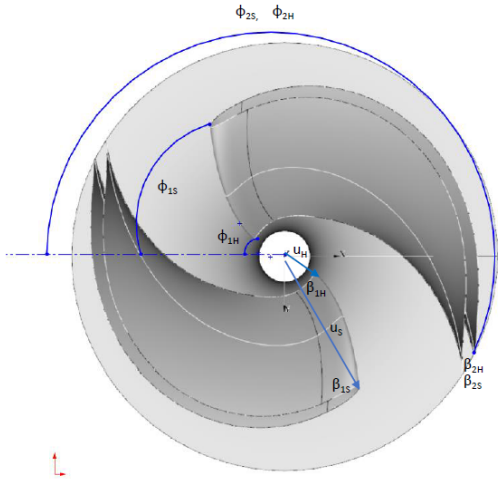

Figure 2. Parameters for DOE

The head H and the efficiency η_{Pump} of the simulated impeller are used as output parameters. The focus here is on maximizing the efficiency, the head plays a subordinate role.

Figure 3 shows the results of the DOE. The sensitivity of the individual varied parameters in relation to the basic impeller with regard to the influence on the efficiency is shown.

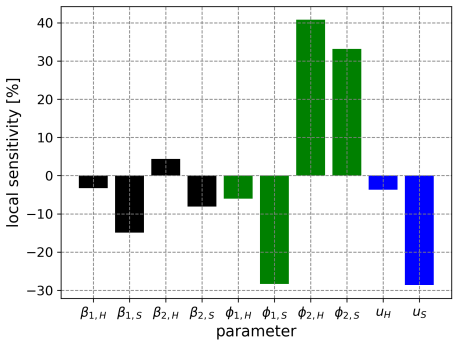

Figure 3. Local sensitivity analsysis for η_{Pump}

Figure 3 shows in particular that increased wrap angles at the outlet ϕ_{2H} and ϕ_{2S} have a significant positive influence on the efficiency of the impeller. In contrast, increased wrap angles at the inlet ϕ_1, especially on the outer streamline ϕ_{1S}, have a negative effect on the efficiency of the basic impeller. The blade angles at the inlet $\beta_{1,H}, \beta_{1,S}$ and outlet $\beta_{2,H}, \beta_{2,S}$ have a subordinate influence. In addition, the position of the leading edge on the outer streamline u_S is decisive for the efficiency of the impeller, while the position of the leading edge on the inner streamline u_H has a minor effect on efficiency. Especially for the outer streamline increased starting positions, which correspond to increased diameters, have a significant reduction in efficiency. This indicates as well, that longer blades, that are starting directly at the suction side of the impeller, are increasing the efficiency for this application.

Based on the individual sample points, it can be seen that particularly high wrap angles lead to high efficiencies. As different blade geometries are to be examined in the further course of the investigations, a target value for a wrap angle at the trailing edge is specified for the optimization in addition to a target value for the maximum efficiency. This wrap angle target value is also selected to be the same for both the inner and outer streamline of the blades, as a two-dimensional trailing edge is desired. The latter is because the use of different blade inlet geometries would otherwise result in unwanted narrow passages between one leading edge and the other blade. The requirements for the optimization are therefore maximizing the efficiency as well as achieving a wrap angle at the trailing edge ϕ_2 of 210° for both streamlines.

For the optimization, the non-dominant sorting genetic alorithm II (NSGA-II) is used as an optimization-algorithm. The selected candidate for optimization meets the boundary conditions of an almost two-dimensional trailing edge with a maximum wrap angle for the end of the blade of approx. 210°. Overall, the impeller has a wrap angle of 189° per blade. In addition, there is a maximum efficiency of 84.2% for the NSGA-II, which results in a simulated efficiency of 83.6% in the geometrically similar volute for the optimization. Due to the range for the estimated efficiency for the semi-open 2-channel impeller, the candidate for the prototype is chosen as the basic modification (MOD 0) for the prototype.

2.2. Prototype Manufacturing

In order to test both the optimized blade geometry and cut-back variants of this blade, a stainless steel prototype is manufactured. This is designed according to the optimized blade contour given by the RSO. In order to be able to test different leading edges in one prototype, the leading edge of the optimized contour for the stainless steel impeller is cut off by 40 % of the outlet diameter and provided with holes on the hub and shroud to which the different leading edges can be screwed as modifications, which are manufactured via 3D-printing. The materials used for the leading edges are polycarbonate (PC) for the optimized blade leading edges (MOD

0) and polylactide (PLA) for the other modifications (MOD 1-2). PC offers increased strength, which is necessary due to the long contour of the optimized blade leading edges, especially regarding the outer streamline. PLA allows fast and cost efficient printing.

To ensure that the impeller has the same gap width of 0.3 mm between the blades and frontliner despite different modifications, an adapter plate is also used, which is screwed onto the back of the stainless steel impeller. This adapter plate holds the shaft-hub connection and represents the same installation situation on the shaft. The frontliner has one groove in all tests, which is used to convey the dusters.

2.3. Impeller Variation

A total of three modifications are used for the impeller in this publication. On the one hand, the blade leading edges resulting from the RSO are used as modification 0 (MOD 0), which form the baseline for the efficiency and functionality measurements. On the other hand, cut-back blade leading edges are implemented, which have the aim of increasing the functionality by slipping off the dusters on the leading edge, while the efficiency is to be maintained. In the first step, the outer streamline of the leading edge is cut-back to 40 % length in relation to the outlet diameter of the impeller, while the inner streamline is unchanged to achieve a resulting curvature between both streamlines. The blade thickness and the elliptical profile remain unchanged. This first modification is continuously described as MOD 1. In addition, starting from MOD 1, the blade leading edges are thickened to 40 mm on the inner streamline in the direction of the impeller screw, which should enable improved slippage. This thickening tapers towards the outer streamline to the thickness of the original blade. In addition, the hub area is reworked to create a plateau between the blades. This plateau is created because previous tests have not only shown severe clogging at the leading edges but also clogging at the screw and hub geometry. This second modification is continuously referred to as MOD 2. Figure 4 shows the individual modifications installed in the stainless steel prototype.

3. TEST SETUP

A clogging test rig at the Chair of Fluid System Dynamics at the Technische Universität Berlin is used for the tests. Three different tests are carried out on this test rig for the various impeller modifications. The first test is a clear water test to record all characteristic values and determine the best efficiency point (BEP). For this purpose, a torque measuring shaft is used on the test rig for the pump in order to record the mechanical power at the pump coupling P_m by measuring the speed with an accuracy of $\pm\,0.05\,\%$ and the torque with an accuracy of $\pm\,0.03\,\%$. Furthermore, a flow meter is used in the pressure pipe of the test rig to measure the flow rate Q with an accuracy of

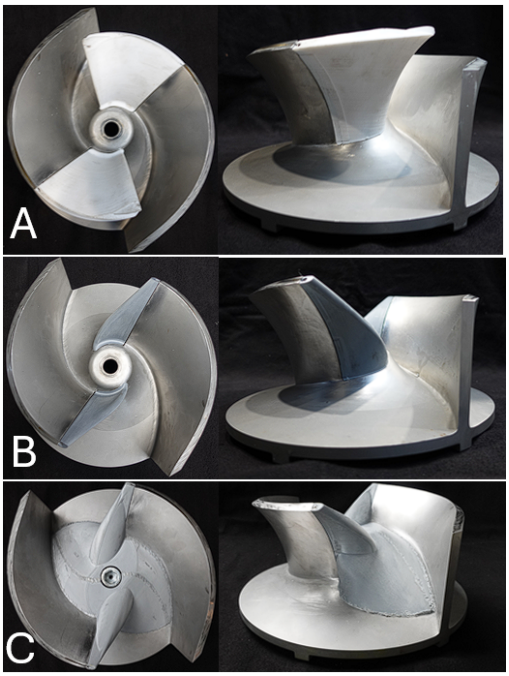

Figure 4. Tested modifications: A) optimized contour MOD 0, B) 40 % cut-back leading edge MOD 1, C) thickened inner streamline MOD 2

$\pm\,0.2\,\%$ and calculate the velocities inside the suction and pressure pipe. A differential pressure sensor with an accuracy of $\pm\,0.5\,\%$ is used to obtain the differential pressure and calculate the head H. With these, the hydraulic power P_h is calculated and the pump efficiency η_{Pump} is calculated with equation 1 [10]:

$$\eta_{Pump} = \frac{P_h}{P_m} \tag{1}$$

The second test is the long-time functional performance test, which is also listed in the DWA-A 120-2 [11] standard. Artificial wastewater is premixed in various contamination classes using tear-resistant dusters. These contamination classes are the low contamination L25, which corresponds to 25 dusters per cubicmeter of water, the medium contamination class L50 with 50 dusters per cubicmeter of water and the high contamination class L100, which represents 100 dusters per cubicmeter of water. Due to the discharge side size of 150 mm for the given volute casing, the tests are carried out with 3 m^3 of water. To carry out the long-time functional performance test, the dry weight of the dusters is determined according to the contamination class. The dusters are inserted into the wastewater tank (WWT). After the dusters have been added, the artificial wastewater is pumped from the WWT back into the WWT for 60 minutes. During the test, the flow rate Q, the head H, the mechanical power P_m and the pump efficiency η_{Pump} are recorded every second. Figure 5 shows the scheme of the long-time functional performance test.

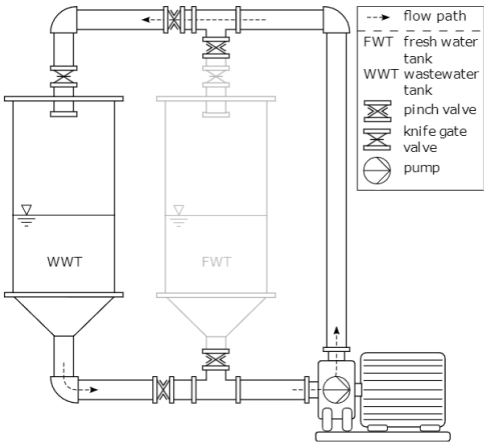

Figure 5. Scheme of the long-time functional performance test [12]

At the end of the 60-minute test period, the pump is switched off, drained and opened. Possible blockages are documented, dried and also weighed. Using the dry weight $m_{W,total}$ added, the weight of the remaining blockages within the pump $m_{W,Pump}$ and the ratio of the average efficiency during the 60-minute test duration $\eta_{test,0-60}$ and the corresponding clear water efficiency at the respective operating point $\eta_{CW,OP}$, the degree of long-time functional performance D_{LTF} is determined according to equation 2.

$$D_{LTF} = \frac{1}{2}\frac{m_{W,total} - m_{W,Pump}}{m_W, total} + \frac{1}{2}\frac{\eta_{test,0-60}}{\eta_{CW,OP}} \qquad (2)$$

A pump is considered to have a low susceptibility to clogging if the D_{LTF} is greater than or equal to 0.7. This value is also the target criterion for the modifications of the prototype impeller in the context of this publication to obtain an impeller with high functionality. The accuracy of the long-time functional performance test is specified according to [13] with an interquartile range of 9 %.

The third test method is an optical measurement, as presented in [14]. For this purpose, a ring made of polymethyl methacylate (PMMA) is connected to the suction side of the pump, which has 8 LED units. Each LED unit has 5595 luminous flux. A polyvinyl chlroide (PVC) ring is also connected in front of the PMMA light ring, which can accommodate a 45° endoscope. In addition, a high-speed camera is connected to the endoscope, which visualizes the interaction between the duster and the impeller at 1000 frames per second. For the tests, 10 dusters per cubic meter of water are used.

These three test procedures are used to evaluate both the efficiency and the functionality of the various modifications.

4. EXAMINATION RESULTS

4.1. Results - Efficiency

Figure 6 shows the results of both the simulated point of the selected optimization candidate with geometrically similar volute and the clear water measurements of MOD 0- MOD 2 on the test rig.

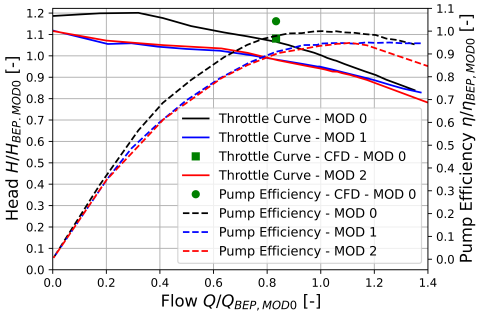

Figure 6. Clear water results for MOD 0-2

When comparing the CFD results for the optimized geometry with a geometrically similar volute to the clear water measurement with the given volute, it is striking that the simulated head of 27.8 m is almost achieved by the clear water measurement for MOD 0. Nevertheless, it can be seen that the simulated efficiency of 83.6 % is not achieved. For the clear water measurement of MOD 0, the BEP has increased in the direction of higher volume flows compared to the design volume flow with a flow rate Q of 480 m^3/h, a head H of 25.7 m and a clear water efficiency of η_{Pump} 80.1 %. Accordingly, the simulated maximum efficiency is relatively 4.4 % above the measured result. This can be related to the assumptions made for the simulation, meaning the use of a stationary simulation without a gap between frontliner and blade tips as well as the lack of the back shroud cavity. In relation to the expected range for maximum efficiency presented in Chapter 2, the results of MOD 0 are within the expected scope.

The clear water results for MOD 1 and MOD 2 each show a reduction in the head H above the flow rate Q due to the shortened blades. In addition, it can be seen that the throttling curves of MOD 1 and MOD 2 are nearly similiar, meaning that the thickening of the inner streamline of the blades and the covering of the impeller screw have a subordinate influence on the hydraulic performance of the impeller in contrast to the blade length. It is also noticeable that cutting back the blade leading edge shifts the BEP of the individual modifications in the direction of higher flow rates. The maximum efficiencies of MOD 1 and MOD 2 are always below the efficiency of MOD 0 due to the modifications of the blade and result in 94.8 % for MOD 1 and 94.9 % for MOD 2 compared to MOD 0. Due to the shift towards higher volume flows, the heads of the two modifications with a shorter blade leading edge are corres-

pondingly lower in the BEP compared to MOD 0, while the mechanical power is higher. Table 1 shows the values of the BEP in relation to MOD 0.

Table 1. BEP results for MOD 0-2

MOD	0	1	2
η/η_{MOD0}	1.000	0.948	0.949
Q/Q_{MOD0}	1.000	1.083	1.104
H/H_{MOD0}	1.000	0.922	0.911
P/P_{MOD0}	1.000	1.050	1.059

4.2. Results - Functionality

For all modifications, the long-time functional performance tests with low contamination L25 in the BEP and optical examinations in the BEP are carried out and compared.

MOD 0: The long-time functional performance test with low contamination for MOD 0 is aborted after approx. 280 seconds of measurement due to a blade breakage of one of the two PC blades. Despite the very short measuring time, a total of 283 g of 283 g of dusters are collected inside the impeller. This results in a $D_{LTF,L25,MOD0}$ of 0.24 with an average normalized pump efficiency during the test of 47.3 %. Even after the short measurement period, this reduced efficiency results from an increase in mechanical power to 111.8 % compared to their clear water value, while the flow rate drops to 78.9 % and the head to 66.1 % compared to the clear water values. The clogging pattern within the impeller after the test and the findings of the optical tests in particular explain why the hydraulically optimized contour is not suitable for media containing fibers. The individual dusters are layered over the leading edges so that subsequent dusters accumulate on them. The blade leading edge, which does not have a sloping edge between the inner and outer streamline, prevents the dusters from slipping off. Figure 7 A) shows an image from the optical test. It can be seen that both blades are covered by dusters. This blockage grows together over the hub area and covers the impeller screw. Figure 7 B) shows the clogging pattern after the long-time functional performance test has been stopped.

MOD 1: The optical tests with 10 dusters per cubic meter show an improved slipping behaviour of the dusters at the leading edges of the blades, as shown in Figure 8.

Figure 8 A) shows a duster that lies on one of the two leading edges. Due to the cut-back of the outer streamline of the blade and the resulting curvature between the outer and inner streamlines, the duster slides along the blade in the direction of the frontliner. Figure 8 B) shows the same experiment after approx. half a revolution. The applied duster has moved in the direction of the outer streamline and ultimately slips towards the suction side of the blade, which shows an improvement compared to MOD 0. However, the optical examinations also show a clogging-prone scenario of MOD 1. Dusters that hit the center of the impeller and thus directly on the hub and on the inner streamline of the blade are not removed and form the beginning of an accumulation. Further arriving dusters are deposited on this initial blockage and grow together over the blades. This initial blockage is shown in Figure 9, in which dusters are attached over the impeller screw and the inner streamline of the blade leading edge and are not discharged until the end of the optical measurement. The low blade thickness on the inner streamline in particular means that there is no slipping behaviour in the optical tests, if the dusters already cover the screw.

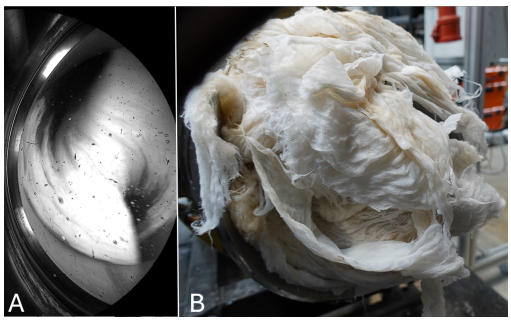

Figure 7. Results for MOD 0. A) accumulation on hub and leading edge during optical investigation, B) blockage inside impeller for L25

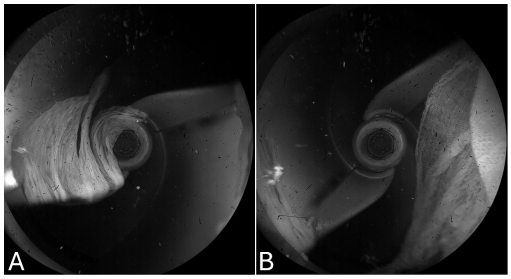

Figure 8. Optical results for MOD 1. A) duster attached on leading edge, B) slipping off duster into channel after half a revolution

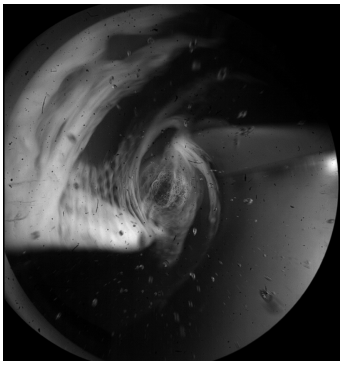

Figure 9. Optical results for MOD 1: clogging on hub, leading edge and impeller screw

This behaviour is also reflected in the long-time functional performance test with low contamination class at BEP. In this test, a total of 221 g of 284 g of dusters are absorbed by the impeller, which corresponds to an improvement compared to the clogging behaviour of MOD 0. Over 60 minutes of measurement, MOD 1 achieves a relative average pump efficiency of 78.9 % compared to clear water operation, which is mainly due to increased mechanical power. This amounts to 115.0 % compared to clear water value, while the volume flow of 97.0 % and the head of 93.5 % are close to the clear water operation. Overall, the $D_{LTF,L25,MOD1}$ is 0.50, which is due to the improved hydraulic performance and the lower absorbed weight during the test. Figure 10 shows the clogged impeller after the end of the long-time functional performance test.

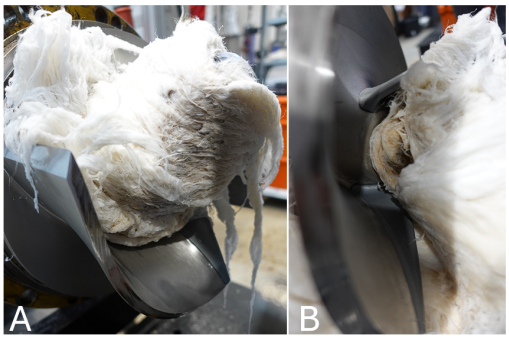

Figure 10. Results for MOD 1: B) accumulation of dusters after completion of test L25, B) accumulation attached to impeller screw

In Figure 10 A) the blockage of 221 g can be seen. Part B) of the figure shows that after lifting the accumulation of dusters, the blockage has grown together over the impeller screw, as could already be observed in the optical examination.

Overall, this results in a gain in functionality of 0.26 for MOD 1, even if this is accompanied by a relative drop in clear water efficiency of 5.2 %, compared to MOD 0.

MOD 2: The optical investigations for MOD 2 show improved slipping behaviour compared to the previous modifications. Figure 11 A) shows two dusters hitting the hub directly. In B), each of these dusters slips into a blade channel after one revolution. The thickened inner streamline of the leading edge helps the dusters to slide either into the blade channel or in the direction of the outer streamline of the leading edge. The plateau, which covers the impeller screw prevents the dusters from sticking on the hub, eventhough a relatively long dwell time of the dusters can be seen during the optical examinations. Due to the flat contour of the plateau, some dusters need several revolutions to be conveyed from the hub towards the channel.

The long-time functional performance test with low contamination L25 in BEP shows a significantly better result compared to the previous modifications. After 60 minutes of measurement, no dusters have accumulated inside the pump. With an average relative efficiency of 95.5 %, this results in a $D_{LTF,L25,MOD2}$ of 0.98 and is therefore above the required 0.7. The mechanical power is unchanged during the test compared to the clear water value, the hydraulic data shows a minimal decrease due to the pumping of the textiles. This results in an average flow rate of 98.6 % and a head of 96.8 % compared to the clear water values.

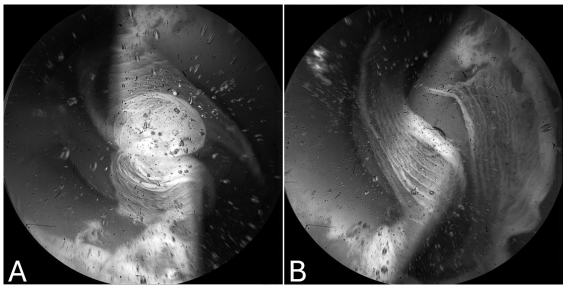

Figure 11. Optical results for MOD 2. A) two incoming dusters on the plateau, B) dusters slipping off into blade channels after one revolution

In addition, due to a result for the $D_{LTF,L25,MOD2}$ greater than 0.7, the long-time functional performance test for MOD 2 is also carried out with medium contamination. In this case, a blockage of 395 g of a total of 572 g of added mass builds up. With an average efficiency over the test duration of 60.7 %, this results in a $D_{LTF,L50,MOD2}$ of 0.46. The flow rate drops to 85.5 % and the head to 75.9 % of the clear water value, while the mechanical performance increases to 107.0 %. Images of the blockages after the end of the test for medium contamination can be seen in Figure 12.

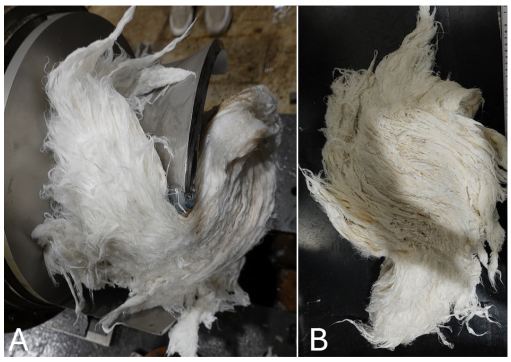

Figure 12. Results for MOD 2: A) clogging inside impeller after completion of test L50, B) removed blockage L50

This behaviour can also be found in the optical tests. Individually arriving dusters slide to the outer streamline, where they are removed by the groove in the frontliner. Due to the fact that only one groove

is used, the dwell time of the dusters on the blades is also too long here. If many dusters hit a blade, an accumulation builds up on the entire leading edge, as can be seen on one blade in the left side of Figure 13. Sliding is no longer possible with this accumulation, so the blockage grows together in the direction of the hub.

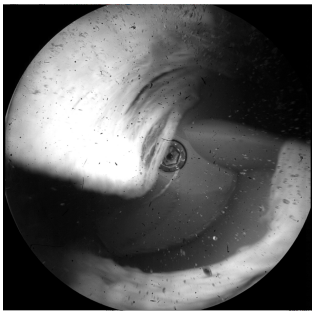

Figure 13. Optical results for MOD 2: clogging scenario on one leading edge

Overall, MOD 2 shows a greatly improved clogging behaviour compared to the previous modifications with a result above the required 0.7 for low contamination while achieving a similiar clear water efficiency compared to MOD 1. In order to further improve the clogging behaviour especially for higher contamination classes, the hub geometry should be further revised to minimize the dwell time of the dusters. In addition, a frontliner with a higher number of grooves should be tested.

5. CONCLUSION

The results of the simulation have shown that the RSO can achieve high efficiencies for wastewater impellers, which are well within the expected efficiency ranges for the corresponding specific speed. However, this flow-optimized contour is highly susceptible to clogging, particularly due to the thin blade leading edges that are strongly exposed to the flow. By cutting back these leading edges, improvements in functionality can already be achieved, but these are accompanied by a moderate drop in efficiency. The thickening of the already cut-back leading edges shows considerable advantages in the slipping behaviour of the dusters, especially in the optical investigations, which also results in an increase in functionality.

REFERENCES

[1] Surek, D., 2014, *Pumpen für Abwasser- und Kläranlagen. Auslegung und Praxisbeispiele*, Springer Vieweg.

[2] Höchel, K., Thamsen, P. U., and Rauwald, H., 2012, "Problem Analysis of sewage pumping stations", *Proceedings of the International Rotationg Equipment Conference*, Düsseldorf, Germany.

[3] Beck, D., Steffen, M., and Thamsen, P. U., 2023, "How to measure the functionality of sewage pumps", *Proceedings of 15th Eurpean Conference on Turbomachinery Fluid dynamics & Thermodynamics*, Budapest, Hungary, Vol. ETC15.

[4] Beck, D., and Thamsen, P. U., 2023, "Development of Sewage Pumps with Numerical and Experimental Support", *International Journal of Turbomachinery Propulsion and Power*, Vol. 8(2).

[5] Beck, D., and Thamsen, P. U., 2024, "Optimization of a Closed 2-Channel Impeller with Experimental and Optical Support", *Proceedings of the ASME 2024 Fluids Engineering Division Summer Meeting*, Anaheim, California, USA, Vol. FEDSM2024.

[6] European Association of Pump Manufacturers, E., 1999, *Attainable efficiencies of volute casing pumps*, Elsevier Science Ltd.

[7] Gülich, J., 2008, *Centrifugal Pumps*, Springer.

[8] Versteeg, H. K., and Malalasekera, W., 2007, *An Introduction to Computational Fluid Dynamics*, Pearson Education Limited.

[9] Mckay, M., Beckman, R., and Conover, W., 2000, "A Comparison of Three Methods for Selecting Values of Input Variables in the Analysis of Output from a Computer Code", *Technometrics*, Vol. 42, No. 1, pp. 55–61.

[10] DIN, 2012, "DIN EN ISO 9906: Kreiselpumpen - Hydraulische Abnahmeprüfungen - Klassen 1,2 und 3", *Tech. rep.*, Deutsches Institut für Normung e.V.

[11] DWA, 2022, "Pumpsysteme außerhalb von Gebäuden - Teil 2: Pumpstationen und Drucksysteme", *Tech. rep.*, Deutsche Vereinigung für Wasserwirtschaft, Abwasser und Abfall e.V.

[12] Brokhausen, F., Herfurth, E., Beck, D., and Thamsen, P. U., 2023, "Exploring characteristics of time-resolved signals in the operation of wastewater pumps", *Proceedings of 15th Eurpean Conference on Turbomachinery Fluid dynamics & Thermodynamics*, Budapest, Hungary, Vol. ETC15.

[13] Pöhler, M., 2020, "Experimentelle Entwicklung eines standardisierten Abnahmeverfahrens für Abwasserpumpen", Ph.D. thesis, Technische Universität Berlin.

[14] Steffen, M., 2023, "Experimentelle Untersuchung der Verstopfungsmechanismen eines Abwasserlaufrades durch Visualisierung der Textil-Laufrad-Interaktion", Ph.D. thesis, Technische Universität Berlin.

Conference on Modelling Fluid Flow (CMFF'25)
The 19th International Conference on Fluid Flow Technologies
Budapest, Hungary, August 26 - August 29, 2025

DYNAMICS AND COLLISION OF NON-SPHERICAL ELLIPSOID PARTICLES IN TURBULENT CHANNEL FLOW

Connor NOLAN[1], Lee MORTIMER[2], Peter JIMACK[3], Michael FAIRWEATHER[4]

[1] Corresponding Author. EPSRC Centre for Doctoral Training in Future Fluid Dynamics, Faculty of Engineering and Physical Sciences, University of Leeds. Leeds LS2 9JT, United Kingdom. E-mail: mm18cn@leeds.ac.uk
[2] School of Chemical and Process Engineering, Faculty of Engineering and Physical Sciences, University of Leeds. Leeds LS2 9JT, United Kingdom. E-mail: l.f.mortimer@leeds.ac.uk
[4] School of Computer Science, Faculty of Engineering and Physical Sciences, University of Leeds. Leeds LS2 9JT, United Kingdom. E-mail: p.k.jimack@leeds.ac.uk
[4] School of Chemical and Process Engineering, Faculty of Engineering and Physical Sciences, University of Leeds. Leeds LS2 9JT, United Kingdom. E-mail: m.fairweather@leeds.ac.uk

ABSTRACT

Non-spherical particle-laden flows in pipes and channels are of importance in numerous industrial, environmental, and biological processes, making their study essential for understanding and optimising particle transport, deposition, and interaction dynamics. In this work the spatial and orientational dynamics of rigid ellipsoidal particles in turbulent channel flow are explored. A high-fidelity spectral element method-based direct numerical simulation is employed to solve for the fluid phase which is coupled to a Lagrangian particle tracker for modelling the dispersed particles. Particle translational motion is governed by inertia, hydrodynamic lift, and drag, while their rotational dynamics is described by the Euler equations of rotation, accounting for external hydrodynamic torques. Quaternions are utilised to track particle orientations over time. Full four-way coupling between the particles and the fluid is implemented, capturing both the influence of the fluid on the particles and the feedback effect of the particles on the continuous phase. The latter is modelled using a local element-based force feedback field in the Navier-Stokes equations. Particle-particle collisions are also resolved. The fluid and particle phases are validated across multiple particle aspect ratios, Reynolds and Stokes numbers with emphasis on reproducing spatial and orientational dynamics consistent with the literature. Fully coupled simulations are then conducted to evaluate collision statistics across all regions of the channel with results being compared to those of spherical particles to elucidate the underpinning micro-scale dynamics present in such flows as well as providing avenues for further research.

Keywords: Collision dynamics, non-spherical particles, turbulent channel flow, Lagrangian particle tracker, four-way coupling

NOMENCLATURE

$\underline{\underline{\boldsymbol{A}}}$	[-]	rotation matrix
A_D	$[m^2]$	projected area normal to drag
A_L	$[m^2]$	projected area normal to lift
C_D	[-]	drag coefficient
C_L	[-]	lift coefficient
$\boldsymbol{F}_D$	$[m/s^2]$	drag force
$\boldsymbol{F}_L$	$[m/s^2]$	lift force
$\boldsymbol{F}_{PG}$	$[m/s^2]$	pressure gradient force on particle
$\boldsymbol{F}_{VM}$	$[m/s^2]$	virtual mass force
$\underline{\underline{\boldsymbol{G}}}$	$[s^{-1}]$	velocity gradient matrix
$\boldsymbol{f}_{PG}$	$[m/s^2]$	pressure gradient force on fluid
$\boldsymbol{f}_{2W}$	$[m/s^2]$	particle force feedback source term
$\boldsymbol{q}$	[-]	quaternion vector
$\boldsymbol{u}_s$	$[m/s]$	slip-velocity
$\boldsymbol{z}'$	[-]	direction of principal particle axis
$\boldsymbol{\Omega}$	$[s^{-1}]$	angular velocity
α	[-]	angle of incidence
δ	$[m]$	half channel height
λ	[-]	aspect ratio
ρ^*	[-]	density ratio
ϕ_p	[-]	volume fraction

Subscripts and Superscripts

p, F	particle, fluid
L, D	lift, drag
PG, VM	pressure gradient, virtual mass
B, τ	bulk, shear
$*$	non-dimensional units (bulk scales)

1. INTRODUCTION

Particle-laden flows are ubiquitous in nature and industry, such as in the formation of riverbeds [1] and the transportation of nuclear waste [2]. In such flows the collision of small, heavy, non-spherical particles occurs frequently, for example in papermaking [3] and in clouds [4]. Understanding both the particle-scale and bulk-scale dynamics in such flows is of importance to be able to effectively predict long-scale phenomena such as deposition, turbulence modulation and blockages. This knowledge allows for the optimisation of processes and ensures the effectiveness and safety of new systems.

In recent years advances in computational performance, direct numerical simulation and Lagrangian particle tracking methodologies have aided the prediction of particle-laden flows at scales relevant to those seen in industry. These models have reproduced many of the bulk-scale dynamics noted in the literature such as turbophoresis and preferential concentration [5]. The development and optimisation of computational fluid dynamics (CFD) has led to these methods surpassing the resolution of experimental methodologies in the study of particle scale interactions. This means that for reliable results first-principles techniques with proven high accuracy, for example direct numerical simulation (DNS) which can resolve relevant length, and time scales down to the Kolmogorov scale [6], currently provide the only means of assessing certain phenomena.

Significant contributions have been made in the study of spherical particle-laden turbulent flows at low-volume fractions ($\phi_p \leq 10^{-6}$) where only the effect of the fluid on the particles is considered in so called one-way coupled simulations. These studies elucidate the mechanisms underpinning particle migration such as preferential concentration and turbophoresis. Preferential concentration is seen most strongly at low Stokes numbers where particle clustering in low-velocity streaks and the near-wall region is noted [7]. Turbophoresis describes the tendency of particles to move towards areas with lower-than-average turbulence kinetic energy and has been shown to scale with the particle Stokes number [8]. The interaction between particles and turbulent structures in the near-wall region has been studied in detail with a wide range of behaviours being noted based upon the material and inertial properties of the system [9]. The dynamics, both translational and rotational, of non-spherical ellipsoidal particles has also been studied using one-way coupled Lagrangian particle tracking (LPT) simulations. Most of the studies on this topic examine prolate ellipsoids with aspect ratios $\lambda > 1$, often referred to in the literature as fibres. It was found that the aspect ratio has little effect on particle clustering, preferential concentration or segregation [10]. An analysis of near-wall dynamics showed that orientational and translational behaviours influence accumulation at the wall with longer fibres being deposited at higher rates. Moreover, it was noted that fibres tend to align with the mean streamwise flow direction near the wall with this alignment being increasingly unstable for higher particle inertia. Complex behaviour is observed in the spanwise and wall-normal directions due to fibre inertia and elongation, with no preferential orientation or significant segregation observed in the channel centre where the turbulent conditions are close to isotropic.

As volume fraction increases ($10^{-6} \leq \phi_p \leq 10^{-3}$) it becomes necessary to account for the impact of the particles back onto the fluid in so-called two-way coupling. This is typically done using the method of particle force feedback on the turbulent fluid phase [11]. Various studies in wall-bounded turbulence found that large particles enhance turbulence while small particles dampen it, and interestingly it has been shown that this effect is muted at low density ratios even when the particle Stokes number is equivalent in each case. In the case of large particle Stokes numbers, the particles have more inertia and are thus less responsive to rapid changes in the local flow, resulting in preferential accumulation in low turbulence regions. This leads to local turbulence attenuation or suppression hindering the energy transfer across turbulence scales [6].

As the volume fraction increases further to around $\phi_p > 10^{-3}$, the translational and rotational motion of the particle begins to be affected by inter-particle collisions which at this point occur very frequently. It is therefore necessary for simulations to be able to detect and resolve such collisions which is computationally expensive, especially in the case of non-spherical particles. Collision-driven turbulent particle-laden flows have been studied extensively, and in one study low Stokes number particle were found to accumulate in regions of irrotational dissipation due to vortex ejection. The authors also noted a relationship between the relative collision velocity and Reynolds number, especially in the case of low Stokes number particles [12]. Work performed simulating a particle-laden vertical channel using a four-way coupled LPT showed that micro particles can modify the fluid turbulence statistics even at very low volume fractions of the order $\phi_p \approx 10^{-5}$ because of the quantity of collisions [13]. Four-way coupling has been applied alongside particle non-sphericity within an LPT but there is little literature quantifying the effect of particle shape on collision dynamics. One study investigated the settling of ellipsoidal particles within isotropic turbulence, finding that ellipsoids collide considerably more often than spherical particles of the same volume and in these collisions the relative velocity was higher [14]. Another study focusing on the collision and coupling effects of high

inertia particles was conducted in [5], revealing that high speed particle collisions lead to larger momentum transfer and directional redistribution, which increases the magnitude and changes the direction of the slip velocity. This study noted the importance of four-way coupling when simulating midrange Stokes numbers.

Various collision detection methods have been developed including nearest-neighbour lists and stochastic models. In this study we use a deterministic partition-based method [15] for collision detection. Post collision calculations are conducted using a hard-sphere model. More sophisticated collision detection algorithms for non-spherical particles have been proposed where the particle volume is approximated by a collection of overlapping fictitious spheres of varying radii [16]. This representation allows for similar contact procedures as those mentioned above for the case of spheres.

The present study aims to advance the understanding of collision dynamics in wall-bounded particle-laden turbulent channel flow, with a focus on the impacts of particle non-sphericity and high inertia. We seek to provide deeper insights into these complex interactions and to generate collision conditions typical of those seen in channels of industrial interest.

2. METHODOLOGY

2.1. Fluid Phase Modelling

To generate accurate predictions of the flow field we utilise the spectral element method-based DNS code Nek5000 [17] to fully resolve all relevant length and time scales. The solver employs an order seven spectral method on each element. We simulate a turbulent channel flow at shear Reynolds number $Re_\tau = u_\tau \delta / \nu_F = 300$, where $u_\tau$is the shear velocity, δ is the half channel height and ν_F is the fluid kinematic viscosity. The reasons for using Nek5000 are twofold, firstly the open-source nature of the solver makes it suitable for modification and extension, secondly the code comes with efficient parallelisation and an extensive history of validation making it an efficient and safe choice. The governing equations for the continuous phase dynamics are the incompressible Navier-Stokes equations, which are given in dimensionless form as follows:

$$\nabla \cdot \boldsymbol{u}_F^* = 0, \tag{1}$$

$$\frac{D\boldsymbol{u}_F^*}{Dt^*} = -\nabla p^* + \frac{1}{Re_B}\nabla^2 \boldsymbol{u}_F^* + \boldsymbol{f}_{PG}^* + \boldsymbol{f}_{2W}^*, \tag{2}$$

where $\boldsymbol{u}_F^*(\boldsymbol{x}^*, t^*)$ is the fluid velocity vector at position $\boldsymbol{x}^*$ and time t^*, $p^*(\boldsymbol{x}^*, t^*)$ is the fluid pressure, $Re_B = u_B \delta / \nu_F$ is the bulk Reynolds number, $\boldsymbol{f}_{PG}^*$ is the constant pressure gradient forcing term and $\boldsymbol{f}_{2W}^*$ is an arbitrary cell-dependent forcing term accounting for two-way momentum exchange between particles and fluid. Parameters marked with an asterisk $(*)$ signify a non-dimensional variable obtained from the bulk properties (δ, u_B, ρ_F) where ρ_F is the density of the fluid. These governing equations are solved on a discretised, structured grid which consists of $27 \times 18 \times 23$ seventh-order spectral elements, equivalent to 3.9 M nodes. Mesh refinement is used in the wall-normal direction, while the distribution of elements is uniform in the streamwise and spanwise directions. For our simulation (x, y, z) correspond to the streamwise, wall-normal and spanwise directions respectively. The simulation domain and corresponding mesh are illustrated in Figure 1.

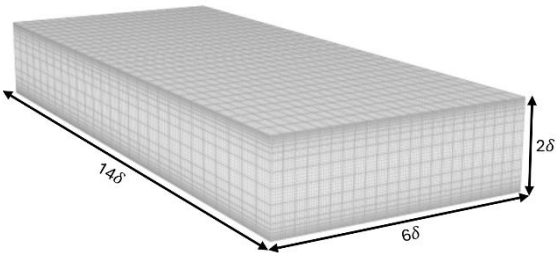

Figure 1. Computational mesh demonstrating element spacings and increased near-wall nodal density

The solver uses a constant time step of $\Delta t^* = 0.0025$. Periodic conditions are imposed in the streamwise and spanwise directions to ensure that the flow remains cyclic. The top and bottom walls at $y^* = \pm 1$ respectively are subject to no-slip and impermeability conditions. The flow is driven by a constant pressure gradient, chosen to obtain a specific Reynolds number, applied in the streamwise direction, the magnitude of which is given as follows:

$$\frac{dp^*}{dx^*} = \left(\frac{Re_\tau}{Re_B}\right)^2. \tag{3}$$

2.2. Lagrangian Particle Tracking

For the tracking of particle trajectories and orientations through the flow, a Lagrangian particle tracking code has been developed to run in parallel with Nek5000. Each particle is represented as a point with its location, velocity, quaternions and angular velocity being updated each time-step by solving a set of dimensionless equations. The equations for the linear motion are derived through considering the balance between the particle's inertia and the fluid. We consider the effects of the following forces: lift, drag, virtual mass and the pressure gradient. The Basset history force is neglected due to its limited impact relative to its computational cost, also neglected are the effects of gravity and buoyancy to allow us to more easily

isolate the effect of the turbulence on the particles. For the rotational motion we use quaternions to track the orientation of the particles and update the angular velocity using Euler's equations of rotation. For these, we consider the torque due to the resistance on a rotating ellipsoid and the cross-coupling between angular velocities along different axes, which arises because the principal moments of inertia are not all the same.

In this work we consider non-spherical ellipsoid particles given by the equation:

$$\left(\frac{x'}{a}\right)^2+\left(\frac{y'}{b}\right)^2+\left(\frac{z'}{c}\right)^2=1, \tag{4}$$

where a, b and c represent the lengths of the three semi-principal axes in the x', y' and z' directions respectively. We enforce that $a=b$ in all cases and define the aspect ratio $\lambda=c/a$. The solid phase can then be characterised by specifying the following bulk parameters: the particle density ρ_p, the aspect ratio and the volume fraction ϕ_p defined as follows,

$$\phi_p=\frac{4}{3}\pi a^2 c\frac{N_p}{V_F}, \tag{5}$$

where N_p is the number of particles and V_F is the volume of the fluid geometry. The particle dynamics are modelled using three reference frames: the particle frame $\boldsymbol{x}'=[x',y',z']$ with its origin at the particle's centroid and its principal axis z', the global (fixed) frame $\boldsymbol{x}=[x,y,z]$ and the co-moving frame $\boldsymbol{x}''=[x'',y'',z'']$ which shares its origin with the particle centroid and has axes parallel to the fixed frame. Transformation between the co-moving frame and the particle frame can be performed as follows:

$$\boldsymbol{x}'=\underline{\underline{\boldsymbol{A}}}\boldsymbol{x}'', \tag{6}$$

Where $\underline{\underline{\boldsymbol{A}}}$ is the time-dependent rotational matrix with elements expressed in terms of four quaternions $\boldsymbol{q}=[q_0,q_1,q_2,q_3]^T$ satisfying the constraint $q_0^2+q_1^2+q_2^2+q_3^2=1$.

The time evolution of the quaternions is used to update the orientation of the particles and is computed as:

$$\frac{d\boldsymbol{q}}{dt^*}=\frac{1}{2}\begin{bmatrix}q_0 & -q_1 & -q_2 & -q_3\\ q_1 & q_0 & -q_3 & q_2\\ q_2 & q_3 & q_0 & -q_1\\ q_3 & -q_2 & q_1 & q_0\end{bmatrix}\begin{bmatrix}0\\ \Omega_{x'}\\ \Omega_{y'}\\ \Omega_{z'}\end{bmatrix}, \tag{8}$$

where $\Omega_{x'}$, $\Omega_{y'}$ and $\Omega_{z'}$ are the components of the particle angular velocity expressed in the particle frame. The particle equations of motion and rotation are given below:

$$\frac{d\boldsymbol{x}_p^*}{dt^*}=\boldsymbol{u}_p^*, \tag{9}$$

$$\frac{\partial\boldsymbol{u}_p^*}{\partial t^*}=\frac{1}{M_{VM}}[\boldsymbol{F}_D+\boldsymbol{F}_L+\boldsymbol{F}_{VM}+\boldsymbol{F}_{PG}], \tag{10}$$

where $\boldsymbol{u}_p^*$ denotes the dimensionless fluid velocity, $M_{VM}=(1+1/2\rho^*)$ is the dimensionless virtual mass factor where $\rho^*=\rho_p/\rho_F$ is the dimensionless density ratio. Here, $\boldsymbol{F}_D$ is the drag force acting on the particle and is given as follows [18]:

$$\boldsymbol{F}_D=\frac{A_D^* C_D|\boldsymbol{u}_s^*|\boldsymbol{u}_s^*}{2\rho^* V_p^*}, \tag{11}$$

where $V_p^*=(4/3)\pi a^{*2}c^*$ is the dimensionless volume of the particle, $\boldsymbol{u}_s^*=\boldsymbol{u}_F^*-\boldsymbol{u}_p^*$ is the slip velocity, and A_D and A_L are the partial projected areas normal to the direction of the drag and lift forces respectively [18]:

$$A_D=\pi a^2\sqrt{\cos^2(\alpha)+\left(\frac{4\lambda}{\pi}\right)^2\sin^2(\alpha)}\,, \tag{12}$$

$$A_L=\pi a^2\sqrt{\sin^2(\alpha)+\left(\frac{4\lambda}{\pi}\right)^2\cos^2(\alpha)}\,, \tag{13}$$

where α is the angle of incidence defined as the angle between the slip velocity $\boldsymbol{u}_s^*$ and the direction of the principal particle axis $\boldsymbol{z}'$. The dimensionless drag coefficient C_D for the non-spherical particles is given by [19]:

$$\frac{C_D}{K_2}=\frac{24}{Re_pK_1K_2}\left[1+0.118\left(Re_pK_1K_2\right)^{0.6567}\right]+\frac{0.4305}{1+3305/\left(Re_pK_1K_2\right)}, \tag{14}$$

where $Re_p=\boldsymbol{u}_s^* d_{ev}/\nu_F$ is the particle Reynolds number computed using the equal volume sphere diameter $d_{ev}=2a\lambda^{1/3}$, $K_1=\frac{1}{3}(d_n/d_{ev}+2\Phi_s^{-0.5})$ and $K_2=10^{1.8148(-\log\Phi_s)^{0.5743}}$ are the Stokes and Newton shape factors that model the particle sphericity and orientation, respectively, $d_n=\sqrt{4A_D/\pi}$ and $\Phi_s=s/S$, where Φ_s is the particle sphericity, defined as the ratio of the surface area of a sphere having the same volume as the particle, s, to the actual surface area of the non-spherical particle, S. The lift coefficient C_L is determined by the following [18]:

$$\frac{|C_L|}{|C_D|}=|\sin^2(\alpha)\cos^2(\alpha)|. \tag{15}$$

The lift force $\boldsymbol{F}_L$ is therefore given by [18]:

$$\boldsymbol{F}_L=\frac{1}{2\rho^* V_p^*}A_L^* C_L\frac{(\boldsymbol{z}'\cdot\boldsymbol{u}_s^*)}{|\boldsymbol{u}_s^*|}[\boldsymbol{z}'\times\boldsymbol{u}_s^*]\times\boldsymbol{u}_s^*. \tag{16}$$

The local pressure gradient force $\boldsymbol{F}_{PG}$ is [5]:

$$\boldsymbol{F}_{PG}=\frac{1}{\rho^*}\frac{D\boldsymbol{u}_F^*}{Dt^*}. \tag{17}$$

The virtual mass force $\boldsymbol{F}_{MV}$ is given by [5]:

$$\boldsymbol{F}_{VM} = \frac{1}{2\rho^*}\frac{D\boldsymbol{u}_F^*}{Dt^*}. \tag{18}$$

The final equations of motion for the rotation of the prolate ($\lambda > 1$) ellipsoid particles are given by Euler's equations of rotation presented below in a simplified dimensionless form [10] :

$$\begin{aligned}
\frac{d\Omega_{x'}^*}{dt^*} &= \frac{20[(1-\lambda^2)d_{z'y'}^* + (1+\lambda^2)(\omega^{*\prime}_{z'y'} - \Omega_{x'}^*)]}{Re_B(\beta_0 + \lambda^2\gamma_0)(1+\lambda^2)\rho^* a^{*2}} \\
&\quad + \left(1 - \frac{2}{1+\lambda^2}\right)\Omega_{y'}^*\Omega_{z'}^*, \\
\frac{d\Omega_{y'}^*}{dt^*} &= \frac{20[(\lambda^2-1)d_{x'z'}^* + (\lambda^2+1)(\omega^{*\prime}_{x'z'} - \Omega_{y'}^*)]}{Re_B(\alpha_0 + \lambda^2\gamma_0)(1+\lambda^2)\rho^* a^{*2}} \\
&\quad + \left(\frac{2}{1+\lambda^2} - 1\right)\Omega_{x'}^*\Omega_{z'}^*, \\
\frac{d\Omega_{z'}^*}{dt^*} &= \frac{20(\omega_{y'x'}^* - \Omega_{z'}^*)}{Re_B(2\alpha_0)\rho^* a^{*2}}.
\end{aligned} \tag{19}$$

Here the elements of the deformation rate tensor ($d_{z'y'}$ and$d_{x'z'}$) and the spin tensor ($\omega_{z'y'}, \omega_{x'z'}$ and$\omega_{y'x'}$) are defined as follows:

$$\begin{aligned}
d_{i'j'} &= \frac{1}{2}\left(\frac{\partial u_{i'}}{\partial j'} + \frac{\partial u_{j'}}{\partial i'}\right), \\
\omega_{z'y'} &= \frac{1}{2}\left(\frac{\partial u_{i'}}{\partial j'} - \frac{\partial u_{j'}}{\partial i'}\right).
\end{aligned} \tag{20}$$

The velocity gradients in the particle frame $G_{i'j'}$ can be obtained by transforming the velocity gradients from the fixed frame$G_{ij} = \partial u_i/\partial x_j$:

$$G_{i'j'} = \underline{\underline{\boldsymbol{A}}}\, G_{ij}\, \underline{\underline{\boldsymbol{A}}}^{-1}. \tag{21}$$

The non-dimensional coefficients $\alpha_0 = \beta_0$, and γ_0 for a prolate ellipsoid ($\lambda > 1$) are defined as [20]:

$$\begin{aligned}
\alpha_0 &= \frac{\lambda^2}{\lambda^2-1} + \frac{\lambda}{2(\lambda^2-1)^{3/2}}\ln\left(\frac{\lambda - \sqrt{\lambda^2-1}}{\lambda + \sqrt{\lambda^2-1}}\right), \\
\gamma_0 &= \frac{2}{\lambda^2-1} + \frac{\lambda}{(\lambda^2-1)^{3/2}}\ln\left(\frac{\lambda - \sqrt{\lambda^2-1}}{\lambda + \sqrt{\lambda^2-1}}\right).
\end{aligned} \tag{22}$$

The governing equations Eqs. (8) to (10) are integrated in time using a fourth-order Runge-Kutta (RK4) algorithm, while Eq. (19) is integrated using a mixed explicit/implicit differencing scheme presented in [20] due to the stiffness of the equations. In both cases the time-step is chosen to be the same as for the continuous phase solver.

For higher volume fractions, as considered in this work, it is essential to account for the particles' impact back onto the fluid and this is done by adding an additional source term in the Navier-Stokes equations. The acceleration applied to cell *i* is given by [11]:

$$\boldsymbol{f}_{2W}^{*i} = \frac{1}{V_i^*}\sum_{j}^{N_{p,i}}\frac{\partial \boldsymbol{u}_{p_j}^*}{\partial t^*}, \tag{23}$$

where $V_i^*$is the volume of the computational cell, and j is an index that iterates over the number of particles contained within a cell, $N_{p,i}$.

All inter-particle and wall collisions assume that the particles are spherical with radius equal to the largest semi-major axis. A deterministic binary collision search algorithm is also used, based on [21]. At each time-step, particles are distributed into cells of a coarse mesh. The collision algorithm detects collisions by comparing relative displacements and velocities within each cell. A secondary search identifies missed collisions. Collisions are resolved using kinetic energy and momentum conservation, with particles deflected to account for penetration. Collisions are assumed fully elastic.

3. RESULTS AND DISCUSSION

Here we focus on the collision dynamics of needle-like particles and compare our findings to those of nearly spherical particles. The fixed particle phase parameters have been chosen to match those of the study [5] and are shown in Table 1. Two particle shapes are considered, and the case specific parameters are outlined in Table 2. Here $St^+ = (\rho^* d_{ev}^{+2})/18\nu_F$ is the dimensionless shear Stokes number where $d_{ev} = 4a\lambda^{1/3}$.

Table 1. Fixed simulation parameters

Fixed Parameter	Value
Number of Particles N_p	300,000
Particle Volume V_p^*	6.55×10^{-4}
Volume Fraction ϕ_p	1.4×10^{-4}
Shear Stokes Number St^+	50
Density Ratio ρ^*	400
Shear Reynolds Number Re_τ	300
Bulk Reynolds Number Re_B	4,900

Table 2. Case specific particle phase parameters

Case	a^*	c^*	λ
Near-Spheres	0.002492	0.002517	1.01
Needles	0.001462	0.007310	5

The particles were injected into the domain with random initial position and orientation. The initial velocity was inherited from the fluid and the initial angular velocity was set to zero. Our analysis breaks the flows into four distinct regions where the flow conditions are known to differ, namely the viscous sublayer (VS) ($0.973 < |y*| \leq 1$), the buffer layer (BL) ($0.834 < |y*| \leq 0.973$), the log-law region (LL) ($0.8 < |y*| \leq 0.834$) and the bulk flow (BF) ($0 \leq |y*| \leq 0.8$). We quantify the

alignment of particles by considering the cosine of the angles $(\theta_x.\theta_y,\theta_z)$ made between the axes of co-moving frame $\boldsymbol{x''}$ and the principal particle axis $\boldsymbol{z'}$. These are known as the direction cosines denoted $\cos(\theta_i)$. Values $\cos(\theta_i) \approx 1$ indicate the fibre is aligned strongly with axis i, while $\cos(\theta_i) \approx 0$ indicate the fibre is unaligned with axis i. The following PDFs are calculated using a Gaussian kernel density estimation.

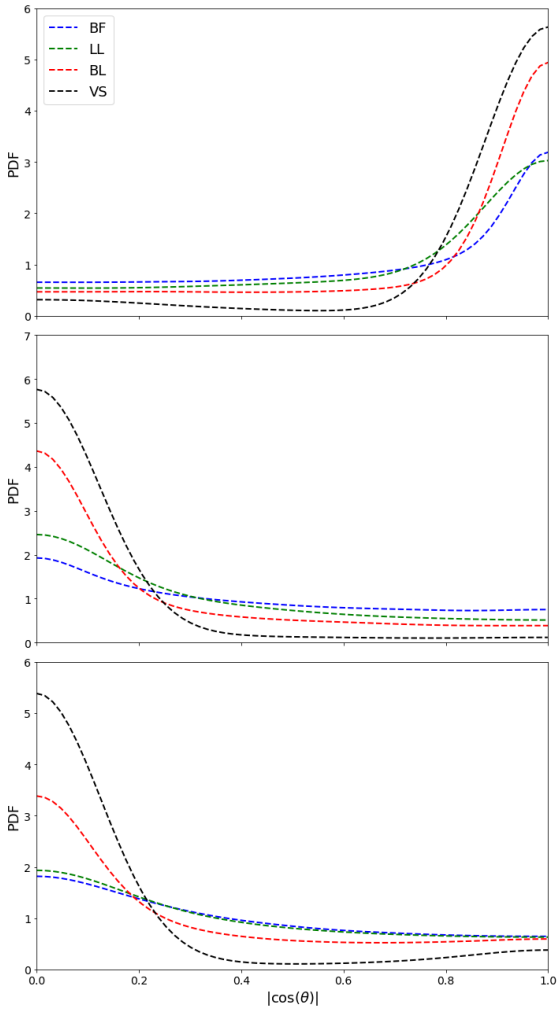

Figure 2: Absolute direction cosine PDFs by wall normal location for needle-like particles, (top) streamwise alignment, (middle) wall normal alignment and (bottom) spanwise alignment

The alignment of the needle-like particles is quantified in Figure 2. We see strong alignment with the streamwise direction close to the wall with the alignment weakening towards the centre of the channel. The spanwise and wall-normal directions behave similarly with strong anti-alignment with the respective axes close to the walls which again weakens toward the channel centre. These findings are consistent with previous studies investigating needle-like particles [10], thus providing validation of the orientational dynamics of the model.

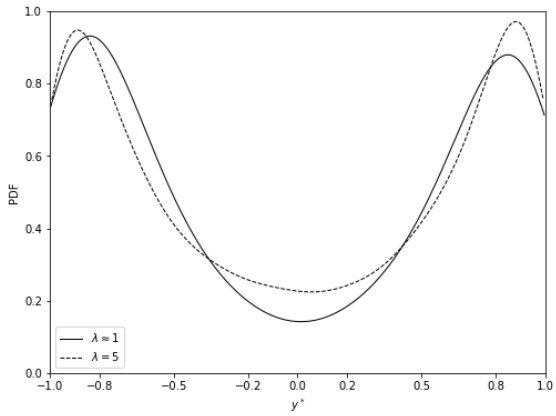

Figure 3: Collision PDFs by wall normal location

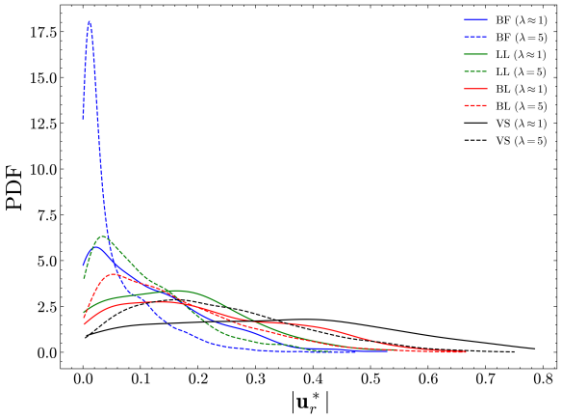

Figure 4: Collided particle absolute relative velocity PDFs separated by flow region

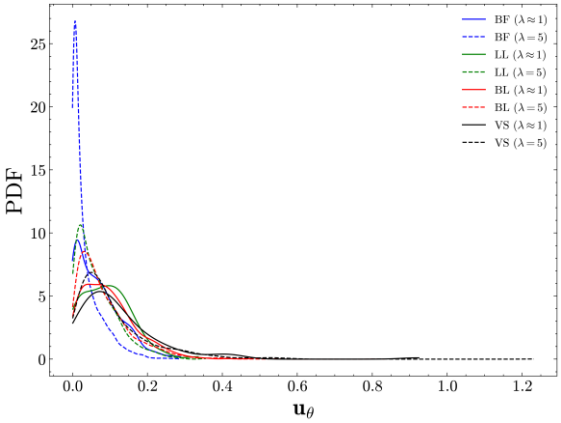

Figure 5: Collided particle relative collision angle (radians) PDFs separated by flow region

We observe that both the near-spheres and needles collide more often closer to the walls, likely due to turbophoresis within the channel leading to preferential concentration in the near wall region (see Figure 3). The needles collide with a higher probability in the very near wall region but the distribution falls more quickly as we move from the wall. Interestingly we also note an increased probability of collision around the channel centre with the needles. Looking at the absolute relative

velocity $|\boldsymbol{u}_r|$ of collided particle pairs it is clear that the needles and near-spheres differ significantly, as shown in Figure 4. While the mean relative velocity is similar in all regions the PDF for the needles shows much less variation, particularly in the bulk flow region. This could be due to the ability of elongated shapes to align more easily with the local flow and collide more predicably. The same relationship is seen for the relative collision angle (the angle between the velocity vectors of two colliding particles), as shown in Figure 5. Here we again see less variance in PDFs for the needle-like particles indicating that more often these particles collide with velocities nearly parallel, $u_\theta = 0$, and this is likely due to the increased tendency of needle-like particles to algin with the local flow.

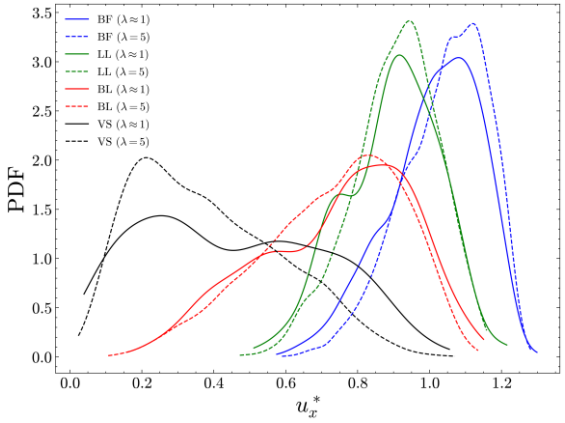

Figure 6: Collided particle streamwise velocity magnitude PDFs separated by flow region

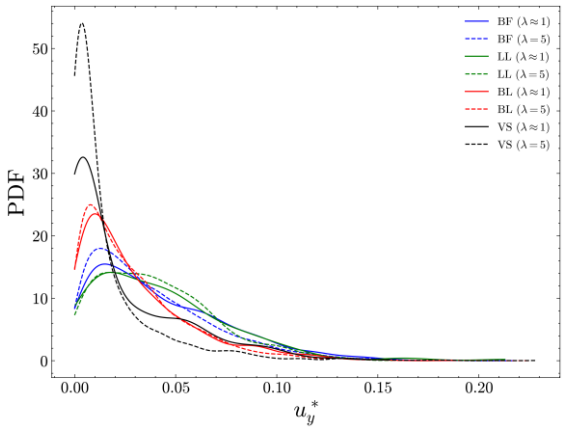

Figure 7: Collided particle wall-normal velocity magnitude PDFs separated by flow region

The mean components of velocity for the nearly spherical particles are in good agreement with the existing literature [5], with similar PDFs observed in all flow regions. The mean streamwise velocity is similar in magnitude between the spherical and needle-like particles, but we do note slightly higher speeds for the needle-like particles in the bulk flow and log-law regions, as shown in Figure 6.

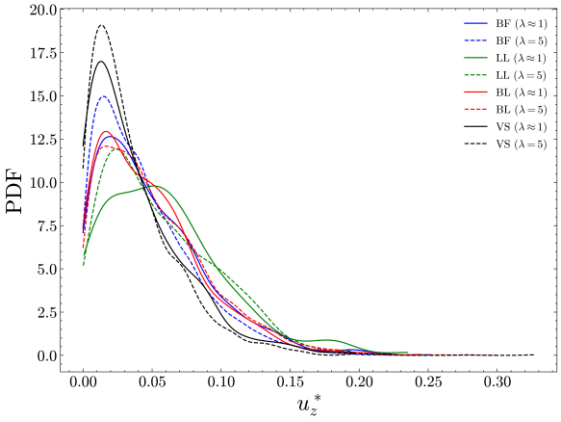

Figure 8: Collided particle spanwise velocity magnitude PDFs separated by flow region

The mean velocity in the wall-normal direction is again similar between the spheres and needles at $\boldsymbol{u_y^* \approx 0}$. Here we again observe that the needles have less variance in their speed (Figure 7.), particularly in the very near wall region where the alignment with the streamwise direction is strong. Here the proximity to the near wall boundary layer combined with the particles' tendency to align with the flow, lead to the angle of incidence and thus the lift and drag forces on the needle particles to be quite small. This results in minimal wall-normal velocity fluctuations and the lower variance observed in the PDFs. The mean velocity in the spanwise direction is slightly higher at around $\boldsymbol{u_z^* \approx 0.02}$, and this is consistent across both spheres and needles in all the regions considered in Figure 8. Again, we see less variation in the PDFs for needles compared to spheres, but this effect is muted compared to the wall-normal direction with, both particle types performing similarly overall.

4. CONCLUSIONS

Numerical simulations of flows of needle-like and nearly spherical particles under similar conditions have been compared. Our findings indicated that needle-like particles exhibited strong alignment with the streamwise direction near the walls, resulting in higher collision probabilities very close to the walls and around the channel centre. A reduced variance in the relative collision velocity and angles for the needles relative to the spheres was also observed, particularly in the bulk flow region. While the mean velocity components for near-spheres aligned with the existing literature (for perfect spheres), needle-like particles showed slightly higher mean streamwise velocities and less variation in wall-normal and spanwise speeds, especially near the walls due to their strong alignment with the flow. These results underscore the significant impact of particle shape on particle collision behaviour and suggest that further research should be undertaken.

ACKNOWLEDGEMENTS

The authors would like to thank the EPSRC (EP/S022732/1) and Sellafield Ltd for funding.

REFERENCES

[1] Allison, M.A., Yuill, B.T., Meselhe, E.A., Marsh, J.K., Kolker, A.S., and Ameen, A.D., 2017, "Observational and Numerical Particle Tracking to Examine Sediment Dynamics in a Mississippi River Delta Diversion", *Estuar Coast Shelf Sci*, Vol. 194, pp. 97-108.

[2] Trojanowicz, M., Kołacińska, K., and Grate, J.W., 2018, "A Review of Flow Analysis Methods for Determination of Radionuclides in Nuclear Wastes and Nuclear Reactor Coolants", *Talanta*, Vol. 183, pp. 70-82.

[3] Lundell, F., Söderberg, L.D., and Alfredsson, P.H., 2011, "Fluid Mechanics of Papermaking", *Annu Rev Fluid Mech*, Vol. 43, pp. 195-217.

[4] Kunnen, R.P.J., Siewert, C., Meinke, M., Schröder, W., and Beheng, K.D., 2013, "Numerically Determined Geometric Collision Kernels in Spatially Evolving Isotropic Turbulence Relevant for Droplets in Clouds", *Atmos Res*, Vol. 127, pp. 8-21.

[5] Rupp, D.A., Mortimer, L.F., and Fairweather, M., 2023, "Stokes Number and Coupling Effects on Particle Interaction Behavior in Turbulent Channel Flows", *Phys Fluids*, Vol. 35, 113307.

[6] Elghobashi, S., 2019, "Direct Numerical Simulation of Turbulent Flows Laden with Droplets or Bubbles", *Annu Rev Fluid Mech*, Vol. 51, pp. 217-244.

[7] Fessler, J.R., Kulick, J.D., and Eaton, J.K., 1994, "Preferential Concentration of Heavy Particles in a Turbulent Channel Flow", *Phys Fluids*, Vol. 6, pp. 3742-3749.

[8] Marchioli, C., and Soldati, A., 2002, "Mechanisms for Particle Transfer and Segregation in a Turbulent Boundary Layer", *J Fluid Mech*, Vol. 468, pp. 283-315.

[9] Mortimer, L.F., Njobuenwu, D.O., and Fairweather, M., 2019, "Near-wall Dynamics of Inertial Particles in Dilute Turbulent Channel Flows", *Phys Fluids*, Vol, 31, 063302.

[10] Marchioli, C., Fantoni, M., and Soldati, A., 2010, "Orientation, Distribution, and Deposition of Elongated, Inertial Fibers in Turbulent Channel Flow", *Phys Fluids*, Vol. 22, 033301.

[11] Eaton, J.K., 2009, "Two-way Coupled Turbulence Simulations of Gas-particle Flows Using Point-particle Tracking", *Int J Multiph Flow*, Vol. 35, pp. 792-800.

[12] Ireland, P.J., Bragg, A.D., and Collins, L.R., 2016, "The Effect of Reynolds Number on Inertial Particle Dynamics in Isotropic Turbulence. Part 1. Simulations Without Gravitational Effects", *J Fluid Mech*, Vol. 796, pp. 617-658.

[13] Dritselis, C.D., 2016, "Direct Numerical Simulation of Particle-laden Turbulent Channel Flows with Two-and Four-way Coupling Effects: Budgets of Reynolds Stress and Streamwise Enstrophy", *Fluid Dyn Res*, Vol. 48, 015507.

[14] Siewert, C., Kunnen, R.P.J., and Schröder, W., 2014, "Collision Rates of Small Ellipsoids Settling in Turbulence, "*J Fluid Mech*, Vol. 758, pp. 686-701.

[15] Chen, M., Kontomaris, K., and McLaughlin, J.B., 1999, "Direct Numerical Simulation of Droplet Collisions in a Turbulent Channel Flow. Part I Collision Algorithm", *Int J Multiph Flow*, Vol. 24, pp. 1079-1103.

[16] van Wachem, B., Zastawny, M., Zhao, F., and Mallouppas, G., 2015, "Modelling of Gas-solid Turbulent Channel Flow with Non-spherical Particles with Large Stokes Numbers", *Int J Multiph Flow*, Vol. 68, pp. 80-92.

[17] Fischer, P.F., Lottes, J.W., and Kerkemeier, S.G., 2008, *Nek5000*, Web page http://nek5000.mcs.anl.gov.

[18] Yin, C., Rosendahl, L., Kær, S.K., and Sørensen, H., 2003, "Modelling the Motion of Cylindrical Particles in a Nonuniform Flow", *Chem Eng Sci*, Vol, 58, pp. 3489-3498.

[19] Ganser, G.H., 1993, "A Rational Approach to Drag Prediction of Spherical and Nonspherical Particles", *Powder Technol*, Vol. 77, pp. 143-152.

[20] Fan, F.G., and Ahmadi, G., 1995, "A Sublayer Model for Wall Deposition of Ellipsoidal Particles in Turbulent Streams", *J Aerosol Sci*, Vol. 26, pp. 813-840.

[21] Breuer, M., and Almohammed, N., 2015, "Modeling and Simulation of Particle Agglomeration in Turbulent Flows Using a Hard-sphere Model with Deterministic Collision Detection and Enhanced Structure Models", *Int J Multiph Flow*, Vol. 73, pp. 171-206.

Conference on Modelling Fluid Flow (CMFF'25)
The 19th International Conference on Fluid Flow Technologies
Budapest, Hungary, August 26-August 29, 2025

EXPLORING TRANSIENT INSTATIONARITIES OF MECHANICAL LOAD IN THE OPERATION OF WASTEWATER PUMPS

Florian BROKHAUSEN[1], Paul Uwe THAMSEN[2],

[1] Corresponding Author. Chair of Fluid System Dynamics, Faculty of Mechanical Engineering and Transport Systems, Technische Universität Berlin. Straße des 17. Juni 135, 10623 Berlin. E-mail: florian.brokhausen@tu-berlin.de
[2] Chair of Fluid System Dynamics, Faculty of Mechanical Engineering and Transport Systems, Technische Universität Berlin. Straße des 17. Juni 135, 10623 Berlin. E-mail: paul-uwe.thamsen@tu-berlin.de

ABSTRACT

The operation of pumps in wastewater conditions is objected to complex failure modes due to the heterogeneous nature of wastewater as a medium. The main operational challenge is the clogging of the pump due to nonwoven wipes accumulating in the impeller. To investigate the operation of wastewater pumps and emulate clogging phenomena, a standardized testing procedure, in which dusters are mixed with clear water to emulate the characteristics of the suspended nonwoven wipes in real wastewater is employed. In this paper, the joint analysis of mechanical and hydraulic measurements provides deeper insights into the characteristic phenomena that constitute clogging events in wastewater pumps. The mechanical data analyzed entails the torque and rotational speed, synchronized with the hydraulic measurement of the pump head and flow. With baseline clear water measurements and constrained wastewater operation tests, salient signatures in mechanical and hydraulic data are attributable to the influence of the wastewater medium and clogging events. The volatile and persistent clogging states of a pump induce transient instationarities in the mechanical load, especially reflected in the high-frequency oscillation of torque in the form of harmonic distortion. This is demonstrated via 19 standardized tests performed on 10 pumps with semi-open two-channel impellers.

Keywords: Clogging Characterization, Frequency Domain Analysis, Instationary Mechanical Load, Wastewater Pumps

NOMENCLATURE

BPF	$[Hz]$	Blade Passing Frequency
DFT	$[-]$	Discrete Fourier Transform
H	$[m]$	Head
M	$[Nm]$	Torque
Q	$[m^3/h]$	Flow
RF	$[Hz]$	Rotational Frequency
VFD	$[-]$	Variable Frequency Drive
m_w	$[g]$	Weight
η	$[\%]$	Efficiency

Subscripts and Superscripts

CW	Clear Water

1. INTRODUCTION

Pumps utilized in wastewater management are crucial components for the transportation and processing of wastewater, which often contains a complex mixture of suspended solids, organic matter, and chemical substances. These pumps are specifically designed to handle such diverse and potentially abrasive materials, ensuring continuous fluid movement. [1] A significant operational challenge, however, is the phenomenon of clogging, predominantly caused by nonwoven wipes. These materials, commonly found in domestic wastewater, have a tendency to accumulate within the pump's impeller, resulting in obstructions that can impair pump performance and, in extreme cases, lead to complete system failure [2].

The consequences of clogging are reductions in flow rate or pump head, increased energy consumption, and amplified mechanical stress and wear. Further, the growing frequency of extreme weather events, in combination with the ongoing trend of urbanization, places additional stress on wastewater infrastructure, increasing the urgency of maintaining the operational integrity of pumps. As such, it is imperative that the design of wastewater pumps incorporates features that enhance resistance to clogging, thereby ensuring long-term efficiency.

While previous research has identified nonwoven wipes as a primary contributor to clogging, much of the existing literature has been limited to theoretical models or simulations. Empirical investigations into the interaction between wastewater impellers and fibrous materials remain scarce. This gap underscores the need for more experimental studies

that provide concrete insights into the mechanisms of clogging and its deduced influence on a pump's operating conditions.

Hence this study provides new and valuable insights into the impact of clogging and general wastewater operating conditions on the mechanical power driving the wastewater pump. To deduce these influences, the chair of Fluid System Dynamics at the Technische Universität Berlin employs a designated test rig to emulate wastewater conditions in a controlled environment. This test rig enables the investigation of a pump's susceptibility to clogging and provides valuable insights into the detailed mechanisms constituting diverse clogging phenomena.

In this work, the designated test rig is leveraged to gain insights into the influence of wastewater operating conditions and clogging events on the mechanical powertrain, namely the torque and rotational speed. In total, 19 tests are carried out on 10 different pumps equipped with a range of different semi-open two-channel impeller designs, objected to varying degrees of emulated contamination. In these tests, the hydraulic performance in terms of flow and pump head are tracked as well as the mechanical load in terms of rotational speed and torque. Besides the analysis in the value domain, the torque is additionally analyzed in the frequency domain to observe the oscillatory behavior and how this is impacted by clogging of the pump's impeller.

2. RELATED WORK

The research area of investigating and characterizing clogging in wastewater pumps and its influence on common process measurements is scarce. Especially so when focusing on experimental works with realistic testing scenarios.

The work of Kallweit [3] presents a baseline for the change of parameters under clogging conditions. Here, the author presents experiments with fixed, constant, artificial clogging on an axial impeller's blades and analyzes the implications. In particular, the authors analyze pressure pulsations in the frequency domain which are shown to substantially deviate for clogging conditions of the tested impeller.

However, a focus on the changes in mechanical load in wastewater pumps with respect to clogging events has not yet been presented. Many studies do employ rotational speed and torque measurements or calculations, but exclusively with the aim to determine mechanical power leveraged for pump efficiency investigations [4, 5]. These investigations do not, however, focus on the implications of clogging but instead on the optimization design aspects for the reduction of power consumption. As the majority of related work on wastewater pumps, these studies also mainly present a simulation of the setup, with only reduced experiment capacities for verification purposes.

The work of Barrio et al.[6] does consider frequency domain analysis of the torque of a pump in terms of the blade passing frequency amplitude of torque. However, these reports are only based on simulation results. Further, the impeller is designed for clear water operation.

Consequentially, to the best of the author's knowledge, this is the first work to investigate mechanical load and particularly torque, in realistic wastewater conditions to this depth and show the large oscillations in the torque harmonics induced by clogging events. This work falls in line with previous efforts in characterizing signal patterns for clogging in wastewater pumps carried out at the Technische Universität Berlin [7, 8, 9, 10].

3. MATERIALS AND METHODS

3.1. Test Rig Setup

The chair of Fluid System Dynamics at the Technische Universität Berlin operates a designated test rig for standardized testing of wastewater pumps.

Test Rig and Procedure. Figure 1 shows the test rig used to carry out the standardized wastewater tests. The test rig is composed of two 3.5 m^3 tanks that are connected through looped pipes, integrating the pump under test. The various valves enable the configuration of different circuits to move the water. For the standardized testing, water is pumped in a circle from and to the wastewater tank. The test medium is artificial wastewater consisting of clear water mixed with dusters. These dusters have a size of 22x33 cm with a fabric weight of 60 g/m^2. They have been found to most closely reproduce the clogging phenomena observed in wastewater pumps in the field induced by nonwoven wipes [2, 11]. The standardized test is called the *long-time functional performance test*, where the artificial wastewater is pumped in a loop for the duration of an hour. The operation of the motor, and thus the pump, is facilitated with a variable frequency drive (VFD). The VFD is set to maintain a constant speed of rotation.

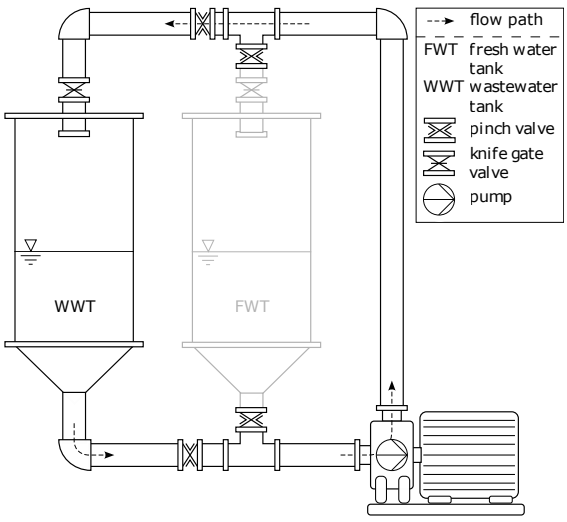

Figure 1. Schematic of the test rig and the flow paths.

After a test, the pump is opened to retrieve the dusters clogged in the impeller of the pump. With this, the weight ratio of all dusters introduced in the test and the ones remaining clogged in the pump at the end of the test is determined. This weight ratio assumes a value of 1 when all introduced dusters are clogged inside the pump at the end of the test. Oppositely, a weight ratio of 0 implies that all dusters have been continuously pumped without being accumulated in the pump at the end of the test. This test can be repeated for three different so-called *contamination classes*. These modify the number of dusters introduced in the test in steps of 25, 50, or 100 dusters per cubic meter of water.

For each long-time functional performance test of a pump, the so-called *degree of long-time functionality (D_{LTF})* is calculated according to the following equation [7]:

$$D_{LTF} = \frac{1}{2} \cdot \frac{\overline{\eta}}{\eta_{CW}} + \frac{1}{2} \cdot \frac{m_{w,total} - m_{w,pump}}{m_{w,total}}, \qquad (1)$$

where $\overline{\eta}$ is the average efficiency of the test, η_{CW} is the efficiency of the pump in clear water operation and $m_{w,\_}$ are the weights of the total introduced dusters in the test and the weight of dusters remaining in the pump at the end of the test.

In addition to the long-time functional performance tests, a clear water reference measurement of 30 s is recorded for each operating point of the pump under test. The obtained clear water values serve as a reference for the changes in the hydraulic, mechanical, and electric characteristics which are induced in the long-time functional performance tests due to wastewater operating conditions and potential clogging.

Sensor Setup. In order to analyze the operation of the pump under wastewater conditions, several measurements are carried out to determine important performance metrics. The differential pressure is measured between the inlet and outlet of the pump, according to DIN EN ISO 9906 [12]. The flow is determined with an inductive flow meter. These measurements enable the calculation of the pump head. All measurements are recorded with a sampling frequency of 1 Hz.

For the purposes of this study, the test rig is equipped with an additional torque transducer. The torque transducer is the measurement flange T40B by HBK . This enables not only the measurement of the torque but the rotational speed as well. The torque is measured with a high accuracy of a maximum 0.03 %. As the previously defined metrics, the rotational speed is recorded with a frequency of 1 Hz. Since the torque is analyzed in the frequency domain as well, the sampling frequency is set to 1000 Hz.

3.2. Pumps under Test

In total, a number of 10 pumps are tested for the purposes of this investigation. For these 10 pumps, 19 tests are performed with varying contamination classes. Generally, with any pump, the testing starts at the lowest contamination class and increases gradually across the denoted classes. A pump is only tested with the next higher contamination class if the respective D_{LTF} value is above 0.4, as otherwise the pump will only exhibit even more severe clogging with no added insights. For the purpose of this study, the D_{LTF} is merely a means to formalize the experimentation and will not be discussed and analyzed further.

The pumps under test are all equipped with semi-open two-channel impellers. The impellers vary in their leading edge configuration in terms of thickness and streamlines. The pumps P1 to P3 exhibit increasing degrees of cutback on the leading edge, i.e. decreasing how far the leading edge reaches into the inlet of the casing. The impellers of pumps P4 to P6 are modifications of P4 with increased leading edge thickness. Finally, pumps P7 to P10 are equipped with impellers observing connected leading edges of varied thickness. All impellers exhibit a diameter of 310 mm. The volute casing is the same for all tests, as is the motor, VFD, and sensor setup. The in- and outlet of the casing are DN200 and DN150, respectively.

In all tests of the different impellers, the rotational speed of the motor is set to 1450 min^{-1} via the VFD.

3.3. Frequency Domain Transfer

Fourier transform. The frequency domain transfer is set up in a similar fashion as in the work of Brokhausen et al. [10]. The process will be briefly described here as well.

The frequency domain transfer is executed via a discrete Fourier transform (DFT) since the data it is applied to is characterized as real-valued and digitized. The result of this transform is a complex amplitude spectrum over the frequencies. These complex amplitudes are converted to real, absolute values and are converted back to their original value domain for ease of interpretation. This is implemented as follows (adapted from [13, p. 61]):

$$A_M = \frac{2 \cdot |A_c|}{N}, \qquad (2)$$

where A_M are the amplitudes in the original value domain, A_c are the complex amplitudes, and N is the number of data points the DFT was applied to.

Windowed DFT. The frequency transform is applied in a windowed fashion. The window is shifted by a certain number of samples across the data, where a DFT is carried out per window. This enables the resolution of the amplitudes over time. The number of samples, the window is shifted by therefore defines the resolution in time. The frequency resolution is defined by the size of the window. The smallest frequency that can be resolved is determined by

the division of the sampling frequency by the window size.

The extracted windows of data need to be further conditioned. When extracting a subsection of data, the constituent waveforms are cut at a point that is unequal to their period. This leads to the detection of amplitudes for frequencies, which in reality do not exist in the data. This phenomenon is called spectral leakage. It is countered by applying a window function to each window. In this study, the Hamming window is used. The Hamming window represents a bell curve with reduced kurtosis and is formulated as follows [14]:

$$w(n) = 0.54 - 0.46 \cdot \cos\left(\frac{2\pi n}{N-1}\right), \quad with\ 0 \leqq n \leqq N-1 \tag{3}$$

where N represents the number of samples in a window. The window function essentially dampens the edges of the windows to reduce their influence in terms of spectral leakage. With the application of this function, however, the resulting amplitudes of the DFT are of course altered. In order to counter this and be able to still interpret the amplitude spectrum in the original value domain, an amplitude correction factor needs to be applied. The correction factor is calculated by Equation 4 [15, p. 212]:

$$CF = \frac{N}{\sum_{n=0}^{N-1} w(n)}, \tag{4}$$

where, again, N is the size of the window. The resulting amplitudes are all multiplied by this correction factor.

Implementation details. The frequency domain transfer via the windowed discrete Fourier transform is executed with a window size of 1000 samples. As mentioned, the sampling frequency of the torque measurement is $1000\,Hz$, making the window one second long. Moreover, this results in a frequency resolution of $1\,Hz$. This is a sufficient resolution in frequency as the frequencies of interest are not as close to one another as to necessitate a sub-Hertz resolution. This is demonstrated in the subsequent chapter.

With this setup, the maximum frequency that can be identified is $500\,Hz$, which is far enough for the harmonics being observed in the measurements, as demonstrated later on in the results. Lastly, the number of samples the window is shifted by is set to 500, i.e. $0.5\,s$. This ensures a sufficient resolution in time.

3.4. Definition of Harmonics

The reason for the frequency domain analysis is to be able to identify and trace harmonics in the torque signal. The expected and observed harmonics originate due to the inherent periodic nature of the mechanic rotation. Therefore, the main base frequency is the rotational frequency (RF). One specific additional frequency of interest is the so-called blade passing frequency (BPF), i.e. the frequency with which the blades of the pump's impeller rotate. Naturally, this depends on the number of blades and manifests as the product of the latter and the rotational frequency. As all pumps in this study employ two-channel impellers, i.e. possessing two distinct blades, their blade passing frequency is twice the rotational frequency.

The notion of harmonics manifests as integer multiples of these base frequencies. Table 1 shows the frequencies of interest evaluated in this study. The table shows both, the exact frequency as well as the binned frequency at which the respective harmonic will be identified due to the frequency resolution of $1\,Hz$.

The table shows another important peculiarity. In this case, the second harmonic of the rotational frequency is synonymous with the blade passing frequency, as both manifest at twice the rotational frequency. Therefore, only the odd harmonics of the rotational frequency are regarded.

Additionally, as the third harmonic of the rotational frequency showcases, the exact frequency of occurrence can be located in the center of two integer frequencies. In this case, due to instationarities in the operation, the frequency bin the harmonic manifests in can change between the two values. In order to account for cases like this and general variance in the exact occurrence of the harmonic amplitude peaks, these are identified as the most prominent peak within a range of $\pm 5\,Hz$ around the theoretically defined center frequency.

In the remainder of the paper, these harmonics may be referred to with a shortened descriptor in the format of $(X\cdot)RF$ and $(X\cdot)BPF$ to represent the X^{th} harmonic.

3.5. Analysis Strategy

Aggregate analysis in the time domain. As a first step, the focal metrics of this study are analyzed separately and time-independent. For this, the distribution of the assumed values of the rotational speed and torque are presented and analyzed per long-time functional performance test. The values are reported in a normalized fashion by being divided by the respective clear water value at the set operating point. Therefore, the spread of the deviation of torque and

Table 1. Non-exhaustive list of frequencies of interest

Description	Exact Value	Binned Value
Rotational Frequency	$24.1\overline{6}\,Hz$	$24\,Hz$
Third Harmonic of RF	$72.5\,Hz$	$73\,Hz$
Fifth Harmonic of RF	$120.8\overline{3}\,Hz$	$121\,Hz$
Blade Passing Frequency	$48.\overline{3}\,Hz$	$48\,Hz$
Second Harmonic of BPF	$96.\overline{6}\,Hz$	$97\,Hz$

speed due to wastewater operating conditions can be deduced.

Aggregate analysis in the frequency domain. The second part of the aggregate analysis is focused on the averaged harmonic amplitudes for all tests. All amplitudes for the frequencies of interest from Table 1 are averaged over time for each test, resulting in a metric per harmonic per test. These amplitudes are normalized by the amplitude of the respective clear water operation as well, therefore representing the relative increase or decrease in amplitude. This analysis gives a first insight into the impact of wastewater operation and clogging on the harmonic amplitudes in the torque.

Integrated time and frequency domain analysis. In order to analyze the hydraulic and mechanical time-related metrics jointly with the frequency domain metrics, the latter are resolved in time as well via the reported windowing approach. Therefore, the head, flow, and torque, as well as the amplitudes of the harmonics of the torque can be reported in a synchronized fashion on a shared time base. This is done for demonstrative tests which are chosen based on the aggregate analyses to represent the prevalent findings.

4. RESULTS

4.1. Aggregate Analysis in Time Domain

Rotational speed. For the aggregate analysis of the distribution of values of the rotational speed, the normalized, relative values are shown as individual box plots per test in Figure 2a. These values can be interpreted as a percentage increase or decrease in rotational speed compared to the set clear water speed. The x-axis shows the labels for the respective pump as well as the contamination class employed in the test.

As can be seen by the very small range of the y-axis, the rotational speed does not vary a lot during the long-time functional performance test with artificial wastewater. The largest deviation from the set rotational speed of any test is below ±0.3 %. The median rotational speed of all tests even falls within ±0.1 % of the set speed.

Torque. The distribution of assumed torque values during the test is represented in the same way as the rotational speed, as boxplots of normalized values in Figure 2b. This figure additionally shows the weight ratio of each test as a bar, mapped to the right-sided y-axis. The weight ratio signifies the amount of dusters that accumulated in the pump at the end of the respective test.

In contrast to the rotational speed, the torque shows a lot more variation, with maximum values exceeding 40 % increase of the needed torque for clear water operation. Further, many more outliers can be observed, as seen by the amount of markers beyond the whiskers of the boxplots. This represents the occurrence of sudden spikes and peaks in the torque induced by the dusters' interference with the impeller.

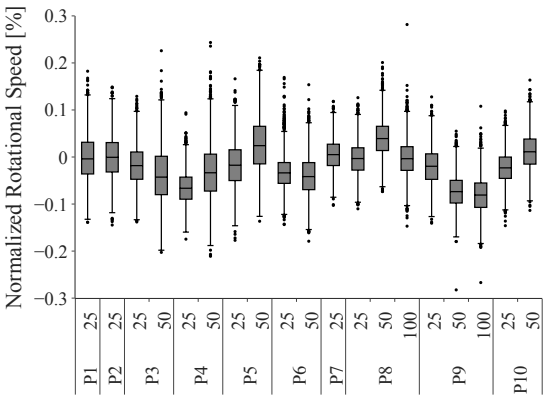

(a) Rotational Speed.

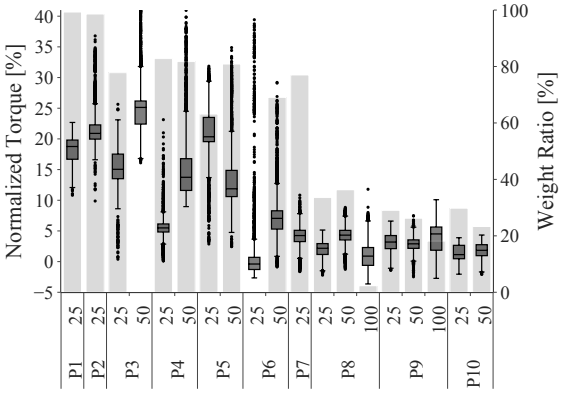

(b) Torque.

Figure 2. Boxplots for all tests showing the distribution of the rotational speed (a) and torque (b), normalized by their respective clear water operation values. Plot (b) additionally shows the weight ratio as bars mapped to the second, right-sided y-axis.

The overlayed weight ratio shows the relation between the severity of clogging of the pump and the attributed increase in the necessary torque. The tests where more severe clogging occurs, i.e. observing a higher weight ratio, also show a higher median of the torque and tend to generally exhibit more variance with more prominent peak values. Moreover, this tendency is also reversely true: tests, where few dusters are accumulated in the pump, tend to show a median closer to zero and less variance.

Discussion. The analysis of the rotational speed shows how well the VFD regulates and controls the delivered speed. Despite the demonstrated increases in torque, the set rotational speed can be very accurately maintained by the control.

The deviations in the operating conditions present due to the clogging of the pump mechanically only reflect in the supplied torque. This is supported by the observed tendency that the median and variance are increased when there are more dusters clogged in the pump. There are some exemptions,

like the test with contamination class 25 for pump P7. Here, 77 % of the dusters remain clogged in the pump, but the median torque is only increased by about 3.5 % compared to clear water operation.

Another obvious exemption to these observations is the test of pump P6 with contamination class 25. Here, no clogging occurred at the end of the test. The median torque in this test also exhibits the lowest value out of all tests, which falls in line with the overall tendency. However, the variance of torque from this test is among the largest of all tests. This can be attributed to transient clogging states occurring over the duration of the test. Since the weight ratio only describes the state at the end of the test, any short-lived and transient clogging events are not reflected in this metric. Therefore, analyses need to be carried out over time as well.

4.2. Aggregate Analysis in Frequency Domain

For the aggregate analysis in the frequency domain, Figure 3 shows the relative change of the average amplitudes for the frequencies of interest for each test. The change is reported relative to the amplitudes of the harmonics in clear water operation.

For the rotational frequency, there are no discernible tendencies to be observed. Only for the tests of pumps P1, P2, and P3, there is a notable increase in amplitude to be seen of up to 300 % in the case of pump P1. For the remainder of the tests, the amplitudes for the RF do not increase or decrease drastically and show no apparent pattern. The amplitudes of the third harmonic of the rotational frequency show a more unified response in that for all tests but one, there is an increase in the amplitude. For tests P1-25, P5-50, and P6-50, there is a particularly strong gain in amplitude. These observations are similar for the fifth harmonic of the RF.

An entirely different effect can be seen for the blade passing frequency, where the amplitude actually decreases for all but one test. The exemption being the test P1-25, which increasingly manifests as an outlier to the overall tendencies. Lastly, the second harmonic of the BPF increases for all performed tests. The highest increase for any harmonic is observed for test P4-50 with an increase of 317 %.

Discussion In the aggregate analysis in the frequency domain, some harmonics of the rotational and blade passing frequencies show tendencies to change in common ways when operating in wastewater conditions. This is further supported when revisiting the weight ratios of the individual tests reported in Fig. 2b. In the tests for pumps P1 through P7, with the exemption of test P6-25, the severity of clogging in terms of the weight ratio is a lot more prominent than for the remainder of the tests. This is reflected in the averaged relative change of the harmonic amplitudes. Here, the increase in the 2·BPF is especially prominent. The harmonic amplitudes of 3·RF also mainly show a larger increase than in the tests with

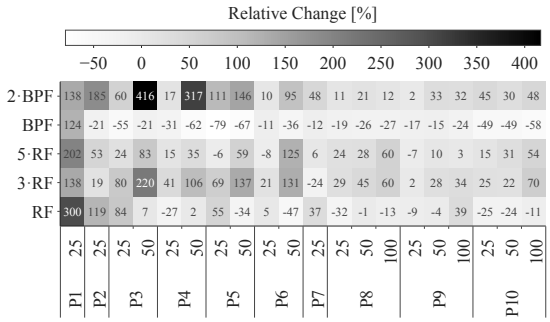

Figure 3. Relative increase of amplitudes at harmonic frequencies for all tests.

less severe clogging. This holds true as well for the observed decrease in magnitude of the BPF.

4.3. Integrated Time and Frequency Domain Analysis

The synchronized analysis of time and frequency domain components of the torque and the hydraulic performance metrics is facilitated by Figure 4. The figure shows the data for three exemplary tests, namely the test of pump P1 at the lowest contamination class 25 as well as tests of pumps P4 and P6 for the medium and lowest contamination classes, respectively.

Each of the subplots is assembled the same way: the respective top plot shows the five harmonics of interest. Here, the amplitudes are normalized by their clear water operation values to get the relative changes in amplitude induced by the wastewater conditions. The bottom plots show the head, flow, and torque data, normalized by their respective clear water operation values as well and transformed to a percentage. All values can directly be interpreted as percentage-wise increases or decreases.

In Figure 4a, it can be seen that especially the amplitude of the rotational frequency increases drastically during the first 1000 *s* of the test, with relative increases of up to nearly 700 %. Additionally, all other harmonics observe increased amplitudes as well, with increases between 100 and 300 %. The overall level of the torque increases by 20 percent at the start of the test and drops to about a 15 % increase at the 2000 *s* mark. In contrast, the flow and head drop to a continuously lower level over the whole duration of the test, with respective losses of 10 % in flow and 20 % in head.

The test in Figure 4b exhibits very different trends. Here, the second harmonic of the BPF is the most prominent harmonic with increases of up to 580 %. The rotational frequency shows no elevated amplitude levels while its third and fifth harmonic increase around 200 % on average, the latter peaking at as much as 520 % increase at the beginning of the test. In contrast, the amplitude of the BPF shows continuously lower levels than in clear water operation with a drop of 60 to 70 %. Concurrently, the

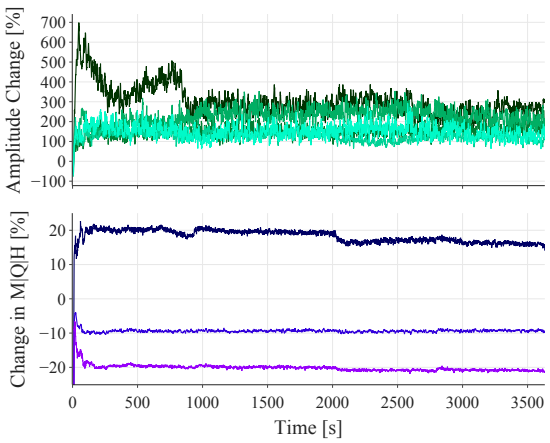

(a) P1-25.

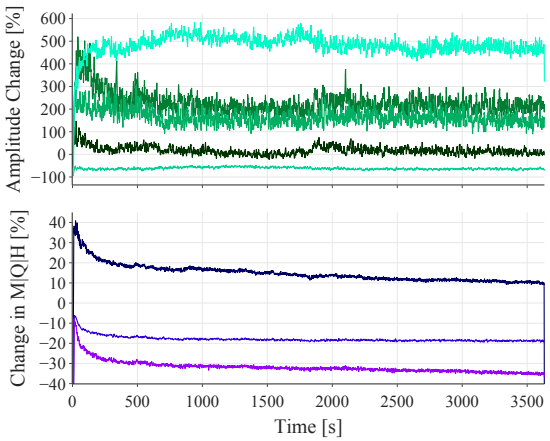

(b) P4-50.

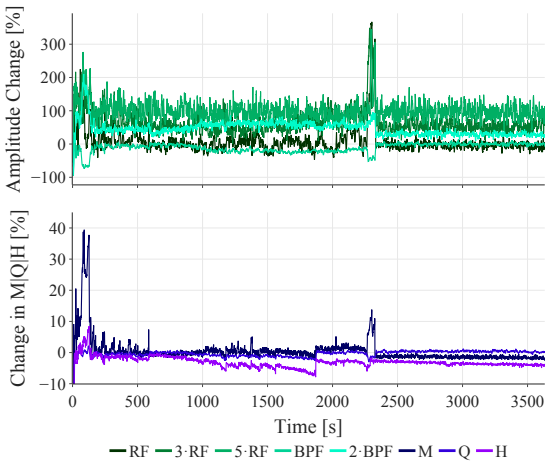

(c) P6-25.

Figure 4. Harmonic and hydraulic metrics over time for three different tests. The respective top plot shows the relative difference in harmonic amplitudes. The bottom plots show the relative difference in head, flow, and torque. The joint legend is located in (c).

hydraulic performance metrics decrease from the beginning of the test, with the flow dropping to a continuously lower level of around 80 % of its clear water reference. The head drops most prominently at the beginning as well, but then keeps slowly declining to a final value of 65 % of its clear water value. The magnitude of the torque again develops contrarily with increases of 40 % at the start and a continuous slow decline from this peak over the duration. The torque is still increased by about 10 % at the end of the test.

Lastly, the third test, reported in Figure 4c, shows rather inconspicuous harmonic levels most of the time. The same holds true for the hydraulic metrics and the overall torque level. However, there are two distinct events, at the beginning of the test and between 2250 and 2350 s, where the torque values increase drastically for a short duration. These events are reflected in the harmonics as well, where for both events the amplitude of the BPF drops below its clear water levels and the other harmonics show increased amplitudes.

Discussion The first two presented tests P1-25 and P4-50 both represent tests where clogging of the pump's impeller occurs from the start of the test. The final clogging accounts for 99 and 82 % respectively for the two tests. The state of clogging of the impeller is depicted in Figure 5.

The test P1-25 is the previously identified outlier from the overall observable harmonics trends in the data. This is also true when regarding the harmonics in a time-resolved manner, as all harmonics show a considerable increase due to severe clogging.

Test P4-50 features even more severe clogging, with, despite the smaller weight ratio, an overall higher weight of dusters remaining clogged in the impeller. This is especially reflected in the hydraulic performance as the head and flow decrease extensively. In the frequency domain, the harmonics show representative patterns as discovered to be prevalent in the aggregate analysis. The BPF is continuously smaller than in clear water operation while its second harmonic is highly increased. The increased torque at the beginning of the test is especially reflected in the third and fifth harmonic of the RF.

In the last test, P6-25, there was no clogged material inside the pump at the end of the test. Over most of the test duration, the pump is only very minorly clogged as observed during the test via a borescope. This minor clogging is reflected in the harmonics of the torque, especially through the increased levels of the third and fifth harmonic of the RF. The salient event after 2250 seconds, where the torque and its harmonics suddenly spike and then revert to their original levels again after about 100 seconds represents an event where more material is spontaneously accumulating in the impeller. Subsequently, all clogged material evacuates from the impeller and it stays clog-free until the end of the test. This presents the imprint of self-cleansing mechanisms as often observed in wastewater pumps [8] onto the required torque and its harmonics.

(a) P1-25. **(b) P4-50.**

Figure 5. Accumulated clogging after the respective test.

5. CONCLUSION

The work presents insights from 19 standardized functional performance tests in realistic wastewater operating conditions for a total of 10 different wastewater pumps with semi-open two-channel impellers. The focus of the investigation lies on the mechanical load and clogging-induced instationarities in it. These are demonstrated in the value as well as frequency domain of the torque signal. In particular, clogging of the impeller was shown to lead to increased required torque levels as well as large increases in torque oscillation. The latter manifests as amplitude increases of harmonic frequencies of the rotational and blade passing frequencies with transient, relative increases of more than 600 %.

In future work, the aim is to project these torque deviations onto electrical power and current measurements within the variable frequency drive. This will mostly be achievable for the value domain, the application of frequency domain analyses, however, will presumably show different characteristics.

REFERENCES

[1] Von Sperling, M., 2007, *Wastewater characteristics, treatment and disposal*, IWA publishing.

[2] Pöhler, M., 2020, *Experimentelle Entwicklung eines standardisierten Abnahmeverfahrens für Abwasserpumpen*, Mensch und Buch Verlag.

[3] Kallweit, S., 1994, *Untersuchungen zur Erstellung wissensbasierter Fehlerdiagnosesysteme für Kreiselpumpen*, Technische Universitaet Berlin (Germany).

[4] Caruso, F., and Meskell, C., 2021, "Effect of the axial gap on the energy consumption of a single-blade wastewater pump", *Proceedings of the Institution of Mechanical Engineers, Part A: Journal of Power and Energy*, Vol. 235.

[5] Keays, J., and Meskell, C., 2006, "A Study of the Behaviour of a Single-Bladed Waste-Water Pump", *Proceedings of the Institution of Mechanical Engineers, Part E: Journal of Process Mechanical Engineering*, Vol. 220.

[6] Barrio, R., Blanco, E., Parrondo, J., González, J., and Fernández, J., 2008, "The Effect of Impeller Cutback on the Fluid-Dynamic Pulsations and Load at the Blade-Passing Frequency in a Centrifugal Pump", *Journal of Fluids Engineering*, Vol. 130 (11).

[7] Beck, D., Holzbauer, Y., and Thamsen, P. U., 2021, "Different Clogging Behavior of Wastewater Pumps", *Fluids Engineering Division Summer Meeting*, American Society of Mechanical Engineers.

[8] Beck, D., Brokhausen, F., and Thamsen, P. U., 2022, "Time-Resolved Measurements for the Detection of Clogging Mechanisms", *Fluids Engineering Division Summer Meeting*, American Society of Mechanical Engineers.

[9] Brokhausen, F., Herfurth, E., Beck, D., and Thamsen, P., 2023, "Exploring characteristics of time-resolved signals in the operation of wastewater pumps", *European Conference on Turbomachinery Fluid Dynamics and Thermodynamics*.

[10] Brokhausen, F., Rost, L. M., and Thamsen, P. U., 2024, "Frequency Domain Analysis of Transient Discharge Pressure Harmonics for Clogging Detection in Wastewater Pumps", *Fluids Engineering Division Summer Meeting*, American Society of Mechanical Engineers.

[11] Mitchell, R.-L., Gunkel, M., Waschnewski, J., and Thamsen, P. U., 2020, "Nonwoven Wet Wipes Can Be Hazardous Substances in Wastewater Systems—Evidences from a Field Measurement Campaign in Berlin, Germany", *Frontiers in Water-Energy-Nexus—Nature-Based Solutions, Advanced Technologies and Best Practices for Environmental Sustainability*.

[12] DIN EN ISO 9906, 2012, "Rotodynamic Pumps—Hydraulic Performance Acceptance Tests—Grades 1, 2 and 3", .

[13] Lyons, R. G., 2004, *Understanding Digital Signal Processing (2nd Edition)*, Prentice Hall PTR, USA.

[14] Blackman, R. B., and Tukey, J. W., 1958, "The measurement of power spectra from the point of view of communications engineering—Part I", *Bell System Technical Journal*, Vol. 37.

[15] Brandt, A., 2023, *Noise and vibration analysis: signal analysis and experimental procedures*, John Wiley & Sons.

Conference on Modelling Fluid Flow (CMFF'25)
The 19th International Conference on Fluid Flow Technologies
Budapest, Hungary, August 26-August 29, 2025

The Effect of Housing Recess Geometry on Fiber Entry into the Back Shroud Cavity of a Wastewater Pump

Tobias RINNERT[1], Paul Uwe THAMSEN[2],

[1] Corresponding Author. Department of Fluid System Dynamics, Faculty of Mechanical Engineering and Transport Systems, Technische Universität Berlin. Straße des 17. Juni 135, 10623 Berlin, Germany. Tel.: +49 30 314 70930, E-mail: t.rinnert@tu-berlin.de
[2] Department of Fluid System Dynamics, Faculty of Mechanical Engineering and Transport Systems, Technische Universität Berlin. Straße des 17. Juni 135, 10623 Berlin, Germany. Tel.: +49 30 314 25262, E-mail: paul-uwe.thamsen@tu-berlin.de

ABSTRACT

In this paper, the influence of several housing recess geometries on the fiber entry into the back shroud cavity of a single volute wastewater pump with a semi-open two-channel impeller is investigated. The test rig used is a wastewater pumping station model that provides optical access into areas in wastewater pumps that are at risk of clogging. Three operating points are examined for each configuration, one at part load, one at best efficiency point and one at overload. The introduced configurations feature varying radial gap widths between back shroud and outer diameter of the recess as well as different degrees of back shroud coverage. The axial gap width between recessed rear housing wall and flat disk back shroud corresponds to 5 *mm*. Tested configurations are evaluated on the basis of dry fiber mass permanently accumulated in the back shroud cavity after pumping artificial wastewater for 60 *min*. The evaluation of the experimental data shows that housing recesses with partial or complete back shroud coverage significantly reduce or completely eliminate fiber entry while increasing efficiency.

Keywords: back shroud cavity, clogging, fibers, housing recess, wastewater pump

NOMENCLATURE

H	$[m]$	head
N_S	$[min^{-1}]$	specific speed (US customary)
P	$[W]$	power
Q	$[m^3 s^{-1}]$	flow rate
R	$[mm]$	radius
Re	[-]	Reynolds number
S	[-]	gap ratio
T	$[min]$	time
c	[-]	degree of coverage
d	$[mm]$	depth
g	$[ms^{-2}]$	gravitational acceleration
n_q	$[min^{-1}]$	specific speed (metric)
s	$[mm]$	gap width
t	$[mm]$	thickness
η	[-]	efficiency
ρ	$[kgm^{-3}]$	mass density

Subscripts and Superscripts

BS	back shroud
HR	housing recess
a	aggregate
ax	axial
c	critical
el	electrical
$hydr$	hydraulic
r	radial

1. INTRODUCTION

Being part of critical infrastructure, wastewater pumps are expected to operate clogging-free, safely and efficiently [1, 2]. However, continuous entry of fibers from nonwoven wipes is one of major obstacles for the reliable operation of wastewater systems all over the world [3]. Although the yearly nonwoven wipe production throughout Europe has declined slightly since its all-time high of almost 3.25 million tons in 2021, in 2023 it was still 2.8 times the amount produced in 2000 [3, 4]. The fibers contained in the wastewater frequently accumulate in wastewater pumps at the blade inlet, on the cutwater and in the front and back shroud cavity [2, 5, 6]. In addition to the risk of clogging, fibers entering the back shroud cavity can pose a risk to the mechanical seal [7]. The *functionality*, i.e. the ability of a pump to transport fiber-laden wastewater without clogging [8], is therefore of utmost importance, as it may furthermore reduce the aforementioned requirements operational safety and efficiency [3, 9]. The only thing worse than an inefficiently operated wastewater pump is one that cannot be operated when needed. Cities such as London, New York and Sydney each bear annual resulting costs of tens of millions USD [3].

In order to meet the requirements discussed, there are numerous design guidelines available that vary depending on wastewater composition [10, 11]. In wastewater pumps, vortex as well as one-, two- and three-channel impellers are commonly in use [2]. When pumping large solids, clogging can be easily avoided by choosing wastewater impellers that feature a sufficiently large *ball passage* [5]. When it comes to pumping fiber-laden wastewater, however, the susceptibility to clogging is independent of the ball passage, as experimentally determined by Pöhler and Thamsen [12] for a wide variety of wastewater pump impellers. Wastewater pumps are usually designed as single-stage pumps with a volute or annular casing [2, 5]. This is due to the fact that the bladed guide vanes found in multistage pumps are prone to clogging [5, 10]. Furthermore, balance holes in the back shroud are avoided in wastewater pumps as well for the same reason, so that axial thrust reduction is typically achieved by back vanes [5].

However, only vague design guidelines are available to keep the back shroud cavity free of fibers or other solids. Housing recesses as well as back vanes are stated as solutions [5, 7, 13, 14]. In preliminary tests on the wastewater pump investigated in this paper, the fiber entry into the back shroud cavity was found to significantly decrease as the axial gap width s_{ax} between flat disk-shaped back shroud and rear housing wall decreases [15]. Further investigations on this wastewater pump focused on the influence of specific design parameters for backward curved back vanes and back channels on fiber entry into the back shroud cavity [16]. It showed, that backward curved back vanes can eliminate fiber entry into the back shroud completely even at low back vane height and with minor efficiency drawbacks. In contrast, only the one back channel configuration investigated at minimum axial gap width between the unmodified part of the back shroud and rear housing wall, as well as maximum channel depth, was found to be capable of slightly decreasing fiber entry at a disproportionate reduction in efficiency.

2. BACK SHROUD CAVITY FLOW

Hardly anything in a centrifugal pump has as powerful an influence on other essential components and operating behavior due to its design characteristics as the cavities between impeller and housing. The flow prevailing there not only largely defines axial thrust [5, 10]. It is furthermore well known, that the shroud cavity design may significantly affect radial thrust as well [5]. Besides axial thrust, the pressure within the back shroud cavity is also to be considered when choosing the shaft seal. With regard to pump efficiency, shroud cavity design impacts leakage losses and, in particular, disk friction losses [10, 17]. The latter is nothing less than the fundamental motivation for the experiments on disks rotating in cylindrical housings, as conducted by Schultz-Grunow [18], Ippen [19] or Daily and Nece [20, 21], from which the basic understanding of back shroud cavity flow is derived [5, 10].

2.1. Theory

Based on analytical and experimental investigations on *enclosed rotating disk flow* conducted by Daily and Nece [20, 21], it has become common practice to distinguish between the following four flow regimes, depending on the properties of disk and rear housing wall boundary layers:

I. merged, laminar
II. separated, laminar
III. merged, turbulent
IV. separated, turbulent

Reynolds number Re and axial gap width s_{ax} define the corresponding flow regime prevailing. However, surface roughness can increase boundary layer thickness and decrease the critical Reynolds number Re_c. [20, 21]

Within the disk boundary layer, the circumferential velocity is increased compared to the rest of the fluid. Directly on the rotating disk surface, the fluid moves with the local circumferential velocity of the disk itself, due to the no slip boundary condition. Accordingly, the no slip boundary condition causes the circumferential speed to be zero directly on the stationary rear housing surface. Compared to the rest of the fluid, the circumferential velocity is decreased within the rear housing boundary layer. Due to the increased circumferential speed within the rotating disk boundary layer, the fluid is therein centrifuged outward. Continuity enforces a radially inward directed flow within the housing wall boundary layer, which leads to the characteristic radial-axial circulation between disk and rear housing wall. Together with the explained circumferential velocity distribution, this yields the three-dimensional flow around enclosed rotating disks. For sufficiently large axial gap widths s_{ax}, the boundary layers are separated from each other and a co-rotating rigid-body vortex develops between them. [5, 10, 18, 20]

Normally, flow regime IV is present in water pumps [5, 10]. For the constellation of separated turbulent boundary layers, the radial velocities are always low compared to the circumferential velocities [5]. With regard to avoiding fiber entry into the back shroud cavity of a pump, this together with the above-mentioned flow pattern appears very convenient. It is tempting to assume that, due to the continuous and isolated radial-axial circulation, fibers contained in the main flow could not enter the back shroud cavity. And even if fibers were to be near parts within the back shroud cavity that are to be kept free of them, it could be expected that they are once more circulated away. However, in reality wastewater pumps have to be taken out of operation due to clogged back shroud cavities or destroyed mechanical seals.

2.2. Practice

In practice, the flow in the back shroud cavity differs considerably from the flow described for enclosed rotating disks. In both, annular and volute housings, the velocity and pressure distribution is rotationally asymmetrical at all operating points, causing the flow inside the back shroud cavity to be asymmetrical as well. Secondary flows through the back shroud cavity then occur as a result. [2, 5, 22, 23]

Furthermore, experiments and numerical simulations have shown that by actively dominating the flow through a suitable shroud geometry [22, 23] or by passively protecting the respective shroud cavity [24], asymmetric flow within front or back shroud cavity can, to a certain degree, be homogenized.

For instance, Bubelach [23] applied front vanes to the front shroud of a wastewater pump with a closed one-channel impeller. Compared to the flat disk-shaped front shroud configuration, the flow inside the front shroud cavity was less dependent of the circumferential pressure distribution in the annular housing.

Will et al. [22] numerically and experimentally investigated the flow inside the front as well as the back shroud cavity of a commercial standard pump with a single volute and a closed seven-channel impeller. Flow regime III was observed to prevail in the back shroud cavity due to low axial gap width s_{ax}. Viscous effects therefore had, to a certain degree, a homogenizing influence on the back shroud cavity flow.

Numerical and experimental investigations carried out by Knop et al. [24] showed that, in addition to the pressure distribution in the housing, the pressure distribution in the impeller eye can also affect the flow in the front shroud cavity. The pressure field in the impeller eye was homogenized by adapting the impeller geometry, which prevented further clogging of the one-channel wastewater impeller.

2.3. Housing Recesses

The extent to which the back shroud cavity is influenced by outer boundary conditions can be controlled by the design of the back shroud cavity, i.e. the design of the housing and the back shroud [5]. When the back shroud cavity is relatively open at the outer impeller diameter, the back shroud cavity flow is strongly coupled to the flow in the housing and the main flow behind the impeller outlet [5, 22]. In contrast, when recessing the rear housing wall in a way that the radial gap width s_r is small, whereas the degree of back shroud coverage c_{BS} is high, the back shroud cavity flow can be decoupled from outer boundary conditions to a large extent [5]. The degree of back shroud coverage c_{BS} is determined as follows, using the parameters shown in Fig. 1:

$$c_{BS} = \frac{d_{HR} - s_{ax}}{t_{BS}} \tag{1}$$

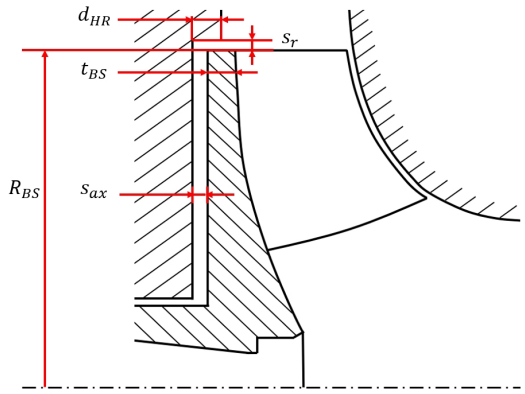

Figure 1. Back shroud cavity parameters

With regard to the fiber entry, it is therefore expected that the discussed local, centripetally directed secondary flows in particular lead to an increase in fiber entry and thus to a decrease in functionality in open and accordingly strongly coupled back shroud cavities. It is vice versa assumed that with increasing degree of back shroud coverage c_{BS} and decreasing radial gap width s_r, the back shroud cavity flow is increasingly decoupled from the external boundary conditions stated above, thus decreasing fiber entry. It is of special interest for the investigation presented to obtain information on both the effectiveness as well as the corresponding magnitude of the parameters back shroud coverage c_{BS} and radial gap width s_r. Increased radial thrust is to be expected for increasingly decoupled back shroud cavity designs, as pressure balancing secondary flows through the back shroud cavity are weakened [5].

3. EXPERIMENTAL INVESTIGATION

3.1. Investigated Pump

The dry-installed wastewater pump investigated has a semi-open two-channel impeller with a specific speed n_q and N_s at best efficiency point (Q100) of 58 min^{-1} and 3000 min^{-1}, respectively. Its outer diameter is 277 mm. The impeller is modified in a way that different back shroud geometries can be mounted. Therefore, the original back shroud geometry was turned off and subsequently featured threaded holes. The investigated pump has a volute housing and is driven by a 4-pole asynchronous motor. The rear housing wall is made of acrylic glass and hence fully transparent. It is furthermore equipped with threaded holes on different radii, so that the flat disk-shaped rear housing wall can be modified.

3.2. Test Rig

Figure 2 shows the open loop test rig operated for the experiments conducted. The water tank (WT) replicates a wastewater pumping station suction chamber. It has a capacity of 6 m^3 as well as fully transparent acrylic glass walls. During each test, artificial wastewater moves from the water tank through

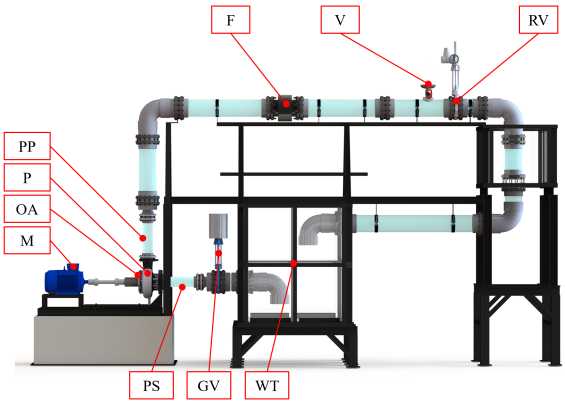

WT	water tank	OA	optical access
GV	gate valve	M	electric motor
PS	pressure measuring section (suction side)	F	flowmeter
PP	pressure measuring section (pressure side)	V	(de-) aeration valve
P	wastewater pump	RV	regulation valve

Figure 2. Test rig [15]

a DN 250 elbow pipe into the DN 150 suction line, where the static pressure upstream the pump is obtained (PS). From there, the artificial wastewater is transported through the test pump (P) and the DN150 discharge line, where the static pressure downstream the pump is measured (PP). From there, the artificial wastewater passes a shock diffuser and continues flowing through a magneto-inductive flowmeter (F). It subsequently passes a valve (V) installed for aeration as well as deaeration before passing the regulation valve (RV). Downstream, the artificial wastewater flows back into the water tank (WT).

3.3. Artificial Wastewater

To replicate fiber-laden wastewater, a defined quantity of microfiber rags is mixed with clear water in accordance with the standard DWA-A 120-2 [8] and other work investigating the functionality of wastewater pumps such as [9] or [12]. The *loading class* chosen corresponds to 25 rags per 1 m^3 of clear water, which complies with the lowest loading class defined in [8]. The total amount of microfiber rags thus corresponds to 150 per each of the tests conducted.

3.4. Housing Recess Configurations

Figure 1 shows the main parameters relevant for the housing recess configurations. The axial gap with s_{ax} was kept constant at 5 *mm*. This axial gap width was chosen due to the results of previous experiments [15] on the influence of the axial gap width s_{ax} between flat disk shaped back shroud and rear housing wall on fiber entry into the back shroud cavity of the same wastewater pump. The tests with axial gap widths s_{ax} of 1, 2, 3, 4 and 5 *mm* showed a general decrease in fiber entry with decreasing axial gap width. In order to assess the effectiveness of the recess configurations presented in this paper, it was decided to select the maximum gap width as a reference, at which the chance of fiber entry is high. Radial gap width s_r as well as degree of back shroud

Table 1. Housing recess configurations

Designation	c_{BS} [-]	s_r[mm]	S_r[-]
HR 0.8	0	8	0.0578
HR 50.8	0.5	8	0.0578
HR 100.8	1	8	0.0578
HR 0.2	0	2	0.0144
HR 50.2	0.5	2	0.0144
HR 100.2	1	2	0.0144

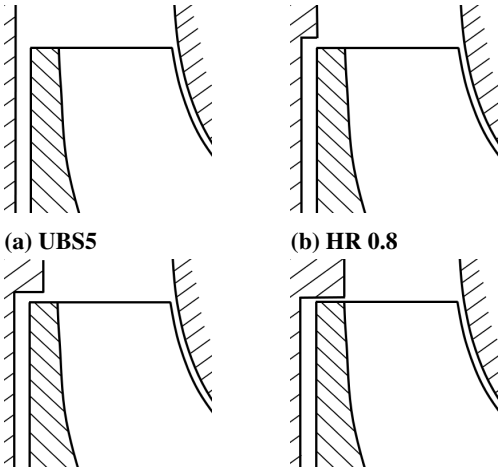

(a) UBS5 **(b) HR 0.8**

(c) HR 50.8 **(d) HR 100.2**

Figure 3. Selected configurations in comparison

coverage c_{BS} were varied throughout the tests. Table 1 provides an overview over the investigated housing recess geometries. Several of these configurations as well as the reference configuration UBS5 are illustrated in Fig. 3. The given designations correspond to the type of modification, the back shroud coverage c_{BS} and the radial gap width s_r. In order to easily compare the housing recess geometries presented with those in other pumps, it is also useful to specify the radial gap ratio as follows:

$$S_r = \frac{s_r}{R_{BS}} \tag{2}$$

The various configurations were implemented by screwing 3D printed polylactide rings onto the acrylic glass back wall, as shown for configuration HR 100.8 in Fig. 4.

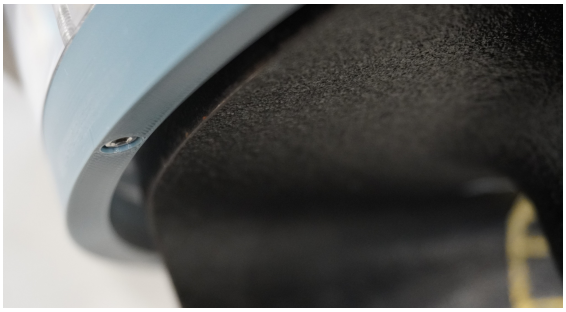

Figure 4. Radial gap of housing recess configuration HR 100.8

3.5. Test Procedure

For each configuration, three different operating points were investigated, one at part load (Q50), one at best efficiency point (Q100) and one at overload (Q120). For a corresponding configuration, three tests were performed per operating point. Each configuration was evaluated regarding the permanent dry fiber mass entry into the back shroud cavity after a test duration of 60 *min* after completion of the ramp-up process.

Prior to each test, reference values for head and electrical power were obtained for the flow rate of interest under clearwater conditions. The reference values are needed to monitor the operating behavior throughout each test as well as to determine any geometry-induced influence on both, operating behavior and aggregate efficiency. The latter is obtained as follows:

$$\eta_a = \frac{P_{hydr}}{P_{el}} = \frac{\rho g Q H}{P_{el}} \tag{3}$$

At the end of each test, the pump was switched off and the test rig was drained into a filtration system, where the fiber-laden water was prepared for the next test. The bearing bracket and the impeller were then removed. After taking the impeller off the shaft, possible fiber accumulations were collected and subsequently dried in a dehydrator until no more evaporation-induced weight loss was detectable. Table 2 provides an overview of the uncertainties of the measurement methods used.

Table 2. Measurement uncertainties

Quantity	Uncertainty
flow rate	± 0.2 % of value
differential pressure	± 0.05 *bar*
electrical power	± 1 % of value
mass	± 0.005 *g*

4. RESULTS

The configurations listed in Table 1 are evaluated below on the basis of the dry fiber mass entry into the back shroud cavity. Results for the reference configuration of equal back shroud geometry without housing recess *UBS5* obtained in [15] are used as a reference. In Fig. 5 and 7, the markers, upper bars and lower bars represent the mean, maximum and minimum values of dry fiber mass entry, respectively.

4.1. Radial Gap Width s_r of 8 mm

Figure 5 shows the results for the housing recess geometries with a radial gap width s_r of 8 *mm*. At part load Q50, no fiber entry into the back shroud cavity was detected for all configurations investigated.

At best efficiency point Q100, however, significant fiber entry into the back shroud cavity took place when testing configuration HR 0.8, as shown

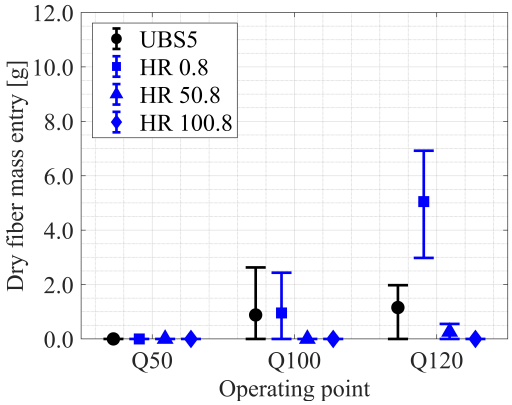

Figure 5. Dry fiber mass entry at s_r of 8 *mm*

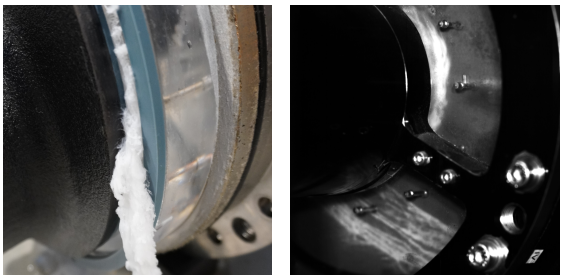

(a) best efficiency point **(b) overload**

Figure 6. Fiber accumulations observed when operating configuration HR 0.8

in Fig. 6a. For this configuration, which fully covers the back shroud cavity but not the back shroud, the fiber entry was quantitatively very similar to that of the recess-free reference configuration UBS5. In contrast, configurations HR 50.8 as well as HR 100.8 showed no fiber entry at best efficiency point, effectively reducing fiber entry into the back shroud cavity.

At overload operation Q120, fiber entry was distinctly increased by configuration HR 0.8. Compared to configuration UBS5, mean fiber entry more than quadrupled. As shown in Fig. 6b, once more fibers were observed to jam the passage to the back shroud cavity. In addition, fibers wound up on the rotating hub. With partial back shroud coverage c_{BS} of 0.5 in contrast, fiber entry was significantly reduced, as the mean value of 0.26 *g* corresponds to 22.5 % of the fiber entry registered for configuration UBS5 at this operating point. Configuration HR 100.8, due to its full back shroud coverage, eliminated any fiber entry at overload operation Q120.

4.2. Radial Gap Width s_r of 2 mm

For the housing recess geometries with a smaller radial gap width s_r of 2 *mm*, the operating point-dependent dry fiber mass entry is shown in Fig. 7.

With exception of configuration HR 50.2, none of the configurations examined at part load Q50 showed any significant fiber entry into the back shroud cavity. This is remarkable, since significant fiber entry into the back shroud cavity proved to be

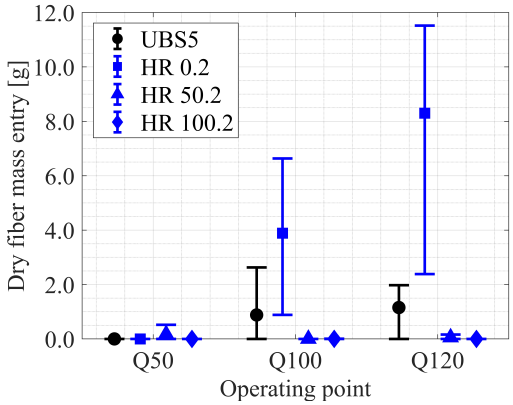

Figure 7. Dry fiber mass entry at s_r of 2 *mm*

rare for the investigated pump at part load. However, two of the three tests carried out with configuration HR 50.2 at part load were free of any fiber entry.

At best efficiency point Q100, HR 0.2 was found to be the only housing recess configuration with significant fiber entry into the back shroud cavity. In Fig. 8a fibers jammed in the passage to the back shroud cavity can be seen. Figure 8b shows the massive amount of fibers wound up on the hub after the same test at best efficiency point with a dry mass fiber entry of more than 6.6 g.

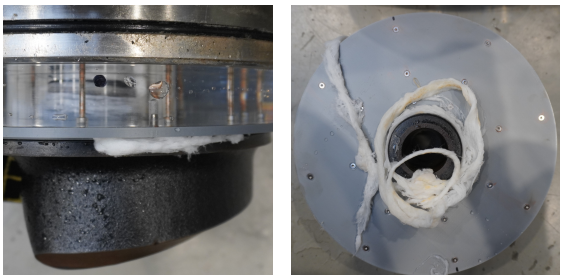

(a) jammed fibers **(b) wound up fibers**

Figure 8. Fiber accumulations after operating configuration HR 0.2 at best efficiency point

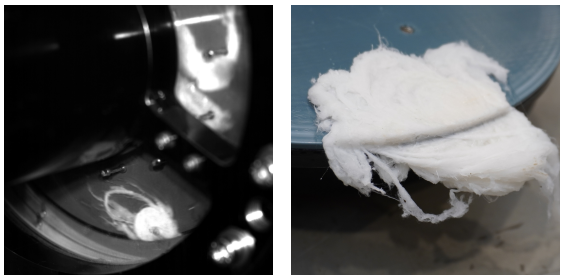

(a) during operation **(b) after operation**

Figure 9. Configuration HR 0.2 at overload

When operating the housing recess configurations with a radial gap width s_r of 2 *mm* at overload Q120, strongly increased fiber entry was detected for HR 0.2 once more. With a maximum value of 11.52 g for this configuration at this operating point, the largest dry fiber mass entry of the entire test series was determined. Again, fibers were seen to both wind up on the rotating hub and jam the passage to the back shroud cavity, as shown in Fig. 9a. As can be further seen in Fig. 9b, the fiber entry was so severe, that the back shroud as well as the recess geometry were damaged and had to be replaced. With a value of 0.16 g, maximum dry fiber mass entry was much less due to increased back shroud coverage c_{BS} but still considerable when operating housing recess configuration HR 0.5 at overload. It was again the configuration with the maximum back shroud coverage c_{BS}, that showed no fiber entry at overload.

4.3. Influence on Performance

In Fig. 10 it can be seen that fibers jamming the passage to the back shroud cavity were particularly evident when examining the recorded performance data, including electric power input P_{el}, hydraulic power output P_{hydr} as well as the resulting aggregate efficiency η_a. Reference values P_{el} and P_{hydr} obtained prior to this test corresponded to 12.45 kW and 8.06 kW, respectively. As can be seen in Fig. 10a, P_{el} increased to 12.89 kW by the end of the test due to the frictional torque caused by the jammed fibers, while P_{hydr} was reduced to 7.84 kW. Aggregate efficiency η_a was thus significantly reduced from 0.648 to 0.609. This influence on the performance data could only be determined for strong jamming of fibers accumulated in the passage to the back shroud cavity. In the case of minor fiber accumulations of this type as well as fibers wound up on the hub or the shaft, no such influence on the operating behavior was determined.

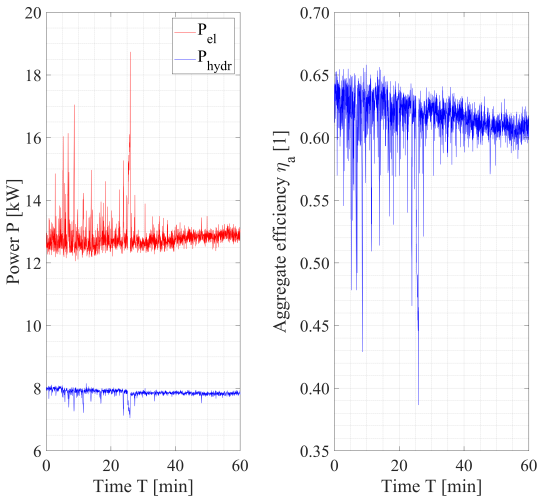

(a) power **(b) efficiency**

Figure 10. Performance data for configuration HR 0.2 at overload

4.4. Clear Water Efficiency Comparison

Measures to increase functionality are also to be evaluated on the basis of their influence on efficiency. Improving the clogging behavior of a wastewater pump often goes together with a reduction in efficiency. Figure 11 shows the aggregate efficiency η_a averaged over the three operating points for all housing recess configurations investigated as well as the recess-free reference configuration UBS5. It can be seen that the aggregate efficiency η_a for the introduced housing recess configurations is generally equal or higher compared to configuration UBS5. Furthermore, aggregate efficiency overall proved to increase with increasing degree of back shroud coverage c_{BS} and decreasing radial gap width s_r.

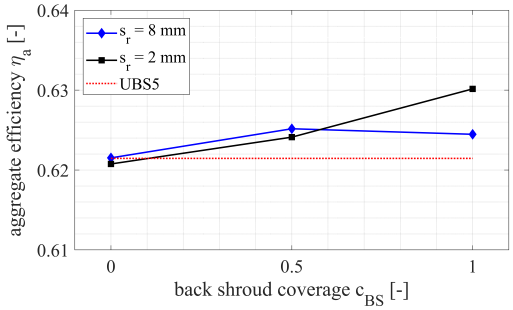

Figure 11. Operating point-averaged aggregate efficiency

4.5. Discussion

For the investigated pump and range of the parameters back shroud coverage c_{BS} and radial gap width s_r, the presented results lead to the finding that to prevent fiber entry into the back shroud cavity by decoupling back shroud cavity and housing using a suitable recess geometry, high back shroud coverage c_{BS} is to be preferred over small radial gap width s_r. This deduction is based on the fact that for all radial gap widths s_r investigated, the increase to moderate and to complete back shroud coverage c_{BS} generally led to a significant reduction and complete elimination of fiber entry, respectively. In contrast, for configurations with insufficient back shroud coverage c_{BS}, an increase in fiber entry with decreasing radial gap width s_r was evident.

As discussed in section 2.3, decoupling the back shroud cavity flow from the flow in the housing was expected to decrease fiber entry into the back shroud cavity. It was further elaborated, that the extent to which these flows are decoupled generally increases with increasing back shroud coverage c_{BS} and decreasing radial gap width s_r. These expectations have only proven to be valid for housing recess configurations in which the decoupling of the back shroud cavity flow was pursued by sufficiently large back shroud coverage c_{BS} and radial gap widths s_r that are not too small. However, this does not directly contradict the literature from which the expectations were derived, as the findings stated therein refer to clear water conditions without fibers or other solids. With only 2 *mm*, the minimum radial gap width s_r selected in this work may provide a significant decoupling of the back shroud cavity from external boundary conditions under clear water conditions. Despite this, however, this proved to result in an unfavorable passage to the back shroud cavity, which causes fiber accumulations to get jammed as well as prevents them from easily exiting the back shroud cavity.

In cases of severe jamming, electrical power input P_{el} was observed to increase, whereas hydraulic power output P_{hydr} was determined to decrease, thus decreasing aggregate efficiency η_a. In the case of minor jamming or fibers wound up on the hub or the shaft, no such influence was detected. Compared to the recess-free reference configuration, clearwater aggregate efficiency η_a of the housing recess configurations presented was equal or higher by up to nearly 0.01.

5. SUMMARY

Based on the literature discussed, potential influences of housing recesses on the back shroud cavity flow and the resulting fiber entry were derived. In order to determine the respective influence of the relevant parameters back shroud coverage c_{BS} and radial gap width s_r, suitable back shroud cavity configurations with housing recesses were designed. A test procedure to assess the functionality of these housing recess configurations was presented. The corresponding configurations were experimentally investigated and evaluated on the basis of dry fiber mass permanently accumulated in the back shroud cavity after pumping artificial wastewater for 60 *min*. The experiments conducted lead to the finding that fiber entry into the back shroud cavity is significantly reduced or completely eliminated as the back shroud coverage c_{BS} is increased. In contrast, an increase in fiber entry was determined when reducing the radial gap width s_r for configurations with insufficient back shroud coverage c_{BS}. Fibers were then frequently observed to jam the passage to the back shroud cavity, reducing aggregate efficiency η_a in severe cases. Fibers were also seen to wind up on the hub or the shaft. However, a related significant influence of this phenomenon on pump performance was not detected. The investigated housing recess geometries showed equal and, in case of partial or full back shroud coverage, increased aggregate efficiency η_a.

However, further knowledge about the prevailing flow within the back shroud cavity is to be determined numerically or experimentally. Since the results presented only apply to the investigated wastewater pump, it is of further interest to find out whether the findings apply to other pumps as well.

REFERENCES

[1] Gerlach, S., and Thamsen, P. U., 2017, “Cleaning Sequence Counters Clogging: A Quantit-

ative Assessment Under Real Operation Conditions of a Wastewater Pump", *Volume 1A, Symposia: Keynotes; Advances in Numerical Modeling for Turbomachinery Flow Optimization; Fluid Machinery; Industrial and Environmental Applications of Fluid Mechanics; Pumping Machinery*, American Society of Mechanical Engineers, Fluids Engineering Division Summer Meeting, p. V01AT05A001.

[2] Surek, D., 2014, *Pumpen für Abwasser- und Kläranlagen - Auslegung und Praxisbeispiele*, Springer Vieweg Wiesbaden, Wiesbaden.

[3] Mitchell, R.-L., 2019, "Causes, effects and solutions of operational problems in wastewater systems due to nonwoven wet wipes", *Environmental Science*.

[4] Hochstrat, I., 2024, "European nonwovens production decreased again", *FS Journal - Filtrieren und Separieren*.

[5] Gülich, J. F., 2020, *Kreiselpumpen - Handbuch für Entwicklung, Anlagenplanung und Betrieb*, Springer Vieweg, Heidelberg.

[6] Ren, Y., Zhao, L., Mo, X., Zheng, S., and Yang, Y., 2024, "Visualization investigation of the motion of rags in a double blades pump", *AIP Advances*, Vol. 14 (1), p. 015070.

[7] Nardone, R., and Flitney, B., 2006, "The effect of impeller back pump-out vanes on seal performance", *Sealing Technology*, Vol. 2006 (2), pp. 9–11.

[8] Deutsche Vereinigung für Wasserwirtschaft, A. u. A. e. V. D., 2022, *Arbeitsblatt DWA-A 120-2: Pumpsysteme außerhalb von Gebäuden – Teil 2: Pumpstationen und Drucksysteme*, DWA, Hennef.

[9] Beck, D., Brokhausen, F., and Thamsen, P. U., 2022, "Time-Resolved Measurements for the Detection of Clogging Mechanisms", *ASME 2022 Fluids Engineering Division Summer Meeting*.

[10] Wesche, W., 2016, *Radiale Kreiselpumpen: Berechnung und Konstruktion der Hydrodynamischen Komponenten*, VDI-Buch, Springer Vieweg, Berlin.

[11] Schindl, H., and Payer, H.-J., 2015, *Strömungsmaschinen. Band 1, Inkompressible Medien*, De Gruyter Oldenbourg, Munich ; Vienna, ISBN 3110343819.

[12] Pöhler, M., and Thamsen, P. U., 2019, "Mythos Kugeldurchgang – Aussage über Verstopfungsanfälligkeit bei Abwasserpumpen?", *WWT Wasserwirtschaft Wassertechnik*, Vol. 7 (8), pp. 12–17.

[13] Karassik, I. J., and McGuire, T., 1998, *Centrifugal Pumps*, Springer, New York.

[14] Schulz, H., 1977, *Die Pumpen*, Springer, Berlin/Heidelberg.

[15] Rinnert, T., and Thamsen, P. U., 2025, "Experimental Investigation of the Influence of the Axial Gap Width in the Back Shroud Cavity on the Clogging Behavior of a Wastewater Pump", *Submitted to Proceedings of the 16th European Turbomachinery Conference (ETC16)*.

[16] Rinnert, T., and Thamsen, P. U., 2025, "The Effect of Backward Curved Back Vanes and Back Channels on Fiber Entry Into the Back Shroud Cavity of a Wastewater Pump", *Submitted to Proceedings of the ASME 2025 Fluids Engineering Division Summer Meeting (FEDSM 2025)*.

[17] Pfleiderer, C., and Petermann, H., 2005, *Strömungsmaschinen*, Springer, Berlin.

[18] Schultz-Grunow, F., 1935, "Der Reibungswiderstand rotierender Scheiben in Gehäusen", *ZAMM - Zeitschrift für Angewandte Mathematik und Mechanik*, Vol. 15 (4), pp. 191–204.

[19] Ippen, A. T., 2022, "The Influence of Viscosity on Centrifugal-Pump Performance", *Transactions of the American Society of Mechanical Engineers*, Vol. 68 (8), pp. 823–838.

[20] Daily, J. W., and Nece, R. E., 1960, "Chamber Dimension Effects on Induced Flow and Frictional Resistance of Enclosed Rotating Disks", *Journal of Basic Engineering*, Vol. 82 (1), pp. 217–230.

[21] Nece, R. E., and Daily, J. W., 1960, "Roughness Effects on Frictional Resistance of Enclosed Rotating Disks", *Journal of Basic Engineering*, Vol. 82 (3), pp. 553–560.

[22] Will, B.-C., Benra, F.-K., and Dohmen, H.-J., 2012, "Investigation of the flow in the impeller side clearances of a centrifugal pump with volute casing", *Journal of Thermal Science*, Vol. 21, pp. 197–208.

[23] Bubelach, T., 2009, *Untersuchung der Radseitenraumströmung in einer Einschaufelrad-Abwasserpumpe*, Mensch und Buch Verlag, Berlin.

[24] Knop, M., Baack, T., Hohmeier, B., Di Brino, M., Petrak, G., Kamps, M., Dohmen, H.-J., and Benra, F.-K., 2022, "Erfolgreicher Kampf gegen die Verzopfung - Entwicklung, Bau und erste Betriebserfahrungen eines optimierten Laufrads für Schmutzwasserpumpen", *Korrespondenz Abwasser, Abfall*, Vol. 69, pp. 387–398.

Conference on Modelling Fluid Flow (CMFF'25)
The 19th International Conference on Fluid Flow Technologies
Budapest, Hungary, August 26 - August 29, 2025

DIRECT NUMERICAL SIMULATION OF THE JET ATOMIZATION PROCESS OF SHEAR THINNING GEL FUEL

Kangbo Yang[2], Yuqi Huang [1] ,Weijuan Yang [3] ,Shuai Wang [4] ,Haiou Wang [5] ,Jianren Fan [6]

[1] Corresponding Author. Department of Energy Engineering, Zhejiang University, Hangzhou, 310027, China. Tel.: +86 13867472242, E-mail: huangyuqi@zju.edu.cn
[2] Department of Energy Engineering, Zhejiang University, Hangzhou, E-mail:12127067@zju.edu.cn
[3] Department of Energy Engineering, Zhejiang University, Hangzhou, E-mail: yangwj@zju.edu.cn
[4] Department of Energy Engineering, Zhejiang University, Hangzhou, E-mail: wshuai2014@zju.edu.cn
[5] Department of Energy Engineering, Zhejiang University, Hangzhou, E-mail: wanghaiou@zju.edu.cn
[6] Department of Energy Engineering, Zhejiang University, Hangzhou, E-mail: fanjr@zju.edu.cn

ABSTRACT

Gel fuels have significant potential in aerospace applications. The shear-thinning behavior of gel fuel significantly impacts its atomization process. This study uses direct numerical simulation (DNS) with a coupled three-dimensional Volume-of-Fluid (VoF) and Lagrangian Particle Tracking (LPT) model to investigate the jet atomization of shear-thinning gel fuel (50 *m/s*, 0.6 mm injection diameter), comparing it with Newtonian fluid atomization. The gelatinized fuel is harder to atomize due to its higher viscosity. High-viscosity regions are concentrated in the jet core and shed in the jet direction, influenced by the velocity distribution within the liquid column. Shear-thinning fluids display unique dynamics: surface instability waves form earlier and primarily grow radially. In contrast, instability waves in Newtonian fluids grow radially while also developing in the direction opposite to the jet velocity. The high-viscosity core suppresses radial expansion, causing hole formation due to gas backflow and liquid film wrapping. A parabolic velocity inlet may optimize atomization by reducing the high-viscosity core. This study reveals how shear rate-viscosity coupling affects instability and fragmentation, providing insights for nozzle design and atomization efficiency.

Keywords: Direct numerical simulation; Instability waves; Shear thinning

NOMENCLATURE

Latin Capital Letters

$\underline{F}$	[N]	force
$\underline{F_D}$	[N]	drag force
$\underline{F_G}$	[N]	gravity and buoyancy force
$\underline{F_{SRM}}$	[N]	aerodynamic force

Latin Lowercase Letters

$\underline{g}$	[m/s^2]	gravitational acceleration
k	[$Pa\ s^n$]	consistency coefficient
m	[kg]	mass
n	[-]	power-law index
p	[Pa]	pressure
t	[s]	time
$\underline{u}$	[m/s]	velocity
$\underline{x}$	[m]	position

Greek Symbols

α	[-]	liquid volume fraction
$\dot{\gamma}$	[$1/s$]	shear rate
ρ	[kg/m^3]	density
μ	[$Pa\ s$]	dynamic viscosity
η_K	[m]	Kolmogorov scale

Other Symbols

$\underline{f_\sigma}$	[N]	surface tension force
φ_V	[-]	Liquid Volume Retention Ratio
φ_S	[-]	Interface Generation Rate
Re	[-]	Reynolds number
We	[-]	Weber number
Oh	[-]	Ohnesorge number
V_{sim}	[m^3]	simulated liquid volume
V_{theory}	[m^3]	theoretical volume of the unatomized cylindrical liquid jet
S_{sim}	[m^2]	simulated surface area of the liquid jet
S_{theory}	[m^2]	surface area of the unbroken liquid jet

Subscripts

g	gas phase
l	liquid phase
p	parcel
max	maximum
min	minimum

1. INTRODUCTION

Gel fuels, characterized by their unique shear-thinning behavior, have emerged as a promising candidate for aerospace propulsion systems due to their dual advantages of liquid-like flowability and solid-like storability. The atomization process of gel fuels directly affects combustion efficiency and thrust performance. Unlike Newtonian fluids, the viscosity of shear-thinning gels decreases significantly under high shear rates (e.g., during injection through narrow nozzles), complicating the atomization dynamics. However, the interplay between shear-thinning rheology, jet instability, and atomization patterns remains poorly understood. Traditional experimental methods struggle to resolve transient interfacial dynamics and localized viscosity variations, while conventional numerical approaches (e.g., RANS or LES [1]) often fail to capture the multiscale interactions between turbulent vortices and non-Newtonian fluid interfaces. Direct Numerical Simulation (DNS), capable of resolving all turbulent scales without modeling assumptions, offers a powerful tool to unravel the intrinsic mechanisms governing shear-thinning jet atomization.

Current research on jet atomization primarily focuses on Newtonian fluids. Menard et al. [2] combined the VOF, Level Set method, and GFM method to resolve the droplet formation and interface fragmentation in the primary breakup of high-speed liquid jets via DNS. The data obtained from DNS further validated and advanced the ELSA model [3]. Shinjo et al. [4] employed DNS with the combination of Level Set and VOF methods to study primary atomization phenomena of high-speed liquid jets under high-pressure conditions, revealing that the main droplet formation mode is driven by capillary waves. The Weber number significantly influences the size of ligaments and droplets in atomization. Further studies, conducted at high grid resolution, explored the formation of a conical structure at the tip of the jet and its subsequent atomization process. They also highlighted that droplet formation could transition from a short-wave mode to a long-wave mode under the stretching effect of the gas [5]. Research on intermittent diesel injection atomization processes also revealed that the surface instability of the liquid core is primarily induced by the gas-phase TS instability mode, with initial instability being two-dimensional, which evolves into three-dimensional instability over time. Most of these studies, however, did not consider the impact of nozzle perturbations on jet atomization. Jiao et al. [6] used DNS to study the effects of different liquid-gas density ratios and nozzle sizes on the turbulent fluctuation effects in diesel jets. Their findings showed that turbulent fluctuations promoted the evolution from a columnar liquid flow to an irregular droplet cluster, with higher gas density and smaller nozzle diameter accelerating this process. Salvador et al. [7] used DNS to investigate the effects of turbulent inflow conditions on the primary atomization process at low Reynolds numbers. They found that turbulence length scales significantly affected droplet fragmentation patterns, with higher turbulence intensity promoting earlier atomization and shorter core lengths. Additionally, Crialesi-Esposito et al. [8] compared the effects of isotropic (SBC) and anisotropic (MBC) turbulent conditions on spray breakup using DNS. Their results indicated that while the total number of droplets generated differed under different turbulence conditions, the overall atomization dynamics remained consistent, and larger turbulent structures more readily promoted atomization and the formation of smaller droplets. Srinivasan et al. [9] studied the influence of different jet velocity profiles on primary breakup using DNS, revealing that parabolic velocity profiles had deeper penetration and more pronounced surface wave changes, leading to more fragmentation features.

While DNS provides unparalleled resolution of interfacial dynamics and turbulent interactions, its computational cost remains prohibitive for industrial-scale applications. To reduce computational costs, some researchers have adopted Eulerian-Lagrangian coupled methods to simulate atomization processes, significantly reducing computational time while maintaining accuracy [10, 11].

In the study of shear-thinning fluid jet atomization, Ertl et al. [12] used DNS to investigate the primary breakup of shear-thinning fluid jets with different velocity profiles, emphasizing that the choice of velocity profile had a more significant impact on breakup than the shear-thinning properties themselves. Zhao et al. [13] employed a VOF-DNS coupled method to study the spray characteristics of power-law biodiesel, finding that shear-thinning fluids exhibited jet breakup patterns similar to Newtonian fluids, with higher Reynolds numbers and gas densities accelerating the breakup process. Abdelsayed et al. [14] conducted DNS to study the primary atomization process of Newtonian and shear-thinning fluids, finding that droplets generated by shear-thinning fluids were more fibrous and exhibited higher surface irregularities. However, numerical simulations of shear-thinning fluid jet atomization are still limited, with few studies comparing simulation results with experimental data and insufficient understanding of the unique atomization morphology of shear-thinning fluids.

This study adopts a three-dimensional coupled Volume-of-Fluid and Lagrangian Particle Tracking (VOF-LPT) model [10], combined with Direct Numerical Simulation (DNS), to analyze the jet atomization process of shear-thinning fluids. Through a quantitative comparison of atomization morphology and experimental observations [15], the numerical model's ability to capture interfacial

evolution is validated. A comparison between shear-thinning and Newtonian fluid jet atomization highlights the more frequent wave structures and internal hole formation observed in shear-thinning fluid atomization, providing valuable insights for enhancing shear-thinning fluid jet atomization.

2. NUMERICAL SIMULATION METHODOLOGY

2.1. Governing equation

The simulations in this study were performed using a two-phase flow solver in OpenFOAM, based on the Volume-of-Fluid (VOF) and Lagrangian Particle Tracking (LPT) coupling method. The governing equations for the two-phase flow consist of mass and momentum conservation laws:

$$\nabla \cdot \underline{u} = 0 \tag{1}$$

$$\frac{\partial \rho \underline{u}}{\partial t} + \nabla \cdot \left(\rho \underline{u}\underline{u}\right) = -\nabla p + \nabla \cdot \left[\mu\left(\nabla \underline{u} + \nabla \underline{u}^T\right)\right] + \underline{f_\sigma} \tag{2}$$

where the ρ and μ are given by the following relations:

$$\rho = \alpha\rho_l + (1-\alpha)\rho_g \tag{3}$$

$$\mu = \alpha\mu_l + (1-\alpha)\mu_g \tag{4}$$

and $\underline{f_\sigma}$ is modeled via the CSF approach .

Interface dynamics during the primary breakup are resolved using a Volume-of-Fluid (VOF) method with geometric interface reconstruction via the isoAdvector method. The phase fraction transport equation is given by:

$$\frac{\partial \alpha}{\partial t} + \nabla \cdot \left(\alpha \underline{u}\right) = 0 \tag{5}$$

The Lagrangian Particle Tracking (LPT) method is used to track the movement of Lagrangian particles within the computational domain:

$$\frac{d\underline{x_p}}{dt} = \underline{u_p} \tag{6}$$

$$m_p \frac{d\underline{u_p}}{dt} = \underline{F_D} + \underline{F_G} + \underline{F_{SRM}} \tag{7}$$

$$\underline{F_G} = m_p\left(1 - \frac{\rho_g}{\rho_l}\right)\underline{g} \tag{8}$$

where $\underline{F_D}$ follows Schiller-Naumann correlation, and $\underline{F_{SRM}}$ accounts for secondary breakup via the Reitz-Diwakar model. The coupling between VOF and LPT is detailed in the reference [10], and will not be repeated here.

For the viscosity of shear-thinning fluids, this study uses a modified power-law model:

$$\mu_l = min\left(\mu_{l,max}, max\left(\mu_{l,min}, k \cdot \gamma^{n-1}\right)\right) \tag{9}$$

2.2. Boundary Conditions

In this study, numerical simulations are conducted for the jet atomization process of JP-10 solution (Newtonian fluid) and its shear-thinning modified solution [16]. Both solutions have a density of 970 *kg/m³*, surface tension coefficient of 0.032 *N/m*, and Newtonian fluid has a constant kinematic viscosity of 1.2×10^{-6} *m²/s*. For the shear-thinning solution, the parameters are $\mu_{l,max}=1.2\times10^{-2} m^2/s$, $\mu_{l,min}=1.2\times10^{-6}$ m^2/s, $k=0.012 Pa\ s^n$, $n=-0.132$. The power-law index n of the shear-thinning solution is less than 0, indicating that this gel solution has a stronger thinning ability than typical shear-thinning fluids ($0 < n < 1$) [16]. The jet breakup process can be divided into four regions based on different Reynolds and Ohnesorge numbers [17]. In this study, the viscosity of shear-thinning fluids is not constant, making it impossible to directly calculate the Reynolds number. Previous studies have used a modified Reynolds number for power-law fluids [18], but this method is not applicable in this study due to the n<0 for the shear-thinning fluid. In this study, the dimensionless parameters are calculated using the average μ_l at the nozzle cross-section, yielding Re=22058, with We=45469 and Oh=0.0097 calculated subsequently. Based on the reference [17], the jet flow in this study falls into the atomization region. The computational domain is set as a rectangular region of $6D\times6D\times25D$, the nozzle length is 1 mm, and the initial jet velocity is 50 *m/s*. The boundary conditions include a velocity inlet, pressure outlet (at atmospheric pressure), and no-slip wall conditions. During the calculation, the maximum Courant number is kept below 0.3 to ensure numerical stability.

3. NUMERICAL SIMULATION VALIDATION AND GRID INDEPENDENCE ANALYSIS

This study employs dynamic adaptive mesh refinement (AMR) techniques to simulate the jet atomization process. Four different grid resolutions were tested, with minimum grid sizes of 20 μm, 15 μm, 10 μm, and 7.5 μm. To evaluate the results, the following metrics were defined based on the liquid phase volume fraction and interface surface area:

$$\varphi_V = \frac{V_{sim}}{V_{theory}} \times 100\% \tag{10}$$

$$\varphi_S = \frac{S_{sim}}{S_{theory}} \times 100\% \qquad (11)$$

Figures 1 and 2 show the variation of φ_V and φ_S with the number of grids. It can be seen that as the grid size is refined from 20 μm to 7.5 μm: The liquid volume retention ratio increases from 98.35% to 99.65%, indicating that the finer grid significantly reduces numerical diffusion at the interface. The interface generation rate shows a growth trend consistent with the physical mechanism of surface area increase due to droplet breakup during atomization. Moreover, the fluctuation amplitude for the 7.5 μm grid is similar to that for the 10 μm grid, suggesting that the grid resolution is sufficient to capture the interface instability.

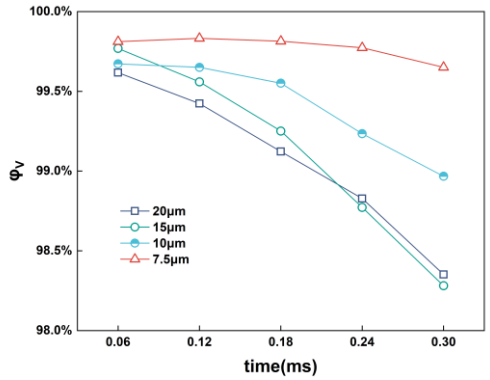

Figure 1. Time-dependent variation of φ_V under different grid sizes

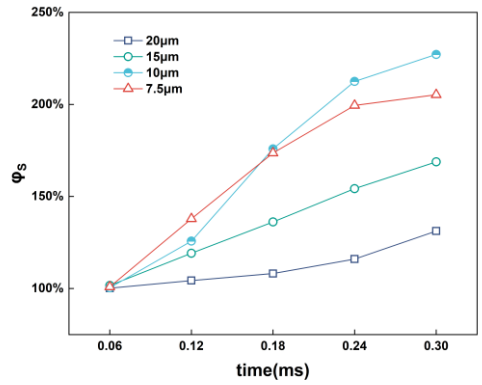

Figure 2. Time-dependent variation of φ_S under different grid sizes

Based on these analyses, a grid size of 7.5 μm was selected as the final grid resolution. This size is of the same order of magnitude as the theoretical Kolmogorov scale (η_K=1.2μm) and satisfies the sensitivity requirements for resolution in interface-dominated atomization processes. Additionally, the simulation results were validated by comparing the jet morphology with experimental results from the reference [15], as shown in Figure 3. The simulation conditions for the verification case are as follows: Case 1. 0.3 *MPa*, velocity 22.32 *m/s*; Case 2: 0.6 *MPa*, velocity 31.22 *m/s*.

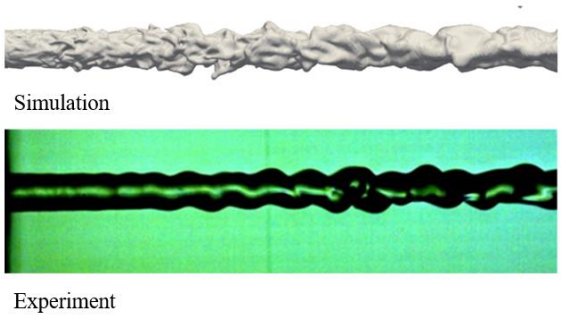

a. Case1: 0.3 MPa

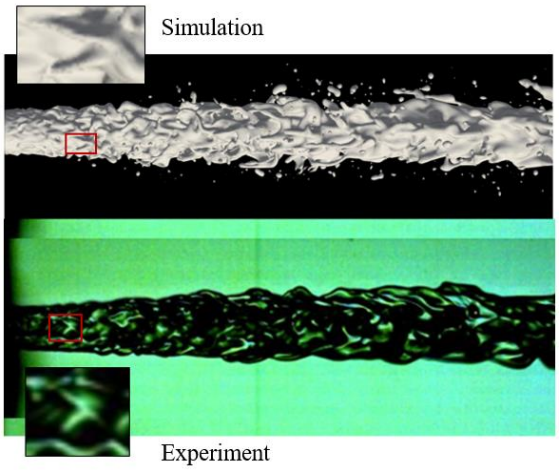

b. Case2: 0.6 MPa

Figure 3. Comparison of experimental and simulation results

Under the 0.3 *MPa* condition, the simulated results successfully capture the jet column structure, resembling a helical distortion, which aligns with experimental observations. For the 0.6 *MPa* condition, the jet surface shape is more complex, and the jet is no longer a simple cylindrical form. The simulated results capture the expansion of the liquid column under these conditions, and the typical V-shaped wave structure observed in experiments is also reproduced. Therefore, it can be concluded that the simulation method used in this study is capable of accurately capturing the atomization structure in shear-thinning fluid jet atomization processes.

4. RESULTS AND ANALYSIS

Figure 4 presents the liquid column cross-sections of Newtonian fluid and its shear-thinning solution at 3×10^{-4}s. It is evident that the surface instability waves of the non-Newtonian fluid appear closer to the nozzle, and large voids are more likely to form inside the liquid column. To further explore the differences between the shear-thinning fluid and

Newtonian fluid jets, the variations in liquid column diameter with axial distance, as well as the cumulative differences between the two fluids, were statistically analyzed, as shown in Figure 5. It can be observed that the cumulative difference is initially greater than 0, further indicating that surface instability waves appear earlier in the non-Newtonian fluid. As the axial distance increases, the cumulative difference shows a gradual decline, suggesting that Newtonian fluids expand more easily in the radial direction. This may be because the high-viscosity region in the center of the non-Newtonian liquid column inhibits this process.

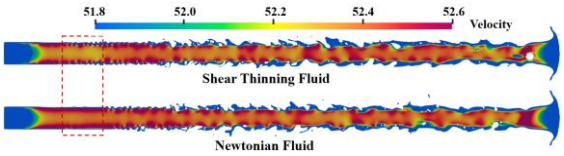

Figure 4. Liquid column cross-sections of Newtonian fluid and shear-thinning fluid at 3×10^{-4} s.

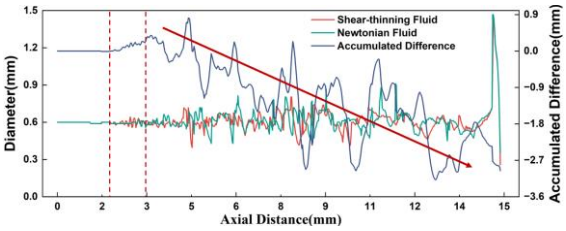

Figure 5. Variations in liquid column diameter with axial distance and cumulative differences between shear-thinning fluid and Newtonian fluid jets

As shown in Figure 6, the high-viscosity region of the shear-thinning fluid (indicated by the yellow area, where viscosity > 2.4×10^{-6} m^2/s) is concentrated in the core of the liquid column and is primarily influenced by the velocity distribution within the liquid column. Near the nozzle, the distribution of surface instability waves causes the formation of intermittently distributed high-speed zones within the liquid column. The presence of these high-speed zones leads to corresponding arc-shaped depressions in the high-viscosity region, which is the main factor influencing the shape of the high-viscosity region in the radial direction. The shedding and separation of the high-viscosity region in the axial direction of the jet are mainly influenced by the axial velocity gradient. Despite the relatively small velocity difference within the liquid column (compared to the jet velocity), it still results in the continuous shedding of the high-viscosity region along the jet direction.

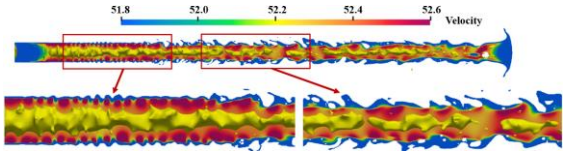

Figure 6. Distribution of high-viscosity regions in the shear-thinning fluid jet and their correlation with velocity distribution and surface instability waves

In the study by Balaji et al. [9], it was found that for Newtonian fluids, a flat velocity distribution at the nozzle produces the highest degree of atomization, while a parabolic velocity distribution exhibits the best penetration performance and results in the fastest reduction of liquid column diameter. Thus, it can be inferred that for shear-thinning fluids, using a parabolic velocity inlet could reduce the high-viscosity region in the liquid core, potentially enhancing the atomization process.

To further compare the different behaviors of shear-thinning and Newtonian fluids in jet atomization, Figure 7 shows the jet structures of both fluids at $t=3\times10^{-4}$s. It can be observed that, compared to the Newtonian fluid, the surface of the shear-thinning fluid jet is more prone to generating instability wave structures perpendicular to the axial direction of the liquid column. Such phenomena are observed at both the neck and middle regions of the jet liquid column.

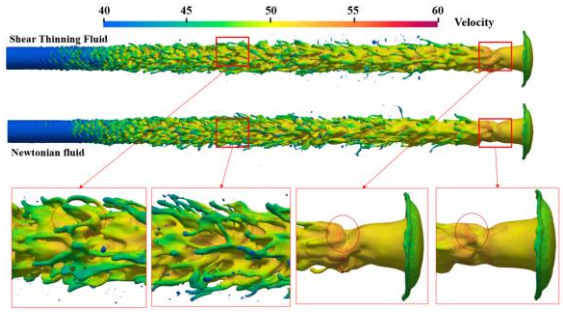

Figure 7. Jet structures of shear-thinning and Newtonian fluids at 3×10^{-4} s

To explore the reasons behind this phenomenon, the development of surface instability wave structures for both fluids was tracked, as shown in Figure 8. For the shear-thinning fluid, the instability waves on the liquid column surface initially appear as large V-shaped structures. Over time, these large V-shaped structures transition into smaller continuous V-shaped waves, which then grow radially along the liquid column. As time progresses further, the connections between the continuous V-shaped structures break, and the V-shaped structures continue to develop radially, while the ends of the instability waves stretch along the axial direction of the liquid column, reaching their final form.

In contrast, for the Newtonian fluid, the instability waves initially also take the form of large V-shaped structures, which gradually transform into smaller V-shaped waves. However, unlike the shear-thinning fluid, the instability waves on the surface of the Newtonian fluid grow radially while simultaneously tilting in the direction opposite to the jet flow. This results in the small V-shaped structures eventually evolving into liquid filaments.

The primary cause of this difference is the distribution of high-viscosity regions in the core of the shear-thinning fluid. Higher viscosity suppresses the growth of instability waves in the opposite direction of the jet. Additionally, previous studies have shown that the viscosity gradient within the fluid promotes instability propagation along the gradient [19]. In this study, the viscosity gradient in the shear-thinning fluid jet promotes the radial propagation of instability waves.

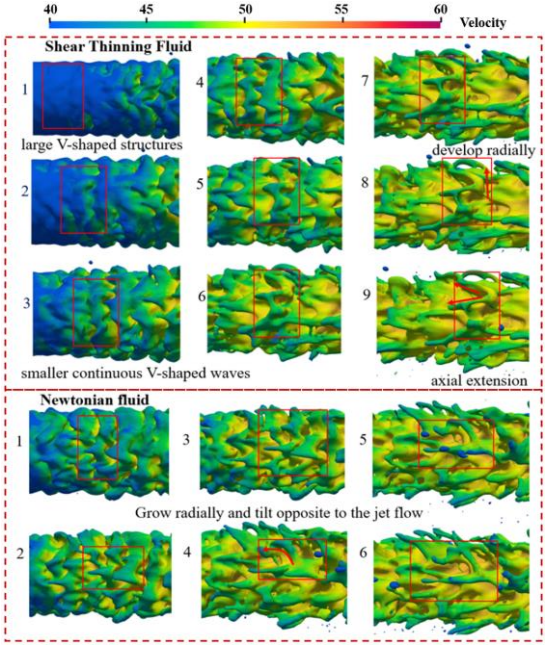

Figure 8. Development of surface instability waves in shear-thinning and Newtonian fluids

The unique wave structure exhibited by shear-thinning fluids during jet atomization is likely the main reason for the frequent formation of voids inside the liquid core. Figure 9 illustrates the formation process of a void structure in the shear-thinning fluid jet atomization. Initially, the void structure appears as a continuous V-shaped instability wave. As time progresses, the V-shaped instability wave grows radially along the liquid column. The incoming air flows past the continuous V-shaped structure and recirculates, generating a void on the liquid column surface. As time goes on, the gas recirculated through the continuous V-shaped structure enters the void, which causes the void to expand, penetrating deeper into the liquid core. Simultaneously, the liquid film on the upper surface of the void moves in the opposite direction to the jet flow, ultimately encapsulating the void and forming an internal hole.

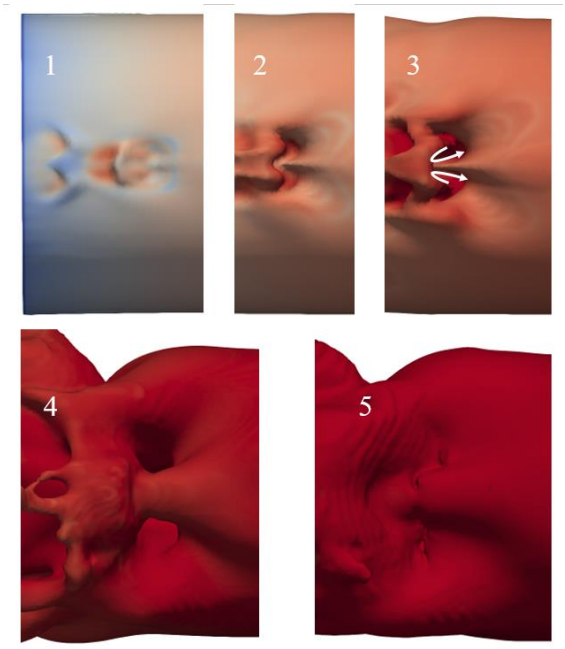

Figure 9. Formation process of a void structure in shear-thinning fluid jet atomization, showing the growth and expansion of the void within the liquid core

5. SUMMARY

This study investigates the jet atomization of shear-thinning gel fuels using direct numerical simulation (DNS) with a coupled three-dimensional Volume-of-Fluid (VOF) and Lagrangian Particle Tracking (LPT) model. The simulation results were validated through comparison with experimental observations, and key differences between shear-thinning and Newtonian fluids in atomization were highlighted.

Effect of Velocity Distribution on Viscosity: In shear-thinning fluids, high-viscosity regions are concentrated in the liquid core. The viscosity distribution is influenced by both the surface instability waves and the velocity distribution within the liquid column, which significantly affects the atomization behavior.

Unique Structure Due to Viscosity Distribution: The high viscosity in the core of the shear-thinning fluid leads to the development of surface instability waves that form earlier and grow radially. In contrast, Newtonian fluids exhibit instability waves that grow radially and also tilt in the opposite direction of the jet flow.

Formation of Voids: The instability waves in shear-thinning fluids contribute to the formation of internal voids within the liquid core. The voids are

primarily driven by air backflow, which deepens and expands the holes within the liquid column.

In conclusion, this study provides insights into the atomization mechanisms of shear-thinning fluids, highlighting the influence of viscosity distribution and the resulting unique structural formations. These findings, along with comparisons between shear-thinning and Newtonian fluids, offer valuable implications for improving atomization processes in gel fuel applications.

ACKNOWLEDGEMENTS

This work is supported by the National Natural Science Foundation of China (Grant No: U2341283). We are grateful for this.

APPENDICES

REFERENCES

[1] Abdelsayed M, Hasslberger J, Ertl M, Weigand B, Klein M. Toward large eddy simulation of shear-thinning liquid jets: A priori analysis of subgrid scale closures for multiphase flows. Physics of Fluids (1994). 2024;36(8).

[2] Ménard T, Tanguy S, Berlemont A. Coupling level set/VOF/ghost fluid methods: Validation and application to 3D simulation of the primary break-up of a liquid jet. International Journal of Multiphase Flow. 2007;33(5):510-24.

[3] Lebas R, Menard T, Beau PA, Berlemont A, Demoulin FX. Numerical simulation of primary break-up and atomization: DNS and modelling study. International Journal of Multiphase Flow. 2009;35(3):247-60.

[4] Shinjo J, Umemura A. Simulation of liquid jet primary breakup: Dynamics of ligament and droplet formation. International Journal of Multiphase Flow. 2010;36(7):513-32.

[5] Shinjo J, Umemura A. Detailed simulation of primary atomization mechanisms in Diesel jet sprays (isolated identification of liquid jet tip effects). Proceedings of the Combustion Institute. 2011;33(2):2089-97.

[6] Jiao D, Zhang F, Du Q, Niu Z, Jiao K. Direct numerical simulation of near nozzle diesel jet evolution with full temporal-spatial turbulence inlet profile. Fuel (Guildford). 2017;207:22-32.

[7] Salvador FJ, S. R, Crialesi-Esposito M, Blanquer I. Analysis on the effects of turbulent inflow conditions on spray primary atomization in the near-field by direct numerical simulation. International Journal of Multiphase Flow. 2018;102:49-63.

[8] Crialesi-Esposito M, Gonzalez-Montero LA, Salvador FJ. Effects of isotropic and anisotropic turbulent structures over spray atomization in the near field. International Journal of Multiphase Flow. 2022;150:103891.

[9] Srinivasan B, Sinha A. Primary breakup of liquid jet—Effect of jet velocity profile. Physics of Fluids (1994). 2024;36(3).

[10] M. Heinrich, R. Schwarze. 3D-coupling of volume-of-fluid and Lagrangian particle tracking for spray atomization simulation in OpenFOAM. SoftwareX, 11 (2020), Article 100483

[11] Chéron V, Brändle de Motta, Jorge César, Ménard T, Poux A, Berlemont A. A coupled Eulerian interface capturing and Lagrangian particle method for multiscale simulation. Computers & Fluids. 2023;256:105843.

[12] Ertl M, Weigand B. Analysis methods for direct numerical simulations of primary breakup of shear-thinning liquid jets. Atomization and Sprays. 2017;27(4):303-17.

[13] Zhao L, Jiao D, Xie X, Jiao K, Peng Z, Du Q. Direct numerical simulation of primary breakup for power-law biodiesel sprays. Energy Procedia. 2019;158:612-8.

[14] Abdelsayed M, Trautner E, Berchtenbreiter J, Klein M. Primary atomization of shear-thinning liquid jets: a direct numerical simulation study. Scientific Reports. 2024;14(1):23896-15.

[15] Guo JP, Bai FQ, Chang Q, Du Q. Investigation on asymmetric instability of cylindrical power-law liquid jets. Energies (Basel). 2019;12(14):2785.

[16] Cao J, Pan L, Zhang X, Zou J. Physicochemical and Rheological Properties of Al/JP-10 Gelled Fuel. Hanneng Cailiao = Chinese Journal of Energetic Materials. 2020(5):382.

[17] Csizmadia P, Till S, Hős C. An experimental study on the jet breakup of Bingham plastic slurries in air. Experimental Thermal and Fluid Science. 2019;102:271-8.

[18] Csizmadia P, Hős C. CFD-based estimation and experiments on the loss coefficient for Bingham and power-law fluids through diffusers and elbows. Computers & Fluids. 2014;99:116-23.

[19] Burghelea T, Wielage-Burchard K, Frigaard I, Martinez DM, Feng JJ. A novel low inertia shear flow instability triggered by a chemical reaction. Physics of Fluids (1994). 2007;19(8):083102,083102-13.

Conference on Modelling Fluid Flow (CMFF'25)
The 19th International Conference on Fluid Flow Technologies
Budapest, Hungary, August 26 - August 29, 2025

MOLECULAR DYNAMICS SIMULATION OF THE RHEOLOGICAL BEHAVIOUR OF GEL FUELS

Mengfan Si[1], Shuai Wang[2], Haiou Wang[3], Kun Luo[4], Jianren Fan[5]

[1] State Key Laboratory of Clean Energy Utilization, Zhejiang University, Hangzhou 310027, China E-mail: 12527013@zju.deu.cn
[2] State Key Laboratory of Clean Energy Utilization, Zhejiang University, Hangzhou 310027, China E-mail: wshuai2014@zju.deu.cn
[3] State Key Laboratory of Clean Energy Utilization, Zhejiang University, Hangzhou 310027, China E-mail: wanghaiou@zju.deu.cn
[4] State Key Laboratory of Clean Energy Utilization, Zhejiang University, Hangzhou 310027, China E-mail: zjulk@zju.deu.cn
[5] Corresponding Author. State Key Laboratory of Clean Energy Utilization, Zhejiang University, Hangzhou 310027, China E-mail: fanjr@zju.deu.cn

ABSTRACT

The rheological behaviour of JP-10-based gelled fuels enhanced with nano-aluminium (Al) particles and low-molecular-weight gelators (LMWGs) was studied by molecular dynamics (MD) simulations. Non-equilibrium molecular dynamics (NEMD) methods were used to evaluate shear viscosity across a range of shear rates. The results demonstrate that the hybrid system exhibits non-Newtonian shear-thinning behaviour, with Al particles enhancing shear sensitivity through mechanical interactions, while LMWGs serve to stabilise the gel network. Increasing Al content leads to a reduction in the time constant in Cross model, which accelerates structural degradation under shear. These findings underscore the synergistic roles of Al nanoparticles and LMWGs in fine-tuning the viscosity profiles of gelled fuels for high-shear propulsion systems, offering a molecular-level framework for optimising gelled fuel performance.

Keywords: gel fuel, MD, nanoparticle, viscosity

NOMENCLATURE

E	$[J]$	energy
F	$[N]$	force
ρ_i	[C/m^3]	electron density
ϕ	$[eV]$	interatomic potential energy
r	$[m]$	distance
η	$[mPa{\cdot}s]$	viscosity
A_1	$[mPa{\cdot}s]$	zero- shear viscosity
A_2	$[mPa{\cdot}s]$	infinite-shear viscosity
τ	$[Pa]$	shear stress
m	[-]	shear-thinning index
$\dot{\gamma}$	[1/s]	shear rate

Subscripts and Superscripts

NVT	Canonical Ensemble
NPT	Isothermal-Isobaric Ensemble

1. INTRODUCTION

Gelled fuels are modified liquid fuels with unique rheological properties, comprising hydrocarbon fuel, gelling agents, and high-energy particles. The gelling agents form a network that increases viscosity, enabling solid-like behaviour at rest and fluid-like flow under shear forces, ensuring efficient injection and atomization. High-energy particles enhance calorific value and energy density, making gelled fuels suitable for high-performance propulsion systems [1]. Upon injection, they undergo a two-stage breakup: primary fragmentation due to turbulent shear forces, followed by secondary dispersion into finer droplets, which evaporate and ignite under high temperatures. These processes involve complex multiphase flows and non-Newtonian fluid dynamics, presenting challenges for stable combustion [2]. Furthermore, multiscale coupling effects—from microscopic particle dispersion to macroscopic flow dynamics under extreme conditions—affect fuel performance. Investigating rheological properties and microscopic mechanisms is essential for optimizing gelled fuels in aerospace propulsion.

Experimental studies have advanced the understanding of gelled fuel rheology but struggle to capture molecular-scale interactions and extreme conditions. Li et al. [3] demonstrated that shear-thinning and thixotropic properties in organic kerosene gels are influenced by pre-shear effects. Sun et al. [4] found that a 1.0% glycyrrhizic acid hydrogel supports efficient atomization, while higher concentrations hinder fuel breakup. Liu et al. [5] developed stable, shear-thinning gelled fuels using low-molecular-mass gellants, improving combustion. Ma et al. [6] synthesized poly glycyrrhizic acid (PGly) with pH-responsive emulsification for controlled release. Despite these insights, experimental constraints highlight the need for molecular simulations.

Molecular dynamics (MD) simulations effectively model gel behavior under extreme shear and pressure. Cui et al. [7] identified nanoparticle-induced interfacial effects in copper-water nanofluids, while Loya et al. [8] showed CuO nanoparticles enhance hydrocarbon-based fluid conductivity. Blanco-Díaz et al. [9] linked shear-thinning in ionic liquids to hydrogen bond disruption, and Liu et al. [10] showed that shear alignment reduces lubricant viscosity. These findings establish MD simulations as essential for understanding and optimizing gelled fuel rheology. Experimental studies lack molecular-level insights under extreme conditions, while simulations mainly focus on single-component systems. The interplay between small-molecule gelators, nanoparticles, and their behaviour under such conditions remains unresolved, requiring advanced models to predict rheological properties across shear regimes.

This study develops a MD model to analyze rheological properties of gelled fuels under varying shear rates using non-equilibrium molecular dynamics (NEMD). The primary contributions are: (i) constructing a complex model incorporating aviation kerosene, low molecular weight gelators (LMWG), and nano-aluminum particles at different mass fractions, and (ii) elucidating the shear response of high-energy hydrocarbon fuels under extreme conditions, linking macroscopic behavior to molecular interactions. The article is organized as follows: Section 2 presents the modelling method. Section 3 summarizes the simulation setting details including the mass fraction and numerical settings. Section 4 gives the results and discussion. Section 5 shows the conclusion.

2. METHODOLOGY

2.1. MD model

This study employed Packmol [11] and LAMMPS [12] for MD simulations of JP-10-based gel fuel. As shown in Fig.1, the system involved three key components: JP-10 (modeled as exo-tetrahydrodicyclopentadiene) serving as the high-energy-density base fuel, diacetone-D-mannitol as the gel-forming LMWG, and Al nanoparticles for combustion enhancement.

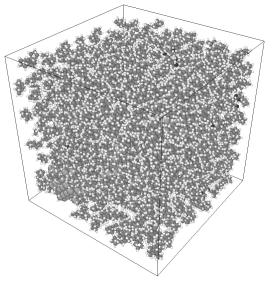

Figure 1. Molecular model of JP-10 gel fuel

The simulations utilized hybrid force fields to describe interparticle interactions. Organic components (JP-10 and LMWGs) were modeled with the Polymer Consistent Force Field (PCFF) [13] selected for its proven reliability in polymer/organic systems. Metallic interactions in nano-aluminum particles were addressed through the Embedded Atom Method (EAM) potential [14]. A mixed potential approach (Heinz et al., 2008) enabled cross-interaction modeling between different material phases.

Derived from the CFF91 framework, the PCFF potential function originally described small organic molecules and proteins, later extending to polymers and inorganic materials. Its mathematical formulation provides comprehensive coverage of bond stretching, angle bending, torsional interactions, and van der Waals forces critical for gel network characterization.

The Embedded Atom Method (EAM) potential, a semi-empirical model for metallic systems, decomposes atomic energy into two components: pairwise interatomic interactions and embedding energy derived from local electron density. This framework enables efficient simulation of metal/alloy behaviour by accounting for both direct atomic bonds and the energy cost of embedding atoms within their electron cloud environment. The functional expression is formulated as Eq. (1).

$$E_{\text{total}} = \sum_i F(\rho_i) + \frac{1}{2}\sum_{i \neq j} \phi(r_{ij}) \qquad (1)$$

where $F(\rho_i)$ represents the embedding energy of atom i which depends on the total electron density ρ_i surrounding the atom. $\phi(r_{ij})$ represents the pairwise interaction energy between atoms, which depends on the distance r_{ij} between the atoms.

2.2. Non-equilibrium conditions

The SLLOD equations, originally developed by Hoover and Ladd [15], provide a validated framework for simulating shear flow in molecular dynamics. Refinements by Tuckerman et al. [16] enhanced their capability to model nonlinear velocity gradients, enabling transport property analysis in complex fluids. In LAMMPS implementations, these equations govern particle dynamics under shear by updating velocities/positions via applied velocity gradients, with triclinic simulation boxes enabling consistent shear strain application.

Simulation protocols involved sequential equilibration stages: initial Packmol-generated configurations underwent iterative energy minimisation through temperature-cycling relaxation. Subsequent NVT/NPT ensembles stabilised system density prior to nonequilibrium studies. For NEMD runs, adaptive step adjustments

ensured sampling adequacy across shear rates. Also, multiple parallel simulations per shear rate were statistically averaged to enhance data reliability.

3. COMPUTATIONAL SETTINGS

The gel fuel model contains 10% nano-aluminium particles by mass, ensuring consistent metallic additive proportions. LMWG was tested at 2% mass fractions to exploit its efficient gelation at minimal concentrations. Component quantities were determined from molecular weights (JP-10, LMWG, Al) for precise formulation control.

All simulations adhered to standard conditions (298 K, 1 atm). The conjugate gradient method performed energy minimisation to optimise molecular configurations. Thermal regulation employed combined Langevin (stochastic collisions) and Nose-Hoover (deterministic coupling) thermostats, while pressure was maintained via a Nose-Hoover barostat. This dual-thermostat approach balanced computational efficiency with thermodynamic accuracy under shear conditions.

4. RESULTS AND DISCUSSION

4.1. Rheological behaviour at ambient conditions

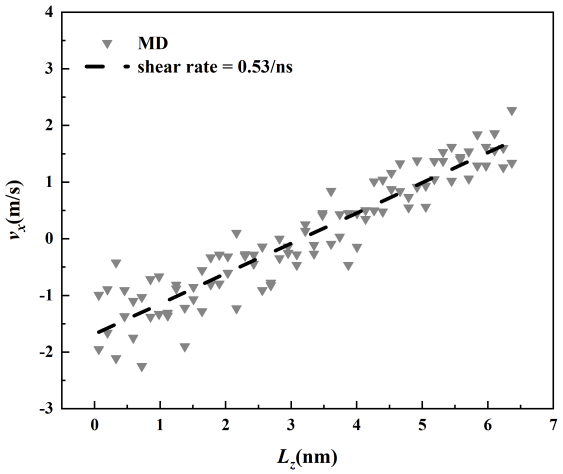

Figure 2. Fitting curves of molecular velocity

NEMD simulations quantified the shear viscosity of gel fuel systems across shear rates spanning 4×10^7 s⁻¹ to 2×10^{11} s⁻¹. As illustrated in Fig.2, thermal fluctuations dominate at shear rates below 8×10^8 s⁻¹, exemplified by the unstable velocity profiles observed at 2×10^8 s⁻¹, a regime where measurement uncertainties preclude reliable viscosity determination. Beyond this threshold, shear-induced forces suppress thermal noise, enabling stable velocity gradients and reproducible viscosity measurements.

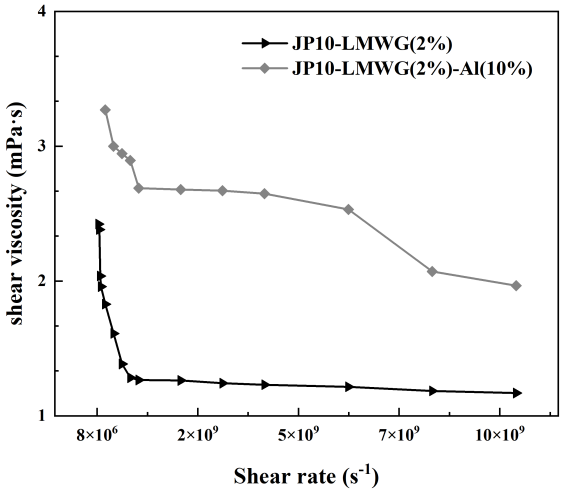

Figure 3. Shear viscosity of gel fuel systems at different shear rates

The incorporation of 10% nano-aluminium particles elevates shear viscosity by 18 - 32% relative to gelator-only systems, as demonstrated in Fig.3. This enhancement stems from nanoparticle-mediated reinforcement of the gel network's mechanical integrity. Notably, particle-free systems exhibit shear-thinning behaviour until reaching a viscosity plateau above 2×10^9 s⁻¹, indicative of a critical shear rate where structural reorganisation counterbalances further viscosity reduction. The divergence in rheological response underscores the nanoparticles' role in stabilising the gel matrix under extreme shear conditions.

4.2. Correlation formulation

This section details the rheological characterisation of JP-10-based gel fuel across shear rates spanning 1×10^{-2} to 2×10^{11} s⁻¹. Experimental measurements [17] provided low shear-rate data (1×10^{-2} - 1×10^2 s⁻¹), complemented by NEMD simulations for high-rate regimes (4×10^7 - 2×10^{11} s⁻¹). The intermediate shear-rate range (1×10^2 - 4×10^7 s⁻¹), inaccessible to reliable simulation due to computational constraints and viscosity instabilities, was bridged through interpolation. The Cross model further enabled extrapolation to ensure rheological curve continuity across the full shear spectrum. The model is expressed as Eq. (2).

$$\eta(\dot{\gamma}) = A_2 + \frac{A_1 - A_2}{1 + (\tau \cdot \dot{\gamma})^m} \qquad (2)$$

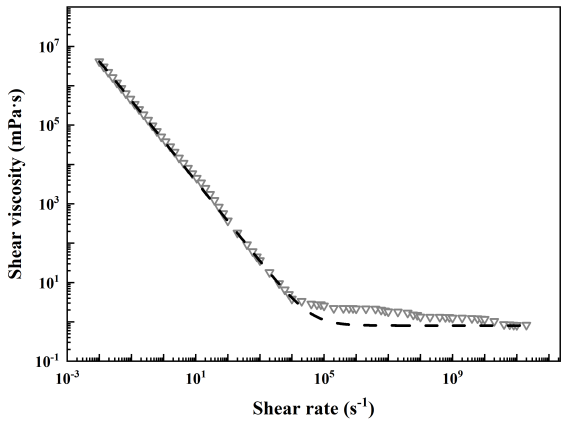

(a)

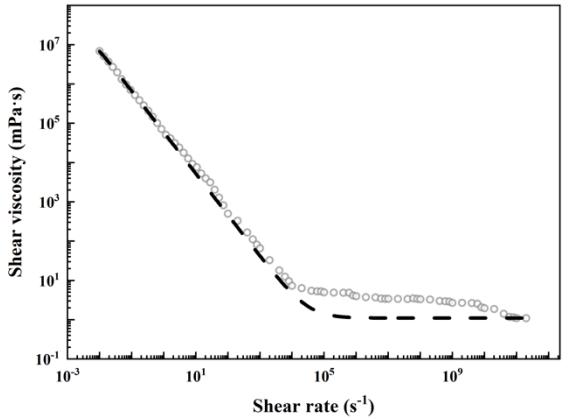

(b)

Figure 4. Rheological curves of gel fuels fitted using Cross model (a) $C_{JP\text{-}10}$ = 98%, C_{LMWG} = 2%, τ = 1160.55, m = 0.98;(b) $C_{JP\text{-}10}$ = 88%, C_{LMWG} = 2%, C_{Al} = 10%, τ = 828.48, m = 0.96

As shown in Fig.4.,nano-aluminium additives (10% mass) increased infinite-shear viscosity, indicating enhanced structural integrity, while reducing characteristic time τ, implying faster shear-induced network breakdown. Higher LMWG content with nanoparticles marginally lowered shear-thinning sensitivity (m), attributed to strengthened gel-particle interactions. At extreme shear rates (>2×10^{10} s^{-1}), viscosity fell below pure JP-10 levels, signalling complete structural collapse, though MD scaling constraints contributed to fitting deviations.

5. SUMMARY

This study utilised molecular dynamics simulations to analyse the rheological properties of JP-10-based gel fuels, revealing the critical influence of nano-aluminium particles and LMWGs on shear viscosity. Nano-aluminium additives (10% mass fraction) enhanced viscosity at low shear rates through structural reinforcement, while LMWGs stabilised the three-dimensional gel network, dictating bulk rheological responses.

The Cross model outperformed the Power-law model in characterising non-Newtonian behaviour, accurately capturing the transition from gel-like (Newtonian plateau) to liquid-like (shear-thinning) regimes at elevated shear rates. This approach resolved limitations of conventional models in describing multiphase systems, particularly the viscosity collapse observed beyond 2×10^{10} s^{-1} where simulated values dropped below pure JP-10 levels. These findings validate molecular dynamics as a robust tool for probing complex fluid systems, offering practical guidelines for tailoring gel fuel formulations. The synergy between nanoparticle reinforcement and gellants concentration optimisation provides a pathway to enhance fuel performance in aerospace propulsion and munitions systems requiring stability under extreme shear conditions. The use of specific modelling assumptions and extrapolation of intermediate values may introduce uncertainties. In future work, we plan to incorporate reactive potentials or machine-learned force fields to address these limitations and enhance the predictive capability of our model.

ACKNOWLEDGEMENTS

We are grateful for the support from the National Natural Science Foundation of China (grant No. U2341283).

REFERENCES

[1] Starkovich, J., & Palaszewski, B., 1993, "Technology for Gelled Liquid Cryogenic Propellants-Metallized Hydrogen/Aluminum," *29th Joint Propulsion Conference and Exhibit*, pp. 1878.

[2] Rahimi, S., Hasan, D., & Peretz, A., 2004, "Development of Laboratory-Scale Gel Propulsion Technology," *Journal of Propulsion and Power*, Vol. 20, pp. 93-100.

[3] Li, M. G., Wu, Y., Cao, Q. L., Yuan, X. Y., Chen, X., Han, J. L., & Wu, W. T., 2022, "*Rheological Properties of Organic Kerosene Gel Fuel*," Gels, Vol. 8, pp. 507.

[4] Sun, H., Jiang, J., Zhang, L., Yuan, C., Jiang, Y., & Liu, P., 2022, "Rheological and Atomization Behavior of Glycyrrhizic Acid Based Supramolecular Gel Propellant Simulant," *Colloids and Surfaces A: Physicochemical and Engineering Aspects*, Vol. 640, pp. 128460.

[5] Liu, Y., Zhang, H., Pan, L., Xue, K., Zhang, X., & Zou, J. J., 2022, "High-Energy-Density Gelled Fuels with High Stability and Shear Thinning Performance," *Chinese Journal of Chemical Engineering*, Vol. 43, pp. 99-109.

[6] Ma, Y., Hao, J., Zhao, K., Ju, Y., Hu, J., Gao, Y., & Du, F., 2019, "Biobased Polymeric Surfactant:

Natural Glycyrrhizic Acid-Appended Homopolymer with Multiple pH-Responsiveness," *Journal of Colloid and Interface Science*, Vol. 541, pp. 93-100.

[7] Cui, W., Shen, Z., Yang, J., & Wu, S., 2015, "Molecular Dynamics Simulation on Flow Behaviors of Nanofluids Confined in Nanochannel," *Case Studies in Thermal Engineering*, Vol. 5, pp. 114-121.

[8] Loya, A., Najib, A., Aziz, F., Khan, A., Ren, G., & Luo, K., 2022, "Comparative Molecular Dynamics Simulations of Thermal Conductivities of Aqueous and Hydrocarbon Nanofluids," *Beilstein Journal of Nanotechnology*, Vol. 13, pp. 620-628.

[9] Blanco-Díaz, E. G., Castrejón-González, E. O., Alvarado, J. J., Estrada-Baltazar, A., & Castillo-Borja, F., 2017, "Rheological Behavior of Ionic Liquids: Analysis of the H-Bond Formation by Molecular Dynamics," *Journal of Molecular Liquids*, Vol. 242, pp. 265-271.

[10] Liu, P., Lu, J., Yu, H., Ren, N., Lockwood, F. E., & Wang, Q. J., 2017, "Lubricant Shear Thinning Behavior Correlated with Variation of Radius of Gyration via Molecular Dynamics Simulations," *The Journal of Chemical Physics*, Vol. 147, pp. 084904.

[11] Martínez, L., Andrade, R., Birgin, E. G., and Martínez, J. M., 2009, "Packmol: A package for building initial configurations for molecular dynamics simulations," *J. Comput. Chem*., Vol. 30, pp. 2157-2164.

[12] Thompson, A. P., Aktulga, H. M., Berger, R., Bolintineanu, D. S., Brown, W. M., Crozier, P. S., in 't Veld, P. J., Kohlmeyer, A., Moore, S. G., Nguyen, T. D., Shan, R., Stevens, M. J., Tranchida, J., Trott, C., Plimpton, S. J., , 2022, "LAMMPS - a flexible simulation tool for particle-based materials modeling at the atomic, meso, and continuum scales," *Comp. Phys. Comm*., Vol. 271, pp. 10817.

[13] Sun, H., Mumby, S. J., Maple, J. R., & Hagler, A. T., 1994, "An Ab Initio CFF93 All-Atom Force Field for Polycarbonates," J*ournal of the American Chemical Society*, Vol. 116, pp. 2978-2987.

[14] Daw, M. S., Foiles, S. M., & Baskes, M. I., 1993, "The Embedded-Atom Method: A Review of Theory and Applications," *Materials Science Reports*, Vol. 9, pp. 251-310.

[15] Evans, D. J., & Morriss, G. P., 1984, "Nonlinear-Response Theory for Steady Planar Couette Flow," *Physical Review A*, Vol. 30, pp. 1528.

[16] Tuckerman, M. E., Mundy, C. J., Balasubramanian, S., & Klein, M. L., 1997, "Modified Nonequilibrium Molecular Dynamics for Fluid Flows with Energy Conservation," *The Journal of Chemical Physics*, Vol. 106, pp. 5615-5621.

[17] Cao, J., Zhang, Y.-C., Pan, L., Shi, L., Zhang, C., Zou, X., and Ji, J., 2020, "Synthesis and characterization of gelled high-density fuels with low-molecular mass gellant," *Propellants, Explosives, Pyrotechnics*, Vol. 45, pp. 1018-1026.

Conference on Modelling Fluid Flow (CMFF'25)
The 19th International Conference on Fluid Flow Technologies
Budapest, Hungary, August 26 - August 29, 2025

EFFICIENT RADIAL-AXIAL JET FOR IMPROVING THE FLEXIBILITY IN OPERATION OF HYDRAULIC TURBINES

Ilie Alin BOSIOC[1], Constantin TANASA[2], Adrian STUPARU[3], Romeo SUSAN-RESIGA[4]

[1] Corresponding Author. Department of Mechanical Machines, Equipment and Transportation, Politehnica University Timișoara, Timișoara, Romania, E-mail: alin.bosioc@upt.ro
[2] Research Institute for Renewable Energies, Politehnica University Timisoara, Timișoara, Romania. E-mail: constantin.tanasa.upt.ro
[3] Department of Mechanical Machines, Equipment and Transportation, Politehnica University Timișoara, Timișoara, Romania, E-mail: adrian.stuparu@upt.ro
[4] Department of Mechanical Machines, Equipment and Transportation, Politehnica University Timișoara, Timișoara, Romania, E-mail: romeo.resiga@upt.ro

ABSTRACT

In industrialized nations, the prevailing mandates necessitate the adoption of renewable energy to the maximum extent practicable. A substantial challenge associated with renewable energy is the intrinsic variability in power generation. The exclusive mechanism currently available for rapid compensation of energy is facilitated by hydroelectric power plants. Notably, hydroelectric power plants, particularly those with hydraulic turbines featuring fixed blades (e.g., Francis turbines), are designed to operate near the optimal operating point with an allowable deviation of up to ±10%. The conventional configuration of a Francis turbine consists of stationary stay vanes, guide vanes, and a radial-axial runner with fixed pitch blades. The swirling flow emerging from the runner blades is typically optimized for peak overall efficiency, thereby reducing losses in the draft tube cone. However, at off-design operating points, there is a sudden increase in draft tube cone losses, alongside pronounced flow instabilities.

This paper introduces a novel approach involving the injection of a radial-axial water jet into the draft tube cone. The radial-axial jet injection necessitates a lower flow rate compared to traditional axial water injection, while effectively mitigating hydraulic instabilities (such as the vortex rope) within the draft tube cone. The investigations will be conducted numerically by examining the flow dynamics and analysing the unsteady static pressure from the walls within the draft tube cone. Ultimately, the paper will assess the ratio between the draft tube pressure amplitude and the requisite flow rate to alleviate these instabilities.

Keywords: Hydraulic Turbines, LDA, Numerical Simulation, Part Load Operation, Radial-Axial Water Jet.

NOMENCLATURE

D_h	[m]	main runner hub diameter
D_t	[m]	main runner tip diameter
n	[rpm]	rotational speed
Q_n	[m^3/sec]	nominal flow rate discharge
V_m	[m/sec]	meridional velocity
V_m	[m/sec]	meridional velocity
V_u	[m/sec]	circumferential velocity
V_{ref}	[m/sec]	reference velocity

1. INTRODUCTION

In the last decades the renewable energy experienced a spectacular development all over the globe. The same trend was observed in Europe and also in Romania, where the renewable energy was developed especially on solar and wind energy generation. Accordingly, the amount of renewable energy in the electricity generation in Romania increase with approximately 10% in less than 8 years, and this trend is increasing constantly. A significant challenge associated with renewable energy is the variability of the produced power. At present, the sole method available for prompt energy compensation is provided by hydroelectric power plants, [1].

Hydroelectric power plants, particularly those equipped with hydraulic turbines featuring fixed blades, such as Francis turbines, are engineered to function near the optimal operating point, allowing for a deviation of up to ±10%. The classical Francis turbines design includes the stationary stay vanes and

guide vanes and a radial-axial runner with fixed pitch blades. The swirling flow exiting the runner blades, usually optimised for a peak overall efficiency with corresponding minimum draft tube cone losses. At off-design operating point, the draft tube cone losses abruptly increase, with severe flow instabilities, [1], [2].

The energy market necessitates that hydraulic turbines operate within an increasingly expansive range, between -35% and 20% from the optimum operational point [2]. Operating hydraulic turbines far from their optimal point results in the emergence of a decelerated swirling flow with instabilities downstream from the turbine, a phenomenon referred to in the literature as the vortex rope. Hydraulic instabilities form at the boundary between the main flow zone—when operating at partial flow near the cone wall—and the stalled area situated at the center of the conical diffuser [3][4][5]. The primary objective of the draft tube cone is to convert the surplus kinetic energy into static pressure, thereby recovering a significant portion of the hydraulic energy and enhancing turbine efficiency. Typically, hydraulic instability originating from the draft tube cone is accompanied by high-pressure pulsations that propagate throughout the hydraulic system, diminishing hydraulic losses and subsequently reducing turbine efficiency. Operating at partial flow rates often results in cracks on the runner blades or the removal of the ogive from the crown type of the runner. These adverse effects and incidents necessitate the cessation of the hydroelectric power plant's operations, leading to substantial economic losses due to repairs and its withdrawal from electricity production, as noted by Casanova et al. [6]. Generally, mitigating the effects of pressure fluctuations induced by hydraulic instabilities involves constraining the turbine's operating range. Consequently, the hydroelectric power plant's function as an energy compensator within the national electrical system remains unfulfilled. Numerous methods have been developed over the years to extend operating regimes while moderately developing hydraulic instabilities. Most solutions are related primarily to the effects, rather than addressing the root cause of hydrodynamic instability. Among the most prevalent solutions are filling the stalled region within the middle of the draft tube cone with air or solid bodies [8][9], or reducing decelerated swirling flow near the conical diffuser wall by installing different fins or channels [10]. Nonetheless, all these methods focus on the effects of hydraulic instabilities rather than addressing the root cause, which, in this context, is the decelerated swirling flow emanating from the runner turbine's outlet. The Laboratory of Hydraulic Machinery and the Research Centre for Engineering of Systems with Complex Fluids (RCESCF) at the Politehnica University Timișoara (UPT) focusses on the investigation of hydraulic machines. An experimental test rig has been developed to study the decelerated swirling flow from the conical diffuser of hydraulic turbines, as depicted in Fig. 1.. The vortex rope is developed in the draft tube cone (or conical diffuser) with higher pressure fluctuations and vibrations, Fig. 1.

In the last decade, a new active control method has been proposed and patented by Resiga et al. [11][12], axial water injected through the runner's crown along the draft tube cone. The method was intensively experimented by Bosioc et al. [13][14] in the laboratory, where the control method proved the efficiency and diminish the flow instabilities from the draft tube cone. The method addresses directly to the cause of flow instabilities, and it acts on dynamic behaviour (by reducing the pressure fluctuations and vibrations) and flow behaviour (modifies the structure of the flow, by eliminating the formation of the vortex rope). As a result, the water jet injection trough the runner crown has been tested in other laboratories on model turbines and has been implemented in real hydropower plants, [15] [16]. Anyway, the major obstacle on implementing this control method in the power plants on large scale, is related by the higher volume of water (more than 15% from the main flow rate) necessary to be axially injected through the ogive in the draft tube cone.

2. METHOD FOR REDUCING THE HYDRAULIC INSTABILITIES AND THE EXPERIMENTAL SETUP

Recently a series of numerical investigations, reheated the idea of water injection in the draft tube cone, [16][17] with similar results in diminishing the flow instabilities from the draft tube cone at part load operation. The investigations performed by two different research collectives [17][18] concentrated on ogive or nozzle modification with the purpose to reduce the amount of water necessary for injection. The results show that a radial-axial water jet can reduce the effects of the vortex rope while using a water jet flow rate of approximately 10% from the main operating flow rate or even less.

The main goal of the paper is to investigate a new concept by using an actuator mounted at the end of the ogive. The actuator will provide a radial-axial water jet in the draft tube cone. According with Fig. 2, the swirl generator which consist by the fixed stay vanes and the runner and continues with the ogive, has an actuator (shown in red) with the possibility to move and positioning at the inlet in the draft tube cone. In comparison with the axial water jet control technique already validated in the laboratory, the concept for radial-axial water jet it comes with the following advantages: 1) efficient jet - reduces the amount of flow rate for water injection from 14% up to 10%; 2) efficient jet - the displacement system has the possibility to provide axial or radial-axial or radial jets, depending by the hydrodynamic instability developed in the drat tube cone.

The main purpose of the new concept of efficient jet is to add flexibility in operation for the hydraulic turbines to avoid the draft tube performance deterioration at off-design operating conditions. Moreover, the main runner operation is not influenced, and the radial-axial water jet will function only when the machine is operated at part load or full load with the development of the vortex rope.

The principle of modulating the decelerated swirling flow within the conical diffuser has been investigated through numerical analysis [18]. In alignment with this theoretical framework, the research objective is to provide an optimal configuration at the draft tube cone inlet. To achieve this optimum configuration, three conditions must be addressed: minimizing hydraulic losses, maximizing pressure recovery, and minimizing pressure pulsations within the draft tube cone. The implementation of a radial-axial water jet facilitates the fulfilment of these conditions with the least energy required for radial-axial water injection.

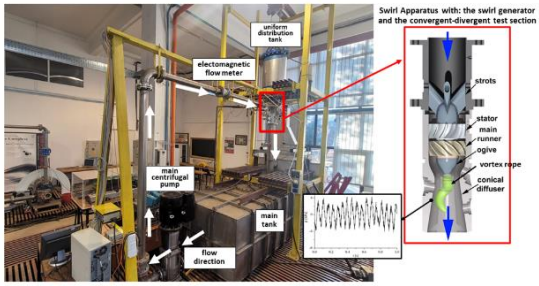

Figure 1. The test rig from the laboratory similar with the numerical model employed in this paper.

The computational model utilized for evaluating the radial axial jet within the discharge cone of hydraulic turbines is linked to the swirl apparatus present within the laboratory environment. This swirl apparatus facilitates the investigation of various control methodologies aimed at alleviating flow instabilities associated with the vortex rope phenomenon. The apparatus, integrated into the primary hydraulic circuit of the test rig, comprises two principal components: the swirl generator and the test section. The swirl generator itself is composed of three parts: the ogive, the stator, and the main runner, which are installed within a cylindrical Plexiglas section with an internal diameter of 0.150 m, as illustrated in Figure 1. At the inlet of the conical diffuser, the stator and main runner generate a rotating flow analogous to that observed downstream of a Francis runner operating at 70% of the nominal flow rate, [13].

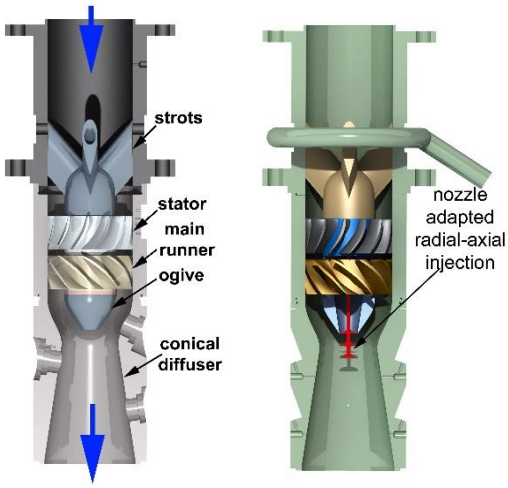

Figure 2. The swirl apparatus and test section from the experimental test rig are illustrated. The left image depicts the original configuration, whereas the right image displays the setup with the device designed to facilitate a radial axial jet rig.

The main dimensions of the components from the swirl apparatus together with the dimensions of the radial axial concept are presented in Table 1.

3. NUMERICAL SETUP

The computational domain pertains to the convergent-divergent segment of the swirling flow apparatus developed at Politehnica University Timisoara (UPT) [19]. The convergent segment is delineated by the annular inlet section and the throat, as depicted in Figure 2. Figure 3 illustrates the computational domain inclusive of the jet injection device. A mixed mesh, comprising approximately 2.8 million cells, has been generated.

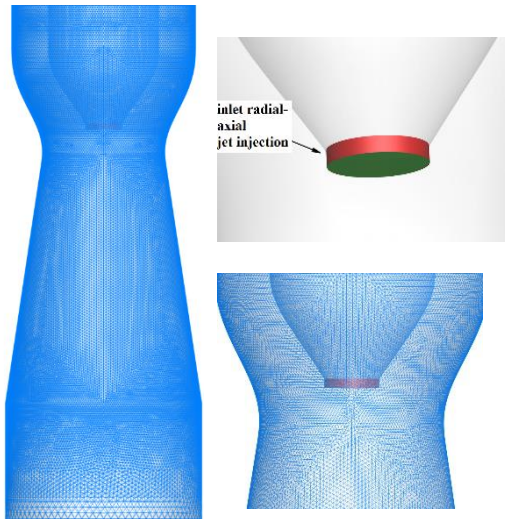

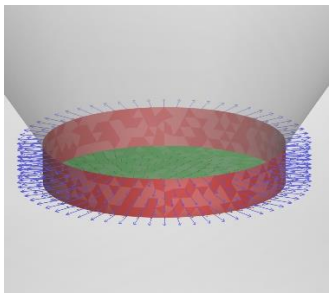

Figure 3. Mesh domain for the convergent-divergent test section and the detail of the inlet for radial-axial jet injection.

For each scenario, boundary conditions are prescribed utilizing a velocity profile at the domain's inlet and an outflow condition at the outlet section. The inflow boundary conditions are derived by computing the flow upstream of the numerical domain from our preceding research work. Consequently, the inlet velocity profile (covering axial, radial, and circumferential velocity components) in addition to the turbulent quantities (kinetic energy and turbulence dissipation rate) corresponding to a runner speed of 920 rpm are applied to the annular inlet section. Figure 5 shows the velocity profiles from the inlet test section. Two flow rates values were tested for the jet injection device: 1.5 l/s and 3 l/s. For the two values of the flow rate of the jet, corresponding constant velocity values were imposed on the outer section of the jet injection device.

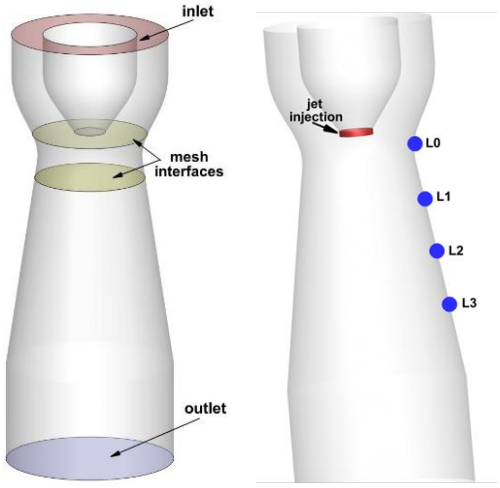

Figure 4. Full 3D domain: with the development of the vortex rope (left), with nozzle for radial axial jet injection (right)

Three-dimensional unsteady numerical simulations, both with and without jet injection, were undertaken utilizing Ansys FLUENT 2023 R2 software to evaluate the efficacy of the novel approach in mitigating the vortex rope. In modelling the turbulent flow within the domain, the k-ω GEKO turbulence model was employed. This turbulence model has been recently introduced into Ansys FLUENT and is more adept at accurately capturing the flow characteristics specific to hydraulic machines. The advantage of this turbulence model lies in its flexibility to encompass a wide array of applications. The model offers free parameters that may be adjusted for specific application types, without adversely affecting its fundamental calibration. This attribute constitutes a potent tool for model optimization; however, it necessitates a thorough understanding of the coefficients' impact to prevent mistuning. It is vital to underscore that the model possesses strong default settings, enabling its application without modification, although any adjustments should be substantiated by high-quality experimental data. The time step applied for the unsteady simulation for all the investigated cases was t = 0.002 s. All numerical solutions were converged down to residuals as low as 10^{-4}. Pressure monitors, L0…L3, have been placed on 4 levels on the cone wall, at 50 mm on each other, in order to acquire the pressure evolution of the flow phenomena.

Table 1. Hydraulic parameters for the numerical setup.

Parameters	Value	Unit
Nominal discharge Qn	0,03	[m^3/s]
Main runner - rotational speed n	920	[rpm]
Main runner - tip diameter D_t	0,150	[m]
Main runner - hub diameter D_h	0,09	[m]
Main runner - blade number z	10	[-]
Nozzle opening	5	[mm]
Control 1 - Flow rate injection	1.5	[l/s]
Control 1 – Procent from main flow	5	[%]
Control 2 - Flow rate injection	3	[l/s]
Control 2 – Procent from main flow	10	[%]

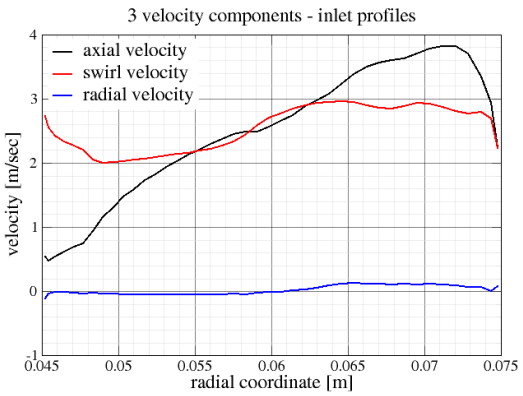

Figure 5. Velocity profiles imposed at the inlet test section

4. VALIDATION, RESULTS AND ANALYSIS

First, the standard case with the development of the vortex rope it was validated with the experimental results, and after the boundary conditions will be replicated for the flowing two investigated cases. The validation results are presented in Figure 6, for the two velocity profiles corresponding to the minimum radius of the test section and for unsteady wall pressure corresponding at the L0 level. Both, the velocity profiles validation and the unsteady pressure are presented in non-dimensional parameters. The paper was concentrated on the validation of numerical against experimental results and the analysis of the new concept of radial-axial jet concept only. The velocity was validated for two velocity components: the meridian component v_m (composed from axial and radial velocity component) and the swirl velocity component v_u. From Figure 6 the velocity profiles obtained from the numerical simulation with the turbulence k-ω GEKO model surprise quite well the velocity measurements, the numerical results being fitted in the error band of the experimental measurements. In case of unsteady pressure validation, the wall point is in L0 level, presented in Figure 5.

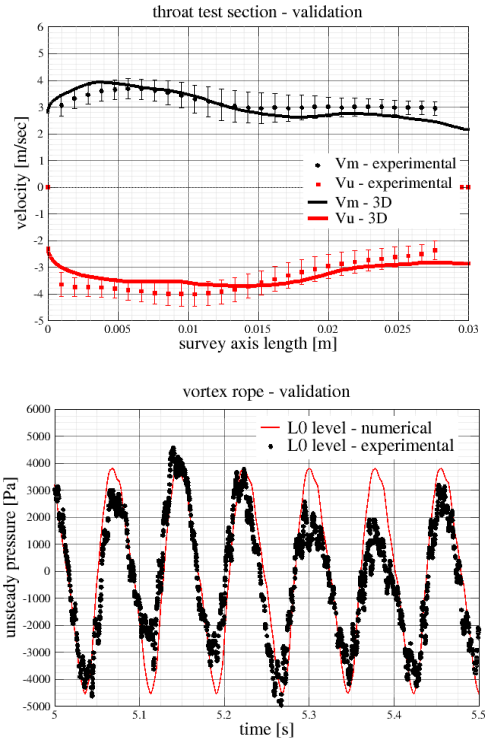

Figure 6. Validation of the vortex rope in case of velocity profiles (close to the throat of the test section) at the inlet in the conical diffuser and in case of unsteady pressure at the wall in L0 level

As it observed in the figure, the numerical validation was registered after 5 seconds iteration, after the case was stabilised, the numerical result having a similar signal as the experiment. The subsequent step involves the analysis of the flow and pressure obtained from the numerical simulation for the scenarios investigated: the vortex rope and two cases for the control: 5% and 10% axial radial injection.

Figure 7 illustrates the flow evaluation within the conical diffuser for all scenarios, focussing on the formation of the vortex rope. To visualise the vortex rope, a constant pressure isosurface was plotted, represented in green, and the vortex cores of the flow field were calculated and depicted as grey. The images show that the vortex rope is present in the conical diffuser in the context of all cases. It forms near the ogive and extends over two-thirds of the conical diffuser's length. When the radial axial jet is introduced into the extension of the ogive, the vortex rope begins to increase in both length and thickness for a flow rate of 5% and begins to decrease for 10%.

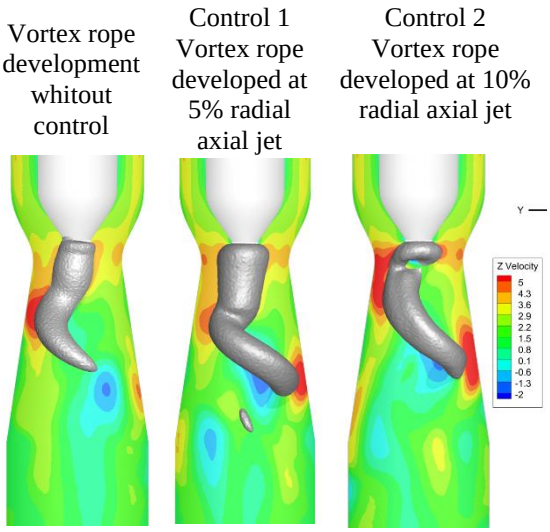

Figure 7. Visualisation of the vortex rope for the case: without and with radial axial jet.

To enhance the understanding of flow dynamics within the conical diffuser, Figure 8 presents a contour plot displaying axial and swirl velocities superimposed with streamlines. It is observed that in the case of the vortex rope, the form is distinctly delineated and extends over more than 50% of the length of the conical diffuser. Upon the introduction of the radial-axial water jet through the ogive inlet, the vortex rope elongates and its angle increases. This augmentation in angle results in the fragmentation of the vortex rope, initiating from the ogive.

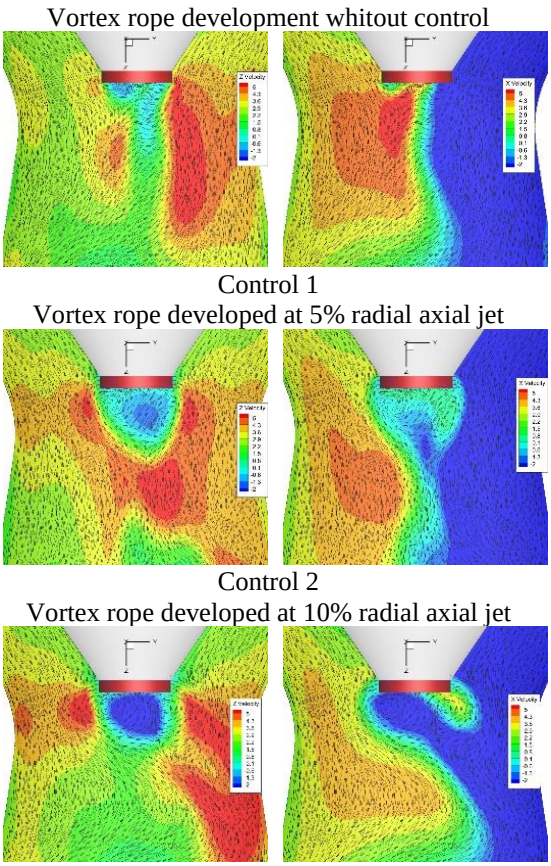

Figure 8. Contour of the axial velocity (left) and of the swirl velocity (right) for the investigated cases where are overlapped the streamlines.

An additional analysis involves the assessment of unsteady pressure recorded on levels L0, L1, L2 and L3 downstream from the inlet within the conical diffuser, as depicted in Figure 9. The unsteady pressure data is obtained from numerical simulation, followed by the execution of FFT. The FFT analysis identifies the primary frequency of the vortex rope of approximately 14 Hz. In the absence of control with axial radial jet, the maximum amplitude attains a value of 4000 Pa. Upon the introduction of the radial axial jet, the maximum amplitude is, and the frequency does not change for 5% flow rate injection. At the maximum flow jet injection of 10% the amplitudes and the frequency in the draft tube cone are diminished completely.

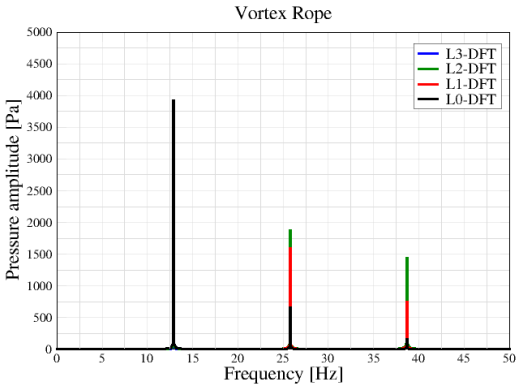

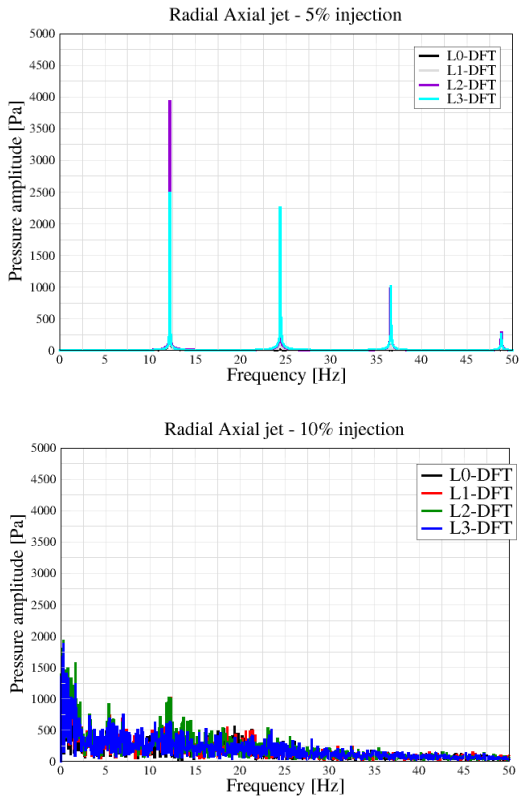

Figure 9. Evaluation of the Fourier transform on the levels L0-L3, downstream of the inlet in the conical diffuser, for the vortex rope case and with radial axial jet from the numerical simulation.

The analysis of the pressure pulsations validates the velocity contours, which means that once the radial axial jet is introduced in the draft tube cone, the vortex rope starts to defragment due to changing the angle. This leads to decrease of frequency and changing the shape of pressure amplitude. Accordingly, the Fourier pressure signal is transforming from a narrowband signal (vortex rope case) to a broadband signal (control with radial axial jet). In practice the defragmentation of the vortex rope into small pieces will lead to a more flexible operation with small pressure amplitudes and without a dominant frequency of the pressure pulsations in the draft tube cone.

5. CONCLUSIONS

The paper explores a method to reduce hydraulic instabilities in draft tube cones by utilizing a radial-axial water jet. Recent numerical investigations have shown that water injection, especially with modifications to the nozzle, can diminish flow instabilities at part load operations, reducing the flow rate required from 14% to about 10%. The study introduces a new concept using an actuator mounted on the ogive to provide a flexible radial-axial water jet that adjusts to different hydrodynamic conditions.

This approach aims to prevent performance deterioration in hydraulic turbines at off-design conditions without affecting the main runner's operation. Numerical simulations with the swirl apparatus and the radial-axial jet injection device were conducted. The Ansys FLUENT 2023 R2 software, employing the k-ω GEKO turbulence model, was used for the simulations, offering flexibility and accuracy for hydraulic machine flows. The study tested two flow rates (1.5 l/s and 3 l/s) for the jet injection, which account for 5% and 10% of the main flow, respectively. Results indicated that radial-axial jet introduction changes the vortex rope characteristics within the draft tube, with increased length and thickness at 5% flow rate and reduced presence at 10%. Unsteady pressure analysis showed that the maximum amplitude of vortex-induced pressure pulsations was significantly reduced with higher flow rate injections, indicating improved hydraulic stability.

ACKNOWLEDGEMENTS

This work was supported by a grant of the Ministry of Research, Innovation and Digitization, CCCDI - UEFISCDI, project number PN-IV-P7-7.1-PED-2024-1113, within PNCDI IV.

REFERENCES

[1] Quaranta E., Hydropower and pumped hydropower storage in the European Union, Status Report on Technology Development, Trends, Value Chains and Markets, 2023.

[2] Kougias I., Aggidis G., Avellan F., Deniz S., Moro A., Muntean S., Novara D., Lundin U., Pérez-Díaz J.I., Quaranta E., Schild P., Theodossiou N., "Analysis of emerging technologies in the hydropower sector", Renewable and Sustainable Energy Reviews, 113, p. 109257, 2019

[3] Nishi, M., S. Matsunaga, M. Okamoto, M. Uno, and K. Nishitani. “Measurement of three-dimensional periodic flow on a conical draft tube at surging condition.” Flows in Non-Rotating Turbomachinery Components, FED 69: 81-88, 1988.

[4] Neidhardt T., Magnoli M., Gummer J., "High part-load fluctuations in Francis turbines and the applicability of model test data", Hydro 2017, Seville, Spain, 2017.

[5] Foroutan H., Simulation, Analysis, and Mitigation of Vortex Rope Formation in the Draft Tube of Hydraulic Turbines, PhD Thesis, 2014.

[6] Casanova, F., "Failure analysis of the draft tube connecting bolts of a Francis-type hydroelectric power plant" In Engineering Failure Analysis, pp. 2203-2208, Elsevier Ltd, 2009.

[7] Qian, Z., J. Yang, and W. Huai. “Numerical simulation and analysis of pressure pulsation in Francis turbine with air admision.” Journal of Hydrodynamics 19, no. 4, p. 467-472, 2007

[8] Thike, R.H. “Practical solutions for draft tube instability.” Vols. 33, No. 2. Water Power and Dam Construction, pp. 31-37, 1981

[9] Peter Joachim Gogstad, Ole Gunnar Dahlhaug. Evaluation of runner cone extension to dampen pressure pulsations in a Francis model turbine. IOP conference series: earth and environmental science, vol. 49, pp. 082019, 2016.

[10] Nishi, M., X.M. Wang, K. Yoshida, T. Takahashi, and T. Tsukamoto. “An experimental study of fins. Their role in control of the draft tube surging.” Proc. of the XVIII IAHR Symposium on Hydraulic Machinery and Cavitation,pp. 895-905, 1996

[11] Susan-Resiga R., Thi V., Muntean S., Ciocan G., Nennemann B., “Jet Control of the draft tube vortex rope in Francis turbines at partial discharge”, 23rd IAHR Symposium, 2006

[12] Ciocan G.D., Vu T., Nennemann B., Demers E., Susan-Resiga R., Liquid Control Jet During Part Load Operation in a Hydraulic Turbine, European Patent EP 2027388 B1, 2007.

[13] Bosioc A., Susan-Resiga R., Muntean S., Tanasa C., “Unsteady pressure analysis of a swirling flow with vortex rope and axial water injection in a discharge cone”, Journal of Fluids Engineering, 134(8), p. 0081104, 2012

[14] Bosioc A., Tanasa C., Experimental study of swirling flow from conical diffusers using the water jet control method, Renewable Energy, 152, pp. 385-398, 2020.

[15] Mohammadi M., Hajidavaloo E., Behbahani-Nejad M., „Investigation on Combined Air and Water Injection in Francis Turbine Draft Tube to Reduce Vortex Rope Effects”, Journal of Fluids Engineering, 141(5), p. 051301, 2019

[16] Juposhti H.J., Maddahian R., Cervantes M., „Optimization of axial water injection to mitigate the Rotating Vortex Rope in a Francis turbine”, Renewable Energy, 175, pp. 214-231, 2021.

[17] Kumar S., Gandhi K., “Axial water jet injection in low head Francis turbine at part load”, Phys. Fluids, 35, p. 065132, 2023.

[18] Litvinov I, Suslov D., Tsoy M., Gorelikov E., Shtork S., Alekseenko S., Oberleithner K., “Active control of the Vortex Induced Pressure Fluctuations in a Hydro Turbine Model via Axial

Radial Jets at the Crown Tip", Int. Journal of Fluid Machinery and Systems, 16(4), pp. 320-331, 2023

[19] Bosioc A I et al, "Numerical Analysis of the Flow by Using a Free Runner Downstream the Francis Turbine", *Int. J. Turbomach. Propuls. Power* 8(2) 10.3390/ijtpp8020014, 2023.

Conference on Modelling Fluid Flow (CMFF'25)
The 19th International Conference on Fluid Flow Technologies
Budapest, Hungary, August 26 - August 29, 2025

OPTIMISATION OF INLET GUIDE VANE FOR LARGE AXIAL FANS BASED ON BIG DATA ANALYSIS

Zijian Mao[1,2], Laifa Lu[1,2], Shuiqing Zhou[1,2,3], Weiya Jin[1,2], Zengliang Gao[1,2], Diping Xu[1,2]

[1] College of Mechanical Engineering, Zhejiang University of Technology, Hangzhou 310023,China.
[2] Institue of Innovation Research of Shengzhou and Zhejiang University ofTechnology, Shengzhou 312400,China.
[3]Corresponding Author. College of Mechanical Engineering, Zhejiang University of Technology, Hangzhou 310023,China. E-mail: zsqwh666@163.com

ABSTRACT

Large axial fans are widely used in nuclear power station ventilation systems due to their high flow rate, high total pressure, compact construction, and excellent economic performance under various operating conditions. This paper discusses a large medium-pressure axial fan with a diameter of 1250 mm, a rated air volume of 82,400 m³/h, and a rated air pressure of 2300 Pa. To address complex and variable operating conditions, as well as performance and noise requirements under extreme conditions, a method for optimizing the inlet guide vane (IGV) of the fan based on big data analysis is proposed. The large axial flow fan audio signal is extracted to analyze structural features of non-steady flow, and discrete peak and non-linear frequencies in the frequency domain are obtained. The PANS model based on the v2-f non-linear turbulence model is validated through simulations, with multi-objective optimization using a support vector machine (SVM) and SVM parameter selection optimized using particle swarm optimization (PSO). Results show that with 15 IGVs, an installation angle of 80°, and a distance of 260 mm between the IGV and dynamic vane, a total pressure increase of 187.64 Pa and a noise reduction of 5.32 dB are achieved.

Keywords: Inlet guide vane, Large axial flow fan, Multi-Objective Optimization, PANS model, SVM

NOMENCLATURE

C_p	[-]	Pressure coefficient
D	[m]	Diameter
E	[-]	Mathematical expectation
F	[-]	Sample matrix
L_{ref}	[m]	Reference Lenth
m_1	[-]	Number of IGVs
m_2	[-]	Number of OGVs
n	[*r*/min]	Rotating speed
p	[Pa]	Pressure
p_{tp}	[Pa]	Total pressure
Q	[m³/min]	Volume flow
r	[-]	Failure indicator function
R^2	[-]	Linear regression coefficient
S_i	[-]	Global Sensitivity Indicator
$V(\cdot)$	[-]	Variance Operator
V_{ref}	[m/s]	Reference velocity
x_i	[-]	Random variable
y^+	[-]	A dimensionless parameter
y_l	[-]	Response
Z	[-]	Number of moving blades
z_l	[-]	Random variables
ρ	[kg/m³]	Density
η	[-]	Efficiency
v	[m²/s]	Kinematic viscosity

Subscripts and Superscripts

RSM	Response Surface Model
GERSM	Gradient-Enhanced Response Surface Model
IGV	Inlet guide vane
MSE	Mean Square Error
NSGA-II	Non-dominated Sorting Genetic Algorithm-II
OGV	Outlet Guide Vane
PANS	Partially-Averaged Navier–Stokes
SPL	Sound Pressure Level

1. INTRODUCTION

This study focuses on optimizing the structure of a large nuclear-grade axial fan (1250 mm diameter) used in nuclear power plant ventilation systems, operating at medium pressure (Mach < 0.3, Reynolds > 4000). Optimizing the fan is urgent due to potential risks in the internal flow field that could lead to motor damage, instability, and shutdowns, causing significant economic and social impacts [1,2].

The goal is to increase pressure and reduce noise without increasing fan size, in line with China's carbon neutrality policies [3,4].

Approximate models are often employed to reduce computational costs in fan optimization. For example, CHOI et al. [5] used RSM to improve total pressure and efficiency by 5.2% and 2.0%, TANG et al. [6] applied GERSM to a transonic fan, and NISHI et al. [7] achieved a 9.1% efficiency increase with RSM in a small axial fan.

Unlike previous studies on single-stage blades, this work optimizes a large axial fan by applying global sensitivity analysis to identify key factors for pressure and noise, uses a Kriging model with NSGA-II for optimization, and validates the results with performance and noise tests, offering guidance for other complex fan designs [8,9].

2. NUMERICAL SIMULATION ANALYSIS AND VERIFICATION

2.1. Research objects

Large axial flow fan mainly consists of a fairing, inlet guide vanes, moving blades, outlet guide vanes and a motor, as shown in Figure 1.

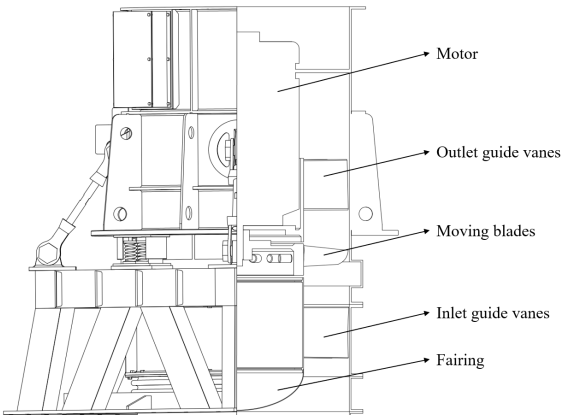

Figure 1 Axial fan structure diagram

2.2. Computational model and verification

For internal area calculations and mesh generation, the fan geometry was divided into five components: inlet, IGV, rotor, OGV, and outlet, as illustrated in Figure 2.

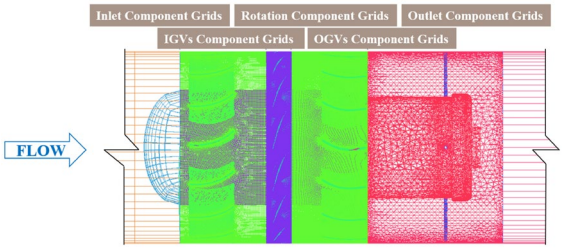

Figure 2. Division of axial fans

Figure 3 shows grid delineation. The important parts (moving vanes, IGVs, OGVs) were structurally meshed to improve the mesh quality. The meshes of IGV, rotation and OGV grids are respectively displayed in Figure 3. In this case, the first node was placed in the region of the viscous substratum with $y^+ \leq 5$. The y^+ empirical formula is expressed as Eq. 1:

$$Y_{wall} = 6\left(\frac{V_{ref}}{\nu}\right)^{-\frac{7}{8}}\left(\frac{L_{ref}}{2}\right)^{\frac{1}{8}} y^+ \qquad (1)$$

where, V_{ref} denotes the reference velocity characteristic of the area-averaged inlet velocity, and L_{ref} represents the reference the fan diameter.

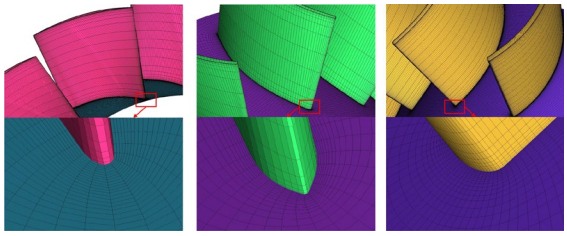

Figure 3. Computational grid of blade

For experimental validation, a C-type air chamber was used according to "GB/T 1236-2017"[10] . The fan was tested at room temperature and pressure, with air parameters recorded using an atmospheric pressure, temperature, and humidity tester at the inlet.

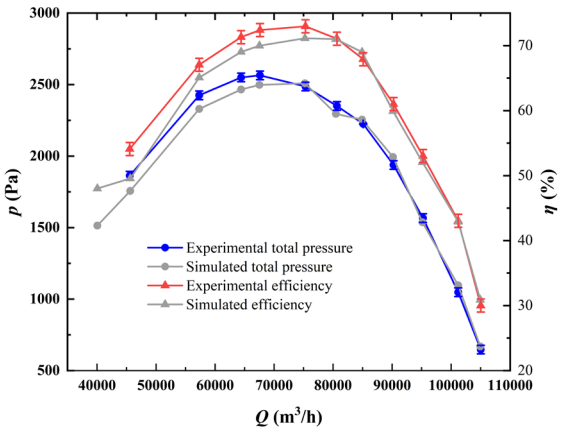

Figure 4. Comparison of experimental and numerical simulation performance curves

Figure 4 compares the numerical simulation with experimental data, showing good agreement. The total pressure simulation was slightly lower, with a maximum error of under 5%. Efficiency differences were minimal, with a maximum error of 9.09% at low flow rates and under 3% at other points, indicating high reliability of the model.

Noise tests followed "GB/T 2888-2008 Fan and Roots Blower Noise Measurement Method,"[11] with the noise receiving point set at 1,250 mm and 45°

horizontally from the outlet center. The schematic of the noise monitoring points and experimental setup is shown in Figure 5(a).

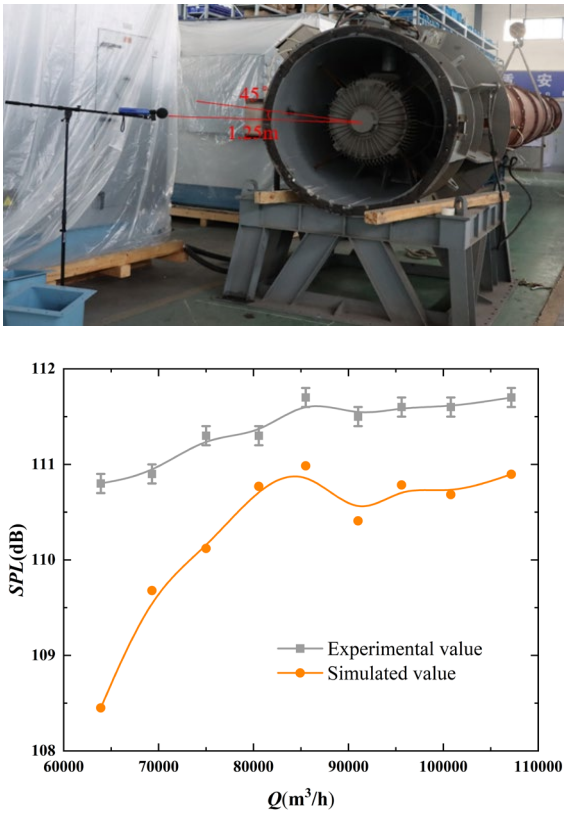

Figure 5. Noise test (a) Noise experimental setup (b) Experimental and numerical simulation noise results

Figure 5(b) shows experimental and simulation noise results. At a flow rate of around 70,000 m³/h, the simulated noise was slightly lower than the experimental value, with a maximum error of under 3%. At flow rates above 75,000 m³/h, the values became more consistent. At the designed flow rate, the average experimental and simulated noise were 111.52 dB and 110.88 dB, respectively, with a relative error of $\leqslant$ 0.57%.

According to JB/T 8690-2014 (Fan Noise Limits)[12], the maximum permissible operational noise level for axial flow fans is 109 dB, and its aerodynamic performance was suboptimal, necessitating optimization. Given the fan's non-standard design and complex structure, analyzing these factors is crucial.

3. DETERMINATION OF OPTIMIZED STRUCTURE

3.1. Global sensitivity analysis method and implementation method

Global sensitivity analys is gives the relationship between the partial derivatives of the output concerning the input variables over the entire input variable space, i.e. $f(\theta)=\partial P_f(\theta)/\partial\theta|_{\theta\in\Theta}$, or a sensitivity indicator used to indicate the importance of the input variables and to rank the importance of the input variables, so it is also known as importance measure analysis.

The global sensitivity metric is defined[13-15] as:

$$S_i=\frac{V[E(I_F\mid x_i)]}{V(I_F)} \tag{2}$$

$$I_F(x)=\begin{cases}1, x\in \text{Invalid Domain}\\ 0, x\notin \text{Invalid Domain}\end{cases} \tag{3}$$

$$V(I_F)=E(I_F^2)-E^2(I_F)=E(I_F)-E^2(I_F) \tag{4}$$

where $V(I_F)$ is the variance operator, $E(I_F\mid x_i)$ is the mathematical expectation of the failure indicator function I_F under the condition of random variable x_i, and I_F is the failure domain indicator function.

For some input variable xi, the global sensitivity principal indicator is:

$$S_i=\frac{V[E(I_F\mid x_i)]}{V(I_F)}=\frac{E(E^2(I_F\mid x_i))-E^2(E^2(I_F\mid x}{E(I_F^2)-E^2(I_F)}=\frac{E(E^2(I_F\mid x_i))-E^2(I_F)}{E(I_F)-E^2(I_F)} \tag{5}$$

The fan mainly consisted of IGV, moving vane, OGV, etc. Therefore, a total of 14 parameters[13], namely the number of IGV ω_1, the number of moving vane ω_2, the number of OGV ω_3, hub ratio ω_4, IGV and moving vane spacing ω_5, moving vane and OGV spacing ω_6, blade top clearance ω_7, IGV bending angle ω_8, IGV chord length ω_9, moving vane bending angle ω_{10}, moving vane swept angle ω_{11}, OGV bending angle ω_{12}, OGV chord length ω_{13}, fan diameter ω_{14}, were analyzed by the Sobol' global sensitivity analysis method. The analysis procedure is specifically displayed in Figure 6 and the schematic diagram of structural parameters is shown in Figure 7.

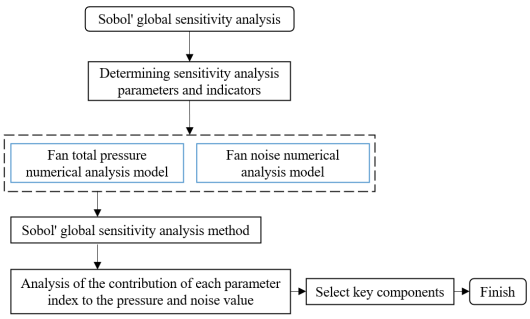

Figure 6. Flow chart of sensitivity analysis

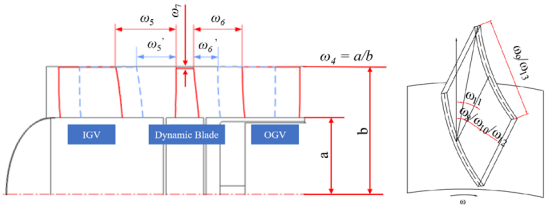

Figure 7. Structural parameters

The global sensitivity values of each parameter to the total pressure and noise of the fan were obtained, as illustrated in Figure 7. In general, the influence of parameters such as IGV bend angle ω_8, IGV and moving vane spacing ω_5, and IGV chord length ω_9 was greater, among which moving vane bend angle ω_{10} and IGV bend angle ω_8 had the highest total global sensitivity values to pressure, which were 31.214 % and 30.113 %, respectively, and IGV bend angle ω_8 and IGV and moving vane spacing ω_5 had the highest total global sensitivity values to noise, which were 33.124 % and 30.145 %, respectively.

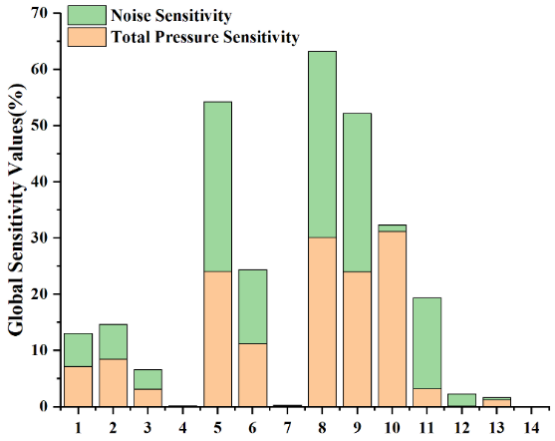

Figure 8. Summary of global sensitivity

According to the above analysis, IGV and moving vane had a large impact while OGV had a relatively small impact on the aerodynamic performance and noise. The internal flow characteristics of the fan will be analyzed as follows to further clarify the optimization objective.

3.2. Analysis of the internal flow characteristics of the fan

The radial section of the hub with blade flow surface R = 280 mm (0.5 times the blade height, Plane1) was selected to study the internal flow characteristics of the fan, and a vertical section was made over the center of the fan circle (as shown in Plane 2). Figure 9 shows the schematic diagram of the radial section of the hub.

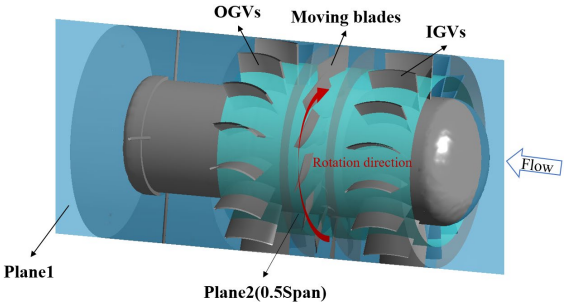

Figure 9. Internal structure of the fan

Figure 10 shows the velocity vector distribution on Plane 1. There was an obvious vortex in the IGV area, which was located between the IGVs. The vortex was mainly concentrated on the pressure surface of the IGV, which was attributable to the blade shape of the guide vane. At the same time, there was a low-speed region in the reflux area, while a high-speed region on the suction surface of the moving blade, which resulted in flow disorder in the dynamic-static coupling zone between the IGV and the moving vane.

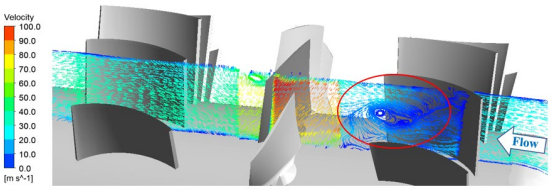

Figure 10. The velocity vector distribution

As a part of the fan, IGV deflected the air flow before entering the hub, increased the flow rate and pressure drop. It was hence an important part of a large axial flow fan. The above analysis also indicates that the structural design of the IGV was not rational and had a significant impact on the performance and noise of the fan, so IGV was identified as the optimization objective of this study.

4. KRIGING MULTI-OBJECTIVE OPTIMIZATION

4.1. Parameterization

The parameters of the IGV are shown in Figure 11. The IGV midline was determined by chord length σ_a, angle α corresponding to the chord, tip deflection angle was defined as β, and the axial distance from the nearest point of the IGV midline to the leading edge of the moving vane as σ_b. These four parameters were optimized in this study.

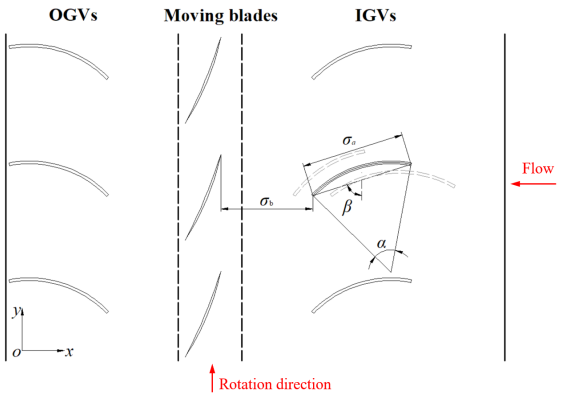

Figure 11. Structure parameters of IGVs

A single circular arc blade is generally adopted in the nuclear power fans. The new IGV midline can be obtained by controlling parameter change and characterizing profile change. Under the premise of ensuring the smooth curvature of the blade, the variable range of each parameter is determined as follows: σ_a: 234~350 mm, α: 44~68 °, β: 58~86 °, σ_b: 208~312 mm.

4.2. Kriging model and optimization

This study and [13] share similar test rigs and parameter ranges, but here we introduce a big data-driven optimization workflow and broader sensitivity analysis, making the results more robust and widely applicable.

Kriging model is an unbiased estimator with minimum variance. The design variables $x_i \in X = [x_1, x_2, \cdots, x_n]^T$ and response values $y_l \in Y = [y_1, y_2, \cdots, y_n]^T$ were assumed to follow a standard normal distribution. The unbiased estimation y_l^* of the random inputs x_l corresponding to y_l is shown as:

$$y_l^* = f(x)^T \beta + z_l(x), \quad l = 1, 2, \cdots, q \tag{6}$$

$$\beta = \left(F^T R^{-1} F\right)^{-1} F^T R^{-1} Y \tag{7}$$

$$\gamma^* = \frac{z_l(x)}{r(x)^T} = R^{-1}(Y - F\beta) \tag{8}$$

To establish the Kriging model, samples should be obtained through experimental design. The optimal Latin hypercube experiment design (Opt LHD) is generally adopted to overcome the deficiencies of random sample space selection and sample concentration in Latin hypercube method. And its formula is expressed as:

$$G_{(L)} = \sum_{i=1}^{N} \sum_{j=i+1}^{N} \frac{1}{\left\| x_i - x_j \right\|^2} \tag{9}$$

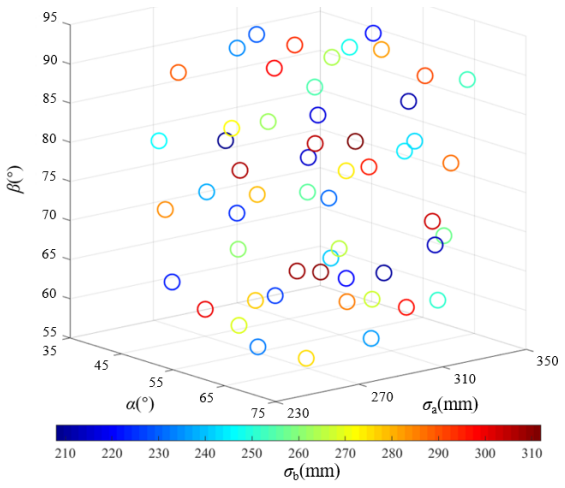

Figure 12. Spatial distribution of samples

As shown in Figure 12, 55 spatial samples were generated using the overshoot method, with the first 50 used to draw IGV profiles. The samples are evenly distributed in the design space. The design variables are IGV chord length (σa), rounding angle (α), tip deflection angle (β), and shortest axial distance (σb), with total pressure and noise as optimization objectives. The mathematical model is as follows:

$$\begin{cases} Max\left(P(\sigma_a, \alpha, \beta, \alpha_b)\right) \\ Min\left(SPL(\sigma_a, \alpha, \beta, \alpha_b)\right) \\ s.t. \quad 234 \le \sigma_a \le 350 \\ 44 \le \alpha \le 68 \\ 57 \le \beta \le 86 \\ 208 \le \alpha_b \le 312 \end{cases} \tag{10}$$

The constraint is:

$$\begin{cases} Q = 82400 \\ SPL \le 111.7 \end{cases} \tag{11}$$

$$MSE = \sum_{i=1}^{n} \frac{1}{n} (f(x_i) - y_i)^2 \tag{12}$$

$$R^2 = 1 - \frac{\sum_{i=1}^{n} (y_i - \hat{y}_i)^2}{\sum_{i=1}^{n} (y_i - \bar{y})^2} \tag{13}$$

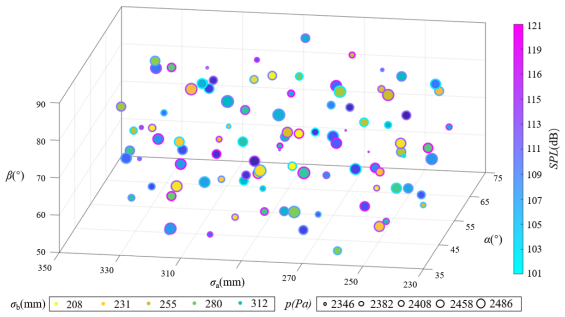

Figure 13. Kriging model fitting results of design variables and total pressure and SPL

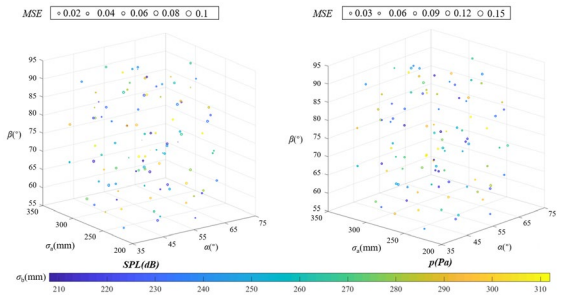

Figure 14. Fitted mean square error MSE

Figures 13 and 14 show the Kriging model fitting results and MSE, with values below 0.1 for noise and 0.15 for pressure, indicating good accuracy. NSGA-II was used for optimization, with optimal results in Table 2. Table 3 shows further reduced MSEs, confirming the effectiveness of the multi-objective optimization.

Table 2. Comparison of parameters before and after optimization

	σ_a (mm)	α (°)	β (°)	σ_b (mm)
Original	292	56	72	260
Optimization	298	61	76	310

Table 3. MSE before and after optimization

	Variable	MSE
Original	*SPL*	0.0434
	p	0.0895
Optimization	*SPL*	0.0235
	p	0.0338

4.3. Optimization result and model

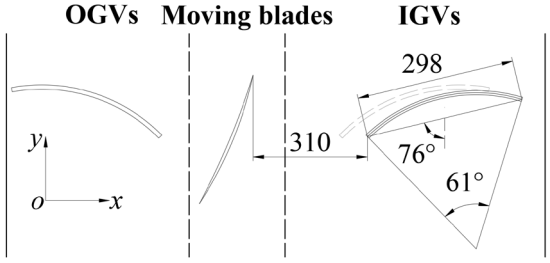

Figure 15. Settings optimization model structure

Fig. 15 shows the settings optimization of IGV. The chord length σ_a of the IGV was increased by 55 mm, the corresponding circular angle α by 5°, the nearest distance σ_b from the IGV to the moving vane by 48 mm, and its angle with the y-axis β by 3°. The physical models are compared in Figure 16.

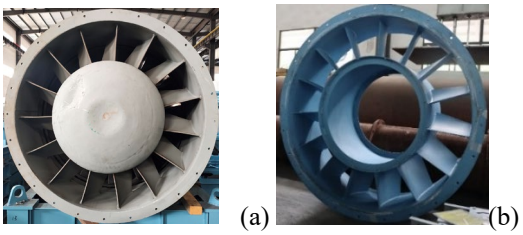

Figure 16. Comparison models (a) Original model (b) Optimization model

5. COMPARISON BEFORE AND AFTER OPTIMIZATION

5.1. Simulation result before and after optimization

To study the internal flow characteristics of the optimized fan, three planes were intercepted in the hub radial direction along the blade height located at R=150 mm (10% blade height), R = 280 mm (50 % blade height) and R = 430 mm (90 % blade height) in the hub radial direction. The rotary surface is shown in Figure 17.

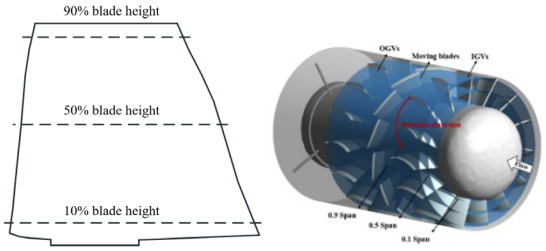

Figure 17. Schematic diagram of the rotating surface

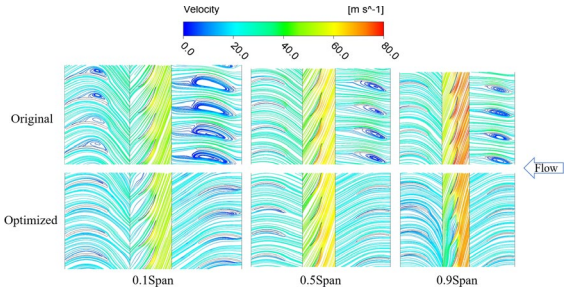

Figure 18. Streamlines coloured by flow velocity at different spans

Figure 18 compares IGV streamlines before and after optimization, showing that vortices present at all heights were eliminated, leaving only low-speed zones. Figure 19 displays simulated static pressure distributions at IGV heights, with Cp calculated using Eq. 13 [16,17].

$$C_p = \frac{p - p_\infty}{\frac{1}{2}\rho_\infty v_\infty^2} \tag{14}$$

Figure 20 shows static pressure distributions. After optimization, Cp increased, pressure gradients decreased, and the separation point shifted, leading to smoother pressure and fewer vortices, thus reducing noise.

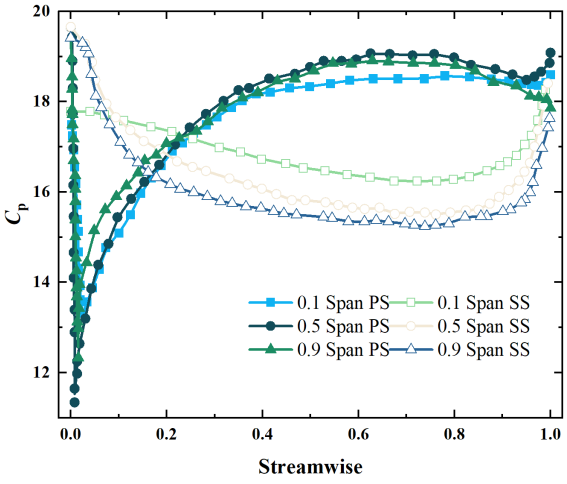

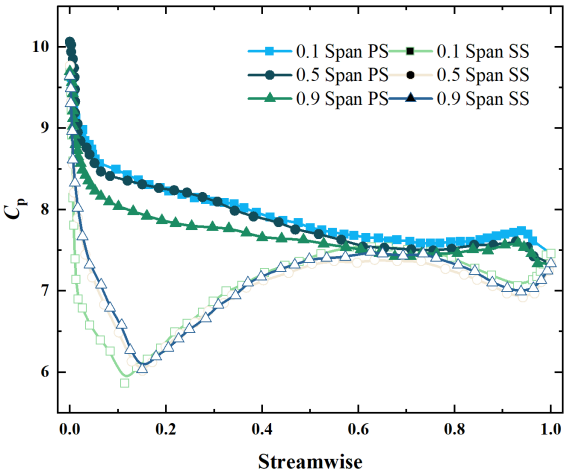

Figure 20. IGVs pressure distribution (a) Original (b) Optimization

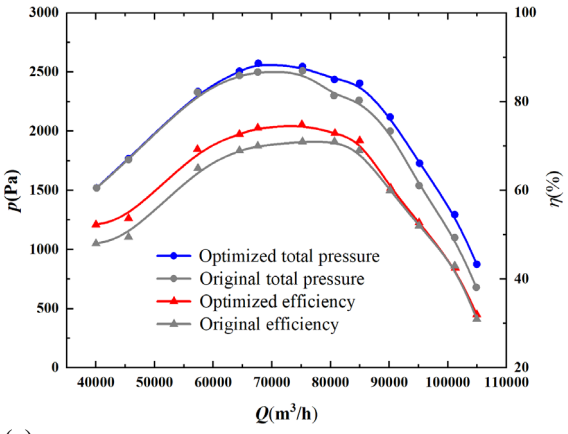

(a)

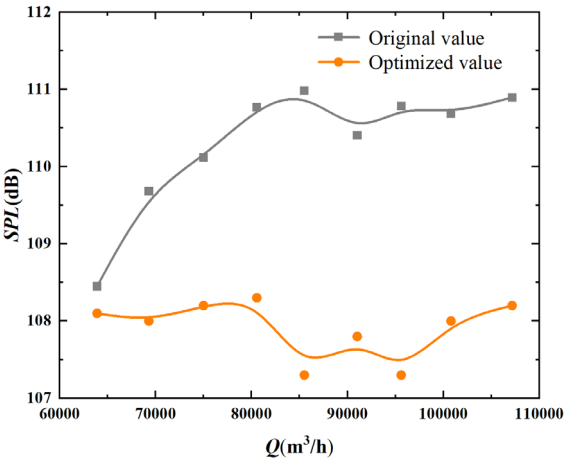

(b)

Figure 21. Numerical simulation results of aerodynamic performance (a) *Q* (b) SPL

Figure 21 shows the numerical simulation results before and after optimization. After optimization, total pressure and efficiency improved at all flow rates. Total pressure increased by 140.97 Pa at flow rates above 70,000 m³/h, while efficiency improved by 2.06% at flow rates below 85,000 m³/h, as shown in Figure 21(a). Noise was reduced by 3.08 dB at all flow rates at the design condition, as shown in Figure 21(b).

5.2. Experimental result before and after optimization

Figure 22 shows the total pressure and efficiency curves for the original and optimized fans across the full range of flow rates. At the design operating point (82,400 m³/h), the optimized model achieves a total pressure increase of 156.4 Pa and an efficiency improvement of 0.86% compared to the original design. All values are area-averaged outlet measurements based on the GB/T 1236-2017 standard. Minor differences between plotted and tabulated values are due to sampling and measurement uncertainty.

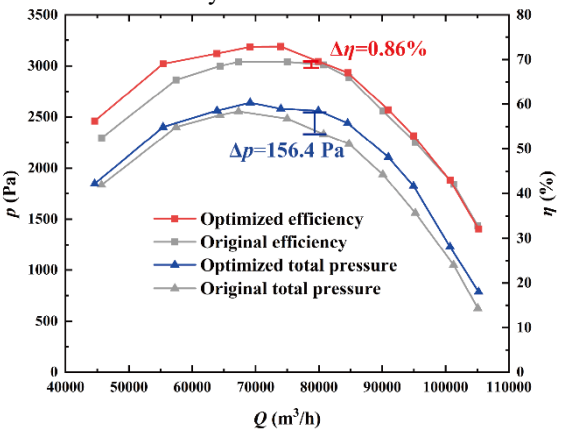

Figure 22. Comparison of performance curves

Referring to the noise test standard, noise receiving points were set at 45 ° from the center of the outlet surface, one time that of the diameter at a horizontal position, and the noise of the optimized fan was also tested.

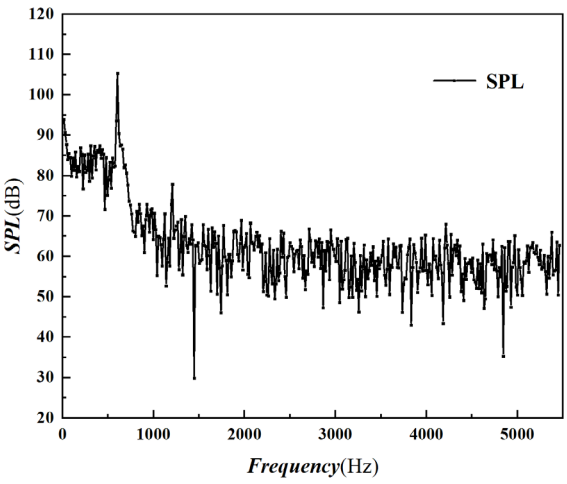

Figure 23. Comparison of noise spectrum

Figure 23 compares the far-field SPL spectra of the original and optimized fans at 82,400 m³/h. Both

show peaks at 14, 302, and 604 Hz. After optimization, the fundamental frequency peak drops from 111.7 dB to 105.3 dB, indicating reduced discrete noise.

6. CONCLUSIONS

This study conducted multi-objective optimization of an IGV for a large axial fan using NSGA-II, validated through experiments and simulations.

(1) Sobol' global sensitivity analysis showed that the IGV bending angle and moving blade bending angle are most sensitive to total pressure, while the distance between the IGV and moving blade affects noise the most. Internal flow analysis revealed significant vortex formation between IGVs, concentrated on the pressure surface.

(2) Numerical simulations of IGV pressure distribution showed smoother static pressure gradients and reduced vortex shedding post-optimization. Experimental results confirmed improved fan performance, with a total pressure increase of 156.4 Pa, a 0.85% efficiency gain, and a 6.4 dB noise reduction.

(3) The NSGA-II optimized Kriging model proved effective for multi-objective IGV design and provides new ideas for optimizing large axial fans.

REFERENCES

[1] Zhao, F.T., Jing, X.D., Yang, M.S., Wang, D.Y., Sha, Y.D., and Luan, X.C. (2020). Experimental study of rotor blades vibration and noise in multistage high pressure compressor and their relevance. Chinese Journal of Aeronautics 33(3), 870-878.

[2] Gu, Z.Y., Zhu, Y.Y., Xiang, J.L., and Zeng, Y. (2021). A prediction method of operation trend for large axial-flow fan based on vibration-electric information fusion. Journal of Central South University 28(6), 1786-1796.

[3] Zhang, W.J., Yuan, J.P., Zhou, B.L., Li, H., and Yuan, Y. (2018). The influence of axial-flow fan trailing edge structure on internal flow. Advances in Mechanical Engineering 10(11).

[4] Fakhraei, A., Faghihi, F., Rabiee, A., and Safarinia, M. (2021). Coolant flow rate instability during extended station blackout accident. Progress in Nuclear Energy 131.

[5] Zhang, C., Li, A.G., Li, J.X., Hou, Y.C., and Chen, X. (2021a). Radiation noise control of a 90 degrees rectangular elbow in ventilation and air conditioning systems. Journal of Building Engineering 37.

[6] Hu, Z.H., and Lu, W. (2017). "Numerical Investigation on Performance and Aerodynamic Noise of High Speed Axial Flow Fans", IAEAC, 885-889.

[7] Kromer, F.J., Moreau, S., and Becker, S. (2019). Experimental investigation of the interplay between the sound field and the flow field in skewed low-pressure axial fans. Journal of Sound and Vibration 442, 220-236.

[8] Tanasic, N., Jankes, G., and Skistad, H. (2011). Cfd analysis and airflow measurements to approach large industrial halls energy efficiency: A case study of a cardboard mill hall. Energy and Buildings 43(6), 1200-1206.

[9] Choi, Y.S., Kim, Y.I., Kim, S., Lee, S.G., Yang, H.M., Lee, K.Y., et al. (Year). "A Study On Improvement Of Aerodynamic Performance For 100hp Axial Fan Blade And Guide Vane Using Response Surface Method", in: ASME-JSME-KSME Joint Fluids Engineering Conference (AJK-FED 2019)).

[10] GB/T 1236-2017(2017). Standardized Air Duct Performance Test for Industrial Ventilators. Beijing: China Standard Press.

[11] GB/T 2888-2008(2008). Methods of noise measurement for fans blowers compressors and roots blowers. Beijing: China Standard Press.

[12] JB/T 8690-2014 (2014). Fans Noise Limited value. Beijing: China Standard Press.

[13] Tang, X., Luo, J.Q., and Liu, F. (2017). Aerodynamic shape optimization of a transonic fan by an adjoint-response surface method. Aerospace Science and Technology 68, 26-36.

[14] Nishi, Y., Mori, N., Yamada, N., and Inagaki, T. (2022). Study on the design method for axial flow runner that combines design of experiments, response surface method, and optimization method to one-dimensional design method. Renewable Energy 185, 96-110.

[15] Venturelli, G., and Benini, E. (2016). Kriging-assisted design optimization of S-shape supersonic compressor cascades. Aerospace Science and Technology 58, 275-297.

[16] Zhou, S.Q., Hu, Y.J., Lu, L.F., Yang, K., and Gao, Z.L. (2022). IGV Optimization for a Large Axial Flow Fan Based on MRGP Model and Sobol' Method. Frontiers in Energy Research 10.

[17] Cui, L.J., Lu, Z.Z., and Zhao, X.P. (2010). Moment-independent importance measure of basic random variable and its probability density evolution solution. Science China-Technological Sciences 53(4), 1138-1145.

Conference on Modelling Fluid Flow (CMFF'25)
The 19th International Conference on Fluid Flow Technologies
Budapest, Hungary, August 26 - August 29, 2025

ESTIMATION OF RELATION BETWEEN PRESSURE DIFFERENCE AND FLOW RATE IN A FRANCIS-TURBINE SPIRAL CASE USING NUMERICAL COMPUTATION

Muris TORLAK[1], Adis BUBALO[2], Ehlimana JUGO[3], Safet ISIĆ[4]

[1] Corresponding Author. Department of Energy, Process Technology and Environmental Engineering, Faculty of Mechanical Engineering, University of Sarajevo. Vilsonovo šetalište 9, BA-71000 Sarajevo, Bosnia and Herzegovina. Tel.: +387 62 14 00 77, E-mail: torlak@mef.unsa.ba
[2] JP Elektroprivreda BiH dd Sarajevo, Podružnica Hidroelektrane na Neretvi. Jaroslava Černija 1, BA-88420 Jablanica, Bosnia and Herzegovina. E-mail: a.bubalo@epbih.ba
[3] Department of Energy, Process Technology and Environmental Engineering, Faculty of Mechanical Engineering, University of Sarajevo. Vilsonovo šetalište 9, BA-71000 Sarajevo, Bosnia and Herzegovina. E-mail: jugo@mef.unsa.ba
[4] Corresponding Author. Faculty of Mechanical Engineering, University "Džemal Bijedić" of Mostar. University Campus, BA-88104 Mostar, Bosnia and Herzegovina. Tel.: +387 62 99 48 77, E-mail: safet.isic@unmo.ba

ABSTRACT

Pressure differences at given locations along radial direction on the walls of the spiral casing of a hydraulic turbine, anticipated for the use in Winter-Kennedy measuring, are computed for a range of water flow rates through the turbine. Different types of boundary condition at the stay-vane side (zero-gradient outlet, average pressure, integral flow rate) are tested first. Several approaches to turbulence handling are also investigated (eddy-viscosity models: realizable k-ε and k-ω SST, then elliptic-blending Reynolds-stress model, as well as large-eddy simulation without subgrid-scale modelling). The simulations are done for a case from an operating hydropower plant, and the results are compared to the pressure values measured in the spiral casing and the flow rates obtained from the recorded output power of the electric generator in real working conditions. The results of numerical simulation agree very well with the measured pressure values. Consequently, a relation between the pressure difference at the monitoring points and the incoming flow rate is established in the form of a power function.

Keywords: computational fluid dynamics (CFD), flow rate measuring, hydraulic turbines, hydropower plants, Winter-Kennedy method

NOMENCLATURE

D	$[m]$	inner diameter of the inlet pipe
P_T	$[W]$	turbine output power
Q	$[m^3/s]$	flow rate
c	[-]	a coefficient of proportionality
g	$[m/s^2]$	gravitational acceleration
h	$[m]$	net head
n	[-]	exponent
p	$[Pa]$	static pressure
t	$[s]$	time
y^+	[-]	non-dimensional wall distance
z_{ps}	$[m]$	vertical position of the pressure sensor
Δ		operator of subtraction, difference
η_T	[-]	turbine efficiency
ρ	$[kg/m^3]$	water density

1. INTRODUCTION

Output power of water turbines is a time-dependent function of the available water net head in a power plant, the water flow rate, and the turbine efficiency, which is usually written in form such as in Eq. (1):

$$P_T(t) = \rho\, g\, h\big(Q(t)\big)\, Q(t)\, \eta_T\big(Q(t)\big)\,. \qquad (1)$$

Time variation of the turbine output power is imposed by electric-grid demands. Neither net head nor turbine efficiency can be directly controlled and varied during regular everyday turbine operation. Practically, the only remaining quantity to control and adapt the turbine output power is the flow rate. The output power is directly dependent on the flow rate Q, but variation of the flow rate also produces variable power losses, affecting thus the net head and the turbine efficiency. Hence, monitoring and management of the water turbines' performance

require reliable estimation of the water flow rate during their operation.

One of the methods used for measuring water flow rate in hydropower plants is the Winter-Kennedy method [1-8]. The method is based on action of centrifugal forces in curved pipes or ducts. The centrifugal forces result in increase of static pressure on the outer side of the curved pipe, and its decrease on the inner side of the pipe. In theory, the pressure difference in radial direction is proportional to the square of the mean velocity of flow through the pipe, thus it is proportional to the square of the flow rate. Accordingly, the dependence of the flow rate on the radial pressure difference is described by Eq. (2):

$$Q = c\,(\Delta p)^n\,. \qquad (2)$$

Theoretically, the exponent n is equal to 0.5, while the coefficient c is a positive real number describing the fluid properties, the geometric properties, and real conditions of the curved pipe. In reality, complex shapes and other geometric properties, such as surface irregularities, roughness, flow regime etc., yield certain deviations from theoretical values, so in practice $n \neq 0.5$.

By measuring Δp, one can get the information on the flow rate using the relation Eq. (2). The method is simple, it does not require moving parts, it is not invasive in the pipe flow, so it does not trigger additional energy loss. It can be applied continuously during the operation. In hydropower plants pressure measuring is installed on spiral casing of a turbine. However, the method requires reliable *a priori* calibration of the coefficients c and n for each specific turbine, usually by (model) experiments in the lab conditions.

Accuracy of water pressure measurement in realistic operational conditions in the spiral casings of hydraulic turbines may decrease over long time periods. This may be a consequence of water debris, sedimentation in the pipe interior, malfunction of an element in the measuring system, occurrence of local pressure variations due to temporary irregular flow patterns etc. Therefore, use of numerical simulation to establish pressure – flow-rate relation for the purpose of flow-rate assessment in operating conditions, or some of protective functions, can be important and improve working processes in hydroelectric power plants.

In this paper a method to obtain coefficients in relation of the pressure difference and the water flow rate in a spiral case of a water turbine by computer simulation using computational fluid dynamics (CFD) instead of experimental calibration is investigated.

2. METHOD

Relation between flow rate and radial pressure difference, as anticipated for use with Winter-Kennedy method, is investigated in case of a real Francis turbine of a medium-head hydropower plant.

Computer program Simcenter STAR-CCM+ [9] is used for meshing, computing, and visualization, where a finite-volume method is applied to discretize the balance equations of mass and momentum, as well as turbulence transport equations (where these are used). Thus obtained systems of linear equations are solved by an algebraic-multigrid method.

Water is considered as incompressible, viscous fluid. The flow field is calculated in parallel using 6 processors for steady-state runs or 64 processors for time-dependent runs. For a series of prescribed water flow rates, the pressure values are evaluated at the monitoring points, corresponding to the locations used in Winter-Kennedy measuring method [1-2], see Figure 1.

Verification of the results is done comparing the results with the data recorded in the power plant in real conditions or the data calculated from them.

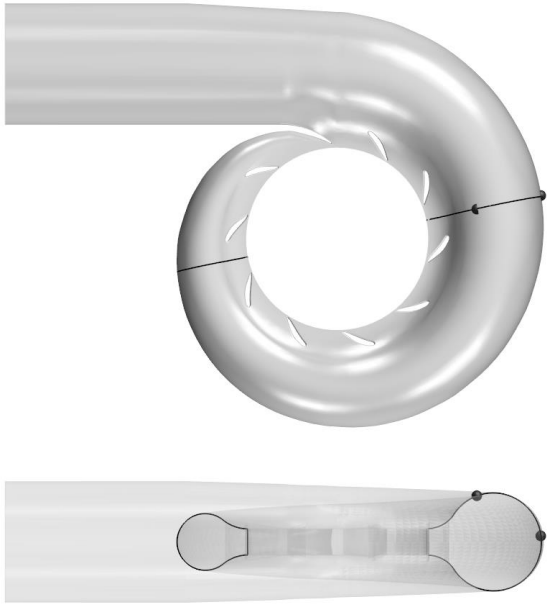

Figure 1. Geometric model of the spiral casing, with the pressure monitoring locations indicated (dark-grey points): the top view (above) and the horizontal view perpendicular to the axis of the inlet pipe, with the section through the monitoring points (below)

2.1. Computational setup

In order to increase the overall processing speed the computational domain is focused on spiral casing, including stay vanes, Fig. 1. The guide vanes and the turbine runner are avoided. Instead, outflow boundary of cylindrical shape is created in the region between the stay vanes and the guide vanes.

The geometric model of the spiral casing is obtained by 3D scanning from the interior (this can be done, for example, during a regular inspection period, when the spiral casing and the turbine are

empty). The resulting point cloud is used to create an appropriate triangulated surface.

The inflow boundary (not shown in figure) is defined as a perpendicular cross section of the inlet pipe, located 4*D* upstream from the entrance to the spiral casing. At the inflow boundary, integral flow rate is prescribed and kept constant in every single calculation run. Spiral casing and stay vanes are considered as fixed, impermeable no-slip walls. Hence, both the tangential and normal component of velocity are set to zero. The wall pressure values are obtained by extrapolation from the near-wall cells.

Three different types of boundary condition are tested at the outflow boundary, in the region between the stay vanes and guide vanes: (a) integral flow rate with specified slope of flow direction, (b) developed outlet flow (with local flow directions extrapolated from the domain interior and zero-gradient condition of physical quantities), and (c) specified *surface-averaged* pressure over the boundary.

The computational mesh inside the CAD model is automatically generated and refined depending on the boundaries' curvature, see Figure 2. The mesh consists of cubic cells, trimmed near the boundaries to adapt to their shape, and 20 layers of prisms along the walls in order to capture velocity gradients in the boundary layer regions. The final mesh contains about 5 030 000 cells.

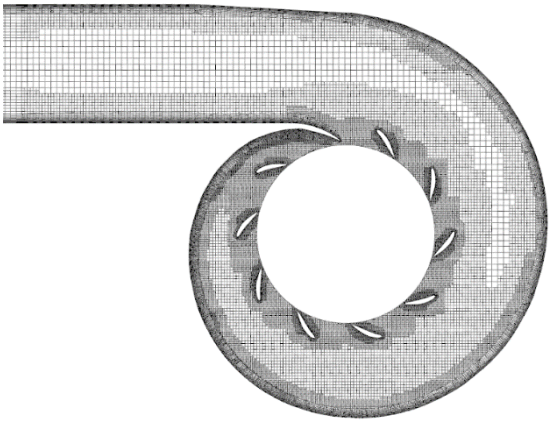

Figure 2. Computational mesh in the horizontal section plane of the spiral casing

Turbulence is resolved using: realizable k-ε model [10] (in this paper also denoted as R KE), k-ω SST model [11] (denoted as KW SST), elliptic-blending Reynolds-stress model [12] (EB RSM), and large-eddy simulation without subgrid-scale modelling (denoted as LES or LES w/o SGS). Implementations of all Reynolds-averaged Navier-Stokes equations (RANS) models used in this work are capable of handling a wide range of y^+ values, from viscous sublayer to logarithmic region. LES w/o SGS reduces, practically, to solution of laminar-flow model, so its wall boundary condition does not involve any special wall treatment and wall distance was not calculated.

Although, formally, LES methods require much finer spatial resolution than RANS models, for sake of keeping computing costs and time demands reduced, LES w/o SGS is done on the same mesh as the RANS models, yielding thus comparison of results obtained with conditions the same or similar, as much as possible.

All simulations are done aiming at steady-state scenario, so the RANS models (R KE, KW SST, and EB RSM) are run ignoring the time dimension and the inertial contribution to the balance of forces, while LES, as imposed by the model, is run in time. Once again, all boundary conditions are kept constant. Since the final solution is expected to be stationary, in case of LES the inertial term of the momentum equation is first discretized by 1st-order accurate implicit Euler scheme, and the time step of 0.005 *s* was adopted, to provide some numerical damping while marching in time. Also convective term is discretized by 1st-order accurate upwind scheme at the beginning. In order to refine the computation, discretization order is increased during simulation (described later in the text), typically after 2 *s* to 3 *s* of simulated time, depending on the flow rate. For the details on numerical methods and discretization techniques the reader is referred to, for example, the books [13, 14] or the software documentation [9].

2.2. Reference measuring

The pressure in the spiral case is measured on a turbine operating in real conditions, at two points along the same radial section, already shown in Fig. 1. Pressure transducers with strain gauges, a measuring range of 0–20 *bar*, accuracy class 0.3, and nominal sensitivity of 0.2 *mV*/*bar*, are used. One transducer is calibrated using a hydraulic scale with an accuracy class of 0.1, and the sensitivity of the second sensor is adjusted to match the readings of the first one. The measurement signal is acquired and amplified by a SPIDER8 amplifier and recorded using CATMAN software [15]. The pressure difference is measured during stationary turbine operation at seven different power levels, ranging from 12 *MW* to 30 *MW*. Power stabilization and achievement of conditions for pressure measurement is monitored by measuring the signal from the opening grade of the turbine guide vanes.

Due to different vertical positions of the two paired sensors, gravity-induced pressure difference is obtained in the recorded values. These are corrected through manual calculation, subtracting the gravity contribution $\rho g \Delta z_{ps}$.

In addition to the pressure differences, a number of corresponding operating data is recorded, including net head, and the output power of the electric generator.

For the reference and comparison with the simulated results, the flow rate is not directly measured, but it is found through a "backward"-calculation from the recorded generator output-power, which is a common procedure for hydraulic turbines in operating conditions. One takes into account efficiency of the generator, power losses in mechanical transmission, and the efficiency of the turbine (from the corresponding hill chart, for the given net head and vane opening). Thus, the input power of the turbine P_T/η_T is obtained, from which the water flow rate is obtained using Eq. (1) having the net head known.

3. RESULTS

In Figure 3 the results of computer simulation are shown for two different types of the outflow boundary condition: zero-gradient outlet and constant average pressure, both of them computed with R KE turbulence model. The reference values – the measured pressure difference and the corresponding flow-rate calculated from the recordings in the power-plant – are shown as well. Both boundary conditions provide the expected trend of the pressure-difference variation. Deviations of the results obtained with zero-gradient outlet condition from the reference data exhibit overestimation in the entire range of the observed flow rates, and are larger than deviations arising in use of average-pressure condition. For both types of boundary condition, the deviations increase with the increase of the flow rate. The computations with the integral flow-rate condition with specified flow direction at the outflow boundary are not shown in the diagram, but they yield the results similar to those achieved with average-pressure condition.

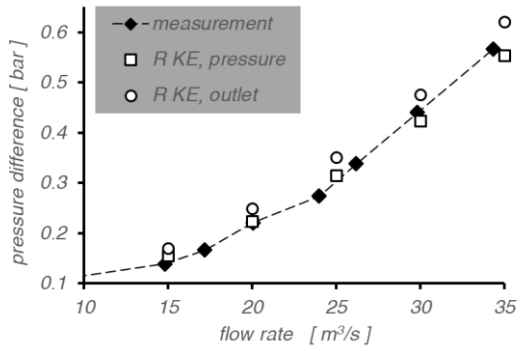

Figure 3. Comparison of average-pressure and zero-gradient-outlet boundary condition

Figure 4 shows a comparison of the results obtained with different types of turbulence modelling applied to the case with the average-pressure outflow boundary condition. The results are quite close to each other, and they are very close to the reference data. This allows conclusion that the choice of turbulence model is not decisive for the overall flow behaviour reflected in the observed pressure-difference and flow-rate relation.

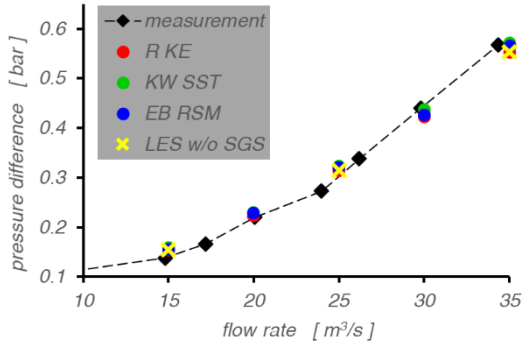

Figure 4. Different turbulent flow simulations with average-pressure outflow boundary

The trend of the curves in Figs. 3 to 4, representing the computational results, approximates quadratic parabola, as expected. By fitting a curve in form of Eq. (2) through the these data (i.e. through arithmetic average of results obtained with different turbulence models for each single flow rate), including corrective translation along the Δp-axis, which accounts for the part of pressure difference caused by gravitational effect and difference in pressure-sensor elevations $\rho g \Delta z_{ps}$, one can obtain the relation:

$$Q = 49.6392 \left(\frac{\Delta p - \rho g \Delta z_{ps}}{100\,000} \right)^{0.5004} . \qquad (3)$$

Note that this relation holds only for the speific spiral casing geometry in the presented simulations. Eq. (3) delivers an error less than 0.5% as compared to the flow rates at sampling points (simulated results).

Fitting a curve of the same form through the measured data delivers the relation:

$$Q = 46.1312 \left(\frac{\Delta p - \rho g \Delta z_{ps}}{100\,000} \right)^{0.4348} . \qquad (4)$$

The resulting exponent in Eq. (4) is clearly lower than the theoretical one. This can be addressed to realistic conditions in the measurement, such as wall roughness and other sources of energy losses. On the other hand, simulation does not take these into account, so the relation resulting from fitting of simulation data has the exponent much closer to the ideal conditions.

Figure 5 shows convergence history of simulations with R KE turbulence model for the minimum (above) and the maximum (below) flow rate from the investigated range, Q=15 m^3/s and Q=35 m^3/s respectively, using all three types of outflow boundary condition. While the average-pressure and the integral flow-rate boundary condition show very similar convergence behaviour,

the zero-gradient outlet condition shows again an overestimation. According to the case of the lowest flow rate (Fig. 5, above), the rate at which the final result is approached is the fastest (i.e. it is achieved in the fewest number of iterations) in the condition of flow-rate with the prescribed flow direction (about 500 iterations).

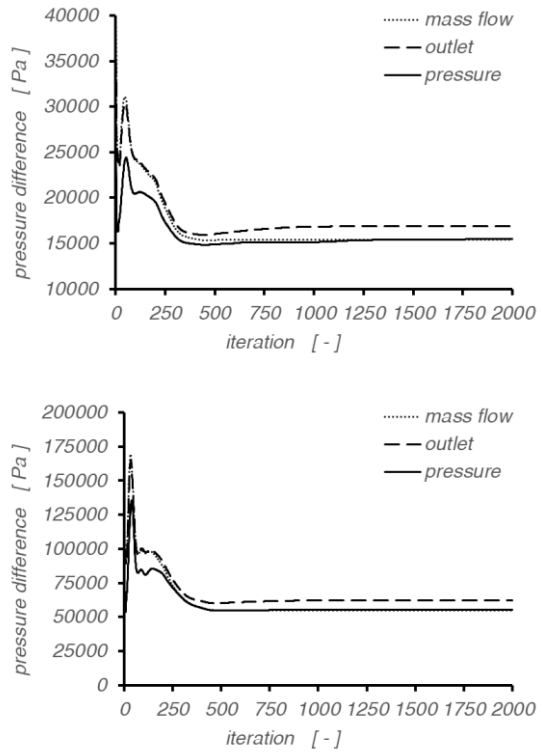

Figure 5. History of the pressure difference at the monitoring points, calculated for different types of outflow boundary condition: Q=15 m^3/s (above) and Q=35 m^3/s (below)

The computational results obtained by LES reveal that the flow exhibits small unsteady effects. In Figure 6, history of the pressure difference is shown. In the period from 0 *s* to 2 *s*, the flow is calculated using the 1st-order accurate upwind scheme for discretization of the convective term in the momentum-balance equation to promote stability and damping with the relatively coarse time step. From 2 *s* to 2.5 *s* of simulated time, discretization scheme for the convective term is switched to the 2nd-order accurate linear-upwind scheme, and after 2.5 *s* of simulated time the discretization scheme of inertial term is also switched to the 2nd-order accurate one, with the time step reduced to 0.001 *s*. Consequently, the simulation detects slight oscillations of the pressure difference between the monitoring points about 0.314 *bar* for the flow rate of 25 m^3/s. Fluctuations of the pressure difference amount to less than 0.5 %, which can be regarded as negligible. Also, a look at the pressure field, such as shown in Figure 7 for a typical instant of time, implies that the monitoring pressure locations are installed in the region of stable, non-fluctuating flow.

4. CONCLUSIONS

Water flow through the spiral casing of a hydraulic turbine is simulated using a computer program for CFD analysis. For the given range of water flow rates static pressure at the pre-defined monitoring points is calculated. The results of numerical simulation with the created computational model give a very good agreement with the measured pressure values. Thus, a relation between the pressure difference at the monitoring points and the incoming flow rate is established. This relation can be used for continuous estimation of the water flow rate in the turbine in operating conditions, by measuring static pressure at the given points.

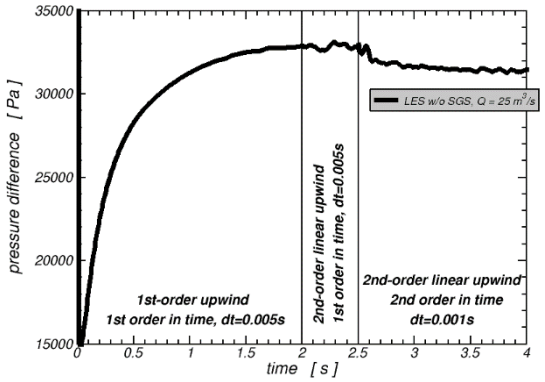

Figure 6. History of the pressure difference at the monitoring points, calculated with LES w/o SGS for Q=25 m^3/s

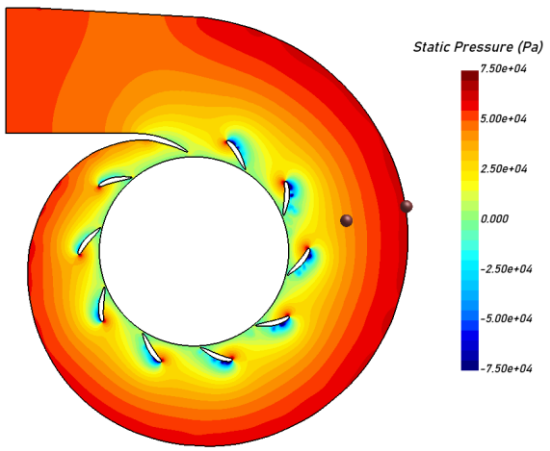

Figure 7. Instantaneous static-pressure field from LES w/o SGS, with the pressure monitoring locations indicated

Since the computational domain includes only inlet pipe, spiral casing, and the stay-vanes ring, for proper simulation appropriate boundary condition is needed at the outflow surface (downstream the stay

vanes). Imposed surface-averaged pressure at the outflow boundary gives the best agreement with the reference data. Testing different turbulent handling approaches did not give substantial differences. Based on the authors' experience, realizable k-ε can model can be adopted for steady-state runs or unsteady runs with relatively slow dynamics, and LES w/o SGS modelling with at least 2nd-order accurate discretization in space and time can be used for the simulations, where small-scale time variations of the flow properties are analysed.

ACKNOWLEDGEMENTS

Financial support is provided by Federal Ministry of Education and Science of FBiH, Bosnia and Herzegovina in year 2023, contract no. 05-35-2489-1/23 from 06.10.2023, which is gratefully acknowledged.

REFERENCES

[1] Winter, I.A., and Kennedy, A.M., 1933, „Improved type of flow meter for hydraulic turbines", *ASCE Proceedings*, Vol. 59, No. 4, Part 1, pp. 563-584.

[2] International Electrotechnical Commission, 1991, "Field acceptance tests to determine the hydraulic performance of hydraulic turbines, storage pumps and pump-turbines", *International Standard* IEC 60041:1991 (E), 3rd edition, Geneva, Switzerland.

[3] Baidar, B., Nicolle, J., Trivedi, C., and Cervantes, M.J., 2016, "Winter-Kennedy method in hydraulic discharge measurement: Problems and Challenges", *11th International conference on hydraulic efficiency measurement*, IGHEM 2016.

[4] Baidar, B., Nicolle, J., Trivedi, C., and Cervantes, M.J., 2018, "Numerical Study of the Winter-Kennedy Method – A Sensitivity Analysis", *Journal of Fluids Engineering*, Vol. 140, No. 5, 051103.

[5] Baidar, B., Nicolle, J., Gandhi, B.K., and Cervantes, M.J., 2020, "Numerical Study of the Winter–Kennedy Flow Measurement Method in Transient Flows", *Energies*, Vol. 13, No. 6, 1310.

[6] Rau, T., and Eissner, M., 2014, „Experience with Winter-Kennedy coefficients on hydraulic identical units", *The 10th International conference on hydraulic efficiency measurements*, IGHEM 2014.

[7] Baidar, B., Nicolle, J., Gandhi, B. K., and Cervantes, M. J., 2020, „Effects of runner change on the Winter-Kennedy flow measurement method – A numerical study", *Renewable Energy*, Vol. 153, pp. 975-984.

[8] Swain, T.K., Garimella, R., and Rahman, M. F., 2025, "Winter Kennedy Method — An Online Tool for Efficiency Monitoring of Hydro Power Plants", In: Pandey, M., Umamahesh, N., Das, J., and Pu, J.H. (eds) *Hydrology and Hydrologic Modelling*, *HYDRO 2023*, Lecture Notes in Civil Engineering, Vol. 410, Springer, Singapore.

[9] Siemens, *Simcenter STAR-CCM+ User Guide*.

[10] Shih, T.-H., Liou, W.W., Shabbir, A., Yang, Z., and Zhu, J., 1994, "A New k- Eddy Viscosity Model for High Reynolds Number Turbulent Flows – Model Development and Validation", *NASA Technical Memorandum*, 106721, ICOMP-94-21, CMOTT-94-6.

[11] Menter, F.R., 1994, "Two-equation eddy-viscosity turbulence modeling for engineering applications", *AIAA Journal*, Vol. 32, No. 8, pp. 1598-1605.

[12] Manceau, R., and Hanjalić, K., 2002, "Elliptic blending model: A new near-wall Reynolds-stress turbulence closure", *Physics of Fluids*, Vol. 14, No. 2, pp. 744-754.

[13] Patankar, S., 1980, *Numerical Heat Transfer and Fluid Flow*, CRC Press.

[14] Ferziger, J.H., Perić, M., and Street, R.L., 2020, *Computational Methods for Fluid Dynamics*, 4th ed., Springer.

[15] Hottinger, Brueel and Kjaer GmbH, *CATMAN, Operating Manual*.

Conference on Modelling Fluid Flow (CMFF'25)
The 19th International Conference on Fluid Flow Technologies
Budapest, Hungary, August 26-August 29, 2025

DEFINITION AND COMPUTATION OF A FLUTTER SAFETY MARGIN FOR QUADCOPTERS BY CHAINING TOGETHER MULTIPLE 2-DOF AEROELASTIC MODELS

Dávid András HORVÁTH[1], János LELKES[2], Balázs FARKAS[3], Tamás KALMÁR-NAGY[4]

[1] Corresponding Author. Department of Fluid Mechanics, Faculty of Mechanical Engineering, Budapest University of Technology and Economics. Bertalan Lajos u. 4 - 6, H-1111 Budapest, Hungary. E-mail: horvathd1@edu.bme.hu
[2] Robert Bosch Kft. E-mail: janos.lelkes@hu.bosch.com
[3] Department of Fluid Mechanics, Faculty of Mechanical Engineering, Budapest University of Technology and Economics. E-mail: farkas.balazs@gpk.bme.hu
[4] Department of Fluid Mechanics, Faculty of Mechanical Engineering, Budapest University of Technology and Economics. E-mail: kalmar.nagy.tamas@gpk.bme.hu

ABSTRACT

When thin, flexible structures, such as the rotors of a quadcopter, are subjected to airflow, aeroelastic phenomena can occur due to the interaction of elastic, inertial, and aerodynamic forces. Due to these phenomena, the flexible structures lose their stability at a critical flow velocity. Flutter is an aeroelastic instability that leads to dynamic stability loss. In this paper, we examine the flutter of the rotor blades during the forward flight of the quadcopter. In this regime, the relative wind experienced by the rotor blades changes periodically. This results in parametric excitation, which can lead to a reduced critical velocity compared to the case without parametric excitation. To consider that the relative wind changes along the radius of the rotor, we construct a three-dimensional reduced-order model by chaining multiple two-degree-of-freedom aeroelastic models. The aerodynamic forces acting on the two-degree-of-freedom models are computed using a quasi-steady aerodynamic model.

We apply the reduced-order model to compute the stability chart of a real quadcopter. To achieve this, we perform simple measurements on the rotor to obtain the geometric parameters, the stiffness, and the damping coefficients. We then compute the stability chart for the quadcopter by solving the equations of motion of the reduced-order model numerically. Using the computed stability chart, we can determine, for a given rotor speed and forward flight velocity, the minimal speed increase required for the rotors of the quadcopter to lose their stability. We call this minimal speed increase the flutter safety margin. We gather velocity data during the flight of a quadcopter and compute the flutter safety margin during the flight.

Keywords: aeroelasticity, fluid-structure interaction, numerical stability analysis, parametric excitation, quadcopter

1. INTRODUCTION

Aeroelastic phenomena affect several types of slender elastic structures subjected to airflow, such as flexible wings, helicopter rotor blades, and wind turbines. Aeroelasticity studies the interactions between inertial, elastic, and aerodynamic forces on flexible structures that are exposed to airflow. The theory of aeroelasticity is extensively covered in the literature [1, 2, 3]. One dangerous aeroelastic instability is called flutter, which is a dynamic stability loss [4]. A famous example of flutter is the vibrations and structural failure of the Tacoma Narrows bridge [5, 6].

Airflow oscillations can cause parametric excitation in aeroelastic systems [7]. Parametric excitation differs from external forcing. The excitation source during parametric excitation is the time-varying modification of a system parameter. In the case of airflow oscillations, the parameters of the aerodynamic lift and moment are time-varying. The interaction of self- and parametric excitation can increase or decrease the critical wind velocity.

Typically, a two-degrees-of-freedom (2-DOF) reduced-order model is used to investigate flutter and compute the critical velocity [8]. However, one major disadvantage of this model is that it assumes a uniform velocity along the wing, while rotorcraft, such as drones, have a linear velocity distribution along the span of their wings. Thus, it is important to study a more complex reduced-order model to gain a better understanding of flutter safety for these aircraft.

This work investigates a three-dimensional reduced-order model subjected to periodically varying airflow to study flutter in flying drones. In Section 2, we introduce the mathematical model. In Section 3, we compute the stability charts. In Section 4, we introduce the flutter safety margin and compute it during the flight of the drone. In Section 5, we summarize the results.

2. MATHEMATICAL MODEL

In this section, we will describe the three-dimensional reduced-order aeroelastic model. The building block of this model is a two-degrees-of-freedom (2-DOF) aeroelastic model shown in Figure 1. The two degrees of freedom in the model are the pitching (α) and plunging (h) degrees of freedom.

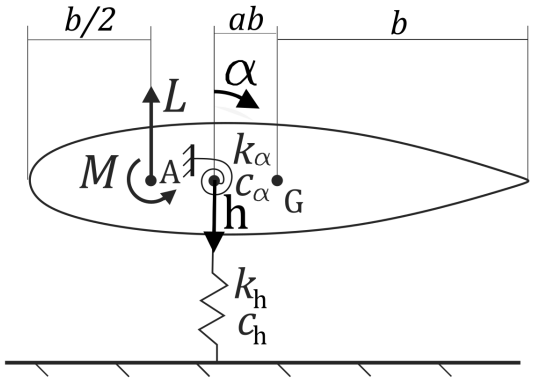

Figure 1. The 2-DOF aeroelastic model.

In this model, we assume that the center of gravity (denoted by G) is located in the middle of the wing. We denote the distance between the elastic axis and the center of gravity by ab and the semi-chord by b. The equations of motion of this model are [9].

$$\begin{aligned} m\ddot{h} + c_h\dot{h} + k_h h &= -L, \\ I_\alpha\ddot{\alpha} + c_\alpha\dot{\alpha} + k_\alpha\alpha &= M, \end{aligned} \tag{1}$$

where h and α describe the vertical (plunge) displacement (positive downwards) and angular (pitch) displacement (positive in the clockwise direction), respectively. The mass of the wing is m and I_α is the moment of inertia. The stiffness and damping coefficients for the plunge DOF are denoted by k_h and c_h, respectively. For the pitch DOF, these coefficients are denoted by k_α and c_α. L and M denote the aerodynamic lift and moment (together they will be called the aerodynamic forces). To compute the aerodynamic forces L and M, we apply the quasi-steady approximation of the Theodorsen lift function [10]. Thus,

$$\begin{aligned} L &= 2\pi\rho U^2 bS\left[\alpha + \frac{\dot{h}}{V} + b\left(\frac{1}{2} - a\right)\frac{\dot{\alpha}}{V}\right], \\ M &= 2\pi\rho U^2 b^2 S\left(a + \frac{1}{2}\right)\left[\alpha + \frac{\dot{h}}{V} + b\left(\frac{1}{2} - a\right)\frac{\dot{\alpha}}{V}\right], \end{aligned} \tag{2}$$

where S is the span of the wing, a is defined via Figure 1, ρ is the density of the air and V is the velocity of the air. One big disadvantage of this model is that it assumes a constant velocity distribution along the span of the wing. This assumption is not valid for rotorcraft, since in their case the velocity increases linearly from the hub to the tip of the wing.

We eliminate this disadvantage by chaining multiple two-degrees-of-freedom (2-DOF) models into a three-dimensional reduced-order model through a pair of springs. Each wing segment (i.e., a single 2-DOF model) has a pitch and plunge DOF, with the plunge DOF corresponding to the bending motion of the wing. These DOFs are coupled to those of the neighboring wing segments by springs. The construction is shown in Figure 2 for two wing segments.

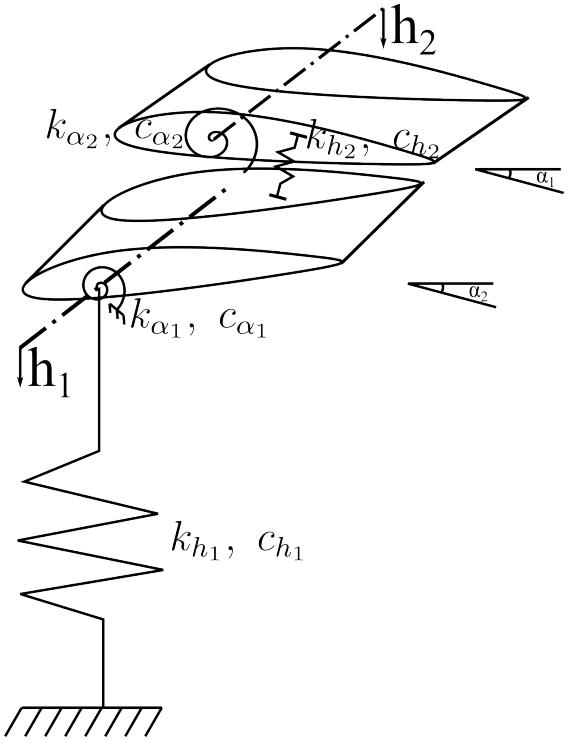

Figure 2. The three-dimensional reduced order model.

This construction consists of wing segments connected to each other by identical springs in a series configuration. The model is shown for two wing segments for simplicity, but it can be easily generalized for more segments. The equation of motion for this three-dimensional model is

$$\underline{\underline{M}}\ddot{x} + \underline{\underline{C}}\dot{x} + \underline{\underline{K}}x = \begin{bmatrix} L_1\left(\ddot{h}_1, \dot{h}_1, \alpha_1, \dot{\alpha}_1, \ddot{\alpha}_1\right) \\ M_1\left(\ddot{h}_1, \dot{h}_1, \alpha_1, \dot{\alpha}_1, \ddot{\alpha}_1\right) \\ L_2\left(\ddot{h}_2, \dot{h}_2, \alpha_2, \dot{\alpha}_2, \ddot{\alpha}_2\right) \\ M_2\left(\ddot{h}_2, \dot{h}_2, \alpha_2, \dot{\alpha}_2, \ddot{\alpha}_2\right) \end{bmatrix}, \tag{3}$$

where $L_i\left(\ddot{h}_i, \dot{h}_i, \alpha_i, \dot{\alpha}_i, \ddot{\alpha}_i\right), M_i\left(\ddot{h}_i, \dot{h}_i, \alpha_i, \dot{\alpha}_i, \ddot{\alpha}_i\right)$ are the lift and moment acting on the i-th wing segment, $\underline{\underline{M}}$, $\underline{\underline{C}}$, and $\underline{\underline{K}}$ are the mass, damping, and stiffness

matrices respectively, and $\underline{x} = [x_1, x_2, x_3, x_4]^T$ is the state vector. The four variables in the state vector are the two plunging displacements h_1, h_2 and the two pitching displacements α_1, α_2, i.e., $x_1 = h_1, x_2 = \alpha_1, x_3 = h_2, x_4 = \alpha_2$. The mass and stiffness matrices are derived using the principles of Lagrangian mechanics and are given by

$$\underline{\underline{M}} = \left[\frac{\partial^2 E_k}{\partial \dot{x}_i \partial \dot{x}_j}\right] \tag{4}$$

$$\underline{\underline{K}} = \left[\frac{\partial^2 U}{\partial x_i \partial x_j}\right], \tag{5}$$

where E_k is the kinetic energy and U is the potential energy of the system. We assume proportional damping, meaning that the damping matrix $\underline{\underline{C}}$ is a multiple of the stiffness matrix $\underline{\underline{K}}$, i.e.,

$$\underline{\underline{C}} = d\underline{\underline{K}}, \tag{6}$$

where d is a constant.

For the model we have taken the structural parameters from [9] but scaled them to match the dimensions and mass of our drone's propeller. The resulting parameters are shown in Table 1.

Parameter name	Parameter value
a	0
b	0.017 m
c_h	0.003 kg/s
c_α	0.006 kgm^2/s
Θ	0.00023 kgm^2
k_h	250 N/m
k_α	0.49 Nm/rad
m	0.008 kg
S	0.167 m
ρ	1.2 kg/m^3.

Table 1. Numerical values of the parameters in the three-dimensional reduced order model.

Now we will describe the parameters of the individual wing segments based on the parameters of the whole wing given in Table 1. The mass, moment of inertia, and span of the i-th wing segment are given by

$$m_i = \frac{m}{n}, \quad \Theta_i = \frac{\Theta}{n} \quad S_i = \frac{S}{n}, \tag{7}$$

where m_i, Θ_i, S_i are the mass, moment of inertia, and span of the i-th wing segment, respectively, and n is the number of wing segments. We approximate the stiffness coefficients by a linear function as

$$k_{\alpha_i} = k_\alpha(n - i + 1), \quad k_{h_i} = k_h(n - i + 1), \tag{8}$$

where k_{α_i}, k_{h_i} are the pitching and plunging stiffness coefficients of the i-th wing segment, respectively. It is not straightforward to determine the damping coefficient of the i-th wing segment. However, it was determined by [11] that the use of

$$c_{\alpha_i} = c_\alpha \sqrt{n}, \quad c_{h_i} = c_h \sqrt{n}, \tag{9}$$

leads to the fastest convergence of the critical velocity as a function of n. For this reason, we use these functions to obtain the damping coefficient of the i-th wing segment.

We will now compute the critical velocity of the model, which is the flow velocity at which the system loses its stability and flutter oscillations occur. First, we assume a constant velocity distribution along the wing. To compute the critical velocity, we determine the eigenvalues of the system's Jacobian for wind velocities starting from 0, increasing by 1 m/s up to 100 m/s. As the velocity increases, a pair of complex conjugate eigenvalues will cross the imaginary axis. The velocity at which this occurs is the critical velocity. The critical velocity as a function of the number of wing segments is shown in Figure 3.

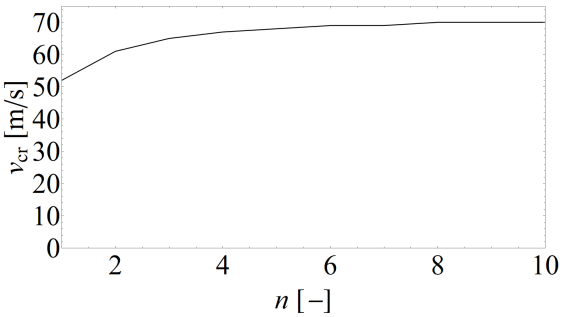

Figure 3. The critical velocity as a function of the number of wing segments assuming constant velocity distribution.

The critical velocity of the two-degrees-of-freedom (2-DOF) model is $52m/s$, which corresponds to $n = 1$. As the number of wing segments increases, the critical velocity also increases and converges to $70m/s$. Thus, the use of the three-dimensional model results in approximately 35% higher critical velocity, which confirms that this more complex model is indeed necessary to obtain accurate results even for fixed-wing aircraft.

Now we will investigate the critical velocity for drones, which have a linear velocity distribution along the wing, as follows:

$$v_i = v\frac{i}{n}, \tag{10}$$

where v_i is the wind velocity at the i-th wing segment. The critical velocity as a function of the number of wing segments is shown in Figure 4.

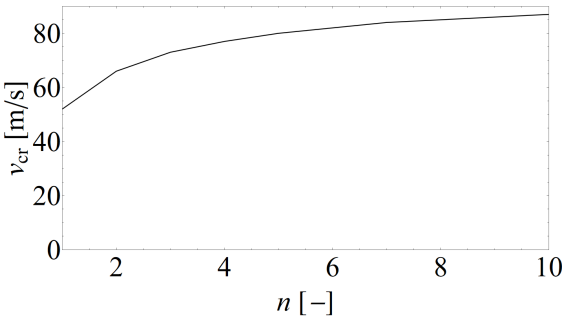

Figure 4. The critical velocity as a function of the number of wing segments assuming linear velocity distribution.

The critical velocity of the two-degrees-of-freedom (2-DOF) model is $52m/s$, which corresponds to $n = 1$. As the number of wing segments increases, the critical velocity also increases and converges to $82m/s$. Thus, the use of the three-dimensional model results in approximately 58% higher critical velocity. This critical velocity is also approximately 17% higher than in the previous case where we assumed constant velocity distribution along the wing.

3. STABILITY CHARTS

In this section, we will compute stability charts for the three-dimensional model, which show as a function of the rotor speed and the forward flight velocity, whether flutter occurs, i.e., the stability of the system.

As a first step, we need to compute the time-varying relative wind velocity experienced by the rotor blade as a function of the rotor speed and the forward flight velocity. This velocity is time-varying because, as the rotor blade travels forward (in the same direction as the rotorcraft is flying), the relative velocity due to the flight of the drone is subtracted from the relative velocity due to the rotor rotation. As the blade travels backward (in the opposite direction to the rotorcraft flight), the opposite happens and the relative velocity increases. The relative velocity can thus be written as

$$v(t, s) = \omega s + v_f \sin(\omega t), \tag{11}$$

where s is the distance from the hub of the rotor ω is the angular velocity of the rotor and v_f is the forward velocity of the drone. Additionally we define the rotational velocity of the wing tip as

$$v_r = \omega s. \tag{12}$$

We computed the stability chart of the three-dimensional model by carrying out numerical simulations with the initial condition $\alpha_1(0) = 0.1$. We ran the simulations for 100 s and considered the system unstable if the tip rotation exceeded 0.1 at any point during the simulation, i.e., the system is considered unstable if

$$\exists t : \alpha_n(t) > 0.1. \tag{13}$$

The stability charts for different n values are shown in Figures 5, 6, 7. The blue region indicates the unstable region, while the yellow region indicates the stable region.

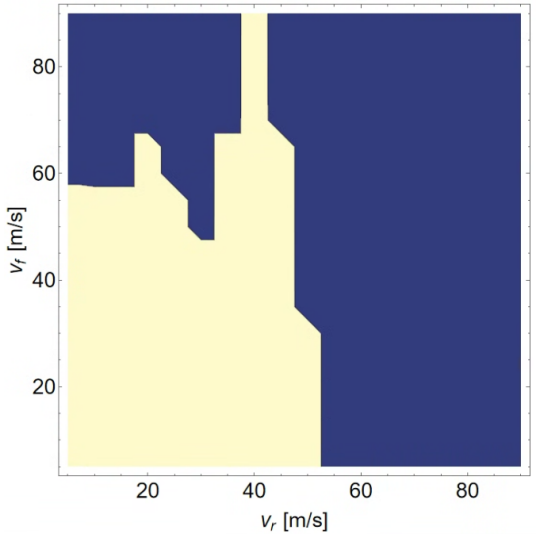

Figure 5. Stability chart for $n = 1$.

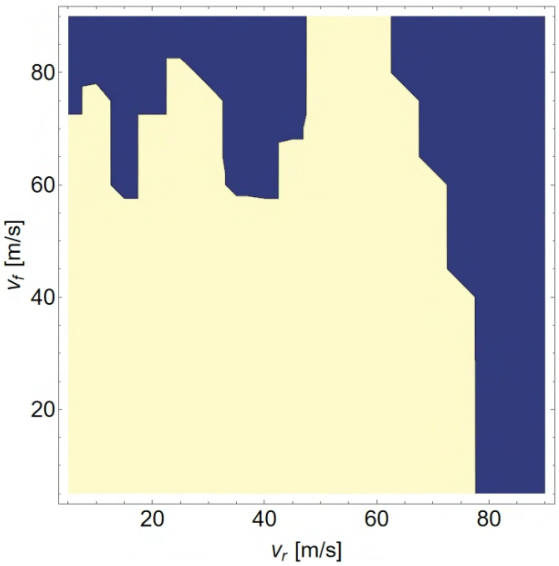

Figure 6. Stability chart for $n = 5$.

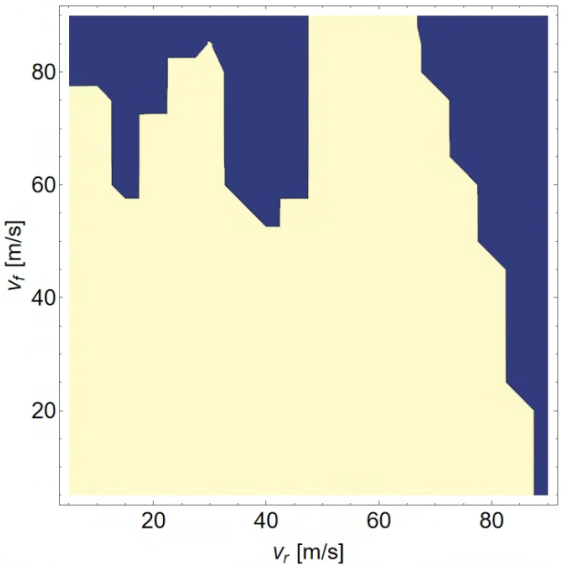

Figure 7. Stability chart for $n = 10$.

For a stationary drone, where the forward velocity $v_f = 0$, the critical velocity is 88 m/s as shown in the previous section. As the forward velocity v_f increases, the rotor will lose its stability at various v_f values depending on the tip velocity v_r. If $v_r < 50$ m/s, the stability loss occurs at $50 \leq v_f \leq 90$ m/s. However, these forward velocities are not attainable since the drone is not able to fly forward faster than the tip velocity. For $50 < v_r < 65$ m/s, the stability loss occurs at $v_f > 90$ m/s. Above $v_r = 65$ m/s, the stability boundary starts to decrease as v_r increases and reaches $v_f = 0$ m/s at the critical velocity $v_r = 88$ m/s. The stability charts corresponding to a lower number of wing segments have a similar shape but the unstable regions are larger.

4. FLUTTER SAFETY MARGIN

In this section, we define the flutter safety margin and compute it during a flight of the drone. The flutter safety margin is defined as the minimal increase in the relative wind velocity at the tip of the wing, which would result in flutter oscillations. This is defined mathematically as the distance between the point (v_f, v_r) and the stability boundary, i.e.,

$$\mathcal{S}(v_f, v_r) = \text{dist}((v_f, v_r), \mathcal{B}), \tag{14}$$

where $\mathcal{S}$ is the flutter safety margin, v_f is the forward velocity of the drone, v_r is the rotational velocity of the wing tip, and $\mathcal{B}$ is the stability boundary in the (v_f, v_r) plane.

To compute the flutter safety margin during the flight of the drone, we first measured the rotor speed corresponding to different forward flight velocities. The goal of the measurement was to determine the working range of a general drone propeller, not to validate the model. We carried out this measurement in the departmental wind tunnel. The drone was fixed inside the wind tunnel on a force measurement device so that we could measure the aerodynamic forces acting on the drone. We then set a constant wind velocity and increased the velocity of the drone rotors until the net force acting on the drone was zero. In this state, the lift of the rotors counteracts the aerodynamic drag and gravity. This means that the velocity of the drone rotors is the same as it would be during forward flight. The measurement setup is shown in Figure 8.

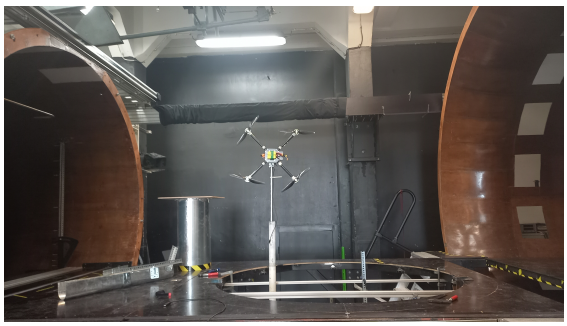

Figure 8. The measurement of the drone rotor velocities in the wind tunnel.

The result of the measurement is shown in Figure 9 and Table 2, where f denotes the rotational velocity of the propeller in revolutions per minute.

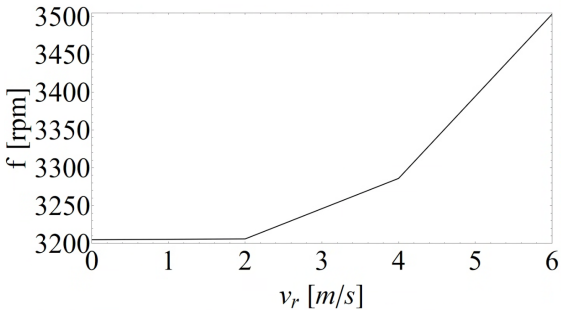

Figure 9. The rpm of the drone rotor at different forward flight velocities

v [m/s]	n [rpm]
0	3205
2	3206
4	3286
6	3503

Table 2. The velocity of the drone rotor at different forward flight velocities

As the forward velocity of the drone increases, the rotor velocity also increases, which becomes more apparent at higher forward velocities. Note that these rotor velocities result in a rotor tip velocity above the critical velocity for the two-dimensional reduced-order model (which is 52 m/s). Thus, this measurement confirms that the three-dimensional reduced-order model is indeed more accurate than the two-dimensional one.

We show the drone's forward flight velocities

and the corresponding rotor tip velocities on the stability chart in Figure 10 with a black line.

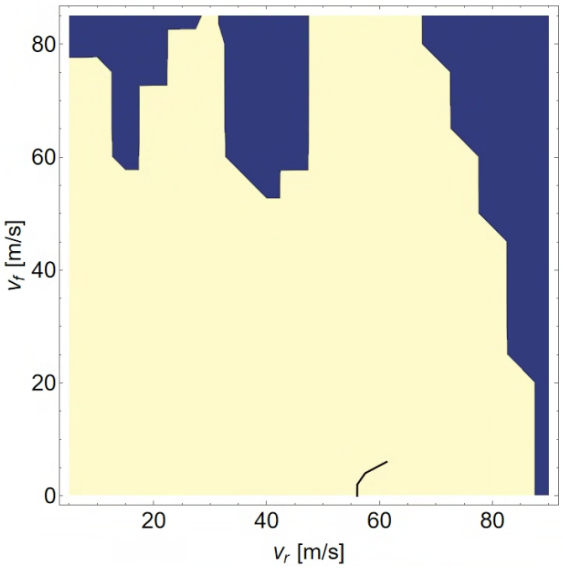

Figure 10. The rotor tip velocities and their corresponding forward flight velocities shown on the stability chart.

The drone stays well away from the stability boundary during forward flight, so flutter does not occur. This again confirms that the three-dimensional model results in more accurate results than the two-dimensional model since the latter predicts that the drone is in the unstable regime during flight. The flutter safety margin is shown in Table 3. As the drone accelerates, the flutter safety margin decreases, but remains above $20m/s$, so there is no risk of flutter.

$v\ [m/s]$	$n\ [rpm]$	$\mathcal{S}\ [m/s]$
0	3205	25.95
2	3206	25.93
4	3286	24.53
6	3503	20.74

Table 3. The flutter safety margin during forward flight

5. SUMMARY

In this paper, we develop a three-dimensional reduced-order model for wing flutter. This model is built by chaining multiple two-dimensional reduced-order models together using linear springs. As a result, each wing segment in the three-dimensional model has a pitch and a plunge degree of freedom, but these are influenced by the motion of the neighboring wing segments.

First, we computed the critical velocity (i.e., the smallest velocity at which flutter is present) for the three-dimensional model as a function of the number of wing segments. We found that the use of multiple wing segments results in an increase in the critical velocity. As the number of wing segments increases, the critical velocity converges to a fixed value and does not increase indefinitely. We also concluded that the use of a linear velocity distribution along the wing results in an even greater critical velocity.

Next, we computed stability charts using the three-dimensional model for various n values and found that increasing the number of wing segments results in the enlargement of the stable region. Based on the stability chart, we defined a flutter safety margin as the distance from the stability boundary. To compute the flutter safety margin during flight, we performed wind tunnel measurements to obtain the rotor tip velocity for different forward flight velocities. Based on the measurement results, we computed the flutter safety margin during forward flight and found that it decreases as the drone accelerates, but never approaches zero, so flutter does not develop during the flight of the drone.

ACKNOWLEDGEMENTS

This work has been supported by the Hungarian National Research, Development and Innovation Fund under contract NKFI K137726.
The research reported in this paper is part of project no. TKP-6-6/PALY-2021 has been implemented with the support provided by the Ministry of Culture and Innovation of Hungary from the National Research, Development and Innovation Fund, financed under the TKP2021-NVA funding scheme. The project supported by the Doctoral Excellence Fellowship Programme (DCEP) is funded by the National Research Development and Innovation Fund of the Ministry of Culture and Innovation and the Budapest University of Technology and Economics.

REFERENCES

[1] Bisplinghoff, R. L., Ashley, H., and Halfman, R. L., 2013, *Aeroelasticity*, Courier Corporation.

[2] Dowell, E. H., 2015, *A Modern Course in Aeroelasticity*, Springer.

[3] Fung, Y. C., 2008, *An Introduction to the Theory of Aeroelasticity*, Courier Dover Publications.

[4] Dowell, E. H., Curtiss, H. C., Scanlan, R. H., and Sisto, F., 1989, *A modern course in aeroelasticity*, Vol. 3, Springer.

[5] Harish, A., "Why the Tacoma Narrows Bridge Collapsed: An Engineering Analysis", `https://www.simscale.com/blog/2018/07/tacoma-narrows-bridge-collapse/`, accessed: 2020-07-10.

[6] "Tacoma Narrows Bridge (1940)", `https://en.wikipedia.org/wiki/Tacoma_Narrows_Bridge_(1940)`, accessed: 2020-07-10.

[7] Meshki, M. M., Nobari, A. S., and Sadr, M. H., 2020, "A study on nonlinear, parametric aeroelastic energy harvesters under oscillatory airflow", *Journal of Vibration and Control*, pp. 1–11.

[8] Lelkes, J., Horváth, D. A., Lendvai, B., Farkas, B., Bak, B. D., and Kalmár-Nagy, T., 2023, "Data-driven aerodynamic models for aeroelastic simulations", *Journal of Sound and Vibration*, Vol. 593, p. 117847, URL `https://www.sciencedirect.com/science/article/pii/S0022460X23002961`.

[9] Abdelkefi, A., Vasconcellos, R., Nayfeh, A. H., and Hajj, M. R., 2013, "An analytical and experimental investigation into limit-cycle oscillations of an aeroelastic system", *Nonlinear Dynamics*, Vol. 71 (1-2), pp. 159–173.

[10] Theodorsen, T., 1935, "General theory of aerodynamic instability and the mechanism of flutter", *NACA Technical Report*, (496).

[11] Horváth, D. A., 2021, "Investigation of a reduced mathematical model of a rotor blade", Bachelor Thesis, Budapest University of Technology and Economics.

Conference on Modelling Fluid Flow (CMFF'25)
The 19th International Conference on Fluid Flow Technologies
Budapest, Hungary, August 26 - August 29, 2025

DEVELOPMENT OF A CYLINDRICAL-BLADE WIND TURBINE DRIVEN BY A NECKLACE VORTEX

Tsutomu TAKAHASHI[1], Ryuga SADAOKA[2], Yasunori SATO[3]

[1] Corresponding Author. Department of Mechanical Mechanics, Faculty of Engineering, Nagaoka University of Technology. 1603-1 Kamitomioka, Nagaoka, Niigata. 940-2188 Japan. Tel.: +81 258 47 9728, E-mail: ttaka@nagaokaut.ac.jp
[2] Department of Mechanical Mechanics, Graduate School of Nagaoka University of Technology. E-mail: s213027@stn.nagaokaut.ac.jp
[3] Department of Mechanical Mechanics, Faculty of Engineering, Nagaoka University of Technology. E-mail: yasusato@nagaokaut.ac.jp

ABSTRACT

When the blade of a horizontal-axis wind turbine is replaced with a circular cylinder and a ring plate is installed downstream, a necklace vortex forms at their intersection. As the cylinder rotates, this vortex remains stationary on the opposite side of its motion, generating lift and driving the turbine. This is known as a necklace vortex-driven cylinder-blade wind turbine. Developed by the authors, this turbine rotates at less than 1/20th of the peripheral speed of conventional blade-type turbines while generating over ten times the torque. Its low speed eliminates noise and vibration, and the soft-material cylinder blades enhance safety, making it suitable for installation near human living spaces. The turbine consists of a single cylinder as the blade and a ring plate positioned in its wake. Key design parameters include the cylinder's diameter and length, the ring plate's diameter and radial width, and their spacing. This presentation examines how these factors influence power characteristics.

Keywords: cylindrical blade, horizontal axis wind turbine, necklace vortex, vertical vortex

NOMENCLATURE

C_P	[-]	power coefficient
d	[mm]	diameter of cylinder blade
D	[mm]	diameter of ring plate
F_L	[N]	lift force on cylinder blades
L	[mm]	length of cylinder blade
n	[rpm]	rotational speed of blades
N	[-]	number of blades
s	[mm]	gap between blade and ring plate
T	[Nm]	Torque acting on rotating shaft
U	[m/s]	wind velocity
W	[mm]	width of ring plate

Subscripts and Superscripts

max maximum value a series of measurements

1. INTRODUCTION

When a cylindrical bluff body is placed in a uniform flow, periodic shedding of Kármán vortices from both sides generates fluctuating lift forces. If the shedding frequency matches the natural frequency of the structure, resonance can occur, leading to large-amplitude oscillations that may damage the structure. To suppress such wake instabilities and vortex shedding, Rashidi et al. [1] systematically reviewed existing control strategies

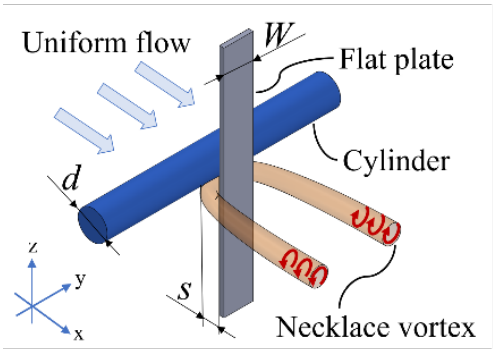

Figure 1. Longitudinal vortices at cross-section of cruciform system with cylinder and flat plate.

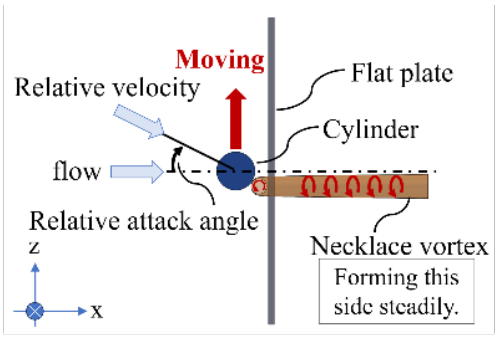

Figure 2. Mechanism of lift force generation by Necklace vortex.

and classified them into two categories: **active control** and **passive control**. Active control involves manipulating the flow using external energy, while passive control modifies the flow without external input by changing the geometry of the body or attaching devices such as splitter plates[2-5]. Passive control is generally simpler in structure and easier to implement, making it more practical for engineering applications [6].

Our group has developed a passive control method to suppress Kármán vortex-induced excitation by placing a secondary circular cylinder downstream in a cruciform arrangement [7,8]. Experiments revealed that this configuration not only reduces oscillation amplitude but can also induce vibrations in the upstream cylinder. Two types of longitudinal vortices—trailing vortex (TV) and necklace vortex (NV)—were observed near the intersection, depending on the gap ratio (s/d). Kato et al. [9] later replaced the downstream cylinder with a strip plate, which proved more effective in enhancing resonant vibrations. This concept was further applied to develop a micro power generator utilizing longitudinal vortex-induced vibration (LVIV) [10].

Longitudinal vortices, with their rotational axis aligned with the flow direction, are periodically generated in the cylinder-plate system shown in Figure 1, which consists of a crossed arrangement with a prescribed gap in uniform flow. As shown in Figure 2, when the cylinder moves parallel to the plate, a relative angle of attack is introduced, disrupting the periodicity of the necklace vortex and localizing it on the opposite side of the cylinder's motion. At this point, a steady lift force acts on the cylinder due to the reaction force of the suction flow at the front of the cylinder, induced by the necklace vortex [11].

The longitudinal vortex-driven cylindrical blade wind turbine is a novel wind turbine concept in

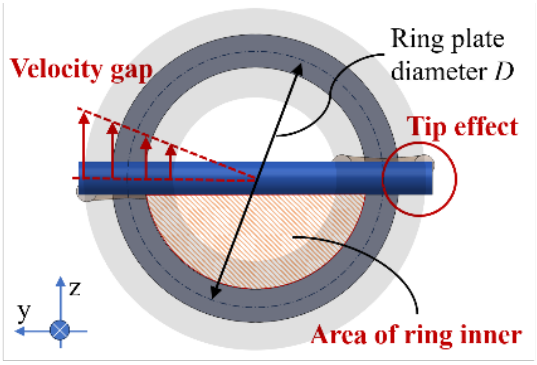

FIGURE 3. DIFFERENCE DUE TO THE CURVATURE GIVEN TO THE FLAT PLATE.

which a rotating shaft is attached to the cylinder as a blade, driven by the necklace vortex flowing through the gap between the ring plate and the trailing edge of the cylinder [12]. However, the effects of this phenomenon have not been fully considered in practical wind turbine systems (Figure 3). Sakamoto et al. demonstrated that varying the ring plate width W for a given cylindrical blade diameter d influences performance and that an optimal face width ratio exists [13].

Therefore, this study aims to clarify the effect of curved flats on performance characteristics and propose a method for predicting wind turbine performance based on geometric parameters.

2. EXPERIMENTAL APPARATUS AND METHODS

Figure 4 shows the experimental apparatus and each parameter. The apparatus was set up in a wind tunnel with a test section of 320 mm × 320 mm × 1000 mm. The center diameter D of the ring plate was varied for different combinations of the cylindrical blade diameter d and the ring plate width W, while maintaining a constant wind velocity U.

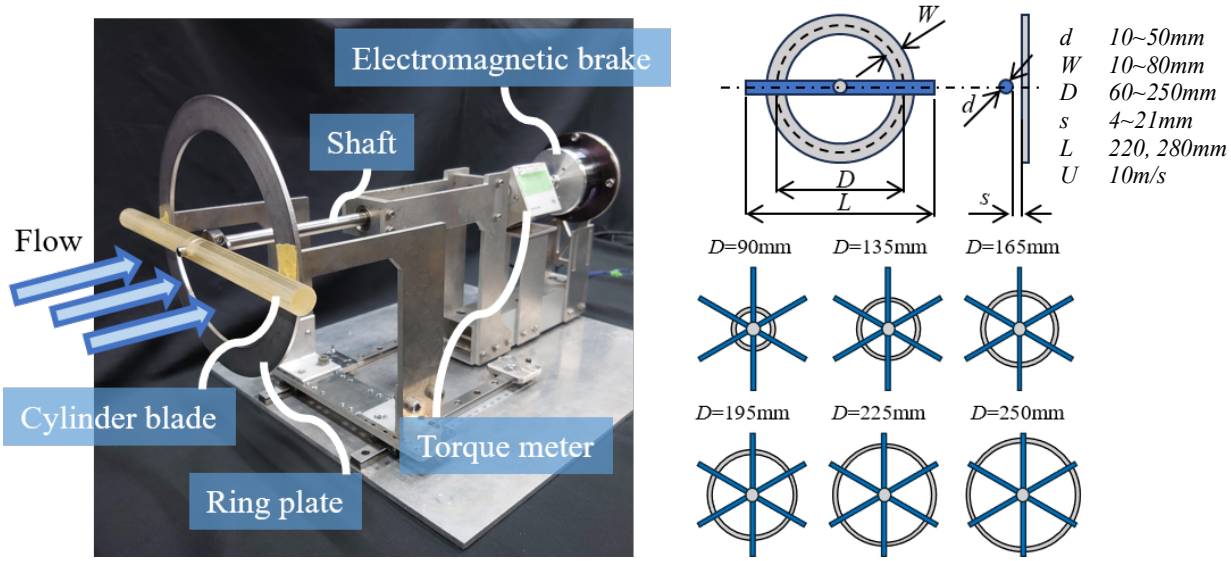

Figure 4. Schematic of wind turbine device and each parameter.

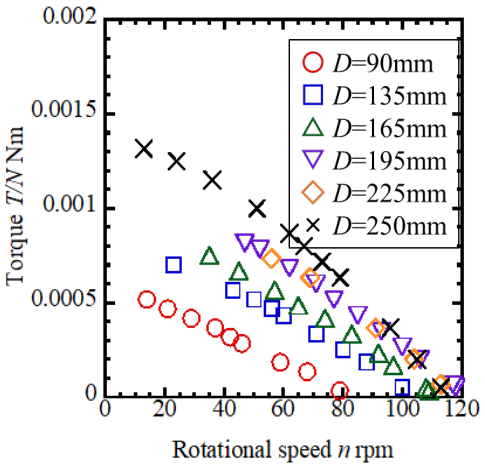

(a) Rotational speed vs. Torque

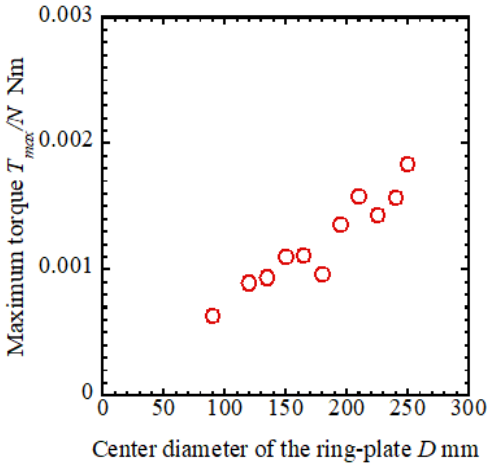

(b) Center diameter of the ring-plate vs. Maximum torque

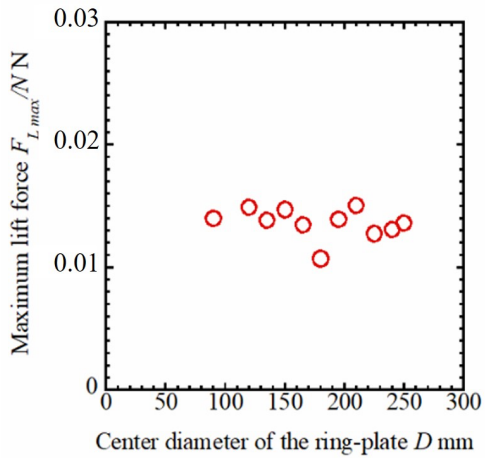

(c) Center diameter of the ring-plate vs. Maximum lift force

Figure 5. Effect of ring plate diameter *D* on the measured torque and lift per blade. (*d*=10mm, *W*=10mm, *s*=4mm, *L*=280mm, *N*=6, *U*=10m/s)

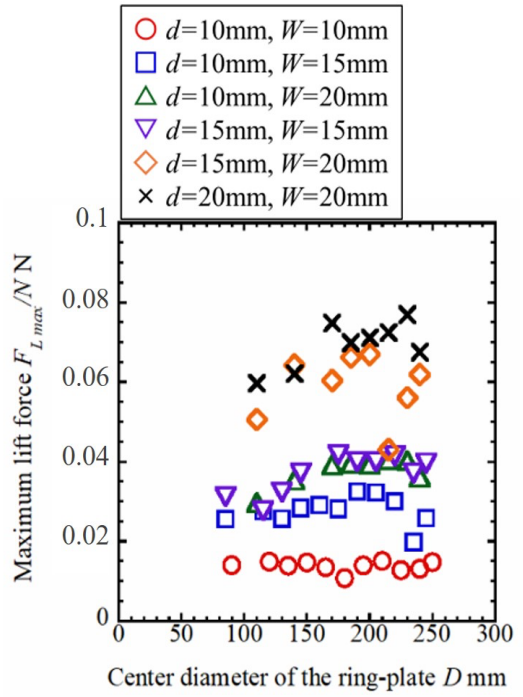

Figure 6. Relationship between the ring plate diameter and the maximum lift force for various cylinder blade diameters and ring plate widths (*L*=280mm, *s*=4-7mm, *U*=10m/s, *N*=2-6).

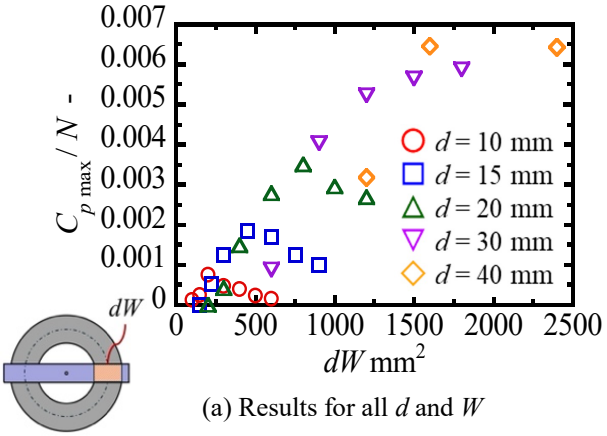

(a) Results for all *d* and *W*

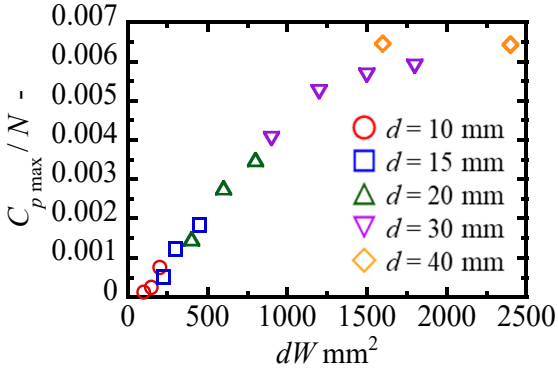

(b) Results restricted to $1 \le W/d \le 2$

Figure 7. Effect of Effective Area of Blade *dW* on Maximum Power Coefficient (*d*=10-40mm, *W*=10-60mm, *D*=155 mm, *L*=220 mm, *s*=4-15 mm, *N*=2, *U*=10m/s).

A load was applied to the wind turbine's rotating shaft using an electromagnetic brake (HB0.5, OGURA CLUTCH Co., Ltd.). The torque T and rotational speed n were measured with a torque meter (UTMII-0.2Nm, Unipulse Co., Ltd.).

3. RESULTS AND DISCUSSION

3.1. Measured toque and evaluated lift force per blade

As shown in Figure 5(a), the torque of this wind turbine increases linearly as the rotational speed decreases when a load is applied to the rotating shaft under a constant mainstream wind speed. Therefore, this torque curve was extrapolated using a linear approximation, and the maximum torque T_{max} was defined as the value obtained when the rotational speed reaches zero. Figure 5(b) illustrates the relationship between the diameter D of the ring plate and T_{max}, while Figure 5(c) presents the relationship between the maximum steady lift force per blade $F_{L\,max}/N$ and D, which was obtained by dividing T_{max} by D. Figure 5(c) indicates that $F_{L\,max}/N$ is nearly independent of D under these conditions.

This suggests that when the cylindrical blade's diameter d and ring width W are sufficiently small, the difference in radius of curvature or circumferential velocity between the inner and outer regions of the ring does not affect the lift, even as the ring diameter D decreases. Additionally, the effect of the vortex generated at the wingtip remains minimal, even if D increases and approaches the wingtip.

Figure 6 shows the maximum steady lift per blade, $F_{L\,max}/N$, when D is varied for an arbitrary combination of d and W. For the d = 10 mm, W = 10 mm combination shown in Figure 5(c), $F_{L\,max}/N$ remained approximately constant regardless of changes in D. However, for the d = 10 mm, W = 15–20 mm combinations, a decrease in $F_{L\,max}/N$ was observed for both large and small values of D. When D is small, the difference in circumferential velocity between the inner and outer diameters of the ring becomes relatively large. Additionally, as D decreases, the size of the hub that supports the rotating shaft and blades remains unchanged, increasing the ratio of flow obstruction to the inner opening area of the ring. These factors contribute to the decrease in $F_{L\,max}/N$ in the small D region.

3.2. Effective area of blade relative to lift

In a cylindrical-blade wind turbine driven by a necklace vortex, the lift force is concentrated near the intersection of the blade and the ring plate. Increasing the blade diameter d and ring width W expands the area over which the lift force acts, leading to a corresponding increase in lift. To quantify this effect, dW is introduced as a new parameter representing the lift-affected area.

Figure 7(a) shows the maximum power coefficient per blade for various combinations of blade diameter d (10 mm to 40 mm) and ring width W (10 mm to 60 mm), obtained by measuring power characteristics. The proportionality to dW does not hold due to performance-interfering phenomena affecting the wind turbine.

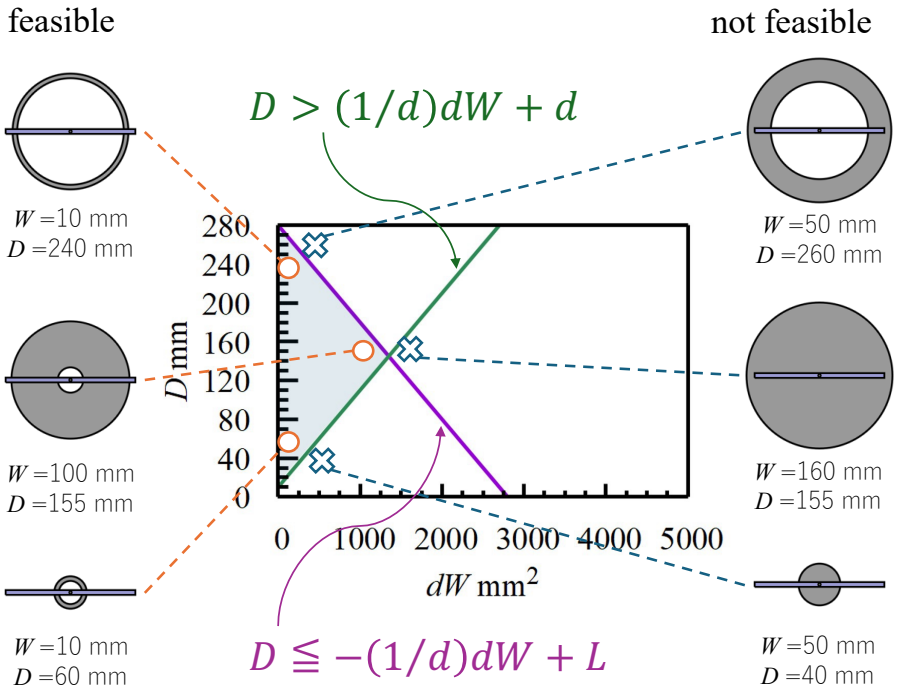

Figure 8. Map illustrating the shape factors required for a viable cylindrical-blade wind turbine.

Figure 7(b) plots a subset of results from Figure 7(a), including only cases where the normalized ring width W/d is between 1 and 2. In this range, the proportional relationship between the power coefficient and dW is maintained across a wide range. This suggests that designing wind turbines within $1 \leq W/d \leq 2$ can help suppress performance-deteriorating effects.

3.3. Conditions for shape factor to be valid as a wind turbine

A cylindrical-blade wind turbine has four shape factors: blade diameter d, blade length L, diameter of ring center D, and ring width W. These factors are not entirely independent, and two constraints must be satisfied to ensure the formation of a necklace vortex and the generation of lift.

The first condition is that the cylindrical blade must not obstruct the inner hole of the ring plate. Since the necklace vortex forms by wrapping around the ring in the direction of its width, a large d with a small D may block the hole, preventing stable vortex formation. Therefore, the inner hole diameter, $D-W$, must be larger than d. Given that dW is used as a design index for wind turbines, this relationship can be expressed as Equation (1).

$$D > (1/d)dW + d \tag{1}$$

The second condition is that the blade must extend beyond the outer edge of the ring. If the blade length L is too short and its tip remains inside the outer diameter of the ring ($D+W$), the necklace vortex will not form. This condition can be expressed as the following equation.

$$D \leqq -(1/d)dW + L \tag{2}$$

For wind turbine design, these conditions are plotted on a plane with the ring plate diameter D on the vertical axis and dW on the horizontal axis, producing the map shown in Figure 8. A wind turbine is geometrically feasible if its parameters fall within the triangular region bounded by the magenta Equation (1) and the green Equation (2). Figure 8 also illustrates examples of wind turbine shapes at characteristic locations both inside and outside this region.

3.4. Distribution of maximum lift force in dW-D map

The maximum lift force of wind turbines with various shapes, measured experimentally, are plotted on the dW-D map in Figure 8. An example is shown in Figure 9, where the color of each point represents the magnitude of the maximum lift coefficient. Additionally, the two blue vertical lines in the figure correspond to W/d=1 and W/d=2. Wind turbines with shapes outside the triangular region defined by Equations (1) and (2) hardly rotated. However, within this triangular region and between the blue vertical lines, the cylinders experienced a stable lift force. Furthermore, within this region, a larger dW results in a higher maximum power coefficient.

4. SUMMARY

In cylindrical-blade wind turbines, which rotate using the lift force from the necklace vortex as the driving mechanism, four key geometric parameters, blade diameter, blade length, ring plate diameter, and ring plate width, were analyzed for their combined effect on power characteristics. Based on these findings, a design guideline was developed to maximize the maximum power coefficient for a given blade length.

REFERENCES

[1] Rashidi, S., Hayatdavoodi M., Abolfazli J., "Vortex shedding suppression and wake control:

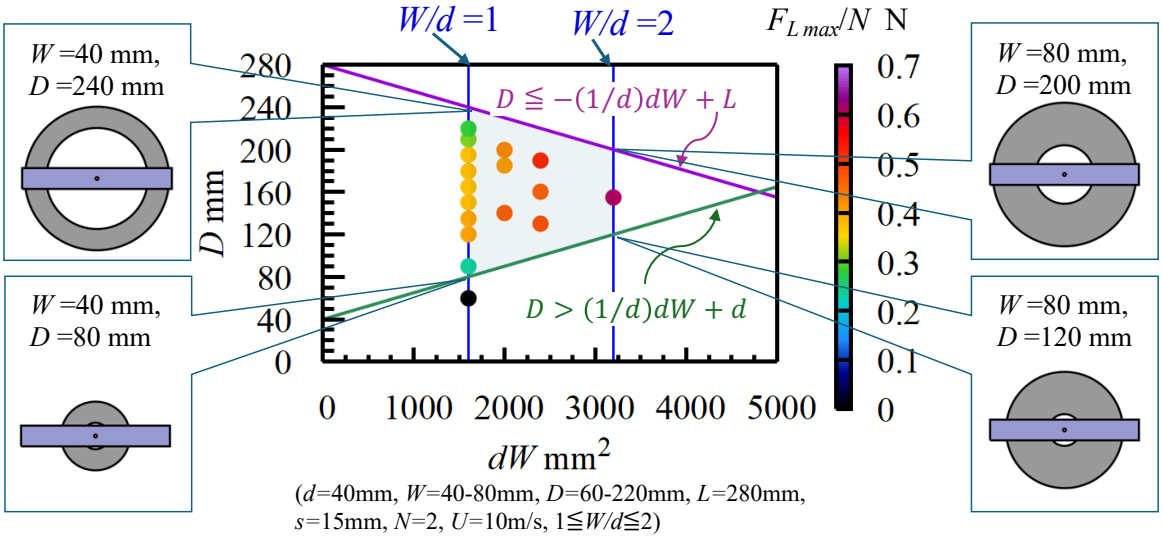

Figure 9. Distribution of the maximum lift force on the *dW-D* map.

a review", Ocean Eng (2016) 126:57–80. https://doi.org/10.1016/j.oceaneng.2016.08.031

[2] Ozono, S., "Vortex suppression of the cylinder wake by deflectors", J Wind E w ng Ind Aerodyn (2003), 91(1–2):91–99. https://doi.org/10.1016/ S0167-6105(02)00337-9.

[3] Hwang, J.Y., Yang, K.S., "Drag reduction on a circular cylinder using dual detached splitter plates", J Wind Eng Ind Aerodyn, (2007), 95(7):551–564. https://doi.org/10.1016/j.jweia.2006.11.003.

[4] Shukla, S., Govardhan, R.N.Ã., Arakeri, J.H., "Flow over a cylinder with a hinged-splitter plate#, J Fluids Struct, (2009), 25(4):713–720. https://doi.org/10.1016/j.jfluidstructs.2008.11.004.

[5] Gozmen, B., Akilli, H., Sahin, B., "Passive control of circular cylinder wake in shallow flow", Measurement, (2013), 46:1125–1136. https://doi.org/10.1016/j.measurement.2012.11.008.

[6] Lee, S-J., Lee, S-I., Park, C-W., "Reducing the drag on a circular cylinder by upstream installation of a small control rod", Fluid Dyn Res (2004) 34:233–250. https://doi.org/ 10.1016/ j.fluiddyn.2004.01.001.

[7] Bae, H.M., Baranyi, L., Koide, M., Takahashi, T., Shirakashi, M., "Suppression of Karman vortex excitation of a circular cylinder by a second cylinder set downstream in cruciform arrangement", J Comput Appl, (2001) Mech 2(2):175–188. https://doi.org/10.1007/s13398-014-0173-7.2.

[8] Kumagai, I., Matsumoto, T., Takahashi, T., Shirakashi, M., "Necklace vortex excitation of upstream cylinder in crisscross circular cylinder system (influence of cylinder diameter, gap and damping factor). JSME Int J Ser B, (2001), 44(4):756–763. https://doi.org/10.1299/jsmeb.44.756.

[9] Kato, N., Koide, M., Takahashi, T., Shirakashi, M, "VIVs of a circular cylinder with a downstream strip-plate in cruciform arrangement. J Fluids Struct 30:97–114. https://doi.org/10.1016/j.jfluidstructs.2012.02.007.

[10] Koide, M., Sekizaki, T., Yamada, S., Takahashi, T., Shirakashi, M., "Prospect of micro power generation utilizing VIV in small stream based on verification experiments of power generation in water tunnel", J Fluid Sci Technol, (2013), 8(3):294–308. https://doi.org/10.1299/jfst.8.294

[11] Sakamoto, K., Hemsuwan, W. and Takahashi, T., "Development of circular cylinder blade wind turbine driven by longitudinal vortex", Transactions of the JSME (in Japanese), Vol. 87, No.894 (2021), pp. 20-00365

[12] Sakamoto, K., Hemsuwan, W. and Takahashi, T., "Numerical investigation of lift-force generation on a moving circular cylinder in a uniform flow driven by longitudinal vortex", Journal of Fluids and Structures, Vol. 83, (2018), pp. 448-470

[13]Sakamoto, K., Hemsuwan, W. and Takahashi, T., "Development of a wind turbine driven by longitudinal vortex: Wind tunnel experiment to investigate the basic characteristics of the wind turbine using a single circular cylinder blade", Journal of Wind Engineering and Industrial Aerodynamics, Vol.210 (2021), pp.104492

Conference on Modelling Fluid Flow (CMFF'25)
The 19th International Conference on Fluid Flow Technologies
Budapest, Hungary, August 26 - August 29, 2025

A THROMBOSIS MODEL FOR BLOOD-CONTACTING MEDICAL DEVICES

Yuning Lin[2], Shuai Wang[3], Jianren Fan[1]

[1] Corresponding Author. State Key Laboratory of Clean Energy Utilization, Zhejiang University, 38 Zheda Road, Hangzhou 310027, China. Tel.: +0571-87951764, E-mail: fanjr@zju.edu.cn
[2] State Key Laboratory of Clean Energy Utilization, Zhejiang University. E-mail: linyuning@zju.edu.cn
[3] State Key Laboratory of Clean Energy Utilization, Zhejiang University. E-mail: wshuai2014@zju.edu.cn

ABSTRACT

Thrombus formation is crucial for blood-contacting medical devices. Current models focus on platelet activity or coagulation factors but overlook the interplay between these two processes, essential for accurate thrombus prediction. In this work, a thrombus generation model was developed, which couples platelet activity with the coagulation cascade. By utilizing the fibrin and thrombin, the product of the coagulation cascade, to regulate thrombus formation, the two processes are integrated. A reduced-order coagulation cascade model is employed, enabling the model to more closely align with human physiological processes while improving computational efficiency. The model's prediction of volume exhibited an error within 20% compared to experimental results and can effectively capture the evolutionary patterns of thrombus formation over time. This thrombus model is expected to be a reliable predictive tool for thrombus generation in blood-contacting medical devices.

Keywords: thrombus, blood-contacting medical devices, hemodynamics

NOMENCLATURE

C_i	$[mol/m^3]$	concentration of component i
D_i	$[N]$	diffusion coefficient of i
k_{apa}	$[/s]$	rate of platelet chemical activation
k_{spa}	$[/s]$	rate of shear-induced activation
k_{aps}	$[/s]$	activation rate due to other platelet-synthesized agonists
t	$[s]$	time
$\underline{v}$	$[m/s]$	absolute velocity vector of blood
$\underline{v_T}$	$[m/s]$	absolute velocity vector of thrombus
μ	$[Pa\cdot s]$	dynamic viscosity of blood
ϕ	[-]	thrombus volume fraction
τ	$[Pa]$	scalar shear stress
γ	$[/s]$	shear rate

1. INTRODUCTION

Blood-contacting medical devices have gained widespread clinical use in the management of cardiovascular and cardiopulmonary diseases. However, hemocompatibility-related complications, including bleeding and thrombosis, remain critical clinical challenges. For instance, left ventricular assist devices (LVADs) are an effective treatment for end-stage heart failure-related diseases. Nevertheless, device-induced thrombus may lead to stroke, neurological events, or compromised mechanical efficiency, ultimately necessitating device replacement [1]. Consequently, elucidating the mechanisms underlying thrombus formation in blood-contacting medical devices constitutes a critical research imperative to advance both device design optimization and clinical implementation.

Thrombus formation is a complex phenomenon governed by the coupled hemodynamic and physiological mechanisms, wherein platelets and biochemical mediators interact through cascade reactions, ultimately driving platelet activation, aggregation, adhesion, and stabilization. Given the incomplete understanding of device-induced thrombotic mechanisms and the inherent risks and difficulties of conducting clinical trials in patient populations, computational modeling of thrombus formation has emerged as an indispensable tool for bridging the fap between in vivo and in vitro experimentation [2]. For example, Fogelsen [3] pioneered simulations integrating platelet activation, agonists transport, and platelet bulk aggregation within continuum-model framework. The inherent complexity of modeling thrombus formation in blood-contacting devices - stemming from the coupled interactions of platelets with numerous biochemical species - necessitates a critical compromise between model fidelity and computational efficiency. Fogelsen and Guy [4] compared a microscale model of platelet aggregation with a continuum model of platelet aggregation and found that the continuum model took only 1% of the

computational time of the microscale model to obtain results similar to those of the microscale model. Based on the Fogelsen continuum model, Sorensen et al. [5] proposed a two-dimensional thrombus model for blood contact with medical devices that incorporates multiple biochemical agonists of platelets to more accurately describe the mechanisms of platelet activation. Goodman et al. [6] extended previous models [3, 5] by incorporating shear stress effects on platelet activation, enabling their model to achieve real-time spatial prediction of thrombus growth. Taylor et al. [7] modified the model of [3, 5] by proposing a simple computational network capable of doing verifiable macro-scale prediction of thrombus at the same spatial scale as cardiovascular devices on time scales ranging from minutes to hours. Wu et al. [8,9] further extended the former model [5] that accurately predicted thrombus generation under different flow conditions and biological environments and was the first to predict thrombus generation and growth in an axial blood pump, with results consistent with clinical observations. Blum et al. [10] developed an accelerated thrombosis model by simplifying a previous model [7] with a time step 10,000 times larger than the time step required by the pre-simplified model, which significantly improves the computational efficiency. Moreover, Li et al. [11–13] established a predictive model focusing on platelet dysfunction induced by supraphysiological shear stresses in blood-contacting devices. While these models focus on platelet activity, but as mentioned earlier, thrombus formation remains intrinsically regulated by coagulation cascades. Meanwhile, some studies have also started from the coagulation cascade reaction to predict thrombus generation and growth by modeling the kinetic process of the coagulation cascade [14–17]. Existing thrombus models typically focus on a single specific subprocess in thrombus formation, limiting their ability to comprehensively reveal the complex mechanisms of thrombus formation. This limitation arises from the trade-off between computational efficiency and the precision of capturing physiological processes. Specifically, thrombus models based on platelet activity often overlook the regulatory effects of the coagulation cascade on platelet behavior, while models based on the coagulation cascade, due to involving numerous reactants and complex reaction networks, result in excessively high computational costs, making efficient simulations challenging.

To address the limitations of previous research, this work proposes a coupled thrombosis model that integrates hemodynamics, platelet activity, and the coagulation cascade. The model regulates platelet activation, aggregation, adhesion, and stabilization through the intermediate and terminal products of the coagulation cascade. To improve computational efficiency, this study utilizes a reduced-order coagulation cascade model. Additionally, the model incorporates dynamic interactions between blood flow and thrombus formation, with particular consideration of shear stress effects in thrombus breakdown under hemodynamic conditions. This thrombus model was then applied to a backward-facing step geometry and validated in space and time against the experiments to assess the accuracy of the predictions of model.

2. METHODS

This work develops a mathematical model of thrombosis. The model couples the fluid governing equations and introduces convection-diffusion-reaction equations (CDR equations) to describe the transport of a range of biochemicals such as platelets and coagulation factors. Chemical activation and shear activation are considered for platelets, and platelet deposition is considered in terms of biochemical concentration aspects and flow aspects. A resistance term is added to the fluid governing equation to represent the obstruction of blood flow by thrombus.

2.1 Governing Equations of Blood Flow

The flow of blood was represented using a modified Navier–Stokes equations (N-S equations):

$$\nabla \cdot \underline{v} = 0 \tag{1}$$

$$\rho\left(\frac{d\underline{v}}{dx} + \underline{v}\cdot\nabla\underline{v}\right) = -\nabla p + \mu\nabla^2\underline{v} + \frac{C_2}{(1-\phi)} f(\phi)(\underline{v} - \underline{v}_T) \tag{2}$$

where ρ is the density of the blood, μ is the kinetic viscosity of the blood, $\underline{v}$ is the flow rate of the blood, and $\underline{v}_T$ is the speed of the thrombus. The source term $C_2 f(\phi)(\underline{v}-\underline{v}_T)/(1-\phi)$ is the resistance exerted by the thrombus to the fluid, where $f(\phi) = \phi\,(1+6.5\phi)$; ϕ is the thrombus volume fraction.

2.2 Biochemical Component Equations

The thrombus model contains two sub-models, the platelet activity model and the coagulation cascade model, which describes the process of platelet aggregation, adhesion, deposition on the surface of a blood-contacting device, which is modulated by the coagulation cascade reaction, and finally by the concentration of fibrin monomers leading to the formation of a stable thrombus. The platelet activity model incorporates a platelet-released agonist, adenosine diphosphate (ADP), three states of platelets: resting platelets (RP), activated platelets (AP), and bound platelets (BP), and residence time. The residence time (RT) is used to determine the flow stagnation and recirculation zones. The coagulation cascade model contains nine coagulation factors and heparin. Some coagulation factors promote thrombin production, while some coagulation factors consume already produced thrombin thereby slowing down the progress of the coagulation cascade reaction. As shown in Figure 1,

when blood contacts the foreign surface, factor XII adsorbs to the surface, and triggers the coagulation cascade response.

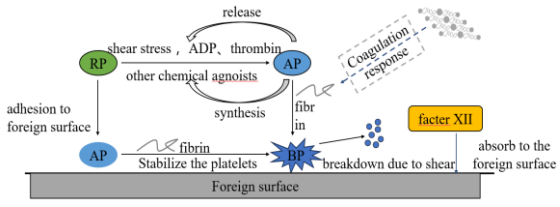

(a)

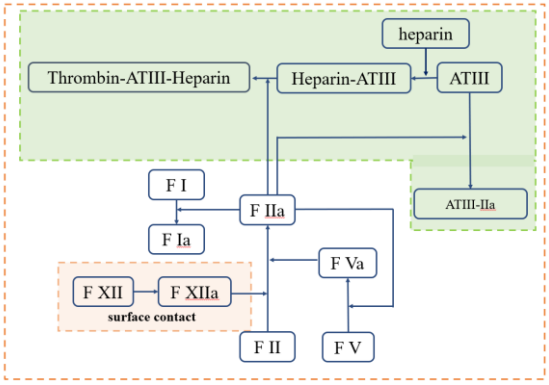

(b)

Figure 1. Schematic diagram of thrombus modeling mechanisms showing the role of the coagulation cascade in regulating platelet activity. (a) Platelet activity model. (b) Simplified coagulation cascade reaction with fibrin as the end product.

The transport phenomenon of biochemical substances is represented by the CDR equation:

$$\frac{\partial[C_i]}{\partial t}+\nabla\cdot\left(\underline{v}\cdot[C_i]\right)=\nabla\cdot\left(D_i\cdot\nabla[C_i]\right)+S_i \qquad (3)$$

where $[C_i]$ denotes the concentration of component i, D_i denotes the diffusion coefficient of i, and S_i is the source term of component i. The detailed diffusion coefficients and source terms are presented in [18].

The source term for platelet activation is defined as (Eq. (4)):

$$S_{AP}=k_{apa}\cdot RP+s_{spa}\cdot RP+k_{aps}\cdot RP \qquad (4)$$

where k_{apa} represents the rate of platelet chemical activation, k_{spa} denotes the rate of shear-induced activation, and k_{aps} refers to the activation rate due to other platelet-synthesized agonists.Since BP is not transported with blood, its governing equation is:

$$\frac{\partial BP}{\partial t}=S_{BP}-k_{tb}\phi \qquad (5)$$

where k_{tb} denotes the rate for thrombus breakdown, with a detailed definition provided in Table A1 in the appendices and [18].

RP directly attaches to the wall surface, transforming into AP, while FXII adhesion to the foreign surface. Both processes are governed by flux boundary conditions [5]. ADP is released when RP is converted to AP, and FXII adsorbed to the surface of the device is converted to FXIIa. Consequently, the boundary conditions for both processes are also expressed using flux boundary conditions. The boundary condition expressions are provided in Table A2 in the appendices.

2.3 Simulation Setup

The thrombus model is first validated in the backward-facing step (BFS) geometry, and the simulation results are quantitatively compared with the experimental data of Yang et al. [19]. The detail of the BFS geometry and mesh is shown in Figure 2. Mesh generation uses structural meshes. A boundary layer consists of 10 layers, and mesh refinement is applied in the BFS region. Given that the coagulation cascade in the model is initiated by contact activation, the numerical algorithm incorporates wall flux boundary conditions to implement this mechanism. Consequently, the size of the wall mesh will influence the accuracy of the model. To address this issue, three sets of grids with varying degrees of refinement were generated in the BFS region: 80% refined mesh, baseline mesh, and 120% refined mesh, in order to validate the accuracy of thrombus formation predictions. Based on the experimental setup, the inlet flow rate was set to 1.67×10^{-5} m³/s, the outlet was specified with a zero-pressure boundary condition, and all wall surfaces were considered as foreign surfaces. Since heparin was not used in the experiments, the initial concentration of heparin was set to 0, and γ_t was adjusted to 10 s^{-1}[20], while other settings remained unchanged. The initial conditions for the thrombus model are outlined in Table 1.

Table 1. Initial conditions for some biochemical species

species	unit	value
RP	PLT/m^3	1.85×10^{14}
AP	PLT/m^3	1%[RP]
XII	mol/m^3	9.36×10^{-8}
heparin	mol/m^3	1×10^{-4}

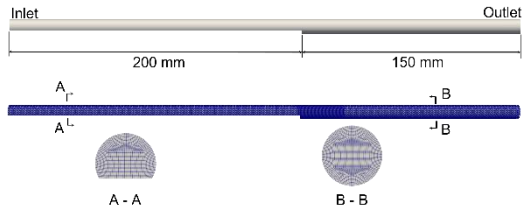

Figure 2. backward-facing step geometry

3. RESULT and DISCUSSION

As the coagulation cascade model is activated through the adsorption of FXII onto foreign surfaces, triggering the intrinsic coagulation cascade, the size of the boundary mesh is one of the key numerical factors in the thrombus model. To validate the mesh independence of the model, point A was selected in the BFS region, as shown in Figure 3(a). Figure 3(b) and Figure 3(c) present the temporal variation of concentrations of fibrin and AP at points A. The maximum deviations between the 80% refined, baseline, and 120% refined meshes were all below 3%, and as time progressed, the discrepancies among the three meshes progressively diminished and converged, ensuring the mesh independence of the thrombus model. Therefore, the baseline mesh, consisting of approximately 540,000 mesh elements, was chosen for the analysis.

Figure 4 shows the streamlines in the BFS region before thrombus formation. A recirculation zone is observed, with zero velocity at the corner after the sudden expansion and at the reattachment point downstream of the expansion, where the strain rate is less than 10 s^{-1}. Figure 5(a) presents a snapshot of the thrombus formed at t=20 s in the BFS region. Figures 5(b-e) illustrate the development of the thrombus and the corresponding velocity contours around the thrombus. The thrombus initially forms at the corner of the sudden expansion, with further thrombus formation occurring at the reattachment point downstream of the expansion. This is due to the low flow velocity and strain rate at both the step corner and reattachment point (Fig. 4), which promotes thrombus formation at these locations. This observation is consistent with the experimental and simulation results of Goodman et al. [6] and the simulations of Taylor et al. [7] However, this phenomenon was not observed in the experiments of Yang et al. [19], possibly due to the resolution limitations of MRI. Subsequently, the thrombus formed at the step corner propagates downstream, while the thrombus formed at the reattachment point propagates upstream, until the thrombi formed at both locations merge into a single thrombus. Additionally, both the thrombus growth and the corresponding velocity contours indicate that the thrombus formation alters its surrounding flow field.

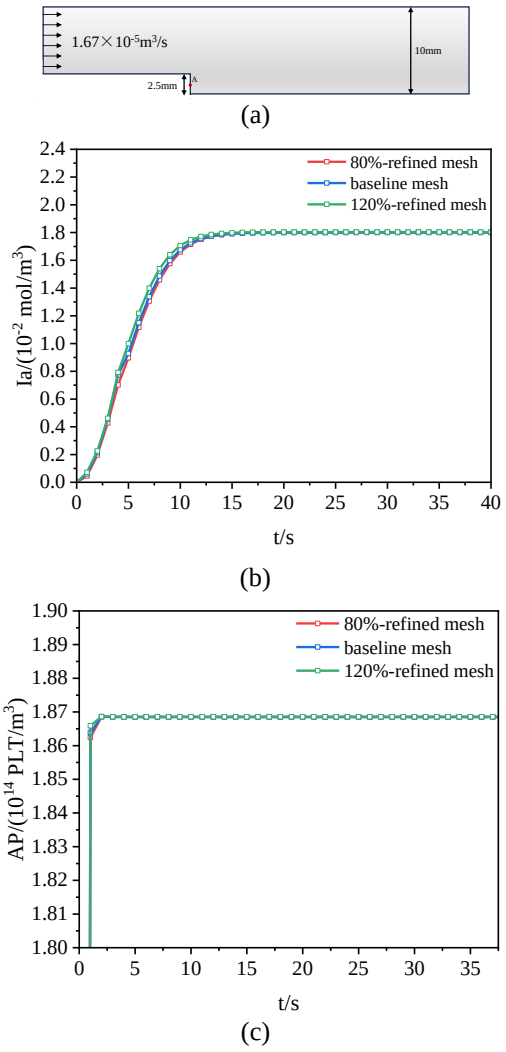

Figure 3. Mesh independence validation of the thrombus model. (a) Points A was selected for mesh independence validation, with coordinates A(0, -0.004, 0). Temporal variation of (b) fibrin and (c) AP concentrations at point A for the three grid

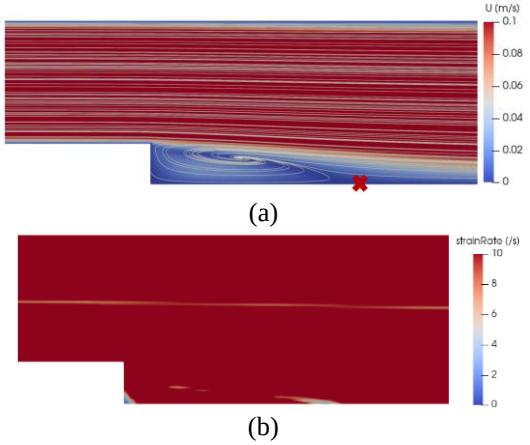

Figure 4. At t=1s, (a) streamline plot with a mark representing the reattachment point, (b) fluid strain rate.

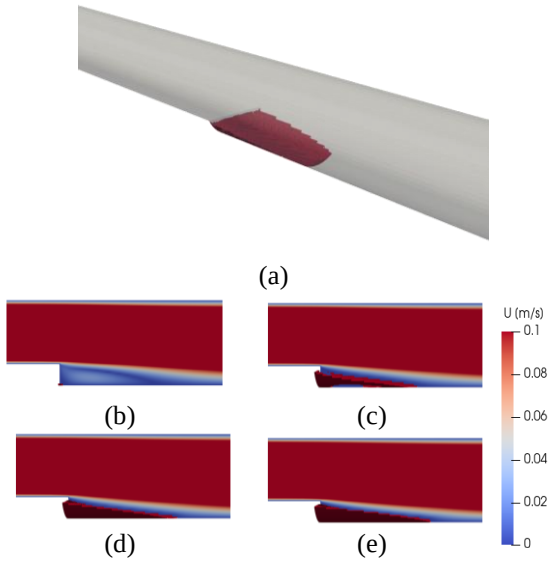

Figure 5. Simulated thrombus and flow field. (a) Simulated thrombus formed at t=20 s and streamline plot. (b-e) Simulated thrombus formed at t=2 s,6 s,10 s,14 s and velocity contours at the central cross-section.

The simulation results of the thrombus model in the BFS geometry are quantitatively compared with the experimental results of Yang et al. in both spatial and temporal domains, as shown in Figure 6. The time scale represented in Figure 6 is accelerated. Simulated results for thrombus volume, length, and height are in good agreement with the experimental data, demonstrating the model's capability to predict thrombus formation. Figure 6(a) compares the simulated thrombus volume with the experimental data. Thrombus formation begins at t=2 s, with the growth rate reaching its peak between t=3 s and t=7 s, after which the thrombus formation rate gradually slows. Figure 6(b) shows the comparison of the simulated thrombus length with the experimental results. Between t=2 s and t=6 s, the thrombus length increases rapidly. From t=6 s to t=8s, the growth rate of thrombus length significantly slows, and after t=8 s, the thrombus length hardly changes. Figure 6(c) illustrates the change in thrombus height over time, with the thrombus rapidly growing to nearly the height of the step before t=6 s, after which the thrombus height shows little further increase. Importantly, it is observed that during thrombus growth, the phenomenon of reattachment point drift occurs in the flow field. The numerical simulation framework is capable of effectively identifying this dynamic process. Notably, the consistency between the predicted thrombus distribution near the reattachment point and experimental results may be attributed to the model's ability to preset the reattachment point location, thereby ensuring a stable computational flow field and aligning simulation predictions with experimental observations.

Figure 7 illustrates the temporal evolution of concentration distributions for certain biochemical species. Figure 7(a) shows the distribution of AP concentration. Due to the strong platelet activation during the computational domain, the temporal variation in AP concentration is not significant. The concentration distribution of fibrin, as depicted in Figure 7(b), is influenced by a recirculation region downstream of the sudden expansion. Consequently, fibrin first accumulate at the corner of the sudden expansion and the reattachment point downstream, resulting in elevated concentrations. However, as the coagulation cascade progresses, the fibrin concentration becomes more uniform downstream. Notably, thrombus formation is influenced by both physiological factors and hemodynamic conditions. Over time, the fibrin concentration on the foreign surface tends to become consistent, but not all regions with high AP and fibrin concentrations develop into thrombi (Figure 7(c)). This is because platelet stabilization also depends on fluid shear stress. Only in low-shear regions can APs convert to BP, thereby forming a thrombus, as shown in Figure 8.

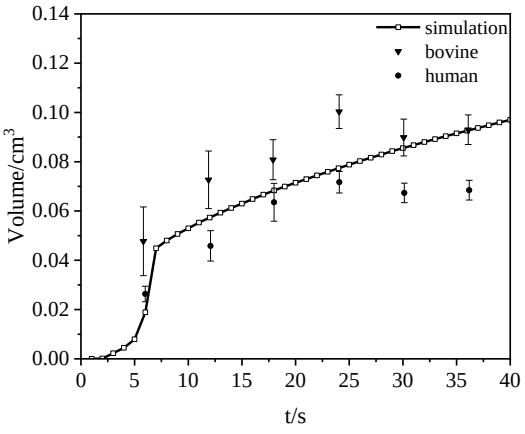

(a)

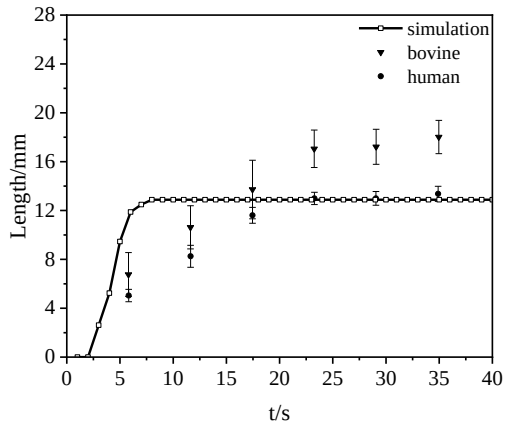

(b)

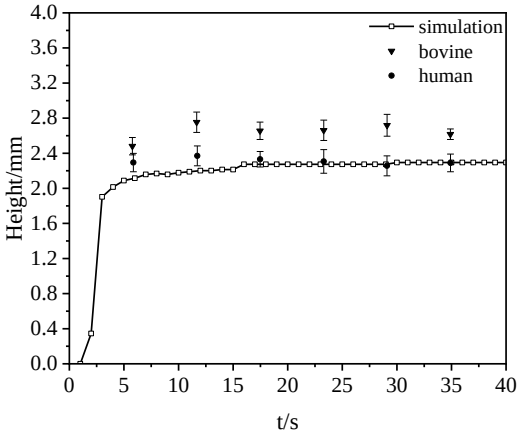

(c)

Figure 6. Quantitative comparison of the simulated thrombus with experimental data in both spatial and temporal domains. (a) Volume, (b) Length, (c) Height, with data obtained from Yang et al. [19].

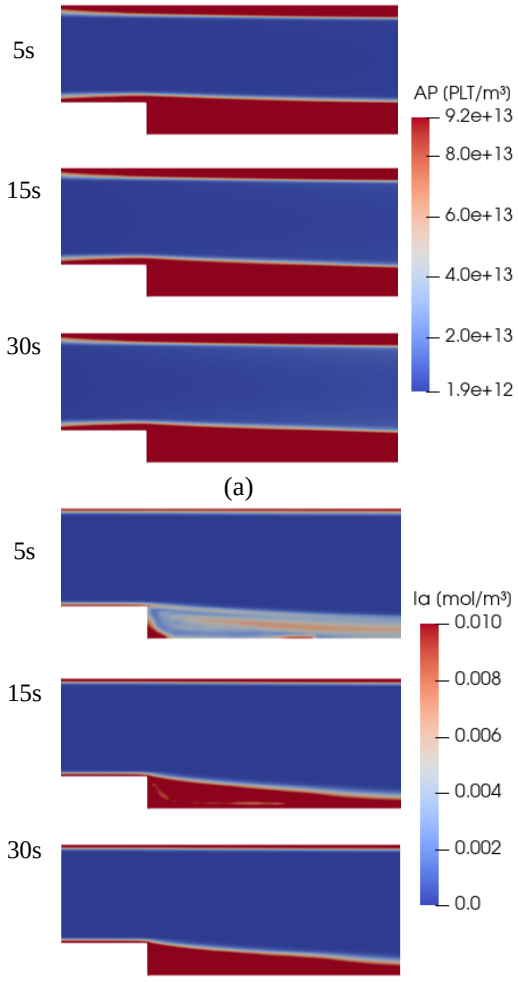

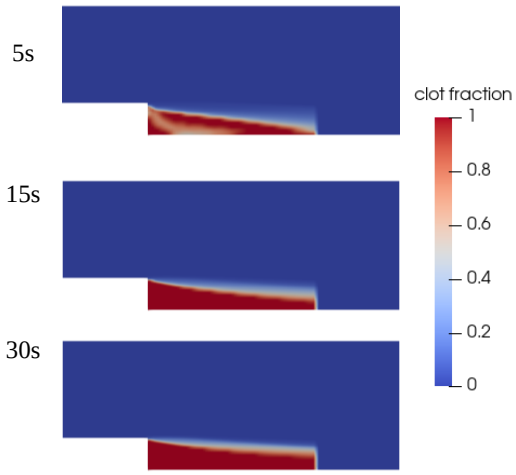

(c)

Figure 7. Concentration distribution of selected biochemicals and simulated thrombus volume fraction at t=5, 15 and 30s. (a) concentration ofAP. (b) concentration of fibin. (c) similated thrombus volume fraction.

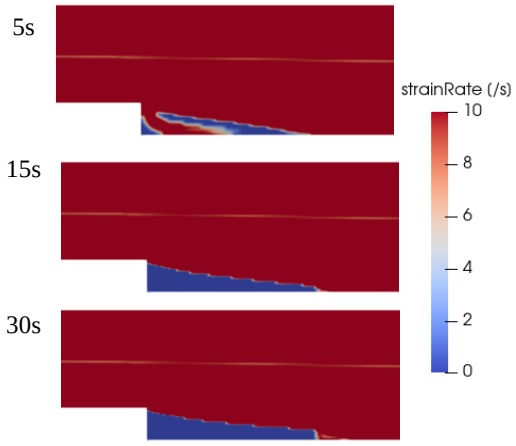

Figure 8. Fluid strain rate at t=5, 15 and 30s.

5. SUMMARY

This study proposes a thrombus formation model that integrates blood flow, platelet activity, and coagulation cascade to predict thrombus formation behavior in blood-contacting medical devices. The model was validated in a backward-facing step geometry, with its numerical simulation results achieving a high degree of consistency with experimental data. This research establishes a foundation for future studies and applications. By applying the proposed model to thrombus prediction in blood-contacting medical devices, it provides a scientific basis for optimizing device design, clinical treatments, and prognostic evaluations.

APPENDICES

Table A1. Parameter relate to platelets activity model

terms	expression	description
k_{apa}	$\begin{cases} 0, & \Omega < 1.0 \\ \frac{\Omega}{t_{ct}}, & \Omega \geq 1.0 \\ \frac{1}{t_{act}}, & \frac{\Omega}{t_{ct}} \geq \frac{1}{t_{act}} \end{cases}$	Platelet activation due to chemical agonists occurs only when the agonist concentration exceeds a certain threshold, triggering the chemical activation reaction.
Ω	$w_{ADP}\frac{[ADP]}{ADP_t}+w_{IIa}\frac{[IIa]}{IIa_t}$	The agonist equivalence, w_{ADP} and w_{IIa} , represent the specific weight factors of ADP and thrombin in their role in platelet activation.
k_{tb}	$k_{bb}\times f(\tau)$	The rate of thrombus breakdown[21]
k_{bb}	200	constant related to the thrombus breakdown rate[21]
$f(\tau)$	$\frac{\tau^2}{\tau^2+\tau_t^2}$	Switching function related to k_{tb}, the greater the scalar shear force acting on the thrombus unit, the faster the thrombus breakdown.
ϕ	$\frac{[BP]}{BP_t}$	Thrombus volume fraction. BPt=1×10^{12}PLT/m^3
λ_j	2.4×10^{-8}	The amount of ADP released by each activated platelet.

Table A2. Expressions of flux boundary conditions

species	expression	description
RP	$-S\theta k_{rpab}[RP]_{wall}$	Consumption due to RP directly adsorbing onto the foreign surface
AP	$S\theta k_{rpab}[RP]_{wall}$	Generated due to RP directly adsorbing onto the foreign surface
ADP	$\lambda_j S\theta k_{rpab}[RP]_{wall}$	ADP released by platelets during the conversion of RP to AP.
XII	$-k_1[XII]$	Consumption due to FXII directly adsorbing onto the foreign surface
XIIa	$k_1[XII]$	Generated due to FXII directly adsorbing onto the foreign surface

REFERENCES

[1] Nascimbene, A., Bark, D., and Smadja, D. M., 2023, "Hemocompatibility and Biophysical Interface of Left Ventricular Assist Devices and Total Artificial Hearts," Blood, Vol. 143, pp. 661–672.

[2] Manning, K. B., Nicoud, F., and Shea, S. M., 2021, "Mathematical and Computational Modeling of Device-Induced Thrombosis," Curr. Opin. Biomed. Eng., Vol. 20, p. 100349.

[3] Fogelson, A. L., 1992, "Continuum Models of Platelet Aggregation: Formulation and Mechanical Properties," SIAM J. Appl. Math., Vol. 52, pp. 1089–1110.

[4] 2008, "Immersed-Boundary-Type Models of Intravascular Platelet Aggregation," Comput. Methods Appl. Mech. Eng., Vol. 197, pp. 2087–2104.

[5] Sorensen, E. N., Burgreen, G. W., Wagner, W. R., and Antaki, J. F., 1999, "Computational Simulation of Platelet Deposition and Activation: I. Model Development and Properties," Ann. Biomed. Eng., Vol. 27, pp. 436–448.

[6] Goodman, P. D., Barlow, E. T., Crapo, P. M., Mohammad, S. F., and Solen, K. A., 2005,

"Computational Model of Device-Induced Thrombosis and Thromboembolism," Ann. Biomed. Eng., Vol. 33, pp. 780–797.
[7] Taylor, J. O., Meyer, R. S., Deutsch, S., and Manning, K. B., 2016, "Development of a Computational Model for Macroscopic Predictions of Device-Induced Thrombosis," Biomech. Model. Mechanobiol., Vol. 15, pp. 1713–1731.
[8] Wu, W.-T., Jamiolkowski, M. A., Wagner, W. R., Aubry, N., Massoudi, M., and Antaki, J. F., 2017, "Multi-Constituent Simulation of Thrombus Deposition," Sci. Rep., Vol. 7, p. 42720.
[9] Wu, W.-T., Yang, F., Wu, J., Aubry, N., Massoudi, M., and Antaki, J. F., 2016, "High Fidelity Computational Simulation of Thrombus Formation in Thoratec HeartMate II Continuous Flow Ventricular Assist Device," Sci. Rep., Vol. 6, p. 38025.
[10] Blum, C., Groß-Hardt, S., Steinseifer, U., and Neidlin, M., 2022, "An Accelerated Thrombosis Model for Computational Fluid Dynamics Simulations in Rotary Blood Pumps," Cardiovasc. Eng. Technol., Vol. 13, pp. 638–649.
[11] Li, Y., Wang, H., Fu, X., Xi, Y., Sun, A., Chen, Z., and Fan, Y., 2024, "A Comprehensive Study of Oxygenator Gas Transfer Efficiency and Thrombosis Risk," Phys. Fluids, Vol. 36, p. 081916.
[12] Li, Y., Wang, H., Liu, X., Xi, Y., Sun, A., Wang, L., Deng, X., Chen, Z., and Fan, Y., 2024, "Comprehensive Study on Simulation, Performance Evaluation and Optimization Strategies for Blood Pumps," Eng. Appl. Comput. Fluid Mech., Vol. 18, p. 2369690.
[13] Li, Y., Zhang, M., Sun, A., Wang, X., Fan, Y., and Chen, Z., 2024, "Evaluation and Optimization of Interventional Blood Pump Based on Hydraulic Performances and Hemocompatibility Performances," Phys. Fluids, Vol. 36, p. 111903.
[14] Méndez Rojano, R., Mendez, S., and Nicoud, F., 2018, "Introducing the Pro-Coagulant Contact System in the Numerical Assessment of Device-Related Thrombosis," Biomech. Model. Mechanobiol., Vol. 17, pp. 815–826.
[15] Méndez Rojano, R., Mendez, S., Lucor, D., Ranc, A., Giansily-Blaizot, M., Schved, J.-F., and Nicoud, F., 2019, "Kinetics of the Coagulation Cascade Including the Contact Activation System: Sensitivity Analysis and Model Reduction," Biomech. Model. Mechanobiol., Vol. 18, pp. 1139–1153.
[16] Anand, M., Rajagopal, K., and Rajagopal, K. R., 2003, "A Model Incorporating Some of the Mechanical and Biochemical Factors Underlying Clot Formation and Dissolution in Flowing Blood," J. Theor. Med., Vol. 5, pp. 183–218.
[17] Wang, Y., Luo, K., Qiao, Y., and Fan, J., 2021, "An Integrated Fluid-Chemical Model toward Modeling the Thrombus Formation in an Idealized Model of Aortic Dissection," Comput. Biol. Med., Vol. 136, p. 104709.
[18] Wang, Y., Luan, J., Luo, K., Zhu, T., and Fan, J., 2023, "Multi-Constituent Simulation of Thrombosis in Aortic Dissection," Int. J. Eng. Sci., Vol. 184, p. 103817.
[19] Yang, L., Neuberger, T., and Manning, K. B., 2021, "In Vitro Real-Time Magnetic Resonance Imaging for Quantification of Thrombosis," Magn. Reson. Mater. Phys. Biol. Med., Vol. 34, pp. 285–295.
[20] Menichini, C., and Xu, X. Y., 2016, "Mathematical Modeling of Thrombus Formation in Idealized Models of Aortic Dissection: Initial Findings and Potential Applications," J. Math. Biol., Vol. 73, pp. 1205–1226.
[21] Wang, K., Armour, C. H., Gibbs, R. G. J., and Xu, X. Y., 2023, "A Numerical Study of the Effect of Thrombus Breakdown on Predicted Thrombus Formation and Growth," Biomech. Model. Mechanobiol., Vol. 23, pp. 61–71.

Conference on Modelling Fluid Flow (CMFF'25)
The 19th International Conference on Fluid Flow Technologies
Budapest, Hungary, August 26 - August 29, 2025

STUDY OF THE MIXING PERFORMANCE OF CURVED BLADE TURBINES IN A SOLID-LIQUID DUAL IMPELLER STIRRED SYSTEM

Laifa Lu[1,2], Jiacheng He[1,2], Shuiqing Zhou[1,2], Weiya Jin[1,2], Zengliang Gao[1,2], Diping Xu[1,2]

[1] College of Mechanical Engineering, Zhejiang University of Technology, Hangzhou,310023, China.
[2] Institue of Innovation Research of Shengzhou and Zhejiang University ofTechnology, Shengzhou,312400, China.
[3] Corresponding Author. College of Mechanical Engineering, Zhejiang University of Technology, Hangzhou 310023, China. E-mail: zsqwh666@163.com

ABSTRACT

Improving mixing efficiency, product quality and process sustainability are the core challenges in the design of multi-impeller stirred tank reactors. In this study, Euler-Euler numerical simulation and Particle Image Velocimetry (PIV) technology were used to systematically explore the solid-liquid mixing performance in a double-impeller mixing tank. Combined with the surrogate model and sensitivity analysis method, the flow field characteristics and suspension performance in the mixing tank of itched blade turbine (PBT) and curved blade turbine (CBT) were studied qualitatively and quantitatively. The results show that the solid-liquid suspension performance of CBT is better than that of PBT. The arc chord distance of the upper impeller and the blade angle have a great influence on the power consumption and particle distribution. When the arc chord distance of the upper impeller is 4mm and the blade inclination angle is 50°, the stirred tank can significantly improve the mixing performance and reduce the power consumption. The research results have certain guiding significance for the optimization design of curved blade turbine and similar mixing tank.

Keywords: solid-liquid mixing, CFD, PIV, sensitivity analysis

NOMENCLATURE

B	[mm]	baffle width
C	[mm]	off-bottom clearance
D	[mm]	impeller diameter
d_s	[mm]	solid particles diameter
g	[m/s^2]	gravitational acceleration
H	[mm]	liquid height
h	[mm]	baffle height
K	[-]	interphase momentum transfer coefficient
p	[Pa]	phase pressure
S	[mm]	blade spacing
T	[mm]	tank diameter
α	[-]	phase volume fraction
θ	[K]	particles temperature
λ	[m^2/s]	phase dynamic viscosity
μ	[$Ps{\cdot}s$]	phase dynamic viscosity
ρ	[kg/m^3]	phase density
τ	[-]	viscous stress tensor of phase

Subscripts and Superscripts

l	liquid phase
s	solid phase
u	upper impeller

1. INTRODUCTION

As a typical fluid machinery, the multi-impeller stirred tank has been widely used in the industrial field due to its excellent mixing and mass transfer performance [1]. However, with the development of the industry, the requirements for hydraulic performance, mixing efficiency and energy consumption are increasing [2], and the mixing equipment is facing the trend of transformation and upgrading. The traditional empirical standard design method is difficult to meet the growing demand for product performance. It has become a hot issue for scholars at home and abroad to improve the comprehensive performance of the tank by designing a new stirring main structure [3].

The solid-liquid double impeller stirred tank is one of the conventional multi-impeller reaction equipment, and its solid particle suspension performance directly affects the product crystallization and precipitation quality [4, 5]. In order to optimize the performance of the mixing tank, the process parameters are often used as the research object. Gu et al. [6] found that at the same speed, the

fractal blade impeller is superior to the inclined blade impeller in terms of particle dispersion. Davoody et al. [7] showed that the impeller parameters were the key factors affecting the performance of the mixing system, and the structure of the curved blade impeller had a significant effect on the volumetric mass transfer coefficient of the gas-solid-liquid three-phase mixing. The above research shows that the non-standard blade structure design at the appropriate scale can effectively improve the mixing efficiency.

Nowadays, Computational Fluid Dynamics (CFD) has been widely used in the performance analysis of various types of stirred tanks, which can effectively simulate the nonlinear and strong pulsation characteristics in the flow field [8]. However, numerical simulation methods usually need to be combined with experimental analysis to verify the accuracy of the prediction results. Martina et al. [9] used conductance probe to measure the local solid concentration at different heights and radial positions in the container, and studied the particle distribution and suspension state. Guha et al. [10] used radioactive particle tracer technique to investigate the hydrodynamic characteristics of high concentration solid-liquid suspension system in stirred tank, which provided data support for evaluating the accuracy of CFD model of slurry reactor. Montante et al. [11] used Particle Image Velocimetry (PIV) technology to study the behavior of dilute solid particles, and analyzed the influence of dispersed phase on the average velocity and turbulence intensity of continuous phase. The purpose of this study is to combine CFD and PIV methods to optimize the performance of mixing tanks more conveniently and accurately.

In order to clarify the optimization direction in the design process, many scholars have introduced sensitivity analysis technology to identify the key parameters that affect the design objectives [12, 13]. In this study, the effects of key structural parameters of the curved blade turbine on the solid-liquid mixing performance were systematically analyzed by Euler-Euler numerical calculation and PIV experimental technology, combined with Multiple-response Gaussian Process (MRGP) approximation model and Extended Fourier Amplitude Sensitivity Testing (EFAST) method. Finally, a curved blade turbine structure with better comprehensive performance was obtained, and the optimization results were verified by PIV test.

2. CALCULATION METHOD AND MODEL VALIDATION

2.1. Numerical simulation calculation method

In this study, the Eulerian-Eulerian multiphase flow model is used to simulate the flow of two phases, each of which is considered as a mutually coherent continuum, in order to solve the Reynolds-averaged continuity equation and the momentum conservation equation for each phase. The controlling equations for phase q (liquid phase q=l, solid phase q=s) are as shown below [14]:

Continuity equation:

$$\frac{\partial}{\partial t}\left(\alpha_{\mathrm{q}}\rho_{\mathrm{q}}\right)+\nabla\bullet\left(\alpha_{\mathrm{q}}\rho_{\mathrm{q}}\vec{u}_{\mathrm{q}}\right)=0 \tag{1}$$

where α_{q} is the volume fraction of the q-phase, $\vec{u}_{\mathrm{q}}$ is the velocity of the q-phase, and ρ is the density of the q-phase.

Liquid phase momentum conservation equation:

$$\begin{aligned}&\frac{\partial}{\partial t}\left(\alpha_{\mathrm{l}}\rho_{\mathrm{l}}\vec{u}_{\mathrm{l}}\right)+\nabla\bullet\left(\alpha_{\mathrm{l}}\rho_{\mathrm{l}}\vec{u}_{\mathrm{l}}\vec{u}_{\mathrm{l}}\right)=\\&-\alpha_{\mathrm{l}}\nabla p+\nabla\bullet\bar{\bar{\tau}}_{\mathrm{l}}+K\left(\vec{u}_{\mathrm{l}}-\vec{u}_{\mathrm{s}}\right)+\alpha_{\mathrm{l}}\rho_{\mathrm{l}}\vec{g}\end{aligned} \tag{2}$$

where p denotes the thermodynamic pressure, $\vec{g}$ is the gravitational acceleration, $\bar{\bar{\tau}}$ is the viscous stress tensor of the liquid phase, and K is the interphase momentum transfer coefficient.

Solid phase momentum conservation equation:

$$\begin{aligned}&\frac{\partial}{\partial t}\left(\alpha_{\mathrm{s}}\rho_{\mathrm{s}}\vec{u}_{\mathrm{s}}\right)+\nabla\bullet\left(\alpha_{\mathrm{s}}\rho_{\mathrm{s}}\vec{u}_{\mathrm{s}}\vec{u}_{\mathrm{s}}\right)=\\&-\alpha_{\mathrm{s}}\nabla p-\nabla p_{\mathrm{s}}+\nabla\bullet\bar{\bar{\tau}}_{\mathrm{s}}+K\left(\vec{u}_{\mathrm{l}}-\vec{u}_{\mathrm{s}}\right)+\alpha_{\mathrm{s}}\rho_{\mathrm{s}}\vec{g}\end{aligned} \tag{3}$$

where $\bar{\bar{\tau}}$ is the viscous stress tensor of the solid phase, and p_s is the solid phase pressure.

In this study, a *k*-*ε* mixed turbulence model is used to calculate the turbulent kinetic energy and dissipation rate of the liquid phase, assuming that both phases have the same *k* and *ε*. The *k* and *ε* equations describing the model are as follows:

$$\begin{aligned}&\frac{\partial}{\partial t}\left(\rho_m k\right)+\nabla\cdot\left(\rho_m\vec{u}_m k\right)=\\&\nabla\cdot\left(\mu_m+\frac{\mu_{\mathrm{t,m}}}{\sigma_{\mathrm{k}}}\nabla k+G_{\mathrm{k,m}}+G_{\mathrm{b,m}}-\rho_m\varepsilon\right)\end{aligned} \tag{4}$$

$$\begin{aligned}&\frac{\partial}{\partial t}\left(\rho_m\varepsilon\right)+\nabla\cdot\left(\rho_{\mathrm{m}}\vec{u}_{\mathrm{m}}\varepsilon\right)=\\&\nabla\cdot\left(\frac{\mu_{\mathrm{t,m}}}{\sigma_\varepsilon}\nabla\varepsilon\right)+\frac{\varepsilon}{k}\left(C_{1\varepsilon}G_{\mathrm{k,m}}-C_{2\varepsilon}\rho_m\varepsilon\right)\end{aligned} \tag{5}$$

where ρ_m is the mixture density, μ_m is the molecular viscosity, $\vec{u}_m$ is the velocity.

Neglecting the effects of virtual mass force, lift force and mass transfer, this paper only considers the drag force which has a large impact on the simulation

results [15]. The momentum exchange coefficients are calculated using the Huilin-Gidaspow model.

This study employs the Multiple Reference Frame (MRF) method, designating the rotating region of the impeller as the moving zone and the remaining regions as stationary zones. A pressure-based transient implicit solver was utilized, with pressure-velocity coupling handled by the Phase Coupled SIMPLE algorithm. A second-order upwind differencing scheme was adopted, with the convergence criterion set to variable residuals falling below 10^{-4} or exhibiting stabilized residual curves. Standard wall functions were applied to model near-wall fluid motion. The top boundary was assigned a symmetric boundary condition to simulate the free surface, while all other geometric walls were assumed to have no-slip boundary conditions.

2.2. PIV Experimental validation

With the development of experimental measurement techniques, PIV is widely used in hydrodynamic measurements as a non-contact type measurement technique capable of providing rich fluid flow information for stirred reactors. In this study, a 2D PIV system was used. The two-dimensional (2D) PIV system adopted in the present work consisted of a dual Vlite series 532 nm dual pulse laser, a high-resolution CCD camera with 6600*4400 pixels, a synchronizer, and the commercial software MicroVec-V3.6.9 The test principle is shown in figure 1(a) and the experimental setup is shown in figure 1(b).

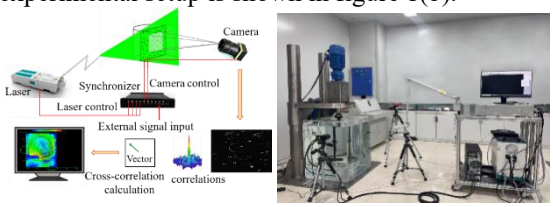

Figure 1. PIV test system (a) PIV test principle (b) PIV Experimental Apparatus

The designated region for PIV experimentation is delineated in Figure 2, wherein H signifies the cylinder's height, T corresponds to the cylinder's diameter, and B denotes the width of the baffle. The laser plane intersects the baffle plane at a 5° angle, and the LED light source forms a 30° angle with the measurement plane. This setting ensures that the image is clear and undistorted. In the context of the solid-liquid biphasic flow field under examination through PIV, the application of specific filters facilitates distinct analyses: a laser light source enables liquid flow assessment, while an LED light source enables particle flow evaluation. The PIV experiment employs fluorescent particles as tracer agents and hollow glass beads as representative solid particles. The liquid medium utilized is pure water. Table 1 provides the relevant parameters for liquid and solid particles.

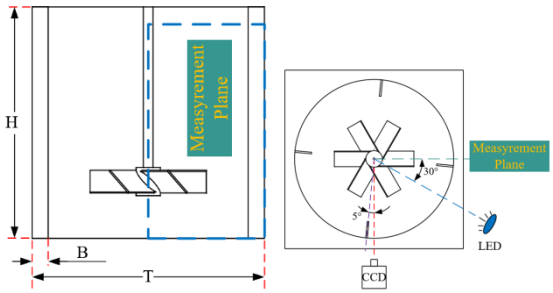

Figure 2. PIV measurement area (a) Mixing tank (b) PIV measurement plane

Table 1. Physical properties parameters

Parameter	Symbol	Value
Liquid density	ρ_L	1000kg/m^3
Hydrodynamic viscosity	μ	0.001Pa·s
Solid particles density	ρ_S	1430 kg/m^3
Solid particles diameter	d_S	0.15mm
Solid volume fraction	φ_S	5.6%

Owing to the inherent rotational periodicity of the stirring process, only half the flow area requires measurement during flow field characterization in stirred tanks. As depicted in Figure 3, liquid-phase average velocity fields obtained from numerical simulations and PIV experiments demonstrate close agreement. Within the r/R range of 0.3 to 0.4, a circulating vortex structure forms near the blade tip, from which fluid discharges diagonally downward at maximum velocity. Upon impinging the tank bottom, the majority of fluid establishes impeller-induced global circulation, while localized particles gradually settle to form an inverted conical region at the base.

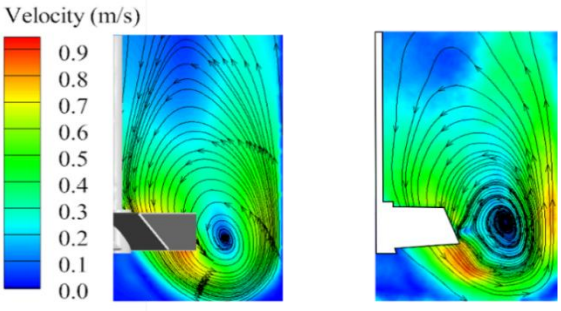

Figure 3. Fluid mean velocity field (a) CFD simulation (b) PIV experiment

3. RESEARCH OBJECT AND ITS PARAMETERIZATION

3.1. Stirring equipment

In the context of a mixing tank characterized by a substantial height-to-diameter ratio, the utility of a solitary impeller becomes limited. This study focuses on a dual-impeller configuration for solid-liquid mixing, as illustrated in Figure 4. The primary

flow field constituents encompass the tank body, tank bottom, baffle, and agitator, encompassing the mixing shaft, upper impeller, and lower impeller. Refer to Table 2 for the structural specifications of the mixing tank and impeller. Within the prototype configuration, the upper and lower impellers are designed as pitched blade turbine (PBT), representing a prevalent choice for mixed-flow impellers within solid-liquid mixing systems. Both impellers are in up pumping mode.

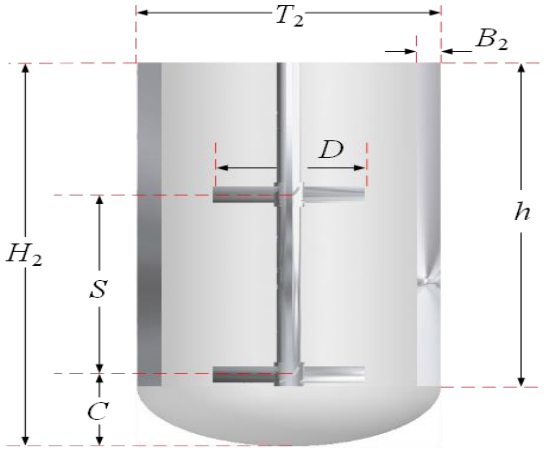

Figure 4. Structure of dual impeller mixing tank

Table 2. Structural parameters of mixing tank and impeller

Parameter	Symbol	Value
Tank diameter	T	500 mm
Liquid height	H_2	1.6 T
Baffle width	B_2	0.1 T
Baffle height	h	1.35 T
Impeller diameter	D	0.5 T
Off-bottom clearance	C	0.3 T
Blade spacing	S	0.75 T

3.2. Impeller structure parameterization

The structural characteristics of the stirrer significantly influence the tank's flow field and the mixing performance of two-phase media. Axial impellers are good for improving the deposition of particles at the bottom, while the shear flow generated by radial impellers is crucial for particle suspension. In the dual impeller mixing tank under study, impeller size, blade spacing, and off-bottom clearance all affect particle suspension performance. However, due to constraints from the shaft bore and motor positioning, the latter is typically difficult to adjust. Traditional PBT impellers fail to meet practical requirements, making impeller structural redesign essential. Consequently, a curved blade turbine (CBT) design is introduced aimed at enhancing energy utilization efficiency. Figure 5 illustrates the structural configuration of the CBT impeller.

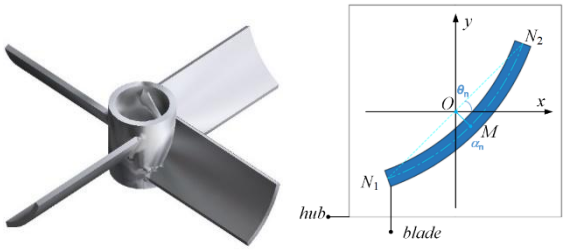

Figure 5. Impeller structure diagram (a) CBT impeller (b) structure parameters of impeller

As in Figure 5, the cross-sectional profile of the blade is shown schematically. The point O is the center of the impeller hub, and there is a straight line N_1N_2 across the point O, which is the chord length of the curved blade, and N_1MN_2 is the mid-arc of the blade. In this study, the position of point O is fixed, and the length of straight line N_1N_2 is unchanged. Take the upper impeller OM distance as 1, ON_2 and x-axis angle as θ_1. Take the lower impeller OM distance as α_2, $ON2$ and x-axis angle as θ_2. These four parameters are the main design variables. Define α_n as the arc-chord distance and θ_n as the blade angle. When $\alpha_n = 0$ mm and $\theta_n = 45°$, the CBT form is the same as PBT.

4. SENSITIVITY ANALYSIS

A distinct interface forms between the suspended solids and the clear liquid layer in the stirred tank, and the height of this interface is defined as the cloud height. Matthias indicated that cloud height reaches full suspension at 90% of the liquid height. Therefore, the cloud height can be used as an important parameter to evaluate the mixing degree. In this study, cloud height is analyzed by numerically tracking the average solids concentration isosurface, defined as the maximum axial height of this isosurface. Taking the four parameters mentioned above as input variables, cloud height and power as output values, the corresponding surrogate model is established by MRGP model, and the sensitivity analysis of variables is carried out by EFAST method.

The MRGP model is an extension of the Kriging model. The traditional Kriging model can only deal with multivariate single response output problems, while for multi-dimensional response output, multiple Kriging models need to be constructed, and this approach does not consider the coupling-related problems of response values. Therefore, the MRGP model for multivariate multi-response problems is gradually gaining attention. MRGP model unites m functions into a specific implementation of a multi-response Gaussian process [16]:

$$G(x) = f(x)^{\mathrm{T}} B + Z(x) \tag{6}$$

where the polynomial regression function $f(x)$ is the same as the Kriging model, but the regression coefficient B is an $n*m$ matrix and $Z(x)$ is also

expanded to a *1*m* row vector. The covariance of Z(x) is expressed as a covariance matrix of size *m*m*:

$$\sum^{m}=\begin{bmatrix}\sigma^2(g_1,g_2) & \cdots & \sigma^2(g_1,g_m)\\ \vdots & \ddots & \vdots\\ \sigma^2(g_m,g_1) & \cdots & \sigma^2(g_m,g_m)\end{bmatrix} \tag{7}$$

In this paper, the MRGP model is selected as the approximation function, and the approximation model is established using the sample data of 50 sets of variables with corresponding responses obtained through Optimal Latin Hypercube Design (Opt LHD) combined with numerical simulations.

Due to the limitation of parameter selection, the constructed MRGP model will have certain errors. In order to verify the accuracy of the model, it is necessary to test it by the relevant accuracy test formula before prediction solving. In this paper, a global sensitivity analysis based on the EFAST method is used. The basic idea of the EFAST method is derived from Bayes' theorem, which holds that the sensitivity of the model output results can be reflected by the variance of the model results. The sensitivity of parameter x can be expressed by the following equation:

$$Sensitivity_{\mathrm{x}}=\frac{var_{\mathrm{x}}\left[E\left(Y|X\right)\right]}{var\left(Y\right)} \tag{8}$$

where *Y* is the output value of the model, *x* is the input parameter, *E*(*Y*|*X*) is the expectation of *Y* when *x* takes a certain value, and var_x is the variance when *x* traverses a range of values.

The total variance of the model and the first-order variance due to parameter *i*, neglecting the coupling with other parameters, yields the first-order sensitivity values:

$$S_{\mathrm{i}}=\frac{\mathrm{var}_{\mathrm{xi}}\left[E\left(Y|x_{\mathrm{i}}\right)\right]}{var(Y)} \tag{9}$$

And for the total sensitivity index of a parameter i after considering the effect of parameter coupling, we need to consider the coupling part between the parameters:

$$S_{\mathrm{Ti}}=1-\frac{var_{\mathrm{xi}}\left[E\left(Y|x_{\mathrm{-i}}\right)\right]}{var(Y)} \tag{10}$$

The first-order sensitivity indicates the degree of influence of a single influencing factor on cloud height and power, while the overall sensitivity reflects not only the degree of influence of a single influencing factor on cloud height and power, but also the interaction with other influencing factors. Therefore, when the difference between the first-order sensitivity of a variable and the overall sensitivity is large, it can be considered that the factor has an obvious interaction. The normalized influence factors of each variable parameter are shown in Figure 6.

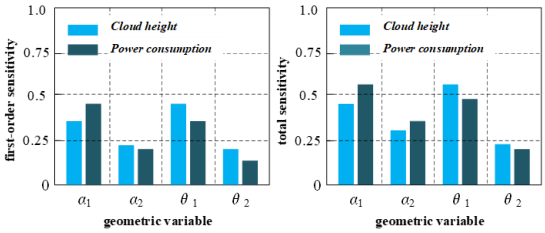

Figure 6. Influence factors of different variables (a) First-order sensitivity (b) Total sensitivity

The first-order sensitivity and overall sensitivity analyses show that the upper impeller structure parameters α_1 and θ_1 have a greater degree of influence on the cloud height and power of the mixing tank. Therefore, it can be inferred that the upper impeller possesses a more significant effect on the mixing performance of the flow field. In order to reduce the complexity of the study, the subsequent study in this paper will keep the lower impeller as the prototype structure and mainly study the flow field characteristics and mixing effect of the upper impeller after the modification.

5. ANALYSIS OF RESULTS

5.1. The effect of impeller form on the flow field

Due to the symmetry of the stirring structure, the flow field shows a symmetrical distribution, which is consistent with the uniform segmentation of the baffle. Figure 7 shows the velocity contours of PBT and CBT impellers, showing similar radial and circumferential flow patterns. When the fluid rotates with the impeller, the flow in the front of the baffle is relatively smooth, but the backflow vortex will be formed after flowing through the rear of the baffle. Compared with the PBT impeller, the vortex scale generated by CBT is smaller, indicating that the mixing efficiency is higher and the energy consumption is lower. The CBT impeller design enhances the circumferential emission capacity, which can promote high-speed circulation and reduce the flow stagnation area compared to the PBT impeller.

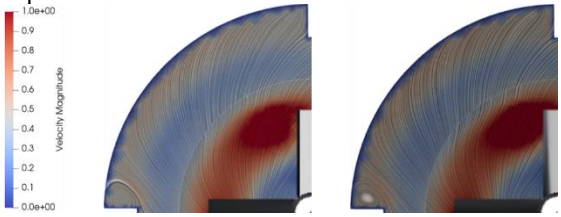

Figure 7. Plane velocity distribution of different impellers (y=0.25H₂) (a) PBT (b) CBT

It is very important to analyze the vortex structure of the impeller to optimize the efficiency of the stirred tank. Figure 8 shows the three-dimensional structure of the wake vortex downstream of the impeller blade. It can be found that each blade channel produces obvious vortex structure. These vortices absorb most of the energy transmitted by the impeller and limit its diffusion to the distant flow field. The wake vortex of PBT impeller has large scale, narrow shape and wide diffusion range, which hinders efficient energy transfer. In contrast, the CBT impeller design changes the dynamic characteristics of the wake vortex, resulting in a more compact wake and significantly reducing energy dissipation.

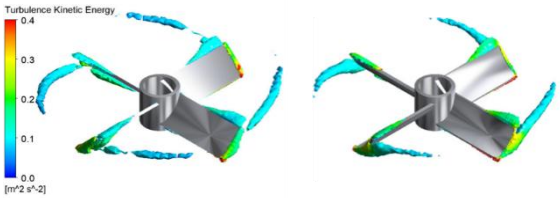

Figure 8. Three-dimensional structure of the tail vortex for different impellers (a) PBT (b) CBT

5.2. Effect of impeller form on solid phase distribution.

Understanding the distribution characteristics of solid particles within stirred tanks holds fundamental research significance. Figure 9 illustrates the three-dimensional distribution of solid-phase volume fraction. For both impeller types, particle accumulation zones form beneath the impellers while clear liquid layers emerge at the upper liquid surface. However, compared to PBT impeller, CBT impeller significantly mitigate particle sedimentation at the tank bottom while simultaneously enhancing particle suspension capability in upper regions. This demonstrates the superior mixing performance of the CBT design, attributable to its curved-blade configuration. The blade curvature expands the discharge area, generating a more powerful high-speed jet. This jet flow enhances the velocity gradient between fluid layers, increasing local energy dissipation rates and thereby improving mixing efficiency.

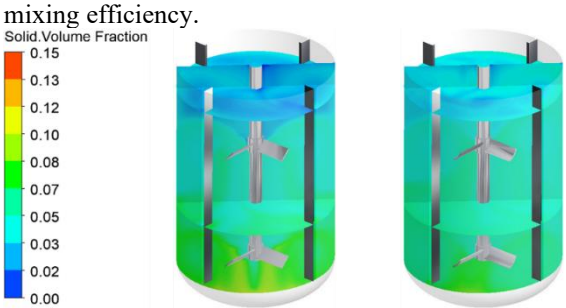

Figure 9. Overall solid phase distribution of different impellers (a) PBT (b) CBT

Figure 10 presents the solid concentration distribution along the axial height at different radial positions (r=0.1~0.9R) in the stirred tank. Compared with PBT impeller, the CBT structure shows a more uniform solid phase concentration distribution, and its concentration gradient is significantly reduced, indicating that the particle suspension performance is improved, especially in the near-axis area and near the tank wall. Under the synergistic effect of CBT and PBT double impellers, the original symmetrical flow field structure is broken, and the energy transfer efficiency between fluids is enhanced, thereby improving the mixing efficiency of the system.

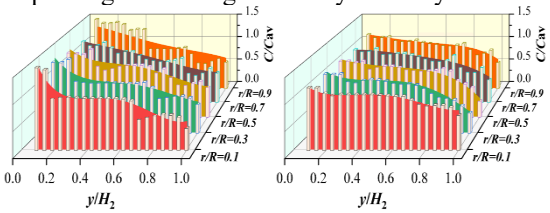

Figure 10. Local axial solid phase distribution of different impellers (a) PBT (b) CBT

5.3. The effect of arc-chord distance

Turbulent kinetic energy and turbulent energy dissipation rate serve as pivotal determinants in the assessment of both mixing duration and the quality of solid-liquid suspension [17]. Manipulation of parameters such as mixing time is facilitated by elevating turbulent kinetic energy and turbulent energy dissipation rate. The non-dimensional distribution of turbulent kinetic energy and turbulent energy dissipation rate across varying arc-chord distances is illustrated in Figures 11 and 12, respectively. Across all instances, the apex values of turbulent kinetic energy and turbulent energy dissipation rate emerge proximate to the impeller blade's tip, while values away from the blade's influence tend to be subdued. CBT engenders a discernible enhancement in the turbulent kinetic energy and turbulent energy dissipation rate within the mixing tank, particularly in proximity to the impeller. This phenomenon can be attributed to the alteration in flow field angle of incidence brought about by CBT's arc curvature. This modification augments shear forces and concurrently diminishes discharge resistance. As the arc-chord distance increases, turbulent kinetic energy and turbulent energy dissipation rate initially rise, exhibiting a slight decline once the arc-chord distance surpasses an optimal range. The most substantial increments in turbulent kinetic energy and turbulent energy dissipation rate occur at the arc-chord distance of 4 mm.

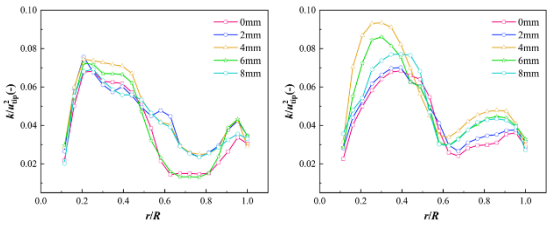

Figure 11. Effect of arc-chord distance on local radial turbulent kinetic energy (a) y = 0.25H₂ (b) y = 0.65H₂

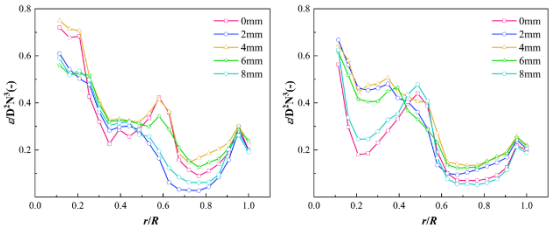

Figure 12. Effect of arc-chord distance on the dissipation rate of local radial turbulent kinetic energy (a) y = 0.25H₂ (b) y = 0.65H₂

5.4. The effect of blade angle

Figures 13 and 14 depict the profiles of dimensionless turbulent kinetic energy and turbulent energy dissipation rate, respectively, for varied blade angles. CBT accomplishes a judicious transition between axial and radial flows through blade angle adjustment. The turbulent kinetic energy and turbulent energy dissipation rate exhibit an initial rise in tandem with an increase in blade angle; however, they exhibit a marginal reduction when the blade angle surpasses a certain threshold. The most noteworthy escalation in both turbulent kinetic energy and turbulent energy dissipation rate is discerned at a blade angle of 50°.

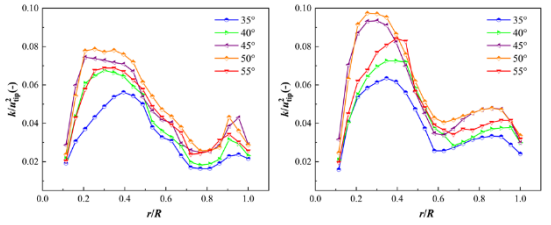

Figure 13. Effect of blade angle on the kinetic energy of local radial turbulence (a) y = 0.25H₂ (b) y = 0.65H₂

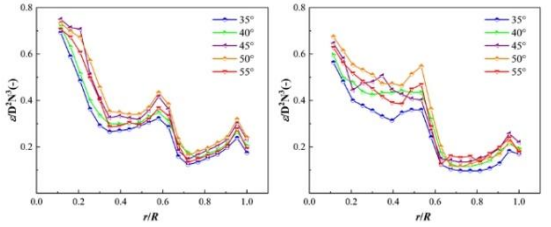

Figure 14. Effect of blade angle on the kinetic energy dissipation rate of local radial turbulence (a) y = 0.25H₂ (b) y = 0.65H₂

5.5. PIV experiments

A CBT with an arc chord distance of 4 mm and a blade angle of 50° was processed and analyzed for PIV experiments. The volume fraction distribution of solid phase particles in the stirred tank is shown in Figure 15, where it can be seen that the particle buildup at the bottom of the CBT is significantly lower than that of the PBT, and the upper clear zone is significantly reduced. Figure 16 shows the velocity distribution of the particles in the stirred tank. It can be seen that the degree of axial circulation of CBT particles is obviously increased, and the transient visible moving particles are obviously increased, which indicates that the suspension effect of particles in the stirring tank of CBT is obviously better than that of PBT, and proves that the analytical results are reliable.

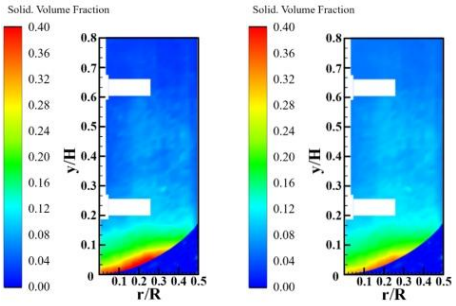

Figure 15. Volume fraction of solid particles measured by PIV (a) PBT (b) CBT

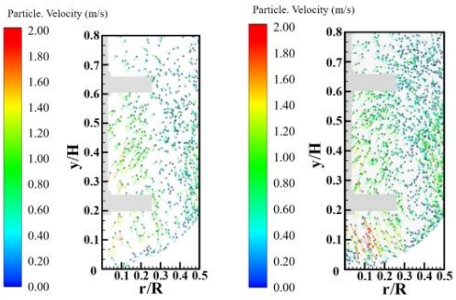

Figure 16. Particle velocity distribution measured by PIV experiment

6. CONCLUSION

In this paper, the MRGP approximation model and EFAST sensitivity analysis method are used to optimize the solid-liquid mixing performance of the double-impeller stirred tank under solid-liquid mixing conditions, and the optimization results are verified by PIV experiments. The main conclusions are as follows:

(1) The CBT impeller generates a high-speed jet during the rotation process, which effectively reduces the wake vortex scale and increases the turbulent kinetic energy and turbulent dissipation rate, thereby improving the solid-liquid suspension quality.

(2) The curved blade parameters significantly impact the solid-liquid mixing performance within stirred tanks. When the arc chord spacing is 4mm and the blade inclination angle is 50°, the mixing performance of the stirred tank can be significantly enhanced while reducing power usage.

(3) In this paper, the influence of arc blade parameters on mixing performance is systematically studied, which provides theoretical guidance for the design of non-standard curved blade turbines in similar stirred tanks.

ACKNOWLEDGEMENTS

This research is supported by the National Natural Science Foundation of China (Grant no. 51706203) and the Natural Science Foundation of Zhejiang Province exploration project (Y,LY20E090004). Thanks to ZJUT for providing computing resources and technical support, The authors also appreciateall other scholars' advice and assistance in improving this article.

REFERENCES

[1] Hu X, Ilgun AD, Passalacqua A, et al. CFD simulations of stirred-tank reactors for gas-liquid and gas-liquid-solid systems using OpenFOAM (R). International Journal of Chemical Reactor Engineering 2021; 19: 193-207. Article.

[2] Ramm P, Terboven C, Neitmann E, et al. Optimized production of biomethane as an energy vector from low-solids biomass using novel magnetic biofilm carriers. Applied Energy 2019; 251. Article.

[3] Fan L, Wang WJ, Yang C, et al. Numerical simulation of laminar flow field in a stirred tank. Chinese Journal of Chemical Engineering 2004; 12: 324-329. Article.

[4] Carletti C, Bikic S, Montante G, et al. Mass Transfer in Dilute Solid-Liquid Stirred Tanks. Industrial & Engineering Chemistry Research 2018; 57: 6505-6515. Article.

[5] Montante G and Magelli F. Modelling of solids distribution in stirred tanks: analysis of simulation strategies and comparison with experimental data. International Journal of Computational Fluid Dynamics 2005; 19: 253-262.

[6] Gu DY, Cheng C, Liu ZH, et al. Numerical simulation of solid-liquid mixing characteristics in a stirred tank with fractal impellers. Advanced Powder Technology 2019; 30: 2126-2138.

[7] Davoody M, Raman AAA, Ahmadi A, et al. Determination of Volumetric Mass Transfer Coefficient in Gas-Solid-Liquid Stirred Vessels Handling High Solids Concentrations: Experiment and Modeling. Iranian Journal of Chemistry & Chemical Engineering-International English Edition 2018; 37: 195-212.

[8] Kumaresan T and Joshi JB. Effect of impeller design on the flow pattern and mixing in stirred tanks. Chemical Engineering Journal 2006; 115: 173-193.

[9] Micheletti M, Nikiforaki L, Lee KC, et al. Particle concentration and mixing characteristics of moderate-to-dense solid-liquid suspensions. Industrial & Engineering Chemistry Research 2003; 42: 6236-6249.

[10] Guha D, Ramachandran PA, Dudukovic MP, et al. Evaluation of large Eddy simulation and Euler-Euler CFD models for solids flow dynamics in a stirred tank reactor. Aiche Journal 2008; 54: 766-778.

[11] Montante G, Paglianti A and Magelli F. Analysis of dilute solid-liquid suspensions in turbulent stirred tanks. CHEMICAL ENGINEERING RESEARCH & DESIGN 2012; 90: 1448-1456.

[12] Wu B. CFD PREDICTION OF MIXING TIME IN ANAEROBIC DIGESTERS. Transactions of the Asabe 2010; 53: 553-563.

[13] Wu BX. COMPUTATIONAL FLUID DYNAMICS STUDY OF LARGE-SCALE MIXING SYSTEMS WITH SIDE-ENTERING IMPELLERS. Engineering Applications of Computational Fluid Mechanics 2012; 6: 123-133.

[14] Liu L, Chen ZB, Yan HJ, et al. Numerical simulation of gas-liquid heat and mass transfer in pressurized leaching stirred tanks[J]. Transactions of Nonferrous Metals Society of China, 2022, 32(10): 3111-3122.

[15] Wang SY, Jiang XX, Wang RC, et al. Numerical simulation of flow behavior of particles in a liquid-solid stirred vessel with baffles. Advanced Powder Technology 2017; 28: 1611-1624.

[16] Liu FC, Wei PF, Tang CH, et al. Global sensitivity analysis for multivariate outputs based on multiple response Gaussian process model. Reliability Engineering & System Safety 2019; 189: 287-298.

[17] Kumaresan T, Nere NK and Joshi JB. Effect of internals on the flow pattern and mixing in stirred tanks. Industrial & Engineering Chemistry Research 2005; 44: 9951-9961.

Conference on Modelling Fluid Flow (CMFF'25)
The 19th International Conference on Fluid Flow Technologies
Budapest, Hungary, August 26 - August 29, 2025

MINIMIZING SEDIMENTATION IN ROUND WASTEWATER PUMPING STATIONS WITH THE ASSISTANCE OF PHYSICAL MODELS

Tim NITZSCHE[1], Horst BAXPEHLER[2], Paul Uwe THAMSEN[3]

[1] Corresponding Author. Chair of Fluid System Dynamics, Faculty of Mechanical Engineering and Transport Systems, Technische Universität Berlin. Straße des 17. Juni 135, 10623 Berlin, Germany. E-mail: tim.nitzsche@tu-berlin.de
[2] Sewer operation, Erftverband, Am Erftverband 6, 50126 Bergheim, Germany E-mail: horst.baxpehler@erftverband.de
[3] Chair of Fluid System Dynamics, Faculty of Mechanical Engineering and Transport Systems, Technische Universität Berlin. Straße des 17. Juni 135, 10623 Berlin, Germany. E-mail: paul-uwe.thamsen@tu-berlin.de

ABSTRACT

Wastewater pumping stations play a crucial role in modern sewage systems by transporting wastewater from lower to higher elevation areas, ensuring a continuous flow to the following pumping stations or treatment facilities. These stations are vital for preventing blockages, overflows, and health hazards associated with untreated sewage. They help maintain the efficiency of sewage systems, safeguarding both public health and the environment.

However, several challenges surround wastewater pumping stations. These stations are frequently susceptible to clogging due to debris, grease, and non-biodegradable materials, which can disrupt their operation. In addition, suction chambers that tend to accumulate extensive sedimentation deposits have to be cleaned more frequently, which requires additional personnel and results in high costs.

In the presented paper, a planned suction chamber concept is scaled using hydraulic similarity principles using the Froude number and checked for its susceptibility to sedimentation. Subsequently, optimisation cycles are carried out in order to minimize the sedimentation that occurs. In the course of this process, inlets, pumps, intake manifolds, sloped walls, among others are analysed and modified with regard to the DWA 120 – „Pumping systems outside of buildings". The average sedimentation in the suction chamber was significantly reduced in the course of this project.

Keywords: physical model, pumping station, sedimentation, wastewater

NOMENCLATURE

d	$[mm]$	Particle size
Fr	[-]	Froude number
Q	$[m^3/s]$	flow rate
Re	[-]	Reynolds number
T	$[s]$	time
v	$[m/s]$	velocity
We	[-]	Weber number
ν	$[m^2/s]$	kinematic viscosity
ρ	$[kg/m^3]$	density
σ	$[N/m]$	surface tension

Subscripts and Superscripts

A	Average
M	model
MAX	Maximum
O	original
P	Peak

1. INTRODUCTION

The coordinated removal of domestic and industrial wastewater and its subsequent treatment is a vital contribution to both public health and a responsible treatment of the environment. An undisturbed wastewater transport through the sewer systems to the treatment plant plays a crucial role in maintaining this flow. Essential components in this system are wastewater pumping stations, which can be used to transport wastewater from the incoming free-flow sewer via pressure pipes to elevated regions. However, due to the high proportion of solids in the composition of wastewater [1, 2], a variety of challenges such as sedimentation, swimming layers, pump clogging [3] or air entrainment [4] occur in pumping stations. In order to implement the most trouble-free and low-maintenance operation possible, special attention must be paid in the design phase to aspects such as the shape of the pit, the layout of the inlet, the geometry of the sloped walls, the pumps and much more. To validate these parameters, an investigation using hydraulic models is recommended [5, 6].

1.1. Wastewater Pumping Stations

Wastewater transport using pressure pipes can be realized by upstream wastewater pumping stations. These structures can vary greatly in size and design. In principle, they can be classified according to the pumps used. Dry-installed pumps are housed in separate machine rooms, as shown in Figure 1a). While this allows easier maintenance and inspection of the machines, it requires increased constructional investment. Wet-installed pumps are placed directly in the suction chamber, as shown in Figure 1b) [7].

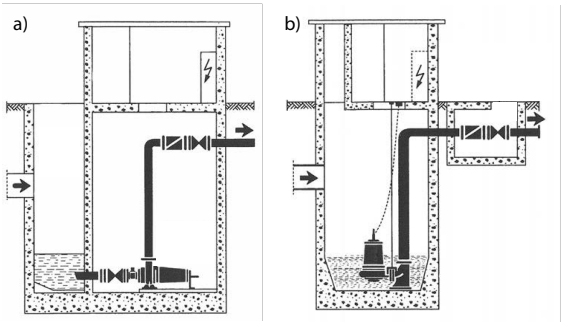

Figure 1. Wastewater pumping station with a) dry-installed and b) wet-installed pumps [7]

The pumping station described in this paper is a variant with dry-installed pumps. The relevant standards contain recommendations for these systems for pumps positioned next to each other. This constellation often results in a suction chamber which is rectangular in shape and provides increased opportunities for particle deposits around the edges. In order to achieve a higher flow velocity and thus better activation of particles, a circular suction chamber with dry-installed pumps was developed as the initial concept. A central cone was used to increase particle movement and prevent the formation of a swimming layer in the outer channel. A schematic top view of the pump station is shown in Figure 2a). A sectional view is shown in Figure 2b). Dashed arrows symbolize the wastewater flow in both illustrations from inlet to the pumps. The left and middle outlets represent the two rainwater pumps, and the right pipe shows the position of the dry weather pump.

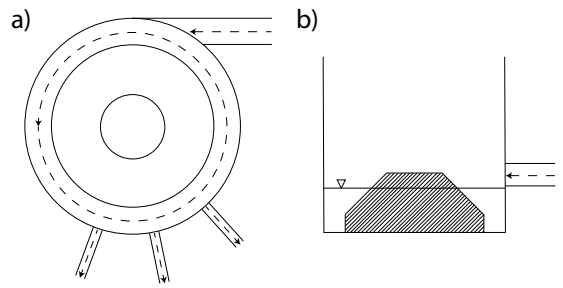

Figure 2. Concept of a round suction chamber with central cone, a) top view, b) sectional view

The connection to the wastewater network takes place in two stages over several years, during which the number of inhabitants covered increase. In order to cover the two operating requirements, both expansion stage 1 with a lower incoming volume flow and expansion stage 2 with an increased flow are taken into consideration in the following investigations.

2. METHOD

2.1. Dimensioning

In order to carry out a fluidic analysis using a hydraulic scaled model, a calculation according to the relevant similarity laws is of immense importance. For an application with free water surfaces, as it is the case in the suction chamber under consideration, modelling according to the Froude similarity, which shows a ratio of inertial force to gravitational forces, is suitable [8, 9].

$$Fr = \frac{v}{\sqrt{g \cdot D}} \tag{1}$$

In order to calculate the similarity, the Froude numbers of the original and the model must remain identical [8, 9].

$$\frac{Fr_M}{Fr_G} = 1 \tag{2}$$

When determining the scaling dimension, viscosity effects and surface tensions must be taken into account. By including the Reynolds number Re and Weber number We, scaling limits can be identified [6].

Inertial and viscous forces are considered using the Reynolds number Re.

$$Re = \frac{v \cdot D}{\upsilon} \tag{3}$$

The Weber number We is used to account for inertia and surface forces.

$$We = \frac{v^2 \cdot D \cdot \rho}{\sigma} \tag{4}$$

Recommendations for value limitations for the selection of these two key figures can be found in the relevant literature. According to [6, 10], the Reynolds number should be in a range of $Re > 3x10^4$ and the Weber number should be greater than $We > 120$. An additional safety factor of 2 is recommended for both values.

The geometrical similarity must likewise be maintained. In this context, all dimensions od the systems under consideration must be in a fixed ratio to reach other [8].

$$M = \frac{L_M}{L_O} = const. \quad (5)$$

Table 1 provides the conversion of various dimensioning parameters between the model and the original.

Table 1. Froude similarity scaling rules [9]

Parameter	Conversion
Lengths	$L_O/L_M = M$
Areas	$A_O/A_M = M^2$
Velocities	$v_O/v_M = M^{1/2}$
Times	$T_O/T_M = M^{1/2}$
Flow rates	$Q_O/Q_M = M^{5/2}$
Forces	$F_O/F_M = M^3$

2.2. Test Rig Design

After applying the design parameters presented in advance, a scaling factor of 1:3.66 was selected. In order to be able to observe comprehensive sedimentation investigations, the suction chamber was constructed out of transparent polyvinyl chloride (PVC) and methyl methacrylate (PMMA). In addition, a water supply network with a water supply tank and speed-controlled pumps were implemented to enable different volume flows and water levels in the modelled suction chamber. A particle injection and filter were installed as well. All components assembled form the test rig are shown in Figure 3.

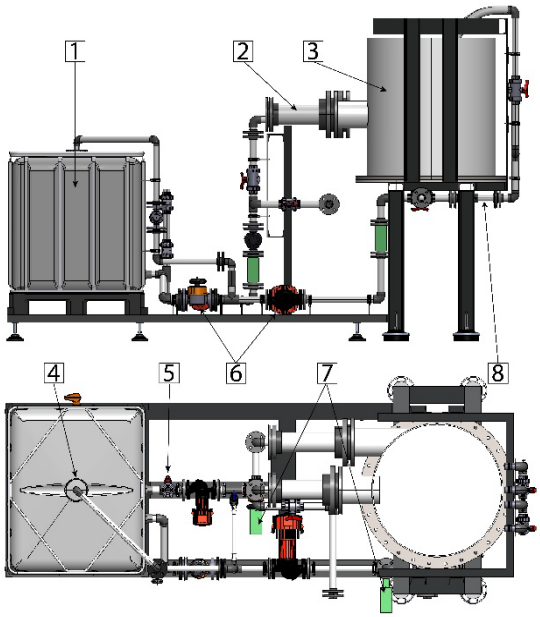

Figure 3. Test rig

The components shown in the graphic include 1) the water supply tank, 2) inlet pipe into the model tank, 3) the model tank, 4) particle filter, 5) particle injection chamber, 6) pumps, 7) magnetic-inductive flow meter, 8) suction pipe exciting the model tank. The inlet and outlet pipes as well as the pumps are fitted with additional connecting pipes to ensure a dispensing of air of the individual lines.

The selected resulted scale of the model tank is shown in Table 2.

Table 2. Model suction chamber dimensions

Parameter	Value
Scale	1:3.66
Diameter	0.93 [m]
Height	1.46 [m]
Volume	0.99 [m^3]
Number of Pumps	3

2.3. Artificial Wastewater

The composition of particles in wastewater systems has been subject of numerous studies. Crabtree [1] created a classification of different sediments, which was expanded by Kirchheim [2]. Further investigations regarding the wastewater medium were conducted by Mitchell in [3]. Table 3 shows a selection of the particles found in sewer systems.

Table 3. Selection of wastewater particles

Label	Density ρ [kg/m^3]	Particle size d [mm]
Gravel, sand, sludge	1,000-2,150	0.4-15
Fine sand	1,230-2,000	0.5-9

As the sources describe very high deviations in the weight and density of the respective particles, depending for example on the time of year and the catchment area, different coloured plastic granules were selected to illustrate the different particle behaviour. Red granulate, which is shown in Figure 4a), with a density of 1,080 [kg/m^3] describes fine sand. Heavy black granulates, which is shown in Figure 4b), with a density of 1,470 [kg/m^3] represents heavy particles.

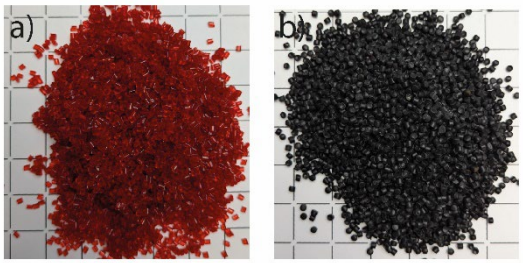

Figure 4. Sediments used to replicate artificial wastewater a) light granulate, b) heavy granulate

The purpose of the particles used is not to achieve an accurate representation of the wastewater, due to its high deviation of particles, but to identify zones with average high sediment accumulations. By using two different types of particles, it is easier to visualise the deposition areas of lighter and heavier sediments. Optimisation of these areas can be achieved in subsequent steps.

2.4. Experimental Procedure

The test sequences are based on a realistic pumping station operation. The inlet volume flows and pump volume flows are applied based on the average daily hydrograph. The average dry-weather discharge Q_A, the expected dry-weather peak Q_P and the maximum volume flow during a rain event with mixed water inflow Q_{MAX} provide the operating points under consideration. The scaled values of the inflow, respective pump flow and the corresponding activation and deactivation levels of the two expansion stages can be found in Table 4.

Table 4. Parameters of used volume flows and water levels

Expansion stage 1	Q_A	Q_P	Q_{MAX}
Inflow [l/s]	0.71	1.24	2.49
Outflow [l/s]	1.99	1.99	2.40
Activation level [m]	0.22	0.22	0.30
Deactivation level [m]	0.11	0.11	0.11
Expansion stage 2			
Inflow [l/s]	1.24	3.11	4.56
Outflow [l/s]	3.00	3.00	4.40
Activation level [m]	0.27	0.36	0.42
Deactivation level [m]	0.11	0.11	0.11

At the respective operating point, a constant inlet volume flow fills the model tank. When the defined activation level is reached, the respective pump is switched on and discharges water from the tank until the water level reaches the deactivation level. Filling and draining the tank between these two levels is referred in the following as a pump iteration. When carrying out experiments, a defined quantity of red and black particles is added to the inlet flow, which are collected again with a filter unit at the end of the test rig. 420 g red particles and 267 g of black particles, which correspond to a poured volume of 600 ml and 300 ml in the respective cases, are used. The particle injection takes place in the active inlet flow during the first pump iteration. After a thorough review phase, the maximum number of pump iterations was set to 10. In almost all cases, particle movement could hardly be observed after the intervals had elapsed. If all particles are removed from the model tank before the tenth pump cycle is reached, it is regarded as a stop criterion. At the end of the test, the black and red particles are removed from the filter, separated, dried and then weighed.

In addition, to the validation of the discharged particles, remaining sediments in the model tank are documented. To ensure a precise description of the deposition formation, the base of the test setup was marked as illustrated in Figure 5.

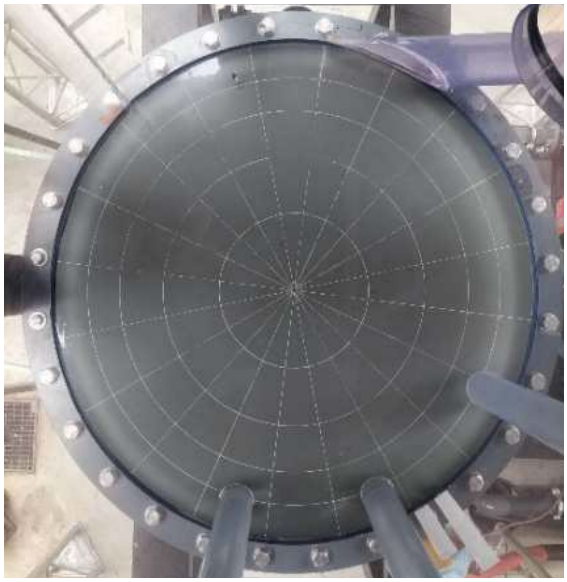

Figure 5. Marked model tank base

These investigations help to understand the basic behaviour of the pump sump and to identify the isolated influence of volume flows and water levels on the particles.

3. RESULTS

3.1. Modification A

Modification A is the implementation of the concept of a suction chamber with a central cone presented in chapter 1.1., which is illustrated in Figure 6.

Figure 7 shows the sketched particle deposits after ten pump iterations during operation in expansion stage 1. As depicted in Figure 7a), both the lighter red particles and the heavier black particles sediment immediately after reaching the pump sump. The detachment of some particles and the movement along the clockwise direction, i.e. against the intended flow direction in the channel to the pumps, can be seen. During operation, the suction flow of the pump dominates and activates a part of the sedimented particles. In Figure 7b), when using a higher volume flow of Q_P, an activation of red particles towards the pumps can be seen. However,

due to the channel flow that appears, sedimentation zones form again in the area of the cone, which cannot be broken down. Nevertheless, the flow conditions in the pump sump are not yet sufficient to activate the black particles. As expected, the best effect can be observed during a rain event with a volume flow of Q_{MAX} depicted in Figure 7c). Both types of particles were almost completely removed.

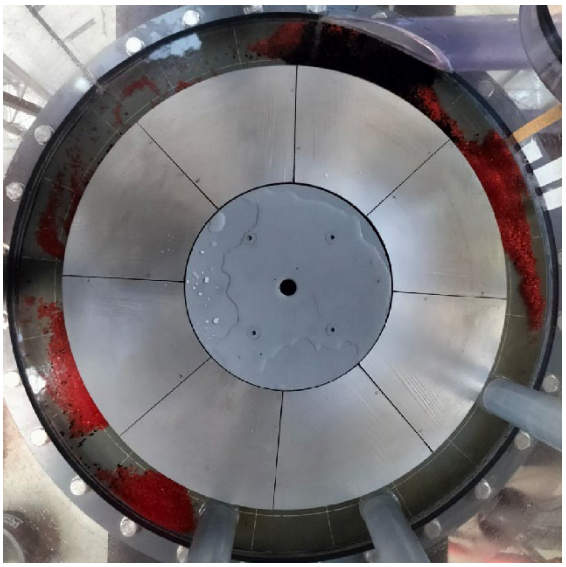

Figure 6. Round suction chamber with a central cone

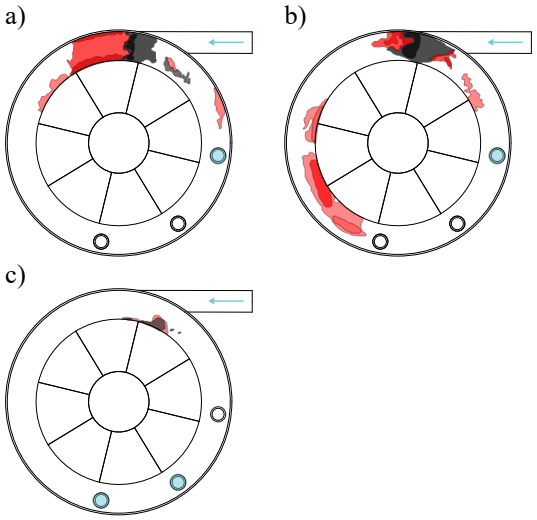

Figure 7. Outline of the particle depositions in expansion stage 1 at a volume flow of a) Q_A, b) QP and c) Q_{MAX}

Figure 8 shows the discharges particle quantities in percent of the respective investigations.

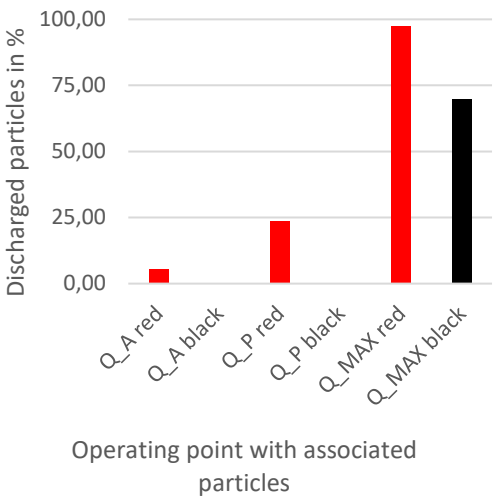

Figure 8. Percentage of discharges particles at expansion stage 1

For the subsequent expansion stage 2 with a higher volume flow, a significantly better movement of the particles can be observed compared to expansion stage 1. During operation at Q_A in Figure 9a), activation of the light sediments can already be seen. However, the heavier black sediments still did not reactivate. Significantly higher discharge quantities of particles were achieved in operation at Q_P as shown in Figure 9b). As in the previous expansion stage 1, almost all particles could be discharges from the model at the high-volume flow Q_{MAX} during a rain event as illustrated in Figure 9c).

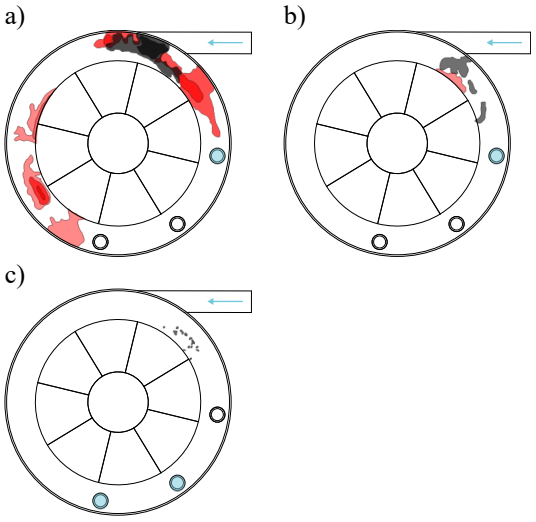

Figure 9. Outline of the particle depositions in expansion stage 2 at a volume flow of a) Q_A, b) QP and c) Q_{MAX}

A significantly better removal of the particles in expansion stage 2 is also underlined by the increased discharge quantities shown in Figure 10.

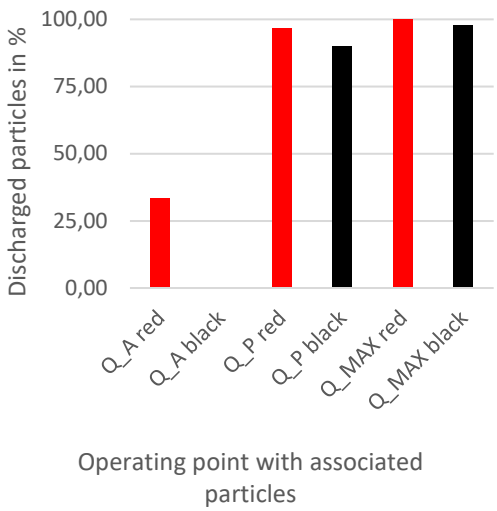

Figure 10. Percentage of discharges particles at expansion stage 2

In the course of further investigations, several additional concepts were developed and examined. These included, among other things:

- Test series with different pump positions
- Eccentric cone placement
- Increasing of the cone diameter

Even though some of the measures listed were able to remove higher quantities of particles, it was not possible to achieve a conversion with a complete particle removal after ten pump iterations in any of the test series. For this reason, a fundamentally different modification was implemented.

3.3. Modification B

Modification B follows the approach of making maximum use of the vortex created by the tangential inflow and the particle transport it supports. Figure 11 shows the particle transport for a) Q_A, b) Q_P, c) Q_{MAX} without built-in sloped walls. Even without installations, a clear movement of the particles towards the center of the model tank can be observed.

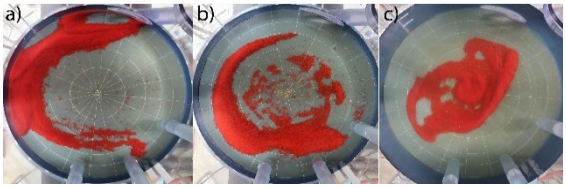

Figure 11. Particle transport with tangential inflow at a) Q_A, b) Q_P and c) Q_{MAX}

Based on this idea, a circular suction chamber with three dry-installed pumps was developed, in which the pump positions are shifted by 45°. Movable pipes make it possible to vary the positions of the individual suction intakes and to investigate different considerations, such as a central suction intake or three intakes at an identical distance from the center. A design layout with a) top view and b) sectional view is given in Figure 12.

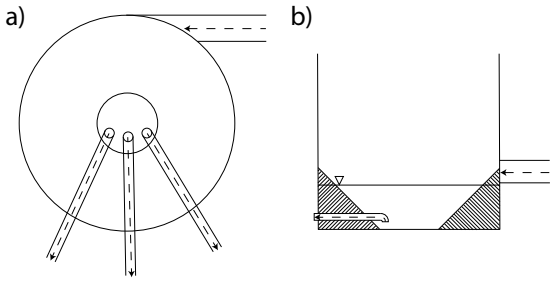

Figure 12. Design of Modification B, a) top view, b) sectional view

The investigations with the new pump sump design started with the test series of expansion stage 1 with the lowest volume flow Q_A. All particles were discharges from the suction chamber after just the third pump iteration. Figure 13 shows a view from below of the model tank after a) one, b) two and c) three pump iterations.

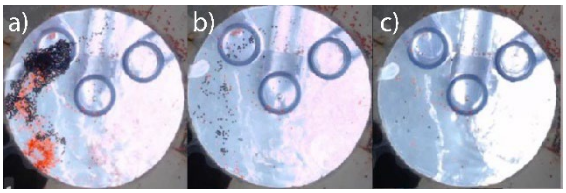

Figure 13. View from below into the model tank at a volume flow Q_A and a) one, b) two, c) three pump iterations

The high discharge performance was maintained across all test scenarios at operating point Q_A, Q_P and Q_{MAX} for both expansion stage 1 and expansion stage 2.

3.4. Comparison of Results

Modification A showed good results in removing the particles at higher volume flows Q_{MAX} and partially Q_A. However, with the exception of rain events, it was never possible to completely remove all particles within ten pump iterations. Even further optimizations of modification A could only show partial improvements.

The use of modifications B resulted in a significant increase in particle removal. Even at expansion stage 1 with volume flow Q_A, it was possible to achieve early test termination due to complete particle discharge.

In further investigations, an adjustment of the activation and deactivation level as well as a flow simulation of the pump sump should be aimed for.

4. CONCLUSION

It was shown that hydraulically scaled model investigations are a very efficient tool for the validation and optimization of a wastewater pumping station with regard to sedimentation. Numerous parameters can be varied and evaluated for their influence.

REFERENCES

[1] Crabtree, R. W.. *A Classification of combined sewer sediment types and characteristics*, 1988

[2] Kirchheim, Norma. *Kanalablagerungen in der Mischkanalisation*, 2005

[3] Mitchell, R. L., 2019, "Causes, Effects and Solutions of Operational Problems in Wastewater Systems Due to Nonwoven Wet Wipes", *Dissertation Technische Universität Berlin, Fakultät V Verkehrs- und Maschiensysteme*

[4] Ackl, R. A., 2018, "Enhancing the Design of the Wet Pit Pumping Stations Based on Experimental and Numerical Investigations", *Dissertation Technische Universität Berlin, Fakultät V Verkehrs- und Maschiensysteme*

[5] DWA-Regulation, DWA-A 120 - 2 *Pumpsysteme ausserhalb von Gebäuden – Teil 2 Pumpstationen und Drucksysteme,* 2022

[6] ANSI/HI 9.8-2018, 2013, "American National Standard for Rotodynamic Pumps for Pump Intake Design"

[7] Surek, D., 2014, *Pumpen für Abwasser- und Kläranlagen*, Springer Fachmedien Wiesbaden

[8] Surek, D., Stempin, S., 2017, *Technische Strömungsmechanik*, Springer Fachmedien Wiesbaden

[9] Strobl, T., Zunic, F., 2006, *Wasserbau*, Springer Berlin Heidelberg

[10] Heller, V., 2011, "Scale Effects in physical hydraulic engineering models", *Journal of Hydraulic Research,* Vol. 49, No. 3, pp. 293-306

Conference on Modelling Fluid Flow (CMFF'25)
The 19th International Conference on Fluid Flow Technologies
Budapest, Hungary, August 26-August 29, 2025

CFD MODELLING OF THE THERMO- AND HYDRODYNAMIC CAPABILITIES OF LONG-NECKED PLESIOSAURS (REPTILIA, SAUROPTERYGIA)

Miguel MARX[2], Róbert-Zoltán SZÁSZ[1], Johan LINDGREN[3]

[1] Corresponding Author. Department of Energy Sciences, Lund University. PO.Box 118, S-22100, Lund, Sweden. Tel.: +46 46 222 0480, E-mail: robert-zoltan.szasz@energy.lth.se
[2] Department of Geology, Lund University. E-mail: miguel.marx@geol.lu.se
[3] Department of Geology, Lund University. E-mail: johan.lindgren@geol.lu.se

ABSTRACT

Plesiosaurs are secondarily aquatic reptiles with a fossil record that extends for over 140 million years, and their remains have been found in localities representing both warm, equatorial waters and cold, high-latitude environments. They are usually portrayed as a snake threaded through the body of a sea turtle. However, due to a general absence of preserved soft tissues, reconstructing the life appearance of particularly long-necked forms is anything but a straightforward task. Moreover, animals with such an oddly-shaped body are unlikely to survive in cold-water environments. To investigate the ability of these ancient marine reptiles to inhabit high-latitude waters, we examined the heat transfer in two virtually reconstructed plesiosaurs: one built according to conventional wisdom (i.e., with a long and narrow neck) and one equipped with a peripheral layer of insulating blubber. We compared several modelling approaches (gradually increasing the complexity of our approach) to assess their pros and cons. We also investigated the temperature distribution within the two body types and tested their hydrodynamic performance by simulating a cruising plesiosaur at a steady velocity. The results of our endeavours show that an insulating blubber layer must have been present to assure a suitable temperature distribution within the plesiosaur body when it inhabited cold water regions.

Keywords: blubber, heat transfer, plesiosaurs, temperature distribution

NOMENCLATURE

c_p	$[J/(kg\,K)]$	specific heat at constant pressure
L	$[m]$	length
MR	$[W/kg]$	metabolic rate
R	$[m]$	radius
T	$[K]$	temperature
t	$[s]$	time
q	$[W/m^3]$	heat source
α	$[m^2/s]$	thermal diffusivity
κ	$[W/(m\,K)]$	heat conductivity
ϕ	$[W/m^2]$	heat flux per unit area
ρ	$[kg/m^3]$	density

1. INTRODUCTION

Palaeontology is an interdisciplinary science that incorporates methods from various fields, including Computational Fluid Dynamics (CFD) [1]. Plesiosaurs (an iconic group of Mesozoic marine reptiles) have garnered some attention in recent years due to their peculiar body shape (long neck, turtle-like body, and four flippers), making them interesting subjects for CFD analyses [2, 3]. While some experiments have been conducted on their swimming performance [2, 3], little is known about their thermodynamic capabilities. Notably though, plesiosaur fossils have been recovered from high-latitude environments [4, 5], to suggest that they were capable of surviving in cold water regimes, something that likely would have necessitated some sort of insulation. Modern whales and even a species of sea turtle (*Dermochelys coriacea*; the Leatherback turtle) utilize a combination of high metabolism, large body size and blubber (a peripheral insulating tissue) to resist the effects of cold water. Blubber was apparently also present in at least some derived ichthyosaurs, another group of extinct marine reptiles [6]. Thus, we hypothesize that plesiosaurs, in which endothermy (warm-bloodedness) has been proposed [7, 8, 9], likewise employed some sort of peripheral tissue layer to enable life in cold water environments.

Modelling heat transfer in an animal poses a number of challenges. To start with, there are several body regions (e.g., muscles, the brain) with heat production that are hard to assess. The heat conductivity of tissues is also difficult to measure accurately, and the circulatory system that regulates heat transfer

between different body parts is challenging to model [10]. Furthermore, if a species is extinct, then the required parameters have to be estimated from analogies in living animals.

Several models are available that replicate physical phenomena involved in heat transferring processes. However, by adding more details, the complexity of the models is amplified, in turn increasing both the required computing resources and human efforts to set-up and analyse the cases. Furthermore, when there are several unknown parameters, a model with increased complexity does not necessarily yield better results.

The purpose of this study is to compare modelling approaches at different levels of complexity to simulate a plesiosaur living in a cold water environment. We also test the effects of an added blubber layer on hydrodynamic drag.

2. METHODS

2.1. One-dimensional analysis

The simplest model assumes that the blubber layer thickness is small relative to the surface area of the skin. For such a condition, the heat transfer through the blubber can be presumed to be one-dimensional and thus assessable by Fourier's law of heat conduction (Eq. 1). Fourier's law can be used, e.g., to estimate the heat flux if the heat conductivity, blubber thickness and temperature difference between the surrounding environment and inner body temperature are known.

$$\phi = -\kappa \frac{\Delta T}{\Delta x} \tag{1}$$

For this initial model, blubber thicknesses and thermal conductivity values for various whale species were adapted from [10, 11] and references therein. Leatherback turtle blubber thickness was obtained from [12], and the thermal conductivity value was assumed to be 0.24 $W/(m\,K)$. The thermal conductivity value for human fat was acquired from [11].

2.2. Cylindrical model

Due to their overall elongate body form, the heat transfer characteristics of several marine animals were investigated by assuming a cylindrical shape. For example, Hokkanen [10] studied the temperature regulation of marine mammals using such a model. By neglecting end-effects, heat transfer can be evaluated in one (radial) direction. This model has the advantage of considering volume and surface area effects compared to the one-dimensional model presented in the previous sub-section.

Here, we estimated the heat flux transferred across a blubber layer with an inner radius R_{in} and outer radius R_{out} for an animal of length L using Eq. 2[13].

$$Q = 2\pi\kappa L \frac{\Delta T}{ln(R_{out}/R_{in})} \tag{2}$$

The heat flux was calculated using body dimensions of the modern Right whale [10, 14], Harbour porpoise [10, 15], Leatherback turtle [12, 16], and two plesiosaur models: one with a thin (1 cm) layer of blubber and a second geometry with a thicker (7 cm) layer of blubber; the required parameters being adopted from [10, 12, 14]. The total length of the plesiosaur cylinder model was set to 11.7 meters based on a reconstruction of the extremely long-necked elasmosaurid, *Albertonectes vanderveldei* (TMP 2007.011.0001).

2.3. 3D heat conduction

Heat conduction in an arbitrary three-dimensional geometry, which can include heat sources, can be investigated by solving the Poisson equation (Eq. 3). For this purpose, the laplacianFoam solver implemented in OpenFOAM v.2306 [17] was used.

$$\frac{\partial T}{\partial t} = \nabla \cdot (\alpha \nabla T) + \frac{q}{\rho\, c_p} \tag{3}$$

Two plesiosaur geometries were constructed using FreeCAD [18]: one without blubber and a second one coated in an insulating layer (based on actual blubber thicknesses of the Leatherback turtle [12]). The total length of the geometry was set to 11.7 meters. The thickness of the muscle tissues encasing the skeleton was approximated from comparisons with modern reptiles [19, 20, 21]. In the blubber-coated model, this peripheral tissue was added to all parts of the body except the flippers. Figure 1 shows a perspective view of the reconstructed geometry without (top) and with blubber (bottom).

The heat conductivity of blubber ($\approx$ 0.30 $W/(m\,K)$) is significantly lower than that of muscles ($\approx$ 0.57 $W/(m\,K)$) [10]; therefore, it is important to investigate the impact of regions with different heat conductivity on the resulting thermal balance. Furthermore, the heat source in the present case is due to metabolism, which depends on the activity level of the animal [22].

As a result, a third geometry was created to include simplified viscera (internal organs), arteries and a brain (which, for simplicity, hereafter is referred to as the 'organ region'). This simplified region is located inside the reconstructed plesiosaur body as shown in Figure 2. The division of the geometry into multiple regions primarily affects the mesh generation process. At the interfaces separating the regions, internal boundaries (referred to as 'baffles' in OpenFOAM terminology) are introduced. Additionally, the mesh is refined in these regions to better capture temperature gradients. From the solver's perspective, the entire mesh remains as a single computational domain; the purpose of the

various regions is solely to assign different material properties.

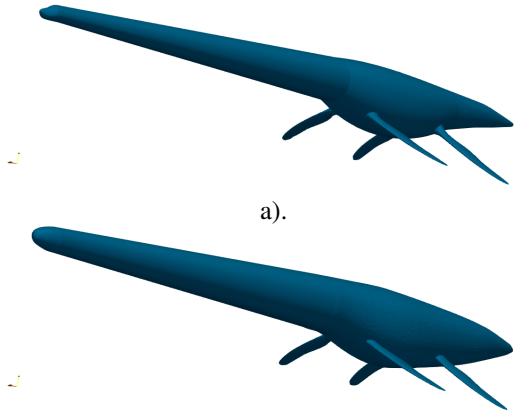

a).

b).

Figure 1. Perspective view of the adopted plesiosaur geometry a) without and b) with blubber.

Figure 2. Side view of the adopted plesiosaur geometry with the internal region marked in red.

Tissues in the geometries were assigned thermal conductivity values reported for extant marine animals: muscle and organ region (0.57 $W/(m\,K)$) [10], and blubber (0.30 $W/(m\,K)$) [10, 11, 22]. In certain cases, the thermal conductivity of the blubber was adjusted to 0.57 $W/(m\,K)$ to replicate vasodilation of the circulatory system in the blubber tissue [23], since this is a known physiological adaptation of marine animals [10, 24]. A specific heat of 3.75 $kJ/(kg\,K)$ was applied to all tissues [22]. Two different metabolic rates were assigned to the models: a lower rate ($MR = 0.083\ W/kg$) corresponding to an inactive cold blooded animal, and an elevated value ($MR = 1.51\ W/kg$) typical of a Leatherback turtle exercising [24]. The heat-generating regions were either assigned to the entire body or only to the organ region. A metabolic rate was not, however, assigned to the blubber as this is not a heat generating tissue. A water temperature of $12\,^oC$ ($285.15\,K$) was chosen because it is comparable to what *A. vanderveldei* would have experienced [4]. Prescribing the water temperature directly on the skin neglects the thermal boundary layer formed in the water in the immediate vicinity of the body. As a consequence, the cooling effect of the water is over predicted. Nevertheless, according to the analysis in [10], the associated error likely is small.

2.4. Hydrodynamic force computations

In addition to heat balance, an added blubber layer affects the hydrodynamic forces acting on the body. In order to estimate this impact, two additional computations were performed. The flow around the two plesiosaur geometries was solved using the simpleFoam solver included in OpenFOAM v.2306. The pressure-velocity coupling is based on the SIMPLE algorithm (see, e.g., [25]). The computational domain extended from (-40 m, -25 m, -25 m) to (100 m, 25 m, 25 m) (Figure 3), the model being located at (0,0,0). The k-omega SST turbulence model developed by Menter [26, 27] was employed. The velocity magnitude was set to 1.5 m/s; i.e., close to the estimated cruising speed of other extinct marine reptiles [28]. A sensitivity study involving grids with 1.2, 3.0, 9.1, and 31.4 million cells indicated that 9.1 million cells were sufficient for our purposes.

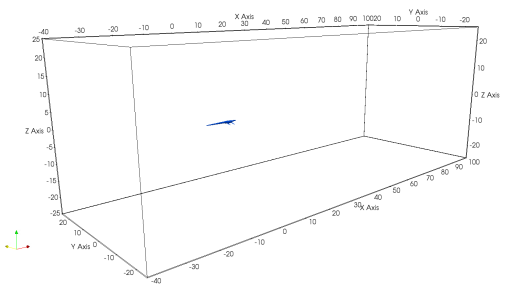

Figure 3. The computational domain used in our flow computations.

3. RESULTS

3.1. One-dimensional analysis

The effects of blubber thickness and the thermal conductivity of this tissue can be clearly seen in Figure 4. The proportionally thin layer of fat in a human allows for a larger heat flux relative to fluxes predicted for cetaceans that have both thicker blubber and lower thermal conductivity values. Notably, a plesiosaur inhabiting cold water environments would benefit from possessing a peripheral layer of insulating blubber.

3.2. Cylindrical model

Using Eq. 2, the total heat flux was estimated for two versions of the modelled plesiosaur (one with and one without blubber), as well as for a number of comparative extant tetrapods. The adopted parameters and the estimated heat fluxes for an assumed temperature difference of $\Delta T = 20\,K$ are summarized in Table 1.

A Northern right whale (a species that is well-adapted for life in cold waters) at approximately the same length as our modelled plesiosaur (~12 meters), but with a greater volume and blubber thickness, has a significantly lower heat flux compared to the plesiosaur version without blubber. An addition of seven

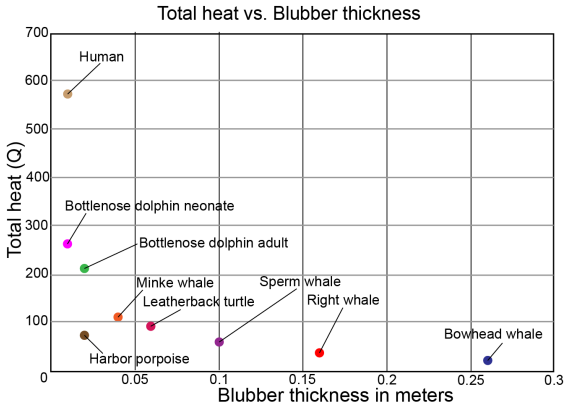

Figure 4. Predicted heat flux values for select extant tetrapods.

Table 1. Heat flux predicted for plesiosaurs and select modern animals.

Animal	R_{out} $[m]$	R_{in} $[m]$	L $[m]$	κ $[\frac{W}{mK}]$	Q $[W]$
Harbour porpoise	0.08	0.06	1.6	0.1	70
Right whale	1.45	1.29	12	0.3	3867
Leatherback Turtle	0.52	0.45	2	0.3	1093
Plesiosaur (no blubber)	0.43	0.42	11.7	0.3	18736
Plesiosaur (blubber)	0.49	0.42	11.7	0.3	2860

centimetres of blubber (which is similar to the blubber layer covering an adult Leatherback turtle) to the plesiosaur model significantly reduces the heat flux to an order of magnitude that is comparable to that of the other considered species. This reduction suggests that plesiosaurs would have benefited from an insulating blubber layer.

3.3. Three-dimensional heat transfer calculations

The purpose of these computations was to investigate the temperature within the plesiosaur body in a variety of scenarios. In all simulations, the water temperature was set to 12^oC. Moreover, based on experiments conducted on hatchling sea turtles [29], the lowest temperature that a plesiosaur probably could comfortably tolerate is 15^oC, whereas the highest temperature is 40^oC. Hence, the color scales used in the figures that follow span the 12–40^oC interval (i.e., 285.15–313.15 K) (Optimal temperatures are considered to be regions coloured either dark-blue or red).

There are two important regions to consider. Firstly, due to the long and narrow neck, the water might cool the brain to dangerously low temperatures. Secondly, the torso has a low surface area-to-volume ratio, and thereby may be prone to overheating.

We investigated the impact of the main parameters (such as the metabolic rate, heat conductivity and presence of a peripheral blubber layer) on the temperature distribution in the body. Additionally, a case with three regions was set-up, where the effect(s) of enhanced heat transfer due to an introduced circulatory system was modelled, albeit in a simplified manner.

3.3.1. Influence of metabolic rate

The impact of metabolic rate on the temperature distribution was evaluated for a model without blubber. Two extreme cases were considered: one corresponding to an inactive individual (MR = 0.083 W/kg) and one to a highly active animal (MR = 1.585 W/kg). In both cases, the heat conductivity was set to 0.57 $W/(m\,K)$.

In the low activity case (Fig. 5), the temperatures across the body are suboptimal, the head and neck essentially being of the same temperature as the surrounding water. It is exceedingly unlikely that a plesiosaur would have survived under such conditions over an extended period of time. Conversely, in the high-activity case, the temperatures are closer to optimal in the brain region; however, in the torso they are too high for comfort.

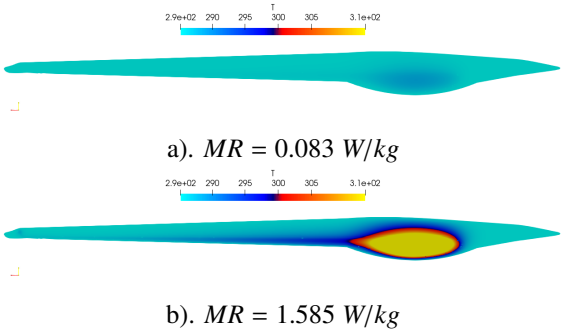

a). MR = 0.083 W/kg

b). MR = 1.585 W/kg

Figure 5. Temperature distribution in a plesiosaur model without blubber at low a) and high b) metabolic rates, respectively (κ = 0.57 $W/(m\,K)$).

3.3.2. Influence of heat conductivity

The heat conductivity can vary not only between tissues, but also for the same tissue depending, e.g., on the influence of the circulatory system. Three values were considered. The lowest one (κ = 0.30 $W/(m\,K)$ is typical for blubber [10], whereas the second one (κ = 0.57 $W/(m\,K)$) is representative of muscles. The third considered value (κ = 2.0 $W/(m\,K)$) was adopted to mimic improved heat transfer by convection effects caused by the circulatory system.

Figure 6 shows the temperature distribution for the low metabolic rate case. As expected, higher heat conductivity values lead to a more uniform heat distribution, but also to a stronger cooling effect in the torso region.

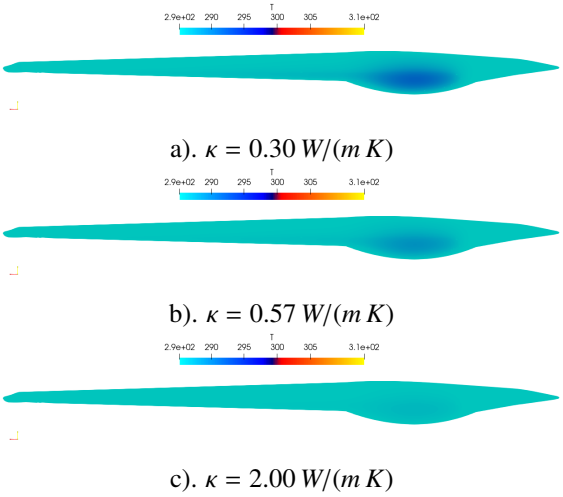

a). $\kappa = 0.30\ W/(m\,K)$

b). $\kappa = 0.57\ W/(m\,K)$

c). $\kappa = 2.00\ W/(m\,K)$

Figure 6. The impact of heat conductivity on the temperature distribution in the plesiosaur without blubber. $MR = 0.083\ W/kg$

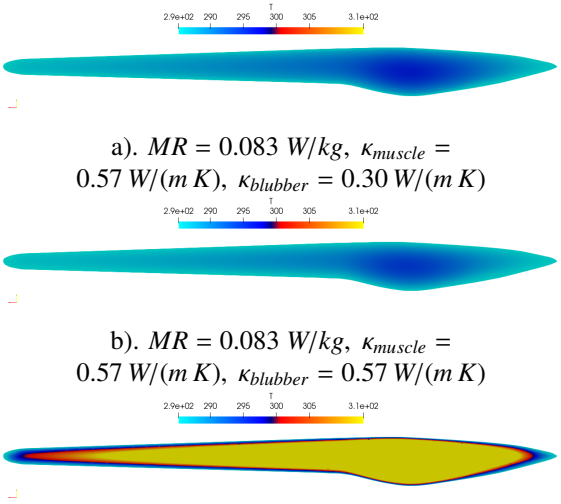

a). $MR = 0.083\ W/kg$, $\kappa_{muscle} = 0.57\ W/(m\,K)$, $\kappa_{blubber} = 0.30\ W/(m\,K)$

b). $MR = 0.083\ W/kg$, $\kappa_{muscle} = 0.57\ W/(m\,K)$, $\kappa_{blubber} = 0.57\ W/(m\,K)$

c). $MR = 1.51\ W/kg$, $\kappa_{muscle} = 0.57\ W/(m\,K)$, $\kappa_{blubber} = 0.57\ W/(m\,K)$

Figure 7. Impact of blubber layer on the temperature distribution.

3.3.3. Influence of blubber

The temperature distribution of a plesiosaur model covered by an external blubber layer was evaluated for a number of metabolic rates and heat conductivity values. In Figure 7, three parameter combinations are depicted.

Figure 7a shows the temperature distribution in a low metabolic rate case. Here, the heat conductivities are typical of muscle and blubber tissues. Compared to the corresponding setup of the case without blubber (Fig. 6a), it is noticeable that there are more favourable temperatures in most parts of the body. Nevertheless, in the brain region, the predicted temperatures are still very low.

In the second case (Fig. 7b), the blubber heat conductivity is increased to $0.57\ W/(m\,K)$. Such a condition could mimic, e.g., improved heat transfer due to vessel dilatation. As expected, there is a stronger cooling effect in the body, but the temperatures are still more viable than in the case without blubber (Fig. 6b).

The third case is characterised by a high metabolic rate (Fig. 7c). Even if the blubber heat conductivity is set to higher values (typical of muscles), and therefore a more intense cooling is assumed, the predicted temperatures for most parts of the body remain too elevated, suggesting that the analysed metabolic rate is too high for the adopted blubber layer thickness.

3.3.4. Three-region model

Heat transfer due to convection by blood is an important phenomenon that is difficult to account for. Due to the range of the involved scales, an explicit computation, even if restricted to the larger diameter parts of the vascular system would still be too demanding from a computational point of view. Accordingly, here we employed a simplified approach where the convective heat transfer by the vascular system is accounted for by an increased heat conductivity coefficient. According to Hokkanen [10], realistic blood flow rates are in the range of 1–4 $kg/(m^3\,s)$ which cause a heat transfer of approximately 4000–16000 $W/(m^3\,K)$. By dimensional analysis, the adopted heat conductivity coefficient ($\kappa = 2\ W/(m\,K)$) results in cross sectional area magnitudes of 125–500 mm^2, which are reasonable, given the size of the animal (the largest diameter of the torso is approximately 1 m).

In the three-region set-up, the outermost region corresponded to blubber ($\kappa = 0.30\,W/(m\,K)$), the middle region muscle ($\kappa = 0.57\ W/(m\,K)$) and the inner region was adjusted for higher heat transfer rates ($\kappa = 2\,W/(m\,K)$). The metabolic rate was set to a high level ($MR = 1.51$); however, heat was generated only in the core region of the body. The resulting temperature distribution is shown in Figure 8. One may notice the relatively strong heat transfer in the inner region (compare, e.g., with Fig. 5b), which results in more favourable temperatures in the brain region. In the torso, the temperatures remain elevated, to suggests that an added blubber layer likely is unnecessary in this region.

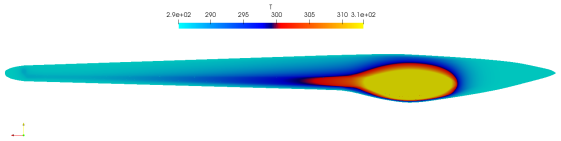

Figure 8. Temperature distribution in the three-region model.

3.3.5. Summary of the three-dimensional cases

A quantitative summary of the three-dimensional cases is shown in Figure 9, where the recorded temperatures are plotted at two monitoring points: the first one located near the brain and the second one located close to the centre of the torso. For reference, the inferred minimum and maximum viable temperatures are also plotted. There are several cases where the torso temperature is within viable limits. Conversely, there is only one case where the brain temperature is suitable for survival. However, in that particular case the torso temperature significantly exceeds the upper allowable limit. Nevertheless, there are other cases where the brain temperature is close to the lower limit. With slightly higher metabolic rates than the minimum value and with less insulation in the torso region, both the brain and torso temperatures should be within viable limits.

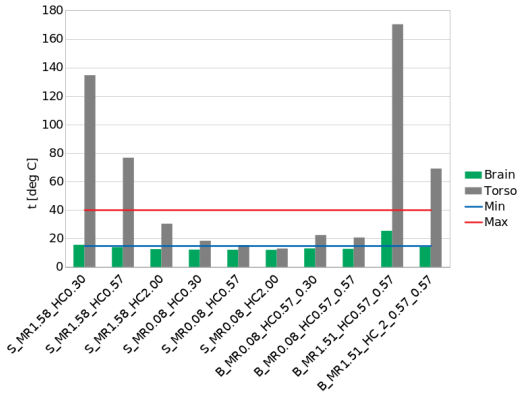

Figure 9. Summary of the observed temperatures in monitoring points located in the brain and torso areas. The labels along the horizontal axis indicate each case. 'S' stands for cases without blubber, 'B' for the ones with an extra blubber layer. The number after 'MR' shows the metabolic rate, while the numbers after 'HC' indicate the heat conductivities.

Models with increased complexity lead to longer computation times. Table 2 summarizes the typical execution times to convergence when running 16 parallel processes on an AMD Ryzen 9 7950X3D 16-core processor. As expected, execution time increases significantly with higher mesh resolution. Moreover, higher thermal conductivity values result in faster convergence, suggesting that longer timesteps could have been used for the lower conductivity cases. Nevertheless, the required computing times are relatively short compared to the more complex CFD simulations, and the impact of suboptimal timestep selection is considered to be negligible.

Table 2. Typical CPU times.

Case type	MR $[\frac{W}{kg}]$	κ $[\frac{W}{mK}]$	N_{cells} $[\cdot 10^6]$	t_{conv} $[s]$
No blubber	1.58	0.30	1.9	509
No blubber	1.58	0.57	1.9	314
No blubber	1.58	2.00	1.9	134
No blubber	0.083	0.30	1.9	430
No blubber	0.083	0.57	1.9	307
No blubber	0.083	0.30	1.9	137
With blubber	1.51	0.57 0.57	3.8	5260
With blubber	0.83	0.57 0.30	3.8	6434
With blubber	0.83	0.57 0.57	3.8	5496
Three regions	1.51	2.0 0.57 0.25	16.2	35036

3.4. Flow computations

These computations were performed to evaluate the impact of the added blubber layer on hydrodynamic drag. Figure 10 shows the pressure distribution along the surface of both the original (top) and blubber-coated (bottom) geometries. No significant difference can be seen in the pressure distributions, which is quantitatively reflected in a tiny (1%) increase of the drag force from 100.92 (original geometry) to 101.93 N (with blubber). This minor rise indicates that the addition of blubber did not lead to any significant penalty in hydrodynamic performance of the selected body shapes.

4. DISCUSSION AND SUMMARY

The impact of an added blubber layer on the heat balance of a plesiosaur (marine reptile) was investigated using numerical models of varying complexity. The simple one-dimensional and cylindrical models predicted a need for an extra insulating layer to reduce the simulated heat fluxes to levels observed in modern animals living in cold-water environments.

The three-dimensional computations further showed that a peripheral insulatory layer was a necessity to achieve a viable internal body temperature. Without an extra blubber layer, the predicted internal temperatures were lethally low for animals at low metabolic rates. Conversely, when a high metabolic rate was introduced, the predicted core temperatures were abnormally high. Nevertheless, as a consequence of the long and slender neck, the temperatures in the brain region remained too low for a real animal.

The addition of a layer of blubber significantly improved the viability chances for individuals with low metabolic rates. For a highly active animal, the added insulation turned out to be too much; the predicted temperature levels exceeded the viable limits in the majority of the body. This suggests that,

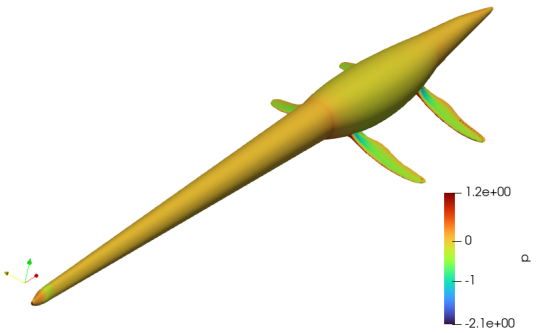

a).

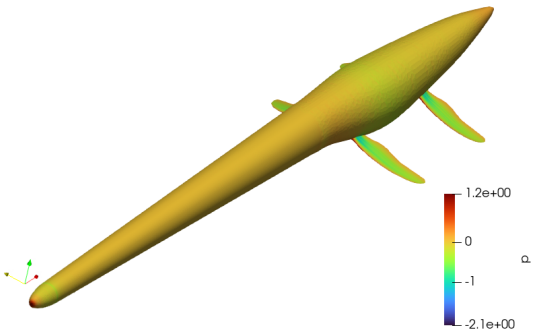

b).

Figure 10. Pressure distribution along the body for a case a) without and b) with blubber

in reality, the thickness of the blubber was probably rather thin in certain regions of the body.

There are several inherent uncertainties in the presented predictions. First of all, there is no widely accepted overall body shape for a plesiosaur; our geometry is a simplification of the general body design, based on a real specimen [30]. The thermodynamic properties of tissues were further approximated based on data from modern animals. Most of these vary between organs and tissues, and sometimes even for the same tissue. Nevertheless, our sensitivity study adopted realistic extreme values. Thus, real-case scenarios are expected to occur within the predicted limits.

The predictions also significantly simplified the heat generation within the body. For better accuracy, several heat generation zones of different magnitudes would be needed. Unfortunately, the information required to set up such simulations is, at present, scarce.

Another limiting factor in the accuracy of our predictions is the difficulty to account for heat convection by the vascular system. A simple model was adopted to account for this phenomenon, but more advanced modelling approaches are expected to substantially improve the accuracy of this parameter.

The adoption of a constant temperature boundary condition implies that the cooling effect of the surrounding water is overpredicted by our models. Although the published literature suggests that this effect is small, it will be verified in the future by a conjugate heat transfer simulation.

We conclude that even if there are unavoidable sources of error in the predictions presented in this paper, our results nonetheless suggest that the currently widely accepted plesiosaur body shape needs to be refined by the addition of a peripheral blubber layer.

ACKNOWLEDGEMENTS

The computations were enabled by resources provided by the National Academic Infrastructure for Supercomputing in Sweden (NAISS), which is partially funded by the Swedish Research Council through grant agreement no. 2022-06725. Additional financial support was provided by a project grant (no. 2020-03542) from the Swedish Research Council awarded to Johan Lindgren.

REFERENCES

[1] Gutarra, S., and Rahman, I., 2022, "The locomotion of extinct secondarily aquatic tetrapods", *Biological Reviews*, Vol. 97 (1), pp. 67–98.

[2] Troelsen, P.V.and Wilkinson, D., Seddighi, M., Allanson, D., and Falkingham, P., 2019, "Functional morphology and hydrodynamics of plesiosaur necks: does size matter?", *Journal of Vertebrate Paleontology*, Vol. 39 (2).

[3] Gutarra, S., Stubbs, T., Moon, B., Palmer, C., and Benton, M., 2022, "Large size in aquatic tetrapods compensates for high drag caused by extreme body proportions", *Communications Biology*, Vol. 5, p. 380.

[4] Petersen, S., Tabor, C., Lohmann, K., Poulsen, C., Meyer, K., Carpenter, S., Erickson, J., Matsunaga, K., Smith, S., and Sheldon, N., 2016, "Temperature and salinity of the Late Cretaceous Western Interior Seaway", *Geology*, Vol. 44 (11), pp. 903–906.

[5] Rogov, M. A., Zverkov, N. G., Zakharov, V. A., and Arkhangelsky, M. S., 2019, "Marine reptiles and climates of the Jurassic and Cretaceous of Siberia", *Stratigraphy and Geological Correlation*, Vol. 27, pp. 398–423.

[6] Lindgren, J., Sjövall, P., T. V., Zheng, W., Ito, S., Wakamatsu, K., and et al., 2018, "Soft-tissue evidence for homeothermy and crypsis in a Jurassic ichthyosaur", *Nature*, Vol. 564 (7736), pp. 359–365.

[7] Wiemann, J., Menéndez, I., Crawford, J., Fabbri, M., Gauthier, J., Hull, P., Norell, M., and Briggs, D., 2022, "Fossil biomolecules reveal

an avian metabolism in the ancestral dinosaur", *Nature*, Vol. 606, pp. 522–526.

[8] Fleischle, C., Wintrich, T., and Sander, P., 2018, "Quantitative histological models suggest endothermy in plesiosaurs", *PeerJ*, Vol. 6 (e4955).

[9] Bernard, A., Lécuyer, C., Vincent, P., Amiot, R., Bardet, N., Buffetaut, E., and et al., 2010, "Regulation of body temperature by some Mesozoic marine reptiles", *Science*, Vol. 328 (5984), pp. 1379–1382.

[10] Hokkanen, J., 1990, "Temperature regulation of marine mammals", *Journal of Theoretical Biology*, Vol. 145, pp. 465–485.

[11] Dunkin, R. C., McLellan, W. A., Blum, J. E., and Pabst, D. A., 2005, "The ontogenetic changes in the thermal properties of blubber from Atlantic bottlenose dolphin Tursiops truncatus", *Journal of Experimental Biology*, Vol. 208 (8), pp. 1469–1480.

[12] Wyneken, J., 2015, "Anatomy of the Leatherback Turtle", *The Leatherback Turtle Biology and Conservation*, Johns Hopkins University Press, pp. 34–50.

[13] Cengel, Y., 2004, *Heat Transfer: A Practical Approach*, McGraw-Hill Education, ISBN 9780071236447.

[14] Christiansen, F., Dawson, S., Durban, J., Fearnbach, H., Miller, C., Bejder, L., and et al., 2020, "Population comparison of right whale body condition reveals poor state of the North Atlantic right whale", *Marine Ecology Progress Series*, Vol. 640, pp. 1–16.

[15] Read, A., Keener, W., Webber, M., and Siebert, U., 2025, "Harbour porpoise Phocoena phocoena (Linnaeus, 1758)", *Handbook of Marine Mammals*, Academic Press., p. 427.

[16] Price, E., Wallace, B., Reina, R., Spotila, J., Paladino, F., Piedra, R., and Velez, E., 2004, "Size, growth, and reproductive output of adult female leatherback turtles Dermochelys coriacea", *Endangered Species Research*, Vol. 1, pp. 41–48.

[17] OpenFOAM, "OpenFOAM, https://www.openfoam.com", URL `https://www.openfoam.com`, checked 2025.02.18.

[18] FreeCAD, "FreeCAD, https://www.freecad.org", URL `https://www.freecad.org`, checked 2025.02.18.

[19] Cieri, R., 2018, "The axial anatomy of monitor lizards (Varanidae)", *Journal of Anatomy*, Vol. 233 (5), pp. 636–643.

[20] Klingler, J., 2016, "On the morphological description of tracheal and esophageal displacement and Its phylogenetic distribution in Avialae", *Plos one*, Vol. 11 (9), p. e0163348.

[21] Davenport, J., Fraher, J., Fitzgerald, E., McLaughlin, P., Doyle, T., Harman, L., and Cuffe, T., 2009, "Fat head: an analysis of head and neck insulation in the leatherback turtle (Dermochelys coriacea)", *Journal of Experimental Biology*, Vol. 212 (17), pp. 2753–2759.

[22] Bostrom, B., and Jones, D. R., 2007, "Exercise warms adult leatherback turtles", *Comparative Biochemistry and Physiology Part A: Molecular Integrative Physiology*, Vol. 147 (2), pp. 323–331.

[23] Dudley, P., Bonazza, R., Porter, and W.P., 2016, "Climate change impacts on nesting and internesting leatherback sea turtles using 3D animated computational fluid dynamics and finite volume heat transfer", *Ecological Modelling*, Vol. 320, pp. 231–240.

[24] Paladino, F., O'Connor, M., and Spotila, J., 1990, "Metabolism of leatherback turtles, gigantothermy, and thermoregulation of dinosaurs", *Nature*, Vol. 344 (6269), pp. 858–860.

[25] Versteeg, H., and Malalasekera, W., 2007, *An introduction to computational fluid dynamics: the finite volume method*, Pearson Education Limited, second edn.

[26] Menter, F., and Esch, T., 2001, "Elements of Industrial Heat Transfer Predictions", Vol. 20, pp. 117–127.

[27] Menter, F. R., Kuntz, M., and Langtry, R., 2003, "Ten Years of Industrial Experience with the SST Turbulence Model", *Heat and Mass Transfer*, Begell House, pp. 625–632.

[28] Motani, R., 2002, "Swimming speed estimation of extinct marine reptiles: energetic approach revisited", *Paleobiology*, Vol. 28 (2), pp. 251–262.

[29] Schwartz, F., 1978, "Behavioral and tolerance responses to cold water temperatures by three species of sea turtles (Reptilia, Cheloniidae) in North Carolina", *Florida Marine Research Publications*, (33), pp. 16–18.

[30] Kubo, T., Mitchell, M. T., and Henderson, D. M., 2012, "Albertonectes vanderveldei, a new elasmosaur (Reptilia, Sauropterygia) from the Upper Cretaceous of Alberta", *Journal of Vertebrate Paleontology*, Vol. 32 (3), pp. 557–572.

Conference on Modelling Fluid Flow (CMFF'25)
The 19th International Conference on Fluid Flow Technologies
Budapest, Hungary, August 26 - August 29, 2025

A 0D-3D MODEL FOR THE ANALYSIS OF THE TRANSIENT THERMAL BEHAVIORS OF AN ELECTRIC POWER TRAIN

Alessio SUMAN[1], Riccardo BONDESAN[2], Luca CONDOTTA[2], Lorenzo ANTONIOLI[2], Nicola ZANINI[2], Mattia BATTARRA[2], Emiliano MUCCHI[2], Mattia PIOVAN[2], Michele PINELLI[2]

[1] Corresponding Author. Department of Engineering, University of Ferrara, Ferrara, Italy. E-mail: alessio.suman@unife.it
[2] Department of Engineering, University of Ferrara, Ferrara, Italy. E-mail: first name.family name@unife.it

ABSTRACT

Electric vehicles are recognized as the solution for the future to reduce emissions, especially in the city center, where health-related issues are due to the high population density and pollutant concentration. Due to this, the automotive industry has to change several paradigms to introduce more efficient vehicles and overcome the reluctance to change the user. In this sense, the thermal management of the vehicles has to be re-designed to manage the operating temperature of high-power devices such as drivers and motors. In the present investigation, a lumped parameter model has been developed to study the dynamic thermal behaviors of electric vehicle power trains. The study analyses the interaction between the heat exchanger and the operation of two electric motors and a single inverter. To set up the model, a computational fluid dynamics simulation has been carried out to characterize the thermal-fluid dynamic characteristics of the relevant components of the system, such as the cooling systems of the inverter and the electric motor. Stationary and transient analyses have been carried out considering the variation of the thermal load according to the vehicle route. The effects of thermal inertia and the effects of the control logic system have also been highlighted.

Keywords: electric vehicle, thermal management, lumped-parameter model, computational fluid dynamics, dynamic simulations

NOMENCLATURE

H	[bar]	pump head
h	[W/m^{2}K]	heat transfer coefficient
P	[W]	power
p	[bar]	static pressure
Q	[l/min]	volume flow rate
T	[°C]	temperature
t	[s]	time
Δ	[-]	difference

1. INTRODUCTION

Thermal management of an electric vehicle is crucial to extend the rangeability and reduce electric consumption. Recent estimations show that the thermal management system accounts for 60 % of the total electric usage [1 – 3]. The modeling of such systems determines several challenges related to the cross-correlation between devices designed to accomplish different tasks (e.g., cabin temperature, heat rejection of the power train, etc.) [1]. To study such a system, low-order models help run several scenarios representing the operating conditions involved in automotive applications. Lumped-parameter models (LPM) are among the most known low-order models. The LPM model is based on a set of equations representing the physical phenomenon and, simultaneously, a set of coefficients or datasets representing the relationship between independent variables and the characteristics of each modeled device/system. Lumped parameter models allow the schematization of the system with details related to cross-correlation phenomena coming from the thermal systems, transmission, and driver characteristics [4, 5], showing the possibility of using the model to optimize the systems by reducing fuel consumption.

Similarly, LPM has been used to assess the interaction between electrical devices in electric-powered vehicles, showing the possibility of studying complex phenomena using low-order models [6]. The LPM could be fed by experimental data or numerical data obtained by high-order models such as computational fluid dynamic simulations. In [7], the LPM of a heat pipe based on CFD simulations is proposed. The three-dimensional simulations were used to estimate the heat transfer coefficients in a complex geometry. At the same time, the LPM results could be checked by CFD simulations, increasing the usefulness of the LPM model to reduce the computational effort in the case of several simulating runs [8 – 10].

1.1. Aim of the paper

In the present paper, an LPM has been developed to study the thermal behavior of the electric power train of a single-seater racing car. The present results refer to the analysis of the cooling circuits designed for the racing car involved in the Formula SAE competition [11]. The present modeling process consists of a framework created using a lumped parameter model in which a set of data and parameters have been obtained by CFD simulations. The CFD analysis was used to characterize the on-purpose design component devoted to managing the thermal behavior of electric motors and inverter. Using the LPM, stationary and dynamic simulations were carried out to describe the cooling systems and assess temperature variation during an endurance test. In this scenario, the control logic based on temperature data can increase car efficiency, reduce consumption, and manage electric power trains.

2. COOLING CIRCUIT

The designed cooling circuit consists of numerous components designed or selected for this specific application. The full-electric racing car includes four electric motors (four-wheel drive concept) and a single inverter that manages the electric power supplied by the battery pack to the electric motor according to the driver's needs and circuit layout. To control the operating temperature of motors and inverter, the cooling circuit is composed of the following elements:

- recirculation pump;
- heat exchanger with cooling fan;
- water jacket for cooling the electric motor;
- cold plate for cooling the inverter;
- rubber hose and fittings.

The cooling circuit and its devices have been reported in a three-dimensional layout proposed in Fig. 1. A recirculating pump supplies the flow rate through the cold plate. After that, the tee fitting was placed to split the water flow rate into two water jackets to cool down the electric motor. After the water jacket, the two lines were re-joined immediately before the heat exchanger. This layout was implemented in the LPM by using Simcenter Amesim software.

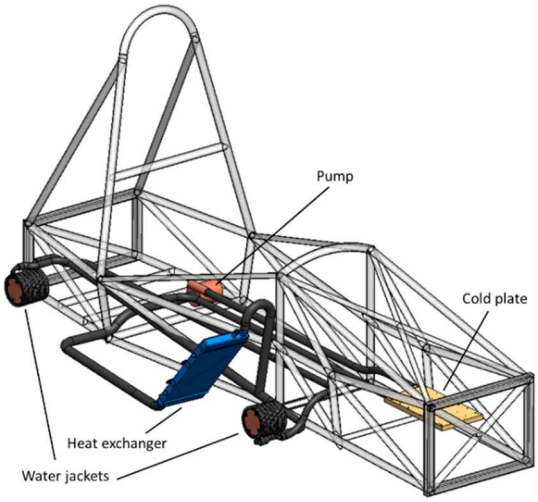

Figure 1. The cooling circuit layout

3. COMPONENTS CHARACTERIZATION

In the following paragraphs, the characterization of the relevant devices has been reported to create the most representative LPM of the cooling circuit.

3.1. Pump, heat exchanger and fittings

The pump and the heat exchanger were selected from the market based on their performance, space requirements, and weight. Such components were characterized by manufacturers, and in this section, only the relevant characteristics related to the LPM have been reported.

The pump performance (provided by Vovyo Technology Co., LTD.) is reported in Fig. 2 according to the flow rate versus head. Since the competition rules impose water as cooling media, the characteristics curve used in the LPM corresponds to that reported in Fig. 2.

Regarding the heat exchanger, the AKS DASIS model DASIS320100N has been selected for the present application. The heat exchanger has a heat rejection value of 10 kW. Such a value is greater than the estimated thermal power that has to be exchanged. However, installing the heat exchanger in the car's side pods determines the nominal air flow rate reduction, reducing the heat exchanger capability. The heat exchanger has been coupled with a circulating fan to ensure the greatest safety of the electric circuits. The fan is the type VA14-BP7 from the manufacturer SPAL Automotive Spa. In the present design, the fan activation is controlled by a control logic based on the temperature value measured in correspondence with critical devices such as the electric motor and inverter. Such a condition will be implemented in the LPM to study the most severe condition of the circuits.

Finally, the connection between the devices has been described. According to Fig. 1, the cooling circuit develops according to the car length, from the

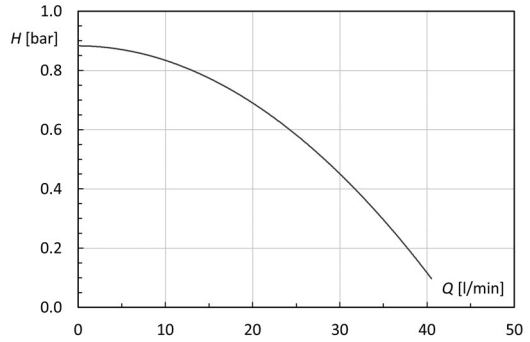

Figure 2. Pump performance: head (*H*) versus flow rate (*Q*)

rear to the front section. The circuit consists of pipes suitable for hot water delivery, mainly used as a flexible connection in the cooling circuits of automotive engines. They are made of black EPDM rubber with synthetic textile reinforcing inserts inside to overcome the pressure.

3.2. Water jacket

The water jacket is used to cool the electric motor. Using a water jacket is known in the literature as a good solution to manage the temperature of electric motors, increasing efficiency and reliability. In [12, 13], analyses of different water jackets designed for cooling the electric motor are reported. In the present analysis, the water jacket's specific design must be accounted for. The water jacket is designed to adhere externally to the electric motor. It is characterized by a coil that wraps around them through which the cooling fluid flows. The external surface of the electric motor is smooth, allowing a sealing process with grooves in the water jacket. Therefore, the cooling water is directly in contact with the electric motor and is supplied through the water jacket in a spiral shape. In Fig. 3, the three-dimensional shape of the designed water jacket and the sketch with relevant dimensions are reported. It is realized using a 3D printer process and PA 12 material filled with carbon fiber.

The water jacket performance was discovered through CFD simulations. A numerical analysis is mandatory to find the relationship between water flow rate and performance data, such as pressure losses and heat exchange parameters. To do this, a numerical model was setup. The computational domain comprises the electric motor external surface and the entire geometry of the water jacket reported in Fig.3. The model setup is similar to that described in [14]. The calculation is based on commercial Flow Simulation software embedded in the Solidworks suite. The computational model is discretized using a cut-cell approach by 530k Cartesian-grid elements while the low Reynolds number k–ε model, as in the Lam–Bremhorst formulation, is used [15]. A proper independent grid analysis was performed to assess the model's reliability. A refinement ratio 1.2 was used, and the selected mesh was the finest. A deviation from the coarsest grid (370k elements) and the finest (530k) was estimated to equal 6.3 % on the water jacket pressure drop. The spatial derivatives are approximated with implicit difference operators of second-order accuracy. The CPU time for the finest grid was 2 h on a workstation equipped with 8 physical processors.

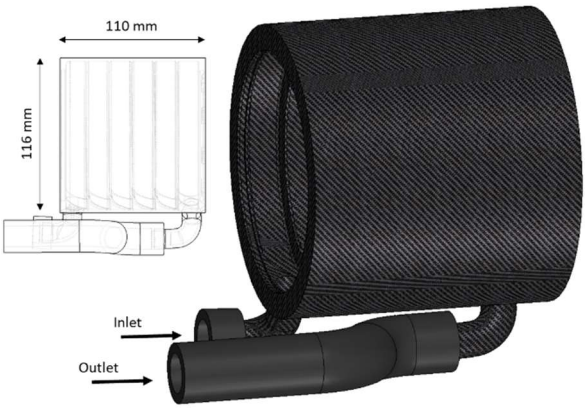

Figure 3. Water jacket to cool the electric motor

A volume flow rate value was imposed at the inlet section, while a static gauge pressure equal to 0 Pa was imposed at the outlet section. Three representative volume rates have been used to characterize the thermal behavior equal to 4, 8, and 12 l/min. From the CFD simulations, the heat transfer coefficient at the electric motor surface and the water jacket pressure losses have been assessed. In Fig. 4, the contour plot of the heat transfer coefficient obtained for the highest flow rate value is reported. Table 1 reports the CFD results helpful to represent the water jacket performance in the LPM as a function of the volume flow rate Q. Pressure losses (Δp) are intended as the difference between the static pressure at the inlet and the outlet. The heat transfer coefficient (h) is intended as the average value on the electric motor surface.

3.3. Cold plate

The inverter gets significantly overheated during the operation at the full power. The latter is placed on top of a cold plate to dissipate the heat developed by the inverter. This is an aluminum alloy plate traversed on the inside by tubes through which the cooling fluid passes. The design of the cold plate is reported in Fig. 5. It was provided by the manufacturer of the inverter (AMKmotion GmbH), who reported the proper fittings for the inverter and

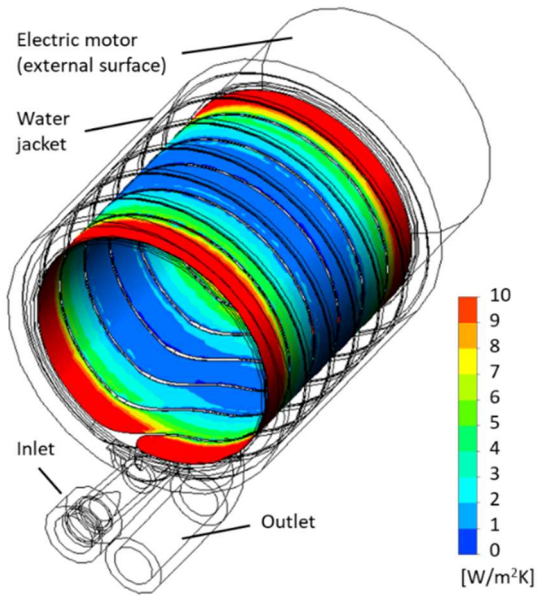

Figure 4. Heat transfer coefficient at the electric motor surface (12 l/min)

Table 1. Water jacket performance

Q [l/min]	Δp [bar]	h [W/m^{2}K]
4	0.01	7.6
8	0.05	8.3
12	0.11	8.6

all the electrical devices. The cold plate is made of aluminum alloy (AlMgSi0.5), and an internal circular-shaped groove characterizes it.

Similar to the previous analysis, the cold plate has to be characterized in terms of pressure drop and heat exchange performance. A numerical model has been defined in line with the model proposed for the water jacket (software suite, turbulence model, and boundary conditions). A cut-cell approach by 400k Cartesian-grid cell has been used. A similar analysis related to the grid independence analysis was adopted. Even in this case, a refinement ratio of 1.2 was used, and the deviation between the coarsest and the finest (selected) grid was 3.2 % for the cold plate pressure drop. The CPU time for the finest grid was 1.5 h on a workstation equipped with 8 physical processors. The cold plate performance was computed for three different volume flow rate values equal to 8, 16, and 24 l/min. In Fig. 6, the contour plot of the heat transfer coefficient obtained for the highest flow rate value is reported. Table 2 reports the CFD results helpful in representing the cold plate performance in the LPM.

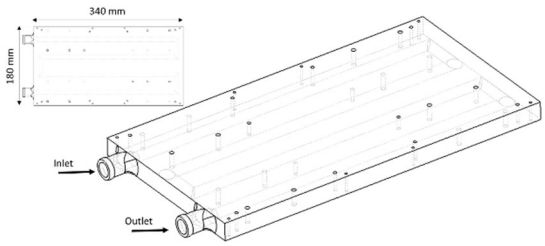

Figure 5. Cold plate design

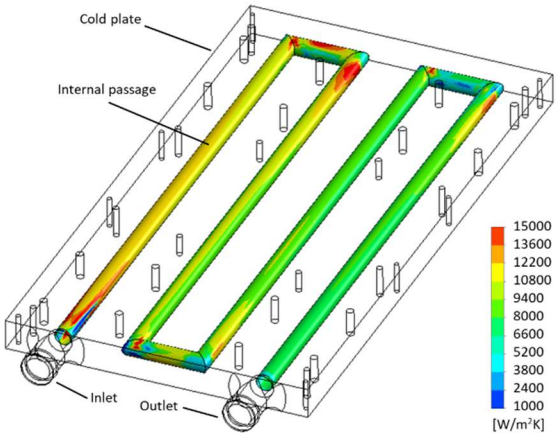

Figure 6. Heat transfer coefficient at the cold plate internal passage (24 l/min)

Table 2. Cold plate performance

Q [l/min]	Δp [bar]	h [W/m^{2}K]
8	0.18	4046
16	0.46	6491
24	1.01	8879

4. LUMPED PARAMETER MODEL

After the component characterization, the LPM can be assembled. The LPM comprises libraries and specific blocks used to define the behavior of relevant components. The LPM has been created in the Simcenter Amesim environment. The first step is to select the proper libraries. In this project, five libraries have been used:

- *Cooling system*: this library includes a set of specific components fully compatible with the *Thermal Hydraulic* and *Thermal* libraries useful to study cooling systems in which temperature variation and fluids are involved;
- *Thermal Hydraulic*: this library is dedicated to designing hydraulic systems in which fluid temperature variations greatly influence the overall system behavior. It is based on a transient heat transfer approach used to model thermal phenomena in liquids (energy transport, convection) and to study the thermal evolution of these liquids in a hydraulic system;
- *Thermal*: this library deals with modeling heat transfer phenomena (conduction, free and forced convection, and radiation) involving solid materials;
- *Thermal Hydraulic Resistance*: this library is dedicated to the analysis of the evolution of pressure drops and flow rates in hydraulic networks where changes in fluid temperature have a significant influence on the overall behavior of the system being modeled;
- *Signal Control*: this library describes the power signal characterizing the inverter and electric motors.

After defining the proper libraries, a block was selected to create the adequate boundary condition and modeling strategy for the relevant components.

The boundary conditions blocks are listed as follows:

- THSD00: to define the materials of the devices (cold plate and water jackets);
- CSMP1: represents the mission profile. This block helps study both stationary (100 km/h, 600 s) and dynamic conditions (endurance test);
- CSES0: to define the ambient condition of the simulation;
- CSED0: to define the vehicle data;
- TFFD3: to define thermal-hydraulic

properties.

Specific blocks were used to model the relevant components. The description of such blocks is reported in the following paragraphs.

4.1. Pump, heat exchanger, and fittings models

The recirculating pump was modeled by the TFPUC0 block (*Thermal-hydraulic resistance* library) coupled with a PM000 electric motor to realize the assembly called the *electric pump*. The motor block allows the modification of the pump rotational speed if required. The pump performance curve (volume flow rate versus head) was added by using the AMETable subprogram. This curve is expressed through discrete values obtained from the manufacturer (see Fig. 2).

The most appropriate solution to model the heat exchanger is based on the CSRA022 block. Two additional blocks were used to increase the reliability of the present model. The TRIG0 block allows, being connected to a temperature sensor at the radiator's output, to detect if the temperature in the radiator is getting too high (above a threshold value imposed by the user) and consequently give the input to activate the fan. The CSDATA000 block helps in the specification of vehicle velocity (e.g., the air velocity on the radiator surface).

Using the layout proposed in Fig. 1, the tube length and diameter have been assessed. To model the cooling circuit in terms of length and fittings (bend, tee, etc.), the following blocks have been used:

- TFL000: used for straight pipe;
- TFBP11: used for bend;
- TFDC10: used for diameter changes;
- TF206: used for three-way fitting.

4.2. Water jacket and cold plate models

The water jacket and the cold plate have been modeled by the CSEN032 block. Such a submodel allows the definition of the heat flow source and a heat flow rate, which are specified according to the data related to inverter and electric motor heat generation. In stationary conditions, such a value will be kept constant. In contrast, in dynamic simulation, the values of the heat flow rate will vary according to the power consumption related to the endurance test. In addition to these data, the heat transfer coefficient is mandatory, representing the heat exchange process between the coolant fluids (simulated in the LPM) and the electrical devices (inverter and electric motor). These numbers were obtained by the CFD simulations, and they are reported in Tables 1 and 2.

5. STATIONARY CONDITION

A sensitivity analysis of the LPM was performed to evaluate the cooling circuit's performance in several operating conditions (thermal power, vehicle speed, cooling flow rate, etc.). In the present manuscript, a representative stationary condition has been reported. The ambient temperature has been set at 36 °C (summer condition), while the threshold temperature for the cooling fan is imposed equal to 65 °C. The thermal power at the cold plate was equal to 2000 W, while at the electric motor, a thermal power of 1200 W was imposed. The vehicle speed was imposed equal to 100 km/h, representing the condition in which the estimated maximum speed is reached using the maximum of the inverter and the electric motor. The results of the LPM model allow the identification of the operating point of the cooling pump and the related head that overcomes the pressure losses over

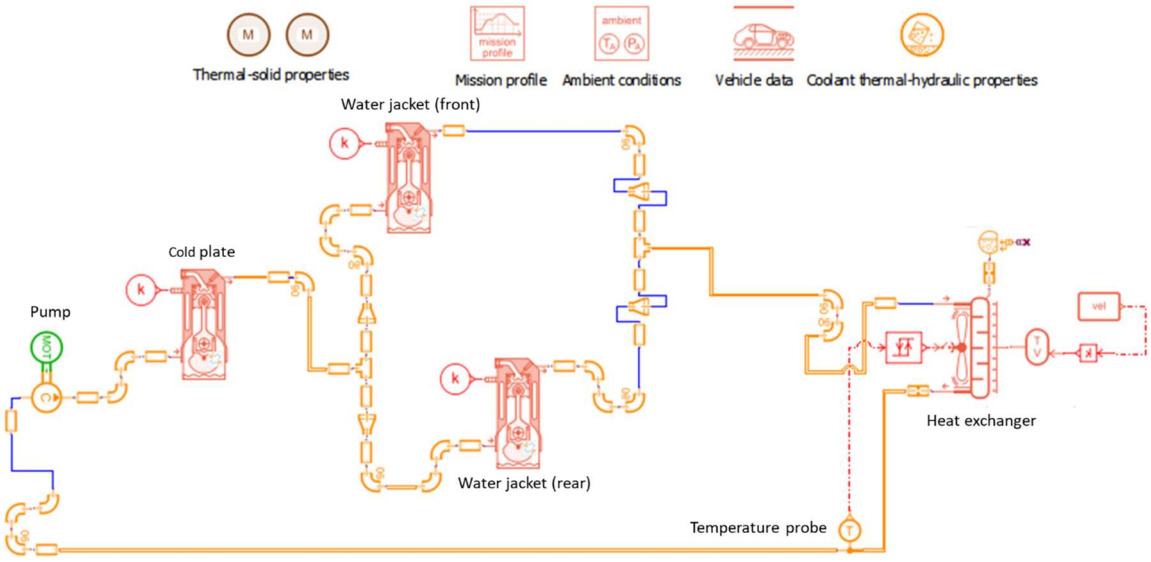

Figure 7. LPM of the cooling circuit realized in the Simcenter Amesim environment

Table 3. Results of the stationary simulation

Component	Δp [bar]	ΔT [°C]
Water jacket	0.056	1.8
Cold plate	0.619	1.5
Heat exchanger	0.002	3.3
Pump head	0.721	0.0

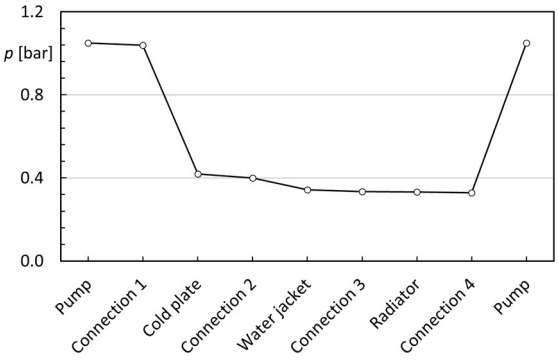

Figure 8. Pressure trend over the cooling circuit

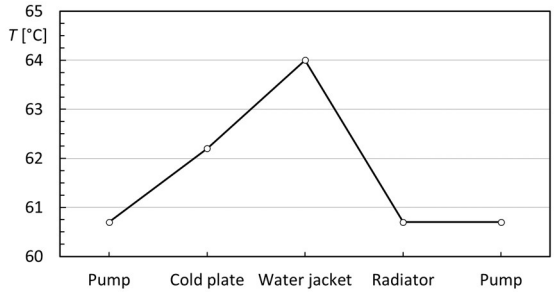

Figure 9. Temperature trend over the cooling circuit

the circuit. Similarly, the temperature difference across each component can be obtained. The results are reported in Table 3. Figures 8 and 9 report the pressure and the temperature values over the cooling circuits. The charts show the pressure and temperature values according to the cooling water flow path, which starts from the pump outlet section.

From the results obtained in the stationary condition for the worst scenario, it is possible to draw several indications. The internal pressure is lower than the critical value reported for each component and suitable for the selected rubber hose.

Similarly, the highest temperature is lower than the critical values for pure water. At the same time, the working temperature values of the electrical device (inverter and motor) are within the safe range defined by the manufacturer. At the same time, the temperature differences obtained with the LPM simulation are lower than the critical values ($\Delta T < 5$ °C for cold plate and water jacket).

6. DYNAMIC SIMULATION

A dynamic simulation was carried out using the LPM in order to simulate the car performance during the endurance test, with particular attention paid to the behavior of the cooling system during the execution of subsequent identical laps.

The first step is the definition of the typical lap. From the data previously recorded by the racing team, a typical is 1 km long and repeated 22 times. In addition to this overall data, the electrical power for the inverter and electric motor have been assessed. These data represent the thermal load of the cooling circuits, which change according to the lap layout (straights and curves). Using the mission profile block (CSMP1), the sequence of straights and curves (15 steps) regarding thermal power and vehicle velocity has been reproduced. In Fig. 10, the mission profile regarding vehicle speed has been reported. The maximum speed is reached at the end of the straight, while the average velocity is between 50 km/h and 60 km/h. The vehicle speed is divided into 15 steps and is the basis for estimating the thermal input for the cooling circuit.

The electrical power and vehicle speed can be matched by using the datasheet provided by the manufacturer. The calculation estimated the current intensity coupled to the voltage values for the electrical motor and, thus, the water jackets. The combination of these values results in the thermal power profile proposed in Fig. 11. It is important to note that the thermal power experienced at the inverter section follows the trend of the water jacket and vice versa. This is due to the correlation between

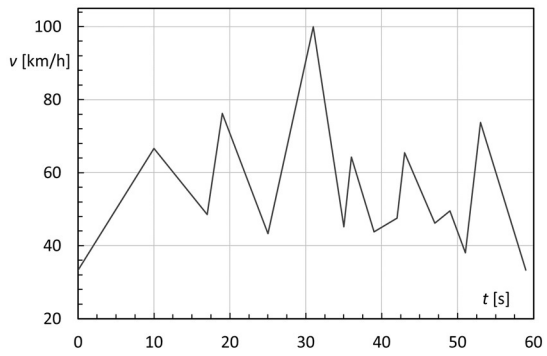

Figure 10. Mission profile: vehicle speed

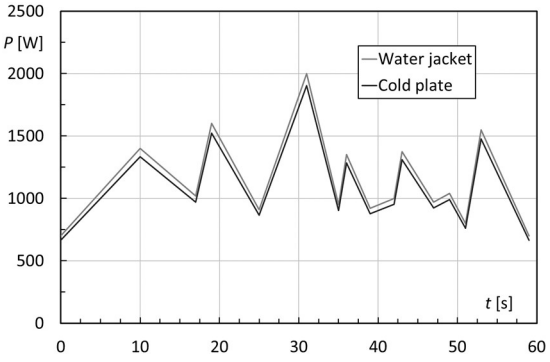

Figure 11. Mission profile: thermal input at the cold plate and water jacket

the power supplied by the inverter and the electric power at the motor. Such a condition determines that the cooling circuit has to overcome the contemporary presence of the highest values of thermal input in both the cold plate and water jacket.

The last required data for the dynamic simulation is the initial condition. Since no data are available, the initial condition will be kept equal to the worst scenario, as represented by the stationary condition that was reported early. This allows the cooling circuit performance to be evaluated when it operates at full load immediately before the start of the endurance test.

Figures 12 – 15 report the temperature trend obtained during the simulation of the endurance test. Figures 12 – 14 refer to the temperature values obtained in correspondence with the inlet and outlet sections for the water jacket, cold plate, and heat exchanger. It can be noted that after the initial phase (which is estimated to be 8 laps long), the cooling circuit achieves a cyclic condition characterized by the repetitive sequence of straight and curves described with the mission profile reported in Fig. 10. All temperature differences remain approximately constant, and the proper performance of the system is constantly verified and satisfied, ensuring adequate heat removal from the inverter and electric motors during the endurance test.

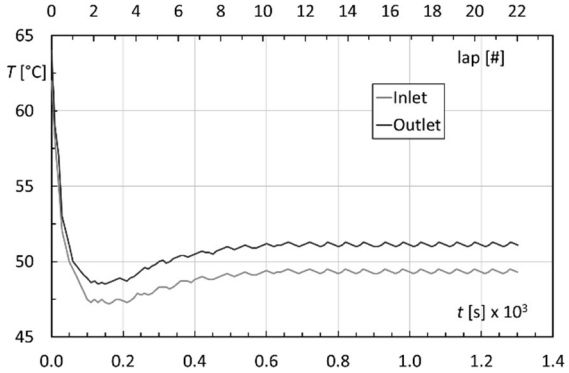

Figure 12. Inlet and outlet temperature trends for the water jacket during the endurance test

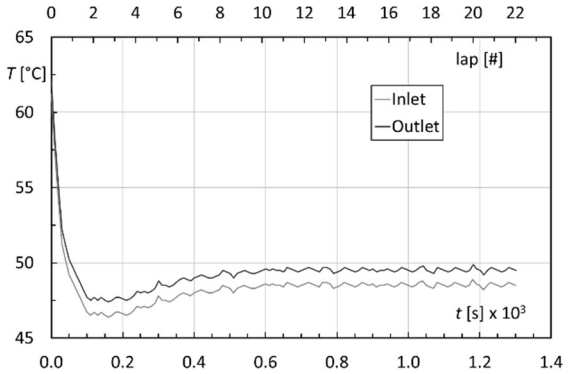

Figure 13. Inlet and outlet temperature trends for the cold plate during the endurance test

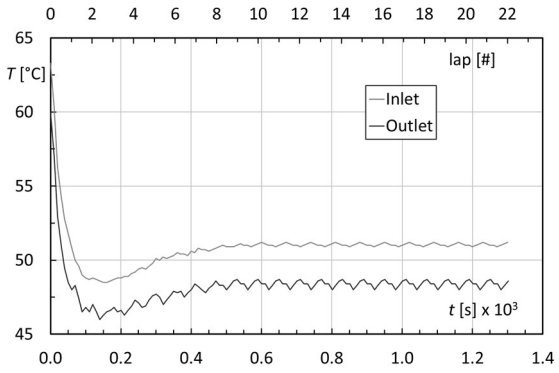

Figure 14. Inlet and outlet temperature trends for the heat exchanger during the endurance test

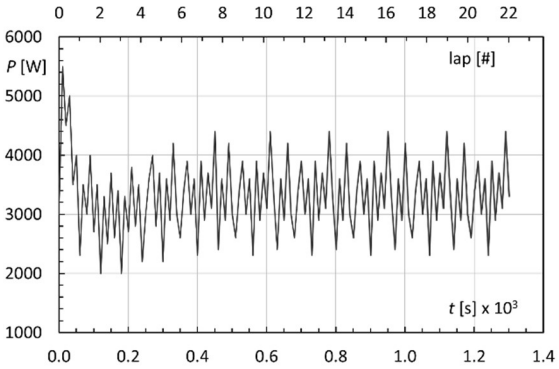

Figure 15. Thermal power trends at the heat exchanger during the endurance test

Figure 15 shows the thermal power exchanged by the radiator. The local variations (peaks and valleys) are visible due to the instantaneous variation of the thermal inputs. At the same time, an almost constant average value of the thermal power can be seen, approximately 3500 W.

7. CONCLUSIONS

In the present analysis, a lumped parameter model has been used to assess the stationary and dynamic performance of a cooling circuit used in an electric car. The present design refers to the thermal management of an electric powertrain used in a single-seater racing car.

The modeling process involves the schematic representation of the three-dimensional layout of the circuits and the analysis of the devices devoted to cooling the inverter and the electric motors. In particular, the designed-on-purpose cold plate (for the inverter) and the water jacket (for the electric motor) were characterized using CFD simulations. The LPM model has been completed by adding the manufacturer's pump and heat exchanger data.

After defining the library set and the most suitable block, a stationary simulation was performed. The worst scenario regarding operating temperature and thermal power input has shown that the cooling circuit allows the preservation of the

operating characteristics of devices, matching the safe condition provided by the manufacturer. Starting from the stationary condition, a dynamic simulation was set up to study the cooling circuit performance during an endurance test. The model results show the temperature and the thermal power trends according to the laps. Even starting from the conditions related to the maximum thermal load, the cooling circuit can overcome the endurance test, ensuring suitable thermal management of the entire system.

Using the methodology presented in the present work, it is possible to check the system's reliability during the design phase and, simultaneously, increase the efficiency of the vehicle, reducing the consumption and thus increasing the rangeability or the performance of the entire vehicle.

ACKNOWLEDGEMENTS

This work has been carried out in the framework of the regional grant N. 2/2023 “Invito agli atenei e agli istituti afam a presentare progetti “team di sviluppo di prototipi/soluzioni per la partecipazione a competizioni nazionali e internazionali”, founded by Emilia Romagna region. The authois wish to thanks Siemens Industry Software srl, and Frig Air Spa for their support.

REFERENCES

[1] Zhao L., Zhou Q., Wang Z. A systematic review on modelling the thermal environment of vehicle cabins (2024) *Applied Thermal Engineering*, Vol. 257, art. no. 124142

[2] Wang X., Li B., Gerada D., Huang K., Stone I., Worrall S., Yan Y. A critical review on thermal management technologies for motors in electric cars (2022) *Applied Thermal Engineering*, Vol. 201, art. no. 117758

[3] Carriero A., Locatelli M., Ramakrishnan K., Mastinu G., Gobbi M. A Review of the State of the Art of Electric Traction Motors Cooling Techniques (2018) *SAE Technical Papers*, 2018-April

[4] Ganesan A., Jaiswal R., Pitchaikani A. A Study of an Integrated HVAC-Vehicle Model for Automotive Vehicles (2018) SAE *International Journal of Passenger Cars - Mechanical Systems*, Vol. 11 (2), pp. 151 – 166

[5] Huang Y., Khajepour A., Bagheri F., Bahrami M. Modelling and optimal energy-saving control of automotive air-conditioning and refrigeration systems (2017) *Proceedings of the Institution of Mechanical Engineers, Part D: Journal of Automobile Engineering*, Vol. 231 (3), pp. 291 – 309

[6] Chen B., Wulff C., Etzold K., Manns P., Birmes G., Andert J., Pischinger S. A Comprehensive Thermal Model for System-Level Electric Drivetrain Simulation with Respect to Heat Exchange between Components (2020) InterSociety Conference on Thermal and Thermomechanical Phenomena in Electronic Systems, ITHERM, 2020-July, art. no. 9190448

[7] Bernagozzi M., Charmer S., Georgoulas A., Malavasi I., Michè N., Marengo M. Lumped parameter network simulation of a Loop Heat Pipe for energy management systems in full electric vehicles (2018) *Applied Thermal Engineering*, Vol. 141, pp. 617 – 629

[8] Akawung A.F., Fujimoto Y. Thermal Analysis of Air Cooling System for Electric Machines Using Lumped Parameter and Flow Resistance Network (2021) IEEE International Symposium on Industrial Electronics, 2021-June

[9] Grunditz E.A., Lundmark S.T., Alatalo M. Evaluation of three cooling concepts for an electric vehicle motor - Lumped parameter models (2020) Proceedings - 2020 International Conference on Electrical Machines, ICEM 2020, art. no. 9271015, pp. 860 – 866

[10] Stuppioni U., Natali C., Battarra M., Blum A., Suman A., Pinelli M., Dalpiaz G., Mucchi E. Experimental and numerical characterization of the under-vane pressure in balanced vane pumps (2024) *Results in Engineering*, Vol. 23, art. no. 102439

[11] Formula ata (2024) https://www.formula-ata.it/formula-sae-italy/, accessed 30th december, 2024

[12] Satrústegui M., Martinez-Iturralde M., Ramos J.C., Gonzalez P., Astarbe G., Elosegui I. Design criteria for water cooled systems of induction machines (2017) *Applied Thermal Engineering*, Vol. 114, pp. 1018 – 1028

[13] Grunditz E.A., Lundmark S.T., Alatalo M. Evaluation of three cooling concepts for an electric vehicle motor - Lumped parameter models (2020) Proceedings - 2020 International Conference on Electrical Machines, ICEM 2020, art. no. 9271015, pp. 860 - 866

[14] Pinelli M., Suman A. Thermal and fluid dynamic analysis of an air-forced convection rotary bread-baking oven by means of an experimental and numerical approach (2017) *Applied Thermal Engineering*, Vol. 117, pp. 330 – 342

[15] Lam C.K.G., Bremhorst K. A modified form of the k-ε model for predicting wall turbulence (1981) *ASME J of Fluids Engineering*, Vol. 103 (3), pp. 456 - 460

Conference on Modelling Fluid Flow (CMFF'25)
The 19th International Conference on Fluid Flow Technologies
Budapest, Hungary, August 26-August 29, 2025

Equilibrium Positions and Dynamic behavior of Thermal Prolate Particles in Shear Flow: Influence of Particle Size

Farshad GHARIBI[1], Dominique THÉVENIN[2]

[1] Corresponding Author. Laboratory of Fluid Dynamics and Technical Flows, University of Magdeburg "Otto von Guericke", D-39106 Magdeburg, Germany, E-mail: farshad.gharibi@ovgu.de
[2] Laboratory of Fluid Dynamics and Technical Flows, University of Magdeburg "Otto von Guericke", E-mail: Thevenin@ovgu.de

ABSTRACT

An accurate characterization of the trajectory and dynamic behavior of particles is crucial for processes such as particle manipulation, design of efficient heating and cooling mechanisms, pollutant dispersion, and biomedical applications. Despite significant progress in the simulation of particle-fluid interactions, the dynamics of non-spherical particles, especially when heat transfer is considered, is still an active area of research. The focus of this study is on prolate particles in shear flows using four-way direct numerical simulation (DNS). For this purpose, we employ a hybrid computational framework, in which the lattice Boltzmann method is used for simulating the fluid flow, the finite-difference approach for solving the energy equation, the immersed boundary method (IBM) to capture fluid-particle interactions and the Discrete Element Method (DEM) for modeling particle collisions. This enables us to accurately model the behavior of particles under isothermal and non-isothermal conditions while varying particle size. The effect of heat transfer on final equilibrium position and dynamic behavior of prolate particles in shear flows are computed and analyzed. The results indicate that the confinement ratio, defined as the ratio of particle major radius to channel width, has a significant impact on both the time it takes for a particle to reach its equilibrium position and the vertical location of that position.

Keywords: Lattice Boltzmann method, Particulate flow, Prolate particle, Shear flow

1. INTRODUCTION

Understanding particle behavior in fluid flows is fundamentally important for a broad spectrum of industrial, environmental, and biological applications. The investigation of particle migration under varying flow conditions is essential for advancing the understanding of particulate motion in complex fluid environments. Given that particles in real-world applications often deviate from idealized spherical geometries, a detailed investigation into the dynamics of non-spherical particles is essential for enhancing the predictive accuracy and applicability of particle-laden flow models. The dynamics of spheroidal particles suspended in shear flows have long been a subject of fundamental research in fluid mechanics. Jeffery [1] already provided an analytical description of the rotational kinematics of isolated spheroidal particles immersed in a viscous fluid under linear shear conditions, assuming negligible inertial effects corresponding to the limit of zero particle Reynolds number. While analytical methods are generally constrained to simplified flow configurations, direct numerical simulations enable the exploration of a broader spectrum of physical phenomena in diverse flow regimes. However, with increasing fluid inertia, the symmetry of the flow field surrounding the particle is broken, giving rise to more intricate and nonlinear particle dynamics. Fox et al. [2] conducted a study on spherical particles in inertia-dominated shear flows and identified a supercritical pitchfork bifurcation occurring beyond a critical particle Reynolds number (Re_p), resulting in the stabilization of two symmetric off-center equilibrium positions. More recently, Lauricella et al. [3] demonstrated that ellipsoidal particles exhibit distinct behavior, tending to return to the centerline at elevated Re_p, in contrast to spherical particles, which display instability under similar conditions. In our previous work [4], we studied the dynamic behavior of a thermal spheroidal particle with fixed size in shear flows. The present study investigates the influence of particle size on the dynamic behavior of thermal non-spherical particles. Such insights may serve as a foundational step toward the development of novel techniques for the thermal and hydrodynamic manipulation of particles. The lattice Boltzmann method (LBM) has emerged as a widely adopted computational framework for simulating fluid flow systems in-

volving particulate suspensions [2, 5, 6]. In the present study, a hybrid computational framework is utilized, combining LBM for fluid flow, Finite-Difference (FD) schemes for the thermal field, the Immersed Boundary (IB) method for fluid–structure interaction, and the Discrete Element Method (DEM) for modeling particle dynamics and collisions. This integrated approach enables high-fidelity simulations of coupled fluid-particle-thermal interactions. All simulations are carried out using the extensively validated in-house solver ALBORZ [7].

2. NUMERICAL METHODS

Employing the LBM, this study conducts flow field simulations. Using a finite-order spectral method with Hermite polynomials, the Boltzmann equation is discretized in phase space. The ensuing system of interconnected hyperbolic equations is resolved by integrating along the characteristics, yielding the "stream-collide" equation for discrete populations f_i:

$$f_i(\mathbf{x} + \mathbf{e}_i\delta t, t + \delta t) = f_i(\mathbf{x}, t) + \Omega_i + F_i^{ext}, \tag{1}$$

where $\mathbf{x}$ represents the fluid node's spatial location, t denotes time, F_i^{ext} describes the external forces, and $\mathbf{e}_i$ corresponds to the discrete velocity vectors, determined based on the lattice structure chosen, and $\mathbf{e}_i\delta t$ denotes the positional shift in different directions. Throughout this investigation, the focus will be exclusively set on the D3Q27 stencil. In Equation (1), Ω_i is the discrete collision operator. In this study, a modified Hermite central moments space collision operator is utilized, which allows to control bulk viscosity independently. Unlike the traditional Hermite polynomial space, this modified formulation allows for the independent relaxation of trace-free and trace components of the second order moments,

$$\Omega_i = \mathcal{T}^{-1} S \mathcal{T}(f_i^{eq} - f_i) + E_i, \tag{2}$$

where S corresponds to the diagonal matrix of the relaxation rates, $\mathcal{T}$ represents the transform tensor for moments, while $\mathcal{T}^{-1}$ represents its inverse, which are determined based on the set of Hermite polynomials. In Equation (2), f_i^{eq} is the discrete equilibrium distribution. The equilibrium distribution function in discrete form is determined through an expansion at a given reference temperature of the Maxwell-Boltzmann distribution, equivalently reference isothermal speed of sound c_s, via Hermite polynomials. The expansion allows then the use of the Gauss-Hermite quadrature to satisfy exact recovery of the desired number of moments of the distribution function on the selected set of discrete velocity vectors leading to:

$$f_i^{eq} = w_i \sum_{n=0}^{N} \frac{1}{n! c_s^{2n}} H_n(\mathbf{e}_i) : a_n^{eq}\left(\rho, \mathbf{u}, \frac{p}{\rho}\right), \tag{3}$$

where ":" represents the Frobenius inner product and w_i represents the lattice weight factor based on Equation (4) for three-dimensional cases. H_n denotes the Hermite polynomial tensor of rank n. The quantity a_n^{eq} is the corresponding equilibrium Hermite coefficient, $\mathbf{u}$ corresponds to velocity, p signifies pressure, ρ represents fluid density, and N indicates the expansion order.

$$\begin{aligned} w_i = \{ & w_0 = \frac{8}{27}, w_{1-6} = \frac{2}{27}, w_{7-18} = \frac{1}{54}, \\ & w_{19-26} = \frac{1}{216} \} \end{aligned} \tag{4}$$

In Equation (2), E_i is a term that takes into account for variations in the diagonal elements of the equilibrium third-order moments [6]. This term ensures that Galilean invariance is maintained in the discretized representation. In fact, the lack of independent support for diagonal terms in third-order moments by standard lattices causes viscosity to exhibit an unconventional dependence on fluid velocity, i.e., non-Galilean-invariant (GI) viscous stress. Defined as follows, the moments transformation tensor $\mathcal{T}$ is constructed using a series of modified central Hermite polynomials:

$$\mathcal{T} = [|\overline{\mathcal{T}}_0\rangle, ..., |\overline{\mathcal{T}}_N\rangle], \tag{5}$$

where column vectors $|\overline{\mathcal{T}}_i\rangle$ are based on Hermite polynomials.

The energy equation for incompressible flows but variable properties, when disregarding viscous heating, can be simplified to:

$$\frac{\partial(\rho C_p T)}{\partial t} + \nabla.(\mathbf{u}\, \rho C_p T) = \nabla.(k \nabla T) + Q, \tag{6}$$

in which T denotes temperature, k signifies thermal conductivity, C_p represents the specific heat capacity, and Q represents the heat source term. A Finite-Difference (FD) technique is employed here for solving the energy equation. The third-order WENO approach is employed for discretizing the advection term in the energy equation, ensuring stability even in regions with large gradients. For handling the diffusion terms, a fourth-order central finite difference (FD) scheme is used for spatial discretization, while a first-order explicit Euler discretization is applied in time to update the relevant fields. The term for buoyancy force ($\mathbf{F}_B$) within the flow-field equation is computed using the Boussinesq approximation in this investigation. This approximation assumes a linear relationship between the buoyancy term and the temperature difference. As a result, the momentum and energy relations become coupled, as expressed by:

$$\mathbf{F}_B = \rho_{f,0} \mathbf{g} \beta (T - T_0), \tag{7}$$

The thermal expansion coefficient β, reference temperature T_0, gravity acceleration $\mathbf{g}$, and fluid density at the specified reference temperature $\rho_{f,0}$ appear in this equation. The Exact Difference Method (EDM) force scheme is used to incorporate the bulk forces $\mathbf{F}$ and buoyancy force $\mathbf{F}_B$ arising from particle-fluid interaction through IBM into Equation (1). The Grashof number, defined in Eq. (8), quantifies buoyancy in

relation to viscosity

$$\mathrm{Gr} = \frac{\rho_f^2 \, g \, \beta \, D_p^3 \Delta T}{\mu^2}, \tag{8}$$

In this study, the Direct-Force IBM is employed to represent the fluid-particle interaction forces including heat transfer. Following the approach introduced by Uhlmann [8] and later extended to thermal IBM by [9], the force term ($\mathbf{F}_b$) at each Lagrangian node ($\mathbf{X}_b$) is computed based on the desired velocity ($\mathbf{U}^d$), as outlined in Equation (9). At each Lagrangian node, the heat source term (Q_b^n) is computed using the same way based on the desired particle temperature (T_p^d) using Equation (10):

$$\mathbf{F}_b^n = \frac{\mathbf{U}^d - \mathbf{U}^{noF}}{\Delta t}, \tag{9}$$

$$Q_b^n = \frac{T_p^d - T^{noH}}{\Delta t}, \tag{10}$$

in which Δt is the time step, n denotes current time step, and $\mathbf{U}^{noF}$ denotes the velocity at next time step that would be calculated in the absence of any external forcing (*noF*, for no forcing). For simulations conducted in three dimensions, the computation of $\mathbf{U}^{noF}$ is based on Equation (11), relying on velocity values at Eulerian points ($\mathbf{u}_{i,j,k}$).

In the same way, regarding heat source term computations at each Lagrangian node, the "no heat source" temperature T^{noH} can be calculated using Equation (12) according to the temperature at the Eulerian points ($T_{i,j,k}$). This leads finally to:

$$\mathbf{U}^{noF} = \sum_{i,j,k} \mathbf{u}_{i,j,k} \, D\left(\mathbf{x}_{i,j,k} - \mathbf{X}_b\right) (\Delta h)^3, \tag{11}$$

$$T^{noH} = \sum_{i,j,k} T_{i,j,k} \, D\left(\mathbf{x}_{i,j,k} - \mathbf{X}_b\right) (\Delta h)^3. \tag{12}$$

Here, $\mathbf{x}_{i,j,k}$ is the Eulerian nodes' position, the lattice size is denoted by Δh, and $\mathbf{X}_b$ indicates the Lagrangian points' position. The discretized Dirac delta function (D) is calculated using the 4-point delta function, as proposed by Peskin [10].

The force applied to each Eulerian node and the heat source on the Eulerian nodes can be determined using Equations (13) and (14).

$$\mathbf{F}_{i,j,k} = \rho_f \sum_{\mathbf{b,n}} \mathbf{F}_b^n \, D\left(\mathbf{x}_{i,j,k} - \mathbf{X}_b\right) \, \Delta V_b, \tag{13}$$

$$Q_{i,j,k} = \rho_f C_{p,f} \sum_{\mathbf{b,n}} Q_b^n \, D\left(\mathbf{x}_{i,j,k} - \mathbf{X}_b\right) \, \Delta V_b, \tag{14}$$

where ΔV_b represents the unit volume of the relevant Lagrangian boundary point segment. To incorporate the particle forces into the LBM, the force $F_{i,j,k}$ is added to Equation (1) using EDM force scheme; to incorporate the particles heat source term into the FD solver, the heat source $Q_{i,j,k}$ is included in Equation (6).

At each Lagrangian point, the desired velocity $\mathbf{U}^d$ is formulated as follows:

$$\mathbf{U}^d = \mathbf{U}_p + \Omega_p \times (\mathbf{X}_b - \mathbf{X}_c), \tag{15}$$

where $\mathbf{X}_c$ represents the particle center, and Ω_p and $\mathbf{U}_p$ denote the particle angular and translational velocities, respectively. By applying the fundamental laws of motion, both velocities can be updated using Equations (16) and (17):

$$M_p \frac{d\mathbf{U}_p}{dt} = -\int \mathbf{F}_b dV + M_f \frac{d\mathbf{U}_p}{dt} + (\rho_p - \rho_f) V_p \mathbf{g} + \mathbf{F}^c, \tag{16}$$

$$\mathbf{T} = I \frac{d\Omega_p}{dt} + \Omega_p \times I\Omega_p, \tag{17}$$

where the subscripts "p" indicate particle properties, while "f" refers to fluid properties. The quantity $\mathbf{F}^c$ is the summation of particle–particle and wall-particle collision forces, M represents the mass, I stands for the moment of inertia and $\mathbf{T}$ denotes the total torque experienced by the particle's center.

In the case of heat transfer, for a particle considered as being at a given temperature, one can directly set the values of T_p^d. Otherwise, for particles with varying temperature, the exchanged heat (in the following example, a heat generation Q_p^g) is added to Equation (10):

$$Q_b^n = \frac{T_p^d - T^{noH}}{\Delta t} + Q_p^g. \tag{18}$$

In this study, the contact interactions between particles are modeled using the soft-sphere Discrete Element Method (DEM), wherein the contact forces are computed based on the overlap between interacting particles. The total collision force consists of both normal and tangential components, each derived according to Hertzian contact mechanics [11]. The normal contact force between particle i and particle j is given by:

$$\mathbf{F}_{n,ij} = -k_n \, \delta_n \, \mathbf{n}_{ij} - \eta_n \, \Delta \mathbf{v}_{n,ij}, \tag{19}$$

where, k_n is the normal stiffness coefficient and is considered to be $8 \times 10^4 \frac{N}{m}$ in this work, δ_n is the overlap distance in the normal direction, η_n is the normal damping coefficient and is considered to be $10^2 \frac{kg}{s}$, $\Delta \mathbf{v}_{n,ij}$ is the relative normal velocity between particles. The tangential contact force, based on the Mindlin-Deresiewicz [12] model, is computed as:

$$\mathbf{F}_{t,ij} = -k_t \, \delta_t \, \mathbf{t}_{ij} - \eta_t \, \Delta \mathbf{v}_{t,ij}, \tag{20}$$

where, k_t is the tangential stiffness coefficient and is set to $4 \times 10^4 \frac{N}{m}$, δ_t is the integrated tangential displacement over the contact duration, η_t is the tangential damping coefficient and is considered to be $50 \frac{kg}{s}$, $\Delta \mathbf{v}_{t,ij}$ is the relative tangential velocity between particles.

To ensure consistency with physical frictional lim-

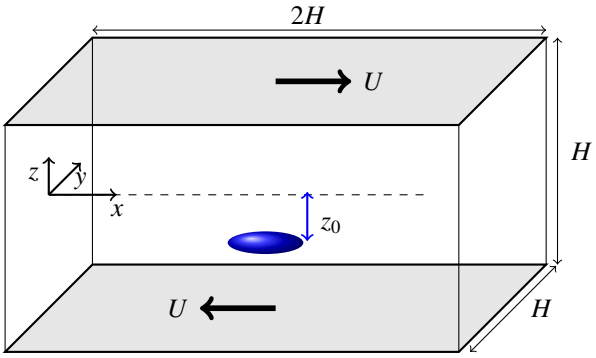

Figure 1. Illustration of the computational domain.

its, the tangential force is bounded by the Coulomb friction criterion:

$$|\mathbf{F}_{t,ij}| \leq \mu_{ij}|\mathbf{F}_{n,ij}|, \tag{21}$$

where μ_{ij} is the coefficient of friction between particles i and j.

3. RESULT

In the present investigation, we examine the flow behavior between two parallel plates moving in opposite directions, each with a constant velocity U, as depicted in Figure 1. The separation distance between the plates is denoted by H, and the computational domain is defined with dimensions $2H \times H \times H$, such that the flow direction extends twice the length of the transverse dimensions. The velocity of the fluid at the walls satisfies the no-slip condition, while periodic boundary conditions are imposed along the remaining directions of the domain.

The suspended particle under consideration is a thermally active prolate spheroid, characterized by a major radius a and a minor radius b. The particle's aspect ratio is defined as $r = a/b$, and its degree of spatial confinement within the channel is quantified using the confinement ratio $K = a/H$. The shear rate for the considered geometry is defined as

$$G = \frac{2U}{H}, \tag{22}$$

To analyze particle dynamics within the flow, we consider a particle initially positioned at (x_0, y_0, z_0) in the computational domain. The particle Reynolds number, using the major radius a as the characteristic length scale, is expressed as:

$$\mathrm{Re}_p = \frac{Ga^2}{\nu}, \tag{23}$$

where ν denotes the kinematic viscosity of the fluid.In this study, a particle Reynolds number of $\mathrm{Re}_p = 30$ is considered for all cases.

This study aims to investigate the influence of the confinement ratio on the equilibrium lateral position of the heated prolate particle in the shear-driven flow. Figure 2 illustrates the migration trajectory of a neutrally buoyant prolate spheroidal particle, initially positioned at $z_0^* = z_0/H = -0.1$, in an isothermal Couette flow. In this scenario, the balance among hydrodynamic forces, inertial lift and wall-induced interactions drives the particle toward a stable vertical equilibrium position near the lower wall. Particles with lower confinement ratios (i.e., smaller relative size compared to the channel height) tend to take longer to reach this equilibrium, which itself occurs at a lower vertical position due to altered balance of forces.

Next, the particle is assumed to be hot with a constant temperature, and a Dirichlet boundary condition—set to the same temperature as the initial fluid domain—is applied on the moving plates. When thermal effects are introduced, as shown in Figure 3 for a thermal case with $\mathrm{Gr} = 80$, the presence of heat transfer significantly alters the particle's equilibrium behavior. In the case with a Grashof number $\mathrm{Gr} = 80$, the thermally induced drag forces arising from buoyancy-driven convection dominate over gravity and other hydrodynamic contributions. As a result, the particle stabilizes in the upper region of the channel. Interestingly, decreasing the confinement ratio in the thermally active case leads to an increase in the final equilibrium height, bringing the particle closer to the upper wall. This behavior indicates a stronger influence of convective forces in less confined environments.

To examine the influence of neighboring particles on the migration dynamics and equilibrium positioning of a heated particle, a configuration of eight particles with aspect ratio $K = 0.1$ is considered. With this consideration, the packing ratio—i.e., the ratio of particle volume to total volume—is equal to 0.004. All particles are initially positioned at $z_0^* = -0.1$, but have different initial streamwise locations x_0 within the domain, with a center-to-center distance of $2.5a$. by th Figure 4 presents the time evolution of the normalized vertical position $z^* = z/H$ for eight thermally active prolate spheroidal particles. The trajectories labeled P0 through P7 correspond to individual particles, while the curve labeled *Mean* represents the ensemble averaged position over time.

Initially, all particles undergo a transient migration phase, during which they move from their initial positions toward a stable equilibrium location. This transient period is most pronounced for $T^* < 50$, reflecting rapid vertical displacement primarily driven by the dominance of convective drag forces in the early stages.

As reported earlier for the single-particle case, the vertical position eventually stabilizes near $z^* \approx 0.4$. However, the presence of multiple particles introduces considerable fluctuations around this equilibrium height. These deviations are attributed to hydrodynamic interactions and flow disturbances caused by neighboring particles. Nevertheless, the mean trajectory converges to a steady-state position similar to the single-particle case, with reducing fluctuations at later times.

Based on the simulation results, the time-averaged

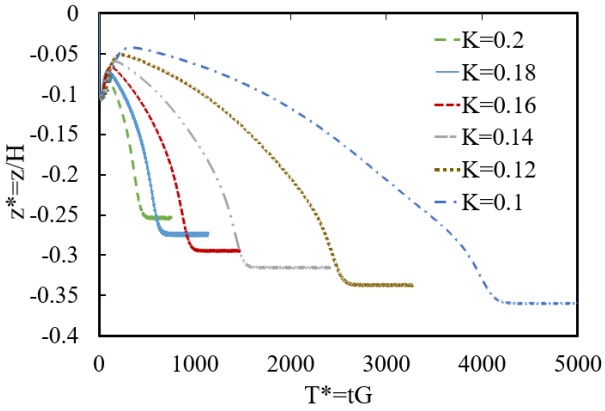

Figure 2. Migration trajectory of an isothermal prolate particle vs. dimensionless time (Gt) at various confinement ratios.

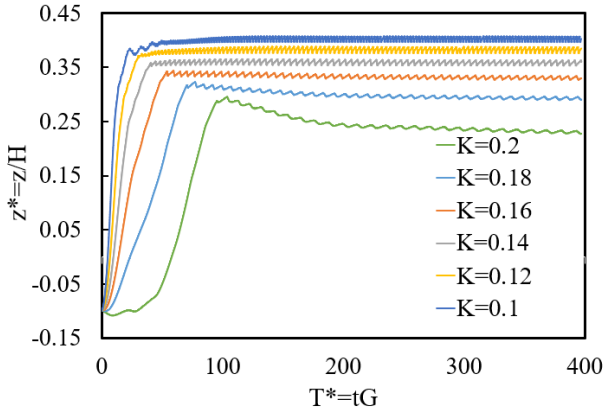

Figure 3. Migration trajectory of a hot prolate particle vs. dimensionless time (Gt) at various confinement ratios for Gr=80.

center-to-center nearest neighbor distance is approximately 3a. The increased fluctuation amplitude observed in the multi-particle case highlights the transient influence of inter-particle interactions, although the long-term equilibrium behavior remains qualitatively consistent with that of single particle. how ever that such behavior may change significantly at higher packing fractions. However, it is important to note that this behavior may change significantly at higher packing fractions.

4. CONCLUSION

In this study, we employed a hybrid computational framework combining the Lattice Boltzmann Method (LBM), Immersed Boundary Method (IBM), a finite-difference (FD) scheme, and the Discrete Element Method (DEM) to investigate the dynamic behavior of non-spherical particles in a shear-driven flow. The results reveal that the confinement ratio significantly influences both the time required for a particle to reach its equilibrium position and the vertical location of that position.

In the isothermal case, particles with lower confinement ratios (i.e., smaller particles relative to the channel height) migrate more slowly toward their equilibrium positions compared to larger particles. Conversely, in the thermal case, smaller particles reach equilibrium more quickly, suggesting that thermally induced forces accelerate vertical migration.

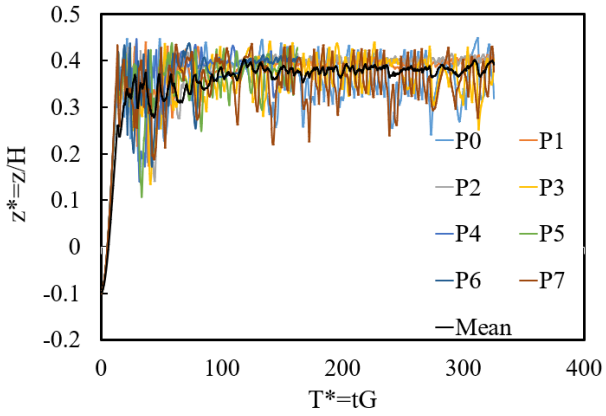

Figure 4. Migration trajectory of eight hot prolate particle vs. dimensionless time (Gt) at confinement ratio K=0.1 for Gr=80.

Furthermore, in both isothermal and thermal configurations, particles with lower confinement ratios tend to equilibrate farther from the channel centerline. The presence of multiple particles within the domain introduces complex interactions. Particle-particle collisions, coupled with hydrodynamic interactions and flow disturbances, lead to chaotic fluctuations in the vertical equilibrium positions. However the mean trajectory position is consistent with that of single particle.

5. ACKNOWLEDGEMENTS

The authors gratefully acknowledge funding by the Deutsche Forschungsgemeinschaft (DFG, German Research Foundation) within Project number 465872891. Also, the authors gratefully acknowledge the Gauss Centre for Supercomputing e.V. (www.gauss-centre.eu) for funding this project by providing computing time on the GCS Supercomputer [HAWK| HUNTER] at Höchstleistungsrechenzentrum Stuttgart (www.hlrs.de)

REFERENCES

[1] Jeffery, G. B., 1922, "The motion of ellipsoidal particles immersed in a viscous fluid", *Proceedings of the Royal Society of London Series A, Containing papers of a mathematical and physical character*, Vol. 102 (715), pp. 161–179.

[2] Fox, A. J., Schneider, J. W., and Khair, A. S., 2021, "Dynamics of a sphere in inertial shear flow between parallel walls", *Journal of Fluid Mechanics*, Vol. 915, p. A119.

[3] Lauricella, G., Naderi, M. M., Zhou, J., Papautsky, I., and Peng, Z., 2024, "Bifurcation of equilibrium positions for ellipsoidal particles in iner-

tial shear flows between two walls", *Journal of Fluid Mechanics*, Vol. 984, p. A47.

[4] Gharibi, F., Fard, A. E., and Thévenin, D., 2025, "Dynamic behaviour of a thermal spheroid particle in shear flows", *Journal of Fluid Mechanics*, Vol. 1013, p. A40.

[5] Khalili, B., Rahnama, M., Jafari, S., Gharibi, F., and Jahanshahi Javaran, E., 2017, "Lattice Boltzmann simulation of solid particles motion in a three dimensional flow using smoothed profile method", *Journal of Applied Fluid Mechanics*, Vol. 10 (4), pp. 1091–1103.

[6] Gharibi, F., Hosseini, S. A., and Thévenin, D., 2024, "A hybrid lattice Boltzmann/immersed boundary method/finite-difference model for thermal fluid-solid interactions", *International Communications in Heat and Mass Transfer*, Vol. 155, p. 107525.

[7] Eshghinejadfard, A., 2017, "Lattice Boltzmann simulation of laminar and turbulent two-phase flows", Ph.D. thesis, Otto-von-Guericke-Universität Magdeburg.

[8] Uhlmann, M., 2005, "An immersed boundary method with direct forcing for the simulation of particulate flows", *Journal of Computational Physics*, Vol. 209 (2), pp. 448–476.

[9] Eshghinejadfard, A., and Thévenin, D., 2016, "Numerical simulation of heat transfer in particulate flows using a thermal immersed boundary lattice Boltzmann method", *International Journal of Heat and Fluid Flow*, Vol. 60, pp. 31–46.

[10] Peskin, C. S., 2002, "The immersed boundary method", *Acta Numerica*, Vol. 11, p. 479–517.

[11] Johnson, K. L., 1987, *Contact mechanics*, Cambridge university press.

[12] Mindlin, R. D., and Deresiewicz, H., 2021, "Elastic Spheres in Contact Under Varying Oblique Forces", *Journal of Applied Mechanics*, Vol. 20 (3), pp. 327–344.

Conference on Modelling Fluid Flow (CMFF'25)
The 19th International Conference on Fluid Flow Technologies
Budapest, Hungary, August 26 - August 29, 2025

A NOVEL SPH MODEL FOR THROMBUS FORMATION

Sumanta LAHA[1,2], Georgios FOURTAKAS[1], Prasanta.K. DAS[2], Amir KESMIRI[1,3]

[1] Corresponding Author. School of Engineering, The University of Manchester, M13 9PL, UK E-mail: sumanta.laha@manchester.ac.uk
[2] Department of Mechanical Engineering, Indian Institute of Technology Kharagpur, India
[3] Manchester University NHS Foundation Trust, Manchester, M13 9PL, UK. E-mail: a.keshmiri@manchester.ac.uk

ABSTRACT

Cardiovascular diseases remain a major global health challenge, often driven by uncontrolled thrombus formation. A comprehensive understanding of its biochemical, biological, and mechanical mechanisms is crucial. Due to the complexities and limitations of in-vivo studies, computational fluid dynamics (CFD) has emerged as a viable and cost-effective alternative. This research presents a novel smoothed particle hydrodynamics (SPH)-based methodology for modelling thrombus formation and growth. Optimised for graphics processing unit (GPU) execution, the approach significantly reduces computational time for thrombus simulations. Two distinct thrombus growth strategies—the penalty approach and the dissipation approach—are investigated to determine the most effective method. The penalty approach incorporates a fibrin-linked velocity penalty term, while the dissipation approach integrates the Einstein equation with fibrin concentration. The model captures the coagulation cascade by simulating key biochemical components, including thrombin, prothrombin, fibrinogen, fibrin, and both activated and resting platelets. The implementation utilises the DualSPHysics solver, incorporating wall shear stress effects to enhance thrombus modelling. To validate the model, simulations were performed in a backward-facing step, demonstrating the effectiveness of SPH in predicting device-induced thrombosis. This study offers a promising step toward advancing cardiovascular research and improving clinical outcomes.

Keywords: Thrombosis, Thrombus formation, Coagulation cascade, Thrombin, Fibrin, DualSPHysics, GPU, CFD, Smoothed particle hydrodynamics.

NOMENCLATURE

Due to space constraints, only a selection of key nomenclature used in this study is provided below.

Biochemical Parameters		
C_{th}	[M]	Thrombin concentration
C_{fb}	[M]	Fibrin concentration
C_{pt}	[M]	Prothrombin concentration
C_{rp}	[PLT ml^{-1}]	Resting platelet concentration
C_{ap}	[PLT ml^{-1}]	Activated platelet concentration
k_{th}	[UPLT^{-1}s^{-1}μM^{-1}]	Thrombin generation rate constant
τ	[Pa]	Wall shear stress

1. INTRODUCTION

Thrombosis is a major contributor to cardiovascular diseases, as it can obstruct blood flow within vessels, potentially leading to life-threatening emergencies by restricting circulation to vital organs. The symptoms vary depending on the clot's location and may include chest pain, breathing difficulties, and skin discoloration, as well as severe conditions like stroke, pulmonary embolism, or ictus. According to Virchow's triad [1], three primary factors contribute to vascular thrombosis: increased blood coagulability, altered blood flow (stasis), and damage to the vessel wall or endothelium. The process of thrombus formation, also known as the coagulation cascade, involves a series of complex biochemical reactions. It is primarily initiated through two pathways—the intrinsic and extrinsic pathways—which eventually converge in the coagulation process. In vascular injury, subendothelial cells become exposed to blood flow, and prolonged exposure triggers biochemical interactions between tissue factors and blood cells, leading to platelet activation and adhesion. Simultaneously, the coagulation cascade is activated, promoting fibrin formation, which stabilizes the clot and facilitates thrombus growth.

Over the years, extensive efforts have been devoted to understanding the intricate mechanisms underlying thrombus formation, drawing from both

fluid mechanics and chemical kinetics. Given the complexity of this process, numerical methods, including semi-empirical and computational modelling, play a crucial role in gaining a macroscopic understanding of thrombus formation.

Computational fluid dynamics (CFD) has emerged as a powerful tool for integrating the hydrodynamics of blood flow with biochemical reactions, building on the success of computational techniques in analysing and predicting haemodynamics in various cardiovascular diseases and medical devices [2]–[5]. While research in this field is not new, its continued importance drives ongoing efforts to refine existing models and develop novel methodologies. Leiderman and Fogelson [6] were pioneers in developing an early spatiotemporal mathematical model for platelet aggregation and blood coagulation under flow conditions. Their model provides a comprehensive framework for understanding coagulation biochemistry, chemical activation, platelet deposition, and the dynamic interaction between fluid dynamics and the growing platelet mass. In a similar vein, Govindarajan et al. [7] introduced an innovative model designed to simulate thrombus formation under venous flow conditions. After validating their model against the work of Colace et al. [8], they further explored the hydraulic resistance caused by platelets and thrombus, offering valuable insights into the complex interactions within the bloodstream.

Particle tracking and time history are crucial for thrombus modelling and are well-suited to the Lagrangian description of motion. Additionally, fluid-structure interaction (FSI) between thrombus, blood, and the cardiovascular vessel plays a key role in accurately simulating thrombus growth and its subsequent breakdown. Recently, there has been an increasing trend in using particle-based Lagrangian approaches for modelling thrombus formation. Tsubota et al. [9] investigated thrombus formation following Fontan surgery using a moving particle semi-implicit scheme. In their model, thrombus formation and attachment were governed by shear rate thresholds and spring attraction forces. While other simplified particle-based models, which consider thrombus shells as thrombin species, exist, they fail to incorporate biochemical reactions.

In recent years, meshless methods, particularly Smoothed Particle Hydrodynamics (SPH), have gained traction as effective tools for simulating cardiovascular haemodynamics [10], [11]. Chui et al. [12] applied SPH to develop a basic clotting model based on local shear rate, where clotting begins in areas subjected to shear stress below a certain threshold. Al Saad et al. [13] advanced SPH modelling by describing thrombus formation with platelet adhesion and aggregation, utilising elastic forces dependent on the distance from an injured vessel. Wang et al. [14] built on this by introducing biochemical reactions and a velocity decay term linked to fibrin concentration. However, focusing solely on fibrin presents a potential limitation. More recently, Monteleone et al. [15] presented an SPH model incorporating various biochemical factors like thrombin, prothrombin, fibrin, and activated platelets. This model used convection-diffusion equations to estimate primary concentrations and switching functions based on threshold concentrations to simulate platelet activation. Upon reaching a critical concentration of bound platelets, particles transition to solid form, mimicking thrombus formation. However, this model overlooks advection terms, wall shear stress in thrombus modelling, and the gradual reduction of platelet velocity in response to rising fibrin concentrations.

The current study proposes a novel methodology based on SPH to model thrombus formation, accumulation, and growth, addressing the limitations of Monteleone et al.'s model [15]. The key innovation lies in combining SPH nearest-neighbour searching to simulate platelet activation with the mesh-like effects of fibrin networks. This approach also incorporates advanced modelling techniques to capture particle deposition within the thrombus. Two unique approaches are employed: a penalty approach, which applies a velocity penalty term based on fibrin concentration to simulate restriction effects, and a dissipation approach, where fibrin concentration is linked to the Einstein equation to introduce an additional dissipation term. To further enhance the model, wall shear stress from recent work is integrated to couple mechanical influences with biochemical processes. A novel method has been introduced to dynamically activate and drive the model based on wall shear stress. The methodology has been rigorously validated against experimental data, including thrombus formation. The more detailed work of the thrombus modelling could be found in the recent publication from same authors [16].

2. MATERIAL AND METHODS

In this section, a brief description of the SPH formulation is provided. In SPH, the continuous approximation of a scalar field function $A(r)$ at a point r in a one-dimensional domain is expressed in by integral representation, written as:

$$A(r) := \int W(r - r', h) A(r')\, d\omega \tag{1}$$

where W is a smoothing function or smoothing kernel, h is the smoothing length in the support domain of the kernel function and ω is the volume of the integral.

The discrete form of Eq. (1) can be written as,

$$A_i = \sum_j^N W(r_i - r_i, h) A_j\, V_j \tag{2}$$

where ω is discretized into N computational nodes or particles. Here, i and j represent the interpolating and neighbouring particles,

respectively, and V is the volume of the particle, defined as $V = m/\rho$, with m being the mass and ρ the density of the particle.

The choice of a smoothing function directly impacts the solution. Various smoothing kernels are available in the literature [17]. In this work, Wendland C^2 kernel has been selected due to its higher-order (5th) nature, which allows it to capture higher-order effects with improved accuracy [17]. The Wendland kernel is defined as follows [18],

$$W(r,h) = \begin{cases} \alpha_d \left(1-\frac{q}{2}\right)^4 (2q+1), & 0 \le q \le 2 \\ 0 & q > 2 \end{cases} \quad (3)$$

where $q = |r_{ij}|/h$ and α_d is $\frac{3}{4h}$, $\frac{7}{4\pi h^2}$, $\frac{21}{16\pi h^3}$ for 1D, 2D, and 3D, respectively. For further information on the SPH method, the reader is directed to [19] and [20].

The governing equations for the haemodynamics are the mass and momentum conservation. To solve these equations, the domain is discretised, and approximate values for the field functions are calculated at specific points. Throughout the SPH simulation, the mass of each particle is kept constant while the density of the particles changes according to the continuity equation. The general form of the continuity equation is as follows,

whereas the SPH discrete form of Eq. (4) can take the following form [21],

$$\frac{\mathrm{D}\rho}{\mathrm{Dt}} = -\rho \nabla \cdot (\mathbf{u}) \quad (4)$$

$$\frac{\mathrm{D}\rho}{\mathrm{Dt}} = \rho_i \sum_{j \in P} \frac{m_j}{\rho_j} (\mathbf{u}_i - \mathbf{u}_j) \cdot \nabla W_{ij} \quad (5)$$

where $\mathbf{u}$ is the velocity of the particle and t denotes physical time. Herein, i and j denote the interpolating and neighbouring particles respectively and $P = F \cup B$ where F and B denote the fluid and boundary particles respectively.

The momentum conservation equation can be written as,

$$\frac{\mathrm{D}\mathbf{u}}{Dt} = -\frac{1}{\rho}\nabla p + \Gamma + \mathbf{f} \quad (6)$$

where p is the pressure, Γ is the dissipative term and $\mathbf{f}$ represents external forces. In SPH notation, Eq. (6) can be expressed as,

$$\frac{\mathrm{D}\mathbf{u}}{\mathrm{Dt}} = -\sum_{j \in P} \left(\frac{p_i + p_j}{\rho_i \rho_j}\right) \nabla W_{ij} m_j + \langle \Gamma \rangle + \mathbf{f} \quad (7)$$

The above equation satisfies the momentum conservation.

Instead of the widely used artificial viscosity scheme, a combination of Shao and Lo operators a large eddy Sub-Particle Scale (SPS) [22] turbulence model has been used in the present study as described by Dalrymple and Rogers [23] to define the dissipation term. In this scheme, the momentum equation is given by,

$$\frac{\mathrm{D}\mathbf{u}}{\mathrm{Dt}} = -\frac{1}{\rho}\nabla p + \mathbf{g} + \nu \nabla^2 \mathbf{u} + \frac{1}{\rho}\nabla \cdot \boldsymbol{\tau} \quad (8)$$

where $\nu\nabla^2\mathbf{u}$ is the laminar viscous stress and it can be expressed as [24],

$$(\nu \nabla^2 \mathbf{u})_i = \sum_{j \in P} m_j \left(\frac{4\nu \mathbf{r_{ij}} \cdot \nabla_i W_{ij}}{(\rho_i + \rho_j) + (r_{ij}^2 + 0.01h^2)}\right) \mathbf{u}_{ij} \quad (9)$$

The last term in the right-hand side of Eq. (8) is accounted for by the SPS stress tensor and that term can be expressed by the means of Favre averaging which is generally used to compute compressibility in weakly compressible SPH [23]. The term is as follows,

$$\frac{1}{\rho}\nabla \cdot \tau_i^{\alpha\beta} = \sum_{j \in P} m_j \left(\frac{\tau_i^{\alpha\beta} + \tau_j^{\alpha\beta}}{\rho_i \rho_j}\right) \cdot \nabla_i W_{ij} \quad (10)$$

here, τ is the SPS stress tensor and has been defined in Einstein notation over superscripts α and β (spatial coordinates).

Therefore, the momentum Eq. (8) can be expressed in SPH terms by,

$$\frac{\mathrm{D}u_i^a}{\mathrm{Dt}} = -\sum_{j \in P} \left(\frac{p_i + p_j}{\rho_i \rho_j}\right) \frac{\partial W_{ij}}{\partial x_i^\alpha} m_j + \mathrm{f}_i^a + \sum_{j \in P} m_j \left(\frac{4\nu r_{ij}^\beta \frac{\partial W_{ij}}{\partial x_i^\beta} W_{ij}}{(\rho_i + \rho_j) + (r_{ij}^2 + 0.01h^2)}\right) u_{ij}^a + \sum_{j \in P} m_j \left(\frac{\tau_i^{\alpha\beta} + \tau_j^{\alpha\beta}}{\rho_i \rho_j}\right) \frac{\partial W_{ij}}{\partial x_i^\beta} W_{ij} \quad (11)$$

Most of the hydrodynamic problems can be approximated by the weakly compressible SPH (WCSPH) scheme. To compute the fluid pressure based on the density of the particle, an equation of state (EOS) is employed, and by regulating the compressibility, the speed of sound is kept artificially low. As a result, the numerical speed of sound is restricted to be at least ten times the speed of the maximum velocity of the system which retains the density variation to less than 1%. This resembles closely an incompressible flow approach.

In the present study, Tait's EOS is used [25], [26] which is given by,

$$P = \frac{c^2 \rho_0}{\gamma} \left(\left(\frac{\rho}{\rho_0} \right)^{\gamma} - 1 \right), \quad (12)$$

where $\gamma = 7$ is the polytrophic index, ρ_0 is the density of the reference fluid at the beginning of the simulation, and the c is the speed of sound at the reference density. In the present work the smoothing length has been taken 1.7 times of the particle spacing and the viscosity of the fluid has been chosen like blood which is 3cP.

2.1. Physiology of the thrombus formation

The key physical processes involved in thrombus formation, which will be incorporated into the present model, are outlined below. Thrombus formation begins with primary haemostasis, where a platelet plug is formed, followed by the activation of the coagulation cascade. When vascular injury occurs, the exposure of collagen initiates this process.

Vasoconstriction: The initial response to vascular injury involves the constriction of blood vessels, reducing blood flow to the affected area.

Platelet plug formation: Platelets adhere to the exposed collagen at the injury site, become activated, and aggregate to form a temporary plug that helps prevent further blood loss.

Activation of the coagulation cascade: Once primary haemostasis is established, the coagulation cascade is triggered, leading to secondary haemostasis.

Final clot formation: As the coagulation cascade progresses, fibrin concentration increases, reinforcing the clot with a dense fibrin network. This marks the final stage of thrombus formation. Eventually, after tissue repair is complete, fibrinolysis occurs, breaking down and dissolving the clot.

2.2. Modelling of the thrombus formation

The modelling process begins with identifying damaged zones where high wall shear stress ($\tau_h > 10Pa$) is activating platelets on a damaged vessel surface, and low wall shear stress ($\tau_l < 0.02Pa$) promotes platelet adhesion and accumulation. Fluid particles within a distance of $2h$ (smoothing radius) from the damaged wall are considered contributors to thrombus formation. Prothrombin concentration reduces with thrombin formation, governed by an advection-diffusion equation (Eq. 13) Following the methodology proposed by Monteleone et al. [15], a source term has been selected based on the chemical kinetics.

$$\frac{\partial C_k}{\partial \mathrm{t}} = \nabla \cdot (D_k \nabla C_k) - \nabla \cdot (\mathbf{u_k} C_k) + R_k \quad (13)$$

where C is the concentration of the bio-chemical species, D is the diffusion coefficient, $\mathbf{u}$ is the velocity of the particle and R is the respective source term. Eq. (13) has been solved for prothrombin, thrombin, fibrin and activated platelet respectively. The above equation discretised and computed through SPH approximation. The SPH version of the equation for a particular species is as follows, where i and j represent the interpolating and neighbouring particles, respectively,

The source term for the prothrombin and thrombin are as follows,

$$\frac{\partial C_i}{\partial \mathrm{t}} = \sum_{j \epsilon P} m_j \left(\frac{4 D_i \mathbf{r_{ij}} \cdot \nabla_i W_{ij}}{(\rho_i + \rho_j) + (r_{ij}^2 + 0.01h^2)} \right) C_{ij} + C_i \sum_{j \epsilon P} \frac{m_j}{\rho_j} (\mathbf{u}_i - \mathbf{u}_j) \cdot \nabla W_{ij} + \mathbf{u}_{\mathrm{i}} \sum_{j \epsilon P} \frac{m_j}{\rho_{\mathrm{j}}} (C_i - C_j) \cdot \nabla W_{ij}, \quad + R_i \quad (14)$$

$$R_{th} = k_{th}^{rp} C_{rp} C_{pt} + k_{th}^{ap} C_{ap} C_{pt} \quad (15)$$

$$R_{pt} = -R_{th} \quad (16)$$

where k_{th}^{rp} and k_{th}^{ap} is the kinetic constant of the resting and activated platelets for the thrombin conversation from the prothrombin. C_{rp}, C_{ap}, C_{pt} are the concentration of the resting platelet, activated platelet and prothrombin, respectively.

When thrombin concentration of a particle exceeds a threshold (C_{th_th}), they are considered as activated platelets. Biochemical interactions between prothrombin, thrombin, and fibrin, governed by Michaelis-Menten kinetics, drive this process, while activated platelets are drawn toward the wall or nearby activated platelets, promoting aggregation.

In the final mechanistic step, velocities of the particles must be reduced based on the fibrin concentration. In the penalty approach, a velocity penalty term proposed by Wang et al. [14] has been introduced,

$$u_{penalty} = \beta \left(1 - \left(\frac{C_{fb,i}}{C_{fb,i}, th} \right)^{1.5} \right) \quad (17)$$

Here $C_{fb,i}$ is the concentration of the fibrin of the interpolating particle and β is a penalty factor considered 1 in the present case. This term gradually reduces particle velocity depending on fibrin concentration, ultimately setting it to rest.

$$\mathbf{u_{i\_new}} = \mathbf{u_i}\, u_{penalty} \quad (18)$$

Table 1. Details of the computational hardware and simulation parameters

Hardware	Geometry domain	No of particle	Run Time
NVIDIA RTX V100 GPU	120×10×10mm (L × B × H)	60,550	40 min
		317,818	4 hours
		1,072,832	32 hours

It has been demonstrated that reasonable prediction of thrombus formation is achieved based on the above modelling technique. However, the gradual decrease in local velocity during fibrin formation is based on an empirical penalty function. This gradual decrease in velocity is due to the deposition of fibrin being similar to fluid flow with dispersion where the viscosity may be predicted through Einstein constitutive equation. Therefore, in the dissipation approach, an additional viscous term is proposed. In the momentum equation the kinematic viscosity ν has been replaced by ν_c by using the Einstein constitutive equation for the viscosity, thus

where φ is an arbitrary constant tuned based on the initial fluid viscosity and has a value of $O(10)^{12}$, sufficiently large to bring the fluid to a complete stop. Therefore, the modified momentum equation based on Eq. (8) can be written as,

$$\frac{\mathrm{D}\mathbf{u}}{\mathrm{D}t} = -\frac{1}{\rho}\nabla p + \mathbf{f} + \nu\nabla^2\mathbf{u} + \left(C_{fb,i}\varphi\right)\nabla^2\mathbf{u} + \frac{1}{\rho}\nabla.\boldsymbol{\tau} \tag{19}$$

Evidently, while the concentration of fibrin (i.e. the fibrin mesh) increases, the term ν_c rises, leading to the deposition of the particles. This approach aligns closely with the physics of clot formation, as the fibrin mesh captures more platelets and reduces flow velocity, supporting the final clot formation. Thereafter, at the final stage while the concentration of the fibrin exceeds a threshold, velocity of the particles is set to zero.

2.3. Implementation and Hardware Acceleration

In this study, the thrombus model has been implemented in DualSPHysics [27], an open-source, C++-based code that leverages graphics processing unit (GPU) hardware acceleration. The code utilises the WCSPH formulation, as discussed in sub sections 2.1 and 2.2. The modified dynamic boundary condition (mDBC) proposed by English et al. [28] has been applied in all the validation test cases. For a more detailed explanation of the boundary condition implementation, please refer to [28]. Given that thrombosis is a time-intensive phenomenon, relying solely on CPU-based models can be impractical due to prolonged simulation runtimes. To enhance computational efficiency, the thrombus model in this study has been specifically designed and optimised for execution on GPUs. All simulations were conducted using the University of Manchester's Computational Sharing Facility (CSF3) with NVIDIA RTX V100 GPUs.

Validation test case was performed in a 3D backward-facing step (BFS) [29]. A detailed description of these test cases is provided in Section 3. Additionally, Table 1 presents the computational time required to run the 3D BFS test cases at different resolutions, illustrating the average simulation runtime of the thrombus model.

3. RESULTS AND DISCUSSIONS

Generally, direct validation of any thrombus model is challenging due to the limited availability of experimental data. Nevertheless, in the present work, the efficacy of the proposed model is demonstrated through case study as validation basis. considering thrombus formation in a backward-facing step geometry as proposed by Taylor et al. [29].

Here, a three-dimensional backward-facing step has been chosen for the thrombus formation. This is a common configuration in fluid dynamics to study flow recirculation, separation and attachment, all of

$$\nu_c = (1 + C_{fb,i}\varphi)\nu \tag{20}$$

which are favourable for the thrombus formation. Moreover, this test case is one of the popular benchmark test cases for the validation of the thrombus model. A geometry of the BFS proposed by Taylor et al. [29] has been reconstructed as depicted in Fig. 1 (side view). A steady flow of 0.2 m/s has been prescribed at the inlet, while the outlet is kept at a zero constant pressure. More detailed parameters for this case study could be found in [16].

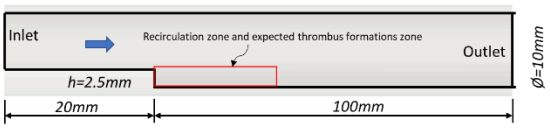

Figure 1. Schematic diagram of the fluid domain of the backward facing step test case.

3.1. Penalty Approach

Using the penalty approach, Fig. 2 illustrates that thrombus formation begins at the step corner and expands both axially and radially. The maximum thrombus length is ten times the step height, aligning with the findings of Taylor et al. [29]. The top view

of the thrombus in BFS geometry, resembling an expanding triangle, is compared in Fig. 2 with the experimental data from Taylor et al. [29], showing good agreement.

Fig. 4 further validates the proposed model quantitatively by comparing thrombus height, length, and surface area over time. The model accurately predicts thrombus length, as also visually confirmed in Fig. 2. However, while the SPH model closely matches the experimental thrombus shape and length at the 5th time instant, it tends to slightly over-predict experimental results qualitatively. In terms of thrombus height and exposed surface area, the model's predictions align well with the experimental data from Taylor et al. [29].

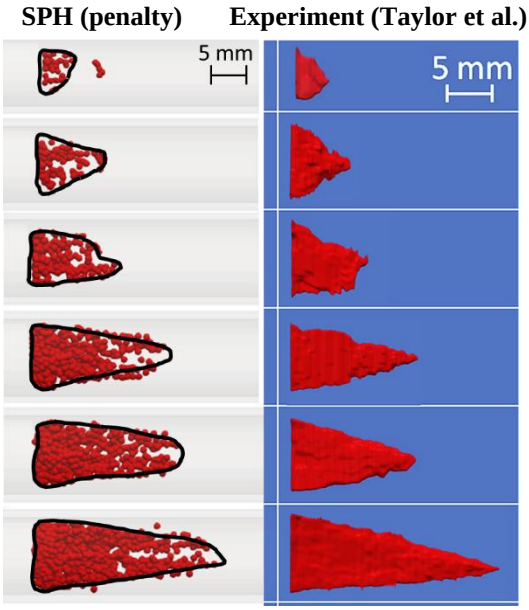

Figure 2. Comparison of predicted thrombus shape in the BFS geometry against the experimental observation by Taylor et al. using the penalty approach at different times

Nevertheless, at the 4th and 5th time instants, the simulated thrombus height slightly exceeds the experimental error range, with an estimated deviation of 5%. A similar deviation is observed for the exposed surface area. These results highlight the accuracy and reliability of the proposed model. It is important to note that this model represents an accelerated approach to thrombus formation, designed to reduce computational runtime. This expedited methodology is inspired by similar approaches found in the existing literature [15].

3.2. Dissipation approach

After successfully implementing the penalty approach for thrombus modelling using the velocity penalty term, an alternative dissipation approach was explored. As previously discussed, this method is more physiologically relevant, incorporating an additional fibrin-linked dissipation term based on Einstein's viscosity equation. The same test on the BFS geometry was repeated using the dissipation approach, while maintaining identical boundary conditions.

As shown in Fig. 3, the dissipation approach reasonably predicts thrombus shapes, though some noise in the form of unwanted random particles—absent in the penalty approach—is observed due to numerical instabilities. The thrombus shapes predicted by the dissipation approach are slightly more compressed radially than those obtained using the penalty approach, resulting in a closer match with experimental observations [29].

For quantitative validation, the thrombus length, height, and surface area predicted by the dissipation approach were compared with experimental results from Taylor et al. [29], as shown in Fig. 4. While the predicted thrombus length closely matches or slightly overestimates the initial model's results, the height and surface area are slightly underestimated, aligning more closely with experimental data. This highlights the improved accuracy of the dissipation approach.

It is important to note that, while the dissipation approach provides more physically accurate results, it is computationally demanding. Unlike the penalty approach, which employs a straightforward velocity reduction mechanism with small time-steps, the dissipation approach incorporates an additional viscous dissipation term, significantly increasing computational costs. Furthermore, the coefficient in Einstein's viscosity equation plays a crucial role and must be carefully calibrated before implementation. Despite these challenges, when properly executed, the dissipation approach enhances the accuracy of thrombus modelling

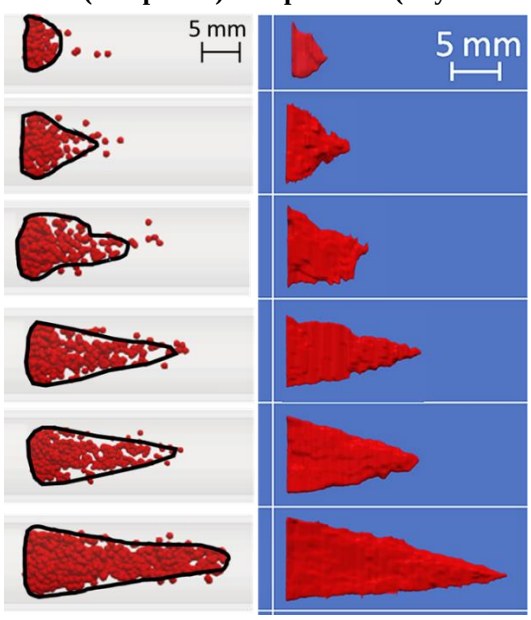

Figure 3. Comparison of predicted thrombus shape in the BFS geometry against the

experimental observation by Taylor et al. using the dissipation approach at different times

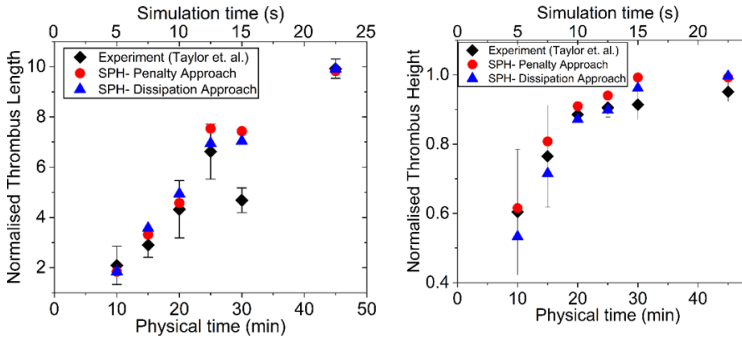

Figure 4. Comparison of the length height, and the surface area of the thrombus shape in the BFS geometry predicted by the present model against the experimental observation by Taylor et al. The length and height have been normalised by the step height

4. CONCLUSION

This study presents a novel SPH-based computational model for thrombus formation, integrating biochemical reactions and fluid dynamics to capture key aspects of clot development. A unique platelet activation and aggregation mechanism, implemented through the nearest neighbours searching method, enhances the model's physiological accuracy. Two distinct velocity reduction approaches were introduced: an empirical velocity penalty term and a physics-driven dissipation method based on Einstein's viscosity equation. While both approaches effectively simulate thrombus formation, the dissipation method provides improved accuracy by incorporating a more realistic representation of fibrin-linked dissipation. The model successfully replicates thrombus formation in pressure-driven microchannels and a backward-facing step, demonstrating strong agreement with experimental observations in terms of thrombus size, shape, and surface area. However, the complexity of thrombus formation necessitates certain simplifications. One key limitation is the high computational cost, which scales with resolution, requiring a scaled-down time frame rather than real physical time- a common trade-off in similar studies. Despite these limitations, the model demonstrates the potential of SPH in simulating thrombus formation in complex geometries where traditional mesh-based methods face challenges. Its ability to predict device-induced thrombosis further highlights its relevance for cardiovascular research and medical applications. Future work will focus on enhancing the model's physiological accuracy by incorporating initial pathway reactions, antithrombin dynamics, and a more refined treatment of clot evolution, ultimately improving its applicability in biomedical simulations.

ACKNOWLEDGEMENTS

The first author would like to acknowledge the Ph.D. funding under the 'Dual Doctoral Programme with the IIT Kharagpur' awarded by the University of Manchester. The underpinning research in this work has also been supported by the UKRI Engineering and Physical Sciences Research Council (EPSRC), under the grant EP/M015599/

REFERENCES

[1] R. Virchow, *Gesammelte abhandlungen zur wissenschaftlichen medicin*. BoD--Books on Demand, 2022.

[2] M. Mcelroy *et al.*, "Identification of the haemodynamic environment permissive for plaque erosion," *Sci. Rep.*, pp. 1–10, 2021, doi: 10.1038/s41598-021-86501-x.

[3] A. Keshmiri and K. Andrews, "Vascular Flow Modelling Using Computational Fluid Dynamics," in *Handbook of Vascular Biology Techniques*, 2015. doi: 10.1007/978-94-017-9716-0.

[4] A. Ruiz-Soler, F. Kabinejadian, M. M. A. Slevin, P. J. P. J. Bartolo, and A. Keshmiri, "Optimisation of a Novel Spiral-Inducing Bypass Graft Using Computational Fluid Dynamics," *Sci. Rep.*, vol. 7, no. 1, 2017, doi: 10.1038/s41598-017-01930-x.

[5] M. McElroy, A. Xenakis, and A. Keshmiri, "Impact of heart failure severity on ventricular assist device haemodynamics: a computational study," *Res. Biomed. Eng.*, vol. 36, no. 4, pp. 489–500, 2020, doi: 10.1007/s42600-020-00088-2.

[6] K. Leiderman and A. L. Fogelson, "Grow with the flow: A spatial-temporal model of platelet deposition and blood coagulation under flow," *Math. Med. Biol.*, vol. 28, no. 1, pp. 47–84, 2011,

[7] V. Govindarajan, V. Rakesh, J. Reifman, and A. Y. Mitrophanov, "Computational Study of Thrombus Formation and Clotting Factor Effects under Venous Flow Conditions," *Biophys. J.*, vol. 110, no. 8, pp. 1869–1885,

2016, doi: 10.1016/j.bpj.2016.03.010.
[8] T. V Colace, R. W. Muthard, and S. L. Diamond, “Thrombus growth and embolism on tissue factor-bearing collagen surfaces under flow: Role of thrombin with and without fibrin,” *Arterioscler. Thromb. Vasc. Biol.*, vol. 32, no. 6, pp. 1466 – 1476, 2012, doi: 10.1161/ATVBAHA.112.249789.
[9] K. I. Tsubota, K. Sughimoto, K. Okauchi, and H. Liu, “Particle method simulation of thrombus formation in fontan route,” *Model. Simul. Sci. Eng. Technol.*, pp. 387–396, 2016, doi: 10.1007/978-3-319-40827-9_30.
[10] S. Laha, G. Fourtakas, P. K. Das, and A. Keshmiri, “Fluid-Structure Interaction Modelling of Bi-Leaflet Mechanical Heart Valves Using Smoothed Particle Hydrodynamics,” *Phys. Fluids*, pp. 1–24, 2023, doi: 10.1063/5.0172043.
[11] S. Laha, G. Fourtakas, P. K. Das, and A. Keshmiri, “Smoothed particle hydrodynamics based FSI simulation of the native and mechanical heart valves in a patient-specific aortic model,” *Sci. Rep.*, vol. 14, no. 1, pp. 1–18, 2024, doi: 10.1038/s41598-024-57177-w.
[12] Y. P. Chui and P. A. Heng, “A meshless rheological model for blood-vessel interaction in endovascular simulation,” *Prog. Biophys. Mol. Biol.*, vol. 103, no. 2–3, pp. 252–261, 2010,
[13] M. Al-Saad, C. A. Suarez, A. Obeidat, S. P. A. Bordas, and S. Kulasegaram, “Application of smooth particle hydrodynamics method for modelling blood flow with thrombus formation,” *C. - Comput. Model. Eng. Sci.*, vol. 122, no. 3, pp. 831–862, 2020, doi: 10.32604/cmes.2020.08527.
[14] F. Wang *et al.*, “Particle hydrodynamic simulation of thrombus formation using velocity decay factor,” *Comput. Methods Programs Biomed.*, vol. 207, p. 106173, 2021, doi: 10.1016/j.cmpb.2021.106173.
[15] A. Monteleone, A. Viola, E. Napoli, and G. Burriesci, “Modelling of thrombus formation using smoothed particle hydrodynamics method,” *PLoS One*, vol. 18, no. 2 February, pp. 1–24, 2023, doi: 10.1371/journal.pone.0281424.
[16] S. Laha, G. Fourtakas, P. K. Das, and A. Keshmiri, “Graphics processing unit accelerated modeling of thrombus formation in cardiovascular systems using smoothed particle hydrodynamics,” *Phys. Fluids*, vol. 37, no. 2, 2025, doi: 10.1063/5.0250640.
[17] W. Dehnen and H. Aly, “Improving convergence in smoothed particle hydrodynamics simulations without pairing instability,” *Mon. Not. R. Astron. Soc.*, vol. 425, no. 2, pp. 1068–1082, 2012,
[18] H. Wendland, “Piecewise polynomial, positive definite and compactly supported radial functions of minimal degree,” *Adv. Comput. Math.*, vol. 4, no. 1, pp. 389–396, 1995, doi: 10.1007/BF02123482.
[19] D. Violeau and B. D. Rogers, “Smoothed particle hydrodynamics (SPH) for free-surface flows: past, present and future,” *J. Hydraul. Res.*, vol. 54, no. 1, pp. 1–26, 2016, doi: 10.1080/00221686.2015.1119209.
[20] D. Violeau, *Fluid Mechanics and the SPH Method*. Oxford University Press, 2012.
[21] A. J. C. Crespo *et al.*, “DualSPHysics: Open-source parallel CFD solver based on Smoothed Particle Hydrodynamics (SPH),” *Comput. Phys. Commun.*, vol. 187, pp. 204–216, 2015, doi: 10.1016/j.cpc.2014.10.004.
[22] H. Gotoh, T. Shibahara, and T. Sakai, “Sub-particle-scale turbulence model for the MPS method - Lagrangian flow model for hydraulic engineering,” *Comput. Fluid Dyn. J.*, vol. 9, no. 4, pp. 339 – 347, 2001,
[23] R. A. Dalrymple and B. D. Rogers, “Numerical modeling of water waves with the SPH method,” *Coast. Eng.*, vol. 53, no. 2–3, pp. 141–147, 2006, doi: 10.1016/j.coastaleng.2005.10.004.
[24] E. Y. M. Lo and S. Shao, “Simulation of near-shore solitary wave mechanics by an incompressible SPH method,” *Appl. Ocean Res.*, vol. 24, no. 5, pp. 275–286, 2002, doi: 10.1016/S0141-1187(03)00002-6.
[25] C.Batchelor and G. K. Batchelor, *An introduction to fluid dynamics*. Cambridge university press, 2000.
[26] J. J. Monaghan, R. A. F. Cas, A. M. Kos, and M. Hallworth, “Gravity currents descending a ramp in a stratified tank,” *J. Fluid Mech.*, vol. 379, pp. 39 – 70, 1999, doi: 10.1017/s0022112098003280.
[27] J. M. Domínguez *et al.*, “DualSPHysics: from fluid dynamics to multiphysics problems,” *Comput. Part. Mech.*, vol. 9, no. 5, pp. 867–895, 2022, doi: 10.1007/s40571-021-00404-2.
[28] A. English *et al.*, “Modified dynamic boundary conditions (mDBC) for general-purpose smoothed particle hydrodynamics (SPH): application to tank sloshing, dam break and fish pass problems,” *Comput. Part. Mech.*, vol. 9, no. 5, pp. 1–15, 2022, doi: 10.1007/s40571-021-00403-3.
[29] J. O. Taylor *et al.*, “In vitro quantification of time dependent thrombus size using magnetic resonance imaging and computational simulations of thrombus surface shear stresses,” *J. Biomech. Eng.*, vol. 136, no. 7, pp. 1–11, 2014, doi: 10.1115/1.4027613.

Conference on Modelling Fluid Flow (CMFF'25)
The 19th International Conference on Fluid Flow Technologies
Budapest, Hungary, August 26-August 29, 2025

Gas Accumulation Behavior in Diverging Channels with Grooves and Bars of Varying Sizes

Michael MANSOUR[1;2], Mena SHENOUDA[3], Nicola ZANINI[4], Dominique THÉVENIN[5],

[1] Corresponding Author. Mechanical Power Engineering Department, Faculty of Engineering - Mataria, Helwan University, 11718 Cairo, Egypt. E-mail: m.botros@m-eng.helwan.edu.eg
[2] Lab. of Fluid Dynamics & Technical Flows, University of Magdeburg "Otto von Guericke", 39106 Magdeburg, Germany. Tel.: +493916758569, Fax: +493916742840, E-mail: michael.mansour@ovgu.de
[3] Lab. of Fluid Dynamics & Technical Flows, University of Magdeburg "Otto von Guericke", 39106 Magdeburg, Germany. E-mail: mena.shenouda@ovgu.de
[4] Department of Engineering - University of Ferrara, Via Saragat 1, 44122, Ferrara, Italy. E-mail: nicola.zanini@unife.it
[5] Lab. of Fluid Dynamics & Technical Flows, University of Magdeburg "Otto von Guericke", 39106 Magdeburg, Germany. E-mail: thevenin@ovgu.de

ABSTRACT

Two-phase flows in diffusers often result in significant gas accumulation due to the presence of low-pressure separation zones, which adversely impacts pressure recovery. This phenomenon limits the performance of centrifugal pumps transporting gas-liquid mixtures. Unlike pumps with rotating components, diffusers offer a simpler setup for precise experimental analysis. This study investigates the effects of geometric modifications on the upper diffuser side, specifically grooves and bars of varying sizes. The goal is to reduce gas accumulation by enhancing turbulence and gas dispersion near the accumulation. A diffuser with an increasing opening angle was used to induce flow separation and gas accumulation. High-speed imaging was employed to capture the two-phase interactions. The results indicate that small-sized grooves and bars have only a limited impact on gas accumulation. In some cases, geometric modifications even intensify flow separation, resulting in a greater gas buildup, especially under low water flow and high air flow conditions. However, larger-sized bars, especially the biggest ones, prove to be most effective in reducing gas accumulation, particularly at higher water flow rates. The outcomes of this research will support the validation of computational models and facilitate design modifications of centrifugal pumps to improve their performance in two-phase flow conditions.

Keywords: Grooves and bars, Turbulent two-phase flow, Gas accumulation, Diverging channels, Diffusers, Centrifugal pumps

NOMENCLATURE

A_u	$[m^2]$	upstream cross-sectional area
D	$[m]$	Depth of groove (or bar)
I	$[cd]$	Light intensity
L_1	$[m]$	upstream straight pipe length
L_2	$[m]$	downstream straight pipe length
Q_G	$[m^3/s]$	gas volume flow rate
Q_L	$[m^3/s]$	liquid volume flow rate
W	$[m]$	Width of groove (or bar)
Re_G	$[-]$	superficial gas Reynolds number
Re_L	$[-]$	superficial liquid Reynolds number
d_{hd}	$[m]$	downstream hydraulic diameter
d_{hu}	$[m]$	upstream hydraulic diameter
p	$[Pa]$	local pressure
p_2	$[Pa]$	reference pressure (sensor 2)
u_G	$[m/s]$	superficial gas velocity
u_L	$[m/s]$	superficial liquid velocity
x	$[m]$	axial distance
y	$[m]$	vertical distance
$\dot{\varepsilon}$	$[\%]$	gas volume fraction
μ_G	$[Pa \cdot s]$	viscosity of gas
μ_L	$[Pa \cdot s]$	viscosity of liquid
ρ_G	$[kg/m^3]$	density of gas

Subscripts and Superscripts

d	downstream
G	gas
h	hydraulic
L	liquid
u	upstream

Abbreviations

% RD	Percentage of reading
LDA	Laser Doppler Anemometry
LED	Light Emitting Diode
LES	Large Eddy Simulation
RSM	Reynolds Stress Model
RTD	Resistance Temperature Detector
VOF	Volume Of Fluid

1. INTRODUCTION

Transporting gas-liquid two-phase mixtures is necessary in various industrial and engineering systems, including pipelines, heat exchangers, nuclear reactors, chemical processing units, solar systems, and oil wells [1–4]. These flows exhibit complex behavior due to the interaction between the two phases, leading to uneven flow patterns and unsteady dynamics. The characteristics of these flows are highly influenced by channel geometry, flow rates, and phase properties, making their prediction and control essential for optimizing system performance and avoiding operational issues such as flow instabilities, pressure fluctuations, and phase separation.

In channels with variable cross-sectional areas, e.g., diverging channels or diffusers, the dynamics of gas-liquid flows become even more intricate. Diverging or expanding cross-sectional areas can lead to significant variations in velocity due to the possibility of flow separation, influencing pressure and void fraction distribution, leading to local gas accumulation [5]. Such large pockets of gas undesirably prevent the diffuser from effectively increasing pressure. Developing techniques to inhibit or decrease gas accumulation in diverging channels is therefore crucial for ensuring effective pressure recovery.

The gas-liquid flow patterns in this expanding channel resemble those in centrifugal pump impellers, where gas buildup causes flow instabilities and reduces pump head and efficiency [6–8]. The complex turbulence and rotational effects in pumps further challenge the accuracy of numerical simulations, especially at high flow rates [5, 9, 10]. Thus, more experiments and improved numerical models are essential for better prediction and control.

This research builds on turbomachinery studies, focusing on how gas buildup in diverging impeller channels degrades centrifugal pump performance. Designed for single-phase flows, these pumps suffer efficiency losses, strong vibrations, flow instabilities, and potential failure when gas accumulates [4, 6, 11, 12]. Understanding gas-liquid interactions is therefore crucial for minimizing gas accumulation and managing two-phase flows effectively.

Researchers have often studied gas-liquid two-phase flow in channels with constant cross-sections to identify flow patterns and measure pressure drops [2, 13, 14]. Similar studies have focused on channels with abrupt cross-sectional changes, like sudden expansions or contractions [2, 15–18]. Other research examined gas-liquid flow in diffusers, such as vertical circular diffusers for pressure recovery [19] and micro-scale converging-diverging rectangular channels for pressure drops [20]. Hwang et al. [20] found that gas velocity decreased in diverging sections, leading to bubble coalescence and significant flow changes. However, most studies used diverging sections with constant opening angles (straight walls) [18–24], which may not fully capture complex flow phenomena like large gas accumulations. The study of two-phase flow in gradually expanding channels with increasing opening angles has received less attention, underscoring the need for further investigation into gas accumulation in these geometries.

A prior study examined two-phase flow regimes in a horizontal, gradually diverging channel [5], identifying key parameters affecting gas accumulation. It was found that large recirculation zones, caused by flow separation, trap gas bubbles, leading to significant accumulations. Increasing the air flow rate resulted in larger accumulations, while increasing the water flow rate initially expanded recirculation zones, increasing accumulation size, until turbulence intensified and reduced the accumulation again. A notable air pocket remained near the end of the diffuser, even at low gas volume fractions (0.05%), negatively affecting velocity distribution and pressure recovery. The study concluded that reducing flow separation or increasing turbulence intensity can help minimize gas accumulation size [5].

The potential of upstream cross-flow steps to reduce gas accumulation in separated turbulent flows was recently explored [25]. These steps enhanced turbulence intensity, breaking larger bubbles into smaller ones and redirecting them towards the channel center, away from the accumulation region. Some step configurations also improved pressure recovery, particularly at higher water flow rates. However, it is important to note that these flow modifications are intrusive elements, affecting inlet conditions.

Several studies [9, 26, 27] validated numerical models against experimental data from [5] to improve prediction accuracy. Kopparthy et al. [9] found that coupling the Reynolds stress model (RSM) with the volume of fluid (VOF) method accurately predicted gas accumulation size and shape, but faced increased errors at high flow. Hundshagen et al. [26] highlighted the impact of turbulence model inaccuracies, noting that the dispersed two-fluid approach sometimes failed to detect gas accumulation. Nguyen et al. [27] achieved the most accurate predictions with a hybrid multiphase model combining Eulerian-Eulerian, VOF, and large eddy simulations (LES), though it was sensitive to prescribed bubble size, requiring further development. These limitations emphasize the continued importance of experimental studies in two-phase flow simulations with significant gas accumulation.

Grooves have been shown to enhance performance and mitigate undesirable phenomena in turbomachinery [28]. In centrifugal compressors, they control rotating stall, though with increased hydraulic losses [29], and in Francis turbine draft tubes, they suppress swirl at the cost of added losses [30, 31]. Grooves have also reduced cavitation in pump inducers [32, 33]. In single-phase centrifugal pumps, micro-grooves on impeller shrouds improve velocity distribution, reduce hydraulic losses, and lessen diffuser separation by smoothing the surface and reducing turbulence [34]. Macro-grooves in mixed

and centrifugal flow pumps reduce inlet swirl, axial thrust, and improve tip leakage flow [35–37]. Additionally, grooved front shrouds in centrifugal pumps enhance secondary flow and improve gas-liquid mixing, reducing gas accumulation [38].

This study investigates the potential to reduce gas accumulation in two-phase flow within a horizontal diverging channel by modifying the upper diffuser wall, where gas typically accumulates. Grooves and bars of various sizes were introduced to enhance turbulence and promote gas dispersion, thus reducing accumulation. The experimental setup and diffuser geometry from previous work [5, 9, 25–27] were retained. A diffuser with a progressively increasing opening angle was used to induce flow separation and gas accumulation. Two-phase flow conditions were varied, with Reynolds numbers for the water and air phases ranging from Re_L = 59530–78330 and Re_G = 3–9.25, respectively. Single-phase flow velocities were measured using Laser Doppler Anemometry (LDA), while high-speed imaging captured two-phase flow dynamics. Some tested designs effectively reduced gas accumulation. The results of this study will be valuable for validating computational models and exploring design modifications for centrifugal pumps operating under two-phase flow conditions, eventually improving their performance.

2. DETAILS OF THE EXPERIMENTS

Figure 1 illustrates the experimental test rig. The diverging section is made of transparent acrylic glass for clear flow observation and optical measurements. A submersible pump circulates water from a 6.0 m^3 tank, while compressed air is introduced through 21 circumferentially arranged 1.0 *mm* holes in a mixing joint. Water and air flow rates are independently measured and regulated using control valves. An electromagnetic flow meter (Endress+Hauser Promag 30F with ± 0.5% RD accuracy) measures water flow, while a rotameter (Yokogawa RGC1263 with ± 2.5% RD accuracy) measures air flow. Two RTD (Resistance Temperature Detector) sensors (Pt100, Class B, ± 0.3 K error) monitor water and air temperatures before mixing. The air supply system includes a service unit, control valve, pressure regulator, and restriction valve for precise control. Eight pressure sensors (Cerabar T PMC131, -1 : $+1$ bar, ± 0.5% RD accuracy) track pressure changes along the diffuser. The estimated average uncertainty in pressure measurements is 2.9% of the reading. Further details on measurement devices can be found in [5, 25].

The flow channel has rectangular cross-sections of 40 × 44 *mm* upstream and 100 × 44 *mm* downstream, yielding a hydraulic diameter ratio of 1.45, with upstream and downstream hydraulic diameters of d_{hu} = 42 *mm* and d_{hd} = 61 *mm*, respectively. The upstream section ($L_1 = 34d_{hu}$) ensures fully developed flow, while the downstream section extends $L_2 = 15.5d_{hu}$. The diffuser features a gradually increasing opening angle to induce flow separation and air accumulation. It starts with a half-included angle of 6°, with the upper curve defined by $x = 13.5y - y^2/10 - 230$ (where x represents the axial direction and y the vertical direction), increasing to 16°. The horizontal flow orientation, while not exactly replicating Coriolis effects in pumps, preserves lateral force interactions, unlike vertical channels where gravity acts parallel to the flow. This setup effectively mimics gas accumulation as observed in impeller channels, enabling investigations into gas accumulation reduction methods.

Single-phase (water) velocity measurements were performed on the upper side of the diffuser using a two-component Laser Doppler Anemometry (LDA) system (Dantec Dynamics 2-D), with an estimated measurement uncertainty below 0.5%. This accounts for statistical (sample size), spatial (grid resolution), and calibration uncertainties. An automatic traversing system acquired velocity data at 325 grid points (10 *mm* horizontal spacing, 7.5 *mm* vertical spacing, see Figure 2a). The velocity was determined from 25,000 samples per point, collected at an average acquisition rate of 1.5 kHz to ensure statistical stability in such turbulent flow. The measurements were performed in the mid-longitudinal section, which provides insights into flow phenomena such as jet direction, flow separation, and turbulence intensity, which are all essential for understanding gas accumulation in two-phase conditions. The precise location of each point was determined through calibration, correcting for laser beam refraction through the acrylic glass and water. Further details about the LDA system and the refraction calibration are available in [39]. Glass spheres with 10 μm mean diameter and 1000 kg/m^3 density were used as tracers. A high-speed camera captured shadowgraphy images, where the channel was backlit by two LED panels positioned opposite the cameras, as shown in Figure 2b). This setup created a dark border at the water-air interface, providing a clear visualization of the size and shape of gas accumulation.

The tested cases involve surface modifications on the upper diffuser wall, specifically three grooves and three bars of varying sizes (Figure 3). The grooves and bars were embedded along the upper wall with the following dimensions (Width, W × Depth, D) 1.0 *mm* × 0.4 *mm* for G1 and B1, 3.0 *mm*× 1.5 *mm* for G2 and B2, and 6.0 *mm*× 3.0 *mm* for G3 and B3. Expressed in dimensionless form relative to the upstream hydraulic diameter (d_{hu}), the corresponding sizes (W/d_{hu}×D/d_{hu}) are 2.4 %×1.0 % for G1 and B1, 7.2 % × 3.6 % for G2 and B2, and 14.3 % × 7.2 % for G3 and B3. These surface structures enhance turbulence and bubble dispersion by introducing localized disturbances along the gas accumulation path. By periodically obstructing the flow, they promote mixing and disturb gas accumulation. The study examines their impact on velocity profiles, gas accumulation, and pressure recovery under single-phase and two-phase flow conditions.

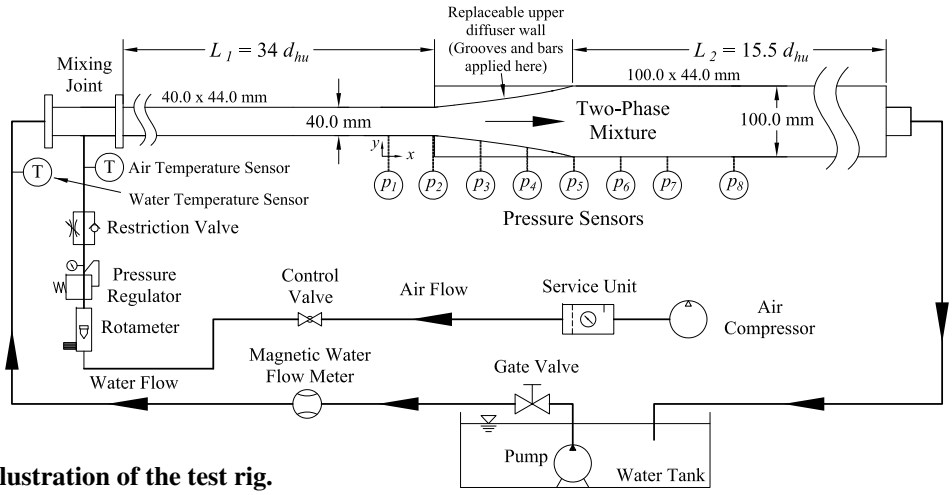

Figure 1. Illustration of the test rig.

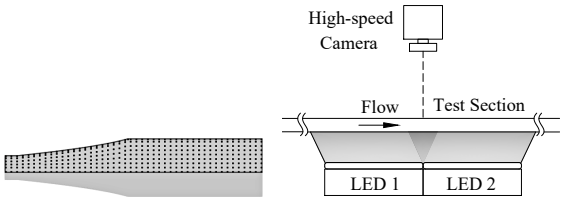

(a) Grid points of LDA **(b) Shadowgraphy top view**

Figure 2. Details of the experiments

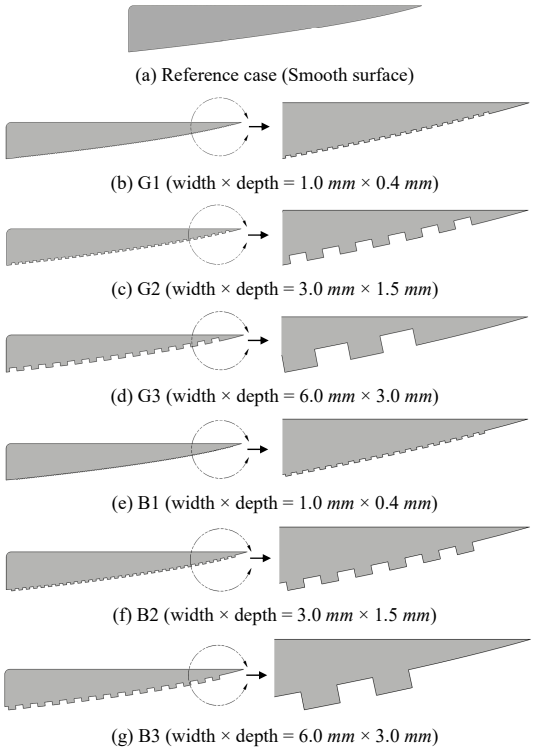

Figure 3. Schematic illustration of diffusers with different artificially introduced grooves and bars.

3. RESULTS

Building on previous studies [5, 9, 26, 27, 39], specific flow conditions were selected to investigate gas accumulation under varying two-phase flow regimes. Two water flow rates (Q_L) and two air flow rates (Q_G) were chosen, resulting in four distinct cases to analyze the influence of different surface modifications. Table 1 summarizes the selected conditions. The superficial Reynolds numbers (Re) for each phase were determined using Eq.1, where ρ represents density, u is the superficial inlet velocity (calculated via Eq.2), μ is dynamic viscosity, and subscripts L and G refer to liquid (water) and gas (air), respectively. The upstream channel cross-sectional area is denoted as A_u. These Reynolds numbers characterize the flow regime of each phase, assuming it occupies the full channel cross-section. The inlet gas volume fraction ($\dot{\varepsilon}$) of each case is determined by by Equation 3. The experimental setup ensured operation under non-cavitating conditions to prevent misinterpretation between air bubbles and vapor cavities. The minimum cavitation number was computed as $\sigma = 18.5$, significantly exceeding the critical threshold ($\sigma_{crit} = 0.3$), even at the maximum velocity, accounting also for flow fluctuations. Consequently, no cavitation was observed during the experiments.

$$\mathrm{Re}_{L,G} = \frac{\rho_{L,G}\, u_{L,G}\, d_{hu}}{\mu_{L,G}} \tag{1}$$

$$u_{L,G} = \frac{Q_{L,G}}{A_u} \tag{2}$$

$$\dot{\varepsilon} = \frac{Q_G}{Q_G + Q_L} \tag{3}$$

Table 1. Flow conditions examined in this study

Case#	Q_L (m^3/s) $\times 10^{-3}$	Q_G (m^3/s) $\times 10^{-6}$	Re_L	Re_G	$\dot{\varepsilon}$ (%)
1	2.64	0	59530	0	0
2	3.47	0	78330	0	0
3	2.64	1.964	59530	3.10	0.074
4	2.64	5.892	59530	9.25	0.223
5	3.47	1.964	78330	3.10	0.056
6	3.47	5.892	78330	9.25	0.169

Figure 4 shows the single-phase velocity magnitudes and fluctuations for all configurations for Case 2. The flow separation increases with groove size due to greater boundary layer disturbance. Similarly, diffusers with bars (B1, B2, B3) exhibit greater flow separation than the smooth reference, with larger bars amplifying velocity fluctuations. Regions of high velocity fluctuations expand as the bar size increases. Further, bars, especially B2 and B3, induce stronger turbulence near the diffuser inlet than grooves, with B3 showing the highest velocity fluctuations, potentially enhancing two-phase mixing.

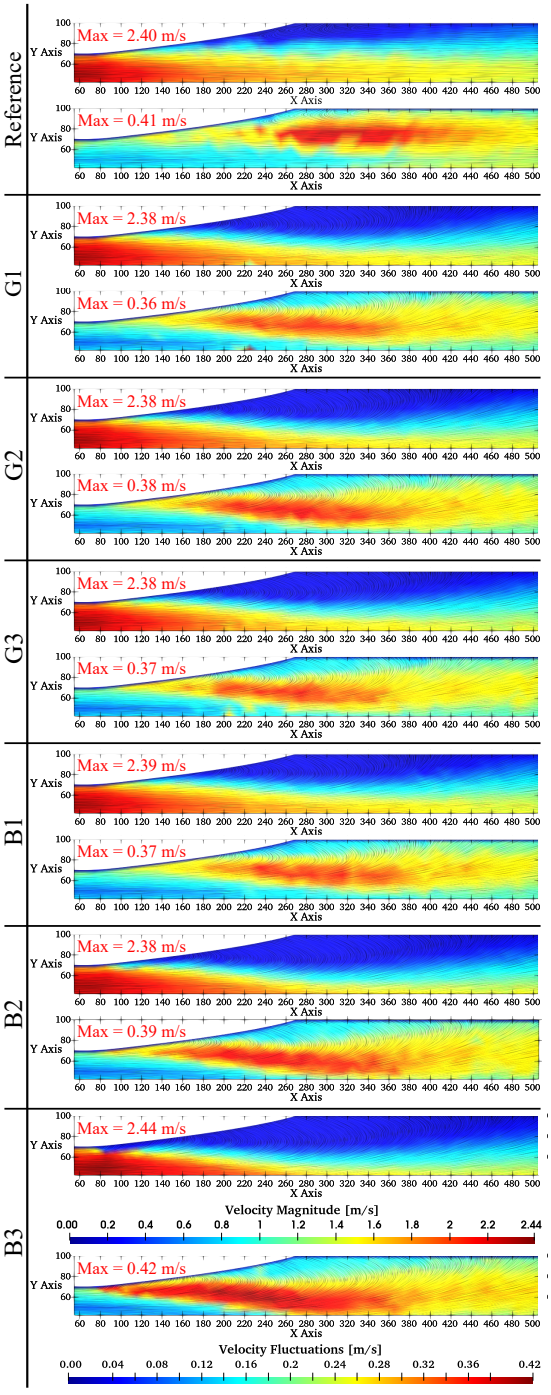

Figure 4. Measured velocities for different configurations (Case 2, Re_L = 78330, Re_G = 0).

Figure 5 illustrates the effects of grooves and bars on gas accumulation in two-phase flow. G1 behaves similarly to the reference case, showing minimal impact of small grooves, while G2 and G3 increase gas accumulation at low water flow, with G3 forming a huge gas cavity in Case 4 due to the increased flow separation. At Re_L = 78330, both G2 and G3 reduce gas buildup by enhancing turbulence and bubble dispersion. Among bars at low flow of water (Re_L = 59530), B1 has little effect, B2 increases accumulation at high gas flow (Case 4), while B3 reduces it in Cases 3 and 4. At Re_L = 78330, B2 and B3 significantly decrease gas accumulation, with B3 performing best across all conditions.

The accumulated air consistently spanned the entire channel width, with minor unsteady variations near the onset of accumulation. To determine the average accumulation size, 1,500 instantaneous images were captured at 50 Hz and processed into a grayscale average image. This stabilized the air-water interface by filtering out transient effects and minimizing potential three-dimensional variations. The grayscale images were then binarized using an intensity threshold (I) derived from their brightness spectra. A MATLAB script automated boundary detection to obtain the accumulation size. Further details on this calculations are available in [5, 39].

Figures 6 and 7 present gas void fraction results, defined as the ratio of mean accumulated gas volume to total channel volume from the diffuser inlet. As shown in Fig. 6, G1 closely follows the reference case, while G2 and G3 increase void fractions at low water flow, with G3 peaking in Case 4. At higher flow, both G2 and G3 reduce gas accumulation, with G3 most effective in Case 5. For bars (Fig. 7), B1 mirrors the reference, B2 increases gas buildup at low water flow (Case 4), and B3 consistently minimizes void fractions, especially at high flow. These findings highlight that G2, G3, B2, and B3 effectively reduce gas accumulation at high liquid velocity, while G1 and B1 provide little improvement. Again, B3 provide improvements for all different conditions. However, the geometry should be carefully selected to control gas accumulation, as the effectiveness varies with flow conditions.

Lastly, Figure 8 shows pressure recovery within the diffuser for all cases, measured at eight axial locations (Fig. 1). To account for turbulence, data were recorded three times at 8 Hz over 15 minutes and averaged. Pressure differences were calculated relative to sensor 2 at the diffuser inlet (x = 0). For the reference case, larger gas accumulations generally reduce pressure recovery. Grooves have little effect at low liquid flow (Re_L = 59530) and worsen recovery at high gas flow (Re_G = 9.25) due to excessive gas buildup. This limited pressure recovery at low liquid flow rates can be attributed to the adverse interaction between the embedded structures (grooves and bars) and the flow dynamics. Specifically, surface structures intensify flow separation along the upper

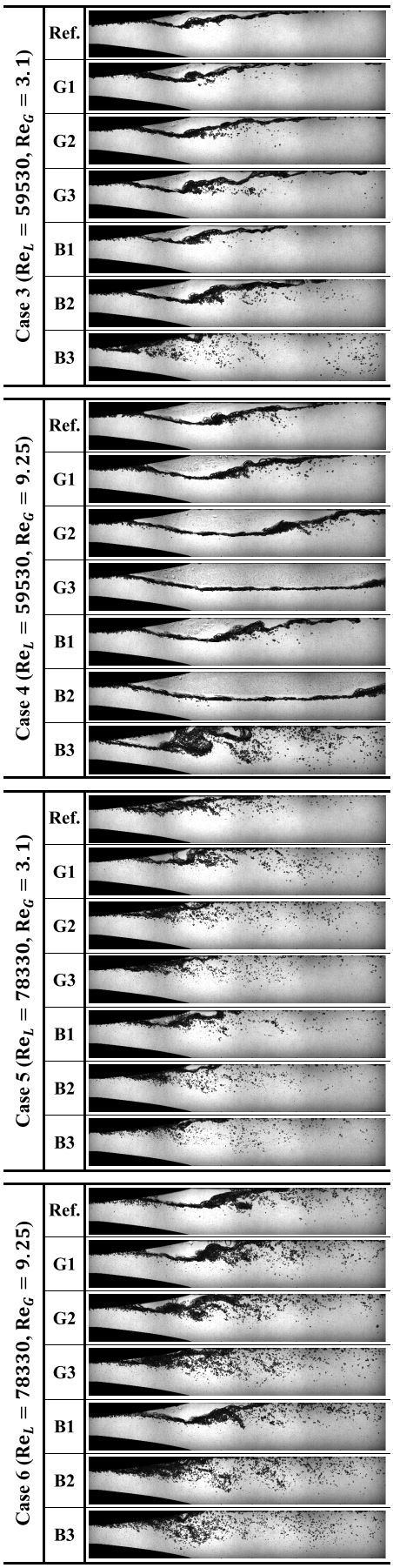

Figure 5. Gas accumulations for different diffusers with grooves and bars.

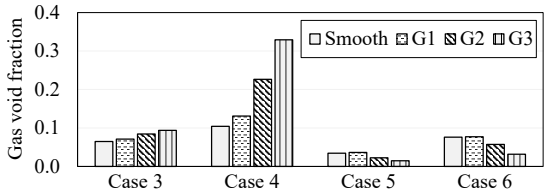

Figure 6. Gas void fractions for different grooves.

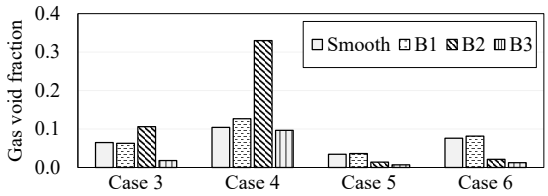

Figure 7. Gas void fractions for different bars.

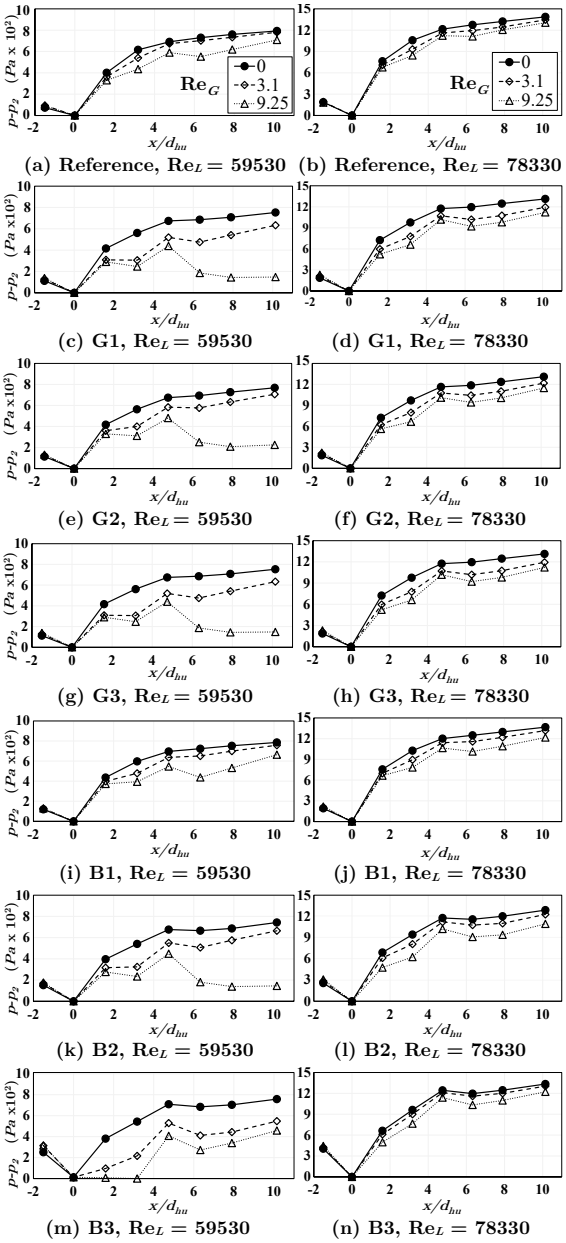

Figure 8. Pressure recovery for all cases (Legend applies to all sub-figures).

wall, which promotes gas accumulation and disrupts the pressure recovery. Furthermore, in the cases of the larger bars (B2 and B3), the reduced inlet cross-sectional area causes flow acceleration, contributing again to reduced pressure recovery. At higher liquid flow, the impact of grooves remains minimal, while all bars closely match the reference case, with B3 offering slight improvement by consistently reducing gas accumulation.

4. CONCLUSIONS

This study examined the effects of surface modifications on the upper diffuser side, specifically grooves and bars of varying sizes, to mitigate gas accumulation in two-phase flow conditions. The findings reveal that small-sized grooves and bars have minimal influence on gas dispersion and, in some cases, exacerbate flow separation, leading to increased gas buildup. Conversely, larger-sized bars, particularly the largest ones, demonstrate significant effectiveness in reducing gas accumulation, especially at higher water flow rates. Pressure recovery is strongly influenced by gas accumulation, with larger accumulations leading to reduced recovery. While grooves have minimal impact, the diffuser with bars, particularly B3, shows a more balanced effect, mitigating gas accumulation while maintaining relatively stable and slightly improved pressure recovery. These insights contribute to a better understanding of two-phase flow behavior in diffusers and provide valuable input for improving computational models and optimizing centrifugal pump designs handling gas-liquid two-phase flows.

ACKNOWLEDGEMENTS

This work is part of a project funded by VDMA (Verband Deutscher Maschinen- und Anlagenbau) and BMWi (Bundesministeriums für Wirtschaft und Energie) under number IGF 23051.

REFERENCES

[1] Ewing, M. E., Weinandy, J. J., and Christensen, R. N., 1999, "Observations of Two-Phase Flow Patterns in a Horizontal Circular Channel", *Heat Transf Eng*, Vol. 20 (1), pp. 9–14.

[2] Chen, I. Y., Tseng, C.-Y., Lin, Y.-T., and Wang, C.-C., 2009, "Two-phase flow pressure change subject to sudden contraction in small rectangular channels", *Int J Multiph Flow*, Vol. 35 (3), pp. 297–306.

[3] Sharma, A., Tyagi, V., Chen, C., and Buddhi, D., 2009, "Review on thermal energy storage with phase change materials and applications", *Renew Sustain Energy Rev*, Vol. 13 (2), pp. 318–345.

[4] Mansour, M., Wunderlich, B., and Thévenin, D., 2018, "Effect of tip clearance gap and inducer on the transport of two-phase air-water flows by centrifugal pumps", *Exp Therm Fluid Sci*, Vol. 99, pp. 487–509.

[5] Mansour, M., Kováts, P., Wunderlich, B., and Thévenin, D., 2018, "Experimental investigations of a two-phase gas/liquid flow in a diverging horizontal channel", *Exp Therm Fluid Sci*, Vol. 93, pp. 210–217.

[6] Mansour, M., Wunderlich, B., and Thévenin, D., 2018, "Experimental study of two-phase air/water flows in a centrifugal pump working with a closed or a semi-open impeller", *ASME Turbo Expo 2018: Turbomachinery Technical Conference and Exposition, Oslo, Norway*, p. V009T27A012.

[7] Mansour, M., Kopparthy, S., and Thévenin, D., 2022, "Investigations on the effect of rotational speed on the transport of air-water two-phase flows by centrifugal pumps", *Int J Heat Fluid Flow*, Vol. 94, p. 108939.

[8] Mansour, M., and Thévenin, D., 2023, "State of the art on two-phase non-miscible liquid/gas flow transport analysis in radial centrifugal pumps Part B: Review of experimental investigations", *Int J Turbomach Propuls Power*, Vol. 8 (4), p. 42.

[9] Kopparthy, S., Mansour, M., Janiga, G., and Thévenin, D., 2020, "Numerical investigations of turbulent single-phase and two-phase flows in a diffuser", *Int J Multiph Flow*, Vol. 130, p. 103333.

[10] Hundshagen, M., Mansour, M., Thévenin, D., and Skoda, R., 2019, "Numerical investigation of two-phase air-water flow in a centrifugal pump with closed or semi-open impeller", *Proceedings of 13th European Turbomachinery Conference on Turbomachinery Fluid Dynamics and Thermodynamics, ETC 2019*.

[11] Zhu, J., Guo, X., Liang, F., and Zhang, H.-Q., 2017, "Experimental study and mechanistic modeling of pressure surging in electrical submersible pump", *J Nat Gas Sci Eng*, Vol. 45, pp. 625–636.

[12] Monte Verde, W., Biazussi, J. L., Sassim, N. A., and Bannwart, A. C., 2017, "Experimental study of gas-liquid two-phase flow patterns within centrifugal pumps impellers", *Exp Therm Fluid Sci*, Vol. 85, pp. 37–51.

[13] Wambsganss, M., Jendrzejczyk, J., France, D., and Obot, N., 1992, "Frictional pressure gradients in two-phase flow in a small horizontal rectangular channel", *Exp Therm Fluid Sci*, Vol. 5 (1), pp. 40–56.

[14] Vallée, C., Höhne, T., Prasser, H.-M., and Sühnel, T., 2008, "Experimental investigation and CFD simulation of horizontal stratified two-phase flow phenomena", *Nucl Eng Des*, Vol. 238 (3), pp. 637–646.

[15] Chen, I. Y., Liu, C.-C., Chien, K.-H., and Wang, C.-C., 2007, "Two-phase flow characteristics across sudden expansion in small rectangular channels", *Exp Therm Fluid Sci*, Vol. 32 (2), pp. 696–706.

[16] Abdelall, F. F., Hahn, G., Ghiaasiaan, S. M., Abdel-Khalik, S. I., Jeter, S. S., Yoda, M., and Sadowski, D. L., 2005, "Pressure drop caused by abrupt flow area changes in small channels", *Exp Therm Fluid Sci*, Vol. 29 (4), pp. 425–434.

[17] Ahmed, W. H., Ching, C. Y., and Shoukri, M., 2008, "Development of two-phase flow downstream of a horizontal sudden expansion", *Int J Heat Fluid Flow*, Vol. 29 (1), pp. 194–206.

[18] Pakhomov, M. A., and Terekhov, V. I., 2022, "Modeling of turbulent heat-transfer augmentation in gas-droplet non-boiling flow in diverging and converging axisymmetric ducts with sudden expansion", *Energies*, Vol. 15 (16).

[19] Anupriya, S., and Jayanti, S., 2014, "Experimental and modelling studies of gas–liquid vertical annular flow through a diverging section", *Int J Multiph Flow*, Vol. 67, pp. 180–190.

[20] Hwang, J. J., Tseng, F. G., and Pan, C., 2005, "Ethanol-CO_2 two-phase flow in diverging and converging microchannels", *Int J Multiph flow*, Vol. 31 (5), pp. 548–570.

[21] Deniz, E., and Eskin, N., 2015, "Hydrodynamic characteristics of two-phase flow through horizontal pipe having smooth expansion", *ISI Bilim Ve Tek Dergisi-Journal Therm Sci Technol*, Vol. 35 (1), pp. 1–9.

[22] Kourakos, V. G., Rambaud, P., Chabane, S., Pierrat, D., and Buchlin, J. M., 2009, "Two-phase flow modelling within expansion and contraction singularities", *Comput Methods Multiph Flow V*, Vol. 63, p. 27.

[23] Eskin, N., and Deniz, E., 2012, "Pressure Drop of Two-Phase Flow through Horizontal Channel with Smooth Expansion", *Int. Refrig. Air Cond. Conf.*, pp. 1–10.

[24] Ahmadpour, A., Noori Rahim Abadi, S., and Kouhikamali, R., 2016, "Numerical simulation of two-phase gas–liquid flow through gradual expansions/contractions", *Int J Multiph Flow*, Vol. 79, pp. 31–49.

[25] Mansour, M., Zanini, N., Shenouda, M., Pinelli, M., Suman, A., and Thévenin, D., 2025, "Minimizing gas accumulation in two-phase flow within a diverging horizontal channel using cross-flow millimeter-size steps", *Proceedings of 16th European Turbomachinery Conference on Turbomachinery Fluid Dynamics and Thermodynamics, ETC16, Hannover, Germany*.

[26] Hundshagen, M., Mansour, M., Thévenin, D., and Skoda, R., 2021, "3D simulation of gas-laden liquid flows in centrifugal pumps and the assessment of two-fluid CFD methods", *Exp Comput Multiph Flow*, Vol. 3 (3), pp. 186–207.

[27] Nguyen, B.-D., Popp, S., Hundshagen, M., Skoda, R., Mansour, M., Thévenin, D., and Hasse, C., 2022, "Large eddy simulations of turbulent gas-liquid flows in a diverging horizontal channel using a hybrid multiphase approach", *J Fluids Eng*, Vol. 145 (3), p. 031501.

[28] Kurokawa, J., 2011, "J-groove technique for suppressing various anomalous flow phenomena in turbomachines", *Int J Fluid Mach Syst*, Vol. 4 (1), pp. 1–13.

[29] Kurokawa, J., Saha, S. L., Matsui, J., and Kitahora, T., 2000, "Passive control of rotating stall in a parallel-wall vaneless diffuser by radial grooves", *J Fluids Eng*, Vol. 122 (1), pp. 90–96.

[30] Chen, Z., Singh, P. M., and Choi, Y.-D., 2017, "Suppression of unsteady swirl flow in the draft tube of a Francis hydro turbine model using J-Groove", *J Mech Sci Technol*, Vol. 31 (12), pp. 5813–5820.

[31] Chen, Z., Baek, S.-H., Cho, H., and Choi, Y.-D., 2019, "Optimal design of J-groove shape on the suppression of unsteady flow in the Francis turbine draft tube.", *J Mech Sci Technol*, Vol. 33 (5).

[32] Choi, Y.-D., Kurokawa, J., and Imamura, H., 2007, "Suppression of Cavitation in Inducers by J-Grooves", *J Fluids Eng*, Vol. 129 (1), pp. 15–22.

[33] Shimiya, N., Fujii, A., Horiguchi, H., Uchiumi, M., Kurokawa, J., and Tsujimoto, Y., 2008, "Suppression of cavitation instabilities in an inducer by j groove", *J Fluids Eng*, Vol. 130 (2).

[34] Skrzypacz, J., and Bieganowski, M., 2018, "The influence of micro grooves on the parameters of the centrifugal pump impeller", *Int J Mech Sci*, Vol. 144, pp. 827–835.

[35] Saha, S. L., Kurokawa, J., Matsui, J., and Imamura, H., 2000, "Suppression of performance curve instability of a mixed flow pump by use of J-groove", *J Fluids Eng*, Vol. 122 (3), pp. 592–597.

[36] Shimura, T., Kawasaki, S., Uchiumi, M., and Matsui, J., 2011, "Internal flow and axial thrust balancing of a rocket pump", *Fluids Engineering Division Summer Meeting*, Vol. 44403, pp. 145–152.

[37] Khoeini, D., and Shirani, E., 2019, "Influences of Diffuser Vanes Parameters and Impeller Micro Grooves Depth on the Vertically Suspended Centrifugal Pump Performance", *J Mech*, Vol. 35 (5), pp. 735–746.

[38] Mansour, M., Kopparthy, S. B., and Thévenin, D., 2023, "Improving air-water two-phase flow pumping in centrifugal pumps using novel grooved front shrouds", *Chem Eng Res Des*, Vol. 197, pp. 173–191.

[39] Mansour, M., 2020, "Transport of two-phase air-water flows in radial centrifugal pumps", Ph.D. thesis, University of Magdeburg, Germany.

Conference on Modelling Fluid Flow (CMFF'25)
The 19th International Conference on Fluid Flow Technologies
Budapest, Hungary, August 26 - August 29, 2025

NUMERICAL ANALYSIS OF THE DECELERATED SWIRLING FLOW REGIMES OBTAINED BY USING A MAGNETORHEOLOGICAL CONTROL DEVICE

Raul Alexandru SZAKAL[1], Alin Ilie BOSIOC[2], Sebastian MUNTEAN[1]

[1] Corresponding Author. 2Center for Advanced Research in Engineering Sciences, Romanian Academy- Timisoara Branch, Bv. Mihai Viteazu, No. 24, 300222, Romania. E-mail: raul.szakal@student.upt.ro
[2] University Politehnica Timisoara, Mechanical Engineering Faculty, Bv. Mihai Viteazu, No. 1, 300222, Romania, E-mail: alin.bosioc@upt.ro

ABSTRACT

The paper focuses on 3D numerical simulations of the decelerated swirling flow conditions in a swirling flow generator. The swirling flow regimes from 1020 *rpm* runaway speed to 870 *rpm* are obtained using a magnetorheological (MR) device at a constant discharge of 30 *l/s*. An 2D Lasser Doppler Velocimetry (LDV) measuring system has been used to measure the mean meridional and tangential velocity profiles in the divergent part of the test section. The 3D numerical simulations have been performed in agreement with real operation conditions. A mixing plane method has been used to transfer the flow between the 3D simplified domains of the swirling flow generator and full 3D test section. The turbulence model *k- ω* and structured mesh type were used for computing the flow in the leaned strouts, stator and rotor's domain. RSM turbulence model has been selected for computing the unsteady flow field in the test section at regimes corresponding to rotor's speed from 990 *rpm* to 870 *rpm*. A time step of 10^{-4} *seconds* has been considered for the numerical simulations in the test section. The numerical results against experimental data shows that the employed methodology leads to good results.

Keywords: decelerated swirling flow, 3D numerical simulation, vortex rope, 2D LDV flow field validation

NOMENCLATURE

k	[m^2/s^2]	turbulence kinetic energy
ε	[m^2/s^3]	turbulence dissipation
ω	[1/s]	specific turbulence dissipation
l	[-]	dimensionless axis length
$Rref$	[m]	reference throat radius
v	[-]	dimensionless velocity
Va	[m/s]	axial dimensionless velocity
Vu	[m/s]	tangential dimensionless velocity
Vr	[m/s]	dimensionless velocity
u_{RMS}	[-]	dimensionless root mean square
Q_{op}	[l/s]	operation discharge
$Vref$	[m/s]	reference throat velocity

1. INTRODUCTION

Decelerated swirling flow is a particular type of flow common to various hydraulic machinery and combustion applications. The same for the cases of hydraulic turbines with fixed blades as Francis or propeller. While operated at partial discharges for power regulation of the electrical grid the decelerated swirling flow at the conical diffusers of Francis turbines leading to strong pressure pulsations and associated vibrations that hinder the good operation [1]. Moreover, start-stop cycles associated with nowadays operation requirements leads to stress loads on mechanical components and eventually failure of them [2-3]. To better understand the flow behaviour in such operating conditions and to address them with proper flow control methods both experimental and numerical work has been done in the last years [4-6]. Moreover, proper flow control methods should be address to particular flow configurations for better results [7].

The paper aims to investigate via both numerical and experimental procedures the decelerated swirling flow from the swirling flow generator from University Politehnica Timisoara [8]. This device is a surrogate of Francis FLINDT hydraulic turbine and mimics the decelerated swirling flow from the draft tube cone. A magnetorheological (MR) device has been utilized to modify the swirling flow conditions. The swirling flow generator together with experimental and numerical setup are presented in section 2. Section 3 presents the flow field validation

and numerical results. The summarize and conclusions of the performed both numerical and experimental work are presented in the last part of the paper together with future research.

2. SWIRLING FLOW GENERATOR. EXPERIMENTAL AND NUMERICAL SETUP

2.1. Experimental setup

To examine the swirling flow phenomena and quantify their effects, the swirling flow generator from University Politehnica Timisoara has been used. The test rig was designed to mimics the swirling flow conditions from Francis Flindt hydraulic turbine. As depicted in Figure 1, the test section installed on the test rig is assembled by a swirl generator [8] and a convergent divergent plexiglass test section [9]. The swirl generator consists of two rows of blades placed coaxially on a hub fixed by a nozzle. The stationary first row of blades generates an excess of tangential momentum as a 30 *l/s* discharge passes through the hydraulic passage. The flux of moment of momentum is then redistributed by the second row of blades called rotor. The rotor was designed with 10 blades and acts like a turbine near to the hub and as a pump near to the shroud. In this way, the total pressure of the main flow is increased at the shroud and decreased in the centre area. The conical shape of the nozzle together with the upper part of the test section assembly a convergent duct which diminishes the drag from the rotor's outlet. In this way, a clean swirling flow is generated at the inlet of the cone of the test section. A magneto-rheological brake was embedded in the rotor`s hub to modify the swirl at the inlet of the convergent-divergent test section [10]. Breaking the rotor speed of the rotor leads to different swirling flow configurations. Both mean velocity profile and unsteady pressure can be measured downstream to the magnetorheological controlled rotor by using a Dantek 2D LDV system and unsteady pressure sensors. The major advantage of using an LDV system for flow characterization consists of the non-invasive measuring technique. The 2D LDV measuring system consists of a measuring probe and a 3D traverse system. This setup ensures a displacement of the probe with a step of 0.2 *mm* step along all coordinates (e.g., x, y, z). The W0, W1 and W2 measuring windows allows to measure the mean velocity profiles on both convergent and divergent part of the test section. The associated axis of each measuring window is placed perpendicular to the wall of the test section. The test section has a throat diameter of 0.1 *m* and the cone half-angle is 8.5° on a height of 0.2 *m*. The downstream pipe connected to the outlet of the divergent part of the test section has a diameter of 0.16 *m* and a length of ≈2m.

2.2. Numerical setup and operating regimes

A 3D numerical simulation was performed using commercial software Ansys Fluent 6.3[11]. For all numerical investigated flow conditions, a constant discharge of 30 l/s was imposed in agreement with experimental setup. The full 3D unsteady computations for the swirl generator apparatus may not be a very cost-effective method due to the substantial computational resources required. Hence, some simplifications were considered. Instead of considering the full 3D domain of the swirling flow apparatus, the leaned strouts, stator and rotor domain were simplified in agreement with both flow and geometrical periodicity. In order to couple the flow between the simplified computational domains of the swirling flow generator, a mixing plane method has been used. According to Figure 2, the simplified leaned strouts domain (90°) has been discretized with 65k cells, the simplified domain of the stator (27.69°) with 132k cells and the rotor`s domain (36°)

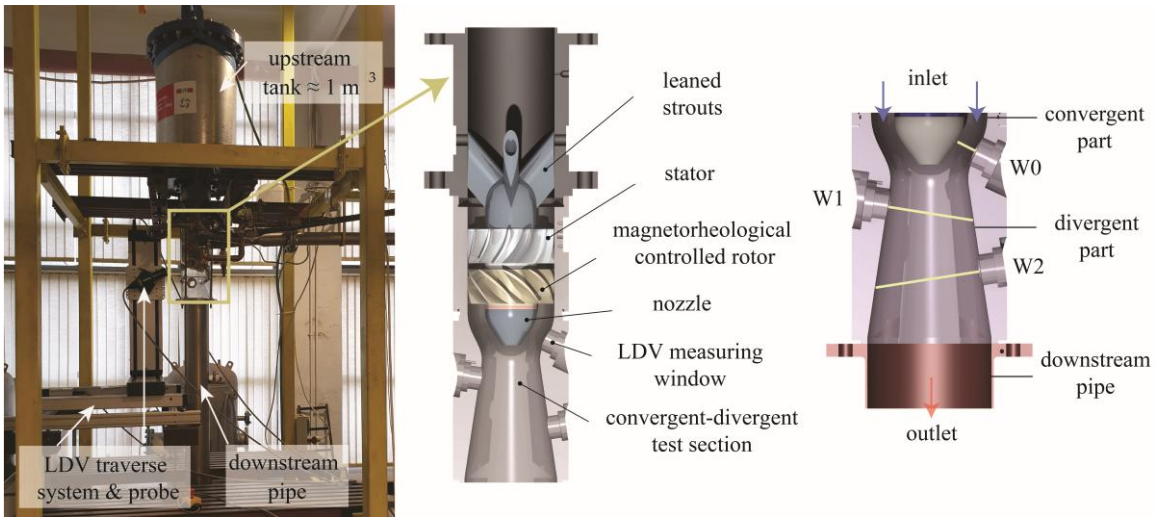

Figure 1. Test rig for decelerate swirling flow investigation (left), the swirling flow generator (center), detail of the convergent divergent test section (right)

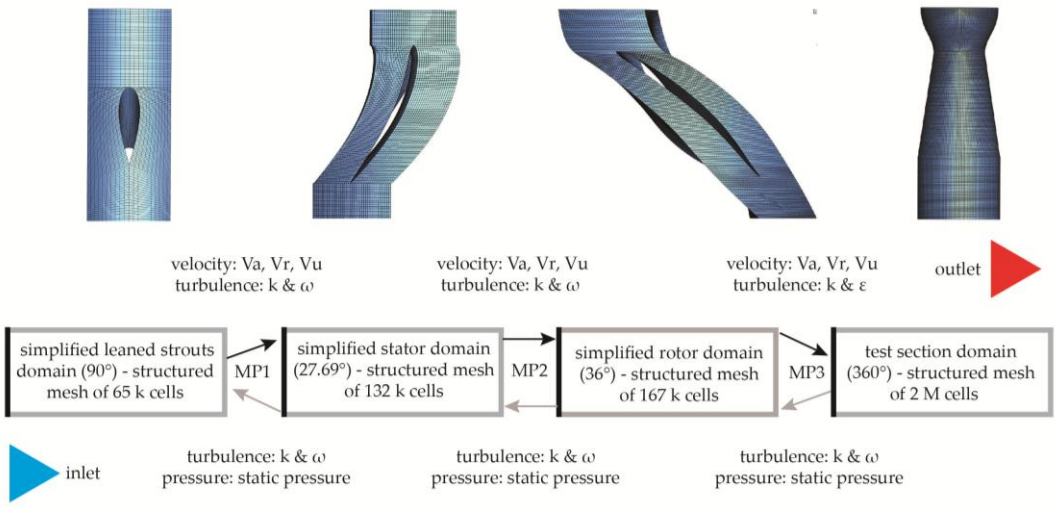

Figure 2. The computational domain of the swirling flow generator and mixing plane algorithm utilized in numerical simulations

with 167k cells, respectively. The convergent-divergent test section domain (360°) has been discretized with about 2 million cells. The flow has been transferred in the normal flow direction by imposing at each domain's inlet the following: (i) axial mean velocity (ii) radial mean velocity and (iii) tangential mean velocity profiles together with (iv) turbulence quantities (e.g., k, ω or ε). At the outlet of each domain, the turbulence quantities have been imposed together with the static pressure distribution. Absolute steady state numerical simulations have been performed for the leaned strouts and stator's domain using fast and reliable k-ω turbulence model. For the rotor's domain, a relative steady-state has been considered using same k- ω turbulence model and the angular velocity of it has been imposed in agreement with rotational speed of the rotor from experimental work. The unsteady flow behaviour in the convergent-divergent test section domain with a time step of 10^{-4} has been considered together with RSM turbulence model, which has already proven capabilities within such flow configurations [12]. A SIMPLE pressure-velocity coupling method and second order discretization scheme for the equation system have been used. For the flow computations in strouts, stator and rotor's domain the absolute convergence criterion were set to 1e-9 to ensure an accurate enough result. Due to lack of experimental data at the outlet of the test section a radial equilibrium boundary condition has been imposed together with hydraulic diameter of 0.16 and 3% turbulence intensity. RSM model involve dissipation rate term ε which has been obtain from specific dissipation rate ω by using the following equation:

$$\omega = \frac{\varepsilon}{kC_\mu} \tag{1}$$

where k is the turbulent kinetic energy and C_μ an emphiric constant (0.09).

3. FLOW FIELD VALIDATION AND NUMERICAL RESULTS

Global parameters as volumetric flow rate and flux of moment of momentum are critical parameters to be conserved along each domain considered for the numerical simulations performed. They have been monitored at each mixing plane to ensure that the operating regime has been conserved and ultimately, the computed flow in the convergent divergent test section is closer to the real one. According to our previous work, a maximum relative deviation of 0.3% and 3.5% has been obtained for volumetric flow rate and flux of moment of momentum, respectively along the mixing planes [13]. These results underlined a good transfer of the flow along the mixing planes.

Since our previous work underlined that the computational efforts describe well the flow on the convergent part of the test section (mean velocity profile validation on measuring window W0 at 920 and 870 *rpm*) those results can be found in [14] together with pressure pulsation validation. Hence, the paper extends and discuss the results and validation of the velocity profiles on W1 and W2 measuring windows. W1 and W2 measuring windows are placed in the divergent part of the test section where decelerated swirling flow occurs. Due to the strong adverse pressure gradient and the conical shape, close to the axis a quasi-stagnant region is developed in agreement with both experimental and theoretical studies [15-16]. The mean velocity profile for meridian and tangential velocity has been extracted from the performed numerical simulation. Around 40 time-steps were considered to average the velocity components and obtain the velocity profiles. Both experimental and numerical data were represented in dimensionless form and the following formulas has been used to express the length of the measuring axis l (e.g.,

associated length of W1, W2 measuring windows) and velocity:

$$l = \frac{x}{R_{ref}} \quad (2)$$

$$v = \frac{V}{V_{ref}} \quad (3)$$

$$V_{ref} = \frac{Q_{op}}{\pi \cdot R_{ref}^2} \quad (4)$$

l represents the dimensionless axis length, and it has been obtained by the ratio between x – x coordinate on the R_{ref} – the throat radius ($0.05m$). v represents the dimensionless velocity, and it has been obtained by the ratio between the measured and calculated velocity V to the refence velocity V_{ref} corresponding to the throat velocity. Eq. (4) has been used to obtain the V_{ref}, by the ratio of the operating flow rate (Q_{op}-$30l/s$) to the throat area. The dimensionless root mean square $uRMS$ of each measuring points has been plotted in vertical bars to express the velocity fluctuation. The dimensionless form has been obtained using the following formula:

$$u_{RMS} = \frac{\sqrt{\sum_{i=o}^{N-1} \frac{1}{N} (u_i - \bar{u})^2}}{Vref} \quad (5)$$

where N is the number of measured points, u_i the instantaneous measured velocity and $\bar{u}$ the average value of the measured velocity.

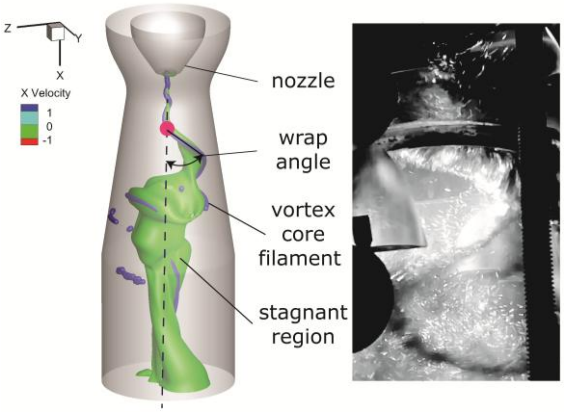

Figure 3. Vortex rope sketch and experimental visualization

The structure of the decelerated swirling flow into the draft tube cone is presented in Fig. 3. A vortex rope sketch together with experimental visualization underline the presence of the vortex rope phenomena. The vortex core filament has a spiral-like shape and wraps around a quasi-stagnant region (mean meridian velocity component is negligible). The wrap angle of the vortex core and associated filament is modified by the hydrodynamic regime (e.g. modifying the rotors speed with the magnetorheological device).

The mean velocity field validation for W1 measuring window is presented in Figures 4-6 for the four analysed operating regimes corresponding to rotors speed of 870, 960 and 990 *rpm*, in agreement with speeds obtained using magnetorheological breaking.

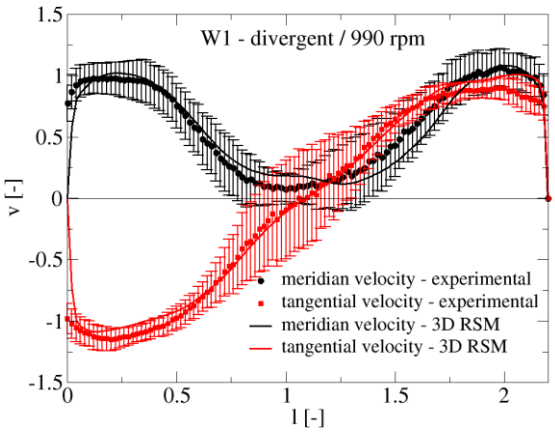

Figure 4. Mean velocity field – meridian and tangential numerical velocity profiles against experimental data on W1 at 990 *rpm*

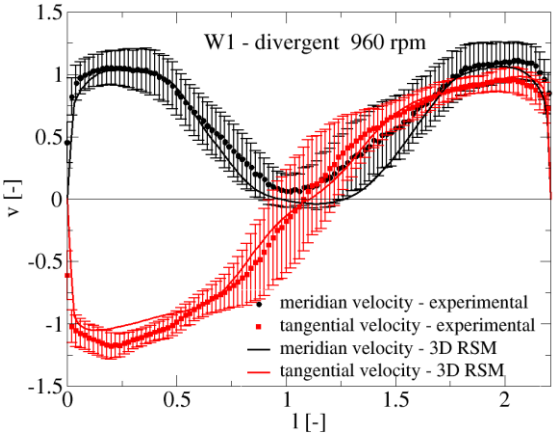

Figure 5. Mean velocity field – meridian and tangential numerical velocity profiles against experimental data on W1 at 960 *rpm*

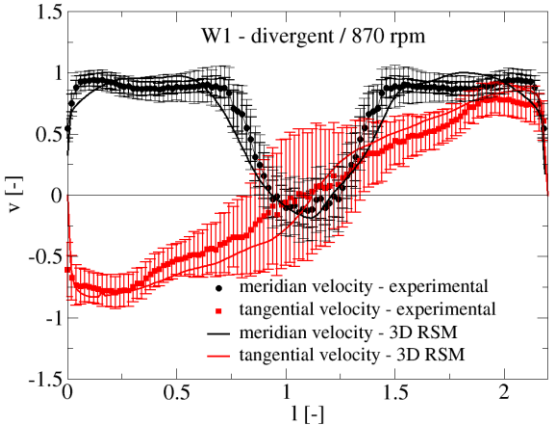

Figure 6. Mean velocity field – meridian and tangential numerical velocity profiles against experimental data on W1 at 870 *rpm*

The breaking down the rotor's speed using the magnetorheological device from 1020 *rpm* to 870 *rpm* leads to decreasing the flux of moment of momentum at the inlet of the test section [17]. This fact is supported by the results obtained both from 3D numerical simulations using RSM model and 2D LDV mean velocity field on measuring window W1. At 990 *rpm*, the decelerated swirling flow conditions leads to a meridian velocity deficit (values close to 0) of almost 0.3/*l* close to the axis. The maximum dimensionless value of the meridian velocity component is around 1 and it's located at the extremities, close to the wall of the test section. A linear distribution of meridian velocity component was observed within 15% of the axis length (*l*) close to the wall at 990 *rpm*. While slowing down the rotor to 870 *rpm*, the meridian velocity deficit is diminished at around 0.1/*l* in the central area of the test section. However, the linear distribution evidenced at larger rotational speeds increase up to 35% of *l* at 870 *rpm*.

Moreover, while the meridian velocity field tends to become uniform, the central deficit area becomes a recirculation region with negative values for the mean meridian velocities. This behaviour is a consequence of the strong tangential velocity component together with strong adverse pressure gradient which tends to push the main flow close to the wall of the test section. The maximum tangential dimensionless velocity is around 1.2 close to the wall at 990 *rpm* and decrease up to 0.8 at the same area at 870 *rpm*.

Figures 7-9 provides the results obtained from numerical simulation vs. 2D LDV experimental data on W2 measuring window placed in the second part of the divergent area of the test section. At large rotor's speed (e.g., 990-960 *rpm*), the strong swirling flow conditions support the formation of the central quasi stagnant region close to the axis of the test section. The quasi-stagnant region (with meridian velocities oscillates around 0 value) covers up to 40-45% of *l* at 990 and 960 *rpm*, respectively. In the performed 3D numerical simulations, the quasi-stagnant region identified on W2 at large rotor's speeds in meridian velocity component is overestimated due to the lack of backflow pressure conditions and the radial equilibrium condition imposed at the outlet. As opposed to the W1, on W2 measuring window the meridian velocity distribution is not linear close to the wall and has a peak-like distribution due to larger area of the test section at that region. However, while the rotor's speed decreased to 870 *rpm*, the meridian velocity component distribution tends to achieve the linear distribution but just on around 5-10% of *l* closed to the wall. If al large rotos speed of 990-960 *rpm*, the tangential velocity distribution has a central solid-rigid behaviour close to the axis, at 870 *rpm*, a flatten region of tangential velocity has been identified. The results at 870 *rpm* show more scattering in the experimental data, which appears to be due to the magnetorheological device s failure keep the rotor speed constant. This happened due to washing out effect of magnetorheological fluid evidenced in our previous work [10].

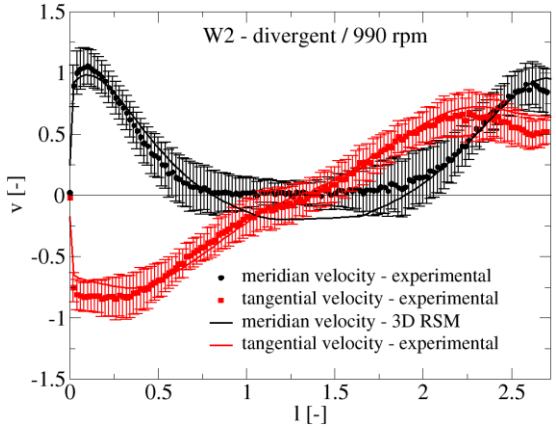

Figure 7. Mean velocity field – meridian and tangential numerical velocity profiles against experimental data on W2 at 870 *rpm*

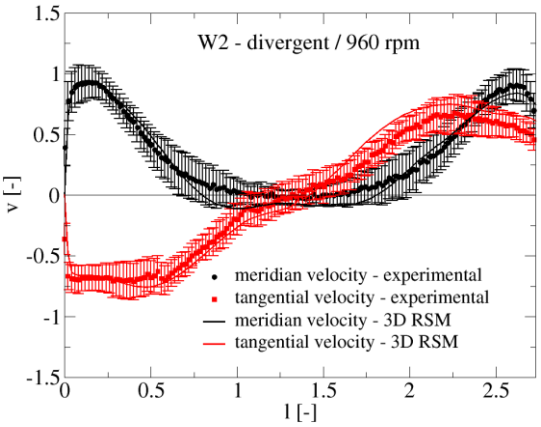

Figure 8. Mean velocity field – meridian and tangential numerical velocity profiles against experimental data on W2 at 920 *rpm*

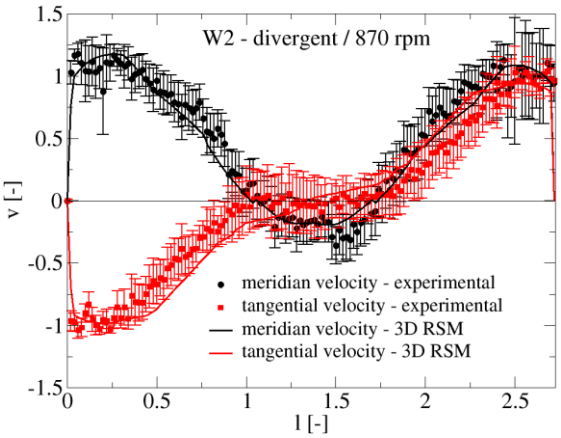

Figure 9. Mean velocity field – meridian and tangential numerical velocity profiles against experimental data on W2 at 990 *rpm*

Using the RSM turbulence model to compute the flow in the swirling flow generator is a good cost-

effective choice due to the results obtained at analysed operating points. The 3D numerical results describe the mean flow fields in the divergent area of the test section in agreement with experimental data measured with 2D LDV system. Moreover, this good agreement is supported by overlap of the numerical results with experimental ones within the u_{RMS} band presented in vertical bars. The improved flow conditions of the swirl generator obtained with the magnetorheological device validates the 3D numerical simulations.

4. CONCLUSIONS

The numerical experiment has been conducted to better understand and validate a reliable working methodology for computing 3D decelerated swirling flow conditions in the swirling flow generator.

The paper presents the numerical and experimental results obtained for different decelerated swirling flow configurations in the swirling flow generator. A 2D LDV measuring system has been used to obtain the mean flow field in the divergent part of the test section on the associated W1 and W2 measuring axis. A magnetorheological brake has been used in experimental work to control the rotor's speed from 1020 to 870 *rpm*. The boundary conditions imposed in the 3D numerical setup were set to fulfil the real operating conditions. The overall setup and particular RSM turbulence model together with imposed boundary conditions showing good agreement with experimental data.

The study stands for a good validation of the mean velocity flow field in the swirling flow generator and together with unsteady pressure field validation would ensure a proper understanding of flow behaviour. The analysis of the mean velocity flow field shows that the flow can be improved overall if the flux of moment of momentum decreases, and the central stagnant region is filled.

Hence, a control method to address these particular types of flow should ensure a filling the meridian velocity deficit identified in the central area and diminishing the excess of high tangential velocity component close to the wall of the cone in hydraulic turbines. Building upon the validated numerical analysis, future work will be done to extend the understanding of vortex rope evolutions at different decelerated swirling flow configurations. The evolution of the associated filament of the vortex rope together with both unsteady pressure and mean velocity flow filed validation will be further done.

ACKNOWLEDGEMENTS

The work of the first author was supported both by the RA-TB/CFATR/LHC multiannual research program 2021–2025 and by a grant of the Ministry of Research, Innovation and Digitization, CCCDI UEFISCDI, project number PN-IV-P7-7.1-PED-2024-1113, within PNCDI IV.

REFERENCES

[1] Kougias. I., et al., 2019, "Analysis of emerging technologies in the hydropower sector", *Renewable and Sustainable Energy Reviews,* Vol. 113, pp. 109257.

[2] Frunzăverde. D., *et al.*, 2010, "Failure analysis of a Francis turbine runner", *IOP Conference Series: Earth and Environmental Science,* Vol. 12, pp. 012115.

[3] Luna-Ramírez. A., Campos-Amezcua, A., Dorantes-Gómez, O. Mazur-Czerwiec, Z. and R. Muñoz-Quezada, 2016, "Failure analysis of runner blades in a Francis hydraulic turbine — Case study", *Engineering Failure Analysis,* Vol. 59, pp. 314-325.

[4] Ciocan, G., Iliescu, M., Vu, T.C., Nennemann, B. and Avellan, F., 2007, "Experimental Study and Numerical Simulation of the FLINDT Draft Tube Rotating Vortex", *Journal of Fluids Engineering,* Vol. 129, pp. 146-158.

[5] Javadi, A., Bosioc, A., Nilsson, H., Muntean, S. and Susan-Resiga, R., 2016, "Experimental and Numerical Investigation of the Precessing Helical Vortex in a Conical Diffuser, With Rotor-Stator Interaction", *Journal of Fluids Engineering-Transactions of the Asme*, Vol. 138(8), pp. 081106.

[6] Bosioc, A.I., and Tanasa, C., 2020, "Experimental study of swirling flow from conical diffusers using the water jet control method", *Renewable Energy*, vol. 152, pp. 385-398.

[7] Skripkin, S. and Shtork, S., 2025, "Active vortex control downstream the turbine runner in the Francis hydro turbine model", *Thermophysics and Aeromechanics*. Vol. 31, pp. 819-830.

[8] Susan-Resiga, R., Muntean, S., Tanasa, C. and Bosioc, A.I., 2008. Hydrodynamic Design and Analysis of a Swirling Flow Generator, in Proc. *4th German-Romanian Workshop on Turbomachinery Hydrodynamics* (Stuttgart, Germany)

[9] Bosioc A, Susan-Resiga R and Muntean S 2008 Design and manufacturing of a convergent-divergent test section for swirling flow apparatus, in Proc. *4th German-Romanian Workshop on Turbomachinery Hydrodynamics* (Stuttgart, Germany)

[10] Szakal, R., Bosioc, A.I., Muntean, S., Susan-Resiga, D. and Vekas, L., 2019, "Experimental Investigation of a Magento-Rheological Brake Embedded in a Swirl Generator Apparatus", *Materials Design and Application II Advanced Structured Materials,* Vol. 98, pp. 265-279.

[11] Fluent Inc 2001 Fluent 6. User Guide

[12]Muntean, S., Tanasa, C., Bosioc, A.I. and Mos, D.C., 2016. "Investigation of the Plunging Pressure Pulsation in a Swirling Flow with Precessing Vortex Rope", *IOP Conf. Ser.: Earth Environ. Sci.* Vol. 49, pp. 082010.

[13]Muntean, S., Susan-Resiga, R. F. and I. Anton, 2004, "Mixing interface algorithm for 3D turbulent flow analysis of the GAMM Francis turbine", *Modelling Fluid Flow*, pp. 359-372.

[14]Szakal, R. A., Muntean, S., Bosioc, A. I., Susan-Resiga, R. and Vékás, L., 2021, "3D numerical investigations of the swirling flow in a straight diffuser for the variable speed values of the rotor obtained with a magneto-rheological brake," in *IOP Conference Series: Earth and Environmental Science*, Vol. 774, pp. 012019.

[15]Nishi, M., Matsunaga, S., Okamoto, S,. Uno, M., and Nishitani, K., 1988, "Measurement of Three-dimensional Periodic Flow in a Conical Draft Tube at Surging Condition," *Flow in Non-Rotating Turbomachinery Components*, Vol. 69, pp. 173-184.

[16]Keller, J. J., Egli, W., and Althaus, R., 1988, "Vortex Breakdown as a Fundamental Element of Vortex Dynamics," *Journal of Applied Mathematics and Physics*, Vol. 39, pp. 404-440.

[17]Muntean, S., Bosioc, A.I., Szakal, R.A., Vékás, L., and Susan-Resiga, R.F., 2017, "Hydrodynamic Investigations in a Swirl Generator Using a Magneto-Rheological Brake," in *Materials Design and Applications*, L. F. M. d. Silva, Ed. Cham: Springer International Publishing, Vol. 65, pp. 209-218.

Conference on Modelling Fluid Flow (CMFF'25)
The 19th International Conference on Fluid Flow Technologies
Budapest, Hungary, August 26-August 29, 2025

MODELING OF FACE MASK FLOW AND DROPLET FILTRATION

Shijie XU[2], Leilei XU[2], Róbert Z. SZÁSZ[1], Xue-Song BAI[2], I.A.Sofia LARSSON[3], Per GREN[3], Mikael SJÖDAHL[3], Joel WAHL[3], Mihai MIHAESCU[4], Marco LAUDATO[4], Dario MAGGIOLO[5], Srdjan SASIC[5], T. Staffan LUNDSTRÖM[3]

[2] Department of Energy Sciences, Lund University, Lund, Sweden
[1] Corresponding Author. Department of Energy Sciences, Lund University, Sweden, E-mail: robert-zoltan.szasz@energy.lth.se
[3] Luleå University of Technology, Sweden
[4] KTH Royal Institute of Technology, Stockholm, Department of Engineering Mechanics, FLOW Research Center, Sweden
[5] Department of Mechanics and Maritime Sciences, Chalmers University of Technology, 412 96, Gothenburg, Sweden.

ABSTRACT

This paper presents experimental and numerical investigations of liquid droplet/air two-phase flow through face masks. The study aims to provide a deeper understanding of the droplet filtration process, generate experimental data for modeling droplet/air two-phase flow across face masks, and develop and validate numerical models to simulate droplet motion through the mask and downstream. Droplet interception and collection in the mask are investigated by detailed lattice Boltzmann simulations. Experiments are conducted in a branching pipe rig to measure filtration efficiency and droplet distribution at the outlet. The numerical models are applied to predict droplet motion within the experimental setup, demonstrating good agreement in terms of droplet emissions. The model is further employed to simulate airflow and droplet behavior around a human face during coughing. The results reveal a significant reduction in flow velocity across the face mask and more than a 60% decrease in droplet penetration distance.

Keywords: LES, IPI, face mask, droplets, filtration

NOMENCLATURE

D	$[m^{-4}]$	Darcy coefficient
F	$[m^{-3}]$	Forchheimer coefficient
L	$[m]$	thickness
d	$[m]$	diameter
p	$[Pa]$	pressure
$\underline{u}$	$[m/s]$	velocity
η	$[-]$	filtration efficiency
μ	$[m]$	dynamic viscosity
ρ	$[kg/m^3]$	density
$\wp$	$[-]$	size distribution

1. INTRODUCTION

Among different measures, the use of face masks is a key component of preventive strategies to minimize the spread of respiratory diseases. Due to the large number of masks used in an potential future pandemic, it is imperative to reduce their environmental footprint while preserving their functionality and user comfort.

Disposable masks, such as surgical masks, N95-100 in the U.S., and FFP1-3 in Europe, pose a significant environmental burden. It is estimated that over 140 billion disposable masks were used globally per month during the early stages of the pandemic [1]. This burden encompasses everything from greenhouse gas emissions during production to landfilling and littering. The World Health Organization (WHO) recommends that disposable masks be discarded as municipal waste, preferably through incineration [2]. While this approach has both benefits and drawbacks, it is problematic that waste is often disposed of in open landfills, especially in developing countries with limited resources for proper waste management [3].

Additionally, the landfilling of mask waste generates microplastics, which are present in landfill leachates and subsequently released into the surrounding environment [4]. Recycling disposable masks is also a complex challenge, as it may require prior decontamination and specialized procedures for separating the various polymer types used in masks, which can then be repurposed, for example, as energy sources [5].

The environmental impact of face masks largely depends on their usage. For instance, the greenhouse gas emissions associated with producing simple cotton cloth masks and disposable surgical masks are comparable. Still, factors such as washing and transportation can shift the environmental balance in favor of either option [6].

Thus, future face masks need to be carefully designed to achieve the desired low environmental impact, ensure proper comfort, and avoid significant economic penalties. Due to the pandemic, a large amount of published research has focused on various aspects of face masks. Mittal et al. [7] gives a detailed overview of the relevant physical phenomena, as well as the experimental and numerical methods used in their investigation, identifying the droplet filtration model used in macroscale simulations as one of the key challenges for numerical simulations. The review article by Hu et al. [8] presents an overview of various experimental methods used to investigate the distribution of particle sizes and the airflow behaviors of human respiration, concluding that there is a need for better spatial and temporal resolution and better quantification of the impact of face coverings.

This paper reports the first steps to reach our overall goal of developing a state-of-the-art experimental and numerical platform connecting experimental investigations of filtration efficiencies, Lattice Boltzmann simulations of droplet interception in the mask material, and large-scale Computational Fluid Dynamics (CFD) simulations to study the impact of face masks in realistic scenarios. The paper presents a novel idea, inspired by the thickened flame (see, e.g., [9]) model, to alleviate issues due to large gradients in the mask region. Furthermore, we investigate the potential of using machine learning methods to incorporate pore-scale physics in large-scale CFD simulations efficiently.

2. METHODS

2.1. Experiments

In the experiments, the droplet distribution in the downstream proximity of the masks is quantified using two different interferometric techniques. The double-pulsed interferometric particle imaging (IPI) technique is used to measure droplets larger than approximately 5 μm. The basic principle of IPI is the generation of two dominant glare points when a monochromatic plane wave, such as a laser, illuminates a particle [10]. When the glare points are defocused, they overlap, producing a fringe pattern at the defocused spot. The number of fringes is proportional to the size of the observed particle. IPI measurements allow the determination of both the size and position of individual particles. By introducing double-pulsed registration, it is also possible to estimate velocities between two frames [11].

For smaller particles, down to a few tens of nanometers, the dual-view polarization-resolved holographic method is used [12]. Smaller droplets scatter light differently depending on the polarization of the illumination, meaning that the state of polarization of the scattered light can be used as a metric to determine the size of individual particles. Combined with double-pulsed holographic registration and reconstruction, this method enables detailed determination of 3D size distributions and velocities. The interferometric data serve as input and validation data for the numerical simulations.

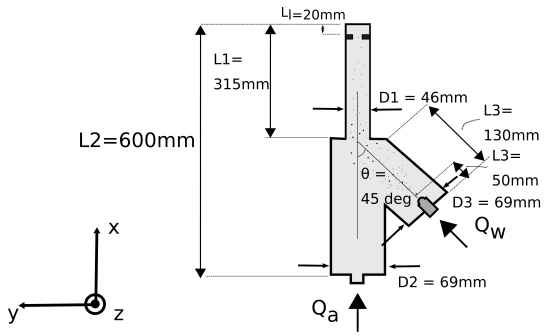

Figure 1. Experimental set-up. Air with flowrate Q_a enters through pipe 2 of diameter D2. Water is injected with a flow rate Q_w into pipe 3 with a diameter D3. The mask material is attached at the outlet of pipe 1 with diameter D1.

Figure 1 illustrates the experimental setup, which consists of three interconnected pipes. The first pipe, with a diameter of 69 mm, supplies air and connects to a second pipe of the same diameter at a 45-degree angle. Downstream of these branching pipes, a smaller pipe with a 46 mm diameter is attached. A face mask is mounted to the outlet. Various face masks are used in the experiments, including surgical masks, C-19 masks, synthetic cloth masks, and cotton cloth masks.

The experiments were conducted with or without leakage at the sides of the face mask. To control leakage, two slits perpendicular to the airflow are positioned 20 mm upstream of the face mask and can be toggled open or closed as needed.

Air with a constant speed of 1.62 m/s enters through the inlet denoted Q_a. Water droplets are injected into the upper branch of the geometry (Q_w) with a constant mass flow rate of 1.317×10^{-3} kg/s. More details about the experiments are given in [11].

2.2. Modeling of droplet dynamics in face mask

In this work, we employ two types of numerical studies: pore-scale high-fidelity simulations and Lagrangian Particle Tracking (LPT) of parcels representing saliva droplets. For the former, we carry out direct numerical simulations using a lattice Boltzmann framework to elucidate the effects of fibrous microstructures of real face masks on the dynamics, coalescence, and collection of droplets that are comparable in size to the pores (10-40 microns). The mechanisms of transport and capture of such droplets are primarily mechanical interception and then capillary transport, and in this work, we focus on the former. Our simulations will predict the average distance traveled by droplets before being captured and the penetration length that takes place in different layers of a face mask. We primarily focus

here on the role of fiber and pore sizes rather than on the effect of, for example, different wettabilities of fibrous structures. Such a study is a necessary step in formulating guidelines for designing face mask microstructures, where machine learning tools are also to be employed.

Scientific machine learning methods represent a promising tool to model droplet dynamics within the face mask microstructure. A neural operator network such as DeepONet [13] can be used to implement a surrogate model that predicts the droplet invasion time at the microscopic scale of a face mask. The model comprises a trunk network, which encodes the pore microstructure and current invasion state, and a branch network, which processes the water front height and distance from the inlet. Training data are produced via detailed numerical simulations of droplet transport in representative pore geometries, ensuring that the physics of the invasion process is accurately captured. The model outputs a single scalar value representing the invasion time of the central pore, thus offering a refined description of the local dynamics. This surrogate model can then be integrated into a computational fluid dynamics (CFD) simulation, where a simple and numerically efficient interface can represent the mask. The possibility of bridging the scales between the microscopic particle-level description of the droplet dynamics within the pore geometry and the continuum-level description of the airflow through the mask represents the perfect stage for the employment of architectures like neural operators [14, 15]. The efficiency of this approach is particularly useful under realistic respiratory boundary conditions, as it bridges the gap between fine-scale accuracy and large-scale performance for droplet transport analysis.

2.3. Numerical simulations of droplet/air two-phase flow

The transport of saliva droplets has been modeled using the reactingParcelFoam solver from OpenFOAM v21.06 [16]. Turbulence in the continuous phase can be accounted for using either Reynolds-Averaged Navier-Stokes (RANS) or Large Eddy Simulation (LES) models. LPT is employed to track parcels of saliva droplets.

The presence of a face mask must be modeled in both the continuous and discrete phases. In the continuous phase, the face mask induces a pressure drop. Similarly to published literature (see, e.g., [17, 7]), this pressure drop is modeled by introducing a porous region using the Darcy-Forchheimer model, which describes the pressure drop across a porous material of thickness L according to Eq. 1.

$$\Delta p/L = \mu D\underline{u} + 0.5\rho F\underline{u}^2 \tag{1}$$

The model coefficients (D, F) are obtained from the pressure drop measurements reported in [11].

A complicating factor is that the face mask is typically very thin compared to the scales of other geometries that need to be considered. Consequently, adding source terms to impose the required pressure drop may lead to numerical stability issues. Similar numerical challenges arise in combustion modeling, where very thin flame fronts create large temperature gradients.

An approach to handle these gradients without requiring an extremely refined mesh is the so-called thickened flame model (see, e.g., [9]). In this method, the diffusivity coefficient is multiplied by a constant, while the reaction rates are divided by the same constant, effectively thickening the flame front by the same factor while preserving the laminar flame speed. Here, we adopt a similar approach to artificially thicken the face mask zone while maintaining the required pressure drop.

In the computational domain, the face mask is represented with a thickness multiplied by a factor C (see Figure 2). Simultaneously, the coefficients in the Darcy-Forchheimer model are divided by the same factor, ensuring that the imposed pressure drop remains unaffected (see Eq. 1).

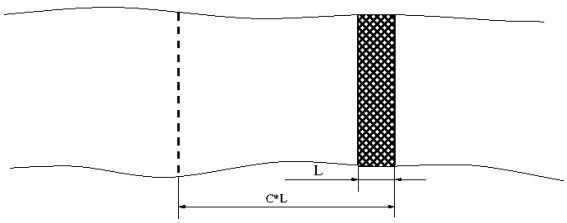

Figure 2. Sketch of the thickened face mask model.

To model the filtration effect of the mask on the discrete phase, two coupled internal boundaries are introduced in the computational domain, corresponding to the two sides of the mask. When a parcel hits one of these boundaries, the number of droplets in the parcel is reduced according to a prescribed filtration efficiency as a function of the droplet diameter. If all droplets are filtered out in the parcel, the parcel is removed. If there are droplets remaining after filtration, the parcel is transferred to the other side of the mask and transported further by the flow.

3. RESULTS

3.1. Droplet dynamics in a face mask microstructure

On the way to formulating a predictive model for droplet interception, we argue that the distance a droplet travels before interception largely depends on the probable size of the pore that the incoming droplet encounters when entering the fibrous medium. Among other things, it is of interest to look at the susceptibility of pores of different sizes to droplet invasion and subsequent collection. In that sense, we differentiate small, medium, and large pores, defined by the relative ratios of a characteristic droplet-to-fiber size ratio to a microstructural parameter of a

mask (defined using porosity of the fibrous medium, the specific surface area, and the fiber diameter). For small pores, which are smaller than droplets, it is straightforward that they will not be easily accessible, given the high capillary pressure required for their invasion. The medium-sized pores are instead more accessible, and should thus allow droplet invasion and collection. These arguments are indeed intuitive, which is not the case for large pores, where we observe a low probability of droplet invasion. Figure 3 shows that only one out of three large pores is invaded. We explain this by the fact that large pores are delimited by a high number of fibers along their perimeter, which significantly reduces the pore-throat size in their proximity. Droplet coalescence also plays a role here, since droplets tend to accumulate at these small pore throats, thus limiting to an even greater extent the access to the large pores.

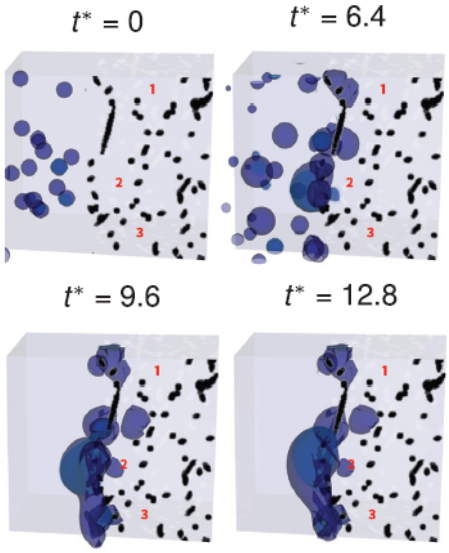

Figure 3. Snapshots of 10–40 micron droplets intercepted in a mask fibrous microstructure obtained by lattice Boltzmann simulations. Large pores are indicated by numbers 1-3, with only pore 2 being invaded.

3.2. Experimental results

Figure 4 shows the droplet distribution after the mask (green triangles), alongside the distribution of the droplets before the mask (blue diamonds) and the filtration efficiency (red rectangles). The droplet distribution before the mask is assumed to match the droplet distribution measured at the outlet when the mask is removed. The results correspond to the cotton cloth and C-19 face masks, both of which exhibited similar filtration efficiency [11]. For better visibility, the droplet size distributions are normalized by the maximum value without a mask.

The droplet size distribution after the face mask is calculated according to Eq. 2, where $\wp(d)$ represents the normalized size distribution of the droplets

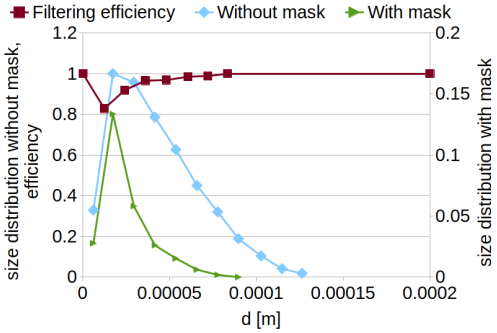

Figure 4. Filtering efficiency and droplet size distributions with and without the face mask.

before the mask at droplet size d, and $\wp_m$ denotes the size distribution of droplets after passing through the face mask. The parameter η represents the filtration efficiency, which is a function of droplet diameter.

$$\wp_m(d) = (1 - \eta(d))\wp(d) \tag{2}$$

The lowest filtration efficiency is approximately 80%, occurring for droplet sizes around 10 μm. Increasing or decreasing the droplet size leads to higher filtration efficiency. When the droplet size exceeds 80 μm, the droplets are completely stopped by the mask. Most droplets emitted at the outlet fall within the size range of 20–50 μm. Ref. [11] gives a more detailed presentation of the results.

3.3. Validation of numerical simulations (LPT)

Figure 5 presents the velocity field and droplet distribution in the branching pipes. The upper figure illustrates the water droplets. The exit of the computational domain is slightly extended to include the flow downstream of the face mask. This facilitates the counting of the leaked droplet numbers and their size distribution. These results align well with the experimental findings discussed in the previous section.

The numerical results provide insight into the droplet dynamics in the branching pipes. First, as shown in the upper sub-figure of Fig. 5, a large number of water droplets adhere to the walls and do not move toward the outlet. Second, the interaction between the droplet-laden flow in the upper branch pipe and the airflow from the lower pipe at the interconnection section creates a recirculating flow. As a result, some droplets move upstream in the lower air pipe and eventually deposit on the walls. Thus, the droplets arriving at the face mask are only a fraction of those injected.

The filtration efficiency obtained from the experimental measurements, shown in Figure 4 as red rectangles, was used in the LES to determine the particle size distribution after the mask. The particle size distribution at the outlet without a face mask was used as the droplet size distribution at the inlet. While

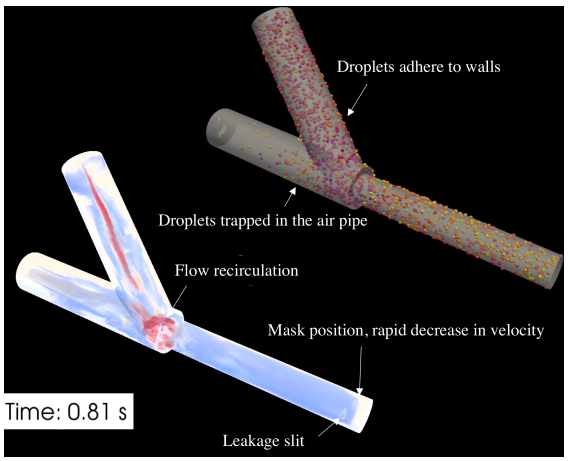

Figure 5. Instantaneous flow velocity and droplet distribution in the pipes.

this provides a qualitatively good approximation of the actual two-phase flow process, a more precise assessment should ideally be based on measurements of droplets directly at the inlet. As seen from the droplet distribution in the branching pipes, a fraction of the droplets is deposited on the walls; thus, the size distribution at the outlet and inlet differ. The particle size distribution near the leakage slit was sampled to validate against the experiments.

3.4. Simulation of flow and droplet distribution during coughing

LES is applied to study droplet distribution during human coughing. The one-equation dynamic k model is used to account for sub-grid scale effects. These computations aim to assess the impact of wearing a mask by comparing two cases: with and without a mask. In both cases, a single coughing event is simulated, with the velocity profile based on the data reported in [18] and plotted in Figure 6.

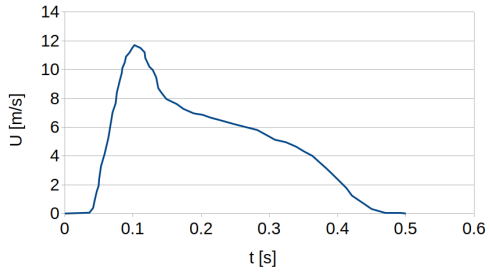

Figure 6. Velocity profile used to simulate a coughing event

A realistic face is included only in the case where the face mask is fitted, as it is important to account for potential leakage in this scenario. Figure 8 illustrates the adopted face geometry, highlighting the placement of the face mask region and the possible leakage areas around the jaw and nose, which are marked with red ellipses. The mouth shape is simplified as a 4×1 cm^2 rectangle. As shown in Fig. 6, a realistic velocity profile is used to mimic the coughing process. The duration of the cough is 0.5 ms, and the maximum velocity is set to 11.7 m/s [19]. The LPT approach is adopted here, and 3000 parcels are used to track the evolution of saliva droplets. The total mass is 7.7 mg, and the droplet size distribution is plotted in Figure 7. Following suggestions in Ref. [20], the size distribution of saliva droplets is initialized using the Rosin-Rammler distribution law. The mean and maximum diameters of 80 and 600 μm are adopted based on measurements in Ref. [21].

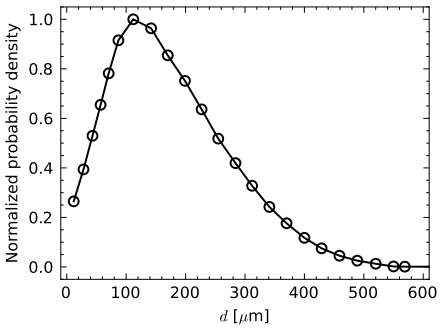

Figure 7. Size distribution of the injected droplets.

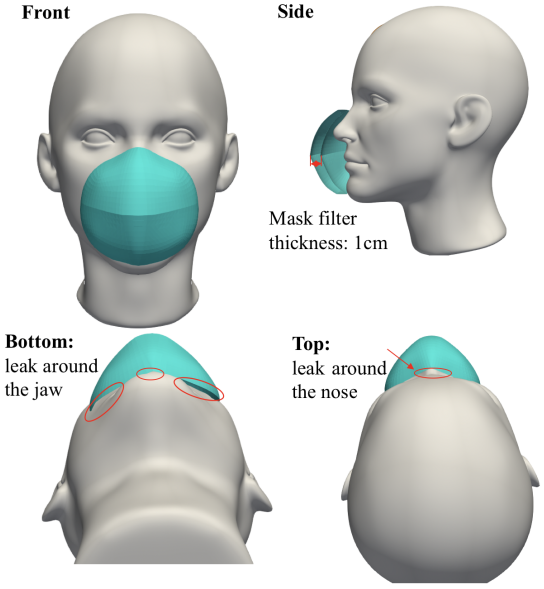

Figure 8. Face model with the mask.

Figure 9 shows the recorded flow rate with and without the face mask. In the numerical simulations, the face mask consists of a set of computational cells, delimited by two patches, i.e., the inner patch and the outer patch. The inner patch is the one close to the inlet, i.e., the mouth, and the outer patch is on the opposite side. The flow rates are calculated as $\sum \rho \underline{u} \cdot \underline{n} A_i$, where $\underline{n}$ and A_i are the normal vector and surface area of the i-th face on the outer patch.

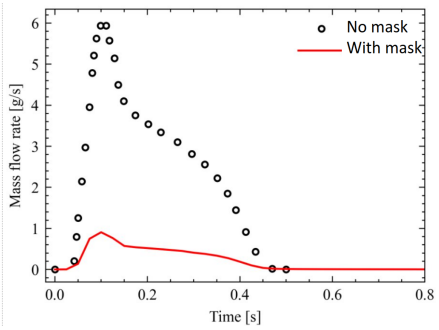

Figure 9. Flowrate with and without mask.

In the case without a face mask, the flow rate is estimated using a virtual patch, i.e., a sampling surface consisting of identical faces to the outer patch. It can be observed that the maximum flow rate is reduced by approximately a factor of six when the face mask is fitted. This factor is slightly lower after 0.15 ms. The flow speed significantly decreases after passing through the face mask due to the pressure loss across it and the leakage of the gas around the nose and jaw. This implies that the leakage cannot be ignored, as it may play an important role in flow fields and the evolution of droplets.

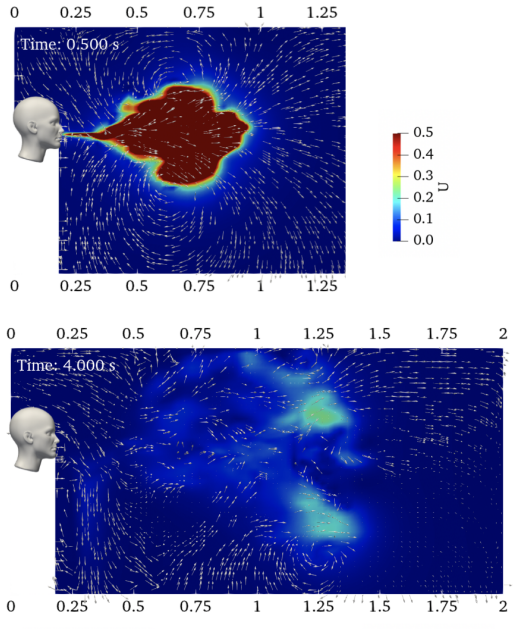

Figure 10. Velocity distribution during human coughing without wearing a face mask.

Figure 10 shows the velocity field at two time instances, i.e., at 0.5 s (top) and 4 s (bottom). The face mask is absent for this case. At 0.5 s, which corresponds to the end of the coughing event, a high-speed flow region with a velocity of approximately 0.5 m/s extends up to 1 m from the human face. By 4 s, the velocity decreases to 0.2 m/s, reaching a distance of 1.5 m. This suggests that a coughing event may affect flow fields at a distance of at least 1.5 meters, consistent with the safety distance.

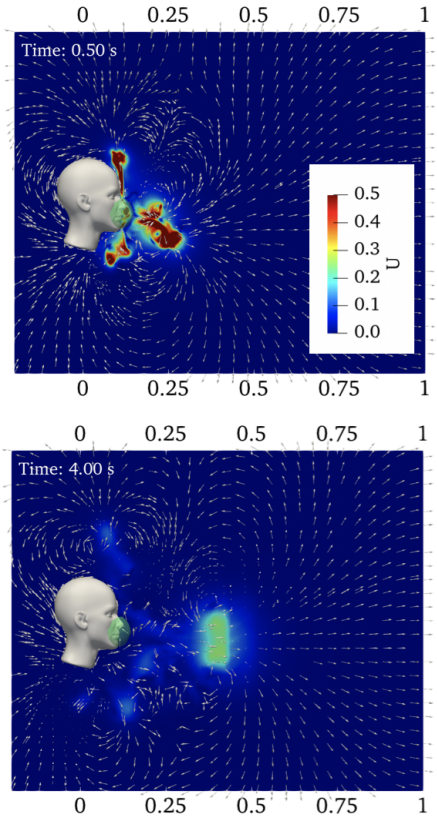

Figure 11. Velocity distribution during human coughing when wearing a face mask.

Figure 11 shows the corresponding velocity field for the case with a face mask. At 0.5 s, three high-speed streams are observed, directed forward, upward, and downward. The upward and downward flow streams result from gaps between the face and the mask around the nose and jaw. This is consistent with observations in Fig. 9, i.e., the penetration of the coughing in the bulk flow direction is reduced, attributed to the mass flow rate of leakage near the nose and jaw.

From Figs. 10 and 11, the impact of the face mask on flow and droplet distribution becomes evident. Due to the significant velocity decrease across the mask, the momentum of droplets moving forward in the horizontal direction is substantially reduced. By 4 s, the velocity of the front stream decreases to approximately 0.2 m/s, reaching only 0.5 m from the face, one-third of the distance observed without the face mask. Additionally, the high filtration efficiency effectively blocks the majority of droplets, thereby reducing the spread of the virus in the air.

3.5. Predicting invasion time with a neural-operator surrogate

As outlined in Sec. 2.2, we employ a DeepONet-style neural operator to predict the invasion time at the pore scale of a facemask. Both subnetworks share a compact, fully connected architecture: Branch net (2 hidden layers, 32 and 16 neurons, respectively), Trunk net (3 hidden layers with 32, 32, and 16 neurons).

All hidden layers use ReLU activation; the latent dimension of each subnetwork is fixed to 32. A single linear neuron in the output layer returns the (scalar) invasion time. The network is trained with Adam and mean–squared error loss; convergence is reached after ≈ 200 epochs.

Model I: absolute time without distance. The first model feeds the pillar diameters (*branch*) and the binary occupation state of the immediate neighbours (*trunk*). Its target is the *absolute* invasion time, measured from $t = 0$ of the simulation. The parity plot in Fig. 12 (top) and the low coefficient of determination ($R^2 = 0.285$) reveal that these inputs are insufficient to capture the invasion dynamics.

Model II: absolute time with distance. To provide a clear physical proxy for front progression, we append the absolute distance from the mask edge to the trunk input. As expected, the network now attains excellent accuracy ($R^2 = 0.989$; Fig. 12 middle), essentially learning the monotonic relationship between distance and arrival time of the wetting front.

Model III: relative time without distance. Finally, we withdraw the distance feature and ask the network to predict the *relative* invasion time, defined as the time elapsed since one of the adjacent pores was first invaded. Although trained on the same data volume as the previous models, Model III already achieves a promising $R^2 = 0.825$ (Fig. 12, bottom). This indicates that local geometry and short-range state information are sufficient to reconstruct the temporal ordering of pore invasion, provided a larger training set.

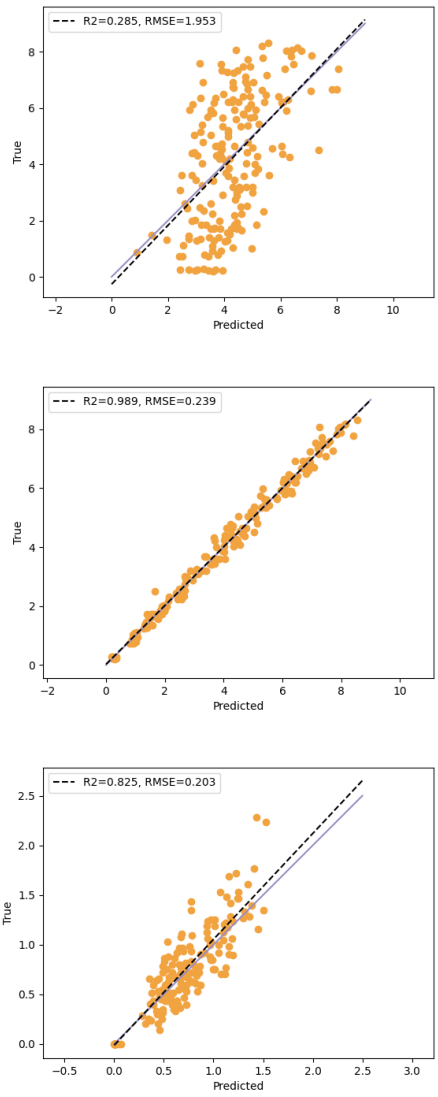

Figure 12. Parity plots for Model I (top), II (middle) and III (bottom). The dashed line is $y = x$.

4. SUMMARY

This paper presents experimental and numerical studies on the filtration of liquid droplets through face masks. Experimental investigations were conducted using a branching pipe rig to analyze water droplet filtration across various face masks, measuring particle size distributions at the outlet with and without masks. The results showed that droplets larger than 80 μm were effectively filtered out, while the lowest filtration efficiency, approximately 80%, was observed for droplets around 10 μm in diameter.

Lattice Boltzmann simulations of droplet interception and collection in the mask revealed that, counterintuitively, not all large pores are penetrated by droplets.

The analysis based on the neural operator revealed that, with additional data, a distance-free surrogate could faithfully reproduce pore-scale invasion dynamics. This represents an essential step toward embedding pore physics in continuum-scale CFD simulations.

A thickened mask model was developed within the large eddy simulation (LES) framework to simulate droplet/air two-phase flow across the mask. Numerical simulations using this model were performed to study droplet and turbulent flow behavior within the branching pipe rig. The results provided insights into droplet motion, wall deposition, recirculating flow, and the rapid velocity drop across the mask.

The thickened mask model was further applied to simulate airflow during human coughing, both with and without a face mask. The results revealed a significantly reduced penetration distance of the forward flow and detailed the airflow structure through gaps between the mask and the nose and jaw. Future work will focus on using the model to optimize the

design of reusable face masks.

ACKNOWLEDGEMENTS

This work was supported by Formas (Project number 2022-01116). The computations were enabled by resources provided by NAISS at NSC and PDC, partially funded by the Swedish Research Council through grant agreement no. 2022-06725 and no. 2018-05973.

REFERENCES

[1] Prata, J. C., Silva, A. L., Walker, T. R., Duarte, A. C., and Rocha-Santos, T., 2020, "COVID-19 pandemic repercussions on the use and management of plastics", *Environmental science & technology*, Vol. 54 (13), pp. 7760–7765.

[2] Corburn, J., Vlahov, D., et al., 2020, "Slum health: arresting COVID-19 and improving well-being in urban informal settlements", *Journal of urban health*, Vol. 97, pp. 348–357.

[3] WHO, "Coronavirus Disease (COVID-19) Advice for the Public: When and How to Use Masks", URL `https://www.who.int/emergencies/diseases/novel-coronavirus-2019/advice-for-public/when-and-how-to-use-masks`, checked 2025.03.06.

[4] Silva, A. L., Prata, J. C., Duarte, A. C., Soares, A. M., Barceló, D., and Rocha-Santos, T., 2021, "Microplastics in landfill leachates: The need for reconnaissance studies and remediation technologies", *Case Studies in Chemical and Environmental Engineering*, Vol. 3, p. 100072.

[5] Jain, S., Yadav Lamba, B., Kumar, S., and Singh, D., 2022, "Strategy for repurposing of disposed PPE kits by production of biofuel: Pressing priority amidst COVID-19 pandemic", *Biofuels*, Vol. 13 (5), pp. 545–549.

[6] Klemeš, J. J., Van Fan, Y., and Jiang, P., 2020, "The energy and environmental footprints of COVID-19 fighting measures–PPE, disinfection, supply chains", *Energy*, Vol. 211, p. 118701.

[7] Mittal, R., Breuer, K., and Seo, J. H., 2023, "The Flow Physics of Face Masks", *Annual Review of Fluid Mechanics*, Vol. 55 (1), pp. 193–211.

[8] Hu, N., Yuan, F., Gram, A., Yao, R., and Sadrizadeh, S., 2024, "Review of experimental measurements on particle size distribution and airflow behaviors during human respiration", *Building and Environment*, Vol. 247 (October 2023), p. 110994.

[9] Detomaso, N., Hok, J.-J., Dounia, O., Laera, D., and Poinsot, T., 2023, "A generalization of the Thickened Flame model for stretched flames", *Combustion and Flame*, Vol. 258, p. 113080.

[10] Semidetnov, N., and Tropea, C., 2003, "Conversion relationships for multidimensional particle sizing techniques", *Measurement Science and Technology*, Vol. 15 (1), p. 112.

[11] Öhman, J., Gren, P., Sjödahl, M., and Lundström, T. S., 2022, "Experimental investigation of face mask filtration in the 15-150 μm range for stationary flows", *Journal of Applied Physics*, Vol. 131, p. 044702.

[12] Öhman, J., and Sjödahl, M., 2020, "Identification, tracking, and sizing of nano-sized particles using dual-view polarization-resolved digital holography and T-matrix modeling", *Applied Optics*, Vol. 59 (14), pp. 4548–4556.

[13] Lu, L., Jin, P., Pang, G., Zhang, Z., and Karniadakis, G. E., 2021, "Learning nonlinear operators via DeepONet based on the universal approximation theorem of operators", *Nature machine intelligence*, Vol. 3 (3), pp. 218–229.

[14] Laudato, M., Manzari, L., and Shukla, K., 2024, "High-Fidelity Description of Platelet Deformation Using a Neural Operator", *arXiv preprint arXiv:241200747*.

[15] Laudato, M., Manzari, L., and Shukla, K., 2025, "Neural Operator Modeling of Platelet Geometry and Stress in Shear Flow", *arXiv preprint arXiv:250312074*.

[16] OpenFOAM, "OpenFOAM, https://www.openfoam.com", Checked 2025.02.18.

[17] Jia, Z., Ai, Z., Yang, X., Mak, C. M., and Wong, H. M., 2023, "Towards an accurate CFD prediction of airflow and dispersion through face mask", *Building and Environment*, Vol. 229 (November 2022), p. 109932.

[18] Gupta, J. K., Lin, C. H., and Chen, Q., 2009, "Flow dynamics and characterization of a cough", *Indoor Air*, Vol. 19 (6), pp. 517–525.

[19] Gupta, J. K., Lin, C.-H., and Chen, Q., 2009, "Flow dynamics and characterization of a cough", *Indoor air*, Vol. 19 (6), pp. 517–525.

[20] Dbouk, T., and Drikakis, D., 2020, "On coughing and airborne droplet transmission to humans", *Physics of Fluids*, Vol. 32 (5).

[21] Xie, X., Li, Y., Sun, H., and Liu, L., 2009, "Exhaled droplets due to talking and coughing", *Journal of the Royal Society Interface*, Vol. 6 (suppl_6), pp. S703–S714.

Conference on Modelling Fluid Flow (CMFF'25)
The 19th International Conference on Fluid Flow Technologies
Budapest, Hungary, August 26 - August 29, 2025

THE CFD-BASED DESIGN OF A BYPASS TUNNEL TO PROVIDE THE CROSS-FLOW USED IN THE CASE OF BLADE CASCADE AEROELASTIC STUDY

Pavel PROCHÁZKA[1], Chandra S. Prasad[2], Pavel ŠNÁBL[3], Vladislav SKÁLA[4]

[1] Corresponding Author. Institute of Thermomechanics, The Czech Academy of Sciences, Prague, Czech Republic. Tel.: +420266053313, E-mail: prochap@it.cas.cz
[2] Institute of Thermomechanics, The Czech Academy of Sciences, Prague, Czech Republic, E-mail: cprasad@it.cas.cz
[3] Institute of Thermomechanics, The Czech Academy of Sciences, Prague, Czech Republic, E-mail: snabl@it.cas.cz
[4] Institute of Thermomechanics, The Czech Academy of Sciences, Prague, Czech Republic, E-mail: skala@it.cas.cz

ABSTRACT

Aeroelastic stability phenomenon is still in the center of interest for many research groups and engineers, particularly in applications involving compressor or turbine blades in various turbomachinery devices. There is a lack of experimental data which could help to validate CFD simulations. Typically, the tests are running in an aerodynamic wind tunnel providing uniform flow conditions. Obviously, there is a significant radial flow component in the real applications when lower mass flow ratio occurs. The radial component can be responsible for the stall flutter occurrence and consequently the stability loss in many cases. Current experimental setups using planar blade cascades do not adequately model this radial flow effect. This study is devoted to the design of bypass (cross) flow based on CFD calculation to create appropriate flow conditions. The presence of cross-flow affecting the tilted blade cascade performing harmonic motion driven by force excitation creates a complex 3D turbulent flow field. Advanced experimental techniques, including HW and PIV anemometry, are planned in the future to analyse flow dynamics. Additionally, the blade response will be measured to determine the aerodynamic damping parameter, providing valuable insights into aeroelastic stability in turbomachinery.

Keywords: cross-flow, turbomachinery, blade cascade, CFD, PIV, HW

NOMENCLATURE

Δp	[Pa]	pressure drop
v, U	[m/s]	velocity magnitude
λ	[-]	friction coefficient
ξ	[-]	local coefficient of resistance
l	[m]	length of the tube
D	[m]	diameter of the tube
ρ	[kg/m^3]	density
y^+	[-]	dimensionless wall distance

Subscripts and Superscripts

inlet	at the inlet of the section
outlet	at the outlet of the section
STD	standard deviation
x, y, z	Cartesian coordinate system
V1-V3	design designation

1. INTRODUCTION

Nowadays, steam turbines are very often operated in non-design conditions due to the significant share of renewable energy sources in the energy network. In such a case, a lower mass flow ratio results in a redistribution of the pressure field along the blades and the creation of a spatial flow structure with a pronounced radial component in the middle area of the blades. Due to lower mass flow ratio occurrence, the inlet velocity is too low and the relative angle of attack is changed causing the tendency to stall flutter. This phenomenon, combined with a large radial velocity component, results in the appearance of vortex structures at a location approximately 90 percent of the blade span. Another vortical structure is apparent near the blade root as presented in Fig 1.

A project dealing with the aeroelastic stability of turbine-blade cascades and the influence of 3D flow structures is being solved within the Institute of Thermomechanics. To successfully achieve the goals of this project, which will be solved mainly experimentally, it is necessary to design an aerodynamic tunnel with the test section that meets the required conditions for the non-rotating blades. The 3D flow condition is met even with the

presence of the elastic blade bodies as these blades will perform harmonic oscillation with torsional and bending modes resulting in time-varying inter-blade channel width. Nevertheless, the presence of two vortical structures (first one close to the blade root and second one behind the blade tip – see figure 1) cannot be physically modelled without creation of inlet flow with a radial flow component that can be controlled according to requirements.

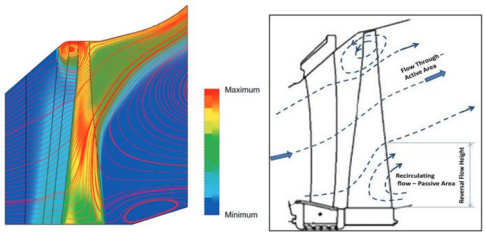

Figure 1. 3D flow structure around LP stage blade during low-load condition (Ref : [5-6])

There are several ways to introduce a radial component to channel axial flow. For example, one can utilize a fine mesh screen bended to an S-shape [1] where a shear flow is generated using the so-called Elder´s generator. However, this is a passive method ensuring the desired flow parameters only in limited space behind the screen. Another passive possibility is to change the shape of the tunnel bottom and upper wall to change the flow direction or apply the test section with diverging cross section [2]. The design of such a test section adaptation is quite simple but does not offer to control the radial flow under various flow regimes. Active flow control is highly desired in this case. The air jet blowing [3] or suction effects [4] seems to be meaningful but the spatial range is not sufficient to excite the presence of the radial flow component in the entire volume of the test section. Finally, the authors have chosen the most robust solution which is not published in detail in available literature. This design was named as a bypass tunnel to create a radial velocity component across the tunnel test section. The bypass flow will be driven by a powerful ventilator which can be set independently of the main tunnel propulsion. This will allow for continuous regulation of the axial - to - radial component ratio and regulation of the size of the recirculation area.

This article will describe the calculation of desired flow rate to introduce sufficient powerful cross-flow, the calculation of pressure losses in the bypass and the choice of appropriate fan and mainly the CFD simulation of the flow in the bypass critical parts.

2. DESIGN

The aeroelastic experiments on the blade cascade will be performed inside the tunnel of Eiffel type with under pressure test section 700 x 700 mm. This tunnel has an axial motor - 14kW, 709 Pa, 44 000 m^3/h (12 m^3/sec), maximal airflow velocity 20-24 m/s. The model of the blade cascade will consist of 13 NACA0010 blades oriented with the stagger angle 90° and located across the test section (see figure 2). There were many numerical simulations which determined the flow rate and proper orientation of the blowing orifice (in front of the blade roots) and suction orifice (behind blade tips). The details about CFD simulation and optimization are presented in the following section. Also due to the constructional reason, it was chosen the variant with the blowing gap 650 x 100 mm located approximately 350 mm in front of the blade cascade and with one suction gap with the same cross-section (0,065 m^2) which can be placed at any location on the ceiling (preferably behind the cascade). The desired flow rate was assessed as approximately 5 000 m^3/h (the volume velocity 20-25 m/s). For similar flow conditions, the flow topology (figure 2) around blade cascade shows similar characteristics as required.

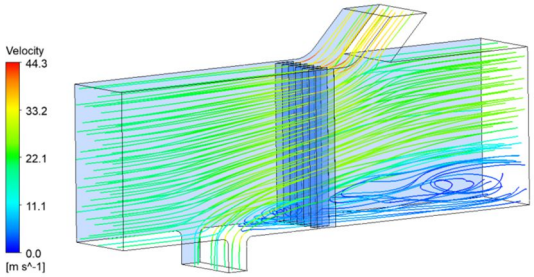

Figure 2. Flow field topology for main inlet and bypass velocity set to 20 m/s

To choose an adequate ventilator for a bypass tunnel it is crucial to know both the desired flow rate and the pressure losses due to friction and due to shaped pieces of pipeline (fittings). The main sources of resistance to flow are fluid velocity through the pipe and fluid viscosity. Pressure drop increases proportionally to the frictional shear forces within the piping network. High flow velocities or high fluid viscosities result in larger pressure losses. Low velocity will result in less pressure losses. Pressure drop is related inversely to pipe diameter to the fifth power. Pressure drop in the pipeline is directly proportional to the length of the tube. The pressure drop can be expressed as

$$\Delta p = \lambda \frac{l}{D} \frac{v^2}{2} \rho \qquad (1)$$

$$\Delta p = \xi \frac{v^2}{2} \rho \qquad (2)$$

for friction taking place on the inner surface of the pipes and for drop due to shape changing. The exact value of this coefficient must be determined experimentally for each fitting part.

The flow rate through the gap is Q= 5850m^3/h for planned volume velocity 25 m/s. However, the calculation should allow for much greater velocity in case of emergency. The table 1 shows the corresponding volume velocity for different tubing cross sections and two flow rates. It is apparent that dimensions less than DN300 would result in too high velocity values and unacceptable pressure losses. The assessed pressure drop for the bypass tunnel and for velocity 30 m/s by DN300 reached the value of 3,8 kPa. Bigger dimension of the pipes is not practical because it involves too heavy and big parts and, more importantly, the solution is really costly.

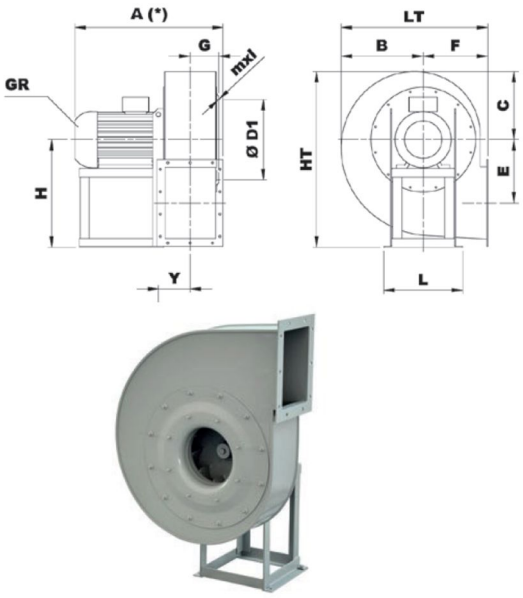

Figure 3. Radial fan ART 501N, main dimensions: outlet 322 x 229mm, inlet Ø 310mm

The ventilator which can deliver flow rate about 5 000 – 7 000 m^3/h at pressure drop 4 kPa is already quite powerful. The axial fan cannot be used as the pressure drop is not sufficient. The radial fan ART 501, which is an industrial type usable for grain cleaners, air transport and strong filtering systems and cyclones, were finally selected. The operating point of this fan is 5000 m^3/h at 4 kPa (see fan characteristic) but it can deliver about 15 000 m^3/h at minimal pressure drop.

Table 1. Tube dimensions and flow rates

	A [m^2]	7500 m^3/h	15000 m^3/h
DN200	0,03	69m/s	139m/s
DN300	0,07	30m/s	59m/s

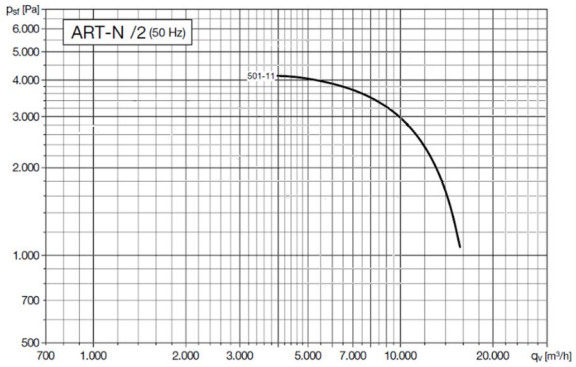

Figure 4. Radial fan performance curves, www.solerpalau.com

The pipeline of upper parts of the bypass tunnel is easy to build (figure 6 – DN300 to connect suction gap with the radial fan) as well as the tubing (322 x 229 mm) from radial fan to blowing gap. Nevertheless, there are two critical sections where the transition parts have to be applied to fit the narrow gap. The most sensitive concerning flow condition is the blowing orifice because it is preceded by one elbow. These parts of the pipeline had to be designed by CFD tools together and will be presented below.

3. CFD OPTIMIZATION

The CFD optimization was mainly used for the bypass tunnel blowing design as presented in the figure 6, to achieve 20 m/s vertical flow in front of the blade cascade. There are three design iterations that have been carried out to achieve the desired flow field.

3.1 CFD numerical model discretization

In the first step for the CFD modelling, geometry of the blowing cone is discretized using 2D and 3D FV-elements. The discretization scheme of the 1st design iteration model is presented in Fig 5.

To generate 3D FV elements first the solid wall and intel/outlet geometry is discretized with 2D mix of rectangular/triangular elements - Fig. 5b. The fluid volume is discretized using 3D tetrahedral FV-elements - Fig. 5c. In order to capture the viscous effect accurately, 3D BL discretization is adopted. There are 7 3D BL elements used with 1st layer thickness 0.0135 mm, to obtain y+ < 1, Fig. 5d. The mesh parameters are given in table 2 below.

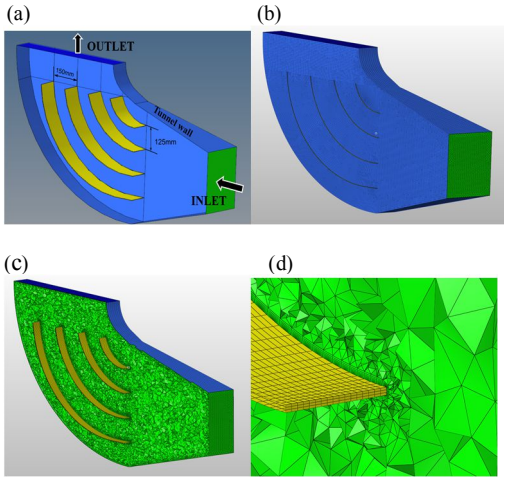

Figure 5. CFD numerical model geometry discretization using 3D FVM. (a) 1st iteration geometry (b) 2D wall surface mesh for CFD (c) interior flow field discretization using 3D tetrahedral FV-elements. (d) 3D boundary layer elements around the solid walls

Table 2. CFD numerical model discretization parameters

Mesh parameters	**Value**
Mesh type	FV
Average element size	7 mm
Number BL	7
Y+	< 1
First layer thickness	0.0135 mm
Mesh size	0.56 millions

Therefore, the entire fluid domain is discretized into 0.56 million FV elements. A mesh convergence study is performed prior to selecting the correct element size for discretization.

3.2 CFD numerical model

A k-omega (K-ω) SST (Shear-Stress Transport) Reynold Averaged Navier-Stokes (RANS), turbulence model is employed as CFD numerical method for the incompressible flow field simulation. Furthermore, K-ω SST turbulence model is a widely used two-equation eddy-viscosity model in computational fluid dynamics (CFD). It is designed to combine the advantages of the k-omega and k-epsilon (k-ε) models, providing accurate predictions in both near-wall and far-field regions [7]. The details about mathematical formulation K-ω SST RANS model can be found in any standard CFD textbook on RANS turbulence modelling or ANSYS Fluent user manual. The 2 equation K-ω SST model is available in ANSYS Fluent 2023R1, commercial software package. All the CFD simulation for the optimization purpose is carried out in the ANSYS-Workbench 2023R1 environment.

In order to obtain the correct solution the proper boundary conditions (BC) need to be imposed in CFD models. Therefore, three main BC is imposed to correctly estimate the flow field within the blowing cone: 1) Velocity inlet type BC at INLET section of the cone - Fig 5a, 2) pressure outlet type BC at the OUTLET section - Fig 5a 3) No-slip BC are applied at the tunnel walls.

The steady state CFD simulation is carried out for all cases of optimization. The simulation time for each case approximately takes 5 hrs on 6-core AMD Ryzen 7 9800X3D processors to fully converge. Time for discretization and post processing is not included in this. However, the computational time can be reduced by using reduced order CFD methods, [8-10]. But in the present case it is not the utmost priority.

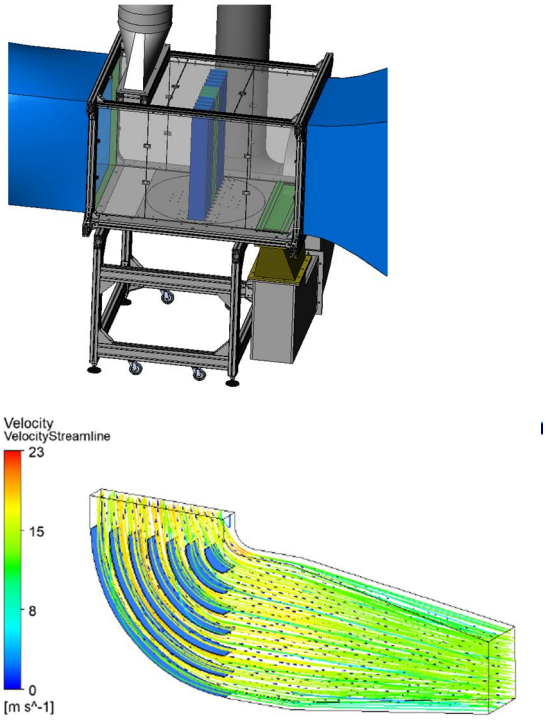

Figure 6. The design of bypass tunnel with circular pipes for suction part and an elbow and a transition part for blowing (a); CFD-optimized blowing part with several vanes to preserve the flow separation - preliminary design (b)

4. RESULTS

There were designed many variants of the pipeline to get from almost square cross-section to a very narrow rectangular shape (650 x 100 mm) while the flowing air must be turned by 90° to penetrate the main channel flow perpendicularly with perfect homogeneity. There is one of the preliminary variants in figure 6 where the change in cross-section takes place in the horizontal part, which is followed by an elbow with six guide vanes and constant cross-section. This strategy will be also applied for further variants as it is the easiest to manufacture.

There were progressively designed and CFD-verified final three variants (V1, V2 and V3) which meet the requirements also with regard to spatial possibilities. V1 is the least space-demanding as it utilizes a relatively sharp inner radius and four equidistant blades. Second and third variants are designed according to general requirements [7] utilizing four and five blades, respectively. The blade radius is 300 mm and the trailing edge is extended by 80 mm. The leading edge is shortened by 4 angular degrees. All blades are positioned proportionally with a 45° inclination. The blade thickness was set to 2 mm. The considered flow rate was set to 1.258 m^3/s.

For all three variants, the design is not space-intensive and the elbow has very low pressure drop. There is a demand for outlet velocity profiles to be homogeneous along the gap width with velocity vectors only slightly deviated from the perpendicular axis. There is velocity distribution for mentioned variants inside the elbows in figure 7.

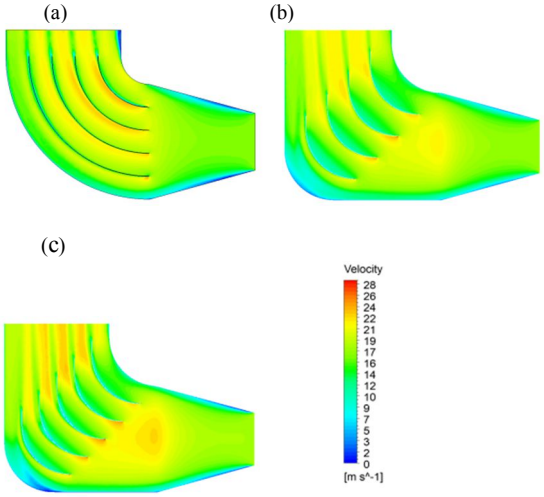

Figure 7. CFD simulation of the flow distribution inside the elbows. (a) 1st variant, (b) 2nd variant and (c) 3rd variant

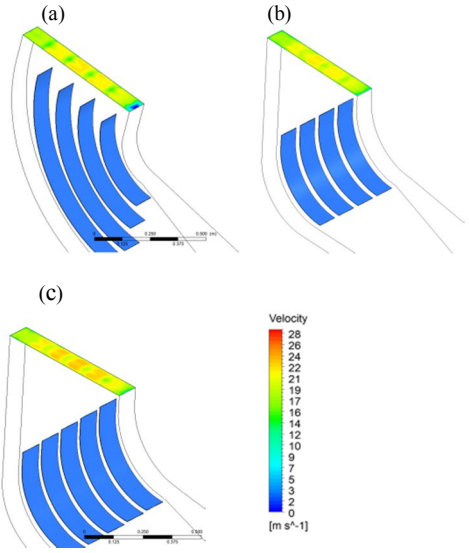

Figure 8. CFD simulation of the velocity distribution within the outlet gap. (a) 1st variant, (b) 2nd variant and (c) 3rd variant

The figure 8 is plotted to show the homogeneity of the jet to be blown. This is a crucial parameter to get a constant radial flow velocity component across the tunnel test section. It is obvious from the velocity distribution that the first variant suffers from the flow separation just behind the inner elbow radius and also the wakes behind all vanes negatively influence the smoothness of velocity distribution. Likewise, the third variant is not homogeneous along the gap. To compare more precisely, the velocity profiles at the centerline will be plotted in figure 9 for all three variants.

A solid red profile is plotted for the 1st variant. A blue dashed line and a green dash and dot line is made for variant No. 2 and 3, respectively.

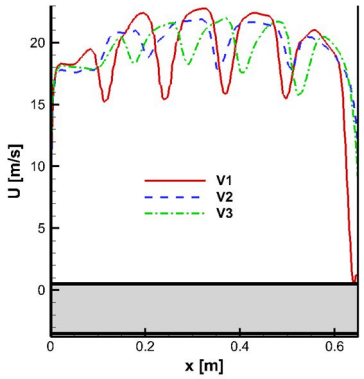

Figure 9. Velocity profiles at the outlet from the elbows V1, V2 and V3; grey area denotes the gap dimensions

All variants have an almost equivalent averaged velocity value (19.5 m/s) at the centerline. However, the velocity is not constant along this line

at all. Variant No. 1 suffers from outstanding velocity decrease inside vane wakes (peak-to peak value 7.6 m/s). The other two variants have smaller deviations (peak-to-peak is 4.1 and 5.8 m/s for V2 and V3). A decisive indicator is the standard deviation of outlet velocity magnitude. The worst value is connected with the 1st variant where standard deviation is equal to 2.98 m/s. The third option is much better - 1.59 m/s. Second variant with only four vanes demonstrates the smallest value equal to 1.52 m/s. To specify the direction of outlet velocity vectors, the averaged angle α was evaluated based on streamwise and spanwise velocity components. The third variant has the best ratio, the second design is only slightly worse (see table 3).

Table 3. Results summary

	V1	V2	V3
STD_U [m/s]	2.98	1.52	1.59
α [°]	3.87	1.66	0.81

5. CONCLUSIONS

The bypass tunnel was designed to meet the criteria by a solution of the project dealing with 3D flow structures affecting the aeroelastic behaviour of the blade cascade with two degrees of freedom. The radial flow component will be controlled by setting of the radial fan revolutions and also by a possibility to change to position of the suction gap. While blowing jet is applied it is very crucial to design the orifice and connecting pipeline to get constant flow features along the blowing gap. This part was designed using CFD tools. Based on numerical calculations and data analysis, the second design of the elbow was selected.

Ansys Fluent proved to be very helpful in designing the partial sections of the bypass tract, which saved a lot of time when it was not necessary to tune the properties of the outlet flow. Even so, it must be taken into account that other improvements will have to apply to improve the output flow parameters.

The CFD results will be validated by the experimental measurement using hot wire (HW) anemometry. Potentially, it would be possible to add a honeycomb section and a fine mesh screen behind the elbow vanes to improve the character of the output jet.

ACKNOWLEDGEMENTS

This work was supported by the research project of the Czech Science Foundation No. 24-12144S.

REFERENCES

[1] Antoš, P., 2014, "Development of Temperature Fluctuation in a 2D Shear Turbulent Flow", *32. stretnutie katedier mechaniky tekutín a termomechaniky*, Conference proceeding pp. 1-4.

[2] Uruba, V., 2012, "Stability and Dynamics of Flow in a Turbulent Boundary Layer Separation Region", *Progress in Turbulence and Wind Energy IV*, *Vol. 141, pp 105-108.*

[3] Wang, J., Jiang, Ch., Zhou, X., Kang, J., Yu, S. and Bai, G., 2024, "Experimental Study on Flow Characteristics of Jet Ventilation in Crossflow in Confined Mine Spaces", *Scientific Reports, Vol. 14, No. 8022.*

[4] He, X., Williams, D. R. and Dawson, S. T. M., 2022, "Transverse gust generation in a wind tunnel: a suction-driven approach", *Experiments in Fluids, Vol. 63, No. 125.*

[5] Mambro, A., Congiu, F., Galloni, E. and Lanni, D., 2022. "Blade Drag Resistance in Windage Operating of Low Pressure Steam Turbines". *Fluids*, *7*(12), p.372.

[6] *Turbines, Generators and Associated Plant (Third Edition)*, Pergamon, 1991, Pages 1-123, ISBN 9780080405131.

[7] Mehta, R. D., Bradshaw, P., "Design rules for small low speed wind tunnels", *The Aeronautical Journal of the Royal Aeronautical Society*, 1974.

[8] Prasad, C.S. and Pešek, L., 2018. "Analysis of classical flutter in steam turbine blades using reduced order aeroelastic model", In *MATEC Web of Conferences* (Vol. 211, p. 15001). EDP Sciences.

[9] Sepúlveda, H., Valle, R., Pincheira, G., Prasad, C.S., Salas, A., Medina, C. and Tuninetti, V., 2023. "Dynamic numerical prediction of plasticity and damage in a turbofan blade containment test", *Proceedings of the Institution of Mechanical Engineers, Part L: Journal of Materials: Design and Applications*, *237*(12), pp.2551-2560.

[10] Prasad, C.S., Šnábl, P. and Pešek, L., 2021. "A meshless method for subsonic stall flutter analysis of turbomachinery 3D blade cascade", *Bulletin of the Polish Academy of Sciences. Technical Sciences*, *69*(6).

Conference on Modelling Fluid Flow (CMFF'25)
The 19th International Conference on Fluid Flow Technologies
Budapest, Hungary, August 26-August 29, 2025

PIPE FLOW ANALOGY IN A PLANAR MASS-SPRING-DAMPER SYSTEM

Róbert ROCHLITZ[1], Bendegúz D. BAK[2]

[1] Corresponding Author. Department of Fluid Mechanics, Faculty of Mechanical Engineering, Budapest University of Technology and Economics. Bertalan Lajos u. 4 - 6, H-1111 Budapest, Hungary. E-mail: rochlitzr@edu.bme.hu
[2] Department of Fluid Mechanics, Faculty of Mechanical Engineering, Budapest University of Technology and Economics. E-mail: bak.bendeguz@gpk.bme.hu

ABSTRACT

We construct a chain oscillator whose block masses are connected by linear springs and linear dampers and each block is capable of 2D movement. This capability for moving in two directions gives rise to geometric nonlinearity in both the spring and the damping forces.

We investigate the behaviour of the planar system for initial conditions resulting in both linear and nonlinear response. The oscillator chain will be subjected to simultaneous forcing of each of its block masses, whose results will be compared for different forcing magnitude and parametrisations of the system.

The mean positions of the planar oscillator's block masses are compared to the velocity fields arising in simple fluid flows in pipes. It is demonstrated that for certain parametrisations of the oscillator, the model can reproduce the velocity profiles of real pipe flows. In particular, the mean position of the masses follows a quadratic profile for forcing similar to the constant pressure gradient which facilitates Poiseuille flows.

Keywords: flow modelling, nonlinear dynamics, pipe flow

NOMENCLATURE

E	[−]	energy
c	[−]	damping
f_0	[−]	scaling parameter of the forcing
k	[−]	spring stiffness
l	[−]	free spring length
m	[−]	element mass
n	[−]	number of elements
p	[−]	fitted polynomial
t	[−]	time
x	[−]	horizontal position
y	[−]	vertical position
R^2	[−]	fit quality
$\mathbf{F}_\mathrm{d}$	[−]	damping force
$\mathbf{F}_\mathrm{f}$	[−]	forcing
$\mathbf{F}_\mathrm{s}$	[−]	spring force
$\mathbf{r}$	[−]	position vector
σ	[−]	scaling parameter

Subscripts and Superscripts

i, j	indices
$\bar{}$	temporal average

1. INTRODUCTION

The mechanistic turbulence (MT) model depicted in Fig. 1 was first introduced as an attempt to explain Richardson's eddy hypothesis [1] with a mechanical system. It consists of a binary tree of masses connected by springs, with damping between the blocks that constitute the two bottom levels. For gradually decreasing block masses connected by with linear springs it is able to exhibit an energy distribution across its scales, that is similar to the turbulent energy spectrum [2] derived by Kolmogorov [3] for 3D homogeneous isotropic turbulence. This turbulent energy cascade is enabled by irreversible transfer of energy from the largest scales of the turbulent flow towards the smallest, dissipative scales.

By introducing cubic nonlinearity to the springs connecting the last two levels of the binary tree (as seen in Fig. 1), the model was found to be capable of efficient targeted energy transfer (TET) towards the nonlinear, dissipative elements for both impulsive and harmonic excitation of the top blocks which have the largest masses [4]. This irreversible transfer of energy results in efficient dissipation [5], and has been used for both vibration absorption [6, 7] and energy harvesting [8]. Thus, the TET found in the nonlinear MT model produces an energy cascade from the largest mass scales to the smallest mass scales, where the energy is ultimately dissipated. This process is chaotic for impulsive excitation of the largest block masses. The model also has chaotic bands [4], which are frequency regions where harmonic excitation induces chaos in the system according to Chen et al. [9].

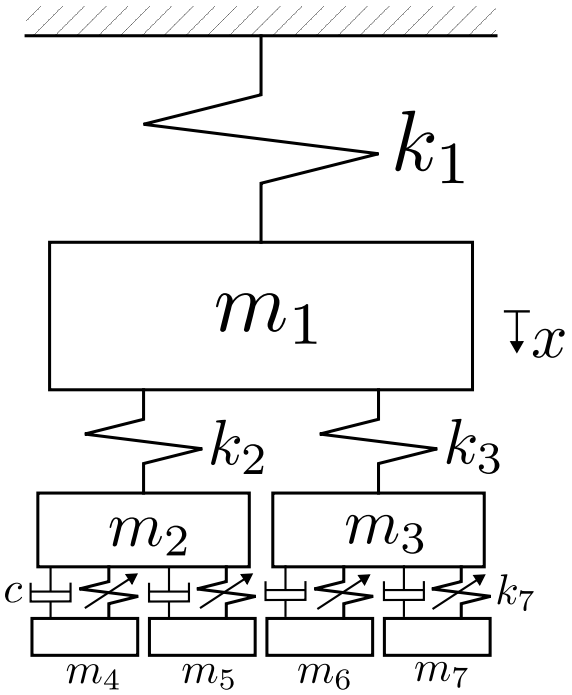

Figure 1. Mechanistic turbulence model with $n = 3$ levels, and springs with cubic nonlinearity between the last two levels

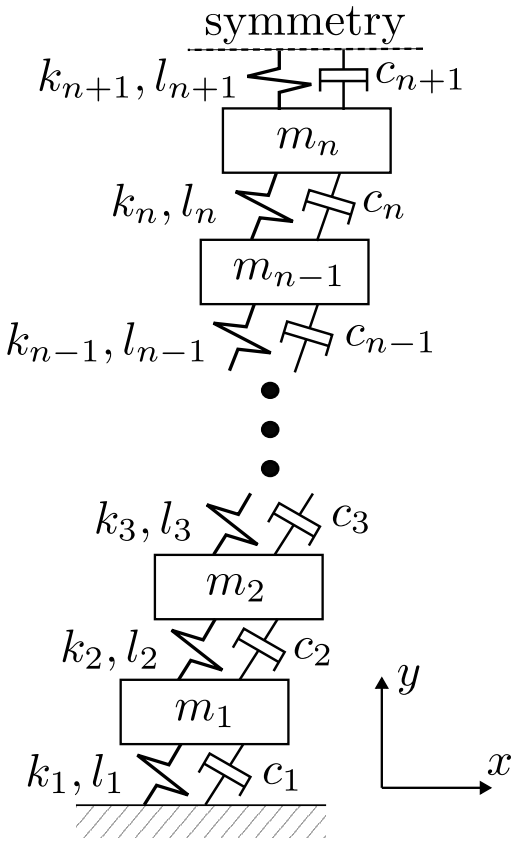

Figure 2. General form of the planar oscillator with a wall and a symmetry boundary condition

Despite its success in nonlinear dynamics, the MT model so far had only limited applications in modelling fluid mechanics. The aim of this paper is to introduce a planar version of the MT model that features geometric nonlinearity as shown in Fig. 2. We show that this planar oscillator is capable of expressing certain features of simple fluid flows – namely the velocity profile of a Poiseuille flow with constant pressure gradient [10] – while being able to exhibit nonlinear phenomena found in the MT model as well.

2. MODEL DESCRIPTION

The planar oscillator shown in Fig. 2 consists of a chain oscillator with n blocks connected by springs and dampers with linear characteristics. A wall and a symmetry boundary condition is applied at the bottom and the top blocks, respectively. The m_i masses, c_i dampings, k_i stiffnesses, and l_i spring lengths follow the relations

$$\begin{aligned} m_i &= \sigma^{n-i}, & i &= 1,\dots,n \\ c_i &= 0.01, & i &= 1,\dots,n+1 \\ k_i &= 1, & i &= 1,\dots,n+1 \\ l_i &= \sigma^{n+1-i} & i &= 1,\dots,n+1, \end{aligned} \tag{1}$$

where $\sigma > 0$ is a scaling parameter. Note that the quantities introduced throughout this paper are taken to be dimensionless, as it focuses on the qualitative behaviour of the system. The power laws and the light damping in Eq. (1) are introduced to obtain a parametrisation in line with the MT model that is described in [2, 4].

The elements of the chain oscillator are the block masses. These are treated as point masses, i.e. they have no rotational degrees of freedom. The equation of motion determining the $\mathbf{r}_i = (x_i, y_i)$ position of element $i = 1,\dots,n$ is

$$m_i\ddot{\mathbf{r}}_i = \mathbf{F}_{\mathrm{d},i,i+1} - \mathbf{F}_{\mathrm{d},i-1,i} + \mathbf{F}_{\mathrm{s},i,i+1} - \mathbf{F}_{\mathrm{s},i-1,i} + \mathbf{F}_{\mathrm{f},i}, \tag{2}$$

where $\mathbf{F}_{\mathrm{d},i,j}$ and $\mathbf{F}_{\mathrm{s},i,j}$ are the damping and spring forces acting on element i, defined as

$$\begin{aligned} \mathbf{F}_{\mathrm{d},i,j} &= \frac{\left(\mathbf{r}_j - \mathbf{r}_i\right)\cdot\left(\dot{\mathbf{r}}_j - \dot{\mathbf{r}}_i\right)}{\left\|\mathbf{r}_j - \mathbf{r}_i\right\|^2} c_i\left(\mathbf{r}_j - \mathbf{r}_i\right), \\ \mathbf{F}_{\mathrm{s},i,j} &= \left(1 - \frac{l_i}{\left\|\mathbf{r}_j - \mathbf{r}_i\right\|}\right) k_i\left(\mathbf{r}_j - \mathbf{r}_i\right), \end{aligned} \tag{3}$$

and $\mathbf{F}_{\mathrm{f},i}$ is the forcing applied to element i. This means that the damping force $\mathbf{F}_{\mathrm{d},i,j}$ and the spring force $\mathbf{F}_{\mathrm{s},i,j}$ act only along the line connecting the elements i and j.

Element $i = 1$ is connected to a wall, i.e., the boundary condition

$$\mathbf{r}_0(t) = \mathbf{0}, \tag{4}$$

is applied. At the other end of the chain oscillator a symmetry boundary condition is applied to element

n, resulting in

$$\begin{aligned} x_{n+1}(t) &= x_n(t), \\ y_{n+1}(t) &= 2\sum_{i=1}^{n} l_i + l_{n+1} - y_n(t). \end{aligned} \tag{5}$$

This means that the position of the masses m_n and m_{n+1} are reflections of each other with respect to the symmetric boundary.

The total energy of the system is defined as the sum of the potential energy of the springs and the kinetic energy of the blocks, i.e.,

$$\begin{aligned} E(t) = &\sum_{i=1}^{n+1} \frac{k_i}{2(1+\delta_{n+1,i})} \left(\|\mathbf{r}_i(t) - \mathbf{r}_{i-1}(t)\| - l_i\right)^2 \\ &+ \frac{1}{2}\sum_{i=1}^{n} m_i \|\dot{\mathbf{r}}_i(t)\|^2 , \end{aligned} \tag{6}$$

where $\delta_{n+1,i}$ is the Kronecker delta.

3. SIMULATION RESULTS

The equation of motion (2) of the planar oscillator was solved numerically with boundary conditions (4)-(5) for different values of the σ scaling parameter introduced in Eq. (1). While the qualitative behaviour of the system is not sensitive for the particular value of σ, different issues arise upon choosing a too high or low value significantly increasing the computational time. For high values (when σ is close to 1) the system requires a large number of blocks to include a wide range of mass scales. For lower values of the scaling parameter ($\sigma \leq 0.5$) simulating more than $n \approx 10$ levels is computationally challenging, because the proportion of the largest and the smallest mass and length scales becomes large enough that the simulation requires much finer time discretisation, leading to increased computational time.

3.1. Impulsive excitation

The planar oscillator is considered with $n = 30$ levels and $\sigma = 0.8$, as this combination of parameters was found to provide a sufficiently broad range of mass scales in Eq. (1) without adversely affecting the computation accuracy and time.

The initial conditions providing the impulsive excitation for the simulations are given by

$$\begin{aligned} \mathbf{r}_i(0) &= \begin{bmatrix} 0 \\ 1 \end{bmatrix} \sum_{j=1}^{i} l_j, \quad i = 0, \ldots, n, \\ \dot{\mathbf{r}}_i(0) &= 0, \quad i = 0, \ldots, n-1, \\ \dot{\mathbf{r}}_n(0) &= \begin{bmatrix} 0 \\ 1 \end{bmatrix} \text{ or } \begin{bmatrix} 1 \\ 0 \end{bmatrix}, \end{aligned} \tag{7}$$

meaning that every element starts in equilibrium and only element n has nonzero initial velocity. As this section considers impulsive excitations, no forcing was applied to the system, i.e.

$$\mathbf{F}_{\mathrm{f},i} = \mathbf{0}, \quad i = 1, \ldots, n. \tag{8}$$

As indicated in Eq. (7), two cases are considered with the same initial velocity magnitude for element n. In the first one, the initial velocity $\dot{\mathbf{r}}_n(0)$ has a zero x component, i.e.,

$$\dot{\mathbf{r}}_n(0) = \begin{bmatrix} 0 \\ 1 \end{bmatrix}. \tag{9}$$

This results in linear behaviour, as the only source of nonlinearity in the planar oscillator is the geometric nonlinearity facilitated by movement in the x direction. The second case has a nonzero x component and a zero y component, i.e.,

$$\dot{\mathbf{r}}_n(0) = \begin{bmatrix} 1 \\ 0 \end{bmatrix}, \tag{10}$$

introducing nonlinear effects.

Interestingly, the linear case given by the initial condition in Eq. (9) provides a stronger dissipation of the total energy $E(t)$ compared to the nonlinear case given by Eq. (10), as seen in Fig. 3. This means that the geometric nonlinearity did not facilitate the efficient energy dissipation seen in some nonlinear dynamical systems [5, 6, 7, 8].

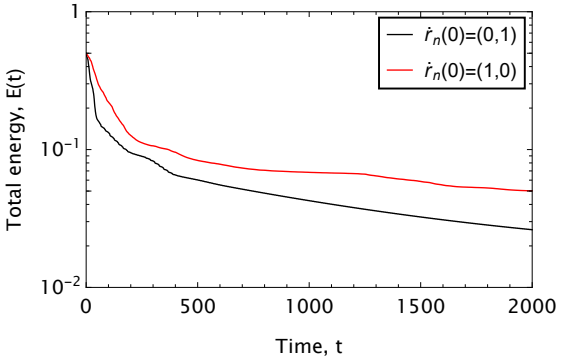

Figure 3. Total energy over time with impulsive excitation given by the initial conditions in Eqs. (7)**-**(10)

3.2. Poiseuille flow

As a next step, the equation of motion of the planar oscillator was solved with a forcing similar to those driving Poiseuille flows [10]. The investigations are carried out for three different values of the scaling parameter σ, which are shown in Tab. 1. along with the number of blocks in the oscillator and the chosen forcing parameters f_0.

Table 1. Number of blocks in the oscillator for the different values of the scaling parameter σ

σ	n
0.5	10
0.8	30
0.9	30

Poiseuille flows arise as a result of a constant pressure gradient [10]. Assuming constant density of the fluid, this results in a force acting on any fi-

nite fluid element proportional to the fluid element's mass. Analogously to Poiseuille flows, the static force applied to element i is defined here as

$$\mathbf{F}_{\mathrm{f},i}(t) = \begin{bmatrix} f_0 m_i \\ 0 \end{bmatrix}, \quad i = 0, \ldots, n, \tag{11}$$

where f_0 is the parameter determining the strength of forcing. In this section, possible values of 0.01, 0.1, and 1 are examined.

This time the initial conditions for the equation of motion (2) were set as

$$\begin{aligned} \mathbf{r}_i(0) &= \begin{bmatrix} 0 \\ 1 \end{bmatrix} \sum_{j=1}^{i} l_j, \quad i = 0, \ldots, n, \\ \dot{\mathbf{r}}_i(0) &= 0, \quad i = 0, \ldots, n, \end{aligned} \tag{12}$$

which means that every spring is initially relaxed and every element starts at rest.

The displacement solutions $x(t)$, $y(t)$ were calculated, then the total energy of the system was also obtained using Eq. (6). The resulting time histories of the total energy $E(t)$ are shown in Fig. 4. for some values of f_0 and σ. In every examined case, Fast Fourier Transform shows that the total energy has harmonic behaviour, with the exception of the case $\sigma = 0.5$ and $f_0 = 0.01$, which has the smallest energy content. In that case, additional modes are present in the $\mathbf{r}_n(t)$ solution compared to every other investigated case.

The oscillations of the total energy $E(t)$ are caused by the fact that the potential energy corresponding to the $\mathbf{F}_{\mathrm{f},i}$ static forces is not taken into account when calculating $E(t)$ according to Eq. (6).

The horizontal displacements exhibit the same qualitative behaviour as $E(t)$. For instance, the horizontal displacement $x_n(t)$ of the block at the symmetry boundary is shown in Fig. 5.

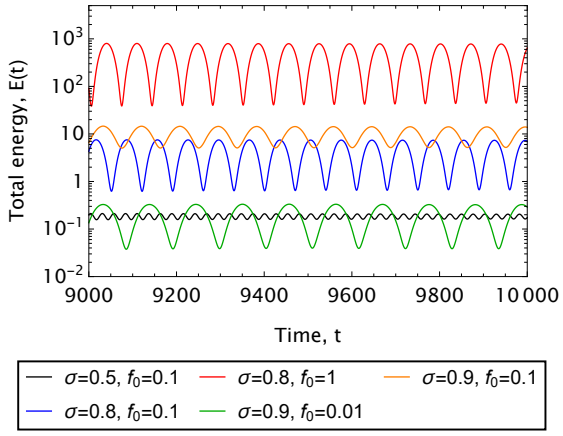

Figure 4. The total energy $E(t)$ of the system as a function of time for some values of σ, n, and f_0 according to Tab. 1, forcing according to Eq. (11), and ICs given in Eq. (12)

The vertical displacement $y_n(t)$ of the block at the symmetry boundary is shown in Fig. 6. for some

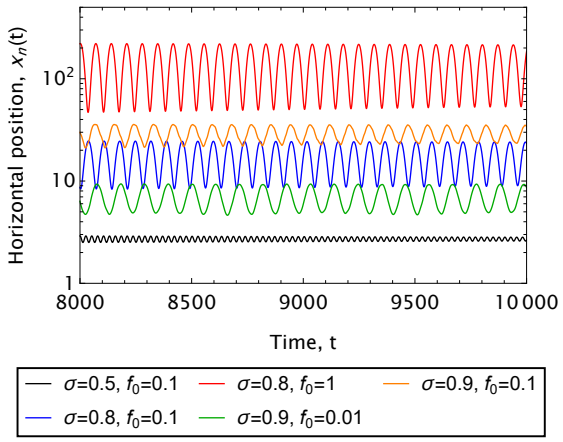

Figure 5. The horizontal displacement $x_n(t)$ of the block at the symmetry boundary as a function of time for some values of σ, n, and f_0 according to Tab. 1, forcing according to Eq. (11), and ICs given in Eq. (12)

of the examined values of σ and f_0. We observed that the frequencies of the components in $y_n(t)$ change as f_0 varies for each value of σ. Nonetheless, for $\sigma = 0.5$ and $\sigma = 0.9$ the emergent behaviour remains the same. In contrast, $y_n(t)$ for $\sigma = 0.8$ shows drastically different behaviour for different f_0 values. Thus we conclude that unlike the horizontal position $x_n(t)$, the qualitative behaviour of the vertical displacements of the blocks are strongly dependent on the parametrisation of the system and the magnitude of the forcing.

For Poiseuille flows in a circular pipe or between two plates with constant cross section and pressure gradient, the velocity profile is a second degree polynomial of the distance from the pipe axis [10]. As the Hagen-Poiseuille equation is a second order differential equation for the flow velocity, similarly to the equation of motion (2) for the displacement of the blocks, it is reasonable to test a second degree polynomial $p(y)$ fit to the $(\bar{x}_i, \bar{y}_i)$ mean displacement of the blocks.

An example of this is shown in Fig. 7 with $f_0 = 0.1$ for each value of the scaling parameter σ given in Tab. 1. Similarly good quality fits were found for the remaining combinations of σ and f_0. This result is non-trivial, as the second degree polynomials of the mean displacements arise despite the fact that the forcing given in Eq. (11) is an exponential function of the block index.

Tabs. 2-4 show the best fit found for the examined cases by minimising the root-mean-square of the $x_i - p(y_i)$ differences. The table suggests a trend towards decreasing R^2 values as the f_0 forcing parameter is increased, regardless of the value of σ. This observation, along with the relatively large drop in R^2 for $f_0 = 1$ suggests that for sufficiently large values of the forcing parameter, the system undergoes a transition whereby the $\bar{x}_i$ mean horizontal displace-

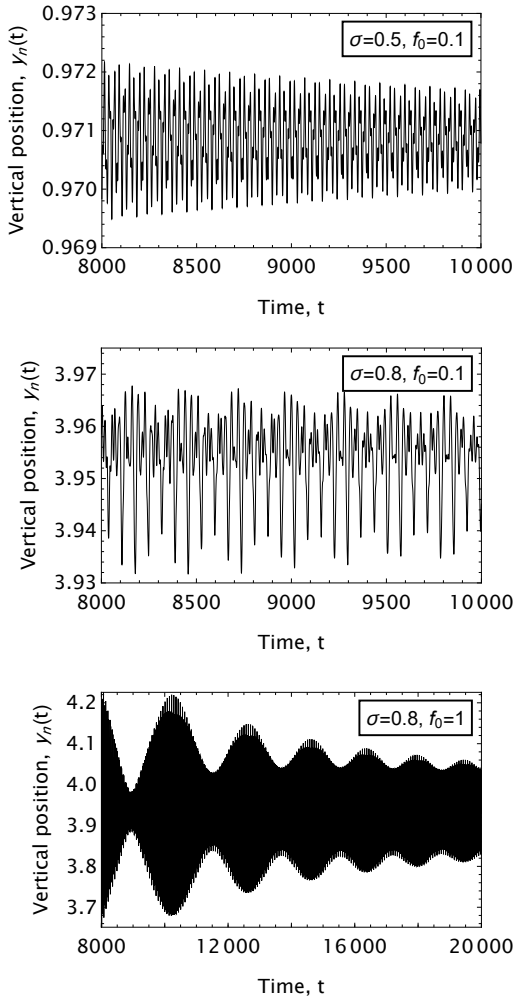

Figure 6. The vertical displacement $y_n(t)$ of the block at the symmetry boundary as a function of time for some values of σ, n, and f_0 according to Tab. 1, forcing according to Eq. (11), and ICs given in Eq. (12)

ments lose their quadratic characteristic.

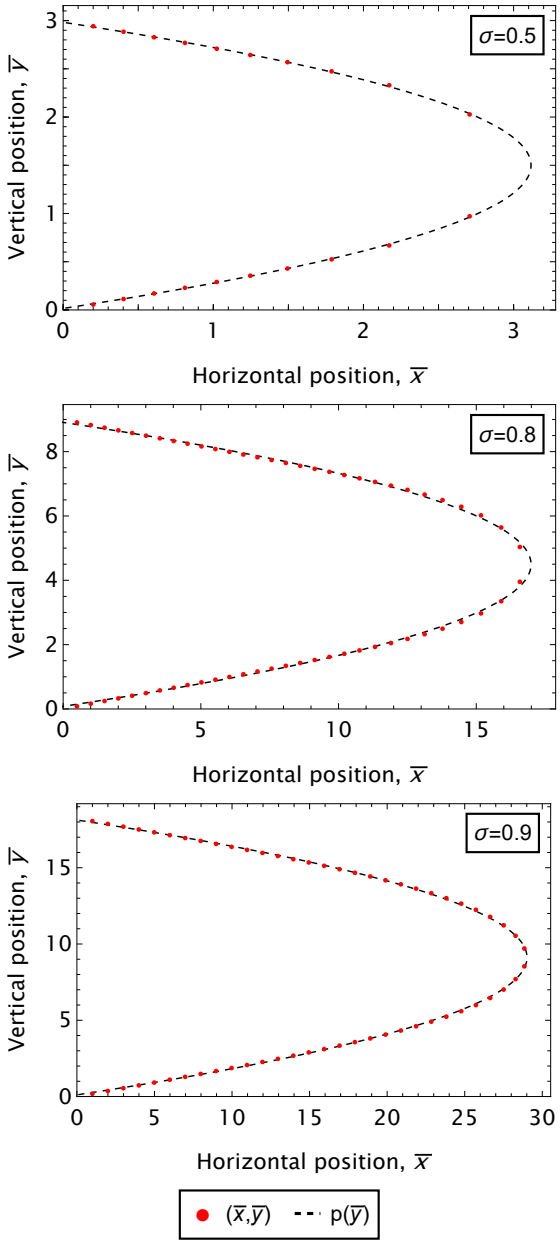

Figure 7. The $(\bar{x}_i, \bar{y}_i)$ mean displacement of the elements and the fitted second order polynomial for $f_0 = 0.1$, with σ and n according to Tab. 1, forcing according to Eq. (11), and ICs given in Eq. (12)

Table 2. Second degree polynomials fitted to the $(\bar{y}_i, \bar{x}_i)$ dataset for different values of the f_0 forcing parameter, with $\sigma = 0.5$

f_0	Fitted polynomial	R^2 value
0.01	$-0.380y^2 + 1.14y - 0.00102$	0.9999
0.1	$-1.42y^2 + 4.25y - 0.0669$	0.9993
1	$-10.3y^2 + 30.7y - 1.23$	0.9965

Table 3. Second degree polynomials fitted to the $(\bar{y}_i, \bar{x}_i)$ dataset for different values of the f_0 forcing parameter, with $\sigma = 0.8$

f_0	Fitted polynomial	R^2 value
0.01	$-0.188y^2 + 1.69y + 0.000403$	0.9997
0.1	$-0.872y^2 + 7.84y - 0.634$	0.9979
1	$-7.03y^2 + 63.2y - 12.2$	0.9864

Table 4. Second degree polynomials fitted to the $(\bar{y}_i, \bar{x}_i)$ dataset for different values of the f_0 forcing parameter, with $\sigma = 0.9$

f_0	Fitted polynomial	R^2 value
0.01	$-0.0835y^2 + 1.52y + 0.0608$	0.9995
0.1	$-0.357y^2 + 6.52y - 0.705$	0.9994
1	$-2.81y^2 + 51.3y - 12.9$	0.9961

4. SUMMARY

A planar oscillator chain was introduced with geometric nonlinearity. The behaviour of this oscillator was tested for initial conditions resulting in linear and nonlinear behaviour (see Eqs. (9) and (10), respectively) for impulsive excitations. It was found that the vertical initial velocity resulting in linear behaviour is somewhat more efficient at dissipating the initial energy of the system.

A constant forcing was introduced, analogously to the Poiseuille flow with a constant pressure gradient. The forced system was examined for three different values of the scaling parameter σ, each with three different f_0 forcing parameters. The total energy and the horizontal displacement of the block at the symmetry boundary showed harmonic behaviour over time in all cases, except for $\sigma = 0.5$ and $f_0 = 0.01$.

The vertical displacement of the blocks exhibited massive qualitative changes for the investigated combinations of σ and f_0 indicating high sensitivity of the system to these parameters. Yet, the oscillator is capable of reproducing the quadratic profile seen in Poiseuille flows regardless of the value of σ and f_0.

In future works, we plan to compare the results of constant forcing to Poiseuille flows quantitatively as well, and extend the analysis by comparing the behaviour of the planar oscillator chain during harmonic forcing with flows induced by an oscillating pressure gradient.

ACKNOWLEDGEMENTS

The project supported by the Doctoral Excellence Fellowship Programme (DCEP) is funded by the National Research Development and Innovation Fund of the Ministry of Culture and Innovation and the Budapest University of Technology and Economics.

The research reported in this paper is part of project no. TKP-6-6/PALY-2021. Project no. TKP-6-6/PALY-2021 has been implemented with the support provided by the Ministry of Culture and Innovation of Hungary from the National Research, Development and Innovation Fund, financed under the TKP2021-NVA funding scheme.

This work has been supported by the Hungarian National Research, Development and Innovation Fund under contract NKFI K 137726.

One of the authors, Bendegúz D. Bak has also been supported by the János Bolyai Research Scholarship of the Hungarian Academy of Sciences.

REFERENCES

[1] Richardson, L. F., 1922, *Weather Prediction by Numerical Process*, Cambridge University Press.

[2] Kalmár-Nagy, T., and Bak, B. D., 2019, "An intriguing analogy of Kolmogorov's scaling law in a hierarchical mass–spring–damper model", *Nonlinear Dynamics*, Vol. 95 (4), pp. 3193–3203.

[3] Kolmogorov, A. N., 1941, "The local structure of turbulence in incompressible viscous fluid for very large Reynolds numbers", *Dokl. Akad. Nauk SSSR*, JSTOR, Vol. 30, pp. 301–305.

[4] Bak, B. D., Rochlitz, R., and Kalmár-Nagy, T., 2023, "Energy transfer mechanisms in binary tree-structured oscillator with nonlinear energy sinks", *Nonlinear Dynamics*, Vol. 111 (11), pp. 9875–9888.

[5] Vakakis, A. F., Gendelman, O. V., Bergman, L. A., McFarland, D. M., Kerschen, G., and Lee, Y. S., 2008, *Nonlinear Targeted Energy Transfer in Mechanical and Structural Systems*, Vol. 156, Springer Science & Business Media.

[6] Starosvetsky, Y., and Gendelman, O. V., 2009, "Vibration absorption in systems with a nonlinear energy sink: Nonlinear damping", *Journal of Sound and Vibration*, Vol. 324, pp. 916–939.

[7] Yang, K., Zhang, Y.-W., Ding, H., Yang, T.-Z., Li, Y., and Chen, L.-Q., 2017, "Nonlinear Energy Sink for Whole-Spacecraft Vibration Reduction", *Journal of Vibration and Acoustics*, Vol. 139 (2).

[8] Kremer, D., and Liu, K., 2014, "A nonlinear energy sink with an energy harvester: Transient responses", *Journal of Sound and Vibration*, Vol. 333 (20), pp. 4859–4880.

[9] Chen, J. E., Theurich, T., Krack, M., Sapsis, T., Bergman, L. A., and Vakakis, A. F., 2022, "Intense cross-scale energy cascades resembling "mechanical turbulence" in harmonically driven strongly nonlinear hierarchical chains of oscillators", *Acta Mechanica*, Vol. 233 (4), pp. 1289–1305.

[10] Drazin, P. G., and Riley, N., 2006, *The Navier-Stokes Equations: A Classification of Flows and Exact Solutions*, London Mathematical Society Lecture Note Series, Cambridge University Press.

Conference on Modelling Fluid Flow (CMFF'25)
The 19th International Conference on Fluid Flow Technologies
Budapest, Hungary, August 26-August 29, 2025

Investigation of Radius Ratio Effects on Velocity Statistics in Annular Pipe Flow using One-Dimensional Turbulence

Pei-Yun Tsai[1,2,3], Li Toong Yap[2,3], Marten Klein[2,3], Heiko Schmidt[2,3]

[1] Corresponding Author. Tel.: +49 (0) 355 69 5127, Fax: +49 (0) 355 69 4891, E-mail: tsaipeiy@b-tu.de
[2] Chair of Numerical Fluid and Gas Dynamics, Faculty of Mechanical Engineering, Electrical and Energy Systems, Brandenburg University of Technology Cottbus-Senftenberg. Siemens-Halske-Ring 15A, 03046 Cottbus, Germany
[3] Scientific Computing Lab, Energy Innovation Center, Brandenburg University of Technology Cottbus-Senftenberg. Universitätsstraße 22, 03046 Cottbus, Germany

ABSTRACT

Concentric coaxial (annular) pipe flows are numerically investigated using a stochastic one-dimensional turbulence (ODT) model. ODT offers full-scale resolution of the radial boundary layers and their dynamical variability. Based on the latter, it is demonstrated for various Reynolds numbers that spanwise wall-curvature affects low-order and detailed velocity statistics. Wall curvature leads to radial asymmetry in the flow statistics, limiting the applicability of conventional wall-function models that assume a universal von Kármán constant and a locally flat surface. Resolving the near-wall turbulence is essential for predictive capabilities, but a computational burden that is addressed by the dimensionally reduced modeling within ODT. The model is able to reproduce and predict consistent low-order and detailed turbulence statistics. By utilizing boundary-layer theory, it is shown how the model can be used to obtain curvature-aware velocity wall function, which is of broader relevance for modeling engineering applications such as coaxial heat exchangers.

Keywords: annular pipe flow, spanwise wall curvature, stochastic modeling, turbulence statistics, turbulent boundary layer

NOMENCLATURE

$\mathcal{E}$	$[-]$	Eddy event
D^+	$[-]$	Parametrization coefficient
P	$[Pa]$	Pressure
R_i, R_o	$[m]$	Radius of inner and outer cylinders, respectively
Re_b	$[-]$	Bulk Reynolds number: $4\overline{u}_b\delta/\nu$
$Re_{\tau i}$, $Re_{\tau o}$	$[-]$	Friction Reynolds number at inner and outer walls: $u_{\tau,i}\delta/\nu$, $u_{\tau,o}\delta/\nu$
β^+	$[-]$	Parametrization coefficient
δ	$[m]$	Half width of the gap between inner and outer pipe walls: $(R_o - R_i)/2$
$\delta(\cdot)$	$[-]$	Dirac distribution function
δ_ν	$[-]$	Viscous length scale: ν/u_τ
η	$[-]$	Radius ratio: R_i/R_o
ν	$[m^2/s]$	Kinematic viscosity
ρ	$[kg/m^3]$	Mass density of fluid
r_m	$[m]$	Radial location of maximum mean axial velocity occurs
t	$[s]$	Time
t_e	$[s]$	Sampled times of eddy event
$\overline{u}_b$	$[m/s]$	Bulk mean velocity
τ_{wi}, τ_{wo}	$[N/s^2]$	Mean wall shear stress on the inner and outer walls, respectively
$u_{\tau i}$, $u_{\tau o}$	$[m/s]$	Wall friction velocity at inner and outer walls : $\sqrt{\tau_{wi}/\rho}$, $\sqrt{\tau_{wo}/\rho}$

Subscripts and Superscripts

DNS	Direct numerical simulation
ODT	One-dimensional turbulence
PDF	Probability density function
RSS	Reynolds shear stress
u, v, w	Velocity component in the x, r, θ direction, respectively
x, r, θ	Coordinates of the axial, radial, and azimuthal directions, respectively
$\overline{(\cdot)}$	Temporal mean
$(\cdot)^+$	Wall coordinate
$(\cdot)'$	Fluctuating component
$(\cdot)_i$, $(\cdot)_o$	Values at the inner and outer walls, respectively
$(\cdot)_{max}$	Maximum value
$(\cdot)_{rms}$	Root-mean-square value

1. INTRODUCTION

Annular pipe flow is found in various engineering applications, such as coaxial geothermal heat ex-

changers, photochemical reactors, and gas-cleaning devices. The investigation of turbulent annular pipe flow is a canonical problem that provides detailed insights into radial transport processes and boundary layers over both convex and concave walls. Unlike turbulent channel flow, the presence of curved surfaces leads to a closure problem, as the inner and outer pipe wall contributions to skin friction drag and pressure loss are undetermined and differ from each other, resulting in a simulation result [1]. This circumstance needs to be addressed with predictive modeling capabilities.

In recent decades, numerous numerical and experimental studies have been carried out to better understand the characteristics of pressure-driven (Poiseuille) turbulent flow in concentric annular pipes. In the last century, a major debate centered on whether the location of maximum radial velocity coincides with the point of zero shear stress. Several experimental studies were conducted on this topic [2, 3]. Chung et al. [4] performed the first comprehensive DNS study of turbulent annular pipe flow at a fixed bulk Reynolds number $Re_b = 8900$, analyzing the effect of spanwise curvature in turbulent properties for two radius ratios, $\eta = R_i/R_o = 0.1$ and 0.5, where R_i (R_o) denotes the radius of the inner (outer) pipe as sketched in Fig. 1 below. Here, the bulk Reynolds number is defined as $Re_b = 4\overline{u}_b\delta/\nu$, with $\overline{u}_b$ representing the bulk mean velocity, $\delta = (R_o - R_i)/2$, and ν being the kinematic viscosity of the fluid. Boersma and Breugem [1] studied turbulent flow in an annular pipe using DNS at a small radius ratio ($\eta \leq 0.1$) over a moderate range of Reynolds numbers. More recently, Bagheri and Wang [5] conducted a DNS study to examine the effects of radius ratio on turbulent statistics and structures in both physical and spectral spaces across multiple radius ratio cases ($eta = 0.1, 0.3, 0.5,$ and 0.7). As an extension, turbulent heat transfer in the annular pipe flow, coupled with passive scalar, has also been discussed [6, 7].

Despite the efforts described above, a theoretical justification of empirical pressure loss properties has remained elusive, as the boundary layer near the curved inner wall is virtually inaccessible to measurement. Furthermore, high-fidelity numerical simulations have high-resolution requirements [1] such that high Reynolds numbers have not been assessed until recently for wide annular gaps [8, 9]. Klein et al. [9] conducted annular pipe flow simulations using the conventional LES-WALE model and found that this approach may not be ideal for accurately capturing small-scale flow physics near curved walls. The objective of this study is to pave the way toward the development of improved wall functions applicable to spanwise curved walls for utilization in classical large-eddy and Reynolds-averaged simulations. This is achieved by adopting an alternative approach that utilizes Kerstein's one-dimensional turbulence (ODT) model [10, 11], which evolves instantaneous boundary layer profiles. The model extension to cylindrical geometry [12], calibrated for annular pipe flow [13], is utilized here as a stand-alone tool. The model formulation and mesh-adaptive implementation provide full-scale resolution of the instantaneous radial profiles of the velocity vector across the annular gap. Dimensional model reduction offers major cost reduction, making high Reynolds number cases feasible.

The rest of this paper is organized as follows. Section 2 gives some details of the annular pipe flow setup investigated. Section 3 provides an overview of the ODT model formulation and the governing equations. Section 4 discusses the main results in terms of velocity statistics, focusing on examining the impact of spanwise curvature on some turbulence properties. Last, section 6 summarizes the key findings of this work.

2. ANNULAR PIPE FLOW

An incompressible, constant-property Poiseuille flow confined between two concentric coaxial cylinders is considered, as sketched in Fig. 1. No-slip boundary conditions are prescribed at the pipe walls, and an axial mean pressure gradient force is applied to drive the flow. The numerical domain of the stochastic ODT simulations (ODT domain) represents a single radial coordinate spanning the entire gap between the cylinders.

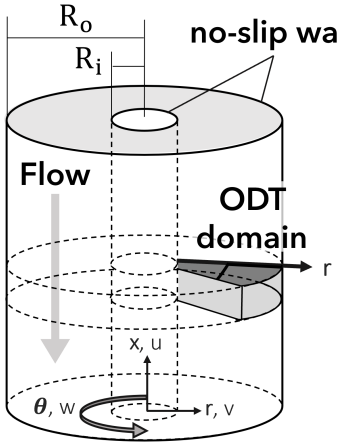

Figure 1. Schematic of the annular pipe flow configuration investigated. The wedge-shaped, radially oriented ODT domain is exaggerated. No-slip boundary conditions are prescribed at the walls as indicated.

3. NUMERICAL MODEL

3.1. ODT Model Formulation

In the ODT model, the conservation equations are dimensionally reduced and solved numerically by representing turbulent advection as a stochastic process. The flow in axial and azimuthal directions is assumed to be statistically homogeneous. This process employs instantaneous spatial mapping events that

intermittently modify the deterministic flow evolution. Following [12] and applying the notation from [14], the dimensionally reduced ODT equations for temporally evolving flow are given by

$$\frac{\partial u_i}{\partial t} + \sum_{t_e} \mathcal{E}_i \, \delta\left(t - t_e\right) = \frac{1}{r}\frac{\partial}{\partial r}\left(r\nu\frac{\partial u_i}{\partial r}\right) - \frac{1}{\rho}\frac{\mathrm{d}P}{\mathrm{d}x}\,\delta_{ix} \; . \tag{1}$$

Here, u_i, $i = x, r, \theta$, represents the model-resolved instantaneous velocity vector with cylindrical components $u_x = u$, $u_r = v$, $u_\theta = w$, corresponding to the axial, radial, and azimuthal directions, respectively. t indicates the time, t_e the stochastically sampled times of eddy event $\mathcal{E}_i$ ($i = x, r, \theta$) occurrences, $\delta(t)$ the Dirac distribution function. $\mathrm{d}P/\mathrm{d}x$ denotes the prescribed mean pressure-gradient force in the axial direction, δ_{ij} the Kronecker delta, ν the kinematic viscosity, and ρ the mass density of the fluid.

ODT utilizes map-based advection modeling [10] to represent instantaneous modifications to the flow profile associated with the turnover of a notional eddy. In this study, the generalized baker's map denoted "triplet map B" (TMB) [12] is specifically used, as it ensures scale-locality, equidistant fluid parcel displacement, and adheres to physical conservation principles for radial transport. Further details on the formulation of the eddy events $\mathcal{E}_i$ and the cylindrical mapping techniques can be found in [12, 14]. The calibration of ODT model parameters for turbulent annular pipe flow is thoroughly discussed in [13, 8] and is not repeated here.

3.2. Grid Sensitivity Analysis

The radially oriented ODT domain is discretized using an adaptive grid, capable of resolving all relevant scales of the flow locally. The grid must be fine enough to resolve the viscous sublayer and the smallest emerging features at and off the wall in the evolving transient solution. To ensure that the results are independent of the grid resolution and that numerically, mesh-adaptive transport is negligible, a grid sensitivity study was conducted.

Table 1 presents the ODT test cases with varying grid resolutions. Case A represents the resolution used throughout this study. Case B uses a finer grid, with half the grid size of Case A; Case C employs a medium resolution with double the grid size of Case A; and Case D corresponds to a coarser resolution, with four times the grid size of Case A. The parameters Δr_min and Δr_max denote the minimum and maximum grid cell sizes in the ODT model, respectively, keeping the adaptivity range constant at $\Delta r_\mathrm{max}/\Delta r_\mathrm{min} = 20$. The difference in friction Reynolds number between Case A and the finer Case B is found to be less than 0.1%. Compared to the reference DNS data from [4], where $Re_{\tau i} = 179$ and $Re_{\tau o} = 141$, Case A achieves excellent agreement, with deviations of less than 0.1% at both the inner and outer walls. This confirms that Case A provides a sufficiently effective resolution to ensure accurate predictions of near-wall small-scale physics. Additionally, since ODT does not involve multi-dimensional mesh geometry, traditional grid quality metrics, such as skewness and aspect ratio, are not applicable in this modeling framework.

Table 1. Friction Reynolds numbers at the inner and outer walls for different grid resolutions. Case A corresponds to the resolution used for all simulations in this study, while the other three cases (B, C, and D) are included for grid resolution testing and comparison.

Cases	Δr_{min}	Δr_{max}	$Re_{\tau i}$	$Re_{\tau o}$
A	$\delta/1000$	$\delta/24$	179.12	144.46
B	$\delta/2000$	$\delta/48$	179.24	144.69
C	$\delta/500$	$\delta/12$	182.73	144.56
D	$\delta/250$	$\delta/6$	206.01	149.15

3.3. Statistical Convergence

The ODT model presents the simulation results in ensemble-averaged form over long simulation times. To ensure statistical stationarity, the data collection began after a warm-up phase that was estimated by short presimulations.

To assess statistical convergence, mean axial velocity profiles from two test cases with different numbers of generated eddy events (N_eddy) are shown in Fig. 2. On average, the model generates approximately three eddy events per second of wall-clock time. The case with 4400 eddy events is shown to be sufficiently qualified to reproduce the mean profile of the reference DNS. In practice, all simulations used in this study were run for a sufficient duration to generate an adequate number of eddy events such that second-order statistical moments converged in a similar manner. These results confirm the robustness of the reported statistics with respect to both random initialization and simulation duration, indicating that the simulations have achieved statistical convergence.

4. RESULTS AND DISCUSSION

4.1. Mean Velocity Profile

Fig. 3 compares the mean axial velocity profiles with the DNS data [4]. Mean velocity is normalized by bulk mean velocity $\overline{u}_b$. An excellent agreement is observed between the ODT results and DNS data for radius ratio $\eta = 0.1$ and 0.5 with fixed bulk Reynolds number $Re_b = 8900$, that the boundary layer radial asymmetry is correctly represented. The asymmetry results in the development of a thicker boundary layer over the outer cylinder surface compared to the inner cylinder surface. This is more pronounced in the radius ratio $\eta = 0.1$ case than $\eta = 0.5$ case.

The influence of wall curvature is noticeably stronger near the inner pipe wall than at the outer pipe wall. This effect becomes even more significant

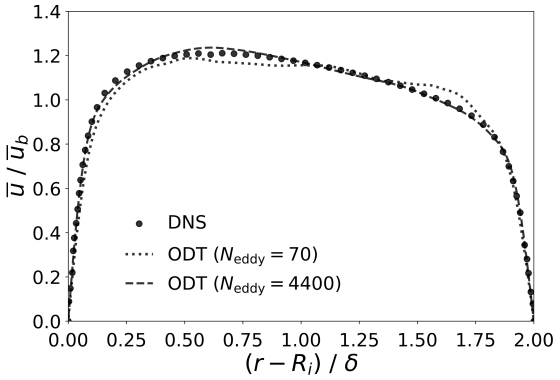

Figure 2. Comparison of two ODT axial mean velocity profiles, normalized by $\overline{u}_b$, at $\eta = 0.1$ and $Re_b = 8900$, after accumulation of $N_{\text{eddy}} = 700$ and 4400 implemented stochastic eddy events, respectively. Reference DNS data is from [4].

in smaller radius ratios, where the velocity gradient at the inner pipe wall is steeper. The dotted vertical lines in Fig. 3 represent the calculated location of the maximum mean axial velocity $\overline{u}_{max}$ determined using the Kays–Leung relation, which has been experimentally validated [3]. The location r_m, where the maximum mean axial velocity occurred, depends on the radius ratio of the inner and outer pipes and is parameterized as

$$\frac{r_m - R_i}{R_o - r_m} = \left(\frac{R_i}{R_o}\right)^{0.343} \quad . \tag{2}$$

A quantitative comparison of r_m as predicted by ODT to the Kays–Leung relation yields an error of less than 0.5. This is remarkable, considering the simplicity of the ODT model, and demonstrates that the map-based stochastic modeling approach effectively captures large-scale mixing-length effects.

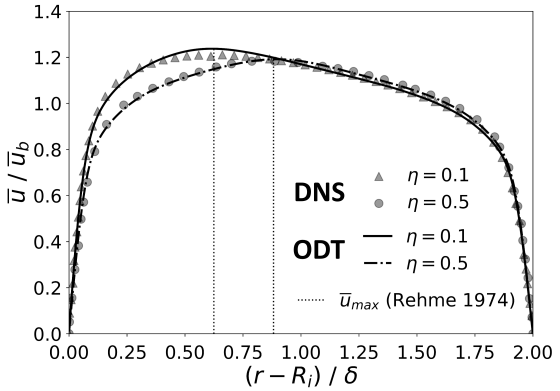

Figure 3. Radial profiles of the mean velocity $\overline{u}$ normalized with the bulk velocity $\overline{u}_b$ for radius ratio $\eta = 0.1$ and 0.5, respectively. The bulk Reynolds number is $Re_b = 8900$. Reference DNS data is from [4].

4.2. Velocity Boundary Layer

Fig. 4 extends the comparison from mean velocity profiles to the logarithmic velocity profiles. For the normalization purpose, the local friction velocities at the inner and outer walls are defined as

$$u_{\tau i} = \sqrt{\nu \left|\frac{\mathrm{d}u}{\mathrm{d}r}\right|_{wall,i}} \quad , \quad u_{\tau o} = \sqrt{\nu \left|\frac{\mathrm{d}u}{\mathrm{d}r}\right|_{wall,o}} \quad , \tag{3}$$

where $u_{\tau i}$ and $u_{\tau o}$ denote the friction velocity on the inner and outer pipe walls, respectively. The normalized mean velocity is defined as $u^+ = u/u_{\tau,o/i}$ and the corresponding radius as $r^+ = |r - R_{o/i}|\, u_{\tau,o/i}/\nu$. The friction Reynolds numbers are defined as $Re_{\tau i} = u_{\tau i}\delta/\nu$ and $Re_{\tau o} = u_{\tau o}\delta/\nu$ at the inner and outer walls, respectively.

Fig. 4(*top*) shows the velocity boundary layer profiles at the inner and outer pipe walls for radius ratio $\eta = 0.5$. It is found that wall curvature does not significantly impact the inner and outer velocity boundary layer profiles in the radius ratio $\eta = 0.5$ case. Both normalized profiles align with the master profile, corresponding to the classical law-of-the-wall for pipe flow [15]. The linear viscous sublayer and logarithmic-law region are captured for radius ratio $\eta = 0.5$. However, this is not the case for radius ratio $\eta = 0.1$.

Fig. 4(*bottom*) exhibits the velocity boundary layer profiles at both sides of the pipe walls for radius ratio $\eta = 0.1$ compared with DNS data [4]. It is seen that the deviation between the inner and outer boundary layers is significant, and the law-of-the-wall profile cannot capture the behavior of the inner profile. This deviation is attributed to the effect of wall curvature, which results from the decrease in the inner cylinder radius. To quantify the effect, velocity boundary layer analysis is applied to the model results, using a similar approach as previously employed in [1]. Consequently, the boundary layer over the inner pipe wall is divided into a viscous-dominated region and a mixing-length-dominated region.

4.2.1. The viscous-dominated region

Assuming that the flow is fully developed, all flow statistics are invariant in the axial and azimuthal direction, so that only steady balance equations for the radial dependence of the statistical moments of the flow variables remain. Application of the Reynolds-averaging procedure to Eq. (1), rearranging, and integrating once over the radial coordinate r yields the shear stress balance equation as

$$\overline{u'v'} - \nu\frac{\partial u}{\partial r} = -\frac{r}{2}\frac{1}{\rho}\frac{\mathrm{d}P}{\mathrm{d}x} + \frac{C_1}{r} \quad , \tag{4}$$

$$C_1 = -\frac{1}{\rho}\frac{\tau_o R_i - \tau_i R_o}{R_i/R_o - R_o/R_i} \quad . \tag{5}$$

Here, C_1 is an integration constant determined by the flow solution and the wall-shear stresses. The

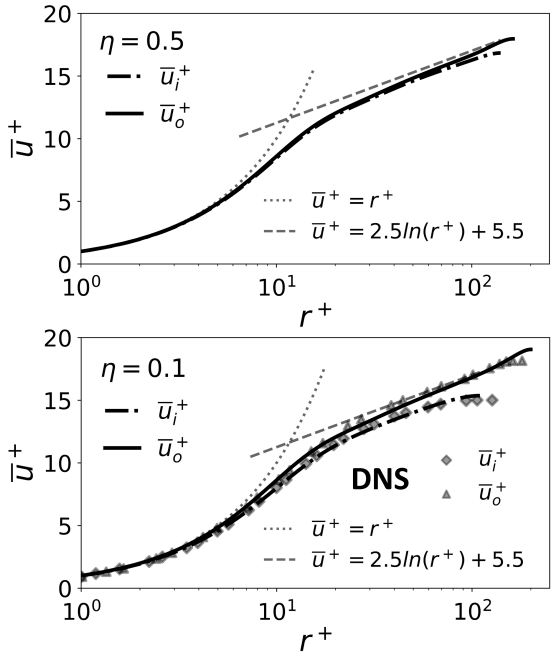

Figure 4. Velocity boundary layer at the inner $\overline{u_i}^+$ and outer $\overline{u_o}^+$ pipe wall, respectively, normalized by the local friction velocity for radius ratio $\eta = 0.1$ and 0.5 with fixed bulk Reynolds number $Re_b = 8900$.

term $\overline{u'v'}$ represents the ensemble effect of turbulent eddy events and serves as the model analog of the Reynolds stress [10, 14]. In the region very close to the wall, where $r < \delta_\nu$ (with the viscous length scale defined as $\delta_\nu = \nu/u_\tau$), it is assumed that the viscous stress dominates, meaning $\overline{u'v'} \ll \nu(\mathrm{d}u/\mathrm{d}r)$. For asymptotically small radius ratios, as $\eta \to 0$, Eq. (4) simplifies to

$$u_i^+(r^+) \approx R_i^+ \ln\left(\frac{r^+ + R_i^+}{R_i^+}\right) \quad , \tag{6}$$

where $R_i^+ = R_i\, u_{\tau,i}/\nu$ is not a constant but a parameter influenced by the wall geometry and the turbulent flow state. Specifically, it depends on the curvature radius and the wall-shear stress acting on the cylindrical inner wall. It is noted that, in this expression, the near-wall region deviates from the purely linear behavior described by the classical law of the wall and instead transitions to a logarithmic behavior.

4.2.2. The mixing-length-dominated region

In the mixing-length-dominated region, it is assumed that the total stress is primarily carried by the turbulent stress, such that $\nu(\mathrm{d}u/\mathrm{d}r) \ll \overline{u'v'}$. The influence of the radius is not negligible. For small asymptotic values of $\eta \to 0$, C_1 is simplified by assuming $R_o \gg R_i$, which retains radial information. Next, following [1], a conventional turbulent eddy viscosity ν_t parameterization is adopted. As suggested by [1], turbulent eddy viscosity can be expressed as $\nu_t = \beta\sqrt{\tau_i/\rho}\,(r - R_i)$, where β is an unknown proportionality factor that has to be estimated with data. Eq. (4) reduces to

$$u_i^+(r^+) \approx \frac{1}{\beta^+} \ln\left(\frac{r^+}{r^+ + R_i^+}\right) + D^+ \quad , \tag{7}$$

where β^+ and D^+ are parametrization coefficients that need to be determined with flow profile data.

Figure 5 presents the velocity boundary layer profiles at the inner pipe wall for three bulk Reynolds numbers ($Re_b = 8900$, 10^5, and 10^6), with the radius ratio fixed at $\eta = 0.1$. The profiles are validated using boundary layer theory. The corresponding values of the coefficients β^+ and D^+ for each case are summarized in Table 2. Based on these three test cases, empirical correlations for the coefficients β^+ and D^+ as functions of Re_b (at fixed $\eta = 0.1$) are proposed as: $\beta^+(Re_b) = 0.02\ln(Re_b) - 0.02$ and $D^+(Re_b) = 6.92Re_b^{0.1}$. These correlations serve as a preliminary model for characterizing the boundary layer behavior in annular pipe flow.

In the viscous-dominated region, Eq. (6) provides an accurate prediction of near-wall velocity profile, with a slightly extended validated length up to $r^+ \leq 10$, compared to the conventional linear wall expression. In the mixing-length-dominated region, Eq. (7) effectively captures the dominant statistical features of the turbulent boundary layer on the cylindrical inner wall across a range of Reynolds numbers. It is found that as the Reynolds number increases, a thicker boundary layer is found, and the curvature effect remains noticeable up to $Re_b = 10^6$.

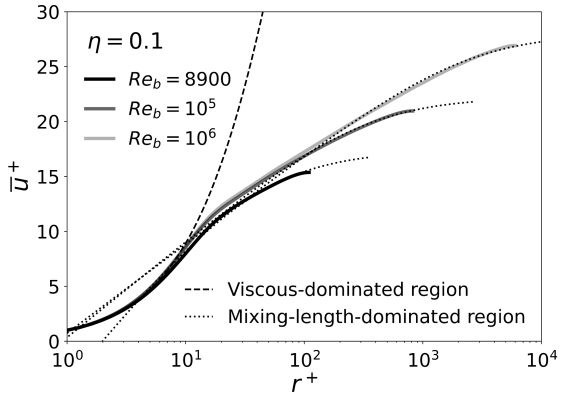

Figure 5. Velocity boundary layer at the inner pipe wall for various bulk Reynolds numbers $Re_b = 8900, 10^5, 10^6$ keeping the radius ratio $\eta = 0.1$ fixed.

Table 2. Coefficients in Eq. (7) for three test cases with fixed $\eta = 0.1$ varying the bulk Reynolds number.

Re_b	8900	10^5	10^6
β^+	0.1756	0.2617	0.2841
D^+	17.34	22.21	27.99

4.3. Reynolds Stress Components

Fig. 6 shows the Reynolds shear stress (RSS) $-\overline{u'v'}^+$ as a function of the wall-normal distance $(r - R_i)/\delta$ for radius ratio $\eta = 0.1$ and 0.5. The results show good agreement with the reference DNS data [5]. It is notable that the zero-crossing point for Reynolds shear stress (where $-\overline{u'v'}^+ = 0$) aligns with the location of the maximum mean axial velocity $\overline{u}_max$. This position is closer to the inner pipe wall for the minor radius ratio case, and the RSS profile becomes more symmetrical as the radius ratio increases. The difference in boundary layer thickness on the inner and outer pipe walls can also be clearly compared in this plot, as it is determined by the point where $-\overline{u'v'}^+ = 0$. This finding has already been discussed in Fig. 3. It is also observed that the magnitude of the RSS $-\overline{u'v'}^+$ is higher on the outer pipe wall than on the inner pipe wall, and this difference is more pronounced as the radius ratio decreases.

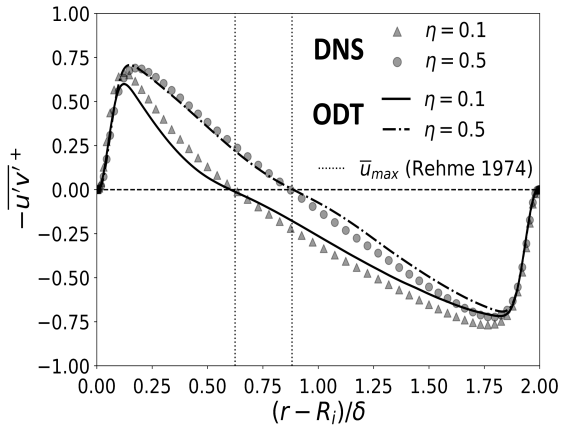

Figure 6. Radial profile of the Reynolds shear stress $-\overline{u'v'}^+$ for radius ratio $\eta = 0.1$ and 0.5, respectively, and fixed bulk Reynolds number $Re_b = 8900$. Reference DNS data is from [5].

Fig. 7 shows radial profiles of the axial component, $\overline{u'u'}^+$, of the normal Reynolds stresses in the vicinity of the inner and outer pipe walls with fixed radius ratio $\eta = 0.1$ and bulk Reynolds number $Re_b = 8900$ compared with reference DNS data [5]. Recall that $\overline{u'u'}^+ = (u_{rms}{}^+)^2$ is the variance or squared root-mean-square (RMS) axial velocity fluctuation. The axial velocity variance is a proxy for the turbulence intensity. The objective is to asses the model's capabilities to capture the radial asymmetry of velocity fluctuations across the gap. High $\overline{u'u'}^+$ value indicates the intense turbulence region. It is found that the maximum value of $\overline{u'u'}^+$ appears in the buffer layer, within the interval $5 < r^+ < 30$, which is in accord with the boundary layer over a flat surface. Compared to the profile of $\overline{u'u'}^+$ on the inner pipe wall, it is evident that the turbulence intensity on the outer pipe wall is stronger than on the inner pipe wall.

In contrast to the reference DNS data [5], ODT significantly underestimates the near-wall turbulent fluctuation peak at $r^+ \approx 15$, but it does capture the trend for the curvature influence. This behavior is consistent with the mean profiles discussed earlier, while underestimating turbulent fluctuations is a known modeling artifact [16, 12, 14]. The magnitude deficit of fluctuation and the underestimation of turbulence intensity do not necessarily imply incorrect radial fluxes. In fact, accurately capturing radial asymmetry requires a physical representation of radial fluxes in the dimensionally reduced model. As already shown in Fig. 6, this is achieved through map-based turbulence modeling within the eddy events, which are responsible for the advection of the radial velocity fluctuations, denoted as v'. It is also suggested that the ODT model may not be ideal for the low Reynolds number investigated. The model is primarily designed for highly turbulent flows, where no reference DNS data is available for turbulent annular pipe flow to support its application in this context. Therefore, the weaker turbulent fluctuations observed, in comparison to the DNS data, can be attributed to the effects of a finite Reynolds number. According to other ODT model studies [14], this type of modeling error tends to vanish for fluxes at high asymptotic Reynolds numbers. Therefore, based on the current model validation, the ODT model can be applied with greater confidence to heat exchangers, chemical reactors, and gas-cleaning devices that involve concentric pipe flows.

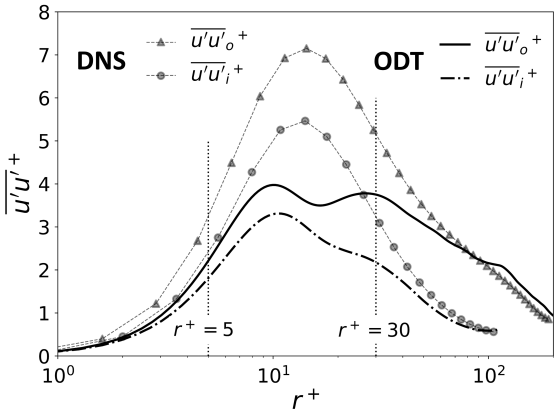

Figure 7. Radial profiles of the axial component of the Reynolds normal stresses in the vicinity of the inner and outer pipe wall, respectively, for bulk Reynolds number $Re_b = 8900$ and radius ratio $\eta = 0.1$.

4.4. Detailed Velocity Statistics

To better understand the variation in axial velocity fluctuation statistics with distance from the wall, the probability density function (PDF) of the fluctuating axial velocity is analyzed over the simulation time. Two distinct locations from both sides of the walls are selected: $r^+ = 5$ in the viscous-dominated

region and $r^+ = 30$ in the mixing-length-dominated region. From Fig. 7, it is known that at $r^+ = 30$, the difference of turbulent intensity between the outer and inner profiles is more extensive than at $r^+ = 5$.

Fig. 8 compares the PDF of the normalized fluctuating axial velocity u/u_{rms}, on the inner and outer pipe walls for two selected r^+ locations, with a radius ratio $\eta = 0.1$ and a bulk Reynolds number $Re_b = 8900$. The results indicate that the PDF curves generally exhibit a Gaussian-like distribution. However, as the location of r^+ changes, the peak of the PDF shifts toward higher magnitudes of u/u_{rms}, leading to a modification in the shape of the distribution profiles. It is seen that the shape of the profiles on the inner and outer pipe walls remains similar. Notably, at $r^+ = 30$, the difference in the magnitudes of u/u_{rms} between the inner and outer PDF profiles is more pronounced than at $r^+ = 5$. This indicates that the curvature effect on the fluctuating axial velocity is more significant at $r^+ = 30$ than at $r^+ = 5$. It is also observed that, compared to the PDF profile on the outer pipe wall, the magnitude of u/u_{rms} on the inner wall is generally higher, with the difference between each other becoming more pronounced as the distance from the pipe wall increases.

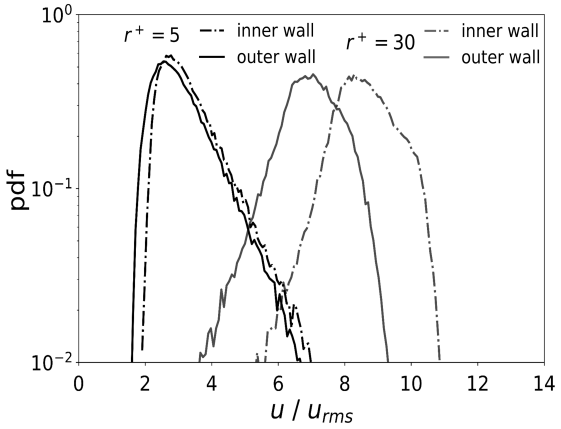

Figure 8. Probability density functions (PDFs) of the axial velocity fluctuations u normalized by the RMS u_{rms} at $r^+ = 5$ in the viscous sublayer and $r^+ = 100$ in the turbulent log layer on the inner and outer pipe walls for fixed radius ratio $\eta = 0.1$ and bulk Reynolds number $Re_b = 8900$.

5. UTILIZATION OF THE CURVATURE-AWARE WALL FUNCTION IN RANS

The application of the modified law-of-the-wall to predictive RANS-based modeling is demonstrated next. Equation 6 is applied as a wall function for the turbulent eddy viscosity in a 1-D finite-volume RANS solver using cylindrical coordinates (infinitesimal wedge). A mixing-length turbulence model with van Driest damping is used as a starting point, with the model coefficients obtained via fitting to DNS data from [4].

Figure 9 shows the mean velocity profile predicted by RANS using the modified wall function on the inner pipe wall in comparison to the reference DNS solution for $\eta = 0.1$ and $Re_b = 8900$. The two profiles are in close agreement, although the mean velocity on the inner pipe wall appears to be underestimated. Forthcoming research is devoted to evaluating the effectiveness of the spanwise curvature-aware wall function when utilized in multi-purpose CFD software.

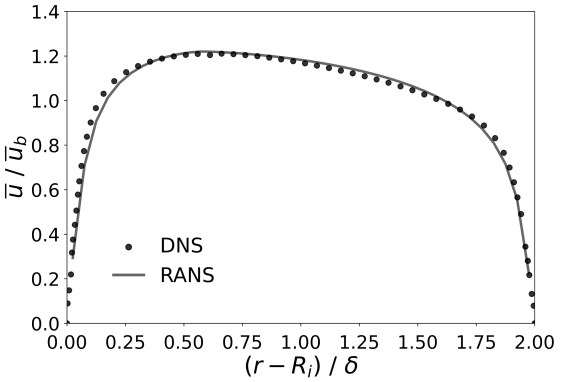

Figure 9. Comparison of RANS coupled with wall function from equation 6 with reference DNS data [4].

6. CONCLUSIONS

In the present study, stochastic one-dimensional turbulence (ODT) modeling of the pressure-driven flow in a concentric annular pipe has been presented and validated with available reference DNS.The stochastic model is formulated using the boundary-layer approximation. It can capture radial transport processes with full-scale resolution, even at high Reynolds numbers. The results demonstrate that the standalone ODT model offers a cost-effective approach to investigate statistical and dynamical features of fluctuating boundary layer flows.

For model validation, the profiles of mean velocity, law-of-the-wall on the inner and outer pipe walls, Reynolds shear stress, and axial Reynolds stress components are compared with reference DNS data [4, 5] at a fixed bulk Reynolds number of $Re_b = 8900$. Overall, the calibrated model reasonably reproduces low-order flow statistics. However, the model tends to underestimate axial velocity fluctuations, especially in the buffer layer, which is a well-known modeling artifact [16] that persists here at low radius ratios and high Reynolds numbers. Nevertheless, the model is able to capture fairly accurately the radial asymmetry and Reynolds shear stress distribution, which is a key asset for the present application.

It is observed that spanwise curvature affects the asymmetry of the mean velocity profile and, consequently, the thickness of the boundary layers on the inner and outer pipe walls. A lower radius ratio results in a thinner boundary layer on the inner

pipe wall. To enhance the wall-function-based prediction for the velocity boundary layer on the inner pipe wall, a theoretical analysis has been conducted, separately examining the viscous-dominated and mixing-length-dominated regions. By applying boundary-layer and mixing-length theories, the analysis successfully predicts the exact boundary layer profiles close to and farther away from the walls. This provides a reasonable basis for the development of curvature-aware wall functions as demonstrated by preliminary results for a low-Reynolds-number formulation.

ACKNOWLEDGEMENT

This research is supported by the German Federal Government, the Federal Ministry of Research, Technology and Space, and the State of Brandenburg within the framework of the joint project EIZ: Energy Innovation Center (project numbers 85056897 and 03SF0693A) with funds from the Structural Development Act for coal-mining regions.

REFERENCES

[1] Boersma, B. J., and Breugem, W.-P., 2011, "Numerical simulation of turbulent flow in concentric annuli", *Flow, Turbulence and Combustion*, Vol. 86 (1), pp. 113–127.

[2] Quarmby, A., 1967, "An experimental study of turbulent flow through concentric annuli", *International Journal of Mechanical Sciences*, Vol. 9 (4), pp. 205–221.

[3] Rehme, K., 1974, "Turbulent flow in smooth concentric annuli with small radius ratios", *Journal of Fluid Mechanics*, Vol. 64 (2), pp. 263–288.

[4] Chung, S. Y., Rhee, G. H., and Sung, H. J., 2002, "Direct numerical simulation of turbulent concentric annular pipe flow: Part 1: Flow field", *International Journal of Heat and Fluid Flow*, Vol. 23 (4), pp. 426–440.

[5] Bagheri, E., and Wang, B.-C., 2020, "Effects of radius ratio on turbulent concentric annular pipe flow and structures", *International Journal of Heat and Fluid Flow*, Vol. 86, p. 108725.

[6] Chung, S. Y., and Sung, H. J., 2003, "Direct numerical simulation of turbulent concentric annular pipe flow: Part 2: Heat transfer", *International Journal of Heat and Fluid Flow*, Vol. 24 (3), pp. 399–411.

[7] Bagheri, E., and Wang, B.-C., 2021, "Direct numerical simulation of turbulent heat transfer in concentric annular pipe flows", *Physics of Fluids*, Vol. 33 (5), p. 055131.

[8] Tsai, P.-Y., Schmidt, H., and Klein, M., 2023, "Investigating Reynolds number effects in turbulent concentric coaxial pipe flow using stochastic one-dimensional turbulence modeling", *Proceedings in Applied Mathematics and Mechanics*, Vol. 23 (4), p. e202300167.

[9] Klein, M., Tsai, P.-Y., and Schmidt, H., 2024, "Stochastic Modeling and Large-Eddy Simulation of Heated Concentric Coaxial Pipes", A. Dillmann, G. Heller, E. Krämer, C. Wagner, and J. Weiss (eds.), *New Results in Numerical and Experimental Fluid Mechanics XIV - Contributions to the 23rd STAB/DGLR Symposium Berlin, Germany 2022*, Springer, Vol. 154 of *Notes on Numerical Fluid Mechanics and Multidisciplinary Design*, pp. 435–444.

[10] Kerstein, A. R., 1999, "One-dimensional turbulence: model formulation and application to homogeneous turbulence, shear flows, and buoyant stratified flows", *Journal of Fluid Mechanics*, Vol. 392, pp. 277–334.

[11] Kerstein, A. R., Ashurst, W. T., Wunsch, S., and Nilsen, V., 2001, "One-dimensional turbulence: vector formulation and application to free shear flows", *Journal of Fluid Mechanics*, Vol. 447, pp. 85–109.

[12] Lignell, D. O., Lansinger, V. B., Medina, J., Klein, M., Kerstein, A. R., Schmidt, H., Fistler, M., and Oevermann, M., 2018, "One-dimensional turbulence modeling for cylindrical and spherical flows: model formulation and application", *Theoretical and Computational Fluid Dynamics*, Vol. 32 (4), pp. 495–520.

[13] Tsai, P.-Y., Schmidt, H., and Klein, M., 2023, "Modeling simultaneous momentum and passive scalar transfer in turbulent annular Poiseuille flow", *Proceedings in Applied Mathematics and Mechanics*, Vol. 22 (1), p. e202200272.

[14] Klein, M., Schmidt, H., and Lignell, D. O., 2022, "Stochastic modeling of surface scalar-flux fluctuations in turbulent channel flow using one-dimensional turbulence", *International Journal of Heat and Fluid Flow*, Vol. 93, p. 108889.

[15] Eggels, J. G., Unger, F., Weiss, M., Westerweel, J., Adrian, R. J., Friedrich, R., and Nieuwstadt, F. T., 1994, "Fully developed turbulent pipe flow: a comparison between direct numerical simulation and experiment", *Journal of Fluid Mechanics*, Vol. 268, pp. 175–210.

[16] Lignell, D., Kerstein, A., Sun, G., and Monson, E., 2013, "Mesh adaption for efficient multiscale implementation of one-dimensional turbulence", *Theoretical and Computational Fluid Dynamics*, Vol. 27, pp. 273–295.

Conference on Modelling Fluid Flow (CMFF'25)
The 19th International Conference on Fluid Flow Technologies
Budapest, Hungary, August 26 - August 29, 2025

COMBUSTION- AND POLLUTANT-MODELLING OF DIMETHYL ETHER IN A SWIRL-STABILIZED COLD AIR BURNER

Moritz DIEWALD[1], Leona GÖHLER[2], Nico SCHMITZ[2], Christian WUPPERMANN[2]

[1] Corresponding Author. Department for Industrial Furnaces and Heat Engineering, RWTH Aachen University. Kopernikusstraße 10, 52074 Aachen, Germany. E-mail: diewald@iob.rwth-aachen.de
[2] Department for Industrial Furnaces and Heat Engineering, RWTH Aachen University

ABSTRACT

The European Green Deal aims to make Europe the first climate-neutral continent by 2050, emphasizing the transformation of energy systems towards affordability, efficiency and circularity. Within this context, biofuels like renewable Dimethyl Ether (rDME) are pivotal in reducing carbon footprints by replacing fossil fuels. Dimethyl Ethers (DME) advantage over hydrogen lies in its transportability and combustion properties, making it a viable alternative for energy-intensive industries such as steel industry.

As part of the EU-funded "Butterfly" project, DME is synthesized from organic residues using advanced processes like Sorption Enhanced DME Synthesis (SEDMES). This method positions DME as a carbon-neutral biofuel option when derived from syngas produced through organic waste materials. [1]

This paper explores various simulation approaches for DME combustion within a swirl-stabilized cold air burner and compares them with experimental data obtained from an in-house test stand. The study focuses on key parameters such as exhaust gas composition, furnace temperature and the energy balance within the furnace. Particular attention is given to air pollutants like nitrous monoxide (NO) and carbon monoxide (CO).

The results offer insights into how conventional burners designed for natural gas and propane respond when fired with DME and contribute to understanding how renewable fuels can be integrated into existing infrastructure while meeting stringent environmental standards. By comparing simulated outcomes with real-world data, this research supports the transition towards cleaner energy sources in line with global climate goals.

Keywords: CFD, Combustion, dimethyl ether, pollutant formation, RANS

NOMENCLATURE

$\dot{H}$	$[kW]$	enthalpy stream
LHV	$[J/kg]$	lower heating value
M	$[kg/mol]$	molar mass
$\dot{Q}$	$[kW]$	heat stream
T	$[°C]$	temperature
c_p	$[J/K]$	heat capacity at constant pressure
l_{min}	[-]	stoichiometric air-fuel-ratio
m	[-]	stochiometric factor
$\dot{m}$	$[kg/s]$	mass flow
n	[-]	stochiometric factor
o	[-]	stochiometric factor
$o_{2,min}$	[-]	stoichiometric oxygen-fuel-ratio
p	[-]	stochiometric factor
q	[-]	stochiometric factor
r	[-]	stochiometric factor
λ	[-]	air-fuel-equivalence-ratio

Subscripts and Superscripts

DME	regarding DME
air	regarding air
combustion	regarding enthalpy of combustion
cool	regarding cooling air
in	streaming in
off-gas	regarding off-gas
out	streaming out
wall	regarding wall
$\bar{}$	averaged over relevant temperature range

1. INTRODUCTION

The exploration of renewable alternatives to fossil fuels is a subject of current research. The transition to renewable alternatives is indispensable to achieve the goals of the Paris Climate Agreement. However, the use of chemical energy carriers remains the state of the art, especially for energy-intensive processes that require high spatial energy

density. Current research is therefore focused on how fossil fuels like natural gas (NG) or liquefied petroleum gas (LPG) can be replaced by renewable alternatives such as hydrogen (H_2). The paper addresses this research question and examines the use of DME as a fuel in a conventional cold air burner. Focus is placed on the effects of DME combustion on the formation of air pollutants such as NO or CO.

The simulation of combustion processes is very computationally intensive, as it requires modelling not only the flow field but also a temperature field and reaction kinetics. Reaction modelling can be realized through various approaches. This paper examines the results of Flamelet Generated Manifold (FGM) combustion modelling. It then compared the results of different kinetic mechanisms and different NO-postprocessing approaches and compares them with experimental data obtained from a burner test stand.

2. METHODOLOGY

In this work, different combustion simulations are conducted and compared with measurements from a burner test stand.

Similar studies have already been carried out in a previous conference paper by this author [2]. However, in that case, the combustion modelling was performed using an adiabatic FGM. One conclusion of that study was to simulate the combustion using a non-adiabatic FGM matrix to achieve more accurate results regarding NO- and CO-concentrations in the exhaust gas. Additionally, other kinetic mechanisms such as those proposed by Li et al. [3] should be considered. [2]

Besides optimising the combustion simulation, a more precise simulation of heat losses through cooling should also be pursued. [2]

2.1 Combustion Calculation

With the help of combustion calculations, theoretical values for the exhaust gas composition of the main reaction products can be determined. The basis for this calculation is Eq. (1) [4].

$$C_m H_n O_o + \left(m + \frac{n}{4} - \frac{o}{2}\right) O_2 \rightarrow mCO_2 + \frac{n}{2} H_2O \quad (1)$$

Here, it is assumed that carbon atoms fully react to carbon dioxide (CO_2) and hydrogen atoms fully react to water (H_2O). This simplification is possible because it involves a fuel-lean combustion where unburned oxygen (O_2) is found in the exhaust gas.

From Eq. (1), Eq. (2) [4] can be derived to determine the stoichiometric oxygen-fuel-ratio.

$$o_{2,min} = m + \frac{n}{4} - \frac{o}{2} = 3 \quad (2)$$

with

$m = 2$
$n = 6$
o $= 1$

For pure DME combustion, this results in a stoichiometric oxygen-fuel-ratio of 3 mol_{O2}/mol_{DME}. With a simplified air composition of 21 *vol.-%*, the stoichiometric oxygen-fuel-ratio can be converted into the stoichiometric air-fuel-ratio using Eq. (3) [4].

$$l_{min} = \frac{3}{0{,}21} = 14{,}29 \quad (3)$$

The stoichiometric air-fuel-ratio for DME is thus 14,29 mol_{air}/mol_{DME}.

In the next step, based on the given power and air ratio, the required mass flows for fuel and combustion air are calculated. The experiments discussed in this paper are operated at a power of 30 *kW* and an air-fuel-equivalence-ratio of 1,1. Using the known lower heating value (LHV_{DME} = 16,46 kWh/m^3) from Teng et al. [5], Eq. (4) [4] yields a fuel mass flow rate of 0,001039 *kg/s*.

$$\frac{\dot{H}_{\mathrm{combustion}}}{LHV_{\mathrm{DME}}} = \dot{m}_{\mathrm{DME}} = 0{,}001039 \frac{kg}{s} \quad (4)$$

Based on the known stoichiometric air-fuel-ratio, together with the air-fuel-equivalence-ratio, Eq. (5) [4] results in an air mass flow rate of 0,01028 *kg/s*.

$$l_{min} \cdot \lambda \cdot \dot{m}_{\mathrm{DME}} \cdot \frac{M_{\mathrm{air}}}{M_{\mathrm{DME}}} = \dot{m}_{\mathrm{air}} = 0{,}01028 \frac{kg}{s} \quad (5)$$

These mass flows ensure consistent energy input for both numerical modelling and investigations at the test stand. The same combustion values are set for both simulations and burner tests to compare numerical modelling results with test stand experiments effectively.

Additionally, using known mass flows and combustion reactions, a theoretical exhaust gas composition can be calculated. Eq. (6) [4] shows the adjusted reaction equation for a fuel-lean combustion with correct exhaust ratios.

$$C_2H_6O_1 + p\ O_2 + q\ N_2 \rightarrow 2CO_2 + 3H_2O + r\ O_2 + q\ N_2 \quad (6)$$

with

$$p = \lambda \cdot o_{2,min}$$
$$q = \lambda \cdot o_{2,min} \cdot \frac{0{,}79}{0{,}21}$$
$$r = (\lambda - 1) \cdot o_{2,min}$$

These chemical considerations result in a calculated moist exhaust gas composition, which is shown in Chapter 3, along with measurement and simulation results.

2.2 Test stand

The combustion chamber has a square base with a side length of 640 *mm*. The height of the combustion chamber is 1000 *mm*. Figure 1 shows a cross-section through the middle of the combustion chamber.

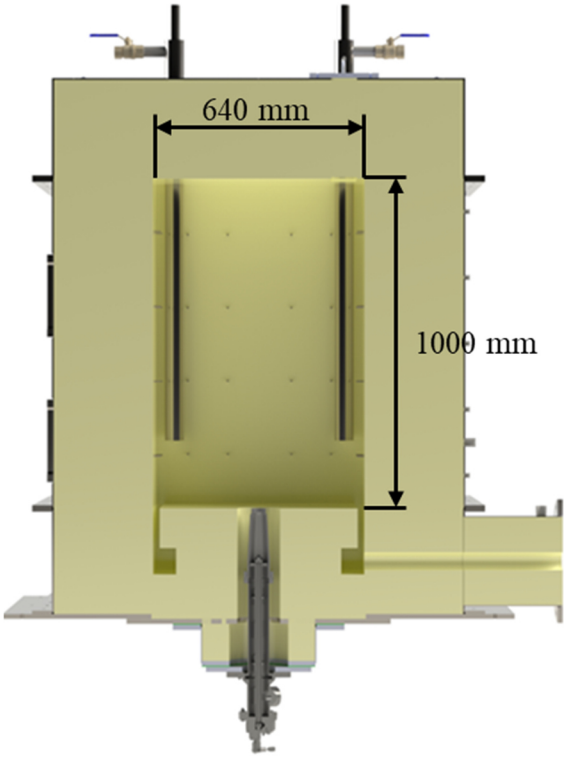

Figure 1. Cut through the burner test stand

The burner, type BIC HB65 by Honeywell [6], is mounted firing upwards in the centre of the bottom plate. At the top of the combustion chamber, four cooling tubes are installed. These are air-cooled to establish a load condition, allowing the test stand to reach a steady state.

The cooling tubes are designed as a pipe-in-pipe construction. Cool air flows in through the outer tube and out again through the shorter inner tube. The lower end of the outer pipe is welded shut so that the oven atmosphere and the cooling air are not mixed. The heat flux of the cooling air corresponds to the power acting on the process or product in an industrial furnace. The cooling tubes are cylindrical with a diameter of 60 *mm* and a length of 800 *mm*. The central axis of the cooling tubes is positioned at 56 *mm* from the wall.

The square bottom plate has a side length of 600 *mm*, creating a gap of 20 *mm* through which exhaust gases can be extracted from the combustion chamber. The extraction is controlled to maintain a constant furnace pressure of 35 *Pa*. The test stand is insulated with a 300 *mm* thick refractory layer.

The off-gas concentration measurements are performed using different measurement systems. The Ultrakust Hygrophil H 4230-10 is uses psychrometric humidity measurement to measure the wet off gas concentration of H_2O. The other concentrations in the off gas are measured in the dry offgas. An Emerson X-Stream measures CO and CO_2 concentration using a Non-Dispersive Infrared (NDIR) Sensor and O_2 using a paramagnetic sensor. An Emerson CLD is used to measure the NO_X-Concentration using Chemiluminescence.

In experiments at the burner test stand, besides measuring exhaust gas composition and temperature, both volumetric flow rate and temperatures of the cooling air before and after passing through the cooling tubes are measured.

Additionally, the wall temperature is measured at mid-height on the inner side of the refractory material. All thermocouples used were of type N class 1. At temperatures over 1100 *°C* the error of these thermocouples is rounded up to 2 *K*.

The volume flow of the cooling air is measured using a pitot tube. The measurement uncertainty results in an error of 1 *Pa*.

2.3 Energy Balance

From the values measured in the test stand, along with the known mass flows from Section 2.1, the exhaust gas enthalpy and the enthalpy difference of the cooling air can be calculated. The enthalpy input from the heat of combustion air and fuel gas is neglected due to low entry temperatures. The energy flows considered are shown in Figure 2.

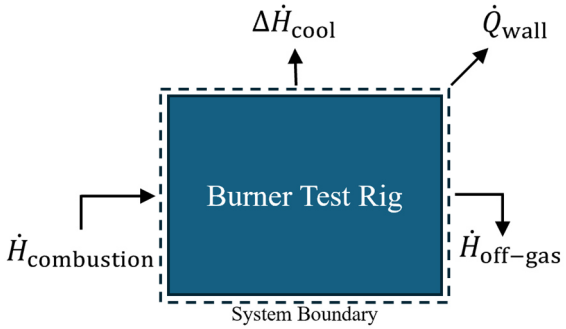

Figure 2. Energy Balance (after [7])

Previous experiments have demonstrated that a steady state can achieved with a cooling air heat flux of around 8 *kW*. The test stand and simulation boundary conditions are set accordingly. Based on the considered energy streams, an energy balance of the furnace can be established. Thus, the energy balance can be calculated using Eq. (7).

$$\dot{H}_{\text{combustion}} = \dot{H}_{\text{off-gas}} + \Delta\dot{H}_{\text{cool}} + \dot{Q}_{\text{wall}} \tag{7}$$

The combustion enthalpy amounts to 30 *kW* and remains constant for all experiments. The exhaust gas enthalpy is determined according to Eq. (8), where the average heat capacity is determined based on each measured exhaust concentration according to VDI 4670 (2016) [8].

$$\dot{H}_{\text{off-gas}} = (\dot{m}_{\text{DME}} + \dot{m}_{\text{air}}) \cdot \bar{c}_{p,\text{off-gas}} \cdot \left(T_{\text{off-gas,out}} - T_0\right) \tag{8}$$

The off-gas enthalpy is calculated in this way for the test stand and the simulation data.

The cooling air enthalpy difference is calculated using Eq. (9).

$$\Delta\dot{H}_{\text{cooling}} = \dot{m}_{\text{cool}} \cdot \bar{c}_{p,\text{air}} \cdot \left(T_{\text{cool,out}} - T_{\text{cool,in}}\right) \tag{9}$$

The average heat capacity is also determined according to VDI 4670 (2016) [8].

Additionally, wall losses are compared, although they are difficult to determine experimentally. Therefore, they are only calculated from the energy balance for experiments.

2.4 Mesh and Boundary Conditions

The simulation volume exactly corresponds to that of the test stand. It begins 30 *mm* below the swirl plate and ends in the exhaust channel 75 *mm* below the base plate. The exhaust channel is simulated to this extent to prevent backflow.

The mesh is based on a poly-hexcore mesh and is created using ANSYS© Fluent. Firstly, a grid independence study is performed. Therefore, the cell sizes are varied. In the coarsest mesh the largest hexahedra have an edge of 20 *mm*, with the finer meshes having maximum cell lengths of 16 mm, 14,4 *mm* and 12,8 *mm* respectively. A simulation is performed for all four mesh sizes and the temperature over different hights is compared. Figure 3 shows the temperature over the height along the burner axis.

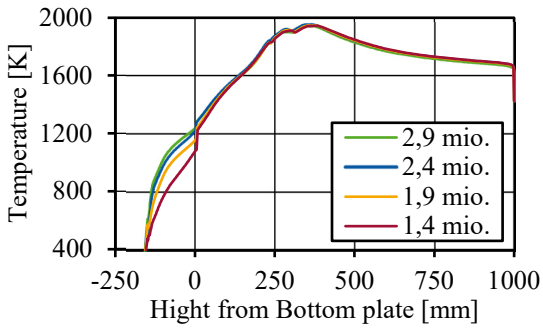

Figure 3. Temperature over the height along the burner axis

After the grid independence study the 2,4 mio. cell mesh is chosen as the temperature curve deviates only slightly from the 2,9 mio. cell mesh. The 2,4 mio. cell mesh corresponds to a maximum edge length of 14,4 *mm*. The mesh includes five mesh refinement levels that are determined based on the flame shape. Consequently, the smallest cells within the swirl plate have a size of 0,45 *mm*. Figure 4 shows the simulation geometry and the form of the mesh refinement levels.

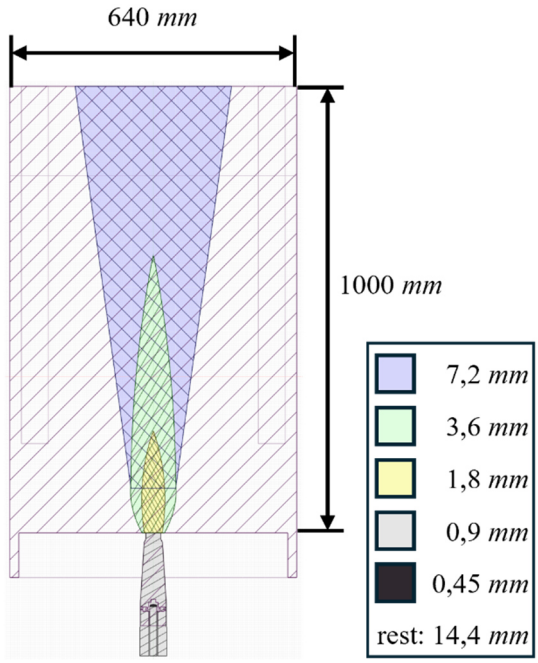

Figure 4. Simulation Geometry and Mesh Refinement

The outer walls of the combustion chamber are simulated using one-dimensional heat conduction with external convection. The conduction consists of two layers. An inner layer representing the refractory material with a thickness of 300 *mm* and an outer layer modelled after the 15 *mm* thick steel body of the test stand. The external temperature is assumed to be 300 *K*. The burner walls and the inner side of the exhaust channel are assumed as adiabatic. The

cooling tubes are assumed to have a constant heat flux, resulting in the previously defined cooling capacity of 8 *kW*. The fuel and air temperatures are 300 *K*.

2.5 Numerical Modelling

The simulations in this work are conducted using the commercial simulation software ANSYS© Fluent 2024R2. The simulations are Reynolds-Averaged Navier-Stokes (RANS) simulations.

Previous simulations showed that the k-omega SST turbulence model [9] generates unsteady flow fields that negatively affect combustion modelling. For this reason, the realizable k-epsilon model [10] was selected for the simulations in this study. Radiation is represented using a 4x4 Discrete Ordinates model [11–13].

Combustion modelling, alongside the choice of kinetic mechanism, is an important consideration in combustion calculations. There are various modelling approaches that differ in accuracy and computational time.

In this paper, combustion is modelled using the Flamelet Generated Manifold (FGM) model [14], which is coupled with a presumed-shape Probability Density Function (PDF) to capture turbulence-chemistry interaction.

Two simulations with different kinetic mechanisms are performed. One simulation is based on the mechanism by Prince et al. [15,16] and the other on the mechanism by Li et al. [3]. Further comparisons between these mechanisms can be found in the preceding paper [2].

The spatial discretisation becomes more complex with increasing simulation accuracy. The final simulation uses the PRESTO! algorithm for pressure interpolation and a first-order upwind scheme for radiation calculation. The other transport equations are solved using a second-order upwind scheme.

2.6 NO-Post-Processing

The FGM model resolves only the twelve most significant species by proportion, so NO is not calculated. Therefore, various post-processing calculations were conducted to determine the NO concentration. These transport equations are post-processed from converged combustion simulations. This approach is valid, as the NO concentration is minuscule compared to the main combustion products.

For this work, three approaches to NO modelling integrated in ANSYS© Fluent were selected:

1. NO_X Modelling (NO_X)
2. Decoupled Detailed Chemistry (DDC)
3. Reactor Network Modelling (RNM)

The ANSYS© Fluent NO_X model used in this work simulates thermal and prompt NO_X formation. NO_X prediction is achieved by solving transport equations for NO and intermediate nitrous oxide (N_2O). The incorporated rate models originate from the Department of Fuel and Energy at the University of Leeds and open literature. [17]

The Decoupled Detailed Chemistry Model in Fluent is based on the same idea as the NO_X model. However, instead of using rate models embedded in Fluent, any kinetic mechanisms can be loaded. [17]

The reactor network model simulates species and temperature fields in a combustor using detailed chemical kinetics. A kinetic mechanism is imported and solved within the reactor network. Therefore, the combustor is divided into a few perfectly stirred reactors, with mass fluxes determined from the CFD solution. This approach efficiently captures finite-rate chemistry effects, particularly for NO, CO and unburnt hydrocarbons. Since the number of reactors is much smaller than the cells of the mesh, it allows faster simulations. [17]

The kinetic mechanism and combustion modelling approaches used in this work are listed in Table 1. The converged FGM combustion simulation before post-processing is labelled as FGM.

Table 1. List of combustion models

No.	Name	Combustion Model	Kin. Mech.
1	FGM Prince	FGM	Prince [15,16]
2	NOX Prince	NOX	Prince [15,16]
3	DDC Prince	DDC	Prince [15,16]
4	RNM Prince	RNM	Prince [15,16]
5	FGM Li	FGM	Li [3]
6	NOX Li	NOX	Li [3]

Only the Prince mechanism includes NO_X chemistry. Therefore, DDC and RNM which are based on the chosen kinetic mechanism are only used in combination with the Prince kinetic mechanism.

3. RESULTS AND DISCUSSION

When switching from natural gas to pure DME combustion, the burner shut off repeatedly. To ensure a stable combustion, a minimal volume flow of 3,15E-7 *kg/s* natural gas is added constantly. This results in a DME concentration of 99,9 *Vol.-%* in the fuel. Further trials must be performed to test if the malfunction arises from the burner itself or the burner control system. The simulated combustion asumes 100 *Vol. %* DME nonetheless.

Table 2 illustrates the temperatures from the simulations and test stand experiments. The FGM

Prince simulation deviates by 35 *K*. The exhaust temperature is overestimated, with a deviation of 23 *K*. The RNM Prince simulation results in the highest temperatures, with both exhaust and wall temperatures at 1209 *K*, exceeding measured values by 96 *K* and 65 *K*, respectively. The FGM Li simulations also demonstrate higher temperatures than those recorded in the test stand, with exhaust temperature being 60 *K* and wall temperature 67 *K* above the measurements.

Table 2. Results of Temperature

	$T_{\text{off-gas}}$ [°C]	T_{wall} [°C]
Trial	1113±2	1144±2
FGM Prince	1136	1179
RNM Prince	1209	1209
FGM Li	1173	1211

There could be various reasons for these deviations. One possible reason could be inaccurate modelling of the wall and cooling tubes heat-fluxes or a not fully heated test stand. Another reason with regards to the off-gas temperature are the differing measurement positions between experiments and simulations leading to larger discrepancies in the exhaust channel.

Next, the temperature fields are displayed. Therefore, a plane is placed diagonally along the burner axis so that it cuts through the centres of two cooling tubes. Figure 5 displays the temperature field of the FGM Li simulation. As the temperature field of the FGM Prince simulation is very similar it is not shown.

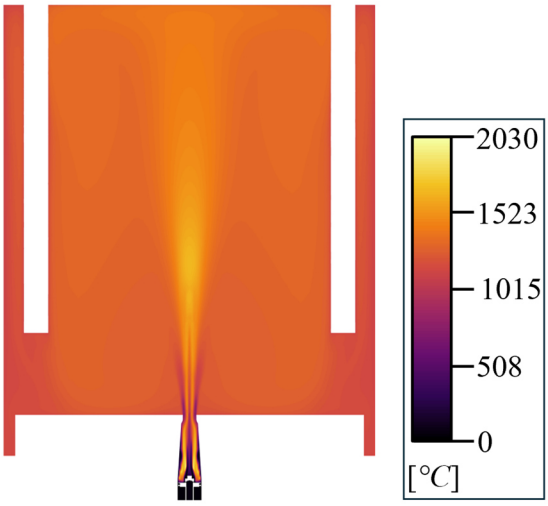

Figure 5. Temperature Field of FGM Li

The temperature before the burner swirl plate is the lowest. In the area after the burner swirl plate the temperatures in the centre and at the outer wall are the coolest. Between these cooler areas is a high-temperature zone. This is explained through the mixing of fuel and air. Fuel is injected in the centre of the swirl-plate and air is injected along the outside. As the combustion can only take place if mixture between air and fuel takes place, it makes sense that the hot zones are between these zones. Therefore, the outer cold zone corresponds to an air-rich area and the inner cold zone corresponds to a fuel rich area. After the burner orifice the colder outer layer diffuses outwards, whereas the hotter layer narrows to a point as it consumes the fuel inside the central colder layer. At one point, the outer hot layer separates from the hot zone. Inside this separation a second hot zone begins. This layer not as clearly defined but it diffuses outward reaching its biggest extend right at the tip of the first hot zone and then gradually diffuses so that the hottest area narrows again. Inside this area a secondary reaction takes place. The remaining temperature field has a relative constant temperature except for the temperatures in the corners of the test stand which are shielded from radiation by the cooling tubes.

The energy balance results are presented in Table 3. The values for cooling air enthalpy difference are in good agreement. Exhaust gas enthalpy is well captured in the simulation, even though the measured value is slightly higher. The wall losses are overestimated by the simulations by 1,54 *kW* for the FGM Prince case and 1,75 *kW* for FGM Li.

Table 3. Results of Energy Balance

	$\Delta\dot{H}_{cooling}$ [kW]	$\dot{H}_{offgas}$ [kW]	$\dot{Q}_{wall}$ [kW]
Trial	8,0±0,3	16,4±0,3	5,6±0,4*
FGM Prince	7,94	14,92*	7,14
FGM Li	7,94	14,71*	7,35

*calculated acc. to Eq. (7)

The off-gas enthalpies of the simulation are lower than during the trial. By contrast, the wall losses calculated for the test stand are lower than the wall losses of the simulations. This can either be explained by the inaccurate wall modelling or is a sign, that the steady state of the temperatures inside the test stand wasn't reached when the measurements were taken.

The wet exhaust gas concentrations are detailed in Table 4. The off-gas concentrations for both FGM simulations deviate only by a maximum of 0,1 *vol.-%* from the calculated concentrations. The RNM Prince simulation yields unrealistic results regarding exhaust composition.

Table 4. Off-gas Concentrations

	O_2 [*vol.-%, wet*]	H_2O [*vol.-%, wet*]	CO_2 [*vol.-%, wet*]
Calculated	1,7	16,9	11,3
Trial	1,6±0,3	18,7±0,1	11,0±0,2
FGM Prince	1,7	16,8	11,2
RNM Prince	2,0	10,8	17,6
FGM Li	1,7	16,9	11,3

The comparison of experimental values with calculated ones shows that O_2 and CO_2 concentrations align well. However, H_2O concentrations from experiments exceed those calculated by 2 *vol.-%*. This is an unrealistic deviation. Therefore, the O_2 concentration measurements should be checked for errors and repeated if necessary.

Table 5 presents air pollutants in dry off-gas concentration. The greatest deviation from measured values arises from Decoupled Detailed Chemistry. Here, NO concentration is less than 1 *%* of the measured value, while CO concentration is significantly overestimated at an absolute value of 1,2 *vol.-%*. As discussed in Section 2.6, FGM modelling does not capture NO phase. Prince FGM significantly overestimates CO concentration at 749,5 *ppm*. Since NO_X modelling only considers species involved in NO_X formation (excluding CO), CO concentration also amounts to 749,5 *ppm*. However, the NO concentration closely matches measured values at 54,6 *ppm* compared to 72 *ppm*. Prince RNM underestimates NO concentration by about 61,2 *ppm* while overestimating CO concentration by 35,1 *ppm*.

The FGM Li simulation provides the best results regarding CO concentration with an underestimation of just 4,9 *ppm*. The corresponding NO concentration of the NO_X Li Simulation achieves also good results, with slightly lower-than-expected readings around 35,6 *ppm*.

Table 5. Off-gas Concentrations Pollutants

	NO [*ppm, dry*]	CO [*ppm, dry*]
Trial	72±5	17±3
FGM Prince	-	749,5
NOX Prince	54,6	(749,5)
DDC Prince	0,4	12337,2
RNM Prince	10,8	52,1
FGM Li	-	12,1
NOX Li	35,6	(12,1)

The simulations based on the Prince mechanism tend towards exaggeration when calculating the carbon monoxide emissions. The simulations using the Li mechanism achieve more realistic outcomes.

The NO_X modelling of the NO postprocessing models available in ANSYS© Fluent achieves the most realistic results.

4. SUMMARY

In this paper, two FGM simulations based on different kinetic mechanisms were conducted. Once the simulations reached steady states, various post-processing models were applied to determine NO concentration. The simulation values were compared with test stand measurements in terms of temperature, energy balance and exhaust gas composition.

The burner was not able to combust pure DME. This should be investigated going forward.

Temperatures were overestimated by all simulations. A possible cause could be inaccurate wall and cooling tube boundary conditions or a not fully established steady state during the experiments.

The heat losses from the experiments are comparable to those simulated, although wall losses in the simulation exceed those measured. This suggests inaccurate representation of wall boundary conditions.

When comparing the values of the main exhaust products, it is noticeable that the RNM simulation leads to an unrealistic exhaust composition. The same applies to the water content in the conducted burner trial. All other measurement and simulation values are in good agreement. The measurements should be checked for errors and repeated if necessary.

Regarding air pollutants in the exhaust gas, CO concentration is significantly overestimated by the Prince mechanism. The Li mechanism results in more realistic CO concentrations, which are slightly below those measured. The most realistic simulation results regarding NO concentrations are achieved through NO_X post-processing.

In conclusion, FGM simulation followed by NO_X post-processing and using the Li mechanism leads to the most realistic results. However, it would be of interest to investigate other mechanisms such as those proposed by Khare et al. [18].

The simulation accuracy and validation could be improved further. One improvement could be to measure the outer wall temperatures of the test stand to calculate the wall losses. This could be achieved by using a thermographic camera. It could also be of interest to model the air stream inside the cooling tubes to achieve a spatial distribution of the heat flux through the cooling tube. Additionally, OH* visualisation measurements would be valuable for comparing the flame shape from simulations with that of a real flame.

ACKNOWLEDGEMENTS

Funded by the European Union

This work has been performed as part of BUTTERFLY project which has received funding from the European Union's Horizon Europe Research and Innovation Programme under Grant Agreement No. 101118241.

REFERENCES

[1] Peinado, C., Liuzzi, D., Sluijter, S. N., Skorikova, G., Boon, J., et al., 2024, "Review and perspective: Next generation DME synthesis technologies for the energy transition," *Chemical Engineering Journal*, Vol. 479, p. 147494.

[2] Diewald, M., Kaiser, H., and Schmitz, N., 2024, "Comparison Of Dimethyl Ether And Natural Gas Combustion In A Swirl-Stabilized Industrial Burner," *Selected papers from the 15th International Conference on Industrial Applications of Computational Fluid Dynamics, Trondheim, Norway, June 11–13, 2024,* Trondheim, Norway, pp. 141–148.

[3] Li, Y., Su, S., Wang, L., Yin, J., and Idiaba, S., 2022, "Reduction and optimization for combustion mechanism of dimethyl ether–air mixtures," *International Journal of Chemical Kinetics*, Vol. 54, pp. 142–153.

[4] Pfeifer, H., 2018, *Praxishandbuch Thermoprozesstechnik. Band I: Grundlagen - Prozesse - Verfahren*, Vulkan-Verlag GmbH.

[5] Teng, H., McCandless, J. C., and Schneyer, J. B., 2004, "Thermodynamic Properties of Dimethyl Ether - An Alternative Fuel for Compression-Ignition Engines," *SAE Technical Paper Series,* SAE International.

[6] Honeywell Kromschröder, 2022, "Burners with ceramic tube BIC, BICA, BICW, ZIC, ZICW," URL: https://docuthek.kromschroeder.com/download.php?lang=de&doc=66423&download=1.

[7] Pfeifer, H. (ed.), 2013, *Handbuch industrielle Wärmetechnik. Grundlagen, Berechnungen, Verfahren,* 5th ed., Vulkan Verl., Essen, Ruhr.

[8] Verein Deutscher Ingenieure (VDI), 2016, "Thermodynamische Stoffwerte von feuchter Luft und Verbrennungsgasen: Thermodynamic properties of humid air and combustion gases," 17.200.01, No. 4670 (2016).

[9] Menter, F. R., 1994, "Two-equation eddy-viscosity turbulence models for engineering applications," *AIAA Journal*, Vol. 32, pp. 1598–1605.

[10] Shih, T.-H., Liou, W. W., Shabbir, A., Yang, Z., and Zhu, J., 1995, "A new k-ϵ eddy viscosity model for high reynolds number turbulent flows," *Computers & Fluids*, Vol. 24, pp. 227–238.

[11] Chui, E. H., and Raithby, G. D., 1993, "Computation of radiant heat transfer on a Nonorthagonal mesh using the Finite-Volume-Method," *Numerical Heat Transfer, Part B: Fundamentals*, Vol. 23, pp. 269–288.

[12] Raithby, G. D., and Chui, E. H., 1990, "A Finite-Volume Method for Predicting a Radiant Heat Transfer in Enclosures With Participating Media," *Journal of Heat Transfer*, Vol. 112, pp. 415–423.

[13] Murthy, J. Y., and Mathur, S. R., 1998, "Finite Volume Method for Radiative Heat Transfer Using Unstructured Meshes," *Journal of Thermophysics and Heat Transfer*, Vol. 12, pp. 313–321.

[14] van OIJEN, J. A., and GOEY, L. de, 2000, "Modelling of Premixed Laminar Flames using Flamelet-Generated Manifolds," *0010-2202*, Vol. 161, pp. 113–137.

[15] Prince, J. C., and Williams, F. A., 2015, "A short reaction mechanism for the combustion of dimethyl-ether," *Combustion and Flame*, Vol. 162, pp. 3589–3595.

[16] Mechanical and Aerospace Engineering, Combustion Research, University of San Diego, 2012, "Chemical-Kinetic Mechanisms for Combustion Applications,".

[17] ANSYS, Inc., 2024, "Fluent Theory Guide,".

[18] Khare, R. S., Parimalanathan, S. K., Raghavan, V., and Narayanaswamy, K., 2018, "A comprehensively validated compact mechanism for dimethyl ether oxidation: an experimental and computational study," *Combustion and Flame*, Vol. 196, pp. 116–128.

Conference on Modelling Fluid Flow (CMFF'25)
The 19th International Conference on Fluid Flow Technologies
Budapest, Hungary, August 26-August 29, 2025

Development of a Cerebral Peripheral Vasculature Model for Quantitative Assessment of Collateral Blood Flow using SPECT and 4D Flow MRI

To Chi Hang[1], Shigeki Yamada[2], Marie Oshima[3]

[1] Corresponding Author. Graduate School of Engineering, Department of Mechanical Engineering, University of Tokyo. 7-3-1 Hongo, Bunkyo-ku, Tokyo 113-8654, Japan. Tel.: +81 80 4476 3065, E-mail: to-chi-hang524@g.ecc.u-tokyo.ac.jp
[2] Graduate School of Medical Sciences, Department of Neurosurgery, Nagoya City University Graduate School of Medical Sciences. E-mail: shigekiyamada393@gmail.com
[3] Institute of Industrial Science / Graduate School of Interdisciplinary Information Studies, The University of Tokyo. E-mail: marie@iis.u-tokyo.ac.jp

ABSTRACT

Collateral blood flow redistribution is crucial in ischemic stroke recovery, yet the role of leptomeningeal anastomoses (LMAs) remains poorly characterized. Current computational models lack representation of patient-specific redistribution under varying ischemic conditions. As such, this study investigates LMA functionality using patient-specific data. A 0D peripheral artery model, informed by anatomical measurements and Circle of Willis (CoW) vessel radii from medical images, is constructed using a stochastic sampling approach. To identify LMA configurations that align with measured data, island Genetic Algorithm (iGA) optimises LMA configuration by minimizing residuals between computed and measured perfusion flow rates from Single Photon Emission Computed Tomography (SPECT), with 4D flow MRI (magnetic resonance imaging) data serving as inlet flow rates. Case studies of two patients with varying degrees and locations of internal carotid artery stenosis reveal redistribution patterns consistent with physiological observations, including anterior-directed perfusion and inter-hemispheric redistribution. Topology analysis reveals a trade-off between LMA radius and pressure difference, with larger radii forming between arteries at lower bifurcation depths, enhancing flow rate despite diminishing pressure differences. By leveraging measurement techniques, this study offers new insights into patient-specific LMA morphology, with potential applications in refining more detailed vascular models for clinical and research use.

Keywords: cerebrovascular haemodynamics, collateral blood flow, genetic algorithm, leptomeningeal anastomosis, stochastic vasculature generation

NOMENCLATURE

G	$[\frac{\text{mL/s}}{\text{mmHg}}]$	conductance
H	$[-]$	number of vascular regions
J	$[-]$	cost function
L	$[mm]$	length
Q	$[mL/s]$	flow rate
R	$[\frac{mmHg}{\text{mL/s}}]$	resistance
d	$[-]$	bifurcation depth
p	$[mmHg]$	pressure
r	$[mm]$	radius
μ	$[Pa \cdot s]$	viscosity
τ	$[mmHg]$	fluid shear stress
$\lambda_{l/r}$	$[-]$	length-to-radius ratio
$\mathcal{N}$	$[-]$	node
R_{eff}	$[\frac{mmHg}{\text{mL/s}}]$	effective resistance

Subscripts and Superscripts

Co	computed
Sp	SPECT
int	internal

1. INTRODUCTION

Collateral blood flow plays a critical role in maintaining cerebral perfusion during arterial occlusions [1, 2], yet its assessment remains a challenge in both clinical and computational settings [3]. Traditional imaging techniques such as 4D Flow MRI and SPECT provide valuable insights into cerebral haemodynamics but are often limited by spatial resolution and qualitative interpretation, particularly in the context of small collateral vessels such as LMAs. These vessels, typically less than 0.3 mm in diameter [4], contribute to blood flow redistribution between vascular territories, yet their functional significance and flow dynamics remain difficult to quantify directly from imaging data.

Computational fluid dynamics (CFD) offers a complementary approach by enabling quantitative assessment of collateral circulation. Unlike imaging-based methods, CFD allows for controlled parameter variation, facilitating sensitivity analyses and predictive modelling of haemodynamic changes under different physiological and pathological conditions. However, conventional CFD methods, including 3D and even 1D simulations, are computationally intensive and impractical for large-scale uncertainty analyses or real-time clinical application [5]. As a result, 0D modelling has emerged as a viable alternative, offering an efficient means to simulate cerebral blood flow while preserving essential flow redistribution characteristics [6].

Despite its advantages, traditional 0D models often simplify vascular territories as isolated compartments, with collateral connections represented by literature-derived resistances rather than patient-specific data [7]. This simplification limits the ability to investigate collateral recruitment dynamics in an anatomically realistic manner.

To improve the physiological accuracy of flow simulations while maintaining computational efficiency, a more refined 0D modelling framework is needed—particularly for representing the peripheral vascular network. A key challenge in this approach is the scarcity of patient-specific vascular data, as direct segmentation of small vessels like LMAs is often impractical in clinical settings. To address this, synthetic vasculature generation offers a viable solution, enabling the creation of vascular networks that reflect anatomical variability with minimal input data [8].

This study presents a 0D modelling framework that integrates flow rate measurements with synthetic vascular network generation to enhance collateral circulation assessment. By minimizing reliance on explicit vascular segmentation, this approach enables the simulation of patient-specific flow dynamics without requiring detailed anatomical reconstructions. The model is designed to be computationally efficient via vasculature lumping to a certain extent without the loss of essential structural information, allowing for rapid simulation of collateral flow scenarios under varying conditions. Through this framework, it is hoped that it would advance the practical application of CFD in cerebrovascular research, bridging the gap between imaging-based assessments and predictive haemodynamic modelling.

2. METHOD

This study aims to create an explicit and computationally efficient vascular network model that includes LMAs, to study how they redistribute blood flow. Synthetic vascular trees are generated using anatomical data, such as bifurcation patterns and artery sizes from cadaver studies, with a stochastic approach to model variability in the generated structures. Six vascular trees, one for each vascular region, are selected for fluid simulations, with patient-specific 4D flow MRI data providing boundary conditions to reflect real physiological conditions. LMAs are then positioned to connect these trees, mimicking the restoration of blood flow in response to blockages. The placement of LMAs is optimized using iGA, which minimizes the difference between simulated flow rates and those measured by SPECT. This process is repeated over multiple iterations to generate different combinations of vascular trees and LMA configurations, ensuring that the best arrangements are found while adhering to physiological constraints. The overall goal is to identify the LMA placements under a range of potential patient-specific peripheral vasculature that recreate the blood flow redistribution shown in measured data.

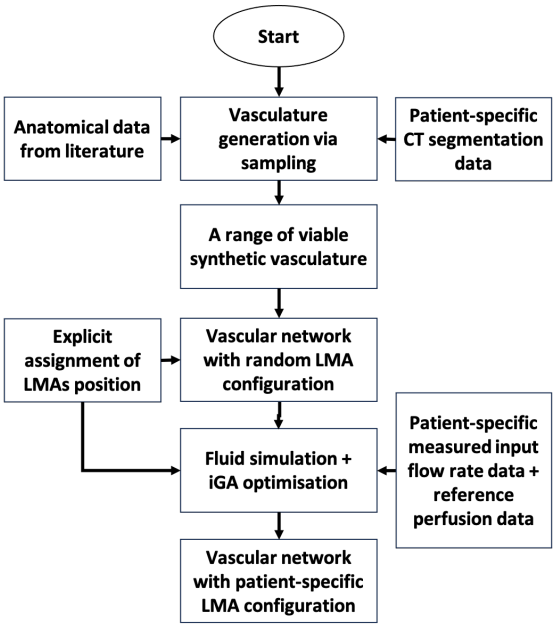

Figure 1. Flowchart depicting the process of deducing patient-specific LMA placement for blood flow redistribution using synthetic vascular trees and patient-specific flow rate data.

2.1. Data Acquisition

To generate a synthetic vasculature model for each of the six vascular regions, only the radii of the six efferent arteries of the CoW —the anterior, middle, and posterior cerebral arteries (ACA, MCA, PCA) on both hemispheres—are required. This differs from traditional methods that rely on imaging beyond the CoW, reducing the dependency on high-resolution medical images. Any loss in model resolution is addressed through uncertainty analysis, considering all plausible vasculature based on available data.

The inlet radii of the peripheral vasculature were derived from segmented CT images, with vessel centrelines extracted and smoothed using software "V-Modeler" [9]. The average radii along these centrelines were computed for use as model inlets.

Regional perfusion distributions were derived from SPECT imaging [10], with patient-specific vascular regions identified through shape registration between SPECT images and an atlas vascular region map. Voxel intensity values were then used to estimate regional flow rates. Since total cerebral blood flow (CBF) measured by SPECT and 4D Flow MRI differs, SPECT-derived flow rates were adjusted to match total CBF, which was determined by summing the MRI-measured flow rates of the internal carotid and basilar arteries, as 4D Flow MRI provides the most accurate measurements in larger arteries. Meanwhile, flow entering the peripheral regions through the six efferent arteries of the CoW was obtained from 4D Flow MRI. Similar to the SPECT-derived values, the outflow rates at the CoW were scaled based on inlet MRI data.

2.2. Sampling and Generation of Vascular Tree Models

To ensure anatomical accuracy, the vascular tree model is constructed based on observed anatomical structures, referencing Perlmutter and Rhoton [11], Gibo et al. [12], and Zeal and Rhoton [13]. Across all six vascular regions, the vasculature follows a consistent bifurcation pattern: perforating trunks traverse the brain, cortical branches extend perpendicularly, and perfusion arterioles supply the cortex. The model is represented as a graph, with nodes corresponding to bifurcation points and edges representing vessel segments, starting with an inlet node at the CoW, marking the entry to the peripheral vascular region. Given a list of candidate cortical branches from literature, each branch is probabilistically determined based on observed frequencies. If fenestration (multiple copies of the same branch) is observed, the number of copies is sampled from a Poisson distribution, and the branch radius is sampled from measured data ranges. After the first cortical branch radius is assigned, the subsequent perforating trunk segment radius is calculated using Murray's law, which states that the cube of the parent vessel radius equals the sum of the cubes of the daughter vessel radii. This process repeats for all candidate branches in the vascular region. If at any point the perforating trunk radius reduces to zero due to sampling variability, the entire process restarts from the first cortical branch candidate.

Perfusion arterioles extend from each cortical branch, assuming equal bifurcation at each level, until reaching the cut-off radius of 0.025 mm. Given depth d as the number of bifurcations from the cortical branch, the arteriole radius at depth d is given by Eq. (1):

$$r_d = r_0 \cdot \left(\frac{1}{2^{1/3}}\right)^d \tag{1}$$

Assuming a constant length-to-radius ratio $\lambda_{l/r}$, the vessel resistance is computed using Eq. (2), based on Poiseuille's law, which is derived from the Navier-Stokes equation under the assumptions of steady, incompressible flow in a cylindrical vessel:

$$R = \frac{8\mu \cdot l_{\text{lma}}}{\pi r^4} \tag{2}$$

Given the homogeneous structure of perfusion arterioles, the total resistance of the arteriole tree at depth d is obtained by series-parallel resistance aggregation, as described by Eq. (3):

$$R_{\text{eff}} = \sum_{k=0}^{d} \frac{R_k}{2^k} \tag{3}$$

Where the radius and resistance at each depth k can be calculated using Eq. (1) and Eq. (2). This reduces the number of nodes from $2^d + 1$ to just 2, significantly improving computational speed for LMA optimization, which is essential for the large number of fluid simulations required.

In the context of this model, an LMA's location is fully defined by the two arterioles it connects, characterized by three parameters: vascular region, cortical branch, and bifurcation depth. To incorporate an LMA, a new node representing its connection point is added between the cortical branch bifurcation and the distal end of its arteriole tree. The arteriole tree's resistance is split into upstream and downstream portions, ensuring efficient flow traversal while maintaining computational efficiency.

Figure 2 presents a schematic representation of a vascular tree, illustrating the node placements for LMA connections. Nodes represent bifurcation points, and edges correspond to blood vessel segments. Arrows indicates the direction of blood flow from inlet to outlet. Red dashed lines depict LMA connections to another vascular region.

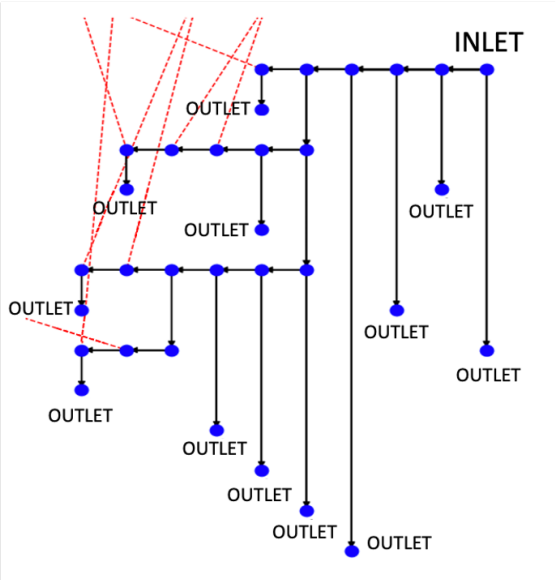

Figure 2. Schematic representation of a vascular tree

2.3. Fluid simulation

Blood flow in this study is simulated using a 0D haemodynamic model based on steady-state flow assumptions, where vessel segments are treated as resistive elements. Blood is modeled as an incompressible Newtonian fluid with a viscosity of 4.7 mPa·s.

The vascular network consists of six primary inlet nodes, corresponding to arterial branches from the CoW, and multiple outlet nodes representing cortical branch terminations. Flow rate boundary conditions are imposed at the inlet nodes, derived from patient-specific 4D Flow MRI data. At the outlet nodes, a fixed pressure value of 50 mmHg is assigned, which approximates typical pial arteriole pressures ($\sim 50\,\mu$m in diameter). Although physiological variability exists in outlet pressures, this fixed value serves as a practical approximation. Future iterations of the model could incorporate a venous compartment to dynamically compute outlet pressures, eliminating the need for fixed boundary conditions.

Pressure distribution within the vascular network is computed using a conductance-based approach, where each vessel segment is characterized by the inverse of its resistance. The pressure at each node is determined by solving the conservation of momentum equation, Eq. (4):

$$G_{ij}(p_i - p_j) = Q_{ij}, \tag{4}$$

where G_{ij} represents the conductance between nodes i and j, p_i and p_j denote the pressure at nodes i and j, respectively, and Q_{ij} represents the flow rate between the two nodes.

To satisfy mass conservation, the sum of all incoming and outgoing flows at each internal node must be zero. Mathematically, this is presented as Eq. (5).

$$\sum_j Q_{ij} = 0, \quad \forall i \in \mathcal{N}_{\text{int}}, \tag{5}$$

where $\mathcal{N}_{\text{int}}$ denotes the set of all internal nodes, excluding inlets and outlets.

Boundary conditions are imposed such that a prescribed net inflow $Q_i \neq 0$ is applied at inlet nodes, while outlet nodes have fixed pressure values. This formulation results in a sparse linear system for the unknown nodal pressures. To efficiently solve this system, the model employs the Compressed Sparse Column (CSC) format, which minimizes memory usage and computational cost. A direct solver optimized for sparse matrices is used, ensuring stability and efficiency in handling large vascular networks. Once the pressure field is computed, the flow rates through each vessel segment are determined based on Eq. (4). The total distal flow rate for each vascular region is obtained by summing the contributions from all outlet nodes within that region. The overall computational framework allows for rapid analysis, with the average runtime for solving the CSC system and determining node pressures being approximately 0.02 seconds.

2.4. Obtaining patient-specific LMA configuration

This section details the optimisation process to identify the LMA configurations that replicate observed flow redistribution in cerebral vasculature. Given the measured 4D flow MRI flow rates at inlets, the goal is to find the LMA configuration that produces regional distal flow rates that match the measured SPECT flow rates in each region. The distal flow rate $Q_{\text{com},h}$ for each vascular region h is determined by summing the flow rates at all outlet nodes within that region.

Given the discrete nature of the problem, where LMA placement is represented by a set of discrete decisions rather than continuous parameters, the problem is classified as a discrete combinatorial optimisation problem. The search space grows exponentially with the number of candidate locations, making an exhaustive search computationally infeasible. Therefore, an iGA was chosen to perform the optimisation. LMA configuration, encoded as a set of potential LMA locations, serves as the decision variable. Meanwhile, the cost function J, shown in Eq. 6, is defined as the RMS error between computed and observed flow rates.

$$J = \sqrt{\frac{1}{H}\sum_{\text{h}=1}^{H}(Q_{\text{Co,h}} - Q_{\text{Sp,h}})^2} \tag{6}$$

The constraints on formation of solution are as follows: (1) Only inter-vascular-region LMAs are considered, with connections defined based on previous studies. These include connections from the ACA to MCA superior trunk branches, PCA to MCA inferior trunk branches, ACA to PCA across hemispheres, and left ACA to right ACA. (2) The difference in radii at the connected arterioles is constrained to a maximum of 0.1 mm. This ensures that the assumption of arteriogenesis, by which LMAs form, requires connections between similarly sized arterioles. (3) Only arterioles that are at least three bifurcations downstream from the cortical branch are considered for LMA connections. This reflects the fact that LMAs most commonly form on the meningeal surface rather than within the cortical network. (4) The maximum number of LMAs allowed in any given configuration is set to 400, a value sufficiently high for the cases tested. It should be noted that, in practice, the number of LMAs in optimized configurations typically remains well below this upper bound.

Shear stress is a crucial factor in arteriogenesis, as the mechanical forces induced by blood flow through vessels promote endothelial activation and subsequent vessel remodelling [14]. In the context of the optimisation, a shear stress constraint is imposed

to prevent the formation of inefficient LMAs. The fluid shear stress (FSS) for a blood vessel, assuming Poiseuille flow and neglecting tortuosity, is given by Eq. 7.

$$\tau = \frac{4\mu Q}{\pi r^3} \tag{7}$$

The FSS constraint enforces that each LMA must maintain a minimum shear stress value for the connection to be valid in the solution. The minimum FSS limit is set at 2.5 Pascals, referencing the lower end of the range measured in [15].

The inherent uncertainty in SPECT measurements is assumed conservatively to be 10% [6]. Given this assumption, a solution is considered satisfactory if the residuals for each vascular region—i.e., the difference between the SPECT-derived and computed distal flow rates in the region—falls within 10% of the scaled SPECT flow rate. This ensures that the maximum discrepancy between the two values remains within the uncertainty range, effectively allowing the computed flow rate to be considered a match to the SPECT flow rate once it falls within this threshold. Mathematically, this can be expressed as Eq. 8.

$$\left|Q_{\mathrm{Co,\,h}} - Q_{\mathrm{Sp,h}}\right| \leq 0.05 \cdot Q_{\mathrm{Sp},h}, \quad \forall h \in \{1, 2, \ldots, H\} \tag{8}$$

At the start of the optimisation process, a set of 6 vascular tree models is chosen from a pre-generated pool of models. A population is initialised through random generation of valid solutions. To enhance the diversity of the search space and avoid premature convergence, the population is divided into multiple subpopulations, or "islands," that evolve independently. Regular migration between islands ensures the exchange of promising solutions. Once the initial population is set, each solution is evaluated by adding the encoded LMAs to the vasculature and performing fluid simulations. The cost of each solution is determined by comparing the computed distal flow rates with the target flow rates from SPECT data.

In the next phase, the rank-based exponential selection algorithm is applied to promote solutions with lower costs. Solutions are ranked based on their cost, and the probability of selection for reproduction is higher for solutions with better performance. After selection, crossover, mutation, and solution length adjustment operations are applied to generate new solutions for the next generation. Crossover involves combining parts of two parent solutions, while mutation introduces small random changes to the solutions. Length adjustment modifies the number of LMAs in a solution to explore different regions of the solution space. Solutions of the next generation is then evaluated, and the iterative process continues until a satisfactory solution is found, or when the maximum number of allowed generations has elapsed, at which point no successful LMA configuration is found for the set of vascular tree models. The models will be returned to the selection pool to be selected again.

3. RESULTS

Two patient cases are examined to illustrate the model's practical application: CEA12, a 68-year-old male with bilateral ICA stenosis (63% left, 65% right), and CEA13, a 72-year-old male with severe right ICA stenosis (91%). For each case, 2,000 vascular tree models were generated per vascular region, and 250 optimized peripheral vasculature-LMA configuration pairs were collected using a stochastic selection methodology. The time required to obtain one optimized LMA configuration varied, with CEA13 taking 257.93 ± 106.53 seconds and CEA12 taking 169.87 ± 118.20 seconds, both of which are acceptable in the scope of this study.

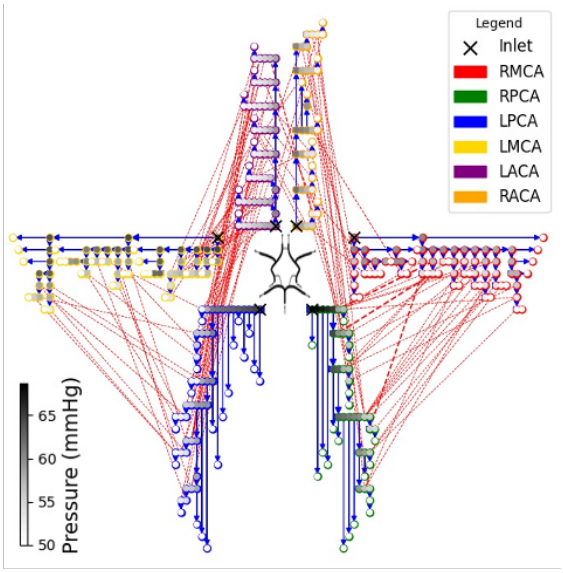

Figure 3. Representative model for case CEA12. Flow direction is indicated by blue arrows, and nodal pressure is visualized using in greyscale.

Figure 3 and 4 present schematic graph plots for cases CEA12 and CEA13, with one peripheral vasculature model from each case selected as a representative sample. In CEA13, due to stenosis on the right-hand side, the pressure in the left hemisphere is elevated compared to the right. LMAs are highlighted in red, with line thickness representing conductance of LMA. In CEA13, a greater number of high-conductance LMAs are observed between the left and right anterior cerebral arteries (ACA), reflecting an increased reliance on inter-hemispheric collateral flow. This recruitment of LMAs is driven by the pressure gradient across hemispheres, created by the single-sided stenosis in case CEA13. The pressure in the right PCA of case CEA13 is also higher, reflecting the reliance on perfusion via the healthy BA instead of the stenosed right ICA.

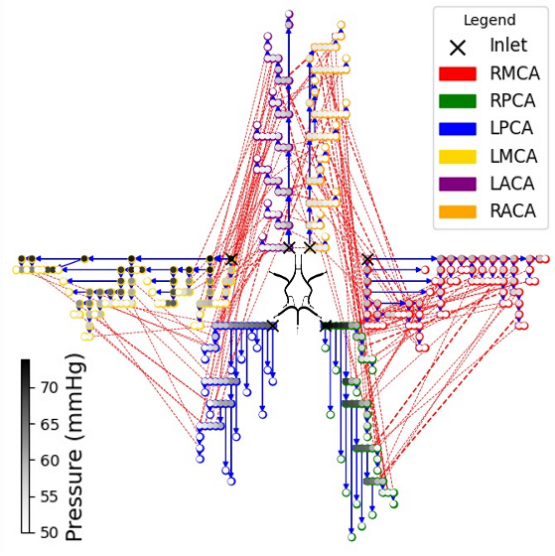

Figure 4. Representative model for case CEA13, in the same format as that for case CEA12.

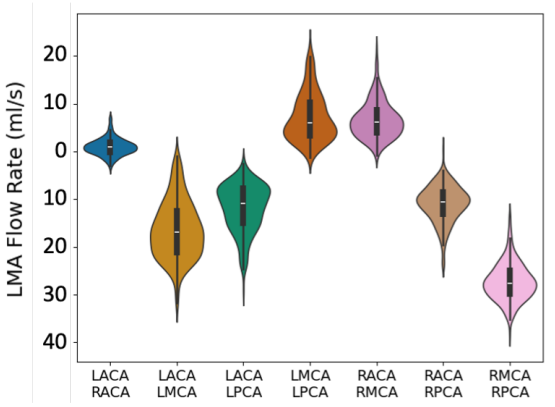

Figure 5. Redistribution of flow rates through each collateral pathway for case CEA12

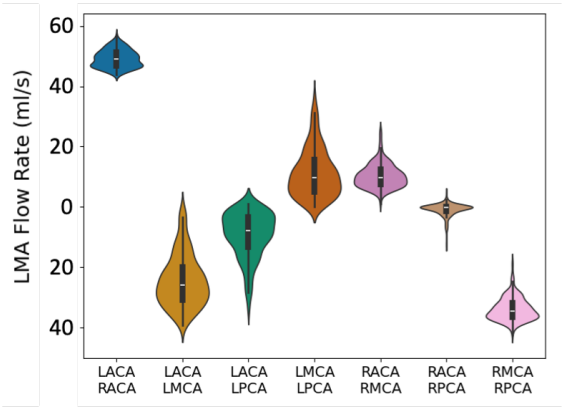

Figure 6. Redistribution of flow rates through each collateral pathway for case CEA13

Figure 5 and 6 present violin plots illustrating the redistribution of flow rates through each collateral pathway, with its pattern differing between cases. Flow rates positioned below zero indicate redistribution from the second vascular region in the label to the first, whereas positive values indicate flow in the opposite direction. In CEA13, inter-hemispheric flow accounts for 11.5% of the total cerebral blood flow, whereas in CEA12, it is significantly lower at 0.23%. Significant flow from right PCA to right MCA aligns with expectation of collateral flow from posterior to anterior circulation. The observed range of redistribution is a result of variations in the vascular tree structure, which alter the relative pressure distribution between regions, in turn leading to differences in LMA recruitment and adaptation. Notably, changes in the vascular structure do not result in unrealistic or excessive variability in flow redistribution patterns. The distribution remains unimodal, as confirmed by Hartigan's Dip Test, indicating a stable adaptation mechanism despite differences in vascular topology.

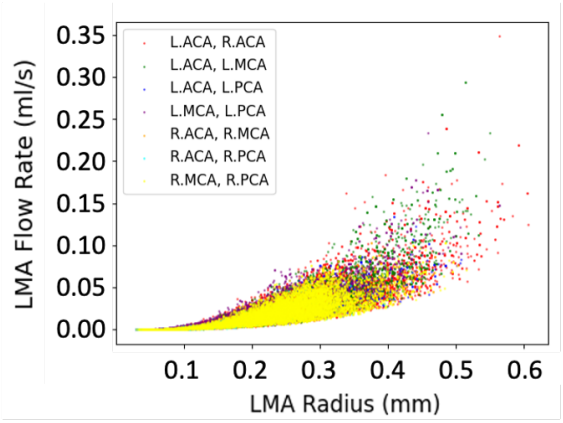

Figure 7. Flow rate vs. radius of LMA, CEA13

Figure 7 presents a flow rate versus radius plot for CEA13, illustrating the redistributed flow rate of each individual LMA across 250 optimized configurations as a function of its respective radius. Each dot represents a single LMA, with the colour scale indicating the associated collateral pathway. The fan-shaped void near the $y = 0$ line suggests that FSS constraint is functioning as intended, as LMAs with a high radius but low flow rate are correctly suppressed, with larger radius leading to higher flow rates in general. This confirms that the fluid simulation operates as expected.

Figure 8 presents a plot of pressure difference versus radius for CEA13, illustrating the pressure difference between the two arterioles connected by each LMA, plotted against their respective radii across all 250 optimized configurations. The results reveal a trade-off between radius and pressure difference. Due to the physiologically-based constraint that the radius difference between the two arterioles connected by an LMA must remain under 0.1 mm, LMAs with larger radii typically form between arteries at lower bifurcation depths, which are located

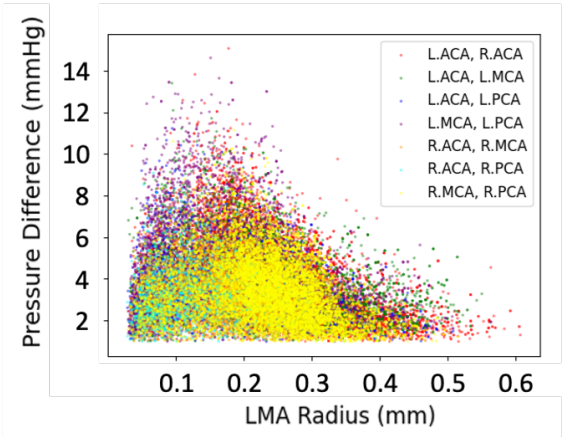

Figure 8. Pressure difference across LMA vs. their respective radii, CEA13

more proximally in the vascular tree. As pressure dissipates downstream, arteries at similar depths exhibit smaller pressure differences compared to arteries at significantly different depths, where the upstream end has a much higher pressure relative to the downstream end. In such cases where the pressure difference is favourable for more efficient redistribution, the smaller radius of the downstream arteriole limits the LMA's overall radius.

While the maximum pressure difference occurs around a radius of 0.2 mm, the maximum flow rate continues to increase with radius, despite lower pressure differences. This behaviour aligns with Poiseuille's equation, which states that flow rate is proportional to the pressure difference but inversely scales with the cube of the radius. Consequently, radius exerts a dominant influence over flow rate, reinforcing that the model accurately reflects the expected behaviour of LMAs from a fluid dynamics perspective.

Finally, it is important to note that the mean LMA radius for each case was found to be 0.212 ± 0.0927 mm for CEA13 and 0.169 ± 0.0857 mm for CEA12. These values are consistent with existing literature, with CEA12 showing a smaller LMA radius compared to CEA13. This difference is likely due to CEA12 needing to prioritize the pressure difference across LMAs by connecting upstream arterioles to downstream ones. Since the inherent pressure difference between vascular regions—and between arterioles at the upstream end of the cortical branch trees—is relatively small, CEA12 compensates by relying on the pressure difference generated by the depth disparity between these arteries.

4. DISCUSSION

This study employs a 0D model due to its suitability for capturing global flow distribution in a simplified and computationally efficient manner. The decision to explicitly compute the radius of each blood vessel segment, and directly derive resistance from anatomical parameters, eliminates the need for empirical tuning. This approach makes the model ideal for steady-state analysis of systemic haemodynamics, as outlined by Shi et al. [5]. It also retains flexibility and simplicity when modelling arterial flow redistribution.

One limitation of this study is the lack of capillary-level analysis, which is essential for understanding microvascular perfusion. Additionally, the model is relatively coarse, considering only six vascular regions, which introduces significant uncertainty in the redistribution of flow values. The study, however, lays the foundation for future research that will incorporate larger datasets and finer perfusion partitioning at the cortical region level. This would be particularly beneficial given the rapid advancements in imaging techniques that are less invasive, more affordable, and increasingly applicable in clinical settings [16]. The increased precision in these imaging techniques would reduce uncertainty in flow redistribution calculations. As more regions are considered, the model would be required to satisfy more complex redistribution conditions. While this adds difficulty, it ultimately leads to more precise and refined insights into haemodynamic behaviour.

Here, the model's scalability should be noted, as it can easily adapt to perfusion data of different precision levels by adjusting the partitioning of regions of interest. Currently, the model is based on just six vascular regions, but it can be extended down to the level of individual cortical branches. This flexibility will allow for the integration of more detailed pial perfusion data, which will contribute to advancing the understanding of local blood flow dynamics. Ultimately, this will enable the development of more accurate, patient-specific predictive models for stroke management.

Validation of both vasculature structure and LMA topology remains a challenging task. It is hoped that future advancements in imaging techniques will provide more quantitative data for validation, allowing for more robust assessments of the model's accuracy. The study is currently advancing in the direction of performing comparative analyses with a broader range of patient cases. This work aims to deepen the understanding of the relationship between variations in both LMA topology and overall vasculature network structure, particularly in response to changes in pressure environments, physiological conditions, and distal perfusion demands.

5. CONCLUSION

A 0D modelling framework that integrates synthetic vascular network generation with flow rate measurements to enhance the assessment of cerebral collateral circulation was introduced. This approach enables patient-specific simulations without requiring detailed vascular segmentation whilst taking in account peripheral collateral network, addressing

key limitations in traditional peripheral vasculature models, thus representing a step toward bridging the gap between imaging-based assessments and predictive haemodynamic modelling, offering a practical approach for investigating cerebrovascular haemodynamics in both research and clinical settings. Future work will focus on validating LMA topology and model performance, increasing model granularity, and expanding the analysis to a broader range of patient cases.

6. ACKNOWLEDGEMENTS

This work was supported by the Fugaku project titled *Development of human digital twins for cerebral circulation using Fugaku*, carried out at the RIKEN Center for Computational Science (Project ID: **hp240220**); as well as by the JSPS KAKENHI grant *Development of an analysis system of systemic-cerebral circulatory metabolism for stroke risk prediction* (Project ID: **22H00190**).

REFERENCES

[1] Odano, I., Tsuchiya, T., Nishihara, M., Sakai, K., Abe, H., and Tanaka, R., 1993, "Regional Cerebral Blood Flow Measured With N-Isopropyl-p- [123I] Iodoamphetamine and Its Redistribution in Ischemic Cerebrovascular Disease", *Stroke*, Vol. 24, pp. 1167–1172.

[2] Shuaib, A., Butcher, K., Mohammad, A., Saqqur, M., and Liebeskind, D., 2011, "Collateral blood vessels in acute ischaemic stroke: a potential therapeutic target", *The Lancet Neurology*, Vol. 10, pp. 909–921.

[3] Brozici, M., van der Zwan, A., and Hillen, B., 2003, "Anatomy and functionality of leptomeningeal anastomoses: a review", *Stroke*, Vol. 34 (11), pp. 2750–2762.

[4] Vander Eecken, H. M., and Adams, R. D., 1953, "The anatomy and functional significance of the meningeal arterial anastomoses of the human brain", *J Neuropathol Exp Neurol*, Vol. 12 (2), pp. 132–157.

[5] Shi, Y., Lawford, P., and Hose, R., 2011, "Review of zero-D and 1-D models of blood flow in the cardiovascular system", *Biomed Eng Online*, Vol. 10, p. 33.

[6] Zhang, H., Fujiwara, N., Kobayashi, M., Yamada, S., Liang, F., Takagi, S., and Oshima, M., 2016, "Development of a Numerical Method for Patient-Specific Cerebral Circulation Using 1D-0D Simulation of the Entire Cardiovascular System with SPECT Data", *Annals of biomedical engineering*, Vol. 44 (8), pp. 2351–2363.

[7] Ryu, J., Hu, X., and Shadden, S. C., 2015, "A Coupled Lumped-Parameter and Distributed Network Model for Cerebral Pulse-Wave Hemodynamics", *Journal of Biomechanical Engineering*, Vol. 137 (10), p. 101009.

[8] Ii, S., Kitade, H., Ishida, S., Imai, Y., Watanabe, Y., and Wada, S., 2020, "Multiscale modeling of human cerebrovasculature: A hybrid approach using image-based geometry and a mathematical algorithm", *PLoS Comput Biol*, Vol. 16 (6), p. e1007943.

[9] Kobayashi, M., Hoshina, K., Yamamoto, S., Nemoto, Y., Akai, T., Shigematsu, K., Watanabe, T., and Ohshima, M., 2015, "Development of an image-based modeling system to investigate evolutional geometric changes of a stent graft in an abdominal aortic aneurysm", *Circulation Journal*, Vol. 79, pp. 1534–1541.

[10] Yamada, S., Kobayashi, M., Watanabe, Y., Miyake, H., and Oshima, M., 2014, "Quantitative measurement of blood flow volume in the major intracranial arteries by using 123I-iodoamphetamine SPECT", *Clinical Nuclear Medicine*, Vol. 39 (10), pp. 868–873.

[11] Perlmutter, D., and Rhoton, A. L. J., 1978, "Microsurgical anatomy of the distal anterior cerebral artery", *Journal of Neurosurgery*, Vol. 49 (2), pp. 204–228.

[12] Gibo, H., Carver, C. C., Rhoton, A. L. J., Lenkey, C., and Mitchell, R. J., 1981, "Microsurgical anatomy of the middle cerebral artery", *Journal of Neurosurgery*, Vol. 54 (2), pp. 151–169.

[13] Zeal, A. A., and Rhoton, A. L. J., 1978, "Microsurgical anatomy of the posterior cerebral artery", *Journal of Neurosurgery*, Vol. 48 (4), pp. 534–559.

[14] Hoefer, I. E., van Royen, N., Buschmann, I. R., Piek, J. J., and Schaper, W., 2001, "Time course of arteriogenesis following femoral artery occlusion in the rabbit", *Cardiovascular Research*, Vol. 49 (3), pp. 609–617.

[15] Cheng, H., Chen, X., Zhong, J., Li, J., Qiu, P., and Wang, K., 2022, "Label-free measurement of wall shear stress in the brain venule and arteriole using dual-wavelength third-harmonic-generation line-scanning imaging", *Optics Letters*, Vol. 47 (21), pp. 5618–5621.

[16] Yamada, S., Otani, T., Ii, S., Ito, H., Iseki, C., Tanikawa, M., Watanabe, Y., Wada, S., Oshima, M., and Mase, M., 2024, "Modeling cerebrospinal fluid dynamics across the entire intracranial space through integration of four-dimensional flow and intravoxel incoherent motion magnetic resonance imaging", *Fluids and Barriers of the CNS*, Vol. 21 (1), p. 47.

Conference on Modelling Fluid Flow (CMFF'25)
The 19th International Conference on Fluid Flow Technologies
Budapest, Hungary, August 26-August 29, 2025

Effects of Wall Slip on Large-Scale Flow in Turbulent Rayleigh–Bénard Convection

Sai Ravi Gupta Polasanapalli[1,2,3], Marten Klein[2,3], Heiko Schmidt[2,3]

[1] Corresponding Author. E-mail: polasana@btu.de
[2] Chair of Numerical Fluid and Gas Dynamics, Faculty of Mechanical Engineering, Electrical and Energy Systems, Brandenburg University of Technology Cottbus-Senftenberg. Siemens-Halske-Ring 15A, 03046 Cottbus, Germany
[3] Scientific Computing Lab, Energy Innovation Center, Brandenburg University of Technology Cottbus-Senftenberg. Universitätsstraße 22, 03046 Cottbus, Germany

ABSTRACT

The current study investigates the effects of surface boundary conditions—no-slip, free-slip, and finite-slip—on flow dynamics and heat transfer in turbulent Rayleigh–Bénard (RB) convection for different Prandtl numbers. Using a three-dimensional lattice Boltzmann method (LBM) solver in direct numerical simulation (DNS) mode, simulations are performed for three Prandtl numbers $Pr = 0.786, 4.38, 10$ and two Rayleigh numbers $Ra = 2 \times 10^6, 10^7$. The aim is to understand how surface conditions influence flow patterns, thermal mixing, and heat transfer efficiency in a cubic cavity with heated bottom and cooled top walls. Results show that free-slip conditions significantly enhance heat transfer, yielding higher Nusselt numbers due to thinner thermal boundary layers and stronger convective currents. In contrast, finite-slip conditions produce results similar to no-slip cases, indicating minimal impact for the slip lengths considered. The results demonstrate that surface boundary conditions play a role in modulating flow dynamics and heat transfer in RB convection.

Keywords: Lattice Boltzmann method (LBM), Navier-slip, Prandtl number effects, Rayleigh–Bénard (RB) convection, Surface boundary conditions, Turbulent flows.

NOMENCLATURE

H	$[m]$	Cavity height
Nu	$[-]$	Nusselt number
Pr	$[-]$	Prandtl number
Ra	$[-]$	Rayleigh number
TKE	$[m^2/s^2]$	Turbulent kinetic energy
g	$[m/s^2]$	acceleration due to gravity
rms	$[-]$	Root mean square
x, y, z	$[-]$	Coordinates
T_h	$[K]$	Bottom wall temperature
$T_\mathbf{c}$	$[K]$	Top wall temperature
$U_\mathbf{b}$	$[m/s]$	Free-fall velocity
ΔT	$[K]$	Temperature difference
β	$[1/K]$	Thermal expansion coefficient
κ	$[m^2/s]$	Thermal diffusivity
ν	$[m^2/s]$	Kinematic viscosity

1. INTRODUCTION

Surface coatings play a pivotal role in engineering applications, offering benefits such as drag reduction, corrosion resistance, wear resistance, and enhanced surface properties like thermal and electrical insulation. These coatings not only improve durability and efficiency but also passively influence scalar transfer in technical flows by modifying surface energy properties and altering boundary conditions. Flows over slippery surfaces are prevalent in both natural phenomena and industrial applications [1, 2]. Hydrophobic and super-hydrophobic surfaces, in particular, are widely used for drag reduction and self-cleaning in transportation systems. Numerically, the hydrophobicity of such surfaces can be modeled using tailored slip velocity boundary conditions.

A common mathematical framework for these applications involves the use of a finite slip length formulation. The Navier slip length, defined as the distance from the surface to the point where the extrapolated wall-parallel velocity component vanishes, is a standard choice [3]. A slip length of zero corresponds to a no-slip surface, while an infinite slip length represents a free-slip surface. Typical slip lengths range from 100 nm for hydrophobic surfaces to 100 μm for super-hydrophobic surfaces [4].

Previous studies ([5, 6]) have explored the effects of slip length in turbulent channel flows, focusing on isotropic and anisotropic slip conditions for drag reduction. In the context of Rayleigh–Bénard (RB) convection, Mayeed et al. (2016) [7] demonstrated heat transfer enhancement using hydrophobic bottom and hydrophilic top walls, though their work was limited to two-dimensional flows and low Rayleigh numbers. Experimental studies by Wu et al. (2013) [8] further investigated the impact of surface wettability on RB convection.

In this study, we investigate the influence of various surface conditions on turbulent Rayleigh–Bénard convection, a canonical problem involving fluid confined in a cubic cavity with a heated bottom wall, a cooled top wall, and adiabatic side walls [9, 10]. Three-dimensional numerical simulations are performed using a lattice Boltzmann method (LBM) solver [11], which is well-suited for efficient upscaling to high Rayleigh number regimes with strong thermal forcing. The LBM solver operates in direct numerical simulation (DNS) mode, ensuring full-scale resolution of the flow dynamics. The primary objective is to examine the effects of no-slip, free-slip, and finite-slip boundary conditions on flow and heat transfer characteristics for fluids and chemical solvents with different Prandtl numbers.

2. FLOW SETUP AND CONFIGURATION

Figure 1 illustrates the schematic setup for Rayleigh–Bénard convection in a cubic cavity of dimensions $H \times H \times H$ in the x-, y-, and z-directions, respectively, where H is the height and serves as the characteristic length scale. The simulations are parameterized by the Rayleigh number, $Ra = \frac{\beta g H^3 \Delta T}{\nu \kappa}$, and the Prandtl number, $Pr = \frac{\nu}{\kappa}$. Here, β is the volumetric expansion coefficient of the fluid, g is the gravitational acceleration, and $\Delta T = T_h - T_c$ is the temperature difference across the cavity height H. ν and κ represent the kinematic viscosity and thermal diffusivity of the fluid, respectively.

The cubic cavity is bounded by walls on all sides. The bottom wall is heated and maintained at a higher temperature T_h, while the top wall is cooled and kept at a lower temperature T_c. The vertical side walls are treated as adiabatic, meaning no heat flux is allowed across them. For velocity boundary conditions, three configurations are considered: no-slip, free-slip, and Navier-slip. In the no-slip condition, all velocity components on the walls are set to zero. For the free-slip condition, the wall-normal velocity component is zero, while the wall-parallel components are specified using a Neumann boundary condition. In the finite-slip (Navier-slip) cases, the wall-normal velocity component is zero, and the wall-parallel components follow the Navier-slip condition: $u_s = l_s \frac{\partial u}{\partial n}$ as illustrated in Figure 2, where u is the wall-parallel velocity component, n is the wall-normal direction, and l_s is the slip length. The simulations are performed for the two Rayleigh numbers $Ra = 2 \times 10^6$, 10^7 and three Prandtl numbers $Pr = 0.786$ (air), 4.38 (water),10 (ethyl alcohol). For the finite-slip cases, isotropic slip lengths of $l_s = 0.00005, 0.0001, 0.0005$ are considered.

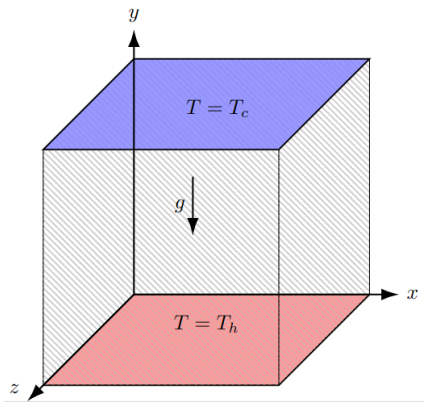

Figure 1. Schematic diagram of the cuboidal Rayleigh–Bénard convection set-up.

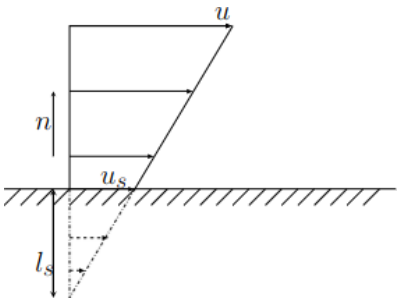

Figure 2. Schematic of the Navier-slip boundary condition parameterization based on a slip velocity u_s and a slip length l_s.

3. OVERVIEW OF THE NUMERICAL METHODOLOGY

The current study employs an off-lattice Boltzmann method (OLBM). The numerical solver implements the discrete velocity and temperature Boltzmann equations within the lattice Boltzmann method (LBM) framework to simulate flow and thermal fields. The implementation is based on a finite-difference approach, specifically designed for non-isothermal flows under the linear Oberbeck–Boussinesq approximation. To enhance numerical stability, the LBM collision term is treated implicitly. Time integration of the LBM equations is performed using a characteristic-based Lax–Wendroff scheme, while the advection terms are discretized using an explicit second-order central-difference scheme. To mitigate oscillations arising from non-dispersive central difference schemes, a sixth-order compact spatial filter is applied. The solver has been validated through various benchmark problems in earlier studies [11, 12, 13], and the same solver is utilized for the present simulations.

Here, a stretched grid to achieve finer resolution near the wall boundaries, ensuring accurate capture of boundary layer dynamics. Initial perturbations, analogous to those proposed by Schoppa and Hussain (2000) [14], are introduced to the conductive initial condition. These finite-amplitude perturbations are designed to trigger convective instabilities, accelerating the transition from the initial state.

4. RESULTS

In a previous study, preliminary results on the influence of different surface boundary conditions (no-slip, free-slip, and finite Navier-slip) and varying slip lengths on RB convection had been obtained for a fixed Rayleigh number $Ra = 2 \times 10^6$ and Prandtl number $Pr = 4.38$. In the present study, we extend this analysis to explore the effects of surface boundary conditions on RB convection for fluids with different Prandtl numbers ($Pr = 0.786, 4.38, 10$). Statistical data were collected over sufficiently long time periods to ensure statistical independence. The analysis includes spanwise and time-averaged isotherm and flow pattern contours, as well as profiles of mean temperature $\langle T \rangle$, turbulent kinetic energy (TKE), and root mean square (RMS) fluctuation of temperature (T_{rms}) along the cavity height for each case. The impact on heat transfer is quantified using the Nusselt number (Nu). Temperature is normalized by $\Delta T = T_h - T_c$. Velocity components are normalized using the free-fall velocity $U_b = \sqrt{\beta g \Delta T H}$ as the bulk velocity scale. TKE and T_{rms} are normalized using U_b^2 and ΔT, respectively.

4.1. Effect on flow and thermal patterns

The formation of convection rolls or vortex modes is discussed in this section for different surface boundary conditions for $Ra = 2 \times 10^6$ and varying Pr. Additionally, results are presented for $Ra = 10^7$ and $Pr = 4.38$. Instantaneous flow contours reveal multiple chaotic flow patterns for no-slip and finite-slip boundary conditions, whereas a single large vortex is observed for free-slip cases. Flow reversal behavior is evident in instantaneous contours for all configurations except the free-slip (FS) case. Figures 3 - 11 present spanwise and time-averaged isotherm and streamline contours, illustrating the temperature distribution and flow patterns across the domain. While the x- and z-directions are geometrically equivalent in our cubic domain, the choice of spanwise averaging along the z-direction is made for consistency in visualization. Arrows indicate flow direction, with their lengths representing velocity magnitude, while the background color reflects the temperature field. The vortex patterns arise due to the buoyancy force generated by the temperature gradient between the top and bottom walls. In RB convection, the structure of these rolls typically depends on the aspect ratio of the domain and significantly influences heat transfer rates. In this study, the aspect ratio is fixed at 1 for all simulations. The surface boundary conditions induce substantial changes in both the flow and thermal fields.

A finite slip length of $l_s = 0.0005$ is considered for slip conditions for all Prandtl number cases. The results corresponding to $Pr = 4.38$ are presented in Figures 3 - 5 for different surface conditions. For $Pr = 4.38$ and 10, the flow patterns under no-slip and finite-slip conditions exhibit a (2, 2) vortex mode, characterized by two vortices along each horizontal and vertical direction. Usually, the (M, N) vortex mode denotes a flow pattern with M vortices in the horizontal plane and N vortices along the vertical direction. The (2, 2) vortex mode is attributed to the relatively low thermal diffusivity compared to momentum diffusivity at higher Prandtl numbers. As a result, heat is transported more slowly than momentum, and the flow is dominated by viscous effects. The results corresponding to $Pr = 0.786$ are presented in Figures 6 - 8 for different surface conditions. In contrast to higher Prandtl number cases, for the lower Prandtl number ($Pr = 0.786$), the flow under no-slip and finite-slip conditions is dominated by a single large diagonal vortex, accompanied by two smaller vortices near the other corners. This behavior arises because thermal diffusion dominates at lower Prandtl numbers, allowing heat to diffuse more rapidly than momentum. The weaker momentum diffusion promotes the formation of larger coherent structures, while the smaller corner vortices result from local recirculation effects and nonlinear interactions near the boundaries. Notably, higher velocity magnitudes are observed for the lower Prandtl number case, with velocity magnitudes decreasing as the Prandtl number increases. For free-slip boundary conditions, a single large vortex is observed across all Prandtl numbers. This is consistent with the reduced frictional resistance at the boundaries, which allows the flow to organize into a more coherent, large-scale structure.

The results for $Ra = 10^7$ and $Pr = 4.38$ are illustrated in Figures 9 - 11, showcasing surface conditions. Two different finite-slip lengths ($l_s = 0.0001$ and 0.00005) are considered in the simulations. At the higher Rayleigh number $Ra = 10^7$, the flow becomes more turbulent, and the influence of buoyancy forces dominates over viscous effects. Under no-slip and finite-slip conditions, the flow patterns are characterized by a single large diagonal vortex accompanied by two smaller corner vortices, even for the higher Prandtl number $Pr = 4.38$. This behavior is attributed to the strong buoyancy forces and turbulent mixing at higher Ra, which overcome the stabilizing effect of viscosity. The two smaller corner vortices are secondary flows driven by the interaction of the primary vortex with the boundaries. While the no-slip and finite-slip cases exhibit similar flow patterns, the finite-slip case with $l_s = 0.00005$ results in lower velocity magnitudes compared to the no-slip case. Simulations for free-slip boundary conditions at $Ra = 10^7$ are forthcoming and will be addressed

elsewhere.

4.2. Effect on flow and thermal statistics

In this section, the variation of first-order and second-order statistical quantities along the cavity height is presented for different boundary conditions. Horizontal (x-z plane) averages of statistical quantities are presented in Figures 12 - 15 , providing a detailed understanding of the spatial distribution of flow and thermal properties in the Rayleigh-Bénard convection. Figures 12, 13 show the non-dimensionalized mean temperature profiles along the cavity height for $Ra = 2 \times 10^6$ and various Prandtl numbers (Pr = 0.786, 4.38, and 10). The mean temperature profiles for free-slip cases exhibit steeper gradients near the walls compared to no-slip and finite-slip conditions. This is due to the higher flow velocities near the walls in the free-slip configurations, which result in thinner thermal boundary layers and enhanced heat transfer. The finite-slip profiles are similar to those of the no-slip case, indicating that the slip length considered here (l_s = 0.0005) has a small effect on the thermal boundary layer. The thermal diffusion is dominant in the lower Prandtl number (Pr = 0.786) cases, resulting in smoother temperature profiles.

The profiles of non-dimensionalized turbulent kinetic energy (TKE) along the cavity height are presented in Figure 14 for different Prandtl numbers (Pr = 0.786, 4.38, and 10) and boundary conditions. TKE is a key measure of the intensity of turbulent fluctuations in the flow. In free-slip cases, the fluid near the walls experiences minimal frictional resistance, allowing for higher flow velocities and stronger turbulent fluctuations. As a result, the TKE values are significantly larger for free-slip boundary conditions compared to no-slip and finite-slip cases across all Prandtl numbers. The absence of wall friction in free-slip configurations enhances the turbulence intensity, leading to more mixing within the flow. This behavior is consistent with the observed steeper temperature gradients and higher heat transfer rates in free-slip cases, as discussed earlier. The Prandtl number influences the TKE distribution along the vertical coordinate. At lower Prandtl numbers (Pr = 0.786), thermal diffusion dominates over momentum diffusion, resulting in larger flow velocities and stronger turbulent fluctuations. Consequently, the TKE values are higher for the Pr = 0.786 case compared to the higher Prandtl number cases. The difference between finite-slip and no-slip cases is also more pronounced at lower Prandtl numbers, with finite-slip conditions showing slightly larger TKE values due to the reduced frictional resistance at the walls. For higher Prandtl numbers, the TKE values are lower due to the increased viscous damping of turbulent fluctuations. The difference between no-slip and finite-slip cases is relatively small, indicating that the effect of partial slip on turbulence intensity diminishes for higher Prandtl numbers.

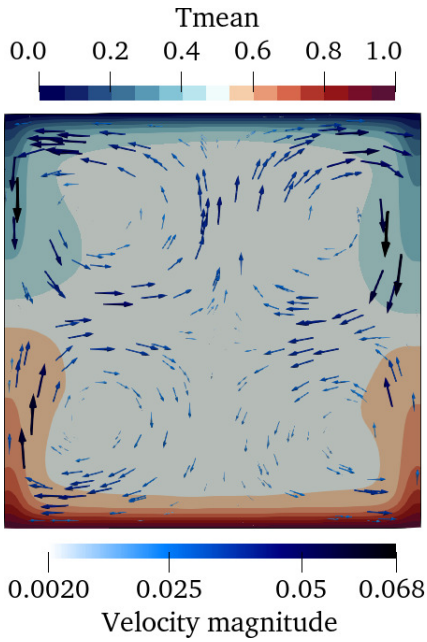

Figure 3. Time- and spanwise-averaged mean velocity vectors (arrows) and temperature distribution (colored contours) for the no-slip case at $Ra = 2 \times 10^6$ and Pr = 4.38.

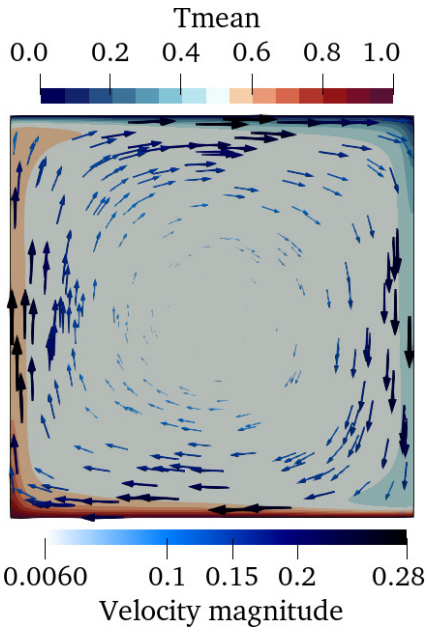

Figure 4. Time- and spanwise-averaged mean velocity vectors (arrows) and temperature distribution (colored contours) for the free-slip case at $Ra = 2 \times 10^6$ and Pr = 4.38.

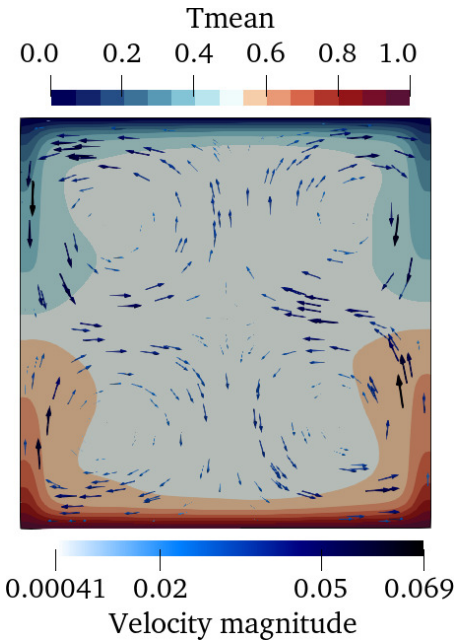

Figure 5. Time- and spanwise-averaged mean velocity vectors (arrows) and temperature distribution (colored contours) for the finite-slip case at $Ra = 2 \times 10^6$ and $Pr = 4.38$.

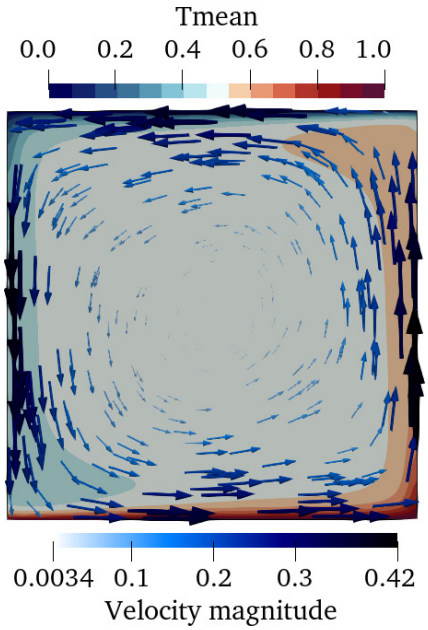

Figure 7. Time- and spanwise-averaged mean velocity vectors (arrows) and temperature distribution (colored contours) for the free-slip case at $Ra = 2 \times 10^6$ and $Pr = 0.786$.

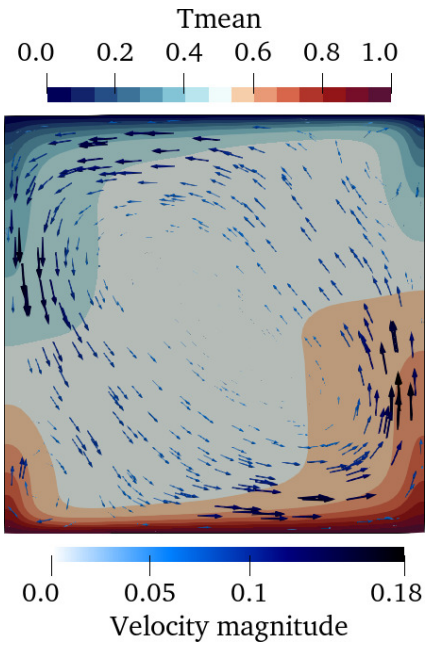

Figure 6. Time- and spanwise-averaged mean velocity vectors (arrows) and temperature distribution (colored contours) for the no-slip case at $Ra = 2 \times 10^6$ and $Pr = 0.786$

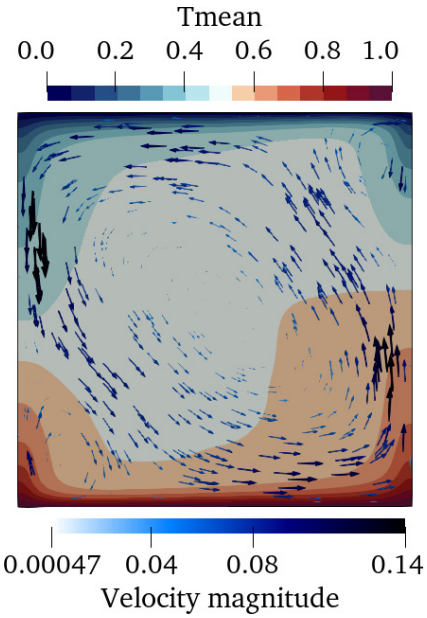

Figure 8. Time- and spanwise-averaged mean velocity vectors (arrows) and temperature distribution (colored contours) for the finite-slip case at $Ra = 2 \times 10^6$ and $Pr = 0.786$.

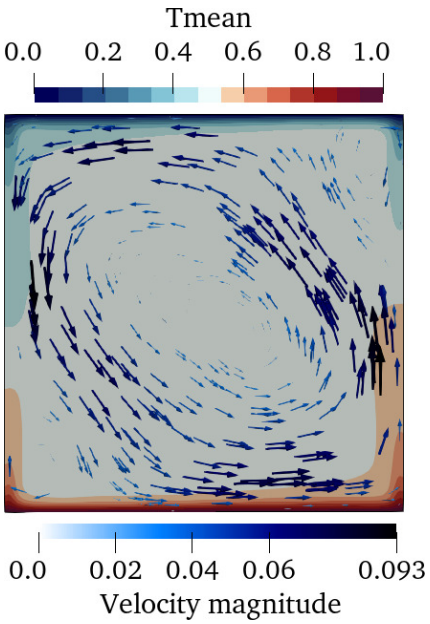

Figure 9. Time- and spanwise-averaged mean velocity vectors (arrows) and temperature distribution (colored contours) for the no-slip case at $Ra = 10^7$ and $Pr = 4.38$.

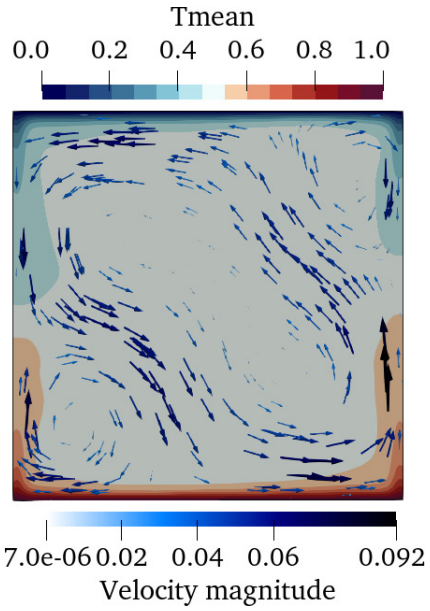

Figure 10. Time- and spanwise-averaged mean velocity vectors (arrows) and temperature distribution (colored contours) for the finite-slip with $l_s = 0.0001$ case at $Ra = 2 \times 10^6$ and $Pr = 4.38$.

The profiles of non-dimensionalized root mean square (RMS) temperature fluctuations (T_{rms}) along the cavity height are shown in Figure 15 for different Prandtl numbers and boundary conditions at $Ra = 2 \times 10^6$. The T_{rms} profiles provide insights into the intensity of thermal fluctuations and the efficiency of thermal mixing in Rayleigh-Bénard con-

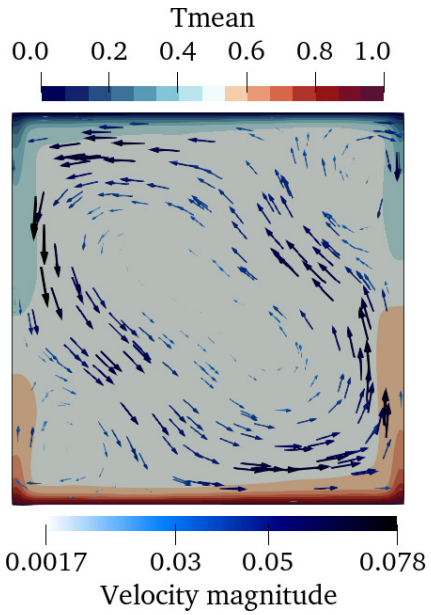

Figure 11. Time- and spanwise-averaged mean velocity vectors (arrows) and temperature distribution (colored contours) for the finite-slip with $l_s = 0.00005$ case at $Ra = 2 \times 10^6$ and $Pr = 4.38$.

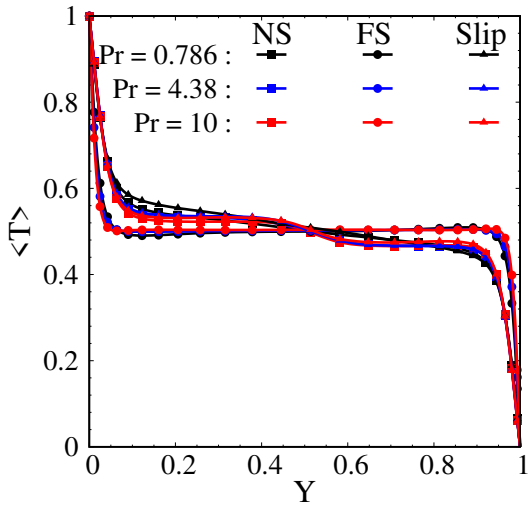

Figure 12. Vertical profiles of the mean temperature.

vection. The steeper gradients near the walls in free-slip cases indicate a thinner thermal boundary layer, which is consistent with the higher heat transfer rates observed in these configurations. The higher T_{rms} values near the walls in free-slip cases are because of intense thermal mixing. The difference between finite-slip and no-slip cases is small, indicating that the slip length considered here ($l_s = 0.00050$) has a minimal effect on the thermal fluctuations. The T_{rms} profiles look smoother for lower Prandtl numbers because of the stronger diffusion effects.

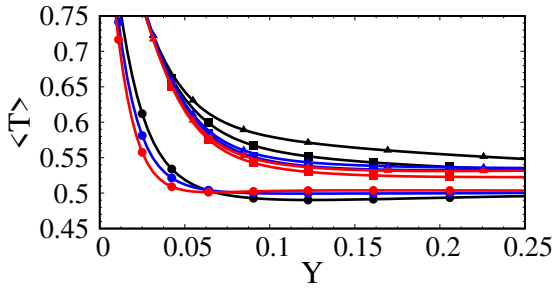

Figure 13. Zoomed-in view of the mean temperature profiles from Figure 12 showing the vicinity of the bottom wall.

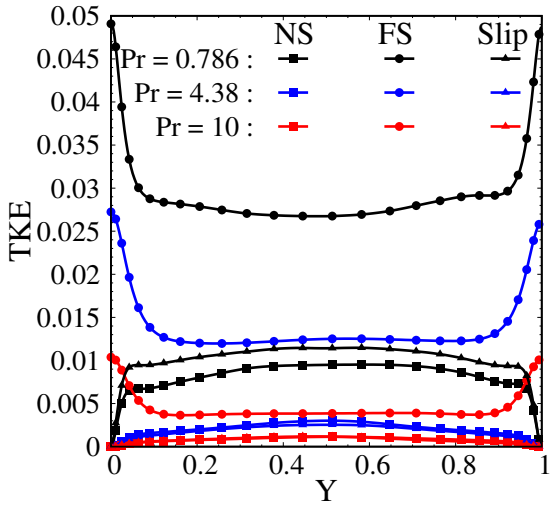

Figure 14. Vertical profiles of the TKE.

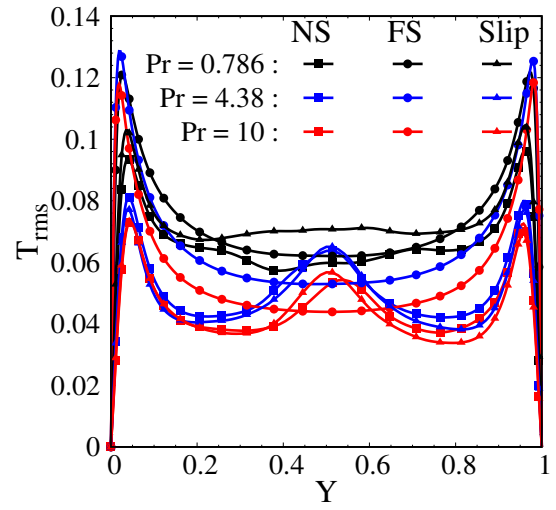

Figure 15. Vertical profiles of the RMS fluctuation temperature.

4.3. Effect on heat transfer

The Nusselt number (Nu) is a key dimensionless parameter used to quantify the heat transfer rate in convective systems. In this study, the overall mean Nusselt number is computed as the area average of $Nu = -\frac{\partial \langle T \rangle}{\partial y} / \left(\frac{\Delta T}{H}\right)$ over the top and bottom walls. The Nusselt number provides a measure of the efficiency of convective heat transfer relative to conductive heat transfer.

The Nusselt numbers for different cases are presented in Table 1. In free-slip cases, the fluid experiences no frictional resistance at the walls, allowing for higher flow velocities near those boundaries. This results in a thinner thermal boundary layer (see Figure 13), which significantly enhance the heat transfer rate. The free-slip condition enables the fluid to move more freely near the walls, increasing thermal gradients and promoting stronger convective heat transfer. As a result, the free-slip condition consistently yields higher Nusselt numbers compared to no-slip and finite-slip conditions across all Prandtl numbers investigated. Notably, the enhancement in heat transfer is most pronounced for $Pr = 10$, where the Nusselt number increases 170% compared to the no-slip case. This is attributed to the combined effects of reduced viscous damping and enhanced thermal gradients at higher Prandtl numbers. Finite-slip boundary conditions, which allow partial slip at the walls, result in heat transfer rates that are nearly identical to those observed for no-slip conditions. This suggests that the finite-slip length considered here ($l_s = 0.0005$) is insufficient to significantly alter the flow dynamics or heat transfer characteristics compared to the no-slip condition. At the higher Rayleigh number $Ra = 10^7$ and $Pr = 4.38$, the heat transfer rates are significantly higher due to the increased buoyancy-driven turbulence. These results indicate that the finite-slip boundary conditions result in only minor changes in heat transfer at high Rayleigh numbers. A small increment in the Nusselt number is observed for the finite-slip case $l_s = 0.0001$. Even at higher turbulent Rayleigh numbers, the effect of partial slip on heat transfer remains limited for the slip lengths considered in this study.

Table 1. Nusselt number obtained from the different boundary conditions simulations.

Ra	Pr	Walls	Nu
2×10^6	0.786	No-slip	10.27
2×10^6		Free-slip	21.43
2×10^6		Slip $l_s = 0.0005$	10.30
2×10^6	4.38	No-slip	9.97
2×10^6		Free-slip	19.99
2×10^6		Slip $l_s = 0.0005$	9.90
2×10^6	10	No-slip	9.81
2×10^6		Free-slip	26.55
2×10^6		Slip $l_s = 0.0005$	9.75
10^7	4.38	No-slip	16.76
10^7		Slip $l_s = 0.0001$	17.27
10^7		Slip $l_s = 0.00005$	16.74

5. CONCLUSION

This study investigates the effects of different surface boundary conditions—no-slip, free-slip, and finite-slip—on flow dynamics and heat transfer in turbulent Rayleigh–Bénard convection for various Prandtl numbers (Pr = 0.786, 4.38, and 10). Three-dimensional numerical simulations were performed using an off-lattice Boltzmann method solver in DNS mode. Free-slip boundary conditions consistently produce a single large vortex across all Prandtl numbers, as the absence of wall friction allows for stronger convective currents and more efficient thermal mixing. Free-slip conditions significantly enhance heat transfer, producing higher Nusselt numbers due to thinner thermal boundary layers and stronger convective currents, while finite-slip conditions yield results similar to those of no-slip cases, indicating minimal impact for the slip lengths considered. Flow patterns vary with Prandtl number, with higher Pr fluids forming smaller vortices and lower Pr fluids exhibiting larger coherent structures. At $Ra = 10^7$, increased turbulence leads to a large vortex flow pattern, even for higher Pr. These findings highlight the critical role of surface conditions in modulating flow dynamics and heat transfer, with free-slip surfaces offering significant thermal performance improvements. Future studies will explore the effect of slip on larger aspect ratio domains and conduct detailed analyses of boundary layers and energy budgets to further advance practical applications.

ACKNOWLEDGEMENT

This research is supported by the German Federal Government, the Federal Ministry of Research, Technology and Space, and the State of Brandenburg within the framework of the joint project EIZ: Energy Innovation Center (project numbers 85056897 and 03SF0693A) with funds from the Structural Development Act for coal-mining regions. The authors gratefully acknowledge the provision of computing resources by the National High Performance Computing Alliance (NHR@ZIB and NHR-NORD@Göttingen) under the project number bbi00022.

REFERENCES

[1] Tritton, D., 1975, "Internally heated convection in the atmosphere of Venus and in the laboratory", *Nature*, Vol. 257 (5522), pp. 110–112.

[2] Choi, C.-H., and Kim, C.-J., 2006, "Large slip of aqueous liquid flow over a nanoengineered superhydrophobic surface", *Physical review letters*, Vol. 96 (6), p. 066001.

[3] Rothstein, J. P., 2010, "Slip on superhydrophobic surfaces", *Annual review of fluid mechanics*, Vol. 42 (1), pp. 89–109.

[4] Voronov, R. S., Papavassiliou, D. V., and Lee, L. L., 2008, "Review of fluid slip over superhydrophobic surfaces and its dependence on the contact angle", *Industrial & Engineering Chemistry Research*, Vol. 47 (8), pp. 2455–2477.

[5] Min, T., and Kim, J., 2004, "Effects of hydrophobic surface on skin-friction drag", *Physics of Fluids*, Vol. 16 (7), pp. L55–L58.

[6] Fukagata, K., Kasagi, N., and Koumoutsakos, P., 2006, "A theoretical prediction of friction drag reduction in turbulent flow by superhydrophobic surfaces", *Physics of fluids*, Vol. 18 (5).

[7] Mayeed, M. S., Patnaik, S. S., and Mitchell, R., 2016, "Heat Transfer Enhancement Using Miniaturized Channel Sections With Surface Modifications", *Proceedings of the ASME 2016 IMECE2016*, ASME, USA.

[8] Wu, C. H., Huang, Y. S., Kuo, L. S., and Chen, P. H., 2013, "The effects of boundary wettability on turbulent natural convection heat transfer in a rectangular enclosure", *International Journal of Heat and Mass Transfer*, Vol. 63, pp. 249–254.

[9] Scheel, J. D., Emran, M. S., and Schumacher, J., 2013, "Resolving the fine-scale structure in turbulent Rayleigh–Bénard convection", *New Journal of Physics*, Vol. 15 (11), p. 113063.

[10] Wagner, S., and Shishkina, O., 2015, "Heat flux enhancement by regular surface roughness in turbulent thermal convection", *Journal of Fluid Mechanics*, Vol. 763, pp. 109–135.

[11] Polasanapalli, S. R. G., and Anupindi, K., 2022, "Large-eddy simulation of turbulent natural convection in a cylindrical cavity using an off-lattice Boltzmann method", *Physics of Fluids*, Vol. 34 (3), p. 035125.

[12] Polasanapalli, S. R. G., and Anupindi, K., 2024, "Turbulent mixed convection in a horizontal cylindrical cavity with the off-lattice Boltzmann method", *International Journal of Heat and Mass Transfer*, Vol. 225, p. 125395.

[13] Polasanapalli, S. R. G., Klein, M., and Schmidt, H., 2024, "Towards stochastic subgrid-scale modeling of turbulent thermal convection in an under-resolved off-lattice Boltzmann method", *PAMM*, Vol. 24 (1), p. e202300223.

[14] Schoppa, W., and Hussain, F., 2000, "Coherent structure dynamics in near-wall turbulence", *Fluid Dynamics Research*, Vol. 26 (2), pp. 119–139.

Conference on Modelling Fluid Flow (CMFF'25)
The 19th International Conference on Fluid Flow Technologies
Budapest, Hungary, August 26-August 29, 2025

Numerical Investigation on the Influence of Internal Carotid Artery Geometry on Wall Shear Stress Distribution

Jianqing FENG[1], Yanbo LIANG[2], Yan CHEN[3], Marie OSHIMA[4]

[1] Department of Mechanical Engineering, Graduate School of Engineering, The University of Tokyo, 7-3-1 Hongo, Bunkyo-ku, Tokyo, Japan. Tel.: +81 080 3448 6133, E-mail: fjq@iis.u-tokyo.ac.jp
[2] Department of Mechanical Engineering, Graduate School of Engineering, The University of Tokyo. E-mail: liangyanbo00@gmail.com
[3] Interfaculty Initiative in Information Studies, The University of Tokyo. E-mail: marie@iis.u-tokyo.ac.jp
[4] Interfaculty Initiative in Information Studies, The University of Tokyo. E-mail: chenyan@iis.u-tokyo.ac.jp

ABSTRACT

The internal carotid artery (ICA) is the primary blood supply to the brain and exhibits complex geometric variations that influence hemodynamic behavior. In particular, the highly curved siphon region is associated with elevated wall shear stress (WSS), which may cause damage to endothelial cells and contribute to disease progression. However, the quantitative relationship between ICA morphology and WSS distribution remains unclear. To clarify this relationship, we developed a novel ICA centerline classification method based on spatial geometric features and categorized the centerlines extracted from the BraVa dataset into four types: U, V, C, and S. Computational fluid dynamics (CFD) simulations were then conducted to analyze the WSS distribution in each classified geometry and to reveal differences in flow patterns. The results show that the U-type has two high-curvature regions, causing large WSS variations. The V-type has concentrated curvature, leading to a localized high WSS region. C-type torsion and non-coplanar bends create a complex WSS distribution. The S-type resembles the U-type but has a larger B2 bending angle, resulting in higher WSS. These findings highlight the impact of vascular morphology on WSS and support further studies on ICA hemodynamics.

Keywords: Blood flow simulation, geometric classification, internal carotid artery, vascular geometry, wall shear stress

NOMENCLATURE

p	[Pa]	pressure
u	[m/s]	velocity
α	[°]	binormal angle
ν	[m^2/s]	kinematic viscosity
ρ	[kg/m^3]	fluid density
θ	[°]	bend angle

1. INTRODUCTION

Cerebrovascular diseases are a leading cause of death worldwide [1], with aneurysms presenting a significant risk due to their potential for rupture, which can lead to severe complications or fatal outcomes [2]. Therefore, early diagnosis and predictive systems are essential for improving patient prognosis and reducing healthcare costs.

The supraclinoid segment of the ICA is a common site for aneurysm formation, and its complex vascular structures pose challenges for treatment [3]. Understanding the relationship between ICA geometry and hemodynamics is essential for early prediction and non-invasive diagnosis, which can be further advanced through CFD simulations.

The formation of aneurysms is influenced by both hemodynamic forces and vascular geometry. Among these, WSS plays a critical role in aneurysm initiation.[4, 5] High WSS and high WSS gradients contribute to media thinning and bulge formation, marking the early stages of aneurysm development. Furthermore, abnormal WSS induces cell apoptosis, extracellular matrix degradation, and inflammation, accelerating aneurysm progression. Vascular geometry directly affects local hemodynamics; studies on ICA curvature have shown that high-curvature regions are subject to elevated WSS and WSS gradients, increasing their susceptibility to aneurysm formation.[6]

To further refine aneurysm risk assessment, classification methods based on vascular geometry have been explored. Zhang's study [7] categorized ICA into U, V, C, and S types, revealing that vascular shape is associated with disease-related hemodynamic patterns. Sangalli et al.[8] analyzed 65 subjects and found that 70% of ICAs with aneurysms located at or beyond the terminal bifurcation were V-type, whereas all ICAs without aneurysms were U-type. These findings suggest that ICA shape classification may serve as an important indicator of in-

tracranial aneurysm risk and its underlying hemodynamic mechanisms.

However, existing classification methods heavily rely on manual segmentation by medical experts, making them highly subjective and difficult to standardize. Such subjectivity may affect the reliability of comparing WSS distributions among different morphological types. To overcome this limitation, our research group has been developing a novel ICA classification method that utilizes shape features of the vessel centerline to objectively classify ICA geometry, dividing it systematically into new U, V, C, and S types. This approach aims to eliminate subjective biases and improve consistency in vascular shape analysis.

Despite advancements in ICA morphology classification, the quantitative impact of different ICA geometries on WSS distribution remains underexplored. Given that WSS plays a important role in the initiation of intracranial aneurysms, further investigation is warranted to quantitatively elucidate its relationship with ICA morphology.

To address these challenges, this study applies the above-mentioned classification method to categorize ICA models from the publicly available BraVa dataset [9, 10] into four distinct types—U, V, C, and S—and analyzes their WSS distributions to identify distinct patterns associated with each morphology, emphasizing the role of geometry in shaping local hemodynamics.

2. DATA ACQUISITION

This study utilizes the BraVa open-source dataset, which provides entire cerebral vascular geometry data from 61 healthy individuals. This study focuses on the ICA and the proximal segment of the middle cerebral artery (MCA) before bifurcation, as shown in Figure 1. To account for variations in vessel length and numerical resolution constraints, only 71 cases were selected for further analysis.

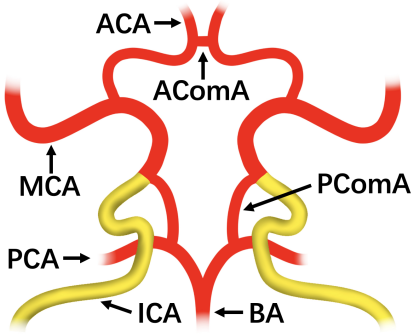

Figure 1. Target region: entire ICA and a portion of MCA prior to MCA bifurcation

The entire cerebral vascular network is extracted into centerline form, and after selecting the target vessels, key parameters such as curvature, torsion, Frenet normals, parallel transport normals, coordinates, and maximum inscribed sphere radius are obtained using V-Modeler [11].

3. CLASSIFICATION METHOD

This study defined ICA shapes using key geometric features, including bend angle (θ), maximum curvature location, superior and inferior extreme points, binormal angle (α), and siphon length, as shown in Fig 2. The UVCS classification follows the scheme illustrated in Fig 3

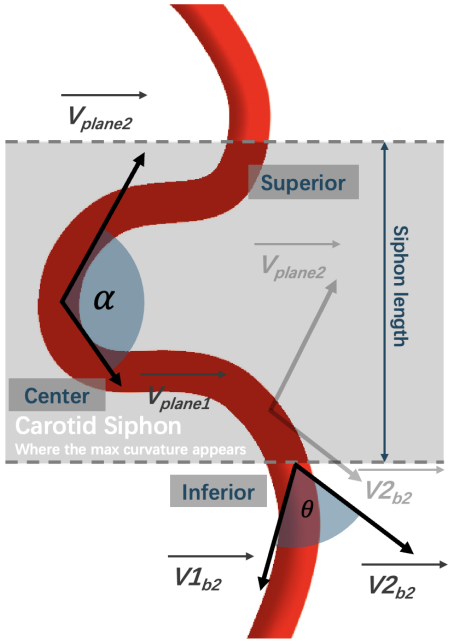

Figure 2. Segmentation of ICA

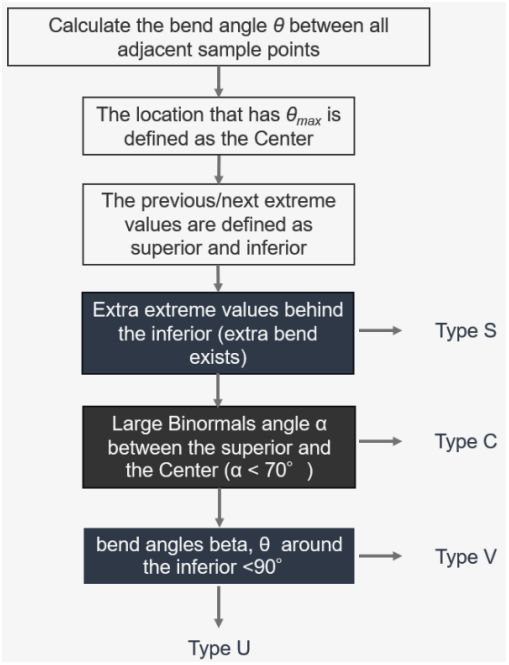

Figure 3. Flowchart of defining the classification

4. 3D MODEL CONSTRUCTION

In this study, the ICA radius was determined based on literature values [12]. Given the significant variation in ICA diameter at different locations—4.67 ± 0.47 mm in the distal ICA and a 40% reduction (to 2.71 ± 0.37 mm) before entering MCA—a constant radius of 1.5 mm was adopted. This choice ensures a physiologically reasonable vessel morphology while preventing surface overlap in highly curved regions. By maintaining a moderate fixed radius throughout the vascular structure, this study aims to minimize the impact of radius variation on hemodynamic computations while preserving the essential geometric characteristics of the ICA.

The vascular model was reconstructed using Vascular Modeling Toolkit (VMTK) [13], which generates the vessel surface based on the extracted centerline data.

5. NUMERICAL METHOD

The governing equations used in this study follow the incompressible Navier–Stokes framework and are solved using the finite volume method via the open-source CFD platform OpenFOAM (OpenFOAM Foundation, 2024). These equations are expressed as follows:

$$\frac{\partial u_i}{\partial x_i} = 0 \tag{1}$$

$$\frac{\partial u_i}{\partial t} + u_j \frac{\partial u_i}{\partial x_j} = -\frac{1}{\rho}\frac{\partial p}{\partial x_i} + \nu \frac{\partial}{\partial x_j}\left(\frac{\partial u_i}{\partial x_j} + \frac{\partial u_j}{\partial x_i}\right) \tag{2}$$

where u_i, u_j, and x_i, x_j denote the components of velocity and spatial coordinates, respectively.

In this study, we assume that the blood flow is in a steady state, which implies no temporal variation in the velocity field. Based on this assumption, the steady-state solver SimpleFoam was employed to solve the governing equations.

Although blood exhibits shear-thinning non-Newtonian behavior at low shear rates, under high shear conditions typical in large arteries, its viscosity remains nearly constant. Thus, blood was modeled as an incompressible Newtonian fluid with a density of $\rho = 1060$ kg/m^3 and a kinematic viscosity of $\nu = 4.43 \times 10^{-6}$ m^2/s. Vessel walls were assumed rigid, with no-slip boundary conditions, and viscoelastic effects were neglected.

To reduce numerical artifacts from boundary conditions, inlet and outlet planes were set perpendicular to the vessel centerline and located sufficiently far from the curved region. Computational meshes were generated using ANSYS ICEM CFD software (ANSYS Inc., 2024). Tetrahedral meshes were applied to the vessel lumen, and refined prism layers were constructed near the wall to improve WSS accuracy. Each model comprised approximately 300,000–400,000 elements.

The velocity field was initialized to zero, and the pressure was uniformly set to 0 Pa. At the inlet, flow rate of 3.63×10^{-6} m^3/s was applied, with a zero-gradient pressure boundary condition. At the outlet, the velocity had a zero-gradient condition, and pressure was fixed at 0 Pa as a reference.

6. RESULTS

6.1. Classification Results

Table 1 presents the distribution of UVCS shape classifications in the BraVa dataset. The results indicate that the U-type is the most prevalent, accounting for 42 cases (59.2%), followed by the V-type with 21 cases (29.6%). The C-type comprises 7 cases (9.8%), while the S-type is the least common, with only 1 case (1.4%). These findings suggest that U-type and V-type structures are more frequently observed in the BraVa dataset, whereas C-type and S-type are relatively rare. The distribution pattern is consistent with the proportions reported in the literature.

BraVa		
Type	Count	(Proportion)
U	42	(59.2%)
V	21	(29.6%)
C	7	(9.8%)
S	1	(1.4%)

Table 1. Results of Classification.

6.2. Geometry Comparison and Simulation Results

Four representative UVCS models were selected from the classified BraVa dataset, with the inlet and outlet lengths extended accordingly, as shown in Fig 4.

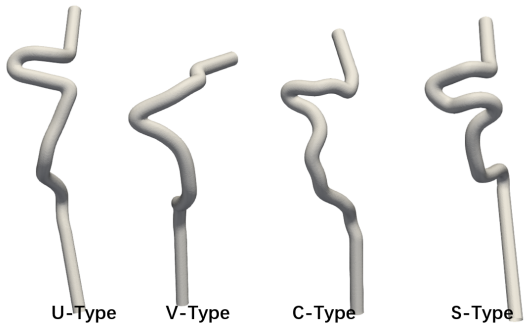

Figure 4. UVCS ICA Model using in CFD

CFD computational meshes were then generated for these models to conduct blood flow simulations. Additionally, the curvature and torsion of the four ICA types were computed, as shown in Fig 5, providing a basis for further exploration of the relationship between geometric characteristics and simulation results.

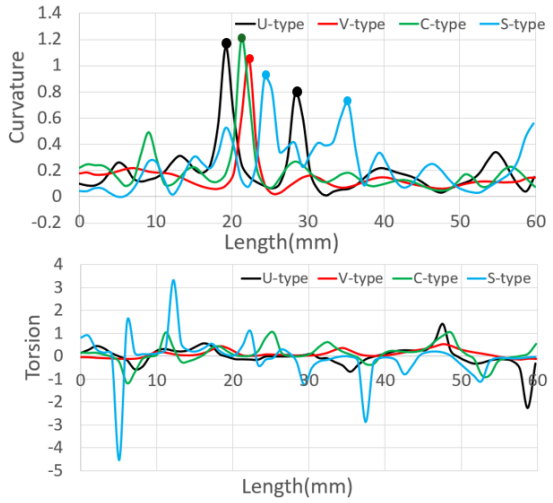

Figure 5. Curvature and Torsion alone Centerline

6.2.1. U-type ICA

The U-type vessel is characterized by a distinct curvature in its midsection, forming a U-type configuration. This morphology results in significant bending angles in both the inferior and posterior segments. Additionally, U-type vessels tend to lie within the same plane, indicating a relatively low torsion and a comparatively small alpha angle.

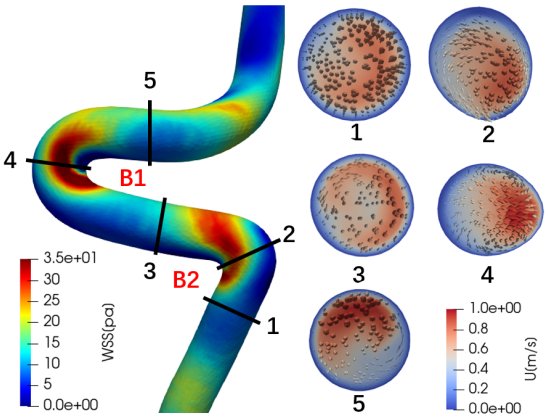

Figure 6. U-type Simulation Result

The curvature pattern of U-type vessels significantly influences blood flow velocity and WSS distribution. As shown in Fig 5, U-type vessels in the ICA siphon region typically exhibit two adjacent curvature peaks, causing rapid flow deviation within the vessel. As illustrated in Fig 6, the first curvature peak directs the main flow toward the outer side of bend B2, while the second curvature peak redirects the flow toward the outer side of bend B1. Consequently, due to these consecutive high-curvature regions, U-type ICAs generally develop two distinct areas of elevated WSS following the bends.

Furthermore, the torsion distribution in Fig 5 indicates that U-type vessels exhibit relatively low torsion peaks, suggesting minimal rotational deformation along the vessel's axis. This implies that U-type vessels primarily undergo planar curvature changes rather than significant spatial twisting, as observed in other vessel types.

6.2.2. V-type ICA

The V-type vessel is characterized by a prominent curvature angle in the ICA siphon region. Compared to U-type vessels, V-type vessels exhibit a more concentrated curvature with fewer bends. The distal bend of the V-type vessel has a relatively smaller curvature angle, and the entire vascular structure primarily lies within a single plane, resulting in a smaller alpha angle.

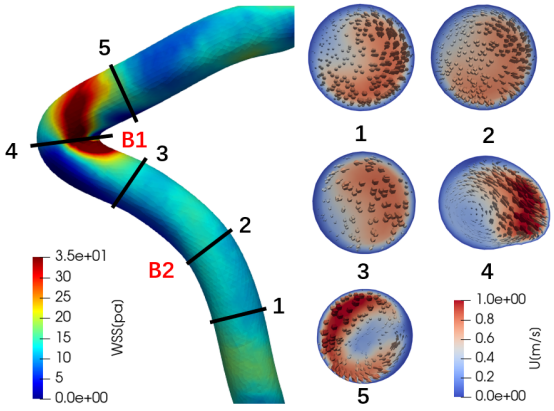

Figure 7. V-type Simulation Result

As shown in Fig 5, V-type ICAs typically exhibit a single major curvature peak in the siphon region. This curvature peak induces significant flow deviation, particularly toward the outer side of bend B1, resulting in a high WSS region, which is noticeably higher than that of U-type vessels, as illustrated in Fig 7. Meanwhile, the central outer region of bend B1 exhibits a low WSS area.

Furthermore, the torsion distribution in Fig 5 indicates that V-type vessels also do not exhibit prominent torsion peaks, suggesting an absence of significant rotational deformation. This implies that V-type vessels primarily exist within the same plane, without noticeable twisting along the vessel's axis.

6.2.3. C-type ICA

The shape of C-type vessels closely resembles that of V-type vessels, they exhibit a distinct feature: a pronounced torsion rate after the center region, particularly near the superior portion. This suggests that C-type vessels do not lie entirely within a single plane and in cases of significant bending, the anterior and posterior segments may be arranged perpendicularly.

As shown in Fig.5, the C-type vascular structures generally share a similar curvature profile with V-type geometries. However, the torsion peaks in

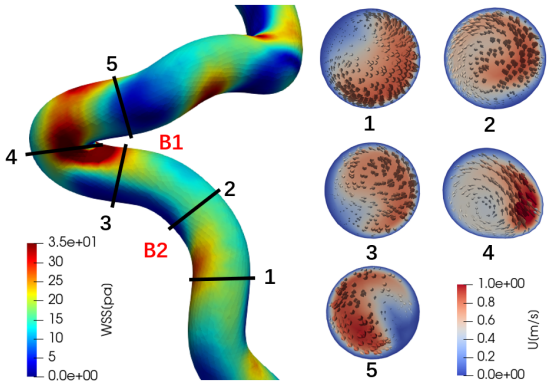

Figure 8. C-type Simulation Result

C-type vessels are significantly higher than those in V-type vessels. Consequently, the elevated torsion after the central portion may induce swirling or eddy formation due to abrupt three-dimensional directional changes in blood flow. In Fig.8, a high WSS region is observed in the high-curvature central portion of the ICA siphon. Additionally, the increased torsion values cause a spatial displacement of the high WSS region in the central part of the ICA siphon. These combined factors contribute to the unique hemodynamic patterns characteristic of the C-type ICA configuration.

6.2.4. S-type ICA

The S-type vascular structure is highly complex, characterized by additional bends appearing before the inferior bend, which further complicates its hemodynamic properties. This vascular configuration is extremely rare in the general population and is scarcely documented in most vascular databases. Consequently, defining the morphological boundaries of S-type vessels remains challenging.

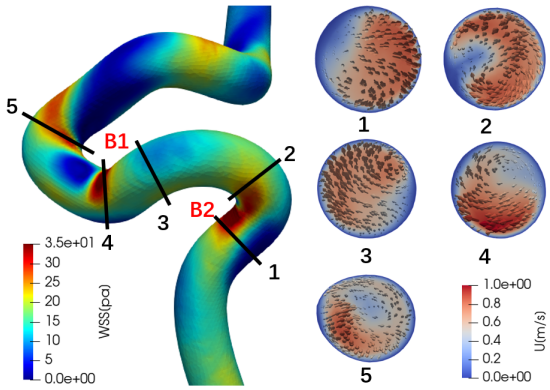

Figure 9. S-type Simulation Result

As observed in Fig 6, the WSS distribution of the S-type vessel is similar to that of the U-type vessel, with two distinct regions of elevated WSS corresponding to the two curvature peaks. In Fig 9, it can be seen that these elevated WSS regions appear before and after the bends. However, compared to the U-type vessel, the S-type vessel exhibits a greater bending angle at B2, leading to higher WSS values in this region.

Additionally, Fig 5 shows that the torsion distribution of the S-type vessel exhibits greater fluctuations compared to that of the U-type vessel. This increased torsional variation may lead to more swirling or vortex formation, resulting in spatial displacement of WSS and contributing to a more complex flow environment.

7. DISCUSSION

In this study, ICA geometries were classified into four types—U, V, C, and S—based on centerline features. CFD simulations were performed to evaluate WSS distributions for each morphology. The results showed that geometric characteristics such as curvature and torsion were associated with the spatial distribution of high WSS, and that each shape exhibited a characteristic high-WSS pattern.

While this study has demonstrated a relationship between ICA morphology and WSS distribution, several limitations should be noted. The sample models were mainly derived from the BraVa dataset, where S-type geometries were rare, limiting morphological diversity. Additionally, a constant vessel radius was used across all models to control for variability, and patient-specific diameter differences were not considered. Although mesh refinement was applied near the wall, a full mesh independence study remains necessary.

Future work may focus on increasing the number of samples and including pathological cases to enhance the statistical power and clinical relevance of the findings. To improve the objectivity of morphological classification, Principal Component Analysis (PCA) could be applied to uniformly resampled centerline coordinates, allowing for the extraction of dominant shape features and identification of clustering patterns in a reduced-dimensional feature space.

Furthermore, if 3D WSS distributions could be projected onto a two-dimensional representation of the vessel surface, unfolded along the centerline, it would allow for more intuitive and quantitative comparisons across different ICA morphologies. Such a mapping approach may also help clarify how local geometric features influence the distribution of wall shear stress. In addition, machine learning techniques may be applied to predict WSS patterns from geometric input, supporting the development of personalized aneurysm risk assessment models.

8. CONCLUSION

This study classified ICA geometries from the BraVa dataset into four distinct types—U, V, C, and S—and analyzed their impact on WSS distribution using CFD simulations. The results highlight the significant influence of curvature and torsion on WSS, with high-curvature regions exhibiting elev-

ated WSS, which may play a role in vascular remodeling and disease progression.

Among the ICA types, U-type is the most common, characterized by a pronounced midsection curvature, leading to two distinct regions of elevated WSS due to consecutive high-curvature zones. V-type, with a single major curvature peak and fewer bends, exhibits a highly localized high WSS region, particularly at bend B1, with values significantly higher than those in U-type vessels. C-type vessels share a similar curvature distribution with V-type but exhibit significantly higher torsion values. The presence of non-coplanar bends and extreme variations in torsion in C-type vessels leads to a more complex WSS distribution, where high torsion contributes to the spatial displacement of WSS regions. S-type, the least frequent configuration, shares a similar WSS pattern with U-type, featuring two WSS peaks before and after the bends; however, its larger bending angle at B2 results in even higher WSS in that region. Additionally, the greater torsional variation in S-type vessels leads to increased vortex formation and WSS displacement, further complicating the flow environment. These findings emphasize the critical role of ICA morphology in shaping hemodynamic conditions, particularly WSS distribution, which could influence vascular disease risks.

In future research, we can increase the sample size to enhance reliability and further investigate the correlation between shape characteristics and WSS distribution. Establishing this relationship will provide a foundation for the future application of machine learning in predicting WSS distribution based on vascular geometry.

9. ACKNOWLEDGEMENTS

This work was supported by the Fugaku project titled *Development of human digital twins for cerebral circulation using Fugaku*, carried out at the RIKEN Center for Computational Science (Project ID: **hp240220**); as well as by the JSPS KAKENHI grant *Development of an analysis system of systemic-cerebral circulatory metabolism for stroke risk prediction* (Project ID: **22H00190**).

REFERENCES

[1] Kalaria, R., and Englund, E., 2024, "Neuropathological Features of Cerebrovascular Diseases", *Pathology*.

[2] Brisman, J. L., Song, J. K., and Newell, D. W., 2006, "Cerebral Aneurysms", *New England Journal of Medicine*, Vol. 355 (9), pp. 928–939.

[3] Muthukumar, K., Moses, V., Keshava, S. N., and Padmanabhan, A., 2021, "Inadvertent Intraprocedural Complication of a Flow Diverter Device During Treatment of Internal Carotid Artery Aneurysm: A Case Report", *Vascular Disease Management*, Vol. 18 (8), pp. E139–E143.

[4] Meng, H., Meng, H., Xiang, J., and Siddiqui, A. M., 2013, "High WSS or Low WSS? Complex Interactions of Hemodynamics with Intracranial Aneurysm Initiation, Growth, and Rupture: Toward a Unifying Hypothesis", *Stroke*, Vol. 35 (7), pp. 1254–1262.

[5] Metaxa, E., Tremmel, M., Natarajan, S. K., Xiang, J., Paluch, R. A., Mandelbaum, M., Siddiqui, A. H., Kolega, J., Mocco, J., and Meng, H., 2010, "Characterization of Critical Hemodynamics Contributing to Aneurysmal Remodeling at the Basilar Terminus in a Rabbit Model", *Stroke*, Vol. 41 (8), pp. 1774–1782.

[6] Lauric, A., Hippelheuser, J., Safain, M. G., and Malek, A. M., 2014, "Curvature Effect on Hemodynamic Conditions at the Inner Bend of the Carotid Siphon and Its Relation to Aneurysm Formation", *Stroke*, Vol. 47 (12), pp. 3018–3027.

[7] Zhang, C., Pu, F., Li, S., Xie, S. Q., Fan, Y., and Li, D., 2012, "Geometric Classification of the Carotid Siphon: Association Between Geometry and Stenoses", *International Journal of Cardiovascular Imaging*, Vol. 35 (5), pp. 385–394.

[8] Sangalli, L. M., Secchi, P., Vantini, S., et al., 2010, "K-mean alignment for curve clustering", *Computational Statistics & Data Analysis*, Vol. 54, pp. 1219–1233.

[9] Wright, S. N., Kochunov, P., Bergamino, F. M. M., Brown, K. M., Mazziotta, J. C., Toga, A. W., Cebral, J. R., and Ascoli, G. A., 2013, "Digital Reconstruction and Morphometric Analysis of Human Brain Arterial Vasculature from Magnetic Resonance Angiography", *NeuroImage*, Vol. 82, pp. 170–181, URL `http://dx.doi.org/10.1016/j.neuroimage.2013.05.089`.

[10] Center for Neural Informatics, Krasnow Institute for Advanced Study, George Mason University, 2013, "BRAVA - Brain Arterial Vascular Atlas", Available at `http://cng.gmu.edu/brava`.

[11] Kobayashi, M., Hoshina, K., Yamamoto, S., Nemoto, Y., Akai, T., Shigematsu, K., Watanabe, T., and Ohshima, M., 2015, "Development of an Image-Based Modeling System to Investigate Evolutional Geometric Changes of a Stent Graft in an Abdominal Aortic Aneurysm", *Circulation Journal*, Vol. 79 (7), pp. 1534–1541.

[12] Baz, R. A., Scheau, C., Niscoveanu, C., and Bordei, P., 2021, "Morphometry of the Entire Internal Carotid Artery on CT Angiography", *Medicina*, Vol. 57 (8), p. 832.

[13] Izzo, R., Steinman, D., Manini, S., and Antiga, L., 2018, "The Vascular Modeling Toolkit: A Python Library for the Analysis of Tubular Structures in Medical Images", *Journal of Open Source Software*, Vol. 3 (25), p. 745.

Conference on Modelling Fluid Flow (CMFF'25)
The 19th International Conference on Fluid Flow Technologies
Budapest, Hungary, August 26-August 29, 2025

A Consistent Approach to Atmospheric Boundary Layer Simulations Using the k-ω SST Model

Márton PRICZ[1], Bálint PAPP[2], Gergely KRISTÓF[3] Miklós BALOGH[4],

[1] Corresponding Author. Department of Fluid Mechanics, Faculty of Mechanical Engineering, Budapest University of Technology and Economics, Műegyetem rkp. 3., H-1111 Budapest, Hungary. Tel.: +36 1 463 2546, E-mail: priczmarton@edu.bme.hu
[2] Department of Fluid Mechanics, Faculty of Mechanical Engineering, Budapest University of Technology and Economics. E-mail: papp.balint@gpk.bme.hu
[3] Department of Fluid Mechanics, Faculty of Mechanical Engineering, Budapest University of Technology and Economics. E-mail: kristof.gergely@gpk.bme.hu
[4] Department of Fluid Mechanics, Faculty of Mechanical Engineering, Budapest University of Technology and Economics. E-mail: balogh.miklos@gpk.bme.hu

ABSTRACT

In the computational investigations of atmospheric flows in urban environments, steady-state Reynolds-averaged Navier-Stokes (RANS) simulations are still preferred to transient scale-resolving ones due to their relatively low computational demand and fast turnover times. An extensively documented challenge associated with RANS models in atmospheric applications is the unwanted alteration of the prescribed velocity and turbulence profiles in the streamwise direction, caused by the inadequate treatment of solid wall boundaries and the well-known inconsistencies between the atmospheric boundary layer (ABL) profiles and general-purpose turbulence models. Although several methods have been proposed to preserve the streamwise homogeneity of the neutral ABL, previously, most of these have been developed for the k-ε model family, which is known to perform poorly in impinging and separated flows, making its applicability in building aerodynamics questionable. The present work proposes and benchmarks two approaches, namely custom wall functions and the sand-grain-roughness-based boundary condition, aimed at maintaining the prescribed atmospheric boundary layer inlet profiles in steady-state calculations using the k-ω SST model, which is better suited for investigating flows around bluff bodies. The same approaches are also applied to the standard k-ε and realizable k-ε models for comparison. The proposed methods are implemented in both Ansys Fluent and OpenFOAM and the results from a test case with a surface-mounted cube are compared. Simulations in an empty domain show significant improvements in the homogeneity of the ABL, with the best performance achieved by a logarithmic atmospheric wall function formulation. The accuracy of the proposed methods is quantified by reproducing the surface pressure distribution of a cuboid building model subjected to an ABL-like approach flow in a wind tunnel.

Keywords: Atmospheric boundary layer, Ansys Fluent, k-ω SST, OpenFOAM, Surface-mounted cube, Wall function

NOMENCLATURE

a_b	$[-]$	blending function parameter
A_k	$[m^2/s^2]$	TKE profile parameter
B_k	$[m^2/s^2]$	TKE profile parameter
C_k	$[m^2/s^2]$	TKE profile parameter
c_p	$[-]$	static pressure coefficient
C_s	$[-]$	roughness constant
C_μ	$[-]$	turbulence model constant
D_k	$[m^2/s^2]$	TKE profile parameter
E	$[-]$	empirical constant
f_b	$[-]$	blending function
H	$[m]$	height of the cube
k	$[m^2/s^2]$	turbulent kinetic energy
K_s	$[m]$	sand-grain roughness height
N	$[-]$	number of pressure probes
O	$[-]$	observed (measured) data set
P	$[-]$	predicted (simulated) data set
p	$[Pa]$	static pressure
q	$[-]$	hit rate
R	$[-]$	correlation coefficient
u	$[m/s]$	x-velocity
u^*	$[m/s]$	friction velocity
v	$[m/s]$	y-velocity
w	$[m/s]$	z-velocity
z	$[m]$	vertical coordinate
z_{0k}	$[m]$	TKE profile reference height
z_{0w}	$[m]$	aerodynamic roughness height
z_0	$[m]$	aerodynamic roughness height
z_{mod}	$[m]$	modified vertical coordinate

α	$[-]$	power-law exponent
β^*	$[-]$	turbulence model constant
δ	$[m]$	boundary layer depth
Δ_{abs}	$[-]$	absolute error
Δ_{rel}	$[-]$	relative error
κ	$[-]$	von Kármán constant
ν	$[m^2/s]$	kinematic viscosity
ω	$[1/s]$	specific dissipation rate
ρ	$[kg/m^3]$	density
σ	$[-]$	standard deviation
τ	$[Pa]$	wall shear stress
ε	$[m^2/s^3]$	turbulence dissipation rate

Subscripts and Superscripts

i	element index of the observed and measured data sets
in	inlet variables
w	values used in the wall function
p	values at the first cell centre
ref	reference values
$+$	nondimensional values

1. INTRODUCTION

A crucial challenge in using Reynolds-averaged Navier-Stokes (RANS) models in atmospheric simulations is creating a so-called horizontally homogeneous atmospheric boundary layer (HHABL) flow by avoiding the unintended streamwise alteration of the prescribed velocity and turbulent kinetic energy profiles as they travel along the numerical domain. This alteration otherwise results in a mismatch between the inflow and approach flow profiles and the flow reaching the area of interest will therefore be different to the intended one – which is a well-documented problem, impacting the fidelity of numerical simulations [1, 2, 3, 4]. This problem stems from the formation of an internal near-wall boundary layer due to inconsistencies between the wall treatment, the transport equations and the inflow profiles[1, 4, 5].

Several studies have proposed methods for the preservation of the inflow profiles of a neutral ABL when using the k-ε model family. These include the modification of model constants [4, 6, 7, 8], the use of corrective source terms [4, 7, 8, 9], and custom wall functions [4, 7, 8, 10] among others. However, the commonly used standard and realizable k-ε models are known to underperform in wall-bounded flows compared to the k-ω SST model [11]. This is apparent in flows around bluff bodies, where the overprediction of k by the k-ε models reduces or even eliminates the separation behind the windward edges of obstacles [11, 12, 13]. The k-ω SST model performs significantly better in impinging and separated flows, making it a preferable alternative for bluff body flow simulations [11].

However, the commonly used Ansys Fluent CFD solver – hereinafter referred to as Fluent – does not provide an option to employ user-defined wall functions when using ω-based turbulence models. Instead, the user must rely on the rough wall boundary condition based on the sand grain roughness model. While formulations for a consistent set of roughness parameters and inlet conditions have already been proposed, these either rely on the drastic modification of model constants [14], or must employ overly large cells near the wall to abide by the requirements for creating a HHABL flow, originally formulated by Blocken et al. [3] [15]. As an example, the optimal set of roughness parameters for a high-roughness ABL flow determined by Townsend et al. [15] requires roughly $29\,m$ high first cells at full scale, which is in itself larger than many low-rise buildings.

The current work proposes a new formulation for obtaining an optimum set of roughness parameters using this boundary condition and shows how the well-known contradiction in the requirements for a high-fidelity HHABL simulation [3] can be circumvented with the current version of Fluent (version 2023 R1). Comparisons are drawn between the applicable wall treatment methods in OpenFOAM and Ansys Fluent as well as between the implementations available for the k-ε and k-ω SST models. The performance of the new method for prescribing appropriate surface roughness for neutral HHABL flows is assessed based on the velocity and TKE profiles in a two-dimensional empty channel and the surface pressure distribution of a surface-mounted cube in a three-dimensional channel.

2. METHODOLOGY

2.1. Inflow conditions

The inlet boundary conditions are determined based on the wind tunnel measurements of [16], with auxiliary data supplemented from [17] and are identical in the OpenFOAM and Fluent simulations. A neutrally stratified, hydrostatic ABL is assumed, where the balancing buoyant and gravitational forces are subtracted from the equation of motion, and the problem is regarded as incompressible. The thermal stratification is therefore not considered in this work. For the velocity profile, a power-law function is fitted to the entire data set. A horizontally homogeneous flow is assumed, with zero mean vertical and lateral velocity components ($v \equiv 0; w \equiv 0$), in the form of

$$u(z) = u_{ref}\left(\frac{z + z_{ref}}{z_{ref}}\right)^{\alpha} - u_{ref}, \tag{1}$$

where u_{ref} denotes the reference velocity, z_{ref} is the reference height and α is the exponent of the power-law profile. For the fitted values of the above parameters, see Table 1.

A four-parameter logarithmic-polynomial profile is used for the turbulent kinetic energy (TKE) profile. This generally offers more flexibility for fitting to wind tunnel data than the commonly used profile proposed by Parente et al. [7] and ensures a zero

Table 1. Fitted parameters for the power law and logarithmic mean x-velocity profiles, the logarithmic-polynomial TKE profile and the f_b blending function.

u_{ref} $[m/s]$	z_{ref} $[m]$	α $[-]$	u_w^* $[m/s]$ (Fluent)	u_w^* $[m/s]$ (OpenFOAM)	z_{0w} $[m]$	
0.4472	1.493×10^{-5}	0.2707	0.3839	0.3759	1.060×10^{-3}	
z_{0k} $[m]$	A_k $\left[m^2/s^2\right]$	B_k $\left[m^2/s^2\right]$	C_k $\left[m^2/s^2\right]$	D_k $\left[m^2/s^2\right]$	δ $[m]$	a_b $[-]$
5×10^{-3}	0.1149	-5.453×10^{-2}	5.699×10^{-3}	0.4912	0.4819	7.591

gradient at the wall [18]:

$$k(z) = A_k \ln^2\left(\frac{z+z_{0k}}{z_{0k}}\right) + B_k \ln^3\left(\frac{z+z_{0k}}{z_{0k}}\right) + C_k \ln^4\left(\frac{z+z_{0k}}{z_{0k}}\right) + D_k, \tag{2}$$

where the value of z_{0k}, A_k, B_k, C_k and D_k parameters are listed in Table 1. The inflow profiles of ε and ω for the respective RANS models are determined based on the profiles of u and k:

$$\varepsilon(z) = \sqrt{C_\mu} k(z) \frac{\partial u(z)}{\partial z} \tag{3}$$

and ω can be expressed from ε via the transformation of Wilcox [19], adopted by Menter [20]:

$$\omega(z) = \frac{\varepsilon(z)}{\beta^* k(z)} = \frac{1}{\sqrt{C_\mu}} \frac{\partial u(z)}{\partial z}, \tag{4}$$

where β^* and C_μ model constants are both kept at the Fluent default value of 0.09 [18].

In the wind tunnel measurements, the appropriate velocity profile was created using physical obstacles, including tripping fences and turbulence-generating spires. These elements did not extend to the top of the wind tunnel and the flow above them remained uniform. To model this effect, a modified z_{mod} vertical coordinate is introduced, expressed as

$$z_{mod}(z) = z(1 - f_b(z)) + \delta f_b(z), \tag{5}$$

where δ is the depth of the boundary layer in the wind tunnel and $f_b(z)$ is given as

$$f_b(z) = \frac{1}{2}\left(1 + \sin\left(\frac{\pi}{2} \max\left(-1, \min\left(a_b(z-\delta), 1\right)\right)\right)\right), \tag{6}$$

where a_b is a fitted blending parameter. The values of δ and a_b are listed in Table 1.

2.2. Wall treatment

2.2.1. Wall treatment in OpenFOAM

In the case of the OpenFOAM simulations, a logarithmic law of the wall is employed. The friction velocity u_w^* and aerodynamic roughness height z_{0w} in Equation 7 are determined by fitting a logarithmic profile to the velocity measurements in the range of $4 \times 10^{-3}\, m < z < 6 \times 10^{-2}\, m$.

$$U_w(z) = \frac{u_w^*}{\kappa} \log\left(\frac{z+z_{0w}}{z_{0w}}\right), \tag{7}$$

where κ is the von Kármán constant, with slightly different default values in the two solvers (OpenFOAM: $\kappa = 0.41$, Fluent: $\kappa = 0.4187$), hence the different friction velocities used in the implementations in the respective solver (see Table 1).

2.2.2. Wall treatment in Fluent

As mentioned in Section 1, user-defined wall functions are not available for the k-ω SST model in Fluent. Therefore, the logarithmic wall function is only used with the standard k-ε and realizable k-ε models, while the rough wall condition is used for the k-ω SST model instead. For fully rough boundary layers – as is the case in ABL flows in general – the velocity in the first cell centre next to the wall is calculated as

$$\frac{u_p u^*}{\tau_w/\rho} = \frac{1}{\kappa} \ln\left(\frac{E z_p^+}{1 + C_s K_s^+}\right), \tag{8}$$

where, from here on, subscript p denotes the values in the first cell centre, at the height of $z = z_p$. Furthermore, $E = 9.793$ is an empirical constant, $u^* = C_\mu^{1/4} k_p^{1/2}$ is the friction velocity, τ_w is the wall shear stress, ρ is the density of the fluid and the C_s roughness constant and K_s sand grain roughness height are provided by the user. The z_p^+ and K_s^+ values are nondimensionalized as $z_p^+ = z_p u^*/\nu$ and $K_s^+ = K_s u^*/\nu$ respectively, where ν is the kinematic viscosity. In the current work, the value of C_s is kept constant (at the Fluent default value of 0.5 [21]), while K_s is chosen so that Eqs. (7) and (8) give the same velocity values for the first cell centre, meaning

$$\frac{\tau_w/\rho}{u^*} \frac{1}{\kappa} \ln\left(\frac{E z_p^+}{1 + C_s K_s^+}\right) = \frac{u_w^*}{\kappa} \log\left(\frac{z+z_{0w}}{z_{0w}}\right). \tag{9}$$

By rearranging Eq. (9), the roughness height can be expressed as

$$K_s = \frac{E z_p z_{0w}}{C_s\left(z_p + z_{0w}\right)} - \frac{1}{C_s^+}, \tag{10}$$

where C_s^+ contains the approximate values of the various formulations of the friction velocity found in

Eqs. (7) and (8):

$$C_s^+ = \frac{\tau_w/\rho}{u^* \nu} C_s \approx \frac{\nu \frac{\mathrm{d}U}{\mathrm{d}z}\Big|_{z_p} + C_\mu^{1/2} k_p}{C_\mu^{1/4} k_p^{1/2} \nu} C_s. \tag{11}$$

With C_s being fixed at 0.5, the resulting roughness height is $K_s = 3.818 \times 10^{-3}\, m$. This value is higher than the first cell centre height $z_p = 3 \times 10^{-3}\, m$ and therefore does not satisfy the minimum cell height criterion formulated by Blocken et al. [3]. However, the authors noted that this limitation was posed by the available 6.2 version of Fluent at the time, and in case of future developments in this regard, this requirement might need to be reconsidered. Indeed, since version 14, Fluent does not restrict the wall-normal mesh resolution based on the roughness height (see section 7.4.15.3.1 in the Ansys Fluent User's Guide [21]). Thus the above-presented parameter values can be employed with no apparent conflict.

2.3. Numerical setup

2.3.1. Empty channel

The wall functions and optimized roughness parameters are first assessed using a two-dimensional empty channel with a length of $1.2\, m$ and a height of $1\, m$, matching the wind tunnel in the experimental investigations [16]. (While this domain will be referred to as a two-dimensional, it is effectively a single-cell-wide three-dimensional domain, as OpenFOAM uses three-dimensional meshes exclusively. For a direct comparison of the results, the same mesh is employed in Fluent.) The numerical mesh consists of 6360 (60×106) hexahedral cells, with uniform horizontal spacing, a first cell layer height of $6 \times 10^{-3}\, m$ and a wall-normal grading with a reference cell expansion ratio of 1.14.

The inflow profiles described in Section 2.1 are imposed at the inlet, while zero gauge pressure is prescribed at the outlet. The wall treatment methods are applied to the channel floor, and a symmetry condition is applied to the top boundary. In the OpenFOAM implementation of the 2D channel, the lateral boundaries are set to "empty", while a symmetry condition is applied to them in Fluent.

2.3.2. Surface-mounted cube

After the preliminary 2D simulations, the methods are employed for a 3D channel containing a surface-mounted cube with an edge length of $H = 0.2\, m$. The vertical and lateral dimensions of the domain match the cross-section of the wind tunnel, while the longitudinal dimensions upwind and downwind of the cube are set in accordance with the guidelines of Franke et al. [22]. For the domain dimension, see Figure 1. The mesh is fully structured and uses the same first cell height and vertical grading as the 2D mesh outside the vicinity of the cube, resulting in 1.15 million hexahedral cells. At the surface of the cube, 26 cells are located along the horizontal edges and 23 along the vertical edges. The

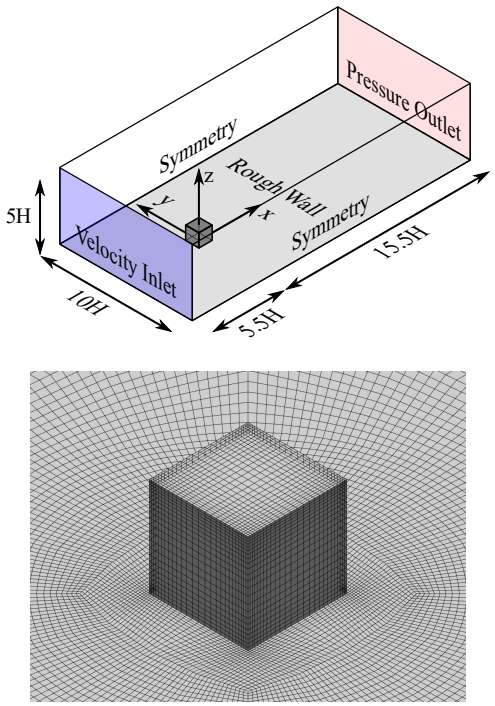

Figure 1. Top: sketch of the 3D computational domain with the surface-mounted cube. Dimensions are displayed relative to the cube height ($H = 0.2\, m$). Bottom: close-up image of the mesh at the surface of the cube.

3D simulation uses the same boundary conditions as the 2D channel, except for the "empty" conditions at the lateral boundaries in OpenFOAM, which are replaced by the slip wall boundary condition. Additionally, the faces of the cube are treated as smooth walls.

2.3.3. Solver settings

Air density was set to $1\, kg/m^3$ and the kinematic viscosity accordingly to $1.5 \times 10^{-5}\, m^2/s$ in the Fluent simulations for direct compatibility with the OpenFOAM calculations. (OpenFOAM solves for the kinematic pressure p/ρ instead of the static pressure in incompressible cases, assuming unit density.)

Table 2. Naming convention of cases. The last character denotes the solver used in the specific case (O– OpenFOAM, F– Fluent)

Notation	Turbulence model	Wall treatment
SSTKW-F	k-ω SST	Rough wall
SSTKW-O	k-ω SST	Log-law
SKE-F	Standard k-ε	Log-law
SKE-O	Standard k-ε	Log-law
RKE-F	Realizable k-ε	Log-law
RKE-O	Realizable k-ε	Log-law

The simulations were performed using steady-state incompressible solvers in both software with a second-order spatial discretization of the pres-

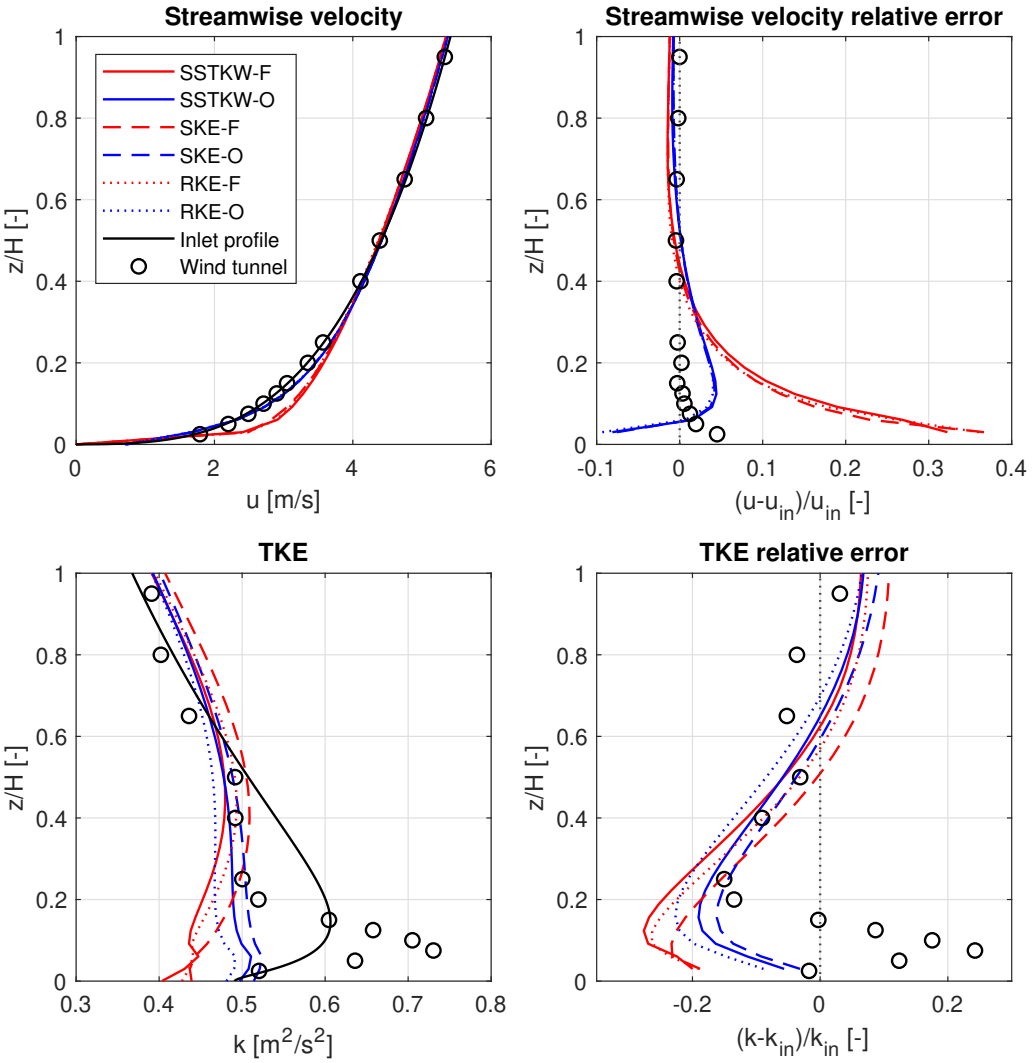

Figure 2. Vertical profiles of u (top) and k (bottom) with their relative errors to the prescribed inlet profiles below $z = H$ height at the outlet, with a distance of $x = 6H$ from the inlet.

sure, second-order upwind discretization for the momentum and first-order upwind discretization for the turbulent variables. All 3D simulations are performed on the CPU partition of the Komondor High-Performance Computer (HPC), using 24 processor cores of an AMD EPYC™ 7763 processor.

3. RESULTS

3.1. Empty channel

The velocity and its relative error at the outlet (at $x = 6H$) of the 2D channel (Figure 2) show that all five implementations utilizing a logarithmic wall function behave similarly, with error values generally below 10% in the most critical, near-ground region. Out of these cases, those using the standard k-ε model produce the highest relative error at the first cell centre, at 9.6% and 9.3% for the Fluent and OpenFOAM implementations respectively. It should also be noted, that the OpenFOAM simulations using the standard and realizable k-ε models result in marginally smaller relative errors than their counterparts in Fluent (average absolute deviations from the prescribed profile below $z = H$: SKE-F - 2.02%, SKE-O - 1.70%, RKE-F - 1.88% and RKE-O - 1.74%). Meanwhile, the rough wall implementation in Fluent (case SSTKW-F) produces noticeably larger errors at almost all locations below $z = H$, with a peak relative error of 32.3% immediately next to the wall (average absolute deviations from the prescribed profile below $z = H$: SSTKW-F - 5.49% and SSTKW-O - 1.84%). This points to the rough wall function behaving differently to the formulation shown in Eq. 8, likely due to the compensation for the cell centre height being smaller than the roughness height [21]. This produces a different velocity at the first cell centre compared to the other simulations, indicating that the local near-wall speedup of the flow may still compromise the results at this height.

The resulting TKE profiles at the outlet show considerable deviations from the inlet profile in all cases. The maximum relative errors to the fitted profile range from 16.19% to 24.61%, with the highest

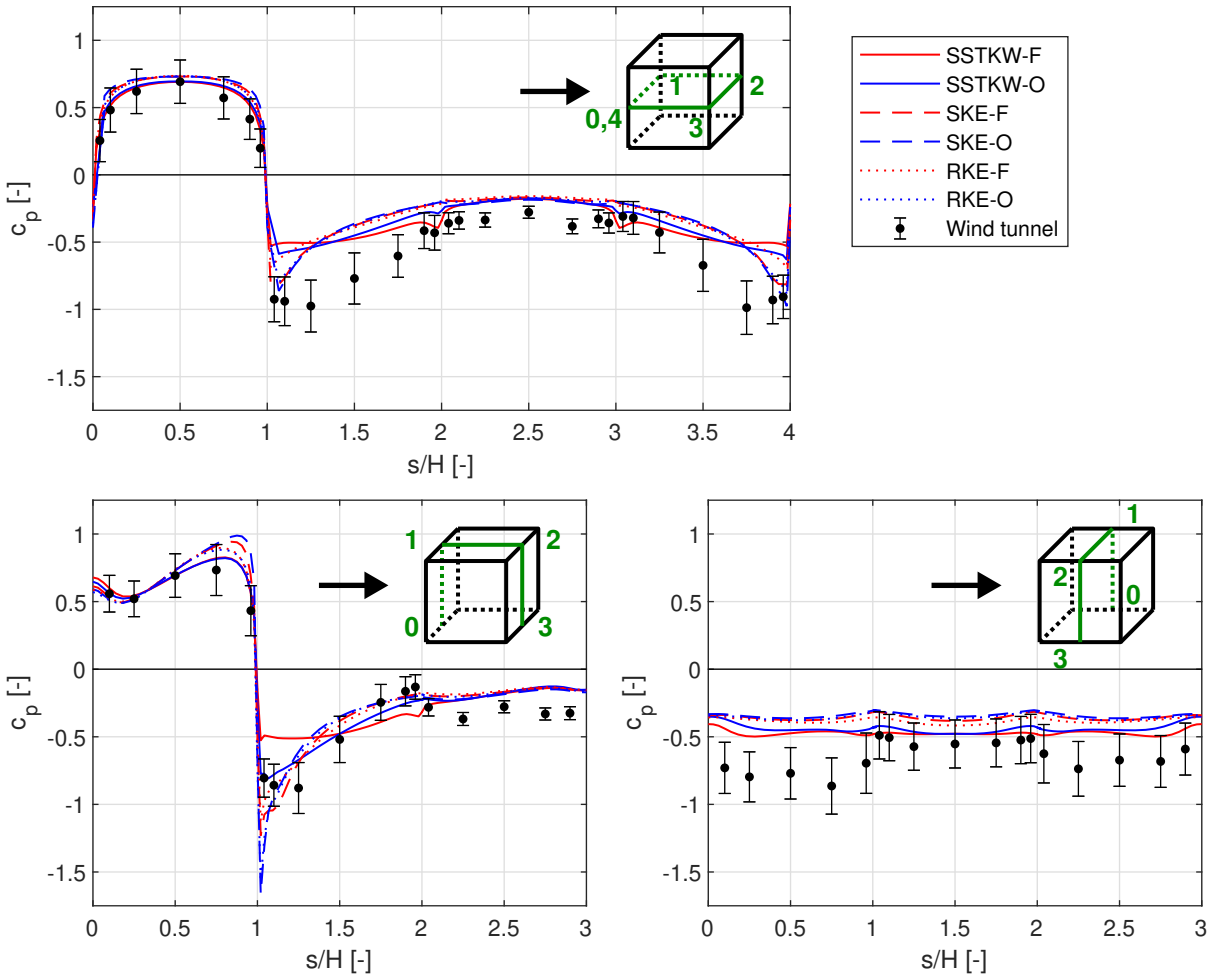

Figure 3. Distribution of the pressure coefficient along the horizontal and vertical centre lines of the cube. Error bars correspond to rms measurement values. s/H denotes the nondimensional distance along the centre lines. (For the orientation, see the sketches in the top right corners of the plots, where the black arrow shows the wind direction.)

error once again produced by the SSTKW-F case, using the rough wall condition. Despite the improved formulation of the TKE profile, the fit to the experimental data is far from ideal and the measured values themselves deviate from this profile considerably, with errors comparable to those produced by the simulations.

3.2. Surface-mounted cube

The results of the simulations in the three-dimensional domain are validated with the experimental surface pressure data from [16]. For this purpose, the static pressure values are presented as pressure coefficients, calculated as

$$c_p = \frac{p - p_0}{\frac{1}{2}\rho u_H^2}, \tag{12}$$

where $u_H = 5.412\,m/s$ is the prescribed inflow velocity at $z = H$ and the p_0 reference static pressure is sampled in the numerical domain at the same location as in the measurement; at the channel wall, in the lateral midplane of the cube and at the height of 0.25 m.

Figure 3 shows the distribution of the pressure coefficient along the horizontal and vertical centre lines of the cube. The depression on the sides of the cube (s/H between 1-2 and 3-4 in the top plot of Figure 3) is underpredicted by both k-ω SST simulations, while it is only significantly underpredicted behind the top leading edge ($s/H = 1$ in the bottom left plot of Figure 3) by the Fluent implementation of the k-ω SST model. As this location is sufficiently far from the channel floor, it is likely that this discrepancy between the two simulations is not the result of the different wall treatment methods but rather a difference in the implementations of the k-ω SST model itself in the two solvers. The Fluent and OpenFOAM simulations, which use the standard k-ε and realizable k-ε models, produce largely similar pressure distributions, invariably overestimating the magnitude of the front overpressure and the depression behind the top leading edge. All turbulence models generally overestimate the pressure on the windward, side and leeward walls, with the most noticeable deviations from the experimental data shown on

the side walls. Overall, the k-ω SST cases, and specifically the SSTKW-O case provide the best agreement between the simulated and measured values.

Following the qualitative remarks, four different scalar metrics were employed to provide a basis for comparing the performance of the individual implementations quantitatively. These are the correlation coefficient (R), the hit rate (corresponding to the value of the measurement uncertainty, $q_{0.142}$), the factor of two observations ($FAC2$) and the average absolute deviation (AAD). Their calculation is as follows:

$$R = \frac{\overline{\left(O_i - \overline{O}\right)\left(P_i - \overline{P}\right)}}{\sigma_O \sigma_P} \tag{13}$$

$$q = \frac{1}{N}\sum_{i=1}^{N} n_i, \text{ where}$$
$$n_i = \begin{cases} 1 & \text{if} \quad (1 - \Delta_{rel}) \leq \frac{P_i}{O_i} \leq (1 + \Delta_{rel}) \\ 1 & \text{if} \quad |P_i - O_i| < \Delta_{abs} \\ 0 & \text{otherwise,} \end{cases} \tag{14}$$

$$FAC2 = \frac{1}{N}\sum_{i=1}^{N} n_i, \text{ where}$$
$$n_i = \begin{cases} 1 & \text{if} \quad 0.5 \leq \frac{P_i}{O_i} \leq 2 \\ 1 & \text{if} \quad |P_i| < \Delta_{abs} \text{ and } |O_i| < \Delta_{abs} \\ 0 & \text{otherwise,} \end{cases} \tag{15}$$

and

$$AAD = \overline{|O_i - P_i|}. \tag{16}$$

In the above definitions, O_i and P_i respectively denote observed (measured) and predicted (simulated) pressure coefficient values at the i^{th} static pressure tap on the surface of the cube, with σ_O and σ_P denoting the standard deviation of the observed and predicted dataset, the overbars above quantities denoting mean values and $N = 175$ standing for the total number of pressure taps on the surface of the cube. For the arrangement of the pressure taps, the reader is referred to Papp et al. [16]. Furthermore, $\Delta_{abs} = 0.142$ and $\Delta_{rel} = 0.25$ absolute and relative errors are taken from the experimental investigations.

A high correlation coefficient serves as a necessary but not sufficient condition for a good statistical match. This condition is satisfied by all simulations, with values of R ranging from 0.921 to 0.957. However, a simulated pressure distribution achieving a higher correlation coefficient than another does not automatically constitute a better overall agreement with the measurement data. The hit rate and the $FAC2$ metrics are calculated on a similar basis but the latter is generally more robust as it is not affected by outliers. It should also be noted, that assuming smaller errors for the experimental results would automatically narrow the criterion for a "hit" ($n_i = 1$ in Equation 14), leading to a lower hit rate, indicating a worse match between the otherwise unchanged experimental and simulated data.

Table 3. Validation metrics of the surface-mounted cube simulations.

Case	R	$q_{0.142}$	$FAC2$	AAD
SSTKW-F	0.935	0.583	0.909	0.184
SSTKW-O	**0.955**	**0.606**	**0.966**	**0.161**
SKE-F	0.954	0.463	0.886	0.180
SKE-O	0.921	0.451	0.869	0.206
RKE-F	0.957	0.463	0.886	0.186
RKE-O	0.932	0.457	0.903	0.192
Target values	1	1	1	0

The validation metrics show that the SSTKW-O case outperforms all other simulations, with the second-best match achieved by the SSTKW-F case in the hit rate and $FAC2$ metrics. In comparison, the validation metrics generally indicate that the k-ε simulations underperform, with the Fluent implementations achieving somewhat higher hit rates and lower average absolute deviation values than the OpenFOAM cases, although the same trend is not present for the FAC2 metric.

4. CONCLUSIONS

The various implementations of the logarithmic wall functions produced similar results in the empty channel simulations, with maximum relative error values for the velocity consistently below 10%, achieving a good match between the inflow and outflow profiles. The rough wall formulation (necessitated by the limited wall function capabilities of Ansys Fluent) produced the largest velocity errors next to the wall, which points to further improvements needed regarding this method. Meanwhile, the errors in the TKE profiles were significantly higher in every case and the distinction between the performance of the logarithmic wall function and the rough wall function became less clear. The pressure distribution on the surface of the surface-mounted cube shows the clear advantages of using the k-ω SST model, which achieved a better match to the experimental data. Based on the employed validation metrics, the best overall agreement with the experimental data was achieved by the OpenFOAM implementation of the k-ω SST model, with significant differences noted between the behaviour of the Fluent and OpenFOAM implementations.

ACKNOWLEDGEMENTS

The authors would like to thank the Digital Government Development and Project Management Ltd. for awarding them access to the Komondor HPC facility based in Hungary. This study was funded by grant no. OTKA K23-146158 from the National Re-

search, Development, and Innovation Office, Hungary. Project no. TKP-6-6/PALY-2021 has been implemented with the support provided by the Ministry of Culture and Innovation of Hungary from the National Research, Development and Innovation Fund, financed under the TKP2021-NVA funding scheme. The work of Bálint Papp was supported by the EKÖP-24-4-I-BME-357 University Research Scholarship Program of the Ministry for Culture and Innovation, from the source of the National Research Development and Innovation Fund.

REFERENCES

[1] Richards, P. J., and Hoxey, R. P., 1993, "Appropriate boundary conditions for computational wind engineering models using the k-ε turbulence model", *Journal of Wind Engineering and Industrial Aerodynamics*, Vol. 46-47, pp. 145–153.

[2] Hargreaves, D. M., and Wright, N. G., 2007, "On the use of the k-ε model in commercial CFD software to model the neutral atmospheric boundary layer", *Journal of Wind Engineering and Industrial Aerodynamics*, Vol. 95 (5), pp. 355–369.

[3] Blocken, B., Carmeliet, J., and Stathopoulos, T., 2007, "CFD simulation of the atmospheric boundary layer: wall function problems", *Atmospheric Environment*, Vol. 41 (2), pp. 238–252.

[4] Parente, A., Gorlé, C., van Beeck, J., and Benocci, C., 2011, "A Comprehensive Modelling Approach for the Neutral Atmospheric Boundary Layer: Consistent Inflow Conditions, Wall Function and Turbulence Model", *Boundary-Layer Meteorol*, Vol. 140 (3), pp. 411–428.

[5] Richards, P. J., and Norris, S. E., 2019, "Appropriate boundary conditions for computational wind engineering: Still an issue after 25 years", *Journal of Wind Engineering and Industrial Aerodynamics*, Vol. 190, pp. 245–255.

[6] Gorlé, C., van Beeck, J., Rambaud, P., and Van Tendeloo, G., 2009, "CFD modelling of small particle dispersion: The influence of the turbulence kinetic energy in the atmospheric boundary layer", *Atmospheric Environment*, Vol. 43 (3), pp. 673–681.

[7] Parente, A., Gorlé, C., van Beeck, J., and Benocci, C., 2011, "Improved k-ε model and wall function formulation for the RANS simulation of ABL flows", *Journal of Wind Engineering and Industrial Aerodynamics*, Vol. 99 (4), pp. 267–278.

[8] Balogh, M., Parente, A., and Benocci, C., 2012, "RANS simulation of ABL flow over complex terrains applying an Enhanced k-ε model and wall function formulation: Implementation and comparison for fluent and OpenFOAM", *Journal of Wind Engineering and Industrial Aerodynamics*, Vol. 104-106, pp. 360–368.

[9] Balogh, M., and Parente, A., 2015, "Realistic boundary conditions for the simulation of atmospheric boundary layer flows using an improved k-ε model", *Journal of Wind Engineering and Industrial Aerodynamics*, Vol. 144, pp. 183–190.

[10] Chang, C.-Y., Schmidt, J., Dörenkämper, M., and Stoevesandt, B., 2018, "A consistent steady state CFD simulation method for stratified atmospheric boundary layer flows", *Journal of Wind Engineering and Industrial Aerodynamics*, Vol. 172, pp. 55–67.

[11] Cindori, M., Čajić, P., Džijan, I., Juretić, F., and Kozmar, H., 2022, "A comparison of major steady RANS approaches to engineering ABL simulations", *Journal of Wind Engineering and Industrial Aerodynamics*, Vol. 221, p. 104867.

[12] Gao, Y., and Chow, W. K., 2005, "Numerical studies on air flow around a cube", *Journal of Wind Engineering and Industrial Aerodynamics*, Vol. 93 (2), pp. 115–135.

[13] Blocken, B., 2018, "LES over RANS in building simulation for outdoor and indoor applications: A foregone conclusion?", *Build Simul*, Vol. 11 (5), pp. 821–870.

[14] Yang, Y., Xie, Z., and Gu, M., 2017, "Consistent inflow boundary conditions for modelling the neutral equilibrium atmospheric boundary layer for the SST k-ω model", *Wind and Structures*, Vol. 24 (5), pp. 465–480, publisher: Techno-Press.

[15] Townsend, J. F., Xu, G., and Jin, Y., 2024, "Roughness constant selection for atmospheric boundary layer simulations using a *k-ω* SST turbulence model within a commercial CFD solver", *Advances in Wind Engineering*, Vol. 1 (1), p. 100005.

[16] Papp, B., Kristóf, G., and Gromke, C., 2021, "Application and assessment of a GPU-based LES method for predicting dynamic wind loads on buildings", *Journal of Wind Engineering and Industrial Aerodynamics*, Vol. 217, p. 104739.

[17] Gromke, C., and Ruck, B., 2005, "Die Simulation atmosphärischer Grenzschichten in Windkanälen", *Proceedings of the 13 GALA Fachtagung "Lasermethoden in der*

Strömungsmesstechnik", 6-8 September 2005, Cottbus, Germany, pp. 1–8.

[18] ANSYS Inc., Canonsburg, PA, 2023, *Ansys Fluent Theory Guide*, release 2023 R1.

[19] Wilcox, D. C., 1988, "Reassessment of the scale-determining equation for advanced turbulence models", *AIAA Journal*, Vol. 26, pp. 1299–1310, aDS Bibcode: 1988AIAAJ..26.1299W.

[20] Menter, F., 1993, "Zonal two equation kw turbulence models for aerodynamic flows", *23rd fluid dynamics, plasmadynamics, and lasers conference*, p. 2906.

[21] ANSYS Inc., Canonsburg, PA, 2023, *Ansys Fluent User's Guide*, release 2023 R1.

[22] Franke, J., Hellsten, A., Schlunzen, K. H., and Carissimo, B., 2011, "The COST 732 Best Practice Guideline for CFD simulation of flows in the urban environment: a summary", *International Journal of Environment and Pollution*, Vol. 44 (1-4), pp. 419–427, publisher: Inderscience Publishers.

Conference on Modelling Fluid Flow (CMFF'25)
The 19th International Conference on Fluid Flow Technologies
Budapest, Hungary, August 26-August 29, 2025

LES AND DES OF FLOW AND ICE ACCRETION ON WIND TURBINE BLADES.

Johan REVSTEDT[1], Robert SZÁSZ[2], Stefan IVANELL[3]

[1] Corresponding Author. Department of Energy Sciences, Faculty of Engineering, Lund University, P.O. Box 118, SE-22100 Lund, Sweden
Tel.: +46 46 222 4302, E-mail: johan.revstedt@energy.lth.se
[2] Department of Energy Sciences, Faculty of Engineering, Lund University E-mail: robert-zoltan.szasz@energy.lth.se
[3] Department of Earth Sciences, Uppsala University E-mail: stefan.ivanell@geo.uu.se

ABSTRACT

The aerodynamic effects of ice accretion on wind turbine blades has been studied using numerical methods. The ice accretion process on an aerofoil was simulated using RANS based simulations. The aerodynamic performance of the iced aerofoil was then investigated using several turbulence models, including both LES and DES. The results show that the shape of the ice has a profound influence on the lift and drag of the aerofoil and a small change in the ice shape can have a significant impact on the performance. Also, the choice of turbulence model is found to be important, with the results varying more than 100% between models.

Keywords: aerodynamic performance,vice accretion, LES, wind turbine

NOMENCLATURE

A	$[m^2]$	cell surface area
C	$[-]$	force coefficient
F	$[N]$	aerodynamic force
M	$[kg]$	accreted ice mass
Nt	[-]	number of triangles
U	$[m/s]$	droplet velocity
c	$[m]$	chord length
d	$[m]$	droplet diameter
m	$[kg/m^2]$	mass surface density
α	[deg]	angle of attack
ρ	$[kg/m^3]$	density

Subscripts and Superscripts

L, D	lift, drag
LWC	liquid water content
cl	clean aerofoil
air	properties of air
d	properties of droplet
i	cell number
j	coordinate direction
v	triangle number

1. INTRODUCTION

During the past decade, a substantial amount of wind power capacity has been developed in cold climate regions. Driving factors for this development are low population densities, as well as favourable atmospheric conditions featuring low air densities and often higher average wind speeds than in more moderate climates. In recent years, particularly large developments took place in Inner Mongolia (China), Northern Scandinavia and Finland, as well as Canada.[1] Despite the overall potential for wind power in cold-climate regions, the risk of blade icing poses a serious challenge for the operation of wind turbines in such areas. On the one hand, this relates to associated security issues such as ice throw. On the other hand, the aerodynamic degradation of the blades due to icing can bring about notable production losses as well as increased turbine loads. Today, about a quarter of the global installed wind energy capacity is expected to be prone to the risk of icing.[2] In counties like Sweden, with more than 80% of the installed capacity in 2020 being located in the most northerly quarter of the country, even higher shares of the turbine fleet are situated in icing-affected regions.[3] The modelling and forecasting of icing events and their impact on turbine performance and loads is therefore gaining importance for both planning and operation of wind farms.

Modelling the impact of icing on the blades of multi-megawatt wind turbines entails various coupled processes that need to be incorporated. The modelling challenge thus not only relates to the difficulties in modelling each individual process, but also in their connectivity and, consequently, the sensitivity of individual processes to the outputs of preceding modelling steps. Significant efforts have been made to investigate these processes including the meteorological forecasting of potential icing conditions, the modelling of ice accretion processes on airfoil sections [4, 5, 6], the prediction of airfoil degradation due to accumulated ice and, finally, the modelling of power and loads of the full turbine. While some

work purely focused on one of the aforementioned involved processes, most studies seek to establish an entire *model chain* comprising several connected models, each for one respective process.

To date, the majority of studies with an engineering perspective typically start from a given time series of liquid water content (LWC), temperature and wind speed. Based on such a set of input variables the accretion of ice on the airfoil sections of the turbine blade can generally be modelled. The first studies of the impact of icing on airfoils date back to 1930's and originated in the aerospace community.[7, 8] Over the past two decades various authors presented more specific studies on the accretion on wind turbine blades. Among these one may mention the work of Kangash et al [9] and Son and Kim [10].

Due to the scale separation in time between the flow and ice accretion, a common approach is to compute the ice accretion and the flow around the ice accreted airfoils in separate stages. For the flow computations a common approach is to use simplified methods to reduce the computational efforts. For example, a potential flow solver is used in LEWICE (although there is a possibility to import flow fields from other solvers) [11], whereas the panel method is used in TURBICE (see e.g. [12]). Recently, thanks to the increase in computational power and to the need to account for 3D effects, it is more and more common to solve the full set of Navier-Stokes equations (see e.g. [13, 14, 15]). Droplet transport is commonly modeled either in an Eulerian (e.g. [15]) or Lagrangian (e.g. [16, 17, 13]) framework.

In the case of rime ice conditions one can assume that all droplets hitting the surface freeze instantaneously, thus there is no need for heat transfer computations. The amount of droplets hitting the surface is determined explicitly or specified via the collection efficiency, depending if a lagrangian or eulerian model is used for droplet transport. To model glaze ice, the most common approach is to compute 1D heat transfer problems based on the so-called Stefan's problem formulated for aeronautical applications by Messinger in 1953 and further improved by Myers in 2001 (see e.g. [13]).

In the case of severe icing conditions the ice structures formed on the surfaces may significantly change the flow topology. In order to account for such changes, a common approach is to divide the time interval of the entire icing event in sub-intervals. During each sub-interval the geometry is considered constant. Before the next time interval is computed, the surface (and the mesh used for the flow computations) is updated to account for the ice accreted during the previous interval. Such a multi-step approach is used e.g. in [13]. A sensitivity study to physical and modeling parameters affecting airfoil icing is shown in [15].

The modified lift and drag curves of the airfoil sections resulting from the ice accretion computations can then be employed in an aerodynamic model of the wind turbine, typically based on the blade element momentum (BEM) method [18]. Homola *et al.* [19], for instance, employed such a model chain to investigate the impact of a generic 1h icing event on the NREL 5MW reference turbine [20]. A similar study was conducted by Etemaddar *et al.* [21]. Again imposing generic constant icing events, the authors investigated the sensitivity of the icing degradation to different meteorological and operational conditions. Later, Zanon *et al.* [22] also employed the aforementioned models but not in a sequential but in a weakly coupled manner. More specifically, the BEM approach provided the instantaneous rotational speed of the turbine during the icing event which allowed for an adaptation of the inflow conditions in the RANS-based accretion simulation. Others replaced the plain BEM model with a coupled aero-elastic solver in order to investigate the impact of icing on the structural dynamics of the turbine [23, 24, 25].

Hence, the overarching aim of this project is building the the model chain for meteorological simulations through ice accretion simulations of the wind turbine blades to simulating the performance of an ice accreted turbine. The particular focus of this paper is the sensitivity of the middle link in the chain, i.e. simulations of the ice build-up and the aerodynamic performance of a blade section.

2. METHOD

We are considering incompressible flow around an aerofoil, which is governed by the incompressible Navier-Stokes equations. Two kinds of simulation are performed, ice accretion simulations mainly performed using RANS models and simulations to acquire the aerodynamic forces where we employ LES and DES models. The methods used for the different simulations are given below.

2.1. Ice accretion simulations

In this work we assume that only rime ice is formed, i.e. the air contains super cooled water droplets that will freeze instantly in contact with the wing section. To model this, we represent the liquid water droplets using a statistical Lagrangian particle tracking method. Each motion of each droplet parcel is described by

$$\frac{dU_j}{dt} = \left(\rho_{\text{air}} - \rho_d\right) g \frac{\pi d^3}{6} + F_j \tag{1}$$

i.e. we only account for drag and gravity forces. Since the droplets are very small ($d = 27\mu m$) we neglect their influence on the air, i.e. one-way coupling. Effects of turbulence on the droplet motion are accounted for using a statistical particle dispersion model in which both the direction and magnitude are randomised and for the latter related to the local magnitude of turbulent kinetic energy, i.e. what is commonly known as a random walk model. The ice accretion simulations are performed using Open-

FOAM 4.1 in combination with an in-house tool for morphing the aerofoil surface based on the amount of ice accreted. The simulations are, in general, performed in several steps, alternating between generating a flow field, calculating the ice accretion and morphing the surface. Details within these steps may vary depending on simulation strategy (i.e. choice of turbulence model etc.). We have found that an efficient approach to create the iced aerofoil shape is to first create a statistically stationary flow field using a RANS simulation. Thereafter, the LPT is performed using this steady flow field and we account only for particle drag force and turbulent dispersion in the resulting differential equation of each droplet parcel. The turbulent dispersion is done with a stochastic model (a.k.a random walk). Each parcel of Lagrangian particles that impacts the aerofoil surface is registered. Since we are only considering rime ice, a droplet impacting the surface is considered to freeze immediately. It should be noted here that the time scale of the flow and the ice accretion differ substantially, with the icing time scale being much longer. To increase the computational efficiency we have therefore shortened the time scale by increasing the LWC artificially. Our previous investigations show that it is possible to decrease the time scale of ice accretion by a factor 1000, i.e. one hour of ice accretion is represented by 3.6 seconds of flow time. Following each hour of ice build-up the simulation is halted and the nodes of the aerofoil surface mesh are moved in accordance with the amount of ice accreted in each cell ensuring that the ice mass is conserved. Thereafter a new computational mesh is generated using snappyHexMesh and the aforementioned simulation steps are repeated. An example of the mesh of morphed aerofoils are depicted in Fig. 1.

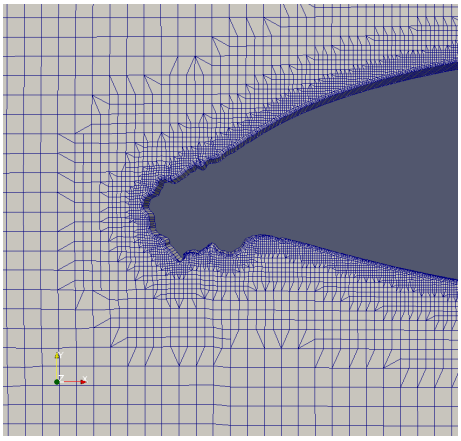

Figure 1. Example of a mesh from the ice accretion simulations

2.2. Surface smoothing

The ice distribution is smoothed over the airfoil surface. This step is motivated by the fact, that even if the length of the LPT computations is long enough to achieve a statistically converged ice distribution, depending on the mesh resolution used to discretise the airfoil, there might be small cells with no ice accreted, leading to physically irregular shape of the ice accreted surface.

The smoothing is done by transferring the information about the amount of accreted ice from cell centers to cell vertices and vice versa. The amount of accreted ice is stored during the CFD simulations in cell centers. The smoothing operates on the mass surface density, m_i:

$$m_i = M_i/A_i \tag{2}$$

where M_i is the amount of ice accreted in cell i and A_i is the area of cell i. Assuming that the amount of ice accreted in a cell contributes equally to the three vertices of the cell, the vertex values are computed as:

$$m_v = \sum_{i=1}^{Nt_v} m_i/3 \tag{3}$$

In the second step the information is transferred back to the cell centers:

$$m_i = \sum_{v=1}^{3} m_v/Nt_v \tag{4}$$

where Nt_v is the number of triangles (cells) sharing vertex v. The effect of smoothing is increasing with increasing number of loops applying Eqs. 3 and 4. After smoothing, the accreted mass in each cell is updated as:

$$M_i = m_i A_i \tag{5}$$

2.3. Turbulence modeling

In the ice accretion phase of the simulations we are using the SST k-ω model[26]. To study the aerodynamic performance of the iced aerofoils we also use LES and DES models. The LES approces considered are the WALE model [27] and the one equation eddy model [28]. The hybrid model considered is the IDDES based on the Spalart-Allmaras model [29]

3. COMPUTATIONAL SET-UP

The case considered in this study has the same specifications as one of the rime ice cases in the wind tunnel study by Hochart et al [30] (case 5).

The computational domain is outlined in Figure 2. The aerofoil shape is a NACA 63-415 which is placed 6 chord lengths (c) from the inlet, the distance to the outlet from the leading edge is $10c$ and the upper and lower boundaries are placed $6c$ from the aerofoil. The width of the aerofoil is $0.4c$. The chord length is $0.2m$ and the wind speed is $36m/s$ which corresponds to a Reynolds number of

Figure 2. Computational domain

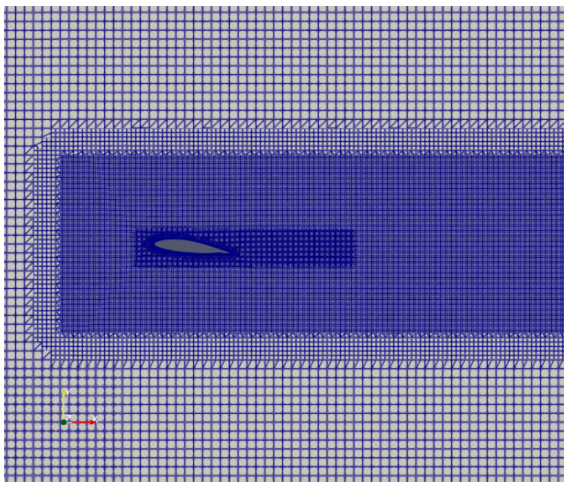

Figure 3. Mesh configuration, showing the local refinements arounf the aerofoil

$Re_c = 475,000$. The meshes used are hexahedral with unstructured refinements created using *snappyHexMesh*. The number of cells is about $2.2 \cdot 10^6$ in the LES cases and somewhat less for the RANS based simulation $1.5 \cdot 10^6$, but also varies slightly between cases due to the differences in ice shape. The cell size in the refinement closest to the wing section is $c/320$, however, where ever possible further refined in the surface normal direction. A typical mesh layout is shown in Figure 3. To get an indication of the mesh sensitivity, we compare the lift coefficient for the case of $\alpha = 7^o$ with resolutions $c/320$ and $c/160$, respectively. For the RANS based simulations, the difference is then about 5 %, while it is about 20% for the one equation eddy model. Considering the wall normal resolution, y^+ varies between 0.025 and 9.0 with an average value of 1.7. The velocity and the variables for the turbulence are set as constant values at the inlet and using the Neumann conditions at the outlet. The pressure is defined as constant at the outlet. The other outer boundaries of the domain specified using the slip condition. On the aerofoil we use no-slip conditions. For the ice accretion simulations a RANS model is used (SST k-ω model[26]).

In the accretion based simulations the following steps are taken. First a flow field is created using a steady state simulation. The particle simulation is then run using this "frozen" flow field. After a certain time the simulation is stopped and the aerofoil geometry is updated based on the number of droplets on the surface using the method outlined in Section 2.2. Here we use either 200 or 500 smoothing steps. An new mesh is then generated and a new flow field simulated. This is repeated until the required icing time is achieved. It should be noted that in reality the time scales for the flow and for the ice accretion process differ by several orders of magnitude. The ice accretion process has therefore been accelerated by a factor 1000 in order to reach reasonable simulation times. This is done by increasing the number of droplets in each parcel. The total ice accretion time in Hochart's wind tunnel experiment was 11.8 minutes, which corresponds to 0.708 s in our simulation. This was divided into 24 simulations of 0.0295 s each with morphing and smoothing of the geometry in between simulation.

The study of the aerodynamic performance of the iced aerofoil is performed using both geometries originating from using 200 and 500 smoothing steps respectively. Most of the simulations here are performed using the one equation eddy model [28], however, in some cases we have also used the WALE model, the IDDES model ant the SST model for comparison. In these simulations the angle of attack, α, has been varied between 2 and 12 degrees.

The RANS simulations are performed using SIMPLE approach (*simpleFoam*). The convective terms are discretised using a bounded second order upwind scheme and for the diffusive terms a second order central scheme is used. In the LES a bounded central scheme is used for the convective terms instead and we use the *pimpleFoam* solver instead.

4. RESULTS

4.1. Ice mass and profiles

As can be seen from Table 1 our simulations slightly overestimates the amount of ice accreted on the surface compared to Hochart et al [30]. As can also be observed, the difference in ice mass between out two cases is also fairly small. Turning our attention to how the ice mass is distributed on the surface we can see from Figure 4 that the iced profiles from the two simulations are very similar. Most of the ice is located close to the leading edge of the aerofoil with also a a fairly large amount accreted on the lower side, while the upper side is almost clean. This coincides fairly well with the measured profile (red dotted line in Figure 4. However, there are some important features missing in the simulation. The most pronounced of these are the horn shape created on

the upper side of the aerofoil and the waviness in the lower side. These features, especially the horn, might have a significant impact on the aerodynamic performance of the aerofoil.

Table 1. Accreted ice mass for the two levels of smoothing also comparing to the data of Hochart et al [30] of $0.182 kg/m$

Smooth steps	Accreted mass $[kg/m]$	Difference compared to [30] in %
200	0.190	4.4
500	0.198	8.8

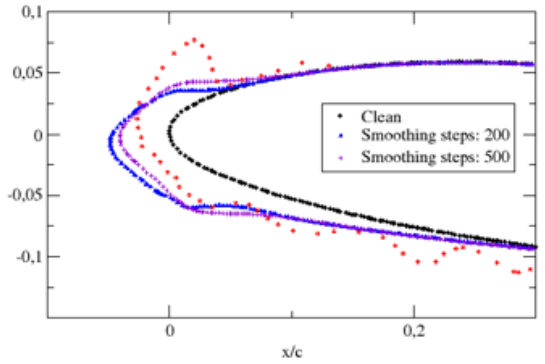

Figure 4. Aerofoil shape with ice at midspan for different levels of smoothing during the accretion process

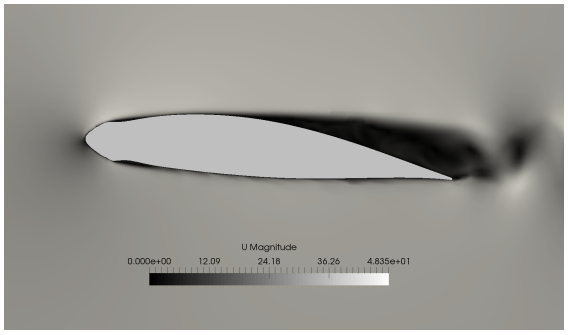

Figure 5. Velocity field at α = 7 deg.

4.2. Aerodynamic forces

One would expect that an aerofoil subjected to ice accretion would perform worse aerodynamically than a clean one. Considering Figure 6 this is indeed the case with two exceptions. Fo almost all angles of attack α the lift coefficient is lower and the drag coefficient is higher for the iced aerofoils. However, in two cases we locally observe an opposite trend. For the case with 200 smoothing steps in the ice accretion simulations (SM200) the performance is instead significantly better at $\alpha = 9^o$ and for SM500 similar results are found at $\alpha = 7^o$. In an effort to explain this behaviour let us consider snapshots of the speed at the four cases of interest. First consider the situation at $\alpha = 7^o$ shown in Figure 8. In the SM200 case the flow stays attached up to about half the chord length, where after a laminar separation occurs causing a fairly large wake. However, for SM500 the ice layer is at a slightly different angle causing a separation close to the leading edge with an almost immediate reattachment and the flow stays attached all the way to the trailing edge, with the boundary layer becoming turbulent at about 60% of the chord. From this the locally improved performance of the SM500 is obvious. Looking instead at $\alpha = 9^o$ the situation is slightly different. Here the SM200 geometry behaves almost identically to what we observed for SM500 at $\alpha = 7^o$, while the SM500 here displays a strong leading edge separation deteriorating the aerodynamic performance.

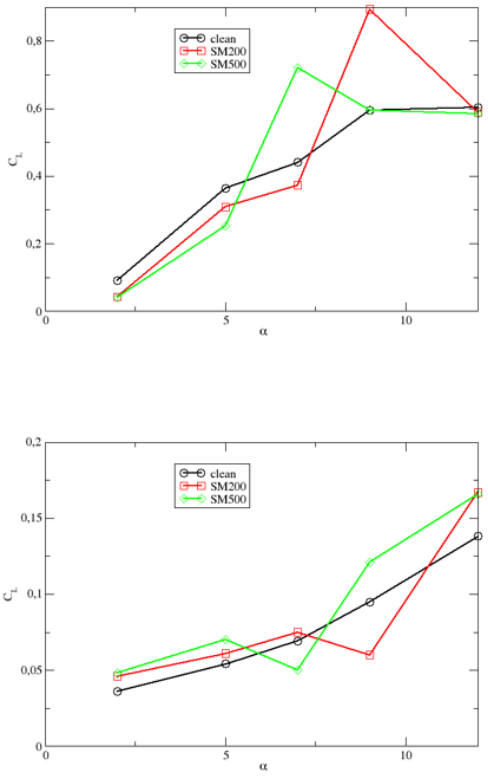

Figure 6. Lift and drag coefficient as a function of angle of attack of the iced aerofoils compare to the clean one. All simulations performed using the one-equation eddy model

4.3. Influence of turbulence model

It might also be of interest to investigate the sensitivity to turbulence model for the ice accreted aerofoil. Her we limit the study to the case $\alpha = 7^o$, since that is the angle of attack used by Hochart et al [30] and to the smoothing SM200.

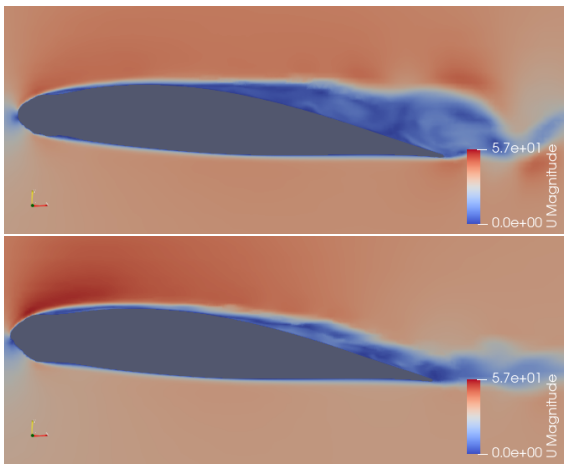

Figure 7. Snapshot of the speed for SM200 (top) and SM500 (bottom) for $\alpha = 7^o$. All simulations performed using the one-equation eddy model

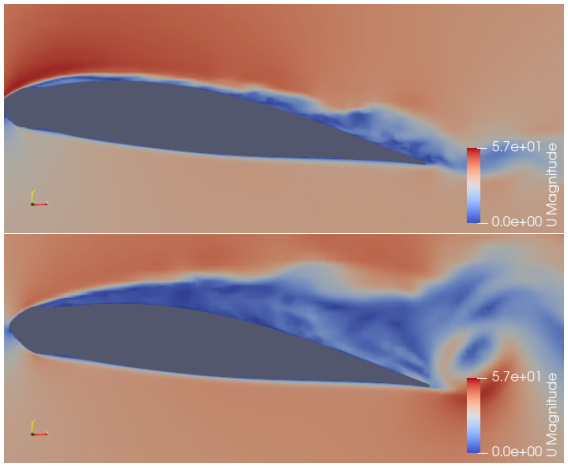

Figure 8. Snapshot of the speed for SM200 (top) and SM500 (bottom) for $\alpha = 9^o$. All simulations performed using the one-equation eddy model

As can be seen from Table 2 the variation in drag and lift between turbulence models is significant. Nevertheless, all these models show an increase in drag and a decrease in lift compared to a clean aerofoil simulated with the same turbulence model and instead tabulating the ratios of lift and drag coefficients shows a slightly different picture, as is seen in Table 2.

5. SUMMARY

Predicting the aerodynamic performance of an aerofoil subjected to ice accretion is a complex task. We have shown that slight differences in the iced geometry can have an enormous impact on the outcome at certain angles of attack, even showing improved performance. Comparing the different turbulence models used we can conclude that none of them are close to matching the data from Hochart et al [30]. I would seem as the one equation eddy model

Table 2. Lift and drag coefficients for $\alpha = 7^o$, SM200 for various turbulence models. To be compared by the results of Hochart et al [30]: $C_L = 0.491$, $C_D = 0.064$

Model	C_D	C_L
One equation eddy	0.078	0.360
WALE	0.021	0.808
IDDES	0.038	0.449
SST k-ω	0.026	0.850

Table 3. Ratios between lift and drag coefficients for an ice accreted and a clean aerofoil at $\alpha = 7^o$, SM200 for various turbulence models.

Model	$C_{\mathrm{D,ice}}/C_{\mathrm{D,cl}}$	$C_{\mathrm{L,ice}}/C_{\mathrm{L,cl}}$
One equation eddy	1.13	0.80
WALE	1.44	0.88
IDDES	1.66	0.66
SST k-ω	1.35	0.96

does a decent job but that model significantly under predicts the lift on the clean profile. This puts its suitability for use in this Reynolds number range in question. One should also mention that we have not taken into account the effects of surface roughness the ice generates beyond what we can resolve in our mesh. OUr earlier studies (not yet published) indicates that also adding surface roughness to a RANS simulation of an iced aerofoil significantly alters the aerodynamic performance.

ACKNOWLEDGEMENTS

The financial support for this work from the Swedish Energy Agency, project no. 47053-1, is gratefully acknowledged. Computational resources were provided by the centre for scientific and engineering calculations (LUNARC) at Lund University.

REFERENCES

[1] Wallenius, T., and Lehtomäki, V., 2016, "Overview of Cold Climate Wind Energy: Challenges, Solutions, and Future Needs", *WIREs Energy and Environment*, Vol. 5 (2), pp. 128–135.

[2] Stoyanov, D. B., and Nixon, J. D., 2020, "Alternative Operational Strategies for Wind Turbines in Cold Climates", *Renewable Energy*, Vol. 145, pp. 2694–2706.

[3] Badman, D., and Tengblad, Y., 2021, "Roadmap 2040Wind Power: Combating Climate Change and Improving Competitiveness", *Tech. rep.*, Swedish Wind Energy Association.

[4] Bragg, M., a.P. Broeren, and Blumenthal, L., 2005, "Iced-airfoil aerodynamics", *Progress in Aerospace Sciences*, Vol. 41 (5), pp. 323–362.

[5] Fu, P., and Farzaneh, M., 2010, "A CFD approach for modeling the rime-ice accretion process on a horizontal-axis wind turbine", *Journal of Wind Engineering and Industrial Aerodynamics*, Vol. 98 (4-5), pp. 181–188.

[6] Ronsten, G., Wallenius, T., Hulkkonen, M., Baring-Gould, I., Cattin, R., Durstewitz, M., Krenn, A., Laakso, T., Lacroix, A., Tallhaug, L., Byrkjedal, Ö., and Peltola, E., 2012, "State-of-the-Art of Wind Energy in Cold Climates", *Tech. rep.*, IEA Wind Task 19.

[7] Jones, R., and Williams, D., 1936, "The Effect of Surface Roughness of the Characteristics of the Airfoils NACA 0012 and RAF 34", *Tech. Rep. Report No.1708*, British ARC.

[8] Gulick, B., 1938, "Effect of Simulated Iced Formation on the Aerodynamic Characteristics of an Airfoil", *Tech. Rep. R.N. NACA- Wr.L-292*, NACA.

[9] Kangash, A., Virk, M., and Maryandyshev, P., 2022, "Numerical study of icing impact on the performance of pitch-regulated large wind turbine", *Wind Engineering*, Vol. 47 (2).

[10] Son, C., and Kim, T., 2020, "Development of an icing simulation code for rotating wind turbines", *Journal of Wind Engineering & Industrial Aerodynamics*, Vol. 203, p. 104239.

[11] Wright, W., 2008, "User ' s Manual for LEWICE Version 3 . 2", *Tech. Rep. NASA/CR–2008-214255*, NASA.

[12] Homola, M. C., Virk, M. S., Wallenius, T., Nicklasson, P. J., and Sundsbø, P. A., 2010, "Effect of atmospheric temperature and droplet size variation on ice accretion of wind turbine blades", *Journal of Wind Engineering and Industrial Aerodynamics*, Vol. 98 (12), pp. 724–729.

[13] Gori, G., Zocca, M., Garabelli, M., Guardone, A., and Quaranta, G., 2015, "PoliMIce: A simulation framework for three-dimensional ice accretion", *Applied Mathematics and Computation*, Vol. 267, pp. 96–107.

[14] Jin, J. Y., and Virk, M. S., 2019, "Study of ice accretion and icing effects on aerodynamic characteristics of DU96 wind turbine blade profile", *Cold Regions Science and Technology*, Vol. 160 (September 2018), pp. 119–127.

[15] Prince Raj, L., Yee, K., and Myong, R., 2020, "Sensitivity of ice accretion and aerodynamic performance degradation to critical physical and modeling parameters affecting airfoil icing", *Aerospace Science and Technology*, Vol. 98, p. 105659.

[16] Szasz, R., and Fuchs, L., 2012, "Numerical modeling of ice accretion on a wing section", J. Vad (ed.), *Proceedings of the Conference on Modelling Fluid Flow*, pp. 292–298.

[17] Szasz, R.-Z., Ronnfors, M., and Revstedt, J., 2016, "Influence of ice accretion on the noise generated by an airfoil section", *International Journal of Heat and Fluid Flow*, Vol. 62, pp. 83–92.

[18] Hansen, M. O. L., 2008, *Aerodynamics of Wind Turbines*, London, UK: Earthscan.

[19] Homola, M. C., Virk, M. S., Nicklasson, P. J., and Sundsbø, P. A., 2012, "Performance Losses Due to Ice Accretion for a 5 MW Wind Turbine", *Wind Energy*, Vol. 15 (3), pp. 379–389.

[20] Jonkman, J., Butterfield, S., Musial, W., and Scott, G., 2009, "Definition of a 5-MW Reference Wind Turbine for Offshore System Development", *Tech. Rep. NREL/TP-500-38060*, NREL.

[21] Etemaddar, M., Hansen, M. O. L., and Moan, T., 2014, "Wind Turbine Aerodynamic Response under Atmospheric Icing Conditions", *Wind Energy*, Vol. 17 (2), pp. 241–265.

[22] Zanon, A., De Gennaro, M., and Kühnelt, H., 2018, "Wind Energy Harnessing of the NREL 5 MW Reference Wind Turbine in Icing Conditions under Different Operational Strategies", *Renewable Energy*, Vol. 115, pp. 760–772.

[23] Rissanen, S., Lehtomäki, V., Wennerkoski, J., Wadham-Gagnon, M., and Sandel, K., 2016, "Modelling Load and Vibrations Due to Iced Turbine Operation", *Wind Engineering*, Vol. 40 (3), pp. 293–303.

[24] Gantasala, S., Luneno, J.-C., and Aidanpää, J.-O., 2016, "Influence of Icing on the Modal Behavior of Wind Turbine Blades", *Energies*, Vol. 9 (11), p. 862.

[25] Gantasala, S., Tabatabaei, N., Cervantes, M., and Aidanpää, J.-O., 2019, "Numerical Investigation of the Aeroelastic Behavior of a Wind Turbine with Iced Blades", *Energies*, Vol. 12 (12), p. 2422.

[26] Menter, F., 1994, "Two-Equation Eddy-Viscosity Turbulence Models for Engineering Applications", *AIAA Journal*, Vol. 32, pp. 1598–1605.

[27] Nicoud, F., and Ducros, F., 1999, “Subgrid-Scale Stress Modelling Based on the Square of the Velocity Gradient Tensor”, *Flow Turbulence and Combustion*, Vol. 62 (3), p. 183–200.

[28] Yoshizawa, A., 1986, “Statistical theory for compressible turbulent shear flows, with the application to subgrid modeling”, *Physics of Fluids*, Vol. 29 (7), p. 2152–2164.

[29] Spalart, P., Jou, W., and Strelets, M., 1997, “Comments on the Feasibility of LES for Wings, and on Hybrid RANS/LES Approach”, C. Liu, and Z. Liu (eds.), *Proceedings of First AFOSR International Conference on DNS/LES*.

[30] Hochart, C., Fortin, G., Perron, J., and Ilinca, A., 2008, “Wind turbine performance under icing conditions”, *Wind Energy*, Vol. 11, pp. 319–333.

Conference on Modelling Fluid Flow (CMFF'25)
The 19th International Conference on Fluid Flow Technologies
Budapest, Hungary, August 26-August 29, 2025

ODTLES: Large-Eddy Simulation with Autonomous Stochastic Subgrid-Scale Modeling Applied to Turbulent Duct Flow

Pavle Marinković[1,2,3], Juan A. Medina Méndez[2], Marten Klein[2,3], Heiko Schmidt[2,3]

[1] Corresponding Author. Tel.: +49 (0) 355 69 6034, Fax: +49 (0) 355 69 4891, E-mail: marinkov@b-tu.de
[2] Chair of Numerical Fluid and Gas Dynamics, Faculty of Mechanical Engineering, Electrical and Energy Systems, Brandenburg University of Technology Cottbus-Senftenberg. Siemens-Halske-Ring 15A, 03046 Cottbus, Germany
[3] Scientific Computing Lab, Energy Innovation Center, Brandenburg University of Technology Cottbus-Senftenberg. Universitätsstraße 22, 03046 Cottbus, Germany

ABSTRACT

In this work, we discuss the application of the One-Dimensional Turbulence-based (very) Large-Eddy Simulation model, abbreviated as ODTLES, to turbulent duct flow. ODTLES is a multi-scale flow model in which an autonomous stochastic One-Dimensional Turbulence (ODT) model, capable of simulating the full bandwidth of time and length-scales in a 1-D domain, is supplemented with large-scale 3-D information coming from a very large eddy simulation (VLES) grid. ODTLES is more expensive than any other VLES, but could be cheaper than highly resolved LES or, naturally, than Direct Numerical Simulation (DNS). Unlike Reynolds-Averaged Navier–Stokes (RANS) and VLES, ODTLES does neither need a wall model, nor a damping function. The correct near-wall behavior is naturally obtained from one SGS ODT domain that is locally wall-normal. The proposed hybrid (3-D/1-D) approach allows the resolution of all relevant scales, modeling certain aspects of 3-D turbulence on the SGS scale. Here, turbulent duct flow is considered as an example, which poses a moderate challenge for traditional LES due to emerging secondary flows that manifest themselves by corner vortices that crucially depend on the accurate capturing of small and large scale motions. Preliminary results indicate a reasonable match with DNS for mean velocity profiles, although capturing secondary flow structures remains a challenge at this stage. Further refinements of the solver and modeling approach are ongoing to improve accuracy and predictive capabilities.

Keywords: Duct flow, Large Eddy Simulation (LES), Multiscale modeling, One-Dimensional Turbulence (ODT), ODTLES, Turbulence modeling

NOMENCLATURE

C	[–]	eddy rate parameter
$C_i^{j->k}$	$[\frac{m}{s^2}]$	Coupling term from grid j to grid k for velocity component i
F_i^k	$[\frac{N}{m^3}]$	i-th component of the forcing field residing on an ODT line indirection k
K	[-]	kernel function
P	$[Pa]$	pressure field on the LES level
$P_{a,eddy}$	[–]	eddy acceptance probability
Re_{tau}	[-]	friction Reynolds number
T	$[s]$	simulation time
U_i	$[\frac{m}{s}]$	i-th component of the velocity field on the LES level
Z	[–]	small-scale suppression parameter
c_i	[-]	kernel coefficient
$f(l)$	[-]	assumed exponential distribution of eddy sizes
$g(x_{k,0})$	$[\frac{1}{m}]$	eddy position PDF
$h(l)$	$[\frac{1}{m}]$	eddy size PDF
l	$[m]$	eddy size
l_k^{-1}	[-]	Deconvolution operator
l_k	[-]	Convolution operator
u_i^k	$[\frac{m}{s}]$	i-th component of the velocity field on an ODT line in k direction
x_k	[-]	ODT aligned direction
$x_{k,0}$	[m]	eddy position
$f(x_k)$	[-]	mapping function
$\Delta\tau_\nu$	$[s]$	viscous time-scale
Δt_{VLES}	[s]	time step for VLES
Δt_{samp}	$[s]$	eddy sampling interval
ν	$[\frac{m^2}{s}]$	kinematic viscosity
ρ	$[\frac{kg}{m^3}]$	density
τ	$[s]$	local time scale of a mapping candidate
τ^{-1}	$[\frac{1}{s}]$	eddy frequency
H	[m]	duct height
L	[m]	duct length

Re_τ	[–]	friction Reynolds number
u_τ	[m/s]	friction velocity
$\mathcal{M}\{u_i^k(x_k,t)\}$	[-]	eddy mapping event

Subscripts and Superscripts

e	eddy event
i	component of vector
k	direction of ODT line
$*$	intermediate values (non-divergence-free values)

1. INTRODUCTION

Turbulence, known for its intricate and chaotic flow patterns, is a phenomenon of great importance in various engineering and scientific fields. From optimizing the aerodynamic performance of aircraft to enhancing mixing processes in chemical reactors, a thorough understanding of turbulent flows is crucial for improving design efficiency, predicting system behavior, and ensuring operational safety. Turbulent flows impact the effectiveness of transportation systems, the spread of pollutants in the environment, and the thermal management in industrial applications. Despite its ubiquity, accurately modeling turbulence remains one of the most challenging aspects of fluid dynamics.

Direct Numerical Simulation (DNS) offers full resolution of all turbulent scales and structures. The computational demands of DNS are, therefore, extremely high when flows are highly turbulent (the highest Reynolds number achieved to date with DNS for turbulent channel flow is $Re_\tau \approx 10{,}000$ [1]). In contrast, Reynolds-Averaged Navier–Stokes (RANS) simulations and Large Eddy Simulations (LES), which are more commonly used in practical engineering applications, often struggle to achieve the necessary accuracy, particularly in complex flow scenarios. This is especially true for wall-bounded flows, where traditional turbulence models rely on simplifying assumptions such as small-scale isotropy or local equilibrium of the near-wall flow, which has notable limitations due to which alternative approaches are still being actively researched (e.g. [2]). These assumptions, including low-order statistical closure models and the law-of-the-wall, are inadequate when the details of small-scale turbulent fluctuations are critical. To overcome the limitations of wall models and diffusive or filter-based turbulence models, alternative approaches such as stochastic turbulence models have been developed. One such model is the One-Dimensional Turbulence-based Large Eddy Simulation (ODTLES) model [3, 4] introduced more than a decade ago, and further developed more recently by [5, 6]. ODTLES aims to achieve the fidelity of DNS by resolving all relevant time and length scales within columnar stacks of dimensionally reduced subdomains. In these stacks, the three-dimensional aspects of turbulence are modeled using a stochastic process on a one-dimensional domain, significantly reducing computational costs while maintaining full-scale resolution. Although still in its developmental stages, ODTLES has demonstrated promising results, particularly in simulating turbulent channel flows with friction Reynolds numbers up to $Re_\tau \approx 2040$ on a single Banana Pi M64 computer [6].

2. PRELIMINARY STUDY CASE

As a preliminary test case, we apply the ODTLES model to turbulent flow in a square duct and validate the results against Direct Numerical Simulation (DNS) data provided by Zhang et al. [7]. The geometric dimensions of the duct are chosen to match those used in the DNS study, and are illustrated in Figure 1.

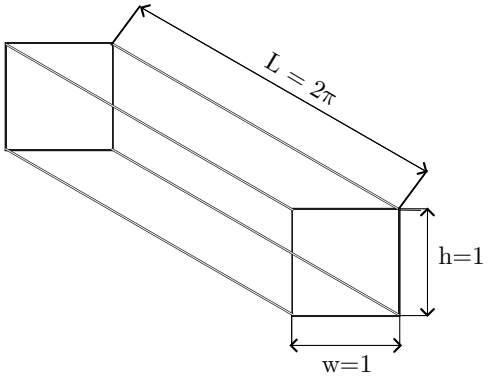

Figure 1. Computational domain of the square duct configuration.

No-slip boundary conditions are applied at the duct walls, while periodic boundary conditions are imposed at the inlet and outlet in the streamwise direction. To drive the flow, a constant streamwise pressure gradient is applied. The magnitude of the pressure gradient is prescribed as $\frac{u_\tau^2}{H}$, where u_τ is the friction velocity and H is the duct width. The value of the kinematic viscosity is then calculated as $\nu = \frac{u_\tau \frac{H}{2}}{Re_\tau}$.

Simulations were performed for friction Reynolds numbers $Re_\tau = 300$ and 600. In both cases, the base LES grid has a resolution of $10 \times 10 \times 10$, while the auxiliary ODTLES grids (see figure 3) are refined to ensure that the first cell sizes in the y and z directions correspond to wall units y^+ and z^+ less than one.

This very coarse base LES resolution has been utilized because we are still working on the algorithm, although in previously it has been shown that using a base resolution that is slightly higher (16x16 resolution in the cross section) to be sufficient for moderately turbulent duct flows [5].

3. ONE-DIMENSIONAL TURBULENCE

Kerstein's One-Dimensional Turbulence model (ODT) [8] is a stochastic modeling approach that utilizes dimensionally reduced map-based advection modeling. It is conceptualized as a standalone turbulence model that operates on a one-dimensional domain, akin to the visualization of a turbulent flow

field from within a turbulence line-of-sight, see also [8, 9]. The model simulates the effects of three-dimensional turbulence through a discrete sequence of stochastic events, which are commonly known as eddy events. These eddy events are represented by a model representation of the effect that vortical motions cause in 1-D scalar profiles within turbulent flows. Assuming a 1-D domain aligned in direction x_k, where $k \in \{1, 2, 3\}$, eddy events are implemented as a triplet map of one-dimensional scalar profiles, $\psi(x_k) \rightarrow \psi[f(x_k)]$, where $f(x_k)$ is the mapping function. The eddy events are sampled in time with an interval Δt_{samp}, where $\Delta t_{samp} \ll \tau_\nu$, with τ_ν being the viscous time-scale. This guarantees full time-scale resolution of the turbulent flow. Operationally, the sampling follows a Poisson stochastic process, achieving a pre-specified mean acceptance probability and a corresponding mean eddy rate. Details of the sampling process can be found in [10]. The mean acceptance probability is calculated as the online average of the different acceptance probabilities for each eddy event candidate, $P_{a,eddy}$, which is estimated as

$$P_{a,eddy} = \frac{\Delta t_{samp}}{l^2 \tau(y_0, l, t) h(l) g(y_0)}. \tag{1}$$

In this equation, $h(l)$ and $g(x_{k,0})$ are presumed probability density functions (PDFs) for eddy sizes l and eddy positions $x_{k,0}$, respectively. Indeed, $g(x_{k,0})$ is a uniform PDF, given that it is assumed that turbulent eddies can occur with equal probability everywhere along the 1-D domain. Conversely, $f(l)$ is an assumed exponential distribution of eddy sizes, see details in [9]. The local time scale of an individual mapping candidate is denoted by τ. The term "candidate" is used because not all mappings yield a physical time-scale or eddy turnover time τ. This is best explained when defining the eddy frequency τ^{-1} based on dimensional arguments for extractable kinetic energy. Operationally, τ^{-1} considers the following integral kinetic energy balance for the eddy candidate with size l, where a proportionality coefficient C has been inserted in order to indicate the direct proportionality, see details in [8, 9]

$$\tau^{-1} = C \frac{\nu}{l^2} \sqrt{\left[\frac{l}{\nu} \sum_i^3 \frac{1}{l^2} \int_l u_i^k(t, f(x_k)) K(x_k) \mathrm{d}x_k \right]^2 - Z} \tag{2}$$

In order for τ^{-1} to be a real number, the quantity within the square root must be positive. To that extent, the parameter Z acts as a dimensionless coefficient for eddy suppression. Specifically, it restricts the implementation of small eddies, and can take the form of either a Reynolds number or a viscous coordinate following algebraic manipulation of Equation 2. Both C and Z are then turbulence model coefficients indicating the empiricism associated with the ODT model. Note that $u_i^k(t, f(x_k))$ represents the mapped profile for the velocity component u_i (which is represented in the domain aligned in x_k) at time t, while $K = x_k - f(x_k)$ is a kernel function (see [8]). Note that we also use $i \in \{1, 2, 3\}$, similar to k. Reasons for the apparent notation redundancy regarding index k will be clarified later. Acceptance of an eddy event candidate, i.e., the mapping $u_i^k(x_k) \rightarrow u_i^k(f(x_k))$, also implies a linear transformation of the post-mapped profile $u_i^k(f(x_k)) + c_i K$, where c_i is a (uniform) kernel coefficient which depends on the form of the scalar velocity profile. Details of the calculation of c_i can be found in [11, 9].

For an ODT line oriented in the x_k-direction, there is also a 1-D governing partial differential equation, which in the case of low Mach constant property flow can be written as

$$\left.\frac{\partial u_i^k}{\partial t}\right|_{\mathrm{ODT}} = \int_0^T \sum_e \mathcal{M}\{u_i^k(x_k, t)\} \delta(t - t_e) \mathrm{d}t + \nu \frac{\partial^2 u_i^k}{\partial x_k^2} + F_i^k \tag{3}$$

where $\mathcal{M}\{u_i^k(x_k, t)\}$ is one transformation of the form $u_i^k(x_k, t) \rightarrow u_i^k(f(x_k), t) + c_i K(x_k)$. This transformation can be implemented several times in an intermittent fashion during the numerical time integration of the 1-D PDE, which is the reason why a summation over eddy events e appears in Equation 3. The delta function in Equation 3 is only written for the purpose of its integral identity returning a discrete value (discrete eddy events in time), whereas said integral implies the entire simulation time T. As commented before, eddy events are evaluated using a predictive approach based on the current flow state and a sampled eddy size l and position $x_{k,0}$. When an eddy event is accepted, the diffusive (and forcing) terms of Equation 3 are advanced in time up to the moment in which the eddy event trial is set to occur. This process is commonly referenced as a catch-up diffusion event in ODT. Additionally, in Equation 3, F_i^k is an acceleration term due to a corresponding body force.

To illustrate the impact of eddy events and the subsequent diffusion process on the velocity profile, we present a plot showing an initial velocity profile, the profile after the mapping of an eddy event, and the profile after the catch-up diffusion in Figure 2.

4. MODEL EXTENSION: 3-D ODTLES

In order to supplement VLES information to ODT, and extend the model to its 3-D counterpart, ODTLES, it is necessary to consider modifications to the standalone ODT implementation. Instead of representing a 3-D velocity field with three velocity components, as it is usual in the standalone ODT vector formulation, see [11], the ODT module in ODTLES represents only two velocity components within the 1-D domain. To that extent, we redefine the ODT velocity field u_i^k by making i and k permuta-

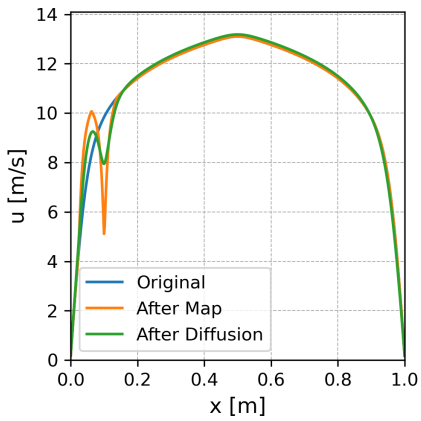

Figure 2. Visualization of map-based advection and diffusion operators for a smooth initial profile, the profile after eddy mapping, and the profile after catch-up diffusion.

tions of $\{1, 2, 3\}$, with $i \neq k$. Thus, the velocity component aligned in the direction of the ODT domain is not governed by Equation 3. Having said that, in order to develop a coherent interpretation of ODTLES, it is necessary to define operators relating the different scales and numerical grids (e.g., the VLES and the ODT grid). The one-dimensional filtering operator $[l_k]$ generates a coarsely resolved velocity variable from the finely resolved velocity in the x_k direction:

$$U_i(X_k, t) = [l_k]u_i^k(x_k, t) = \frac{1}{\Delta X_k} \int_{X_k - \frac{\Delta X_k}{2}}^{X_k + \frac{\Delta X_k}{2}} u_i^k \, dx_k \quad (4)$$

Here, X_k is the resulting coarsened grid (previously x_k) with grid cell sizing Δ_{X_k}, while U_i is the corresponding large-scale velocity field.

4.1. Spatial discretization strategy

ODTLES is a multi-scale model that operates on meshes with different levels of refinement. The coarsest resolution or large-scale information level is represented in a (V)LES grid, whose resolution is set according to the standard practices used in VLES or coarse RANS simulations. Additional to the VLES grid, we introduce three supplementary grids, which we reference as ODTLES grids. Each of these three grids are equivalent to the VLES grid, but feature refinements in each of the three principal Cartesian directions, respectively. The level of said refinements is set according to the Direct Numerical Simulation (DNS) resolution requirements for the smallest turbulent scales in each respective direction. To that extent, the memory requirements for ODTLES can be estimated as approximately $\sim 3N_{\text{VLES}}^2 N_{\text{DNS}}$, where N_{VLES} and N_{DNS} are the VLES and ODT grid resolutions, respectively. This is significantly lower than the memory requirements for DNS, which can be roughly estimated as $\sim N_{\text{DNS}}^3$. Consequently, for a fixed LES resolution, the cost of ODTLES for increasing Reynolds numbers varies linearly, in contrast to the cubic variation expected for DNS [12]. Overall, each ODTLES grids is the result of an embedding of a set of parallel 1-D ODT domains, as seen in Figure 3. This geometric configuration restricts the application of the current ODTLES model to structured meshes. Although ODTLES is not fundamentally restricted to equidistant meshes, the current implementation prioritizes equidistant meshes for simplicity (grid discretization in every direction is equidistant, although it may be different across directions).

In ODTLES, the velocity components u_i^k correspond to velocity fields represented in an ODTLES grid refined in direction x_k. Conversely, the coarsely resolved pressure and velocity variables in the VLES grid are denoted as P and U_i, respectively.

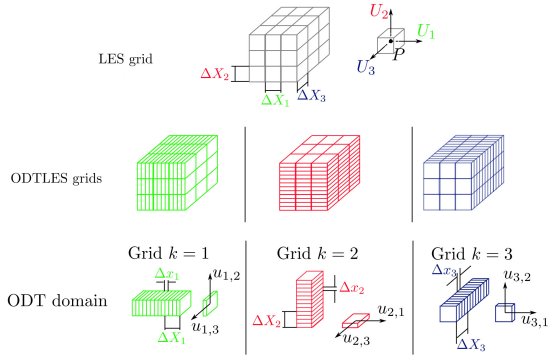

Figure 3. ODTLES model structure, showing the primary LES grid and the three supplementary ODTLES grids with refinements in the principal Cartesian directions.

A consistency condition needs to be fulfilled between the velocity fields, such that

$$U_i = [l_k]u_i^k, \quad \text{for every } k \quad (5)$$

The latter consistency condition implies that the filtered velocity field representation of all ODTLES grid represented velocity fields should be equivalent, see also [5].

In contrast with the precepts of the filtering operation defined in Equations 4 and 5, it is in general not possible to perfectly reconstruct a field u_i^k from its large-scale counterpart. That is, the filtering operator has no unique inverse, such that, in general, $[l_k^{-1}][l_k] \neq 1$. Nevertheless, Schmidt et al. [3] proposed a numerical approximation for the refinement of coarsely resolved information, i.e., an algorithm for the deconvolution operator of coarse fields $[l_k^{-1}]$. Said algorithm was later improved by Glawe [5] to address the issue of artificial extrema generation near no-slip boundary conditions. The algorithm in [3, 5] is high-order accurate and avoids the introduction of noticeable discontinuities. It also fulfills an import-

ant integral constraint, namely,

$$U_i = [l_k][l_k^{-1}]U_i \tag{6}$$

An example of the application of $[l_k^{-1}]$ with k being the wall normal direction in our duct case is visualized in Figure 4.

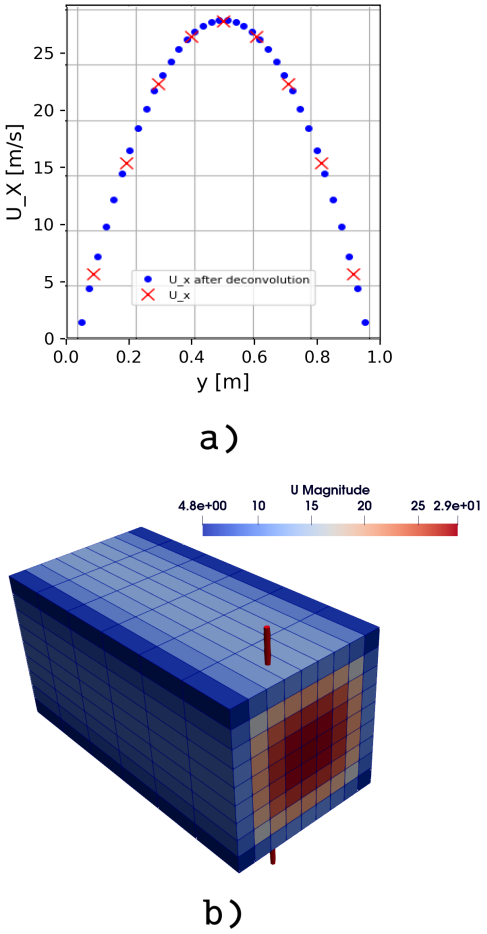

Figure 4. Example of the deconvolution algorithm at work. a) The deconvoluted fine-scale-resolved velocity together with the coarse-scale velocity. b) Visual representation of the VLES grid and the selected ODT domain along which the deconvolution was done (indicated by the extended local y axis shown in red).

4.2. ODTLES governing equations

The 3-D extension of the standalone ODT model with LES support, ODTLES, can be written as follows for the velocity component u_i, $i \in \{1,2,3\}$ in a grid refined in direction x_k, $k \neq i$, $k \in \{1,2,3\}$

$$\frac{\partial u_i^k}{\partial t} = -[l_k^{-1}]\left\{\frac{\partial(U_iU_i)}{\partial X_i} + \frac{\partial\left(U_jU_i\right)}{\partial X_j} + \frac{\partial(U_kU_i)}{\partial X_k}\right\} + \nu\frac{\partial^2 u_i^k}{\partial X_i^2} + \left.\frac{\partial u_i^k}{\partial t}\right|_{\mathrm{ODT}} + C_i^{j\to k} - \frac{1}{\rho}\frac{\partial P}{\partial X_i} \tag{7}$$

Note that the Einstein summation convention is omitted in equation 7, implying that there are actually six equations similar to 7 which must be solved simultaneously (2 velocity components in 3 ODTLES grids). The corresponding ODTLES continuity equation, or zero divergence condition, is only satisfied at the VLES level, see [5], and it is written as

$$\frac{\partial U_i}{\partial X_i} + \frac{\partial U_j}{\partial X_j} + \frac{\partial U_k}{\partial X_k} = 0 \tag{8}$$

In equations 7 and 8, ρ denotes the density. Also, the term $\partial u_i^k/\partial t|_{\mathrm{ODT}}$ is the entire ODT acceleration (or time-advancement) given by Equation 3. Such term considers the standalone ODT time-advancement of one ODT *stack* within the ODTLES grid, during $T = \Delta t_{\mathrm{VLES}}$, the latter being a time-step required for stable numerical integration on the coarse VLES grid level. This implies that the numerical time-advancement of Equation 3 utilizes an eddy sampling procedure $\Delta t_{\mathrm{samp}} \ll \tau_\nu$, and catch-up diffusion events with time-stepping $\Delta t_{\mathrm{ODT}} \ll \Delta t_{\mathrm{VLES}}$, where again, Δt_{ODT} is a numerical time-step required for stable time-integration in the ODT domain (hence, compliant with the corresponding CFL condition). We note that the standalone ODT time-advancement imposes a limit on the maximum eddy size to be sampled from the presumed eddy size PDF $h(l)$, see [10, 13]. This limit is maintained in the standalone ODT advancement which is part of ODTLES.

It is also noted that we indicated lowercase and uppercase variables distinctively in Equations 7 and 8. On one hand, lowercase variables indicate the finely resolved fields or directions, while, on the other hand, uppercase variables denote the VLES fields and directions. As a notation example, we note $\partial^2 u_i^k/\partial X_i^2$ as being a coarse diffusion operator on u_i^k, the finely resolved velocity field defined on grid k (finely resolved in x_k direction); said coarse diffusion operator considers the VLES grid cell size ΔX_i for the diffusion estimation (recall that $i \neq j \neq k$). Also, note that all advection terms are defined at VLES level, with the VLES velocity components U_i, U_j, U_k. All advection effects are simply deconvoluted from the VLES grid to each ODTLES grid.

The term $C_i^{j\to k}$ in Equation 7 is a coupling term that facilitates the communication between ODTLES grids. This allows the coupling of the ODT-modeled turbulent advection from the array of 1-D domains which conform the ODTLES grid refined in x_j direction to the ODTLES grid refined in x_k direction. In order to avoid double-counting of the forcing term from the standalone ODT advancement in ODTLES grid j in the ODTLES grid k, the forcing term is subtracted from the time-advancement. In fact, the acceleration term $\partial u_i^k/\partial t|_{\mathrm{ODT}}$ is better understood as a velocity change in a time interval $T = \Delta t_{\mathrm{VLES}}$, for the purpose of the coupling represented by $C_i^{j\to k}$. These

considerations lead to the definition of $C_i^{j\to k}$ as

$$C_i^{j\to k} = [l_k^{-1}][l_j]\left(\left.\frac{\partial u_i^j}{\partial t}\right|_{\text{ODT}} - F_i^j \right) \tag{9}$$

Figure 5 shows a visualization of the instantaneous vortical structures, represented by Q-criterion iso-surfaces, alongside the instantaneous velocity magnitude.

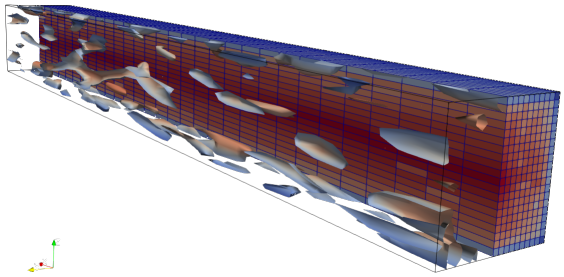

Figure 5. Instantaneous flow structures in the square duct. The left half of the domain shows iso-surfaces of the Q-criterion highlighting vortical structures, while the right half displays the instantaneous velocity magnitude. Visualization performed on a mesh of a higher resolution for visualization quality.

Equation 7 is solved using a finite-volume method (FVM) discretization with the standard midpoint rule for locating all flow variables at cell centers. Standard upwind interpolation schemes are used for the advective fluxes, and linear interpolation schemes are used for the diffusion fluxes. It is noted that this discretization method is different from previous ODTLES implementations relying on a staggered grid logic, see [6, 5]. That is, we have transitioned to a collocated approach. The numerical time integration method is defaulted to an explicit Euler scheme. However, we note that an implicit-explicit scheme for better stability was proposed in the staggered grid logic in [6].

Finally, we comment on the pressure gradient term $\partial P/\partial X_i$ in Equation 7. It is important to note that the pressure variable P is only defined on the VLES grid level. Applying a projection method, we split the time-advancement of Equation 7 into a predictor and a corrector step. The predictor step considers all momentum contributions other than the pressure gradient. This causes a change in the ODTLES velocity fields, e.g., $u_i^{k,n}$ to $u_i^{k,*}$ where we have used the superindex n to indicate a time discretization, such that time-advancement takes place from t^n to t^*, with $\Delta t_{\text{VLES}} = t^* - t^n$. Note that all advection effects are calculated on the VLES grid at time t^n, e.g., using the velocity field U_i^n. Following the predictor step, we obtain the intermediate non-divergence-free velocity fields u_i^{k*}. Due to $C_i^{j\to k}$, these velocity fields are consistent across ODTLES grids, such that we can obtain the VLES intermediate velocity field using the filtering operator,

$$U_i^* = [l_k]u_i^{k*} \tag{10}$$

The intermediate predicted VLES velocity fields are then used for the corrector step in order to enforce zero-divergence at the VLES level by solving the following pressure Poisson equation,

$$\begin{aligned}\frac{\partial^2 P}{\partial X_i^2}+\frac{\partial^2 P}{\partial X_j^2}+\frac{\partial^2 P}{\partial X_k^2} \\ = \frac{\rho}{\Delta t_{\text{VLES}}}\left(\frac{\partial U_i^*}{\partial X_i}+\frac{\partial U_j^*}{\partial X_j}+\frac{\partial U_k^*}{\partial X_k}\right)\end{aligned} \tag{11}$$

After P is found from equation 11, the VLES velocity field U_i is updated to the next time-step for advancement t^{n+1} as

$$U_i^{n+1} = U_i^* - \frac{\Delta t_{\text{VLES}}}{\rho}\frac{\partial P}{\partial X_i} \tag{12}$$

The change $U_i^{n+1} - U_i^*$ over Δt_{VLES} is considered a source term (after deconvolution) to update $u_i^{k,*}$ to $u_i^{k,n+1}$. This updates the information in the ODTLES grids. Note that we obtain the mass-fluxes required to evaluate the divergence of U_i^* in equation (11) by linear interpolation. Said face-centered mass-fluxes are also updated with equation 12 using a face-centered pressure gradient (calculated using the collocated pressure values). They are stored and used later for the calculation of the upwinded VLES advection effects in equation 7.

5. SOLVER IMPLEMENTATION

The current ODTLES codebase represents the second C++ rewrite of the original Fortran code developed by Christoph Glawe in [6]. The initial C++ codebase, a porting used in a previous publication in [6], was developed in order to modernize the original code and achieve high modularity and expandability. The current version is a highly refactored iteration of that codebase. The strategy and experiences of this process have been documented in [14], highlighting the importance and benefits of clean code principles. By adhering to these practices, we have completed a comprehensive refactor of the remaining parts of the algorithm, which we anticipate will facilitate quick and relatively easy improvements and expansions of the current ODTLES algorithm.

As discussed in [12], ODTLES greatly benefits from parallelization. In its current version, we utilize OpenMP to parallelize major parts of the algorithm. Most notably, we advance the ODT part of the momentum equations in parallel for each ODT line. Running the ODTs in parallel is observed to have excellent parallel efficiency due to the numerous individual tasks, each taking roughly the same amount of time, with tasks that are substantial enough such that the overhead of thread creation is not significant.

Similarly, all deconvolution operations, being one-dimensional, are parallelized using the same logic. These operations are also observed to exhibit high parallel efficiency, although we expect slightly worse performance as in the ODT part, since the tasks are not as computationally expensive.

For the advancement of the remaining parts of the momentum equations, we have divided the available threads into three groups—one for each ODTLES grid—and perform the explicit advancement in parallel within each group. This approach is also observed to yield a good parallel efficiency.

In the current code version, the pressure Poisson problem of Equation 11 is solved using the Eigen library's SparseLU solver [15]. While a strict performance measurement has not been carried out for this part of the algorithm, we anticipate that it will greatly benefit from further parallelization efforts. In the future, we plan to utilize Hypre's multigrid solvers [16] as in the older ODTLES versions in [5, 6], which are designed to run in parallel and are well-suited for large-scale linear systems. This transition is expected to further enhance the efficiency and scalability of our solver, although we stress that the bottleneck of the algorithm should not be in the Poisson problem anyway, since this is only solved at the large-scale VLES grid level.

6. PRELIMINARY RESULTS

We have conducted simulations of turbulent flow in a square duct at friction Reynolds numbers Re_τ = 300 and 600.

In the current setup, we are actively fine-tuning the value of the model's C parameter, while keeping the Z parameter fixed at the standard value commonly used in standalone ODT studies. These adjustments aim to optimize the balance between model fidelity and computational efficiency.

So far, preliminary results demonstrate that the refactored ODTLES implementation is capable of producing mean streamwise velocity profiles along the wall bisector that agree reasonably well with reference DNS data by Zhang et al. [7], as shown in Figure 6.

While previous work has shown that ODTLES can capture the emergence of secondary flows in duct geometries [5]), the present solver—undergoing substantial algorithmic restructuring—has not yet successfully reproduced these secondary motions. This limitation is currently under investigation.

Furthermore, we are exploring additional algorithmic improvements, particularly concerning the treatment of advection terms within the ODTLES framework, with the aim of enhancing accuracy while not significantly decreasing performance.

7. SUMMARY AND OUTLOOK ON ONGOING AND FUTURE WORK

In this study, we presented the implementation of a recent version of the One-Dimensional Turbulence-based Large-Eddy Simulation (ODTLES) model within a newly refactored C++ codebase. This framework provides increased flexibility, maintainability, and testing capabilities, allowing for the use of arbitrary boundary conditions on a structured finite-volume collocated grid.

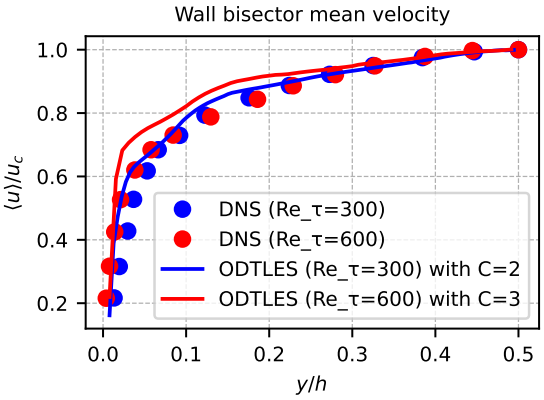

Figure 6. Comparison of mean streamwise velocity profiles from ODTLES and DNS [7] at Re_τ = 300 and 600.

We applied the model to turbulent flow in a square duct, a challenging test case due to the presence of secondary flows and corner vortices. While preliminary results show reasonable agreement with DNS data in terms of mean velocity profiles along the wall bisector, the current solver has not yet been able to fully capture the complex secondary flow structures observed in experiments and previous ODTLES studies [5].

This limitation is attributed to ongoing algorithmic restructuring, especially concerning the treatment of advection terms, and highlights the need for further refinement. Future work will focus on addressing these challenges and performing additional tests and comparisons, with the goal of achieving robust and accurate predictions of three-dimensional flow features in duct geometries.

ACKNOWLEDGEMENTS

This research is supported by the German Federal Government, the Federal Ministry of Education and Research and the State of Brandenburg within the framework of the joint project EIZ: Energy Innovation Center (project numbers 85056897 and 03SF0693A) with funds from the Structural Development Act for coal-mining regions.

REFERENCES

[1] Hoyas, S., Oberlack, M., Alcántara-Ávila, F., Kraheberger, S. V., and Laux, J., 2022, "Wall turbulence at high friction Reynolds numbers", *Phys Rev Fluids*, Vol. 7, p. 014602, URL `https://link.aps.org/doi/10.1103/PhysRevFluids.7.014602`.

[2] Heinz, S., and Fagbade, A., 2025, *A critical review of hybrid RANS-LES concepts: Continuous eddy simulation versus classical methods*, American Institute of Aeronautics and Astronautics, Inc.

[3] Schmidt, R. C., Kerstein, A. R., and McDermott, R., 2010, "ODTLES: A multi-scale model for 3D turbulent flow based on one-dimensional turbulence modeling", *Comput Methods Appl Mech Eng*, Vol. 199 (13), pp. 865–880.

[4] Gonzalez-Juez, E. D., Schmidt, R. C., and Kerstein, A. R., 2011, "ODTLES simulations of wall-bounded flows", *Phys Fluids*, Vol. 23, p. 125102.

[5] Glawe, C., 2015, "ODTLES: Turbulence Modeling Using a One-Dimensional Turbulence Closed Extended Large Eddy Simulation Approach", Ph.D. thesis, Freie Universität Berlin.

[6] Glawe, C., Méndez, J. A. M., and Schmidt, H., 2018, "IMEX based multi-scale time advancement in ODTLES", *Z Angew Math Mech*, Vol. 98, pp. 1907–1923.

[7] Zhang, H., Trias, F. X., Gorobets, A., Tan, Y., and Oliva, A., 2015, "Direct numerical simulation of a fully developed turbulent square duct flow up to Re=1200", *International Journal of Heat and Fluid Flow*, Vol. 54, pp. 258–267, URL `https://www.sciencedirect.com/science/article/pii/S0142727X15000685`.

[8] Kerstein, A., 1999, "One-Dimensional Turbulence: Model formulation and application to homogeneous turbulence, shear flows, and buoyant stratified flows", *J Fluid Mech*, Vol. 392, pp. 277–334.

[9] McDermott, R. J., 2005, "Toward one-dimensional turbulence subgrid closure for large-eddy simulation", Ph.D. thesis, University of Utah.

[10] Lignell, D. O., and Rappleye, D. S., 2012, "One-dimensional-turbulence simulation of flame extinction and reignition in planar ethylene jet flames", *Combust Flame*, Vol. 159 (9), pp. 2930–2943.

[11] Kerstein, A. R., Ashurst, W. T., Wunsch, S., and Nilsen, V., 2001, "One-Dimensional Turbulence: Vector formulation and application to free shear flows", *J Fluid Mech*, Vol. 447, p. 85–109.

[12] Méndez, J. A. M., Glawe, C., Starick, T., Schöps, M. S., and Schmidt, H., 2019, "IMEX-ODTLES: A multi-scale and stochastic approach for highly turbulent flows", *Proc Appl Math Mech*, Vol. 19, p. e201900433.

[13] Klein, M., Schmidt, H., and Lignell, D. O., 2022, "Stochastic modeling of surface scalar-flux fluctuations in turbulent channel flow using one-dimensional turbulence", *Int J Heat Fluid Flow*, Vol. 93, p. 108889.

[14] Marinković, P., Medina, J. A., Schöps, M. S., Klein, M., and Schmidt, H., 2025, "Experiences From the Bottom-Up Development of an Object-Oriented CFD Solver with Prospective Hybrid Turbulence Model Applications", *Proc Appl Math Mech*, Vol. 25 (1), p. e202400190, `https://onlinelibrary.wiley.com/doi/pdf/10.1002/pamm.202400190`.

[15] Guennebaud, G., Jacob, B., et al., 2010, "Eigen v3", http://eigen.tuxfamily.org.

[16] "*hypre*: High Performance Preconditioners", `https://llnl.gov/casc/hypre`, `https://github.com/hypre-space/hypre`.

Conference on Modelling Fluid Flow (CMFF'25)
The 19th International Conference on Fluid Flow Technologies
Budapest, Hungary, August 26-August 29, 2025

NUMERICAL ANALYSIS OF SWIRLING FLOW INDUCED BY AXIAL FAN

Aleksandar Ćoćić[1], Balazs Pritz[2]

[1] Corresponding Author. University of Belgrade - Faculty of Mechanical Engineering, Chair for Fluid Mechanics. Kraljice Marije 16, 11120 Belgrade, Serbia. Email: acocic@mas.bg.ac.rs
[2] Institute for Thermal Turbomachinery (ITS), Karlsruhe Institute of Techonology (KIT), Kaiserstraße 12, D-76131 Karlsruhe, Germany. Email: pritz@kit.edu.

ABSTRACT

In this paper, swirling flow generated by axial fan at the beginning of long, horizontal pipe is studied in great detail using numerical computations. In order to have the least possible effect of mesh parameters to the accuracy of computations, great attention is dedicated to creation of high quality block-structured grid, which also includes the geometry of axial fan. Flow is then studied using two approaches: frozen-rotor with RANS models (RNG k - ε and k - ω SST). For aforementioned computation OpenFOAM® is used. Additionally, using block-structured in-house code SPARC at KIT, flow is computed using LES with MILES approach. Experimental results of mean velocity profiles and turbulent kinetic energy were used as validation tool. Obtained results give deeper insights into the dynamics of vortex structures and the process of swirl decay, where good agreement is found with experimental results.

Keywords: swirling flow, axial fan, CFD, RANS, LES.

NOMENCLATURE

$\underline{U}$	$[m/s]$	averaged (filtered) velocity vector
$\underline{U}_r$	$[m/s]$	relative averaged velocity vector in rotating frame of reference
P	$[m^2/s^2]$	averaged (filtered) kinematic pressure
$\underline{\tilde{u}}$	$[m/s]$	instantaneous velocity vector
$\tilde{p}$	$[m^2/s^2]$	instantaneous kinematic pressure
k	$[m^2/s^2]$	turbulent kinetic energy
ν	$[m^2/s^2]$	molecular viscosity
ν_t	$[m^2/s^2]$	turbulent viscosity
ω	$[1/s]$	specific rate of dissipation of turbulent kinetic energy
ε	$[m^2/s^3]$	dissipation rate of turbulent kinetic energy
$\underline{\Omega}$	$[1/s]$	angular velocity vector

1. INTRODUCTION

Swirling flows occurs frequently, both in nature and engineering. Typical examples from nature are hurricanes and tornadoes in Earth's atmosphere and whirlpools in seas and oceans. Fluid flows in turbomachinery, cyclone separators, combustion chambers and pipeline systems - to name a few, are examples from engineering. These flows can be viewed as combination of plane rotational flow and axial flow perpendicular to the plane, which causes the fluid to move in helicoidal trajectories. Essentially, in these flow fields we have large three-dimensional vortex structures and their interaction. In terms of modeling, we have velocity gradients in radial direction of axial and circumferential velocity with the same order of magnitude, streamline curvature and highly anisotropic structure of turbulence. Because of all that, swirling flows are typical example where RANS eddy-viscosity models fail to predict the flow development in correct manner. Some improvements are made by adding additional terms in model equations which takes the fluid rotation into the account, or by introducing the non-linearity in eddy-viscosity concepts. Reynolds stress transport models (RSTM) gives better predictions, but they have issues with computational stability.

2. FLOW MODELING

First, details about the geometry of the flow domain is presented. Then, the procedure about the creation of numerical mesh is explained in details. Finally, governing equations and constitutive model equations are presented.

2.1. Geometry, computational domain and numerical mesh

Photograph of experimental installation is shown in Fig. 1. It consists of axial fan mounted at the entrance of the long pipe. At the pipe entrance, before the fan, bell mouth is installed to minimize local losses and to produce smooth entrance of the air. Axial fan has seven straight blades, with angle of

26° toward the flow direction. Comprehensive measurements were performed on this experimental rig in past decades. It is designed and constructed by late prof. Miroslav Benišek. His was a pioneer in experimental investigation of swirling flow at Belgrade University - Faculty of Mechanical Engineering, [1]. After his original work, detailed research with various experimental techniques were performed at the same rig. Detailed description about the results and more can be found in review paper [2].

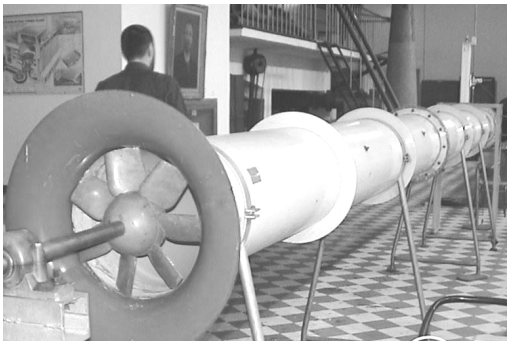

Figure 1. Photograph of experimental installation (Laboratory for Hydralic Machines, Universtity of Belgrade - Faculty of Mechanical Engineering).

The sketch of the installation, with relevant geometrical parameters is shown in Fig. 2. Their values are: $D = 400\,mm$, $D_1 = 659.6\,mm$, $\delta = 3\,mm$, $L_1 = 60\,mm$ and $L_2 = 5\,m$. It can be noted that the shaft of the fan impeller is not taken into the account. This is due to the fact that our region of interest is behind the fan.

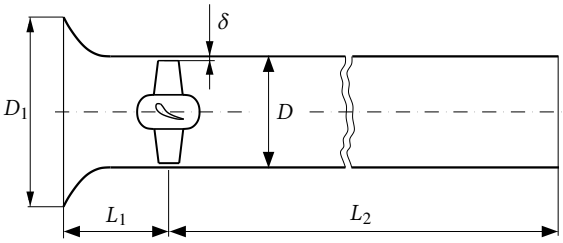

Figure 2. Sketch of experimental installation with relevant geometrical parameters.

The main goal from the start was to create numerical mesh with high quality cells, so great care is taken to create the block-structured grid, and for that purpose commercial software ICEM-CFD was used. Since it is practically impossible to create the unified block topology in whole computational domain, it is divided in three subdomains $\mathcal{D}_1$, $\mathcal{D}_2$ and $\mathcal{D}_3$. Additionally, the inlet is further extended by adding semi-spherical domain before the bell mouth in order to simulate the entrance of the air to the impeller more accurately. This is shown in Fig. 3. In flow direction, subdomain $\mathcal{D}_1$ ends up with the surface (patch) named SRI-1. This surface is geometrically the same as surface RSI-1, which is the left boundary surface of subdomain $\mathcal{D}_2$. Similar story is with right boundary surface RSI-2 and left boundary surface of subdomain $\mathcal{D}_3$, named SRI-2. Now, in these subdomains block-structured grid is created, with different topology of the blocks in each one of them.

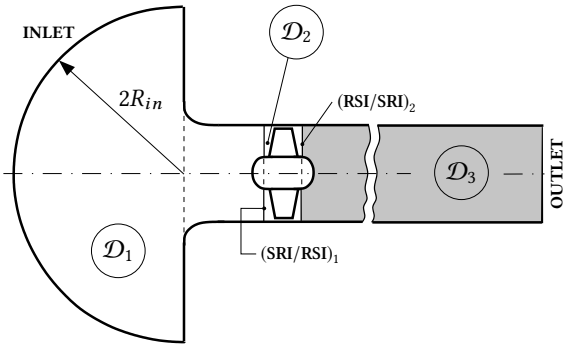

Figure 3. Computational subdomains with characteristic surfaces.

It is assured that aspect ratio between the cells in the boundary region between the domains has approximately the same size. Number of the faces of interface surfaces (SRI/RSI) is not the same, but it is assured that the difference is as small as possible, in order to reduce the error of interpolation during numerical computations. The result of that is the mesh which part around the fan impeller is shown in Fig. 4.

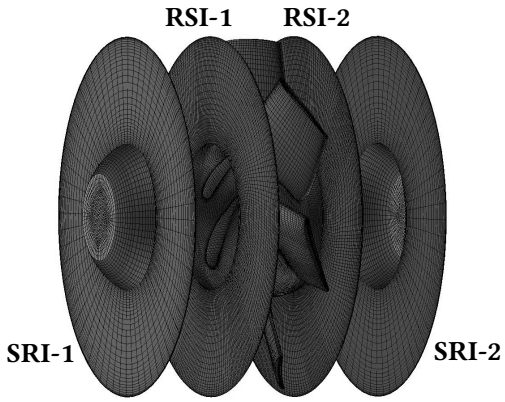

Figure 4. Part of numerical mesh with interface surfaces between the domains.

For each subdomain the minimum value of Jacobian determinant for hexahedral cells was 0.8 (mesh quality parameter in ICEM CFD; "ideal" mesh has the value of determinant 1.0 for each cell). These three meshes are exported to *.msh format, and then separately imported to OpenFOAM format using fluent3DMeshToFoam utility. Finally, they are merged together to one unique mesh with mergeMeshes utility. Cell zones in domains $\mathcal{D}_1$ and $\mathcal{D}_3$ are named STATOR-1 and STATOR-2, respectively. Cell zone in domain $\mathcal{D}_2$ is named ROTOR, and the physical rotation of the fan is treated in two different ways, which will be explained in details in following section. The results presented here are obtained on the mesh with 8265989 cells. Grid sensitivity study is performed previously and presented in [3].

2.2. Governing equations

Experiments showed that mean velocities in the pipe are around $10\,m/s$, so it is assumed that the flow is incompressible (density ρ = const). The starting point is the Navier-Stokes equations

$$\begin{aligned} &\nabla \cdot \underline{\tilde{u}} = 0 \\ &\frac{\partial \underline{\tilde{u}}}{\partial t} + \nabla \cdot \left(\underline{\tilde{u}}\, \underline{\tilde{u}} \right) = \nabla \tilde{p} + \nu \nabla^2 \underline{\tilde{u}} \end{aligned} \tag{1}$$

Because of high range of time scales and spatial vortex sizes in turbulent flows, direct numerical solution of system (1) is practically not possible for most cases. Navier-Stokes equations need additional treatment in order to reduce the range of scales. In that sense, there are two main approaches:

- time averaging, where we get the RANS equations; or ensemble averaging where we get unsteady RANS or URANS equations
- spatial filtering, where we get the filtered Navier-Stokes equations, which are the starting point for LES.

In both cases, we are splitting pressure and velocity into two parts - averaged (filtered) U_i and fluctuating remaining part u_i

$$\tilde{u}_i = U_i + u_i, \qquad \tilde{p} = P + p$$

Inserting this into the equation (1) we end up with the same type of the equations. They are

$$\begin{aligned} &\nabla \cdot \underline{U} = 0 \\ &\frac{\partial \underline{U}}{\partial t} + \nabla \cdot \left(\underline{U}\, \underline{U} \right) = \nabla P + \nu \nabla^2 \underline{U} - \nabla \cdot \underline{\underline{T}}_{\text{tur}} \end{aligned} \tag{2}$$

where $\underline{U}$ and P are ensemble (Reynolds) averaged velocity and pressure in URANS (RANS) approach, while in LES approach it is filtered velocity and filtered pressure. Symbol T_{tur} represent the second order tensor which originates from averaging or filtering procedure of the original nonlinear convective term in Navier-Stokes equations. In RANS modeling turbulence tensor T_{tur} is called Reynolds stress tensor and it is modeled by introducing turbulent viscosity ν_t, which was known as Boussinesq approximation

$$\underline{\underline{T}}_{\text{tur}} = \nu_{\text{t}} \left(\nabla \underline{U} + \nabla \underline{U}^T \right) + \frac{2}{3} k\, \underline{\underline{I}}$$

where k is time averaged turbulent kinetic energy. Turbulent viscosity is determined from auxiliary model equations. Here we'll compare the results obtained with RNG k-ε and k-ω SST models, [4] and [5]. Similar approach is in LES, where we are introducing sub-grid scale viscosity ν_{sgs} for modeling residual stresses T_{tur}.

2.2.1. Momentum equation in rotating frame of reference

Equations (2) can be further simplified using so called "frozen-rotor" approach. Here we're assuming that the turbulence is statistically steady, we're using RANS. Rotation of the fan is taken into the account in the following way. In any fluid domain which rotates with constant angular velocity $\underline{\Omega}$ we can represent absolute velocity vector via two components, relative and rotational

$$\underline{U} = \underline{U}_r + \underline{\Omega} \times \underline{r}$$

Inserting this into the RANS equations, we'll get the equation with two additional terms: centrifugal and Coriolis force per unit mass, while the velocity vector will be $\underline{U}_r$. That is, we get RANS equation in rotating frame of reference. Since we have also the other parts of domain where we don't have physical rotation of the fluid, it is convenient to use the same convective velocity throughout the domain, which is $\underline{U}$, velocity absolute frame of reference. For that purpose, convective term with relative velocities + Coriolis force + centrifugal force, can be written as

$$\nabla \cdot (\underline{U}_r\, \underline{U}) + \underline{\Omega} \times \underline{U}$$

and system of equations (2) becomes

$$\begin{aligned} &\nabla \cdot \underline{U} = 0 \\ &\nabla \cdot (\underline{U}_r\, \underline{U}) = \nabla P + \nu \nabla^2 \underline{U} - \underline{\Omega} \times \underline{U} - \nabla \cdot \underline{\underline{T}}_{\text{tur}} \end{aligned} \tag{3}$$

Finally, in numerical procedure the convective term is split into two parts

$$\nabla \cdot (\underline{U}_r\, \underline{U}) = \nabla \cdot (\underline{U}\, \underline{U}) - \nabla \cdot [(\underline{\Omega} \times \underline{r})\, \underline{U}]$$

Now all the terms in Eq. (3) are written with velocity vector $\underline{U}$ in absolute frame of reference. Convection flux have additional correction term which takes into the account the rotation. Prior to computation, the position of rotational axis in absolute frame of reference needs to be specified, together with the magnitude of angular velocity $\underline{\Omega}$.

2.3. Simulation set-up

In this section detailed description of simulation set up concerning boundary conditions, discretization schemes and iterative solvers used for solution of system of linear equations is given. This is mostly related to OpenFOAM® . Boundary conditions for SPARC code are very similar, and the differences will be mention in later section, where results are presented. For all computations angular velocity of $\Omega = 104.72\,rad/s$ is set, like it was in experiment.

2.3.1. Boundary conditions

At the INLET boundary, Fig. 3, value of total pressure is specified, while at OUTLET boundary fixed value of pressure is specified. These values are assumed to be the same, equal to zero. For velocity, boundary condition called pressureInletVelocity is prescribed. The inflow velocity is obtained during the computation from the flux with a direction normal to the INLET boundary. For turbulence quantities, values based on estimated length and time scales are defined at the INLET, while like for the velocity, zero gradient is applied at the OUTLET boundary. With this setup flow through the domain is estab-

lished due to the fan rotation, which corresponds to the experimental set up. From the Figs. 3 and Figs. 4, in both STATOR cell zones, parts of the hub are located. Constant, nonuniform value of velocity is prescribed, calculated from angular velocity of the fan and the radial distance from rotational axis. At all patches of type wall, zero gradient for pressure is prescribed, while for turbulence quantities wall functions were used. Two version of OpenFOAM were used for computations:

1. ESI-OpenCFD version OpenFOAM® 2306, [6], named OFv2306 in further text, and
2. foam-extend version 4.1, a fork of the OpenFOAM® driven by the community [7], named FE41 in further text

While aforementioned boundary conditions are the same in both version, different boundary conditions are used at the non-conformal interfaces SRI/RSI.

In early stages, when it was announced in 2012, only extended version had the capabilities to compute turbomachinery problems. One on the main issues which needed to be solved is how to handle non-conformal interfaces. At that time the generalized grid interface (GGI) was presented and implemented in the original OpenFOAM code [8]. At the interface, the level of communication between the cells is established first, depending of the relative face overlap. The effect of facets is interpreted by a facet-area-based interpolation scheme across the interface. Interpolation stencil is established by geometrical consideration and weighting factors are calculated as area ratio of the facet and the complete face [8]. Additionally, mixing plane boundary condition is also introduced in [8] where the averaging of the flow variables in circumferential direction is performed at second interface in the pair (SRI-2) at each time step, while preserving the flux through the face. Using that approach, we have axisymmetric conditions at the SRI-2, at the pipe inlet. GGI and mixing plane boundary conditions are further improved in terms of stability, and they're available in FE41.

In OFv2306 boundary condition named cyclicAMI (AMI as abbreviation for Arbitrary Mesh Interface) uses the same principle as GGI, and it's based on the original code of GGI. Additional weighting factors are introduced in order to establish more robust interpolation at the interfaces.

2.3.2. Discretization and iterative solvers

Second order linear upwind scheme is used for discretization of convective terms for velocity and turbulence quantities. Initial computations started with purely upwind schemes on all variables, and later during computations, when converged solution is established, schemes are switched to linear upwind. Computations were performed in parallel mode, on 32 Intel® Xeon® Silver 4108 CPUs.

Concerning iterative solver for pressure, it was found that in FE41 preconditioned conjugated gradient (PCG) solver for pressure was faster and more stable in comparison to generic algebraic multigrid (GAMG). In some cases, computations with GAMG were extremely slow. It is assumed that this problem is related to distribution of computation between the nodes, but it wasn't investigated in greater details, since PCG showed stable and accurate. In OFv2306 GAMG solver showed robust and smooth. Concerning the computational time between two version, we didn't perform real tests. The computations in "frozen-rotor" approach are performed in following way:

(1) OFv2306, RNG k-ε, with constant, near zero values inside the domain for all physical quantities
(2) OFv2306, k-ω SST model, using the converged solution from (1) as the initial values; initial values of omega is calculated from k and ε using turbulenceFields function object
(3) FE41, RNG k-ε, using the converged solution (1) as the initial values
(4) FE41, k-ω SST mode, using the converged solution (2) as the initial values.

Of course, for (3) and (4) we needed to tweak few files, to adopt it to the requested syntax. Additionally, for both (3) and (4) both GGI and mixing plane at the interface RSI-2/SRI-2 are used.

3. RESULTS AND DISCUSSION

In [9] comprehensive measurements were performed at experimental rig shown in Fig. 1. Those experimental results are used as the validation tool.

3.1. Results of "frozen-rotor" approach

First, we analyze the global parameters like volume flow rate through the domain. These results are shown in Table 1, together with percentage difference between the values. In calculation of the

Table 1. Volume flow rate values (in m^3/s).

	FE41	**OFv2306**	**Difference**
RNG k-ϵ	0.61753	0.61005	1.23%
k-ω SST	0.63145	0.62381	1.69%
Difference	2.23 %	2.23 %	

percentage difference, we used the arithmetic mean in denominator, and the absolute value of difference in numerator. Values in last columns corresponds to the difference between versions, with the same turbulence model in both version. Difference given in last row is due to the choice of turbulence model, within the same version. It is notable that k-ω SST predicts larger flow rate in comparison to RNG k-ε model, and that percentage is almost the same in both version. There is also a slight difference for both turbulence models between the versions, and that difference is a bit more pronounced in case of k-ω SST model. In terms of stability and robustness of computations, version OFv2306 showed great advantages. Convergence is monitored in several ways.

First, by values of residuals during iterative procedure. Second, by monitoring the flow rate, and lastly monitoring the values of velocity and pressure in several points inside the domain. In both versions, RNG k-ε model lead to steady-state solution, while in case of k-ω SST we have pseudo-steady solution. This can be seen in Fig. 5.

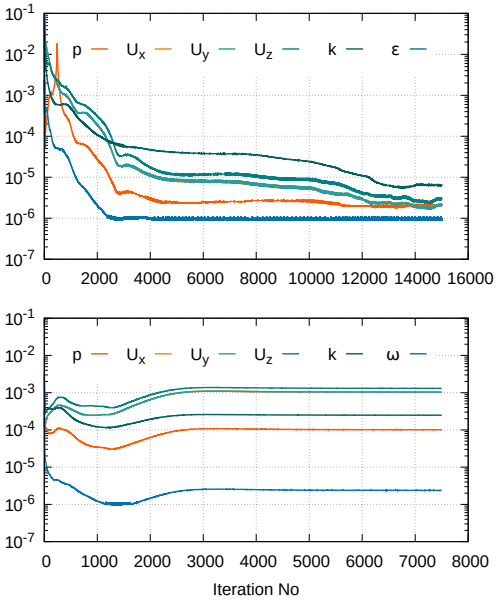

Figure 5. OFv2306. Residuals of physical quantities during computations with RNG k-ε (top) k-ω SST model (bottom).

It is worth mentioning again that initial values of physical quantities inside the domain for computations with k-ω SST are converged solution obtained with RNG k-ε model. After initial decrease in residual values for all physical quantities, they start to increase, and after 3000 iteration they remain constant in further computations. Such changes of residuals indicates the unsteady behaviour of solution.

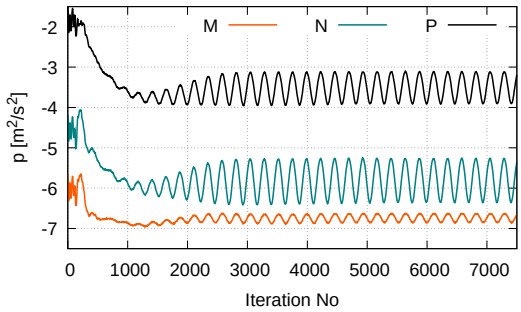

Figure 6. OFv2306, k-ω SST. Variation of pressure in several points in cross-section $z = 0.1\,m$. Coordinates (x, y) of the points are: M(-0.05, 0); N(-0.1, 0) and P(-0.175, 0).

This is evident from the diagram shown in Fig. 6, where oscillations of pressure in different points during iterations are shown. It can be seen that oscillation period is the same for all points, while the amplitude is different. Concerning oscillation period we have roughly four periods in 1000 outer iterations. Of course, we can not talk about accurate unsteady dynamics in this case, but it is interesting to see how global flow field is changing during iterations. The changes of velocity and pressure during iterations are shown in Fig. 7.

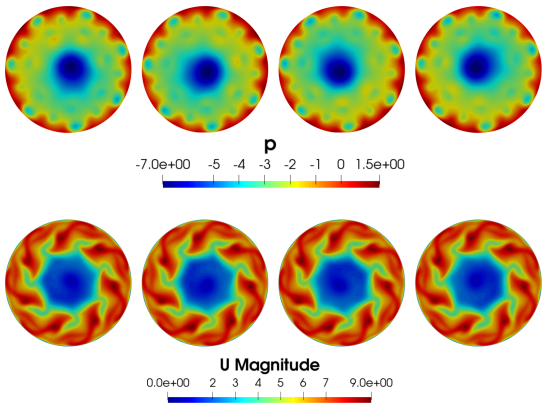

Figure 7. OFv2306, k-ω SST. Contours of pressure (in m^2/s^2) and velocity magnitude (in m/s) in cross-section $z = 0.25\,m$, in outer iterations 4000, 5000, 6000 and 7000. Back view, from pipe outlet.

We can see that main changes are located in the core region of the pipe. Based on contours of low pressure region, these changes of pressure resemble to unsteady vortex rope behind the fan. This vortex rope can be better visualized using Q criterion. Three-dimensional contour of constant Q is shown in Fig. 8.

Figure 8. OFv2306, k-ω SST model. Vortex structures identified as contour of $Q = 1500\,s^{-1}$. Outer iteration number 5000.

Besides coherent vortex structure in the central region of the pipe, e.g. vortex core, we also have additional seven larger structures which originates from the tips of the fan blades. These contours passes through regions of low pressure near the pipe wall shown in Fig. 7. But, contrary to movement of vortex rope in the central region of the pipe, those vortex structures remain still during iterations. This is expected, since in the position of the fan is frozen, and this structures are located near the pipe wall.

Due to fact that we have oscillatory behaviour

during iterations, we can get from this quasi steady to steady solution in following way. Rough estimate is that 4000 iterations is needed for the rope to make one quasi-revolution. In that sense, we can start do compute moving averages (UMean and pMean) from 4000 to 8000 iteration in order to get iteration averaged values of pressure and velocity in each point of computational domain. Using this procedure, we can get the steady state solution. This is shown in Fig. 9 where contours of velocity magnitude are shown, for both turbulence models. In case of RNG k-ε model it is converged velocity, while in case of k-ε SST model it is the iteration averaged velocity.

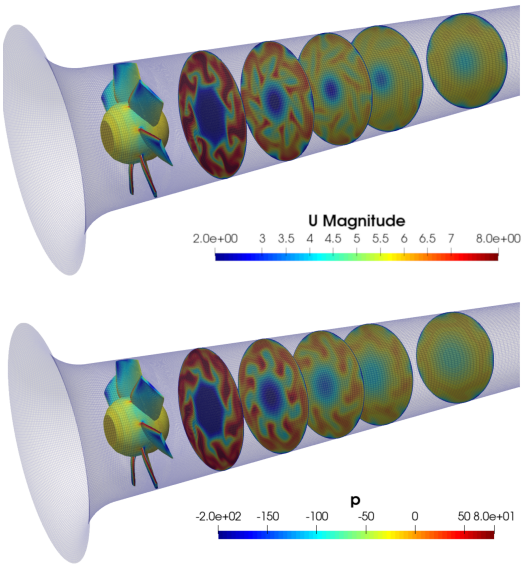

Figure 9. OFv2306. Contours of velocity magnitude (in m/s) in several cross-sections behind the fan: z = 0.25, 0.5, 0.75, 1 and 1.5 m. Contours of kinematic pressure (in m^2/s^2) are shown at fan blades and hub. Top: RNG k-ε, bottom: k-ω SST model.

From Fig. 9 we can clearly see the difference in the results between two models. The effect of the position of fan impeller is more pronounced in case of k-ω SST model. It is evident that the flow is not purely axisymmetric in cross-section close to the fan impeller, it is rather quasi-periodic with $360°/7$ (number of fan blades is seven). Due to many practical reasons, velocity components in OpenFOAM® are stored and calculated in Cartesian coordinates. Based on those results, velocity components in polar coordinates are calculated. For swirling flow, radial distribution of circumferential component can be used to characterize the type of the flow. This distribution is shown in Fig. 10, for both models, in cross-section $z = 1\,m$ of the pipe. For k-ω SST model we used mean velocity vector UMean. From the Fig. 10 it evident that we have so called solid-body rotation, where circumferential velocity reaches maximum values close to the pipe wall, and of course has its minimum in the axis region. Position of

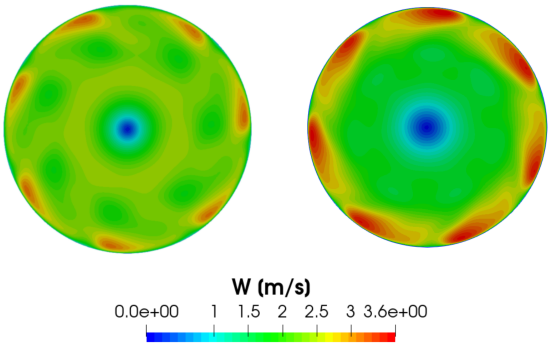

Figure 10. OFv2306. Contours of circumferential velocity W in cross-section $z = 1\,m$. Left: RNG k-ε, right: k-ω SST model.

these regions where circumferential velocity reaches its maximum are directly related to the position of the fan blades, and the profile is not axisymmetric. We can perform circumferential averaging as a part of post-processing in any chosen cross-section, but this is a bit tedious work. For that purpose we used mixing plane at interface, a boundary condition available in version FE41.

3.1.1. Comparison to experimental results

In LDA measurements it was assumed that flow is axisymmetric, and measurements are performed in vertical plane, as shown in Fig. 11.

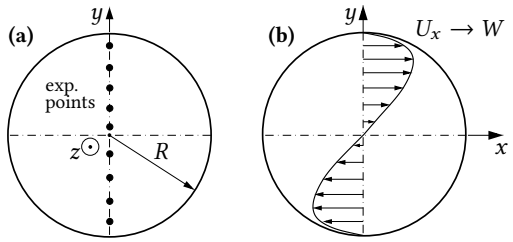

Figure 11. (a) Position of measuring points in cross-section of the pipe. (b) Mean velocity component in direction of x axis corresponds to circumferential component of velocity in polar coordinates.

Additionally, it is assumed that radial velocity component is much smaller in comparison to axial and circumferential, and it wasn't measured. This is usual and accurate approximation for this type of swirling flow. In order to do comparison to the experimental results, i.e. to compare the mean velocity components U_x and U_z, numerical results obtained with mixing plane interface in FE41 are chosen, since they produce axisymmetric flow in the pipe. This is shown in Fig. 12, where symmetry of flow variables in measuring cross-section in circumferential direction is evident. That symmetry is also pronounced in all other cross-sections of the pipe. In that sense, there is no need to calculate velocity components in polar coordinates as a part of post-processing procedure. Instead, velocity component normal to the

sampling line in cross-section will correspond to the circumferential component.

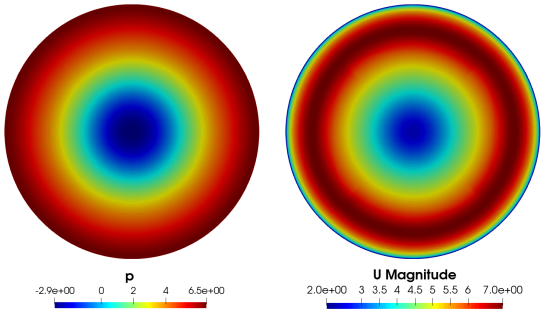

Figure 12. FE41. Contours: kinematic pressure (m^2/s^2), left, and velocity magnitude (right). RNG k-ε turbulence model, measuring section $z = 1\,m$. Mixing plane at the interface pair RSI-2/SRI-2.

Comparison of velocity distribution along vertical axis to experimental results is shown in Fig. 13. Very good agreement is found, for both turbulence models. Decrease in axial velocity in core region is captured in correct manner, and also the type of circumferential velocity profile. There is slight underestimation of the slope of circumferential velocity profile around the axis, which results in underestimation in whole cross-section, except the wall region.

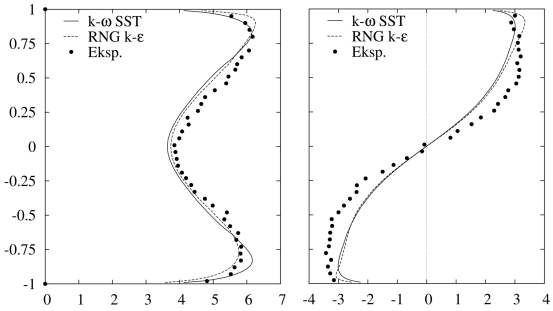

Figure 13. FE41. Comparison of axial and circumferential velocity profiles (see Fig. 11), measuring section $z = 1\,m$. Mixing plane at the interface pair $(\mathrm{RSI/SRI})_2$.

There are numerous experimental points. The reason for that is to check if the assumption of axisymmetry is fulfilled. We can see that there are slight deviation between the values in points which are symmetric around the axis. However, maximum of this deviation is not larger than 2% between the points. Also, in region around the pipe axis, unsteadiness is highly pronounced, specially in circumferential direction. More details about the problems with measurements in this region can be found in [9]. In that region we can also have back flow, or even axial velocity equal to zero. This decrease in axial velocity in core region are directly related to the existence of rotational, i.e. circumferential velocity component.

3.2. Results of the SPARC code

Quasi-steady behaviour shown in Fig. 6 and Fig. 7 clearly shows that this kind flow is unsteady in nature, even on larger scales. This behaviour in results was not found with RNG k-ε model, where we get steady solution. Of course, the most accurate solution with both turbulence models will be with mesh rotation. But, for the purpose of presenting the results in this paper, on this mesh with available computational power, it seems like impossible task. So we turned to the SPARC code. SPARC is in-house block-structured CFD code, written in FORTRAN and developed at KIT Institute of fluid machinery. Foundation of the code are compressible Navier-Stokes equations. Modeling of sub-grid scales in LES are based on MILES algorithm. In contrast to OpenFOAM® , where computations are performed on unstructured mesh by definition, computations in SPARC are performed on mesh defined as multi-block mesh. The topology of the blocks in mesh generation process is important parameter for computations. It turned out that mesh which one part shown in Fig. 4 was very good in that sense, and the simulations ran smooth. For temporal discretization second order dual time stepping is used, with time step in range $\Delta t = 10^{-5}\,s$. For more stable computations, constant flow rate is prescribed at the INLET. At the interfaces SPARC uses sliding mesh approach. After more ten flow through times, values of physical quantities are averaged in time, in order to validate the computation with comparison to the experimental results. Very good agreement is found in terms of axial and circumferential velocities, as shown in Fig. 14. In contrary to Fig. 13 circumferential averaging is performed for both experimental and numerical results.

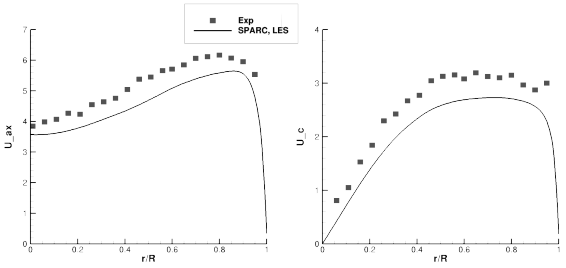

Figure 14. SPARC. Profiles of axial and circumferential velocity in cross-section $z = 1\,m$.

Since in experiments LDA method is used, with sampling rate of $2\,kHz$, it is possible to calculate the root mean square (RMS) of signals that corresponds to axial and circumferential velocity, and compare it with results from SPARC. In Fig. 15 RMS values of axial and circumferential velocity are shown. In contrast to Fig. 13, experimental values are taken as arithmetic mean value of two symmetric points in respect to axis (dependence of radial coordinate). There are two peak values in RMS of axial velocity, which are also predicted numerically. One is located

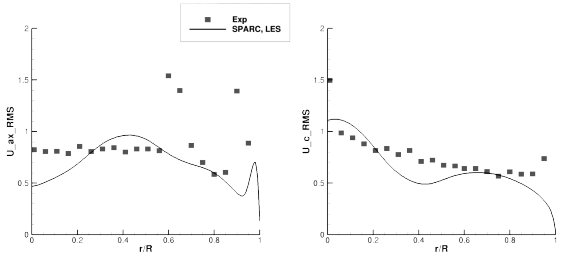

Figure 15. SPARC. Turbulence intensities, i.e. root mean square of axial (left) and circumferential velocity (right) in cross-section $z = 1\ m$.

in the wall region where large velocity gradients produces turbulent kinetic energy, and other at the end of vortex core region where large velocity gradients are also present. Both of these maximums are largely under-predicted in comparison to experimental results. On the other hand, there is good agreement in terms of RMS of circumferential velocity. Figure 16 shows unsteady vortex rope in the region near the pipe axis, in one instant in time. Unsteady behaviour of vortex rope are captured in physically expected manner.

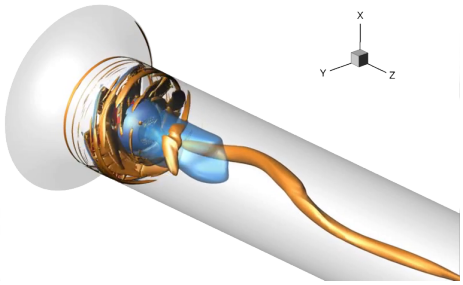

Figure 16. SPARC. Vortex rope identified by contour of constant $Q = 1000\,s^{-1}$ (orange) and contour of zero velocity (blue) in one instants of time.

Computations in SPARC were performed in parallel mode, using MPI on HP XC3000 with 120 CPUs in Scientific Computer Center of KIT. Some issues encountered during computations are given in great detail in [10]. Our opinion is that this behaviour can be reduced with dedicated non-reflecting boundary condition, which will be implemented in the code.

4. CONCLUSION

Numerical analysis of swirling flow straight circular pipe is presented in this paper. Swirl is generated by axial fan, mounted at the pipe inlet. Complete geometry is modeled, while the rotation of the fan is taken into the account in two ways: using frozen-rotor approach and using sliding mesh, with two different CFD codes: OpenFOAM® for first approach and SPARC for the second. Two different version of OpenFOAM® are tested, and it was found that there are slight differences in the results between the versions. Both codes give the results which are in good agreement with experimental results. Future research is dedicated to URANS and hybrid LES/RANS computations with rotating mesh in OpenFOAM® and improvement of LES computations in SPARC.

ACKNOWLEDGMENT

This work has been supported by the Ministry of Education, Science and Technological Development, Republic of Serbia through project 451-03-137/2025-03/20010. First author also wants the express gratitude to the students of University of Belgrade for inspiration and motivation they are giving since the beginning of December 2024.

REFERENCES

[1] Benišek, M., 1979, “Investigation of Swirling Flow in Pipe (in Serbian)”, Ph.D. thesis, University of Belgrade - Faculty of Mechanical Engineering.

[2] Benišek, M., Lečić, M., Čantrak, Dj., and Ilić, D., 2017, “The School of the Turbulent Swirling Flow at the Faculty of Mechanical Engineering University of Belgrade”, *Thermal Science*, Vol. 21, Issue suppl. 3, pp. 899–911.

[3] Ćoćić, A., Ratter, H., Lečić, M. and Gabi, 2014, M. “Numerical Investigations of Flows in Axial and Radial Fans Using OpenFOAM”, 9th International OpenFOAM Workshop - Zagreb, Croatia, June 23-26th

[4] Yakhot, V., Orszag, S., Thangam, S., Gatski, T., and Speziale, C., 1992, “Development of Turbulence Models for Shear Flows by a Double Expansion Technique”, *Physics of Fluids*, Vol. 4, No. 7.

[5] Menter, F., Kuntz, M., and Langtry, R., 2003, “Ten Years of Industrial Experience with the SST Turbulence Model”, *Heat and Mass Transfer*, Vol. 4.

[6] https://www.openfoam.com

[7] https://sourceforge.net/projects/foam-extend

[8] Jasak, H., and Beaudoin, M., 2011, “OpenFOAM Turbo Tools: From General Purpose CFD to Turbomachinery Simulations”, *Proceedings of the ASME-JSME-KSME 2011 Joint Fluids Engineering Conference*, Hamamatsu, Shizuoka, Japan, pp. 1–12.

[9] Čantrak, Dj., 2012, “Analysis of Vortex Core and Turbulence Structure in Circular Pipe With PIV, LDA and HWA methods”, Ph.D. thesis, University of Belgrade - Faculty of Mechanical Engineering.

[10] Pritz, B. and Gabi, M. 2017, “On the Resonant Behaviour of Compressible Flow Simulations”, *Proceedings of the 13th International Symposium on Experimental Computational Aerothermodynamics of Internal Flows*, 7-11 May, Okinawa, Japan

Conference on Modelling Fluid Flow (CMFF'25)
The 19th International Conference on Fluid Flow Technologies
Budapest, Hungary, August 26-August 29, 2025

Flow Diverter Treatment For Intracranial Media Bifurcation Aneurysms: Challenging the Predictive Role of Morphology and Hemodynamics

Anna Bernovskis[1,8], Janneck Stahl[2,8], Gabor Janiga[3,8], Matthias Gawlitza[4], Daniel Behme[5,8], Philipp Berg[6,8], Samuel Voß[7,8]

[1] Corresponding Author. Department of Healthcare Telematics and Medical Engineering, University of Magdeburg, Universitätsplatz 2, 39106 Magdeburg, Germany. E-mail: anna.bernovskis@ovgu.de
[2] Department of Healthcare Telematics and Medical Engineering, University of Magdeburg, Universitätsplatz 2, 39106 Magdeburg, Germany. E-mail: janneck.stahl@ovgu.de
[3] Laboratory of Fluid Dynamics and Technical Flows, University of Magdeburg, Universitätsplatz 2, 39106 Magdeburg, Germany. E-mail: gabor.janiga@ovgu.de
[4] Department of Neuroradiology, University Clinic Jena, Am Klinikum 1, 07747 Jena, Germany. E-mail: matthias.gawlitza@med.uni-jena.de
[5] Department of Neuroradiology, University Hospital of Magdeburg, Leipziger Str. 44, 39120 Magdeburg, Germany. E-mail: daniel.behme@med.ovgu.de
[6] Department of Healthcare Telematics and Medical Engineering, University of Magdeburg, Universitätsplatz 2, 39106 Magdeburg, Germany. E-mail: philipp.berg@ovgu.de
[7] Laboratory of Fluid Dynamics and Technical Flows, University of Magdeburg, Universitätsplatz 2, 39106 Magdeburg, Germany. E-mail: samuel.voss@ovgu.de
[8] Forschungscampus STIMULATE, University of Magdeburg, Universitätsplatz 2, 39106 Magdeburg, Germany.

ABSTRACT

The treatment of intracranial aneurysms (IAs) with flow diverters (FD) has become an established minimally-invasive intervention, showing particularly high rates of complete aneurysm occlusion, especially in the case of sidewall aneurysms. The role of FD in treating bifurcation IAs is still under discussion, as some aneurysms show no long-term improvement. This study aims to explore potential hemodynamic factors contributing to unsuccessful treatment outcome by analyzing retrospective data, with the goal of predicting the success of FD treatment. Twelve intracranial media bifurcation aneurysms patients treated with a state-of-the art FD device are included. Successful treatment was observed in six patients, whereas the other six showed no IA occlusion after follow-up. Patient-specific surface models are extracted based on pre-interventional 3D digital subtraction angiography followed by a morphologic analysis. Post-interventional treatment stages are virtually created using an in-house fast virtual stenting approach. Image-based blood flow simulations compare hemodynamics before and after intervention in successful and unsuccessful treatments. Reductions in all flow-related parameters induced by the FD are observed, regardless of the treatment outcome. IAs with unsuccessful treatment outcome show tendencies to higher morphological parameters, extreme hemodynamic values, and increased stent shear stress. However, these findings suggest that the hemodynamic and morphological results alone do not accurately predict the outcome.

Keywords: cerebral blood flow, CFD, endovascular treatment, flow diverter, hemodynamics, intracranial aneurysms

NOMENCLATURE

AV	$[m/s]$	averaged velocity
$AWSS$	$[Pa]$	averaged wall shear stress
NIR	$[kg/s]$	neck inflow rate
PI	$[-]$	pulsatility index
SSS	$[Pa]$	stent shear stress

1. INTRODUCTION

Intracranial aneurysms (IAs) are pathological vascular dilatations in the cerebral arteries, with a prevalence of 2 to 5 % in adults [1]. 22 % of IAs are localized at the middle cerebral artery (MCA) [2]. In recent years, endovascular treatment methods have become increasingly popular, allowing IAs to be treated in a minimally invasive procedure [3]. In addition to (stent-assisted) coiling, the deployment of a flow diverter (FD) became an established treatment option. The FD is intended to divert the blood flow away from the IA due to its braided wires and ensure thrombosis inside the aneurysm sac, while reendothelializing the aneurysm neck [4]. In up to 76 %

of cases, this procedure results in complete occlusion of the IA [5]. However, the procedure-related morbidity and mortality is between 4 and 5 %, which highlights the importance of accurately assessing the therapy outcome [5].

FDs are particularly successful in fusiform or wide-necked IAs [6, 7]. However, the specific morphological factors that contribute to successful occlusion are still being investigated. Long et al. [8] examined the morphological parameters of small aneurysms treated with FD and observed that aneurysm sacs with branch vessels or a larger aneurysm diameter make occlusion more difficult. The success of a FD for bifurcation aneurysms is also under discussion, as problems can occur due to occlusion of the neighboring vessels [9, 6, 7].

Numerical blood flow simulations and virtual stenting of the FD can be performed to investigate the hemodynamic influence of a FD. There are numerous fast virtual stenting methods and also several studies in which the influence of a FD on hemodynamics is investigated using this method [10]. Larrabide et al. [11] investigated the hemodynamic changes caused by the FD in internal carotid artery (ICA) aneurysms using a fast virtual stent placement method. A significant reduction in wall shear stress (WSS) and velocity is observed. Additionally, the shape of the aneurysms was considered, showing greater reductions in fusiform aneurysms compared to saccular aneurysms. Cebral et al. [12] and Levitt et al. [13] also followed a similar approach in their study. Both studies also demonstrate a significant reduction in flow into the aneurysm dome and in WSS on the aneurysmal wall following FD treatment. These studies suggest that morphological and hemodynamic parameters can be linked to treatment success. However, it is not possible to determine exactly which conditions lead to good occlusion of an IA.

In this study, the focus is on MCA aneurysms. Their localization at a bifurcation poses a particular challenge for flow diversion. The FD necessarily covers one of the two main branches. Therefore, by performing a retrospective analysis this study examines whether the previous results on the relation between morphological and hemodynamic parameters and treatment outcome can be transferred to bifurcation aneurysms.

2. MATERIALS AND METHODS

Figure 1 illustrates the study workflow. Initially, digital subtraction angiography (DSA) is performed pre-interventionally. The vessels are segmented and converted to a 3D vessel model. This model serves as a basis for morphological analysis. Subsequently, a FD is virtually deployed in the model, and numerical blood flow simulations are carried out for both the pre-stented and stented models.

2.1. Patient data

The study contains the retrospective data of 11 patients and includes 12 aneurysms located at the MCA-bifurcation. All patients were treated with the p48 MW Flow Modulation Device (phenox, Bochum Germany) at Leipzig University Hospital. After the procedure, all cases were evaluated using the O'Kelly-Marotta (OKM) [14] and Saatci-Cekrige (SCS) [15] scores, which help to determine the success of the procedure. Based on the scores, this cohort includes six cases in which the aneurysm occlusion is achieved. These cases are referred to as successful in the following. In six cases, incomplete occlusion occurs, these cases are labeled as unsuccessful. An overview of the patient data is provided in Table 1.

Table 1. Overview of the therapeutic success of patient cases using classification by the O'Kelly-Marotta (OKM) and Saatci-Cekrige score (SCS).

Case	OKM	SCS	Success
1	D	1c	yes
2	C1	1c	yes
3	A1	3	no
4	D	1c	yes
5	A1	3	no
6	A1	3	no
7	A1	3	no
8	A1	3	no
9	D	1c	yes
10	D	1c	yes
11	A1	3	no
12	C2	5	yes

2.2. Image acquisition

All endovascular treatments are performed using Philips Allura Xper Biplane AngioSuite (Philipps Medical Systems DMC GmbH, Hamburg, Germany). The procedures and image acquisitions were conducted between January 2018 and December 2023. A monoplanar 3D rotational angiography (3D-RA) is performed with a rotation time of 4 s. A manual injection of 20 ml of contrast medium (Imeron 300, Bracco Imaging GmbH, Konstanz, Germany) is administered during the procedure. The pre-interventional 2D images are acquired shortly before FD deployment. Isotropic voxel sizes is 0.27 mm for all acquisitions.

2.3. Image segmentation

The extraction of patient-specific vascular structures from the 3D DSA data was performed using MeVisLab v3.4.1 (MeVis Medical Solutions AG, Bremen, Germany). To obtain the initial segmentation, threshold-based methods combined with global Laplacian smoothing were employed. Following the segmentation process, the resulting mask was converted into a triangulated 3D surface mesh utiliz-

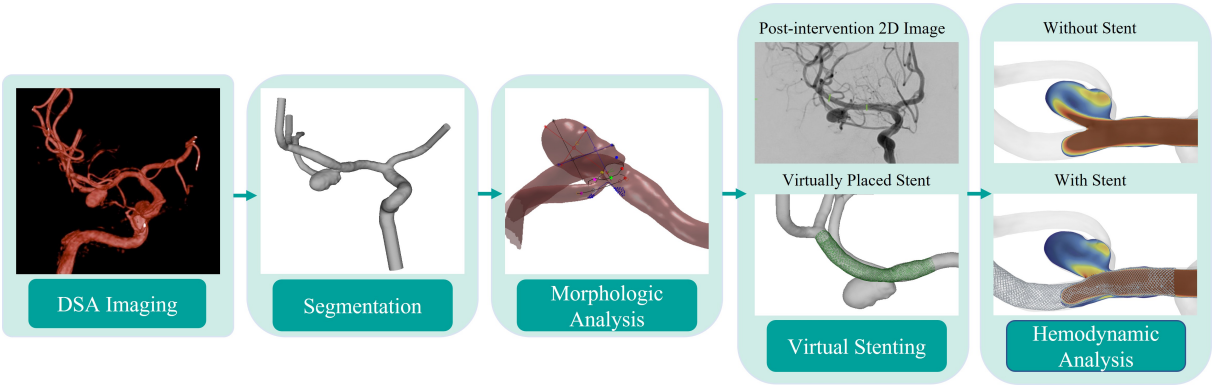

Figure 1. The workflow includes medical imaging, vessel segmentation, and morphological analysis of the extracted 3D vessel model. This is followed by virtual FD placement and a final hemodynamic analysis through numerical blood flow simulations for both pre-stented and stented models.

ing the marching cubes algorithm. For the post-processing of the segmentation the open-source 3D creation suite Blender v2.9 (BlenderFoundations, Amsterdam, Netherlands) is used. The steps performed with this software are the manual removal of artifacts, separating incorrectly fused vessel sections, extrusion of the in- and outlet cross-sections perpendicular to the vessel axis and optimizing the triangulated mesh. A total of 12 pre-interventional patient-specific models are extracted from the 3D DSA data. As shown in Figure 1, these models are used for in house fast virtual stenting approach.

2.4. Fast virtual stenting approach

The virtual FD geometries are created using an in house fast virtual stenting approach. This software is employed to virtually place the FD in patient-specific vascular models [16]. The exact position of the FD within the vessel is determined based on 2D images taken after the intervention. The FD is precisely positioned to match its placement during the initial procedure. The stent lengths and diameters used in the procedure are known and are therefore adapted to the size of the virtual stent. Stent diameters of 2 and 3 mm are used and the stent length varies between 9 and 18 mm.

2.5. Morphologic parameters

The morphologic parameters are calculated using Saalfelds et al. [17] semiautomatic neck curve reconstruction tool. This approach requires a vessel centerline, which is extracted using the VMTK v1.4.0 (Vascular Modeling Toolkit, vmtk.org) software. The morphological parameters investigated are the aneurysm area, the aneurysm volume, the orthogonal height (H_{ortho}) and the aspect ratio. The aspect ratio results from the orthogonal height divided by the maximum distance between two points on the neck curve. Furthermore, with regard to morphology, the 2D images before and after the intervention are qualitatively analyzed to identify possible changes in morphology due to the treatment.

2.6. Hemodynamic simulation and analysis

To analyze the hemodynamic differences before and after FD deployment, numerical blood flow simulations are performed using the finite-volume solver STAR-CCM+ v17.06 (Siemens PLM Software Inc., Plano, TX, USA) following the guidelines by Berg et al. [18]. The IA models were spatially discretized using polyhedral cells with a maximum base size of 0.07 mm, along with five layers of prism cells to ensure accurate resolution of near-wall flow. In order to accurately capture the individual stent struts, the discretization around the FD is refined using a base size of 0.016 mm. (A comparison with a refined 0.0094 mm mesh was conducted, showing a deviation of less than 1 % in the results. Therefore, the 0.016 mm base size was maintained.) These settings result in a total number of cells between 2.5 and 4.8 million for configurations without a FD and between 10.6 and 22.7 million for configurations with a FD, respectively. Inlet and outlet boundary conditions must be defined for the hemodynamic simulations as no patient-specific data is available. For the inlet, a representative inflow curve was taken from Cebral et al. [12]. For configurations without a stent, area-weighted outflow splitting was employed to ensure physiologically appropriate flow distribution across outlets [19]. The resulting time-dependent pressure waveforms were then used as outflow boundary conditions in the corresponding stented configurations, thereby enabling flow redistribution induced by the FD. All vessel walls were modeled as rigid and with no-slip wall condition. Blood is simplified as a fluid with incompressible ($\rho = 1056\ \mathrm{kg/m^3}$) and non-Newtonian properties (Carreau-Yasuda model parameters taken from Robertson et al. [20]). The Reynolds number in the modeled geometries did not exceed 1000. Therefore, laminar flow conditions were assumed for all simulations. Two cardiac cycles are simulated for each of the 24 configurations. The first cycle is used for initialization and the second cycle is used for the actual

hemodynamic evaluation.

Analyzed hemodynamic parameters are the

- Average Velocity inside the aneurysm sac (AV)
- Neck Inflow Rate (NIR): The net flow rate entering the aneurysm through the ostium. [21]
- Pulsatility Index regarding NIR (PI_NIR): PI quantifies the amplitude of NIR along the cardiac cycle in relation to the mean NIR [11].
- Average Wall Shear Stress (AWSS): The AWSS describes the tangential shear stress along the vessel wall over one cardiac cycle.
- Pulsatility Index regarding WSS (PI_WSS): PI quantifies the amplitude of WSS along the cardiac cycle in relation to the mean WSS [11].
- Stent Shear Stress (SSS): The time-averaged SSS describes the tangential shear stress along the stent over one cardiac cycle [22].

3. RESULTS

3.1. Morphologic analysis

The comparison of the morphologic parameters for the pre-interventional geometries is presented in Table 2. It can be observed that all morphologic parameters are higher in the unsuccessful outcome category. For example, the average IA volume is 102.69 mm³ in the unsuccessful cases, while it is 83.57 mm³ in the successful cases. Similarly, the average IA area is 87.83 mm² in the unsuccessful cases, compared to 83.32 mm² in the successful cases.

Table 2. Results of the averaged morphological parameters of the investigated IAs in the corresponding category (successful, unsuccessful)

Parameter	Successful	Unsuccessful
IA area (mm^2)	83.32	87.83
IA volume (mm^3)	83.57	102.69
H_{ortho} (mm)	3.71	4.41
Aspect Ratio (-)	0.82	0.99

Further, 2D images taken before and after the procedure are compared. In certain aneurysms, vessel deformation is evident as a result of FD deployment. Figure 2 presents an example of a case where the vessel deformation induced by the FD is clearly visible. However, these morphological changes do not exhibit a direct correlation with success or unsuccessful treatment outcome.

3.2. Hemodynamic analysis

3.2.1. Quantitative evaluation

Figure 3 shows the quantitative evaluation of the peak-systolic intra-aneurysmal blood flow velocity for two selected cases, representing successful and unsuccessful FD treatment outcome. In both cases, the blood flow in the aneurysm dome is visualized

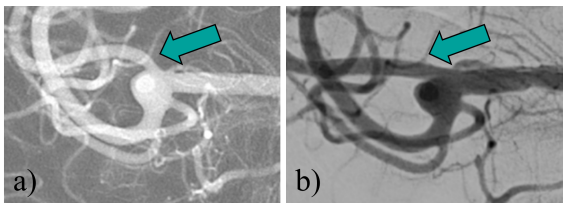

Figure 2. Representative case showing FD-induced vessel deformation; a) before intervention and b) after FD depolyment.

before and after FD deployment. It is evident that the deployment of the virtual FD leads to a reduction in the intra-aneurysmal blood flow velocity in both cases. The direct comparison shows that the reduction is even higher in the unsuccessful outcome than in the successful one. This observation can be confirmed by other cases.

The SSS is presented in Figure 4, with one successful and one unsuccessful case selected as examples. Each case is shown from two different perspectives to enable a more detailed analysis. In Figure 4a), the stent is visible from within the aneurysm, while in Figure 4b), it can be observed from the ostium into the aneurysm. In perspective a), no clear differences in the distribution of the SSS between the successful and unsuccessful cases are noticed. However, this is considerably different for perspective b). In both cases, increased SSS values can be detected near the aneurysm neck region. In the unsuccessful outcome, the SSS on the inside of the stent is notably increased, being more than four times larger. This tendency can be confirmed by the other cases.

3.2.2. Qualitative evaluation

The bar chart in Figure 5 presents the mean relative changes in hemodynamic parameters, categorized into successful and unsuccessful outcome. It can be observed that all parameters exhibit the same pattern of relative changes, with both positive and negative trends being consistent across all cases, regardless of the treatment outcome. For instance, there are negative relative changes in the values for velocity, NIR and AWSS. The parameters related to pulsatility show positive changes in the values. The greatest AWSS reduction (-54.4 %) occurs in unsuccessful cases, compared to -42.8 % in successful ones. AWSS pulsatility increases more in unsuccessful outcomes (36.7 %) than in successful (25.5 %). The largest intergroup difference is in NIR, with a 12.6 % greater reduction in the unsuccessful group.

Finally, Figure 6 presents the absolute values of all selected parameters and analyzed cases before and after FD deployment. Consistent with the observations of relative changes, a reduction in velocity, AWSS, and NIR values are evident following FD placement. The absolute values of the pulsatility regarding AWSS and NIR increase. Additionally, the analysis of absolute values reveals that ex-

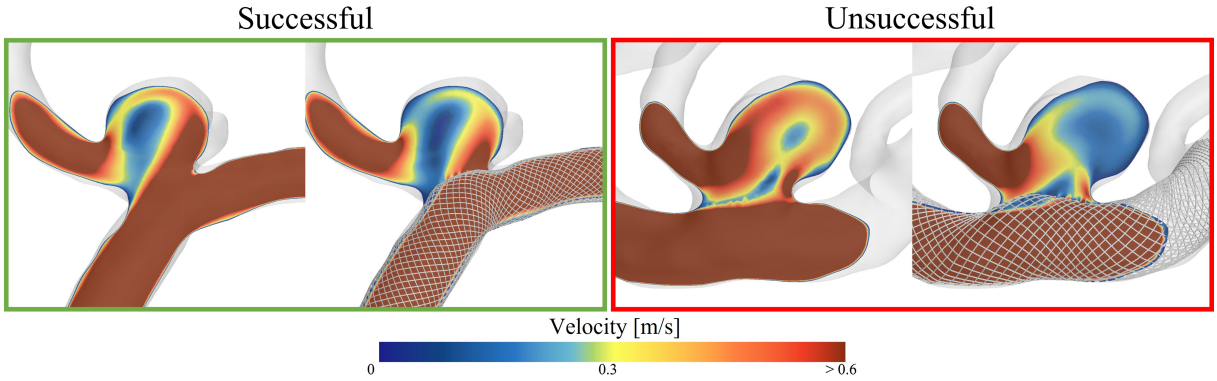

Figure 3. Visualisation of the peak-systolic intra-aneurysmal blood flow velocity before and after virtual stent deployment for a successful case and an unsuccessful case.

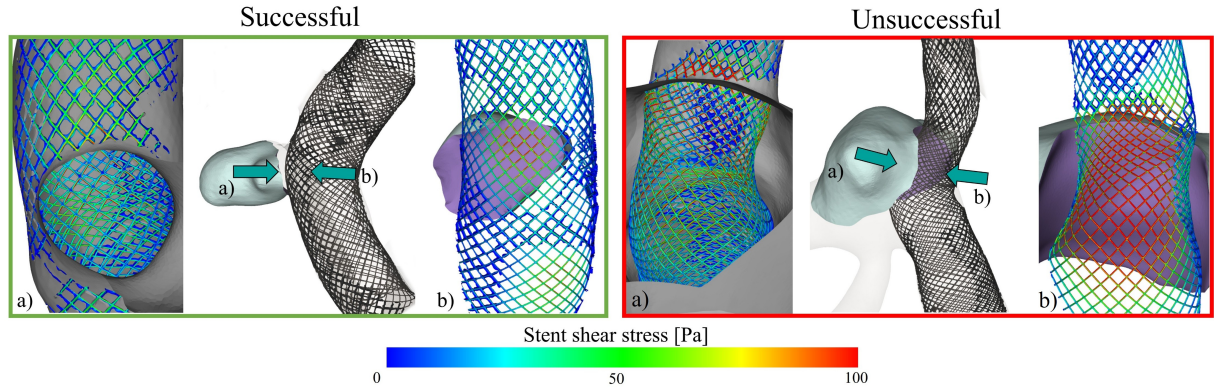

Figure 4. Visualisation of the SSS for a successful and unsuccessful case from two different perspectives. The arrows show the indicated direction of view (a) perspective from the aneurysm dome on the FD, b) perspective on the ostium of the aneurysm).

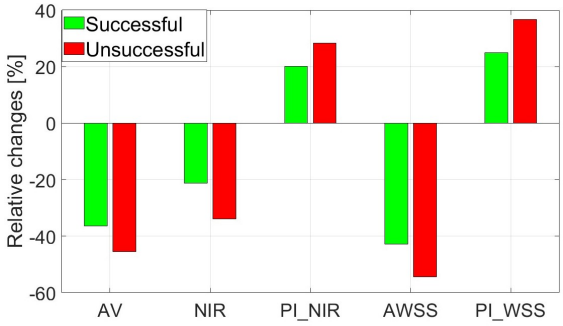

Figure 5. Mean relative changes in AV, NIR, PI_NIR, AWSS, and PI_WSS before and after FD deployment, categorized into successful and unsuccessful outcome.

treme values often occur in unsuccessful treatment outcomes. This is particularly noticeable in the pre-interventional AWSS values, which range from 1.7 to 12.2 Pa. In contrast, for successful cases, the maximum AWSS value is 5.62 Pa, while the minimum is 3.09 Pa.

4. DISCUSSION

The results of the morphological analysis indicate a tendency for FD therapy to be less successful in larger MCA aneurysms. However, no specific parameter or associated threshold can be identified that reliably predicts the success of FD deployment in relation to morphological characteristics. Consequently, the analysis of the morphological parameters of IAs alone does not provide a clear classification of whether the use of a FD will lead to full occlusion of the IA.

The 2D comparison of the images before and after treatment demonstrates, that in some cases there are morphological deformation of the vessels due to the FD. This often appears as a straightening of the surrounding vessels. Even if it is not clearly identifiable whether this deformation has a positive or negative influence on the treatment success, it could make a difference for the subsequent hemodynamic analysis. Voß et al. [23] investigated the effect of vessel deformation on MCA aneurysms and showed that these morphological changes impact intra-aneurysmal hemodynamics. To achieve this, they analyzed 3DRA data collected before and after FD treatment. In this work, only 2D images

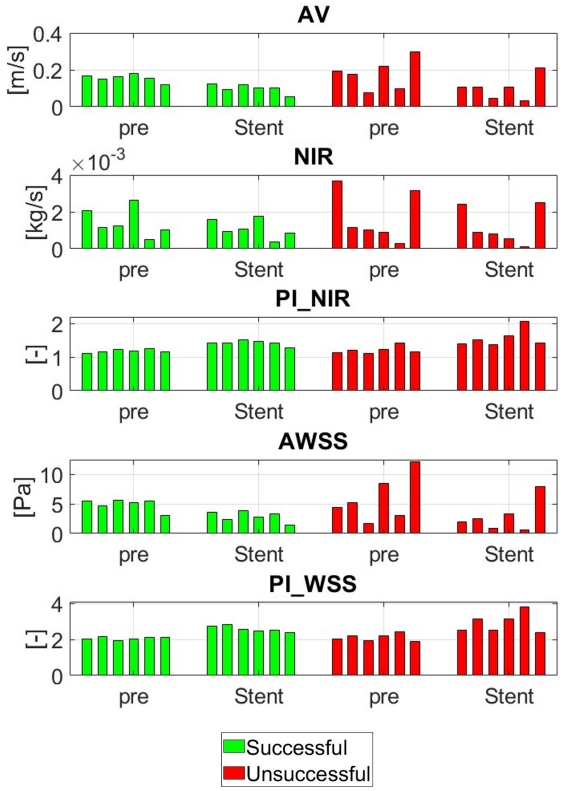

Figure 6. Absolute values of the parameters AV, NIR, PI_NIR, AWSS, and PI_WSS before and after FD deployment, divided into successful and unsuccessful outcome.

after treatment are available. To enable a more comprehensive analysis of the precise morphological and hemodynamic conditions following FD treatment, it would be beneficial for subsequent studies to include post-interventional 3D images. This would provide a more realistic representation of the morphology and stent placement and thus also improve the hemodynamic analysis.

FD deployment aims to occlude the aneurysm and prevent rupture. Two effects play a decisive role in its success. Firstly, thrombus formation in the aneurysm and secondly, endothelization along the FD and the neck of the aneurysm [4].

The FD-induced reduction of blood AV inside the aneurysm, the NIR and the AWSS is expected and confirmed by the presented results. These findings agree with previous studies by Thormann et al. [24] and Kulcsár et al. [25]. It is noticeable that the pulsatility of both the NIR and the WSS increase after FD deployment, independent of the occlusion state. This behavior is also identified in the study by Larrabide et al. [11] who investigated the hemodynamic effects of a FD in a similar study design.

However, it is unexpected that the average reduction of these parameters is greater in the unsuccessful cases in both absolute and relative values. As also stated by Ravindran et al. [4], especially the reduced velocity is a key factor for thrombus formation and thus for occlusion of the aneurysm. These results therefore do not contribute to differentiating between successful and unsuccessful cases.

The study by Mut et al. [26] has a similar design and investigates potential causes for fast or slow aneurysm occlusion following FD treatment. In contrast to the present results, this study identified significant differences regarding AV and NIR. Both were found to be significantly lower in cases with fast occlusion. The key difference is the focus on IAs located at the ICA and posterior communicating artery (PCOM), rather than MCA-bifurcation aneurysms. The results of the present study suggest that Mut et al.'s findings may not be applicable to MCA-bifurcation aneurysms, requiring further analysis of hemodynamic parameters.

Further, the absolute values are analyzed in order to possibly predict the outcome success using hemodynamic analysis. It is noticeable that the unsuccessful cases often represent minimum or maximum values, see Figure 6. This could indicate abnormal flow conditions that could prevent the aneurysm occlusion mechanisms introduced above. Regarding the instability assessment of IAs, abnormal flow is considered as critical factor [27]. Notably, a trend towards abnormal flow conditions or extreme hemodynamic parameters is already visible in the pre-interventional simulations of the unsuccessful cases. Therefore, such an indicator might be used pre-interventionally to assess the success of FD treatment.

In addition, SSS is evaluated. Berg et al. [22] found that an increased SSS is present in regions where endothelialization did not occur. At lower SSS, endothelial proliferation was seen both on the stented parent artery and on the open segments of the stent. Accordingly, this study highlights increased SSS in the unsuccessful cases. This could therefore lead to reduced endothelialization and serve as an explanation for incomplete aneurysm occlusion. Further studies should investigate this in more detail.

Limitations The first limitation is the small cohort size of 12 MCA IAs, with only six in each successful and unsuccessful group. A larger cohort and the consideration of all OKM score classes would provide more precise information on the hemodynamic effects of FD deployment.

Another limitation is the uncertainty caused by the segmentation and manual processing steps involved in creating the patient-specific geometries. This can lead to discrepancies from the original shape of the vessel. However, comparing the medical images and the 3D models was utilized to reduce 3D model uncertainty.

Some simplifications are necessary for the hemodynamic simulations. These include the simplification of the fluid properties of blood as well as a simplified representation of the wall and the inlet and outlet conditions. In this study, it would be of

special interest to apply patient-specific inlet conditions. Unfortunately, patient-specific flow rates are rarely available, but they could make a difference in estimating the success of therapy [28].

Additionally, it should be considered to adopt a more multifactorial approach by incorporating additional patient-specific factors into the prediction of treatment success. This could include diseases such as hypertension, as well as lifestyle factors like smoking. These factors were not considered in the current approach, which focused solely on morphology and hemodynamics. Furthermore, the morphological analysis could be extended, allowing a more detailed analysis of the aneurysm's surroundings and the position of the side branches.

Moreover, the availability of both 2D and 3D DSA images after the intervention would be highly advantageous. This would enable a more accurate assessment of vessel deformation and allow for a more realistic placement of the virtual FD.

5. CONCLUSION

This study addresses the morphological and hemodynamic analysis of MCA-bifurcation aneurysms to evaluate the treatment success of FD deployments. The findings indicate that larger IAs are more likely to experience unsuccessful treatment outcome, and the hemodynamic parameters in these cases show a greater relative change compared to successful cases. Abnormal flow conditions in the unsuccessful cases, along with higher SSS, could delay occlusion. This pilot study represents a first step toward identifying specific parameters for predicting treatment success for MCA aneurysm. While hemodynamic and morphological analysis alone may not be sufficient, these findings highlight the need for a multifactorial approach.

ACKNOWLEDGEMENTS

This study was partly funded by the Federal Ministry of Education and Research in Germany within the Forschungscampus STIMULATE (grant number 13GW0473A and 13GW0674C) and the German Research Foundation (grant number 548907942).

REFERENCES

[1] Xu, Z., Rui, Y.-N., Hagan, J. P., and Kim, D. H., 2019, "Intracranial aneurysms: pathology, genetics, and molecular mechanisms", *NeuroMolecular Medicine*, Vol. 21 (4), pp. 325–343.

[2] Keedy, A., 2006, "An overview of intracranial aneurysms", *McGill Journal of Medicine: MJM*, Vol. 9 (2), p. 141.

[3] Lee, K. S., Zhang, J. J., Nguyen, V., Han, J., Johnson, J. N., Kirollos, R., and Teo, M., 2022, "The evolution of intracranial aneurysm treatment techniques and future directions", *Neurosurgical Review*, Vol. 45 (1), pp. 1–25.

[4] Ravindran, K., Casabella, A. M., Cebral, J., Brinjikji, W., Kallmes, D. F., and Kadirvel, R., 2020, "Mechanism of action and biology of flow diverters in the treatment of intracranial aneurysms", *Neurosurgery*, Vol. 86 (Supplement_1), pp. S13–S19.

[5] Brinjikji, W., Murad, M. H., Lanzino, G., Cloft, H. J., and Kallmes, D. F., 2013, "Endovascular treatment of intracranial aneurysms with flow diverters: a meta-analysis", *Stroke*, Vol. 44 (2), pp. 442–447.

[6] Topcuoglu, O. M., Akgul, E., Daglioglu, E., Topcuoglu, E. D., Peker, A., Akmangit, I., Belen, D., and Arat, A., 2016, "Flow diversion in middle cerebral artery aneurysms: is it really an all-purpose treatment?", *World Neurosurgery*, Vol. 87, pp. 317–327.

[7] Michelozzi, C., Darcourt, J., Guenego, A., Januel, A.-C., Tall, P., Gawlitza, M., Bonneville, F., and Cognard, C., 2018, "Flow diversion treatment of complex bifurcation aneurysms beyond the circle of Willis: complications, aneurysm sac occlusion, reabsorption, recurrence, and jailed branch modification at follow-up", *Journal of Neurosurgery*, Vol. 131 (6), pp. 1751–1762.

[8] Long, S., Shi, S., Tian, Q., Wei, Z., Ma, J., Wang, Y., Yang, J., Han, X., and Li, T., 2024, "Correlation of flow diverter malapposition at the aneurysm neck with incomplete aneurysm occlusion in patients with small intracranial aneurysms: a single-center experience", *American Journal of Neuroradiology*, Vol. 45 (1), pp. 16–21.

[9] Gawlitza, M., Januel, A.-C., Tall, P., Bonneville, F., and Cognard, C., 2016, "Flow diversion treatment of complex bifurcation aneurysms beyond the circle of Willis: a single-center series with special emphasis on covered cortical branches and perforating arteries", *Journal of NeuroInterventional Surgery*, Vol. 8 (5), pp. 481–487.

[10] Stahl, J., Marsh, L. M. M., Thormann, M., Ding, A., Saalfeld, S., Behme, D., and Berg, P., 2023, "Assessment of the flow-diverter efficacy for intracranial aneurysm treatment considering pre-and post-interventional hemodynamics", *Computers in Biology and Medicine*, Vol. 156, p. 106720.

[11] Larrabide, I., Geers, A. J., Morales, H. G., Bijlenga, P., and Rüfenacht, D. A., 2016, "Change in aneurysmal flow pulsatility after flow diverter treatment", *Computerized Medical Imaging and Graphics*, Vol. 50, pp. 2–8.

[12] Cebral, J., Mut, F., Raschi, M., Scrivano, E., Ceratto, R., Lylyk, P., and Putman, C., 2011, "Aneurysm rupture following treatment with flow-diverting stents: computational hemodynamics analysis of treatment", *American Journal of Neuroradiology*, Vol. 32 (1), pp. 27–33.

[13] Levitt, M. R., McGah, P. M., Aliseda, A., Mourad, P. D., Nerva, J. D., Vaidya, S. S., Morton, R. P., Ghodke, B. V., and Kim, L. J., 2014, "Cerebral aneurysms treated with flow-diverting stents: computational models with intravascular blood flow measurements", *American Journal of Neuroradiology*, Vol. 35 (1), pp. 143–148.

[14] O'Kelly, C., Krings, T., Fiorella, D., and Marotta, T., 2010, "A novel grading scale for the angiographic assessment of intracranial aneurysms treated using flow diverting stents", *Interventional Neuroradiology*, Vol. 16 (2), pp. 133–137.

[15] Cekirge, H., and Saatci, I., 2016, "A new aneurysm occlusion classification after the impact of flow modification", *American Journal of Neuroradiology*, Vol. 37 (1), pp. 19–24.

[16] Berg, P., Daróczy, L., and Janiga, G., 2017, "Virtual stenting for intracranial aneurysms: A risk-free, patient-specific treatment planning support for neuroradiologists and neurosurgeons", *Computing and Visualization for Intravascular Imaging and Computer-Assisted Stenting*, Elsevier, pp. 371–411.

[17] Saalfeld, S., Berg, P., Niemann, A., Luz, M., Preim, B., and Beuing, O., 2018, "Semiautomatic neck curve reconstruction for intracranial aneurysm rupture risk assessment based on morphological parameters", *International Journal of Computer Assisted Radiology and Surgery*, Vol. 13, pp. 1781–1793.

[18] Berg, P., Saalfeld, S., Voß, S., Beuing, O., and Janiga, G., 2019, "A review on the reliability of hemodynamic modeling in intracranial aneurysms: why computational fluid dynamics alone cannot solve the equation", *Neurosurgical Focus*, Vol. 47 (1), p. E15.

[19] Chnafa, C., Bouillot, P., Brina, O., Delattre, B., Vargas, M., Lovblad, K., Pereira, V., and Steinman, D., 2017, "Vessel calibre and flow splitting relationships at the internal carotid artery terminal bifurcation", *Physiological Measurement*, Vol. 38 (11), p. 2044.

[20] Robertson, A. M., Sequeira, A., and Owens, R. G., 2009, "Rheological models for blood", *Cardiovascular Mathematics: Modeling and Simulation of the Circulatory System*, pp. 211–241.

[21] Sugiyama, S.-i., Niizuma, K., Sato, K., Rashad, S., Kohama, M., Endo, H., Endo, T., Matsumoto, Y., Ohta, M., and Tominaga, T., 2016, "Blood flow into basilar tip aneurysms: a predictor for recanalization after coil embolization", *Stroke*, Vol. 47 (10), pp. 2541–2547.

[22] Berg, P., Iosif, C., Ponsonnard, S., Yardin, C., Janiga, G., and Mounayer, C., 2016, "Endothelialization of over-and undersized flow-diverter stents at covered vessel side branches: an in vivo and in silico study", *Journal of Biomechanics*, Vol. 49 (1), pp. 4–12.

[23] Voss, S., Beuing, O., Janiga, G., and Berg, P., 2019, "Stent-induced vessel deformation after intracranial aneurysm treatment–A hemodynamic pilot study", *Computers in Biology and Medicine*, Vol. 111, p. 103338.

[24] Thormann, M., Stahl, J., Marsh, L., Saalfeld, S., Sillis, N., Ding, A., Mpotsaris, A., Berg, P., and Behme, D., 2024, "Computational Flow Diverter Implantation—A Comparative Study on Pre-Interventional Simulation and Post-Interventional Device Positioning for a Novel Blood Flow Modulator", *Fluids*, Vol. 9 (3), p. 55.

[25] Kulcsár, Z., Augsburger, L., Reymond, P., Pereira, V. M., Hirsch, S., Mallik, A. S., Millar, J., Wetzel, S. G., Wanke, I., and Rüfenacht, D. A., 2012, "Flow diversion treatment: intra-aneurismal blood flow velocity and WSS reduction are parameters to predict aneurysm thrombosis", *Acta Neurochirurgica*, Vol. 154, pp. 1827–1834.

[26] Mut, F., Raschi, M., Scrivano, E., Bleise, C., Chudyk, J., Ceratto, R., Lylyk, P., and Cebral, J. R., 2015, "Association between hemodynamic conditions and occlusion times after flow diversion in cerebral aneurysms", *Journal of NeuroInterventional Surgery*, Vol. 7 (4), pp. 286–290.

[27] Rayz, V. L., and Cohen-Gadol, A. A., 2020, "Hemodynamics of cerebral aneurysms: Connecting medical imaging and biomechanical analysis", *Annual Review of Biomedical Engineering*, Vol. 22 (1), pp. 231–256.

[28] Voß, S., Niemann, U., Saalfeld, S., Janiga, G., and Berg, P., 2025, "Impact of workflow variability on image-based intracranial aneurysm hemodynamics", *Computers in Biology and Medicine*, Vol. 190, p. 110018.

Conference on Modelling Fluid Flow (CMFF'25)
The 19th International Conference on Fluid Flow Technologies
Budapest, Hungary, August 26-August 29, 2025

NUMERICAL INVESTIGATION OF A LIFTED METHANE/AIR JET FLAME USING STOCHASTIC MAP-BASED TURBULENCE MODELING

Tommy Starick[1], Heiko Schmidt[2,3]

[1] Corresponding Author. Chair of Numerical Fluid and Gas Dynamics, Institute of Transport Technology, Brandenburg University of Technology (BTU) Cottbus-Senftenberg, Siemens-Halske-Ring 15a, 03046 Cottbus, Germany. Tel.: +49 355 69 4813, Fax: +49 355 69 4891, E-mail: Tommy.Starick@b-tu.de
[2] Chair of Numerical Fluid and Gas Dynamics, Institute of Transport Technology, Brandenburg University of Technology (BTU) Cottbus-Senftenberg, Siemens-Halske-Ring 15a, 03046 Cottbus, Germany. Tel.: +49 355 69 4874, Fax: +49 355 69 4891, E-mail: Heiko.Schmidt@b-tu.de
[3] Scientific Computing Lab (SCL), Energy Innovation Center (EIZ), Brandenburg University of Technology (BTU) Cottbus-Senftenberg, 03046 Cottbus, Germany.

ABSTRACT

This numerical study investigates a lifted methane/air jet flame in a vitiated coflow by means of the map-based, stochastic one-dimensional turbulence (ODT) model. The dimensional reduction of ODT allows for simulations with affordable computational costs and provides nonetheless full-scale resolution along a notional line of sight crossing the turbulent flow field. The considered Cabra burner configuration consists of a jet flame issuing from a central nozzle into a vitiated coflow of hot combustion products. Radial and centerline profiles for mixture fraction, temperature and selected species mass fractions obtained from ODT using a reduced and detailed reaction mechanism are in appropriate agreement with the existing experimental measurements. A two-dimensional illustration of the autoignition index is given, which enables the distinction between autoignition and propagation driven reaction zones. Additionally, the sensitivity of the jet combustion to velocity and temperature variations is investigated. Considering the reduced order of ODT and the sensitivity of the subtle interactions of the hot coflow with the cold jet on the entire reaction process, ODT is able to predict the flow characteristics and reasonably matches the experimental data. As a consequence, ODT is an efficient and alternative model for turbulent reactive flow simulations.

Keywords: autoigniton, lifted jet flame, methane/air combustion, ODT, one-dimensional turbulence, stochastic turbulence modeling

NOMENCLATURE

C	$[-]$	ODT model parameter - turbulence intensity
D	$[m]$	jet diameter
E_{kin}	$[J]$	available kinetic energy
E_{vp}	$[J]$	energetic viscous penalty
M_k	$[\frac{kg}{mol}]$	molecular weight of species k
P	$[Pa]$	thermodynamic pressure
R_u	$[\frac{J}{K \cdot mol}]$	universal gas constant
T	$[K]$	thermodynamic temperature
V_k	$[\frac{m}{s}]$	diffusion velocity of species k
X_k	$[-]$	mole fraction of species k
Y_k	$[-]$	mass fraction of species k
Z	$[-]$	ODT model parameter - viscous penalty
Δt_{sample}	$[s]$	sampling time interval
$\dot{w}_k$	$[\frac{kg}{m^3 \cdot s}]$	reaction rate of species k
f	$[-]$	mixture fraction
l	$[m]$	eddy size
r	$[m]$	radial position
r_0	$[m]$	eddy location
t	$[s]$	simulation time
u_i	$[\frac{m}{s}]$	velocity component
z	$[m]$	downstream position
β	$[-]$	ODT model parameter - large eddy suppression
λ	$[\frac{1}{s \cdot m^2}]$	eddy rate
μ	$[\frac{kg}{m \cdot s}]$	dynamic viscosity
ρ	$[\frac{kg}{m^3}]$	density of the gas mixture
τ	$[s]$	eddy event time scale

1. INTRODUCTION

Recirculating burners are a special type of burner that reinjects part of the hot exhaust gases back into the combustion process. This technology is used to enhance combustion efficiency, reduce pollutant emissions (especially nitrogen oxides), control flame temperature and to get wider fuel and operation flexibility. By recirculating the exhaust gases, the oxygen concentration in the combustion chamber is lowered, resulting in slower and more uniform com-

bustion. Recirculating burners are widely used in industrial heating processes, power plants, and chemical processing applications where optimized energy utilization and emission reduction are required.

The numerical study of this special type of burner is challenging due to the recirculation of hot combustion products. Vitiated coflow burners exhibit similar characteristics in terms of chemical kinetics, heat transfer, and molecular transport as recirculating burners, where the stabilized flame is lifted from the burner by increased jet or coflow velocity. However, they avoid the complexities associated with recirculating fluid mechanics, as demonstrated in the experimental measurements of Cabra et al. [1].

Despite the simplified consideration of a recirculating burner as a vitiated coflow burner, the accurate representation of the turbulent reactive flow is a standing challenge in numerical fluid dynamics. The small-scale interactions of the hot coflow with the unburnt jet flow are crucial for the entire reaction of the jet and necessitate a full resolution of all relevant time and length scales in order to completely capture the state-space statistics.

Direct numerical simulation (DNS) would be the ideal method for turbulent reactive flows, as it provides complete resolution of the flow without modeling errors. However, for most industrial applications, DNS remains prohibitively computationally expensive and is therefore also not a feasible option in the foreseeable future [2].

To enable the numerical study of turbulent reactive flows despite computational limitations, turbulence closure models are commonly applied. In contrast to the full resolution of DNS, large-eddy simulation (LES) and Reynolds-averaged Navier-Stokes (RANS) approaches resolve the flow only in a filtered or averaged sense, which reduces the computational effort in the desired way. To compensate for the limited state-space information of the scalar composition, these lower-fidelity models often incorporate transported probability density function (PDF) methods [3].

The considered Cabra burner configuration, consisting of a jet flame issuing from a central nozzle into a vitiated coflow of hot combustion products, represents an important test case and has been investigated by a variety of LES [4, 5, 6, 7] and RANS [1, 8, 9, 10] simulations.

These studies show that the averaged or filtered results generally are in reasonable agreement with the experimental measurements and are able to capture key combustion characteristics. However, despite the use of filtering or averaging, LES and RANS simulations remain computationally demanding due to the need for resolving the expensive chemistry alongside of the transported PDF approach. As a result, their applicability for extensive sensitivity analyses or comprehensive parameter studies is limited.

Reduced order turbulence and mixing models offer an alternative approach, significantly lowering computational costs compared to DNS while preserving fundamental physical conservation principles and accurately capturing turbulent flow phenomenology.

In reduced order stochastic mixing and turbulence models, map-based transformations are applied in one-dimensional domains to mimic the effects of turbulent mixing and advection. Notable representatives are the linear eddy model (LEM) [11] and the hierarchical parcel swapping (HiPS) model [12], both mixing models, and the one-dimensional turbulence (ODT) model [13], all developed by A. Kerstein. These models efficiently utilize available computational resources through dimensional order reduction while fully resolving the entire range of scales within the one-dimensional domain. This makes LEM, HiPS and ODT particularly well-suited for applications where small-scale interactions between advection, diffusion, and reaction play a crucial role.

The main objective of this work is the scale-resolving, pyhsics-based, yet computationally efficient numerical investigation of the Cabra jet flame in a vitiated coflow. The results from the ODT model are thoroughly compared with the experimental data from Cabra et al. [1]. Additionally, the autoignition index is evaluated, and the sensitivity of the lift off height to variations in jet velocity and coflow temperature is examined.

The paper is structured as follows: Section 2 provides a more detailed description of the ODT model formulation. Section 3 describes the flow configuration for the considered methane/air jet flame in a vitiated coflow. Section 4 presents and discusses the model results, followed by concluding remarks.

2. ODT MODEL FORMULATION

The one-dimensional turbulence (ODT) model offers a significantly reduced numerical framework compared to DNS and LES, enabling full-scale resolution in the radial direction of the jet. This makes ODT an ideal tool for the numerical study of a lifted methane/air jet flame in a vitiated coflow. For this round jet flame, a cylindrical ODT formulation is used to account for the geometric proportions. This formulation is detailed in Lignell et al. [14].

ODT employs a stochastic, map-based approach to represent turbulent advection. The diffusion and reaction kinetics along the one-dimensional domain are modeled through the temporal advancement of deterministic evolution equations. Unlike averaged or filtered simulation approaches, such as RANS or LES, ODT integrates molecular processes (e.g., chemical reactions and diffusive transport) without introducing additional approximations or modeling assumptions.

The effects of three-dimensional turbulence are incorporated into ODT through the use of stochastic *eddy events*. These eddy events directly represent the turbulent transport characteristics affecting fluid

properties along the simulated one-dimensional domain. Each eddy event modifies property fields by applying a *triplet map*.

A triplet map is a measure-preserving transformation rule that ensures the continuity of advected fields, leading to the steepening of local property gradients [14, 15]. The map operates by taking a line segment $[r_0, r_0 + l]$ with a randomly selected eddy location r_0 and size l, shrinking it to a third of its original length, and then placing three copies of the segment on the original domain. The middle copy is reversed. The features of the triplet map in the cylindrical ODT formulation can be reviewed in [14].

Eddy events are sampled in time using a marked Poisson process, with assumed Probability Density Functions (PDFs) for eddy locations r_0 and sizes l. This process replicates the statistics of turbulent flows on average by oversampling the number of events representing turbulent transport, while maintaining a target mean acceptance probability for the eddy events, as discussed in [16] and [14]. The acceptance probability of a particular eddy within a given sampling time interval Δt_{sample} is determined by calculating a rate λ of the eddy candidate.

The eddy rate λ, as shown in Eq. 1, depends on r_0, l, and the eddy event time scale τ. The time scale τ is proportional to the difference between the available kinetic energy E_{kin} in the eddy range and an energetic viscous penalty E_{vp} for suppressing excessively small eddies, as described in [14]. While the energetic viscous penalty does not significantly affect the statistical results, it is beneficial for improving the model's performance.

$$\lambda(r_0, l, \tau) \equiv \frac{C}{l^2 \tau} \sim C\left(E_{kin} - Z E_{vp}\right) \tag{1}$$

C and Z are dimensionless ODT model parameters that are initially calibrated and then remain constant.

Due to its reduced dimensionality, ODT does not capture large-scale coherent structures. Occasionally, during the initial phase, the eddy sampling process may accept unphysically large eddies, which can negatively impact turbulent transport. To prevent this, ODT employs a large eddy suppression mechanism.

This mechanism eliminates eddies whose event time scale is disproportionately larger than the elapsed simulation time t. In general, eddies are only implemented if the following condition

$$\tau \leq \beta t \tag{2}$$

is satisfied, where β is another dimensionless ODT model parameter which is determined beforehand [14].

Eddies are sampled sequentially in time. Once an eddy is implemented, a deterministic catch-up process takes place, advancing the diffusive-reactive transport equations up to the physical time at which the eddy was selected for implementation.

In an open system configuration, such as the lifted jet flame examined in this study, the deterministic evolution follows integral conservation laws based on a Lagrangian ODT formulation, as described in [14].

The integral expressions for the conservation of mass, momentum, and energy are presented below. The mass conservation equation is given as follows.

$$\frac{\mathrm{d}}{\mathrm{d}t} \int \rho r \mathrm{d}r = 0 \tag{3}$$

Here, ρ represents the density of the gas mixture, which is determined by its pressure, temperature, and molecular weight, as described by the ideal gas law.

$$P = \rho R_u T \sum_k \frac{Y_k}{M_k} \tag{4}$$

In this equation, P represents the thermodynamic pressure, which remains constant over time and space in the open jet flame configuration. Additionally, R_u denotes the universal gas constant, T is the temperature of the gas mixture, and Y_k and M_k correspond to the mass fractions and molecular weights of the k-th species that make up the gas mixture, respectively. The species conservation equation is given by following equation.

$$\begin{aligned} \frac{\mathrm{d}}{\mathrm{d}t} \int \rho Y_k r \mathrm{d}r = &- \int \frac{1}{r} \frac{\partial}{\partial r} \left(r \rho V_k Y_k\right) r \mathrm{d}r \\ &+ \int \dot{w}_k r \mathrm{d}r \end{aligned} \tag{5}$$

Here, V_k represents the species diffusion velocities, which require the same modeling approximations as those used in reactive DNS. Similarly, $\dot{w}_k$ denotes the species reaction rates, which are determined by an imported reaction mechanism under specified thermodynamic conditions.

For momentum conservation, we assume that radial transport is dominant and model the diffusion of momentum using the gradient of scalar-modeled shear stresses, following the approach described in [14].

$$\frac{\mathrm{d}}{\mathrm{d}t} \int \rho u_i r \mathrm{d}r = \int \frac{1}{r} \frac{\partial}{\partial r} \left(r \mu \frac{\partial u_i}{\partial r}\right) r \mathrm{d}r \tag{6}$$

In the momentum conservation equation, u_i stands for the three velocity components in the cylindrical system and μ is the dynamic viscosity of the gas mixture. Finally, the energy conservation in the open system is being represented by the conservation of enthalpy h in a zero Mach number limit approximation.

$$\begin{aligned} \frac{\mathrm{d}}{\mathrm{d}t} \int \rho h r \mathrm{d}r = &- \int \frac{1}{r} \frac{\partial}{\partial r} \left(r \rho V_k Y_k h_k\right) r \mathrm{d}r \\ &+ \int \frac{1}{r} \frac{\partial}{\partial r} \left(r \lambda_t \frac{\partial T}{\partial r}\right) r \mathrm{d}r \end{aligned} \tag{7}$$

In this equation, h_k stands for the sensible enthalpy of each k-th species and λ_t is the thermal conductivity of the mixture.

The deterministic time advancement of Eq.3-7 is achieved using a finite volume method (FVM) with first-order time integration. For the analyzed lifted methane/air jet flame, an implicit time integration of Eq.3-7 is applied, where the diffusive flux terms, calculated at the start of each time step, are treated as constants. This approach helps to mitigate the potentially restrictive CFL condition caused by stiff chemistry arising from the species chemical reaction source term. However, this converts the time integration in Eq. 6-7 into an explicit Euler method.

The density, which is updated after time-stepping the enthalpy and species conservation equations (Eq.7 and 5), is computed using Eq.4 based on the new mixture composition and temperature. Once the density is updated, mass conservation is enforced through a conservative remeshing of the grid, following the application of the mass conservation equation [17]. The fluid thermophysical properties are determined using the Cantera software suite, as described in [18].

3. FLOW CONFIGURATION

The Cabra burner configuration [1] consists of a lifted methane/air jet flame in a vitiated coflow generated by an array of lean H_2/air flames. The temperature and species concentrations are considered uniform across the coflow, and the flow field of interest is not influenced by mixing with ambient air [1]. Consequently, the coflow is uniformly initialized in all ODT simulations, and the ambient air is not considered. This results in a pure two-stream configuration. For the base case configuration, the jet and coflow is initialized as specified in Table 1. For every single ODT realization, an instantaneous velocity profile is used generated by ODT pipe flow simulations with a fixed bulk velocity of 100 m/s.

Table 1. Initial conditions for jet and coflow. X, mole fraction; u, velocity; T, temperature; D, diameter;

-	Jet	Coflow
D (mm)	4.57	100
u (m/s)	100	5.4
T (K)	320	1350
X_{CH_4}	0.33	0.0003
X_{O_2}	0.15	0.12
X_{N_2}	0.52	0.73
X_{H_2O}	0.0029	0.15
X_{OH} (ppm)	0.0	200
X_{H_2} (ppm)	100	100

The detailed GRI-Mech 3.0 mechanism [19], which includes 53 species and 325 reactions, along with a reduced reaction mechanism [20] containing 19 species and 15 reactions, is used for the representation of chemical reactions and thermophysical properties.

The ODT results are meant to be compared with the stationary, spatially developing round jet flame measurements from [1]. However, the cylindrical ODT formulation applied here only solves for a radial location, r, and time, t. As a result, a transformation between time and the corresponding downstream position, z, is necessary. This is accomplished by downstream advection of the ODT line using an instantaneous bulk velocity, $\bar{u}$.

$$z(t) = z(t_0) + \int_{t_0}^{t} \bar{u}(t')dt' \tag{8}$$

Here, $z(t_0)$ marks the starting position. The bulk velocity, $\bar{u}$, is calculated by the sum of the free-stream (coflow) velocity, u_∞ , and the ratio of integrated momentum flux to integrated mass flux, as detailed in [21].

$$\bar{u}(t) = u_\infty + \left.\frac{\int_{-\infty}^{\infty} \rho(u-u_\infty)^2 r dr}{\int_{-\infty}^{\infty} \rho(u-u_\infty) r dr}\right|_t \tag{9}$$

For the definition of the mixture fraction, the commonly used Bilger's equation [22] is applied.

4. RESULTS AND DISCUSSION

ODT simulations, using both a reduced and a detailed reaction mechanism, were carried out and compared with the experimental data from Cabra et al. [1]. The Favre-averaging of the ODT results was based on an ensemble size of 1500 realizations. For all presented results, the ODT model parameters C and Z in Eq. 1 were set to $C = 18$ and $Z = 400$, matching the parameters used in the study of a round jet flame with a similar cylindrical formulation by Lignell et al. [14]. Furthermore, a fixed model parameter of $\beta = 1.17$ was used to suppress large eddies during the initial phase of the simulation.

4.1. Centerline profiles

Comparisons are made between the experimental measurements of [1] and ODT simulations using both a reduced and a detailed reaction mechanism. The centerline profiles of the Favre-averaged species mass fractions, temperature, and mixture fraction, along with their corresponding fluctuations, are presented in Figure 1. In these plots, the red and blue curves represent ODT simulation results for the reduced and detailed reaction mechanisms, respectively, while the experimental data from [1] is shown as round black markers.

In the initial phase, up to approximately $z/D \approx 40$, the process is dominated by non-reactive mixing between the cold jet and the hot coflow, leading to a gradual rise in centerline temperature with low fluctuations. This is followed by the flame stabilization phase around $z/D \approx 45$, where a sharp temperature increase, rapid oxygen consumption, hydroxyl

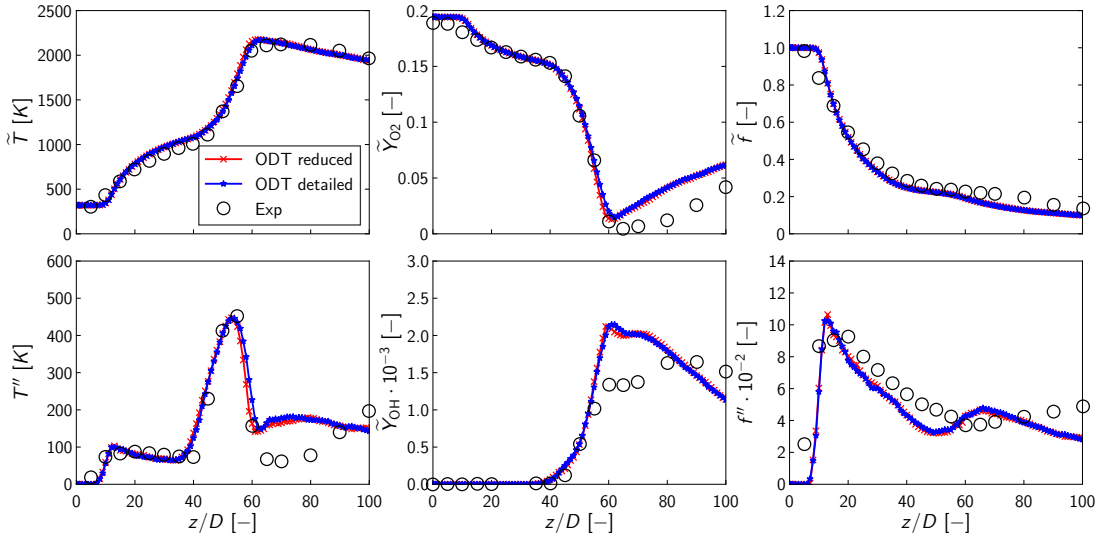

Figure 1. Centerline profiles of Favre-averaged temperature ($\tilde{T}$ and fluctuations T''), species mass fractions (Favre-averaged oxygen mass fraction $\tilde{Y}_{O2}$ and Favre-averaged hydroxyl radical mass fraction $\tilde{Y}_{OH}$), and mixture fraction ($\tilde{f}$ and fluctuations f'') from ODT simulations using a reduced and detailed reaction mechanism for the representation of the methane/air combustion. ODT results are compared to the experimental measurements of [1] (Exp).

radical production, and a peak in temperature fluctuations are observed.

The ODT results for both reaction mechanisms show good agreement with the experimental data, accurately capturing the mixing behavior in the early phase and the subsequent combustion process, as indicated by the steep temperature rise and drop in oxygen mass fraction. Additionally, ODT closely follows the trend and magnitude of the Favre fluctuations observed in the experiments. However, slight overpredictions of the mean mass fractions of O_2 and OH are noted for $z/D > 60$. The differences between the two reaction mechanisms are negligibly small.

4.2. Radial profiles

In addition to the centerline profiles, Figure 2 presents the radial profiles of the Favre-averaged temperature and mixture fraction. Similar to the centerline plots, the red and blue curves represent ODT simulation results using a detailed and a reduced reaction mechanism, respectively. The experimental data for the Favre-averaged values are depicted by round markers.

In the initial phase, where non-reactive mixing occurs between the cold jet and the hot coflow ($z/D = 15$ and $z/D = 30$), the ODT results for both reaction mechanisms show reasonable agreement with the experimental measurements. However, at positions further downstream ($z/D = 50$ and $z/D = 70$), deviations between the ODT results and the experimental data become noticeable. These discrepancies are likely due to the approximation used for determining the downstream position, as described by Eq. 8 and 9.

Unlike the centerline region, where a radially uniform bulk velocity approximation for each time step is more applicable, this approach may not be entirely suitable for the shear region between the cold jet and the hot coflow. A more accurate representation of the downstream advection of the ODT line could potentially be achieved by using a spatial ODT formulation, as suggested in [14].

4.3. Autoignition index

The autoignition index (AI) provides a measure to differentiate between autoignition-driven and propagation-driven reaction zones, as described in [4]. Its definition is based on a reaction rate flux analysis of the HO_2 chemistry. In the detailed GRI-Mech 3.0 mechanism [19], the key reactions governing the consumption of HO_2 play a crucial role in distinguishing between these two types of reaction zones. Specifically, this distinction is made through the following two reactions.

$$HO_2 + H \longleftrightarrow OH + OH \qquad [R46]$$

$$HO_2 + OH \longleftrightarrow H_2O + O_2 \qquad [R287]$$

The autoignition index is given by following definition, as detailed in [4].

$$AI = \left| \frac{\dot{w}_{HO_2}^{R287}}{\dot{w}_{HO_2}^{R287} + \dot{w}_{HO_2}^{R46}} \right| \tag{10}$$

Here, $\dot{w}_{HO_2}^{R287}$ stands for the contribution of reaction 287 to the reaction rate of HO_2 in the detailed reaction mechanism. Similarly, $\dot{w}_{HO_2}^{R46}$ is the contribution of reaction 46 to the reaction rate of HO_2.

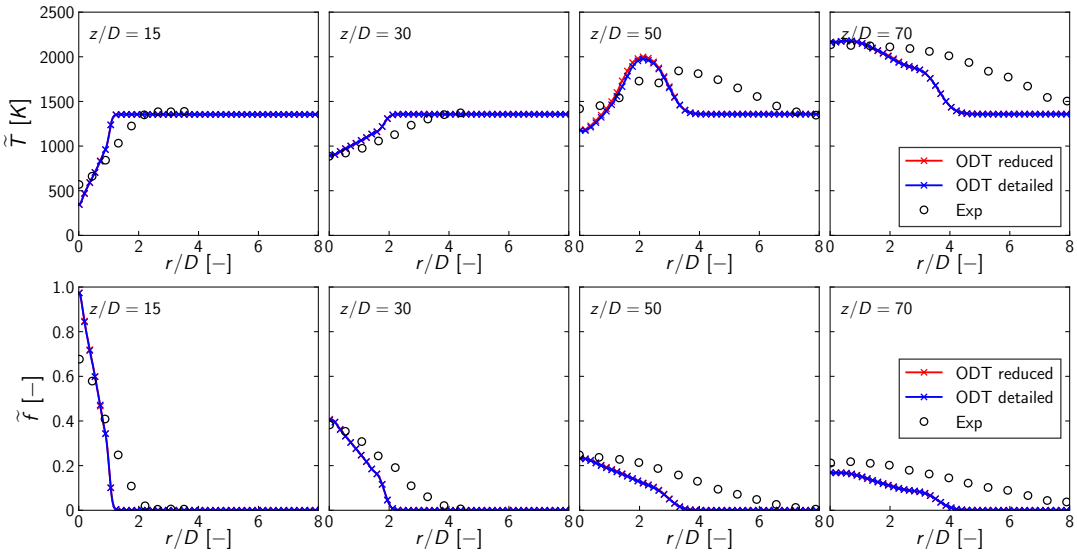

Figure 2. Radial profiles of Favre-averaged temperature and Favre-averaged mixture fraction from ODT simulations using a reduced and detailed reaction mechanism for the representation of the methane/air combustion. ODT results are compared to the experimental measurements of [1] (Exp).

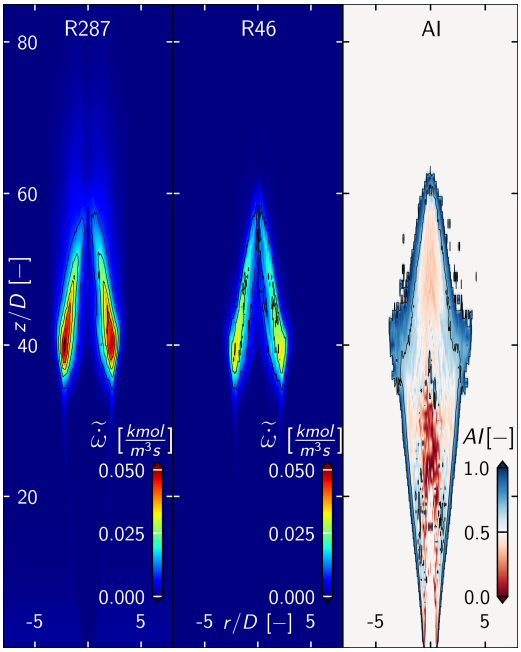

Figure 3. Two-dimensional renderings of the reaction rate of HO_2 of reaction 287, reaction rate of HO_2 of reaction 46, and mean autoignition index (AI). All results are averaged over the full ensemble size of ODT realizations.

Figure 3 illustrates the mean autoignition index, where blue regions (AI > 0.5) indicate autoignition-dominated zones, and red regions (AI < 0.5) represent propagation-dominated zones. In this visualization, propagation primarily occurs in the core of the flame, while autoignition is dominant in the transition region to the hot coflow. Compared to the instantaneous AI results from a 3-D LES simulation reported by [4] (not shown here), the ODT results exhibit similar spatial distributions of autoignition- and propagation-driven reaction zones. Given the reduced-order nature of the ODT model, its ability to provide insights into the autoignition index distribution while maintaining reasonable agreement with the findings of [4] highlights the effectiveness and potential of ODT.

4.4. Sensitivity to velocity and temperature variations

Figure 4 shows the sensitivity of the jet combustion to variations on jet velocity and coflow temperature. The centerline profiles for jet velocity variations reveal a later combustion with increasing jet velocity. This is indicated by a flatter temperature rise and more moderate oxygen consumption in the flame stabilization phase compared to the base case configuration with 100 m/s. A similar effect can be achieved by reducing the coflow temperature, as visible by the profiles for 1270 K, 1290 K, 1310 K, and 1330 K. However, with a higher temperature than the base case configuration of 1350 K, a faster combustion can also be observed. The temperature rise and oxygen consumption is thereby more rapidly. The mixture fraction, however, shows only minor differences between the profiles for different jet velocities and coflow temperatures. These findings are in well agreement with the parametric measurements of Cabra et al. [1] on the sensitivity of flame liftoff height to jet velocity and coflow temperature.

5. CONCLUSIONS

ODT simulation results for a lifted methane/air jet flame in an environment of hot combustion products have been presented. A cylindrical and temporal ODT formulation was employed using both a reduced and a detailed reaction mechanism, with

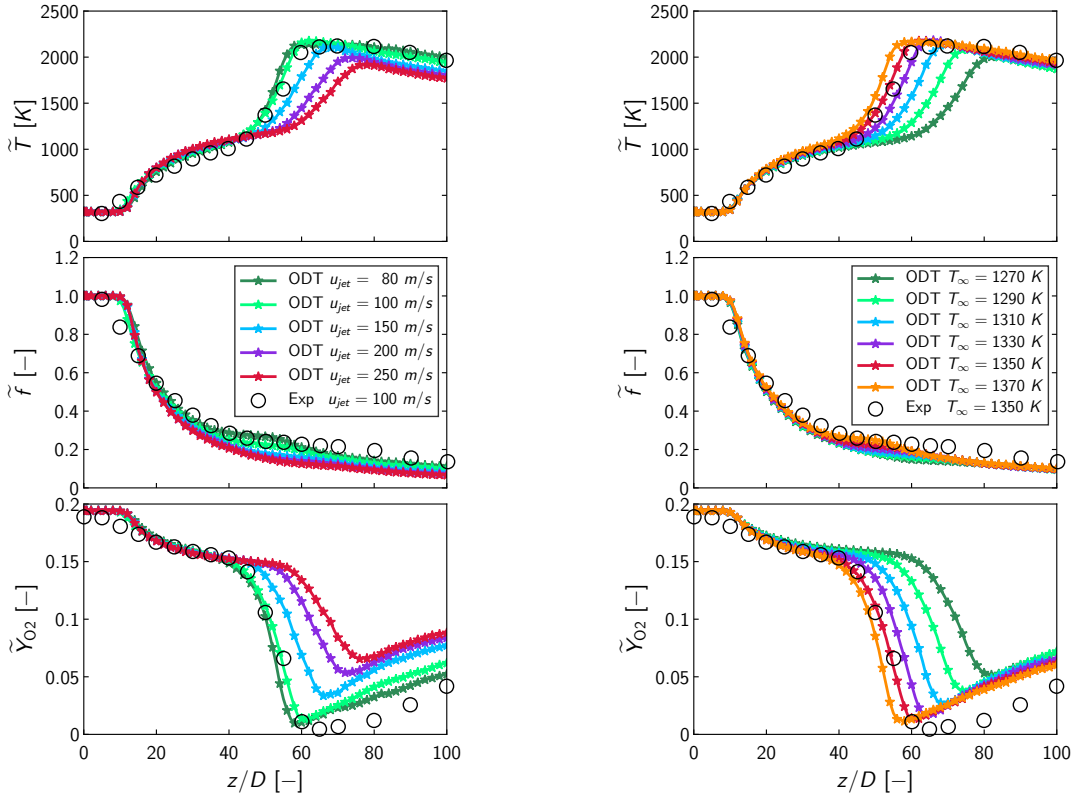

Figure 4. Centerline profiles of Favre-averaged temperature ($\tilde{T}$), mixture fraction ($\tilde{f}$), and oxygen mass fraction ($\tilde{Y}_{O2}$) from ODT simulations using a detailed reaction mechanism. Left: Sensitivity to jet velocity variations. Right: Sensitivity to coflow temperature variations.

comparisons made against the experimental measurements of [1]. The detailed mechanism consists of 53 species and 325 reactions, while the reduced mechanism includes 19 species and 15 reactions.

The comparison of centerline profiles with experimental data showed reasonable agreement for both reaction mechanisms, demonstrating ODT's ability to accurately reproduce Favre-averaged centerline profiles and their corresponding fluctuations. Additionally, the radial profiles for the pure mixing phase (z/D <30) aligned well with experimental observations. However, at positions further downstream (z/D >30), deviations from the experimental data were observed. The differences in the centerline and radial profiles between the detailed and reduced mechanism are negligibly small. The possibility of investigating the autoignition index and the influence of temperature and velocity variations reveals the benefits of the ODT model.

Overall, the results indicate that ODT successfully captures the essential combustion features of the investigated lifted methane/air jet flame in a vitiated coflow. Given its reduced-order nature, ODT proves to be an efficient and scale-resolving turbulence model for reactive jet flame simulations.

ACKNOWLEDGEMENTS

This research is supported by the German Federal Government, the Federal Ministry of Education and Research, and the State of Brandenburg within the framework of the joint project EIZ: Energy Innovation Center [project numbers 85056897 and 03SF0693A] with funds from the Structural Development Act (Strukturstärkungsgesetz) for coal-mining regions and the Brandenburg University of Technology (BTU) Graduate Research School [Conference Travel Grant].

REFERENCES

[1] Cabra, R., Chen, J.-Y., Dibble, R. W., Karpetis, A. N., and Barlow, R. S., 2005, "Lifted methane-air jet flames in a vitiated coflow", *Combustion and Flame*, Vol. 143, pp. 491–506.

[2] Domingo, P., and Vervisch, L., 2022, "Recent developments in DNS of turbulent combustion", *Proc Combust Inst*, Vol. 39 (2), pp. 2055–2076.

[3] Pope, S., 1985, "PDF methods for turbulent reactive flows", *Prog Energy Combust Sci*, Vol. 11 (2), pp. 119–192.

[4] Schulz, O., Jaravel, T., Poinsot, T., Cuenot, B., and Noiray, N., 2017, "A criterion to distinguish autoignition and propagation applied to a lifted methane–air jet flame", *Proceedings of the Combustion Institute*, Vol. 36 (2), pp. 1637–1644, URL https://www.sciencedirect.com/science/article/pii/S1540748916304114.

[5] Zhang, H., Yu, Z., Ye, T., Zhao, M., and Cheng, M., 2018, "Large eddy simulation of turbulent lifted flame in a hot vitiated coflow using tabulated detailed chemistry", *Applied Thermal Engineering*, Vol. 128, pp. 1660–1672, URL https://www.sciencedirect.com/science/article/pii/S1359431117316733.

[6] Domingo, P., Vervisch, L., and Veynante, D., 2008, "Large-eddy simulation of a lifted methane jet flame in a vitiated coflow", *Combustion and Flame*, Vol. 152 (3), pp. 415–432, URL https://www.sciencedirect.com/science/article/pii/S0010218007002519.

[7] Ihme, M., and See, Y. C., 2010, "Prediction of autoignition in a lifted methane/air flame using an unsteady flamelet/progress variable model", *Combustion and Flame*, Vol. 157 (10), pp. 1850–1862, URL https://www.sciencedirect.com/science/article/pii/S0010218010002038.

[8] Michel, J.-B., Colin, O., Angelberger, C., and Veynante, D., 2009, "Using the tabulated diffusion flamelet model ADF-PCM to simulate a lifted methane–air jet flame", *Combustion and Flame*, Vol. 156 (7), pp. 1318–1331, URL https://www.sciencedirect.com/science/article/pii/S0010218009000042.

[9] Gkagkas, K., and Lindstedt, R., 2007, "Transported PDF modelling with detailed chemistry of pre- and auto-ignition in CH4/air mixtures", *Proceedings of the Combustion Institute*, Vol. 31 (1), pp. 1559–1566, URL https://www.sciencedirect.com/science/article/pii/S1540748906003415.

[10] R. L. Gordon, A. R. Masri, S. B. P., and Goldin, G. M., 2007, "A numerical study of auto-ignition in turbulent lifted flames issuing into a vitiated co-flow", *Combustion Theory and Modelling*, Vol. 11 (3), pp. 351–376.

[11] Kerstein, A., 1988, "A Linear Eddy Model of Turbulent Scalar Transport and Mixing", *Combustion Science and Technology*, Vol. 60 (4-6), pp. 391–421.

[12] Kerstein, A. R., 2013, "Hierarchical parcel-swapping representation of turbulent mixing. Part 1. Formulation and scaling properties", *J Stat Phys*, Vol. 153 (1), pp. 142–161.

[13] Kerstein, A., 1999, "One-dimensional turbulence: model formulation and application to homogeneous turbulence, shear flows, and buoyant stratified flows", *Journal of Fluid Mechanics*, Vol. 392, pp. 277–334.

[14] Lignell, D., Lansinger, V., Medina M., J. A., Klein, M., Kerstein, A., Schmidt, H., Fistler, M., and Oevermann, M., 2018, "One-dimensional turbulence modeling for cylindrical and spherical flows: model formulation and application", *Theoretical and Computational Fluid Dynamics*, Vol. 32, pp. 495–520.

[15] Ashurst, W., and Kerstein, A., 2005, "One-dimensional turbulence: Variable-density formulation and application to mixing layers", *Physics of Fluids*, Vol. 17.

[16] McDermott, R., 2005, "Towards One-Dimensional Turbulence Subgrid Closure for Large-Eddy Simulation", Ph.D. thesis, University of Utah.

[17] Lignell, D., Kerstein, A., Sun, G., and Monson, E., 2013, "Mesh adaption for efficient multiscale implementation of One-Dimensional Turbulence", *Theoretical and Computational Fluid Dynamics*, Vol. 27 (3-4), pp. 273–295.

[18] Goodwin, D., 2002, *Cantera C++ User's Guide*, California Institute of Technology.

[19] Smith, G. P., Golden, D. M., Frenklach, M., Moriarty, N. W., Eiteneer, B., Goldenberg, M., Bowman, C. T., Hanson, R. K., Song, S., Gardiner, W. C., Lissianski, V. V., and Qin, Z., 1999, "http://www.me.berkeley.edu/gri_mech/", *Tech rep*.

[20] Lu, T., and Law, C., 2008, "A criterion based on computational singular perturbation for the identification of quasi steady state species: A reduced mechanism for methane oxidation with NO chemistry", *Combustion and Flame*, Vol. 154, pp. 761–774.

[21] Echekki, T., Kerstein, A., and Dreeben, T., 2001, "One-Dimensional Turbulence Simulation of Turbulent Jet Diffusion Flames: Model Formulation and Illustrative Applications", *Combustion and Flame*, Vol. 125, pp. 1083–1105.

[22] Bilger, R., S.H., S., and R.J., K., 1990, "On Reduced Mechanisms for Methane-Air Combustion in Nonpremixed Flames", *Combustion and Flame*, Vol. 80, pp. 135–149.

Conference on Modelling Fluid Flow (CMFF'25)
The 19th International Conference on Fluid Flow Technologies
Budapest, Hungary, August 26 - August 29, 2025

NUMERICAL INVESTIGATION OF LIQUID EMBOLIZATION FOR INTRAVASCULAR TREATMENT USING A PARTICLE METHOD

Marie Oshima[1], Takuya Natume[2], Nobuhiko Mukai[3]

[1] Corresponding Author. Interfaculty Initiative in Information Studies/ Institute of Industrial Science, the University of Tokyo, E-mail: marie@iis.u-tokyo.ac.jp
[2] Graduate School of Integrative Science and Engineering, Tokyo City University, E-mail: takuya.natsume.1102@gmail.com (graduated in 2022)
[3] Graduate School of Integrative Science and Engineering, Tokyo City University, E-mail: nmukai@tcu.ac.jp

ABSTRACT

Subarachnoid hemorrhage is caused by cerebral aneurysm rupture. Since subarachnoid hemorrhage has not only high mortality but also high possibility for complications, it is important to prevent aneurysm rapturing by performing an intravascular treatment.

The advantage of the recently developed photocurable liquid embolization is its controllability compared to conventional treatment such as coiling or clipping. However, as the treatment has not been evaluated extensively, this study presents a nuermical method to investigate applicability of intravascular treatment using photocurable liquid embolization.

The process of photocurable liquid embolization is complicated and involves both geometrical and topological changes like separation. Therefore, a particle method, particularly the moving particle semi-implicit method was used in this paper. A stabilization method was investigated to reduce numerical instability caused by pressure oscillations. In addition, we developed an efficient numerical method that considers the effects of highly viscous fluids of liquid embolization and wettability of a catheter. The proposed method was applied to a simplified injection problem involving highly viscous fluid to replicate intravascular treatment. The simulation results were compared to experimental data and showed good agreement with the experiments.

Keywords: Moving Particle Semi-implicit method, highly viscous fluid, wettability, photocurable liquid embolization. Cerebral aneurysm

NOMENCLATURE

A_0	[m^2]	interfacial area occupied. by one particle
C	[N/m^2]	potential coefficient
F	[N]	force
H	[-]	approximated Heaviside function
N'	[m^2]	number of particles in the radius r_e^{ave}
P	[Pa]	pressure
S	[-]	coefficient for interface
d	[-]	dimension number
g	[m/s^2]	gravitational acceleration
h	[m]	interfacial thickness
n	[m^2]	particle density
n^{in}	[-]	normal vector to the interfacial surface
r	[m]	distance between particles
u	[m/s]	velocity
w	[-]	weighted function
λ	[$1/m^{2]}$	coefficient of the Laplacian term
μ	[P・s]	viscosity coefficient
ρ	[Kg/m^3]	density
ϕ	[-]	scalar

Subscripts and Superscripts

i, j	x-axis, y-axis, and z-axis coordinate system
k, l	particle number
inter	interfacial
$\bar{kl}$	variable between partilce k and particle l
e	effective
av	average
ad	adhesion
sp	spread
in b-c	interface between blood and embolization liquid
in l-c	interface between embolization liquid and

catheter
k-st particle in the structure (catheter)
k-l particle in liquid (embolization liquid)
k-sl particle in the interface between structure and liquid

1. INTRODUCTION

Subarachnoid hemorrhage is a serious cerebral disorder. Due to high mortality rate and sever subsequent complications after the incidence of subarachnoid hemorrhage, a patient at high risk is often recommended surgery [1]. Since subarachnoid hemorrhage generally occurs in patients with a cerebral aneurysm, surgery is necessary to prevent the aneurysm rupture. There are mainly two types of conventional surgical treatments: coiling and clipping. Coiling is less invasive than clipping and therefore more widely used. However, it is an expensive procedure that requires a large number of expensive coils. Further, it is difficult to estimate the number of required coils, and once inserted into the aneurysm, the coils cannot be retracted. In view of the limitations of coiling, liquid embolization methods like Onxy have gained attention [2]. In particular, photocurable liquid embolization has been developed as a novel treatment. The advantage of photocurable liquid embolization is its controllability compared to the conventional treatments.

Photocurable liquid embolization is still under development for a clinical application. A numerical simulation is a variable technique to elucidate the mechanism as well as to examine the procedure. However, replicating the flow behavior of photocurable liquid embolization by simulation is quite challenging. Since it is injected into aneurysm from catheter, its process is quite complicated and involves geometrical and topological changes like separation. Therefore, the simulation is required to perform not only flow analysis but also analyze interaction between blood flow and liquid for emolization and that between liquid for emolzaition and catheter with consideration of wettability.

To solve these complex issues, liquid embolization process was simplified. Specifically, to capture essential physics, viscous fluid imitating embolization liquid was injected into water instead of blood through a Teflon tube assumed to be a catheter. Since the embolization happened through topological changes, the moving particle semi-implicit (MPS) method was used in this study [3]. A stabilization method was investigated to reduce numerical instability caused by pressure oscillations [4-6]. In addition, we developed an efficient numerical method that considers the interfacial tension between water and highly viscous fluids of liquid embolization as well as the iterfacial tension with the wettability of the viscous fluid on the catheter.

There are mainly two types of interfacial models. The first one uses CFS model developed by Nomura et al. [7] , whcih considers a volume force. The other one uses the potential model developed by Kondo et al. [8] , which formalizes an intermolecular force. However, theses models are designed for force in single phase flow, and not for liquid-liquid two phase flow as in the present study. To cosider the influece of interaction between two-phase flows in the interfacial bounday, this study developed a method based on the potential model developed by Kondo et al., [8] combining it with the interfacial tension model developed by Ishii et al. [9].

Therefore, this paper aims to develop a new numeircal technique based on the MPS method to simulate the injection of embolization liquid into aneuryms by considering the interaction between blood and liquid embolization as well as between liquid embolization and catheter with wettability. In order to validate the prposed method, the simulation results were compared to experimental data, in which the problem was simplified as a viscous fluid injected into water through a cylidical Teflon tube [10].

2. NUMERICAL METHOD

In this study, the MPS method was used to simulate the injection of a highly viscous fluid into water through a cylindrical Teflon tube, mimicking the injection of embolization liquid into an aneurysm through the catheter. Since this is a complex multi-physic problem, the simulation not only models the flow of water and highly viscous fluid but also the interaction between them. In addition, the present study developed the interfacial tension model to account for interactions between water and the viscous fluid as well as one between the viscous fluid and cylindrical tube, while considering wettability effects.

2.1. Governing Equations

The present method was applied to an injection problem involving a highly visous fluid to replicate intravascular treatment. Therefore, flow simulations of incompressible Newtonian fluid are performed for water and viscous fluid. The governing equations consist of the continuity and Navier-Stokes equations as follows:

$$\frac{\partial u_i}{\partial x_i} = 0 \tag{1}$$

$$\frac{\partial u_i}{\partial t} + u_j \frac{\partial u_i}{\partial x_j} = \frac{1}{\rho}\frac{\partial P}{\partial x_i} + \frac{\mu}{\rho}\frac{\partial^2 u_i}{\partial {x_j}^2} + F_i \tag{2}$$

The external body force *F*i is given by

$$F_i = \rho g_i + F_i^{inter} \tag{3}$$

The method to determine force F_i^{inter} is described in the later section.

2.1. MPS Method

The MPS method is based on particle interactions, discretizing the partial differential equation using a weight function to calculate an averaged interparticle distance. This study uses the weight function developed by Tamai et al. [11], which is given by

$$w^{\overline{kl}} = \begin{cases} \left(\frac{r^{\overline{kl}}}{r_e^k} - 1\right)^2 & \left(r^{\overline{kl}} \le r_e^k\right) \\ 0 & \left(r_e^k \le r^{\overline{kl}}\right) \end{cases} \quad (4)$$

where $r_{\overline{kl}}$ is the distance between particle k and l, and the effective radius r_e^k is the radius of influence for the particle k. In this study, r_e^k is set as 2.1 times the initial interparticle distance in the gradient and the divergence models while it is set as 3.1 times in the interfacial tension models.

The MPS method requires the density of particles, which is obtained by

$$n_k = \sum_{k \ne l} w^{\overline{kl}} \quad (5)$$

The particle interaction model comprises the gradient, the divergence, and the Laplacian terms. Each term of particle k for an arbitrary scalar ϕ^k can be described in the following partial differential operators:

$$\frac{\partial \phi^k}{\partial x_i} = \frac{d}{n^0} \sum_{l \ne k} \frac{\phi^l - \phi^k}{\left(r^{\overline{kl}}\right)^2} \left(r_i^l - r_i^k\right) w^{\overline{kl}} \quad (6)$$

$$\frac{\partial \phi^k}{\partial x_j} = \frac{d}{n^0} \sum_{l \ne k} \frac{\left(\phi^l - \phi^k\right) \cdot \left(r_j^l - r_j^k\right)}{\left(r^{\overline{kl}}\right)^2} w^{\overline{kl}} \quad (7)$$

$$\frac{\partial^2 \phi^k}{\partial {x_j}^2} = \frac{2d}{\lambda n^0} \sum_{l \ne k} \left(\phi^l - \phi^k\right) w^{\overline{kl}} \quad (8)$$

where λ is defined as

$$\lambda = \frac{\sum_{k \ne l} \left(r^{\overline{kl}}\right)^2 w^{\overline{kl}}}{\sum_{k \ne l} w^{\overline{kl}}} \quad (9)$$

When the governing Eqs. (1) and (2) are solved, numerical instability may increase depending on arrangement of particles. Therefore, the high-order MPS is used to avoid numerical instability. In general, the pressure Poisson equation is solved to obtain pressure. We applied the high-order method to the Laplacian term of pressure in the Poisson equations using the method based on Tanaka et al. [4-6]. In addition, the high-order gradient model developed by Iribe et al. [5] was applied to the pressure gradient term.

2.2. Interfacial Tension Model

The two types of interface force considered in this study are the one between blood (water) and liquid for embolization (viscous fluid) and the other between catheter (cylindrical Teflon tube) and liquid for embolization (viscous fluid). Therefore, when the interfacial tension F_i^{inter} is calculated, it is necessary to consider two types of the interfacial tension models :1) the one between liquid and liquid and 2) the other between solid and liquid considering wettability.

In this study, the simulation is simplified as described in the previous section. Figure 1 describes the interfacial force between water and viscous fluid. A blue particle represents water, and a red represents viscous fluid.

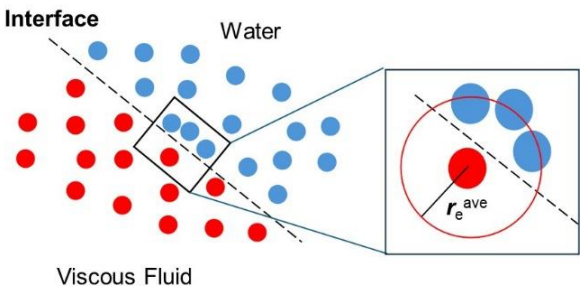

Figure 1. Schematic illustration of the interfacial force between blood and liquid for embolization

Let us consider force balance in the region within the radius of influence r_e^{ave} as shown in Fig.1 The interfacial tension model in the present study is based on the potential model [9]. The interfacial force between water and viscous fluid is given as follows:

$$(F^k)_i^{in\ b-e} = \frac{d\left(P^v - \overline{P^b}\right)}{h} n_i^{k-in} \quad (10)$$

$$P^b = \frac{1}{N'} \sum_{l \ne k}^{N'} \overline{P^b}\, w'^{\overline{kl}} \quad (11)$$

$$w'^{\overline{kl}} = \begin{cases} 1 & \left(r^{\overline{kl}} < r_e^{av}\right) \\ 0 & \left(r_e^{av} \le r^{\overline{kl}}\right) \end{cases} \quad (12)$$

Since this study deals with the contact between a viscous fluid and cylindrical tube, it is important to include the effects of wettability. In general, the contact angle of the embolization liquid on the catheter is used to characterize wettability. However, it is difficult to obtain the angle. Therefore, this study developed a method to replicate the wettability by combining adhesion and spread of liquid on the solid surface of the catheter.

First, the particles at the interface between viscous fluid and cylindrical tube need to be distinguished. The following normal vector is used to identify the particles on such interface:

$$n_i^{k-in} = \begin{cases} \dfrac{F_i^{k-l}}{|F_i^{k-l}|} & \left(|F_i^{k-l}| / |F_i^{k-l}|^{flat} \geq \eta \right) \\ 0 & \left(|F_i^{k-l}| / |F_i^{k-l}|^{flat} < \eta \right) \end{cases} \quad (13)$$

In this paper, η is set to be 0.2[9].

Next, the identification of particles at the interfacial surface is performed to distinguish the particles, where wettability needs to be considered. Figures 2 (a) and 2 (b) show schematic illustration of how particles are identified using the effective radius r_e^{st}. The red particles in Fig. 2 (b) are required to consider wettability while the black particles represent the wall of catheter, and the green ones are the reference particles.

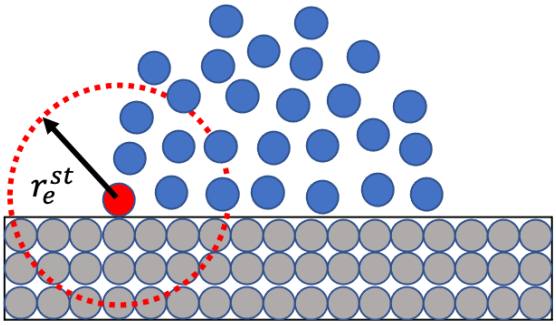

(a) Before identification

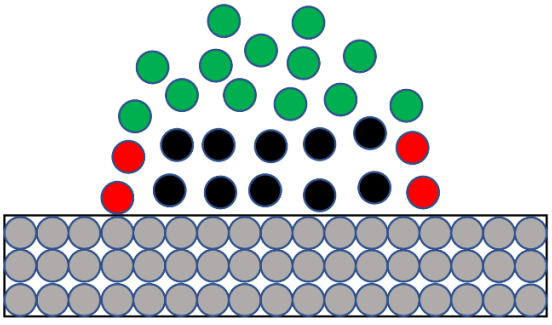

(b) After identification

Figure 2. schematic illustration of identification of particles subject to wettability

If the effects of adhesion in wettability are strong, the force balance can be expressed as follows:

$$F_i^{k-ad} = F_i^{k-st} + F_i^{k-l} + F_i^{k-sl} \quad (14)$$

On the other hand, when the effects of spreading out are stronger, the force balance becomes

$$F_i^{k-sp} = F_i^{k-st} - F_i^{k-l} - F_i^{k-sl} \quad (15)$$

Each term in Eqs. (14) and (15) can be obtained using the following poteital model:

$$F_i^{k-\alpha\alpha} = C^{\alpha\alpha} \sum_{l \neq k} f^{kl} \frac{r_i^l - r_i^k}{r^{\overline{kl}}} \quad (16)$$

The interfacial potential between viscous fluid and cylidical tube can be obtained by cobining F_i^{k-ad} and F_i^{k-sp}, which is given by

$$(F^k)_i^{in\ l-c} = F_i^{k-ad} - HF_i^{k-sp} \quad (17)$$

Therefore, the interfacial tension model in this paper, which comprises the interfacial tension model between liquid and liquid and the one between solid and liquid considering wettability, can be defined as follows:

$$F_i^{k-inter} = S^k \frac{d}{hA_0} \left[\left(\frac{1}{\frac{1}{N}\sum_{l \neq k} \sin \varphi^{\overline{kl}}} - 1 \right) \right] (F^k)_i^{in\ s-c} \quad (18)$$

where S^k is set as 1.0 for convex shape and -1 for concave shape.

3. RESULTS

The simulation results were compared to the experimental data to validate the present numerical method. The conditions for the experiment were applied for the numerical simulations. In this study, epoxy resin was used as embolization liquid and a Teflon tube was used as catheter in the experiment [10]. Table 1 summarizes the experiment and simulation conditions.

Table 1. experimental and Simulation conditions

Physical Properties		
Density [kg/m^3]	Water	1.00×10^3
	Embolization Liquid	1.18×10^3
Viscosity Coefficient [Pa・s]	Water	1.00×10^{-3}
	Embolization Liquid	7.42×10^{-3}
Inflow Velocity [m/sec]		8.50×10^{-3}
Gravitational acceleration [m/s^2]		9.8

The particle size is 1.00 × 10^{-1} mm in the MPS simulation in this study.

The experimental setup is shown in Fig. 3(a). The simulation was performed using the analysis model as described in Fig. 3(b) under the same conditions as the experiment.

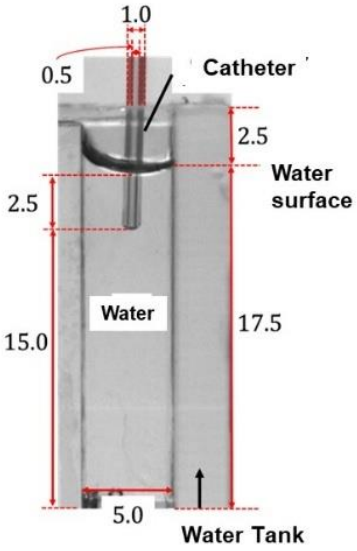

(a) Experimental model

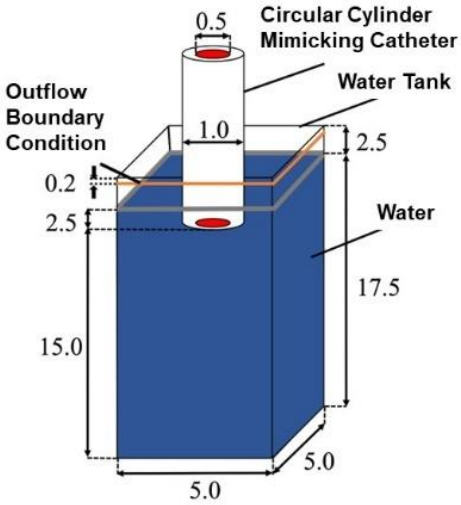

(c) Analysis model

Figure 3. Experimental and analysis models

In order to examine the effects of wettability, a comparison was performed between simulation results obtained without and with considering wettability. Figures. 4 (a) and 4 (b) present the results of comparison.

Although it was difficult to compare behavior of two simulations at the same instantaneous time, the results were sufficiently close for comparison. If wettability is ignored, embolization liquid tends to be elongated due to gravitational force. On the other hand, if wettability is considered, embolization liquid tends to spread out at the edge of circular tube against gravitational force, which makes embolization liquid less elongated, as described in Fig. 4(b).

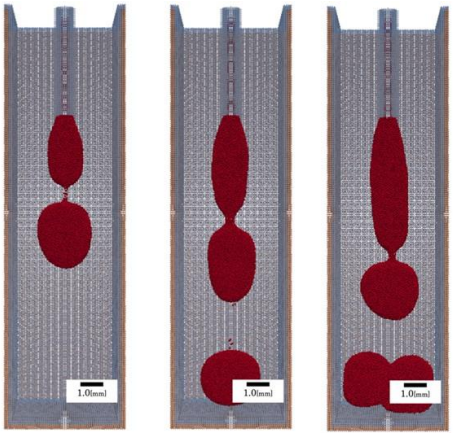

12.6 sec 22.9 sec 34.8 sec

(a) Without wettability

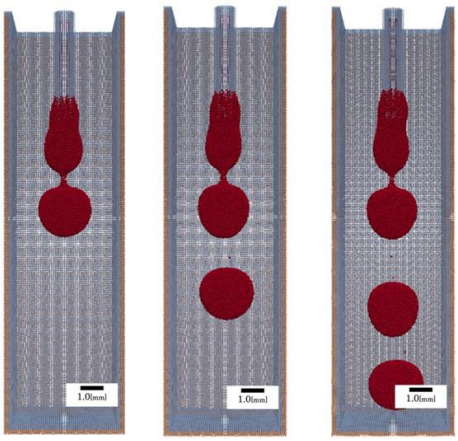

10.0 sec 15.6 sec 21.4 sec

(b) With wettability

Figure4. Comparison for investigation of wettability

Next, we compared the simulation results with experimental data. First, we compared the separation time, which is the time taken by a droplet to detach from the cylindrical Teflon tube. The experiment was performed six times while the simulation using the present method was performed three times. The average separation times for the experiments and simulation were 10.32 sec and 7.09 sec, respectively. The results of droplet volume for experiment and simulation were also compared. The average droplet volume was calculated over three trials for both the experimental measurements and simulations. The averaged droplet volume of simulation was 8.84× 10^{-9} m^3 while it was 1.8 × 10^{-8} m^3 in the experiment. Both droplet volume and separation time were smaller than those in the experiments. Hence, separation in simulations tends to occur faster than that in experiments. This is caused by the

underestimation of the interfacial tension compared to the gravitational force.

Let us compare the process of droplet formation at instantaneous times for both experiment and simulation. The images on the left in Figs. 5 (a) and 5(b) are the experimental measurement data while ones on the right are the simulation results. Both experimental data and simulation results are compared at the same instantaneous times 7.00 sec and 10.0 sec.

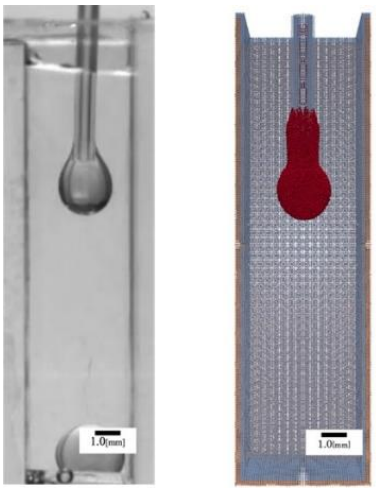

Experiment Simulation

(a) Instantaneous time at 7.00 sec

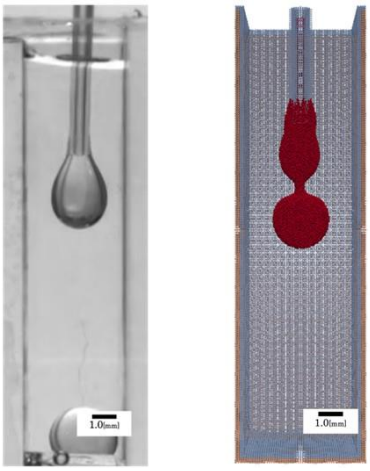

Experiment Simulation

(b) Instantaneous time at 10.00 sec

Figure 5. Comparison between experiment and simulation

As illustrated in Figs 5, the droplet tends to form faster than in the experiment, which leads to shorter droplet formation time and a smaller volume.

5. SUMMARY

In order to investigate flow characteristics of photocurable liquid embolization as a novel treatment for cerebral aneurysms, a simulation method has been developed based on the MPS method to solve topological changes. In addition, the interfacial tension model was developed. Since the treatment involves injecting embolization liquid into blood in the aneurysm, the interfacial tension needs to consider two types of interactions :1) the one between blood (water) and embolization liquid (viscous fluid) and 2) the other between embolization liquid (viscous fluid) and catheter (cylindrical Teflon tube) with wettability. The proposed interfacial tension model was incorporated into the MPS method and applied to the problem similar to the experimental setup, in which viscous fluid was injected into water through the cylindrical Teflon tube. The experiment and simulation were conducted under the same condtions and compared. The simulation results showed relatively good agreement with those of the experiment. However, the simulation results showed a tendency to underestimate the interfacial force compared to the experimental results. Therefore, volume and separation time in the simulation were smaller than those in the experiment.

ACKNOWLEDGEMENTS

This research was supported by JSPS KAKENHI under Grant Number JP22H00190If. relevant.

The authors express appreciation to Dr. Masamichi Oishi for providing experimental data.

REFERENCES

[1] Yamada, S., Koizumi, A., Iso, H., Wada, Y., Watanabe, Y., Date, C., Yamamoto, A., Kikuchi, S., Inaba, Y., Toyoshima, H., Kond, T., and Tamakoshi, A., 2003, “Risk Factors for Fatal Subarachnoid Hemorrhage”, *Stroke*, Vol. 34, No. 12, pp. 2781–2787.

[2] Molyneux, A. J., Cekirge, S., Saatci, I., and Ga’l, G.2004, “Cerebral Aneurysm Multicenter European Onyx (CAMEO) Trial: Results of a Prospective Observational Study in 20 European Centers”, *American Journal of Neuroradiology*, Vol. 25, No. 1, pp. I.

[3] Koshizuka, S. and Oka, Y., 1996“Moving-Particle Semi-Implicit Method for Fragmentationof Incompressible Fluid”, *Nuclear Science and Engineering*, Vol.123, No. 3, pp. 421–434.

[4] Tanaka, M. and Masunaga, T., 2010, “Stabilization and Smoothing of Pressure in MPS Method by Quasi-Compressibility”, *Journal of Computational Physics*, Vol. 229, No. 11, pp. 4279–4290.

[5] Irebe, Y., and Nakazawa, E., 2011, ‘’Improvement of Accuracy of a MPS Method with a New Gradient Calculation Model’’,

Journal of Japan Society of Civil Engineering, Vol.67, pp.36-48(in Japanese).

[6] Monaghan, J. J., 2000, "SPH without A Tensile Instability", *Journal of Computational, Physics*, Vol. 159, No. 2, pp. 290–311.

[7] Nomura, K., Koshizuka, S., Oka, Y., and Obata, H., 2001., "Numerical Analysis ofDroplet Breakup Behavior using Particle Method", *Journal of Nuclear Science and Technology*, Vol. 38, No. 12, pp. 1057–1064,

[8] Kondo M., Koshizuka, S., Takimoto, M., 2017,' Surface Tension Model using Inter-Particle Potential Force in Moving Particle Semi-Implicit Method', *Transactions of JSCES*, Paper No. 20070021.

[9] Ishii E. and Sugii T., 2012, ''Development of Surface Tension Model for a Particle Method'', *Transaction of the Japan Society of Mechanical Engineers*, Vol.78, pp. 1710-1725.

[10] Natsume, T., Oishi, M., Oshima, M., and Mukai, N., 2021, "Droplet Formulation Method for Viscous Fluid Injection Considering the Effect of Liquid-Liquid Two-Phase Flow", ITE Transactions on Media Technology and Applications, Vol. 9, No. 1, pp. 33–41.

[11] Tamai T. and S. Koshizuka, 2014, "Least Squares Moving Particle Semi-Implicit Method: An Arbitrary High Order Accurate Meshfree Lagrangian Approach for Incompressible Flow with Free Surfaces", *Computational Particle Mechanics*, Vol. 1, No. 3, pp. 277‑305.

Conference on Modelling Fluid Flow (CMFF'25)
The 19th International Conference on Fluid Flow Technologies
Budapest, Hungary, August 26 -August 29, 2025

DEVELOPMENT OF THE TURBULENT SWIRLING FLOW VELOCITY PROFILES IN THE AXIAL FAN JET

Novica Z. JANKOVIĆ[1], Đorđe S. ČANTRAK[2], Dejan B. ILIĆ[3], Miloš S. NEDELJKOVIĆ[4]

[1]Corresponding Author. Department of Hydraulic Machinery and Energy Systems, University of Belgrade - Faculty of Mechanical Engineering. Kraljice Marije 16, 11120 Belgrade, Serbia. Tel.: +38 1 11 3302 363, E-mail: njankovic@mas.bg.ac.rs
[2]Corresponding Author. Department of Hydraulic Machinery and Energy Systems, University of Belgrade - Faculty of Mechanical Engineering. Kraljice Marije 16, 11120 Belgrade, Serbia. Tel.: +38 1 11 3302 226, E-mail: djcantrak@mas.bg.ac.rs
[3]Corresponding Author. Department of Hydraulic Machinery and Energy Systems, University of Belgrade - Faculty of Mechanical Engineering. Kraljice Marije 16, 11120 Belgrade, Serbia. Tel.: +38 1 11 3302 226, E-mail: dilic@mas.bg.ac.rs
[4]Department of Hydraulic Machinery and Energy Systems, University of Belgrade - Faculty of Mechanical Engineering. Kraljice Marije 16, 11120 Belgrade, Serbia. Tel.: +38 1 11 3302 226, E-mail: mnedeljkovic@mas.bg.ac.rs

ABSTRACT

Turbulent swirling flow in the jet generated by the axial fan impeller with twisted blades is studied in this paper. Three velocity components are obtained by using three-component laser Doppler velocimetry system in ten measured sections. Downstream flow development and continual deformation of all velocity profiles with gradients in radial and axial directions are obvious. It is shown that circumferential velocity significantly deforms profile of the axial velocity which gets M-shape with weak reverse flow region in the central flow zone in the first two measuring sections. This phenomenon is still not well explained, especially from the mathematical point of view.

Derivatives of all three velocity components in radial direction are calculated for velocity field analysis. Axial velocity profile in the downstream sections becomes more uniform, with the strict hierarchy of the positive gradient of the axial velocity in axial direction in domain $0 < r/R < 0.5$. Character of distribution of the axial velocity out of this region shows jet expansion. Maximum of the axial velocity doesn't belong to the jet core. In the jet axis vicinity profile of the axial velocity is concave even in the last measuring section. It means that the transformation process is not completed.

Keywords: axial fan, jet, swirling flow, three-component LDV, turbulence

NOMENCLATURE

C	$[m/s]$	total velocity
D	$[m]$	inner pipe diameter
Q	$[m^3/s]$	volumetric flow rate
R	$[m]$	inner pipe radius
U	$[m/s]$	mean axial velocity
U_m	$[m/s]$	averaged velocity by area
V	$[m/s]$	mean radial velocity
W	$[m/s]$	mean circumferential velocity
r	$[m]$	radial coordinate
n	$[rpm]$	fan shaft rotation speed
x	$[m]$	axial coordinate along a jet axis
Γ	$[m^2/s]$	average circulation
Ω	[-]	swirl flow parameter
ν	$[m^2/s]$	kinematic viscosity
φ	[°]	coordinate of the polar cylindrical coordinate system (x, r, φ)

1. INTRODUCTION

In this paper is presented experimental research of the turbulent swirling flow in jet generated with the axial fan impeller with twisted blades. Axial fan is in-built in the installation following the setup category A for fans in the international standard ISO 5801 [1]. This installation means free inlet and free outlet.

Experimental research is performed by use of the three-component laser Doppler velocimetry (LDV) system.

A significant number of papers analyze free swirling jets, but only few of them investigate swirling jets generated by the axial fan impeller. A good literature overview of the turbulent swirling flow jet experimental research is presented in [2, 3]. In paper [4] is shown that the entrainment rate and angle of spread for the swirling jet was nearly twice that of the non-swirling free jet.

Study of jets with different initial swirl distributions is presented in [5]. In this case miniature five-hole probe is used for three-

component velocity measurements. Experimental study on the effects of swirl on the development of an axisymmetric turbulent mixing layer is presented in [6]. Single component LDV measurements of the swirling flow generated by the guide vanes placed at the nozzle exit in the horizontal plane are presented in [7].

Here studied turbulent swirling flow in jet is three-dimensional, inhomogeneous and anisotropic. Generated velocity field is very complex, characterized by inhomogeneity and distinct gradients, especially in the radial direction.

2. EXPERIMENTAL TEST RIG

Swirling flow generator is an axial fan impeller with nine twisted blades with variable angle of attack, designed after the law rW = const. Adjusted angle at the axial fan impeller outlet diameter, which is 0.399 *m*, is 30°. The dimensionless hub ratio, which represents the ratio of the hub and outer diameter is 0.5. Inner pipe, i.e. fan casing (Fig. 1, pos. 3), diameter is D = 0.4 *m*. Experimental test rig, with marked flow direction, is presented in Figure 1, where 1- DC motor is regulated with fully automated thyristor bridge with error up to ±0.5 *rpm*, 2- profiled bell mouth inlet and 3- axial fan impeller with casing.

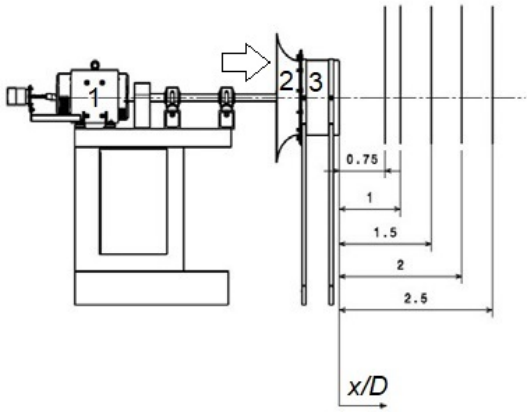

Figure 1.Experimental test rig with marked measuring sections

Three-component LDV measurements have been performed in ten measurement sections along vertical directions at a 10 mm distance each. Measuring sections along the axial fan rotating axis are x = 300, 400, 600, 800, 1000, 1200, 1400, 1600, 1800 and 2000 *mm*, i.e. in the range x/D = 0.75D to 5D, with the step 0.5D, except for the first step 0.25D. In Fig. 1 are presented first five measuring sections.

Measurements have been performed for the axial fan impeller rotation speed n = 1500 *rpm*. Flow seeding is provided by an Antari Z3000 fog machine loaded with the Eurolite Smoke Fluid. It was naturally sucked in the test rig by the axial fan.

Three-component LDV system, by TSI, was used in these experiments. Continuum Ar-Ion laser of 5 *W*, by Coherent is applied. Two probes TSI TR60 with beam expanders XPD60-750 were used to form measurement volume. The TSI Flow Sizer software is used for acquisition and preliminary data analysis. The measurement focus with attached optics was on 757.7 *mm*. Laser wavelengths were 514.5 *nm*, 488 *nm* and 476.5 *nm*. The measurement volume diameter was app. 70 μm, while measurement volume length was app. 280 μm. Both LDV probes work in back scatter mode. The velocity was measured with uncertainty lower than 0.1%. [3]. Uncertainty analysis of the used 3D LDV system is thoroughly analyzed and presented in [2, 8].

3. EXPERIMENTAL RESULTS AND DISCUSSIONS

Experimentally obtained distributions of the total velocities along the jet axis are presented in Figure 2. The flow development is observed. Namely, continuous deformation of the velocity profile with gradients in the axial and radial direction occurs. It is obvious that even 5D downstream turbulent swirling flow still exists.

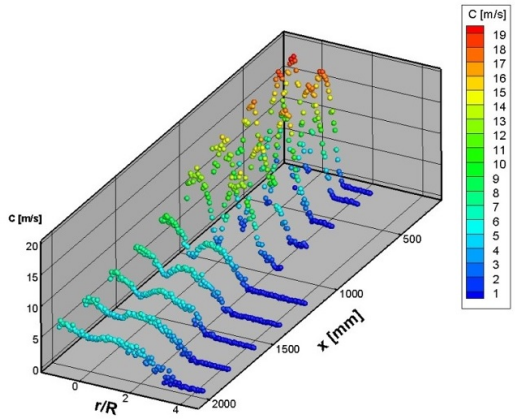

Figure 2.Total velocity distributions $C = C(r,x)$

Circumferential velocity (W) significantly deforms profile of the axial velocity (U). Radial velocity (V) development and distribution is also correlated with the presence and distribution of the circumferential velocity.

Radial-axial distributions of all three velocity components U, V and W in the turbulent swirling jet are presented in the following Figures 3 to 5, where φ = 90° denotes upper half of the measuring section, and, consequently, φ = 270° lower half. They are obtained on the basis of the Reynolds averaging of the measured instantaneous velocity fields. It is obvious that circumferential velocity significantly

deforms profile of the axial velocity which gains M-shape, with weakly formed reverse, i.e. recirculating flow, in the first two measuring sections, i.e. I and II. The condition for the reverse flow is fulfilled, because swirl number $\Omega > 0.4$ [9]. However, this phenomenon is still not well explained, especially from the mathematical point of view.

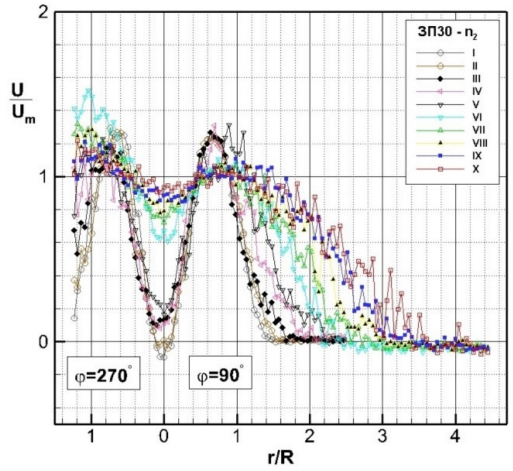

Figure 3.Experimental radial-axial distribution of the axial velocity in the turbulent swirling jet

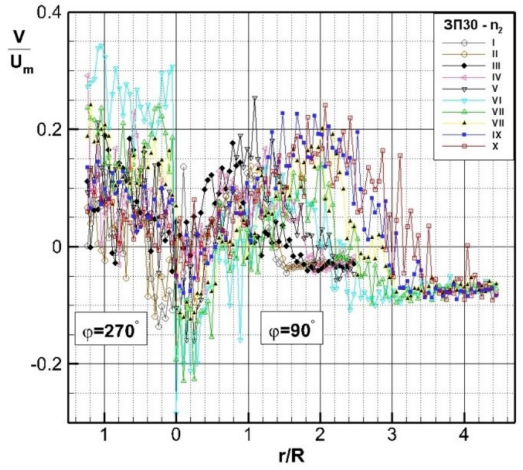

Figure 4.Experimental radial-axial distribution of the radial velocity in the turbulent swirling jet

Swirl number is calculated as follows:

$$\Omega = Q/(R\Gamma), \qquad (1)$$

while average circulation is determined in the following way:

$$\Gamma = 4\pi^2 R^3 \int_0^1 k^2 UW dk / Q, \qquad (2)$$

where $k = r/R$.

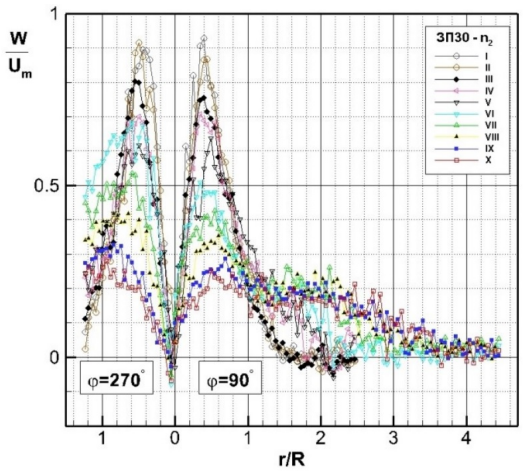

Figure 5.Experimental radial-axial distribution of the circumferential velocity in the turbulent swirling jet

In downstream measuring sections profile of the axial velocity becomes more uniform, with a strict hierarchy of the gradient $\partial_x U > 0$ in a domain $0 < r/R < 0.5$ (Fig. 3). Character of the distribution of the axial velocity, outside this region, points out the expansion of the jet in the radial direction. Maxima values (U_{max}) don't belong to the jet core. That is why the axial velocity profile is concave in the jet axis vicinity, even in the last measuring section X (Fig. 3). Physically, it means that development process is still not finalized, that swirl is still present (Fig. 5) and that the transformation in the axial jet was not possible in the studied case.

Development and transformation of the radial velocity V are also related to the presence and distribution of the circumferential velocity W. Radial velocity profiles in the turbulent swirling jet are very characteristic (Fig. 4). This applies to both the intensity of the radial velocity and its sign. Characteristic domains are the ones where it increases ($\partial_r V > 0$) and decreases ($\partial_r V < 0$), as well as in the points where it changes the sign. It is important for convection and the occurrence of turbulent exchange to analyze the intensity and change in sign of the radial velocity. This is visible in more details in measuring sections: I, III and V (Figs. 6.a-c), where all three velocity components are presented. It is obvious that swirling flow changes character of the radial movement, as well as intensities and signs of the derivative $\partial_r V$. This will be discussed in the case of the measuring section III.

In Figure 6.b are presented distributions of all three velocity components $U_i = U$, V and W in the measuring section III, where $x = 600$ *mm*. Average velocity is $U_m = 12.57$ *m/s*, while Reynolds number is $Re = 358951$ and average circulation, calculated after the Eq. (2), is $\Gamma = 4.93$ m^2/s.

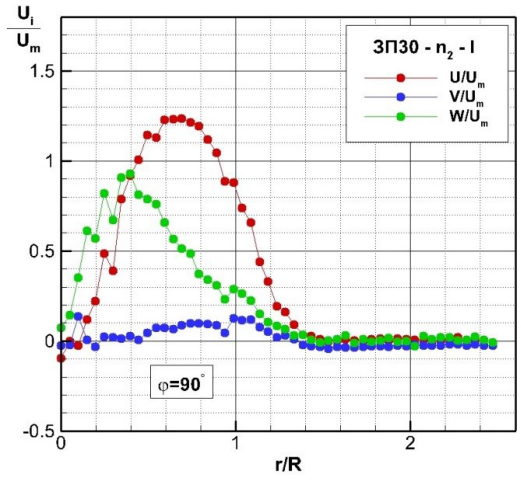

Figure 6.a All three velocities ($U_i = U$, V and W) distributions in the section I

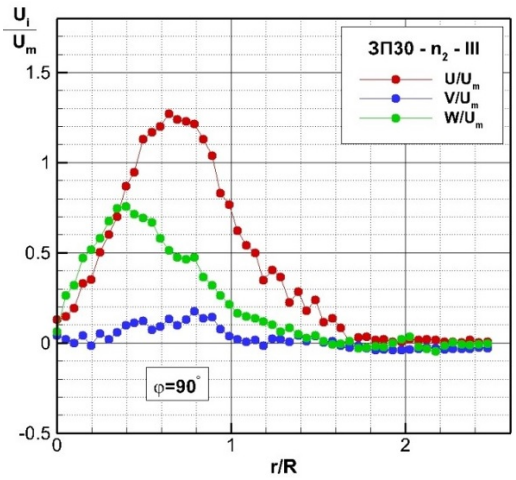

Figure 6.b All three velocities ($U_i = U$, V and W) distributions in the section III

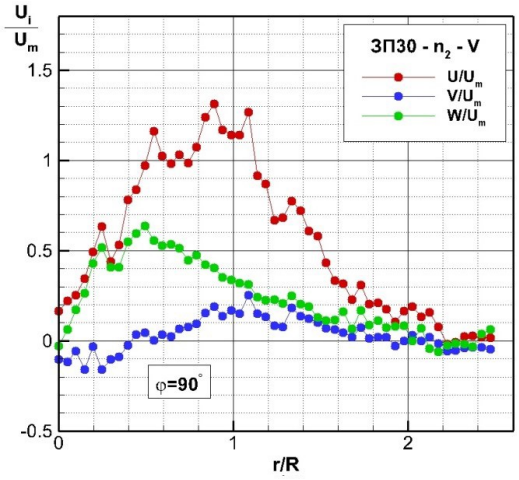

Figure 6.c All three velocities ($U_i = U$, V and W) distributions in the section V

In the vicinity of the axis gradient of the radila velocity is negative ($\partial_r V < 0$), while in the domain $0.3 < r/R < 0.8$ this gradient is positive ($\partial_r V > 0$). Further increase of the radial coordinate, up to $r/R = 1.2$, results, again, with the negative gradient of the radial velocity ($\partial_r V < 0$). In the region with higher radial coordinate, profile of the radial velocity becomes approximately uniform, so radial gradients $\partial_r V$ have lower values, and the change in its sign, when approaching the jet boundary occurs, with the predominant negative values.

Experiments show that for characteristic points where maxima axial and circumferential velocities are reached, in all measuring sections, stands: $r_{W\text{-}max} < r_{U\text{-}max}$. With the increase of the axial coordinate x, circumferential velocity W, in region $0 < r/R < 1$, decreases, so that W-profiles, together with its W_{max} are hierarchically distributed from the first (I) up to the last measuring section (X) (Fig. 5). This is not a case outside this region, because profiles intermix and don't follow hierarchy. This leads to more uniform distributions of the circumferential velocity in the downstream measuring sections (Figs. 5 and 6.a-c).

The presented empirical profiles of all three velocities show that in addition to the global maxima (within the respective sections), for example for section III (Fig. 6.b), U_{max} is reached for $r/R \approx 0.65$ and W_{max} for $r/R \approx 0.4$, there is also a significant number of local maxima for all three velocity components.

The complexity of the structure of the averaged velocity field becomes even more obvious when to the previous elements is added the presence of heterogeneous changes of the $\partial_r U_i$ for all three components in the radial direction of the turbulent swirling jet.

Changes of the average velocity fields in radial direction are calculated on the basis of the experimental results presented in Fig. 6.b and presented in Figures 7.a-c. These diagrams have information on the speed of the change of velocity components U_i in radial direction, positions of their maxima, local maxima and minima, as well as correlation of the averaged and fluctuating velocity field. These diagrams could have an important role in analysis of the turbulent swirling jet.

It could be noted in Fig. 7.a that the first zero value ($\partial_r U = 0$) determines value of the maximum velocity $U/U_m(r/R \approx 0.65) = (U/U_m)_{\max}$, while diagram on Fig. 7.c provides distribution of the circumferential velocity $W/U_m(r/R \approx 0.4) = (W/U_m)_{\max}$.

Changes of the averaged radial velocity in the radial direction are very complex (Fig. 7.b). It is interesting that the intensity of the change of the radial velocity in the measuring section III is significantly higher than the change of the axial velocity, but lower than the circumferential velocity.

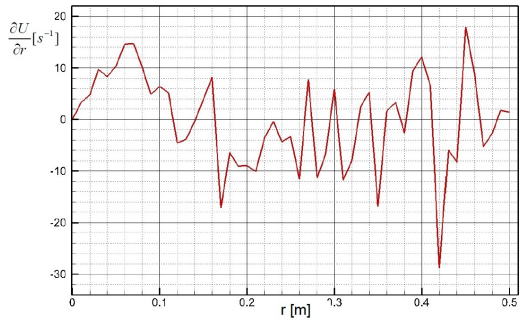

Figure 7.a Change of the average axial velocity in radial direction in the measuring section III

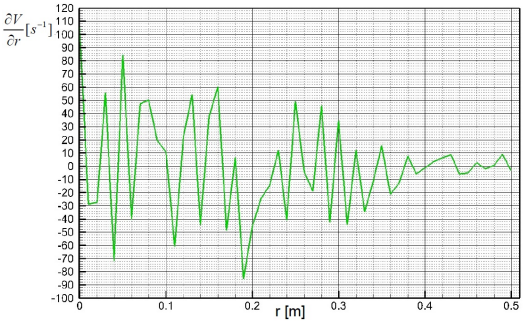

Figure 7.b Change of the average radial velocity in radial direction in the measuring section III

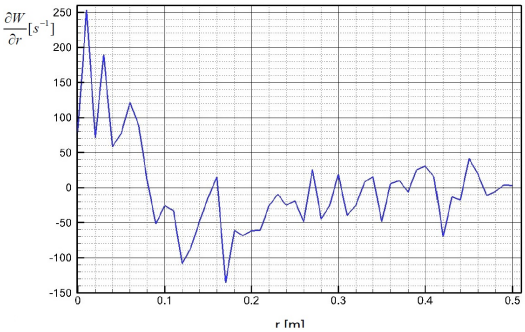

Figure 7.c Change of the average circumferential velocity in radial direction in the measuring section III

This is quantified and presented in the following equation.

$$-20<\left(\partial_r U\right)_{\max}<18,\ -75<\left(\partial_r V\right)_{\max}<85,$$
$$-140<\left(\partial_r W\right)_{\max}<240. \qquad (3)$$

Value intervals are strongly changeable.

Presented distributions in Figs. 7.a-c are of great importance for Reynolds stresses discussion. It could be theoretically discussed interdependence of the $-\overline{uv}\partial_r V$ which determines production of the important Reynolds shear stress $-\rho\overline{uv}$. In the same manner mathematical therm $-\overline{v^2}\partial_r V$ participates in the generation of the normal turbulent stress $-\rho\overline{v^2}$.

It could be, also, emphasized the important influence of the distribution of the circumferential velocity on the structure of turbulence in the swirling jet. The influence of the mathematical therm $-\overline{vw}\partial_r W$ on the production of the Reynolds normal stress $-\rho\overline{w^2}$, as well as the significance of the relation $-\overline{uv}\partial_r W$ on the generation of the turbulent shear stress $-\rho\overline{uw}$ stress could be further discussed.

4. CONCLUSIONS

Conclusions, based on the previously presented experimental results and discussions, could be summarized as follows:

- Measurements have confirmed the assumption of the statistical axisymmetry of the velocity field (Figs. 3-5), what is important from both physical and mathematical point of view.
- Reverse flow occurs in the measuring sections I and II.
- Condition for the reverse flow region is fulfilled, because the swirl number, defined as the $Q/R\Gamma$, where Q is volume flow rate, R is radius and Γ is circulation is higher than 0.4 when the reverse flow region, after [9] occurs.
- In downstream sections axial velocity becomes more uniform, but in the studied case transformation in the axial jet is not completed.
- Development and transformation of the radial velocity profiles are also correlated with the presence and distribution of the circumferential velocity.
- Intensity and change of the sign of the radial velocity is important for the convection and turbulence exchange.
- Position of the circumferential velocity maximum is correlated to the vortex core diameter, as well as with the vorticity distributions.
- Presented results show that $r_{Wmax} < r_{Umax}$ in all measuring sections.
- With increase of the axial coordinate (x) velocity W in the region $0 < r/R < 1$ decreases, so the circumferential velocity profiles are hierarchically distributed downstream from the section I to X. Outside this region this is not a case anymore, and W velocity profiles are mixed.
- The complexity of the structure of the averaged velocity field becomes even more obvious when to the previous elements is

added the presence of heterogeneous changes of the $\partial_r U_i$ for all three components in the radial direction of the turbulent swirling jet.

- It is shown that the changes of the averaged radial velocity in the radial direction are very complex (Fig. 7.b). It is interesting that the intensity of the change of the radial velocity in the measuring section III is significantly higher than the change of the axial velocity, but lower than the intensity of the change of the circumferential velocity.
- All these discussions lead to better understanding of the production of the Reynolds stresses in the generated turbulent swirling jet by the axial fan impeller.

ACKNOWLEDGEMENTS

The results presented in this paper are the result of the research supported by the Ministry of Science, Technological Development and Innovation of the Republic of Serbia under the Agreement on financing the scientific research work of teaching staff at accredited higher education institutions in 2025, no. 451-03-137/2025-03/200105. The work on this paper is finalized during the student demonstrations in Serbia, which started in November 2024. and are still in progress and is dedicated to them who stand for the justice in our society.

REFERENCES

[1] ISO 5801:2017 "Fans – Performance Testing Using Standardized Airways". (https://www.iso.org/standard/56517.html)

[2] Janković, N. Z., 2020, "Experimental and Theoretical Research of the Structure of Turbulent Swirl Flow in Axial Fan Jet", (in Serbian), *Doctoral dissertation, Hydraulic Machinery and Energy Systems Department, Faculty of Mechanical Engineering, University of Belgrade*.

[3] Janković, N. Z., 2017, "Investigation of the Free Turbulent Swirl Jet behind the Axial Fan", *Thermal Science*, Vol. 21, Suppl. 3, pp. S771-S782.

[4] Pratte, B. D., and Keffer, J. F., 1972, "The Swirling Turbulent Jet", *J. of Basic Eng.*, 94, 4, pp. 739-747.

[5] Gilchrist, R. T., and Naughton, J. W., 2005, "Experimental Study of Incompressible Jets with Different Initial Swirl Distributions: Mean Results", *AIAA Journal*, 43, 4, pp. 741-751.

[6] Mehta, R. D., Wood, D. H., and Clausen, P. D, 1991, "Some Effects of Swirl on Turbulent Mixing Layer Development", *Physics of Fluids*, 3, 11, pp. 2716-2724.

[7] Sislian, J. P., and Cusworth, R. A., 1986, "Measurements of Mean Velocity and Turbulent Intensities in a Free Isothermal Swirling Jet", *AIAA Journal*, 24, 2, pp. 303-309.

[8] Ilić, J.T., Janković, N.Z., Ristić, S.S., and Čantrak, Đ.S., 2019, "Uncertainty Analysis of 3D LDA System", Proc., The 7th International Congress of the Serbian Society of Mechanics, Minisymposium M3: Turbulence, Sremski Karlovci, Serbia, Proceedings, paper No. M3j, pp. 189.

[9] Kitoh, O., 1991, "Experimental Study of Turbulent Swirling Flow in a Straight Pipe", *J. Fluid Mech.*, Vol. 225, pp. 445-479.

Conference on Modelling Fluid Flow (CMFF'25)
The 19th International Conference on Fluid Flow Technologies
Budapest, Hungary, August 26 - August 29, 2025

EVALUATING THE PROBABILITY OF INFECTION IN A UK HOSPICE THROUGH A CFD DRIVEN METRIC

Mohammad ELSARRAJ[1], Yasser LARIMI[2], Amir KESHMIRI[3]

[1] Corresponding Author: Department of Fluids & Environment, School of Engineering, The University of Manchester, Manchester, M13 9PL, UK. E-mail: mohammad.elsarraj@manchester.ac.uk
[2] Department of Fluids & Environment, School of Engineering, The University of Manchester, Manchester, M13 9PL, UK.
[3] Department of Fluids & Environment, School of Engineering, The University of Manchester, Manchester, M13 9PL, UK.

ABSTRACT

Hospices house vulnerable patients with severely weakened immune systems, making control of airborne virus transmission critical. This study introduces a Probability of Infection (POI) metric, quantified through Computational Fluid Dynamics (CFD) using a transient Eulerian-Lagrangian (E-L) model to simulate airborne particle transport and exposure. Simulations include exhaled CO_2 and infectious aerosols to explore spatial correlations, revealing that while CO_2 and POI distributions exhibit similarities, they diverge due to differences in diffusion behaviour. Across 13 scenarios, POI heatmaps identify high-risk zones influenced by airflow patterns and infector position, not solely by CO_2 levels. The findings highlight the limitations of relying on CO_2 concentration as a proxy for infection risk and demonstrate the value of direct aerosol modelling in assessing ventilation effectiveness. This approach offers a robust basis for improving infection risk evaluation in sensitive indoor healthcare environments.

Keywords: Finite Volume Method, Indoor Air Quality, Indoor Virus Transmission, CFD, Fluid Dynamics

Nomenclature

C_d	Drag coefficient
P	Pressure [pa]
Pr	Prandtl number
Re_d	Reynolds number of particle
T	Mean temperature [K]
U_i	Mean velocity component in Cartesian

Greek Symbols

μ	Dynamic viscosity [Pa s]
ρ	Density [kg/m^3]

Acronyms

E-L	Eulerian-Lagrangian model
IR	Infection risk
POI	Probability of infection (%)

Additional symbols and acronyms are defined in the text.

1. INTRODUCTION

The risk of infectious particle transport via ventilation systems has gained significant attention, particularly during the COVID-19 pandemic [1–4]. Virus transmission is especially efficient in enclosed, crowded indoor environments such as offices, restaurants, and public transport [5]. Ventilation plays a crucial role in mitigating airborne transmission by removing indoor pollutants and replacing contaminated air. Consequently, organisations such as the Chartered Institution of Building Services Engineers (CIBSE), the American Society of Heating, Refrigerating and Air-Conditioning Engineers (ASHRAE) and the Federation of European Heating, Ventilation and Air Conditioning Associations (REHVA) have issued guidelines advocating increased outdoor air exchange to reduce airborne pathogen exposure [6–8]. However, the optimal ventilation rate required to mitigate airborne contagion remains unclear [9]. Moreover, a trade-off exists: while ventilation dilutes contaminants, it may also contribute to aerosol dispersion, potentially increasing infection risk [10]. This study seeks to establish an optimal balance by refining ventilation strategies for infection risk mitigation.

Traditionally, infection risk has been assessed through airborne pollutant concentration metrics. Several studies have utilised computational fluid dynamics (CFD) simulations to evaluate ventilation strategies and their impact on airborne particle dispersion [9,11,12]. Research has explored natural

and mechanical ventilation designs, air distribution patterns, and physical barriers to control droplet transmission in settings such as classrooms, office spaces, and aircraft cabins[13,14]. However, these studies primarily focus on particle presence and concentration, often overlooking critical transmission parameters such as exposure duration, viral load, and individual susceptibility.

To address these limitations, this study introduces a novel infection risk probability metric based on a transient Eulerian-Lagrangian CFD approach. The metric quantifies long-range airborne transmission by incorporating spatial-temporal particle concentration, exposure time, and clinical viral load data. This allows for a more realistic assessment of cumulative viral exposure over time, which is essential for understanding transmission risk in shared indoor environments. Given that human respiratory activities (e.g., breathing, speaking, coughing) generate droplets ranging from 0.01 to 1000 μm [15], understanding the behaviour of these aerosols in ventilated spaces is essential.

The CFD model is applied to a hospice communal space and captures airflow variations driven by fluctuating wind pressures on operable windows. By analysing the distribution of infectious aerosols and comparing it to exhaled CO_2 concentrations, the study identifies key differences in dispersion behaviour and highlights the importance of particle-based infection modelling for effective ventilation assessment. The communal space is demonstrated by Figure 1.

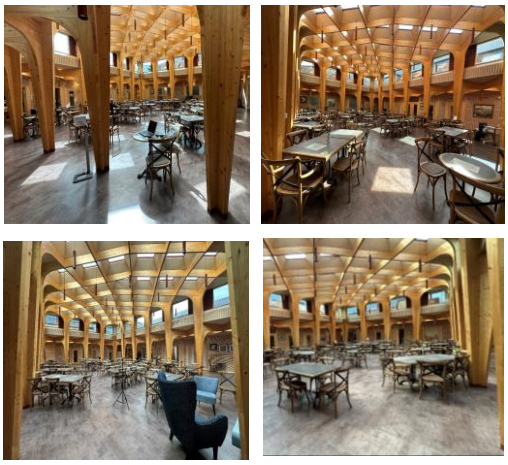

Figure 1. The communal area of the UK Hospice.

2. METHODOLOGY

2.1 The Eulerian-Lagrangian CFD Model

2.1.1 Background

Accurately evaluating airborne infection risk, particularly for COVID-19, requires modelling viral emission, transport, and inhaled exposure over time. Infections may arise from prolonged exposure to low concentrations of virus-laden aerosols, reinforcing the importance of spatial and temporal resolution in dose estimation. The Lagrangian approach is well-established in indoor air quality research for tracking aerosolised particles. It resolves forces such as drag, gravity, and turbulent dispersion, allowing accurate characterisation of airborne transport and deposition patterns and quantifying viral dose [13,14].

This study employs the **Eulerian-Lagrangian CFD approach** based on Crowe et al. [16], modelling air (continuous phase) via Eulerian equations while tracking particles (dispersed phase) with a transient Lagrangian method. The model simulates infectious particle transport during speech, outputting particle volume, count, and fraction per computational cell. This data, combined with clinical inputs, enables spatial-temporal infection probability estimation.

2.1.2 The Eulerian Model

As the governing equations for the mass, momentum, and energy equations, Navier-Stokes is used to model the unsteady incompressible flow field using an Eulerian approach:

$$\frac{\partial \rho}{\partial t} + \frac{\partial (\rho U_i)}{\partial x_i} = 0 \tag{1}$$

$$\frac{\partial (\rho U_i)}{\partial t} + \frac{\partial}{\partial x_j}\left(\rho U_i U_j\right) = -\frac{\partial P}{\partial x_i} + \frac{\partial}{\partial x_j}\left(\mu \frac{\partial U_i}{\partial x_j} - \rho \overline{u_i u_j}\right) \tag{2}$$

$$\frac{\partial (\rho T)}{\partial t} + \frac{\partial}{\partial x_j}\left(\rho U_j T\right) = \frac{\partial}{\partial x_j}\left(\frac{\mu}{Pr}\frac{\partial T}{\partial x_j} - \rho \overline{u_j \theta}\right) \tag{3}$$

where, ρ is the density and $\overline{u_j \theta}$ is the turbulent heat flux vector, respectively.

The present authors have previously shown the importance of the choice of the turbulence model on the prediction of fluid flow and heat transfer [17–19]. Consequently, the present authors have also investigated six different types of eddy viscosity models to determine the most feasible in predicting indoor air flow [20]. The φ–f model was chosen for its stability and near-wall performance and the same

model will be used in this present study. Since this a low-Reynolds-number turbulence model, the grids were adjusted to be very fine along the wall (the wall-adjacent cell typically extends only to $y^+ \leq 1$), in order for the turbulent boundary layers to be fully resolved.

2.1.3 The Lagrangian Model

The momentum equation for particles is derived from the balance between inertial forces and external forces applied to the particle:

$$m_p \frac{dv_p}{dt} = \frac{m_p(v_c - v_p)}{\tau_r} + m_p g + F \qquad (4)$$

Where, for a spherical particle with a diameter of d_p immersed in continuous air, g is the gravitational force exerted on the particle, F represents additional forces acting on the particle surface, specifically the drag force (C_d), virtual mass force, and pressure gradient **force** all of which were modelled using the standard Lagrangian particle tracking approach implemented in the CFD solver. v_c is the velocity of the continuous phase, v_p is the particle velocity and τ_r is the momentum relaxation time scale computed as:

$$\tau_r = \frac{2m_p}{\rho_c A_p C_d (v_c - v_p)} \qquad (5)$$

where, ρ_c is the density of the continuous phase and A_p is the projected area of the particle. The Drag force (C_d) is modelled through the Schiller-Naumann Correlation [21], which is a function of the particle Reynolds number:

$$Re_d = \frac{\rho_c |v_c - v_p| D_p}{\mu_c} \qquad (6)$$

where, μ_c is the dynamic viscosity of the continuous phase and D_p is the diameter of the particle.

2.1 Infection Risk Metric

2.1.1 The Wells-Riley Model

The Wells–Riley model estimates airborne infection probability (POI) as a function of inhaled quanta (n), defined as the dose causing infection in 63% of susceptible individuals [22,23]. Assuming a uniform aerosol concentration:

$$POI = 1 - e^{-n} = 1 - e^{-(q_c \times IR \times t_e)} \qquad (7)$$

where, q_c is the quanta concentration [quanta/m³], IR is the inhalation rate, and t_e is the exposure time. However, the model assumes well-mixed, steady-state conditions, which rarely hold in indoor spaces with complex airflow and localised sources. This limitation motivates the need for spatially and temporally resolved approaches, as detailed in the following subsection.

2.1.2 Virion Concentration and POI at Each Cell

This study employs a Probability of Infection (POI) metric, incorporating particle count, exposure duration, and clinical data. Using CFD and a time-dependent Eulerian-Lagrangian (E-L) model, the emission and distribution of infectious airborne particles (quanta) are computed.

Initially, the quanta concentration at each computational cell is determined using Eq. (7), where the sum of the particle-to-air volume fraction ($\alpha_{p,cell}$) and the initial hydrated particle volume ($Vol_{i,cell}$) is normalised by the evaporated desiccated volume and multiplied by the viral load c_v, taken as 2.35×10^9 [quanta/mL] [24]. This number is multiplied by 10^6 to convert to quanta/m^3.

The total inhaled quanta at each cell, (D_{cell}), is then obtained by integrating the quanta concentration over time, as expressed in Eq. (8). This value is subsequently substituted into the Wells-Riley equation to compute the Probability of Infection (POI) at each cell, using Eq. (9). The resulting POI values generate a spatio-temporal infection risk (IR) map, illustrating areas of elevated exposure risk.

$$q_{c,cell} = c_v \frac{\sum_{j=0}^{t} (\alpha_{p,cell_j} \, Vol_{pi,cell_j})}{Vol_p} \times 10^6 \qquad (7)$$

$$D_{cell} = IR \int_0^T q_{c,cell} \, dt \quad [quanta] \qquad (8)$$

$$POI = \left(1 - e^{(-D_{cell})}\right) \times 100 \, [\%] \qquad (9)$$

2.1.3 Infection Risk Metric and Particle Assumptions

A time-dependent Eulerian–Lagrangian CFD model was used to compute particle transport and quanta concentration at each cell. Concentration was calculated using Eq. (7), combining local particle volume fraction and hydrated droplet volume, scaled by a viral load of $c_v = 2.35 \times 10^9$ quanta/mL and converted to quanta/m³. The inhaled dose was integrated over time (Eq. 8) and used in the Wells–Riley model (Eq. 9) to estimate the POI.

Based on Li et al. [25], the volume-weighted mean diameter of respiratory droplets is 6.62 µm. This study assumes all droplets rapidly dehydrate into aerosols and adopts this diameter as representative of airborne transmission. Dehydrated droplet nuclei are 20–34% smaller due to water loss; Li et al. [25] estimated a final diameter equal to 26.2% of the original, using data from Chao et al.

[26] and Li et al. [27], consistent with Stadnytskyi et al. [28]. Accordingly, a shrinkage factor of 0.262 is applied in volume calculations. Viral decay is neglected to reflect a conservative, worst-case infection scenario. At this size, particle motion is governed by drag, gravity, and turbulence; Brownian diffusion was excluded and is noted as a limitation. Viral load was assumed proportional to droplet volume, as in [37], though finer particles may carry higher concentrations [29].

2.2 CO_2 and Age of Air Numerical Models

Occupant-generated CO_2 emissions are modelled using the species transport equation to compare infection risk (IR) and CO_2 concentration distributions.

The mean ventilation effectiveness in the occupied zone (E_{OZ}) is evaluated using the age of air (θ_{age}) [30], modelled via the passive scalar transport equation. This approach assigns a virtual "clock" to each air volume element, tracking the time elapsed since uncontaminated outdoor air entered a given cell. Consequently, this enables the assessment of air distribution and age across different office space regions.

2.2.1 CO_2 Species Transport Numerical Model

The three-dimensional species transport equation to simulate the transport of CO_2 within the office room is implemented in this study:

$$\frac{\partial(\rho Y_{CO2})}{\partial t} + \frac{\partial(\rho Y_{CO2} U_j)}{\partial x_j} = \frac{\partial}{\partial x_j}\left[\rho D_{CO2}\frac{\partial(Y_{CO2})}{\partial x_j} + \frac{\mu_t}{\sigma_t}\frac{\partial Y_{CO2}}{\partial x_j}\right] \quad (10)$$

where t is the simulation time, ρ is the overall density of the mixture, Y_{CO2} is the mass fraction of CO_2, U_j is the velocity where u_1, u_2, u_3 are the directions in the x, y and z directions respectively, μ_t is the turbulent dynamic viscosity, σ_t is the turbulent Schmidt number and D_{CO2} is the molecular diffusivity of CO_2 in the mixture. The turbulent diffusion is accounted for through the term $\frac{\mu_t}{\sigma_t}$.

The occupants were represented by a box, 0.25 m x 0.4 m x 1.2 m, in the computational model, [31]. The exhaled CO_2 was introduced via a small circular hole of 10-mm at the height of 1.1 m of the box. Table 1 summarises the boundary conditions for the occupant. The peak occupancy is 88 people.

Table 1. Boundary conditions for the occupant CO_2 exhalation for each case.

Activity	CO_2 Exhalation Rate [L/min]	Inlet Type	Heat Source (W)
Sedentary	0.31 [32]	Circular Inlet	75

2.2.2 Age of Air Numerical Model

The age of air is modelled through the passive scalar transport equation:

$$\frac{\partial \rho A}{\partial t} + u_j\frac{\partial \rho A}{\partial x_j} - \frac{\partial}{\partial x_j}\left[D\frac{\partial \rho A}{\partial x_j}\right] - S_A = 0 \quad (11)$$

where A is the passive scalar of the age of air, D is the diffusivity flux of the passive scalar, and S_A is the source term for the age of air, which is a scalar flux with an inferred density of 1/s. The passive scalar's diffusivity characteristics were set by increasing the Schmidt number and the Turbulent Schmidt number to a value of 1×10^9. Consequently, advection can dominate the transport of the time scalar when there is flow motion, whereas diffusion can operate on the scalar when there is little to no advection.

Local and Mean Ventilation Effectiveness

Air Changes per Hour (ACH) quantifies the total volume of air entering a space relative to its internal volume, representing the nominal ventilation rate. However, this metric only accounts for the total fresh air supply without considering its distribution within the space.

To assess air distribution, local ventilation rates are calculated based on the age of air at each cell. This provides a more detailed evaluation of airflow patterns, ensuring a comprehensive understanding of ventilation effectiveness. The age distribution theory, as outlined in [33], forms the basis of this approach:

$$n_{cell} = \frac{1}{A_{cell}} \quad (12)$$

Ventilation effectiveness, denoted as n_{cell}, is determined by comparing the actual delivery rate of outside air with an ideal mixing scenario. In a perfectly mixed environment, where ventilation is uniform and concentrations are equal throughout, the local ventilation efficiency at each cell (E_{cell}) is calculated as:

$$E_{cell} = \frac{n_{cell}}{N} \quad (13)$$

According to ASHRAE [34], the occupied zone, referring to the area where humans occupy, extends up to 1.8 meters from the floor and 0.3 meters from the side walls. To determine the average ventilation

effectiveness in this zone (E_{OZ}), we calculate the volume average of the local ventilation effectiveness within this range. This involves summing up products of E_{cell} and cell volumes, then dividing by the total cell volumes in the occupied zone.

2.3 A Description of IES:VE Energy Modelling

The Integrated Environmental Solutions Virtual Environment (IES:VE) is a comprehensive building performance simulation suite used by architects and engineers to optimise energy efficiency and occupant comfort. It has been validated against international standards, including ASHRAE 140 and CIBSE TM33, ensuring compliance with rigorous industry benchmarks [35].

2.4 Cases Studied

Figure 2 shows the computational domain of the hospice dining space. The passive ventilation system includes upper operable windows (red, labelled 1–4) for exhaust and lower intakes (blue, labelled 1–2) for fresh air supply. Internal doors (green, labelled 1–2) are opened under overheating conditions to allow cross-zone airflow. As a passive system, flow direction can reverse depending on wind and pressure, resulting in either positive or negative airflow through the openings.

To capture realistic ventilation-driven airflow conditions throughout the year, hourly data from dynamic simulation was analysed using a custom script. This process identified 13 representative days that collectively span the full range of ventilation performance across all opening types, covering the minimum, maximum, and key quartiles (Q1, Q2, Q3). These selected cases ensure efficient yet comprehensive CFD coverage of both typical and extreme conditions, where openings may act as inlets or exhausts depending on wind-driven pressure differences. These cases are outlined by Table 2 below.

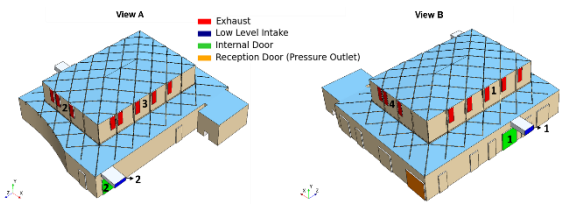

Figure 1. The computational domain of the communal area within the UK hospice used in the present study.

Table 2. Boundary conditions for the occupant CO_2 exhalation for each case.

Date	Time	Intake 1	Intake 2	E1	E2	E3	E4	ID1	ID2	Occupancy	Season
05/07/2023	17:30	-0.039	1.009	-0.327	-0.498	0.888	-0.055	-0.509	1.395	50%	Summer
08/01/2023	12:30	0.000	0.000	-0.004	-0.088	-0.169	0.347	0.000	0.000	100%	Winter
31/05/2023	06:30	0.369	-0.379	0.000	0.000	0.000	0.000	0.000	0.000	25%	Summer
17/01/2023	15:30	0.000	0.000	0.120	0.644	-0.375	-0.263	0.000	0.000	50%	Winter
08/12/2022	08:30	0.000	0.0001	0.004	-0.001	-0.002	-0.002	0.000	0.000	50%	Winter
24/06/2023	07:30	-0.197	0.250	-0.008	-0.009	0.008	-0.028	0.000	0.000	50%	Summer
16/05/2023	16:30	0.0001	0.000	0.043	0.208	-0.090	0.122	0.000	0.000	50%	Summer
10/12/2022	19:30	0.000	0.000	0.108	-0.070	-0.048	-0.020	0.000	0.000	100%	Winter
11/07/2023	15:30	-0.067	-0.358	0.500	0.313	-0.424	-0.156	0.497	-1.246	50%	Summer
03/01/2023	19:30	0.000	0.000	-0.092	0.226	-0.041	-0.026	0.000	0.000	100%	Winter
05/02/2023	09:30	0.000	0.000	0.070	0.071	-0.070	-0.070	0.000	0.000	50%	Winter
31/08/2023	18:30	-0.051	0.000	-0.060	-0.023	0.011	0.129	0.051	0.000	100%	Summer
04/07/2023	14:30	0.000	0.000	-0.089	-0.408	1.068	0.045	0.000	0.000	50%	Summer

2.5 Acceptable POI Level

The acceptable POI level, determined to be 7.5% in England based on worst case government statistics, is based on the methodology proposed by the authors in a companion paper [37].

2.6 Lagrangian Particle Injector

The exhaled droplets (dispersed phase) from the infector are simulated using a transient Lagrangian model. This study implements "one-way" coupling between the dispersed phase (airborne particles) and the continuous phase (air-CO_2 mixture). As confirmed in our companion paper [37], the volume fractions of the airborne particles are so insignificant that their displacement of the air-CO_2 mixture is negligible. Consequently, the particle transport is affected only by the fluid motion, without influencing the air flow in return. The overall simulated time was 5 minutes with a droplet time step of 0.01s. This time was sufficient for the IR level to reach the acceptable limit based on worst-case scenarios. The residuals were left to reach a minimum level of 10^{-6} to regulate the particle tracking's accuracy. Table 3 demonstrates the numerical boundary conditions applied for the particle injector.

Table 3. Boundary Conditions for the Lagrangian Particle Injector.

Variable	Value/Type	Reference
Injector Type	Point injector	-
Injection Rate	1000 [particle/s]	[28]
Injection Direction	Normal	-
Particle Diameter	6.62 [μm]	[25]
Activity	Speaking	-
Particle Injection Velocity	4.07 [m/s]	[38]
Particle Temperature	34 [°C]	[39]
Particle Deposition Rate	0.285 [cm/s]	[40]

3. RESULTS

3.1 Distribution and Behavioural Analysis

3.1.1 Contour Plots

Figures 3 & 4 illustrate the Probability of Infection (POI) and CO_2 concentration contours along the horizontal plane (1.2 m above the floor) and vertical mid-span plane. The results indicate that airflow forces significantly influence the distribution of both infectious particles and CO_2, with higher concentrations in recirculation zones and low-velocity regions, where airborne particles tend to accumulate.

While CO_2 concentration and infection risk share distributional similarities, key differences are observed. The CO_2 species transport model exhibits 'smearing' effects, where CO_2 disperses more uniformly from high- to low-concentration areas due to diffusion. In contrast, the infection risk formulation lacks a diffusion term, resulting in sharper concentration gradients and more localised risk zones.

Given the extensive number of contour plots across multiple cases, only representative cases are presented. To facilitate a comprehensive comparison across all 13 cases assessed in this study, heatmaps are employed, offering a more insightful and quantitative analysis of POI and CO_2 distribution patterns.

3.1.2 Heatmaps

Figures 5 & 6 show the average Probability of Infection (POI) and CO_2 concentration at 1.2 m above the floor across all cases. Surface-averaged values are consistently higher than volume-averaged values, as the latter includes regions with zero infection risk and atmospheric CO_2 levels, lowering overall averages.

Notably, high CO_2 concentration does not imply high infection risk, as CO_2 is exhaled by all occupants, while infectious particles originate from an infector. Infection risk varies with infector position and airflow direction, whereas CO_2 distribution remains unaffected.

Elsarraj et al. [20] trained an Optimised Random Forest (ORF) model using volume-averaged POI and CO_2 concentration, incorporating ventilation rate to distinguish CO_2 thresholds across occupancy levels. However, assuming a single infector led to overlapping CO_2 values for the same POI, affecting model accuracy.

Analysing all surface and volume-averaged data was impractical due to overlapping CO_2 values at a given ventilation rate, which obscures clear trends.

Instead, heatmaps (Figures 5 & 6) were used to identify high-risk zones based on elevated infection probability. For these zones, only surface-averaged POI and CO_2 concentrations were extracted to provide a conservative representation of worst-case exposure conditions.

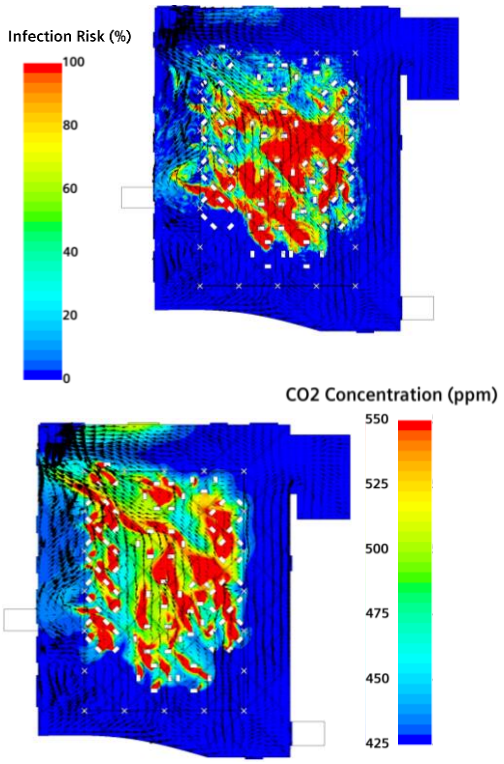

Figure 3. Contour and vector plots of the POI and the CO_2 concentration along the horizontal plane at a height of 1.2 m above the floor

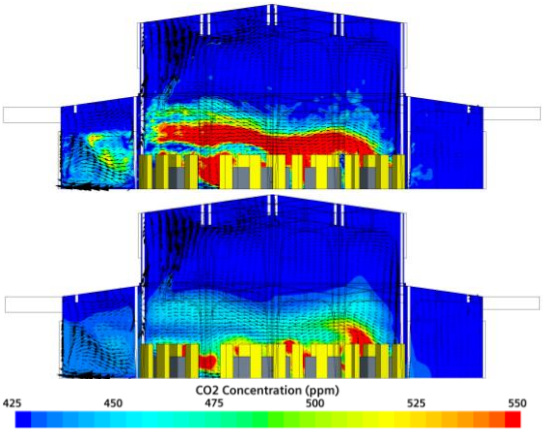

Figure 4. Contour and vector plots of the POI and the CO_2 concentration along the vertical mid-span plane.

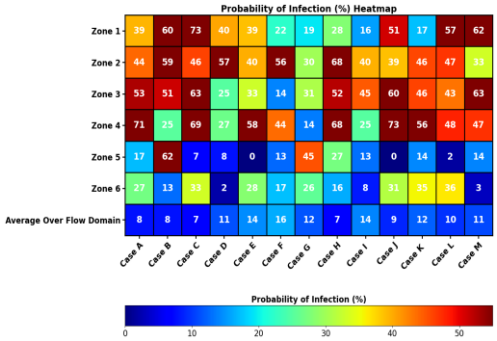

Figure 5. POI heatmaps for all cases for each zone.

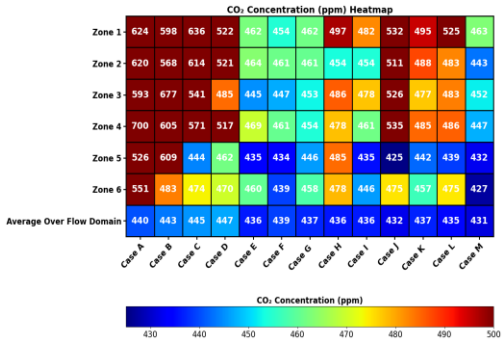

Figure 6. CO_2 concentration heatmaps for all cases for each zone.

4. Conclusion

This study developed a CFD-based framework for evaluating infection risk in a UK hospice using a Probability of Infection (POI) metric derived from an Eulerian-Lagrangian (E-L) model. The results demonstrate that CO_2 distribution, while often used as a ventilation performance indicator, differs significantly from the spatial behaviour of infectious aerosols, primarily due to diffusion effects absent in the POI formulation. This discrepancy validates the need for direct particle-based modelling when assessing airborne infection risk.

Heatmap analysis across multiple cases identified high-risk zones, revealing that infection risk is highly sensitive to infector position and airflow dynamics, rather than CO_2 concentration alone. These insights demonstrate the limitations of relying on CO_2 as a surrogate for exposure and highlight the value of spatially resolved CFD models in guiding ventilation strategies.

By quantifying infection risk based on clinically informed exposure metrics and airflow behaviour, this approach offers a robust tool for assessing and improving ventilation effectiveness in sensitive healthcare settings. The framework may be extended to other high-risk environments, such as care homes or waiting areas, to support evidence-based infection control strategies in post-pandemic building design.

REFERENCES

[1] J. Lu, J. Gu, J. Gu, K. Li, C. Xu, W. Su, Z. Lai, D. Zhou, C. Yu, B. Xu, Z. Yang, COVID-19 Outbreak Associated with Air Conditioning in Restaurant, Guangzhou, China, 2020, Emerg. Infect. Dis. 26 (2020) 1628–1631. https://doi.org/10.3201/eid2607.200764.

[2] L. Morawska, D.K. Milton, It Is Time to Address Airborne Transmission of Coronavirus Disease 2019 (COVID-19), Clin. Infect. Dis. 71 (2020) 2311–2313. https://doi.org/10.1093/CID/CIAA939.

[3] V. Stadnytskyi, C.E. Bax, A. Bax, P. Anfinrud, The airborne lifetime of small speech droplets and their potential importance in SARS-CoV-2 transmission, Proc. Natl. Acad. Sci. U. S. A. 117 (2020) 11875–11877. https://doi.org/10.1073/PNAS.2006874117/ASSET/03A58387-760C-4C37-9D6A-BB2FEF5BC447/ASSETS/GRAPHIC/PNAS.2006874117FIG01.JPEG.

[4] R. Zhang, Y. Li, A.L. Zhang, Y. Wang, M.J. Molina, Identifying airborne transmission as the dominant route for the spread of COVID-19, Proc. Natl. Acad. Sci. U. S. A. 117 (2020) 14857–14863. https://doi.org/10.1073/pnas.2009637117.

[5] Q.J. Leclerc, N.M. Fuller, L.E. Knight, S. Funk, G.M. Knight, What settings have been linked to SARS-CoV-2 transmission clusters?, Wellcome Open Res. 5 (2020). https://doi.org/10.12688/WELLCOMEOPENRES.15889.2.

[6] CIBSE, COVID-19 Ventilation Guidance, (2021) 1–26. https://www.cibse.org/knowledge-research/knowledge-portal/covid-19-guidance-ventilation-v4.

[7] ANSI/ASHRAE, ANSI/ASHRAE standard 62.1-2022:, Vent. Accept. Indoor Air Qual. Atlanta, GA, USA Am. Soc. Heating, Refrig. Airconditioning Eng. (2022).

[8] REHVA, REHVA COVID-19 guidance document version 4.1. How to operate HVAC and other buildings service systems to prevent the spread of the coronavirus (SARS-CoV-2) disease (COVID-19) in workplaces, 2021. https://www.rehva.eu/fileadmin/user_upload/REHVA_COVID-19_guidance_document_V4.1_15042021.pdf (accessed June 14, 2023).

[9] G. Pei, M. Taylor, D. Rim, Human exposure to respiratory aerosols in a ventilated room: Effects of ventilation condition, emission mode, and social distancing, Sustain. Cities Soc. 73 (2021).

https://doi.org/10.1016/j.scs.2021.103090.
[10] G.K. Rencken, E.K. Rutherford, N. Ghanta, J. Kongoletos, L. Glicksman, Patterns of SARS-CoV-2 aerosol spread in typical classrooms, Build. Environ. 204 (2021). https://doi.org/10.1016/j.buildenv.2021.108167.
[11] C. Ren, S.J. Cao, F. Haghighat, A practical approach for preventing dispersion of infection disease in naturally ventilated room, J. Build. Eng. 48 (2022) 103921. https://doi.org/10.1016/j.jobe.2021.103921.
[12] Q. Cao, M. Liu, X. Li, C.H. Lin, D. Wei, S. Ji, T. (Tim) Zhang, Q. Chen, Influencing factors in the simulation of airflow and particle transportation in aircraft cabins by CFD, Build. Environ. 207 (2022). https://doi.org/10.1016/j.buildenv.2021.108413.
[13] Y. Yan, X. Li, Y. Shang, J. Tu, Evaluation of airborne disease infection risks in an airliner cabin using the Lagrangian-based Wells-Riley approach, Build. Environ. 121 (2017) 79–92. https://doi.org/10.1016/J.BUILDENV.2017.05.013.
[14] Z. Liu, W. Zhuang, X. Hu, Z. Zhao, R. Rong, J. Li, N. Li, W. Ding, Potential infection risk assessment of improper bioaerosol experiment operation in one BSL-3 laboratory based on the improved Wells-Riley method, Build. Environ. 201 (2021) 107974. https://doi.org/10.1016/J.BUILDENV.2021.107974.
[15] B. Bake, P. Larsson, G. Ljungkvist, E. Ljungström, A.C. Olin, Exhaled particles and small airways, Respir. Res. 20 (2019). https://doi.org/10.1186/S12931-019-0970-9.
[16] C.T. Crowe, J.D. Schwarzkopf, M. Sommerfeld, Y. Tsuji, Multiphase flows with droplets and particles: Second edition, 2011.
[17] A. Keshmiri, M.A. Cotton, Y. Addad, D. Laurence, A. Keshmiri, M.A. Cotton, Y. Addad, · D Laurence, Turbulence Models and Large Eddy Simulations Applied to Ascending Mixed Convection Flows, Flow Turbul. Combust. 89 (2012) 407–434. https://doi.org/10.1007/s10494-012-9401-4.
[18] A. Keshmiri, A. Revell, H.G. Darabkhani, Assessment of a common nonlinear eddy-viscosity turbulence model in capturing laminarization in mixed convection flows, Numer. Heat Transf. Part A Appl. 69 (2016) 146–165. https://doi.org/10.1080/10407782.2015.1069672.
[19] A. Keshmiri, K. Osman, S. Benhamadouche, N. Shokri, Assessment of advanced RANS models against large eddy simulation and experimental data in the investigation of ribbed passages with passive heat transfer, Numer. Heat Transf. Part B Fundam. 69 (2016) 96–110. https://doi.org/10.1080/10407790.2015.1096641.
[20] M. Elsarraj, Y. Mahmoudi, A. Keshmiri, Quantifying indoor infection risk based on a metric-driven approach and machine learning, Build. Environ. 251 (2024) 111225. https://doi.org/10.1016/J.BUILDENV.2024.111225.
[21] L. Schiller, Über die grundlegenden Berechnungen bei der Schwerkraftaufbereitung, Z. Vereines Dtsch. Inge. 77 (1933) 318–321.
[22] W.F. Wells, Airborne contagion and air hygiene: an ecological study of droplet infections, J. Am. Med. Assoc. 159 (1955) 90. https://jamanetwork.com/journals/jama/article-abstract/302159.
[23] E.C. Riley, G. Murphy, R.L. Riley, Airborne spread of measles in a suburban elementary school, Am. J. Epidemiol. 107 (1978) 421–432. https://doi.org/10.1093/oxfordjournals.aje.a112560.
[24] R. Wölfel, V.M. Corman, W. Guggemos, M. Seilmaier, S. Zange, M.A. Müller, D. Niemeyer, T.C. Jones, P. Vollmar, C. Rothe, M. Hoelscher, T. Bleicker, S. Brünink, J. Schneider, R. Ehmann, K. Zwirglmaier, C. Drosten, C. Wendtner, Virological assessment of hospitalized patients with COVID-2019, Nat. 2020 5817809. 581 (2020) 465–469. https://doi.org/10.1038/s41586-020-2196-x.
[25] X. Li, D. Lester, G. Rosengarten, C. Aboltins, M. Patel, I. Cole, A spatiotemporally resolved infection risk model for airborne transmission of COVID-19 variants in indoor spaces, Sci. Total Environ. 812 (2022) 152592. https://doi.org/10.1016/j.scitotenv.2021.152592.
[26] C.Y.H. Chao, M.P. Wan, L. Morawska, G.R. Johnson, Z.D. Ristovski, M. Hargreaves, K. Mengersen, S. Corbett, Y. Li, X. Xie, D. Katoshevski, Characterization of expiration air jets and droplet size distributions immediately at the mouth opening, J. Aerosol Sci. 40 (2009) 122–133. https://doi.org/10.1016/j.jaerosci.2008.10.003.
[27] X. Li, Y. Shang, Y. Yan, L. Yang, J. Tu, Modelling of evaporation of cough droplets in inhomogeneous humidity fields using the

multi-component Eulerian-Lagrangian approach, Build. Environ. 128 (2018) 68–76. https://doi.org/10.1016/j.buildenv.2017.11.025.

[28] V. Stadnytskyi, C.E. Bax, A. Bax, P. Anfinrud, The airborne lifetime of small speech droplets and their potential importance in SARS-CoV-2 transmission, Proc. Natl. Acad. Sci. U. S. A. 117 (2020) 11875–11877. https://doi.org/10.1073/pnas.2006874117.

[29] D.K. Milton, M.P. Fabian, B.J. Cowling, M.L. Grantham, J.J. Mcdevitt, Influenza Virus Aerosols in Human Exhaled Breath: Particle Size, Culturability, and Effect of Surgical Masks, PLoS Pathog. 9 (2013) 1003205. https://doi.org/10.1371/journal.ppat.1003205.

[30] M. Sandberg, What is ventilation efficiency?, Build. Environ. 16 (1981) 123–135. https://doi.org/10.1016/0360-1323(81)90028-7.

[31] L. Tian, Z. Lin, Q. Wang, Comparison of gaseous contaminant diffusion under stratum ventilation and under displacement ventilation, Build. Environ. 45 (2010) 2035–2046. https://doi.org/10.1016/J.BUILDENV.2010.01.002.

[32] ANSI/ASHRAE, ANSI/ASHRAE standard 62.1-2013:, Vent. Accept. Indoor Air Qual. Atlanta, GA, USA Am. Soc. Heating, Refrig. Airconditioning Eng. (2013). www.ashrae.org/technology.

[33] M. Sandberg, M. Sjöberg, The use of moments for assessing air quality in ventilated rooms, Build. Environ. 18 (1983) 181–197. https://doi.org/10.1016/0360-1323(83)90026-4.

[34] American Society of Heating Refrigerating and Air-Conditioning Engineers (ASHRAE), ASHRAE handbook: Fundamentals, American Society of Heating, Refrigeration and Air-Conditioning Engineers, 2009.

[35] I.E.S. Limited., SOFTWARE VALIDATION AND APPROVAL, (2014). https://www.iesve.com/software/software-validation?utm_source=chatgpt.com (accessed November 27, 2024).

[36] CIBSE, Applications Manual AM 11 - Building performance modelling, 2015. https://www.cibse.org/knowledge-research/knowledge-portal/applications-manual-11-building-performance-modelling-2015?utm_source=chatgpt.com (accessed November 27, 2024).

[37] M. Elsarraj, Y. Mahmoudi, A. Keshmiri, Linking airflow dynamics to infection risk reduction and predictive strategies, J. Build. Eng. 110 (2025) 113027. https://doi.org/10.1016/J.JOBE.2025.113027.

[38] S.B. Kwon, J. Park, J. Jang, Y. Cho, D.S. Park, C. Kim, G.N. Bae, A. Jang, Study on the initial velocity distribution of exhaled air from coughing and speaking, Chemosphere. 87 (2012) 1260–1264. https://doi.org/10.1016/j.chemosphere.2012.01.032.

[39] Z.T. Ai, A.K. Melikov, Airborne spread of expiratory droplet nuclei between the occupants of indoor environments: A review, Indoor Air. 28 (2018) 500–524. https://doi.org/10.1111/ina.12465.

[40] A.C.K. Lai, W.W. Nazaroff, Modeling indoor particle deposition from turbulent flow onto smooth surfaces, J. Aerosol Sci. 31 (2000) 463–476. https://doi.org/10.1016/S0021-8502(99)00536-4.

Conference on Modelling Fluid Flow (CMFF'25)
The 19th International Conference on Fluid Flow Technologies
Budapest, Hungary, August 26-August 29, 2025

NUMERICAL MODEL DEVELOPMENT AND ANALYSIS OF A DROP-ON-DEMAND INKJET APPLICATION

Patrick WAGNER[1], Aurélia VALLIER[2], Hesameddin FATEHI[3]

[1] Sustainable Energy Engineering Program, Lund University, Sweden, E-mail: pa3246wa-s@student.lu.se
[2] Tetra Pak Packaging Solutions AB, Sweden, E-mail: aurelia.vallier@tetrapak.com
[3] Corresponding Author. Department of Energy Sciences, Division of Fluid Mechanics, Lund University, Lund 22100, Sweden, E-mail: hesameddin.fatehi@energy.lth.se

ABSTRACT

The print quality of drop-on-demand (DOD) systems is affected by the jet breakup and the potential occurrence of satellite droplets. This paper presents the development of a numerical model to simulate droplet formation using the volume-of-fluid (VOF) method. A particular focus is on the occurrence of satellite droplets and how different fluid properties influence jetting behavior. The research centers on a printhead with a native droplet size of 2-3 pL and limited data availability. Therefore, an inlet boundary approximation method is developed to simulate the droplet formation for different actuation waveforms accurately based on the experimental results from a JetXpert drop-watcher with two different fluids and several different actuation waveform. Results show that multi-pulse waveforms can enhance droplet detachment and mitigate satellite formation by controlling pressure dynamics in the nozzle. Further simulations on sequential multi-pulse actuation revealed residual meniscus vibrations that influence subsequent droplet formation. The model was used to investigate the effect of viscosity, density, surface tension, and contact angle on the droplet formation process.

Keywords: Drop-on-demand (DOD), Ink Jetting, Satellite Droplet, Volume-of-fluid (VOF), Newtonian Fluid, Waveform Approximation

1. INTRODUCTION

Inkjet printing is one of the most common applications of microfluidics [1]. This technology progressively creates 2D images by depositing thousands of microscopic droplets on a stationary or moving substrate. Those droplets are typically in the range of 1 to 500 pL and move at a speed of 5-8 m/s when hitting the substrate [2]. Multiple mechanisms are involved in this process and have been studied in recent years [1, 3], including the actuation method [4], the acoustics within the printhead [5], the jetting process [6] and the droplet formation and breakup [7, 8]. There are several categories of inkjet printing technologies, with the most general division between continuous inkjet (CIJ) and drop-on-demand (DOD) printers. A DOD printer uses separate pressure pulses at each nozzle to generate individual droplets that can be generated on demand. This pressure pulse and the underlying actuation mechanism strongly influence the controllability and the process of droplet formation in DOD printers.

A common actuation mechanism for DOD printers is the use of microscopic piezoelectric elements [2]. Piezoelectric elements change their shape in the presence of an electric field, which can be utilized to transfer energy to the fluid through a pressure change in the ink chamber [9]. The way these actuators produce a droplet is heavily depending on the electrical signal imposed on them. Since the piezoelectric elements are controlled with a voltage signal, two principal actuation modes can be applied. The element can either initially contract and then expand, resulting in a pull-push mode, or vice versa, leading to a push-pull actuation. Considering the delay of the electric signal and mechanical movement, this leads to a single trapezoidal pulse. This type of actuation has been subject of many numerical studies [10, 11]. Adding together multiple pulses with different amplitudes leads to the formation of more complex actuation methods and waveforms [12, 13, 5]. Apart from the electrical signal, fluid properties also influence the waveform and, consequently, jetting behaviour and droplet formation [14]. Choosing the correct waveform is essential for successfully jetting a selected ink. A simplified geometry of an inkjet nozzle is used in Figure 1 to explain the actuation process, according to [2]. A single unipolar rectangular pulse is applied to the piezoelectric element on the side of the ink chamber leading to an initial contraction. Therefore, a negative pressure pulse is induced during t_{rise}, which travels through the ink chamber

and reflects at the reservoir during t_{dwell}. When the actuator expands, the pulse is superimposed with a positive pressure pulse during t_{fall}. This positive interference leads to a high-pressure pulse that results in the droplet jetting at the meniscus.

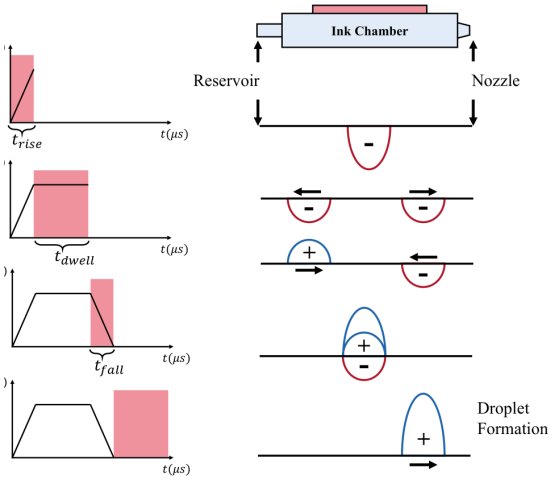

Figure 1. Schematic representation of the actuation principle, based on [2].

A comprehensive understanding of droplet formation is essential to investigate the behavior of ejected liquids. In Figure 2, the DOD droplet formation process is schematically represented and divided into six steps. Initially, the liquid is in an equilibrium state (A). After an actuation is induced, the liquid is pushed out of the nozzle (B). When a certain amount of fluid is pushed through the nozzle, the head droplet starts forming, and the necking of the fluid begins due to surface tension (C). The liquid continues to move out of the nozzle and forms an extending ligament of fluid, which attaches the head droplet to the meniscus (D). The surface tension leads to the pinch-off of the liquid ligament and the formation of a tail droplet (E). Afterwards, the liquid tail begins to catch up with the main droplet and ideally joins with it (F_a). If, however, the tail droplet pinches of from the tail and becomes an individual droplet, it is known as a satellite droplet (F_b). The head droplet formation, the pinch-off, the tail behavior, and the satellite formation are different aspects of the process that influence the final droplet size [3].

The actuation waveform is the main driver of the droplet formation and the most sensitive part of the simulation [2]. A good approximation of the inlet boundary conditions is essential to successfully simulate a DOD system. However, predicting the waveform at the boundary is challenging since the flow within the nozzle chamber is rarely observable. Some researchers have simulated the dynamics within the printhead itself, to predict the boundary condition [12, 15]. Another common method is the use of lumped element models to calculate the pressure response [11]. Analytical equations have also been used in recent papers to predict the pressure at the boundary of the numerical model [13, 5, 10]. The goal of this paper is to develop an analytical approximation method for a boundary condition for a given printhead, with limited information on its geometric characteristics, and to calibrate the boundary equation using experimental data. Through this approach, a simple model is created that can be used to investigate the effects of different waveforms on droplet formation.

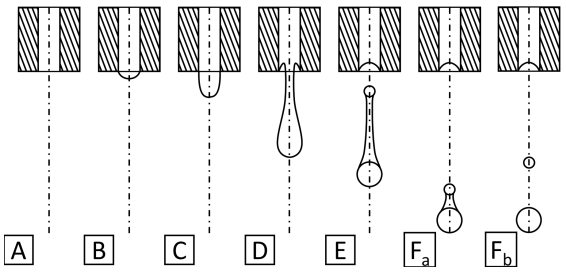

Figure 2. Six stages of the droplet formation process, based on [9]. The explanation of the different stages is presented in the text.

2. NUMERICAL MODELING

The CFD software Star-CCM+ is used for the numerical simulations in this study [16]. The VOF model was selected since it is designed to capture the interface between several immiscible fluids, since resolving the free surface is essential to capture the droplet formation process.

2.1. Volume of Fluid

The Volume of Fluid method allows the simulation of fluid dynamics of two immiscible fluids with a fluid-fluid interface (free surface). A fixed mesh is used, and the free surface moves through the mesh. At each grid cell, a volume fraction α_i is defined, indicating how much of a cell is occupied by the phase i. The material properties in a cell with $0 < \alpha_i < 1$ depend on the material properties of the constituent phases. The fluid properties in the cells are treated as a mixture. The density and viscosity are calculated as:

$$\rho = \Sigma_i \rho_i \alpha_i \tag{1}$$

$$\mu = \Sigma_i \mu_i \alpha_i \tag{2}$$

The distribution of phase i is driven by the phase mass conservation equation:

$$\frac{\partial}{\partial t}\int_V \alpha_i dV + \oint_A \alpha_i \mathbf{v}\cdot d\mathbf{a} = \int_V \left(S_{\alpha_i} - \frac{\alpha_i}{\rho_i}\frac{D\rho_i}{Dt}\right)dV - \int_V \frac{1}{\rho_i}\nabla\cdot(\alpha_i\rho_i\mathbf{v}_{d,i})\,dV \tag{3}$$

where $\mathbf{a}$ is the surface area vector, $\mathbf{v}$ is the mixture (mass-average) velocity, $\mathbf{v}_i$ is the mass-average phase velocity and $\mathbf{v}_{d,i} = \mathbf{v}_i - \mathbf{v}$ is diffusion velocity. S_{α_i} is a

source term of phase i, and $\frac{D\rho_i}{Dt}$ is the material derivation of the phase density ρ_i. For a two-phase flow, the equation is solved only for the primary phase, which in this case is the liquid.

To simulate two immiscible phases, a sharp interface between them is essential. Star-CCM+ uses the High-Resolution Interface Capturing (HRIC) scheme, based on the normalized variable diagram (NVD) [16]. Recent versions of the VOF model include the surface tension via the continuum surface force (CSF) approach. This approach includes surface tension effects as a source term in the Navier-Stokes equations.

The other governing equations include mass conservation and momentum equation. The total mass conservation for all phases is given by:

$$\frac{\partial}{\partial t}\left(\int_V \rho dV\right) + \oint_A \rho \mathbf{v} \cdot d\mathbf{a} = \int_V S\, dV \tag{4}$$

where S is the mass source term, which is defined as:

$$S = \sum_i S_{\alpha_i} \cdot \rho_i \tag{5}$$

This total mass conservation is related to the phase mass conversion (Eq. 3) and includes the fluid mixture through the density. The momentum equation is defined as:

$$\frac{\partial}{\partial t}\left(\int_V \rho \mathbf{v} dV\right) + \oint_A \rho \mathbf{v} \otimes \mathbf{v} \cdot d\mathbf{a} = -\oint_A p\mathbf{I} \cdot d\mathbf{a} + \oint_A \mathbf{T} \cdot d\mathbf{a} + \int_V \mathbf{f}_b dV - \sum_i \int_A \alpha_i \rho_i \mathbf{v}_{d,i} \otimes \mathbf{v}_{d,i} \cdot d\mathbf{a} \tag{6}$$

where p is the pressure, I is the unity tensor, T is the stress tensor and f_b is the vector of body forces.

2.2. Computational Domain

To reduce computational cost, an axisymmetric model was chosen. The simulation domain of the stand-alone jetting model includes parts of the pressure channel, the nozzle, and an air section as presented in Figure 3. The pressure channel has a radius of r_P and a length of l_P. The nozzle is formed into the nozzle plate with a thickness of l_N and has a nozzle radius of r_N. The nozzle has an angle Φ and a neck thickness l_{neck}. The air section has a length of l_A and a radius of r_A. The dimensions of the air section must be sufficiently large to prevent any backflow and boundary condition effects affecting the droplet simulation. Moreover, the air domain should be large enough to capture the crucial aspects of droplet formation. Both the pressure channel and the nozzle are filled with liquid at the start of each simulation.

Several simulations were performed to evaluate the optimal mesh type and resolution, resulting in the selection of a polyhedral mesh. A general guideline is to aim for 10 grid cells to simulate spatial details [3] accurately. For the droplet formation, the smallest length scale is the viscous length scale L_μ, which depends on γ, the surface tension coefficient:

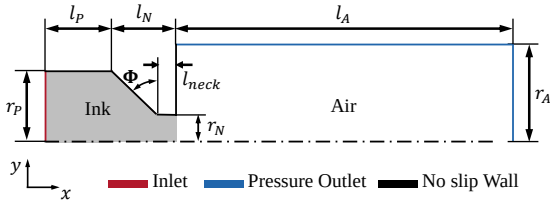

Figure 3. Schematic of the axisymmetric computational domain, including the pressure channel, nozzle, and air region.

$$L_\mu = \frac{\mu^2}{\rho\gamma} \tag{7}$$

This length scale varies depending on the properties of the liquid but is considered to be around 1-5 μm with typical values for fluid properties. This would result in a minimal element size of 0.1-0.5 μm to resolve all flow characteristics.

The minimal element size variation was chosen with the values 1.6 μm, 0.8 μm, 0.4 μm, and 0.266 μm. An example mesh with the smallest element size of 0.8 μm is shown in Figure 4. The refinement zones marked in the top half of this figure were chosen to both capture the meniscus motion within the nozzle and the droplet formation. A base element size of 5 μm was chosen in the coarse zones. A slow growth rate was selected to create a smooth transition between the refinement zone and the coarser mesh area.

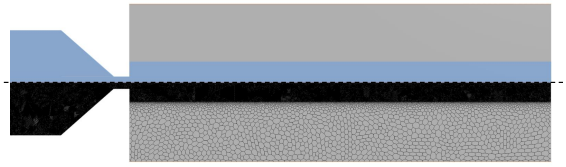

Figure 4. Unstructured mesh of the axisymmetric model. (Top) Refinement zones capturing meniscus motion and droplet formation. (Bottom) Example mesh with a smallest element size of 0.8 μm.

To investigate the mesh dependency and numerical model parameters, a simple velocity waveform, based on the simplifications presented in Figure 1, is used on the inlet. A pull time of 1 μs and a push time of 2 μs was chosen. The printhead in the simulation has a nozzle diameter of 32 μm. For the initial simulation a general time-step of 2e-7 seconds was selected with an adaptive time-step based on the CFL number of the free surface. The CFL limit was set at a maximum condition value of 0.4 and the implicit solver SIMPLE was selected. The arbitrary fluid parameters are $\rho = 1050\ kg/m^3$, $\mu = 7\ cP$, and $\gamma = 72\ mN/m$, resulting in a Ohnesorge number of 0.201. The results of the simulations are presented

in Figure 5, which shows the volume fraction of liquid within the domain. A clear difference can be observed in the tail breakup and the free surface interface between mesh (a) and the rest of the simulations. Mesh (c) and (d) show a sharp free surface interface and a similar droplet behavior.

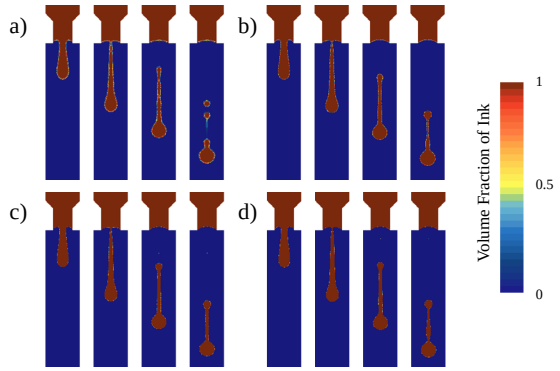

Figure 5. Simulation of the droplet formation at different mesh resolutions with an unstructured mesh at 5, 10, 15 and 20 μs, respectively. Smallest element size: a) 1.6 b) 0.8 c) 0.4 d) 0.266 μm.

When comparing the position and the velocity of the head droplet to the nozzle (Figure 6), similar results between different mesh resolutions could be observed. Both position and velocity show consistency across different resolutions. Since a mesh resolution of 0.4 μm showed a sharp free surface interface with a stable droplet formation, this mesh resolution was selected for further investigations with a total of 660514 cells.

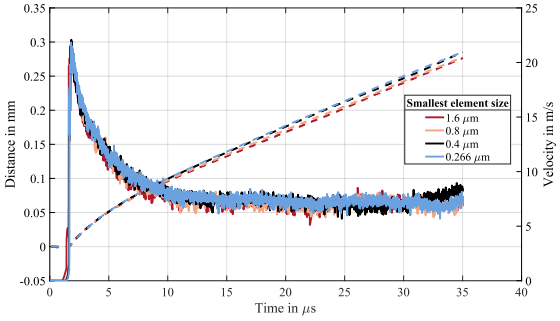

Figure 6. Distance (- -) and velocity (-) of the head droplet over time at different mesh resolutions with an unstructured mesh.

3. EXPERIMENTAL SETUP

Experimental studies were conducted to explore the formation of droplets with a specified printhead. A Newtonian fluid was selected for the experiments. This allows for an accurate description of the fluid properties without requiring complex fluid models. A mixture of 1.2 propandiol and water was chosen for this purpose. To investigate the influence of different fluid properties, two mixtures were studied. The mixtures were based on mass fractions, and the desired composition was mixed in laboratory glass vessels using a commercial scale. The two mixtures have a 1.2 propandiol content of 50% and 25%, respectively. They are referred to as mixture M_{50} and M_{25} in the following sections.

The studies were performed with a Samba printhead from Fujifilm Dimatix. This printhead produces a native droplet size of roughly 3 pL and supports fluids with a viscosity range of 4-9 cP. A single printhead holds 2048 individual nozzles each controlled by separate Silicon MEMS (microelectromechanical system) actuators. Every nozzle is connected to a common refill channel that supplies the ink chamber with a constant flow of ink and is pressurized. The ink flows through the chamber and leaves the printhead through a combined recirculation channel. A piezoelectric actuator on top of the ink chamber can induce the necessary actuation waveform to produce a droplet at the nozzle. Each nozzle has a diameter of 17 μm and is cut into a 50 μm thick nozzle plate with an angle Φ of 45 degrees.

A dropwatcher is directly connected to a JetXpert measurement software, which captures images of the droplet formation and provides multiple analysis tools. The dropwatcher of JetXpert consists of three parts: the printhead with a custom mounting plate, a high-speed LED strobe light, and the high-resolution camera system. All three components are synchronized so when the printhead fires a droplet, the strobe light flashes, and the camera records the droplet in flight at a specific delay. The resolution of the camera is half a micron, and it has an 8 million fps-equivalent exposure time. The printhead can be moved laterally to focus the camera on a single nozzle. The fluid is supplied and recirculated by a heated pipe system. The extracted data consists of image sequences from the JetXpert measurement software which have been used to calculate the velocity and position of the droplets at different timesteps. The delay between each image is 5 μs.

For the experimental investigation, five different pulse widths (t_{dwell}) with an amplitude of 18 V have been selected: 1.65, 1.97, 2.294, 2.55, 2.87 μs. Additionally, several different amplitudes at a constant pulse width of 1.97 μs were tested. Besides the single-pulse actuation, multi-pulse waveforms have been tested. Two tested multi-pulse signals are presented in Figure 11. For both multi-pulse signals, the mixture M_{50} was selected. The first waveform (a) consists of two trapezoidal pulses with the same amplitude. The second waveform (b) consists of three pulses with changing amplitudes. The first two pulses mainly increase the volume of the droplet, while the task of the final pulse is the collection of the tail. It can be observed that the produced droplet from this waveform has an even higher volume and no remaining satellite droplets in comparison to the two-pulse waveform.

4. RESULTS AND DISCUSSIONS

4.1. Calibration and Validation

The movement of the piezoelectric element generates an acoustic wave and a volumetric change that propagates through the ink chamber. This can be translated into a pressure change within the chamber, that can be used as a boundary condition for the CFD model. Since the timescale is short and the travel times are fast, it is assumed that the pressure within the chamber is approximately the same everywhere. At the beginning of an actuation signal, the system is in an equilibrium state. When the piezoelectric actuator expands due to a voltage signal, it creates a lower pressure in the ink chamber (see Figure 1). This low pressure is balanced out over time and falls back to the previous pressure level of the system. Two factors can be seen as responsible for the pressure to go back into its state of equilibrium: the retraction of the meniscus and the fluid flow through the recirculation and re-fill channel. When the piezoelectric element falls back into its non-actuated state, it creates a pressure increase in the ink chamber. This pressure increase is balanced out by the movement of the meniscus, optimally resulting in the formation of a droplet.

To translate the relation between the observable voltage input signal to the unknown pressure change within the printhead, the system is simplified to behave like a resonance circuit. This is based on the Lumped element model approach, which makes the analogy that the electric current (i) and the voltage (V) are equivalent to the volumetric flow rate (Q) and pressure difference (ΔP), respectively. In the resonance case, the system reacts to a change of state with an exponentially damped sinusoid function [17]. The function of the response can be written as:

$$V = Ae^{\zeta t} \sin\left(\frac{2\pi}{\omega}t\right) \tag{8}$$

where A represents the amplitude of the oscillation, ζ the damping factor, and ω the wave period. Applying the aforementioned analogy, the voltage represents the pressure difference and the amplitude of the oscillation depends on the amount of change from the equilibrium state. This results in the following equation:

$$\Delta P = A_p e^{\zeta t} \sin\left(\frac{2\pi}{\omega}t\right) \tag{9}$$

$$A_p = \beta A_V \tag{10}$$

where A_p is the amplitude in Pa, A_V is the amplitude in V, and β is a constant with the unit Pa/V. The voltage signal to the piezoelectric actuator leads to an expansion and contraction of the actuator. This movement leads to a decrease and increase in pressure within the ink chamber. The pressure increase is considered the same everywhere, and the actuation instantaneous. This results in two natural responses of the resonance circuit, which are induced at the beginning of each actuation, as presented in Figure 7. The pull motion of the actuator leads to a negative pulse, while the push motion results in a positive pulse.

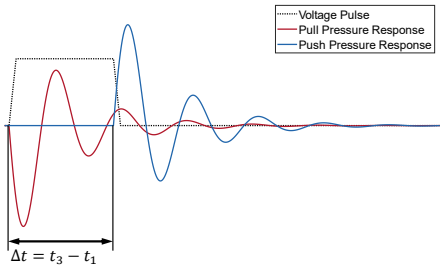

Figure 7. Schematic representation of two pressure wave responses, concerning a voltage signal.

Both responses are superimposed to create the final pressure waveform, which is used as the inlet condition for the numerical model. The amplitude of the response is directly coupled to the amplitude of the voltage signal with the constant β. The final equation for a single voltage pulse response as a pressure waveform depends on the time of the responses and the previous parameters. It can be written as:

$$\begin{aligned}
\Delta P(t) &= 0 && (t < t_1) \\
\Delta P(t) &= A_p e^{\zeta(t-t_1)} sin\left(\frac{2\pi}{\omega}(t-t_1)+\pi\right) && (t < t_3) \\
\Delta P(t) &= A_p e^{\zeta(t-t_1)} sin\left(\frac{2\pi}{\omega}(t-t_1)+\pi\right) \\
&\quad + A_p e^{\zeta(t-t_3)} sin\left(\frac{2\pi}{\omega}(t-t_3)\right) && (t >= t_3)
\end{aligned} \tag{11}$$

where t_1 is the time of the first response, and t_3 is the timing of the second response. This function can be implemented as a field function within StarCCM+ and provides a basis for data fitting with the experimental results by calibrating the parameters. The first step of the calibration process is to select a fitting wave period ω. The experimental results showed, that a sweep across multiple pulse widths results in a near quadratic relationship to the droplet velocity and position over time. This effect is based on the superimposing waveforms of the push pulse and the residual vibration of the pull pulse. At an optimal interference, the pressure peak results in a maximum velocity of the resulting droplet. To recreate this effect, different pulse widths have been simulated, using an amplitude of $A_p = 1.6$ bar, a period of $\omega = 5.2\,\mu s$ and a dampening factor of $\zeta = 250000$. The value Δt was varied in intervals of ±10% starting from $\Delta t = \omega/2$, by changing t_3 in equation 11.

To test the connection between the resonance frequency and optimal pulse width, the same simulations have been repeated for multiple values of ω. In Figure 8, the resulting relative droplet position for

different pulse widths and values of ω are presented. It can be seen that a sweep across Δt results in the described quadratic relationship and a change in resonance period corresponds to a shift of the distribution. This supports the assumption that the optimal droplet ejection is achieved when the pulse width is aligned with the resonance period, which changes with material properties. The slopes of the different distributions are affected by the velocity of the droplet and time when the data is extracted. It is therefore important to focus on the position of the maximum.

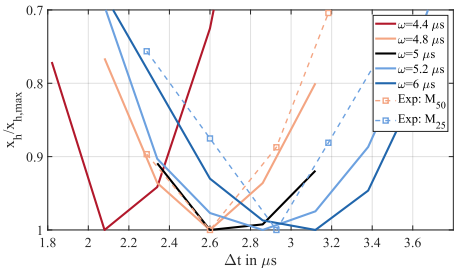

Figure 8. Simulation results of the relative droplet distance resulting from different pulse widths and resonance frequencies. All distances are derived at the same timestep of 50 μs.

To further calibrate the model, the parameter β is used to match the speed of the ejected droplet in the simulation with that in the experiment. In both cases a linear increase in the amplitude results in a linear increase of the droplet speed. The last step of the calibration consists of the definition of a dampening factor ζ. This was achieved by comparing the oscillation of the meniscus in the simulation with that in the experiments. With the designed and calibrated model, a close match between the experimental results and simulated droplet formation across multiple single pulse signals was achieved. Figure 9 shows a visual comparison between experiments and simulation for a case with an actuation amplitude of 15 V. Figure 10 shows the comparison between the recorded and simulated trajectory of multiple actuation amplitudes.

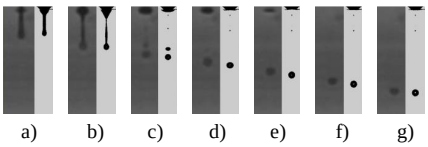

Figure 9. Comparison between experimental results (left) of a droplet formation with an actuation amplitude of 15 V and the simulation (right) with the calibrated model. The images are taken at 10, 15, .., 40 μs, respectively.

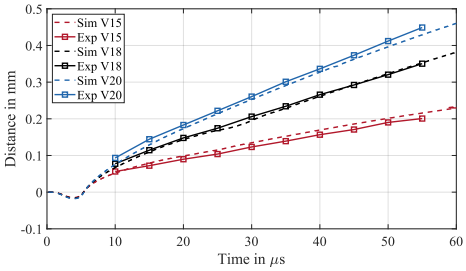

Figure 10. Trajectory comparison between experimental droplets and simulated droplets at different voltage amplitudes showing the distance (x_h) of the head droplet to the nozzle plate.

4.2. Application to different waveforms and fluids

To explore different actuation methods, the two multi-pulse waveforms are used as boundary condition with the calibrated model. For this application, the pressure waveform equation 11 was extended by two additional responses for every added voltage pulse. By superimposing all functions, a combined pressure boundary condition was approximated. The transformed waveforms for both input signals are displayed in Figure 11.

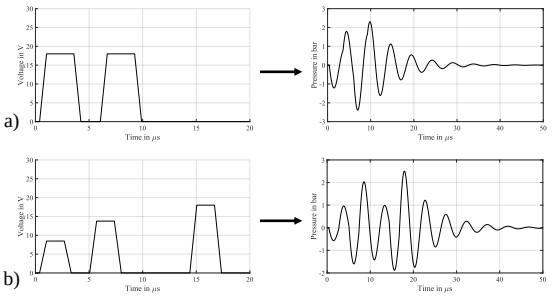

Figure 11. Computed pressure waveform for the multi-pulse actuation. (a) M-shaped waveform with two trapezoidal pulses, (b) complex waveform with three unipolar pulses.

The results of the M-shaped waveform simulation are shown in Figure 12a. A good approximation of the experimental droplet formation could be achieved. The effect of two pulses is visible in the simulation and the experimental observation. After an initial actuation, the second pulse leads to an increase in droplet volume. The final droplet in the experiments consists of a single droplet with a smaller satellite. The same result was predicted with the simulation. Nevertheless, a difference in final velocity can be observed. When comparing the simulations of the three-pulse waveform with the experimental observations, presented in Figure 12b, a close resemblance of the droplet formation was achieved. Two smaller initial pulses lead to the increase in volume,

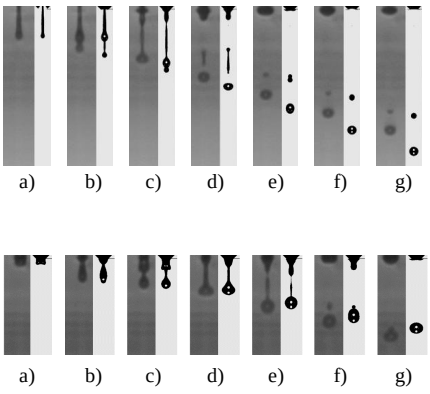

Figure 12. Comparison of experimental and simulated droplet formation using amplitude of 18 V and (a) M-shaped waveform, (b) complex waveform. The images are taken at 10, 15, .., 40 μs, respectively.

while the last pulse collects the tail and leads to a satellite-free droplet. The entire process could be recreated in the simulation. However, the final velocity still slightly differs from the observed experiments.

Besides multi-pulse actuation modes, different concentrations of 1.2 propandiol have been subjected to experimental tests. The numerical fluid parameters in the model were adjusted to examine the performance of the model when using a different fluid. Accordingly, the boundary condition approximation was adapted by selecting a different wave period ω based on Figure 8. The other boundary parameters were not varied from the previous calibration, assuming that ω mainly depends on the fluid properties, while β mainly depends on the displaced volume. The simulation of this fluid showed also a good agreement with the experimental results, as shown on Figure 13.

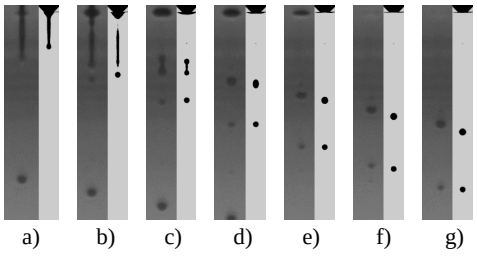

Figure 13. Comparison of experimental and simulated droplet formation for mixture M_{25} using a single trapezoidal waveform. The images are taken at 10, 15, .., 40 μs, respectively.

When simulating a multi-pulse actuation waveform, it is important to consider potential residual vibrations resulting from sequential actuation. In the observed experiments, as presented in Figure 14, it can be noted that the meniscus does not fully retract into the nozzle plate before the next droplet is fired. This can imply that the following droplets are affecting each other at the chosen frequency based on the residual vibration. For all single pulse actuation, the meniscus fully retracts before the next actuation.

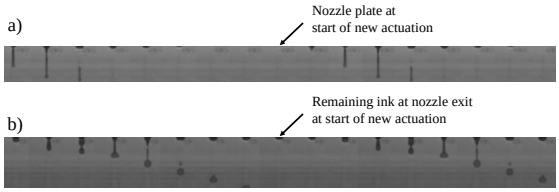

Figure 14. Experimental observations of two actuation cylces of a single pulse actuation (a) and a multi-pulse actuation (b). The arrow indicates the beginning of a new actuation cycle. Remaining ink at the nozzle can be detected during the multi-pulse actuation.

To simulate a possible case with multiple droplets, the complex waveform is repeated four times within the simulation, resulting in four individual droplets. The resulting waveform with the current model is shown in Figure 15. A clear overlapping between the separate actuation is visible. The frequency of the actuation is 20 kHz.

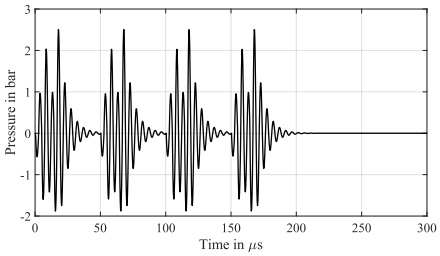

Figure 15. Pressure waveform for a multi-shot simulation with overlapping vibrations between different actuation phases.

When simulating this waveform, a different behavior between the first droplet and the following droplets can be observed, as shown in Figure 16. The first droplet moves with a significantly higher velocity, while the following droplets are slowed down. The difference in the actuation can also be seen in the meniscus movement. When simulating a single droplet, the effect of the previous droplet on the actuation waveform might not be captured. These show that while multi-pulse actuation effectively reduces satellite formation, residual meniscus vibrations in sequential jetting can alter droplet velocity and trajectory, which is of special importance for high-frequency applications.

5. PARAMETER STUDY

With the calibrated model, different fluid and printhead properties were investigated and their influence on jetting behavior with the given printhead

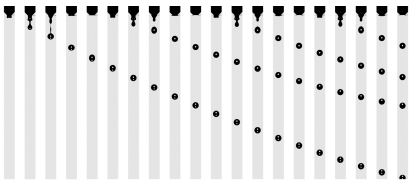

Figure 16. Sequential images of the multi-shot simulation. The images are taken at a rate of 10 μs beginning at 10 μs after the actuation.

dimensions was analyzed. This initial analysis of different fluid properties did not take into account a changing wave period and therefore only allows for a general guideline. An increase in density showed a reduction in jetting velocity and droplet volume while slightly delaying the time of pinch-off. A change in viscosity showed a strong influence on the droplet velocity and volume, as well as the pinch-off timing. Both velocity and volume greatly decreased with an increase in viscosity while the pinch-off time was delayed. An increase in surface tension showed a faster pinch-off and an increase in maximum jetting velocity while only slightly affecting the droplet volume and final velocity. For the given printhead, a change in contact angle only affected the droplet formation when reaching a non-wetting behavior. An increase in contact angle over that point resulted in a decrease in velocity and volume. The effects of viscosity are considered the most influential, given the strong fluctuation of ink viscosity depending on temperature changes.

6. CONCLUSION

A numerical stand-alone model of the jetting process from a DOD printhead was successfully developed. The model was designed to simulate an existing printhead with limited available data by incorporating a resonance circuit assumption and calibrating the boundary condition using experimental observations. A good agreement between the numerical and experimental results was achieved across multiple actuation waveforms and different fluid compositions.

The study confirmed that multi-pulse actuation improves droplet formation by controlling tail breakup and reducing satellite formation. However, new simulations demonstrated that sequential actuation leads to residual meniscus vibrations, affecting the velocity and trajectory of subsequent droplets. These results emphasize the importance of considering inter-droplet interactions in waveform optimization for high-frequency printing applications.

ACKNOWLEDGMENTS

This work was financed by Tetra Pak® Packaging Solutions AB.

REFERENCES

[1] Lohse, D., 2022, “Fundamental Fluid Dynamics Challenges in Inkjet Printing”, *Annual Review of Fluid Mechanics*, Vol. 54 (1).

[2] Hoath, S. D., 2016, *Fundamentals of Inkjet Printing: The Science of Inkjet and Droplets*, John Wiley and Sons, Incorporated, ISBN 9783527684731.

[3] Wijshoff, H., 2008, “Structure- and fluid-dynamics in piezo inkjet printheads”, Ph.D. thesis.

[4] Ezzeldin, M., Van Den Bosch, P. P. J., and Weiland, S., 2013, “Toward better printing quality for a drop-on-demand ink-jet printer: improving performance by minimizing variations in drop properties”, *IEEE Control Systems*, Vol. 33 (1), pp. 42–60.

[5] Li, D., Sun, L., Li, Z., Wu, X., Hu, G., Ma, C., Sun, Q., Liu, Y., and Zhang, Y., 2024, “Suppression of secondary droplet for high-definition drop-on-demand inkjet by actively regulating the channel acoustic waves”, *Acta Mechanica Sinica*, Vol. 40 (3).

[6] Fraters, A., Jeurissen, R., Berg, M. v. d., Reinten, H., Wijshoff, H., Lohse, D., Versluis, M., and Segers, T., 2020, “Secondary Tail Formation and Breakup in Piezoacoustic Inkjet Printing: Femtoliter Droplets Captured in Flight”, *Physical Review Applied*, Vol. 13 (2).

[7] Driessen, T., 2013, “Drop Formation from axisymmetric fluid jets”, *University of Twente*.

[8] Zhong, Y., Fang, H., Ma, Q., and Dong, X., 2018, “Analysis of droplet stability after ejection from an inkjet nozzle”, *Journal of Fluid Mechanics*, Vol. 845, pp. 378–391.

[9] Hutchings, I. M., and Martin, G. D., 2013, *Inkjet technology for digital fabrication*, Wiley Online Library.

[10] Lei, T., Han, J., and Liu, H., 2022, “Numerical Analysis and Optimal CFD Model Verification of Piezoelectric Inkjet Printhead”, *Journal of Applied Fluid Mechanics*, Vol. 15 (4).

[11] Shah, M. A., Lee, D. G., and Hur, S., 2019, “Design and Characteristic Analysis of a MEMS Piezo-Driven Recirculating Inkjet Printhead Using Lumped Element Modeling”, *Micromachines (Basel)*, Vol. 10 (11).

[12] Yang, Z., Tian, H., Wang, C., Li, X., Chen, X., Chen, X., and Shao, J., 2023, “Piezoelectric Drop-on-Demand Inkjet Printing with Ultra-High Droplet Velocity”, *Research (Wash D C)*, Vol. 6, p. 0248.

[13] Jianjun, W., Jin, H., Chuqing, X., Hongxiao, G., Chaoyu, L., Qiang, Z., Jie, Z., Pengbing, Z., Yupeng, Y., Jinzhu, Z., Wang, G., and Ruiqi, C., 2023, "Actuation waveform auto-design of drop-on-demand inkjet for ejection droplet without satellite", *Journal of Manufacturing Processes*, Vol. 102.

[14] Jiao, T., Lian, Q., Zhao, T., and Wang, H., 2021, "Influence of ink properties and voltage parameters on piezoelectric inkjet droplet formation", *Applied Physics A*, Vol. 127 (1).

[15] Wei, H., Xiao, X., Yin, Z., Yi, M., and Zou, H., 2017, "A waveform design method for high DPI piezoelectric inkjet print-head based on numerical simulation", *Microsystem Technologies*, Vol. 23 (12), pp. 5365–5373.

[16] Siemens, 2024, "StarCCM+ Documentation", URL `www.siemens.com`.

[17] Plonus, M., 2020, *Electronics and communications for scientists and engineers*, Butterworth-Heinemann.

Conference on Modelling Fluid Flow (CMFF'25)
The 19th International Conference on Fluid Flow Technologies
Budapest, Hungary, August 26-August 29, 2025

A NOVEL EULERIAN-LAGRANGIAN MULTI-SCALE METHOD FOR CAVITATING FLOW IN AN INJECTOR NOZZLE

Wei Guan[1], Shengnan Zhang[2], Chuqiao Wang[3], Zhixia He[2], Dominique Thévenin[1]

[1] Corresponding Author. Lab. of Fluid Dynamics and Technical Flows, University of Magdeburg "Otto von Guericke", Magdeburg 39106, Germany. E-mail: wei.guan@ovgu.de
[2] Institute for Energy Research, Jiangsu University, Zhenjiang, PR China
[3] School of Energy and Power Engineering, Jiangsu University, Zhenjiang, PR China

ABSTRACT

The cavitation phenomena found in high-pressure fuel injector nozzles have a significant influence on the performance of subsequent spray mixing, combustion, and even emissions in internal combustion engines. In particular, cloud cavitation accompanied by complex interactions between phase transition and turbulent fluctuations induced by the shedding of vapor bubbles, inevitably results in nozzle wall erosion while facilitating the primary breakup of the liquid jet. The in-nozzle cavitating flow is generally captured by using an Eulerian method coupled with large eddy simulation (LES). However, this approach cannot capture the behavior of vapor bubbles at scales smaller than the LES grid. Therefore, an Eulerian-Lagrangian multiscale model is proposed here to simulate the multiscale vapor structure in a scaled-up injector nozzle. The Volume of Fluid (VOF) method is employed to capture the macroscopic characteristics of cavitation, while a Lagrangian method is used to track microscopic bubbles. This combined Eulerian-Lagrangian approach leads to a two-way coupling and reveals the mechanisms controlling cavitation bubble shedding in the nozzle. It accurately reproduces the multiscale features of cavitation, in particular the evolution of large cavities as well as the dynamic characteristics of microscopic bubbles. The results indicate that shedding cycles of cavitation cloud are mainly induced by the re-entrant jet for a cavitation number below 1.64.

Keywords: Injector nozzle, Multi-scale cavitation, Eulerian-Lagrangian model, Re-entrant jet

1. INTRODUCTION

Atomizing liquid jets are utilized across various fields, including medical sprays, rocket engines, and internal combustion engines. In recent decades, numerous studies have focused on enhancing atomization performance in diverse industrial applications, with fuel injection spray processes in internal combustion engines (ICE) being a typical example. Outstanding fuel injection atomization can significantly enhance engine combustion efficiency and reduce emissions [1, 2]. Furthermore, the internal flow behavior within the injector, particularly in the presence of cavitation, has a significant influence on fuel spray characteristics, highlighting the need for a thorough understanding of nozzle cavitating flow [3, 4].

With its tiny geometric scale (~0.1 mm diameter), high injection pressure (>160 MPa), and extremely short injection duration (~3 ms), the nozzle orifice exhibits micro-scale, ultra-high-speed, strongly transient, and highly turbulent internal flow characteristics. The abrupt change in the flow cross-section at the orifice entrance causes the fuel to detach from the wall, resulting in a significant depressurization. When the local pressure drops below the saturation vapor pressure of the fuel, cavitation occurs, causing the fuel to transition from liquid to gas phase and resulting in a complex two-phase cavitating flow within the nozzle. Moreover, shear and vortex flows within the nozzle induce various forms of cavitation, increasing the complexity of the internal flow.

While cavitation within the injector nozzle can enhance jet breakup and improve atomization, it may also reduce orifice flow capacity and cause cavitation erosion, potentially leading to injector failure [5]. Cavitation induces complex flow issues [6], including shock waves and turbulent vortices, and associated effects such as pressure fluctuations, vibrations, and noise [7, 8], all of which have attracted considerable attention in fields such as fluid machinery and fuel injection system. The pressure fluctuations and pulses generated by cavitation are major contributors to pipeline system corrosion [9, 10]. Accordingly, the study of shock wave propagation is essential for gaining a deeper understanding of the mechanisms underlying cavitation bubble growth and collapse. This phenomenon typically occurs during the final stage of cavity collapse, taking place on ex-

tremely small temporal and spatial scales and characterized by the dynamic behavior of a cloud of discrete bubbles and minute mixed-phase cavities.

Nonetheless, accurately capturing the dynamic characteristics of discrete cavities remains a significant challenge. The commonly used homogeneous mixture models within the Eulerian framework effectively capture large cavities but fail to accurately represent smaller cavities that are below the grid resolution. A potential solution is a multi-scale hybrid model, where macro-scale cavity structures are captured using a homogeneous mixture approach, such as the Volume of Fluid (VOF) method with a mass transfer model, while micro-scale cavity structures are modeled using a Lagrangian approach, governed by the Newtonian motion of individual spherical bubbles and by the Rayleigh–Plesset equation for bubble dynamics [11, 12]. In the present work, therefore, a Eulerian–Lagrangian multi-scale cavitation model is employed, in order to investigate cavitation shedding mechanisms induced by shock waves. Coupled to LES simulations, the micro-bubbles performance is obtained in an injector nozzle for different shedding mechanisms.

2. NUMERICAL METHODOLOGY

2.1. VOF method

The VOF method has been utilized for the simulation of cavitating flows in the injector nozzle. The transport equations for continuity, momentum, and for capturing the macro-scale vapor cavities are as follows

$$\frac{\partial \rho_m}{\partial t} + \nabla \cdot (\rho_m \mathbf{U}) = 0, \quad (1)$$

$$\frac{\partial (\rho_m \mathbf{U})}{\partial t} + \nabla \cdot (\rho_m \mathbf{U}\mathbf{U}) = -\nabla p + \nabla \cdot \tau - \vec{F_B}, \quad (2)$$

$$\frac{\partial (\alpha_v \rho_v)}{\partial t} + \nabla \cdot (\alpha_v \rho_v \mathbf{U}) = \dot{R}_e - \dot{R}_c, \quad (3)$$

where ρ_m, ρ_v, $\mathbf{U}$, and p are the mixture density, vapor density, velocity, and pressure, respectively. The viscous stress tensor τ is defined as $\tau = \mu\left(\nabla\mathbf{U} + (\nabla\mathbf{U})^{\mathrm{T}}\right) + \boldsymbol{\tau}_t$, where μ is the mixture viscosity and $\boldsymbol{\tau}_t$ is the turbulent stress. Here, α_v is the volume fraction of vapor, and therefore the volume fraction of liquid is defined as $\alpha_l = 1-\alpha_v$. The source term $\dot{R}_e - \dot{R}_c$ is the phase change mass transfer rate between the liquid and vapor, calculated by using the Zwart–Gerber–Belamri (ZGB) [13] cavitation model in this work. The source terms are given by

$$\dot{R}_e = F_{vap} \frac{3\alpha_{\mathrm{nuc}}(1-\alpha_v)\rho_v}{R_{\mathrm{B}}} \sqrt{\frac{2}{3}\frac{(p_v - p)}{\rho_l}}, \quad p \le p_v, \quad (4)$$

$$\dot{R}_c = F_{\mathrm{cond}} \frac{3\alpha_v \rho_v}{R_{\mathrm{B}}} \sqrt{\frac{2}{3}\frac{(p - p_v)}{\rho_l}}, \quad p > p_v, \quad (5)$$

where F_{vap} and F_{cond} are empirical coefficients, respectively. R_{B} represents the mean radius of bubbles, which is assumed to be 0.001 mm in this model, while α_{nuc} is the nucleation site volume fraction, which is fixed at 0.0005. Considering that the focus of the paper is to resolve cloud cavitation at normal fuel operating temperature within the injection orifice, where the variation of temperature does not vary more than 10 K for the pressure drops considered, the isothermal assumption has been adopted in the present study. Therefore, the energy conservation equation is not considered in the barotropic behavior of the fluid in this work.

2.2. Discrete bubble model

The discrete bubble model (DBM) within the Lagrangian framework for tracing bubbles on the coarse-grid domain is given by

$$\vec{u_{\mathrm{B}}} = \frac{dx}{dt}, \quad (6)$$

$$M_{\mathrm{B}} \frac{d\vec{u_{\mathrm{B}}}}{dt} = \vec{F}_{\mathrm{Drag}} + \vec{F}_{\mathrm{VM}} + \vec{F}_{\mathrm{PG}}, \quad (7)$$

where M is the mass and subscript B represents discrete bubbles, while $\vec{F}_{\mathrm{Drag}}$, $\vec{F}_{\mathrm{VM}}$, $\vec{F}_{\mathrm{PG}}$ are the drag force, the virtual-mass force, and the pressure gradient force, respectively, calculated using the following equations

$$\vec{F}_{\mathrm{Drag}} = M_{\mathrm{B}} \frac{\vec{u} - \vec{u_{\mathrm{B}}}}{\tau_r}, \quad (8)$$

$$\vec{F}_{\mathrm{VM}} = C_{\mathrm{VM}} M_{\mathrm{B}} \frac{\rho_m}{\rho_v}\left(\vec{u}_{\mathrm{B}} \nabla \vec{u} - \frac{d\vec{u_{\mathrm{B}}}}{dt}\right), \quad (9)$$

$$\vec{F}_{\mathrm{PG}} = \frac{\rho_m}{\rho_v} M_{\mathrm{B}} \vec{u}_{\mathrm{B}} \nabla \vec{u}, \quad (10)$$

where C_{VM} is the virtual-mass force coefficient taken equal to 0.5. The quantity τ_r is the relaxation time of discrete bubbles, given by

$$\tau_r = \frac{\rho_v d_{\mathrm{B}}^2}{3\mu_m} \frac{4}{C_d \mathrm{Re}}, \quad (11)$$

where C_d is the drag coefficient calculated by the spherical drag law, and Re is the relative Reynolds number, calculated by the following formula

$$\mathrm{Re} = \frac{\rho_m d_{\mathrm{B}} \left|\vec{u}_{\mathrm{B}} - \vec{u}\right|}{\mu_m}. \quad (12)$$

The integral average in each control volume is expressed as

$$\vec{F}_{\mathrm{B}} = -\frac{1}{V_{\mathrm{cell}}} \sum_{i=1}^{N} \left(\vec{F}_{\mathrm{Drag},i} + \vec{F}_{\mathrm{VM},i} + \vec{F}_{\mathrm{PG},i}\right), \quad (13)$$

where the subscript i represents the bubbles in the control volume. This study employs a simplified Rayleigh–Plesset equation to simulate the growth and collapse of discrete bubbles, leading to

$$\frac{\mathrm{d}R_{\mathrm{B}}}{\mathrm{d}t} = sign(p_v - p)\sqrt{\frac{2}{3}\left|\frac{p_v - p}{\rho_l}\right|}, \quad (14)$$

where R_B is the radius of discrete bubbles with an initial value of 1×10^{-6} m. Since the above equation only considers the first-order term of the Rayleigh–Plesset equation and neglects the second-order term and surface tension, two coefficients C_v and C_c are introduced to correct the growth and collapse rates of the bubbles. Because bubbles are not only produced in parts below the saturation vapor pressure, a nucleation coefficient C_{csp} which is greater than 1 is also introduced, referred to as the nucleation pressure. The growth and collapse of the bubbles can be expressed as

$$\frac{dR_B}{dt} = \begin{cases} C_v \sqrt{\frac{2}{3}\left(C_{csp}p_v - p\right)/\rho_l}, & p \le C_{csp}p_v \\ C_c \sqrt{\frac{2}{3}\left(p - C_{csp}p_v\right)/\rho_l}, & p \ge C_{csp}p_v \end{cases} \quad (15)$$

where C_v, C_c, and C_{csp} are 0.5, 0.01, and 1.2, respectively, as suggested by Li et al. [14]. To simulate the nucleation process, nuclei are randomly injected into the region where the local pressure is lower than the nucleation pressure. Nuclei are allocated with a number of nucleation sites per unit cell volume set to 1×10^{10} m^{-3}.

2.3. Multiscale transformation algorithm

A discrete-continuum transformation algorithm is employed for multiscale modeling of cavitation bubbles across different fluid scales. During fuel injection in the nozzle, large-scale cavities are well-resolved with high grid resolution in LES simulations, enabling the accurate capture of cavity shedding. Sub-grid scale cavities are converted into Lagrangian bubbles, initiating the transition from VOF to DBM, as presented in Figure 1a. When $p_{csp}p_{sat} \leqslant p$ and $\alpha_v < 0.6$ are satisfied simultaneously in one grid cell, the Eulerian cavity within the grid cell is replaced by an equivalent volume of discrete bubbles, triggering the VOF-to-DBM transition.

Nonetheless, when the volume of discrete bubble touches the liquid-vapor interface and the volume fraction of vapor phase exceeds 0.6, further tracking by the DBM is deemed unacceptable. Therefore, two transition modes are considered in this work to achieve the transition from DBM to VOF. The first mode involves the coalescence between the DBM and VOF methods, as shown in Fig. 1b. The second mode represents the transition from DBM to VOF due to the growth of discrete bubbles, as illustrated in Fig. 1c. When a discrete bubble reaches the liquid-vapor interface, the transition depends on the volume ratio of the bubble V_B to the grid cell volume V_{cell}. If $V_B/V_{cell} < 1 - \alpha_v$, the discrete bubble is incorporated into the Eulerian cavity for further calculation, and the gas phase volume fraction in the grid cell is updated as $\alpha_v = \alpha_v + V_B/V_{cell}$. Conversely, if $V_B/V_{cell} \geqslant 1 - \alpha_v$, the vapor volume fraction with the grid cell reaches $\alpha_v = 1$, and the excess bubble volume beyond the grid cell capacity is evenly distributed among the neighboring cells, thereby achieving the DBM-to-VOF conversion. During the transition, the Lagrangian framework removes the bubble and transfers its mass into the VOF simulation. Accordingly, a source term should be incorporated into the volume-fraction equation of the vapor [14], expressed as follows

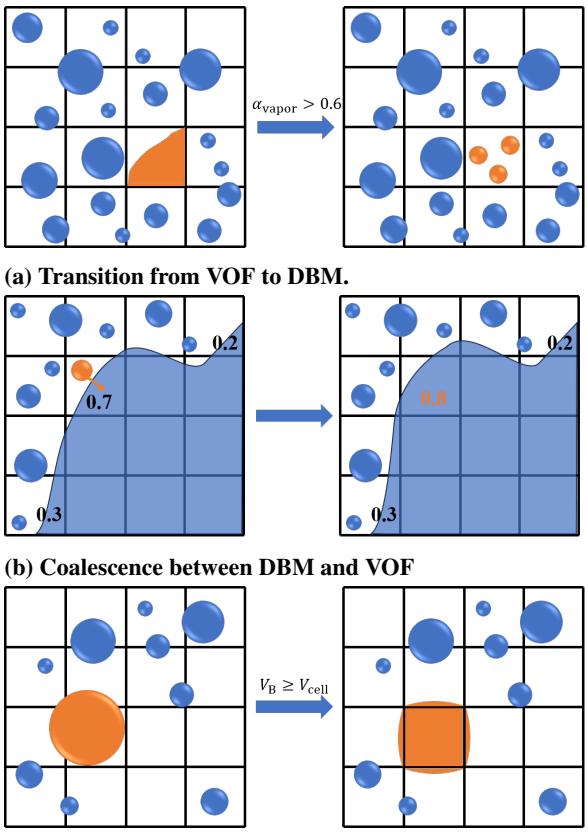

(a) Transition from VOF to DBM.

(b) Coalescence between DBM and VOF

(c) Transition from DBM to VOF.

Figure 1. Diagram of VOF-DBM with two-way transition.

$$\frac{\partial(a_v\rho_v)}{\partial t} + \nabla \cdot (a_v\rho_v\mathbf{U}) = \dot{R}_e - \dot{R}_c + S_B, \quad (16)$$

where S_B represents the source due to the transition from discrete bubbles (DBM) to macro-scale cavities (VOF), which is expressed as follow

$$S_B = \begin{cases} \frac{\rho_v V_B}{V_{cell}\Delta t} & \text{if bubble is removed} \\ 0 & \text{else} \end{cases} \quad (17)$$

2.4. Turbulence modeling

The LES model employs a spatial low-pass filter operation determined by the cell size of the computational domain to separate the eddies at different scales. In this study, for modeling the unresolved turbulence, the Wall-Adapting Local Eddy-Viscosity (WALE) model is employed [15]. The sub-grid scale model (SGS) turbulent closure is defined as

$$\tau_t = \frac{1}{3}\tau_{kk}\delta_{ij} - 2\mu_t\overline{S}_{ij}, \quad (18)$$

where $\overline{S}_{ij}$ is the rate of strain tensor for the resolved scale. τ_{kk} is the isotropic part that is not modeled but added to the filtered static pressure term, while μ_t is the sub-grid-scale turbulent viscosity given as

$$\mu_t = \rho L_s^2 \frac{(\mathbf{S}_{ij}^d \mathbf{S}_{ij}^d)^{3/2}}{(\mathbf{S}_{ij}^d \mathbf{S}_{ij}^d)^{5/4} + (\bar{\mathbf{S}}_{ij} \bar{\mathbf{S}}_{ij})^{5/2}}, \tag{19}$$

where L_s is the length scale based on the cell volume V_{cell} and the distance to the closest wall d.

2.5. Case setup

The geometry of the computational domain is illustrated in Fig. 2. The geometrical topology of the rectangular nozzle is derived from a previous study [16]. The width W and length L of the nozzle are about 2 and 4 mm, respectively. The nozzle has a W/L ratio of 2 and a nominally sharp entrance. This structure can be representative for cavitating flow in fuel injectors, since the velocities and cavitation obtained are similar to the large-scaled fuel injector nozzle and it is easy to investigate cloud cavitation.

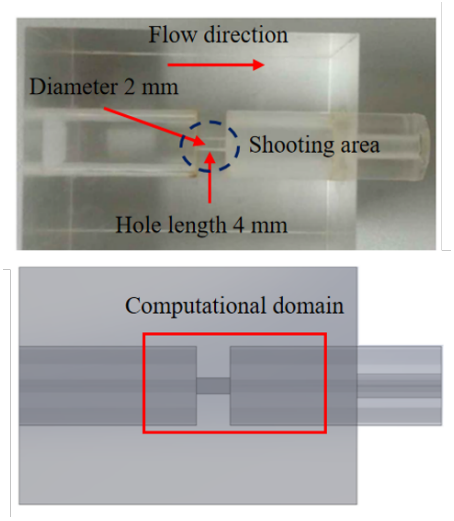

Figure 2. Transparent nozzle geometry.

For a LES simulation, a sufficient mesh resolution is essential for capturing the large-scale turbulent structure. Therefore, a proper balance between computational accuracy and computational cost is required, which is favored by a suitable arrangement of the computational domain grid. The Taylor microscale (λ_g) from the statistical theory of turbulence is used as a common guideline for selecting the LES mesh in the relevant literature [4, 17]

$$\lambda_g = \sqrt{10}\text{Re}^{-0.5} D_{\text{out}} \approx 65\mu\text{m}, \tag{20}$$

The mesh is refined near the walls and the inlet sharp edge as shown in Fig. 3. The minimum cell size near the wall is 2 µm and the maximum dimensionless wall distance (y^+) in the area of interest is about 1.

In this study, simulations were conducted for a

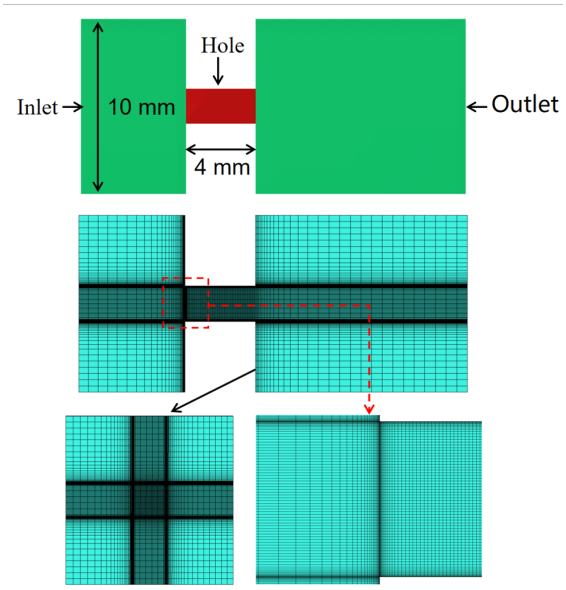

Figure 3. Computational mesh.

cavitation number $\sigma = 1.64$ to investigate the shedding behavior of unsteady cavitation. The cavitation number of the nozzle is defined as

$$\sigma = \frac{p_{\text{in}} - p_{\text{sat}}}{p_{\text{in}} - p_{\text{out}}} \tag{21}$$

where p_{in} and p_{sat} are the inlet pressure and the saturation pressure, and p_{out} is the fixed outlet pressure of 101325 Pa.

The employed solver is the segregated, pressure-based formulation in the ANSYS Fluent platform (Version 18.0). User-defined functions (UDFs) are implemented to achieve the development of DBM for cavitation and the combination between DBM and VOF. The pressure–velocity coupling scheme relies on the PISO scheme. The cell gradients are calculated using Least Square Cell Based method. The pressure interpolation is performed using the body force weighted scheme due to its robustness. The convective terms for the momentum are discretized using a bounded central differencing scheme. Finally, the time integration has been performed by adopting a bounded second-order implicit scheme. An adaptive time step is employed based on a Courant–Friedrichs–Lewy (CFL) number. An empirically value of 0.8 is adopted in the present study, limiting the diffusion of turbulent vortex clusters into the flow.

3. RESULTS AND DISCUSSION

3.1. Validation

The numerical results are validated against the experimental observations by He et al [16]. A detailed description of the experimental setup is provided in [16], in which the typical periodic shedding and collapse of cloud cavitation are observed at a cavitation number of $\sigma = 1.64$. To better visualize

the vapor distribution in the flow field, all cases using the VOF-LES and VOF-DBM-LES methods are represented through the iso-surface of the vapor volume fraction at $\alpha_v = 0.1$. Figure 4 shows the transient experimental flow pattern, the VOF-LES simulation results, and the VOF-DBM-LES simulation results.

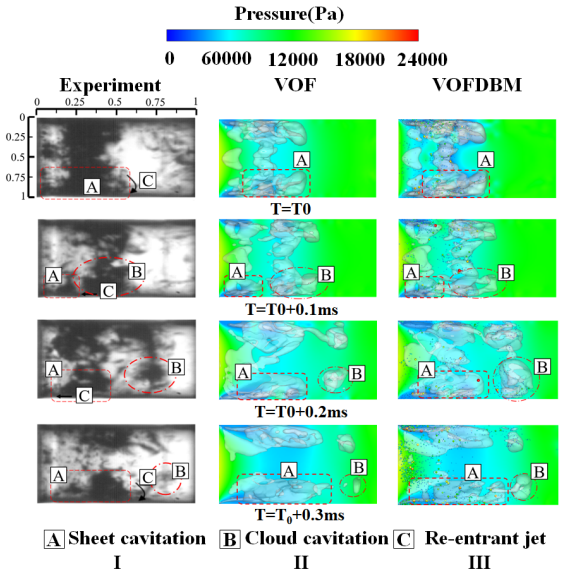

Figure 4. Comparison of simulation results with the experimental data at $\sigma = 1.64$.

As the volume fraction field only captures the macroscopic distribution of the vapor cavity, both simulation results show some discrepancies compared with the experimental results. The results using the VOF-LES method aligns well with the experimental observations in the first two time frames; however, in the latter two, the shed cloud cavitation is noticeably smaller compared to the experiment. Particularly at time frame IV, the cloud cavitation almost entirely collapses, showing a significant deviation from the experimental results. Moreover, this approach fails to capture the development of discrete bubbles during the flow process. In contrast, the VOF-DBM-LES approach not only accurately reproduces the growth of sheet cavitation, the shedding, collapse, and periodic behavior of cloud cavitation observed in the experiment but also provides a clear representation of the development of microscopic bubbles throughout the flow process.

The VOF-DBM method used in this study enables the two-way transition between large-scale cavities and microscopic bubbles, in contrast to the traditional VOF method. The transition occurs when the conversion threshold is reached. To better illustrate the processes of bubble injection, growth, collapse, and two-way transition, all bubbles are magnified by a factor of 3 based on their diameter, as shown in Fig.5. Figure 5(a) shows the injection, growth, and collapse of discrete bubbles over a 3 μs time interval, with different arrows representing different processes. Figures 5(b) and 5(c) illustrate the Lagrangian-to-Eulerian transition, representing different transition mechanisms, which are discussed in Section 2 of this study. Figure 5(d) depicts the

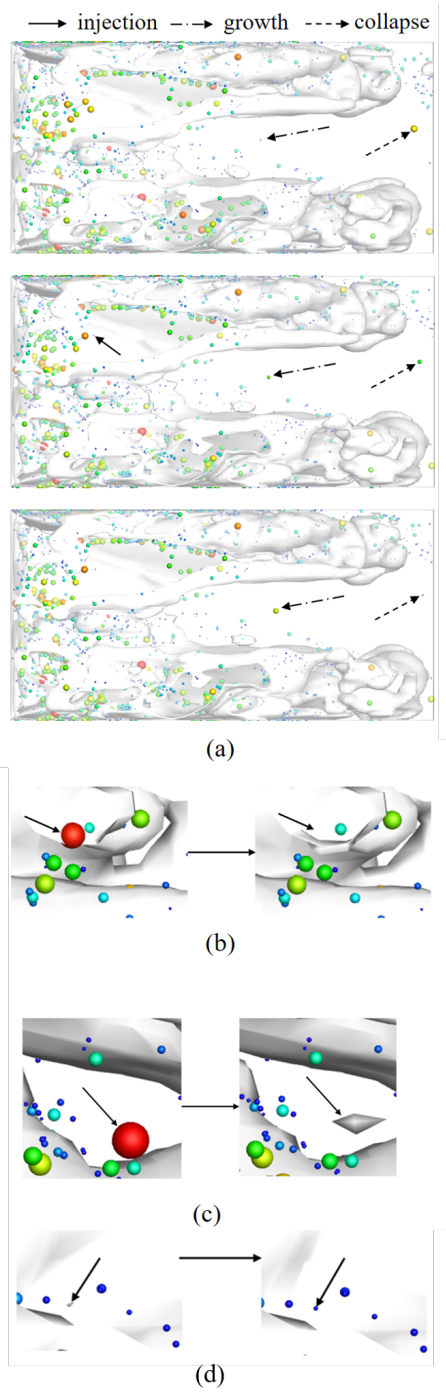

Figure 5. Injection, growth, collapse of discrete bubbles, and the two-way transition between Eulerian and Lagrangian frames: (a) Injection, growth, and collapse of discrete bubbles, (b) Lagrangian-to-Eulerian transition, (c) Lagrangian-to-Eulerian transition, (d) Eulerian-to-Lagrangian transition.

Eulerian-to-Lagrangian transition. The time intervals for Figs.5(b), (c), and (d) are 2 μs.

3.2. Characteristics of cavitation shedding

At $\sigma = 1.64$, the cavitating flow exhibits a periodic process, including the growth of sheet cavitation, the shedding of cloud cavitation, and the collapse of cloud cavitation, as shown in Fig. 6. Once cavitation develops to time t_0, periodic shedding and collapse of cavitation begin to appear in the flow field. The sheet cavitation grows continuously along with the formation of the re-entrant jet, reaching its maximum size at t_0. At this time, the re-entrant jet begins to cut through the sheet cavitation until $t = t_0 + 0.1$ ms. Then, the rear part of the sheet cavitation is severed by the re-entrant jet, leading to a reduction in the length of sheet cavitation, and the detached part immediately forms cloud cavitation. The shed cloud cavitation moves downstream along with the mainstream flow, while the sheet cavitation continues to grow at the point where it was cut off. From $t = t_0 + 0.1$ to $t = t_0 + 0.2$, the sheet cavitation grows, eventually recovering its original length by $t = t_0 + 0.2$, and maintaining a relatively stable state. During this period, small-scale secondary shedding of tiny cavities occasionally occurs from the rear part of the sheet cavitation. At this stage, the re-entrant jet starts forming from the rear of the sheet cavitation and gradually propagates upstream, while the shed cloud cavitation continues to move downstream. Due to the pressure recovery, the cloud cavitation begins to collapse. As the cloud cavitation approaches the nozzle exit at $t = t_0 + 0.3$, the recovered pressure causes the rapid collapse of the cloud cavitation. Finally, at $t = t_0 + 0.4$, the flow field returns to its state at t_0, marking the start of a new cavitation cycle.

Figure 7 shows the $x - t$ diagram of the numerical simulation results at $\sigma = 1.64$. It captures at least one complete cycle of cavitation development. The cavitation structures are represented by the isosurface of vapor volume fraction at $\alpha_v = 0.1$, shown in white, while the background is displayed in black. The green solid line represents the reduction of sheet cavitation, indicating the shedding of cloud cavitation. The yellow solid line represents the growth of sheet cavitation. The blue solid line represents the downstream transport of cloud cavitation with the mainstream flow, while the red dashed line indicates the collapse of cloud cavitation. The shedding type of cloud cavitation can be determined based on the rate of reduction of sheet cavitation, which corresponds to the slope of the green solid line.

As shown in Fig. 7, the cavitation shedding phenomenon exhibits relatively simple characteristics, with only one noticeable instance of sheet cavitation reduction observed. The reduction rate of sheet cavitation is relatively low, at 9.6 m/s, indicating that the cavitation shedding process is slow and stable. Therefore, it can be concluded that, under the conditions of this study, the shedding mechanism of cloud

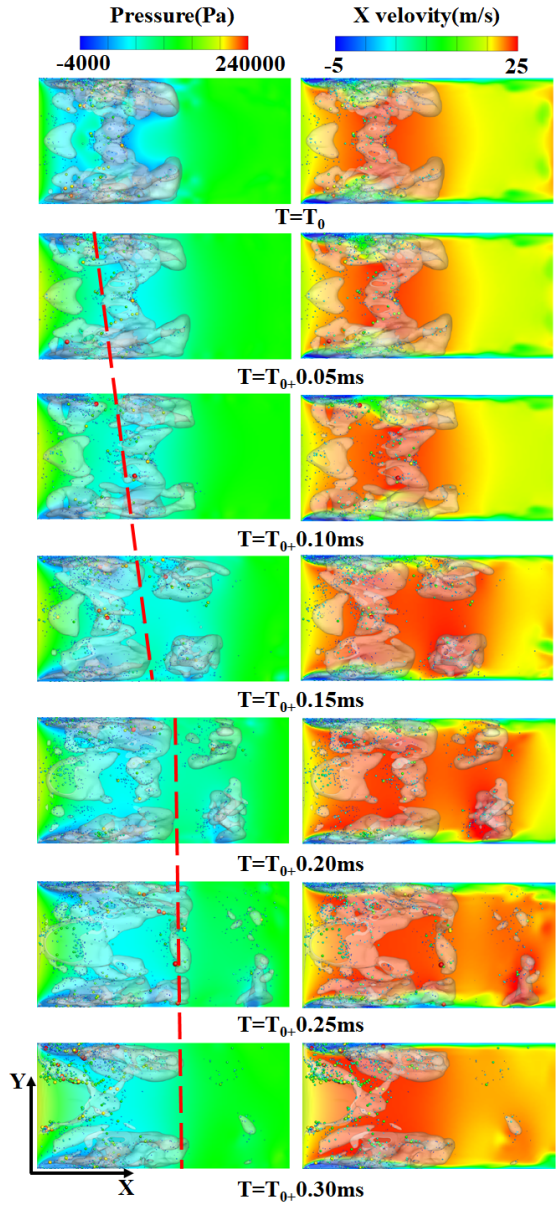

Figure 6. Cloud cavitation shedding and collapse at a cavitation number of $\sigma = 1.64$.

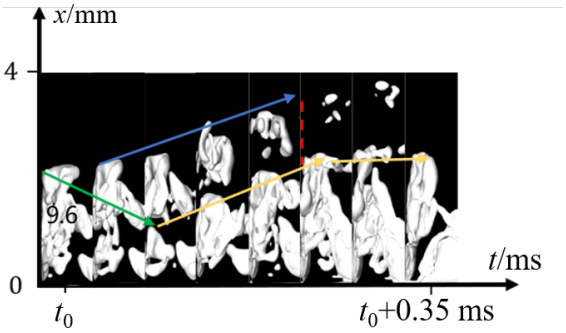

Figure 7. $x - t$ diagram at $\sigma = 1.64$.

cavitation is primarily influenced by the re-entrant jet, with other possible shedding mechanisms playing a negligible role in this process.

4. CONCLUSION

In this study, an Euler-Lagrangian multiscale model is employed to simulate the cavitation process in the nozzle, with a focus on the cavitation shedding mechanism. The VOF method is used to simulate the macroscopic cavity characteristics, while the Lagrangian method is applied to solve for the small-scale structures in the flow field. LES is used to simulate turbulence, and the mechanisms leading to cavitation shedding are investigated at cavitation number of $\sigma = 1.64$. By comparing with experimental results, the accuracy of the multiscale model used in this study is validated. The results reveal that cavitation shedding is primarily induced by the re-entrant jet at the cavitation number of $\sigma = 1.64$. Finally, the clock time per time step when using the VOF-DBM method is 1.17 times longer than that of the VOF method. However, the total simulation clock time with VOF-DBM is 1.2 times shorter due to the larger allowable time step in the VOF-DBM approach.

ACKNOWLEDGEMENTS

This study was funded by the Natural Science Foundation of China (52106155) and the China Postdoctoral Science Foundation (2023M743269).

REFERENCES

[1] Mohan, B., Yang, W., and Kiang Chou, S., 2013, "Fuel injection strategies for performance improvement and emissions reduction in compression ignition engines—A review", *Renewable Sustainable Energy Rev*, Vol. 28, pp. 664–676.

[2] Xuan, T., Maes, N., García-Oliver, J. M., De León-Ceriani, D., Pachano, L., and He, Z., 2022, "Combined experimental and numerical studies on soot characteristics of diesel sprays with split injection strategies", *Combust Flame*, Vol. 246, p. 112384.

[3] Gavaises, M., 2008, "Flow in valve covered orifice nozzles with cylindrical and tapered holes and link to cavitation erosion and engine exhaust emissions", *Int J Engine Res*, Vol. 9, pp. 435–447.

[4] Guan, W., Huang, Y., He, Z., Guo, G., Wang, C., and Thévenin, D., 2024, "Primary breakup of a jet coupled with vortex-induced string cavitation in a fuel injector nozzle", *Phys Fluids*, Vol. 36 (5).

[5] Gavaises, M., Papoulias, D., Andriotis, A., Giannadakis, E., and Theodorakakos, A., 2007, "Link between cavitation development and erosion damage in diesel injector nozzles", *Tech. rep.*, SAE Technical Paper.

[6] Wu, P., Bai, L., Lin, W., and Yan, J., 2017, "Stability of cavitation structures in a thin liquid layer", *Ultrason Sonochem*, Vol. 38, pp. 75–83.

[7] Kadivar, E., el Moctar, O., and Javadi, K., 2018, "Investigation of the effect of cavitation passive control on the dynamics of unsteady cloud cavitation", *Appl Math Modell*, Vol. 64, pp. 333–356.

[8] Oerley, F., Trummler, T., Hickel, S., Mihatsch, M., Schmidt, S., and Adams, N., 2015, "Large-eddy simulation of cavitating nozzle flow and primary jet break-up", *Phys Fluids*, Vol. 27 (8).

[9] Usta, O., Köksal, Ç. S., and Korkut, E., 2023, "A systematic study into the cavitation erosion test for marine propeller materials by cavitating jet technique", *Ocean Eng*, Vol. 284, p. 115252.

[10] Koukouvinis, P., Gavaises, M., Li, J., and Wang, L., 2016, "Large Eddy Simulation of Diesel injector including cavitation effects and correlation to erosion damage", *Fuel*, Vol. 175, pp. 26–39.

[11] Ghahramani, E., Ström, H., and Bensow, R., 2021, "Numerical simulation and analysis of multi-scale cavitating flows", *J Fluid Mech*, Vol. 922, p. A22.

[12] Li, L., Pei, C., Wang, Z., Lin, Z., Li, X., and Zhu, Z., 2024, "Assessment of cavitation erosion risk by Eulerian–Lagrangian multiscale modeling", *Int J Mech Sci*, Vol. 262, p. 108735.

[13] Zwart, P. J., Gerber, A. G., Belamri, T., et al., 2004, "A two-phase flow model for predicting cavitation dynamics", *Fifth International Conference on Multiphase Flow.–Yokohama, Japan.–2004*.

[14] Li, L., Huo, Y., Wang, Z., Li, X., and Zhu, Z., 2021, "Large eddy simulation of tip-leakage cavitating flow using a multiscale cavitation model and investigation on model parameters", *Phys Fluids*, Vol. 33 (9).

[15] Nicoud, F., and Ducros, F., 1999, "Subgrid-scale stress modelling based on the square of the velocity gradient tensor", *Flow Turbul Combust*, Vol. 62, pp. 183–200.

[16] He, Z., Chen, Y., Leng, X., Wang, Q., and Guo, G., 2016, "Experimental visualization and LES investigations on cloud cavitation shedding in a rectangular nozzle orifice", *Int Commun Heat Mass Transfer*, Vol. 76, pp. 108–116.

[17] Pope, S. B., 2000, *Turbulent Flows*, Cambridge University Press.

Conference on Modelling Fluid Flow (CMFF'25)
The 19th International Conference on Fluid Flow Technologies
Budapest, Hungary, August 26 - August 29, 2025

LOW-AMPLITUDE ACOUSTIC MODULATION AS A TOOL FOR CONTROLLING THE VORTEX STRUCTURES OF THE TURBULENT AXISYMMETRIC AIR JET

Nikola ĆETENOVIĆ[2], Dejan CVETINOVIĆ[1], Aleksandar ERIĆ[2], Đorđe ČANTRAK[3], Jaroslav TIHON[4], Kazuyoshi NAKABE[5], Kazuya TATSUMI[5]

[1] Corresponding Author. University of Belgrade, VINCA Institute of Nuclear Sciences, Laboratory for Thermal Engineering and Energy, Belgrade, Serbia, Tel.: +381 63 8433 988, E-mail: deki@vin.bg.ac.rs
[2] University of Belgrade, VINCA Institute of Nuclear Sciences, Laboratory for Thermal Engineering and Energy, Belgrade, Serbia e-mail: nikola.cetenovic@vin.bg.ac.rs
[3] Faculty of Mechanical Engineering, University of Belgrade, Belgrade, Serbia, djcantrak@mas.bg.ac.rs
[4] Institute of Chemical Process Fundamentals, Academy of Sciences of the Czech Republic, Prague, Czech Republic e-mail: tihon@icpf.cas.cz
[5] Mechanical Engineering, Faculty of Engineering, Kyoto University, Kyoto, Japan, e-mail: tatsumi@me.kyoto-u.ac.jp

ABSTRACT

The roll-up of vortex structures in turbulent jets can be influenced by low-amplitude modulations of the nozzle exit velocity. These modulations can be generated either by external low-amplitude oscillations or by self-sustaining oscillations inherent to the operation of specially designed whistler nozzles. The aim of the experimental investigations, mathematical modeling, and numerical simulations carried out as part of the project evaluation was to thoroughly investigate the characteristics and vortex dynamics of acoustically modulated and non-modulated nozzles. A major focus was on identifying effective methods to control vortex structures, as these play an important role in improving heat transfer processes.

This paper presents the results of mathematical modeling and numerical simulations of free and impinging turbulent axisymmetric air jets, both unmodulated and modified by low-amplitude oscillations. The modeling results showed strong agreement with experimental findings confirming the ability to manipulate vortex structures in the jet by acoustically modulating the nozzle exit velocity. This study provides a basis for the development and optimization of technological processes using air jets, particularly in applications where improved heat transfer is critical.

Keywords: Impinging jet, flow control, heat transfer, mathematical modelling, turbulent axisymmetric air jet, vortex structures.

NOMENCLATURE

D	$[m]$	diameter of the nozzle
L	$[m]$	distance of the impact plate from the nozzle exit along the jet axis
Nu	[-]	Nusselt number
Pr	[-]	Prandtl number
Re	[-]	Reynolds number
Re_t	[-]	Reynolds number of vortex structures
St_D	[-]	Strouhal number of the jet
T	$[K \text{ or } °C]$	temperature
U	$[ms^{-1}]$	mean velocity
f	$[Hz]$	frequency
h	$[Wm^{-2}K^{-1}]$	heat transfer coefficient
p_w	$[Pa]$	wall pressure
q_c	$[Wm^{-2}]$	heat flux from the heated surface
r	$[m]$	radial distance from the jet axis
t	$[s]$	time
u'	$[ms^{-1}]$	velocity fluctuation
x	$[m]$	distance in the x-axis direction
x_2	$[m]$	distance from the impact surface toward the nozzle
y	$[m]$	distance in the y-axis direction
λ	$[Wm^{-1}K^{-1}]$	thermal conductivity of the fluid
v	$[m^2s^{-1}]$	kinematic viscosity
τ_w	$[Pa]$	wall shear stress
σ_{ij}	$[Pa]$	total stress

1. INTRODUCTION

Impinging jets is a widely used as a way to provide an effective and flexible transfer of energy or mass in diverse industrial applications. Liquid or gaseous flow released against a surface can efficiently transfer thermal energy or mass between the surface and the fluid. Heat transfer applications include cooling during material forming processes, heat treatment of different materials, cooling of electronic components, heating of surfaces for defogging, cooling of turbine components, cooling of critical machinery structures, and many other similar industrial processes. Typical mass transfer applications include drying and removal of small surface particulates. Abrasion and heat transfer are interesting for vertical/short take-off and landing jet devices in the case of direct lift propulsion systems. The heat transfer rate can be assumed as a complex function of many parameters: Reynolds number (*Re*), Prandtl number (*Pr*), the non-dimensional nozzle to plate spacing (*L/D*), and the non-dimensional displacement from the stagnation point (*r/D*), also nozzle geometry, flow confinement, initial turbulence intensity of the jet, dissipation of jet temperature, etc. [1], [2], [3], [4], [5]. Vortex structures of impinging jet are confirmed by a number of authors to have great importance in the impinging jet heat transfer. Primary vortices, which roll-up in the jet shear layer, induce an unsteady flow separation at the wall, prohibiting the heat transfer between the wall and the fluid jet. Thus, controlling of them necessary leads to the control of the heat transfer from the jet to the wall, and vice versa. It is found that the vortex roll-up can be controlled by adding small amplitude modulation of the nozzle exit velocity.

Subject of present work is submerged, round, unconfined impinging air jet, issuing from a bell-shaped converging nozzle [6], [7] and from the specially designed whistler nozzle [8]. The aim of the investigation is to qualitatively describe the vortex structure of the free and impinging jet and to examine the possibility of its control by low-amplitude modulation of the nozzle exit velocity by external source of sound and self-sustained resonant sound oscillations generated in the operation of the whistler nozzles. The vortex roll-up is generally triggered by a perturbation of the shear layer, which is amplified by the shear layer instability [9], [10]. The perturbation can also be a random noise wave arriving from the environment, from an upstream flow system, or from a downstream flow event. The modulation of the nozzle exit velocity acts as an additional source of disturbances, which overwhelms the natural disturbances if the modulation is strong enough. Modulation of the nozzle exit velocity controls the vortex roll-up and hence all structure of the turbulent axisymmetric jet [11], [12].

2. EXPERIMENTAL RESULTS

Series of measurements along the jet centreline and in the plane normal to the jet at the nozzle exit is provided, to explore influence of the small amplitude perturbation to the structure of free turbulent axisymmetric air jet issuing from a bell-shaped nozzle [6], [7].

The experimental configuration used for measuring the flow field in the impinging jet system is schematically depicted in Figure 1. It comprised a bell-shaped converging nozzle, a settling chamber, a flow disturbance mechanism, an impingement plate positioned perpendicular to the jet axis, an air supply system, and a control and data acquisition system. The bell-shaped nozzle, constructed from a plastic material, had an outlet diameter of 25 *mm*. Air entered the settling chamber via two centrally located pipes, subsequently passing through four grids and a honeycomb structure. The final section of the settling chamber was equipped with both a pressure tap and a temperature sensor.

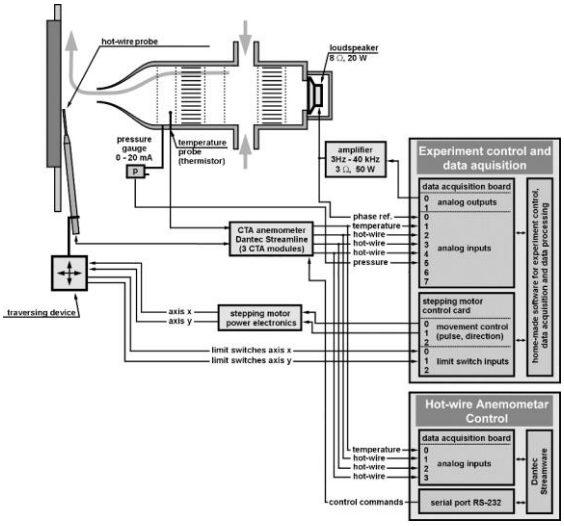

Figure 1. Experimental setup for experiments in an impinging jet configuration

Air jet normalized velocity profiles and normalized velocity r.m.s. profiles at the free jet centreline are shown on the Figure 2. The profiles were measured up to $L=8D$ downstream distances from the nozzle lip. Figure 2. shows the change in the normalized velocity and velocity r.m.s. profiles along the jet axis for a fixed Reynolds number, $Re=10000$, different excitation Strouhal number, $St_D=0.3\text{-}2.12$, and excitation amplitude in the range $u'/U_e=1\text{-}3\%$.

From presented figures can be clearly distinguished four ranges of Strouhal number where jet behaviour can be considered as very similar. First excitation Strouhal number range is around naturally most amplified mod of excitation (called “preferred mode”, [3]), $St_D\approx0.3$. Second belongs to the

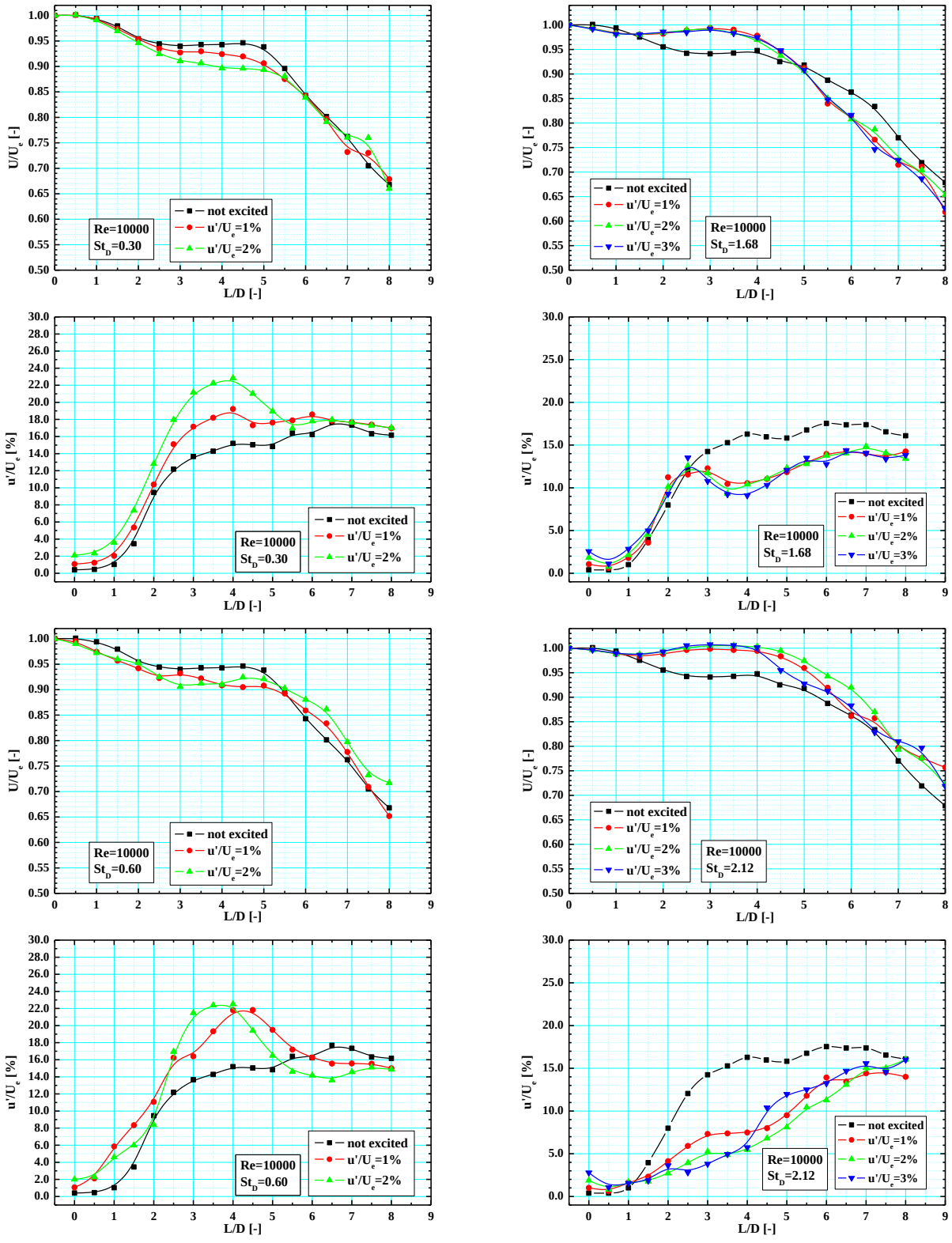

Figure 2. Normalized velocity and velocity r.m.s. profiles along the jet centreline; – flow and excitation conditions: *Re*=10000; St_D=0.3-2.12; u'/U_e=1-3%

frequency range around double most amplified mod value, St_D≈0.6-0.7, denoted in the literature as a stable vortex pairing mode. Third excitation Strouhal number range are values around St_D≈1.0 and fourth is above St_D≈1.8. All excitation modes have their own characteristics that can be explored more deeply.

Looking at the normalized velocity profiles in the excitation Strouhal number range around naturally most amplified mode, St_D=0.2-0.4, can be obviously seen that excitation make influence in shortening of the jet potential core, from previous value between 4.5 and 5 nozzle diameters to value between 3 and 4 diameters, depending on the excitation amplitude. From the shape of the normalized velocity one can conclude that potential core still exists, but peripheral vortices, grown in size, can be found in the centreline on smaller axial distance from the nozzle lip.

Second excitation Strouhal number range, St_D=0.5-0.8, denotes stable vortex pairing mode of excitation, is characterized by more sudden decrease in the jet potential core length. Peak in the normalized velocity r.m.s. appear at the smaller axial distance from the nozzle lip at a slightly higher value than in the previously described excitation range, which coincides with the conclusion that the jet potential core disappears on smaller axial distance. Increase in the excitation amplitude does not produce significant increase in the normalized velocity r.m.s. profile, like some kind of saturation exists. This fact can be explained by redistribution of the energy in the jet faced with a vortex pairing, and high amount of energy used for this process.

Range of excitation around Strouhal number St_D≈1.0, is characterized with a high intermittency and unstable behaviour. Jet potential core is somehow extended, and normalized mean velocity at the jet centreline increased, but depending on the excitation condition some big difference between very close measuring points is found and repeated so many times in experiments. This discontinuity clearly seen in the normalized velocity r.m.s. profiles look like some discrete “jumps” from one jet behaviour to another, from one frequency regime to another.

Excitation in the range above St_D≥1.8, has produced higher velocities in the areas at the higher axial distance from the nozzle lip and significant decrease in the normalized velocity r.m.s. comparing to the not excited case, especially in the excitations with a Strouhal numbers above St_D≥2.0. Influence of excitation amplitude here is negligible in both normalized velocity profiles and normalized velocity r.m.s. profiles in all investigated excitation amplitude range.

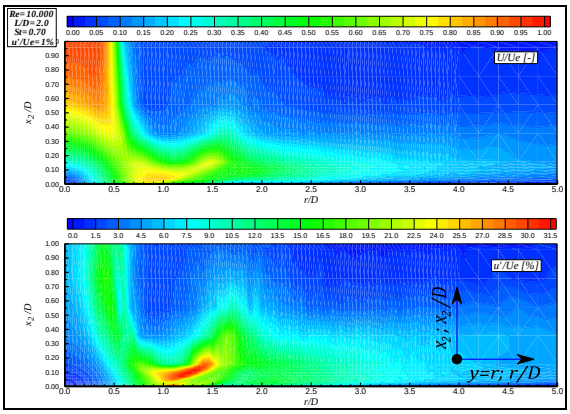

Figure 3. Normalized mean velocity and turbulence intensity fields in the area 1*D*x5*D* above impinging surface - with the sound excitation; Re=10000; St_D=0.7; u'/U_e =1%; *L/D*=2

Figure 3. shows the fields of normalized velocity, and turbulence intensity of the modified axisymmetric turbulent jet of Reynolds number *Re* = 10000 with excitation Strouhal number St_D=0.7 and the initial amplitude of the oscillations u'/Ue = 1%. The jet impinges to the flat surface placed perpendicular to the jet axis at an axial distance *L/D*=2. Measurement results are extracted from very intense net measurements with a hot wire anemometry in the area 1*D*x5*D* above the impinging surface. In spite of jet velocity reduction, as a consequence of sound modification, the profile of the normalized velocity shows great resemblance to the profile of the unmodified stream and the same flow characteristics for the same impinging distance. Jet slightly accelerated on the path around stagnation zone and vortices from the jet shear layer descend into the boundary layer at the wall of the impinging surface, causing the separation streamline at the same radial distance that we observed in the experiments without sound modification. In the turbulence intensity field can be observed intensification of the vortical structures in the shear layer close to the impinging surface, which is accompanied by abrupt changing of the flow direction and acceleration of the flow around the stagnation zone.

Figure 4. illustrates the process of vortex penetration from the jet shear layer into the boundary layer flow on the wall of the impinging surface. Induced velocity angle between the wall and ejected vortex path depends on the speed of rotation of the incoming vortex.

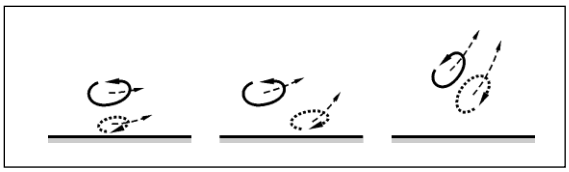

Figure 4. Vortex approaching boundary layer on the impinging surface (injective phase). The primary vortex - a solid line; spot - the secondary vortex; dash-line - induced velocity from the wall (ejective phase)

The analysis of the presented turbulence intensity field, Figure 3., which corresponds to the case of Strouhal number St_D = 0.7 modification, it can be argued that the angle at which the vortex ejects from the impinging surface is greater with respect to the rest of the modification cases investigated. In this mode, the excitation leads to the stable pairing of vortices and the newly formed vortex created in the process of pairing is stronger, with the higher rotation speed, which leads to a larger bounce angle.

The measurement of velocity field in the case of Strouhal number modification St_D = 2.01 is shown in Figure 5. The results confirm the specificity of this modification. Specifically, this case of modification is not characterized with injective and ejective movement of vortices near the impinging surface shown on previous figure. A series of vortices formed in the shear layer of the jet near the impinging surface are with lower vorticity and vortices are not powerful enough to initiate this phenomenon. Stream lines do not separate from the impinging plate wall, even flow was accelerated around stagnation zone, causing uniformity in a turbulence intensity profile on a large range of radial distances from the axis of the jet. The influence of the initial amplitude of the sound oscillations in the jet in this particular excitation Strouhal number range is negligible, so that the modification of the u'/Ue =3%, shown in Figure 5., are not significantly different from the cases of lower-amplitude external excitation investigated.

From the standpoint of controlling fluid structure with the help of external acoustic modifications this Strouhal number range looks most suitable. Very uniform zone of turbulence intensity, which has been verified for all investigated axial distances between the nozzle lip and impinging surface, can be considered as very predictable characteristic controlled by sound modifications with Strouhal number $St_D \geq 2.0$. Here, however, must be noted that the realization of such high value Strouhal number in the special nozzle design that produce self-sustained oscillation – whistler nozzle, can be very difficult.

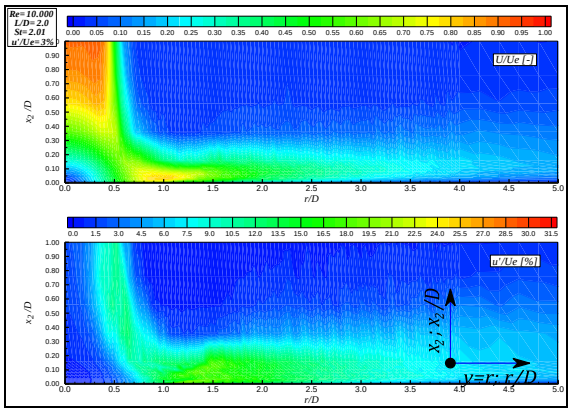

Figure 5. Normalized mean velocity and turbulence intensity fields in the area 1*D*x5*D* above impinging surface - with the sound; *Re*=10000; St_D=2.0; u'/U_e =3%; *L/D*=2

As part of the experimental investigations, visualization of the free jet emerging from the nozzle was also performed. The studied cases correspond to Strouhal numbers of 0, 0.3 and 0.52, while the Reynolds number was 91000 and the nozzle diameter was 18 *mm*. The presented images (Figure 6.) were obtained using a PIV (Particle Image Velocimetry) system. The recorded jet length was 7*D*.

In the first image, corresponding to the unexcited jet, it can be observed that the potential core, characterized by an unchanged velocity relative to the nozzle exit, contracts and vanishes at axial distances of $L/D \geq 5$.

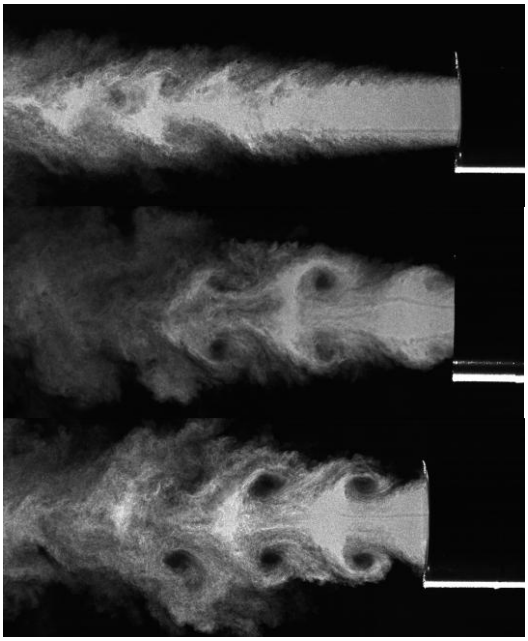

Figure 6. Visualization of the free jet at Reynolds number *Re* = 91000 for Strouhal numbers St_D = 0 (top image), St_D = 0.3 (middle image) and St_D = 0.52 (bottom image)

In the second image, it is evident that excitation with a Strouhal number of St_D = 0.3 (close to the "preferred" excitation mode) generates vortex structures in the form of highly regular vortex rings with high rotational velocity around the vortex core. The potential core is significantly shorter, and pronounced axial oscillations can be observed.

The third image shows the case with excitation at St_D = 0.52, where the potential core is longer than in the previous case. The large vortices are not regular in shape, because they are formed by the pairing of multiple vortex structures along their path from the nozzle exit. At smaller axial distances from the nozzle exit, this case of excitation leads to more pronounced radial spreading of the jet, which has also been confirmed by hot-wire anemometry velocity measurements.

3. MATHEMATICAL MODELLING

In most of practical engineering situations the impinging jets are modelled using different turbulent models. As already pointed out by many researchers, the most of the turbulence models were developed for flows, which are parallel to the wall. Therefore, their applicability to impinging jet is limited because of significant differences from parallel flows:

- kinetic energy of turbulence in the vicinity of the axis of symmetry (i.e. stagnation point) is generated by the normal stresses (for flows parallel to the wall this role have shear stresses);
- the velocity fluctuation component normal to the wall is of the same order, or even larger than the component parallel to the wall; in parallel flows, the normal component is much smaller;
- the local turbulent length scales near the wall are strongly affected by the length scale of jet turbulence; in parallel flows, the length scales are determined by the distance from the wall;
- in impinging jets, there is an important convective transport of turbulence toward the stagnation point; in parallel flow, the convective transport is usually negligible and the turbulence production and dissipation are approximately in equilibrium.

The initial assumption of the model is that the air is an incompressible Newtonian fluid with temperature dependent characteristics. Numerical simulation of temperature and calculation of the flow field in numeric domain requires solving the continuity equation (3.1), Reynolds averaged Navier-Stokes equations of motion (3.2) and time-averaged energy equation (3.3), presented in the index tensor notation in the form of:

$$\frac{\partial U_i}{\partial x_i} = 0 \tag{3.1}$$

$$\frac{\partial U_i}{\partial t} + U_i \frac{\partial U_j}{\partial x_j} = -\frac{1}{\rho}\frac{\partial P}{\partial x_i} + \frac{\partial}{\partial x_j}\left[\nu\left(\frac{\partial U_i}{\partial x_j} + \frac{\partial U_j}{\partial x_i}\right) - \overline{u_i u_j}\right] \tag{3.2}$$

$$\rho\frac{DT}{Dt} = \rho\frac{\partial T}{\partial t} + \rho U_j \frac{\partial T}{\partial x_j} = \frac{\partial}{\partial x_i}\left[\frac{\mu}{\mathrm{Pr}}\frac{\partial T}{\partial x_i} - \rho\overline{\theta u_i}\right] \tag{3.3}$$

Attempts of the numerical calculation of the flow and temperature field of the fluid flow, formed in the case of the jet impinging on a flat heated plate, carried out using standard two-equation turbulence models and standard Reynolds-stress models, showed disagreements with the experimentally determined physical situation. The highest degree of disagreement was observed in the stagnation area of the jets, especially in the calculation of local values of Nusselt numbers.

In the case of two-equation models of turbulence, the reason for these disagreements is usually their known property, to provide relatively wrong predictions for extremely non-isotropic flows. This property is a consequence of their design based on differential transport equations for scalar quantities (k and ε, or k and ω), and the fact that practically all two-equation turbulent models are developed for shear turbulent flows.

Based on the Boussinesq's turbulent viscosity hypothesis, Reynold's stress is a function of the local gradient of velocity and turbulent viscosity ν_t. The coefficient of the turbulent viscosity takes into account viscous interactions of the fluid and is not a physical property of the fluid. By analogy with the constituent relation between the laminar stresses and the deformation rate, the dependence between the turbulent stress and the velocity gradient of averaged fluid flow can be obtained in the form:

$$-\rho\overline{u_i u_j} = \tau_{ij} = \mu_t\left(\frac{\partial U_i}{\partial x_j} + \frac{\partial U_j}{\partial x_i}\right) = \mu_t S_{ij},$$

which is known in the literature as the linear concept of turbulent viscosity. The introduction of the coefficient μ_t (or its kinematic variant ν_t) enables the closure of the system of equations of turbulent motion and the method of its calculation defines the type of model for turbulent flow modelling (μ_t is not a model itself).

In the case of shear turbulent flows, this coincidence and proportionality are more or less present, but in the stagnation zone of the flow generated by impingement of the jet to the surface, the presumption of such dependence is no longer adequate. In this zone, instead of the appearance of the shear, the processes of the fluid particles compression are the dominant ones. This means that those parts of the averaged velocity tensor

responsible for the normal, rather than shear deformations, dominantly change.

If the turbulent stresses for this case of physical fluid flow are modeled in accordance with Boussinesq's hypothesis, this results in a wrong prediction of the turbulence kinetic energy and the linear increase of the corresponding normal turbulent stresses. This erroneous prediction process, for *k-ε* and *k-ω* models, is reflected through an enlarged term of the modeled turbulent viscosity, since the increase in the kinetic energy of turbulence causes the turbulent viscosity to increase in proportion to the square of its value.

Energy equation (3.3) has a term $\frac{\mu_t}{\Pr}\frac{\partial T}{\partial x_i}$, which is not capable to distinguish difference between the effects of certain Reynolds stresses, consequently leads to excessive increase in the enthalpy flow that increase local value Nusselt numbers in the stagnation area.

By moving away from the stagnation point and transformation into the wall jet, the results of numerical calculations are increasingly approaching experimentally measured values. These approximations are not surprising, as with the transition from "non-shear" to a shear turbulent flow, the Boussinesq's hypothesis accurately predicts the relationships between the Reynolds stress tensors and the averaged fluid particle deformation rate tensor. Correctly establishing these relationships leads to an increased accuracy of numerical/mathematical predictions.

In this paper will be shown mathematical models that use turbulent scalar quantities k and ε to calculate ν_t, which are obtained by solving the following set of modeled transport equations:

$$U_i\frac{\partial k}{\partial x_i}=\frac{\partial}{\partial x_i}\left[\left(\mu+\frac{\mu_t}{\sigma_k}\right)\frac{\partial k}{\partial x_i}\right]+\mu_t\left(\frac{\partial U_i}{\partial x_j}+\frac{\partial U_j}{\partial x_i}\right)\frac{\partial U_i}{\partial x_j}-\rho\tilde{\varepsilon} \tag{3.4}$$

$$\rho U_i\frac{\partial \varepsilon}{\partial x_i}=\frac{\partial}{\partial x_i}\left[\left(\mu+\frac{\mu_t}{\sigma_\varepsilon}\right)\frac{\partial \varepsilon}{\partial x_i}\right]+f_1C_1\mu_t\frac{\varepsilon}{k}\left(\frac{\partial U_i}{\partial x_j}+\frac{\partial U_j}{\partial x_i}\right)\frac{\partial U_i}{\partial x_j}-\rho f_2C_2\frac{\varepsilon^2}{k}+E \tag{3.5}$$

$$\mu_t=\rho f_\mu C_\mu\frac{k^2}{\varepsilon} \tag{3.6}$$

$$\tilde{\varepsilon}=\varepsilon+D \tag{3.7}$$

$$\mathrm{Re}_T=\frac{\rho k^2}{\mu\varepsilon};\ \mathrm{Re}_{x_2}=\frac{\rho\sqrt{k}x_j}{\mu};\ \mathrm{Re}_\varepsilon=\frac{\rho(\mu\varepsilon/\rho)^{1/4}x_j}{\mu} \tag{3.8}$$

where C_μ, C_1, C_2, σ_k and σ_ε are the same empirical constants for turbulent models as those used in *k-ε* models for large Reynolds numbers. The "dumping functions" f_μ, f_1 and f_2, and in some models, the used terms *D* and *E* are used to improve the accuracy of the flow model near the wall. The detailed physical meaning of these "dumping functions", as well as terms *D* and *E*, with the criteria for determining the correctness of these functions for the flow near the wall are given in the reference Patel et al., 1985 [13].

The modification of the *k-ε* model for small Reynolds turbulent numbers (so called Low-Reynolds-Number Models) allows their use in the vicinity of the wall. The modification involves inserting a “dumping function” into the original term of the transport equation for *ε*, and in the expression for turbulent viscosity μ_t.

The "damping functions" allow these equations to be used in a turbulent boundary layer, including a viscous sublayer, but on the other hand they apply only to this case of flow and cannot be applied in other fluid flows.

A modified transport equation for *ε* (3.5) for using the dumping functions f_μ, f_1 and f_2 takes the form:

$$\rho U_i\frac{\partial \varepsilon}{\partial x_i}=\frac{\partial}{\partial x_i}\left[\left(\mu+\frac{\mu_t}{\sigma_\varepsilon}\right)\frac{\partial \varepsilon}{\partial x_i}\right]+\frac{\varepsilon}{k}(f_1C_{1\varepsilon}\mu_tS^2-\rho f_2C_{2\varepsilon}\varepsilon) \tag{3.9}$$

Low-Reynolds number modification of the basic *k-ε* model that will be presented in the paper are Abid, 1993, [14], Lam and Bremhorst, 1981, [15], Launder and Sharma, 1974, [16] Abe, Kondoh and Nagano, 1994, [17], and Chang, Hsieh and Chen 1995, [18].

4. RESULTS OF NUMERICAL SIMULATIONS

The subject of numerical analysis in this research was to examine the performance of several different, so called, low-Reynolds number modification of the basic *k-ε* model (Abid, 1993, Lam and Bremhorst, 1981, Launder and Sharma, 1974, Abe, Kondoh and Nagano, 1994, and Chang, Hsieh and Chen 1995) using commercial CFD code Fluent-Ansys, applied to the problem of jet impinging on a flat surface positioned perpendicular to its propagation.

Application of the low Reynolds number k-ε model modification for this phenomenon requires a very high density of the network with the wall itself, y^+ on a cell at the wall must be at least 1. Preferred optimum is 10 cells in the viscous sub-layer. The calculation was made in double precision coupled solver, and the convergence was achieved when normalized residuals of the dependent variable in the last 10 iterations are less than 10^{-7}.

The geometric model used in the simulations is two-dimensional, and only half of the domain was analyzed due to the axisymmetric nature of the problem. The nozzle diameter is 18 *mm* and the axial distance between the nozzle exit and the impingement surface was varied to obtain *L/D* ratios of 2, 4, 6 and 8, thereby altering the control volume accordingly. The radial distance from the nozzle's axis of symmetry to the outer boundary of the domain is 10*D*. The computational mesh is structured and refined in key regions, particularly near the nozzle exit, in the stagnation region, and along the wall-jet zone. The mesh elements are quadrilateral. Boundary conditions were defined such that air exits the nozzle at a temperature of 300 *K*, with a velocity corresponding to Reynolds numbers of 10000 and 20000, discharging into a quiescent ambient air environment with the same temperature. The impingement surface is modeled as an isothermal wall providing a constant heat flux of 1500 W/m^2 to the fluid. The influence of body forces is considered negligible, and the flow is assumed to be incompressible. To enhance the accuracy of the numerical solution, a second-order discretization scheme was employed.

To characteristics of the jet depending on the excitation Strouhal number suitable for the industrial application here will be presented only fragment of the numerical results. Results of unsteady two-dimensional CFD numerical simulation of pressure fields in the free jet modified by acoustic oscillations, give us the opportunity to analyse the influence of the excitation Strouhal number on the type and character of vortex structures on the periphery of the jet that occur as a result of these modifications. Time step in the numerical calculation is carefully selected to strictly reproduce the entire sinusoidal change of jet velocity, depending on the Strouhal number of the excitation [19, 20].

On Figure 7. are shown pressure fields in a free jet (in the selected time) in the case of the Reynolds number Re_D=10000 modified by acoustic oscillations with Strouhal number St_D=0.3, 0.6 and 2.0 and the oscillation amplitude of 20%. Only one half of the jet issuing from the nozzle (bottom left side of Figures) is presented due to the axisymmetry of the problem.

From pathlines of the pressure shown above, representing different excitation conditions with Strouhal number St_D=0.3, 0.6 and 2.0, can be clearly seen shape and size of vortices formed due to excitation modification. Numerical simulation confirmed that conclusions derived from experimental analysis given in previous chapters are correct.

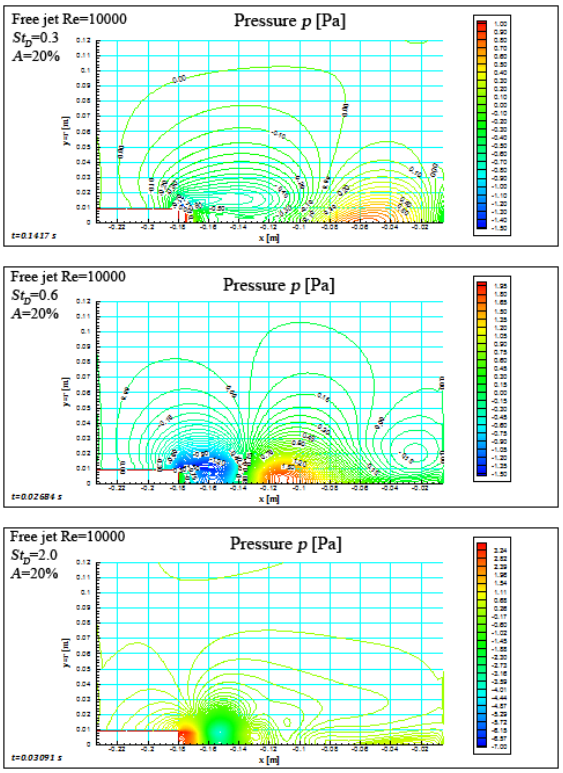

Figure 7. Pressure field in the sound modified turbulent axisymmetric jet; *Re*=10000; St_D=0.3-2.0

Numerical simulation of the excitation case with Strouhal number St_D=2.0 showed that train of vortices small in size formed at the nozzle lip, are very fast disintegrated in the area close to the nozzle making uniformity in the field on a larger axial distance. This analysis also confirms that this excitation range around Strouhal number St_D=2.0 can be very interesting for applications.

It is noted that the agreement with the experimental results is very good at all distances from the jet axis, for which it is certainly because of the inlet velocity setting based on the experimentally determined values. As the analysis of the profiles from Figure 8. can be concluded, the software does not provide calculations in cells that are close to the wall of the impact plate, but it uses a wall function that contains a dumping function that is characterized by each of the tested modifications of the *k-ε* model.

The calculation is not conducted in the whole area in the vicinity of the wall (from the image shows that the first cell of which enter into the calculation at a distance x_2/D=0.025) so that the observed differences in the cells just above the wall zone can be ascribed to the very method of calculation. When further away from the impact plate, the velocity profile follows the profile of the measured values in a satisfactory accuracy.

It may be noted that all five tested modifications of the standard *k-ε* model shows some differences in averaged velocity profiles at four radial cross-

sections shifted from the axis of the jet shown in Figure 8. This was to be expected, since all five modifications *k-ε* models have the same constants of the *k-ε* model, and differ only in the applied coefficients characterized by the "damping" functions, so that the differences can be expected in the profiles of the production of turbulence kinetic energy and the coefficient of heat transfer.

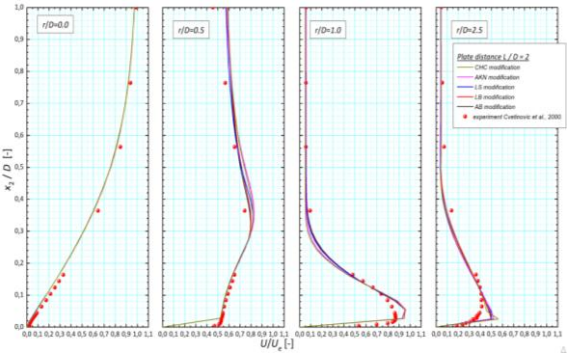

Figure 8. Averaged velocity profiles for Re_D = 20000, *L/D* = 2; Comparison of own experimental results with numerical simulation results for five modifications of the *k-ε* model for low Reynolds turbulent numbers

Changes in the value of local Nusselt number (for comparison with other authors in the form of $Nu/Re^{0.7}$) for several distances from the nozzle are given in the following figures, Figure 9-12.

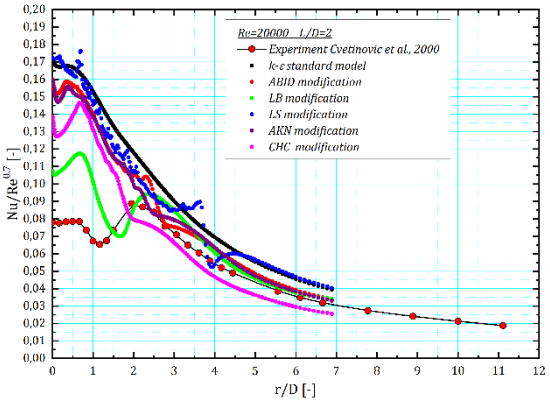

Figure 9. Local Nusselt number profiles for Re_D = 20000, *L/D* = 2; Comparison of own experimental results with numerical simulation results for five modifications of the *k-ε* model for low Reynolds turbulent numbers

Calculated heat transfer coefficients in the case of the smallest distance of the impinging surface from the nozzle outlet *L/D*=2 are given in Figure 9. In general, all 5 modifications of the standard *k-ε* turbulence model for low Reynolds turbulent numbers improve the prediction of local heat transfer coefficients in the impact zone jet against the base model. However, the prediction also exceeds the values of the Nusselt numbers determined experimentally in the *r/D*<2 zone. It can be noticed that some of the proposed modifications and numerically unstable, there was a slight divergence of the solution. There is a particularly notable disagreement with experimentally determined values at higher radial distances from the jet stream which is unacceptable and can be explained by poor selection of damping functions and/or the lack of a justified criterion in the calculation for the application of “damping functions” whose role is to damp production of the kinetic turbulence energy in this zone.

By moving the impinging surface to greater distances from the nozzle outlet, the results of the calculation approach the measured values, as can be seen in Figure 10., which represents the calculated values of the local heat transfer coefficients in the case of distance *L/D* = 4 from the impinging plate from the output from nozzle.

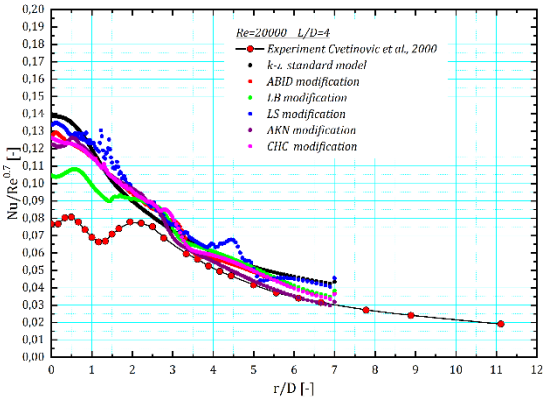

Figure 10. Local Nusselt number profiles for Re_D = 20000, *L/D* = 4; Comparison of own experimental results with numerical simulation results for five modifications of the *k-ε* model for low Reynolds turbulent numbers

The presented results of calculations of the distance *L/D* = 4 still above the measured but still can claim to better anticipate local Nusselt numbers of basic *k-ε* model in the stagnation zone of the jet. Calculations instability is retained in some modifications of the standard turbulence model for low Reynolds turbulent numbers, which is also reflected in the jumps at some of the radial distributions shown in Figure 10. Also, the observed distributions indicate a deviation from the measured values at higher radial distances from the jet axis.

For larger distances of the impinging surface from the outlet of the nozzle of *L/D* = 6 and 8, shown in Figures 11. and 12., it is evident much better agreement with the measured values and, also, evident improvement over the standard *k-ε* turbulence model.

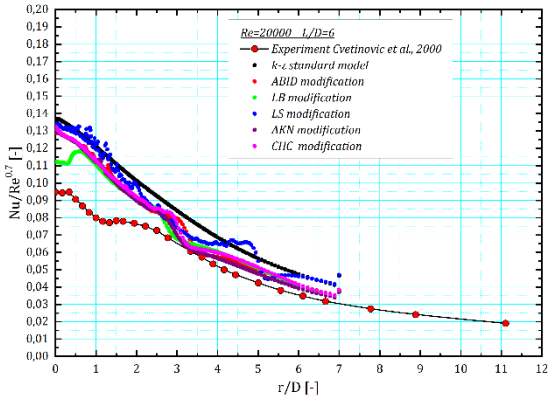

Figure 11. Local Nusselt number profiles for Re_D = 20000, L/D = 6; Comparison of own experimental results with numerical simulation results for five modifications of the k-ε model for low Reynolds turbulent numbers

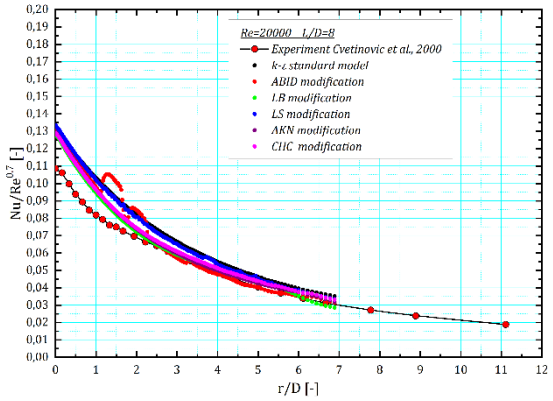

Figure 12. Local Nusselt number profiles for Re_D = 20000, L/D = 8; Comparison of own experimental results with numerical simulation results for five modifications of the k-ε model for low Reynolds turbulent numbers

The objective of the numerical investigation of the heat transfer from a turbulent axisymmetric jet to a flat surface that was set up normally on the jet centerline was to examine the performance and possibilities in predicting local Nusselt numbers of the simplest two-equation turbulence models, and by several authors of the proposed modifications of the standard two-equation k-ε turbulence model for low Reynolds turbulent numbers.

Although the prediction of the local heat transfer coefficients over predicts the experimental data, better predictive results have been achieved than some that are listed in the literature. The reason for this is in the carefully given input parameters in the calculations corresponding to the experimental results with which the comparison was made.

5. CONCLUSIONS

Stagnation heat transfer can be augmented by increasing not only the time averaged approach velocity and turbulence intensity but also the characteristic frequency of the jet to hit the impinging surface with large-scale vortical structure, which is the main characteristic of the late-transitional region of the jet. Large-scale eddies on the heat transfer target surface intermittently impinge onto the boundary layer around the stagnation point. Such areas can be considered to have adverse gradients of the instantaneous surface pressure very often because the gradients of the time averaged surface pressure are almost zero there. If a target plate is situated in the transitional region of a turbulent free jet, therefore, unsteady separation-like reverse flow could occur at and near the stagnation point owing to the intermittent impingement of large-scale vortical structures on the target plate.

In this paper was demonstrated the ability to control eddy structure in the axisymmetric turbulent jet by sound modulations of jet velocity at the exit of the nozzle as an attractive possibility to be used in the technological processes. In fact, sometimes it is necessary to intensify the mixing of primary fluid flow and the surrounding fluid (in the chemical reactor), by sound modulation which intensifies eddy structures in a jet shear layer, while, for example, to achieve uniformity of the heat transfer coefficient on a major surface of the impinging surface it is necessary to apply modulation with totally different frequency.

The objective of the numerical investigation of the heat transfer from a turbulent axisymmetric jet to a flat surface that was set up normally on the jet centerline was to examine the performance and possibilities in predicting local Nusselt numbers of the simplest two-equation turbulence models, and by several authors of the proposed modifications of the standard two-equation k-ε turbulence model for low Reynolds turbulent numbers.

Prediction of the local heat transfer coefficients is better than some that are listed in the literature. The reason for this is in the carefully given input parameters in the calculations corresponding to the experimental results with which the comparison was made. This study can serve as a base for development and optimization of the technological processes that involve air jet.

ACKNOWLEDGEMENTS

This research was funded by the Ministry of Science, Technological Development and Innovation of the Republic of Serbia, Grant no. 451-03-66/2024-03/200017 («Vinča» Institute of Nuclear Sciences, National Institute of the Republic of Serbia, University of Belgrade) and Science Fund of the Republic of Serbia - Green Program of Cooperation between Science and Industry - project STABILISE.

REFERENCES

[1] Jambunathan, K., Lai, E., Moss, M. A., Button, B. L., 1992: A review of heat transfer data for single circular jet impingement, *International Journal of Heat and Fluid Flow*, vol. 13, no. 2, pp. 106-115

[2] Zuckerman, N. and Lior, N., 2006: Jet impingement Heat Transfer: Physics, Correlations and Mathematical Modelling, *Advances in Heat Transfer*, Volume 39, ISSN: 0065-2717, DOI: 10.1016-S0065-2717(06)39006-5, pp. 565-631

[3] Behnia, M., Parneix, S., Durbin, P. A., 1998: Prediction of heat transfer in an axisymmetric turbulent jet impinging on a flat plate, *International Journal of Heat and Mass Transfer*, vol. 41, no. 12, pp. 1845-1855

[4] Chen, H., Chong, K. L., 2025: Heat transfer mechanisms in impinging jets: The role of vortex dynamics, *International Journal of Heat and Mass Transfer*, vol. 248, Article 127142

[5] Rönnberg, K., Duwig, C., 2021: Heat transfer and associated coherent structures of a single impinging jet from a round nozzle, *International Journal of Heat and Mass Transfer*, vol. 173, Article 121197

[6] Cvetinovic D., Tihon J., Verjazka J., Drahos J., 2004: "Effect of external excitations on the axisymmetrical air jet flow structures - Investigations of the Free Jet", *CHISA 2004*, 22-26. August 2004, Prague, Czech Republic, P5.237, ISBN 80-86059-40-5

[7] Cvetinovic D., Tihon J., Verjazka J., Drahos J., 2004: "Effect of external excitations on the axisymmetrical air jet flow structures - investigations of the jet impinging on a flat surface", *CHISA 2004*, 22-26. August 2004, Prague, Czech Republic, P5.236, ISBN 80-86059-40-5

[8] Hussain A.K.M.F. and Hasan M.A.Z., 1983: The "Whistler-nozzle" Phenomenon, *J. Fluid Mech*., vol. 134, pp. 431-458

[9] Zaman, K. B. M. Q., Hussain, A. K. M. F., 1980: Vortex pairing in a circular jet under controlled excitation, Part 1. General jet response, *Journal of Fluid Mechanics*, vol. 101, part 3, pp. 449-491

[10] Hussain, A. K. M. F., Zaman, K. B. M. Q., 1980: Vortex pairing in a circular jet under controlled excitation. Part 2. Coherent structure dynamics, *Journal of Fluid Mechanics*, vol. 101, part 3, pp. 493-544

[11] Hussain, A. K. M. F., 1986: Coherent structure and turbulence, *Journal of Fluid Mechanics*, vol. 173, pp. 303-356

[12] Suresh, P. R., Srinivasan, K., Sundararajan, T., Das, Sarit K., 2008: Reynolds number dependence of plane jet development in the transitional regime, *Physics of Fluids*, vol. 20, Article 044105

[13] V. C. Patel, W. Rodi and G. Scheuerer: Turbulence Models for Near-Wall and Low Reynolds Number Flows: A Review August 1985, *AIAA Journal* 23(9):1308-1319, https://doi.org/10.2514/3.9086

[14] Abid, R., 1993: Evaluation of two-equation turbulence models for predicting transitional flows, *International Journal of Engineering Science* 31 (6) (1993) 831–840.

[15] Lam, C.K.G., Bremhost, K., 1981: A modified form of the k–ε model for prediction wall turbulence, *Transactions of the ASME, Journal of Fluids Engineering* 103 (1981) 456–460.

[16] Launder, B.E., Sharma, B.I., 1974: Application of the energy-dissipation model of turbulence to the calculation of flow near a spinning disc, *Letters in Heat and Mass Transfer* 1 (1974) 131–138.

[17] Abe, K., Kondoh, T., Nagano, Y., 1994: A new turbulence model for predicting fluid flow and heat transfer in separating and reattaching flows I: Flow field calculations, *International Journal of Heat and Mass Transfer* 37 (1) (1994) 139–151.

[18] Chang, K.C., Hsieh, W.D., Chen, C. S., 1995: A modified low-Reynolds-number turbulence model applicable to recirculating flow in pipe expansion, *Transactions of the ASME, Journal of Fluids Engineering*, 117, pp. 417–423.

[19] Cvetinović D. B., Stefanović P. Lj., Bakić V. V., Oka S. N., Review of the research on the turbulence in the laboratory for thermal engineering and energy, Thermal Science 2017 Volume 21, Issue suppl. 3, Pages: 875-898, doi: 10.2298/TSCI160221330C

[20] Cvetinović D. B., Ćetenović N. M., Erić A. M., Anđelković J. D., Čantrak Đ. S., Transient modeling of impinging heat transfer from an acoustically modulated turbulent air jet to a normally positioned flat surface, Thermal Science 2025 Volume 29, Issue 1 Part B, Pages: 767-780, doi: 10.2298/TSCI2501767C

Conference on Modelling Fluid Flow (CMFF'25)
The 19th International Conference on Fluid Flow Technologies
Budapest, Hungary, August 26 - August 29, 2025

BEM SIMULATION OF AN EXPANDING / CONTRACTING BUBBLE IN VISCOELASTIC FLUIDS

Koki Asano[1], Honami Nishimura[2], Haruki Furukawa[3],
Tim Phillips[5], Steven Lind[6], Shuichi Iwata[4]

[1] Department of Life-Science and Applied Chemistry, Graduate School of Engineering, Nagoya Institute of Technology, Gokiso-cho, Showa-ku, Nagoya, Aichi, 466-8555, Japan. Tel: +81-52-735-5256, Fax: +81-52-735-5255, E-mail: k.asano.057@nitech.ac.jp
[2] Department of Life-Science and Applied Chemistry, Graduate School of Engineering, Nagoya Institute of Technology, Gokiso-cho, Showa-ku, Nagoya, Aichi, 466-8555, Japan, E-mail: h.nishimura.929@nitech.jp
[3] Department of Life-Science and Applied Chemistry, Graduate School of Engineering, Nagoya Institute of Technology, Gokiso-cho, Showa-ku, Nagoya, Aichi, 466-8555, Japan, E-mail: furukawa.haruki@nitech.ac.jp
[4] Corresponding Author. Department of Life-Science and Applied Chemistry, Graduate School of Engineering, Nagoya Institute of Technology, Gokiso-cho, Showa-ku, Nagoya, Aichi, 466-8555, Japan, E-mail: iwa@nitech.ac.jp
[5] School of Mathematics, Cardiff University, E-mail: PhillipsTN@cardiff.ac.uk
[6] School of Engineering, Cardiff University, E-mail: LindS1@cardiff.ac.uk

ABSTRACT

We measured motion of rising bubble under pressure-oscillating field, and reported a significant enhancement of the rising velocity up to approximately 400 times for a shear-thinning fluid with 1–5 mm^3 bubbles in 0.8 wt% aqueous sodium polyacrylate (SPA) (Iwata *et al.* JNNFM, 2008). Complex local flow is observed as uniaxial extension occurred at the tail of the bubble during the contraction phase as well as the biaxial extensional deformation occurred at the upper side of the bubble (Iwata *et al*., JNNFM, 2019). To analyze the flow near the bubble, Ito *et al*. analyzed the motion of an expanding/contracting rising bubble in the Carreau-Yasuda model fluid by FEM analysis (Reoroji Gakkaishi, 2020). However, the FEM analysis didn't take into account the effect of viscoelasticity of surrounding fluid.

Therefore, we applied the boundary element method (BEM) to the problem of an expanding/contracting bubble and modelled the fluid external to the bubble as a viscoelastic fluid. The bubble is initially located near a rigid wall. In this study, the Giesekus model is used as a viscoelastic model. We aim to clarify the influence of the rigid wall on the deformation and dynamics of an expanding/contracting bubble.

Keywords: Deformation, Boundary Element Method, Viscoelastic fluid, Rigid wall, Giesekus model

NOMENCLATURE

h	[-]	non-dimensional position of bubble center
P_b	[Pa]	pressure of bubble
P_0	[Pa]	initial bubble pressure
P_{ref}	[Pa]	pressure of viscoelastic fluid
$\dot{\gamma}$	[s^{-1}]	shear rate
η	[Pa·s]	shear viscosity
η_0	[Pa·s]	zero-shear viscosity
η_p	[Pa·s]	viscosity of polymer solutions
η_s	[Pa·s]	solvent viscosity
η_e	[Pa·s]	extensional viscosity
$\dot{\varepsilon}$	[s^{-1}]	elongation velocity
N_1	[Pa]	first normal stress difference
λ_1	[s]	relaxation time
λ_2	[s]	delay time
μ	[Pa·s]	viscosity of viscoelastic fluid
ρ	[kg/m^3]	density of viscoelastic fluid
γ	[J/(kg·K)]	specific heat
ω	[rad/s]	angular frequency
G'	[Pa]	storage modulus
G''	[Pa]	loss modulus
T	[Pa]	extra stress
n	[-]	subscript indicating the normal direction
$T_{nn}{}^p$	[Pa]	the normal-normal component of stress T in the polymeric part
σ	[N/m]	surface tension
C	[m^{-1}]	curvature
∇	[m^{-1}]	gradient operator
V	[m^3]	bubble volume
V_0	[m^3]	initial bubble volume
R_0	[m]	initial bubble radius
R_m	[m]	maximum bubble radius

r	[m]	r-coordinate
z	[m]	z-coordinate
t	[s]	time
$\mathbf{x}$	[-]	position vector
$\mathbf{u}$	[-]	irrotational velocity vector
$\mathbf{S}$	[s^{-1}]	rate of strain of tensor
α	[-]	Giesekus model parameter
Re	[-]	Reynolds number
De	[-]	Deborah number
We	[-]	Weber number
N_b	[-]	number of nodes on the bubble
k	[-]	nodal number
ϕ	[-]	dimensionless velocity potential
r^*	[-]	dimensionless r-coordinate
z^*	[-]	dimensionless z-coordinate
t^*	[-]	dimensionless time
E	[-]	ratio of the solvent viscosity to the zero-shear viscosity

1. INTRODUCTION

A tiny air bubble in viscoelastic fluid moves upward at a very slow rising velocity due to the fluid viscosity. Thus, the bubble may take a very long time to travel through the fluid. To address this issue, Iwata *et al*. proposed the Pressure-Oscillation Deforming (POD) method.

This method involves applying pressure oscillations from the vessel to the fluid containing bubbles, which gives rise to alternating expansion and contraction of the bubbles. The cyclical change in bubble diameter due to pressure oscillations generates strong, continuous local flows and shear near the bubble, giving rise to lower local viscosity in the case of shear-thinning fluids. This viscosity reduction significantly accelerates the bubble rise velocity up to more than 400 times in the case of 1–5 mm³ bubbles in a 0.8 wt% aqueous sodium polyacrylate (SPA) solution (zero-shear viscosity η_0 = 90 Pa·s) [1]. The experimental snapshots indicate that the bubble forms a spherical shape during the expansion phase and develops a cusped shape at the tail of the bubble during the contraction phase.

To further investigate bubble dynamics, Ito *et al*.[2] performed numerical analysis of the flow around a bubble using the unsteady finite element method. The fluid properties of Carreau-Yasuda model were fitted with experimental data with steady shear measurements of a 0.8 wt% SPA solution by a stress-controlled rheometer. The results showed that in a purely viscous fluid subjected to 1 Hz oscillations from below, the local shear rate increased at the bottom of the bubble during the contraction phase and at the top during the expansion phase. However, under these conditions, it was difficult to observe a cusped bubble, as the elastic effects were not considered in this analysis.

Therefore, the boundary element method (BEM) was considered to quantitatively evaluate the behavior of a bubble in viscoelastic fluids. Lind and Phillips [3] performed BEM analysis of an oscillating bubble near a rigid wall in an infinite space filled with an upper convected Maxwell fluid. In the present study, instead of employing the Maxwell model, we introduced the Giesekus model, which exhibits shear-thinning behavior and increases has a first normal stress difference that increases moderately with increasing shear rate. Additionally, to ensure a realistic representation of the system, we fitted the model's rheological properties to match those of the high-viscosity experimental fluid with zero-shear viscosity η_0 of approximately 90 Pa·s. The numerical modelling in the following sections focuses on the effects of viscoelastic properties on bubble shape, stress distribution, surface tension, and jet velocity dynamics.

2. NUMERICAL ANALYSIS

2.1. Governing Equations

The continuity equation, the momentum equation are expressed by equations (1) to (2), given the following assumptions. The internal energy equation is ignored since there is no heat or mass transfer through the boundary, and temperature is assumed to be constant. Since the fluid is assumed to be incompressible, the fluid density remains constant, and the continuity equation reduces to a velocity constraint. Under this condition, equation (3) is derived. The assumption of irrotationality results in the curl of the velocity vanishing, thus implying the existence of a velocity potential, and the velocity field can be expressed as shown in equation (4). Substituting this into equation (4), it can be seen that this potential satisfies Laplace's equation in the fluid domain. In addition, based on arguments due to Joseph and coworkers (see for example, Joseph and Liao[4]), it is assumed that the viscoelastic effects are only introduced through the boundary conditions, and that the viscosity/rheological effects in the fluid bulk are negligible in this case.

The calculations were performed in a two dimensional cylindrical coordinate system. The initial bubble shape was assumed to be spherical and the bubble center was placed at a distance h, the standoff distance, from the rigid wall. The continuity equations (5), equations of motion (6) and constitutive equations (7) at the bubble surface of the Giesekus model are shown below. The pressure p_b in the bubble is obtained from equation (8). Since the flow inside the fluid is assumed to be potential, the momentum equation can be expressed using the potential ϕ, and equation (6) is obtained by reformulating the Navier–Stokes equation using the velocity potential and including the free-surface stress balance in normal direction at the bubble surface. In addition, equation (7) is the constitutive equation of the Giesekus model, which includes a

nonlinear term to represent shear-thinning behavior.

$$\frac{D\rho}{Dt} + \rho\nabla\cdot\mathbf{u} = 0 \tag{1}$$

$$\rho\frac{D\mathbf{u}}{Dt} = -\nabla P_{ref} + \nabla\cdot\boldsymbol{\tau} \tag{2}$$

$$\nabla\cdot\mathbf{u} = 0 \tag{3}$$

$$\nabla^2\phi = 0 \tag{4}$$

$$\frac{D\mathbf{x}}{Dt} = \nabla\phi \tag{5}$$

$$\rho\frac{D\phi}{Dt} = \frac{\rho}{2}|\mathbf{u}|^2 - 2\eta_s\frac{\partial^2\phi}{\partial n^2} - T_{nn}^{\ p} + \sigma C + P_{ref} - P_0\left(\frac{V_0}{V}\right)^{\gamma} \tag{6}$$

$$\lambda_1\frac{DT_{nn}^{\ p}}{Dt} = -T_{nn}^{\ p} + 2\lambda_1 T_{nn}^{\ p}\frac{\partial^2\phi}{\partial n^2} - \alpha\frac{\lambda_1}{\eta_p}T_{nn}^{\ p2} + 2\eta_p\frac{\partial^2\phi}{\partial n^2} \tag{7}$$

$$P_b = P_0\left(\frac{V_0}{V}\right)^{\gamma} \tag{8}$$

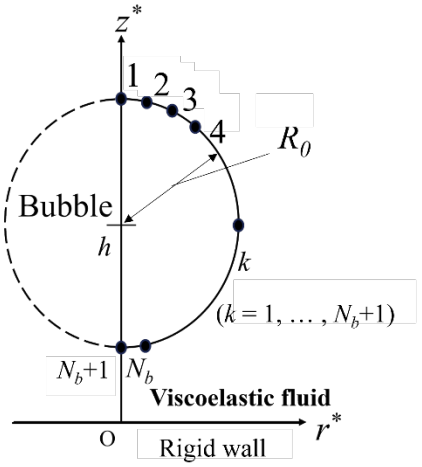

Fig. 1 Schematic diagram of initial conditions when a rigid wall is set up near a bubble.

2.2. Model Set-up

The numerical modelling was performed in a flow field filled with viscoelastic fluid surrounding a single bubble near a rigid wall. As shown in **Fig. 1**, the center of the bubble is initially positioned at a distance h from the rigid wall located at z^*=0, and a two-dimensional axisymmetric flow was assumed with the z-axis in the vertical direction.

2.3. Numerical methods

The bubble surface was discretized into N_b (N_b = 40) segments by distributing N_b+1 nodes on the bubble from the north to south poles of the bubble. Then, the quintic spline representations of the nodal positions (r, z) and potential ϕ were integrated over each interval on the bubble interface using the Gaussian quadrature. The normal stress τ_{nn} is obtained by solving the constitutive equation, and finally, the coordinates (r,z) and the potential ϕ are updated by the fourth-order Runge-Kutta method, respectively.

2.4. Material

The properties of 5 wt% CMC *aq.* measured by a stress-controlled rheometer (MCR302-WESP, Anton Paar, Ltd.) were assumed. Ansys Polymat was used to fit the solution properties to the Giesekus model. The solution density ρ[kg/m^3], initial viscosity η_0, relaxation time λ_1[s], and ratio of the fluid viscosity to the zero-shear viscosity E [-] were determined. A typical value of 1000 kg/cm^3 was used for the density of water. As for the viscoelastic 5wt% CMC solution, the density is ρ = 1049.54 kg/m^3. Zero-shear viscosity η_0 is 90.49 Pa·s.

The viscosity ratio $E = \frac{\eta_s}{\eta_0}$ is obtained as E = 1.105×10^{-5}.

Additionally, two values of the relaxation time λ_1 were considered: λ_1 =0.02 s and λ_1 =10 s. Furthermore, the specific heat ratio γ was set to 1.25, following Walter *et al*.[5].

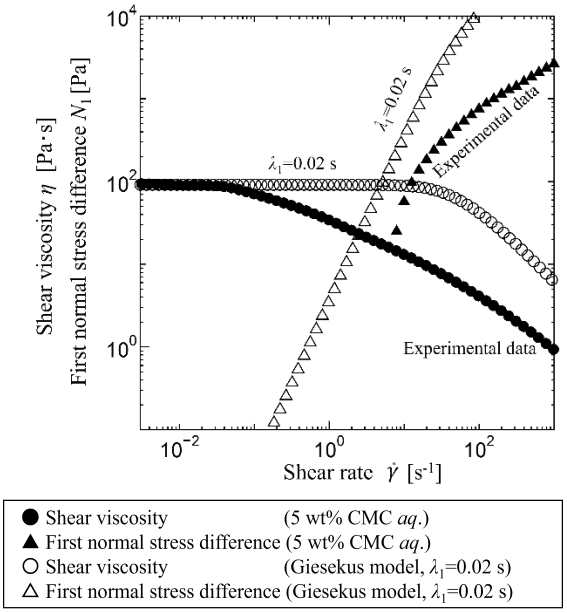

Fig. 2 Profiles of rheological properties of 5 wt% CMC*aq.* and fitting curves of Giesekus model (α = 0.3)

3. RESULTS AND DISCUSSION

We investigated the expansion and contraction phases of a bubble placed near a rigid wall using the Giesekus model (α = 0.3). We analyzed the influence of the initial standoff distance on bubble shape and examined the temporal variations in jet velocity. Furthermore, we conducted a detailed study on the effects of shear stress fields and polymeric stress. In this calculation, the coordinates r and z, as well as

time t, were non-dimensionalized using equations (9) ~ (11) as follows. The dimentionless numbers are defined as shown in equations (12) thorough (14). Here, R_m represents the maximum bubble radius attained by a bubble in an infinite expanse of inviscid fluid.

$$r^* = \frac{r}{R_m} \tag{9}$$

$$z^* = \frac{z}{R_m} \tag{10}$$

$$t^* = \frac{t}{R_m}\left(\frac{p_{ref}}{\rho}\right)^{\frac{1}{2}} \tag{11}$$

$$Re = \frac{R_m}{\eta}\left(\left(P_{ref}\right)\rho\right)^{1/2} \tag{12}$$

$$De = \frac{\lambda_1}{R_m}\left(\frac{P_{ref}}{\rho}\right)^{\frac{1}{2}} \tag{13}$$

$$We = \frac{R_m P_{ref}}{\sigma} \tag{14}$$

3.1. Effect of initial standoff distance

The results corresponding to a relaxation time λ_1= 0.02 s are presented below. As for h = 2.0, the fluid flow acted in the upward direction and obliquely downward, contributing to the formation of an interesting shape during the contraction phase as shown in **Fig. 3 – (c) to (f)**. Local concentration of stress on the lateral sides of the bubble resulted from these oblique jet flows, leading to complex deformation. The maximum of T_{nn} at head of the bubble reached approximately 0.1, highlighting the strong nonlinear effects. This behavior is attributed to the weakened influence of the wall, allowing the fluid to deform more freely.

When the bubble was initially positioned closer to the wall (h = 1.0), a vertically downwards jet flow acted from upward, causing the upper side of the bubble to fold inward during the contraction phase. Strong stress distribution was observed at the upper part of the bubble as shown in **Fig. 4**. In particular, negative stress (negative value defined to be in the outward direction from the bubble surface) concentrated locally in the upper deformation region, indicating a pronounced effect of shear stress. The depressed shape at the bubble top was caused by strong elastic effects and closer proximity to the wall.

In the case of h = 4.0, a horizontal jet flows from the sides contributing to the extension in the vertical direction, with local extra stress up to 0.3 at the center during the contraction phase as shown in **Fig. 5**. As a result, the delayed relaxation of polymer stress caused bubble elongation, leading to a bubble shape at the onset of fragmentation. In this case, the wall's influence was smaller, forming a uniform stress field except for necking area.

(a) t^* = 0 (Initial bubble)

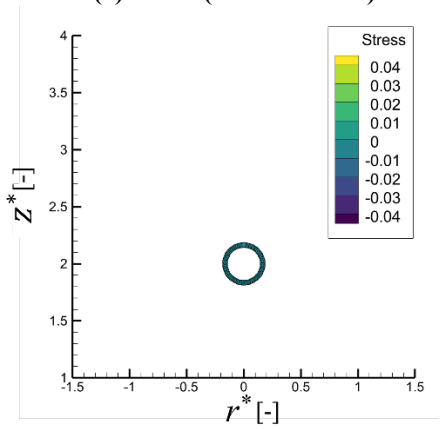

(b) t^*=0.5530 (Expansion phase)

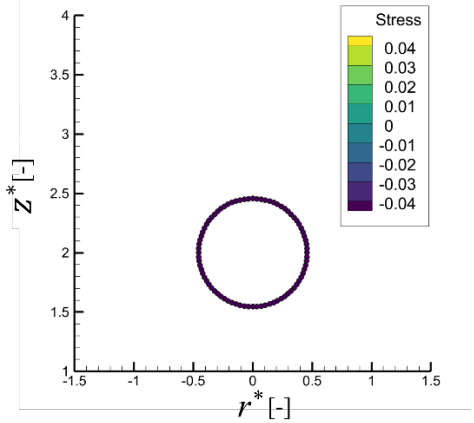

(c) t^*=2.184 (Contraction phase)

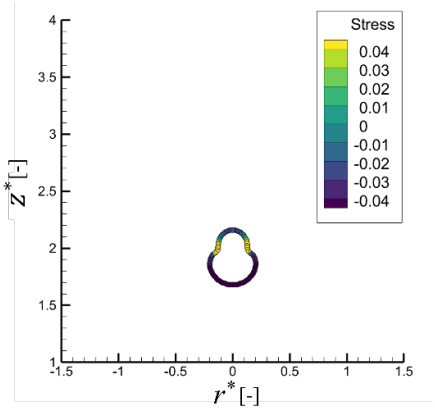

(d) t^*=2.648 (Expansion phase)

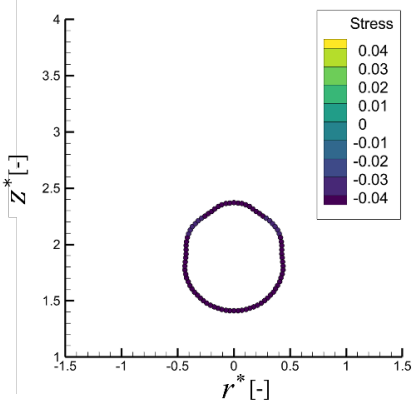

(e) t^*=3.143 (Contraction phase)

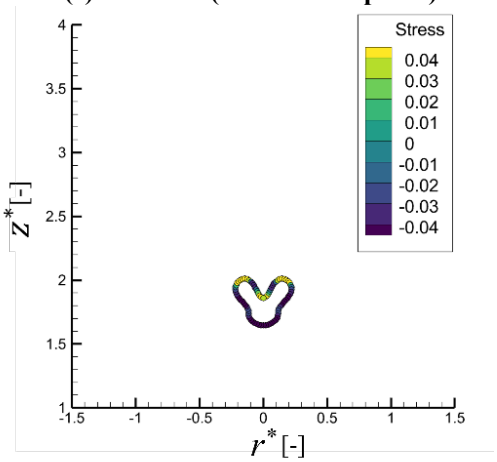

(f) t^*=3.219 (Most contraction phase)

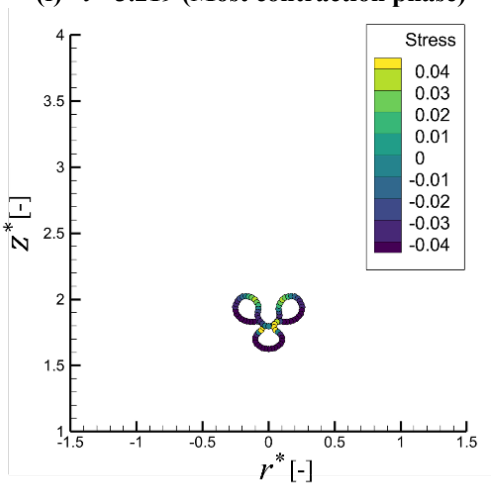

Fig. 3 Profiles of bubble shape and stress distribution in the Giesekus model at h=2.0. (η_0 = 90.49 Pa·s, λ_1 = 0.02 s, σ = 0 mN/m, γ=1.25, α = 0.3, Re = 0.1137, De = 195.2, We^{-1} = 0)

Final shape(t^*=1.100, Contraction phase)

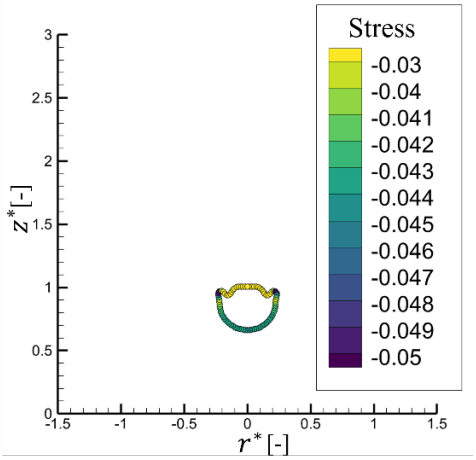

Fig. 4 Profiles of bubble shape and stress distribution in the Giesekus model at h=1.0. (η_0 = 90.49 Pa·s, λ_1 = 0.02 s, σ = 0 mN/m, γ=1.25, α = 0.3, Re = 0.1137, De = 195.2, We^{-1} = 0)

Final shape (t^*=5.191, Contraction phase)

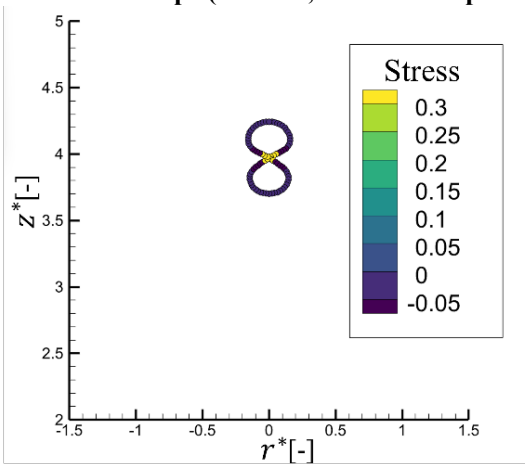

Fig. 5 Profiles of bubble shape and stress distribution in the Giesekus model at h=4.0. (η_0 = 90.49 Pa·s, λ_1 = 0.02 s, σ = 52.5 mN/m, γ=1.25, α = 0.3, Re = 0.1137, De = 195.2, We^{-1} = 0)

3.2. Effect of Surface tension

To help understand the factors which lead to the formation of the various bubble shapes, we examined the effect of surface tension at the bubble surface. The calculations were performed by varying the reciprocal of the Weber number We^{-1}, while keeping the reference pressure of the viscoelastic fluid P_{ref} and the maximum bubble radius R_m constant. When the surface tension is set to zero, i.e., We^{-1} = 0, the results are shown in **Fig. 3**. In contrast, the result for a surface tension σ = 52.5 mN/m, corresponding to a 1 wt% CMC aqueous solution at 25 °C, is presented in **Fig. 9.** In this case, it is observed that the bubble expands and contracts alternately while maintaining its spherical shape. The stress is observed to be uniformly distributed across the entire bubble interface, with no significant local concentration of stress. This is likely occurred because the surface tension helps to maintain the smooth and symmetrical bubble shape. Additionally, the results for near-zero surface tension conditions specifically σ = 0.0725 mN/m and σ = 0.725 mN/m are shown in **Figs. 10** and **11**, respectively. Other unique bubble shapes and significant deformation were observed in both cases. A similar final bubble shape to the zero surface tension case was observed at $We^{-1} = 7.18\times10^{-4}$ as shown in **Fig.10**. The pinch off points can be observed to take place in lateral regions around the bubble, as shown in **Fig.11**.

(a) **Initial bubble (t^*= 0)**

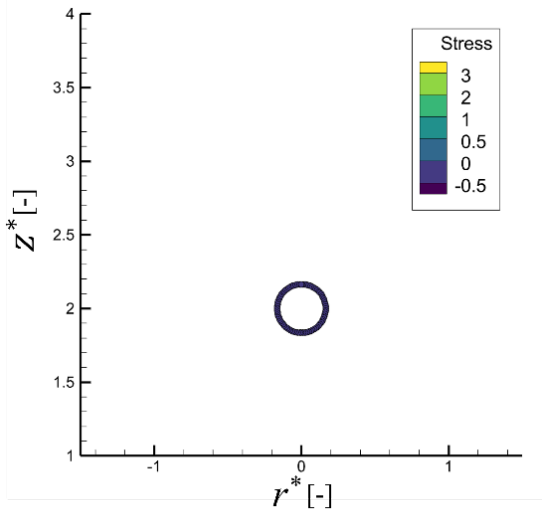

(b) **Expansion phase (t^*= 24.34)**

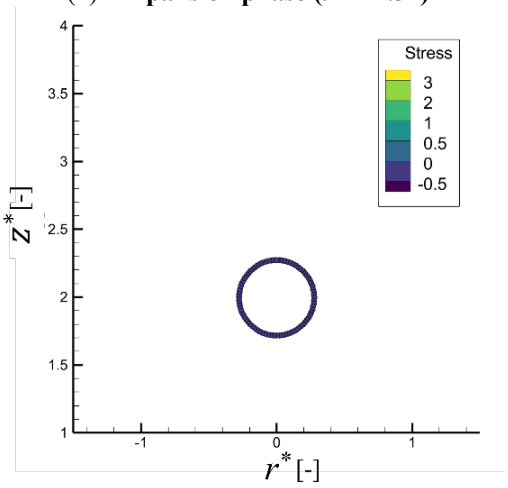

(c) **Final shape (t^*= 84.66, Contraction phase)**

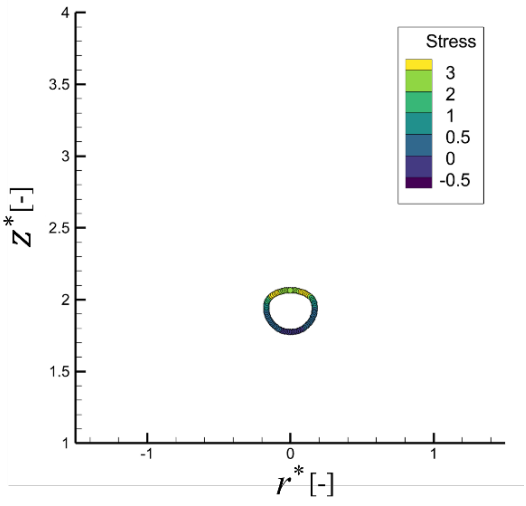

Fig. 9 Profiles of bubble shape and stress distribution in the Giesekus model at h=1.0. (η_0 = 90.49 Pa·s, λ_1= 0.02 s, σ = 52.5 mN/m, γ=1.25, α = 0.3, Re = 0.1137, De = 195.2, We^{-1} = 0.5198)

Final shape (t^*=3.194, Contraction phase)

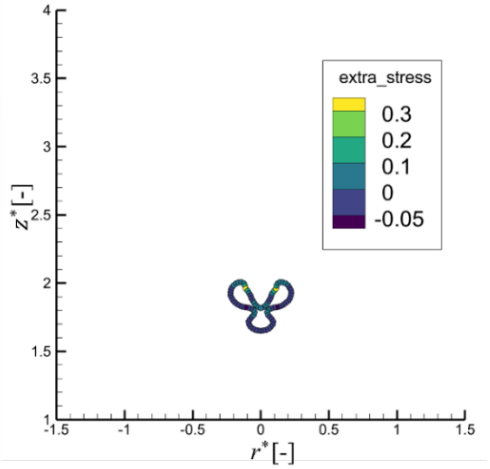

Fig. 10 Profiles of bubble shape and stress distribution in the Giesekus model at h=1.0. (η_0 = 90.49 Pa·s, λ_1=0.02 s, σ = 0.0725 mN/m, γ=1.25, α = 0.3, Re = 0.1137, De = 195.2, We^{-1} = 0.000718)

Final shape (t^*=3.186, Contraction phase)

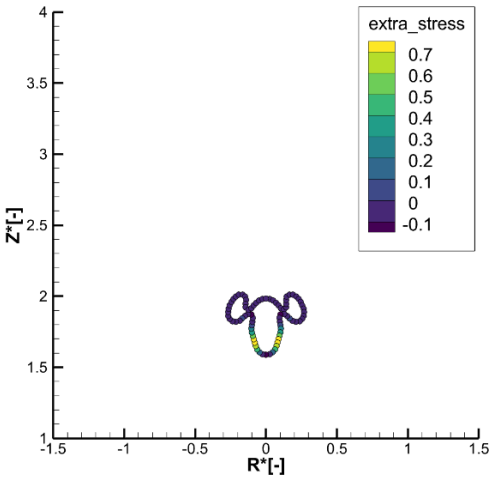

Fig. 11 Profiles of bubble shape and stress distribution in the Giesekus model at h=1.0. (η_0 = 90.49 Pa·s, λ_1= 0.02 s, σ = 0.725 mN/m, γ=1.25, α = 0.3, Re = 0.1137, De = 195.2, We^{-1} = 0.00718)

3.3. Investigation based on Shear rate

For a relaxation time λ_1 = 0.02 s and zero-shear viscosity η_0 = 90.49 Pa·s, the shear rate $\dot{\gamma}$ was calculated using the rate of deformation tensor **S**, defined by following equation (15). Additionally, the shear rate $\dot{\gamma}$ was calculated at the points on the bubble interface where the strongest stress acts during the contraction phase as shown in **Table 1**.

$$\dot{\gamma} = \sqrt{2\mathbf{S}:\mathbf{S}} \qquad (15)$$

$$\mathbf{S} = \frac{1}{2}\left(\nabla\mathbf{u} + \left(\nabla\mathbf{u}\right)^{T}\right) \tag{16}$$

In the case of **Fig.4** (h = 1.0), strong local stress occurred at the upper bubble surface, where the local shear rate at node number k=1 was observed to be up to 687 s^{-1} during the contraction phase. However, a weaker local stress was observed in lower regions with lower local shear rates around 100 s^{-1}.

As for the case of **Fig.3** (h = 2.0), the maximum shear rate was observed at k = 1 during the expansion phase, with a local shear rate of 4.281 s^{-1}. The bubble exhibited an interesting shape during the contraction phase, with the strongest stress acting at the bubble's center. The local shear rate at this point was up to 2960 s^{-1} in the final contraction phase as shown in **Fig.3-(f)**. It can be seen that the bubble is ready to pinch off into three parts.

In the case of **Fig.5** (h = 4.0), the bubble deformed into a vertically contracted shape during the contraction phase, with the strongest stress occurring at k = 21. The local shear rate at this point was 199 s^{-1}.

Table 2 shows the local shear rates under the condition of h = 2.0 as a function of surface tension. Shear rates are extremely higher for all cases during the contraction phase. In the zero-tension case (σ = 0 mN/m), the peak shear rate reaches 2936 s^{-1} at t^*=3.218. Introducing a low surface tension of σ = 0.0725 mN/m reduces this peak by approximately 80% to 522 s^{-1} at the same phase. For σ = 0.725 mN/m, the peak is about 1536 s^{-1}, and the peak is suppressed to just 195s^{-1} at σ = 52.5 mN/m.

Table 1 Details of the local shear rate in the Giesekus model. (η_0 = 90.49 Pa·s, λ_1 = 0.02 s, γ=1.25, α = 0.3)

Height h [-]	Nodal number k [-]	Dimentionless time t^* [-]	Shear rate $\dot{\gamma}$ [s^{-1}]
1.0	1	0.5530 (Expansion phase)	2.88
		1.100 (Contraction phase)	687
2.0	1	0.5530 (Expansion phase)	4.28
		3.218 (Contraction phase)	2960
4.0	21	1.552 (Expansion phase)	0.548
		5.191 (Contraction phase)	199

Table 2 Details of local shear rate in the Giesekus model due to differences in surface tension at the bubble surface. (η_0 = 90.49 Pa·s, λ_1 = 0.02 s, γ=1.25, α = 0.3)

Height h [-]	Surface tension σ [mN/m]	Nodal number k [-]	Dimentionless time t^* [-]	Shear rate $\dot{\gamma}$ [s^{-1}]
2.0	0	1	0.5530 (Expansion phase)	4.28
			3.218 (Contraction phase)	2960
2.0	0.0725	1	0.5527 (Expansion phase)	1.82
			3.186 (Contraction phase)	522
2.0	0.725	1	0.5529 (Expansion phase)	1.82
			3.194 (Contraction phase)	1536
2.0	52.5	1	24.34 (Expansion phase)	2.72
			84.66 (Contraction phase)	195

CONCLUSIONS

We performed a numerical simulation to analyze the expansion and contraction behavior of a bubble placed near a rigid wall in a viscoelastic fluid using the Giesekus model (α = 0.3).

It was found that the deformation of the bubble varied significantly depending on the initial distance between the bubble and the rigid wall. This is due to the combined influence of the restricted fluid movement near the wall and the rheological properties of the viscoelastic fluid, which together influence the deformation of the bubble. Moreover, the results indicate that surface tension significantly affects the morphology of the bubble.

ACKNOWLEDGEMENTS

This work was supported by JSPS KAKENHI Grant Numbers (20K04285 and 23K03673) from the Japan Society for Promotion of Science (JSPS).

REFERENCES

[1] S. Iwata et al., 2008, "Pressure-oscillation deforming for viscoelastic fluid," *Journal of Non-Newtonian Fluid Mechanics*, Vol.151(1-3), pp.30-37.

[2] S. Ito et al., 2020, "Numerical simulation of a rising bubble in a shear-thinning fluid under pressure-oscillating field," *Nihon Reoroji Gakkaishi*, Vol.48, No.3, pp.145-151.

[3] Lind, S.J. and Phillips, T.N., 2012. The influence of viscoelasticity on the collapse of cavitation bubbles near a rigid boundary. *Theoretical and Computational Fluid Dynamics*, *26*, pp.245-277.

[4] Joseph, D.D. and Liao, T.Y., 1994. Potential flows of viscous and viscoelastic fluids. *Journal of Fluid Mechanics*, *265*, pp.1-23.

[5] M.J.Walters et al., 2015, "An Investigation into the Effects of Viscoelasticity on Cavitation Bubble Dynamics with Applications to Biomedicine,", Cardiff University

Conference on Modelling Fluid Flow (CMFF'25)
The 19th International Conference on Fluid Flow Technologies
Budapest, Hungary, August 26 - August 29, 2025

A COMPREHENSIVE ANALYSIS OF VARIABLE INLET GUIDE VANE ON CAVITATION AND HYDRAULIC PERFORMANCE OF AN AXIAL-FLOW PUMP

Duc-Anh NGUYEN[1,2], Jin-Hyuk KIM[1,2*]

[1] Convergence Manufacturing System Engineering (Green Process and Energy System Engineering), University of Science & Technology, Daejeon, 34113, South Korea
[2] Carbon Neutral Technology R&D Department, Korea Institute of Industrial Technology, Cheonan, 31056, South Korea
* Correspondence author: Jin-Hyuk Kim (Ph.D.) E-mail: jinhyuk@kitech.re.kr

ABSTRACT

Addressing cavitation in axial-flow pumps is crucial for enhancing efficiency, reducing vibration, and extending pump lifespan. Therefore, this study proposes a novel approach to increase hydraulic performance and mitigate cavitation at different flow rates by altering the flow direction into the impeller using variable inlet guide vanes (IGV). To analyze the internal flow characteristic, this study employed numerical simulations, utilizing the Reynolds-averaged Navier-Stokes equations in conjunction with a shear stress transport turbulence model. The experiments were performed to validate the accuracy of the numerical results. The results show that changes in efficiency are less pronounced when adjusting the IGV setting angle from negative to positive, whereas the total head consistently increases by an average of 8.06% at the best efficiency point. The formation of the tip leakage vortex within the axial-flow pump at the deep stall point is attributed to the combination of tip leakage flow and flow separation at the leading edge of the impeller. Although negative IGV setting angles can degrade the hydraulic performance at the best efficiency point (BEP) and overload conditions, they also significantly reduce cavitation, reaching up to 86.253% at the BEP. At part-load conditions, positive IGV setting angles effectively reduce cavitation, especially at the deep stall condition with a reduction of up to 40.64%.

Keywords: Axial-flow pump, variable inlet guide vane, impeller, computational fluid dynamics, hydraulic performance, cavitation.

NOMENCLATURE

g	$[m/s^2]$	Gravitational acceleration
H	$[m]$	Total head coefficient
ψ	[-]	Total head
D	$[m]$	Impeller diameter
Q	[-]	Flow rate coefficient
φ	$[m/s]$	Flow rate
φ_d	$[m/s]$	Flow rate at the BEP
n	$[rpm]$	Rotating speed
λ	[-]	Specific speed
η	[%]	Efficiency

Subscripts and Superscripts

IGV	Inlet guide vane
DV	Diffuser vane
LE	Leading edge
TE	Trailing edge
SS	Suction side
PS	Pressure side
TLV	Tip leakage vortex
BEP	Best efficiency point
GCI	Grid convergence index

1. INTRODUCTION

A pump, a device that moves fluids from one place to another, is an indispensable device in daily life. Pumps are used in a variety of applications, including water distribution, sewage treatment, and industrial processes. In addition, the pump is a device that consumes a lot of energy and can cause noise pollution. Research by Capurso et al. [1] indicated that the power usage of centrifugal pumps in Europe amounts to 120 TWh/day, which corresponds to an average carbon generation of 475 gCO2/kWh. A mere 1% enhancement in energy performance can lead to a reduction of at least 570 tCO2/day in greenhouse gas emissions. Therefore, optimizing and improving the performance of the pump is an important factor in saving energy and protecting the environment, particularly for axial-flow pumps, which are large, energy-intensive devices.

Compared to other types of pumps, an axial-flow pump is capable of generating the largest flow rate at high performance and is extensively utilized in water systems, agricultural applications, draining in industrial and city settings. The flow characteristic within an axial-flow pump is characterized by chaos, turbulent and unsteady dynamics, often resulting in the formation of various vortices, including tip leakage vortex (TLV) [2-4], separation flow [5], horseshoe vortex [6], and corner vortex [5, 6]. Additionally, hydraulic losses caused by cavitation and leakage flow at the impeller gap can induce strong vibrations, generate excessive noise, and damage the impeller blades. Therefore, not only the axial-flow pump but all types of pumps, increasing performance, reducing cavitation are important factors in stable and safe pump operation.

Cavitation [7] is an undesirable phenomenon that can cause significant wear and tear on the metal blades of pumps [8, 9], turbines [10-11], and propellers [12]. It reduces operational efficiency, causes unpleasant vibrations, leads to high energy consumption, system instability, and diminished pump component lifespan. According to Orlandi et al. [13], cavitation occurs when the pressure of a liquid drops below its saturation vapor pressure, leading to the formation of gas bubbles. As these bubbles move into regions of higher pressure, they implode, creating powerful shock waves that can damage the blade surface. The repeated implosion of gas bubbles can severely erode the metal surface, especially on the impeller. Zhang et al. [14] noted that cavitation at the tip region of the axial-flow pump varied over time and encompassed several types at tip clearance, in TLV, on the suction side (SS), and at the trailing edge (TE). In the study of Zhang et al. [15], cavitation intensity in axial-flow pumps also changed with flow rate conditions and was categorized into different stages, including non-cavitating, incipient cavitation, critical cavitation, and deep cavitation. Due to its damaging effects, detection and elimination of cavitation are key considerations in pump design.

To enhance the hydraulic performance and reduce vibration in axial-flow pumps, variable IGV is currently being considered as a potential solution [16-19]. However, existing research has not yet demonstrated the effect of variable IGV on the reduction of cavitation. Consequently, this study is performed to comprehensively examine the cavitation phenomenon in axial-flow pumps through both numerical simulations and experimental investigations. In addition, this study proposes a novel approach to mitigate cavitation by altering the flow direction into the impeller using a variable IGV. By changing the flow direction, it is anticipated that flow separation within the impeller will be reduced, leakage flow minimized, and overall cavitation and pump performance significantly improved. Cavitation changes in the axial-flow pump will be carefully analyzed via cavitation visualization and the determination of cavitation volume.

2. METHODOLOGY

2.1. Axial-flow pump model

The axial-pump model utilized in this study consists of four IGVs, four impellers, and seven diffuser vanes (DV) as demonstrated in figure 1(a). The pump is designed to operate at a specific speed of 1204 and the rotating speed coefficient of 0.7893 as calculated according to Eq. (1) and Eq. (2), respectively. At the best efficiency point (BEP), the design head and design flow rate coefficient are 1.584 and 0.4319 as calculated according to Eq. (3) and Eq. (4), respectively.

$$\lambda = n[rpm]\frac{\varphi^{0.5}\left[\frac{m^3}{min}\right]}{\psi^{0.75}\,[m]} \tag{1}$$

$$\chi = \frac{nD}{\sqrt{g\psi}} \tag{2}$$

$$H = \frac{g\psi}{n^2D^2} \tag{3}$$

$$Q = \frac{\varphi}{nD^3} \tag{4}$$

where n, φ, ψ, D, and g denote the rotational speed, flow rate, total head, impeller diameter, and acceleration of gravity, respectively.

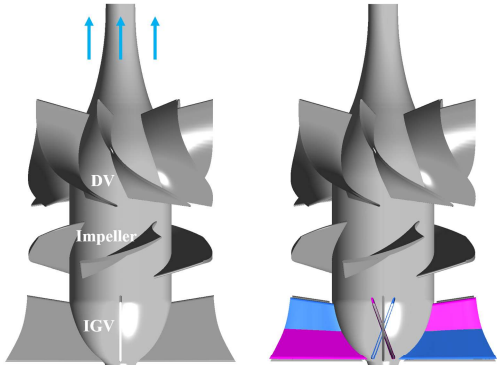

(a) (b)

Figure 1. Axial-flow pump configuration. (a) Original design, (b) New design with variable IGV (green: 20°, pink: −20°)

The axial-flow pump was tested at the Korea Institute of Machinery & Materials with the IGV chamber made transparent to easily see the formation and evolution of cavitation during operation with the help of a high-speed camera and fill light. The NX4-S1 camera model from Integrated Design Tools incorporation was synchronized with the computer system. In addition, to achieve the efficiency and power consumption of the pump, a series of modern measuring devices such as digital pressure gauge,

magnetic flow meter, and power meter were used, as can be seen in figure 2. Accuracy of measuring device is presented in Table 1 and detailed information about the experimental system can be found in previous studies [6, 20].

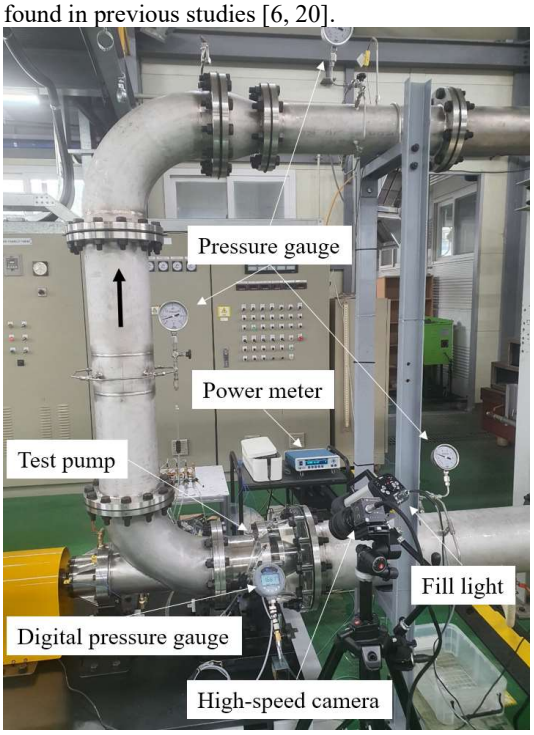

Figure 2. Measuring instruments in the pump test [20]

Table 1. Accuracy of measuring equipment [6]

Equipment	Operational range	Uncertainty
Absolute pressure transducer	0−200 (kPa)	± 0.25%
Differential pressure transducer	0−500 (kPa)	± 0.2%
Torque measurement	0−200 (Nm)	± 0.2%
Rotating measurement	0−20,000 (rpm)	± 0.02%
Flowmeter	0−900 (m^3/hr)	± 0.2%

2.2. Numerical method

Figure 3 shows the grid system for the numerical simulation with a hexahedral grid structure. The grid system is refined at wall surfaces with multiple layers of small meshes to ensure that the averaged y^+ value is less than two. The grid growth rate was maintained below 1.3. The grid independence is checked by utilizing the Grid Convergence Index (GCI) [21] based on three different grid systems (N_1, N_2, and N_3) with a grid refinement ratio of larger than 1.3. The values of the key parameter (efficiency) are normalized according to the efficiency value of the N_1 grid system with only impeller in the computational model. As can be seen in Table 2, the GCI_{fine}^{21} values and extrapolated relative error values (e_{ext}^{21}) are small enough [21] to confirm the convergence of the grid system. Therefore, the optimal grid system in this study consists of 0.55×10^6, 0.67×10^6, and 0.57×10^6 nodes for one IGV, impeller, and DV passages, respectively.

In the numerical simulation, the boundary conditions of the axial-flow pump are established based on ANSYS CFX-Pre with the fluids including water and water vapor at 25°. The inlet and outlet of the computational domain are respectively set as total pressure and mass flow rate. The blade, hub, and shroud surfaces are set as non-slip walls. The interfaces between the stationary and rotating domains are set as the mixing-plane. Rayleigh Plesset is selected as the cavitation model with a saturation pressure of 3170 Pa and the initial average bubble diameter of $2 \times 10^{-6}\ m$. The shear stress transport [22] coupled with the reattachment modification option is used as an optimum turbulence model to be able to accurately predict cavitation, vortex flow, and separation flow in this study.

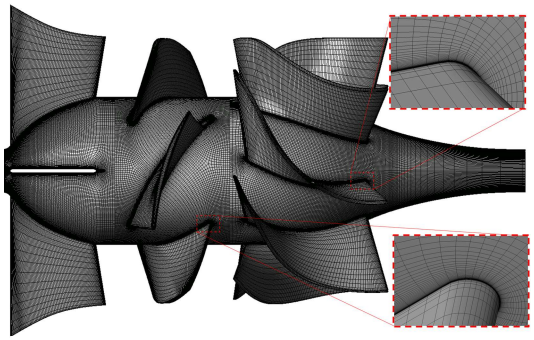

(a)

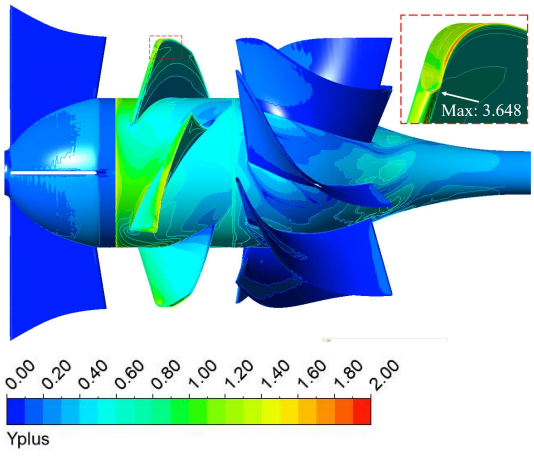

(b)

Figure 3. The established grid for numerical simulation. (a) grid system, (b) y+ distribution.

Table 2. Grid sensitivity analysis [6]

	Only impeller (No. of nodes in impeller)	IGV and impeller (No. of nodes in IGV)	Full component (No. of nodes in DV)
N_1	666,773	550,272	571,540
N_2	265,681	248,100	256,250
N_3	115,260	409,164	114,500
r_{21}	1.359	1.304	1.307
r_{32}	1.321	1.315	1.308
η_1/η_1	1.000	0.976	1.043
η_2/η_1	0.993	0.975	1.042
η_3/η_1	0.972	0.957	1.026
e_{ext}^{21}	0.00325	0.00014	0.00012
$\mathrm{GCI}_{\mathrm{fine}}^{21}$	0.00407	0.00017	0.00016

3. RESULTS AND DISCUSSIONS

3.1. Validation

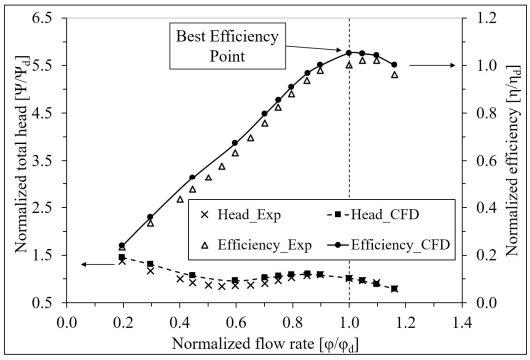

Figure 4. The hydraulic performance curves in simulation and in experiment

Figure 4 compares the efficiency and total head of the axial-flow pump measured in the experiment and in the numerical calculation. The efficiency and total head values are normalized using their values at the BEP of the experimental results. As can be seen in figure 4, the numerical results are consistent with the experimental data. The discrepancy between the numerical and experimental data is about 5.2% for efficiency and 1.256% for total head at the BEP. The relatively large difference in efficiency at the BEP is caused by the instability of the flow field in the experiment at a high flow rate due to the absence of a booster pump. For this reason, the experimental data at overload conditions are not available. In addition, errors in the measuring equipment and extrapolation errors in numerical calculations are also the causes of these differences.

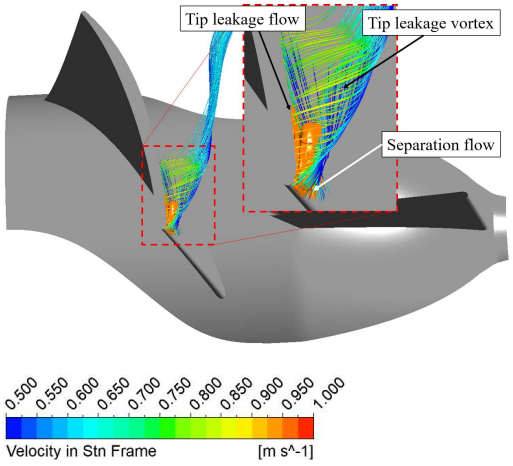

(a)

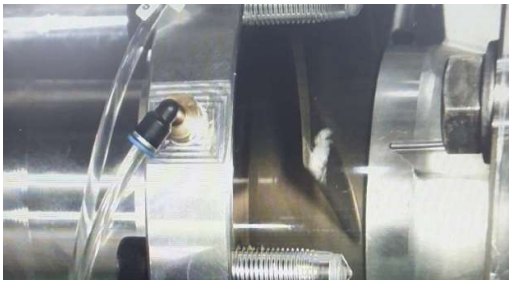

(b)

Figure 5. Cavitation visualization. (a) in simulation (orange: vapor volume fraction of 0.94), (b) in experiment.

To further confirm the accuracy of the numerical results, cavitation visualization is extracted and compared with the experimental result at the deep stall point ($0.6\varphi_d$) as shown in figure 5. The numerical simulation predicts well the cavitation bubbles formed at the leading edge (LE) of the impeller. Based on the simulation results, cavitation formation is based on two main factors including tip leakage flow and separation flow. The combination of these two flows created a TLV that separates from the impeller surface. With high rolling velocity mainly caused by the tip leakage flow, a large void with low pressure inside the TLV is formed. The pressure inside this void drops below the saturation vapor pressure, ultimately leading to the formation of cavitation bubbles.

3.2. Hydraulic performance

Figure 6 presents the total head and efficiency curves across various IGV angles. The total head and

efficiency values are normalized to their respective values at the BEP of the 0° IGV angle model, which serves as the reference model. When varying the IGV angle, changes in efficiency are less pronounced, particularly in the low-flow rate region, compared to the more significant variations observed in the total head. The minimal changes in efficiency can be attributed to the turbulence within the flow field, which elevates the load on the impeller and subsequently increases power consumption. As a result, the efficiency of the reference model remains superior to that of other IGV setting angles, except at high flow rates where a favorable match between the flow and impeller blade angle can occur. Around the BEP, the efficiency for too large and too low IGV angles is significantly lower in comparison to the reference model, with the efficiencies at 20° and −20° IGV under the BEP being reduced by 2.29% and 1.82%, respectively.

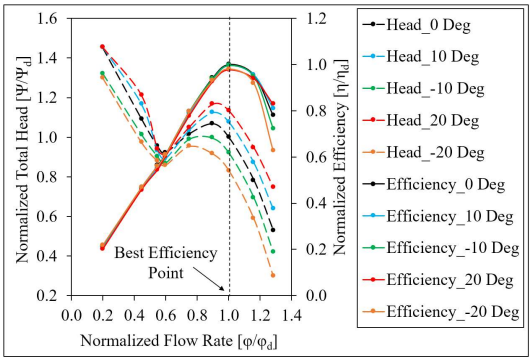

Figure 6. The hydraulic performance at different IGV setting angle

The head of the axial-flow pump progressively rises as the IGV angle transitions from negative to positive, exhibiting an average increase of 8.06% at the BEP. This enhancement is primarily due to the role of IGV in facilitating flow into the impeller; as the IGV angle rises, the absolute velocity of the flow entering the impeller becomes increasingly compatible with the relative velocity. This alignment results in elevated velocity and pressure in the flow exiting the impeller. In addition, the saddle zone also becomes more prominent as the IGV angle rises, owing to significant losses in both IGV and impeller passages at high IGV angles. These high angles also increase the incident angle at LE of the impeller, promoting the flow separation on the SS of the impeller compared to the reference model, particularly under low flow rate conditions. Based on the hydraulic performance curves, it can be seen that at the same head, the axial-flow pump can operate at various flow rates to achieve optimal performance depending on the variable IGV.

3.3. Internal flow characteristics

To clearly observe the impact of variable IGV on cavitation within the impeller, figure 7 depicts cavitation represented by an orange iso-vapor volume fraction of 0.5 across −10°, 0°, and 10° IGV setting angle models at different flow rates. Intense cavitation is observed at the LE of the impeller for all three models at the deep stall point. Although the cavitation of the 10° model is smaller than in the other two models, this difference does not seem to be significant as observed in figure 7(a). However, the bubble volume of the 10° model is reduced by 40.64% and 16.38% compared to the reference model and −10° model as presented in the figure 8. Figure 7 also shows the turbulence kinetic energy (TKE) distribution at different cross-sections to evaluate the energy loss caused by TLV and cavitation. It can be stated that the TKE generated at the deep stall point is the largest among all three IGV models due to the chaotic flow characteristics and the presence of strong cavitation. While the 10° model reduces cavitation, it leads to a 13.51% increase in TKE compared to the reference model, whereas the −10° model yields a 10.68% reduction in TKE.

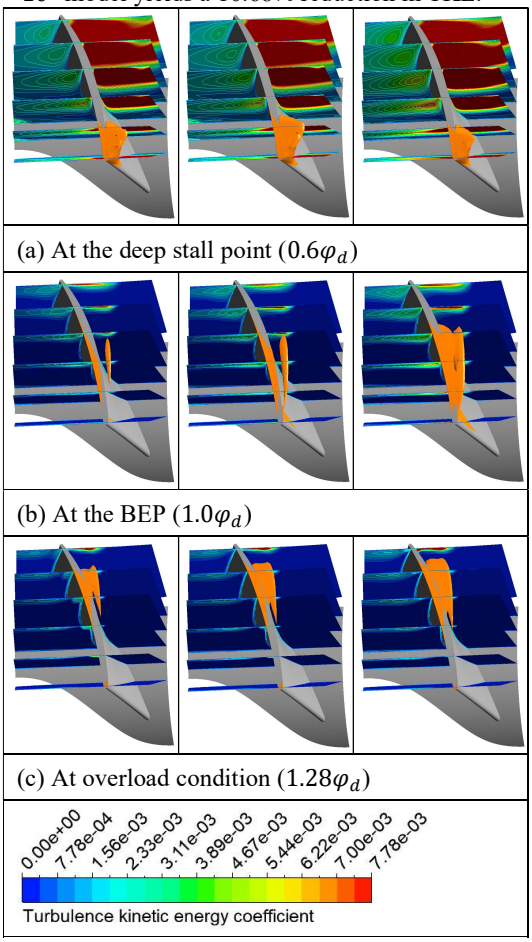

Figure 7. Cavitation in the impeller at different flow rate conditions (left: −10°; middle: 0°; right: 10°)

The difference in cavitation is most apparent at the BEP, as shown in figure 7(b). In all three models, cavitation is markedly reduced in the $-10°$ model, with cavitation streaks nearly disappearing at the LE of the impeller. Furthermore, cavitation induced by leakage flow at the gap and TLV is significantly diminished compared to the reference model. Therefore, the turbulence kinetic energy and bubble volume of the $-10°$ model decreased by up to 19.643% and 86.253%, respectively in comparison with the reference model. While increasing the IGV setting angle may enhance the total head, it also increases the risk of severe cavitation formation and the TKE at the BEP, as demonstrated in figure 7(b, right). The closeness of absolute velocity to relative velocity not only intensifies leakage flow through the gap but also generates a substantial pressure differential, leading to a marked pressure drop on the SS, as can be seen in figure 9(b), thereby fostering conditions favorable for cavitation.

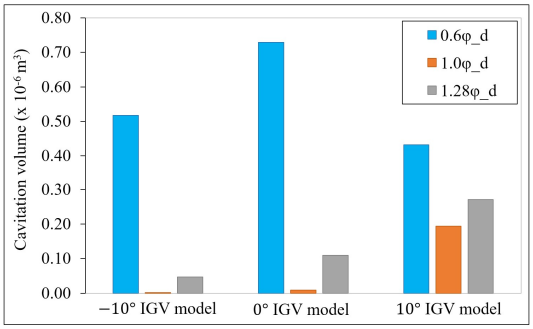

Figure 8. The volume of cavitation in different conditions

Likewise, under overload conditions, cavitation manifests more robustly at positive IGV angles, whereas it diminishes at negative angles when compared to the reference model. Therefore, the bubble volume of the 10° model at the BEP and $1.28\varphi_d$ increased by 20.77 times and 2.47 times compared to the reference model, respectively. Correspondingly, the TKE of the 10° model increased by 39.78% at the BEP and 19.63% at $1.28\varphi_d$ in comparison to the reference model. It should be noted that while the TKE of the 10° model exhibits an increase in comparison with the reference model, the hydraulic performance is also enhanced, especially at overload conditions. This is attributed to the improved compatibility between the flow angle and blade angle at the LE of the impeller, which consequently results in an increase of the velocity and energy within the impeller domain, thereby contributing to both the elevated TKE and the hydraulic performance observed in the10° model.

The cavitation visualization indicates a tendency for cavitation to gradually migrate from the LE to the TE of the impeller as the flow rate increases. Additionally, analysis of the bubble volume in figure 8 reveals that the negative IGV angles are more effective than positive angles in mitigating cavitation within the impeller, particularly around the BEP and under overload conditions.

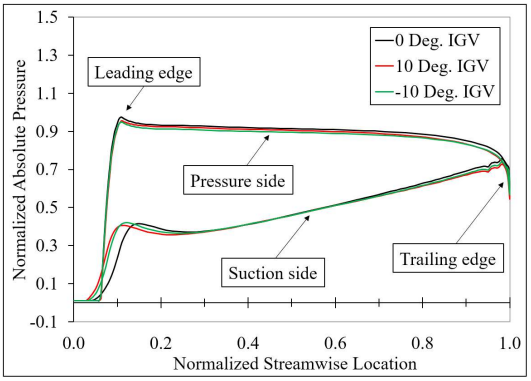

(a)

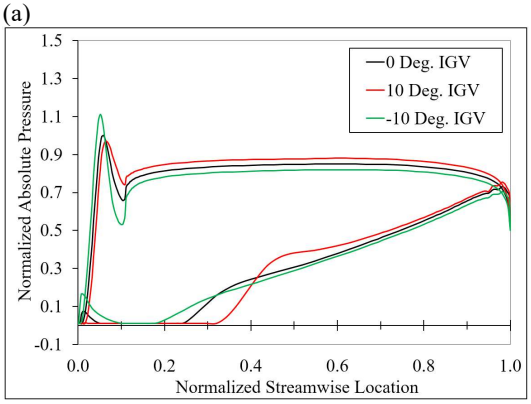

(b)

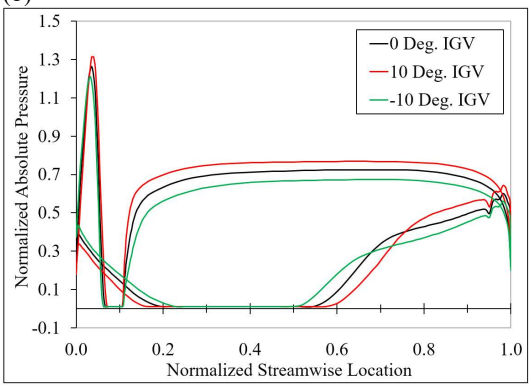

(c)

Figure 9. The pressure distribution at 95% span of the impeller. (a) at the $0.6\varphi_d$, (b) at the BEP (φ_d), (c) at the $1.28\varphi_d$

Figure 9 shows the absolute pressure distribution at 95% span where cavitation occurs prominently for $-10°$, 0°, and 10° IGV angle models across various flow rates. The pressure values are normalized to the maximum pressure of the reference model at the BEP. At the deep stall point, a significant pressure drop is observed at the LE of the impeller, which facilitates the formation and development of

cavitation, as illustrated in figure 7(a). The pronounced differences in pressure distribution among the different models are mainly at the BEP and $1.28\varphi_d$ contributing to noticeable variations in the total head curves, as shown in figure 6. However, the pressure drop at the SS of these flow conditions continues to promote cavitation formation, particularly at the 10° model. At the BEP, the pressure drop extends to a streamwise location of 0.3, resulting in the appearance of elongated cavitation streaks, as depicted in figure 7(b). For the 10° model, while the pressure on the pressure side (PS) is the highest, the pressure drop at the SS is also the most significant, leading to substantial cavitation within the impeller domain. At the $1.28\varphi_d$, the pressure distribution around the LE becomes highly complex, characterized by a peak pressure due to the stagnation point, alongside sharp pressure drops resulting from velocity acceleration on both sides of the impeller. The majority of cavitation observed in figure 7(c) is a consequence of the abrupt pressure drop within the TLV between streamwise positions 0.2 and 0.6. Additionally, the irregular pressure distribution at the TE is also clearly visible in figure 9, attributed to the presence of the TE vortex [23].

To evaluate the energy loss in the axial-flow pump, the distribution of TKE at 95% span is presented in figure 10 for the three IGV models at different flow rate conditions. The TKE value is normalized by the square of the maximum velocity at the impeller tip. It is evident that operation at the deep stall point results in the highest energy loss among the three operational conditions due to the complexity of the flow. A significant amount of loss occurs around the LE of the impeller at the SS and subsequently spreads throughout the impeller passage. Furthermore, the turbulence also affects the IGV, leading to considerable energy loss at the outlet of the IGV. The changes in hydraulic performance at the deep stall point are primarily reflected in the energy loss observed at the outlet of the IGV and the TE of the DV. At the BEP and $1.28\varphi_d$, energy loss is improved markedly compared to that at the deep stall point. However, the presence of cavitation and TLV still results in considerable energy loss within the impeller domain, as clearly illustrated in figures 10(b, right) and 10(c).

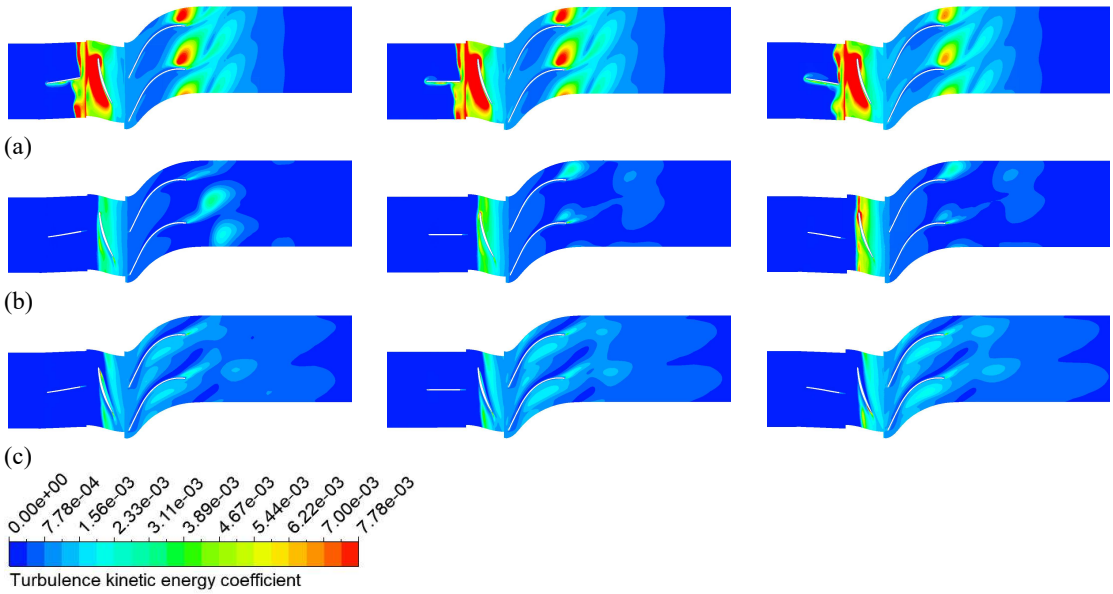

Figure 10. The turbulence kinetic energy distribution at 95% span(left: $-10°$; middle: 0°; right: 10°). (a) at $0.6\varphi_d$, (b)at the BEP (φ_d), (c) at $1.28\varphi_d$

4. CONCLUSIONS

This study investigates the influence of variable IGV on the hydraulic performance and cavitation of the axial-flow pump, utilizing five IGV setting angles, including 0°, $\pm10°$, and $\pm20°$. To validate the numerical simulation results, hydraulic performance curves and cavitation visualizations are compared against experimental data. The key findings derived from the numerical simulations are drawn as follows:

A. The variable IGV does not significantly alter the efficiency of the axial-flow pump, except under high flow rate conditions. However, increasing the IGV angle leads to a substantial increase in the total head with an average increase of around 8.06% and makes the saddle zone more pronounced. Therefore, variable IGV is particularly advantageous for optimizing the efficiency of axial-flow pumps by operating at different flow rates while maintaining the desired head.

B. Cavitation at the deep stall point is primarily attributed to the pressure drop within the TLV, resulting from a combination of tip leakage flow and separation flow at the LE of the impeller. At the deep stall point, while the 10° model achieves a 40.64% reduction in cavitation, it concurrently results in a 13.51% increase in TKE whereas the −10° model demonstrates a 10.68% reduction in TKE compared to the reference model. Under operating conditions around the BEP and under overload conditions, positive IGV angles increase total head, while negative angles mitigate cavitation by up to 86.253% in comparison with the reference model. Furthermore, the study further demonstrates a correlation between flow rate and cavitation location, with higher flow rates resulting in cavitation occurring closer to the TE of the impeller.

It should be noted that the hydraulic performance and cavitation characteristics may vary depending on different pump models. This study has not considered the time-dependent evolution of cavitation through unsteady-state simulations. In the future, the Large Eddy Simulation with the Wall-Adapting Local Eddy-viscosity subgrid-scale model will be employed to observe and thoroughly analyze cavitation behavior and internal flow characteristics of the axial-flow pump at various stages across different IGV setting angles.

ACKNOWLEDGEMENTS

This work was supported by Korea Institute of Energy Technology Evaluation and Planning (KETEP) grant funded by the Korea government (MOTIE) (2021202080026A, Development of Variable Operating Technology for Medium and Large Size Pump) and partially was supported by UST Young Scientist+ Research Program 2024 through the University of Science and Technology. (No. 2024YS21).

REFERENCES

1. Capurso, T., Bergamini, L., Torresi, M., 2022, “A new generation of centrifugal pumps for high conversion efficiency,” *Energy Convers Manage*, Vol. 256, 115341.

2. Zhang, D., Shi, L., Shi, W., Zhao, R., Wang, H., Esch, B. P. M. V., 2015, “Numerical analysis of unsteady tip leakage vortex cavitation cloud and unstable suction-side-perpendicular cavitating vortices in an axial flow pump”, *Int J Multiphase Flow*, Vol. 77, pp. 244-259.

3. Shen, X., Zhang, D., Xu, B., Shi, W., Esch, B. P. M. V., 2021, “Experimental and numerical investigation on the effect of tip leakage vortex induced cavitating flow on pressure fluctuation in an axial flow pump”, *Renew Energy*, Vol. 163, pp. 1195-1209.

4. Shen, X., Zhao, X., Xu, B., Zhang, D., Yang, G., Shi, W., Esch, B. P. M. V., 2022, “Unsteady characteristics of tip leakage vortex structure and dynamics in an axial flow pump”, *Ocean Eng*, Vol. 266, pp. 1-18.

5. Wang, C., Wang, F., Xie, L., Wang, B., Yao, Z., Xiao, R., 2021, “On the vortical characteristics of horn-like vortices in stator corner separation flow in an axial flow pump”, *ASME J Fluids Eng*, Vol. 143, 061201.

6. Nguyen, D. A., Lee, H. J., Kim, S., Choi, B. L., Choi, D. H., Kim, G. S., Sun, S., Kim, J. H., 2024, “Multiobjective hydraulic optimization of the diffuser vane in an axial flow pump”, *Phys Fluids*, Vol. 36, pp. 1-25.

7. Kan, K., Binama, M., Chen, H., Zheng, Y., Zhou, D., Su, W., Muhirwa, A., 2022, “Pump as turbine cavitation performance for both conventional and reverse operating modes: A review”, *Renew Sustain Energy Rev*, Vol. 168, pp. 1-21.

8. Gong, J., Luo, W. Z., Wu, T. C., Zhang, Z. Y., 2022, “Numerical analysis of vortex and cavitation dynamics of an axial-flow pump”, *Eng Appl Comput Fluid Mech*, Vol. 16, pp. 1921-1938.

9. Jia, X. Q., Zhang, Y., Lv, H., Zhu, Z. C., 2023, “Study on external performance and internal flow characteristics in a centrifugal pump under different degrees of cavitation”, *Phys Fluids*, Vol. 35, 014104.

10. Shahzer, M. A., Kim, J. H., 2024, “Investigation of role of fins in a francis turbine model's cavitation-induced instabilities under design and off-design conditions”, *Energy*, Vol. 292, pp. 1-17.

11. Shamsuddeen, M. M., Park, J. W., Choi Y. S., Kim, J. H., 2020, “Unsteady multi-phase cavitation analysis on the effect of anti-cavity fin installed on a kaplan turbine runner”, *Renew Energy*, Vol. 162, pp. 861-876.

12. Tan, Q., Ding, Y., Sui, C., Xiang, L., 2024, “Effects of propeller cavitation on ship propulsion performance in off-design operating conditions”, *Ocean Eng*, Vol. 313, pp. 1-16.

13. Orlandi, F., Montorsi, L., Milani, M., 2023, “Cavitation analysis through CFD in industrial pumps: A review”, *Int J Thermofluids*, Vol. 20, pp. 1-26.

14. Zhang, D., Shi, L., Zhao, R., Shi, W., Pan, Q., Esch, B. P. M. V., 2017, “Study on unsteady tip leakage vortex cavitation in an axial-flow pump using an improved filter-based model”, *J Mech Sci Tech*, Vol. 31, pp. 659–667.

15. Zhang, R., Chen, H. X., 2013, “Numerical analysis of cavitation within slanted axial-flow pump”, *J Hydrodyn*, Vol. 25, pp. 663-672.

16. Yang, F., Hu, W. Z., Li, C., Liu, C., Jin, Y., 2020, “Computational study on the performance improvement of axial-flow pump by inlet guide vanes at part loads”, *J Mech Sci Technol*, Vol. 34, pp. 4905-4915.

17. Zhang, W. P., Shi, L. J., Tang, F. P., Duan, X. H., Liu, H. Y., Sun, Z. Z., 2020, “Analysis of inlet flow passage conditions and their influence on the performance of an axial-flow pump”, *J Power Energy*, Vol. 0, pp. 1-14.

18. Nguyen, D. A., Kim, J. H., 2024, “Co-adjustable guide vane and diffuser vane to improve the energy generation potential of an axial-flow pump as turbine”, *Energy*, Vol. 291, pp. 1-15.

19. Shi. L. J., Chi, Y., Wang, L., Xu, T., Jiang, Y. H., Xing, J., Yan, B. Y., Chen, Y. Y., Han, Y., 2023, “Numerical simulation and model test of the influence of guide vane angle on the performance of axial flow pump”, *Phys Fluids*, Vol. 35, 015129.

20. Nguyen, D. A., Dinh, C. T., Kim, J. H., 2024, “Improvement in energy performance from the construction of inlet guide vane and diffuser vane geometries in an axial-flow pump”, *Sci Rep*, Vol. 14, pp. 1-27.

21. Celik, I. B., 2008, "Procedure for estimation and reporting of uncertainty due to discretization in CFD applications", *J Fluid Eng*, Vol. 130, pp. 1-4.

22. Menter, F. R., 1994, “Two-equation eddy-viscosity turbulence models for engineering applications”, *AIAA J*, Vol. 32, pp. 1598–1605.

23. Zierke, W. C., Straka, W. A., 1996, “Flow visualization and the three-dimensional flow in an axial-flow pump”, J Propul Power, Vol. 12, pp. 250–259.

Conference on Modelling Fluid Flow (CMFF'25)
The 19th International Conference on Fluid Flow Technologies
Budapest, Hungary, August 26-August 29, 2025

SPHERICAL STABILITY AND BREAKUP LIMIT OF OSCILLATING MICROBUBBLES

Dániel NAGY[1], Péter KALMÁR[2], Kálmán KLAPCSIK[3], Ferenc HEGEDŰS[4]

[1] Department of Hydrodynamic Systems, Faculty of Mechanical Engineering, Budapest University of Technology and Economics. Muegyetem rakpart 3, H-1111 Budapest, Hungary. E-mail: dnagy@hds.bme.hu
[2] Department of Hydrodynamic Systems, Faculty of Mechanical Engineering, Budapest University of Technology and Economics. Muegyetem rakpart 3, H-1111 Budapest, Hungary. E-mail: pkalmar@hds.bme.hu
[3] Department of Hydrodynamic Systems, Faculty of Mechanical Engineering, Budapest University of Technology and Economics. Muegyetem rakpart 3, H-1111 Budapest, Hungary. E-mail: kklapcsik@hds.bme.hu
[4] Corresponding Author. Department of Hydrodynamic Systems, Faculty of Mechanical Engineering, Budapest University of Technology and Economics. Muegyetem rakpart 3, H-1111 Budapest, Hungary. E-mail: fhegedus@hds.bme.hu

ABSTRACT

This study investigates the spherical stability and breakup limits of oscillating microbubbles in an acoustic standing wave, employing both a Reduced Order Model (ROM) and a multiphase flow solver. The ROM couples the spherical bubble dynamics, governed by the Keller-Miksis equation, with axisymmetric surface mode oscillations, formulated as a system of ordinary differential equations. The results from the ROM are compared against multiphase CFD simulations performed using the ALPACA flow solver. While multiphase CFD simulations are computationally more intensive, they offer deeper insights into the dynamics, including the ability to capture bubble breakup – a phenomenon that lies beyond the capabilities of the ROM. This study combines the ROM and the CFD simulations to predict spherical stability and breakup thresholds across varying bubble sizes, acoustic pressures, and frequencies. Three regimes are identified: (1) spherically stable bubbles, (2) stable surface mode oscillations, and (3) instability leading to breakup. The key finding is that the ROM reliably predicts breakup through unbounded growth of surface modes, demonstrating strong agreement with the results obtained from ALPACA simulations.

Keywords: bubble dynamics, direct numerical simulation, multiphase flow, sonochemistry, reduced order model

NOMENCLATURE

R_0	[μm]	initial bubble radius
R_E	[μm]	equilibrium bubble radius
T	[K]	temperature
$\hat{a}_n$	[−]	n^{th} dimensionless mode amplitude
a_n	[μm]	n^{th} mode amplitude
c	[m/s]	speed of sound
c_V	[J/K]	heat capacity at const. volume
f	[kHz]	excitation frequency
g_n	[m^2/s^2]	higher order terms
$l_{\max}$	[−]	max. number of refinements
p_0	[Pa]	ambient pressure
p_∞	[Pa]	stiffened gas EoS parameter
p_A	[Pa]	pressure amplitude
p_v	[Pa]	vapour pressure
t	[ms]	time
u	[m/s]	x-directional velocity
v	[m/s]	y-directional velocity
ϵ	[−]	small parameter
γ	[−]	stiffened gas EoS parameter
λ	[m]	wavelength
μ	[Pa · s]	dynamic viscosity
ω	[1/s]	angular frequency
ρ	[kg/m^3]	density
σ	[N/m]	coefficient of surface tension

Subscripts and Superscripts

B	bubble
B, 0	bubble, initial state
L	liquid

1. INTRODUCTION

The study of oscillating microbubbles in acoustic fields is a cornerstone of sonochemistry, where these bubbles play an important role in energy concentration that leads to chemical reactions [1, 2, 3, 4]. When subjected to acoustic excitation, microbubbles can undergo complex dynamics, including spherical oscillations, stable surface wave oscillations, bubble jetting [5, 6] and bubble breakup [7, 8]. Understanding these behaviors is crucial for scaling cavitation-driven chemical synthesis for industrial scales.

A central challenge in modeling non-spherical microbubble oscillations lies in the uncertainty of both measurements and models. Experimental data for non-spherical oscillations are limited to a few parameter combinations [7, 9, 10], and they also often suffer from limitations in accuracy. Computational models must contend with assumptions and approximations that may not fully capture the complexity. To address these challenges, this study employs two complementary approaches: the reduced-order model (ROM) [11, 12, 13] and the high-fidelity ALPACA solver [14, 15]. The ROM provides a computationally efficient framework for analyzing radial bubble dynamics coupled with surface mode oscillations, making it suitable for large-scale parameter studies [16]. However, its validity is constrained to scenarios with small perturbations in surface modes [17]. In contrast, ALPACA is a compressible multiphase computational fluid dynamics (CFD) solver that solves the governing equations of fluid flow directly. Leveraging the level set method for interface capturing and a multiresolution meshing algorithm, ALPACA makes it possible to simulate surface mode oscillations and bubble breakup [18].

This study investigates the spherical stability and breakup limits of oscillating microbubbles by combining the strengths of ROM and ALPACA. A series of parameter studies is conducted to explore the effects of bubble size, pressure amplitude, and excitation frequency on bubble dynamics. ALPACA simulations are used to validate and refine ROM predictions. The second section discusses the ROM and the ALPACA solver. Then, the simulations are introduced in the third section and the results are discussed.

2. MODELING ACOUSTICALLY EXCITED BUBBLES

2.1. Reduced Order Model

The Reduced Order Model handles the non-spherical bubble dynamics as a vibration problem assuming axial symmetry and small deformation. The aim is to avoid partial differential equations by employing modal decomposition, specifically using Legendre polynomials as orthogonal basis functions, and to construct an ordinary differential equation system that describes the time evolution of the mode amplitudes. In this manner, the temporal evolution of the complex bubble shape r_s, expressed via Legendre polynomials as an infinite series in a spherical coordinate system that can be described as:

$$r_s(\theta, t) = R(t) + \sum_{n=2}^{\infty} \varepsilon a_n(t) P_n(\mu), \tag{1}$$

where $R(t)$ is the spherical or 0^{th} mode as the function of time, while a_n denotes the n^{th} mode amplitude corresponding to the Legendre polynomial $P_n(\mu)$ of order n, with $\mu = \cos(\mu)$. Note that the first mode, i.e., the translational motion, is neglected in this paper for simplicity. Additionally, surface distortion is assumed to be small, as indicated by the small parameter ε. Following the work of Shaw [11, 12, 13], the mode amplitudes are described by an implicit second-order nonlinear n-dimensional differential equation system derived from the Lagrangian function composed of the kinetic and potential energy. The nonlinear coupling terms permit interaction between the modes and account for the implicit nature of the system. The volume mode (the radial oscillation $R(t)$) reads as:

$$\left(1 - \frac{\dot{R}}{c_L}\right) R\ddot{R} + \left(1 - \frac{\dot{R}}{3c_L}\right) \frac{3}{2}\dot{R}^2 = G(t) + \frac{1}{c_L}\left(\dot{R} \cdot G(t) + R \cdot \dot{G}(t)\right) + \varepsilon^2 \left(g_0 + g_{0v}\right), \tag{2}$$

where c_L is the speed of sound in the liquid and

$$G(t) = \frac{p_{B_0}}{\rho_L}\left(\frac{R_0}{R}\right)^{3\gamma} + \frac{p_v}{\rho_L} - \frac{1}{\rho_L}\left(p_0 + p_A \sin(\omega t)\right) - \frac{4\mu_L \dot{R}}{\rho_L R} - \frac{2\sigma}{\rho_L R}. \tag{3}$$

In this context, p_{B_0} denotes the equilibrium pressure inside the bubble, while ρ_L represents the density of the liquid. The initial radius of the bubble is given by R_0, and γ refers to the ratio of specific heats. The dynamic viscosity of the liquid is denoted by μ_L, and σ stands for the surface tension. Acoustic excitation is characterized by the angular frequency ω and the pressure amplitude p_A. The ambient pressure, also known as the far-field pressure, is represented by p_0, and p_v indicates the vapour pressure. The higher order terms g_n and g_{nv} are the inviscid and damping terms, which can be found in [11, 12]. The surface modes have the following form:

$$\varepsilon \Big\{ R\ddot{a}_n + 3\dot{R}\dot{a}_n + \left[\left(n^2 - 1\right)(n+2)\frac{\sigma}{\rho_L R^2} - (n-1)\ddot{R}\right] a_n + \frac{2\mu_L}{\rho_L}\left[(n-1)(n+2)\frac{\dot{R}}{R^2}a_n + (n+2)(2n+1)\frac{\dot{a}_n}{R}\right]\Big\} = \varepsilon^2 \left(g_n + g_{nv}\right). \tag{4}$$

Like the 0^{th} mode, the second-order term governs the coupling between the modes, which can be separated into inviscid and damping components; the interested reader can find these terms in [16].

The solution strategy for the model is divided into two main parts: an initial value problem and a nonlinear equation system. The initial value problem is solved using a self-developed Runge–Kutta–Cash–Karp solver. At the same time, the nonlinear equation system is handled using a GPU-optimized iterative technique derived by the authors [16]. With this approach, the parameters of large spherical or closely spherically oscillating bubbles can be found efficiently. The deviation from the spherical shape is characterised by the mode ampli-

tudes divided by the 0^{th} mode; from now on, relative mode amplitude $\hat{a}_n = a_n/R$. The approximated validity limit of the model, i.e., the maximum of the relative mode amplitude corresponding to the dominant mode (mode with the largest amplitude), is between 0.25 and 0.37 [17].

2.2. ALPACA Simulations

The CFD simulation of an oscillating microbubble in an acoustic field requires a compressible multiphase solver. The computational domain must span at least one wavelength to simulate a standing wave, which, in typical cases, is in the order of 10 mm, based on the speed of sound and excitation frequency. In contrast, bubble sizes in sonochemistry are typically around 10 µm, resulting in a scale difference of approximately three orders of magnitude. This significant disparity necessitates specialized numerical meshes.

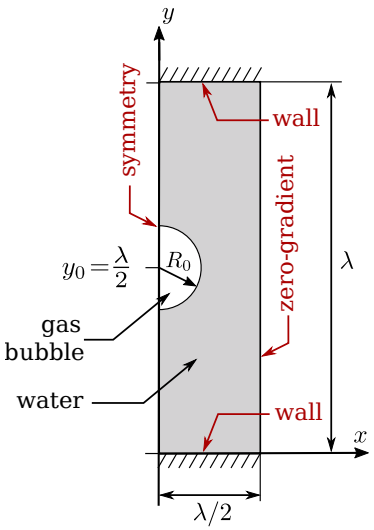

Figure 1. Layout and boundary conditions of the ALPACA simulations.

The chosen solver, ALPACA, meets these requirements, having been specifically developed to study compressible and multiphase phenomena [14]. ALPACA employs the level set method for interface capturing [19] and utilizes high-order, non-dissipative numerical schemes to accurately capture shockwaves [15]. Its meshing process is highly efficient, leveraging a multiresolution algorithm [20] that automatically refines the mesh as needed. The maximum number of refinements is controlled by the user defined parameter $l_{\max} \leq 14$, allowing the cell size to vary by nearly four orders of magnitude.

ALPACA was used to carry out two-dimensional axisymmetric numerical simulations of bubbles in a standing wave. The bubble was positioned at the node of the acoustic standing wave within a rectangular domain of dimensions $\lambda \times \lambda/2$, where λ represents the wavelength. The boundary conditions are illustrated in Figure 1. Reflective walls were placed on the south and north boundaries, causing wave reflections. A zero-gradient boundary condition was applied on the east boundary, while the west boundary served as the axis of symmetry. The standing wave was introduced through the initial conditions, and the bubble was subjected to the following pressure:

$$p(t) = p_0 - p_A \cdot \sin(2\pi f \cdot t). \tag{5}$$

The initial conditions in the bubble correspond to the equilibrium condition, that is

$$p_B(x, y) = p_0 + \frac{2\sigma}{R_0}, \tag{6}$$

where p_B is the bubble pressure, σ is the surface tension and R_0 corresponds to the equilibrium radius. The initial velocities are zero and the density is set according to the ideal gas law:

$$u_B(x, y) = 0, \tag{7}$$

$$v_B(x, y) = 0 \text{ and} \tag{8}$$

$$\rho_B(x, y) = \frac{p_B(x, y)}{(\gamma_B - 1)c_V T_B}, \tag{9}$$

where u_B is the x-directional velocity, v_B is the y-directional velocity and ρ_B is the density in the bubble. In both phases, the stiffened gas equation of state is used [21]:

$$p = (\gamma - 1)\rho e - p_\infty, \tag{10}$$

where e is the internal energy and γ, p_∞ are parameters. In the gas phase $p_{\infty,B} = 0$, thus the stiffened gas EoS results in the ideal gas law, in which $\gamma_B = 1.4$ is the ratio of specific heats. To model the water, parameters $\gamma_L = 4.4$ and $p_{\infty,L} = 6 \cdot 10^8$ Pa are adopted from the literature [22].

To accelerate the formation of surface mode oscillations, the bubble shape is initially perturbed with relative mode amplitudes of $\hat{a}_2 = 0.031$, $\hat{a}_3 = -0.050$, $\hat{a}_4 = 0.008$, and $\hat{a}_5 = 0.016$. These amplitudes are chosen to ensure that the volume of the bubble remains unchanged. A post-processing code was developed in Paraview to extract the mode amplitudes from the numerical simulations.

In total, 62 ALPACA simulations were conducted, with each simulation running for 24 hours on the SUPERMUC-NG supercomputer, utilizing one compute node with 36 cores. In most cases, this computing time was sufficient to run the simulations for at least 10 acoustic cycles, enabling the analysis of long-term behavior. For lower frequencies, simulating the same number of acoustic cycles requires more time, as the period of the oscillation is longer, and more time steps are necessary. Simulating smaller bubbles necessitates a reduction in cell size, and in accordance with the CFL condition, the time step size is also reduced. To account for these factors, the simulations were extended for an additional 24 hours compute time in the case of low frequencies and small bubbles.

3. SIMULATION RESULTS

This section presents the results of the ALPACA and ROM simulations. First, the convergence of the

ALPACA simulations is analyzed by increasing the mesh resolution and comparing the results to ROM predictions. Next, the frequency and bubble radius are fixed to investigate the effect of pressure amplitude, and the classification of surface modes are discussed. Finally, large-scale parameter studies are introduced.

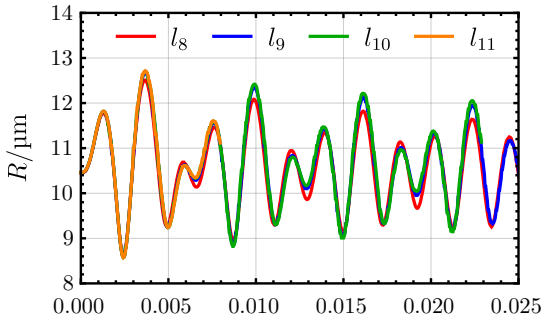

(a) Radius

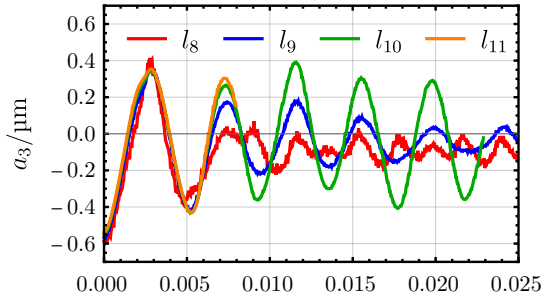

(b) 3rd mode

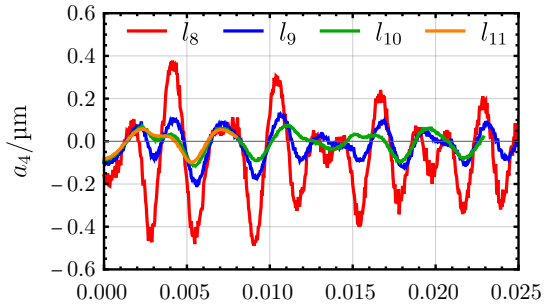

(c) 4th mode

Figure 2. Results of the convergence study with parameters $R_0 = 10.5\,\mu m$, $p_A = 50\,kPa$ and $f = 480\,kHz$.

3.1. Mesh independence study of ALPACA

A bubble with an initial radius of $R_0 = 10.5\,\mu m$ is excited by a standing wave with an amplitude of $p_A = 50\,kPa$ and a frequency of $f = 480\,kHz$. According to the ROM, a stable 3rd mode oscillation is expected to form. Simulations were conducted in ALPACA using four different mesh resolutions. The number of adaptive refinements was varied from 8 to 11 on an initial 80×144 mesh. This resulted in the number of cells along the bubble diameter being $N_{bubble} = 76, 152, 304$, and 608 for the resolutions l_8, l_9, l_{10}, and l_{11}, respectively. Figure 2a demonstrates that the l_9 mesh already produces accurate results in the bubble radius, as further increase of the resolution does not lead to significant changes. Figures 2b and 2c illustrate the 3rd and 4th modes, respectively.

In the figures, clear convergence is visible. Using the l_{10} mesh, the desired 3rd mode oscillation forms with an amplitude of $a_3 \approx 0.3\,\mu m$, while the 4th mode dampens to $a_4 \approx 0.05\,\mu m$. For comparison, the ROM predicts $a_3 = 0.297\,\mu m$ and $a_4 = 0.023\,\mu m$. Based on these results, a mesh resolution of $N_{bubble} \approx 300$ is used for all subsequent ALPACA simulations.

3.2. Effect of pressure amplitude

The effect of increasing pressure amplitude is examined for a bubble with an initial radius of $R_0 = 47.5\,\mu m$ excited by a frequency of $f = 30\,kHz$ acoustic standing wave at various pressure amplitudes in ALPACA. According to the ROM, the bubble remains spherical when the pressure amplitude p_A is below 19 kPa. For pressure amplitudes exceeding 39 kPa, unstable surface mode oscillations occur ($a_n \to \infty$), potentially leading to bubble breakup. In the intermediate range, $19\,kPa < p_A < 39\,kPa$, stable 2nd and 3rd mode oscillations develop. The radius–time curves in Figure 3 depict the radial dynamics in selected ALPACA simulations, showing remarkable agreement between the ALPACA simulations (red line) and the ROM predictions (black dashed line). The mode amplitude–time curves are presented for the same ALPACA simulation in Figure 4. The formation of stable surface mode oscillations takes hundreds of acoustic periods in the ROM; thus, it cannot be compared directly with ALPACA. The following observations can be made:

1. For a low pressure amplitude ($p_A = 10\,kPa$) the initial perturbation in the modes damps down as illustrated in Figure 4a. The bubble is considered spherically stable in that case. This point falls below the spherical stability limit, aligning with the ROM results.

2. For pressure amplitudes $p_A = 32\,kPa$ and $p_A = 36\,kPa$, there is an initial large 3rd mode oscillation observed during the first few acoustic cycles as depicted in Fig. 4b. However, this dampens down and a stable 2nd mode oscillation remains. The ROM predicts a dominant 2nd mode for $p_A = 32\,kPa$, and a dominant 3rd mode for $p_A = 36\,kPa$ that differs from ALPACA results as depicted in Fig. 4c.

3. For a high pressure amplitude ($p_A = 42\,kPa$), the initial perturbation grows, leading to bubble breakup at 0.072 ms. This breakup event is indicated by a vertical dashed line in Figs. 3d and 4d. For this particular parameter combination the ROM predicts diverging mode amplitudes ($a_n \to \infty$).

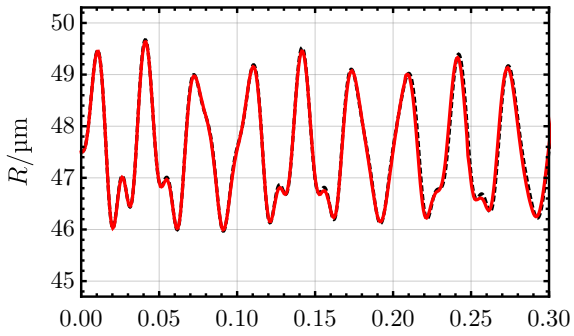

(a) $p_A = 10\,\mathbf{kPa}$

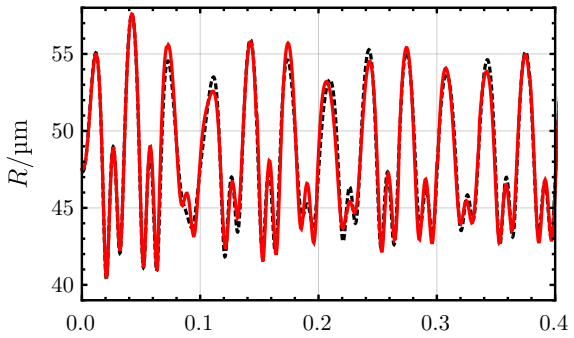

(b) $p_A = 32\,\mathbf{kPa}$

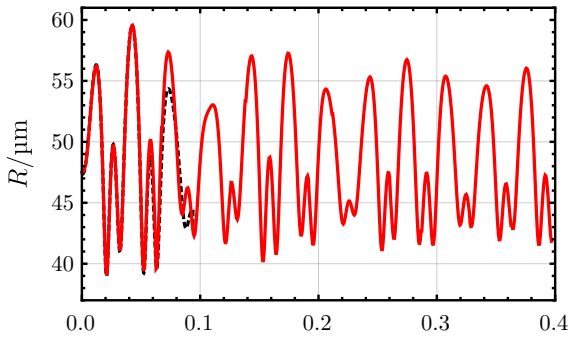

(c) $p_A = 36\,\mathbf{kPa}$

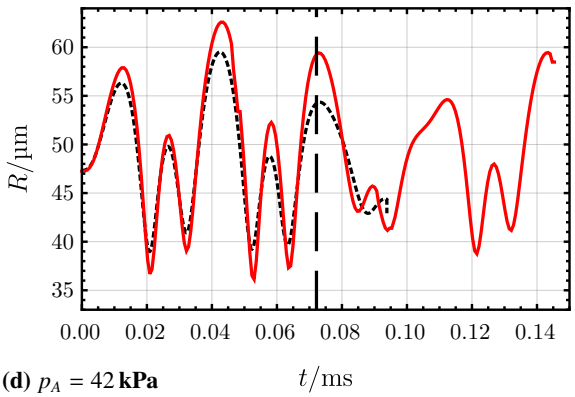

(d) $p_A = 42\,\mathbf{kPa}$

Figure 3. Radius over time for a $R_0 = 47.5\,\mu\mathbf{m}$ bubble excited with $f = 30\,\mathbf{kHz}$ ultrasound. (black dashed: ROM)

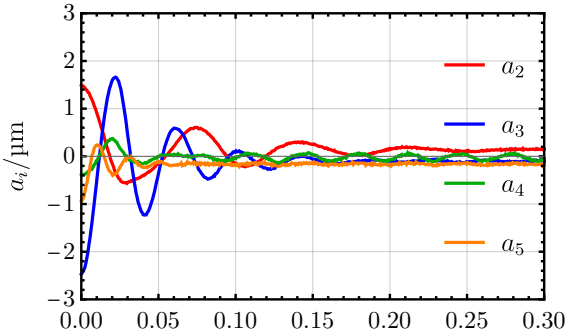

(a) $p_A = 10\,\mathbf{kPa}$

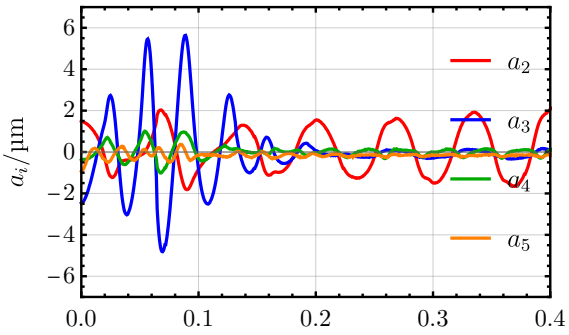

(b) $p_A = 32\,\mathbf{kPa}$

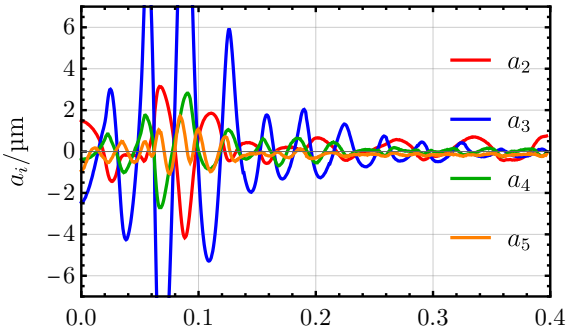

(c) $p_A = 36\,\mathbf{kPa}$

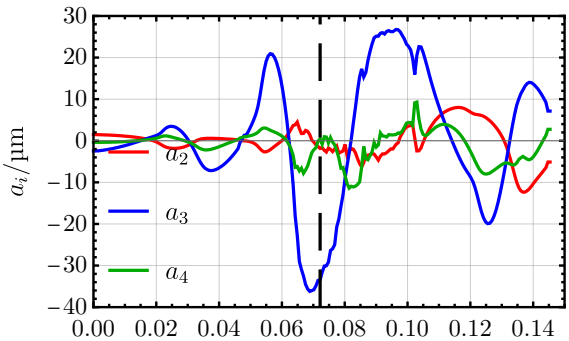

(d) $p_A = 42\,\mathbf{kPa}$

Figure 4. Mode amplitudes over time for a $R_0 = 47.5\,\mu\mathbf{m}$ bubble excited with $f = 30\,\mathbf{kHz}$ ultrasound.

The results indicate that the ALPACA simulations and the ROM predict similar spherical stability and breakup limits. Based on the simulations, the spherical stability limit in ALPACA is between 10 kPa $< p_A <$ 25 kPa, compared to $p_A = 19$ kPa in the ROM. Similarly, the breakup limit in ALPACA lies between 36 kPa $< p_A <$ 42 kPa, while the ROM predicts diverging mode amplitudes above $p_A = 39$ kPa. That indicates that diverging mode amplitudes in ROM can be a sign of bubble breakup.

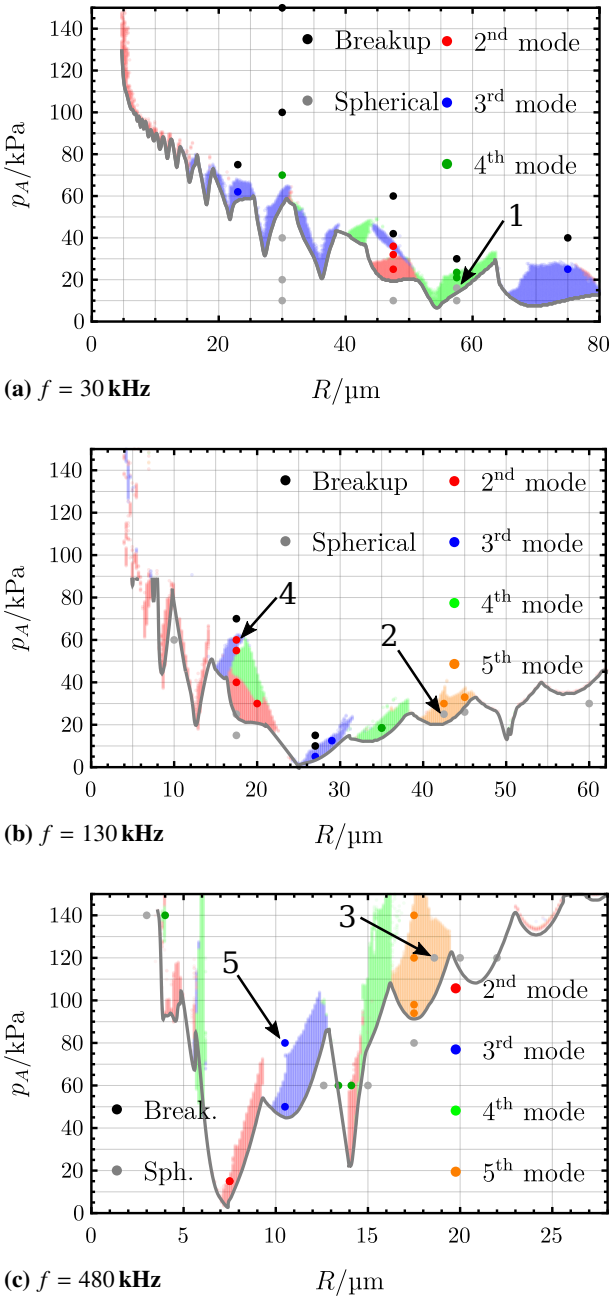

(a) $f = 30$ **kHz**

(b) $f = 130$ **kHz**

(c) $f = 480$ **kHz**

Figure 5. Parameter studies at various frequencies, the background is colored based on the ROM results, the dots show the ALPACA results. The gray line indicates the limit of stability (in ROM).

3.3. Parameter studies

Three parameter studies were conducted using the ROM. In each parameter study, the frequency was held constant while the bubble radius and pressure amplitude were adjusted in the ranges specified in Table 1. The dominant mode (i.e., the mode with the largest amplitude) was identified in each case. If the dominant mode amplitude does not reach $\hat{a}_n = 0.001$, then the bubble is considered spherically stable.

Table 1. Parameters used in the studies

Frequency	f	30 kHz/130 kHz/480 kHz
Equiv. radius	R_E	0 µm . . . 80 µm
Pressure ampl.	p_A	0 kPa . . . 150 kPa

The dominant modes are plotted in the (R, p_A) plane for the $f = 30$ kHz, 130 kHz and 480 kHz cases in Figures 5a, 5b and 5c, respectively. The various colors correspond to the different modes, as indicated in the legend. The gray line shows the limit of spherical stability, below which the bubble is considered spherical according to the ROM. Above the spherical stability line, where there is no color in the plot the bubble undergoes breakup. ALPACA simulations were carried out for selected cases, marked by dots based on the dominant mode amplitude. Below the spherical stability limit, as determined by the ROM (gray line), the bubbles in ALPACA also exhibit spherical stability. Slightly above the stability limit, the surface mode oscillations remain small and cannot be seen in the ALPACA simulations. For instance, in Fig. 5a in point marked by 1, the modes amplitudes are so small that they cannot be resolved by ALPACA with the given mesh resolution.

The stable surface mode oscillations generally show good agreement between the ROM and the ALPACA simulations. However, there are some cases where discrepancies occur, particularly for higher surface modes, as exemplified in Fig. 5b in point 2, and Fig. 5c in point 3. Additionally, cases with high surface mode amplitudes above the validity limit of ROM can also exhibit differences, such as $\hat{a}_2 > 0.3$ in Fig. 5b in point 4. It is important to note that bubble breakup consistently occurs above the region of stable surface oscillations. However, there are instances where the bubble does not break up, although predicted by the ROM (e.g., Fig. 5c point 5). This can be attributed to the validity limit, as it assumes small perturbations in the surface and may not accurately capture the behavior in cases with significant surface perturbations.

Out of the 62 ALPACA simulations, 54 of them (87%), qualitatively align with the ROM predictions. The simulation results are summarized in Tables 2, 3 and 4 in the Appendix. Based on these observations, it can be concluded that the spherical stability limit and the stable surface mode oscillations are accurately predicted by the reduced order model, as long as the validity limit of the ROM is not exceeded. The

approximated validity limit of the model is between $0.25 < \hat{a}_n < 0.37$ [17]. Furthermore, the ALPACA simulations verify that diverging mode amplitudes in ROM can indicate bubble breakup in some cases.

4. CONCLUSION

This study presents a comprehensive comparison of the ALPACA and ROM models for predicting surface oscillations and bubble breakup in oscillating microbubbles. The results demonstrate a high level of agreement between the two approaches, with ALPACA and ROM predictions aligning in 87% of cases. The ALPACA simulations achieved accurate results using a bubble resolution of $N_{\text{bubble}} \approx 300$. Deviations between the models were observed primarily in scenarios where the surface mode oscillations were small, and could not be resolved in ALPACA with the applied resolution, or when the dimensionless mode amplitudes exceeded the validity limit of the ROM.

In conclusion, the two models predict similar spherical stability and breakup limits, highlighting their reliability for simulating bubble dynamics. The results demonstrate that diverging mode amplitudes in ROM can effectively indicate bubble breakup, even when these amplitudes exceed its validity limit. This finding means that ROM could be a computationally effective method to identify bubble breakup, although flow simulations with ALPACA provide more details for capturing high-amplitude surface mode oscillations and bubble breakup. Together, these models offer complementary insights into the stability and breakup phenomena of oscillating microbubbles.

ACKNOWLEDGEMENTS

This research was supported by the EKÖP, Hungary funded by the National Research Development and Innovation Fund under grant number EKÖP-24-3-BME-84. The authors gratefully acknowledge the Gauss Centre for Supercomputing e.V. (www.gauss-centre.eu) for funding this project by providing computing time on the GCS Supercomputer SuperMUC-NG at Leibniz Supercomputing Centre (www.lrz.de). Project no. TKP-6-6/PALY-2021 has been implemented with the support provided by the Ministry of Culture and Innovation of Hungary from the National Research, Development and Innovation Fund, financed under the TKP2021-NVA funding scheme. The authors acknowledge the financial support of the Hungarian National Research Development and Innovation Office via NKFIH grants OTKA FK142376 and OTKA PD142254.

APPENDIX A

Tables 2, 3 and 4 contain all the ALPACA simulation parameters and the identified dominant mode in ALPACA and the ROM.

Table 2. Comparison at $f = 30$ kHz

R/μm	p_A/kPa	Dominant mode ALPACA	Dominant mode ROM
47.5	10	none	none
47.5	25	2	2
47.5	32	2	2
47.5	36	2	3
47.5	42	breakup	breakup
47.5	60	breakup	breakup
75	25	3	3
75	25	breakup	breakup
57.5	10	none	none
57.5	16	none	4
57.5	21	4	4
57.5	23.5	4	4
57.5	30	breakup	breakup
23	62	3	3
23	75	breakup	breakup
30	10	none	none
30	10	none	none
30	10	none	none
30	10	4	breakup
30	10	breakup	breakup
30	10	breakup	breakup

Table 3. Comparison at $f = 130$ kHz

R/μm	p_A/kPa	ALPACA	ROM
17.5	15	none	none
17.5	25	none	none
17.5	40	2	2
17.5	55	2	3
17.5	60	2	3
17.5	70	breakup	breakup
27	5	3	3
27	10	breakup	breakup
27	15	breakup	breakup
45	26	none	none
20	30	2	2
29	12.5	3	3
35	18.5	4	4
42.5	25	none	5
42.5	30	5	5
45	33	5	5
10	60	none	none
60	30	none	none

Table 4. Comparison at $f = 480$ kHz

R/μm	p_A/kPa	ALPACA	ROM
17.5	80	none	none
17.5	94	5	5
17.5	98	5	5
17.5	120	5	5
17.5	140	5	5
18.6	120	none	5
20	120	none	none
22	120	none	none
10.5	50	3	3
10.5	80	3	break
7.5	15	2	2
12.6	60	none	none
13.4	60	4	break
14.1	60	4	2
15	60	none	none
3	140	none	none
3	140	4	4
30	10	none	none
30	20	none	none
30	40	none	none
30	70	none	none
30	100	none	none
30	150	none	none

REFERENCES

[1] Sochard, S., Wilhelm, A., and Delmas, H., 1997, "Modelling of free radicals production in a collapsing gas-vapour bubble", *Ultrasonics Sonochemistry*, Vol. 4 (2), pp. 77–84.

[2] Kubicsek, F., Kozák, Á., Turányi, T., Zsély, I. G., Papp, M., Al-Awamleh, A., and Hegedûs, F., 2024, "Ammonia production by microbubbles: A theoretical analysis of achievable energy intensity", *Ultrasonics Sonochemistry*, Vol. 106, p. 106876.

[3] Cho, S., and Yun, S. H., 2020, "Structure and optical properties of perovskite-embedded dual-phase microcrystals synthesized by sonochemistry", *Communications Chemistry*, Vol. 3 (1), pp. 1–7.

[4] Al-Awamleh, A., and Hegedűs, F., 2024, "Sono-hydrogen: a Theoretical Investigation of its Energy Intensity", *Periodica Polytechnica Mechanical Engineering*, Vol. 68 (3), pp. 254–263.

[5] Rosselló, J., Lauterborn, W., Koch, M., Wilken, T., Kurz, T., and Mettin, R., 2018, "Acoustically induced bubble jets", *Physics of Fluids*, Vol. 30 (12).

[6] Prabowo, F., and Ohl, C.-D., 2011, "Surface oscillation and jetting from surface attached acoustic driven bubbles", *Ultrasonics sonochemistry*, Vol. 18 (1), pp. 431–435.

[7] Versluis, M., Goertz, D. E., Palanchon, P., Heitman, I. L., van der Meer, S. M., Dollet, B., de Jong, N., and Lohse, D., 2010, "Microbubble shape oscillations excited through ultrasonic parametric driving", *Physical review E*, Vol. 82 (2), p. 026321.

[8] Mur, J., Reuter, F., Agrež, V., Ohl, C.-D., et al., 2024, "Optic generation and perpetuation of acoustic bubble clusters", *Ultrasonics Sonochemistry*, Vol. 110, p. 107023.

[9] Guédra, M., and Inserra, C., 2018, "Bubble shape oscillations of finite amplitude", *Journal of Fluid Mechanics*, Vol. 857, pp. 681–703.

[10] Cleve, S., Guédra, M., Mauger, C., Inserra, C., and Blanc-Benon, P., 2019, "Microstreaming induced by acoustically trapped, non-spherically oscillating microbubbles", *Journal of Fluid Mechanics*, Vol. 875, pp. 597–621.

[11] Shaw, S. J., 2006, "Translation and oscillation of a bubble under axisymmetric deformation", *Physics of Fluids*, Vol. 18 (7), p. 072104.

[12] Shaw, S. J., 2009, "The stability of a bubble in a weakly viscous liquid subject to an acoustic traveling wave", *Physics of Fluids*, Vol. 21 (2), p. 022104.

[13] Shaw, S. J., 2017, "Nonspherical submillimeter gas bubble oscillations: Parametric forcing and nonlinear shape mode coupling", *Physics of Fluids*, Vol. 29 (12), p. 122103.

[14] Hoppe, N., Adami, S., and Adams, N. A., 2022, "A parallel modular computing environment for three-dimensional multiresolution simulations of compressible flows", *Computer Methods in Applied Mechanics and Engineering*, Vol. 391, p. 114486.

[15] Hoppe, N., Winter, J. M., Adami, S., and Adams, N. A., 2022, "ALPACA - a level-set based sharp-interface multiresolution solver for conservation laws", *Computer Physics Communications*, Vol. 272, p. 108246.

[16] Kalmár, P., Hegedűs, F., Nagy, D., Sándor, L., and Klapcsik, K., 2023, "Memory-friendly fixed-point iteration method for nonlinear surface mode oscillations of acoustically driven bubbles: from the perspective of high-performance GPU programming", *Ultrasonics Sonochemistry*, Vol. 99, p. 106546.

[17] Kalmár, P., Hegedűs, F., and Klapcsik, K., 2024, "A comparative study of measurements and numerical simulations of acoustically excited non-spherical bubbles oscillation", *International Journal of Multiphase Flow*, Vol. 179, p. 104947.

[18] Nagy, D., and Hegedűs, F., 2023, "Az ALPACA szoftver validációja akusztikusan gerjesztett gázbuborékok szimulációjára: Validation of ALPACA for the simulation of acoustically excited gas bubbles", *Nemzetközi Gépészeti Konferencia–OGÉT*, pp. 360–365.

[19] Osher, S., and Fedkiw, R. P., 2001, "Level set methods: an overview and some recent results", *Journal of Computational physics*, Vol. 169 (2), pp. 463–502.

[20] Harten, A., 1995, "Multiresolution algorithms for the numerical solution of hyperbolic conservation laws", *Communications on Pure and Applied Mathematics*, Vol. 48 (12), pp. 1305–1342.

[21] Harlow, F. H., and Amsden, A. A., 1971, "Fluid Dynamics. A LASL Monograph.", *Tech. rep.*, Los Alamos National Lab.(LANL), Los Alamos, NM (United States).

[22] Kaiser, J. W., Hoppe, N., Adami, S., and Adams, N. A., 2019, "An adaptive local time-stepping scheme for multiresolution simulations of hyperbolic conservation laws", *Journal of Computational Physics*, Vol. 4, p. 100038.

Conference on Modelling Fluid Flow (CMFF'25)
The 19th International Conference on Fluid Flow Technologies
Budapest, Hungary, August 26 - August 29, 2025

FLUID MECHANICS OF CEREBRAL THROMBI

László FUCHS[1], Lisa PRAHL-WITTBERG[2]

[1] Corresponding Author. Department of Mechanics, KTH, Royal Institute of Technology, Stockholm, Sweden. Tel.: +46 705728466, E-mail: fuchs@kth.se
[2] Department of Mechanics, KTH, Royal Institute of Technology, Stockholm, Sweden. Tel.: +46 736756464, E-mail: prahl@kth.se

ABSTRACT

Blood flow in a typical human aorta is considered by numerical simulations. Thrombi fragments (emboli) may reach the arteries leading blood to the brain. The flow in the aorta depends on the geometrical details and the temporal flow rate due to the cardiac output and the outflow from the branching arteries. Aortic flow is unsteady, swirling and may have a retrograde component during parts of the cardiac cycle. Retrograde flow may transport emboli into the branching arteries leading to the brain. Such a situation may occur also for particles, released late in diastole even when released in the descending aorta. The risk of stroke due to retrograde transport has also been observed clinically. Here, we simulate numerically the risk for emboli as a function of different heartbeat types. Particles with different properties were inserted, at different locations and at different time instants during the cardiac cycle. The motion of the particles and the forces acting on them may be used to assess risk for cerebral stroke. The temporal characteristic of the cardiac flow is an important stroke risk factor. It is shown that some clinical reports may underestimate the risk of stroke in thoracic aorta with small plaques (< 4 *mm*).

Keywords: Cerebral embolus. CFD, LPT, Thoracic aorta, retrograde particle transport.

NOMENCLATURE

inlet	[-]	The inlet plane
F_D,F_L	[*N*]	Forces acting on a particle
$F_{Saffman}$	[*N*]	Saffman lift force
F_{mass}	[*N*]	Added mass force
C_D	[-]	Drag coefficient
BC	[-]	Brachiocephalic artery
LC	[-]	Left Carotid artery
LS	[-]	Left Subclavian artery
Exit	[-]	Portion of particles leaving
Remain	[-]	Portion of particle within the aorta
IP1-IP4	[-]	Injection Points (Figure 3).
Re_p	[-]	Particle Reynolds number

1. INTRODUCTION

Stroke due to embolism may occur when a blood clot reaches a major artery supplying blood to the brain. The aortic arch has three major branches: the Brachiocephalic (BC) left Carotid (LC) and left subclavian (LS) arteries. All three arteries are major blood suppliers to the brain. Thus, blood clots from the heart, the ascending aorta, the aortic arch, or the proximal part of the descending aorta are all potential sources for ischemic stroke. Yet, it is not obvious whether a blood clot may enter BC, LC and LS at all. Atheroma in the proximal parts of the thoracic aorta, and in the aortic arch has often been observed in ischemic stroke patients when the atheroma diameter is larger than 4 *mm* [1].

Further evidence for the relation between aortic atheroma and the risk for ischemic stroke has been accumulated over the past decades [3-10]. The observations presented in these references suggested that retrograde diastolic blood flow in the proximal descending aorta having larger plaques (> 4 *mm*) could be associated with brain embolism due to retrograde aortic flow. Such retrograde flows in the aortic arch and proximal descending aorta were observed and characterized several decades ago using ultrasound technique [10-11].

Geometrical details of the aortic arch branching play an important role in ischemic stroke. In general, it has been observed that the percentage of left-sided infarcts are more common. Elsaid et al [12] classified the branches of the aortic arch into three types. The main finding was that cardio emboli caused by atrial fibrillation tends to have left anterior cerebrovascular predilection. Similarly, Xu et al [13] studied the relationship between the different aortic arch types (i.e., geometrical shapes) and the location of large vessel occlusion (LVO) in cardioembolic stroke. It was found that the anatomical shape by itself is inadequate to determine the risk for ischemic stroke. In addition to the shape of the aorta, its mechanical properties (i.e. aortic wall stiffness) and the temporal behavior of the cardiac output affect the extent of flow reversal [14].

The clots found in arteries vary considerably in shape and composition depending on the formation and degradation process that takes place naturally. In-vitro measurements of clots by Nahirnyak et al [15] reported the averaged clot density to be 1.08 10^3 kg/m^3 with an overall uncertainty in the density measurements of about 2%. Thrombi containing large volumes of fibrin have higher density, up to 1300 kg/m^3. The computation study by Choi et al [16], using the data of Nahirnyak et al [15] assumed thrombus size and density of 2-6 *mm* and 1080 kg/m^3, respectively. Pennati et al [17] and Neidlin et al [18] investigated numerically thrombectomy and endovascular mechanical recanalization, using thrombus density of 1300 kg/m^3.

The mechanism of clot transport depends both on the geometrical details of the thoracis aorta and the associated blood flow in it. The spatial and temporal details of the flow reveal the extent and variations of blood flow reversal. Fuchs et al [19-20] studied the volumetric extent of retrograde flow in the thoracic aorta for different cardiac flow rate profiles, concluding that details of the temporal behavior of cardiac flow profile impact on retrograde flow volume more than heart rate (HR) and cardiac output (CO). It was found that ratio of retrograde flow volume relative to the aortic volume depends on time and the character of the temporal variations in the cardiac cycle. Peak retrograde volume was reached at the local minimum of the volumetric flow. Peaks of wall shear-stress were observed at time instances when the time-derivative of the retrograde volume had (instantaneously) large temporal derivative. Rapid deceleration and elevated HR/CO were found to promote retrograde flow when expressed in terms of backflow volume relative to the total aortic volume. Although this measure may not directly reflect the potential of upstream thrombus transport, it raises the question of, and motivates investigating, the influence of retrograde flow dynamics on thrombus transport. The purpose of the current study was to assess the risks for ischemic embolus due to CO-pathology conditions, clot size and density, clot detachment location and instant during the cardiac cycle. The study is based on numerical flow simulations along with corresponding study of particle transport, depending on particle size, density, motion unsteadiness and local shear of the fluid.

The main purpose of this paper was to expose the basic fluid mechanical driving mechanism responsible for transport processes in the thoracic aorta and that may lead to cerebral stroke. These aspects were assessed by tracking solid spherical particles released at some specific locations and at certain times of the cardiac cycles. The cardiac flow rate was kept constant (1 Hz), but the temporal flow-rate distribution was changed such that the effects of deceleration and flow recovery on particle transport could be assessed. The modified cardiac output profiles are used to emulate heart arrhythmia.

2. Methods

The numerical simulations were carried out using a typical geometry of a generic human thoracic aorta (Swedish ethical approval Dnr 2017/258-31). The aortic walls were assumed to be rigid. The thoracic aorta has three major arteries, branching from the aortic arch (Figs 2-3.). These arteries lead blood to the upper parts of the body and to the brain. The flow distribution among the different branches may vary, depending on individual and instantaneous conditions. In the following simulations, the blood flow rate over the cardiac cycle was kept to 5 l/min. The temporal distribution into the inlet corresponded to the flow rate suggested by Benim et al [21]. The flow distribution among the four outlets was set to 15%, 7.5%, 7.5% and 70%, for BC, LC, LS and the exit from the proximal, thoracic part into its abdominal part of the aorta, respectively.

The blood was assumed to be an incompressible, homogenous non-Newtonian liquid with constant density (1102 kg/m^3). The non-Newtonian effect was accounted for through the Quemada model [22], which is based on the local red blood cell concentration and the shear-rate. In the following computations, only the strength of local shear-rate affects the local blood viscosity.

The computational geometry was discretized on a sequence of grids. After evaluation of the accuracy on different grids (Fuchs et al [19-20]), a grid with about 6 million computation cells was used. Given the assumptions made on the blood and the geometrical set-up, the incompressible Navier-Stokes equations were discretized on the final mesh. The equations were integrated in time over several cardiac cycles to eliminate initial condition effects.

The computed results were used to assess particle transport from different locations and different particle properties. Particle transport was simulated in post-processing mode, repeating the final cardiac cycle several times (between 5 to 50 cardiac cycles), depending on the injection mode and location. Commonly, one assumes that the main force acting on particles is the drag force. However, after estimating the effects of flow unsteadiness and the shear-rates found in the simulated cases, we used the contribution of different forces, when accounting for the motion of particles in the aorta. The particle equations are given in the section below.

2.1 Particle tracking and forces

Newton's second law expresses the balance of forces acting on a solid spherical particle and its acceleration:

$$F_p = m_p \frac{du_p}{dt} = F_D + F_{press} + F_{mass} + F_L \quad (1)$$

where F_p, is the force acting on the particle m_p, and u_p are the mass and velocity of the particle; F_D,

F_{press}, F_{mass} and F_L are the considered forces acting on the particle due to drag, pressure gradient, added (virtual) mass and lift, respectively. For a wide range of Reynolds numbers, the drag force, F_D, can be expressed as:

$$F_D = \frac{1}{2} C_D \frac{\pi D_p^2}{4} (u_p - u)|u_p - u| \qquad (2)$$

where u and u_p are the local fluid and particle velocities, respectively. The drag is related to the relative velocity of the particle (u-u_p). The particle Reynolds number, Re_p, is defined as $Re=D_p|u-u_p|/\nu$, with $\nu = m/\rho_f$ being the kinematic viscosity, ρ_p and ρ_f are the density of the particle and the carrier fluid, respectively. As the particle Reynolds number, Re_p, is within the intermediate range (up to the order of 50-100) for the cases considered here, the drag coefficient, C_D was given by:

$$C_D = \begin{cases} \frac{24}{Re} & (Stokes\ flow:\ Re_p < 1) \\ \frac{24}{Re}(1 + 0.15Re^{0.687}) & 1 \le Re_p \le 10^3 \end{cases} \qquad (3)$$

The F_{press} term is related to the pressure gradient in the fluid phase and the volume of the (spherical) particle.

$$F_{press} = \frac{1}{6} \pi D_p^3 \nabla P \qquad (4)$$

The added mass force is due to the acceleration of the fluid, and for Stokes flow it equals to half of the particle mass times its acceleration:

$$F_{mass} = \frac{1}{12} \pi D_p^3 \rho_f \frac{du_p}{dt} \qquad (5)$$

The lift force is based on Saffman's expression and hence it is denoted in the following by $F_{saffman}$ (cf [23]).

$$F_{saffman} = K \rho_f D_p^2 \frac{-\sqrt{\nu}}{\sqrt{|\nabla \times u|}} ((\nabla \times u) \times (-u_p)) \qquad (6)$$

This form of the lift force is valid for small particle Reynolds numbers (Re_p) based on the local shear.

When hitting the aortic wall the particles were assumed to be reflected without losses.

3. COMPUTED CASES

In the following we consider the effects of the dynamics of blood flow in a model of human thoracic aorta, and its effect on the transport of spherical particles. All cases are for a cardiac output of 5 l/min at a rate of 60 beat per minute (1 Hz). The aortic shape was fixed for the computed cases. The following four different cases considered herein, differing from each other in terms of the temporal flow rate over the cardiac cycle: Case A stands for a common, periodic cardiac cycle. Case B is like case A, but with an abrupt termination of the late part of the systole, corresponding to a stop in blood pumping in the late part of systole. Case C is similar also to Case A bout with a 20% shorter diastole whereas Case D has a 20% longer diastole. Case B implies a fast deceleration of the flow, leading to strong adverse pressure in the aorta. The latter two cases are common to patients with cardiac arrythmia and may occur randomly or (less common) periodically. The four temporal volume flow rate vs time are depicted in Fig 1. The blood pumped into the thoracic aorta leaves the vessel through four exits, as described above.

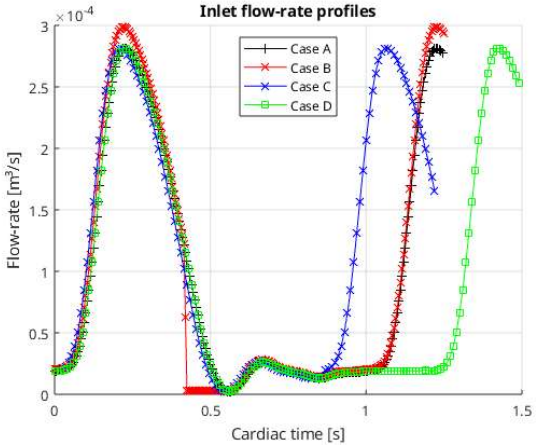

Figure 1. The volumetric flow rate into the aorta. Case A (black marking), "base" case with 60 beats/min and 5 l/min. The length of systole is roughly the same as the length of diastole. Case B (red markings) is like Case A, but with an abrupt termination of systole, leading to the formation of a sudden pressure increase. Case C (blue marking) is the same as Case A but with a 20% shorter diastole and Case D (green marking) has 20% longer diastole time.

The thoracic aorta has a significant curvature in the section termed as the aortic "arch" and a further weaker tortuosity in direction out of the plane of the arch. The curvature of the aorta implies formation of secondary flow. Further curvature out of the plane of arch leads to the formation of vortices of different scales. Time-dependency of the flow adds to the geometrical effects in terms of formation of additional vorticity.

Fig 2. depicts the instantaneous rotation (curvature) and angular velocity of particles released from a spherical region in the distal part of the aortic arch. Note the strong variation of these parameters along the particle paths. This observation, along with the clinical observation as discussed in the introduction, motivated the simulations to assess the interactions between the cardiac flow and particles with different sizes and densities.

The particles were released at four locations along the aorta (IP1 to IP4), as depicted in Fig 3. Particles injected into the aortic inlet were released continuously at the inlet plane. The number of particles leaving the four outlets increased until an asymptotic, final level was reached. These

simulations are useful to assess the accumulated impact of forces that the fluid exerts on the particles. A second mode, in which a given bolus of particles was released at certain instant of time within the cardiac cycle, was used to assess the risk for embolism from releasing particles at the different location at given time instance.

The injected particles were tracked by integrating Eqs (1) to (6) in a post-processing mode. Particles could leave the computational domain through the four exits mentioned above (BC, LCC, LSC and Exit). The injected particles were followed over five cardiac cycles with integration time-step of 1% of the cardiac cycle-time. The total integration time was long enough not to affect the total number of particles existing, the thoracic aorta segment under consideration. The accumulated number of particles leaving each exit plane relative to the number of injected particles was defined as the "Escape Rate" (ER). This criterion was used to reflect the risk for cerebral embolism.

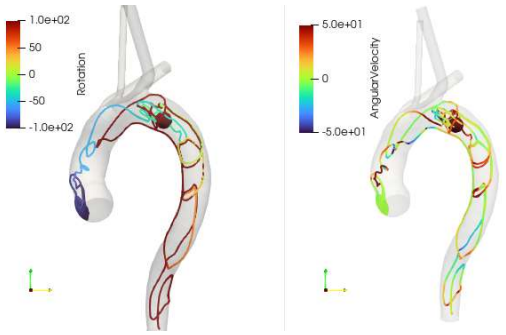

Figure 2. The instantaneous values of rotation and angular velocity on the particle paths. The particles were released from the spherical object downstream of the bifurcating arteries from the aortic arch.

Figure 3. Particles were released at the marked locations (denoted by IP1 to IP4, respectively): The aortic inlet was used to inject particles continuously throughout the simulation at the inlet plane. The evolution of the number of particles leaving each outlet followed in time, over ten to fifty cardiac cycles. In all other cases particles were injected at the marked location only once at a given instant of time in the cardiac cycle (after long enough simulations to attain a periodic flow field). These particles were followed over fine cycles only to assess the portion of particle leaving the different arteries branching from the aortic arch.

In the following we consider injection of particles particle injection into the aortic inlet (IP1), the arch (IP3) and the proximal descending aorta (IP4). The injected particles had the diameter of 2*mm* or 5*mm* and density of 1080 kg/l or 1200 kg/l, respectively. In each simulation, initial computation was carried out such that the effects of initial conditions were eliminated.

Table 1. shows the number of particles leaving the four outlets, relative to the total number of injected particles (ER). Inlet injection was continuous (i.e. throughout the cardiac cycle), and the number of particles was accumulated over time until a balance between injection rate and ER is in balance. The Escape Rate in the table was computed by following particles injected at the entrance to the aorta and during 10 cardiac cycles. As noted, the particle size is more important than the particle density. We also note that the large number of the larger (5*mm*) particles as well as the large portion of remaining smaller particle left through the Brachiocephalic (BC) artery.

The impact of the cardiac cycle on particle transport depends strongly on particle density and size. Irregular cardiac cycles (e.g. Cases C and D) lead to stronger transport of the 2*mm* particles through the aorta. The effect was much smaller for the 5*mm* particles. The risk for transport into the most distal (the left subclavian, LS) artery is almost twice as large for the irregular cardiac cases as compared to the periodic (Case A) cardiac rhythm.

When assessing the risk for embolus transport into the arteries branching from the aortic arch, a single bolus of particles was injected for each particle type at certain instant of time. Table 2 shows the portion of particles leaving the aorta accumulated over five cardiac cycles. The table corresponds to an injection point at the aortic arch (IP3) and at 50% of the cardiac cycle (i.e. approximately the end of systole, IT=0.5). As noted, and as expected most particles leave the aorta in the streamwise direction. The risk for stroke is non-negligible for the larger (5 *mm*) particles. A premature heartbeat (Case C) leads to elevated stroke risk also for the 2 *mm* particles. Particles released at other locations further downstream show similar behavior as shown in Table 2. Particles released further downstream in the ascending part of the aorta do not reach upstream, provided that the release instance takes place before mid-diastole. Fig. 4 depicts particle locations after five cardiac cycles, when the particles are released at the most distal location (IP4, shown in Fig. 3). Three different particle injection instances are shown: Release time at IT=0.25, 0.5 and 0.75 s (equals to

percentages of the time in the cardiac cycle). The particles are colored by the (Frobenius) norm of the stress tensor acting on the particle instantaneously.

Early injection instants (i.e. during systole) lead to the advection of the particles downstream with low degree of retrograde flow that is inadequate to transport particles in the arteries of the aortic arch. Late injection times, such as the one shown in Fig. 4 with IT= 0.75 s, leads to considerable retrograde flow. As the particles are injected during diastole, they are sucked upstream directly. During the next systolic phase (1< T <1.5 s) the particles are transported into all three branching arteries. Repeated simulations show that the highest probability for embolus is through the left subclavian (LS) artery. Indeed, the simulations do confirm clinical observation of higher stroke incident rate through the LC artery [12].

The stress acting on the particles may be large initially, depending on the relative velocity between the blood flow and the stationary thrombus. This stress determines also possible instant of fragmentation of the thrombus, and which is affected by the mechanical property of the thrombus. The norm of the stress acting on the particles increases over time and exceeds in all cases 1 N/m^2. The impact of stress on the particles was not considered here and can be seen as be a limiting factor in the simulations herein.

5. DISCUSSION

The results may be divided primarily into the fluid-mechanical aspect and secondly on potential clinical impact. The results demonstrate that the transport of spherical, rigid particles depends not only the commonly assumed drag, but also the rate of flow deceleration during the cardiac cycle. The deceleration affects enters both into the added mass and the Saffman terms (Eqs (5) and (6)). The results clearly demonstrate the role of retrograde, near-wall flow to transport particles upstream in the thoracic aorta. The results also help in explaining the elevated embolus risk heart arrythmia with prolonged diastole followed by a normal systole. The clinical impact of this work implies that the physical properties and the embolus (i.e. density and diameter) along with the detachment location and instant during the cardiac cycle strongly affect the risk for stroke. The multiple factors leading to stroke make it practically difficult to use patient-specific data to predict the risk for stroke.

The limitations of the study are due to the assumption made on the one-way coupling between the particles and the fluid. Further assumptions are made with respect to particle properties, solid aortic walls, particle-wall interaction and the limited variations in the imposed boundary conditions.

6. CONCLUSIONS

Detached thrombus fragments from the heart or the thoracis aorta was observed clinically as a potential risk for ischemic stroke (embolus). The simulations herein focus on the impact of particle size and diameter, release location and release instant of time in the cardiac cycle and not least irregularities in the cardiac cycle itself. The results indicate that the risk för stroke depends on all these parameters. Classification of stroke risk only by the aortic geometry as attempted clinically is inadequate, as the risk depends strongly also on the flow dynamics. The risk for stroke is very low for embolus released during systole and early diastole. Release in diastole implies risk for stroke with all four particle types. The results show that also smaller particles may lead to elevated stroke risk. This is in contrasts with clinical finings that the risk for stroke applies only for larger aortic atheroma with diameters larger than 4 *mm*.

ACKNOWLEDGEMENTS

Former Ph.D. students (Niclas Berg and Alexander Fuchs) assisted in the earlier stages of the project. Their contribution is highly acknowledged. The funding from the Swedish Heart Lung Foundation (Dnr 20220492) is highly acknowledged.

REFERENCES

[1] Viedma-Guiard, E, et al. Aortic Sources of Embolism. *Front Neurol.* doi: 10.3389/fneur.2020.606663, 2021, Vol. 15, 11:606663.

[2] Kronzon, I and Tunick, P. Aortic Atherosclerotic Disease and Stroke. *Circulation.* doi:10.1161/CIRCULATIONAHA.105.593418, 2006, Vol. 114, 1:63-75.

[3] Harloff, A, et al. Complex plaques in the proximal descending aorta: an underestimated embolic source of stroke. *Stroke* . doi: 10.1161/STROKEAHA.109.577775, 2010, Vol. 41, 6:1145-1150.

[4] Chhabra, L, et al. Retrograde embolism from the descending thoracic aorta causing stroke: an underappreciated clinical condition . *Indian Heart J.* . doi:10.1016/j.ihj.2013.04.024, 2013, Vol. 65, 3:319-322.

[5] Wehrum, T, et al. Aortic atheroma as a source of stroke –assessment of embolization risk using 3D CMR in stroke patients and controls. *J Cardiovascular Magnetic Resonance.* DOI:10.1186/s12968-017-0379-x, 2017, Vol. 19:67.

[6] Wehrum, T, et al. Measurement of cardiac valve and aortic blood flow velocities in stroke patients: a comparison of 4D flow MRI and echocardiography. *The international journal of cardiovascular imaging* . 2018, Vol. 34, 6:939-946.

[7] Wehrum, T, et al. Aortic Atherosclerosis Determines Increased Retrograde Blood Flow as a Potential Mechanism of Retrograde Embolic Stroke. *Cerebrovasc Dis.* doi: 10.1159/000455053, 2017, Vol. 43, 3-4:132-138.

[8] Wehrum, T, et al. Age dependence of pulmonary artery blood flow measured by 4D flow cardiovascular magnetic resonance: results of a population-based study. *J Cardiovasc Magn Reson* . doi:10.1186/s12968-016-0252-3, 2016, Vol. 18:31.

[9] Wehrum, T, et al. Quantification of Retrograde Blood Flow in the Descending Aorta Using Transesophageal Echocardiography in Comparison to 4D Flow MRI. *Cerebrovasc Dis* . doi: 10.1159/000381682, 2015, Vols. 39:287–292 .

[10] Kilner, P J, et al. Helical and Retrograde Secondary Flow Patterns in the Aortic Arch Studied by Three-Directional Magnetic Resonance Velocity Mapping. *Circulation.* 1993, Vol. 88, 5:2235–2247.

[11] Segadal, L and Matre, K. Blood Velocity Distribution in the Human Ascending Aorta. *Circulation.* 1987, Vol. 76, 1:90-100.

[12] Elsaid, N, et al. The Relation Between Aortic Arch Branching Types and the Laterality of Cardio-Embolic Stroke. *J Stroke Cerebrovasc Dis.* . doi:10.1016/j.jstrokecerebrovasdis.2020.104917., 2020, Vol. 29, 7:104917.

[13] Xu, L, et al. The relation between aortic arch branching types and the location of large vessel occlusion in cardioembolic stroke. *J Clin Neurosci.* doi: 10.1016/j.jocn.612 2021.05.013, 2021, Vols. 89:171-176.

[14] Hashimoto, J and Ito, S. Aortic Stiffness Determines Diastolic Blood Flow Reversal in the Descending Thoracic Aorta: Potential Implication for Retrograde Embolic Stroke in Hypertension . *Hypertension.* 2013, Vol. 62, 3:542–549.

[15] Nahirnyak, VM, Yoon, SW and Holland, ChK. Acousto-mechanical and thermal properties of clotted blood. *J. Acoust Soc Am* . doi: 10.1121/1.2201251, 2006, Vol. 119:3766.

[16] Choi, HW, Navia, JA and Kassab, GS. Thrombus deflector stent for stroke prevention: A simulation study. *J Biomech. 2015,.* doi: 10.1016/j.jbiomech.2015.05.006. PMID: 26049978., 2015, Vol. 48, 10:1789-95.

[17] Pennati, G, et al. Numerical simulation of thrombus aspiration in two realistic models of catheter tips. *Artif Organs.* doi: 10.1111/j.1525-1594.2009.00770.x. , 2010 , Vol. 34, 4:301-10.

[18] Neidlin, M, et al. A numerical framework to investigate hemodynamics during endovascular mechanical recanalization in acute stroke. *Int J Numer Method Biomed Eng.* doi: 10.1002/cnm.2748, 2016, Vol. 32, 4:e02748.

[19] Fuchs, A, et al. The Impact of Heart Rate and Cardiac Output on Retrograde Flow in the Human Thoracic Aorta. *ASME J of Medical Diagnostics.* https://doi.org/10.1115/1.4054459, 2022, Vol. 5, 3:031107.

[20] Fuchs, A, Berg, N and Prahl Wittberg, L. Pulsatile Aortic Blood Flow—A Critical Assessment of Boundary Conditions. *ASME J. Med. Diagn.* 2020, Vol. 4:011002, doi: 10.1115/1.4048978.

[21] Benim, AC, et al. Simulation of blood flow in human aorta with emphasis on outlet boundary conditions. *Applied Mathematical Modelling.* 2011, Vols. 35:3175–3188.

[22] Quemada, D. Rheology of concentrated disperse systems ii. a model for non-Newtonian shear viscosity in steady flows. *Rheologica Acta.* 1978, Vol. 17, 6:632-642 .

[23] Saffman, PG. The lift on a small sphere in a slow shear flow. *J Fluid Mechanics.* 1965, Vol. 22, 2:385-400.

Table 1: Continuous injection of particles at the *aorta inlet* (IP1), after 10 cardiac cycles. The relative escape rate (ER) from the outlet planes of the thoracis aorta, expressed in percents. The 2 *mm* and 5 *mm* particles are shown in the upper and lower tables, respectively. The portion of injected particles that are found in the thoracic aorta after 10 cardiac cycle is denoted as "Remain".

	Case A		Case B		Case C		Case D	
	1080	1200	1080	1200	1080	1200	1080	1200
Exit	37.4	36.6	37.0	36.3	44.1	43.3	43.3	42.6
BC	9.5	10.2	9.7	10.4	8.9	9.7	10.3	11.2
LC	6.3	6.7	5.7	6.4	5.0	5.4	5.8	6.0
LS	5.1	5.9	6.8	7.2	4.8	5.4	6.7	7.4
Remain	41.7	40.7	40.9	39.7	37.1	36.3	33.9	32.7

	Case A		Case B		Case C		Case D	
	1080	1200	1080	1200	1080	1200	1080	1200
Exit	25.9	24.4	23.9	22.8	44.1	26.1	31.7	28.7
BC	46.8	48.1	43.5	45.1	8.9	45.6	49.6	50.6
LC	6.5	7.1	4.4	4.7	5.0	8.0	7.3	8.4
LS	4.1	4.0	3.9	4.2	4.8	5.4	6.7	7.5
Remain	16.8	16.4	24.2	23.3	37.1	15.0	4.7	4.7

Table 2: Continuous injection of particles at the *aortic arch* (IP3), after five cardiac cycles. The relative escape rate (ER) from the outlet planes of the thoracis aorta, expressed in percents. The 2 *mm* and 5 *mm* particles are shown in the upper and lower tables, respectively. The portion of injected particles that are found in the thoracic aorta after 5 cardiac cycle is denoted as "Remain".

	Case A		Case B		Case C		Case D	
	1080	1200	1080	1200	1080	1200	1080	1200
Exit	99.1	98.9	99.5	99.4	94.2	94.7	99.8	99.9
BC	0.0	0.0	0.0	0.0	0.0	0.0	0.0	0.0
LC	0.0	0.0	0.0	0.0	0.0	0.0	0.0	0.0
LS	0.3	0.6	0.5	0.5	1.2	1.2	0.0	0.0
Remain	0.5	0.6	0.1	0.1	4.6	4.1	0.1	0.1

	Case A		Case B		Case C		Case D	
	1080	1200	1080	1200	1080	1200	1080	1200
Exit	92.0	91.7	95.3	95.0	93.8	93.7	95.0	93.8
BC	0.0	0.0	0.0	0.0	0.0	0.0	0.0	0.0
LC	0.0	0.0	0.0	0.0	0.0	0.0	0.0	0.0
LS	8.0	8.3	4.7	5.0	6.2	6.3	5.0	6.2
Remain	0.0	0.0	0.0	0.0	0.0	0.0	0.0	0.0

IT=0.25

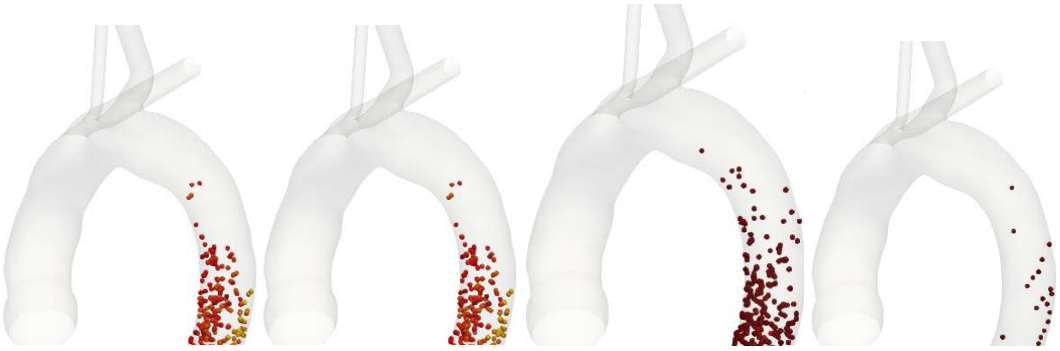

T=0.50 *T=0.75* *T=1.00* *T=1.50*

IT=0.50

T=0.50 *T=0.75* *T=1.00* *T=1.50*

IT=0.75

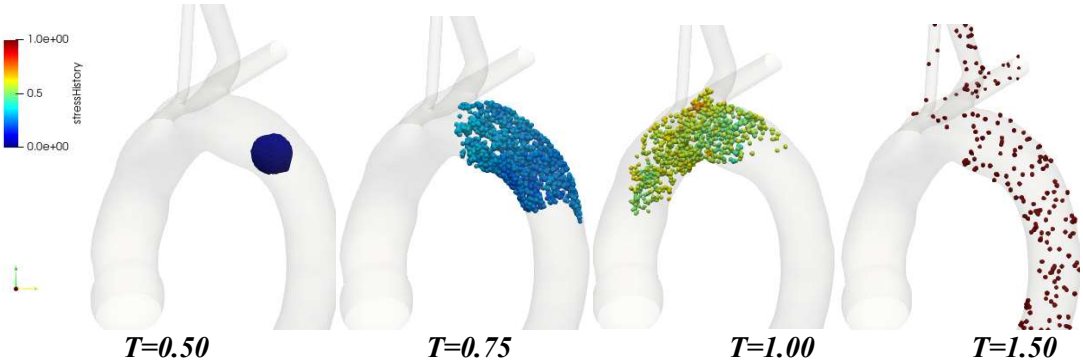

T=0.50 *T=0.75* *T=1.00* *T=1.50*

Figure 4. Injection of a single bolus of particles (Case A) at IP4, marked in left frame in the lowest row. There injection instants in the cardiac cycles are considered in the frames above: IT=0.25, 0.5 and 0.75 of the cardiac cycle, depicted in the three rows, respectively. The instantaneous particle positions, at different cardiac times are shown for each of the cardiac cycle instances is in the horizontal frames. T=0.75, 1, 1.25 and 1.5 stand for cardiac instant corresponding to about mid-diastole, end-diastole, peak- and end systole, respectively. Time T> 1, corresponds to the 2nd cardiac cycle. The injected particles were of density of 1080 kg/l and diameter of 5 *mm*. The norm of stress acting on the particles is used to color the particles (the colormap is shown in the low-left frame). Note (low-right frame) that particles that are injected in diastole are transported upstream into all three arteries that branch out from the aortic arch. Particles injected during systole do not end-up in the branching arteries.

Conference on Modelling Fluid Flow (CMFF'25)
The 19th International Conference on Fluid Flow Technologies
Budapest, Hungary, August 26-August 29, 2025

MODELLING THE TRANSPORT OF OXYGEN IN THE HUMAN VASCULAR SYSTEM

Márta VIHAROS[1], Richárd WÉBER[2], György PAÁL[3]

[1] Department of Hydrodynamic Systems, Faculty of Mechanical Engineering, Budapest University of Technology and Economics. H-1111 Budapest, Műegyetem rkp. 3., Hungary. Corresponding Author. E-mail: viharos.marti@gmail.com
[2] Department of Hydrodynamic Systems, Faculty of Mechanical Engineering, Budapest University of Technology and Economics. H-1111 Budapest, Műegyetem rkp. 3., E-mail: rweber@hds.bme.hu
[3] Department of Hydrodynamic Systems, Faculty of Mechanical Engineering, Budapest University of Technology and Economics. H-1111 Budapest, Műegyetem rkp. 3., E-mail: gypaal@hds.bme.hu

ABSTRACT

Low-dimensional hemodynamic simulations offer the advantage of modelling blood flow across the entire vascular system simultaneously. This approach enables the representation of large-scale physiological processes, including the complete cycle of oxygen transport within the vascular system.

In this cycle, inhaled oxygen diffuses from the alveoli into the pulmonary capillaries. Oxygenated blood is then transported via the pulmonary veins to the left heart and subsequently distributed through the systemic arteries. In the systemic capillaries, oxygen diffuses from the blood plasma into the surrounding tissues. The resulting deoxygenated blood is returned to the right heart through the systemic veins and is then transported back to the lungs via the pulmonary arteries. These processes involve advection-driven blood transport between two diffusion-driven stages: oxygen uptake in the lungs and oxygen delivery to tissues. The heart sustains this cycle by providing the necessary energy to maintain blood flow.

The primary objective of this study is to simulate these processes and replicate a realistic oxygen transport cycle within the whole modeled vascular system using the one- and zero-dimensional hemodynamic solver, first_blood. Evaluation of the simulation results demonstrated that the model successfully reproduces realistic dynamics across the entire vascular system.

Keywords: tissue oxygenation, oxygen uptake, hemodynamics, one- and zero-dimensional simulations

NOMENCLATURE

A	Cross section $[m^2]$
C	Oxygen concentration $\left[\frac{m^3}{m^3}\right]$
D	Diffusion coefficient $\left[\frac{m^3}{m^3}\right]$
$K_{\max}$	- $\left[\frac{m^3(O_2)}{m^3(\text{plasma})\cdot mmHg\cdot s}\right]$
$M_{\max}$	Maximum consumption rate of oxygen $\left[\frac{m^3(O_2)}{s\cdot m^3(\text{plasma})}\right]$
P	Partial pressure $[mmHg]$
h_c	Wall thickness of capillary vessels $[m]$
j	Index of the given division point [1]
n	Number of division points [1]
t	Time $[s]$
x	Axial coordinate $[m]$
α	Oxygen solubility $\left[\frac{m^3}{mmHg\cdot m^3}\right]$
κ	Wall permeability $\left[\frac{m^3(O_2)}{mmHg\cdot mm\cdot s}\right]$
ϕ	Volume fraction [%]
τ	Time constant of oxygen dissolution $[s]$
$\frac{S}{V}$	Vessel surface area to volume $\left[\frac{1}{m}\right]$
C_{RBC}	RBC concentration in blood $\left[\frac{1}{m^3(\text{plasma})}\right]$
HB	Haemoglobin [−]
HB_{O_2}	Haemoglobin saturation [%]
RBC	Red blood cell [−]

Subscripts and Superscripts

a	Alveoli
c	Capillary
p	Pulmonary
sat	Saturation
t	Tissue

1. INTRODUCTION

Studying biological processes through mathematical modeling could become a cornerstone in understanding complex physiological phenomena in the future. Hemodynamics, the dynamics of blood flow, is a fundamental aspect of cardiovascular physiology, directly influencing the delivery of nutrients and oxygen to tissues.

The vascular system has many tasks, one of which is the transport of O_2 (oxygen), which is of

prime importance. O_2 is crucial for the body since human cells need O_2 to produce adenosine triphosphate, which can be used or stored as energy. In case of inadequate blood supply, the body activates certain autoregulation processes to match the demand. For realistic haemodynamic simulations, taking these into account is inevitable.

The simulation of O_2 transport is the first step to simulate certain autoregulation processes, such as the metabolic response. For that reason, this article presents a mathematical model for the O_2 transport. The models include tissue O_2 uptake at the systemic capillaries and blood oxygenation at the pulmonary capillaries. Modelling these two processes ensures that the whole O_2 transport cycle is adequately captured.

1.1. The vascular system model

Low-dimensional haemodynamic simulations have the advantage of being computationally less demanding, making it possible to simulate blood flow in almost the entire vascular system simultaneously. This approach considers each large vessel as an axisymmetric pipeline, which builds up a vascular tree. Two equations describing the behavior of the fluid, the mass and momentum balances, are solved. The vessels are not rigid, so a material model connecting the transmural pressure and vessel deformation is needed [1]. This adds a third independent equation to the previous two. A detailed description of the vascular model is presented in [2]. The three independent equations are solved with the MacCormack scheme and the method of characteristics with the first_blood solver [3, 4].

1.2. Structure of the paper

The paper is structured as follows: After the introduction, a model for transport simulation in lumped models is presented. This is followed by a description of a modified version of the tissue oxygenation model from [5]. Before the results are presented and discussed, the blood oxygenation model is also introduced.

2. METHODS

2.1. Transport model for lumped models

For the vessels modelled in one dimension, the transport equation is solved given by Eq. 1, where C is a general transport variable. The effect of diffusion is small compared to the advection, the minimum of the Péclet number is around $P_{e_{O_2}} = \frac{v_c L_c}{D_{O_2}} = \frac{0.001[\frac{m}{s}] \cdot 0.00315[m]}{1.65 \cdot 10^{-9}[\frac{m^2}{s}]} \approx 1909$[1], where v_c is velocity of the plasma in the capillaries [6], L_c is the length of a capillary (the value is estimated) and D_{O_2} is the diffusion coefficient [5]. Red blood cells are much larger than O_2 molecules, and the effect of diffusion is even smaller, so the diffusion along the vessel axis can be neglected entirely.

The solver calculates the velocity field in every timestep for all vessels; thus, the concentration values can also be determined. At the intersections of the vessels there are nodes, the concentration is determined by assuming perfect mixing, providing boundary conditions. The concentration of the nodes is calculated as the weighted average of concentrations flowing toward the node, and the weights are the volumetric flow rates.

$$\frac{\partial C}{\partial t} = -v\frac{\partial C}{\partial x} \tag{1}$$

Besides the vessels modelled in 1D, there are also lumped models. For example, the peripherals are modelling small vessels, veins and organs. The structure of a peripheral model can be seen in Figure 1. The solver determines the volumetric flow rate and pressure values for these zero-dimensional models in each time step. Velocity and a spatial coordinate are necessary to calculate the transport. The next description briefly describes how these parameters are estimated for the 0D models.

- The time average of the volumetric flow rate corresponding to the resistance at the given peripheral model is calculated from a previous simulation for a cardiac cycle.
- Average velocity values corresponding to each segment can be found in the literature [6]. Time and spatial averages are needed in the simulations for arterioles, capillaries, venules, and veins. Table 1 presents the literature values considered in this work.
- The flow rate and the velocity determine the cross-section area for each segment. This way, in every time step with the previously calculated volumetric flow rate, a realistic velocity value can be obtained.
- Finally, the length is estimated for each segment; see Table 1 for the values. The venous vessel lengths are assumed to be equal to the length of the arterial path from the heart to the considered periphery.

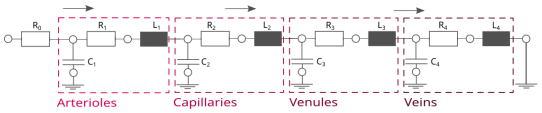

Figure 1. Peripheral models. Each compartment (arterioles, capillaries, venulares and veins) is modeled with an RLC circuit [7]. The left node of the lumped model is connected to a 1D vessel segment.

Providing that all segments at each periphery have every necessary additional parameter (a cross-section area and length), the transport of substances

Table 1. Velocity and length values for each segment. * indicates that for each peripheral model, the sum of the venous vessel lengths is uniquely determined based on the arterial model. The venous vessel lengths are assumed to be equal to the length of the arterial path from the heart to the considered periphery.

	v $[\frac{m}{s}]$	L $[m]$
arterioles	0.02	0.0225
capillaries	0.001	0.00315
venules	0.033	0.00515
veins	0.133	*

can be simulated the same way as for the vessels modelled in one dimension. The described transport model is general, and an arbitrary number of transport variables can be solved simultaneously.

2.2. Tissue oxygenation

The haemoglobin (HB) in red blood cells (RBCs) is mainly responsible for oxygen delivery. An HB molecule can bind a maximum of four O_2 molecules reversibly. Hemoglobin saturation (HB_{sat}) indicates the percentage of bound O_2 molecules relative to the maximum amount possible. If all HB molecules are bound to four O_2 molecules, the saturation is 100%. O_2 molecules stay attached to the HB molecules because of a balance between the partial pressure of O_2, $P_{O_2,p}$, and the HB saturation. This balance can be represented with a sigmoid curve. The curve is obtained by fitting (with the least squares method), while the data points are taken from the relevant interval of $P_{O_2,p}$ ($40mmHg \leq P_{O_2,p} \leq 95mmHg$) from the literature, see Table 2. The function is given by Eq. 2,

$$HB_{O_2} = \frac{L}{1 + e^{-k(P_{O_2} - m)}} + b \tag{2}$$

where $L = 1.251[-]$, $k = 0.0676[1/mmHg]$, $m = 17.71[mmHg]$ and $b = -0.274[-]$, and the curve is shown by Figure 2. The shape of the curve can be explained by the fact that the first O_2 molecule bound to an HB molecule changes the O_2-affinity, making the binding of the second and third O_2 molecule easier [8].

Table 2. Corresponding values of P_{O_2} [mmHg] and HB_{O_2} [1] in normal physiological conditions in the relevant interval ($40mmHg \leq P_{O_2} \leq 95mmHg$

P_{O_2}	40	50	60	70	80	95
HB_{O_2}	0.75	0.85	0.91	0.94	0.96	0.97

As RBC reaches the capillaries, the partial pressure reduces; thus, the O_2 disconnects from the HB molecules and enters the blood plasma. Between the plasma and the tissue, the main driving force is the diffusion because the velocity of plasma is

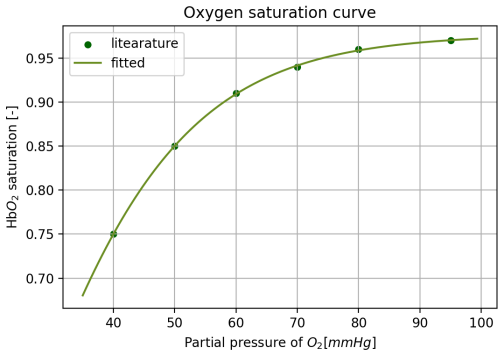

Figure 2. Sigmoid curve fitted with least squares method to data points are taken from Table 2.

$\approx 0.5 - 1[\frac{mm}{s}]$ [6], leaving enough time for the O_2 diffusion from the plasma to tissues through the capillary walls. Altogether, four transport equations are solved to model this complicated phenomenon, one for each: RBC, HB_{O_2}, O_2 concentration in the plasma, and O_2 concentration of the tissue. In larger arteries, arterioles, venules, and veins, O_2 absorption is negligible; thus, Eq. 1 is solved for these parts of the vascular model. However, handling the O_2 diffusion needs special source terms.

Capillaries can be found in the systemic peripherals and also in the pulmonary circulation. First, we discuss the former. The mathematical model describing the tissue oxygenation is based on the work of Bing [5]. The following assumptions are applied in the case of this model:

- O_2 and RBC diffusion is neglected along the vessel axis.
- The dissolution of O_2 from HB to plasma is instantaneous, i.e., Eq. 2 is updated each timestep.
- The inter-segment advection (e.g. arterioles-venules) term is not considered. This means that the partial pressure difference of O_2 between the segments does not inflict a change in O_2 concentration.

All following differential equations are advection transport ones with different source terms to mimic certain biological or chemical effects. The parameters and their values are in Table 3. The first is for the O_2 concentration in the capillaries, C_c, that is

$$\frac{\partial C_c}{\partial t} = \underbrace{-v\frac{\partial C_c}{\partial x}}_{\text{advection}} \underbrace{- \frac{\kappa_c}{h_c}\frac{S_c}{V_c}\left(\frac{C_c}{\alpha_b} - \frac{C_t}{\alpha_t}\right)}_{\text{diffusion from plasma to tissue}} + \underbrace{\frac{1}{\tau}\Delta HB_{O_2} \cdot C_{RBC} \cdot N_{O_2/RBC}\frac{M}{N_A \cdot \rho}}_{O_2 \text{ dissolving from HB to plasma}} \tag{3}$$

The diffusion of O_2 into tissue is driven by the partial pressure difference of dissolved O_2 between the

Table 3. Parameters of tissue oxygenation model. Literature provided an interval for each parameter, and the applied values fall within that range [5]. The exceptions are ϕ_c and $\frac{S_c}{V_c}$, which come from synthetic geometries suggesting different values: $\phi_c = 1.42[\%]$ and $\frac{S_c}{V_c} = 6.1638 \cdot 10^5[\frac{1}{m}]$. ϕ_t is then calculated as 1-ϕ_c.

Notation	Unit	Value
κ_c	$\frac{m^3}{mmHg \cdot mm \cdot s}$	$4.2 \cdot 10^{-14}$
h_c	m	$1.0 \cdot 10^{-6}$
$\frac{S_c}{V_c}$	$\frac{1}{m}$	$4.74 \cdot 10^5$
α_b	$\frac{m^3}{mmHg \cdot m^3}$	$3.11 \cdot 10^{-5}$
α_t	$\frac{m^3}{mmHg \cdot m^3}$	$3.95 \cdot 10^{-5}$
τ	s*	$8.0 \cdot 10^{-2}$
ϕ_c	%	1.1303
ϕ_t	%	98.8697
M_{max}	$\frac{m^3}{s \cdot m^3}$	$2.4 \cdot 10^{-4}$
C_{50}	$\frac{m^3}{mmHg \cdot m^3}$	10^9
$N_{O_2/RBC}$	$\frac{1}{1}$	$2.6 \cdot 10^{-5}$
M	$\frac{kg}{mol}$	0.032
N_A	$\frac{1}{mol}$	$6 \cdot 10^{23}$
ρ	$\frac{kg}{m^3}$	1.43

plasma and the tissue, expressed as $P_{O_2,p} - P_{O_2,t} = \frac{C_c}{\alpha_b} - \frac{C_t}{\alpha_t}$. The term $\frac{\kappa_c}{h_c}\frac{S_c}{V_c}$ represents the rate of change in C_c due to a unit difference in partial pressure. Moreover, the last term models the dissolution of O_2 to plasma from O_2 bound to hemoglobin (HB) according to the following considerations.

- At each timestep there is a given HB_{O_2} and C_c value. These are not necessarily in perfect balance, i.e., the sigmoid relationship given by Eq. 2 is not met. ΔHB_{O_2} gives the difference between the actual state and the sigmoid curve with the current C_c.
- The difference dissolves into the plasma described by the differential equation of a first-order lag.
- The dissolved amount is also substracted from the HB_{O_2} to ensure mass balance.

Eq. (4 describes the O_2 concentration of tissues. The second term, corresponding to the O_2 diffusion from plasma to tissue, is the same as in Eq. (3, but multiplied with $\frac{\phi_c}{\phi_t}$ (the ratio of capillary to tissue volume) and with a different sign to ensure mass balance. The multiplication by $\frac{\phi_c}{\phi_t}$ is necessary since the variables in the equations represent concentration, and the volumes of tissue and blood are different.

$$\frac{\partial C_t}{\partial t} = \underbrace{\frac{\kappa_c}{h_c}\frac{S_c}{V_c}\frac{\phi_c}{\phi_t}\left(\frac{C_c}{\alpha_b} - \frac{C_t}{\alpha_t}\right)}_{\text{diffusion from plasma to tissue}} - \underbrace{\frac{M_{max} C_t}{C_t + C_{50}}}_{O_2 \text{ consumption}}; \quad (4)$$

The O_2 consumption by tissue activity (see last term in Eq. 4) is modelled by the Michaelis–Menten kinetics, where C_{50} is C_t at the half maximum consumption rate [5], as this model is applied to describe nutrient uptake by cells [9].

The third equation describes the HB_{O_2} saturation level. The only source term is the dissolution of O_2 from HB to plasma, same as in Eq. (3).

$$\frac{\partial HB_{O_2}}{\partial t} = \underbrace{-v\frac{\partial HB_{O_2}}{\partial x}}_{\text{advection}} - \underbrace{\frac{1}{\tau}\Delta HB_{O_2}}_{O_2 \text{ dissolving from HB to plasma}} \quad (5)$$

Finally, the last one tracks the flow of RBC cells. As the amount of RBC cells remains constant on the low time scale, no additional source terms exist.

$$\frac{\partial C_{RBC}}{\partial t} = \underbrace{-v\frac{\partial C_{RBC}}{\partial x}}_{\text{advection}} \quad (6)$$

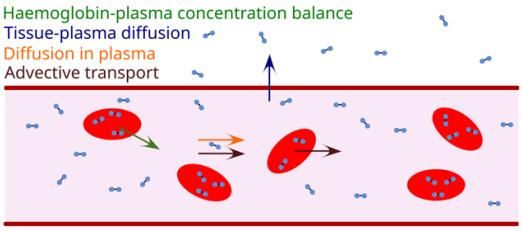

Figure 3. The transport of O_2 in capillaries.

2.3. Blood oxygenation

Gas exchange in the pulmonary circulation occurs with the help of alveoli, which are small air sacs in the lungs that allow gases to enter the blood. The difference between the partial pressure of O_2 in the alveoli and in the capillaries drives the diffusion of O_2. The partial pressure of O_2 in the alveoli is about $P_{O_2,a} = 100[mmHg]$, with minimal fluctuations over time [8]. The applied mathematical method is a modification of the systemic capillaries. The main difference being the direction of O_2 diffusion, and, since the fluctuations of the partial pressure of O_2 in the alveoli is low, it is assumed to be constant, so is the tissue concentration. Overall, there is no need for Eq. 4 in the pulmonary circulation, Eq. 5 and Eq. 6 are the same; however, the development in the source term of the plasma concentration model is crucial to cope the correct O_2 diffusion.

$$\frac{\partial C_{p,c}}{\partial t} = \underbrace{-v\frac{\partial C_{p,c}}{\partial x}}_{\text{advection}} \underbrace{- K_{max} sin^2\left(\frac{j\pi}{n}\right)\left(\frac{C_{p,c}}{\alpha_b} - P_{O_2,a}\right)}_{\text{diffusion from alveoli to plasma}} +$$
$$+ \underbrace{\frac{1}{\tau}\Delta HB_{O_2} \cdot C_{RBC} \cdot N_{O_2/RBC}\frac{M}{N_A \cdot \rho}}_{O_2 \text{ dissolving from HB to plasma}}, j \in \{1; 2...n\}; \quad (7)$$

The second term on the right hand-side of Eq. 7 describes the diffusion of O_2 from the alveoli. K_{max} is a constant parameter representing the maximum concentration change caused by a unit partial pressure difference in one second. The sin^2 function models the gradual change of the vessels rather than a sudden shift, so there is no O_2 diffusion in the start and end of the pulmonary capillaries. $\left(\frac{C_{p,c}}{\alpha_b} - P_{O_2,a}\right)$ is the partial pressure difference driving the diffusion of O_2. Table 4 gives the parameters of Eq. 7.

Table 4. Notations used in Eq. 7 describing the O_2 uptake in the pulmonary capillaries.

Notation	Dimension	(value)
$P_{O_2,a}$	$mmHg$	100
K_{max}	$\frac{m^3}{m^3 \cdot mmHg \cdot s}$	$6.479 \cdot 10^{-4}$

3. RESULTS AND DISCUSSION

Figure 4 represents the results of the O_2 transport simulation. Even though the simulation is transient, it converges to a periodic state. Since the fluctuations of the concentration levels within the periodic state are negligible, the figure contains temporal averages. While the y-axis presents the saturation level and the plasma O_2 concentration for the top- and bottom-side plot, respectively, the x-axis is a quasi-spatial coordinate, i.e., the actual lengths are distorted, giving each segment of the circulatory system the same gap. The HB_{O_2} saturation level (see top-side) is high for the systemic arteries and the pulmonary veins, while it is low for the systemic veins and the pulmonary arteries. The simulation results in a high level of around 97% and a low of 75%, which, as the dashed lines indicate in the figure, match the literature data qualitatively. Similar conclusions can be drawn from the bottom-side figure regarding plasma O_2 concentration. A slight discrepancy is present for the high-oxygenated level, but the low level coincides perfectly. It is interesting to notice the transition from high to low level in both cases. While the saturation level drops linearly, the plasma O_2 concentration shows exponential tendencies.

Even though the model results in physiologically relevant values, the validation can be only considered qualitatively. A significant uncertainty originates from the parameters. Since the original parameters are from different sources, they are not necessarily free from contradictions. The cited article specifically models the human brain, so the parameters determined are not necessarily valid for all body parts. The adopted mathematical model used for the synthetic geometries is given by [10], which focuses solely on the cerebral microvasculature. Some parameters cannot be directly measured, and only estimates can be applied. A patient-specific or even a population-based model needs further in-vivo measurements and calibration of the model. Finally, the modelled biology itself might be more complex than the current model.

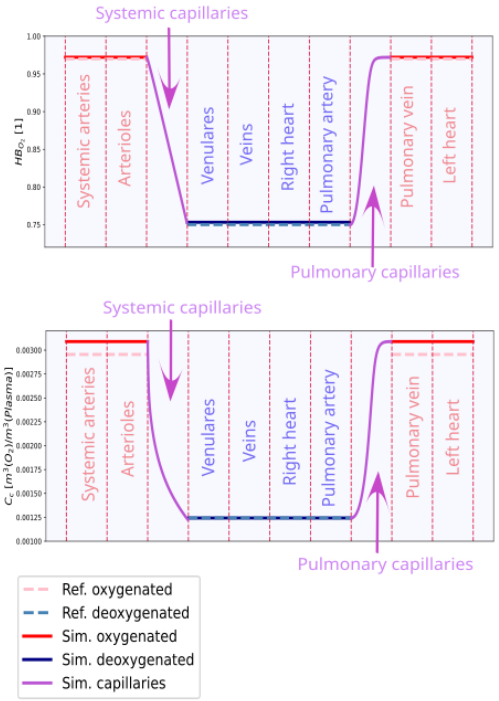

Figure 4. Simulation results of the O_2 transport cycle after the transient. The haemoglobin saturation and plasma O_2 concentration values are physiologically correct at every location in the vascular system.

4. CONCLUSIONS

The paper presents a possible mathematical method to model oxygen (O_2) transport via blood flow in the circulatory system. To obtain the classic hydraulic variables (such as pressure or velocity), the solution of the traditional mass and momentum balance equations and the deformable walls need to be coped. The basis for predicting O_2 concentration is the advection-diffusion equation from fluid dynamics. While diffusion along the vessel axis is negligible due to the high Peclet number, diffusion drives the exchange between the capillaries and tissues in both systemic and pulmonary capillaries. The former provides O_2 for the tissues (such as organs or muscle) using the O_2 for their primary function; the latter is responsible for the O_2 intake to the bloodstream from the lungs.

The presented model is validated qualitatively, i.e., the results coincide with physiological ranges in general. The O_2 saturation level is above 95% after the O_2 intake in the lungs, i.e., the pulmonary veins, the left side of the heart, and the systemic arteries. The O_2 consumption of the tissues at the systemic capillaries reduces O_2 concentration to 75%. However, patient-specific or population-based validation is inevitable in future work, which requires in-vivo measurements performed on real patients. Furthermore,

verification and a thorough uncertainty analysis are necessary to improve the reliability of the model.

ACKNOWLEDGEMENTS

GEMINI has received funding from the European Union's Horizon 2020 research and innovation programme under the grant agreement No 101136438.

The research was supported by the János Bolyai Research Scholarship (BO/00484/23/6) of the Hungarian Academy of Sciences and by the New National Excellence Program of the Ministry for Culture and Innovation from the source of the National Research (Wéber Richárd ÚNKP-22–5-BME-426).

Project no. TKP-6-6/PALY-2021 has been implemented with the support provided by the Ministry of Culture and Innovation of Hungary from the National Research, Development and Innovation Fund, financed under the TKP2021-EGA funding scheme.

REFERENCES

[1] Olufsen, M. S., 1999, "Structured tree outflow condition for blood flow in larger systemic arteries", *American Journal of Physiology-Heart and Circulatory Physiology*, Vol. 276 (1), pp. H257–H268, URL https://www.physiology.org/doi/10.1152/ajpheart.1999.276.1.H257.

[2] Wéber, R., Gyürki, D., and Paál, G., 2023, "First blood: An efficient, hybrid one- and zero-dimensional, modular hemodynamic solver", *International Journal for Numerical Methods in Biomedical Engineering*, Vol. 39 (5), p. e3701.

[3] Richárd, W., "github.com/weberrichard/first_blood.", .

[4] Wéber, R., Viharos, M., Gyürki, D., and Paál, G., 2024, "Improvement for the hemodynamic solver, First Blood, using the MacCormack scheme", *Biomechanica Hungarica*.

[5] Bing, Y., Józsa, T. I., and Payne, S. J., 2024, "Parameter quantification for oxygen transport in the human brain", *Computer Methods and Programs in Biomedicine*, Vol. 257, p. 108433, URL https://linkinghub.elsevier.com/retrieve/pii/S0169260724004267.

[6] Nichols, W. W., O'Rourke, M. F., and Vlachopoulos, C., 2011, *McDonald's blood flow in arteries: theoretical, experimental and clinical principles*, Hodder Arnold, London, 6th ed edn., ISBN 978-0-340-98501-4.

[7] Liang, F., Takagi, S., Himeno, R., and Liu, H., 2009, "Biomechanical characterization of ventricular–arterial coupling during aging: A multi-scale model study", *Journal of Biomechanics*, Vol. 42 (6), pp. 692–704, URL https://linkinghub.elsevier.com/retrieve/pii/S0021929009000268.

[8] Fonyó Attila, Ligeti Erzsébet, Kollai Márk, and Szűcs Géza, 2008, *Az orvosi élettan tankönyve*, Medicina, Budapest, 4., átdolg., bőv. kiad edn., ISBN 978-963-226-126-3, oCLC: 909502283.

[9] Wong, J., Simmons, C., and Young, E., 2017, "Modeling and Measurement of Biomolecular Transport and Sensing in Microfluidic Cell Culture and Analysis Systems", *Modeling of Microscale Transport in Biological Processes*, Elsevier, ISBN 978-0-12-804595-4, pp. 41–75, URL https://linkinghub.elsevier.com/retrieve/pii/B9780128045954000031.

[10] El-Bouri, W. K., and Payne, S. J., 2015, "Multi-scale homogenization of blood flow in 3-dimensional human cerebral microvascular networks", *Journal of Theoretical Biology*, Vol. 380, pp. 40–47, URL https://linkinghub.elsevier.com/retrieve/pii/S0022519315002398.

Conference on Modelling Fluid Flow (CMFF'25)
The 19th International Conference on Fluid Flow Technologies
Budapest, Hungary, August 26-August 29, 2025

MODELLING THE METABOLIC AND MYOGENIC CONTROL IN HUMAN BLOOD CIRCULATION

Richárd WÉBER[1], Márta VIHAROS[2], György PAÁL[3]

[1] Department of Hydrodynamic Systems, Faculty of Mechanical Engineering, Budapest University of Technology and Economics. H-1111 Budapest, Műegyetem rkp. 3., Hungary. Corresponding Author, E-mail: rweber@hds.bme.hu
[2] Department of Hydrodynamic Systems, Faculty of Mechanical Engineering, Budapest University of Technology and Economics. H-1111 Budapest, Műegyetem rkp. 3., E-mail: viharos.marti@gmail.com
[3] Department of Hydrodynamic Systems, Faculty of Mechanical Engineering, Budapest University of Technology and Economics. H-1111 Budapest, Műegyetem rkp. 3., E-mail: gypaal@hds.bme.hu

ABSTRACT

Hemodynamics, the study of blood flow dynamics, is a fundamental aspect of cardiovascular physiology, governing the delivery of oxygen and nutrients to tissues. A critical mechanism, ensuring stable blood flow under varying conditions, such as changes in blood pressure, is autoregulation. The myogenic response, a cornerstone of autoregulation, involves the contraction of arterioles in response to increased intravascular pressure, thereby stabilizing blood flow. Similarly, metabolic responses regulate vascular tone in accordance with the metabolic demands of tissues, ensuring an adequate supply of oxygen [1].

This study introduces refined mathematical models of regulatory mechanisms, implemented within a one- and zero-dimensional hemodynamics solver, first_blood[2]. The simulation mimics the body's response to changes by considering the peripheral resistances varying. Simulation results are systematically evaluated against established physiological knowledge. The findings demonstrate that the simulations can reproduce the behaviour of the control mechanisms. Specifically, the myogenic and metabolic response models yielded qualitatively accurate results. Future work will focus on validation with clinical in-vivo measurement data.

Keywords: metabolic control, myogenic control, haemodynamics, one- and zero-dimensional simulations

NOMENCLATURE

C	Oxygen concentration $\left[\frac{m^3}{m^3}\right]$
G	Static gain [1]
R	Vascular resistance $\left[\frac{m^3}{m^3}\right]$
M	Maximum oxygen consumption rate $\left[\frac{m^3(O_2)}{s \cdot m^3(plasma)}\right]$
a	Inner vessel radius $[m]$
b	Outer vessel radius $[m]$
c	A constant parameter $[m^2]$
f	Parameter of a sigmoid curve $\left[\frac{1}{Pa}\right]$ or $\left[\frac{m^3}{m^3}\right]$
k	A constant parameter [1]
u	A constant parameter [1]
p	Pressure $[Pa]$
t	Time $[s]$
x	Independent variable of a sigmoid curve $[Pa]$ or $[s]$
σ_θ	Circumferential wall tension $[Pa]$

Subscripts and Superscripts

fact	Scaling factor
max	Maximal value
met	Metabolic
min	Minimal value
myo	Myogenic

1. INTRODUCTION

The human circulatory system is responsible for transporting viable nutritions, ions, oxygen, etc. to the tissues. Maintaining blood flow and pressure is inevitable to keep the body functional. Although the complexity of blood flow regulation is high, modelling of such phenomena might help in understanding the fundamental operations, in decision-making or diagnose. Besides physiological and hormonal effects, three major control mechanisms influence blood pressure: myogenic, metabolic and neural. While the neural one uses baroreceptors from various locations of the arterial network controlling the heart, the former two are local mechanisms effecting only the diameter of arterioles.

In suboptimal conditions (e.g., low blood pressure or low tissue O_2 (oxygen) levels), the system attempts to correct this through regulation mechanisms that control the amount of blood flowing through the capillaries. Local regulation consists of two main

phenomena: myogenic and metabolic mechanisms that operate indepedently. The former responds to changes in blood pressure, while the latter responds to changes in the chemical composition [1], from which, the study focuses on the O_2 level. This work aims to capture the known and accepted characteristics of these processes. It also applies the O_2 transport modelling, that is also presented at this conference, titled "Modelling the transport of oxygen in the human vascular system".

Arteries are responsible for delivering oxygenated blood to organs and tissues. These vessels vary in diameter and length, with each type serving a different purpose. Smaller arterial vessels include arterioles, terminal arterioles, and capillaries, with diameters of 20-200 μm, 8-20 μm, and 4-7 μm, respectively. Larger arteries have relatively low vascular resistance, contributing about 10% to the total vascular resistance, while small arteries and arterioles contribute 50-55%, capillaries 30-35%, and the rest comes from venules and veins [3].

When considering autoregulation, the brain often comes to mind first, as it is one of the most vital organs in the body. The blood supply to the intracranial system is therefore a high priority, with a numerical value around $50-60\ \frac{\text{ml}}{\text{min}\ 100\ \text{g}}$, around 20% of the cardiac output when the body is at rest [4]. Cerebral autoregulation can be seen as the body's attempt to maintain this value under various conditions. Physicians often use the mean arterial pressure - cerebral blood flow (MAP-CBF) diagram to represent this phenomenon.

According to the original theoretical cerebral autoregulation curve, for a MAP value between 60 and 150 mmHg (the lower and upper limit of autoregulation), CBF remains almost constant as shown by Figure 1. This theory was described by Lassen in 1959. The classic autoregulation curve was later rejected. The updated autoregulation curve has a similar shape, but its width is different. Recent studies suggest that the plateau is much narrower, around $5-10$ mmHg. It is also unclear whether the autoregulation curve is symmetric, as the brain might respond better to an increase in MAP than to a decrease. Obtaining the real curve is challenging, as measuring CBF has its own difficulties. Two common methods, Doppler ultrasound and magnetic resonance imaging, both have considerable measurement uncertainties [4], [5].

1.1. The myogenic response

The myogenic response is observed in arterioles that supply blood to the brain and heart, among other organs. It works as follows: when blood pressure increases, the vessel wall initially expands. If the pressure remains constant, the vessel then contracts, often to a diameter smaller than its original size [6]. This contraction increases blood flow velocity and decreases pressure. The vascular resistance of vessels depends heavily on their diameter ($R \sim \frac{1}{d^4}$), so

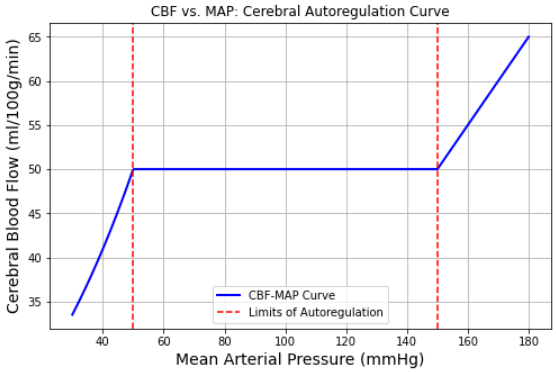

Figure 1. The original CBF-MAP curve.

by adjusting the diameter based on pressure, the body can regulate blood flow distribution to tissues and capillary pressure. Increased and maintained pressure in resistance arteries and arterioles causes these vessels to contract, a phenomenon known as the myogenic response. The steady-state response of these vessels is called myogenic tone. These mechanisms contribute to the autoregulation of blood flow in the brain, heart, skeletal muscles, and other organs [6].

Despite their importance, not all aspects of these biological functions are fully understood due to their complexity. Processes involving G-protein coupled receptors and ion channels, among others, play a role in the development of myogenic tone and response. The goal of mathematical modelling is not to encompass the entire process but focuses on establishing a direct relationship between pressure and peripheral resistance based on documented observations by physicians [6]. Mathematical models for myogenic autoregulation already exists in the literature [7], [8].

1.2. The metabolic response

Cells use Adenosine triphosphate (ATP) as a source of energy. ATP is typically produced through either oxidative phosphorylation or glycolysis, with the body preferring the former, which requires O_2. For this reason the body is in continuous need for O_2. O_2 demand can change for various reasons, including the onset of exercise. If the O_2 supply is insufficient, meaning that it does not match the need of the tissues, adenosine is produced. Adenosine, along with other substances produced as metabolic waste, causes vasodilation. Therefore, if the O_2 concentration is lower than needed, the vessels dilate, reducing their vascular resistance and allowing a larger blood flow to the tissue, increasing the O_2 supply. Literature suggests that the surface area responsible for O_2 diffusion also increases during exercise, increasing the amount of O_2 that can diffuse from the plasma to the tissues. This process results in a balance between the new level of O_2 demand and supply [1] [3].

The paper presents a comprehensive approach to simulate myogenic and metabolic blood flow regula-

tion, integrating insights from both literature research and mathematical modeling. The main objective of this work is to develop first_blood, a zero- and one-dimensional hemodynamic solver [2]. Researches regarding the control mechanisms could have real-world impact on medical research and clinical practice in the future. By advancing our ability to simulate these processes, it may pave the way for better diagnostic methods, targeted therapies, and new treatments for vascular disorders. The results of the simulations are thoroughly evaluated and discussed in the context of existing knowledge. The findings suggest that the simulations can mimic the behavior of the control mechanisms discussed, the myogenic and metabolic response models provide qualitatively correct results.

2. METHODS

2.1. Classic hemodynamic model

The model consists of large vessels modeled as axisymmetric tubes in one dimension (1D), which build up a vascular tree. The geometrical parameters (for example, diameter and length values) are taken from [9]. The vessels are elastic, and the relationship between the vessel deformation and the pressure described by a nonlinear function [10]. This, in addition to two fluid mechanics equations (the one dimensional mass and momentum equations) are solved with the method of characteristics and the MacCormack scheme [11]. Some parts of the cardiovascular system are modelled in zero dimension (0D) using electrical elements, e.g. resistors, inductors, capacitors, diodes and elastances. The smaller vessels (arterioles, capillaries and venules) and the veins are modelled using lumped models also, each compartment is taken into account with an RLC circuit at each periphery [12, 13]. The equations are solved the in-house hemodynamic solver, called first_blood [2].

2.2. Modeling the myogenic response

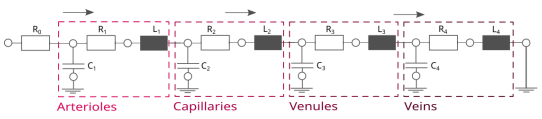

Figure 2. Peripheral models. Each compartment (arterioles, capillaries, venulares and veins) is modeled with an RLC circuit [12].

The simulation models the behavior of arterioles by considering the parameters of the peripheral models varying. For example, resistances vary with geometry, i.e., a smaller diameter results in higher resistance. In this context, the goal is to establish a relationship between peripheral resistances and pressure, since the myogenic response reacts to changes in blood pressure. First, an idealized relationship between pressure and peripheral resistance is given, based on a few assumptions:

- The arterioles are modeled as thick-walled tubes, since the ratio of the inner radius and the wall thickness is around $\frac{3}{4}$ [14].
- Since the Poisson coefficient of the vessel walls is close to 0.5 [2], it is an acceptable approximation to consider it incompressible.
- The shortening of the vessels as a response to increased pressure is neglected. Combining this with incompressible wall means constant area for the annulus.
- Theoretically the vessels response to stretch, trying to maintain constant circumferential wall tension despite changes in pressure [1]. We assume that the body strives to keep the circumferential wall tension constant at the inner diameter of the vessel.
- The pressure outside the arterioles is atmospheric.

The circumferential wall tension for a thick walled-tube can be written as:

$$\sigma_\theta(u) = \frac{pa^2}{b^2 - a^2}\Big(1 + \frac{b^2}{u^2}\Big), \tag{1}$$

where a and b are the inner and outer radius of the tube, p is the internal pressure and u is the radial coordinate ($a \leq u \leq b$). The third assumption above can be written in mathematical form:

$$(r + h)^2 - r^2 = c, \tag{2}$$

where c is a constant parameter, h is the wall thickness and r is the inner radius of the annulus. h can be determined as a function of r as $h = -r \pm \sqrt{r^2 + c}$ from Eq. (2). Since h, r and c are all positive, $h = -r + \sqrt{r^2 + c}$.

From the fourth assumption Eq. (1) should be evaluated at $u = r$. The inner radius of the tube is naturally $a = r$. We obtain:

$$\sigma_{\theta,0} = \frac{pr^2}{b^2 - r^2}\Big(1 + \frac{b^2}{r^2}\Big), \tag{3}$$

where $\sigma_{\theta,0}$ is constant. Substituting $b = r + h$ and $h = -r + \sqrt{r^2 + c}$ to Eq. (3) we get:

$$\sigma_{\theta,0} = p\Big(1 + \frac{2r^2}{c}\Big). \tag{4}$$

As previously mentioned a relationship between the peripheral resistances (R) and the pressure is needed, making the peripheral parametes time-dependent. The resistances are inversely proportional to r^4, so

$$R = \frac{\left(\frac{\sigma_{\theta,0}}{p} - 1\right)^{-2}}{k}. \tag{5}$$

Note that k is a constant parameter. After dividing both sides with the nominal resistance we obtain:

$$R_{fact} = \frac{\left(\frac{\sigma_{\theta,0}}{p} - 1\right)^{-2}}{k^*}, \tag{6}$$

where k^* is also a constant parameter, and R_{fact} is a scaling factor of the nominal resistance. To determine the two constants ($\sigma_{\theta,0}$ and k^*) two equations are needed. $\sigma_{\theta,0}$ can be calculated by substituting $b = r + h$ to Eq. (3), rearranging and using the first assumption ($\frac{h}{r} \approx \frac{4}{3}$ if $p = p_{ref}$).

$$\sigma_{\theta,0} = p\Big(1 + \frac{2}{2\frac{h}{r} + (\frac{h}{r})^2}\Big) = \frac{29}{20} p_{ref} \tag{7}$$

This provides a value for $\sigma_{\theta,0}$, since p_{ref} is a given parameter from the reference model. k^* can be calculated by substituting the value of $\sigma_{\theta,0}$ to Eq. (6), since R_{fact} is 1 if $p = p_{ref}$. This gives $k^* = (\frac{29}{20} - 1)^{-2} = \frac{400}{81}$[1]. At this stage the theoretical idealised curve is given with all it's parameters and constants.

In reality the vessels can not expand or contract without limitations, meaning that function given by Eq. (6) is not realistic. Instead, we assume that the system aims to follow the derived curve but fails. A more realistic sigmoidal connection is assumed between the pressure and the scaling factor of R:

$$R_{fact} = \frac{R_{max} + R_{min} e^{-f \cdot x_{myo}}}{1 + e^{-f \cdot x_{myo}}}, \tag{8}$$

Eq. (6) and Eq. (8) are obviously really different functions. So the next step is to determine the parameters (R_{max}, R_{min} and f) of the sigmoid curve considering the derived curve given by Eq. (6). The applied method sets the parameters so that Eq. (8) approximates the saturation values at roughly the same points as Eq. (6).

For the slope fitting we have to give the value of f. By matching the derivatives of Eq. (8) and Eq. (6) at p_{ref} we get: $f = \frac{8}{R_{max} - R_{min}} \frac{\sigma_{\theta,0}}{p_{ref}^2 k^*} \left(\frac{\sigma_{\theta,0}}{p_{ref}} - 1\right)^{-3}$.

Since the vascular resistance is a function of the diameter, the saturation values can be given with the normalized diameters obtained from [15]. With $sat_{max} = 1.773$ and $sat_{min} = 0.772$, R_{min} and R_{max} can be determined as:

$$R_{min} = \begin{cases} sat_{min}, & \text{if } x_{myo} < 0 \\ 2 - sat_{max}, & \text{otherwise.} \end{cases} \tag{9}$$

$$R_{max} = \begin{cases} 2 - sat_{min}, & \text{if } x_{myo} > 0 \\ sat_{max}, & \text{otherwise.} \end{cases} \tag{10}$$

x_{myo}, the independent variable of the myogenic control can be calculated from p with a low-pass filter. The differential equation for the filter is [7],

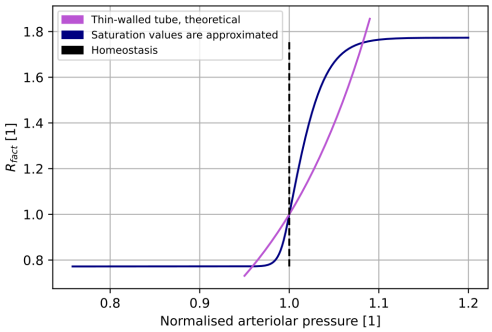

Figure 3. The theoretical curve given by 6 and the more resalistic sigmoidal curve.

$$\tau_{myo} \frac{dx_{myo}}{dt} = -x_{myo} + G_{myo}(\bar{p} - p_{ref}) \tag{11}$$

$G_{myo} = 0.9$ is the static gain, $\tau_{myo} = 40s$ is the time constant of the low-pass filter, $\bar{p}$ is the time-average of the last cardiac cycle and p_{ref} is the reference pressure. For each periphery p_{ref} is determined as the time average of the arteriolar pressure of the last cardiac cycle from a previous simulation (without any autoregulation). The simulation can calculate the scaling factor of resistances (R_{fact}) from the reference and the actual pressure with the given model. The arteriolar resistances are given for the next time step.

2.3. Modeling the metabolic control

Similar to the myogenic control, a sigmoidal connection between tissue O_2 level and the peripheral resistances is assumed. The saturation levels of the sigmoid curve are the same as for the myogenic control since the same vessels are responsible for these mechanisms and there is no information in the literature to suggest otherwise according to the author's knowledge. Similarly to the modelling of the myogenic response, the base simulation without any regulation mechanisms is used as the reference. Based on Eq. (8), the time dependent peripheral resistances can be determined as

$$R_{fact} = \frac{R_{max} + R_{min} e^{-f_{met} \cdot x_{met}}}{1 + e^{-f_{met} \cdot x_{met}}} \tag{12}$$

where f_{met} is scaled, so that the relative central slope is the same as in Eq. (8). The independent variable of the metabolic control (x_{met}) is calculate from C_t with a low-pass filter:

$$\tau_{met} \frac{dx_{met}}{dt} = -x_{met} + G_{met}(\bar{C}_t - \bar{C}_{t,ref}) \tag{13}$$

$G_{met} = 0.9$ is the static gain, $\tau_{met} = 40s$ is the time constant of the low-pass filter and $\bar{C}_t$ is the time average of C_t in the last cardiac cycle. For each periphery $\bar{C}_{t,ref}$ is calculated as the time average of the tissue O_2 concentration of the last cardiac cycle from

a previous simulation (without any autoregulation).

3. RESULTS AND DISCUSSION

3.1. Results of the myogenic response

Figure Figure (4) shows the simulated CBF-MAP curves with and without the myogenic response for the cerebral peripheries (the myogenic response for other peripheries were turned off for all simulations). The MAP values where modified by changing the miniumun of the elastance function of the left ventricle in the heart model that mimics the contraction of the heart. MAP was calculated as the time-average of the aortic pressure, CBF (the time-averaged volumetric flow rate of blood through the arteries supplying the intracranial system) is relative to the simulation computed with the base model.

A third-degree polynomial was fitted to the data points in both cases, since this type of function is recommended by physicians to describe autoregulation [16]. As expected, the myogenic response makes the CBF-MAP curve flatter over a certain range. However, the simulated curve is not as flat as the theoretical CBF-MAP curve, which is usually depicted with a more horizontal plateau. The simulation successfully mimics the body's behavior, meaning it attempts to maintain constant blood flow under varying conditions.

The myogenic mechanism responds to changes in blood pressure, but the body has multiple mechanisms that regulate blood pressure, e.g., the baroreflex. This means that the CBF-MAP curve observed by physicians is influenced by numerous factors [17]. Without accounting for these other processes, the simulated CBF-MAP curve cannot match the one measured in humans. It is also impossible to measure the effect of only the myogenic response in humans, since the other responses cannot be turned on or off independently.

Moreover, there are fairly different CBF-MAP curves found in the literature. The uncertanities of the CBF measurement methods (for example magnetic resonance imaging and transcranial Doppler ultrasound) are high [5], meaning that, achieving accurate numerical data is challenging, and the measurement error accumulates to the MAP-CBF curve. Since the model gives qualitatively correct results the model is found to be acceptable. In-vivo measurements could give the opportunity to calibrate the model to a for a population stochastically, or even a patient-specific level.

3.2. Results of the metabolic response

The metabolic response can be observed when an organ's O_2 demand increases, such as during exercise. The body responds by dilating resistance vessels, which increases blood flow to the organ. The increased O_2 demand can be modeled by changing the O_2 consumption term in the equations. To test whether the metabolic response model accurately mimics the body's behavior, four simulations

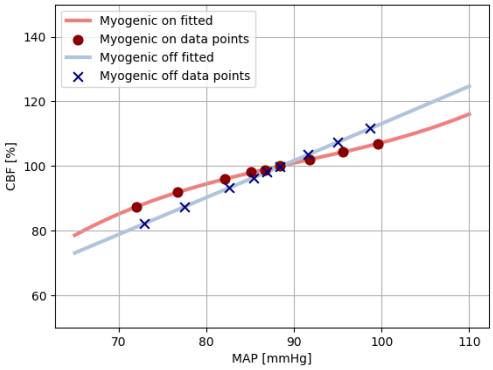

Figure 4. Evaluated CBF-MAP curves of the simulations. The myogenic response is only applied for the cerebral peripherals. The MAP values are modified by changing the miniumun of the elastance function of the left ventricle in the heart model that mimics the contraction of the heart. MAP is calculated as the time-average of the aortic pressure, CBF is relative to the simulation computed with the base model.

are computed. First, regulation is turned off, and all model parameters are set to their default values. In the second scenario, regulation is turned on, but the parameters remain the same. In the third scenario, the maximum oxygen consumption rate is doubled, but the metabolic response is turned off. In the fourth scenario is still doubled, but this time, the metabolic response is turned on. Overall every scenario is considered with the metabolic response and the modelled exercise.

The results of these simulations are shown in Figure (5). In the first two scenarios, the tissue O_2 concentration, the tissue oxygenation stabilizes at the same level, as expected. However, when O_2 consumption increases (in the third scenario), the tissue oxygenation decreases. When the metabolic response is activated (in the fourth scenario), the oxygenation increases and stabilizes between the values from the first two and the third scenarios. These results are consistent with expectations. The increased metabolic demand is regulated by increasing the diameters of the arterioles; thus, the blood flow is increased. The elevated blood flow tries to compensate the increased demand of O_2 in the tissues.

The model gives qualitatively accurate simulation results. The limitation of the study is the available in-vivo measurements. Performing in-vivo measurement on real patients requires both physicians with ethical approval, and expensive measurement setup. Moreover, the available measurement scenarios are highly limited, only certain variables can be measured directly, and only at certain locations. However, the main objective of future research is to collaborate with physicians and to obtain in-vivo

measurement data. Such data gives the opportunity to calibrate the model population- or even patient-wise.

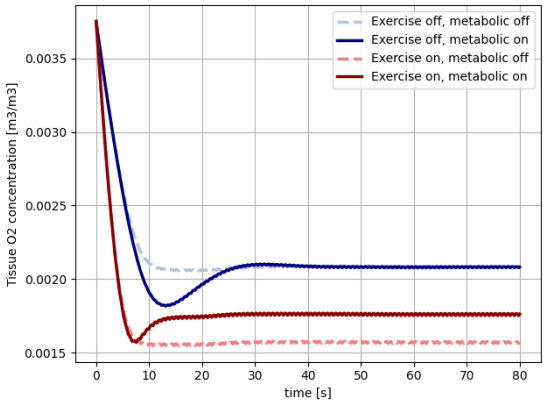

Figure 5. Evaluated CBF-MAP curves of the simulations. The myogenic response was only applied for the cerebral peripherals. The MAP values where modified by changing the minimun of the elastance function of the left ventricle in the heart model that mimics the contraction of the heart. MAP was calculated as the time-average of the aortic pressure, CBF is relative to the simulation computed with the base model.

3.3. Conclusion

The study presented a possible way to model two cardiovascular system control mechanisms, the myogenic and the metabolic response. Although both work locally, the myogenic response aims to ensure the constant circumferential shear stress, and to keep the blood flow constant and protect the vessels from overpressure. Traditional fluid and solid mechanical considerations determine a theoretical function for the pressure - peripheral resistance; however, lower and upper diameter boundaries limit the deformation keeping the physiological relevance. The metabolic response maintain the oxygen saturation level high ensuring the proper function of tissues and organs. The applied mathematical model builds on the same foundations as the myogenic one.

The simulation results suits the physiological relevance and gives qualitatively correct values. The myogenic model mimics the autoregulation, i.e., limits the effect of increased mean arterial pressure to the cerebral blood flow keeping the nutrient supply high despite changing physiological state. Analysing the metabolic response, by creating simulation scenarios with mimicking exercise by an increased oxygen demand could prove the qualitative relevance of the model. The results clearly set the direction for further research: in-vivo measurement can increase the validity of the models.

REFERENCES

[1] Pittman, R. N., 2016, *Regulation of tissue oxygenation*, Morgan & Claypool, San Rafael, California, second edition edn., ISBN 978-1-61504-721-5, oCLC: 957008214.

[2] Wéber, R., Gyürki, D., and Paál, G., 2023, "First blood: An efficient, hybrid one- and zero-dimensional, modular hemodynamic solver", *International Journal for Numerical Methods in Biomedical Engineering*, Vol. 39 (5), p. e3701.

[3] Fonyó Attila, Ligeti Erzsébet, Kollai Márk, and Szűcs Géza, 2008, *Az orvosi élettan tankönyve*, Medicina, Budapest, 4., átdolg., bőv. kiad edn., ISBN 978-963-226-126-3, oCLC: 909502283.

[4] Vitt, J. R., Loper, N. E., and Mainali, S., 2023, "Multimodal and autoregulation monitoring in the neurointensive care unit", *Frontiers in Neurology*, Vol. 14, p. 1155986, URL `https://www.frontiersin.org/articles/10.3389/fneur.2023.1155986/full`.

[5] Jones-Muhammad, M., and Warrington, J. P., 2021, "Redefining the cerebral autoregulatory range of blood pressures: Not as wide as previously reported", *Physiological Reports*, Vol. 9 (17), p. e15006.

[6] Jackson, W. F., 2021, "Myogenic Tone in Peripheral Resistance Arteries and Arterioles: The Pressure Is On!", *Frontiers in Physiology*, Vol. 12, p. 699517, URL `https://www.frontiersin.org/articles/10.3389/fphys.2021.699517/full`.

[7] Toro, E. F., Celant, M., Zhang, Q., Contarino, C., Agarwal, N., Linninger, A., and Müller, L. O., 2022, "Cerebrospinal fluid dynamics coupled to the global circulation in holistic setting: Mathematical models, numerical methods and applications", *International Journal for Numerical Methods in Biomedical Engineering*, Vol. 38 (1), p. e3532.

[8] Ursino, M., and Giannessi, M., 2010, "A Model of Cerebrovascular Reactivity Including the Circle of Willis and Cortical Anastomoses", *Annals of Biomedical Engineering*, Vol. 38 (3), pp. 955–974, URL `http://link.springer.com/10.1007/s10439-010-9923-7`.

[9] Reymond, P., Merenda, F., Perren, F., Rüfenacht, D., and Stergiopulos, N., 2009, "Validation of a one-dimensional model of the systemic arterial tree", *American Journal of Physiology-Heart and Circulatory Physiology*, Vol. 297 (1), pp. H208–H222, URL `https://www.physiology.org/doi/10.1152/ajpheart.00037.2009`.

[10] Olufsen, M. S., 1999, "Structured tree outflow condition for blood flow in larger systemic arteries", *American Journal of Physiology-Heart and Circulatory Physiology*, Vol. 276 (1), pp. H257–H268, URL https://www.physiology.org/doi/10.1152/ajpheart.1999.276.1.H257.

[11] Wéber, R., Viharos, M., Gyürki, D., and Paál, G., 2024, "Improvement for the hemodynamic solver, First Blood, using the MacCormack scheme", *Biomechanica Hungarica*.

[12] Liang, F., Takagi, S., Himeno, R., and Liu, H., 2009, "Biomechanical characterization of ventricular–arterial coupling during aging: A multi-scale model study", *Journal of Biomechanics*, Vol. 42 (6), pp. 692–704, URL https://linkinghub.elsevier.com/retrieve/pii/S0021929009000268.

[13] Jones, G., Parr, J., Nithiarasu, P., and Pant, S., 2021, "A physiologically realistic virtual patient database for the study of arterial haemodynamics", *International Journal for Numerical Methods in Biomedical Engineering*, Vol. 37 (10), p. e3497.

[14] Müller, B., Lang, S., Dominietto, M., Rudin, M., Schulz, G., Deyhle, H., Germann, M., Pfeiffer, F., David, C., and Weitkamp, T., 2008, "High-resolution tomographic imaging of microvessels", San Diego, California, USA, p. 70780B, URL http://proceedings.spiedigitallibrary.org/proceeding.aspx?doi=10.1117/12.794157.

[15] Zhang, C., Rogers, P. A., Merkus, D., Muller-Delp, J. M., Tiefenbacher, C. P., Potter, B., Knudson, J. D., Rocic, P., and Chilian, W. M., "Regulation of Coronary Microvascular Resistance in Health and Disease", .

[16] Brassard, P., Labrecque, L., Smirl, J. D., Tymko, M. M., Caldwell, H. G., Hoiland, R. L., Lucas, S. J. E., Denault, A. Y., Couture, E. J., and Ainslie, P. N., 2021, "Losing the dogmatic view of cerebral autoregulation", *Physiological Reports*, Vol. 9 (15), URL https://onlinelibrary.wiley.com/doi/10.14814/phy2.14982.

[17] Tlałka, K., Saxton, H., Halliday, I., Xu, X., Taylor, D., Narracott, A., and Malawski, M., 2024, "Local Sensitivity Analysis of a Closed-Loop in Silico Model of the Human Baroregulation", L. Franco, C. De Mulatier, M. Paszynski, V. V. Krzhizhanovskaya, J. J. Dongarra, and P. M. A. Sloot (eds.), *Computational Science – ICCS 2024*, Vol. 14835, Springer Nature Switzerland, Cham, ISBN 978-3-031-63771-1 978-3-031-63772-8, pp. 173–187, URL https://link.springer.com/10.1007/978-3-031-63772-8_17, series Title: Lecture Notes in Computer Science.

Conference on Modelling Fluid Flow (CMFF'25)
The 19th International Conference on Fluid Flow Technologies
Budapest, Hungary, August 26 - August 29, 2025

MULTIPHASE MODEL OF THE MELT BLOWING PROCESS IN MULTI-HOLE NOZZLES

Fabian LEMARCHAND[1], Alejandro RIVAS[2], Alaine SALTERAIN[3]

[1] Department of Mechanical Engineering and Materials, TECNUN Escuela de Ingeniería, Universidad de Navarra, Paseo Manuel de Lardizabal, 13, San Sebastian E-20018, Spain. Tel.: +33 6 23 83 43 66, E-mail: flemarchand@unav.es
[2] Department of Mechanical Engineering and Materials, TECNUN Escuela de Ingeniería, Universidad de Navarra, Paseo Manuel de Lardizabal, 13, San Sebastian E-20018, Spain. E-mail: arivas@tecnun.es
[3] Valco Melton, Pol. Industrial Agustinos, Calle G, 34, Orcoyen 31160, Spain. E-mail: alaine.salterain@velcomelton.es

ABSTRACT

Melt blowing is an industrial process used to design various products across different fields like surgical masks, filtration devices, diapers or electronic devices. The process consists in attenuating a fibre of adhesive using gases at a high velocity. Achieving optimal fibre attenuation is of paramount importance to get a convenient industrial application that meets quality requirements. The dynamics of this process is investigated by implementing a multiphase mathematical model that employs the Volume of Fluid (VOF) method. Three-dimensional multiphase simulations are conducted to gain insights into the influence of operating parameters on the fibre dynamics and attenuation. The simulation replicates the interaction between compressible air and the fluid fibre, which is treated as a non-Newtonian fluid with a temperature-dependent viscosity following a Cross-Arrhenius law. Attenuation results are compared with experimental measures and observations. By conducting multiphase simulations leveraging the capabilities of the VOF model, valuable insights into the dynamics and the physical properties of the fibres is obtained, contributing to the optimization of the melt blowing process in various industrial applications.

Keywords : Melt blowing, Volume of Fluid (VOF), Non-Newtonian fluids, Computational Fluid Dynamics (CFD), Holt-melt adhesive, Turbulence damping

NOMENCLATURE

A	$[m^{-1}]$	interfacial area density
B	[-]	turbulence damping factor
c_p	$[J.kg^{-1}.K^{-1}]$	specific heat at a constant pressure
c_v	$[J.kg^{-1}.K^{-1}]$	specific heat at a constant volume
D	$[m]$	fibre diameter
D_0	$[m]$	fibre diameter at the first measurement point (i.e. Z = 0.53 mm)
$\underline{dr}$	$[m]$	cell to face distance vector
E_a	$[J/mol]$	activation energy of the fluid
F_{CSF}	$[N/m^3]$	surface tension force
$\underline{g}$	$[m.s^{-2}]$	gravitational acceleration vector
k	$[J/kg]$	turbulent kinetic energy
l	$[m]$	turbulent length scale
M_f	$[kg]$	mass of fibre present in the domain
$\dot{m}$	$[kg/s]$	mass flow rate
m'	[-]	dimensionless flow rate ratio
$\underline{n}$	[-]	surface normal vector
N	[-]	power-law index
p	$[Pa]$	pressure field
R	$[J.K^{-1}.mol^{-1}]$	gas constant
$S_{\omega,i}$	$[m^2/s^4]$	turbulence damping source term
t	$[s]$	flow time
T	$[K]$	temperature field
T_R	$[K]$	Cross-Arrhenius model reference temperature
T'	[-]	dimensionless temperature ratio
$\underline{u}$	$[m/s]$	velocity vector
α	[-]	volume fraction
β	[-]	turbulence damping destruction term
$\dot{\gamma}$	$[s^{-1}]$	shear rate
δ_s	[-]	dirac distribution concentrated at the interface
Δn	$[m]$	grid size
Δt	$[s]$	time step size
ϑ	[-]	slope limiter value
κ	$[W.m^{-1}.K^{-1}]$	thermal conductivity
λ	$[s]$	Cross-law relaxation time
μ	$[Pa.s]$	dynamic viscosity
μ_0	$[Pa.s]$	zero-shear viscosity
μ_t	$[Pa.s]$	turbulent viscosity
ρ	$[kg/m^3]$	density
σ	$[N/m]$	surface tension coefficient
φ	[-]	flow variable

$\bar{\varphi}$	[-]	flow variable mean value
φ'	[-]	flow variable fluctuating part
χ	$[m^{-1}]$	local curvature at the interface
ω	$[m^2/s^3]$	turbulent specific rate dissipation

Subscripts and Superscripts

a	air phase
amb	ambient
$Coarse$	Coarsest grid
f	fibre fluid phase
$face$	grid face
$Fine$	Finest grid
i	i phase
$Medium$	Medium grid
min	minimum value
t	turbulent
$Z = Z_k$	$Z_k = (7\ mm, 12\ mm)$

1. INTRODUCTION

The melt blowing process involves the extrusion of a polymer called fibre through a nozzle, where convergent air jets attenuate the polymer to create non-woven textiles with reduced adhesive usage. This process has been widely studied since its creation in the 1950s [1] to enhance its efficiency, improve product quality, and reduce energy consumption. This industrial process enables the production of high-filtration devices [2], that can be masks, diapers or disposable hygiene products in general. One of the main issues encountered in the melt-blowing process is the lack of reproducibility, by not being able to fully control the fibre pattern uniformity along the process. Defects like undesired breakups, shot formation and fibre vibrations tend to affect the fibre pattern, potentially leading to imperfections in the final application or altering the filtration functionalities of the product.

Although experimental setups composed of high-speed cameras, halogen lamps and diffuser glasses can capture all these phenomena [3], measuring the diameters and temperatures of the fibres is a challenging and costly process. Therefore, numerical methods techniques need to be explored to set up the process without having to perform these experiments. Computational fluid dynamics (CFD) simulations have been performed to study the airflow in the melt blowing process, focusing on different nozzle geometries and employing three-dimensional turbulent steady-state analyses. Single phase models of the airflow have been implemented to study the impact of different nozzle configurations on turbulence levels and air recirculation, two phenomena that might lead to the splitting of the fibre flow [4] [5]. Nonetheless, such models do not consider the presence of the fibre. A solution is to couple a one-dimensional model of the fibre flow with the airflow. This is done by incorporating drag and heat transfer exchange source terms to the momentum and heat transfer equations of the fibre flow using the fundamental equations of the melt-spinning process [6]. The source term coefficients might need adjustments to validate the melt-blowing process experimental results [7] [8] [9]. Nevertheless, these models do not take into account the fibre motion and its implications on the surrounding airflow. Multiphase models can be contemplated as an alternative to capture the complex physical coupling between the air and the fibre [10]. The computational resources required and the challenges associated with an accurate modelling of the multiphase nature of the process should be considered though, as the fluid properties are complex and the need for adequate spatial and temporal discretisation can result in significant time restrictions [11]. One of the most known models used in gas-liquid simulations is the Euler-Euler model, in applications that involve atomisation in particular. In such model, both phases are treated as interpenetrating continuum. This is particularly useful when breakups and bubble formation are expected, as in spray modelling [12], [13]. A similar approach has been employed to model the interaction between a gas and solid particles [14], [15], [16]. Other approaches combine the Euler-Euler model with the VOF model, the latter being primarily used to track the interface between two immiscible phases. Such hybrid methodology consists in using the Euler-Euler model to capture dispersed flow phenomena while the VOF model is used to model the internal gas-liquid flow [17], [18].
Nonetheless, implementing the VOF model without coupling it with the Euler-Euler model proved to be sufficient for investigating jet-instability and droplet formation in atomisation[19].

The model presented in this study employs the VOF model to track the interaction between the fibre and the airflow in a multi-hole nozzle structure used in the melt-blowing process. Such methodology has already been employed in swirl die structures [20]. Valuable information can be obtained on the flow thermophysical properties, the fibre dynamics and the fibre pattern by simulating under various operating conditions without having to conduct challenging and expensive experiments. The present work shows how CFD can be used as a decision support tool to optimise the configuration of complex manufacturing processes. Two different cases are compared to investigate the influence of the air-polymer flow rate on fibre pattern and fibre dynamics. The fibre attenuation and motion frequencies are analysed and compared with experimental results.

2. GOVERNING EQUATIONS

The VOF model is employed to track the interface between two immiscible fluids here, which are the air, modelled as an ideal gas and the polymer fibre fluid. The volume fraction α is calculated in a control volume to determine the presence of the primary (air) and secondary (polymer fibre fluid)

phases. When α=1, the control volume is full of adhesive, while when α=0, the control volume is full of air. The VOF model is governed by a set of equations that include the mass, momentum and energy conservation and the transport of the volume fraction:

$$\frac{\partial \rho}{\partial t} + div\,(\rho \underline{u}) = 0 \tag{1}$$

$$\frac{D(\rho \underline{u})}{Dt} = -\nabla p + div\left(\mu \nabla \underline{u} + \mu\left(\nabla \underline{u}\right)^T\right) + \sigma \chi \delta_s \underline{n} + \rho \underline{g} \tag{2}$$

$$\frac{D(\rho T)}{Dt} - div(\kappa \nabla T) + div\left(\underline{u} p\right) + \frac{D\left(\rho\left(0.5|\underline{u}|^2\right)\right)}{Dt}\left(\frac{\alpha}{c_{v,f}} + \frac{1-\alpha}{c_{v,a}}\right) = 0 \tag{3}$$

$$\frac{D(\rho \alpha)}{Dt} = 0 \tag{4}$$

$$\rho = \alpha \rho_f + (1-\alpha)\rho_a \tag{5}$$

$$\mu = \alpha \mu_f + (1-\alpha)\mu_a \tag{6}$$

$$\kappa = \alpha \kappa_f + (1-\alpha)\kappa_a \tag{7}$$

with $\underline{u}$ being the velocity vector, χ the local curvature at the interface, δ_s the dirac distribution concentrated on the interface, σ the surface tension coefficient, ρ_f the fibre fluid density, ρ_a the air density, μ_f the fibre fluid viscosity, μ_a the air viscosity, $c_{v,f}$ the fibre fluid specific heat, $c_{v,a}$ the air specific heat, κ_f the fibre fluid conductivity and κ_a the air conductivity. $\underline{n}$ represents the surface normal. Its expression is $\underline{n} = \nabla \alpha$. Capillary effects are taken into account in this study. The Continuum Surface Force (CSF) model [21] is used to model the surface tension effect between the air and adhesive phases. A constant surface tension coefficient value of $\sigma = 0.03\ N/m$ is used in this study. The surface tension force F_{CSF} is calculated using the following formulation:

$$F_{CSF} = \sigma \chi \nabla \alpha \tag{8}$$

where σ is the surface tension coefficient, and $\nabla \alpha$ denotes the gradient of the volume fraction (α) across the interface between the air and adhesive phases.

As for turbulence modelling, the RANS (Reynolds Averaged Navier Stokes) equations of the continuity, momentum and heat transfer are solved. A flow variable $\varphi(X,t)$ is split into two terms: a mean value $\bar{\varphi}$ and a fluctuating part φ':

$$\varphi(X,t) = \bar{\varphi}(X,t) + \varphi'(X,t) \tag{9}$$

The turbulence models that are based on that Boussinesq hypothesis express the turbulent viscosity μ_t as a function of k, the turbulent kinetic energy and length scale l:

$$\mu_t = \rho l \sqrt{k} \tag{10}$$

where k is defined as:

$$k = \frac{1}{2}\overline{\underline{u}' \cdot \underline{u}'} \tag{11}$$

The k-ω SST model [22] is the turbulence model chosen, as it turns out to be more able to solve flows with strong adverse pressure gradient and flow separation, as it is the case of dual rectangular jets melt-blowing die flows [23]. A turbulence damping source term $S_{\omega,i}$ is introduced in the ω equation [24] to dampen the turbulence near the interface to avoid inaccurate results caused by non-physical velocity jumps.

$$S_{\omega,i} = A \Delta n \beta \rho_i \left(B \frac{6\mu_i}{\beta \rho_i \Delta n^2}\right)^2 \tag{12}$$

Where $A = 2.0\ \alpha_i |\nabla \alpha_i|$, α_i being the phase i volume fraction, Δn represents the grid size; $\beta = 0.075$ the destruction term; ρ_i the density of the phase i; μ_i the viscosity of the phase i and B the damping factor. A damping factor of 10 has been selected, with the intention to not completely eliminate all the turbulence at the interface, but rather to capture the behaviour of the multiphase flow avoiding the introduction of numerical instability.

3. FLUID RHEOLOGY AND THERMOPHYSICAL PROPERTIES

The fibre fluid is modelled as a temperature-dependent non-Newtonian fluid. To capture the data of the measurements obtained from a parallel plate viscometer at different temperatures (Figure 1), the Cross-Arrhenius model is employed:

$$\mu_f = e^{\frac{E_a}{R}\left(\frac{1}{T} - \frac{1}{T_R}\right)} \frac{\mu_0}{1 + (\lambda \dot{\gamma})^N} \tag{13}$$

where μ_0 is the zero shear viscosity, λ the relaxation time, $\dot{\gamma}$ the shear rate and N the power-law index. $\frac{E_a}{R}$ is the activation energy of the polymer divided by the ideal gas constant and T_R is the reference temperature. For this fluid, $T_R = 150\ ºC = 423.15\ K$ and $\frac{E_a}{R} = 6843.83\ K$. The values of the cross law parameters are $\mu_0 = 2{,}4\ Pa.s$, $\lambda = 0.2\ ms$ and $N = 0.85$.

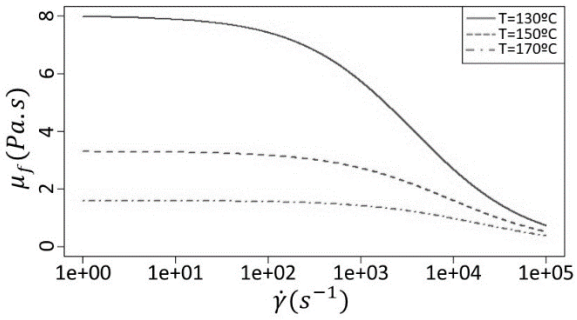

Figure 1. Evolution of the dynamic viscosity μ_f as a function of the shear rate $\dot{\gamma}$ at different temperatures

The air employed to attenuate the fibre follows the ideal gas law. The other thermophysical properties (specific heat, density, thermal conductivity, surface tension) are maintained constant for both the air and the fibre fluid.

4. FLOW DOMAIN AND DISCRETISATION

4.1. The boundary conditions and the flow domain mesh

The flow domain is shown in Figure 2. The three entry ducts are the nozzle components. The central duct contains the fibre fluid, and the other ones air, with a hydraulic diameter of 0.52 mm.

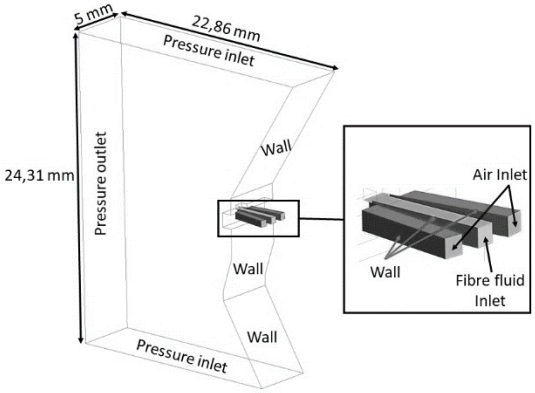

Figure 2. The fluid flow domain boundary conditions with the three entry ducts

The flow domain has been meshed by parametrising the number of division and node distribution at each edge. The structured mesh (Figure 3) is composed of 4 millions of hexahedral cells, with an average orthogonal quality of 0.99 and a mean aspect ratio of 7.29. To capture accurately volumetric fraction gradients at the interface between the air and the adhesive, an adaptive mesh refinement method is employed (see the cut view in Figure 3 for the interface where such method is employed). This approach allows for finer resolution without overly increasing the number of cells.

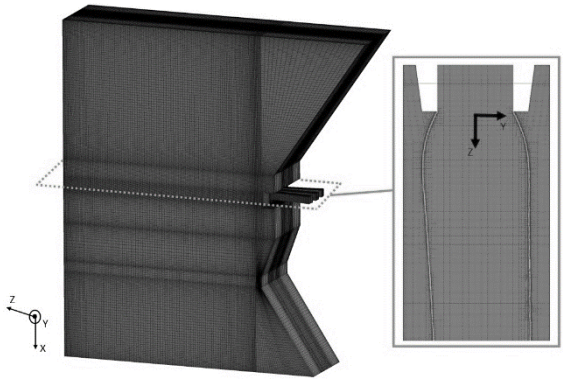

Figure 3. The fluid flow domain mesh isometric view with the cut view showing the mesh interface refinement

4.2. Spatial and temporal discretisation

The governing equations of the flow are discretised using the finite volume method (FVM) and solved using Ansys® Fluent 2020 R1. Second-order accurate schemes are employed, and the PRESTO! (pressure staggering option) scheme is used for the discretisation of the pressure equation. The gradients are computed using the least squares cell based method and the discretised equations are solved in a coupled manner. As the explicit formulation is employed for the discretisation of the volume fraction equation, the first-order implicit method is used to perform the temporal discretisation.

4.3. Interface capturing method

To capture the interface between the air and the adhesive, the compressive scheme [25] is employed. This scheme is based on a slope limiter that is used to handle sharp changes in the solution domain.

$$\alpha_{face} = \alpha_{donor} + \vartheta \nabla \alpha_{donor} \cdot \underline{dr} \qquad (14)$$

where α_{face} is the value of the volume fraction of the face; ϑ is the slope limiter value, α_{donor} is the value of the volume fraction of the donor cell and $\underline{dr}$ is the cell to face distance.

5. RESULTS AND DISCUSSION

In this section, the results obtained from the multiphase model, using the same configuration as in two experiments previously conducted by Formoso et al. [26], are presented. The experimental measurements for the two cases considered (EXP A3 and EXP A5) revealed different results in terms of fibre patterns and motion frequencies, as the combination of air-polymer flow rate ($m' = \frac{\dot{m}_a}{\dot{m}_f}$) is doubled from EXP A3 to EXP A5 while the temperature ratio ($T' = \frac{T_a - T_{amb}}{T_f - T_{amb}}$) is the same. The air-polymer flow rate ratio influence proved to be predominant over that of the temperature ratio,

therefore the study focuses on the effect of the air-polymer flow rate ratio. The frequencies of the fibre oscillations and the attenuation of the fibre are key results, which determine whether if the experiment is within the limits of the operating conditions window. Otherwise, instabilities can appear and are likely to generate defects on the final product. The experimental results indicate that in both cases, no fibre breakup has been observed. However, the range of fibre motion frequencies differs significantly between EXP A3 and EXP A5. To validate the results, the experimental measures are compared with the fibre attenuation of the CFD results as well as the fibre movement in both the YZ and ZX plane. The frequencies obtained from such movement are assessed by studying the temporal evolution of the minimum Y-coordinate of the fibre.

5.1. Grid convergence and time step size influence study

A grid and time step size sensitivity analysis is performed by comparing three spatial resolutions and two temporal resolutions. The variations of the fibre diameter at two locations (Figure 4), as well as the total mass of fibre within the domain are analysed. A Richardson extrapolation is then conducted following the guidelines proposed by Celik [27]. The case considered for this study has an air-polymer flow rate $m' = 1.3$ and a temperature ratio $T' = 1.52$.

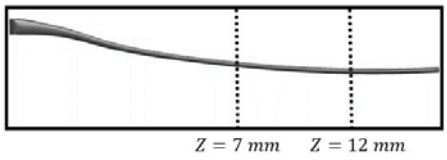

Figure 4. The fibre in the ZX plane and the positions used to monitor the fibre dynamics

The configurations of the three cases considered are presented in Table 1. The medium grid includes three levels of local refinement at the interface between the fibre and the surrounding air. This grid is compared against a coarser grid with two levels of refinement and a finer grid with four levels of refinement. For each grid, the simulation was run for the equivalent of two complete cycles of fibre dynamics (20.25 ms).

Table 1. Grid characteristics

Grid	Δt	Number of time steps simulated
Coarse (3,800,000 cells)	2 μs	10250
Medium (4,600,000 cells)	2 μs	10250
Fine (9,800,000 cells)	1 μs	20500

The grid convergence index (GCI) values obtained from the grid convergence test values (Table 2) proved to be accurate enough as the GCI values are all below 15% (Table 3).

Table 2. Grid convergence test values

	Coarse grid	**Medium grid**	**Fine grid**
$\bar{D}_{Z=7\ mm}$	0.166±0.025 mm	0.179±0.025 mm	0.18±0.024 mm
$\bar{D}_{Z=12\ mm}$	0.124±0.027 mm	0.135±0.025 mm	0.139±0.026 mm
$\bar{M}_f$	1.454±0.03 mg	1.491±0.025 mg	1.492±0.025 mg

Table 3. Grid convergence index values

	GCI_{Coarse}	GCI_{Medium}	GCI_{Fine}
$\bar{D}_{Z=7\ mm}$	9.84%	0.76%	0.058%
$\bar{D}_{Z=12\ mm}$	18.55%	8.77%	4.0%
$\bar{M}_f$	3.188%	0.09%	0.002%

5.2. EXP A3 (m'=1.3; T'=1.52)

As for EXP A3, the point at which the dynamics starts is located at Z=2 mm in both the YZ (Figure 5) and ZX (Figure 6) plane. The dynamics of the fibre in the YZ plane is stronger than in the ZX plane though, as wiggles can be noticed. Such dynamics is likely to create fibre patterns of a similar shape as those observed by Formoso et al. [26].

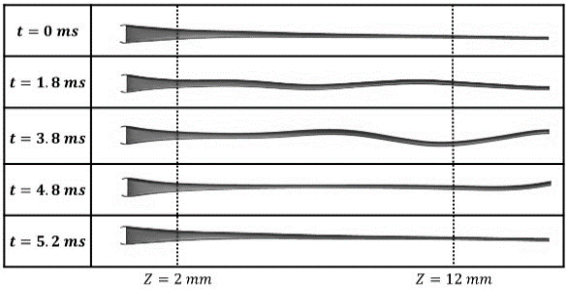

Figure 5. EXP A3 fibre dynamics in the YZ plane

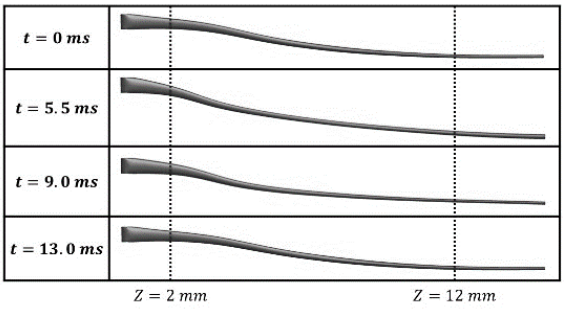

Figure 6. EXP A3 fibre dynamics in the ZX plane

The mean fibre attenuation obtained from the CFD model (Figure 7) is in agreement with the experimental results, as the differences between both results are within a 10% margin.

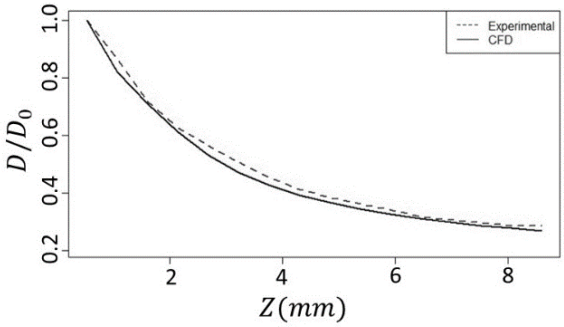

Figure 7. Mean fibre attenuation comparison between experimental and CFD results for EXP A3

The frequencies obtained from the variations in the minimum Y-coordinate of the fibre at $Z = 12\ mm$ (Figure 8) are consistent with the experimental data, displaying a range from 0.05 to 0.8 kHz, with the most significant peak being located between 0.175 and 0.23 kHz (Figure 9).

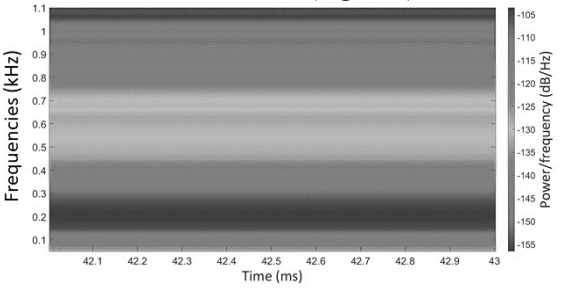

Figure 8. Spectrogram depicting the variations of the minimum Y-coordinate of the fibre at Z=12 mm for EXP A3

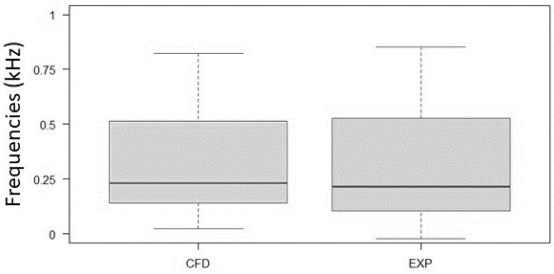

Figure 9. Comparison between the frequencies obtained from experiments and CFD for EXP A3

5.3. EXP A5 (m'=2.7; T'=1.52)

As for EXP A5, where the dimensionless flow rate ratio is more than doubled that of EXP A3 by doubling the airflow rate $\dot{m}_a$, the fibre dynamics is significantly impacted. Hence, the fibre motion is predominantly two-dimensional, as the motion is mainly noticeable in the YZ plane.

Moreover, the amplitudes of the oscillations in the YZ plane are substantially steeper than in EXP A3 (Figure 10), with the highest amplitudes occurring near the starting point of the fibre oscillation (Z=2 mm).

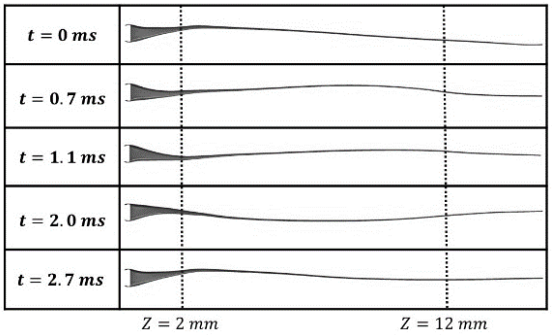

Figure 10. EXP A5 fibre dynamics in the YZ plane

The change in airflow rate also influences the mean fibre attenuation values (Figure 11), which are observed to be lower than those in EXP A3. The values obtained from the CFD model are still in agreement with the experimental ones.

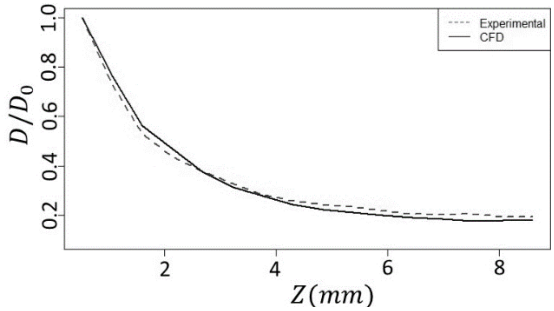

Figure 11. Mean fibre attenuation comparison between experimental and CFD results for EXP A5

As for the fibre motion, the frequency range obtained from simulations is considerably broader than in EXP A3. Indeed, the frequencies (Figure 12) extend from 0.1 to 1.7 kHz, with a high-frequency bandwidth ranging from 0.3 to 0.7 kHz and the most significant peak located between 0.45 and 0.5 kHz (Figure 13).

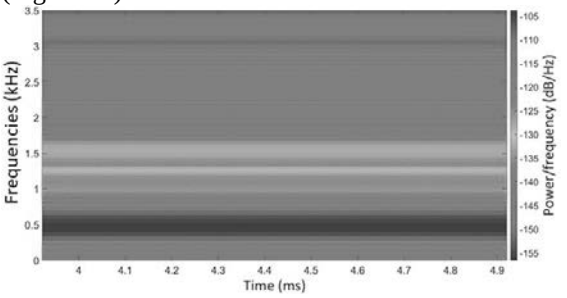

Figure 12. Spectrogram depicting the variations of the minimum Y-coordinate of the fibre at Z=12 mm for EXP A5

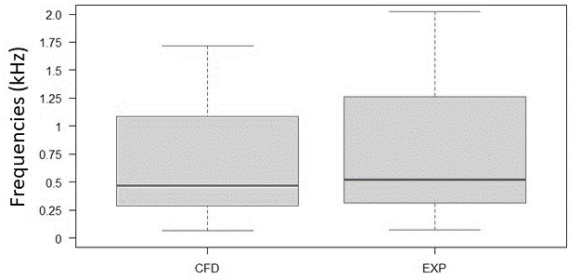

Figure 13. Comparison between the frequencies obtained from experiments and CFD for EXP A5

6. CONCLUSIONS

A mathematical multiphase model of the melt-blowing process in multi-hole nozzles was developed, by employing the VOF model. The fluid flow equations are discretised and solved using the finite volume method. The model provides information on the fibre dynamics as well as the air and temperature fields. The results showed that by doubling the air-polymer flow rate ratio, the attenuation of the fibre and the oscillations of the fibre motion are significantly affected. Furthermore, the agreement between the CFD results and experimental data of the fibre attenuation and dynamics provides confirmation that the adoption of the VOF model is appropriate and effective for studying the melt blowing process. This alignment between the numerical predictions and experimental observations validates the capability of this model to capture the complex phenomena occurring in the process not only qualitatively, but also quantitatively. This further establishes the suitability of multiphase simulations as a valuable tool for investigating and optimising the melt blowing process. By leveraging the capabilities of multiphase simulations, insights can be gained into the impact of the process parameters, and the performance of the melt blowing process can be predicted more efficiently and cost-effectively compared to relying solely on experimental trials.

ACKNOWLEDGEMENTS

The authors gratefully acknowledge the financial support for this project from Ministerio de Ciencia e Innovación, Gobierno de España, RETOS-COLABORACION 2019 (grant number RTC2019007057-7).

REFERENCES

[1] X. Hao and Y. Zeng, ‘A Review on the Studies of Air Flow Field and Fiber Formation Process during Melt Blowing’, *Ind. Eng. Chem. Res.*, vol. 58, no. 27, pp. 11624–11637, Jul. 2019, doi: 10.1021/acs.iecr.9b01694.

[2] Y. Kara and K. Molnár, ‘A review of processing strategies to generate melt-blown nano/microfiber mats for high-efficiency filtration applications’, *Journal of Industrial Textiles*, vol. 51, no. 1_suppl, pp. 137S-180S, Jun. 2022, doi: 10.1177/15280837211019488.

[3] P. Boggavarapu, S. P. Ramesh, M. M. Avulapati, and R. RV, ‘Secondary breakup of water and surrogate fuels: Breakup modes and resultant droplet sizes’, *International Journal of Multiphase Flow*, vol. 145, p. 103816, Dec. 2021, doi: 10.1016/J.IJMULTIPHASEFLOW.2021.103816.

[4] Y. Yang, Y. Zeng, Y. ; Yang, and Y. Zeng, ‘Measurement and Comparison of Melt-Blowing Airflow Fields: Nozzle Modifications to Reduce Turbulence and Fibre Whipping’, *Polymers 2021, Vol. 13, Page 719*, vol. 13, no. 5, p. 719, Feb. 2021, doi: 10.3390/POLYM13050719.

[5] S. Xie, G. Jiang, X. Wu, Y. Wang, H. Fang, and B. Shentu, ‘Air Recirculation and Its Effect on Microfiber Spinning in Blunt-Die Melt Blowing’, *Fibers and Polymers 2021 22:3*, vol. 22, no. 3, pp. 703–710, Mar. 2021, doi: 10.1007/S12221-021-0225-5.

[6] S. Kase and T. Matsuo, ‘Studies on melt spinning. I. Fundamental equations on the dynamics of melt spinning’, *Journal of Polymer Science Part A: General Papers*, vol. 3, no. 7, pp. 2541–2554, Jul. 1965, doi: 10.1002/pol.1965.100030712.

[7] B. Majumdar and R. L. Shambaugh, ‘Air drag on filaments in the melt blowing process’, *Journal of Rheology*, vol. 34, no. 4, pp. 591–601, May 1990, doi: 10.1122/1.550097.

[8] V. Bansal and R. L. Shambaugh, ‘On-line Determination of Diameter and Temperature during Melt Blowing of Polypropylene’, *Industrial & Engineering Chemistry Research*, vol. 37, no. 5, pp. 1799–1806, May 1998, doi: 10.1021/ie9709042.

[9] G. W. Sun, J. Song, L. Xu, and X. H. Wang, 'Numerical modelling of microfibers formation and motion during melt blowing', *https://doi.org/10.1080/00405000.2017.1342522*, vol. 109, no. 3, pp. 300–306, Mar. 2017, doi: 10.1080/00405000.2017.1342522.

[10] Kolev NI ,. Author and Lyczkowski RW ,. Reviewer, 'Multiphase Flow Dynamics, Volume 1: Fundamentals; Volume 2: Thermal and Mechanical Interactions', *Applied Mechanics Reviews*, vol. 56, no. 4, pp. B57–B59, Jul. 2003, doi: 10.1115/1.1579460.

[11] F. Denner, F. Evrard, and B. van Wachem, 'Breaching the capillary time-step constraint using a coupled VOF method with implicit surface tension', *Journal of Computational Physics*, vol. 459, p. 111128, Jun. 2022, doi: 10.1016/j.jcp.2022.111128.

[12] M. Vujanović, Z. Petranović, W. Edelbauer, and N. Duić, 'Modelling spray and combustion processes in diesel engine by using the coupled Eulerian–Eulerian and Eulerian–Lagrangian method', *Energy Conversion and Management*, vol. 125, pp. 15–25, Oct. 2016, doi: 10.1016/j.enconman.2016.03.072.

[13] Z. Petranović, W. Edelbauer, M. Vujanović, and N. Duić, 'Modelling of spray and combustion processes by using the Eulerian multiphase approach and detailed chemical kinetics', *Fuel*, vol. 191, pp. 25–35, Mar. 2017, doi: 10.1016/j.fuel.2016.11.051.

[14] N. C. Markatos, 'Modelling of two-phase transient flow and combustion of granular propellants', *International Journal of Multiphase Flow*, vol. 12, no. 6, pp. 913–933, Nov. 1986, doi: 10.1016/0301-9322(86)90035-2.

[15] D. B. Spalding, 'Numerical computation of multi-phase fluid flow and heat transfer', *In Von Karman Inst. for Fluid Dyn. Numerical Computation of Multi-Phase Flows*, pp. 161–191, 1981.

[16] G. V. Messa and S. and Malavasi, 'Numerical prediction of dispersed turbulent liquid–solid flows in vertical pipes', *Journal of Hydraulic Research*, vol. 52, no. 5, pp. 684–692, Sep. 2014, doi: 10.1080/00221686.2014.939110.

[17] Q. Xue *et al.*, 'An Eulerian CFD model and X-ray radiography for coupled nozzle flow and spray in internal combustion engines', *International Journal of Multiphase Flow*, vol. 70, pp. 77–88, Apr. 2015, doi: 10.1016/j.ijmultiphaseflow.2014.11.012.

[18] W. Edelbauer, 'Numerical simulation of cavitating injector flow and liquid spray break-up by combination of Eulerian–Eulerian and Volume-of-Fluid methods', *Computers & Fluids*, vol. 144, pp. 19–33, Feb. 2017, doi: 10.1016/j.compfluid.2016.11.019.

[19] T. Ménard, S. Tanguy, and A. Berlemont, 'Coupling level set/VOF/ghost fluid methods: Validation and application to 3D simulation of the primary break-up of a liquid jet', *International Journal of Multiphase Flow*, vol. 33, no. 5, pp. 510–524, May 2007, doi: 10.1016/j.ijmultiphaseflow.2006.11.001.

[20] B. Vila, D. Maza, and J. M. Pastor, 'A Three-Dimensional Multiphase Simulation of the Fiber Spiral Motion Under a Melt-Blowing Swirl Die', *Fibers Polym*, vol. 24, no. 7, pp. 2333–2341, Jul. 2023, doi: 10.1007/s12221-023-00228-2.

[21] J. U. Brackbill, D. B. Kothe, and C. Zemach, 'A continuum method for modeling surface tension', *Journal of Computational Physics*, vol. 100, no. 2, pp. 335–354, Jun. 1992, doi: 10.1016/0021-9991(92)90240-Y.

[22] F. R. Menter, 'Two-equation eddy-viscosity turbulence models for engineering applications', *AIAA Journal*, vol. 32, no. 8, pp. 1598–1605, Aug. 1994, doi: 10.2514/3.12149.

[23] Y. Wang and X. Wang, 'Numerical analysis of new modified melt-blowing dies for dual rectangular jets', *Polymer Engineering & Science*, vol. 54, no. 1, pp. 110–116, 2014, doi: 10.1002/pen.23536.

[24] Y. Egorov, M. Boucker, A. Martin, S. Pigny, M. Scheuerer, and S. Willemsen, 'Validation of CFD codes with PTS-relevant test cases', *5th Euratom Framework Programme ECORA project*, vol. 2004, pp. 91–116, 2004.

[25] G. Chen, Q. Wang, and S. He, 'Assessment of an Eulerian multi-fluid VOF model for simulation of multiphase flow in an industrial Ruhrstahl–Heraeus degasser', *Metall. Res. Technol.*, vol. 116, no. 6, Art. no. 6, 2019, doi: 10.1051/metal/2019049.

[26] I. Formoso *et al.*, 'Experimental study on the hot-melt adhesive pattern produced by melt blowing nozzle designs':, *https://doi.org/10.1177/1528083720978401*, Dec. 2020, doi: 10.1177/1528083720978401.

[27] I. Celik, 'Numerical Uncertainty in Fluid Flow Calculations: Needs for Future Research', *Journal of Fluids Engineering*, vol. 115, no. 2, pp. 194–195, Jun. 1993, doi: 10.1115/1.2910123.

Conference on Modelling Fluid Flow (CMFF'25)
The 19th International Conference on Fluid Flow Technologies
Budapest, Hungary, August 26-August 29, 2025

CAVITATION BUBBLE NEAR A WALL: SENSITIVITY TO MODELING CONDITIONS

Bo WANG[1], Zhidian YANG[2], Francesco ROMANÒ[2]

[1] Corresponding Author. Univ. Lille, CNRS, ONERA, Arts et Métiers Institute of Technology, Centrale Lille, UMR 9014 - LMFL - Laboratoire de Mécanique des Fluides de Lille - Kampé de Fériet, F-59000 Lille, France. Tel.: +33 07 81 39 91 74, E-mail: bo.wang_1@ensam.eu
[2] Univ. Lille, CNRS, ONERA, Arts et Métiers Institute of Technology, Centrale Lille, UMR 9014 - LMFL - Laboratoire de Mécanique des Fluides de Lille - Kampé de Fériet.

ABSTRACT

Cavitation near solid surfaces is a critical phenomenon due to its potential to damage materials and impair the performance of machinery such as pumps and turbines. Previous studies have employed compressible multiphase solvers to simulate the collapse of cavitation bubbles near walls, often using equivalent radius as a key parameter for validation. In this work, we aim to deepen the understanding of cavitation bubble dynamics by comparing two modeling approaches: (*i*) the Volume-of-Fluid (VOF) method with the All-Mach approach and (*ii*) the Level-Set method with Euler equations. The simulations are conducted using Basilisk and M2C, respectively, two open-source solvers that leverage adaptive meshes on the one hand and multiphysics on the other hand for high-resolution computations that can tackle complementary regimes. A novel aspect of this study is the simulation of bubble dynamics starting from the breakdown phase, which provides a more comprehensive understanding of the collapse process. Our results indicate that while the equivalent radius shows limited sensitivity to modeling conditions, the maximum wall pressure is strongly dependent on the bubble's stand-off ratio. By comparing the simulation results to experimental measurements and visualizations, we evaluate the accuracy and applicability of the two approaches under various conditions. This study provides new insights into the sensitivity of cavitation bubble collapse to modeling conditions and informs the selection of numerical methods for accurate prediction of cavitation-induced phenomena.

Keywords: bubble dynamics, bubble modeling, laser-induced cavitation

NOMENCLATURE

$max_r(P_w)$	$[MPa]$	maximum wall pressure
R_{eq}	$[mm]$	equivalent radius of bubble
$D(t_{MR})$	$[mm]$	distance from the bubble's centroid to the wall
$\max_t(R_{eq})$	$[mm]$	maximum equivalent radius of bubble

Subscripts and Superscripts

L	laser
t_{MR}	time when bubble reaches its maximum equivalent radius
eq	equivalent
r	radial direction
w	wall

1. INTRODUCTION

Cavitation refers to the formation, growth, and collapse of vapor bubbles in a liquid due to rapid changes in pressure or temperature [1, 2]. Cavitation bubbles commonly occur in hydraulic machinery such as pumps and turbines [3, 4]. On one hand, their collapse can cause erosion and vibration on solid surfaces [5]. On the other hand, cavitation can offer benefits across various fields like enhancing the drilling rate of petroleum wells [6] and performing shotless peening on metals [7]. Understanding bubble collapse near solid surfaces is therefore essential.

There is a substantial body of research dedicated to investigating cavitation bubble dynamics through experimental approaches [8, 9, 10, 11]. However, experiments face limitations such as difficulty in measuring pressure, temperature and velocity fields inside the bubble. In order to address these challenges, numerical simulations have been developed to study bubble dynamics near a solid boundary. One widely used method is the Volume-of-Fluid (VOF) method with All-Mach approach, implemented in Basilisk by [12, 13]. Simulations using this method assume predefined initial conditions, such as pressure, temperature and velocity at a given bubble size. Recently, Zhao et al. [14] employed the Level-Set method

with Euler equations using M2C solver to simulate laser-induced bubble generation, specifically focusing on pear-shaped and elongated bubble formation. Their work provides a robust framework for modeling bubble behavior and greatly advances the understanding of laser-induced bubble dynamics as they model the breakdown phase, hence the formation of the bubble.

In this work, we aim to deepen the understanding of cavitation bubble dynamics by simulating a single axi-symmetric bubble near a solid boundary. We compare the results obtained using two numerical models: the VOF method with the All-Mach approach by [13, 15] and the Level-Set method with Euler equations by [14] which will be conducted in the present study. Key metrics, such as the bubble equivalent radius and maximum wall pressure, are analyzed and validated against experimental data from [16, 17]. This comparison evaluates the accuracy and applicability of the two numerical approaches, contributing to advancements in modeling cavitation-induced phenomena.

2. PROBLEM FORMULATION

2.1. Problem description

Figure 1 illustrates the problem investigated in this work, showing an axi-symmetric vapor bubble induced by laser.

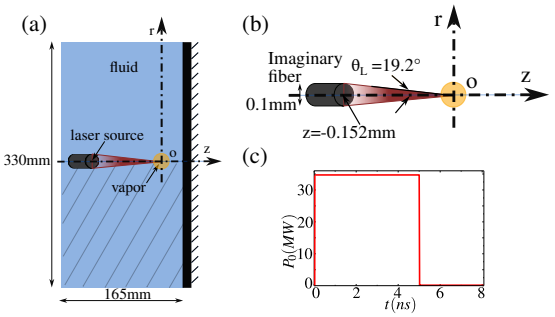

Figure 1. Schematic of laser-induced bubble generation. (a) Computational domain with axi-symmetry. (b) Geometry of the laser radiation domain. (c) Temporal profile of laser power.

In the experiment performed by [16], a Q-switched Nd: YAG laser with a wavelength of 532nm, maximum pulse energy of 200mJ and a pulse duration of 5ns was used as the energy source to induce the cavitation bubble. The experiment was carried out in a $20.3 \times 20.3 \times 20.3\ cm^3$ glass tank filled with pure water under ambient conditions: temperature $T = 293.15K$ and pressure $P = 101325Pa$.

To replicate the experimental conditions in our computational model, we employed an axi-symmetric simulation domain with radius and length of 165 mm. In our simulations, r denotes the radial coordinate. The laser, positioned outside the water tank in the experiment, is modeled as originating at $z = -0.152\ mm$, with a laser source radius of $R_L = 0.05\ mm$, and a convergence angle of $\theta_L = 19.2°$, consistent with the laboratory experiment, as shown in Fig. 1.

Computational domain size is 55 times the maximum bubble radius to avoid the impact of computational boundary on bubble shape and size by constraining its growth. The initial conditions assumed that the domain is filled with liquid water of density $\rho_0 = 0.001\ g/mm^3$, pressure $p_0 = 1atm$, and temperature $T_0 = 293.15\ K$. The flow is initially assumed at rest. In the computational model, the spatial distribution of laser intensity is simplified and treated as a step function, as shown in Fig. 1(c). The laser power increases rapidly to its peak within 0.01ns, remains constant for 5ns, and then decreases to zero over 0.02ns. In our simulation, the absorption coefficient α is set to 101222 m^{-1} for liquid water and $10^{-5}\ m^{-1}$ for the vapor. The vaporization temperature and latent heat of vaporization are specified as $T_{vap} = 373.15\ K$ and $l = 2256.4\ J/g$, respectively.

The bubble dynamics can be analyzed using two key parameters: the equivalent radius, denoted as R_{eq}, and the distance from the bubble's centroid to the solid wall, L. The stand-off ratio, expressed as

$$\gamma = \frac{D(t_{MR})}{\max\limits_{t}(R_{eq})} \tag{1}$$

quantifies the relative distance between the bubble's centroid and the wall, where t_{MR} refers to the time when the bubble reaches its maximum equivalent radius.

2.2. Governing equations

The equations, governing the compressible two-phase flows neglecting the effects of viscosity and surface tension while considering radiative heat transfer, are presented in this section. The governing equations for the conservation of mass, momentum, and energy in a compressible fluid are expressed in a conservative form as follows.

$$\frac{\partial \boldsymbol{W}(\boldsymbol{x},t)}{\partial t} + \nabla \cdot \mathcal{F}(\boldsymbol{W}) = \nabla \cdot \mathcal{G}(\boldsymbol{W}) \tag{2}$$

with

$$\boldsymbol{W} = \begin{bmatrix} \rho \\ \rho \boldsymbol{V} \\ \rho e_t \end{bmatrix}, \mathcal{F} = \begin{bmatrix} \rho \boldsymbol{V}^T \\ \rho \boldsymbol{V} \otimes \boldsymbol{V} + p\boldsymbol{I} \\ (\rho e_t + p)\,\boldsymbol{V}^T \end{bmatrix}, \mathcal{G} = \begin{bmatrix} \boldsymbol{0}^T \\ \boldsymbol{0} \\ (k\nabla T - \boldsymbol{q_r})^T \end{bmatrix}. \tag{3}$$

ρ, $\boldsymbol{V}$, p, and T denote the fluid's density, velocity, pressure, and temperature, respectively. The total energy per unit mass, e_t, is defined as

$$e_t = e + \frac{1}{2}|\boldsymbol{V}|^2 \tag{4}$$

where e represents the fluid's internal energy per unit mass. k is the thermal conductivity coefficient, set to 0.5576 W/mK for liquid and 0.02457 W/mK for vapor. $\boldsymbol{q_r}$ refers to the radiative heat flux induced by the laser. To close the governing equations (2), a complete equation of state (EoS) for each phase, including a temperature equation, is required. In this study, the Noble-Abel stiffened gas ($NASG$) equations are

employed as the pressure and temperature equation [18] for both phases. Specifically,

$$p_I(\rho, e) = (\gamma_I - 1)\frac{e - q_I}{\frac{1}{\rho} - b_I} - \gamma_I p_{cI} \tag{5}$$

$$T_I(\rho, e) = \frac{\gamma_I}{c_{pI}}\left(e - q_I - \left(\frac{1}{\rho} - b_I\right)p_{cI}\right) \tag{6}$$

in which the subscript $I \in \{0, 1\}$ identifies the liquid (0) and vapor (1) phases. For each phase, γ, p_c, q and b are constant parameters that characterize its thermodynamic properties. c_p denotes the specific heat capacity at constant pressure, assumed to be a constant. The values of these parameters and other related thermodynamic properties are adopted from Zein et al. [19] and summarized in Table 1.

Table 1. NASG EoS parameters and thermodynamic properties for liquid and vapour phase.

Parameter	Units	Value
c_{p0}	J kg^{-1} K^{-1}	7094.593
γ_0	–	2.057
p_{c0}	Pa	1.066×10^9
b_0	m^3 kg^{-1}	0
q_0	J kg^{-1}	-1994.674×10^3
c_{p1}	J kg^{-1} K^{-1}	1592.4
γ_1	–	1.327
p_{c1}	Pa	0
b_1	m^3 kg^{-1}	0
q_1	J kg^{-1}	1995×10^3

The laser radiation equation is derived based on energy conservation, taking into account the assumptions that the laser radiation dominates over the black-body radiation and that the laser propagates in a fixed direction with a certain wavelength [14].

$$\nabla \cdot (L\boldsymbol{s}) = \nabla L \cdot \boldsymbol{s} + (\nabla \cdot \boldsymbol{s})L = -\alpha(I)L \tag{7a}$$

$$\boldsymbol{q}_r = L\boldsymbol{s} \tag{7b}$$

where $s = s(x)$ denotes the direction of the laser propagation, which is constant only when the beam is parallel. The spatial variable x refers to the position on the surface of the laser fiber, where the initial laser radiance used to induce the vapor bubble is calculated, and L represents the laser radiance, which can be calculated for uniform beam as:

$$L = \frac{P_0(1 + \cos\theta_L)}{\pi r^2} \tag{8}$$

2.3. Numerical schemes

In this section, we present a summary of the numerical schemes used, and we refer to Zhao et al. [14] for a detailed description. The above governing equations are solved using a finite volume method based on exact multiphase Riemann problem solver. The vapor-liquid interface is tracked by the level set method and the phase transition process is accomplished when the intermolecular potential energy in the liquid phase reaches the latent heat.

In the current study, we do not model the laser fiber as a fixed boundary interacting with the vapor since the bubble in our case is free-floating without interaction with the fiber.

3. SPATIAL CONVERGENCE STUDY

3.1. The global influence of mesh resolution

In this section, the influence of global mesh refinement is investigated to identify an optimal mesh size that ensures convergence in the bubble's generation simulated using M2C. We refer to Yang et al. [17] for a detailed grid convergence study for Basilisk.

As shown in Figure 2(a), the axi-symmetric computational domain is $330mm \times 165mm$. Since the bubble induced by laser has an experimental radius of approximately 2.7mm, a region of $9mm \times 8mm$ (indicated by a cyan dashed box) is designated with finer mesh resolution than the surrounding area, as illustrated in Fig. 2(b). This region, larger than the maximum bubble radius, ensures that the bubble can grow and collapse under a consistent mesh refinement. The red area highlights the location where the bubble will evolve.

At first, only the mesh size within this designated region is varied, while the mesh outside remains unchanged. Seven cases for $\gamma = 1.82$ are examined, with minimum cell size from $\Delta x = 4.5 \times 10^{-6}$m to $\Delta x = 10^{-5}$m.

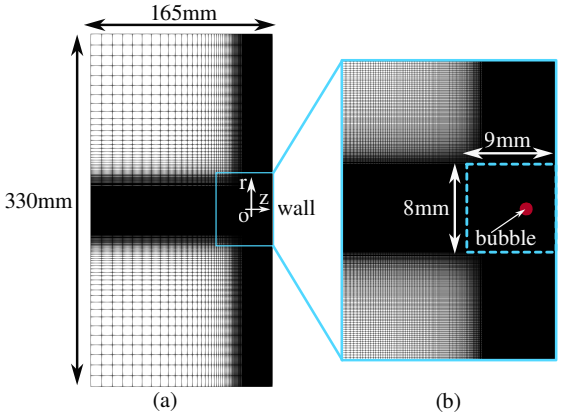

Figure 2. Global mesh distribution

In Figure 3, it can be observed that all cases exhibit a rapid expansion of the bubble in the first 270-300 μs, reaching a maximum radius between 2.6mm and 2.8mm, which corresponds well with the experimentally measured radius of approximately 2.7mm. The maximum bubble radius tends to converge as the mesh is refined. Minimum cell sizes finer than $\Delta x = 5 \times 10^{-6}$m show less variability in the maximum radius and collapse time. Besides, in Figure 4, similar to the bubble radius, the pressure peak at the wall reaches a convergence at $\Delta x = 5 \times 10^{-6}$m. Therefore, based on both the bubble radius and the

pressure peak, $\Delta x = 5 \times 10^{-6}$m is an optimal choice for balancing computational cost and accuracy.

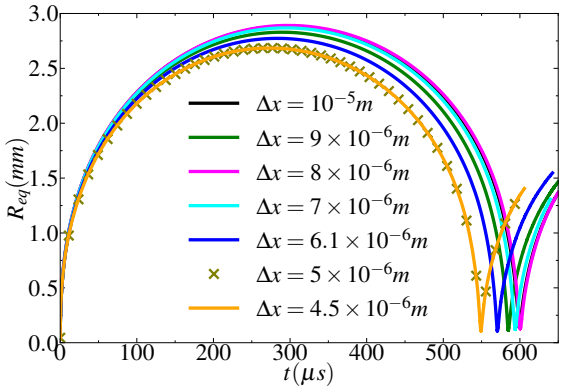

Figure 3. Evolution of bubble radius obtained with different computational meshes. The minimum cell size is reported in the legend.

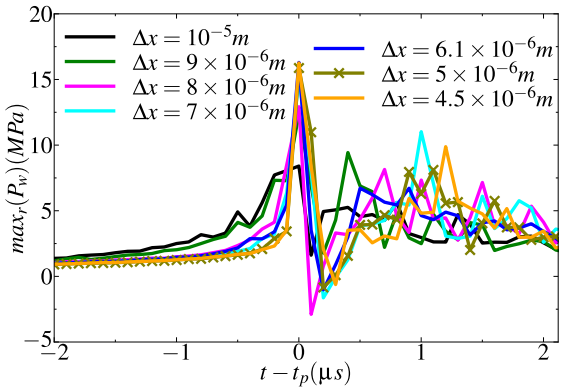

Figure 4. Evolution of pressure at wall obtained with different computational meshes. The minimum cell size is reported in the legend.

3.2. The local influence of mesh resolution

After determining the optimal global mesh size, we further study the sensitivity of bubble nucleation to local spatial resolution. Since our model initially assumes a domain entirely filled with liquid, a bubble is generated as part of the simulation mesh element. Suppose we do not maintain a consistent initial mesh near the region of bubble nucleation. In that case, each simulation will generate different initial bubbles due to the varied spatial resolution, leading to non-comparable results. This makes it imperative to fix the initial mesh to ensure repeatability and consistency across different simulations.

To further validate our numerical approach, three simulations are carried out: **(a)** a first simulation with a fixed extra-fine region at nucleation site whose cell size is Δx=5×10^{-6}m, while $10^{-5}m$ is used elsewhere within the cyan dashed box of fig. 2, **(b)** a second simulation with uniform cell size Δx=5×10^{-6}m within the cyan dashed box of fig. 2, and **(c)** a third simulation with uniform cell size Δx=10^{-5}m within the cyan dashed box of fig. 2. The equivalent bubble radius during the first $45\mu s$ after bubble generation is depicted in figure 5. We observe that the initial bubble generation is highly sensitive to spatial resolution around the nucleation site. Specifically, the difference between the black curve(with a uniform mesh size of 10^{-5}m throughout the domain) and the magenta curve(with a refined mesh size of 5×10^{-6}m in the nucleation region and 10^{-5}m elsewhere) is significantly larger than the difference between cyan and magenta curves. This observation confirms the necessity of fixing the initial mesh around the bubble nucleation site to ensure consistent results.

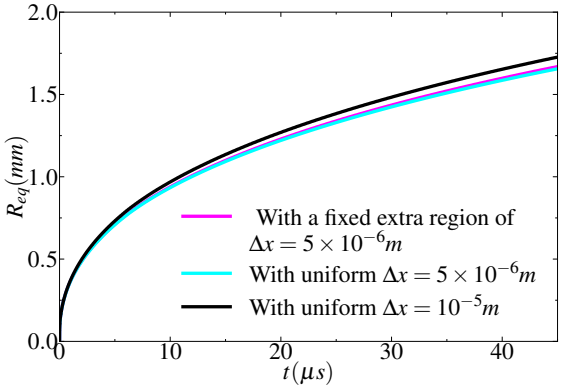

Figure 5. Influence of local mesh refinement at nucleation site.

To make sure that the bubble will be generated under identical initial conditions, we fix the mesh resolution in the region of $0.4mm \times 0.6mm$ near the bubble nucleation site, denoted as Ω0. Specifically, the mesh size is set to 5×10^{-6}m within Ω0 for the first 200 time steps, as Figure 6 . This mesh size was determined to be optimal in the previous section.

Outside this space (Ω1), the mesh size can vary, but the bubble will always start within the extra fine mesh in Ω0. This setup allows for reliable convergence studies, as the bubble's initial formation is consistent across simulations, regardless of the coarser mesh outside Ω0.

Fig. 6 illustrates this mesh configuration, highlighting the denser mesh region around the nucleation site and the coarser mesh outside of it.

To determine the optimal mesh size in the region Ω1, three cases for $\gamma = 1.82$ are considered, with different mesh sizes: $\Delta x = 10^{-5}$m, 2×10^{-5}m, 5×10^{-6}m. In particular, we focus on the evolution of the bubble radius and the pressure exerted at the wall. From Figure 7, all simulations capture the general trend of bubble growth and collapse. The bubble expands and then collapses, following the same qualitative behavior as the experimental measurements. The mesh resolution of $\Delta x = 10^{-5}$m shows a better agreement with the experimental results, reaching a

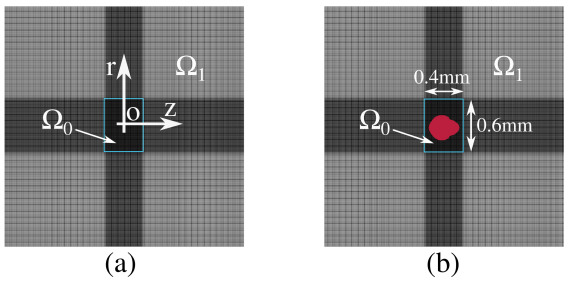

Figure 6. Local mesh distribution near the bubble nucleation site. (a) t=0s. (b) t=10^{-7}s. The red area within Ω_0 represents the bubble right after its nucleation.

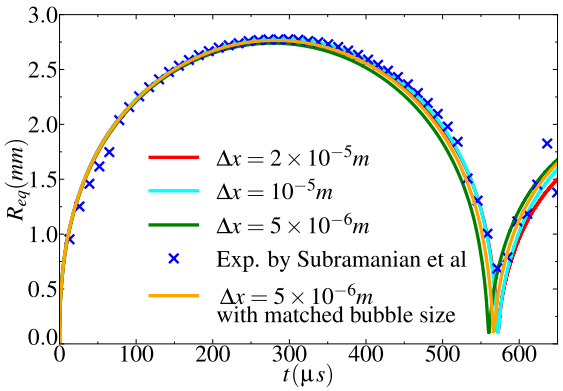

Figure 7. Comparison of radius between experiment and simulation.

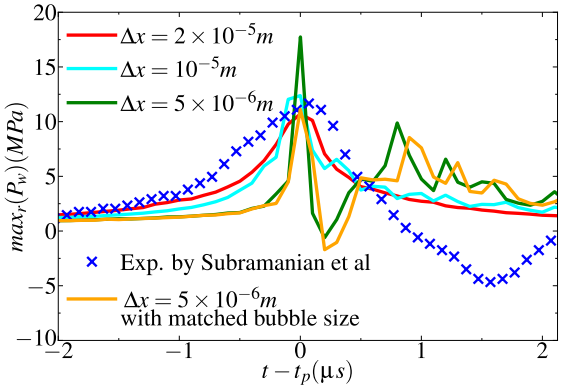

Figure 8. The sensitivity of wall pressure to mesh size.

maximum radius of 2.7 mm which matches well the experimental results. Besides, in Figure 8, the simulation with $\Delta x = 10^{-5}$m exhibits a relative error of 1.3% in the timing of the peak pressure and 6% in the peak pressure value, compared to the experimental measurements.

A notable feature regarding maximum wall pressure for Δx $=5 \times 10^{-6}$m is found to be approximately 17MPa (see green line in fig. 8). This pressure peak is significantly higher than what observed experimentally (see blue crosses in fig. 8) and speculate that it is due to inaccuracies on the prediction of the bubble size rather than to mesh resolution. To verify our assumption, an additional simulation was conducted using the same mesh resolution of Δx $=5 \times 10^{-6}$m but with a 20% higher absorption coefficient. This adjustment led to a 1% increase in the numerical maximum bubble size, matching the experimental measurements by [16] (see orange line in fig. 7). The wall pressure is highly sensitive to the collapse dynamics. As the bubble grows slightly larger, its collapse becomes significantly less sharp due to a reduced collapse velocity and lower compression of the surrounding fluid. This deceleration diminishes the intensity of the pressure wave generated during collapse, and consequently, the impact on the wall is reduced. The resulting pressure peak for the size-matched simulation is now in good agreement with the experiments, as shown by the orange line in fig. 8. This confirms that Δx $= 5 \times 10^{-6}$m gives similar results to $\Delta x = 10^{-5}$m once the bubble dynamics are properly matched with the experiment data. Therefore, $\Delta x = 10^{-5}$m is chosen as the converged mesh size for region Ω1, ensuring accurate and efficient simulations in the following studies.

In conclusion, a spatial convergence study has been conducted and we identified an optimal mesh size of $\Delta x = 5 \times 10^{-6}$m within Ω0 and 10^{-5}m within Ω1 to conduct the following simulations.

4. RESULTS

In this study, three γ are considered, i.e. $\gamma \approx 1$, 1.6, 2.2, in order to investigate three conceptually different cavitation regimes ([16]). A single bubble near a solid wall is modeled by two different approaches. Firstly, we simulate a cavitation bubble initialized at rest. The corresponding simulations are carried out using two numerical solvers, namely Basilisk [12] and M2C [14]. As the two solvers employ different numerical methods and discretization approaches, this preliminary comparison will allow us to single out the discrepancies in the numerical simulations that are due to the numerical solver. Hence, we compare them in terms of the time evolution of (i) the equivalent bubble radius (R_{eq}, i.e. the radius of a fictitious spherical bubble with the same volume), and (ii) the maximum wall pressure ($\max_r(P_w)$).

A second part of our investigation includes the laser generation and the first collapse. In this second part, we use the sole M2C solver, owing to its multiphysics capabilities to simulate a laser-induced bubble from the generation point. By comparing the equivalent radius and the maximum wall pressure between our simulations and the experimental measurements by [16], we will discuss the limitations of simulating a cavitation bubble starting from rest.

4.1. A bubble from rest

This section examines the dynamics of a bubble near a wall assuming that the bubble has been initialized at rest starting from its maximum size. The initial bubble temperature is set to be $T_{G,0}/T_{L,0}$=0.826. The initial pressure ratio between outside and inside the bubble is specified to be $P_{G,0}/P_{L,0}$=1/50. Two solvers are here compared, i.e. M2C and Basilisk, making sure that the simulations have consistent initial configurations and converged mesh resolution. The selected stand-off ratios are γ=1.049, 1.537, 2.152, as for such three stand-off ratios we can initialize the bubble shape using the fitting of [17].

As illustrated in Figure 9, both equivalent radius and collapse time predicted by Basilisk and M2C show a strong agreement. The deviation between the two numerical solvers remains within 5% for the collapse time. Furthermore, the collapse times predicted by both solvers are within the range reported in the experiments by [16, 17]. We further stress that both solvers reproduce the trend observed in the experiments, i.e. $t_c \downarrow$ for $\gamma \uparrow$.

Regarding the maximum wall pressure $\max_r(P_w)$, as shown in Fig. 10, both solvers display a similar trend across all γ. However, M2C tends to predict a sharper increase in $\max_r(P_w)$ in time near the pressure peak time t_p. As γ increases from 1.049 to 2.152, both solvers predict a decrease in the peak pressure.

A significant deviation is observed for γ = 1.049, with M2C predicting a pressure peak approximately 50% higher than Basilisk. Furthermore, an oscillatory behavior appears in the M2C result, which is absent in Basilisk. This highlights the sensitivity of $\max_r(P_w)$ for $\gamma \approx 1$. This discrepancy in pressure peak and the oscillatory behavior may stem from differences in interface capturing methods (VOF vs Level-Set method), as well as variations in discretization schemes. In particular, the nonphysical behavior observed with the Level Set method may be related to its frequent re-initialization process inherent to the method, which can shift the interface position. This becomes especially problematic near the wall, where such shifts can locally violate pressure continuity and lead to non-physical pressure peaks and oscillations. In contrast, for γ = 1.537 and 2.152, the relative error significantly reduces to a range of 5% to 8% in pressure peak.

In conclusion, both M2C and Basilisk can effectively simulate the dynamics of a bubble initially at rest near a wall. While the equivalent radius and collapse time show minimal sensitivity to the modeling approaches, the maximum wall pressure exhibits a stronger variability, particularly for $\gamma \approx 1$. A detailed comparison with the modeling approach including laser generation must therefore focus primarily on the pressure quantification, rather than on interfacial indicators.

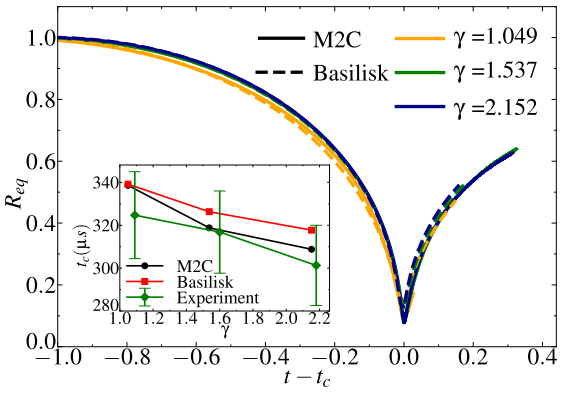

Figure 9. Bubble equivalent radius and collapse time: Comparison between the two numerical solvers for three stand-off ratios. The inset shows the numerical collapse times for the three stand-off ratios, compared with the experimental measurements by [16, 17].

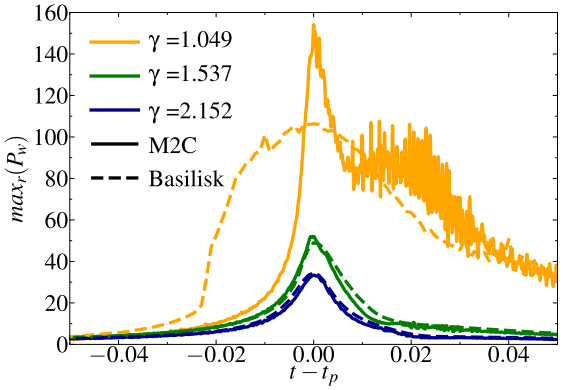

Figure 10. Maximum wall pressure: Comparison between the two numerical solvers for three stand-off ratios.

4.2. A bubble from laser generation

In this section, three slightly different γ are selected, i.e., γ= 1.07, 1.68, 2.18, as they correspond to the stand-off ratios reproduced in the laser-induced cavitation experiments of [16]. We will now simulate bubble generation thanks to the capacitive phase-change approach implemented in M2C.

As illustrated in Figure 11, the maximum wall pressure predicted by the simulation generally matches well with the experimental measurements, although a significant deviation of 34% for γ=1.68 in the pressure peak is observed. This discrepancy is likely attributed to the difference in the equivalent radius and interfacial dynamics between experimental results and the simulation, as shown in Figure 12. For γ=1.07 and for γ=2.18, we observe that the relative error is considerably smaller, around 5% and 2% in pressure peak, respectively. This minimal deviation can also be explained by the nearly-perfect match between the bubble's equivalent radius evol-

ution in M2C simulation and experimental data for these two γ.

Figure 13 shows the comparison in wall pressure among the simulation of bubble initially at rest implemented with both M2C and Basilisk, the simulation of bubble from generation using M2C, and experimental measurements. The results indicate that simulating the bubble generation provides better agreement with the experiments and simulations initiated from rest, regardless of the numerical approach used, largely underestimate the pressure peak at $\gamma > 1$. This highlights the importance of including the memory of the formation and expansion phases in the bubble dynamics simulations.

To further reinforce the significance of modeling the entire bubble evolution from the breakdown phase, two additional cases for $\gamma \approx 1.6$ were simulated with M2C: (*i*) one including only the expansion and collapse phases, initialized with a small radius of 0.16 mm and high internal pressure and temperature ($P_{G,0}/P_{L,0} = 3225$, $T_{G,0}/T_{L,0} = 33.67$); (*ii*) another considering only the collapse phase, starting from the maximum bubble size of 2.7mm with initial pressure and temperature corresponding to a bubble from rest (i.e. $P_{G,0}/P_{L,0} = 1/50$, $T_{G,0}/T_{L,0} = 0.826$), as shown in Figure 14 and 15. These results clearly show that including the bubble breakdown phase provides the best agreement with experimental measurements by [16], while simulations that model only the expansion and collapse phases perform better than those starting solely from the maximum radius, which are the least accurate.

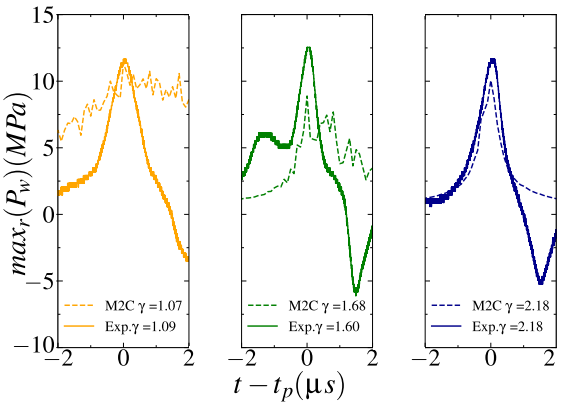

Figure 11. Maximum wall pressure: Comparison between simulations (dashed lines) and experiments by [16] (solid lines).

5. CONCLUSION

Simulations of bubbles from rest, implemented using M2C and Basilisk, demonstrate strong agreement in predicting the equivalent radius and collapse time, with deviations between the two solvers remaining within 5%. Both methods accurately capture the trend of decreasing collapse time as γ increases, and the simulated results match well with

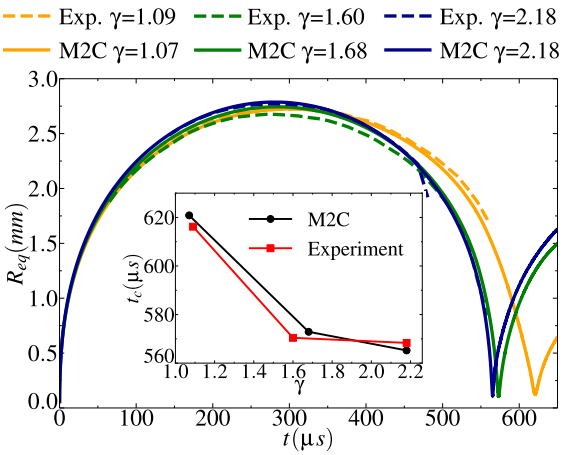

Figure 12. Evolution of R_{eq} simulated by M2C (solid lines) and measured experimentally by [16] (dashed lines), together with the collapse time reported in the inset.

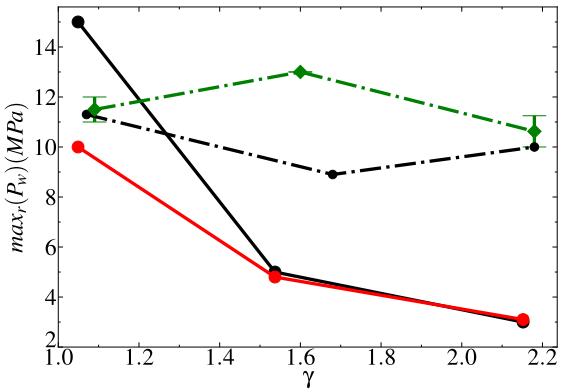

Figure 13. Comparison of maximum wall pressure. The solid lines denote simulations from rest carried out using M2C (solid black line) and Basilisk (solid red line). The black dashed-dotted line refers the M2C simulations including the laser-generation of the cavitation bubble, while the green dashed-dotted line refers to the experiments by [16].

experimental measurements for these metrics. However, the maximum wall pressure ($\max_r(P_w)$) shows greater sensitivity to the modeling approach, particularly at lower γ. For $\gamma \approx 1$, a significant discrepancy of approximately 50% is observed between both solvers, highlighting the influence of differences in interface capturing methods (VOF vs Level-Set method) and numerical discretizations.

Simulations of bubble from its nucleation, conducted with M2C, achieve better agreement with experimental results compared to those started with the bubble at rest. By incorporating the formation and expansion phases of the bubble, the simulation provides more accurate predictions of maximum wall pressure and a comprehensive understanding of

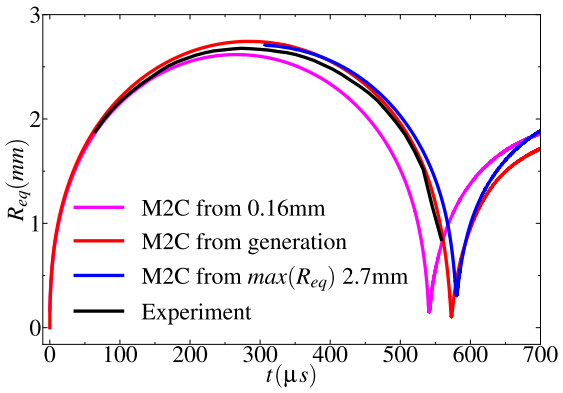

Figure 14. Comparison of R_{eq} for $\gamma \approx 1.6$ obtained from M2C simulations initialized at different starting points and measured experimentally by [16].

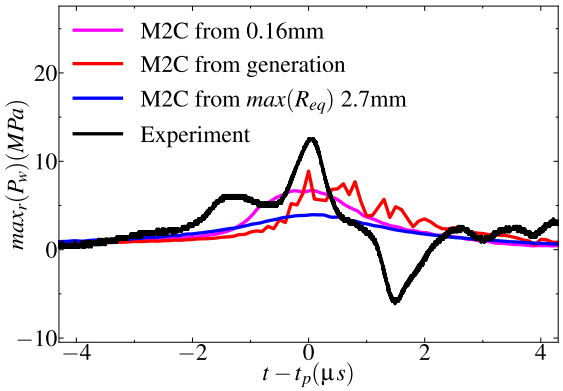

Figure 15. Comparison of $max_r(P_w)$ for $\gamma \approx 1.6$ obtained from M2C simulations initialized at different starting points and measured experimentally by [16].

bubble collapse. For $\gamma \approx 1$ and $\gamma \approx 2.2$, relative errors in wall pressure peak between simulation and experiment are minimal, at approximately 5% and 2%, respectively. However, for $\gamma \approx 1.6$, a significant deviation of 34% in pressure peaks was observed. This discrepancy is attributed to differences in the evolution of bubble radius and interfacial dynamics between the simulation and experiment, as evidenced by the radius evolution analysis.

Overall, simulations of bubbles from generation exhibit superior accuracy in predicting experimental results compared to those from rest. While both modeling approaches are effective in capturing key bubble dynamics such as collapse time and equivalent radius, the inclusion of the formation and expansion phases in the simulation process enhances the predictive capability for maximum wall pressure. These findings underscore the sensitivity to the initialization modeling assumptions and further studies will be aimed to identify the initial conditions capable of simulating the bubble dynamics without necessarily including the bubble generation.

ACKNOWLEDGEMENTS

This work has been financially supported by the Chinese Scholarship Council (CSC) for B. Wang (student number 202206240030) and Z. Yang (student number 202008310185).

REFERENCES

[1] Brennen, C. E., 2014, *Cavitation and bubble dynamics*, Cambridge university press.

[2] Franc, J.-P., and Michel, J.-M., 2006, *Fundamentals of cavitation*, Vol. 76, Springer science & Business media.

[3] Cristofaro, M., Edelbauer, W., Koukouvinis, P., and Gavaises, M., 2020, "A numerical study on the effect of cavitation erosion in a diesel injector", *Applied Mathematical Modelling*, Vol. 78, pp. 200–216.

[4] Balz, R., Nagy, I. G., Weisser, G., and Sedarsky, D., 2021, "Experimental and numerical investigation of cavitation in marine Diesel injectors", *International Journal of Heat and Mass Transfer*, Vol. 169, p. 120933.

[5] Arndt, R. E., 1981, "Cavitation in fluid machinery and hydraulic structures", *Annual Review of Fluid Mechanics*, Vol. 13 (1), pp. 273–326.

[6] Gensheng, L., Zhonghou, S., Changshan, Z., Debin, Z., and Hongbing, C., 2005, "Investigation and application of self-resonating cavitating water jet in petroleum engineering", *Petroleum science and technology*, Vol. 23 (1), pp. 1–15.

[7] Soyama, H., Chighizola, C. R., and Hill, M. R., 2021, "Effect of compressive residual stress introduced by cavitation peening and shot peening on the improvement of fatigue strength of stainless steel", *Journal of Materials Processing Technology*, Vol. 288, p. 116877.

[8] Zhao, B., and Coutier-Delgosha, O., 2023, "The impacts of material acoustic impedance and thickness on single laser-induced bubble dynamics and determining factors in resulting pressure", *Physics of Fluids*, Vol. 35 (10), p. 103303, URL `https://doi.org/10.1063/5.0168349`, `https://pubs.aip.org/aip/pof/article-pdf/doi/10.1063/5.0168349/18151383/103303_1_5.0168349.pdf`.

[9] Zhang, J.-y., Du, Y.-x., Liu, J.-q., Sun, Y.-r., Yao, Z.-f., and Zhong, Q., 2022, "Experimental and numerical investigations of the collapse of a laser-induced cavitation bubble near a solid wall", *Journal of Hydrodynamics*, Vol. 34 (2), pp. 189–199.

[10] Ren, X., He, H., Tong, Y., Ren, Y., Yuan, S., Liu, R., Zuo, C., Wu, K., Sui, S., and Wang, D., 2016, "Experimental investigation on dynamic characteristics and strengthening mechanism of laser-induced cavitation bubbles", *Ultrasonics sonochemistry*, Vol. 32, pp. 218–223.

[11] Zhang, Y., Xie, X., Zhang, Y., and Du, X., 2019, "Experimental study of influences of a particle on the collapsing dynamics of a laser-induced cavitation bubble near a solid wall", *Experimental Thermal and Fluid Science*, Vol. 105, pp. 289–306.

[12] Saade, Y., Lohse, D., and Fuster, D., 2023, "A multigrid solver for the coupled pressure-temperature equations in an all-Mach solver with VoF", *Journal of Computational Physics*, Vol. 476, p. 111865, URL https://www.sciencedirect.com/science/article/pii/S0021999122009287.

[13] Fuster, D., and Popinet, S., 2018, "An all-Mach method for the simulation of bubble dynamics problems in the presence of surface tension", *Journal of Computational Physics*, Vol. 374, pp. 752–768, URL https://www.sciencedirect.com/science/article/pii/S0021999118305187.

[14] Zhao, X., Ma, W., and Wang, K., 2023, "Simulating laser-fluid coupling and laser-induced cavitation using embedded boundary and level set methods", *Journal of Computational Physics*, Vol. 472, p. 111656, URL https://www.sciencedirect.com/science/article/pii/S0021999122007197.

[15] Saade, Y., Lohse, D., and Fuster, D., 2023, "A multigrid solver for the coupled pressure-temperature equations in an all-Mach solver with VoF", *Journal of Computational Physics*, Vol. 476, p. 111865.

[16] Subramanian, R. K., Yang, Z., Romanò, F., and Coutier-Delgosha, O., 2024, "Bubble collapse near a wall. Part 1: An experimental study on the impact of shock waves and microjet on the wall pressure", URL https://arxiv.org/abs/2408.03479, 2408.03479.

[17] Yang, Z., Subramanian, R. K., Wang, B., Coutier-Delgosha, O., and Romanò, F., 2025, "Bubble collapse near a wall: A numerical study on the impact of physical mechanisms for a bubble initially at rest", *submitted*.

[18] Métayer, O. L., Saurel, R., Métayer, O. L., and Saurel, R., 2016, "The Noble-Abel Stiffened-Gas equation of state", Vol. 046102, URL http://dx.doi.org/10.1063/1.4945981.

[19] Zein, A., Hantke, M., and Warnecke, G., 2013, "On the modeling and simulation of a laser-induced cavitation bubble", *International Journal for Numerical Methods in Fluids*, Vol. 73, pp. 172–203.

Conference on Modelling Fluid Flow (CMFF'25)
The 19th International Conference on Fluid Flow Technologies
Budapest, Hungary, August 26 - August 29, 2025

SUPERPOSITION OF SECONDARY FLOWS INSIDE ARTIFICIAL GEOMETRIES

Péter Friedrich[1], Benjamin Csippa[1], György Paál[1]

[1] Corresponding Author. Department of Hydrodynamic Systems, Faculty of Mechanical Engineering, Budapest University of Technology and Economics. Műegyetem rkp 3, H-1111 Budapest, Hungary, E-mail: pfriedrich@hds.bme.hu, bcsippa@hds.bme.hu, gypaal@hds.bme.hu

ABSTRACT

It has been hypothesised in the literature that secondary flows play a role in intracranial aneurysm formation. [1], [2] Complex flow fields develop inside the arteries, affected by several parameters. The irregular shape of the blood vessels means that the effects of the geometry features, such as bends or cross-section changes are superposed. The complexity of the flow-field is further increased by the pulsatile nature of the blood flow.

The aim of this research is to better understand the relationship between the geometry and the developed flow-field in the case of intracranial arteries. Artificial models were created, where the cross-section was assumed to be constant and circular. The models consisted of two bends with a straight section between them. During the study several parameters were changed in the model. These include the diameter of the pipe, the radii of the bends, the length of the straight section between the bends and finally the Reynolds number. All the parameter ranges were selected to correspond to those in real vessels. CFD simulations were carried out on the models using Ansys CFX.

The study is limited by the number of bends and the number of configurations. The simulations were steady state, the transient effects of the pulsatile flow were not studied. Future work can expand on this research by improving on these limitations or by increasing the number of bends.

Keywords: Aneurysm, haemodynamics, CFD, CFX, Secondary flow, Python

NOMENCLATURE

$\underline{Fr}$	[-]	frenet unit vector
$\underline{r}$	[-]	vector
p	[-]	arbitrary point in plane
r_c	[-]	centreline point in plane
$\underline{v}$	[m/s]	absolute velocity vector

Subscripts and Superscripts

n, b, t	normal, binormal, tangent components of the Frenet system
ax	axial velocity
sec	secondary velocity
rad	radial component
circ	circumferential velocity
x, y, z	axes

1. INTRODUCTION

Aneurysms are malformations of the blood vessel wall. Two shapes are known. One is the so-called fusiform aneurysm. These form on arteries in the abdomen, the artery grows out radially in all directions. The other form is the saccular aneurysm. These are typical inside the brain. A sac grows on the side of the blood vessel, and it is connected to it with a smaller neck section.

Aneurysms might not influence the patient and may go unnoticed for long times as they do not have distinctive symptoms. Their danger lies in the rupture of the sac. The rupture of the sac can lead to stroke. Stroke is still one of the leading sources of death in the world. With the use of modern digital medical imaging technologies getting more common more aneurysms are discovered. Once discovered, the aneurysm can be treated effectively. Modern treatments use flow diverter stents, which are a web-like structure made of biocompatible metal alloys. These are placed in the artery at the neck of the aneurysm using a catheter. Another common method is coiling, when a thin metal wire is coiled inside the sac itself. Both of these methods reduce the velocity of the blood inside the sac, so that it starts to coagulate, and then the aneurysm may disappear. Both methods are endovascular procedures, in contrast to older open surgery methods.

As aneurysms do not have distinctive symptoms they are often discovered by accident. Thus, their

formation and development are not well understood. There are several theories on the cause of the aneurysm initiation. The initiation and growth of the sac are complex biomechanical processes. It is also believed that elevated secondary flows also play a role in the formation of the aneurysm sac.

Secondary flows exist in many fields of fluid dynamics. Everywhere it means a flow which is perpendicular to the main flow direction. The importance of secondary flows varies among the various fields of fluid dynamics. For example, in river flows they are well studied. The secondary flows play an important role in the movement of sediment in the river. In the case of mixing vessels, the vertical circulation of the liquid is also a secondary flow. Secondary flows also develop inside pipe networks. Most often bends in the pipe induce the secondary flow, but valves and pumps can also do it. In most engineering cases secondary flows inside a pipe are disadvantageous. Therefore, most studies focus on their reduction or dissipation.

A mathematical approach was proposed by Dean back in 1927 [3]. He assumed a pipe with circular cross-section, constant diameter and bend radius. The work also assumed the radius of the bend to be large compared to the radius of the cross section of the pipe. It also assumed the Reynolds number to be small and the flow to be steady state.

Later research expanded on the work of Dean by focusing on pulsatile flows in curved pipes. The flow varied in a sinusoidal manner. It had similar limitations as the work by Dean. It was again assumed that the curvature of the pipe bend was bigger than the radius of the cross-section of the pipe. [4], [5]

Physiological curved geometries often are non-planar, and thus have torsion besides curvature. Researchers also investigated the effects of torsion on the secondary flows. Yamamoto et al. [6] investigated the effects of torsion numerically in a steady flow. Others demonstrated [7], [8], [9] in helical pipes that torsion causes asymmetric Dean vortices in the cross section of the pipe. The vortex in one half becomes bigger, while the other becomes smaller. Nijjari et al. [10] investigated pulsatile flows in a curved pipe bend with torsion with elastic walls.

The above-mentioned research only focused on helical vessels or singular pipe bends. The radius of the bend was constant, and larger than the radius of the cross-section. However, in physiological blood vessels several bends can occur in a short distance, which may influence the development of the secondary flows in the next bend downstream. The radius of the bend might not be constant throughout the bend.

This paper aims at investigating the superposition of bends within a short distance of each other and their effect on the developing secondary flows using computational fluid dynamics (CFD).

2. METHOD

In order to investigate the superposition of pipe bends and their effect on the secondary flows a simple geometry was created. The geometry had several parameters, and a parametric study was made.

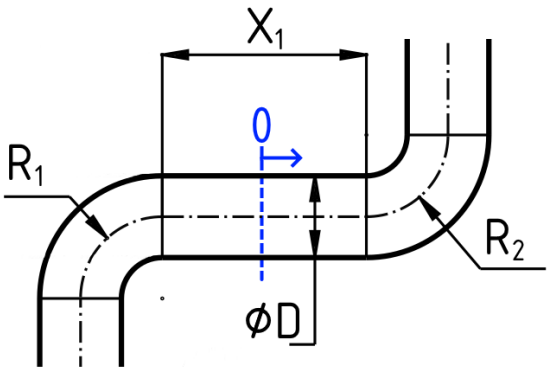

Figure 1. Parameters of the geometry, in blue the zero point for the post-processing coordinate-system

The geometry is a pipe with a circular cross-section and consists of straight and curved sections. The curved sections were each a 90° bend in opposite directions. Between the pipe bends there was a straight section. Before the first bend and after the second bend straight sections were made with 20 diameters in length. This was done to ensure a fully developed flow to arrive at the first bend, and to observe the dissipation of the secondary flows after the second bend. The geometry was created using FreeCAD 0.21.2 via the Python API. The geometry had the diameter of the pipe D, the radii of the bends R_1, R_2 and the length of the straight section between the bends x_1 as parameters. These can also be seen in Figure 1. The geometries were exported as an open surface mesh in the .stl format.

Meshing of the geometries was carried out with the Vascular Modelling Toolkit (VMTK) Python package. The mesh had an element size of 0.3 *mm* with tetrahedral elements. The inflation on the wall consisted of 8 layers, with a growth ratio of 1.25. The mesh settings were identical for all the cases. For the CFD simulations Ansys CFX 23R2 was used. The simulations were steady state. The fluid chosen was water. The inlet was set up as a velocity inlet, with a parabolic velocity profile. The mean velocity of the profile was calculated from the Reynolds-number prescribed for the given simulation. As the possible maximum Reynolds-number in the parameter set was 800, no turbulence model was used. The outlet was set as an opening with 0 *Pa*. The walls were rigid and set as non-slip walls.

The parameters of the study were the diameter of the pipe (D), the radii of the pipe bends (R), the length of the straight section between the bends (x_1) and the Reynolds-number (Re). The radii for the pipe

bends were the same for a given case, so the geometry is centrally symmetrical. They were defined using the R/D ratio. The value of x_1 was also made dimensionless using the diameter of the pipe. The ranges were selected, based on data from real arteries used in previous research. The range and increments of the parameters can be seen in Table 1. By multiplying the number of possible values for each the total number of cases is 990.

Table 1. Ranges and increments of the parameters

Parameter	Minimum	Maximum	Increment
D [mm]	3	5	1
R/D [-]	1	10	1
x_1 [-]	0	10	1
Re [-]	100	800	350

The parametric study was run using the Dakota open-source package. It managed the running of the cases, including modifying the scripts and commands necessary for running the simulations and post-processing. It also managed running the cases parallelly, thus greatly reducing the time required for running all the cases.

3. POST-PROCESSING

The post-processing was carried out using Paraview 5.10.1 and custom in-house built Python scripts. The post-processing focuses on the decomposition of the velocity field into secondary components. The decomposition is done using Frenet frames along the centreline of the geometry. A clear understanding of the Frenet frames is essential.

For each geometry a centreline can be calculated. Along this centreline, at any given point an orthogonal coordinate-system can be defined. In case of a Frenet-system each of the three axes point to a specified direction. The Frenet tangent vector $\underline{Fr_t}$ is parallel to the tangent of the centreline at that point. The Frenet normal vector $\underline{Fr_n}$ is perpendicular to the Frenet tangent vector, and points towards the centre of the tangent circle of the centreline. The third axis is the Frenet binormal vector $\underline{Fr_b}$ and is perpendicular to the other two axes. All of them are unit vectors. By using the Frenet normal and binormal vectors a plane can be defined. The geometry can be sliced with this plane. All further calculations were carried out on these slices.

The centreline was defined according to the geometrical parameters. The centreline was sampled at 0.1 mm intervals. A Python script calculated the Frenet unit vectors at each point.

The velocity field can be decomposed into an axial component and a secondary component. The first are parallel to the centreline, while the second are perpendicular to it, and lies in the plane of the slice. The axial component is calculated first using the Frenet tangent vector as can be seen in Eq. (1). Using Eq. (2) the secondary component can be calculated by subtracting the axial component, $\underline{v}_{ax}$, from the velocity vector $\underline{v}$.

$$\underline{v}_{ax} = (\underline{v} \cdot \underline{Fr_t}) \cdot \underline{Fr_t} \tag{1}$$

$$\underline{v}_{sec} = \underline{v} - \underline{v}_{ax} \tag{2}$$

The secondary velocity is in the plane of the slice it can be further decomposed into two components. Given the circular cross-section switching to a polar coordinate-system around the centreline point $\underline{r}_c$ is beneficial. So the secondary velocity can be decomposed into a radial and a circumferential component. First a radial unit vector is calculated using Eq. (3) between $\underline{r}_c$ and an arbitrary point p in the slice. Using the radial unit vector the radial component, $\underline{v}_{rad}$ of the secondary velocity can be calculated as seen in Eq. (4). The circumferential velocity $\underline{v}_{cir}$ can be calculated by simply subtracting the radial velocity from the secondary velocity as seen in Eq. (5). [11]

$$\underline{r}_{rad} = \frac{\underline{p} - \underline{r}_c}{\left|\underline{p} - \underline{r}_c\right|} \tag{3}$$

$$\underline{v}_{rad} = (\underline{v}_{sec} \cdot \underline{r}_{rad}) \cdot \underline{r}_{rad} \tag{4}$$

$$\underline{v}_{cir} = \underline{v}_{sec} - \underline{v}_{rad} \tag{5}$$

After computing the various velocity components in the slices, the average of each was computed for each slice along the centreline.

4. RESULTS

In the following section the findings will be explained, based on velocity graphs along the centreline between different configurations.

As the length of the centreline varies considerably between different configurations, it was made dimensionless for the graphs. The straight sections of the pipe were made dimensionless with the diameter. For the bend sections the length of the arc was chosen, which is the quarter circle. The reference point was set to the halfway point between the two pipe bends, shown in blue in Fig 1. So negative values along the x-axis are towards the inlet, and positive values are towards the outlet. The inlet straight section is not shown on the graphs to help with readability. The velocity component magnitude averages were normalized with the average of the inlet velocity.

The first grouping was done by fixing the diameter and the value of x_1 and changing the value of the curvature of the pipe bends. For $D = 4\,mm, x_1 = 0,\ Re = 100$ the results can be seen in Figs. 2., 3.

As R/D decreases, the maximum value of the circumferential velocity increases in both bends.

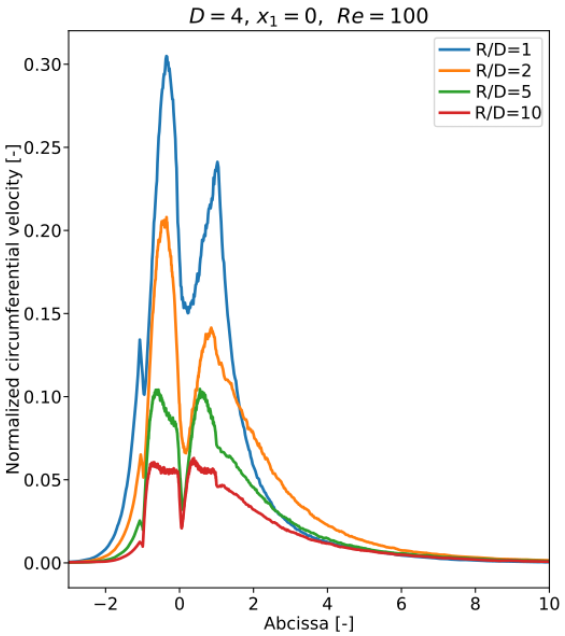

Figure 2. Plot of the circumferential velocity for $D = 4\ mm, x_1 = 0,\ Re = 100$

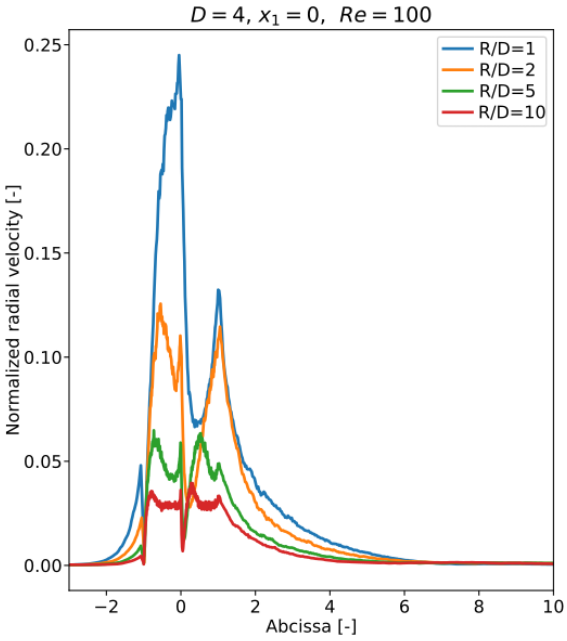

Figure 3. Plot of the radial velocity for $D = 4\ mm, x_1 = 0,\ Re = 100$

This is because a higher R/D ratio means the bend is shallower. An infinitely high ratio would mean straight pipe, where no circumferential velocity would develop. The local maxima in the second bend are lower than in the first bend for $R/D = 1$ and $R/D = 2$. For the other two configurations the maxima in the two bends are equal. With the exception of $R/D = 10$, the velocity in both bends have distinct maximum, while $R/D = 10$ has the shape of a plateau. In the second bend the location of the maximum moves towards the end of the bend as R/D decreases. The circumferential velocity dissipates faster for $R/D = 1$, as in the other cases, while having the highest maximum in the second bend.

The radial velocity graph shows similar findings to the circumferential ones. $R/D = 1$ and $R/D = 2$ have lower local maximum values in the second bend, though the values are similar despite the difference in the maxima in the first bend. The local maxima are further towards the end of the bends in both bends. For $R/D = 2$ and $R/D = 5$ a secondary rise can be seen at the end of the first bend. This rise in radial velocity also appears in the second bend for $R/D = 5$ with a lower value than in the first bend. After the second bend the radial velocity decreases in a similar manner for all the different R/D ratios.

With the increase of the Reynolds-number to 800 both graphs change considerably. The graph for the circumferential velocity can be seen in Fig. 4. and Fig. 5. The maxima are higher than in the case of $Re = 100$, meaning that relative importance of the secondary flows is higher than in the case of the lower Reynolds number.

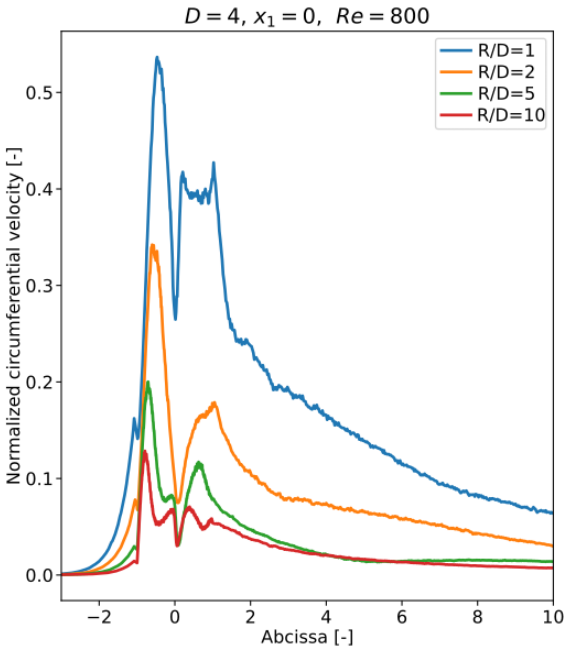

Figure 4. Plot of the circumferential velocity for $D = 4\ mm, x_1 = 0,\ Re = 800$

As for the second bend, the local maxima are smaller than in the first bend for all configurations.

The dissipation of the circumferential velocity takes longer and differs more between the different R/D ratios. The longer dissipation is probably caused by the higher relative velocity values.

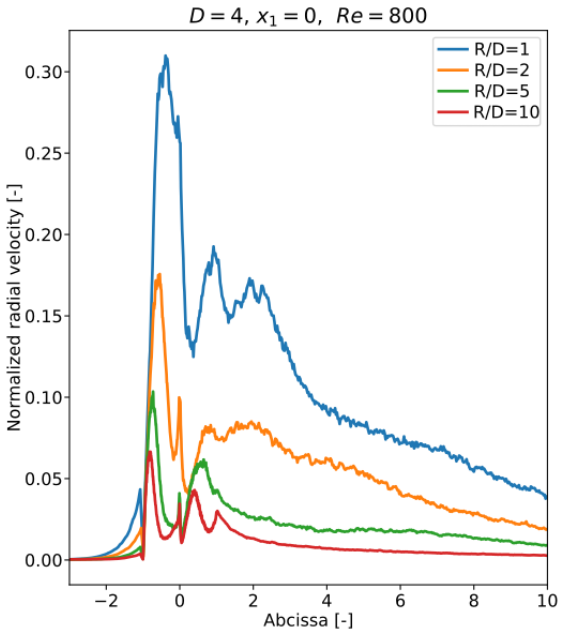

Figure 5. Plot of the radial velocity for $D = 4\ mm, x_1 = 0,\ Re = 800$

The plot of the radial velocity shows the radial velocity in comparable range to Fig. 3. This is in contrast with the circumferential velocity, where with the increase of the Reynolds number the relative velocity increased. The maximum in the first bend moves backwards as the R/D ratio decreases, and the increases as R/D decreases. In the second bend the local maxima are lower than in the first bend for all configurations. After the second bend increases in the radial velocity can be observed for $R/D = 1$ and $R/D = 2$

The effect of the length of the straight section was also investigated. The results will be shown for $R/D = 5$, as it is the shows the trends the best. The first graph in Fig. 6. shows the circumferential velocity for $Re = 100$. The graphs show identical trends in the two bends and between each other too. Also visible is that with the increase of x_1 the minimum value between the two bends decreases. The radial velocity graph seen in Fig. 7. shows similar results to Fig 6. The trends look nearly identical between the different configurations and between each other. As expected, the minimum between the bends decreases as x_1 increases. The difference is that the radial velocity graphs have a secondary peak in each bend.

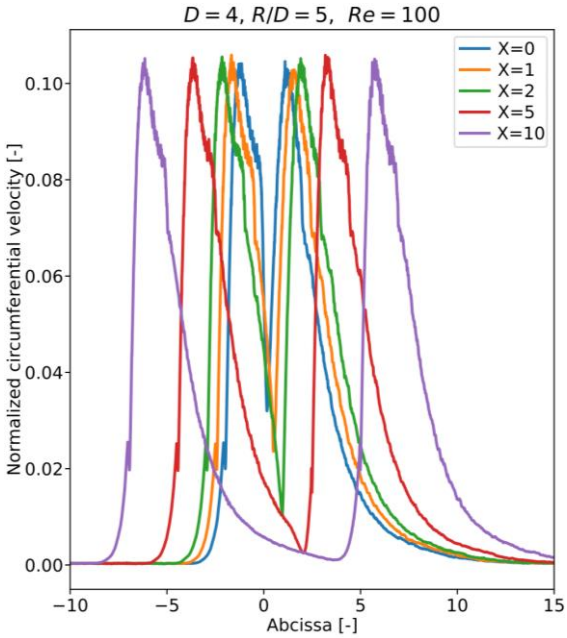

Figure 6. Plot of the circumferential velocity for $D = 4\ mm,\ R/D = 5,\ Re = 100$

For $Re = 800$ the circumferential velocity graph is shown in Fig. 8. The results for the first bend show matching shapes for each configuration. The minimum between the bends decreases as x_1 increases, as seen in the case of $Re = 100$. The results for the second differ though. The maxima are lower than in the first bend. It also increases as x_1 increases. The relative velocity maxima is two times higher than in the case of $Re = 100$.

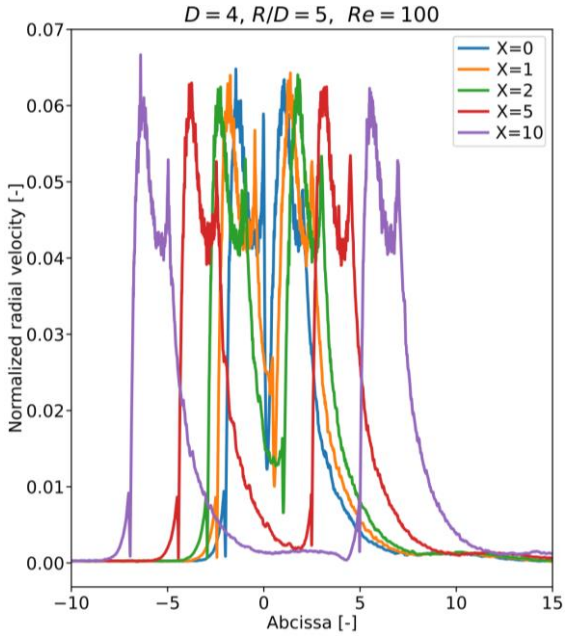

Figure 7. Plot of the radial velocity for $D = 4\ mm,\ R/D = 5,\ Re = 100$

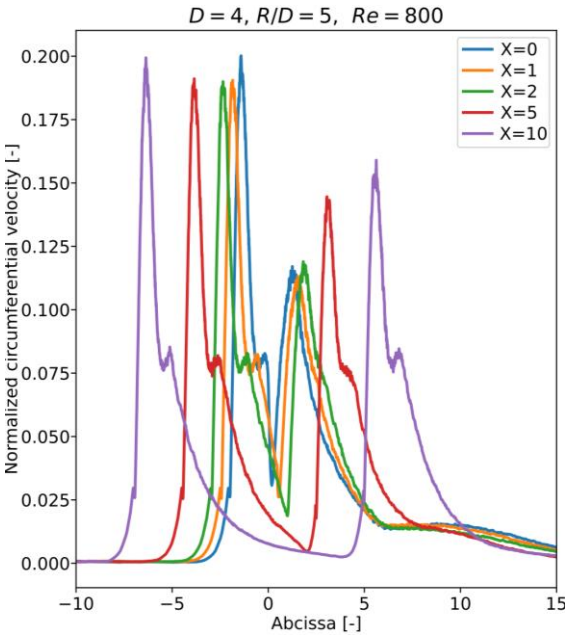

Figure 8. Plot of the circumferential velocity for $D = 4\ mm,\ R/D = 5,\ Re = 800$

The results for the radial velocity can be seen in Fig. 9. The results show similarities to both Fig 8. and Fig. 7. The shape of the graphs for the first bend are nearly identical. The minimum between the bends decreases as x_1 increases. The maxima in the second bend are again lower, than in the first bend, and increases as x_1 increases. The range is again similar to the case of $Re = 100$ and thus lower than the range of the circumferential velocity.

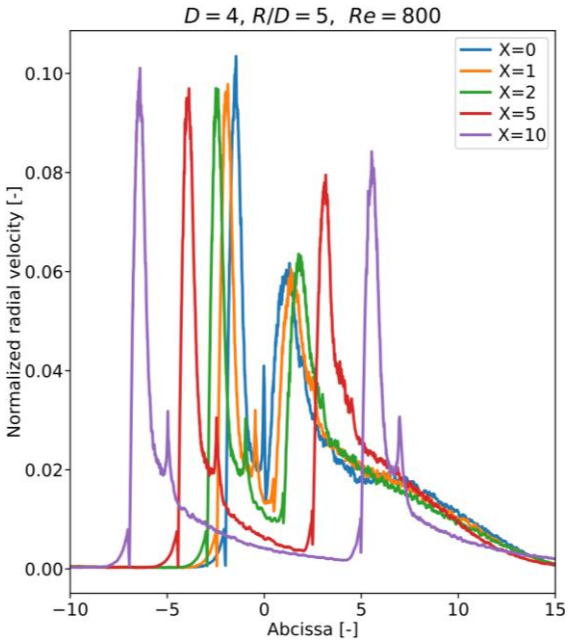

Figure 9. Plot of the radial velocity for $D = 4\ mm,\ R/D = 5,\ Re = 800$

However, the shapes between the first and second bend do not look as similar as in Fig. 7. The exception is $x_1 = 10$. The second rise up in velocity is not present in the second bend.

5. SUMMARY

The goal of the paper was to explore the effects of two pipe bends in opposite directions on secondary flows. A simple geometry was created which consisted of two 90° pipe bends with a straight section between them. It had three parameters which were changed. The flow was studied by steady state CFD simulations at different Reynolds-numbers. All the parameters were chosen to reflect real morphological data, to support research regarding the effect secondary flows on cardiovascular diseases.

At low Reynolds-number the first bend has less effect on the second one in most configurations. The exceptions for both in terms of radial and circumferential velocity happen when $x_1 = 0$ and the bends have a radius of $R/D = 1$ and $R/D = 2$. In these cases, the maximum values were lower than in the first bend. The radial and circumferential velocities were in the same range. At $Re = 800$ the first bend affected the developed flow noticeably. The local maxima in the second bend were smaller than in the first bend. This effect was stronger when x_1 was small. As x_1 increased the maxima in the second bend increased. As the bends were in opposite directions, they induce vortices in opposing rotating directions. So, the second bend first must slow down the vortices from the first bend and then starts to induce vortices in the opposite direction, hence the lower maximum values. Increasing the distance between the bends allows the secondary flows to dissipate more, thus the second bend can induce faster secondary flows. But even with the distance of 10 diameters, the maxima for both secondary velocity components were lower than in the first bend. With the increase of the Reynolds-number and in turn the velocity, the relative circumferential velocity increased considerably more than the relative radial velocity. The relative radius of R/D affected the location of the maximum secondary velocity location inside the bend.

In conclusion the first bend has a significant effect on the flow in the second bend, particularly at higher Reynolds-numbers. The distance between the bends also plays a crucial role in the strength of secondary flows in the second bend. The relative radius affects both the strength of the secondary flows and the location of the maxima inside the bend. These findings have implications for understanding the development of cardiovascular diseases, particularly in relation to aneurysm formation. The exact location of the secondary flow maximum is of interest as elevated secondary flows show correlation with aneurysm formation. [12]

The research can be extended to include more configurations, like non-planar cases or bends with non-constant radius. The effect of oscillatory and pulsatile flow may also be worth considering.

ACKNOWLEDGEMENTS

The project supported by the Doctoral Excellence Fellowship Programme (DCEP) is funded by the National Research Development and Innovation Fund of the Ministry of Culture and Innovation of Hungary and the Budapest University of Technology and Economics

Péter Friedrich and his work were supported by the Gedeon Richter Talentum Foundation in the framework of the Gedeon Richter Excellence PhD Scholarship

REFERENCES

[1] A. Lauric, J. Hippelheuser, M. G. Safain, and A. M. Malek, "Curvature effect on hemodynamic conditions at the inner bend of the carotid siphon and its relation to aneurysm formation," J Biomech, vol. 47, no. 12, pp. 3018–3027, Sep. 2014, doi: 10.1016/j.jbiomech.2014.06.042.

[2] B. Csippa, G. Závodszky, G. Paál, and I. Szikora, "A new hypothesis on the role of vessel topology in cerebral aneurysm initiation," *Comput Biol Med*, vol. 103, no. June, pp. 244–251, Dec. 2018, doi: 10.1016/j.compbiomed.2018.10.018.

[3] W. R. Dean, "XVI. Note on the motion of fluid in a curved pipe," *The London, Edinburgh, and Dublin Philosophical Magazine and Journal of Science*, vol. 4, no. 20, pp. 208–223, Jul. 1927, doi: 10.1080/14786440708564324.

[4] F. T. Smith, "Pulsatile flow in curved pipes," 1975.

[5] C. C. Hamakiotes and S. A. Berger, "Fully developed pulsatile flow in a curved pipe," 1988.

[6] K. Yamamoto ', S. Yanase, and T. Yoshida, "lirilii P Torsion effect on the flow in a helical pipe," 1994.

[7] D. G. Xie, "Torsion effect on secondary flow in helical pipe."

[8] "Steady flow in a helically symmetric pipe," 1998.

[9] "Unsteady blood flow in a helically symmetric pipe," 1998.

[10] M. R. Najjari and M. W. Plesniak, "Secondary flow vortical structures in a 180 elastic curved vessel with torsion under steady and pulsatile inflow conditions," *Phys Rev Fluids*, vol. 3, no. 1, Jan. 2018, doi: 10.1103/PhysRevFluids.3.013101.

[11] B. Csippa, L. Sándor, and G. Paál, "Decomposition of velocity field along a centerline curve using frenet-frames: Application to arterial blood flow simulations," *Periodica Polytechnica Mechanical Engineering*, vol. 65, no. 4, pp. 374–384, 2021, doi: 10.3311/PPME.18517.

[12] B. Csippa, P. Friedrich, I. Szikora, and G. Paál, "Amplification of Secondary Flow at the Initiation Site of Intracranial Sidewall Aneurysms," *Cardiovasc Eng Technol*, 2025, doi: 10.1007/s13239-025-00771-4.

Conference on Modelling Fluid Flow (CMFF'25)
The 19th International Conference on Fluid Flow Technologies
Budapest, Hungary, August 26-August 29, 2025

GEOMETRICAL OPTIMIZATION OF RECTANGULAR MVGS DELAYING BOUNDARY LAYER TRANSITION OVER A FLAT PLATE

Márton KULCSÁR[1], András SZABÓ[2], Péter Tamás NAGY[2], György PAÁL[2]

[1] Corresponding Author. Department of Fluid Mechanics, Faculty of Mechanical Engineering, Budapest University of Technology and Economics. H-1111, Budapest, Műegyetem rkp. 3., D building, 3rd floor. E-mail: mkulcsar@hds.bme.hu
[2] Department of Hydrodynamic Systems, Faculty of Mechanical Engineering, Budapest University of Technology and Economics.

ABSTRACT

It has been shown both numerically [1] and experimentally [2] that employing miniature vortex generators (MVGs) to create spanwise mean velocity gradients (SVGs), which in turn attenuate the growth of Tollmien–Schlichting (TS) waves, can delay the transition from laminar to turbulent flow in a low-turbulence boundary layer over a flat plate.

Recently, a parametric study was carried out by Szabó et al. [3] which showed that the measurements carried out by Sattarzadeh et al. [4] utilised non-optimal vortex generators. Consequently, my aim was to find the optimal geometric parameters of MVGs for a given far-field velocity and streamwise position.

Finally, a Bayesian approach, following Ament et al. [5], is used to optimise the geometric properties of the MVGs.

Keywords: boundary layer, CFD, flow stability, MVG, optimization, transition delay

1. INTRODUCTION

Delaying laminar-turbulent transition is crucial for reducing friction drag on streamlined bodies. Transition occurs via boundary layer instabilities (natural transition) or bypass transition, determined by free-stream turbulence levels [6]. Bypass transition, prevalent at high turbulence, is complex and less suitable for control. Natural transition, occurring at low turbulence, is better understood, driven by the exponential growth of small disturbances like Tollmien-Schlichting (TS) waves, describable by linear stability theory, followed by a non-linear secondary instability phase [7]. Dampening TS waves is thus a key strategy for transition delay.

Various active (e.g., wall movement, suction) and passive (e.g., shape optimisation, localised surface modifications [8, 9]) techniques aim to delay transition. While structures like riblets can inhibit Görtler instabilities, they do not suppress TS waves [10, 11]. An effective TS wave dampening method involves introducing streamwise streaks (alternating slow/fast flow regions) into the boundary layer [12, 13]. These streaks induce spanwise shear, disrupting disturbance energy growth, a principle used in spanwise mean velocity gradient (SVG) methods [12, 14].

Generating boundary layer streaks is effective for flow stabilisation [15]. Higher amplitude streaks offer better stabilisation [12], but excessive amplitudes can trigger secondary sinuous instabilities and premature transition [16]. Passive methods are preferred over active ones due to no external energy requirement. Early passive attempts with cylindrical roughness elements had limited success, as increased height destabilised their wakes [13].

A promising passive approach involves winglet-type miniature vortex generators (MVGs), which create strong, stable streaks for effective boundary layer stabilisation [17]. Extensive experimental studies [18, 19, 20, 2, 21] explored MVG parameter influences, streak reinforcement, instability development, and pressure gradient effects, confirming TS wave [2] and oblique disturbance [22] stabilisation. Most studies utilised triangular MVGs, with some investigating rectangular designs [2, 4]. These findings established MVGs' efficacy in creating streaky boundary layers that attenuate TS wave growth. Recently, [23] applied MVGs to an aircraft fuselage, developing practical parameter selection guidelines.

Numerical investigations have further explored MVG flow stability. Siconolfi et al. [1] used Bi-Global stability analysis, finding reasonable agreement with experiments [19] but noted challenges in comparing disturbance growth near MVGs due to instability scattering. Nobis et al. [24] optimised MVG design using a direct-adjoint looping approach to minimise downstream TS wave energy, significantly improving performance but neglecting spanwise spacing, a key parameter for streak evolution [4, 25]. Most recently, Szabó et al. [3]conducted a

parametric study of 225 rectangular MVG configurations using steady-state simulations, Boundary Region Equations (BRE) for flow extension, and BiGlobal stability analysis. They varied MVG height, inter-pair, and intra-pair distances, finding that taller, more sparsely placed MVGs sustain stronger streaks.

Bayesian optimisation [26] is a technique for optimising expensive-to-evaluate functions, with applications in areas like fluid dynamics [27]. First, a probabilistic surrogate model (typically a Gaussian Process, GP) of the objective function is initialised and built using available data points. Then, an acquisition function determines the next sampling point by balancing exploration and exploitation. Finally, the objective function is evaluated at the new point(s), and the model is updated. The process iterates until a stopping criterion is met.

1.1. Objectives of the study

In this study, the stability of the streaky boundary layer generated by MVGs mounted on a zero-pressure-gradient flat plate is analysed using local modal linear stability analysis. As such, it is important to emphasise that the present study focuses specifically on using MVGs to delay the growth of TS waves. Therefore, the recommendations provided here may not necessarily yield improvements in all aspects of MVG design.

Unlike Pederson et al. [28] and Klauss et al. [29], who used streak amplitude as an indirect measure of boundary layer stabilisation, this study directly characterises the flow by solving local stability equations within the framework of the e^N method. Two N factors are computed, one for TS waves and another for secondary instabilities. While using two N factors to assess flow stability may seem unconventional, it is not unprecedented: Scrauf [30] successfully employed this approach by separately evaluating stationary crossflow instability and TS waves to correlate local stability calculations with in-flight test data.

Although the e^N method may appear simplistic compared to more recently developed stability analysis tools, it remains widely used in industrial applications [31, 32] due to its simplicity, relatively low computational cost, and ability to capture key aspects of the transition process. Its continued success suggests that it can provide valuable predictions.

This study focuses on rectangular MVGs, allowing the investigation of key parameters such as spanwise spacing, an aspect not considered in previous topology optimisation studies [28, 29, 24].

A Bayesian optimisation was conducted where three parameters were varied simultaneously: the height (h), the distance between MVGs in each pair (Λ), and the angle of the MVGs (θ). The aim of this optimisation, consistent with [28] and [29], was to attenuate primary instabilities while avoiding the emergence of secondary instability modes. The results can be found in Section 3.

2. FLOW CONFIGURATION AND MODELLING

2.1. Flow configuration

A zero-pressure-gradient incompressible boundary layer is considered. Dimensional quantities are denoted with a hat ($\hat{\square}$), while non-dimensional quantities are represented without it. The free-stream velocity is set to $\hat{U}_\infty = 6$ m/s, and the kinematic viscosity is $\hat{\nu} = 1.4607\times10^{-5}$ m^2/s. The problem setup is illustrated in Figure 1. The downstream distance from the idealised leading edge to the MVG centre is denoted as $\hat{x}_{\mathrm{MVG}}$. The spanwise distance between two MVGs is $\hat{d}$, and the spanwise distance between MVG pairs is $\hat{\Lambda}$. The MVGs have a width $\hat{w}$, length $\hat{L}$, and height $\hat{h}$, and are oriented at an angle $\hat{\theta}$ relative to the free-stream velocity. Recently, [3] found that an important metric for the distance between MVGs is its ratio to the distance between different pairs, as such, this ratio ($\hat{d}/\hat{\Lambda}$) was kept at a fixed value. The specific constant parameter values are provided in Table 1, along with their ratios to the boundary layer thickness at the MVG location ($\hat{\delta}_{99,\mathrm{MVG}} = 3.610$ mm). The parameters varied during the optimisation and their bounds are provided in Table 2, along with the same ratio as before.

2.2. Modelling

The stability of an incompressible boundary layer over a flat plate is analysed using linear stability theory. For a detailed description of the employed method, the reader is referred to [3]. In summary, the governing equations are non-dimensionalised with the free-stream velocity $\hat{U}_\infty$ and boundary layer length scale $\hat{\delta}_0 = \sqrt{\hat{L}_0\hat{\nu}/\hat{U}_\infty}$. The length scale is $\hat{L}_0 = \hat{x}_{st}$ where $\hat{x}_{st}$ is the start of the BRE calculation, shown on Fig. 1. Because of these, the Reynolds number used in this paper is defined as $\mathrm{Re}_\delta = \hat{\delta}_0\hat{U}_\infty/\hat{\nu}$. The velocity field is decomposed into a steady base flow and small perturbations. The base flow is calculated in two steps. First, near the MVGs, the complete NS equations are solved. Further downstream, they can be simplified under appropriate scaling assumptions. Introducing the small parameter ε, the boundary region equations (BRE) are derived, which extend the boundary layer equations and allow the efficient extension of the base flow downstream during the second step.

The stability of the streaky boundary layer is analysed using the BiGlobal stability framework [33]. Since the base flow varies weakly in the streamwise direction, disturbances are assumed to take the form of modal waves with a prescribed real frequency, while the complex wavenumber is computed as an eigenvalue. This leads to the BiGlobal stability equations, widely used in flow stability studies. The spatial growth rate is given by the imaginary part of the wavenumber, and the eigenvalue problem is solved using standard numerical methods. Finally, the growth rates from each slice are used to calculate

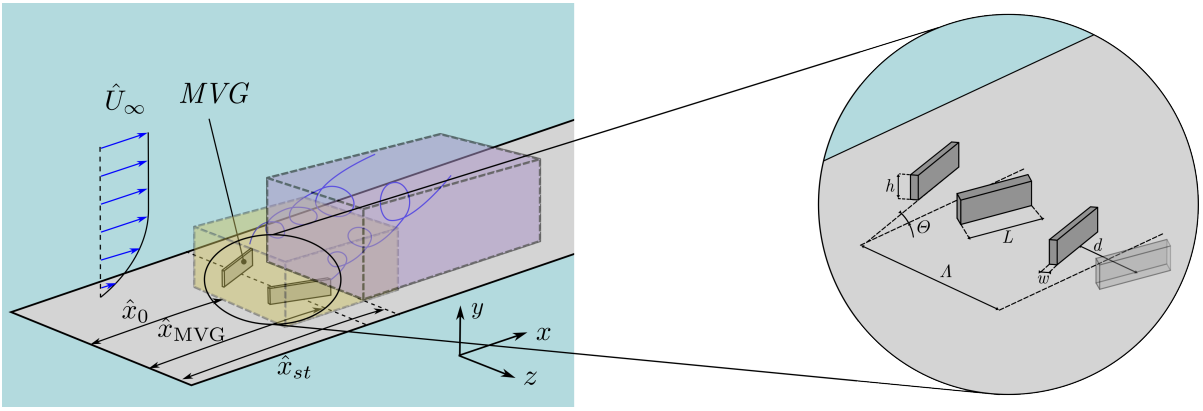

Figure 1. Flow configuration

Table 1. Constant parameters of the computational setup

$\hat{d}/\hat{\Lambda}$ (−)	$\hat{w}$ (mm)	$\hat{L}$ (mm)	$\hat{x}_{\mathrm{MVG}}$ (mm)	$\hat{x}_0$ (mm)	$\hat{x}_{\mathrm{st}}$ (mm)	$\hat{x}_{1,\mathrm{CFD}}$ (mm)
0.5	0.3	3.25	222	213	235	240
	$(0.083\delta_{99,\mathrm{MVG}})$	$(0.90\delta_{99,\mathrm{MVG}})$				

Table 2. Varied parameters of the computational setup

$\hat{\Lambda}$ (mm)	$\hat{h}$ (mm)	Θ (°)
[15, 100]	[0.9, 2.5]	[3, 15]
$[4.15, 27.70]\,\delta_{99,\mathrm{MVG}}$	$[0.25, 0.69]\,\delta_{99,\mathrm{MVG}}$	

the N factor to be used in the e^N method.

The transition to turbulence is predicted using the e^N method, where the transition location correlates with the growth of instability waves. The N factor is computed for each eigenmode, with transition occurring when a critical N value is reached. Two types of instabilities are considered: modified TS waves and secondary instabilities. TS waves, the primary instability in two-dimensional boundary layers, are weakened by streaks and dominate at low frequencies. In contrast, secondary instabilities arise due to streaks and exhibit a broader frequency range, often accelerating transition.

For TS waves, a conservative transition threshold of $N = 7$ is used. No established threshold exists for secondary instabilities, so the maximum N value among all unstable modes is tracked.

2.3. Numerical solution and parameters

The base flow computation consists of two steps: first, the near-MVG flow is computed using 3D CFD, followed by solving the BRE for the downstream flow. BRE calculations start slightly upstream of the CFD domain's end to prevent any effects from the boundary condition.

The CFD simulation employs ANSYS CFX 21 R2 [34], using a steady-state solver. To reduce the computational cost, only half of the geometry (a single MVG) was simulated, while the rest of the computational domain was accounted for by prescribing symmetry boundary conditions to the base flow. A Blasius profile is imposed upstream, while a free-outflow boundary is applied downstream to allow backflow into the domain. The mesh is generated with GMSH [35]. As shown in the figure, the mesh is finest near the MVG, with element size progressively increasing further away. A typical mesh contains approximately $8 - 16 \cdot 10^6$ elements. Second-order spatial discretisation is used, and mesh refinement tests confirm negligible sensitivity in results.

The BRE and BiGlobal stability equations are solved using a finite element method, implemented in the parallel version of the open-source finite element library FreeFem [36]. Taylor-Hood elements are used, where the velocity and pressure fields are discretised using $\mathcal{P}_2$ and $\mathcal{P}_1$ elements, respectively. The mesh, consisting of triangular elements, is generated using BAMG [37], the built-in mesh generator of FreeFem, which utilises Delaunay triangulation to discretise the domain. It adapts element sizes for efficient wall-normal and spanwise resolution. Further mesh refinement studies verified that increased resolution has minimal effect on transition Reynolds numbers.

BRE equations are discretised with a second-order backward Euler scheme, using PETSc [38] for sparse linear algebra and SLEPc [39] for eigenvalue computations. The non-linear system of equations arising from the discretisation of the BRE is solved using a second-order line search (Newton-Raphson) method with the SNES library of PETSc. LU factorisation via MUMPS [40] ensures efficient Jacobian inversion.

BiGlobal stability calculations employ the Krylov-Schur algorithm with shift-invert techniques. This approach enables the extraction of eigenvalues

near an initial guess, referred to as the shift. For each MVG configuration, streamwise location, and frequency, multiple eigenvalue calculations with varying shifts are performed to capture the relevant portion of the spectrum. Shifts are adjusted dynamically to ensure unstable modes are reliably tracked downstream. If an eigenvalue is lost, an additional shift is introduced based on the most unstable mode, guaranteeing accurate instability detection.

Two sets of stability analyses are conducted: one for the modified TS waves and another for the secondary instabilities.

2.4. Optimisation

In order to efficiently explore the parameter space and identify optimal configurations, a multi-objective Bayesian optimisation approach was implemented using the BoTorch [41] package for Python. The logNEHVI (log-constrained Noisy Expected Hypervolume Improvement) [5] acquisition function was employed to maximise two competing objectives. The first of these is the transitional Reynolds number in the low-frequency TS wave domain, which should be maximised. The second is the maximum growth rate of secondary instabilities, which should be minimised, but was multiplied by -1 to reformulate it as a maximisation problem. We assume that our results are exact, so the acquisition function was used in a noiseless setting, this increases numerical stability compared to using the logEHVI (log-constrained Expected Hypervolume Improvement) formulation. The parameter space was constrained using the non-linear constraint handling capabilities of BoTorch to ensure physically relevant configurations. These constraints ensured that two MVGs in the same pair can not touch:

$$\hat{d} - 2 \cdot \hat{L} \cdot sin(\Theta) > \frac{\hat{w}}{2} \tag{1}$$

and that two MVGs in different pairs could not touch:

$$\hat{d} + 2 \cdot \hat{L} \cdot sin(\Theta) < \hat{\Lambda} - \frac{\hat{w}}{2} \tag{2}$$

To accelerate convergence, four new points were queried and evaluated in each iteration step. The goal was to identify a Pareto frontier, balancing both objectives, and the optimisation process was terminated once a sufficient number of Pareto-optimal points were found.

During the optimisation three parameters were varied to validate the viability of the optimisation process, so that it can be used in the future for broader sets of parameters. The constant parameters, such as the streamwise velocity, streamwise position of the MVGs, etc. are shown in Table 1. The bounds of the varied parameters are shown in Table 2. In this three-parameter run, relevant results from the aforementioned parameter study [3] were used as initial data to guide the optimization. This approach facilitated an accelerated convergence toward the Pareto-optimal solutions.

3. RESULTS

In this section, the results obtained from the previously outlined modelling framework are presented. A total of 87 points were evaluated in the model, with 28 taken from the initial parameter study [3] and 59 newly queried points. As demonstrated by the Pareto frontier, Fig. 2a, previous results from [3] and [4] were significantly improved. The best-performing configuration reached the end of the computational domain without triggering the laminar-turbulent transition while maintaining low amplification of secondary instabilities. The convex hull highlights theoretically ideal points, which slightly outperform some of the Pareto-optimal configurations, suggesting that further evaluations could lead to Pareto-optimal points aligning more closely with these theoretically ideal ones. All newly tested points are shown in Fig. 2b, with MVG height and spacing scaled by factors of 10^4 and 10^3, respectively, to emphasise trends rather than absolute values. Full markers indicate Pareto-optimal points, while opaque ones represent suboptimal configurations. The x-axis denotes the transition Reynolds number. The figure reveals distinct optimal ranges for both MVG angle and spacing, while height remains maximised in all optimal cases. The angle effect can be attributed to the need for a sufficiently strong vortex to generate a streaky boundary layer without excessively amplifying secondary instabilities. The optimum MVG spacing arises from the necessity of streak interactions, if too close, they break down prematurely; if too far apart, they fail to sustain each other. The consistently maximal height suggests that vortices generated higher in the boundary layer have a stronger influence on TS wave modulation. However, the upper bound was not extended further, as excessively tall MVGs might trigger transition mechanisms beyond the capabilities of the model.

Two points from the Pareto-frontier, the ones with the highest transitional Reynolds-numbers were further analysed, the parameters of these configurations, along with the best points from [3] and [4] are summarized in Table 3

The amount of drag reduction achieved can be quantified using an averaged drag coefficient (c_D) which is calculated in the following way:

$$c_D = \frac{\frac{\hat{F}_{MVG}}{\hat{U}_\infty^2 \cdot \hat{\rho} \cdot \hat{\Lambda}/2} + \int_{\hat{x}_{st}}^{\hat{x}_1} c_f(\hat{x})\, \mathrm{d}\hat{x}}{\hat{x}_1 - \hat{x}_0} \tag{3}$$

Where c_f is the skin friction coefficient which can be seen in Fig. 3 and F_{MVG} is queried from the laminar CFD of the first phase of the calculation. The figure is shown as a function of Re_δ to be consistent with the other figures. For the turbulent part of the function the Schultz-Grunow formula [42] was used.

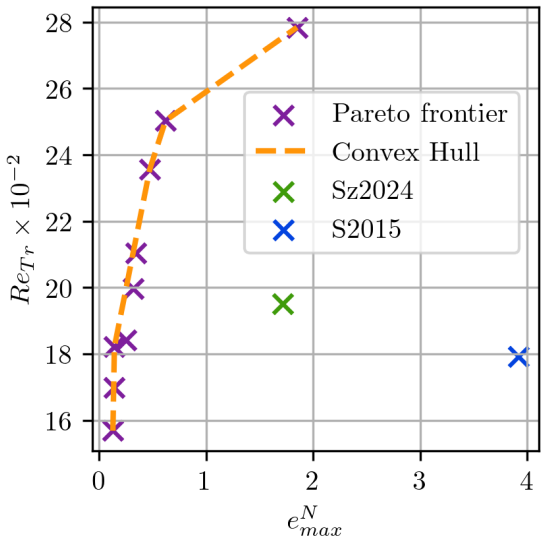

(a) Pareto frontier; the x-axis is the maximum N factor calculated for the secondary instabilities, while the y-axis show the transition Reynolds number. The points from [3] and [4] are the best points from their studies according to our criteria.

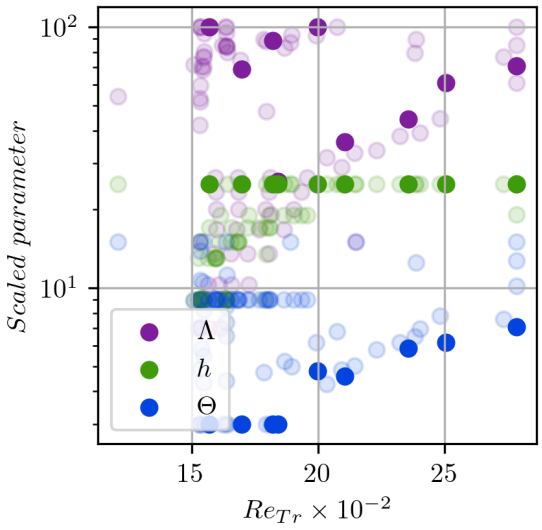

(b) The three varied parameters during the optimisation scaled to fit in the same figure. The x-axis show the transition Reynolds number. Full markers indicate Pareto-optimal points, while opaque ones represent suboptimal configurations.

Figure 2. Results of the three-variable optimisation.

Table 3. Results of the three-variable optimisation

Name	$\hat{\Lambda}$ (mm)	$\hat{d}/\hat{\Lambda}$ (−)	$\hat{\Theta}$ (°)	$\hat{h}$ (mm)	Re_{Tr} (−)	$e^N_{\max}$ (−)
Sz2024	26.5	0.5	9	1.9	1950	1.71
S2015	13	0.25	9	1.3	1793	3.93
Opt1	76.9	0.5	7.58	2.5	$> 2781^*$	1.91
Opt2	61.1	0.5	6.15	2.5	2503	0.62

*There was no transition detected within the computational domain.

The well-known phenomena of the transitional phase overshooting the turbulent phase was neglected.

Due to this effect the results can vary based on the length of the integration, thus the calculation was executed for multiple streamwise coordinates shown with grey dashed lines. In dimensional form, these are the following: $x|_{Re_\delta=1500} = 5.5(m)$, $x|_{Re_\delta=2000} = 9.8(m)$, $x|_{Re_\delta=2500} = 15(m)$, $x|_{Re_\delta=2781} = 19(m)$. The results can be seen in Table 4. In addition, the values for natural transition of the Blasius boundary layer are also included in Table 4.

This shows that, given a shorter body ($L = 5.5(m)$), the drag coefficient between that of a flat plate and of a flow modulated by MVGs can increase by as much as 78%. On the other hand, the strategy works well on longer bodies ($L = 19(m)$), where the same metric can be decreased by 89%. The explanation for this large difference is twofold. In the laminar regime, the vortices generated by the MVGs increase the friction losses. However, by remaining laminar for a much longer distance, the difference in friction between the laminar and turbulent regimes compensates for the higher initial loss.

4. SUMMARY

This paper presents an optimisation method for the geometric properties MVGs, based on local linear stability analysis. Building on prior studies, the base flow near the MVG was computed using 3D CFD simulations, while the downstream evolution of the streaky boundary layer was predicted using the BRE. The stability analysis was performed by solving the BiGlobal stability equations, conducting two sets of calculations for each MVG configuration: one for the modified TS waves and another for identifying potential secondary instabilities that could promote transition. Transition location was estimated using the e^N method for the TS waves with a conservative $N = 7$ value, while for secondary instabilities, the maximum N factor was computed as a destabilisation indicator in the absence of a specific N value. These criteria were used as objectives in a multi-objective Bayesian optimisation approach to find new MVG configurations, which, based on our criteria, outperform previously investigated MVGs. The findings of this study should be further examined through experimental validation or high-fidelity direct numerical simulations.

Table 4. Drag results

Name	$c_D\|_{Re_\delta=1500}$	$c_D\|_{Re_\delta=2000}$	$c_D\|_{Re_\delta=2500}$	$c_D\|_{Re_\delta=2781}$
Blasius	$2.15 \cdot 10^{-4}$	$8.18 \cdot 10^{-4}$	$15.91 \cdot 10^{-4}$	$20.80 \cdot 10^{-4}$
S2015	$3.66 \cdot 10^{-4}$	$7.44 \cdot 10^{-4}$	$14.43 \cdot 10^{-4}$	$16.57 \cdot 10^{-4}$
Sz2024	$3.90 \cdot 10^{-4}$	$5.19 \cdot 10^{-4}$	$12.46 \cdot 10^{-4}$	$14.98 \cdot 10^{-4}$
Opt1	$3.83 \cdot 10^{-4}$	$3.01 \cdot 10^{-4}$	$2.50 \cdot 10^{-4}$	$2.29 \cdot 10^{-4}$
Opt2	$3.82 \cdot 10^{-4}$	$2.99 \cdot 10^{-4}$	$2.71 \cdot 10^{-4}$	$5.56 \cdot 10^{-4}$

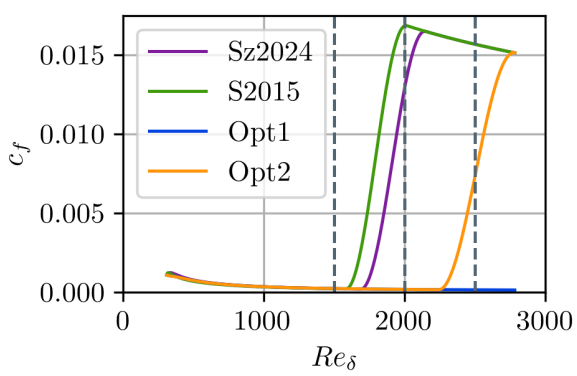

Figure 3. The skin friction coefficients for different configurations. The x-axis shows the non-dimensional streamwise coordinate, Re_δ and the y-axis shows the local friction coefficient c_f. Note that the Opt1 configuration stayed laminar throughout the computational domain ($x1 = 19(m)$).

ACKNOWLEDGEMENTS

This research was performed within the framework of the NKFI Hungary 142675 project. The project is supported by the Doctoral Excellence Fellowship Programme (DCEP) is funded by the National Research Development and Innovation Fund of the Ministry of Culture and Innovation and the Budapest University of Technology and Economics. The work used high-performance computing resources, provided by HPC Competence Center of the Governmental Agency for IT grant ID c_mvgopt03.

REFERENCES

[1] Siconolfi, L., Camarri, S., and Fransson, J. H. M., 2015, "Stability analysis of boundary layers controlled by miniature vortex generators", *Journal of Fluid Mechanics*, Vol. 784, pp. 596–618.

[2] Sattarzadeh, S. S., and Fransson, J. H. M., 2014, "Experimental investigation on the steady and unsteady disturbances in a flat plate boundary layer", *Physics of Fluids*, Vol. 26, p. 124103.

[3] Szabó, A., Nagy, P. T., De Baets, G., Vanierschot, M., and Paál, G., 2024, "Stability analysis of a streaky boundary layer generated by miniature vortex generators", *Computers and Fluids*, Vol. 269, p. 106123.

[4] Sattarzadeh, S. S., and Fransson, J. H. M., 2015, "On the scaling of streamwise streaks and their efficiency to attenuate Tollmien-Schlichting waves", *Experiments in Fluids*, Vol. 56, p. 58.

[5] Ament, S., Daulton, S., Eriksson, D., Balandat, M., and Bakshy, E., 2025, "Unexpected Improvements to Expected Improvement for Bayesian Optimization", `2310.20708`.

[6] Kachanov, Y. S., 1994, "Physical Mechanisms of Laminar-Boundary-Layer Transition", *Annual Review of Fluid Mechanics*, Vol. 26, pp. 411–482.

[7] Herbert, T., 1988, "Secondary Instability of Boundary Layers", *Annual Review of Fluid Mechanics*, Vol. 20, pp. 487–526.

[8] Gad-el-Hak, M., 2000, *Flow Control: Passive, Active, and Reactive Flow Management*, Cambridge University Press, ISBN 9780521770064.

[9] Xu, H., Lombard, J. E. W., and Sherwin, S. J., 2017, "Influence of localised smooth steps on the instability of a boundary layer", *Journal of Fluid Mechanics*, Vol. 817, pp. 138–170.

[10] Luchini, P., and Trombetta, G., 1995, "Effects of riblets upon flow stability", *Applied Scientific Research*, Vol. 54, pp. 313–321.

[11] Nagy, P. T., Szabó, A., and Paál, G., 2022, "The effect of spanwise and streamwise elastic coating on boundary layer transition", *Journal of Fluids and Structures*, Vol. 110 (103521).

[12] Cossu, C., and Brandt, L., 2004, "On Tollmien-Schlichting-like waves in streaky boundary layers", *European Journal of Mechanics - B/Fluids*, Vol. 23, pp. 815–833.

[13] Fransson, J. H. M., Talamelli, A., Brandt, L., and Cossu, C., 2006, "Delaying Transition to Turbulence by a Passive Mechanism", *Physical Review Letters*, Vol. 96, p. 064501.

[14] Fransson, J. H., 2015, "Transition to Turbulence Delay Using a Passive Flow Control Strategy", *Procedia IUTAM*, Vol. 14, pp. 385–393, iUTAM_ABCM Symposium on Laminar Turbulent Transition.

[15] Pearce, H. H., 1961, "Shock-induced separation and its prevention by design and boundary layer control", G. V. Lachmann (ed.), *Boundary layer and flow control: its principles and application*, Vol. 2, Pergamon Press, pp. 1166–1344.

[16] Andersson, P., Brandt, L., Bottaro, A., and Henningson, D., 2001, "On the breakdown of boundary layer streaks", *Journal of Fluid Mechanics*, Vol. 428, pp. 29–60.

[17] Shahinfar, S., Sattarzadeh, S. S., Fransson, J. H. M., and Talamelli, A., 2012, "Revival of Classical Vortex Generators Now for Transition Delay", *Phys Rev Lett*, Vol. 109, p. 74501.

[18] Fransson, J. H. M., and Talamelli, A., 2012, "On the generation of steady streamwise streaks in flat-plate boundary layers", *Journal of Fluid Mechanics*, Vol. 698, pp. 211–234.

[19] Shahinfar, S., Fransson, J. H. M., Sattarzadeh, S. S., and Talamelli, A., 2013, "Scaling of streamwise boundary layer streaks and their ability to reduce skin-friction drag", *Journal of Fluid Mechanics*, Vol. 733, pp. 1–32.

[20] Sattarzadeh, S. S., Fransson, J. H. M., Talamelli, A., and Fallenius, B. E. G., 2014, "Consecutive turbulence transition delay with reinforced passive control", *Physical Review E*, Vol. 89, p. 061001.

[21] Downs, R. S., Fallenius, B. E. G., Fransson, J. H. M., and Mårtensson, H., 2017, "Miniature Vortex Generators for Flow Control in Falkner–Skan Boundary Layers", *AIAA Journal*, Vol. 55, pp. 352–364.

[22] Shahinfar, S., Sattarzadeh, S. S., and Fransson, J. H. M., 2014, "Passive boundary layer control of oblique disturbances by finite-amplitude streaks", *Journal of Fluid Mechanics*, Vol. 749, pp. 1–36.

[23] Weingärtner, A., Mamidala, S. B., and Fransson, J. H., 2023, "Application of Miniature Vortex Generators for Boundary Layer Transition Delay", *AIAA Paper 2023-0097*.

[24] Nobis, H., Schlatter, P., Wadbro, E., Berggren, M., and Henningson, D., 2023, "Topology optimization of roughness elements to delay modal transition in boundary layers", F. Auteri, D. Fabre, F. Giannetti, and A. Hanifi (eds.), *Progress in Flow Instability, Transition and Control*, ERCOFTAC, 15TH ERCOFTAC SIG33 WORKSHOP, p. 44.

[25] Bagheri, S., and Hanifi, A., 2007, "The stabilizing effect of streaks on Tollmien-Schlichting and oblique waves: A parametric study", *Physics of Fluids*, Vol. 19, p. 78103.

[26] Garnett, R., 2023, *Bayesian Optimization*, Cambridge University Press.

[27] Diessner, M., O'Connor, J., Wynn, A., Laizet, S., Guan, Y., Wilson, K., and Whalley, R. D., 2022, "Investigating Bayesian optimization for expensive-to-evaluate black box functions: Application in fluid dynamics", *Frontiers in Applied Mathematics and Statistics*, Vol. 8.

[28] Pederson, C. C., Choudhari, M. M., Zhou, B. Y., Paredes, P., and Diskin, B., 2020, "Shape optimization of vortex generators to control mack mode amplification", *AIAA AVIATION 2020 FORUM*, Vol. 1 PartF.

[29] Klauss, C. W., Pederson, C. C., Paredes, P., Choudhari, M. M., and Diskin, B., 2022, "Stability Analysis of Streaks Induced by Optimized Vortex Generators", *AIAA Paper 2022-3249*.

[30] Schrauf, G., 2004, "Large-Scale Laminar Flow Tests Evaluated with Linear Stability Theory", *Journal of Aircraft*, Vol. 41 (2), pp. 224–230.

[31] Schrauf, G. H., and von Geyr, H., 2020, *Simplified Hybrid Laminar Flow Control for the A320 Fin - Aerodynamic and System Design, First Results*.

[32] Schrauf, G. H., and von Geyr, H., 2021, *Simplified Hybrid Laminar Flow Control for the A320 Fin. Part 2: Evaluation with the e^N-method*.

[33] Theofilis, V., 2003, "Advances in global linear instability analysis of nonparallel and three-dimensional flows", *Progress in Aerospace Sciences*, Vol. 39 (4), pp. 249–315.

[34] ANSYS Inc., 2021, *ANSYS 21 R2 CFX Theory Guide*.

[35] Geuzaine, C., and Remacle, J.-F., 2009, "Gmsh: A 3-D finite element mesh generator with built-in pre- and post-processing facilities", *International Journal for Numerical Methods in Engineering*, Vol. 79 (11), pp. 1309–1331.

[36] Hecht, F., 2012, "New development in freefem++", *Journal of Numerical Mathematics*, Vol. 20 (3-4), pp. 251–266.

[37] Hecht, F., 1998, *BAMG: Bidimensional anisotropic mesh generator*, INRIA.

[38] Balay, S., Gropp, W. D., McInnes, L. C., and Smith, B. F., 1997, "Efficient Management of Parallelism in Object Oriented Numerical Software Libraries", E. Arge, A. M. Bruaset, and H. P. Langtangen (eds.), *Modern Software Tools in Scientific Computing*, Birkhäuser Press, Boston, MA, pp. 163–202.

[39] Roman, J. E., Campos, C., Dalcin, L., Romero, E., and Tomas, A., 2022, "SLEPc Users Manual", *Tech. Rep. DSIC-II/24/02 - Revision 3.18*, D. Sistemes Informàtics i Computació, Universitat Politècnica de València.

[40] Amestoy, P. R., Buttari, A., L'Excellent, J.-Y., and Mary, T., 2019, "Performance and Scalability of the Block Low-Rank Multifrontal Factorization on Multicore Architectures", *ACM Trans Math Softw*, Vol. 45 (1).

[41] Balandat, M., Karrer, B., Jiang, D. R., Daulton, S., Letham, B., Wilson, A. G., and Bakshy, E., 2020, "BoTorch: A Framework for Efficient Monte-Carlo Bayesian Optimization", *Advances in Neural Information Processing Systems 33*.

[42] Schultz-Grunow, F., 1941, "New Frictional Resistance Law for Smooth Plates", .

Conference on Modelling Fluid Flow (CMFF'25)
The 19th International Conference on Fluid Flow Technologies
Budapest, Hungary, August 26 - August 29, 2025

DESIGN AND DEVELOPMENT OF AN AUTOMATIC PUMP TEST RIG FOR CONDITION MONITORING OF MECHANICAL SEALS

David Heel[1], Peter Meusburger[2], Helmut Benigni[3], Johannes Bauer[4], Ferdinand Werdecker[5], Maximilian Raith[6]

[1] Corresponding author, Institute for Hydraulic Fluid Machinery, Graz University of Technology. Kopernikusgasse 24/4, A-8010 Graz, Phone: +43 (0) 316 873 7578, E-mail: david.heel@tugraz.at
[2] Institute of Hydraulic Fluidmachinery, Graz University of Technology. E-mail: peter.meusburger@tugraz.at
[3] Institute of Hydraulic Fluidmachinery, Graz University of Technology. E-mail: helmut.benigni@tugraz.at
[4] EagleBurgmann Germany, Äussere Sauerlacher Str. 6-10 D-82515 Wolfratshausen, E-mail: johannes.bauer@eagleburgmann.com
[5] EagleBurgmann Germany, Äussere Sauerlacher Str. 6-10 D-82515 Wolfratshausen, E-mail: ferdinand.werdecker@eagleburgmann.com
[6] EagleBurgmann Germany, Äussere Sauerlacher Str. 6-10 D-82515 Wolfratshausen, E-mail: maximilian.raith@eagleburgmann.com

ABSTRACT

This paper presents the design and implementation of an experimental pump test rig for investigating mechanical seals. The primary objective of the rig is to conduct long-term tests under varying operating parameters, providing a platform for developing condition monitoring systems for mechanical seals under realistic conditions. The adjustable parameters include pump speed, flow rate, system pressure, and water temperature at the pump inlet. Additionally, the design enables controlled air injection on the suction side, the simulation of dry running of the seal, and the resulting thermal shocks during automatic refilling of the circuit, allowing replication of entire industrial processes. By incorporating vibrations, shocks, and other disturbances generated by the pump, the test rig provides a more comprehensive testing environment compared to conventional spindle-based rigs. It supports both automatic and semi-automatic operation modes, enabling comprehensive evaluation of condition monitoring systems and their practical applicability.

Keywords: Automatic operation, Condition monitoring, Long-term testing, Mechanical seals, Pump test rig

NOMENCLATURE

F_N	[N]	normal force
H	[m]	head
K	[-]	wear coefficient
Q	[m^3/h]	flow rate
Re	[-]	Reynolds number
T	[$°C$]	temperature
V_{wear}	[m³]	wear volume
n	[rpm]	rational speed
p_{abs}	[Pa]	absolute pressure
p_{diff}	[Pa]	differential pressure
p_{rel}	[Pa]	relative pressure
x	[m]	distance
η	[$\%$]	efficiency
σ_0	[N/m^2]	hardness

Subscripts and Superscripts

AE	acoustic emission signal
PS, SS	pressure side, suction side

1. INTRODUCTION

Mechanical seals are high-precision sealing systems specifically developed for pressurized shaft passages. They are characterized by a very narrow sealing interface and low friction. Due to their low-maintenance design and long service life, they are widely used in pumps, compressors, propeller shafts, mixers, and filtration systems. [1,2] A study by the Fraunhofer Institute identified that the mechanical seal is one of the main reasons for the failure of pumps in industrial processes, followed by bearing and gap wear. [3]

Although mechanical seals are designed for long service lives, analysing premature failure or excessive wear remains a significant challenge. The unpredictability of such failures poses the risk of unplanned plant shutdowns, which can result in costs of several million euros per day, depending on the plant's size and production volume. [4] In many cases, repair and associated costs can surpass the initial cost of the seal by factors ranging from 100 to 1000 times. [5] Continuous condition monitoring is therefore a key research focus to detect wear and seal failure at an early stage, enabling planned maintenance and replacement cycles, and ensuring

the operational reliability and cost-effectiveness of the entire system.

Furthermore, API 682 [6], which defines the requirements for shaft sealing systems in centrifugal and rotary pumps in the field of oil-, gas- and process engineering, mandates three years of uninterrupted operation while complying with environmental emission regulations. To meet these standard requirements, condition monitoring of the mechanical seal may be essential.

The sealing interface of a mechanical seal is oriented normally to the shaft and is formed by two opposing faces. These contact surfaces are designed to allow a thin lubricating film to be established under specific operating conditions. The thickness of which significantly influences both leakage and frictional behaviour. [7] Leakage occurs radially through the sealing interface. To better understand the function of a mechanical seal, refer to Figure 1, which illustrates its schematic structure. The axially movable rotating seal face is pressed against a stationary seat by one or multiple springs. This spring ensures automatic adjustment of the sealing interface, compensating for wear and thermal expansion, thereby maintaining continuous contact between the sealing face and the seat. Material pairings such as carbon graphite combined with metal or ceramic are often selected, while O-rings are employed as secondary sealing elements. [8]

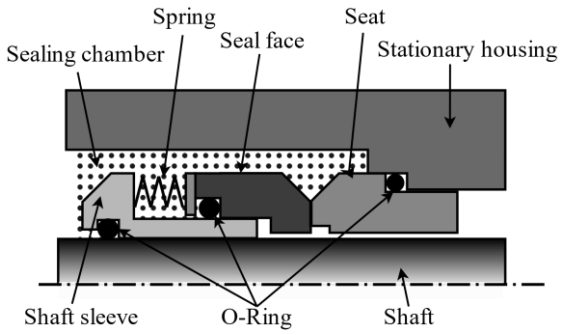

Figure 1. Schematic design of a mechanical seal

Previous efforts to develop condition monitoring systems have predominantly utilized spindle test rigs, where the seal is installed in a dedicated test setup and the shaft is driven externally. The test rig presented in this publication enables the development of condition monitoring systems directly within a pump. In addition to facilitating the design of new monitoring approaches, it also allows for the evaluation of existing condition monitoring systems. By precisely controlling the operating conditions, specific processes and events can be conducted in a reproducible manner.

2. FAILURE OF MECHANICAL SEALS

2.1. Theory of wear

When defining the tribological system of a mechanical seal based on DIN 50320 [9], the stationary seat serves as the base body, while the rotating seal face acts as the counterbody, which is subjected to the applied load. The intermediate substance is the process medium, which forms the sealing gap. Depending on the seal configuration, the process medium and, in some cases, the barrier fluid function as the environmental medium. In general, frictional states can be classified into solid-state friction, boundary friction, mixed friction, fluid friction, which includes hydrostatic, hydrodynamic, and elastohydrodynamic lubrication, as well as gas friction, which can occur under aerostatic or aerodynamic conditions.

All of these frictional states can occur within a mechanical seal, leading to different wear mechanisms. The most common wear mechanisms include adhesion, abrasion, surface fatigue, and tribochemical reactions. [7]

According to Popov [10], the dominant wear mechanism in sliding contacts is adhesive wear. Continuous stress on the sliding surfaces due to adhesive contact leads to crack formation at the welded surface unevenness. If adhesion forces become too high, particles or material grains may detach. These particles are further ground down within the sealing gap until they are flushed out, causing additional cracks and leading to material removal. [10,11] The wear volume V_{wear} can be determined using the Holm-Archard equation [12], which states that the worn volume is proportional to the normal force F_{N} and sliding distance x, while inversely proportional to the hardness σ_0 of the softer sliding partner. Manufacturers typically provide the wear coefficient K based on the material pairing.

$$V_{\text{wear}} = K \frac{F_{\text{N}} \cdot x}{\sigma_0} \tag{1}$$

2.2 Premature failure

A mechanical seal is a wear component designed for a specific service life. The primary factor used to determine its lifespan is the adhesive wear of the sealing surfaces. However, a significant amount of mechanical seals does not reach their expected service life. In such cases, the term "premature failure" is used. [13]

There are numerous reasons why a mechanical seal may fail before reaching its intended lifespan. Some of these factors occur even before the seal is put into operation, including design flaws, manufacturing defects, or installation errors. Regardless of these pre-operational issues, this discussion focuses on failure mechanisms that arise during operation. In many cases, premature failure is

caused by a combination of multiple factors rather than a single issue. [14]

2.2.1 Mechanical overload

Even with proper design and installation, a mechanical seal may experience excessive mechanical stress. One of the primary causes is operational misuse of the equipment. Excessive pressure or sliding speeds can lead to grooving on the sealing surfaces. [5] Sudden pressure surges, often resulting from the rapid closing of a valve or shut-off device, can impose shock loads on the seal, potentially causing cracks or edge chipping. Additionally, mechanical overload can be induced by pump vibrations, whereas damaged bearings may cause these vibrations. Furthermore, improper flow conditions, such as blockages, deposits, or unfavourable operating points, can lead to increased radial forces acting on the seal, further accelerating wear and failure. [15]

2.2.1 Thermal overload

One of the leading causes of thermal overload is dry running of the seal, which can lead to fluid evaporation within the seal chamber. [13] A sudden temperature change, such as flushing the system with a cold medium after a high-temperature process, can cause thermal shock. Similarly, irregular operating conditions, including frequent start-stop cycles or insufficient flushing, can result in excessive heat build-up. [16] The consequences of thermal overload include crack formation, material embrittlement, and deformation of sealing components. [17] Moreover, excessively high temperatures can also cause degradation of secondary seals such as O-Rings, leading to leakage and failure of the entire sealing system.

2.2.3 Chemical degradation

Mechanical seals are also vulnerable to chemical attacks, particularly corrosion of metallic or ceramic components. [5] Additionally, carbonization or crystallization of process media can lead to increased leakage or even complete seal failure. [8] Secondary seals, may also be compromised if the material compatibility with the process fluid is insufficient. Chemical degradation is particularly critical in aggressive operating environments where exposure to acids, solvents, or high-temperature fluids accelerates material deterioration.

3. CONDITION MONITORING FOR MECHANICAL SEALS

The condition monitoring of mechanical seals can take various forms and must be tailored to the specific application. As previously discussed, there are numerous causes of seal failure. The first step in developing an effective monitoring system is to determine which failure mechanisms should be observed. Furthermore, the focus during development should always be on application in real use cases.

A basic method for assessing the condition of a mechanical seal is leakage detection. Additional measurable parameters that provide insights into the frictional state include temperature measurements at the seal face, seat, or within the sealing gap. [18] In particular, during solid-state friction and boundary lubrication, wear is significantly increased due to the conversion of kinetic energy into heat at the tribological contact interface. As a result, the temperature of the entire tribosystem and especially the interfacial temperature rises. [9] To assess the stress conditions acting on the seal, comprising a combination of pressure and sliding velocity (pressure x velocity), it is necessary to measure the operating pressure and rotational speed of the system. [13,19]

Lambert [20] already presented a system which monitors the condition of mechanical seals by measuring operating parameters in 1998. To improve reliability, the surface temperature was calculated using a finite element method.

Beyond these basic condition monitoring techniques, measuring the lubrication film thickness within the sealing gap provides valuable information on the friction state of the sliding surfaces. By defining a critical threshold for fluid film thickness, a distinction can be made between pure fluid lubrication and solid-state contact. [19] Since the fluid film is only a few micrometers thick, the sensors used must have a very high resolution. However, measuring the lubrication film thickness is particularly challenging in transient operating conditions, where temperature variations further complicate the measurement task.

Several sensor-based measurement techniques have been investigated for determining the lubrication film thickness, for example by Zou and Green [21] using an eddy current sensor. The eddy current proximity probes were attached to the end of the housing to measure the static and dynamic distance between the seat and the end face of the rotor.

Another possibility is to use the acoustic emission signal (AE), as this can contain a lot of information on the friction of the end surfaces. Based on the operating conditions, three main mechanisms can contribute to AE generation during sliding, namely viscous friction due to the shearing of lubricant layers, the interaction between surface irregularities and fluid flows, and direct contacts of the surface irregularities. In addition to understanding the formation mechanism of tribological AEs in mechanical seals, there is a difficulty in characterizing the AE signal. [13,22]

A further option is to impose active ultrasonic waves with a piezoelectric ultrasonic transducer and compare them with the signal reflected and received

by the sliding surface. [13] Dwyer-Joyce presents in [23] the theoretical principles for the interaction of ultrasound with the interfaces and the fluid film.

The above list provides a brief overview of the possibilities for condition monitoring. There are many other promising methods. For future research, there are improvements in sensor accuracy, the integration of real-time monitoring systems, and the optimization of data analysis techniques to implement.

4. TEST RIG

The primary circuit, also referred to as the main circuit, is driven by the main pump. The test mechanical seals ensure that the medium in the main circuit is sealed against the environment and the rotating shaft of the main pump.

Following the flow direction from the main pump, the medium passes through a flow control valve (C1), which regulates the volumetric flow rate, before entering the pressure vessel. The pressure vessel serves as a damping element, with an adjustable air cushion in the upper half that allows system pressure modulation. From there, the medium continues its way through a heat exchanger, which allows precise thermal conditioning, before flowing through a dedicated pipeline section designed for controlled air injection. Finally, the medium returns to the pump inlet, closing the loop.

To simulate dry-running conditions, the pump's drainage valve (C6) can be opened, enabling controlled evacuation of the working fluid. Butterfly valves (C2) and (C3) are installed on the suction and pressure sides of the main pump. When closed, they prevent complete drainage of the system, ensuring that only the section between the valves is emptied.

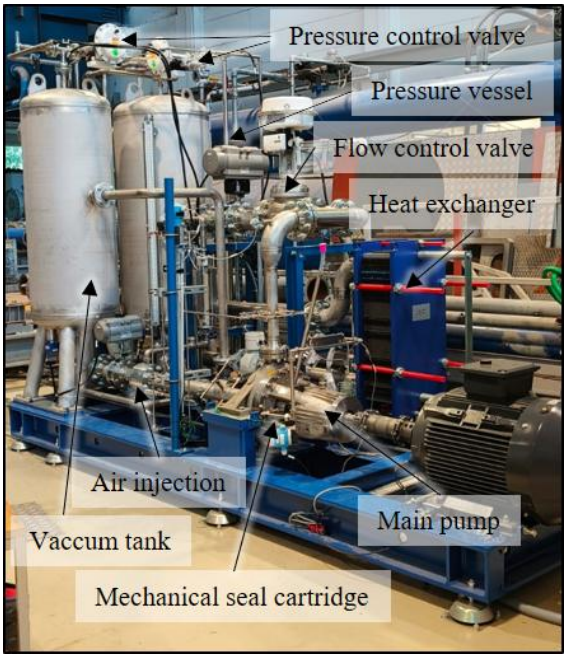

Figure 2. Test rig overview

Table 1. Control valves of the test rig

Flow control valve	C1
Butterfly valve pressure side	C2
Butterfly valve suction side	C3
Pressure boost valve	C4
Pressure relief valve	C5
Pump drain valve	C6
Air injection control valve	C7

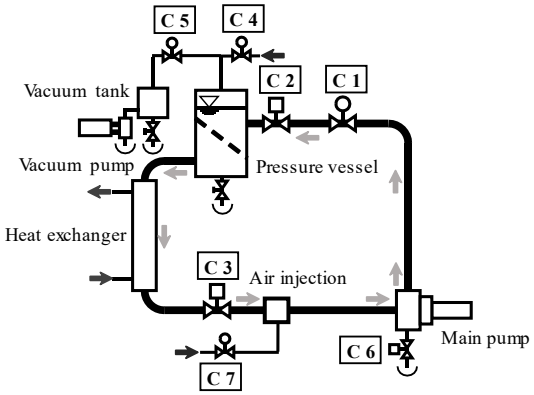

Figure 3. Schematic diagram of main test rig components

4.1 Control variables of the test rig

The test rig can operate fully automatic, with predefined process steps being executed sequentially. Alternatively, a semi-automatic mode allows for manual input of specific control variables. The following sections describe the individual control loops.

The drive motor of the main pump is controlled via a frequency converter, which regulates and monitors the motor operation. The actual speed is measured by a rotary encoder (M13) that records the rotational speed of the motor shaft.

The flow rate in the primary circuit is regulated using a proportional valve (C1). By adjusting the valve position, the volume of liquid flowing through the main circuit can be continuously controlled. A magnetic inductive flow meter (M06) is used to measure the flow rate. To ensure the possibility of reducing the flow to zero discharge, a shut-off valve is installed in the primary circuit.

The system pressure is regulated via an air cushion in the upper section of the pressure vessel. To increase pressure, compressed air from an external supply is introduced via the booster valve (C4), expanding the air cushion until the desired pressure is reached. Pressure reduction is achieved via the pressure relief valve (C5), which is connected to a vacuum tank. This allows air to be released from the pressure vessel into the vacuum tank, which is maintained at a reduced pressure by a vacuum pump. The actual system pressure is recorded by the piezoresistive pressure sensor (M03).

The temperature in the primary circuit is regulated via a heat exchanger, which dissipates excess heat. The setpoint temperature is determined by sensor (M09), a PT100 resistance thermometer. The cooling source of the system is a chiller unit, while heat is introduced into the system through the operation of the main pump.

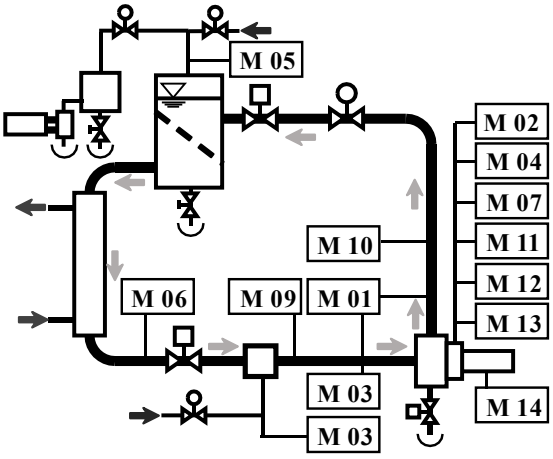

Figure 4. Diagram of the instrumentation

The test rig allows for controlled air injection into the main circuit on the suction side of the pump. This is achieved via a pipe section equipped with mixing nozzles. The pipeline assembly consists of an annular chamber with wall perforations, which is connected to a pressurized air line equipped with a check valve. The air flow rate is regulated using proportional valve (C7) and monitored via an ultrasonic flow meter (M08).

Table 2. Measured variables at the test rig

Pressure	
Differential pressure pump	M01
Relative pressure at seal	M02
Absolute pressure suction side	M03
Absolute pressure ambient	M04
Relative pressure pressure vessel	M05
Flow rate	
Main circuit	M06
Flush mechanical seal	M07
Air injection	M08
Temperatures	
Suction side	M09
Pressure side	M10
Flush mechanical seal	M11
Seal face	M12
Rotational speed	
Main pump speed	M13
Electrical power	
Main pump power	M14

4.2 Condition monitoring of the mechanical seal

As shown in Figure 4, a set of measurement variables is extracted from the main pump, representing the condition monitoring system of the mechanical seal. These measured variables include the relative pressure of the seal (M02) and the ambient pressure (M04) as key pressure parameters. The pressure connection of (M02) is shown in Figure 5. The hole ends very close to the sealing gap, the measured pressure corresponds to the pressure that the seal must also withstand. Additionally, the flow rate in the flushing line from the spiral casing to the seal is monitored using an ultrasonic flow meter (M07). Further monitoring parameters include the temperature in the flushing line (M11) and the temperature near the seal face (M12, thermocouple in Fig. 5). To complete the readings for a load collective, the rotational speed of the main pump (M13) is also recorded.

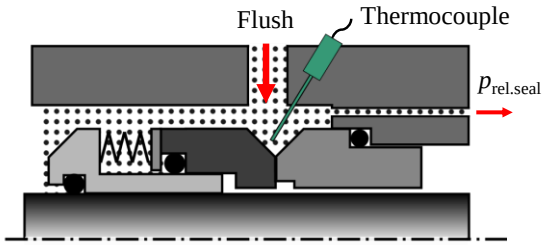

Figure 5. Instrumentation of the mechanical seal

The selected monitoring parameters represent fundamental baseline values. However, the system allows for future expansion. Before extending the monitoring setup, it is essential to determine the specific tests to be conducted on the test rig. If necessary, additional parameters can be integrated into the condition monitoring system.

5. INITIAL MEASUREMENT DATA

For this study, three measurement series were recorded, each representing a pump characteristic curve. The pump characteristics were determined at three constant rotational speeds: 1500 *rpm*, 2500 *rpm*, and 3500 *rpm* In addition, for each measurement series the system pressure was maintained at 6 *bar*, and the temperature was kept constant at 20 *°C* on the suction side of the pump.

Starting from zero discharge, the flow rate was incrementally increased in steps of 10 m^3/h until the pump's maximum achievable flow rate was reached. The pump's delivery head is determined by the before mentioned parameters.

The process sequence executed on the test rig ensures that the system is properly prepared before the actual measurement. Before recording a pump characteristic curve, the pipeline system is flushed, and the test rig is stabilized at a constant temperature

of 20 *°C*. Therefore, the main pump speed is set to 2500 *rpm*, and a flow rate of 80 *m³/h* is held constant for 200 seconds. Following this stabilization phase, an automated flushing for the pressure sensors is performed at reduced speed. After completing this step, the actual measurement process is initiated. In the final stage, the pump speed is brought to a full stop at 0 *rpm*. This standardized procedure ensures repeatable initial conditions for each test run, thereby improving the reliability and reproducibility of the measurements.

Each measurement series was recorded continuously. The measuring software sampled data at 1000 *Hz* and stored averaged values every second.

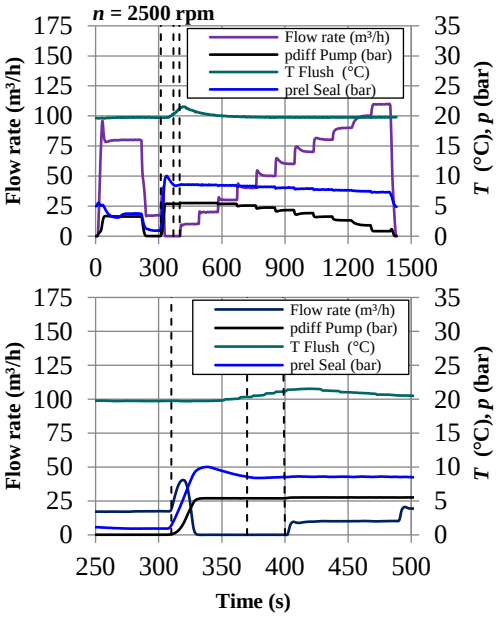

Figure 6. Continuous recording at 2500 *rpm*, (top) full measurement log (bottom) first process step

Figure 6 (top) illustrates the complete process sequence for the measurement series at 2500 *rpm*.The graph (bottom) in Figure 6 shows the time interval of the initial section of the characteristic curve at a flow rate of 0 *m³/s*. Each process step consists of a settling phase and a holding phase. This is indicated by three vertical lines: the first marks the start of the process step and the beginning of the settling phase, the second marks the transition from the settling to the holding phase, and the third marks the end of the holding phase and the completion of the process step.

During the settling phase, the control system adjusts the operating parameters until they stabilize. In the holding phase, the values reached at the end of the settling phase are maintained. If the target system pressure is 6 *bar* but only 4.5 *bar* is achieved within the predefined settling time, then 4.5 *bar* becomes the new target value for the holding phase. As a result, no significant changes occur during the holding phase, allowing for the calculation of an average value that is representative of this operating state of the pump while minimizing variance.

For the measurement series, the settling phase was set to 60 *s*, followed by a 30 *s* holding phase. In Figures 7 to 9, a mean value was calculated from the data recorded during the holding phase, representing a single measurement point.

The authors consistently present the data as a set of two graphs. The upper graph illustrates the pump characteristic curve at the respective rotational speed, along with the pump efficiency and the measured electrical power, compensated by the efficiency of the drive motor. By analysing the pump characteristic curve, its power and its efficiency, the operating point of the pump can be assessed. This evaluation also serves to associate the data related to the seal, which is depicted in the lower graph. For the seal-related data, the selected parameters include the sealed pressure, as well as the flow rate and temperature of the flushing medium. All data is plotted against the flow rate. Based on these representations, the following section analyses the trends observed in the measurement data, focusing on the interaction between pump and seal.

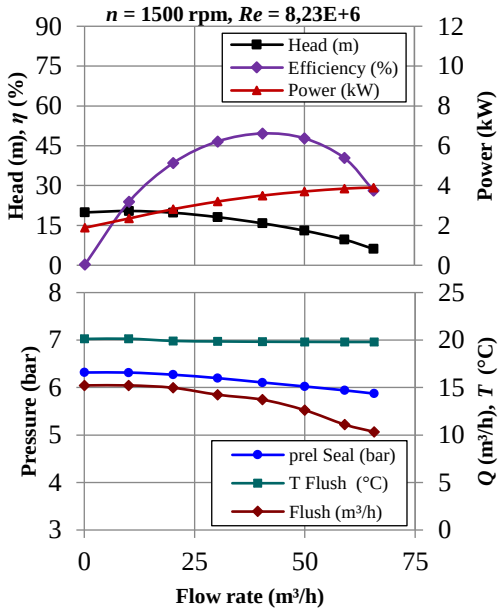

Figure 7. (top) Pump characteristic 1500 *rpm*, (bottom) corresponding measured variables

The results, as shown in Figure 7, illustrate the pump's performance at a rotational speed of 1500 *rpm*. At this speed, the pump reaches a maximum head of 20.4 *m* and a maximum flow rate of 65 *m³/h*, with a peak efficiency of 49.6 *%*. Examining the head curve from the first measurement series reveals that the second measurement point is slightly above the first. Gülich [24] describes characteristic curves where the gradient $\partial H/\partial Q > 0$ is as "unstable." The drop in head at very low flow rates can be attributed to

recirculation within the impeller, a typical behaviour for centrifugal pumps of this specific speed and design. The power and efficiency curves both follow the expected trends.

The relative pressure at the seal decreases as the flow rate increases, which is expected since the pump head also decreases. Notably, the entire pressure generated by the pump does not appear at the seal. This drop in measured static pressure can be explained by the dynamic pressure component, which is influenced by the seal flushing. The dynamic pressure reduction occurs due to the flushing flow, which follows an inverse trend compared to the main pump flow. The flushing line functions as a bypass from the spiral casing to the seal, meaning that the higher the differential pressure generated by the pump, the higher the flushing flow rate. The temperature of the flushing flow remains constant at 20 °C, which is consistent with the suction-side temperature regulation of the pump.

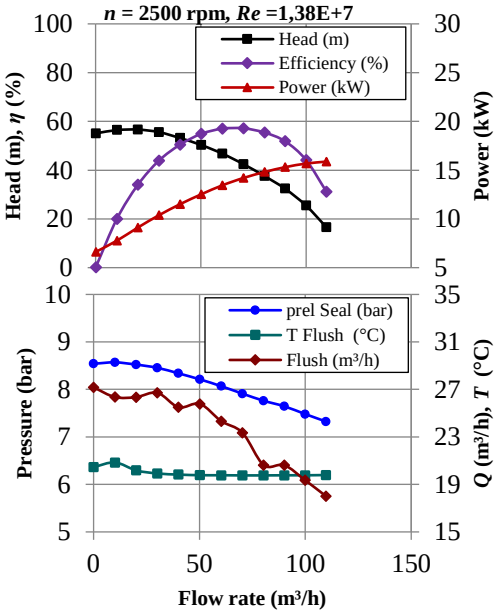

Figure 8. (top) Pump characteristic 2500 *rpm*, (bottom) corresponding measured variables

Figure 8 presents the data from the measurement series at 2500 *rpm*. At this rotational speed, the pump achieves a maximum head of 56.6 *m* and a maximum flow rate of 109.7 *m³/h*. By applying the similarity laws according to EN ISO 9906:2012 [25] or IEC 60193:2019 [26], similar operating points can be converted. In this context, the flow rate scales linearly to the speed ratio, the head scales to the square of the speed ratio, and the power scales to the cube of the speed ratio. Applying these laws to the measurement data reveals a good correlation between the first and second measurement series.

The pump reaches a peak efficiency of 57.2 %, which is significantly higher than the efficiency measured in the first series. According to IEC 60193 [26], the frictional losses in the flow of hydraulic machinery are primarily dependent on the Reynolds number (*Re*). Since the Reynolds number increases by approximately 1.7 times due to the higher rotational speed, an increase in efficiency is also expected. It should be noted: In the evaluation, the outlet diameter of the impeller was used as the characteristic length for calculating the Reynolds number displayed in Figure 7 to 10.

The unstable characteristic curve can be recognized even more clearly. The relative pressure at the seal follows a trend similar to that observed in the first measurement series, and the unstable nature of the pump characteristic curve is also evident in the pressure profile. The temperature of the flush remains at approximately 20 °C, with a slight increase observed at very low flow rates. This temperature rise occurs because, at this operating point, heat accumulates due to insufficient dissipation caused by the low flow rate. Examining the temporal progression in Figure 6 shows a continuous temperature increase once a flow rate of 0 m³/h is reached. As previously discussed, the standardized startup process ensures that this temperature increase does not originate from prior process conditions.

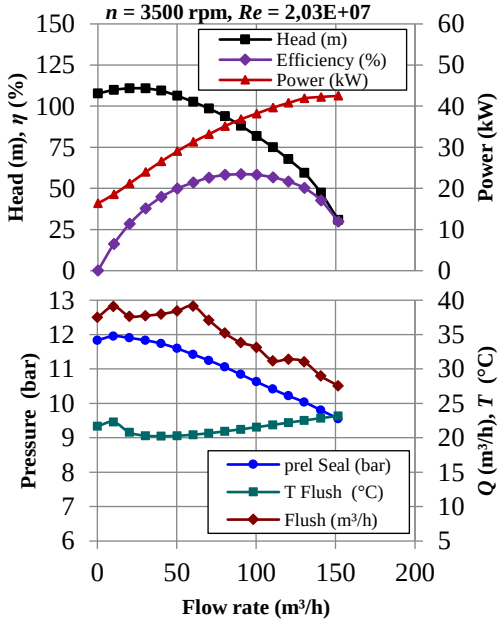

Figure 9. (top) Pump characteristic 3500 *rpm*, (bottom) corresponding measured variables

The data from the latest measurement series at 3500 *rpm* are shown in Figure 9. At this rotational speed, the pump achieves a maximum head of 110.9 *m*, a maximum flow rate of 151.6 *m³/h*, and a peak efficiency of 58.7%. The correlation based on the similarity laws aligns very well with the other measurement series. The trend of the relative pressure at the seal and the flushing flow rate fits the overall pattern. The temperature profile of the

flushing flow shows a slight increase at very low flow rates, subsequently drops back to 20 °*C*, and then rises steadily. A possible explanation for this behaviour could be the power increase, which scales with the cube of the rotational speed ratio. This causes the pump housing and the cartridge to heat up over time until a thermal equilibrium is reached.

To complement the presented measurement results, Table 3 provides quantified uncertainty values for the displayed parameters. The uncertainty analysis follows DIN EN ISO 99006 [25], using representative values near the pump's best efficiency point. Measurement uncertainty may vary across the measurement range, particularly at its boundaries, where deviations tend to be more pronounced. The primary objective is to provide a quantitative estimate of the uncertainty associated with the reported values.

The analysis accounts for the entire measurement chain, including the data acquisition system, galvanic isolation amplifiers, signal conditioners, and the respective sensors. The reported uncertainties represent expanded uncertainties with a confidence level of 95 %. The current setup meets the grade 1 acceptance criteria for pump measurements according to DIN EN ISO 9906 [25].

Table 3. Measurement uncertainty

Head	0.7118 %
Flow rate	0.8684 %
Efficiency	1.7335 %
Power	1.3207 %
Relative pressure at seal	0.7954 %
Temperature flush	0.8211 %
Flow rate flush	1.5793 %

6. SUMMARY

Monitoring the condition of mechanical seals is essential for detecting wear and failures, ensuring operational reliability, and enabling early intervention. To develop and validate existing condition monitoring approaches for mechanical seals, a dedicated test rig was designed and constructed. The test rig allows precise control over key operating parameters, including pump speed, flow rate, system pressure, and water temperature at the pump inlet. Additionally, its design enables controlled air injection on the suction side, the simulation of seal dry-running conditions, and the resulting thermal shocks upon automatic refilling of the circuit. These features allow the replication of entire industrial processes under controlled conditions. Initial measurements were recorded and analysed using the pump performance curve as a reference.

The presented test rig provides a solid foundation for further investigations, particularly long-term tests. Moreover, it can be employed to diagnose application-specific issues by replicating real-world processes in a controlled laboratory environment and applying appropriate measurement techniques to identify the root cause. The setup also facilitates the validation of existing condition monitoring systems, making it a versatile tool for research and practical applications. Future work will focus on optimizing the measurement techniques and further expanding the range of monitored parameters to further enhance the reliability of mechanical seal condition monitoring.

ACKNOWLEDGEMENTS

This work has been supported by the EagleBurgmann Germany GmbH & Co. KG.

AUTHORS' CONTRIBUTION

All authors were involved in the conception and design of this study. D.H. was responsible for material preparation, data collection, and analysis. D.H. wrote the first draft of the manuscript, and all other authors provided feedback on previous versions. All authors read and approved the final manuscript.

REFERENCES

[1] Schlegel R., 1984, "Gleitringdichtungen für Pumpen in der chemischen Industrie", Chemie Ingenieur Technik, Vol. 56(5), pp. 397–399.

[2] Zhang Z., Chen K., Zhang E. Q., and Fu P., 2014, "Mechanical Seal Condition Monitoring Technology Research", AMM, Vol. 529, pp. 344–348.

[3] Kohlmann B., and Schneider S., 2007, "Zuverlässigkeitsprognose von mechatronischen Systemen zur Ableitung restnutzungsdauerbezogener Betriebs- und Instandhaltungsstrategien".

[4] SIEMENS AG, 2024, "The True Cost of Downtime 2024", https://assets.new.siemens.com/siemens/assets/api/uuid:1b43afb5-2d07-47f7-9eb7-893fe7d0bc59/TCOD-2024_original.pdf.

[5] Riedl A., Ed., 2017. *Handbuch Dichtungspraxis*, 4th ed., Vulkan Verlag, Essen.

[6] American Petroleum Institute, 2014, "Pumps—Shaft Sealing Systems for Centrifugal and Rotary Pumps" API STANDARD 682.

[7] Czichos H., and Habig K.-H., 2020. *Tribologie-Handbuch*, Springer Fachmedien Wiesbaden, Wiesbaden.

[8] Müller H., and Nau B., 2024, "Gleitringdichtungen: Grundlagen", www.fachwissen-dichtungstechnik.de.

[9] DIN Deutsches Insitut für Normen, 1979, "DIN 50320: Verschleiß; Begriffe,

Systemanalyse von Verschleißvorgängen, Gliederung des Verschleißgebietes" Deutche Normen.
[10] Popov V. L., 2015. *Kontaktmechanik und Reibung*, Springer Berlin Heidelberg, Berlin, Heidelberg.
[11] Ni X., Sun J., Ma C., and Zhang Y., 2023, "Wear Model of a Mechanical Seal Based on Piecewise Fractal Theory", Fractal Fract, Vol. 7(3), p. 251.
[12] Archard J. F., 1953, "Contact and Rubbing of Flat Surfaces", Journal of Applied Physics, Vol. 24(8), pp. 981–988.
[13] Fan Y. E., Gu F., and Ball A., 2008, "A Review of the Condition Monitoring of Mechanical Seals", ASME 7th Biennial Conference on Engineering Systems Design and Analysis, pp. 179–184.
[14] Plumridge J., and Page R.L, The development of more tolerant mechanical seals, *Shaft sealing in centrifugal pumps*, pp. 9–22.
[15] Shiels S., 2002, "Failure of mechanical seals in centrifugal pumps — part two", World Pumps, Vol. 2002(432), pp. 34–37.
[16] Shiels S., 2002, "Failure of mechanical seals in centrifugal pumps", World Pumps, Vol. 2002(429), pp. 20–22.
[17] Mayer E., 1960, "Doppeltwirkende axiale Gleitringdichtungen in der chemischen Industrie", Chemie Ingenieur Technik, Vol. 32(4), pp. 285–288.
[18] Fan Y. E., 2007. *The condition monitoring of mechanical seals using acoustic emissions*.
[19] Gu F., Towsyfyan H., and Ball A., 2013. *A review of mechanical seal tribology and condition monitoring*, University of Huddersfield, Huddersfield.
[20] Lambert P., 1998, "A condition-based monitoring system for mechanical seals", Sealing Technology, Vol. 1998(57), pp. 7–9.
[21] Zou M., and Green I., 1998, Real-time Condition Monitoring of Mechanical Face Seal, *Tribology for energy conservation: Proceedings of the 24th Leeds-Lyon Symposium on Tribology, held in the Imperial College of Science, Technology, and Medicine, London, UK, 4th-6th September 1997*, Dowson D., ed., Elsevier for the Institute of Tribology University of Leeds and Institut National des Sciences Appliquées de Lyon, Amsterdam, New York, pp. 423–430.
[22] Towsyfyan H., Gu F., Ball A. D., and Liang B., 2019, "Tribological behaviour diagnostic and fault detection of mechanical seals based on acoustic emission measurements", Friction, Vol. 7(6), pp. 572–586.
[23] Dwyer-Joyce R. S., 2005, "The Application of Ultrasonic NDT Techniques in Tribology", Proceedings of the Institution of Mechanical Engineers, Part J: Journal of Engineering Tribology, Vol. 219(5), pp. 347–366.
[24] Gülich J. F., 2020. *Centrifugal Pumps*, Springer International Publishing, Cham.
[25] EUROPEAN COMMITTEE FOR STANDARDIZATION, "DIN EN ISO 9906:2013-03, Kreiselpumpen_- Hydraulische Abnahmeprüfungen_- Klassen_1, 2 und_3 (ISO_9906:2012); Deutsche Fassung EN_ISO_9906:2012".
[26] International Electrotechnical Commission, 2019, "IEC 60193:2019: Hydraulic turbines, storage pumps and pump-turbines – Model acceptance tests" International Standard.

Conference on Modelling Fluid Flow (CMFF'25)
The 19th International Conference on Fluid Flow Technologies
Budapest, Hungary, August 26 - August 29, 2025

SIMULATION AND CHALLENGES FOR A LOW SPECIFIC SPEED PELTON TURBINE

Daniel R. REITERER[1], Lukas SANDMAIER[2], Helmut BENIGNI[3]

[1] Corresponding Author. Institute of Hydraulic Fluid Machinery, Graz University of Technology. E-mail: daniel.reiterer@gmx.net
[2] Institute of Hydraulic Fluid Machinery, Graz University of Technology. E-mail: lukas.sandmaier@tugraz.at
[3] Institute of Hydraulic Fluid Machinery, Graz University of Technology. E-mail: helmut.benigni@tugraz.at

ABSTRACT

This study presents the numerical analysis of a Pelton turbine of low specific speed with the Lagrangian open-source code DualSPHysics [1]. The numerical results were compared with experimental data. The main objective was to determine if the applied numerical approach led to reproducible results and allowed insight into the momentum transfer and water movement in jet, runner, and casing. The influence of numerical parameters like particle size, kernel and smoothing length coefficient, and shifting value on the simulation results has been tested.

As a result, an optimal particle size formulation is suggested. Furthermore, we established a connection for two numerical parameters of DualSPHysics, the "smoothing length coefficient" and the "shifting", to improve the fluid flow behaviour and the resulting torque without modifying the physical parameters. In addition, we investigated the deviation from the optimal achievable torque and the improved fluid behaviour through these numerical parameters.

We discussed the effect of the bucket disturbance in the jet from the particle simulation alongside the similarity law simulation and the actual prototype's measurement outcomes. Identical simulations of the physical properties of the operation points were compared in momentum.

Keywords: Pelton turbine, SPH, DualSPHysics, Particle simulation

NOMENCLATURE

A	$[m^2]$	cross-section
B	$[m]$	bucket width
$coef_h$	[-]	kernel smoothing coefficient
D	$[m]$	runner jet diameter
d_{jet}	$[m]$	diameter of the jet
d_p	$[m]$	particle size
g	$[m^2/s]$	gravitational constant
H	$[m]$	head
k_c	[-]	nozzle losses
k_{dp}	[-]	jet diameter/particle coefficient
k_{jv}	[-]	kinetic energy coefficient
kh	[-]	smoothing length
n	$[1/s]$	rotational runner speed
Q	$[m^3/s]$	discharge
T	$[Nm]$	torque
t	$[s]$	time
TFS	[-]	threshold to detect free surface
v	$[m/s]$	velocity vector
z	[-]	number of buckets
φ	[-]	discharge coefficient
ψ	[-]	pressure coefficient

Subscripts and Superscripts

jet	fluid jet of a single nozzle
M	meridional speed
x, y, s	cartesian coordinate components
I	low specific speed prototype
II,	typical specific speed prototypes
PS, SS	pressure side, suction side

1. INTRODUCTION

Pelton turbines with a low specific speed n_q operate with comparatively low flow rates and high heads. This type of Pelton turbine is often used in systems whose purpose is not primarily power generation, such as in water supply or process engineering systems. Therefore, such turbines' design, analysis, and optimisation are often restricted by low budgets and require cost-effective methods. In general, but especially under these conditions, numerical flow simulations represent a powerful tool. In recent years, smoothed particle

hydrodynamics (SPH) has gained popularity due to the continuous improvement of computer hardware, especially regarding graphic processing units. In addition, only the CAD files are required, which is a significant advantage over Eulerian CFD codes where additional meshing is needed. However, the simulation of Pelton turbines with low specific speed presents additional difficulties owing to their distinct geometrical prerequisites and high velocity compared to the low discharge relation. The low flow rate at high jet velocities usually results in relatively small buckets compared to the size of the runner. This poses challenges not only for flow observation in experimental investigations but also for flow simulation. A minimal particle size would be required for the small bucket size and the thin jet diameter, both represented by particles. As the hardware on the GPU may overstep its capabilities, bigger particles must be used. However, tiny particles are needed to achieve both aims: a good representation of the runner surface and a sufficient resolution in the jet.

Additionally, the high velocity of the particles and the low discharge, leading to a small diameter of the jet, result in a fragile jet. So, modelling the binding forces and surface interaction in the bucket is far more critical than larger jet diameters with lower velocity and must be done carefully. In the Lagrangian approach, the particle-particle interaction and the particle-surface interaction are partly formed by particle size d_p, smoothing kernel length, interaction factor and particle shifting. To better understand the effects of the model behind these parameters, an open-source code was used for the present study, which allowed insight and validation of the mathematical formulations of the code.

This study uses the code DualSPHysics [1], an open-source software that utilises the smoothed particle hydrodynamics (SPH) method to enable the simulation of fluids and other continuous media within three-dimensional environments. With this code, a low specific speed Pelton turbine was analysed in detail based on the geometry of a one-nozzle Pelton turbine (in the following referenced as Prototype I). Particles represent the fluid, rotating, and static bodies. To save computing time, only the surface made of particles (the envelope) is used for the rotating runner and the housing. *Prototype I* has an n_q of 2.5 rpm and a head H of 350 m with a horizontal axis. One additional Pelton turbine with a different specific speed was investigated to evaluate the simulation setup with different geometrical conditions. The six-nozzle *Prototype II* had an n_q of 15.5 rpm ($n_{q,nozzle}$ = 6.3 rpm).

Prototype I has been tested in real size, and *Prototype II* has been tested in model size (scale factor as of 1:4.2, by applying similarity laws) in the Institute of Hydraulic Fluid machinery laboratory, which facilitated the verification of the simulation results.

2. PREPARATORY WORK

The simulation of Pelton turbines using SPH is becoming increasingly popular. Also, the SPH simulation with DualSPHysics [1] was already applied for this kind of turbine. Dominguez et al.'s work contains the mathematical model and code [2, 3]. Works by Furnes [4] conducted a comprehensive investigation into SPH on a Pelton turbine to determine if the approach of Pelton simulation with DualSPHysics is feasible for prediction and identified it as a promising tool. Ge et al. [5] compare mesh and particle-based approaches using the data from Vessaz; while he criticised the accuracy of the torque, he highlights the possibilities for preliminary screening. Further, he mentioned the benefits of droplet observation. Vessaz et al. [6, 7], who researched the finite volume particle method (FVPM) for Pelton turbines, described this method as satisfactory. Kumashiro et al. [8] used the particle-based software project “SPHEROS” to identify differences in torque compared to the mesh-based solution with ANSYS CFX, where the particle-based solver agreed with the experiment's trends. Furthermore, Alimirzazadeh et al. [9] examined the jet interference of six-jet Pelton turbines, utilising, for instance, SPHEROS as a meshless finite volume particle method (FVPM) for simulating fluid flows compared against ANSYS CFX, where the FVPM method was in agreement with the experiment and the jet interference good observable in the simulation.

Koukouvinis researched the flow in the injector of Pelton turbines [10] and improved conservation laws [11] for smoothed particle hydrodynamics. SPH development is still ongoing, as in the thesis of Garzon [12], who proposed a new ALE-WENO (Arbitrary Lagrangian Eulerian - Weighted Essentially Non-Oscillatory formulation) based on DualSPHysics for accurate free surface jets.

Arch and Mayr [13] note that the critical Weber number for droplets (or particles) is approximately 6.5. In this context, the particle Weber number under discussion is significantly higher; around ten times greater than this critical threshold. Additionally, the Weber number for the Pelton turbine aligns with this observation and is supported by the research conducted by Staubli and Hauser [14]. Their study of the Pelton turbine jet, with a similar Weber number, in Moccasin, California, revealed considerable droplet formation and mist, highlighting the instability of the jet's surface structure. “The higher the Weber number, the higher the degree of atomization.”, Grein et al. [15].

3. PARAMETERS

In preparation for the simulation, a parameter study focused on particle size and the smoothing and

shifting parameters. The initial parameters were derived from the so-called "DamBreak" example included in the DualSPHysics code package [16]. Then, an initial optimisation was evaluated by an analytically calculated torque from an impinging jet, with reference to existing literature (e.g. [10, 17]). For the optimisation process, a Nelder-Mead optimiser [18] was utilised to address the non-linear relationship between parameter changes and the resulting torque development [19, 20, 21] during the solving process [22].

After several iterations of jet impingement optimisation, the obtained parameters were applied to a single-bucket simulation. In this case, a full bucket was necessary, as using a half-model was not feasible due to the requirement to represent the edges as spheres (Asymmetry). Additionally, the shape of the jet was constrained by fundamental geometric forms, such as circles, making a half circle impossible within the current code. As a reference, the torque taken from the experiment was used as one benchmark for the simulation.

No numerical target value for correct fluid behaviour was available in the optimisation. Therefore, the parameter ranges for the optimisation were constantly fine-tuned manually to optimise torque and fluid behaviour simultaneously. For reference purposes, the simulation was, e.g., compared with Ruden's analytical analysis [23] concerning jet expansion. Experimental data from Schach [24] and other literature [25, 26, 27] were used to examine the jet's impact on a flat surface. Moreover, surface formation and wetting considerations were deemed important as they significantly influence the energy transfer (e.g., [28, 29]). Referencing from existing literature [30, 31, 32, 33, 34] was also applied to the bucket's fluid behaviour.

Subsequently, the derived parameters were utilised in a comprehensive runner simulation and compared against the measurement results from *Prototype I* and the literature [35, 36, 37]. Consequently, the simulation was analysed, leading to a re-run of the optimisation process at the jet impingement stage, whereas the results have been considered. The parameters acquired from this optimisation, particularly those related to shifting and smoothing, were also successfully used in the simulations for *Prototype II*.

3.1. PARTICLE SIZE

The size of the particle defines the resolution of the solid boundaries and the fluid. Moreover, numeric accuracy and computational performance are directly related to particle size and the boundary interaction between the fluid and the surface [4, 16, 2, 38]. Furthermore, DualSPHysics permits only identical particle sizes in a simulation.

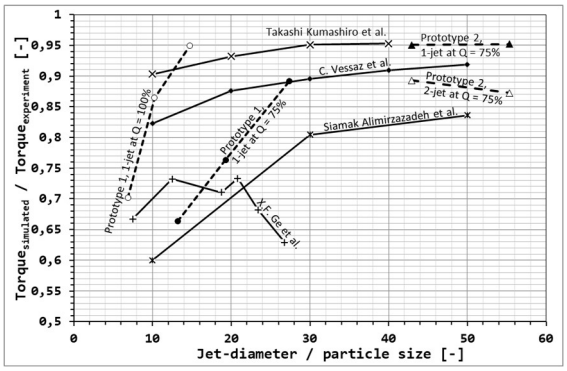

Figure 1. Different simulation results compared to literature values

Research [5, 9, 39, 40] indicates an interest in optimised particle size for particle simulation of Pelton turbines. Figure 1 shows the extracted and normalised data from the referenced researchers.

In addition, the separately simulated data is shown for comparison. On the one hand, the data generally indicates an improvement of the effective torque for higher jet diameter to particle size ratios (k_{d_p}). On the other hand, there is a decline in the achievable torque for different prototypes, similar to the findings of Ge et al. [5]. The assumption that the jet diameter to particle ratio, k_{d_p}, has an optimum or saturates at high values seems plausible, considering the Lagrangian formalisation [41, 42, 43].

$$k_{d_p} = \frac{d_{jet}}{d_p} \tag{1}$$

Considering the proposed ratio k_{d_p}, as expressed in Equation (1), a straightforward transition can be made with the jet velocity. As depicted in Equation (2), the jet diameter can be expressed in terms of discharge and head by reformulating the jet velocity and relating it to these variables, including the velocity coefficient k_c (e.g. K_{C_i} in Raabe [44]), which is a loss coefficient.

$$v_{jet} = k_c \cdot \sqrt{2 \cdot g \cdot H} = \frac{Q_{jet}}{A_{jet}} \tag{2}$$

This leads to the formula shown in Equation (3). The ratio k_{d_p} was taken from the literature (e.g., [8, 45]).

$$d_p = \frac{d_{jet}}{k_{d_p}} = \frac{2}{k_{d_p} \cdot (\pi \cdot k_c)^{\frac{1}{2}}} \cdot \frac{Q_{jet}^{\frac{1}{2}}}{(2 \cdot g \cdot H)^{\frac{1}{4}}} \tag{3}$$

The impact of the head and nozzle losses is smaller than the influence of the discharge. We simplify this further by collecting the jet velocity-related terms k_c and H, including the other constants, to a jet-velocity parameter k_{jv}, as seen in Equation (4).

$$k_{jv} = \frac{d_p \cdot k_{d_p}}{Q_{jet}^{\frac{1}{2}}} = \frac{2}{(\pi \cdot k_c)^{\frac{1}{2}}} \cdot \frac{1}{(2 \cdot g \cdot H)^{\frac{1}{4}}} \quad (4)$$

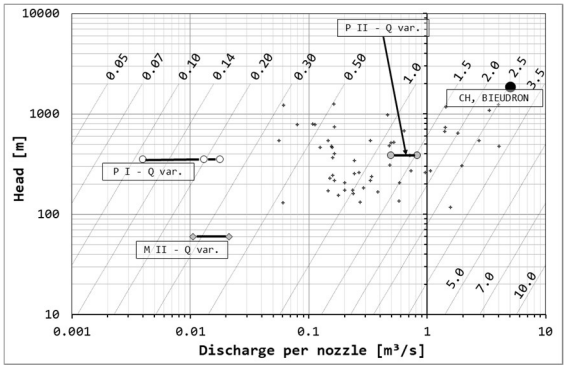

Figure 2. Lines of calculated constant particle size in mm for k_{dp} = 72, presented for discharge and head, g = 9.81 m/s² and k_c = 0.98, (+) are selected prototype units

This leads to the simplified form presented in Equation (5), where the terms are now divided into a kinetic energy factor (k_{jv}), discharge (Q), and numerical resolution (k_{d_p}).

$$d_p = \frac{d_{jet}}{k_{d_p}} = \frac{k_{jv}}{k_{d_p}} \cdot Q_{jet}^{\frac{1}{2}} \quad (5)$$

Figure 2 shows the simulated and other turbine data and the calculated lines for constant particle size with a k_{d_p} of 72, a gravitational acceleration g of 9.81 and a velocity coefficient k_c of 0.98. The value for k_{d_p} is constrained by the hardware and the solver. Selecting a large k_{d_p} value may cause the solver to raise an error due to the numerous potential particles in the system. For example, in DualSPHysics, the solver restricts the particle size by calculating a particle estimation before the simulation. Accordingly, after determining the appropriate particle size, it is essential to note that in DualSPHysics, there is no significant difference between using one or six nozzles in this memory safety measure. However, if the chosen particle size is too close to the limit, it could lead to the GPU running out of memory during the simulation. Consequently, a k_{d_p} value of 72 was employed for bucket simulations, whereas full simulations, including housing, utilised a k_{d_p} of 50, due to the memory of the GPU. Considering the trend presented in the literature and executed simulations, as depicted in Figure 1, it is suggested that an even higher k_{d_p} value of 72 and above could enhance the results.

Figure 3 depicts the particle size over the discharge per nozzle. In addition to the executed simulations, the calculated particle sizes, for example for Prototype I with $k_{d_p} = 100$ and the hardware limit, are included. The calculated particle size for *Prototype I*, where reducing the particle size would lead to an improvement, shows that the needed size is outside of the hardware possibilities. Further, the calculation of the particle size for the literature Pelton turbines shows that most of them would run below the actual hardware limit of an NVIDIA A6000 GPU.

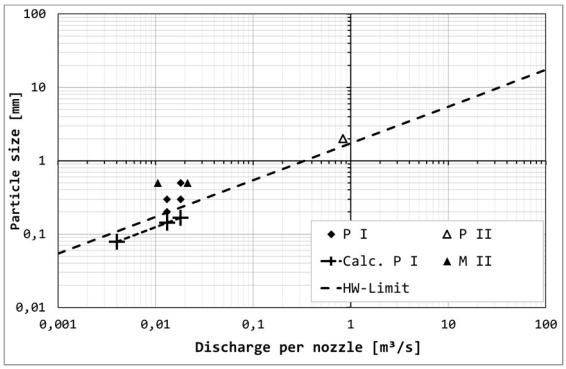

Figure 3. Comparison of applied particle size for various simulated Pelton turbines, calculated particle size (+, k_{dp} = 100) and the identified hardware limit for *Prototype I* (dashed line, k_{d_p} = 72)

When comparing the torque obtained from the simulation to the particle size used, a decline in torque corresponding to increasing particle sizes is observed. Figure 4 illustrates the deviation between simulated and experimental torque, correlating it with the relative increase in particle size compared to the calculation. For particles 5 to 9 times larger than the calculated size, the torque deviation is approximately 40% compared to the experiment. The smallest deviation corresponds to the calculated particle size with a k_{d_p} of 72.

The resulting trend, indicated by the dashed line in Figure 4 for *Prototype I*, suggests a tendency to saturate at both larger and smaller particle sizes. The simulation of *Prototype II* revealed a 5% torque deviation for the calculated particle size.

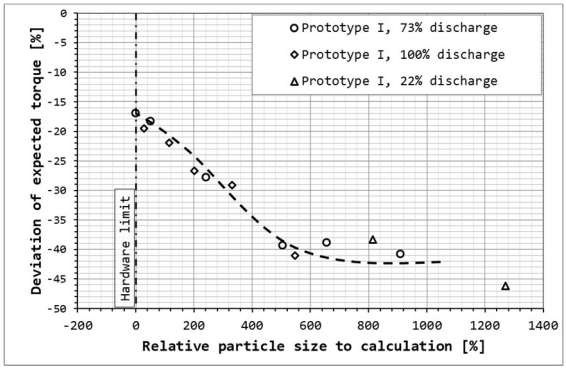

Figure 4. Torque deviation remains at approximately 40% even for particles 9 times larger than the calculated size, while the calculated particle size is the local minimum.

Further reducing the particle size should increase the possibilities of chaotic movement for the particles in the model, which leads to higher fluid-fluid interaction, ultimately reducing the energy transfer through friction. It is reasonable to assert that smaller particles result in only a limited improvement in energy transfer and are still below the expectations (a negative torque deviation far below 0) compared to the measurement for *Prototype I*.

4. SMOOTHING AND SHIFTING

The equation of state governs energy transfer within the Lagrangian framework of DualSPHysics [2] and similar SPH models. Therefore, key focus areas include the physical properties, particularly pressure and density. Taking a Pelton turbine as a reference, actual data should accurately represent these physical properties, which helps to define specific boundaries for parameters such as density, viscosity, and speed of sound. Furthermore, additional factors like solid-fluid binding coefficients [46] must be carefully chosen to maintain their linear characteristics. Model parameters, including kernel smoothing length and shifting [1], can be adjusted to improve fluid dynamics while preserving the integrity of the physical properties.

The kernel smoothing length is determined by the particle size and the smoothing coefficient $coef_h$ [2, 3]. This smoothing length indicates the distance to the considered neighbour particles for calculating the next time step, defined as the compact support area illustrated in Figure 5. For more details, Dominguez et al. [16, 2, 3] established the concepts of kernel and compact support within DualSPHysics.

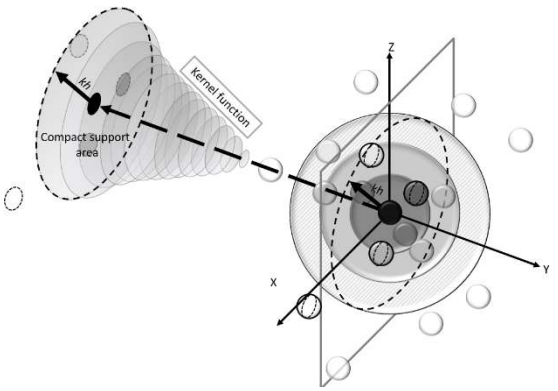

Figure 5. The influence of the kernel function depends on the smoothing length kh and the definition of the compact support area [33]. The right side represents the 3D particle space, while the left shows a conceptual 2D influence section with the kernel (interaction) function as an additional dimension.

An optimal solution would involve using an infinite smoothing length, effectively extending the compact support area to the entirety of the simulation domain, where every particle is considered for calculating a single particle for each time step. The constrained space and modelling predicated upon the ideal gas equation promote then the number of neighbouring elements. This leads to a transition toward regions of increased mass through the missing air particles and the damping of the kernel. With a small smoothing length, the compact support would approximate the particle size, allowing the particle to behave almost independently. Then, the interaction between two fluid particles or a fluid and boundary particle only occurs at a direct collision.

The following parameters in this parameter study are the “threshold to detect free surface”, referred to as the shifting parameter TFS and the coefficient for shifting computation [2]. Shifting defines the possible movement for the next time step, restricting the particle’s freedom.

Reduced freedom of the particles leads to rapid dispersion due to their high velocity. Therefore, a restriction should be imposed to ensure that the particles are forced to adhere to the initial flow. If the restriction is set too high, the particles face increased collisions due to the limited possibilities enforced by the flow and geometry. Thus, the shifting parameters should be chosen carefully to enable the particles to remain in the flow and follow the geometry without unnecessary collisions among the particles themselves.

A suitably selected shifting parameters and smoothing coefficient result in improved flow behaviour, enhancing the energy transfer between fluid and solid. Low parameter values facilitate higher freedom of movement. In comparison, higher values restrict potential motion, causing the fluid to adhere to the initial direction of the flow, consequently being more forced onto the solid when it gets redirected by the geometry of the bucket. This results in an unrealistic and strong deflection of the fluid on the bucket surface, which, due to the still restricted movement and high interaction radius of the particles, leads to the forming of a water bulk instead of a steady flow inside the bucket.

The coefficient for shifting computation was readily optimisable in jet impinging and remained unaffected by other parameters. The shifting coefficient TFS and the smoothing parameter $coef_h$ showed an interesting connection. This relationship suggests that there may be a significant link between them, which deserves further investigation. A simulation examining bucket interactions across various values of TFS and smoothing coefficients revealed that optimal torque occurs at a TFS of 0.3 and a smoothing coefficient of 0.8, as depicted in Figure 6. It is important to note that there is a marked decrease in torque at lower TFS values, while the smoothing coefficient exhibits a consistent decrease in both directions. Overall, the torque gradient for higher values of both parameters remains relatively flat. It is of high interest that the local optimum of the

torque is well-distinguished, which indicates a strong correlation for both parameters when applied to Pelton turbines.

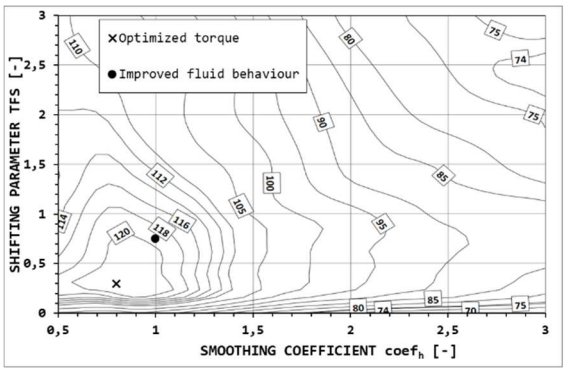

Figure 6. Torque variation in Nm over shifting parameters and smoothing coefficients of the bucket simulation for a fluid velocity of 82 m/s and a rotation speed of 1515 rpm

Further, in the optimum region, the fluid shows a substantial difference in the behaviour. Figure 7 illustrates the optimal torque on the left side, where the higher level of particle dispersion is evident. Moreover, the fluid behaviour is even worse for lower parameter values. By increasing the smoothing coefficient to one and adjusting the shifting parameter to 0.7, the fluid behaviour significantly improves, while the torque only decreases by around 1.5% (Figure 7, right side).

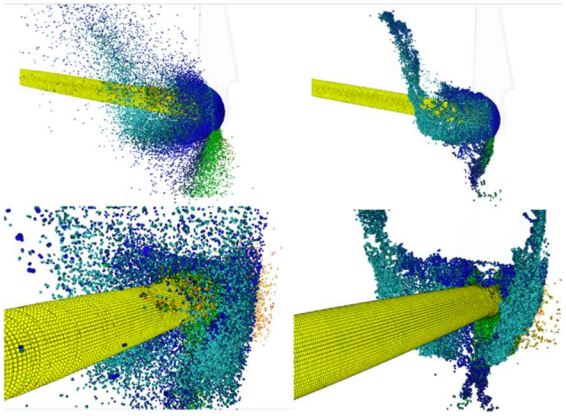

Figure 7. Single rotating bucket simulation with a fluid velocity of 82 m/s and rotation speed of 1515 rpm after torque optimisation (left) and after further manual correction of the shifting and the smoothing coefficient (right)

This divergence between the torque optimum and acceptable fluid movement indicates that energy transfer is better for more dispersive fluid behaviour. Nevertheless, fluid movement is essential for developing the Pelton turbine, particularly in the housing. Therefore, the optimisation must be revised, or an additional condition must be factored into the optimisation.

Table 1. Used parameters for DualSPHysics simulations of *Prototype I*, with highlighted parameters (bold) from the study

Parameter	Used value
Particle size d_p [mm]	**0.3**
Density ρ [kg/m³]	998.207
Dyn. Viscosity ν [Pa s]	8.93×10^{-7}
Speed of sound a [m/s]	1463.62
Boundary method	mDBC
Kernel	Wendland
Viscosity formulation	Laminar+SPS
Solid-fluid binding, ViscoBoundFactor	0.75
Smoothing coefficient $coef_h$	**1.102**
Shifting mode	Full
Threshold to detect free	**0.75**
Coefficient for shifting computation, ShiftCoef	-2.01
Minimum density valid [kg/m³]	900
Maximum density valid [kg/m³]	1100

After automated and manually corrected optimising *Prototype I*, a smoothing coefficient of 1.1 and a shifting parameter of 0.75 were identified. Further, the optimised $coef_h$ and TFS values yielded promising results for the fluid behaviour and the torque. In addition, the parameters used were successfully usable without adaptation for other simulations, such as *Prototypes II*.

Table 1 shows the set of used DualSPHysics parameters for the simulation of *Prototype I*.

5. JET DISTURBANCE

In the bucket work cycle, the bucket cuts through the jet before the filling begins. Observable in the experiment and CFD [47, 48], wetting occurs on the back side of the bucket, leading to a build-up of surface tension. The adhesive forces from the fluid-solid interaction create a pressure gradient called the Coanda effect [26, 27, 49], which pulls parts of the fluid towards the bucket's backside boundary layer.

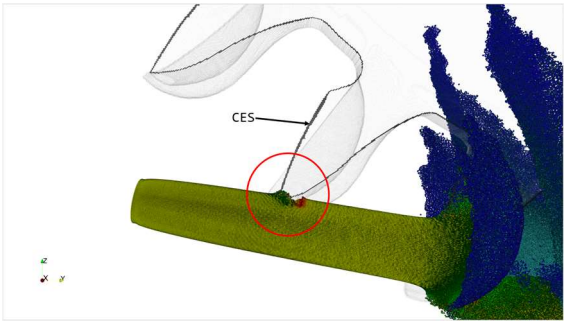

Figure 8. Initiation of jet disturbance (red) by entering the bucket at 7°, with highlighted cutting-edge section (CES)

In contrast, the fluid begins to move towards the bucket-runner connection. When the cohesive and

surface-forming forces reach their limit, the remaining jet after the bucket dissolves the connection.

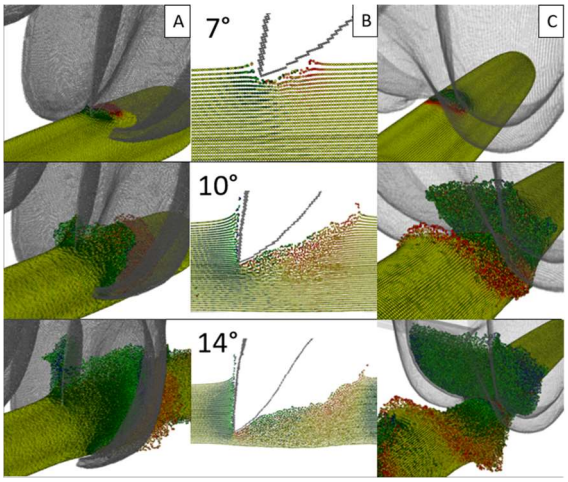

Figure 9. Jet disturbance for various positions over time with reduced (green), accelerated (red) and initial (yellow) particle speed in front view (A), cutting-edge section CES (B) and back view of the bucket

Compared with SPH, after the bucket enters the jet, a gap between the bucket's backside and the jet appears [5]. The needed surface terms are only indirectly considered through the ideal gas equation and the execution of the model [2, 49].

Furthermore, the volume's incompressibility (where density changes in the SPH to compensate for the fluid's incompressibility) leads to a push of the particles from the jet by the bucket, displacing the fluid inside the jet.

As a result, the jet becomes disturbed, and part of the particles accelerate. Figure 8 shows the initial disturbance caused by the bucket, while Figure 9 shows the development of the disturbance. The red marked area in Figure 8 is shown in Figure 9 for 7° in detail, including the highlighted cutting edge section (CES). When the bucket cuts into the jet, the particles of the jet are pushed by the rotating bucket. Hence, the particles change their trajectory, see Figure 10-B.

The pushed particles accelerate and generate additional momentum, which is transported in the jet direction. Furthermore, the accelerated particles in the direction of the jet displace the upstream particles, deforming the jet (see Figure 10-A) and creating a momentum wave within the jet (see Figure 9-C).

Similar to the observation of Ge et al. [5] or Guo et al. [50], this behaviour in the SPH is contrary to the physical expectation, where the surface tension and adhesive forces should create a pull towards the bucket's backside, along with a constriction of the jet.

Figure 10-C shows the development of the particle positioning, average velocity, and number of particles before (left), while bucket entrance (middle) and after (right).

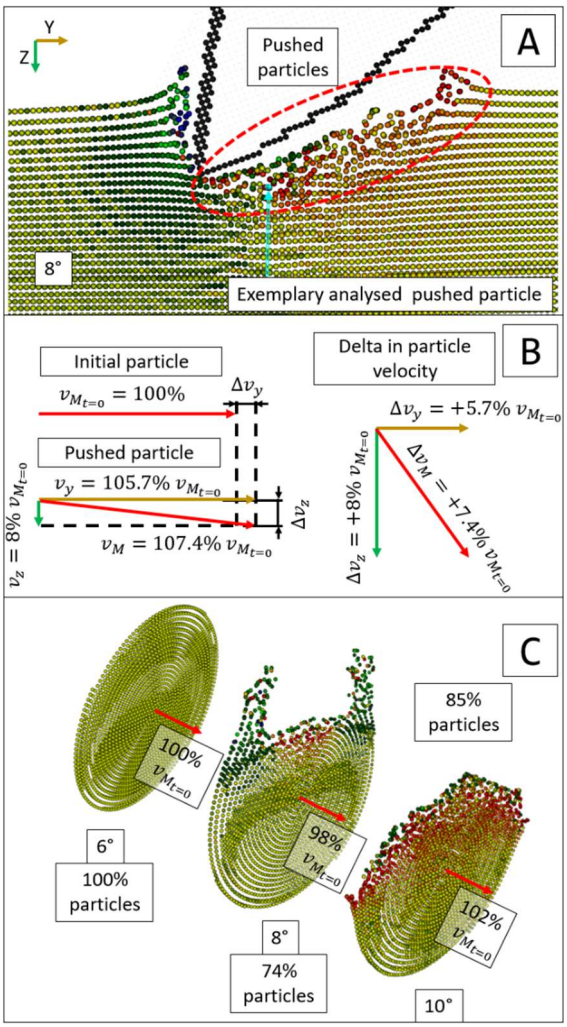

Figure 10. The relative development of velocity through the entrance of the bucket (A), accelerated particles (B), average velocity development (C) for 6° (before impact), 8° (impact) and 10° (after impact), including the number of particles in the sections

When the bucket cuts into the jet, some particles are removed through the bucket, some slow down by passing by the bucket, and others speed up (get pushed). The accelerated particles push against the particles in front of them. This interaction transfers some of their velocity to the front particles and increases the layer density. The first layers of particles that reach the bucket remain unchanged from the disturbance. Some accelerated particles in the following layers must move sideways past the main flow.

The particles that move sideways also impact the inner part of the bucket, causing further disturbances in the flow and resulting in energy loss.

The resulting disturbance is displayed in Figure 11, just before the impact and disturbance of the flow inside the bucket.

Furthermore, the disturbance can also be observed in the torque of a single bucket. Figure 12 illustrates the entrance of a single bucket into the jet for different particle sizes. For relatively large particles, specifically for *Prototype I* with $d_p = 2$ mm, the initial entrance is clearly visible at 2.25 ms (feature I).

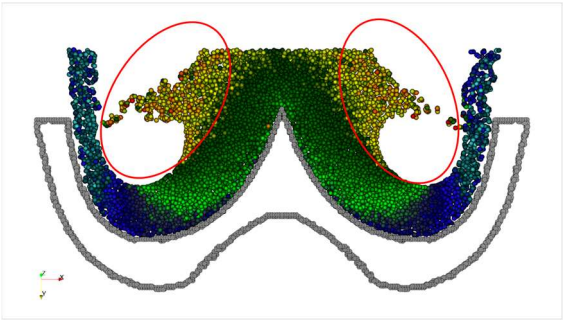

Figure 11. Jet disturbance in the bucket section

This negative torque nearly vanishes for reduced particle sizes. In addition, for a particle size of 2 mm, the initiated wave from the disturbance is distinctly distinguishable over the first milliseconds after bucket entrance (feature 1-4). Here, smaller particles exhibit no distinguishable wave but a weak promoted feature. Additionally, the difference between 0.5 mm and 0.7 mm particle sizes shows a shift of the characteristic peak from the wave impact around 3.25 (feature III) to 3.14 ms (feature II).

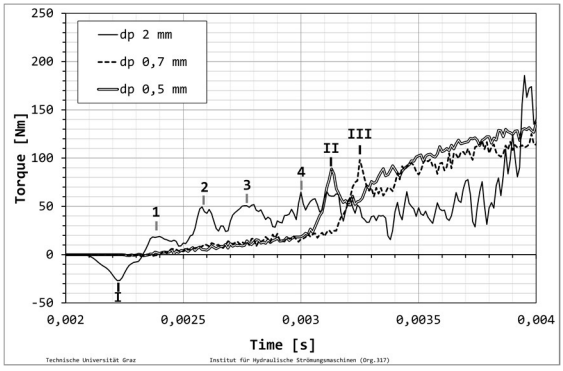

Figure 12: Change in torque through jet disturbance

6. SIMILARITY LAW

As dimensionless parameters for the similarity, φ and ψ are utilised. The discharge coefficient φ is defined with the bucket width B, discharge Q and runner speed n, shown in Equation (6) and normalised with the bucket number z for better comparison to the simulation. Further, the pressure coefficient ψ defined with head H,, runner diameter D and runner speed, depicted in Equation (7), is used.

Figure 13 illustrates discharge variations for *Prototype I* across heads of 350, 275, 200, and 100 m.

$$\varphi = \frac{8 \cdot Q}{B^3 \cdot \pi^2 \cdot z \cdot n} \tag{6}$$

$$\psi = \frac{2 \cdot g \cdot H}{D^2 \cdot \pi^2 \cdot n^2} \tag{7}$$

Additionally, a runner speed variation was conducted for constant discharge and head and a discharge variation for constant ψ. Similarly, several simulations were performed for each head at a constant discharge coefficient φ of 0.072.

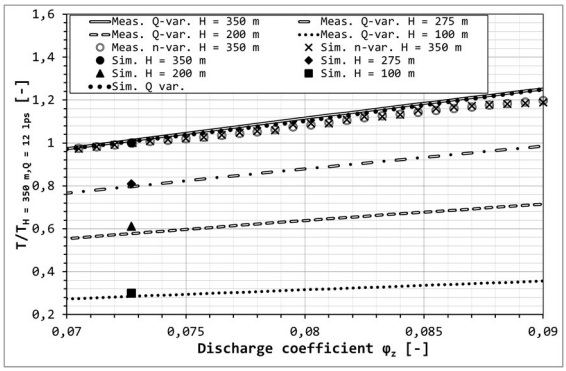

Figure 13 Relative torque of measurement compared to simulation

Furthermore, a simulation of the observed runner speed and discharge variations was conducted using identical values from the experiment. Subsequently, the torque from the measured and simulated operation points is normalised with the torque of the nominal operation point at $H = 350$ m. $n = 1515$ rpm at $\varphi = 0.072$.

In comparison, the relative torque change between the similar operating points for lower heads is nearly identical in both simulation and experiment. The discharge variation in the simulation shows a linear offset for higher discharges compared to the experiment, with a torque deviation below 1%. The variation in runner speed demonstrates a good match in the relative change in torque, which is almost identical to the relative change observed in the experiment.

CONCLUSION

This research examined the parameters in the software package DualSPHysics for particle size, smoothing coefficient, and shifting parameters for Pelton turbines, including the jet disturbance and similarity laws. An automated optimisation, including manual corrections and individual investigations, was conducted for the parameters.

As a result, the particle size was refined based on a simple correlation with discharge or jet diameter. The optimal particle size displayed a strong dependency on the jet diameter.

The shifting and smoothing parameters yielded a local optimum for torque, which does not align with acceptable fluid movement. A slight adaptation of the parameters allows a substantial improvement in fluid behaviour near the torque optimum.

In SPH, the occurring jet disturbance demonstrates the impact of the absent surface tension formulation within the model. Furthermore, the jet disturbance affects the torque, particularly for slender jets or jets with large particle sizes.

The investigation into the similarity law yielded favourable results when comparing operational points for identical geometries. However, an investigation between scaled geometries is still required.

The approach to support investigations with DualSPHysics is advantageous for low specific speed Pelton turbine development due to its limited effort and easy adaptation. Furthermore, the conservation of the similarity law can facilitate straightforward comparisons of changes between geometries and operational points.

ACKNOWLEDGEMENTS

This research has been performed at the Technical University of Graz, Institute of Hydraulic Fluid Machinery.

The product names referenced in this paper may be trademarks of their respective companies.

REFERENCES

[1] A. J. Crespo, J. M. Domínguez, B. D. Rogers, M. Gómez-Gesteira, S. Longshaw, R. Canelas, R. Vacondio, A. Barreiro and O. García-Feal, "DualSPHysics: Open-source parallel CFD solver based on Smoothed Particle Hydrodynamics (SPH)," *Computer Physics Communications,* vol. 187, pp. 204-216, 2 2015.

[2] J. M. Domínguez, G. Fourtakas, C. Altomare, R. B. Canelas, A. Tafuni, O. García-Feal, I. Martínez-Estévez, A. Mokos, R. Vacondio, A. J. Crespo, B. D. Rogers, P. K. Stansby and M. Gómez-Gesteira, "DualSPHysics: from fluid dynamics to multiphysics problems," *Computational Particle Mechanics,* 2021.

[3] J. M. A. Domínguez and G. Fourtakas, "Structure of the DualSPHysics code," in *DualSPHysics Users Workshop*, Manchester (United Kingdom), 2015.

[4] K. Furnes, "Flow in Pelton turbines," Norwegian University of Science and Technology, Department of Energy and Process Engineering, 2013.

[5] J. Sun, X. F. Ge and Y. Zheng, "SPH method used for characteristic predictions at Pelton turbine buckets: comparing with the mesh-based method," *Engineering Computations (Swansea, Wales),* vol. 40, no. 5, pp. 1245-1265, 7 2023.

[6] C. Vessaz, E. Jahanbakhsh and F. Avellan, "Flow simulation of a Pelton bucket using finite volume particle method," *IOP Conference Series: Earth and Environmental Science,* vol. 22, 2014.

[7] C. Vessaz, E. Jahanbakhsh and F. Avellan, "Flow simulation of jet deviation by rotating pelton buckets using finite volume particle method," *Journal of Fluids Engineering, Transactions of the ASME,* vol. 137, no. 7, 7 2015.

[8] T. Kumashiro, S. Alimirzazadeh, F. Avellan and K. Tani, "Application of particle-based numerical analysis to the practical design of Pelton turbine," *IOP Conference Series: Earth and Environmental Science,* vol. 774, no. 1, 6 2021.

[9] S. Alimirzazadeh, T. Kumashiro, S. Leguizamón, E. Jahanbakhsh, A. Maertens, C. Vessaz, K. Tani and F. Avellan, "GPU-accelerated numerical analysis of jet interference in a six-jet Pelton turbine using Finite Volume Particle Method," *Renewable Energy,* vol. 148, pp. 234-246, 4 2020.

[10] P. K. Koukouvinis, J. S. Anagnostopoulos and D. E. Papantonis, "Flow modelling in the injector of a Pelton turbine," in *4th international SPHERIC workshop*, Nantes, 2009.

[11] P. K. Koukouvinis, J. S. Anagnostopoulos and D. E. Papantonis, "An improved MUSCL treatment for the SPH-ALE method: Comparison with the standard SPH method for the jet impingement case," *International Journal for Numerical Methods in Fluids,* vol. 71, no. 9, pp. 1152-1177, 3 2013.

[12] R. A. Garzon, A NEW ALE-WENO FORMULATION OF SMOOTHED PARTICLE HYDRODYNAMICS (SPH) FOR THE ACCURATE SIMULATION OF FREE SURFACE JETS, Freie Universität Bozen, Faculty of Science and Technology, Sustainable Energy and Technologies, 2021.

[13] A. Arch and D. Mayr, "Prototype Measurements on casing flow and air entrainment into the tailwater of Pelton turbines," in *Measurement, 2. Jg., S. 1.*, LYON, 2009.

[14] T. Staubli and H. P. Hauser, "FLOW VISUALIZATION-A DIAGNOSIS TOOL FOR PELTON TURBINES," in *IGHEM*, Lucerne, 2004.

[15] H. Grein, D. Klicov and W. Wieser, "Efficiency scale effects in Pelton turbines," *Water Power & Dam Construction,* pp. 32-36, 1988.

[16] M. J. A. Domínguez, "DualSPHysics: Towards High Performance Computing using SPH technique," Universidad de Vigo, Enciromental Physics Laboratory, 2014.

[17] Z. Zhang, Freistrahlturbinen - Hydromechanik und Auslegung, Springer, 2009.

[18] J. A. Nelder and R. Mead, "A Simplex Method for Function Minimization," *The Computer Journal,* vol. 7, no. 4, pp. 308-313, 1 1965.

[19] C. H. Amon, A. M. Guzmán and B. Morel, "Lagrangian chaos, Eulerian chaos, and mixing enhancement in converging-diverging channel flows," *Physics of Fluids,* vol. 8, no. 5, pp. 1192-1206, 1996.

[20] D. Perrone, S. Stefania Scarsoglio, S. Luca Ridolfi and G. Boffetta, "Lagrangian dynamics in wall-bounded transitional and turbulent flows: Particle tracking and network-based analyses," 2024.

[21] L. P. Wang, M. R. Maxey, T. D. Burton and D. E. Stock, "Chaotic dynamics of particle dispersion in fluids," *Physics of Fluids A,* vol. 4, no. 8, pp. 1789-1804, 1992.

[22] M. M. Jalali and M. R. Jalali, "Curvilinear shallow water solver and Lagrangian particle tracking model for Chaotic advection," 2024.

[23] P. Ruden, "Turbulente Ausbreitungsvorgänge im Freistrahl," *Die Naturwissenschaften, Springer Verlag,* vol. 21, no. 23, pp. 375-378, 1933.

[24] W. Schach, "Umlenkung eines kreisförmigen Flüssigkeitsstrahles an einer ebenen Platte senkrecht zur Strömungsrichtung," *Ingenieur-Archiv, Springer Verlag,* vol. VI, pp. 51-59, 1934.

[25] MABROUKI T., Raissi K. and Cornier A., "Numerical simulation and experimental study of the interaction between a pure high-velocity waterjet and targets: contribution to investigate the decoating process," *ELSEVIER WEAR,* no. 239, pp. 260-273, 1 2000.

[26] F. Chen and P. E. Smith, "Simulated surface tensions of common water models," *Journal of Chemical Physics,* vol. 126, no. 22, 2007.

[27] M. Miozzi, F. Lalli and G. P. Romano, "Experimental investigation of a free-surface turbulent jet with Coanda effect," *Experiments in Fluids,* vol. 49, no. 1, pp. 341-353, 7 2010.

[28] P. Jungwirth and D. J. Tobias, "Specific ion effects at the air/water interface," *Chemical Reviews,* vol. 106, no. 4, pp. 1259-1281, 4 2006.

[29] S. Chempath and L. R. Pratt, "Distribution of binding energies of a water molecule in the water liquid-vapor interface," *Journal of Physical Chemistry B,* vol. 113, no. 13, pp. 4147-4151, 4 2009.

[30] Y. NAKANISHI, T. FUJII and S. KAWAGUCHI, "Numerical and Experimental Investigations of the Flow in a Stationary Pelton Bucket," *Journal of Fluid Science and Technology,* vol. 4, no. 3, pp. 490-499, 2009.

[31] C. Bauer, Visualisierung von Strömungen im Becher einer Peltonturbin, Technische Universität Wien, Institut für Energietechnik und Thermodynamik, Forschungsbereich Strömungsmaschinen, 2011.

[32] J.-C. Marongiu, F. Leboeuf, J. Caro, E. Parkinson and E. Parkinson Free, "Free surface flows simulations in Pelton turbines using an hybrid SPH-ALE method," *Journal of Hydraulic Research,* vol. 48, pp. 40-49, 2010.

[33] F. Beck and P. Eberhard, "Predicting abrasive wear with coupled Lagrangian methods," *Computational Particle Mechanics,* vol. 2, no. 1, pp. 51-62, 5 2015.

[34] A. Rossetti, G. Pavesi, G. Cavazzini, A. Santolin and G. Ardizzon, "Influence of the bucket geometry on the Pelton performance," *Proceedings of the Institution of Mechanical Engineers, Part A: Journal of Power and Energy,* vol. 228, no. 1, pp. 33-45, 2014.

[35] T. Kubota, "Observation d'interférence de jets dans une turbine pelton à 6 injecteurs," *Journal of Hydraulic Research,* vol. 27, no. 6, pp. 753-767, 1989.

[36] F. Beck and P. Eberhard, "Comparison of wear models using a Lagrangian approach," in *IV International Conference on Particle-based Methods–Fundamentals and Applications PARTICLES2015*, 2015.

[37] J.-C. Marongui, M. Rentschler and E. Parkinson, "Study of flow patterns in hydraulic turbines with SPH-Ale," Hydrolink, 2015.

[38] A. Židonis and G. A. Aggidis, "State of the art in numerical modelling of Pelton turbines," *Renewable and Sustainable Energy Reviews,* vol. 45, pp. 135-144, 2015.

[39] C. Vessaz, L. Andolfatto, F. Avellan and C. Tournier, Toward design optimization of a Pelton turbine runner, vol. 55, Springer Verlag, 2017, pp. 37-51.

[40] T. Kumashiro, S. Alimirzazadeh, A. Maertens, E. Jahanbakhsh, S. Leguizamón, F. Avellan and K. Tani, "Numerical investigation of the jet velocity profile and its influence on the Pelton turbine performance," *IOP*

Conference Series: Earth and Environmental Science, vol. 240, no. 7, 3 2019.

[41] A. Frangioni, "About Lagrangian Methods in Integer Optimization," *Annals of Operations Research,* vol. 139, pp. 163-193, 2005.

[42] X. Q. Yang, X. X. Huang and S. J. Optim, "A nonlinear Lagrangian approach to constrained optimization problems," *SIAM journal of optimisation,* vol. 11, no. 4, pp. 1119-1144, 2001.

[43] S. Sabach and M. Teboulle, "Lagrangian Methods for Composite Optimization," 2019.

[44] J. Raabe, Hydro power. The design, use, and function of hydromechanical, hydraulic and electrical equipment, VDI-Verlag, 1985.

[45] C. VESSAZ, "Finite Particle Flow Simulation of Free Jet Deviation by Rotating Pelton Buckets," 2015.

[46] D. team, "XML guide for DualSPHysics," DualSPHysics, 2022.

[47] A. Perrig, "Hydrodynamics of the free surface flow in Pelton turbine buckets," EPFL, Lausanne, 2007.

[48] M. Choi, Y. J. Jung and Y. Shin, Unsteady flow simulations of Pelton turbine at different rotational speeds, vol. 7, Hindawi Publishing Corporation, 2015.

[49] A. ŽIDONIS, OPTIMISATION AND EFFICIENCY IMPROVEMENT OF PELTON HYDRO TURBINE USING COMPUTATIONAL FLUID DYNAMICS AND EXPERIMENTAL TESTING, Lancaster University, 2015.

[50] B. Guo, Y. Xiao, A. K. Rai, Q. Liang and J. Liu, "Analysis of the air-water-sediment flow behavior in Pelton buckets using a Eulerian-Lagrangian approach," *Energy,* vol. 218, 3 2021.

Conference on Modelling Fluid Flow (CMFF'25)
The 19th International Conference on Fluid Flow Technologies
Budapest, Hungary, August 26 - August 29, 2025

APPLICATION RANGES OF THE HAGEN-POISEUILLE LAW TO MODEL NON-NEWTONIAN FLUID-FILLED DAMPERS

Boglárka BALOG[1], Péter NAGY-GYÖRGY[2]

[1] Corresponding Author. Department of Hydrodynamic Systems, Faculty of Mechanical Engineering, Budapest University of Technology and Economics. Bertalan Lajos u. 4 – 6, H-1111 Budapest, Hungary. E-mail: bbalog@hds.bme.hu
[2] Department of Hydrodynamic Systems, Faculty of Mechanical Engineering, Budapest University of Technology and Economics. E-mail: nagy-gyorgy.peter@gpk.bme.hu

ABSTRACT

Non-Newtonian liquids, such as magnetorheological and shear thickening fluids, are increasingly utilized in hydraulic dampers due to better controllability and energy absorption capabilities. Despite these advantages, the design of such dampers remains heavily reliant on empirical experiments, and accurately modelling their damping characteristics presents a persistent challenge. The most common method involves applying the Hagen-Poiseuille law to describe the flow inside the damping channel, and the damping force is calculated from the pressure drop. However, in several practical scenarios, this approach may lead to significant inaccuracies due to the simplifications. We aim to describe the application range, where the law can predict the damping characteristic with reasonable accuracy. We performed steady state CFD simulations with different dimensions and frequencies for Newtonian, and shear thickening fluids. The results were compared to the analytical values, and the relative error was plotted using the function of dimensionless length/diameter ratio. Based on the contour plots, the industry can identify the ranges where the approximations are applicable.

Keywords: CFD, damper modelling, Hagen-Poiseuille law, non-Newtonian fluid, shear thickening fluid

NOMENCLATURE

A	$[m^2]$	piston surface
d	$[m]$	piston diameter
D	$[m]$	outer cylinder diameter
f	[-]	function
F	$[N]$	load
L	$[m]$	channel length
p	$[Pa]$	pressure
Q	$[m^3/s]$	volume flow rate
R	$[m]$	radius
t	$[s]$	time
u	$[m/s]$	velocity component in x direction
v	$[m/s]$	velocity component in y direction
w	$[m/s]$	velocity component in z direction
$\dot{\gamma}$	[1/s]	shear rate
η	$[Pa{\cdot}s]$	dynamic viscosity
τ	$[Pa]$	shear stress

Subscripts and Superscripts

c	critical
max	maximum
w	wall

Abbreviation

STF	shear thickening fluid
CFD	computational fluid dynamics
PL	power-law
PEG	polyethylene glycol

1. INTRODUCTION

Shear thickening fluids (STFs) are increasingly used in hydraulic dampers due to their self-adaptive characteristics and enhanced energy absorption capabilities. However, the accurate prediction of damping characteristics, $F(v)$, remains a significant challenge. In engineering practice, the damping force is commonly estimated using analytical models based on the Hagen-Poiseuille law, which assumes laminar, Newtonian flow through the orifices. While this approach provides a convenient first approximation, its validity for STF-based dampers has not been systematically established, raising concerns about its accuracy in practical applications.

Existing methods for determining damping characteristics rely heavily on experiments [1–6], but the measured data could be compared only to analytical solutions derived from Newtonian [2] or traditional non-Newtonian rheological models such as power law [7] or Herschel-Bulkley [8]. However, these models frequently fail to account for the

distinctive three region viscosity curve of STFs, leading to inaccuracies in predicted damping forces. Furthermore, numerical simulations such as computational fluid dynamics (CFD) provide precise solutions but are computationally expensive and constrained by predefined rheological models (e.g., Newtonian, Bingham, power-law, Herschel-Bulkley, Carreau-Yasuda models) [9].

To address these limitations, our previous study [10] introduced an analytical method for estimating damping characteristics without relying on rheological model fitting. Instead, we directly incorporated measured rheological data, enabling an inverse approach to identify appropriate fluid properties for a given damping requirement. The derivation based on the Hagen-Poiseuille law for pipe flow applying assumption that the entrance and exit losses are negligible compared to the viscous flow losses, so the pipes are sufficiently long to have a fully developed flow. The CFD results prove the accuracy of the novel analytical model when the assumptions are fulfilled.

Our initial validation of these assumptions was performed for power-law (PL) and STF rheologies [10], where parameter sweeps were conducted for cylindrical orifice geometries. Although 3D simulations with multiple orifices provided accurate results [11], they were computationally demanding, leading us to adopt a 2D simplification for broader parameter exploration.

Building on these prior investigations, the present study systematically assesses the validity of the Hagen-Poiseuille law in predicting STF damping characteristics by comparing the CFD and analytical results. The primary objective is to identify the applicability range of this law and quantify deviations beyond its valid range. To achieve this, we map the relative error as a function of the dimensionless length-to-diameter ratio and relative volume flow rate. While previous research has examined the effects of various rheological models, the specific transition boundaries where Hagen-Poiseuille-based predictions break down remain poorly defined. By providing a detailed error analysis and visualization, this study establishes an industry-relevant framework for determining when these simplifications hold, thus guiding the design of STF-based dampers with greater accuracy.

A critical aspect of ensuring the accuracy of these investigations is the reliability of the rheological data used as input for both analytical and numerical models. However, existing studies report significantly different rheological properties for STFs with identical compositions, suggesting inconsistencies in measurement techniques or variations in experimental conditions [12,13]. Under controlled conditions, we synthesized STF samples to ensure consistency in rheological measurements, providing reliable input data for both analytical and numerical models. Building on this foundation, this study systematically evaluates the applicability of the Hagen-Poiseuille law in predicting STF-based damper behaviour by comparing analytical predictions with CFD simulations. We examine a range of flow conditions and geometries to identify the accuracy limits of the analytical approach and quantify deviations beyond its valid range. By analysing the relationship between relative error, dimensionless parameters, and flow characteristics, we establish guidelines for when the Hagen-Poiseuille approximation remains valid. The findings offer practical insights for damper design, highlighting the importance of precise rheological characterization and the conditions under which simplified models can be confidently applied.

2. MATERIALS AND METHODS

2.1. Materials and Experimental Procedures

2.1.1. Materials

The STF is composed of nanoscale silica particles suspended in a carrier liquid. The fumed silica (Aerosil® R816, provided by Evonik) has a primary particle size of 12 nm and a specific surface area of approximately 190 ± 20 m^2/g [14]. The silica is post-treated with hexadecylsilane, consisting of slightly hydrophobic, spherical particles. Due to its large surface area and porous structure, R816 silica effectively adsorbs gases, liquids, and other substances. This type of silica is characterized by an extremely fine powder form. Its key advantages include excellent dispersibility, enabling homogeneous distribution in various media and enhancing product performance. Furthermore, it offers high thermal stability and chemical resistance, making it suitable for applications across a wide temperature range and in oxidative or corrosive environments. The carrier liquid used in the formulation was polyethylene glycol with a molecular weight of 200 g/mol (PEG 200, product code P0840, supplied by TCI Chemicals). It is a colourless, clear liquid but has lower viscosity and is miscible with water. Due to its low viscosity and miscibility, it is advantageous in applications where easy blending or compatibility with other substances is essential.

2.1.2. Sample preparation

During the preparation process, the liquid medium and silica were introduced in alternating increments, each constituting one-third of the total required volume. Following each addition, the sealed bottles were subjected to ultrasonication for 30 minutes to promote dispersion. This process was repeated twice to ensure uniform distribution of the silica within the medium. Subsequently, the sealed bottles were placed in a water bath and gradually heated to 80 °C. Upon reaching the target

temperature, the bottle caps were removed, and the samples were subjected to continuous stirring for 2 hours using an overhead stirrer to achieve thorough homogenization. As a result, a transparent and homogeneous fluid was obtained. For each STF, specific quantities of fumed silica were incorporated into the carrier fluid at a defined weight fraction (12 and 15 wt.%).

2.1.3. Rheological measurements

An Anton Paar MCR 301 rotational rheometer equipped with a cone-plate measuring system was used to determine the rheological properties of the STF samples. The measuring system featured a cone with a diameter of 25 mm and a fixed gap of 0.054 mm, ensuring precise control of the measurement parameters. Based on the defined gap distance, the applied force, and the rotational speed, the instrument recorded and plotted shear rate versus viscosity data. The suspensions were analysed within a shear rate range of 0.1 to 10,000 s^{-1}. All measurements were carried out at a constant temperature of 25°C to ensure accuracy and reproducibility.

2.2. Analytical approach

Rheological measurements provided shear rate and shear stress data, which can be used to estimate the expected velocity-pressure drop function for a given system. The analytical approach presented in this section is based on the methodology detailed in [10], where a comprehensive derivation and validation using CFD simulations can be found. By utilizing these relationships, a predictive framework is established for describing the flow behaviour of the dilatant fluid under given operating conditions.

The hydraulic dampers usually characterised by the *F(v)* force(velocity) characteristic. When the piston with surface A_{piston} moves with a v_{piston} velocity, the liquid flows through the gap with the

$$Q = v_{piston}\, A_{piston} \tag{1}$$

volume flow rate. The Δp pressure difference between the chambers drives the flow, which is proportional to the compressing force, since

$$F = \Delta p\, A_{piston} \tag{2}$$

As a result, we can see that the *Q*-Δp relationship is essential to predict the *F(v)* damping characteristic.

To develop the analytical model, laminar flow was assumed as in the similar research studies such as [15,16]. The governing equations are the momentum and the continuity equation in a cylindrical coordinate system (x, r, θ) applying the assumptions:

1. The fluid is incompressible.
2. The solution corresponds to a steady-state condition with no time dependence.
3. The flow is two-dimensional, meaning all quantities are constant in the θ direction.
4. The axial velocity component u depends only on the radial coordinate ($u = u(r)$), while the other velocity components are zero ($v = w = 0$).
5. The pressure gradient is constant.

With these assumptions, the continuity equation and the momentum equation in the θ tangential and in x longitudinal directions are automatically satisfied. The remaining simplified equation is the

$$0 = -\frac{dp}{dx} + \frac{1}{r}\frac{d}{dr}(r\tau) \tag{3}$$

with the

$$u(r = R) = 0 \tag{4}$$

boundary condition, where $\tau(r)$ represents the local shear stress in the function of the radial coordinate. This equation is valid for any shear rate–shear stress rheology $\tau = g(\dot{\gamma})$. After integrating with respect to r, the local shear stress is

$$\tau = \frac{dp}{dx}\frac{r}{2} + \tau_0, \tag{5}$$

For arbitrary non-Newtonian rheology, where τ_0 is the local shear stress at the centreline of the pipe. Since the bore and, consequently, the flow is axisymmetric, it follows that $\tau_0 = 0$.

Based on these considerations, the volumetric flow rate can be determined using the following equation:

$$Q = \frac{2\pi R^3}{{\tau_w}^3}\left[\frac{{\tau_w}^2}{2}F(\tau_w) - S(\tau_w)\right], \tag{6}$$

where R is the radius, L is the channel length, $\tau_w = \frac{dp}{dx}\frac{R}{2} = \frac{\Delta p R}{2L}$ is the wall shear stress, and

$$F(\tau) = \int_0^{\tau} f(\tilde{\tau})\, d\tilde{\tau} \tag{7}$$

$$S(\tau) = \int_0^{\tau} \tilde{\tau} F(\tilde{\tau})\, d\tilde{\tau} \tag{8}$$

are integral functions where $f(\tau) = g^{-1}(\tau)$ represents the inverse function of the traditional shear stress-shear rate rheological curve.

The authors would emphasize that this method does not require any model fittings, since the integrations in Eq. (7) and (8) can be performed numerically (e.g. with trapezoidal method) using the measurement data directly. Rearranging eq. (6) gives the

$$\tilde{Q} := \frac{Q}{2\pi R^3} = \frac{1}{{\tau_w}^3}\left[\frac{{\tau_w}^2}{2}F(\tau_w) - S(\tau_w)\right], \tag{9}$$

relative flow rate, which depends only on the τ_w wall shear stress. It practically means that the $\tilde{Q}$ - τ_w curve depends only on $f(\tau)$ inverse rheological curve. Since this curve does not depend on the geometric dimensions, we will define the volume flow rate to have uniformly distributed $\tilde{Q}$ values in the range of 10-10000 1/s.

The Eq. (9) has a simpler form for Newtonian case,

$$\tilde{Q} := \frac{\tau_w}{8\eta} \tag{10}$$

when the inverse rheological and the integral functions are

$$f(\tau) = \frac{\tau}{\eta}, \qquad F(\tau) = \frac{\tau^2}{2\eta}, \qquad S(\tau) = \frac{\tau^4}{8\eta} \quad (11)$$

and η is the Newtonian dynamic viscosity.

2.3. CFD setup

To evaluate the accuracy of the Hagen-Poiseuille law in predicting the damping characteristics of non-Newtonian fluids in hydraulic dampers, CFD simulations were performed using OpenFOAM (Version 2112, [17]). The study focused on a single damping channel geometry for various length and diameter configurations. Consistent material properties, boundary conditions, and numerical settings were applied across all cases. The objective was to determine the range of validity for the analytical approach by comparing the CFD results to theoretical predictions.

2.3.1. Geometry and meshing

Fig. 1 show the computational domain. To reduce computational cost while maintaining accuracy, a two-dimensional axisymmetric approach was employed, where only a 5° wedge of the circular domain was modelled. The mesh was generated using the built-in *blockMesh* utility, which decomposes the domain into structured hexahedral elements. Mesh parameters, including nodal coordinates, division counts, and expansion ratios, were computed using a custom MATLAB script to ensure a high-quality structured mesh with minimal distortion. The resulting mesh was composed entirely of hexahedral elements, exhibiting zero non-orthogonality and a maximum skewness of 0.320537.

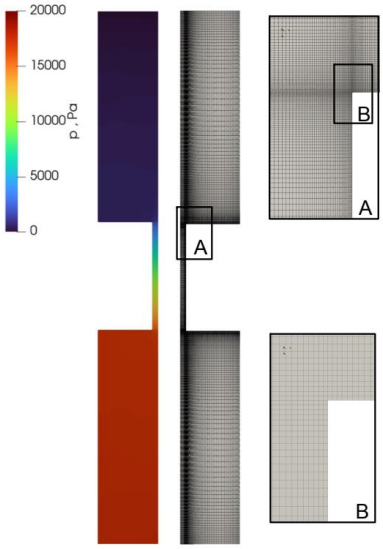

Figure 1. The mesh of the investigated damper and the corresponding pressure distribution

To assess the influence of discretization errors, a mesh independence study was performed by evaluating four different mesh densities: 21.2k, 51.2, 132.6k, and 341.4k elements. The study considered the effects of gap size variations and the shear-thickening rheology by analysing two different diameters, 11 different lengths, 15 different velocities and three rheological models in all combinations. As a result, 2x11x15x3 = 1320 steady state simulations were performed. Mesh independence analysis was performed based on the maximum volume flow rate, and the relative difference in the computed force values was found to be less than 1% between the three finest meshes. Consequently, the mesh with 133.4k cells was selected for all subsequent simulations (see Fig. 1).

2.3.2. Boundary conditions

In the present study, the damper operation was modelled by prescribing a constant velocity at the moving boundary, representing the compression of the damper. The uniform inlet velocity value was defined to have uniform $\tilde{Q}$ relative volume flow rate distribution. Since the working fluid was considered incompressible, the pressure drop remained independent of the absolute pressure level. Therefore, a relative pressure of 0 Pa was imposed at the outlet. No-slip boundary conditions were applied to all solid walls to accurately capture the shear effects within the damping channel.

2.3.3. Numerical options, turbulence model

Turbulence modelling for non-Newtonian fluids presents a significant challenge, as conventional models such as *k-ϵ*, *k-ω*, and *SST* are primarily developed for Newtonian flows. Proper parameter tuning or the development of tailored turbulence models for non-Newtonian behaviour remains an active area of research. However, considering that the analytical approach assumes laminar flow and turbulence is not expected within the studied channel configurations, no additional turbulence model development was employed. Previous studies [18–20] have demonstrated that the SST k-ω model provides reasonable agreement with experimental data for pipe flows; therefore, this model was adopted with the recommended parameter settings. To accurately account for the non-Newtonian viscosity variations, the *strainRateFunction* transport model was employed in the CFD simulations. This approach allowed the viscosity to be directly interpolated from the experimental measurement data rather than relying on an analytical rheological model fit. It is important to emphasize that both the analytical and CFD models utilized raw, pointwise $\tau(\dot{\gamma})$ data instead of assuming a predefined constitutive equation. Numerical discretization schemes were selected to ensure stability and accuracy: the gradient term was

approximated using a Gauss linear scheme, while limited bounded Gauss was used for divergence terms. The Laplacian term was discretized with a Gauss linear orthogonal scheme, and linear interpolation was applied throughout the computational domain.

3. RESULTS

3.1. Rheological results

The rheological behaviour of the prepared STF samples was characterized using an Anton Paar MCR 301 rotational rheometer with a cone-plate measuring system. The viscosity as a function of shear rate was recorded in the range of 0.1 to 10,000 s^{-1} at a constant temperature of 25°C to ensure measurement accuracy and reproducibility.

The results indicate that the STF samples exhibit shear thickening behaviour, see Fig. 2. The flow curve can be divided into three distinct regions: (Region 1) a shear thinning region at low shear rates, (Region 2) a shear thickening region, and (Region 3) a second shear thinning region at higher shear rates. The most relevant segment for this study is the shear thickening region, where two key rheological parameters were identified: the critical shear rate ($\dot{\gamma}_c$), at which shear thickening begins, and the maximum viscosity (η_{max}), marking the end of the thickening process. Additionally, the dilatant effect, defined as the ratio of maximum viscosity to the viscosity at the critical shear rate, was determined as a significant characteristic parameter [21].

These findings confirm the pronounced shear thickening behaviour of the STF samples and highlight the importance of critical shear rate and maximum viscosity in understanding their rheological response. To establish a reference, the dispersion medium without silica—exhibiting Newtonian behaviour—was also measured. As shown in Fig. 2, the viscosity curves of the STF samples (12% and 15% silica concentration) are compared to the Newtonian fluid, illustrating the progressive shear thickening effect with increasing silica content. The addition of silica led to an increase in maximum viscosity and a decrease in the critical shear rate, suggesting that higher silica content results in stronger particle interactions and earlier hydrocluster formation. This rheological response plays a critical role in determining the fluid's performance in damping applications.

Table 1. summarizes the key rheological parameters for each STF sample, including the critical shear rate, maximum viscosity, dilatant effect, and the slope of the viscosity curve in the shear thickening region. These findings emphasize the significant role of silica concentration in modulating the shear thickening behaviour and provide valuable data for further analysis and modelling of STF behaviour in damping systems.

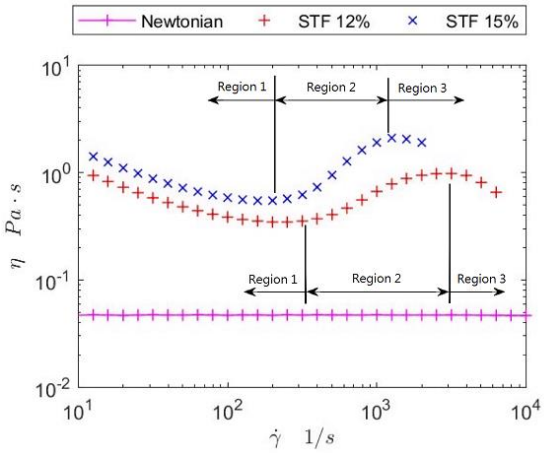

Figure 2. The rheological measurement data of the STF samples and the dispersion medium

Table 1. Critical and maximum rheological values of STF samples and the dispersion medium

	$\dot{\gamma}_c$ [1/s]	η_c [Pa·s]	$\dot{\gamma}_{max}$ [1/s]	η_{max} [Pa·s]	*dilatant effect*
PEG	-	0.46	-	0.46	-
STF12	251	0.35	3160	0.98	2.8
STF15	159	0.55	1260	2.1	3.8

3.2. CFD results

To evaluate the accuracy of the Hagen-Poiseuille equation in predicting the pressure drop across the pipe, CFD simulations were conducted for Newtonian and shear thickening fluids. The results were analysed for various pipe lengths and diameters, with a focus on the relative error

$$e = \left| \frac{\Delta p_{analytical} - \Delta p_{CFD}}{\Delta p_{CFD}} \right| \qquad (12)$$

between the analytical and numerical solutions. This relative error is plotted in the function of L/D relative length and $\tilde{Q} := \frac{Q}{2\pi R^3}$ relative volume flow rate.

3.2.1. Newtonian Fluid Case

Firstly, the flow of the pure PEG-200 liquid was investigated with the Newtonian viscosity of ($\eta = 0.46\ Pas$) In the first subplot of Fig. 3. we plotted the wall shear stress τ_w as a function of the relative flow rate Q̃. The analytical model gives a straight line according to the Eq. (10). The CFD results are marked with cross symbols, which exhibit the same linear relationship. For large L/D ratio the numerical values are aligning well with the analytical solution. However, the error increases as the L/D ratio decreases, indicating that shorter pipes introduce additional effects not accounted for by the Hagen-Poiseuille equation.

The second subplot in Fig. 3. shows the contour plot of the relative error e in the function of the relative volume flow rate and *L/D* ratio. The relative error primarily depends on the length-to-diameter

ratio (*L/D*) and the dependence on the volume flow rate is negligible.

Therefore, we also plotted the error for all of the simulation points in the function of the *L/D* in the third subplot. The points present a second order polynomial behaviour in the function of the *L/D* with R^2 = 0.95 determination coefficient.

As shown in Fig. 3., the error decreases with increasing *L/D*, indicating improved agreement between the analytical and CFD results for longer pipes. For *L/D* > 25, the relative error remains below 5%, suggesting that the Hagen-Poiseuille equation provides a reliable approximation in this range. However, for smaller *L/D* values, the influence of entrance and exit effects leads to higher discrepancies, emphasizing the need for alternative corrections in short pipe configurations.

3.2.2. Shear Thickening Fluid Case

For the shear thickening fluids with 12% (STF 12%) and 15% (STF 15%) concentration, we applied the same evaluation method as in the Newtonian case. Firstly, the flow curves were plotted in the first and second subplot of Figure 4. It is observable that the numerical values marked with cross demonstrate similar behaviour to the analytical curve.

However, the error of the analytical predictions shows a more complex behaviour due to the non-Newtonian viscosity variations. As depicted in the 3rd and 4th panels in Fig. 4, the relative error is strongly influenced by the relative flow rate $\tilde{Q}$ in addition to the *L/D* ratio. Three distinct regions were observed: In *Region 1* (low $\tilde{Q}$ before the thickening range) the error follows a trend similar to the Newtonian case, where longer pipes exhibit better agreement with analytical predictions while the volume flow rate has less significant effect. In *Region 2* (intermediate $\tilde{Q}$, in the thickening region) a sharp reduction in error is observed, likely due to the stabilizing effect of the shear thickening mechanism, which compensates for deviations from the Hagen-Poiseuille assumption. In *Region 3* (high $\tilde{Q}$): The error again follows the Newtonian trend, indicating that at sufficiently high flow rates, the deviations in viscosity do not significantly alter the pressure drop predictions.

A contour plot (Fig. 4) was generated to visualize the relative error as a function of *L/D* for relative volume flow rates corresponding to different regions. The results indicate that for shear thickening fluids, the Hagen-Poiseuille equation derived for the shear thickening fluid can be applied with reasonable accuracy for *L/D* > 50, provided that the flow rate remains outside the critical thickening.

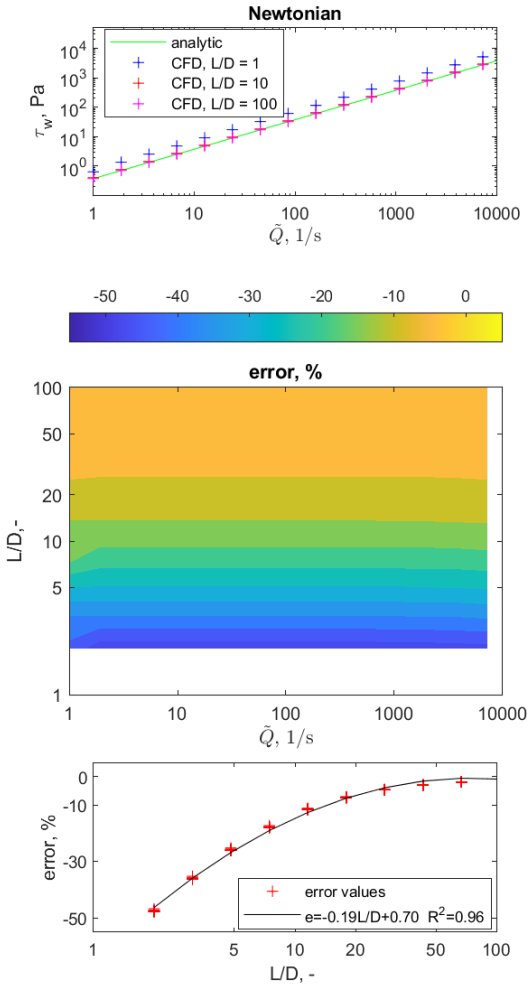

Figure 3. Relative error of the analytical model comparing to CFD results for Newtonian fluid

3.3. Application for Hydraulic Damper Design

The findings from this study provide critical insights into the applicability of the Hagen-Poiseuille law for damper design. For Newtonian fluids, analytical predictions are accurate for *L/D* > 25, while shorter pipes require correction factors to account for entrance and exit effects. For shear thickening fluids, the validity of the Hagen-Poiseuille equation depends not only on *L/D* but also on the flow regime. The equation holds for low and high flow rates but exhibits significant deviations in the thickening region. Industry designing hydraulic dampers with shear thickening fluids should ensure operation within the recommended *L/D* and relative volume flow rate ranges to maintain analytical accuracy.

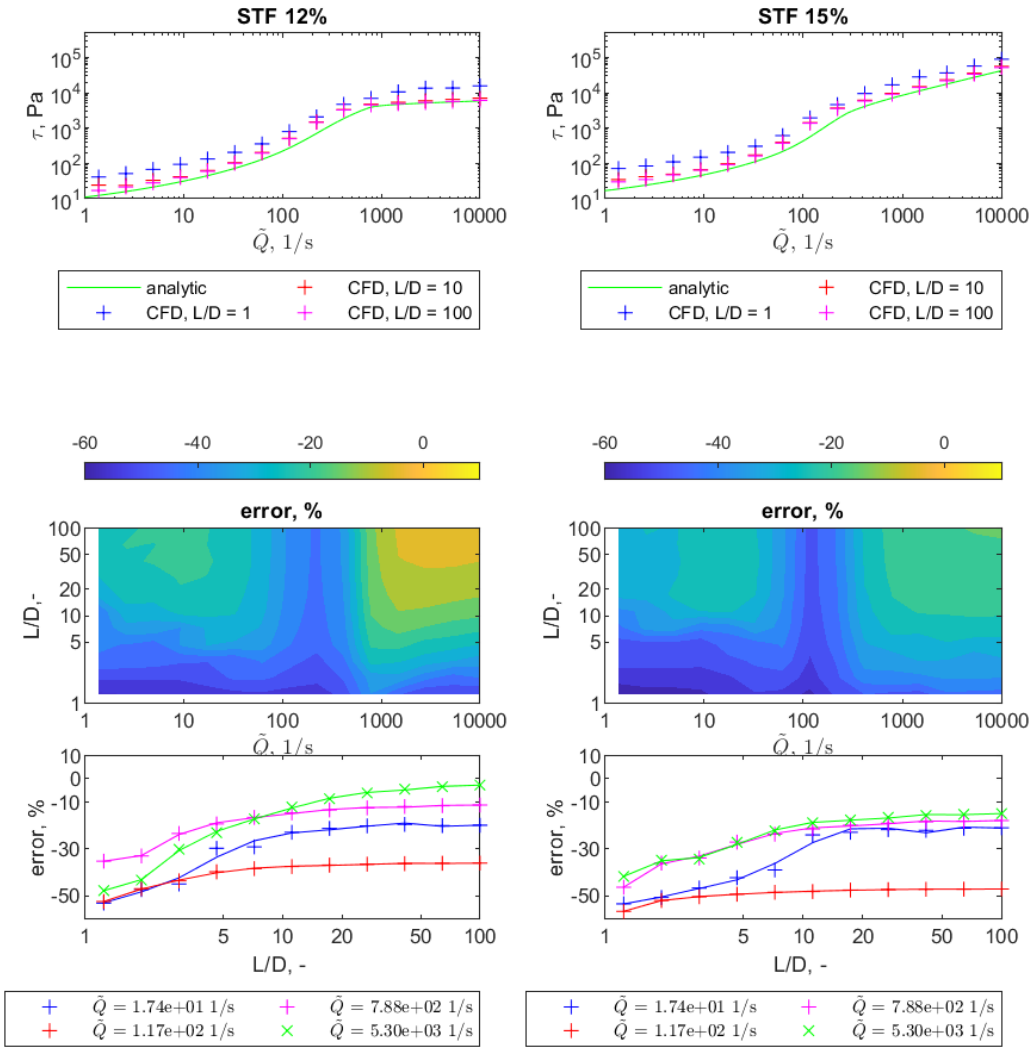

Figure 4. Relative error of analytical and CFD model results for STF12% and STF15%

4. CONCLUSIONS

This study systematically assessed the accuracy of the Hagen-Poiseuille equation in predicting the pressure drop for Newtonian and shear thickening fluids in a pipe flow representative of hydraulic dampers. To achieve this, we prepared shear thickening fluids and measured their rheological properties. We then conducted a series of CFD simulations to calculate the pressure drop for different volume flow rates and various pipe lengths. The error of the analytical approach was evaluated to identify the regions where the assumptions of the analytical derivation remain valid.

For Newtonian fluids, the accuracy of the Hagen-Poiseuille equation depends primarily on the length-to-diameter ratio, with $L/D > 50$ ensuring an error below 5%. For shear thickening fluids, the error is strongly dependent on the relative flow rate, with significant deviations occurring in the thickening region. The equation remains valid for $L/D > 50$ when and the wall shear stress is outside of the shear thickening region. The contour plot of relative error provides a practical guideline for determining the applicability of the analytical approach in damper design.

ACKNOWLEDGEMENTS

This work has been supported by the Hungarian National Research, Development and Innovation Centre under contract No. PD 146259.

REFERENCES

[1] Zhou, H.; Yan, L.; Jiang, W.; Xuan, S.; Gong, X.: Shear thickening fluid-based energy-free damper: Design and dynamic characteristics. Journal of Intelligent Material Systems and Structures, **27**, 208–220 (2016). http://doi:10.1177/1045389X14563869.

[2] Zhang, X. Z.; Li, W. H.; Gong, X. L.: The rheology of shear thickening fluid (STF) and the dynamic performance of anSTF-filled damper. Smart Materials and Structures, **17**

(2008). http://doi:10.1088/0964-1726/17/3/035027.

[3] Yang, J.; Sun, S.; Li, W.; Du, H.; Alici, G.; Nakano, M.: Development of a linear damper working with magnetorheological shear thickening fluids. http://dx.doi.org/10.1177/1045389X15577653, **26**, 1811–1817 (2015). http://doi:10.1177/1045389X15577653.

[4] Yeh, Y.; Chang, K.-C.; Chen, T.-W.: *Smart Viscous Dampers utilizing Shear Thickening Fluids with Silica Nanoparticles*;

[5] Wei, M.; Lin, K.; Guo, Q.; Sun, H.: Characterization and performance analysis of a shear thickening fluid damper. Measurement and Control (United Kingdom), **52**, 72–80 (2019). http://doi:10.1177/0020294018819543/ASSET/IMAGES/LARGE/10.1177_00202940188195 43-FIG8.JPEG.

[6] Wei, M.; Lin, K.; Liu, H.: Experimental investigation on hysteretic behavior of a shear thickening fluid damper. Structural Control and Health Monitoring, **26**, e2389 (2019). http://doi:10.1002/STC.2389.

[7] Gucuyener, I. H.; Gurcay, O. K.; Yanik, S.: A Comprehensive Evaluation of Rheological Models for Non-Aqueous Drilling Fluids. Proceedings of the International Conference on Offshore Mechanics and Arctic Engineering - OMAE, **10** (2022). http://doi:10.1115/OMAE2022-78546.

[8] Gómez, J. R.; Escandón, J. P.; Jimenez, E. M.; Torres, D. A.: Hydrodynamic Analysis of a Magnetorheological Squeeze Film Damper Using the Herschel-Bulkley Model and the Short Bearing Approximation. ASME International Mechanical Engineering Congress and Exposition, Proceedings (IMECE), **8** (2025). http://doi:10.1115/IMECE2024-144750.

[9] Hou, C.-Y.: Fluid Dynamics and Behavior of Nonlinear Viscous Fluid Dampers. http://doi:10.1061/ASCE0733-94452008134:156.

[10] Nagy-György, P.; Hős, C.: Predicting the damping characteristics of vibration dampers employing generalized shear thickening fluids. Journal of Sound and Vibration, **506**, 116116 (2021). http://doi:10.1016/J.JSV.2021.116116.

[11] Gao, H.; Chi, M.; Dai, L.; Yang, J.; Zhou, X.: Mathematical Modelling and Computational Simulation of the Hydraulic Damper during the Orifice-Working Stage for Railway Vehicles. Mathematical Problems in Engineering, **2020**, 1830150 (2020). http://doi:10.1155/2020/1830150.

[12] Zhao, Q.; He, Y.; Yao, H.; Wen, B.: Dynamic performance and mechanical model analysis of a shear thickening fluid damper. Smart Materials and Structures, **27** (2018). http://doi:10.1088/1361-665X/aac23f.

[13] Wei, M.; Lin, K.; Liu, H.: Experimental investigation on hysteretic behavior of a shear thickening fluid damper. Structural Control and Health Monitoring, **26** (2019). http://doi:10.1002/stc.2389.

[14] Galindo-Rosales, F. J.; Rubio-Hernández, F. J.; Velázquez-Navarro, J. F.: Shear-thickening behavior of Aerosil® R816 nanoparticles suspensions in polar organic liquids. Rheologica Acta, **48**, 699–708 (2009). http://doi:10.1007/s00397-009-0367-7.

[15] Fayed, H. E.; Sheikh, N. A.; Iliev, O.: On Laminar Flow of Non-Newtonian Fluids in Porous Media. Transport in Porous Media, **111**, 253–264 (2016). http://doi:10.1007/S11242-015-0592-8/FIGURES/7.

[16] Güzel, B.; Frigaard, I.; Martinez, D. M.: Predicting laminar–turbulent transition in Poiseuille pipe flow for non-Newtonian fluids. Chemical Engineering Science, **64**, 254–264 (2009). http://doi:10.1016/J.CES.2008.10.011.

[17] User Guide Available online: https://www.openfoam.com/documentation/user-guide (accessed on Feb 20, 2025).

[18] Csizmadia, P.; Hos, C.: CFD-based estimation and experiments on the loss coefficient for Bingham and power-law fluids through diffusers and elbows. Computers & Fluids, **99**, 116–123 (2014). http://doi:10.1016/J.COMPFLUID.2014.04.004.

[19] Csizmadia, P.; Till, S.; Paál, G.: CFD-based investigation on the flow of Bingham plastic fluids through 90 ∘ bends. Journal of the Brazilian Society of Mechanical Sciences and Engineering, **45**, 1–13 (2023). http://doi:10.1007/S40430-023-04121-0/FIGURES/10.

[20] Csizmadia, P.; Dombóvári, G.; Till, S.; Minkó, M.: CFD-based Estimation of Friction Factor in Rough Pipes with Herschel-Bulkley Fluids. Periodica Polytechnica Chemical Engineering, **67**, 74–82 (2023). http://doi:10.3311/PPCH.20857.

[21] David Moriana, A.: *Fabrication, characterisation and optimisation of shear thickening fluids*;

Conference on Modelling Fluid Flow (CMFF'25)
The 19th International Conference on Fluid Flow Technologies
Budapest, Hungary, August 26-August 29, 2025

EVALUATION OF CAROTID PLAQUE MORPHOMETRY AND HEMODYNAMICS

Benjamin CSIPPA[1], Márton NÉMETH[1], György PAÁL[1], Zsuzsanna MIHÁLY[2]

[1] Department of Hydrodynamic Systems, Faculty of Mechanical Engineering, Budapest University of Technology and Economics. Műegyetem rkp. 3., H-1111, Budapest, Hungary. E-mail: bcsippa@hds.bme.hu (Corresponding Author), mnemeth@hds.bme.hu, paal@hds.bme.hu
[2] Department of Vascular Surgery, Heart and Vascular centre, Faculty of Medicine, Semmelweis University. E-mail: mihaly.zsuzsanna@med.semmelweis-univ.hu

ABSTRACT

Carotid artery disease is a narrowing in the vessel that forms due to the accumulation of plaque material on the wall of the vessel. These obstructions present a risk of stroke and decrease blood flow into the brain circulation. One of the usual treatments is carotid endarterectomy when a vascular surgeon removes the plaque during open wound surgery.

In this study, we are interested in the relationship between plaque morphometry and hemodynamics in the arterial section. For this purpose, we must develop a capable evaluation technique encompassing the hemodynamic and morphometric quantities in a common reference frame along the arterial centerline. Previously, we developed a solution to evaluate hemodynamic quantities in the geometrical framework of the centerline. Now, we extend this framework to include the geometrical characterization of the plaque morphometry.

Data on plaque morphometry were acquired with VascuCap (now ElucidVivo), a commercial tool that automatically detects plaque characteristics from CT images of the carotid artery. The hemodynamics is calculated with the finite-volume solver of Ansys CFX. With this technique, we can connect the properties of the plaque material to the hemodynamic indices and understand how the characteristics of the plaque material are connected to the dynamic load of the fluid.

Keywords: carotid artery, CFD, hemodynamics, plaque morphometry

NOMENCLATURE

CEA	$[-]$	Carotid endarterectomy
div_W	$[-]$	Wall Shear Stress divergence
LSA	$[-]$	Low time-averaged WSS area
OSI	$[-]$	Oscillatory Shear Index
$\underline{\tau}$	$[Pa]$	wall shear stress vector
$\underline{e}$	$[-]$	wall cell unit vectors
$\underline{FR_t}$	$[-]$	Frenet tangent unit vector
WSS	$[Pa]$	Wall Shear Stress
C	$[m^3/Pa]$	compliance
R_1	$[Pas/m^3]$	Proximal resistance
R_2	$[Pas/m^3]$	distal resistance

Subscripts and Superscripts
b, n, t normal, binormal, tangential

1. INTRODUCTION

Wall Shear Stress (WSS) characterisation of the carotid artery bifurcation has been the centre of scrutiny for a number of years as it has been identified to be linked with atherosclerosis [1, 2, 3] . Carotid stenosis can present a severe risk for stroke since, in the event of plaque rupture, the lipid-rich necrotic core can enter the bloodstream, causing a blockage in the distal vasculature. Treatment can be either vascular stenting or carotid endarterectomy (CEA). In the case of CAE, the surgeon removes the plaque entirely with an open wound surgery, reconstructing the bifurcation. In the literature, research has investigated a number of WSS metrics to identify possible susceptibility factors for carotid stenosis or even the risk of long-term restenosis. Low time-averaged WSS area (LSA) and oscillatory WSS index (OSI) are significant independent risk factors. Furthermore, recently, the divergence of the time-averaged WSS vector field (div_W) gained significant interest as div_W can show the topological skeleton of the WSS field [4] by identifying WSS fixed points and corresponding stable/unstable manifolds around the contraction and expansion regions.

The present study explores and expands these WSS metrics by further analysing the WSS field according to the vessel centerline direction to understand the effect of WSS directionality. WSS directionality was previously proposed by [5], yet not in the context of analysing the hemodynamics of the carotid artery stenosis. This pilot study ties together several evaluation metrics to understand the hemo-

dynamic behaviour affecting the vascular biology.

Additionally, plaque morphometry was calculated using VascuCap, the CT-based technology from Elucid Bio. The aim is to connect the information on plaque composition with hemodynamic modeling to understand the formation of atherosclerotic lesions. In this pilot study, the necessary workflow was built to evaluate the plaque morphometry within the same computational coordinate system of the hemodynamic simulation. In the future, the objective is to analyse a larger patient cohort with the developed methods.

2. METHODS

2.1. Geometry & CFD

A patient who underwent CEA procedure at the Heart and Vascular centre of Semmelweis University were selected for this study. The hospital ethics committee approved the study, and patients provided informed consent. CT-angiography was performed to obtain the pre-CEA and post-CEA 3D geometry by manual segmentation in Slicer (www.slicer.org), followed by surface mesh post-processing in the Vascular Modeling Toolkit (VMTK, www.vmtk.org). The pre-CEA images were used for the VascuCap analysis. The analysis only captured the ICA side of the bifurcation in a range set by the operator, a vascular surgeon. Multiple regions of vasculature and plaque can be analysed with the technology, but for this study, only the plaque composition was used. Namely, the calcified (Ca*) and the lipid-rich necrotic core (LRNC) regions. The pre-and post-CEA geometries with the pre-CEA plaque composition can seen in Figure 1.

Transient CFD simulations were carried out using the ANSYS CFX solver based on the finite volume method. Numerical meshes were created in ANSYS, containing approximately 5 million tetrahedral numerical cells with seven prismatic layers next to the vessel wall. In the present study, mesh independence was not studies. According to the literature, a numerical mesh containing five million numerical cells is well above the usual considerations[6]. Here, we adopted the larger mesh count to adeaquatley calculate the divergence of the WSS. Blood was modeled as a homogenous Newtonian fluid with a density and viscosity of 1055 kg/m^3 and 3.4 $mPa\ s$, respectively. Since the Reynlods numbers are below 1500, it was assumed that the flow is laminar, hence tubulence models were not considered for the simulations. The vessel wall as assumed to be rigid, which is a usual assumption in the literature. Doppler ultrasound velocimetry was used to extract velocity waveforms at the CCA before CEA and used as inlet boundary conditions for the transient simulations. Three-element Windkessel outlet boundary conditions [7] were set on the internal and external carotid arteries (ICA, ECA) with the following parameters:

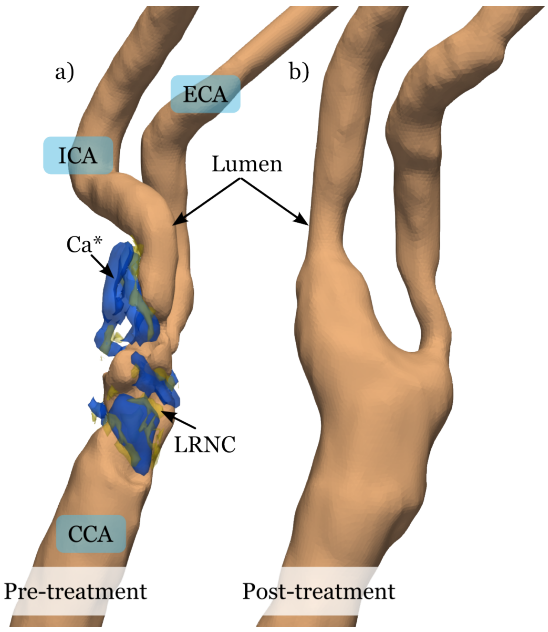

Figure 1. Patient-specific geometry before (a) and after (b) the endarterectomy procedure. Besides the lumen (fluid domain), the calcified (Ca*) region and the lipid-rich necrotic core (LRNC) are visualized with opaque blue and yellow surfaces.

Table 1. Three-element Windkessel paramaters. Proximal resistance R_1, distal resistance R_2 and compliance C for the internal and external carotid artery boundary.

	$R_1\ [Pas/m^3]$	$R_2\ [Pas/m^3]$	$C\ [m^3/Pa]$
ICA	10^8	10^9	10^{-10}
ECA	10^9	10^{10}	10^{-11}

Second-order spatial and temporal discretisation schemes were used, and 5000 time steps were simulated [8]. Three cardiac cycles were computed, and the last was used for further evaluation. The results were exported in vtk format for post-processing with our Python-based workflow.

2.2. WSS characterization

The PyVista Python package was used to develop automated evaluations. Since the WSS field will be evaluated, the surface elements were only extracted from the numerical domain. The unit vectors normal to the wall e_n were calculated for each numerical cell on the surface. Similarly, as in Arzani and Shadden [5], to construct an intrinsic orthonormal coordinate frame (e_n, e_t, e_b) to follow the centerline direction that varies along the vessel surface. The tangential unit vector e_t that mostly aligns with the centerline tangent vector Fr_t can be calculated as follows:

$$\mathbf{e_t} = \frac{\mathbf{Fr_t} - (\mathbf{Fr_t} \cdot \mathbf{e_n})\mathbf{e_n}}{\|\mathbf{Fr_t} - (\mathbf{Fr_t} \cdot \mathbf{e_n})\mathbf{e_n}\|} \tag{1}$$

where $\mathbf{Fr_t}$ is the tangent unit of the closest centerline point transfered to the associated surface cell. Corresponding centerline points and the associated $\mathbf{Fr_t}$ unit vectors are calculated using the CKDTree algorithm and transferred as a vector field on the surface to compute the above equation for each cell. Consequantly, the $\mathbf{e_b}$ the binormal unit vector can be calculated as $\mathbf{e_b} = \mathbf{e_t} \times \mathbf{e_n}$. Using these unit vectors, the WSS vector can be decomposed into a tangential and a binormal direction as:

$$\boldsymbol{\tau} = (\boldsymbol{\tau} \cdot \mathbf{e_t})\mathbf{e_t} + (\boldsymbol{\tau} \cdot \mathbf{e_b})\mathbf{e_b} = \boldsymbol{\tau}_t + \boldsymbol{\tau}_b \tag{2}$$

Here, we want to remark that the decomposition is only valid for the CCA before the bifurcation and on the ICA side since only the centerline going from the CCA to the ICA was considered in this pilot study. The integral average along the cardiac cycle can compute the time-averaged quantities:

$$\|\overline{\boldsymbol{\tau}_t}\| = \left\| \frac{1}{T} \int_0^T \boldsymbol{\tau}_t dt \right\| \tag{3}$$

and for $\|\overline{\boldsymbol{\tau}_b}\|$:

$$\|\overline{\boldsymbol{\tau}_b}\| = \left\| \frac{1}{T} \int_0^T \boldsymbol{\tau}_b dt \right\| \tag{4}$$

Figure 2 demonstrates the the $\overline{\boldsymbol{\tau}_t}$ and $\overline{\boldsymbol{\tau}_b}$ vector fields using the Post-CEA geometry as an example.

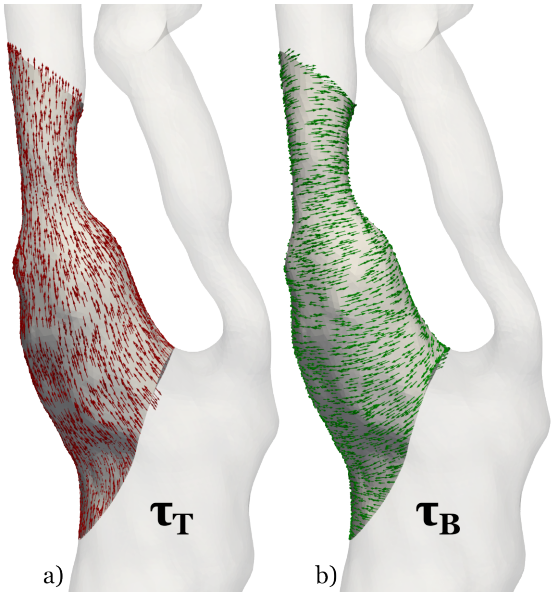

Figure 2. $\overline{\boldsymbol{\tau}_t}$ (a) and $\overline{\boldsymbol{\tau}_b}$ (b) vector fields on the luminal surface of the post-CEA geometry.

Continuing with the definition of the usual WSS parameters used in the literature: $\|\overline{\boldsymbol{\tau}}\|$ is the magnitude of the cycle-averaged WSS vector:

$$\|\overline{\boldsymbol{\tau}}\| = \left\| \frac{1}{T} \int_0^T \boldsymbol{\tau} dt \right\| \tag{5}$$

The time-averaged WSS magnitude is defined as:

$$TAWSS = \frac{1}{T} \int_0^T \|\boldsymbol{\tau}\| dt \tag{6}$$

where T is the time of the cardiac cycle. The oscillatory shear index (OSI) is as follows:

$$OSI = \frac{1}{2}\left(1 - \frac{\|\overline{\boldsymbol{\tau}}\|}{TAWASS}\right) \tag{7}$$

Finally, the divergence of the WSS vector can be calculated to visualize the WSS contraction and expansion regions:

$$div_W = \nabla \cdot \hat{\boldsymbol{\tau}} \tag{8}$$

where $\hat{\boldsymbol{\tau}}$ is the normalized instantaneous WSS vector field on the luminal surface. In the following, an example of the use of these metrics will be demonstrated on the carotid geometry of the patient. Pre-CEA and post-CEA visualizations are confined to the domain close to the carotid bifurcation region. Plaque composition will only be shown for the OSI and div_W metrics to showcase the connection with the WSS vectorial behavior.

3. RESULTS & DISCUSSION

In Figure 3, a threshold area of the TAWSS field can be seen as the Low Shear Area (LSA) corresponding to regions where TAWSS is lower than 3 *Pa*. There is a clear difference between the pre-CEA and post-CEA LSA variation.

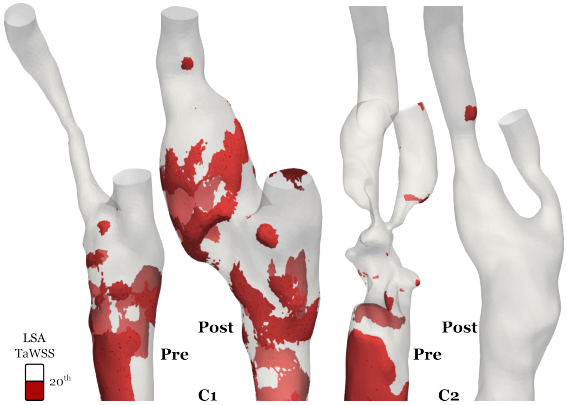

Figure 3. Low WSS area (LSA) with a threshold set at 20th percentile of TaWSS of the accumulated all values from all cases, before (a) and after (b) the CEA procedure.

In the diseased state, multiple recirculation zones are present due to the shape modification of severe stenosis. Following the CEA procedure, these spots of recirculation zones disappeared as the carotid bulb was reconstructed, and only one large vortical region was present in the bulb. A further change in LSA can be attributed to the geometrical difference between

the parent artery before and after the CEA procedure. The shape of the ICA significantly changed after the procedure as the artery became less tortuous, hence the more uniform flow features and WSS field.

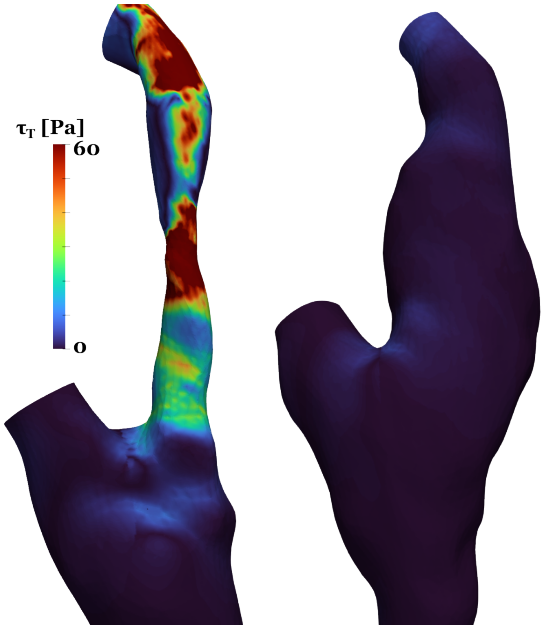

Figure 4. Time-averaged tangential WSS vector field $\|\overline{\tau_t}\|$, before (a) and after (b) the CEA procedure for case C1.

In Figure 4, 5 and 6, 7 the time-averaged decomposition of the WSS field can be seen, the $\|\overline{\tau_t}\|$ and $\|\overline{\tau_b}\|$, respectively. In the stenosis region, both the tangential and binormal components indicate a strong swirling flow, possibly due to the complex shape of the lumen in the atherosclerotic carotid bulb. Disturbed flow features emerge due to the deformed shape of the lumen at the carotid bulb. Therefore, the magnitude of both the tangential and binormal components of the WSS field is high in this region since the inflow region is highly disturbed. It can be seen that before the stenosis, the binormal component dominates as small-scale counter-rotating recirculation zones precede in the different pockets, depicted by the lines of near-zero $\|\overline{\tau_b}\|$ values where the WSS vector component changes direction.

The binormal and tangential WSS on the luminal surface also show that after the CEA procedure, the tangential WSS component will dominate in the slightly stenosed vessel segment. The binormal $\|\overline{\tau_b}\|$ component decreased substantially in the stenosis as less disturbed flow enters the narrowing region. The reconstruction after the CEA procedure of the carotid bulb fundamentally changed the flow and WSS field. Due to the decreased velocity in the segment, the tangential component becomes directionally stable without large zones of backflow. The binormal component displays the expected features of the secondary flow phenomenon as a consequence of the bifurcation. The topology of the WSS vector field after the CEA procedure resembles what would be expected in a healthy state. However, further investigation is needed to understand long-term outcomes in the presence of mild stenosis after the reconstruction.

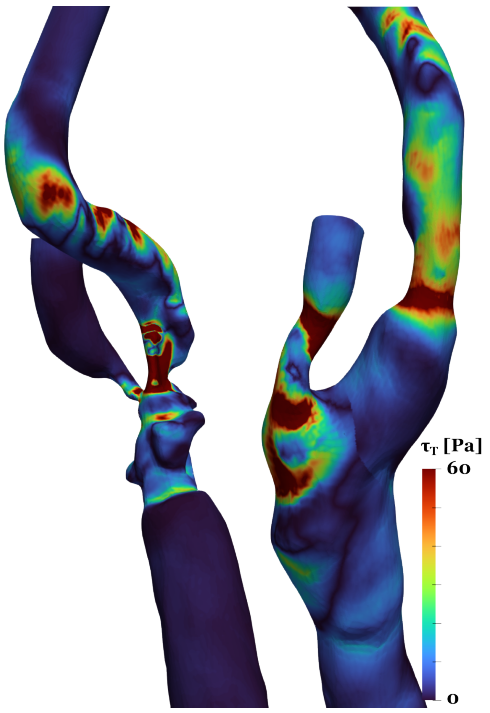

Figure 5. Time-averaged tangential WSS vector field $\|\overline{\tau_t}\|$, before (a) and after (b) the CEA procedure for case C2.

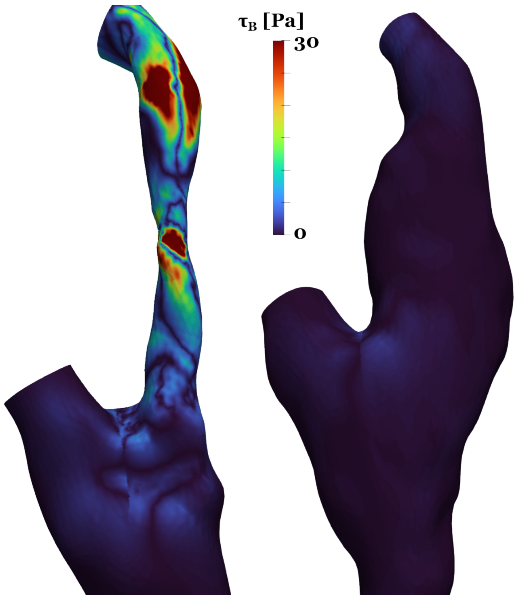

Figure 6. Time-averaged tangential WSS vector field $\|\overline{\tau_b}\|$, before (a) and after (b) the CEA procedure for case C1.

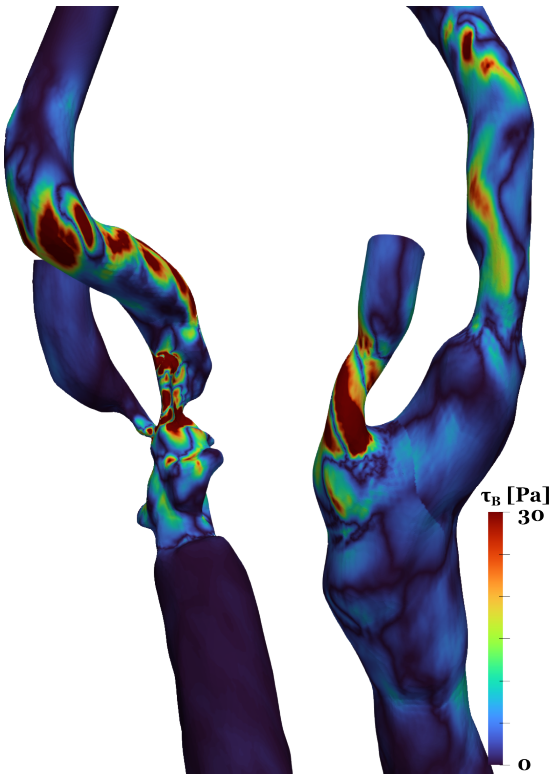

Figure 7. Time-averaged tangential WSS vector field $\|\overline{\tau_b}\|$, before (a) and after (b) the CEA procedure for case C2.

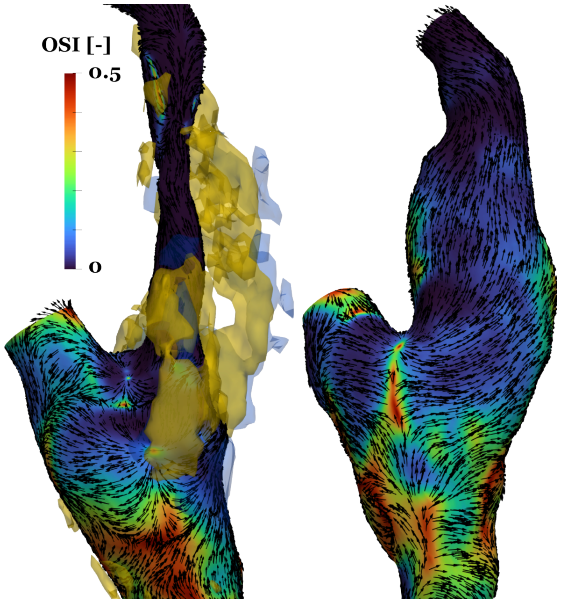

Figure 8. Oscillatory Shear Index (OSI) on the luminal surface for case C1. The time-averaged WSS field is visualized by normalized arrows (black). Besides the lumen (fluid domain), the calcified (Ca*) region and the lipid-rich necrotic core (LRNC) are visualized with opaque blue and yellow surfaces.

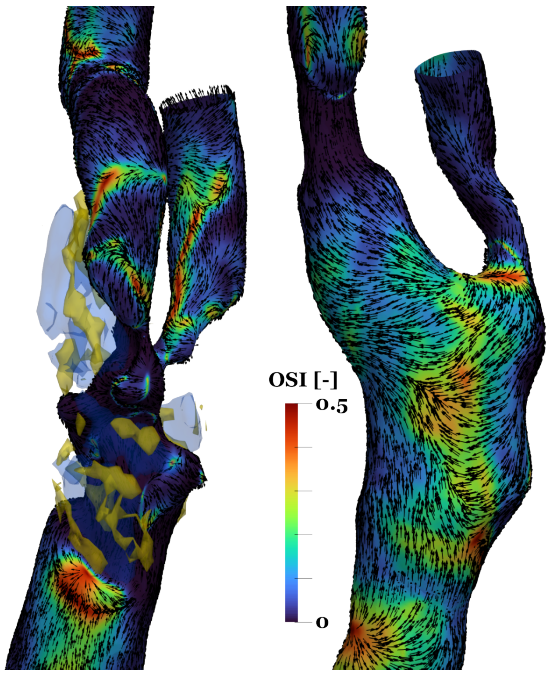

Figure 9. Oscillatory Shear Index (OSI) on the luminal surface for case C1. The time-averaged WSS field is visualized by normalized arrows (black). Vector visualization according to the previous image.

In Figure 8 and 9, the temporal behavior of the WSS field is expressed with the oscillatory shear index. By definition, the index measures the temporal variability of the pointwise directionality change of the WSS vectors. Close to zero values correspond to stable WSS vector directionality, while close to 0.5, the vector has no preferred directions throughout the cardiac cycle. The largest difference comparing the diseased and surgically reconstructed cases is the apparent small values of OSI in the atherosclerotic regions. Case 1: Large regions of oscillatory behaviour can be observed, known to be susceptible to later restenosis formation [9]. Another observation based on OSI maps is that the plaque material accumulated mostly in regions of low OSI. However, a cause-and-effect relationship cannot be drawn from the observation, as the formation of atherosclerotic plaques is not yet understood.

In Figure 10 and 11, the divergence of the WSS vector field can be observed. The WSS contraction/expansion regions are denoted with colder/warmer colors. According to our observations, stronger contraction regions were identified in the atherosclerotic region, both in the carotid bulb and near the stenosis. The post-CEA cases display a stronger expansion region at the apex of the bifurcation and only weaker contraction regions in the carotid bulb. The effect of expansion/contraction on vascular biology needs further quantitative analysis, as according to the literature [4, 2], this WSS-related

action can be connected to the formation of atherosclerosis.

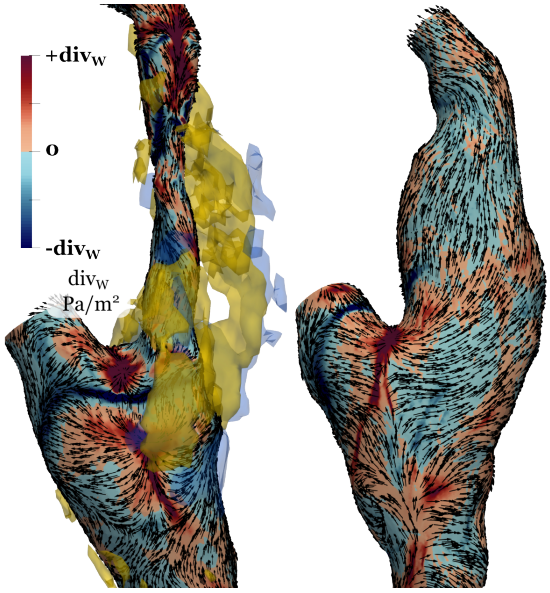

Figure 10. Wall Shear Stress divergence (div_W) on the luminal surface for case C1. The time-averaged WSS field is visualized by normalized arrows (black). Besides the lumen (fluid domain), the calcified (Ca*) region and the lipid-rich necrotic core (LRNC) are visualized with opaque blue and yellow surfaces.

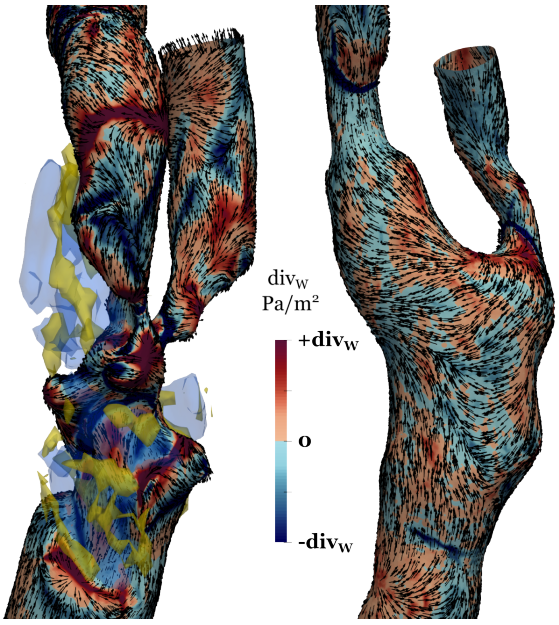

Figure 11. Wall Shear Stress divergence (div_W) on the luminal surface for case C2. Vector visualization according to the previous image.

4. SUMMARY

This pilot study investigates the relationship between plaque morphometry and hemodynamics in the carotid artery, focusing on patients undergoing carotid endarterectomy (CEA). An evaluation method was developed to analyze the interaction between plaque composition and blood flow dynamics, integrating morphometric data from VascuCap (now ElucidVivo) with hemodynamic simulations. Wall shear stress (WSS) characterization was achieved by decomposing the vector field along the vessel centerline to understand the emergence of globally interpreted standard hemodynamic parameters, including time-averaged WSS (TAWSS), oscillatory shear index (OSI), and WSS divergence (div_W). This new insight can shed light on the interplay between directional WSS metrics, oscillatory behaviour [10], and vascular biology. The results demonstrated that CEA significantly alters the WSS field, reducing the spurious appearance of low-shear areas and stabilizing flow patterns. The reconstructed artery exhibited a more uniform WSS distribution, particularly in regions previously affected by stenosis.

This pilot study established the methodology for integrating morphometric and hemodynamic data within a unified computational framework. Future work will expand the analysis to a larger patient cohort to understand the cause-and-effect relationship between hemodynamic metrics and plaque formation.

ACKNOWLEDGEMENTS

This research was funded by NKFI-PD23 146299 grant between 2024 and 2027. NKFI: Nemzeti Kutatási Fejlesztési és Innovációs Hivatal/ National Research, Innovation and Development Office

REFERENCES

[1] Gallo, D., Steinman, D. A., and Morbiducci, U., 2016, “Insights into the co-localization of magnitude-based versus direction-based indicators of disturbed shear at the carotid bifurcation”, *Journal of biomechanics*, Vol. 49 (12), pp. 2413–2419.

[2] Morbiducci, U., Mazzi, V., Domanin, M., De Nisco, G., Vergara, C., Steinman, D. A., and Gallo, D., 2020, “Wall shear stress topological skeleton independently predicts long-term restenosis after carotid bifurcation endarterectomy”, *Annals of biomedical engineering*, Vol. 48, pp. 2936–2949.

[3] Lee, S.-W., Antiga, L., Spence, J. D., and Steinman, D. A., 2008, “Geometry of the carotid bifurcation predicts its exposure to disturbed flow”, *Stroke*, Vol. 39 (8), pp. 2341–2347.

[4] Mazzi, V., Gallo, D., Calò, K., Najafi, M., Khan, M. O., De Nisco, G., Steinman,

D. A., and Morbiducci, U., 2020, "A Eulerian method to analyze wall shear stress fixed points and manifolds in cardiovascular flows", *Biomechanics and Modeling in Mechanobiology*, Vol. 19 (5), pp. 1403–1423.

[5] Arzani, A., and Shadden, S. C., 2016, "Characterizations and correlations of wall shear stress in aneurysmal flow", *Journal of biomechanical engineering*, Vol. 138 (1), p. 014503.

[6] El Sayed, R., Sharifi, A., Park, C. C., Haussen, D. C., Allen, J. W., and Oshinski, J. N., 2023, "Optimization of 4D flow MRI spatial and temporal resolution for examining complex hemodynamics in the carotid artery bifurcation", *Cardiovascular engineering and technology*, Vol. 14 (3), pp. 476–488.

[7] Vignon-Clementel, I. E., Figueroa, C., Jansen, K., and Taylor, C., 2010, "Outflow boundary conditions for 3D simulations of non-periodic blood flow and pressure fields in deformable arteries", *Computer methods in biomechanics and biomedical engineering*, Vol. 13 (5), pp. 625–640.

[8] Mancini, V., Bergersen, A. W., Vierendeels, J., Segers, P., and Valen-Sendstad, K., 2019, "High-Frequency Fluctuations in Post-stenotic Patient Specific Carotid Stenosis Fluid Dynamics: A Computational Fluid Dynamics Strategy Study", *Cardiovasc Eng Technol*, Vol. 10 (2), pp. 277–298.

[9] Domanin, M., Gallo, D., Vergara, C., Biondetti, P., Forzenigo, L. V., and Morbiducci, U., 2019, "Prediction of long term restenosis risk after surgery in the carotid bifurcation by hemodynamic and geometric analysis", *Annals of biomedical engineering*, Vol. 47, pp. 1129–1140.

[10] Morbiducci, U., Kok, A. M., Kwak, B. R., Stone, P. H., Steinman, D. A., and Wentzel, J. J., 2016, "Atherosclerosis at arterial bifurcations: evidence for the role of haemodynamics and geometry", *Thrombosis and haemostasis*, Vol. 115 (03), pp. 484–492.

Conference on Modelling Fluid Flow (CMFF'25)
The 19th International Conference on Fluid Flow Technologies
Budapest, Hungary, August 26-August 29, 2025

Impact of Wave Directionality and Inter-Device Spacing on the Performance of Wave Energy Converter Arrays

Anulekha Majumdar[1], Govindarajulu Venkatesan[2], Abdus Samad[3]

[1] Corresponding Author. Ocean Engineering Department, IIT Madras, Chennai, India, Energy and Fresh Water Department, National Institute of Ocean Technology, Chennai, India. E-mail: anulekha.niot@gmail.com
[2] Energy and Fresh Water Department, National Institute of Ocean Technology, Chennai, India. E-mail: gvenkat@niot.res.in
[3] Ocean Engineering Department, IIT Madras, Chennai, India. E-mail: samad@iitm.ac.in

ABSTRACT

It is well known that there is no significant effect on the wave power extraction from individual devices beyond a certain spacing between the wave energy converters (WEC) in an array, as destructive interference is reduced. However, this arrangement would require a huge amount of money, which would have cost implications. Moreover, restrictions in the available area might limit this arrangement. Hence, exploring alternate wave spacing arrangements is required to optimize the layout. There is no effect of wave directionality on the power obtained for a single-point absorber wave energy device. However, when considering a wave farm, the WEC layout will be affected by the direction of incoming waves. Studies have shown that for the Indian coast, the maximum wave power is observed during the monsoon period, from waves originating from wave direction between 245 - 270 °, which are South westerlies. Thus, it is imperative to consider the wave direction as an important parameter. The paper aims to study the effect of wave directionality, WEC spacing, and layout on wave power. A two-body point absorber is considered for the study.

Keywords: hydrodynamic analysis, point absorbers, time domain simulation, wave energy converter farms, wave farm layout

NOMENCLATURE

F_e	$[N]$	excitation force
F_{ext}	$[N]$	external force
F_{hs}	$[N]$	hydrostatic restoring force
F_r	$[N]$	radiation force
F_v	$[N]$	viscous drag force
g	$[m/s^2]$	Earth's acceleration
m	$[kg]$	mass matrix
m_a	$[kg]$	added mass matrix
ω	$[rad/s]$	wave frequency
ϕ	$[m^2/s]$	velocity potential function
ϕ_D	$[m^2/s]$	diffraction wave potential
ϕ_I	$[m^2/s]$	incident wave potential
ϕ_R	$[m^2/s]$	radiation wave potential
τ	$[s]$	past time
ζ	$[m]$	motion amplitude
A_∞	$[kg]$	instantaneous added mass effect
d	$[m]$	water depth
j	[]	degree of freedom
$K(t-\tau)$	$[kg/s]$	Impulse response function
n	$[m^2/s]$	unit normal vector of the body surface pointing outwards
t	$[s]$	present time
x	$[m]$	position vector
Z	$[m]$	vertical coordinate of a wetted surface

Abbreviations

BEM	Boundary element method
BEMIO	Boundary element method Input/Output
IRF	Impulse response function
JONSWAP	Joint North Sea Wave Project
LA	Line absorber
PA	Point absorber
PTO	Power take-off
WEC	Wave energy converter

1. INTRODUCTION

Wave energy is a renewable energy source that is available in abundance from the oceans. It has a very high energy density; however, the waves are highly dynamic in nature. For the coastal areas near the equator, the waves have lower heights, resulting in lower extractable power. India is such a place. However, it has a vast coastline, with many places having higher wave activity. In addition, many coastal areas lack adequate power and drinking water facilities. Hence, the coastal areas can be supplied with power by utilising a wave energy converter (WEC),

which converts the motion of the waves into electricity in a sustainable way. An optimised array of WEC can extract power from waves on a MW scale. This power can then be used for many things, such as generating potable water from the oceans. Several studies have carried out life cycle analyses for conventional fossil fuel electricity plants and a wave energy farm and reported a 20-40 times reduction in the carbon footprint. To reach the stage of commercialization, WECs need to be grouped in a particular arrangement, considering the wave conditions, the hydrodynamic interactions of the devices, and the cost of the technology. Using models and machine learning techniques, a single wave energy device has previously been optimized for its shape, control method, and power take-off (PTO) system.

1.1. Literature review

Budal conducted the first study on wave arrays [1]. He introduced the concept of point absorber theory and coined the term interaction factor or q factor, which is defined as the power produced by the array to the sum of the power produced by the devices when present individually. q>1 signifies constructive interference, and q<1 represents destructive interference. Thereafter, Falnes [2] and Evans [3] carried out studies on point absorber (PA) arrays to obtain a *q factor* of more than 1. McIver [4] in 1994 studied the change of the q factor with changing wave direction. He also studied the effect of equal and unequal spacing between WECs. Fitzgerald and Thomas [5], in 2007, conducted a study on five WECs considering the effect of the geometry of the WEC and the direction of the wave.

India has a wave energy potential of 40 GW [6], with the southern tip having the highest potential. Researchers studied various WECs for various locations along the Indian coast, for offshore and nearshore conditions [7, 8], and observed that multibody PA and line absorbers (LA) performed better for nearshore and offshore locations, respectively. However, in these studies, a single WEC was considered, with no effect of the directional characteristics or the hydrodynamic changes owing to other devices in the array. In addition, the significant wave height considered was less than 1.5 m, when the maximum significant wave height occurring in the Indian coastal waters can go up to 3 m. Waves of maximum height were also observed to come from 245 - 270 ° [9]. So, it is imperative to understand the effect on power produced due to changing wave direction and the presence of multiple WECs.

Cruz et al. [10] analysed a single-body PA farm with 4 WECs arranged in a square layout for regular and irregular waves. Regular waves are sinusoidal waves with the same wave height and period. Irregular waves can be defined as the superposition of many regular waves of different wave heights and periods. By changing the incident wave angle and applying suboptimal control of the external damping coefficient, they observed a 4% increase in power when the direction was changed from 90 to 45 °. De Andres et al. [11] studied a farm layout of 2-body WEC for optimizing the q factor by analysing wave layout, spacing, the number of WECs, and wave direction. Increasing the number of WECs increased the q factor. The highest q factor was obtained for half of the wavelength of the incident wave; triangle or rhombus layouts were good for multidirectional waves, and square for unidirectional waves; q factor results were similar for triangle and square layouts. Ji et al. [12] studied a circular layout for a six two-body PA array and concluded that as the radius of the circle increased, power first increased, then decreased, and eventually stabilized. They also studied the effect of change in wave direction on power and found power to vary negligibly. However, for a farm of 2 WECs, there was a change in power with changing wave directions. Murai et al. [13] studied array arrangement, incident wave angle, optimal control parameters to maximize power generation, and linear and triangular configurations and drew similar conclusions for linear arrays as de Andres et al. [11]. They also observed that PTO damping had a larger influence on power change than PTO stiffness; also, poor arrangement can negate the effect of choosing optimal control parameters.

This paper presents the study of WEC arrays to understand the effect of wave direction on it. Here, two layouts are studied—3 and 5 devices. Time domain simulations are carried out to estimate the power for both regular and irregular waves. The effect of device spacing is also investigated.

2. WEC MODEL

WEC performance evaluation is carried out in two steps. First is frequency domain calculation, where the problem is linearised, allowing for simplification using linear potential flow theory. The governing equations are transformed into the frequency domain, leading to a set of algebraic equations. This approach assumes harmonic excitation, making it computationally efficient. The Boundary Element Method (BEM) is the most commonly adopted numerical technique for solving this problem. BEM determines the excitation forces, radiation damping, and added mass coefficients. The most popular software for this purpose are ANSYS AQWA, WAMIT, and NEMOH. Since the WEC considered here is a point absorber, that is, the diameter of the device is much smaller than the wavelength of the wave, and the wave conditions are relatively mild, this problem can be solved using potential flow theory. The hydrodynamic coefficients were determined in the linear potential flow BEM solver AQWA. In AQWA, the panel method is used to compute the device's hydrodynamic coefficients. The software considers the following assumptions:

- Bodies have negligible forward speed

- Fluid is inviscid and incompressible
- Flow is irrotational
- Incident wave amplitude are small compared to the wavelength

Assuming a velocity potential function for the body $\phi(x,t)$, the body should satisfy the Laplace equation as follows

$$\nabla^2\phi = 0 \tag{1}$$

The solution of the Laplace equation is based on the boundary conditions considered and the decomposition of the solution into diffraction and radiation forces.
Boundary condition 1: Linear free surface equation

$$-\omega^2\phi + g\frac{\partial\phi}{\partial Z} = 0 \quad on \quad Z = 0 \tag{2}$$

where ω is the wave frequency, g is the Earth's acceleration, and Z is the vertical coordinate of the wetted surface.
Boundary condition 2: Body surface conditions:

$$\frac{\partial\phi}{\partial n} = \begin{cases} i\omega n_j & for \quad radiation \quad potential \\ -\frac{\partial\phi}{\partial n} & for \quad diffraction \quad potential \end{cases} \tag{3}$$

on the mean wetted surface of the body.
where n is the unit normal vector of the WEC surface pointing outwards.
Boundary condition 3: Seabed surface condition at water depth d

$$\frac{\partial\phi}{\partial Z} = 0 \quad on \quad Z = -d \tag{4}$$

A far field radiation boundary condition needs to be considered for the wave to dissipate at a distance.

$$\sqrt{(x^2+y^2)} \to \infty \tag{5}$$

ϕ can be decomposed into

$$\phi = \phi_I + \phi_D + \phi_R \tag{6}$$

where ϕ_I is the incident wave potential, which is the wave potential in the absence of the WEC, ϕ_D is the diffracted wave potential, which is the wave potential due to interaction between the incident wave and a motionless WEC, and ϕ_R is the radiated wave potential, which is the wave field produced by the WEC motion in the absence of any wave. The radiation potential can be expressed as

$$\phi_R = i\omega\sum_{j=1}^{6}\zeta_j\phi_j \tag{7}$$

where ζ_j is the motion amplitude in the jth mode and ϕ_j is radiated potential from body motion in the jth mode. From the radiation potential, added mass and frequency damping are obtained by evaluating the hydrodynamic forces induced by unit motions in each degree of freedom. The excitation force in each degree of freedom is computed from the incident and diffracted wave potentials.
The output from the BEM software is fed into a time domain-based solver. BEMIO (Boundary Element Method Input/Output), an open-source Python library used for hydrodynamic analysis of floating bodies, interfaces with BEM solvers to extract and process hydrodynamic coefficients. It converts hydrodynamic coefficients from the frequency domain to the time domain by computing impulse response functions (IRFs) using the Cummins equation framework. It creates an .h5 file, which, along with the Simulink model and WEC geometry, is given as an input to WEC-Sim, an open-source tool developed in MATLAB, to obtain the power output of the WECs, which is the second step to evaluate the WEC performance. WEC-Sim solves the Cummins equation. The time domain equation of motion for the WEC, with its origin at the centre of gravity, can be represented by Eq. 8 as

$$(m+m_a)\ddot{x} = -F_r + F_e - F_{hs} + F_v + F_{ext} \tag{8}$$

where, m = mass matrix, m_a = added mass matrix at infinite frequency, x = position vector, F_r= radiation force, F_e= excitation force vector, F_{hs} = hydrostatic restoring force vector, F_v = viscous drag force vector, and F_{ext}= external force vector. In the present study, only the heave motion is considered. Therefore, all quantities reduce to scalars. The radiation and excitation forces together constitute the hydrodynamic force. The hydrodynamic simulation models determine the dynamic response of a system or group of devices based on the forces in the above equation. The Cummins equation describes the motion of the WEC due to waves, taking into account the interaction between fluid and structure. The radiation force can be split into two parts: the instantaneous added mass effect, $A_\infty\ddot{x}(t)$ and the convolution integral, $\int_0^t K(t-\tau)\dot{x}(\tau)d\tau$. Therefore, F_r can be represented as

$$F_r = A_\infty\ddot{x}(t) + \int_0^t K(t-\tau)\dot{x}(\tau)d\tau \tag{9}$$

where $K(t-\tau)$ is the IRF, which tells how the force depends on the previous velocities of the WEC, at a time lag $(t-\tau)$, t is the current time at which the forces have to be evaluated, and τ is the past time, ranging from the start of the simulation to the present time, $\dot{x}(\tau)$ describes the past velocities at time τ. These frequency-domain coefficients are converted into the time domain by calculating the IRF. Thus, the Cummins equation takes the following form:

$$(m+m_a)\ddot{x} + A_\infty\ddot{x}(t) + \int_0^t K(t-\tau)\dot{x}(\tau)d\tau = F_e - F_{hs} + F_v + F_{ext} \tag{10}$$

The left-hand side of the equation includes inertia, memory (via convolution), and restoring forces. The right-hand side includes excitation force, viscous damping, and external forces. WEC-Sim uses these

IRFs to solve the Cummins equation and compute motion and power. The system is represented using mathematical blocks in Simulink. The bodies are defined as rigid bodies, which are connected to each other using constraint blocks or a PTO block. A linear spring damper PTO was considered for the study. Figure 1 shows a flowchart illustrating the sequence of steps involved in calculating the power output of the WEC. A study was undertaken to select the appropriate WEC for the farm by considering a single and a two-body WEC [14]. It was observed that the two-body WEC produced 28% higher power than the single-body WEC, thus being the device considered for further studies. Fig. 2 shows the WEC considered for study, and Table 1 shows the dimensions of the WEC. Two configurations of wave farms were studied: a 3-device and a 5-device farm. Several researchers observed that a triangular layout gave better results compared to other layouts, such as linear and square layouts [15, 11]. Hence, for the 3-device and 5-device configurations, a triangular layout was considered, as shown in Figures 3 and 4. A pentagon layout was not considered for analysis previously. Hence, a pentagon layout was considered for the 5-device configuration, as shown in Fig. 5. A 2 m wave height and 6 seconds period were considered.

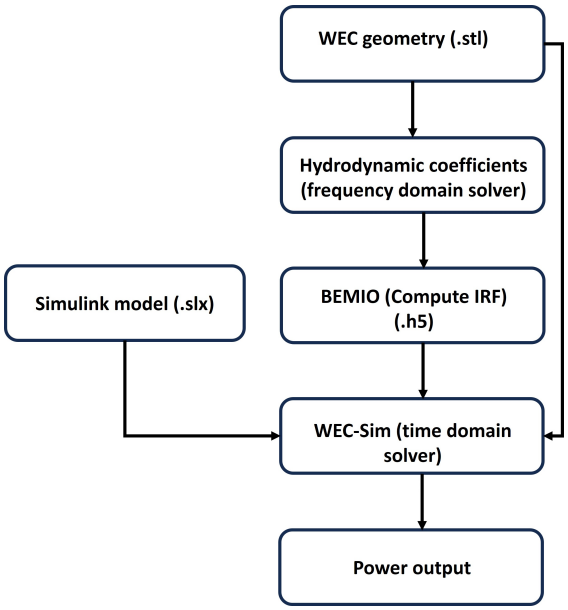

Figure 1. Steps for Calculating WEC Power Output

Table 1. Dimensions of the two-body WEC

Parameter	Value
Diameter of buoy	3 m
Height of buoy	0.8 m
Draft	0.25 m
Diameter of sphere	3.9 m

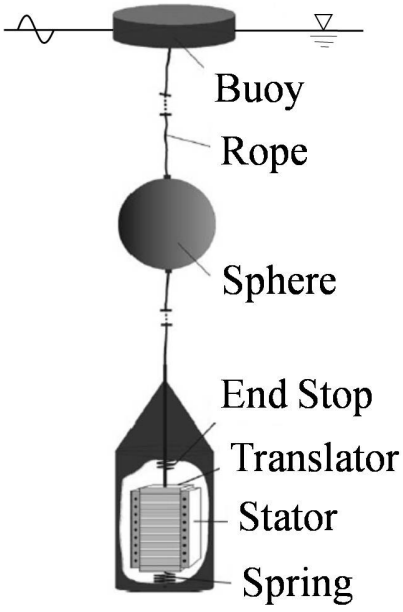

Figure 2. Two-body PA [16]

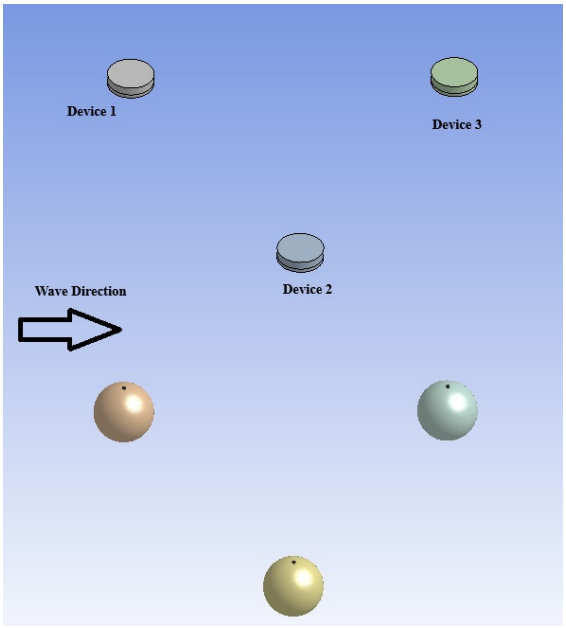

Figure 3. 3-device configuration

3. NUMERICAL RESULTS

3.1. Effect of layout

First, the number of devices on the farm was studied for regular and irregular waves. Irregular waves can be described using many spectra. Here, a Joint North Sea Wave Project or JONSWAP spectrum was used [17]. The inter-device spacing was fixed at 20 m. Figures 6, 7, and 8 show the power obtained for a 3-device and 5-device configuration in regular wave conditions. Here, the 0° incident wave direction was considered. Negative power val-

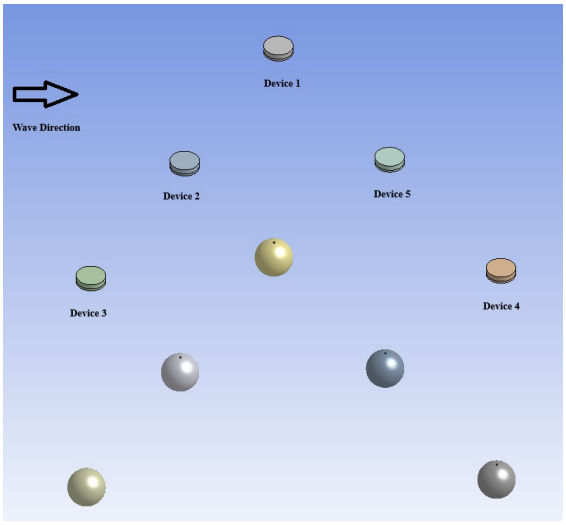

Figure 4. 5-device configuration in triangular layout

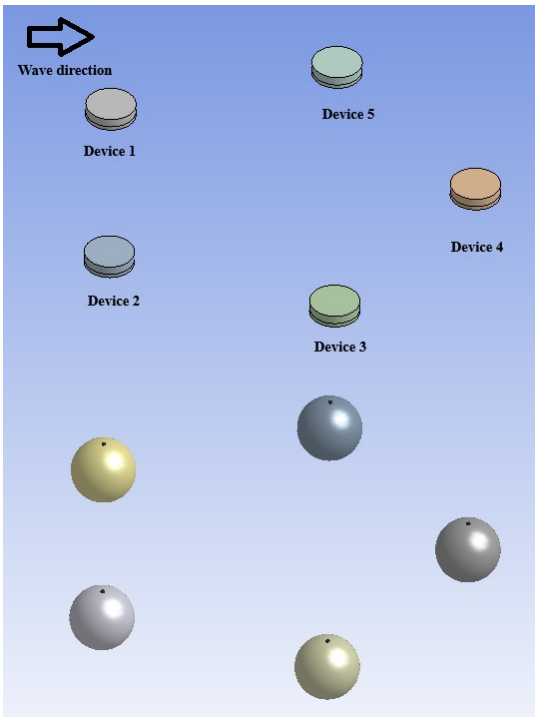

Figure 5. 5-device configuration in pentagon layout

ues indicate energy absorption from waves, as per the WEC-Sim sign convention. It was observed that the power obtained for a 3-device configuration for an individual device is more than the 5-device configuration. Figures 9, 10, and 11 show the average power obtained for a 3-device and 5-device configuration in irregular wave conditions. Even for irregular waves, the power obtained for individual devices in the triangular configuration is more than that of the pentagon configuration.

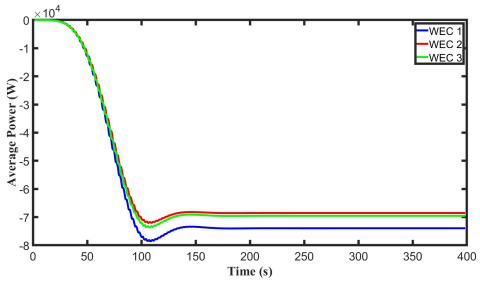

Figure 6. Power obtained for a three-device configuration in regular waves

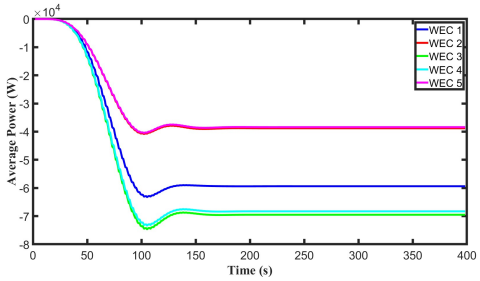

Figure 7. Power obtained for a five-device triangular configuration in regular waves

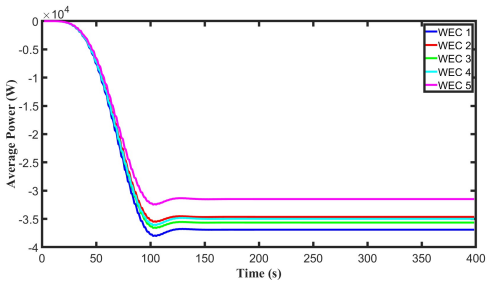

Figure 8. Power obtained for a five-device pentagon configuration in regular waves

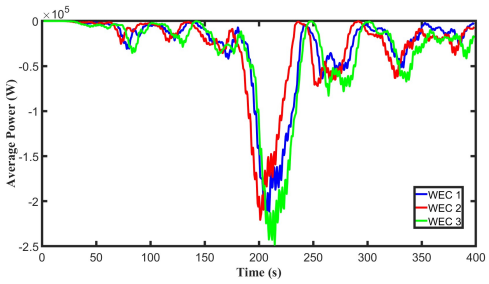

Figure 9. Power obtained for a three-device configuration in irregular waves

3.2. Effect of wave direction

To understand the effect of wave direction, the 5-device triangular layout with 20 m spacing was studied. Fig. 12 shows the comparison of average power for the triangular layout for 8 wave directions: 0, 30,

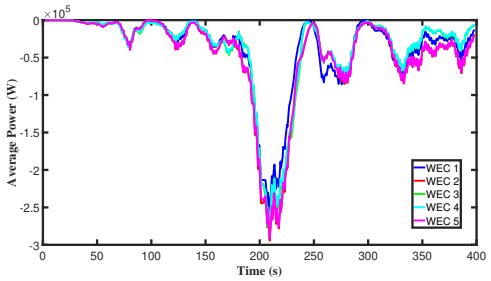

Figure 10. Power obtained for a five-device triangular configuration in irregular waves

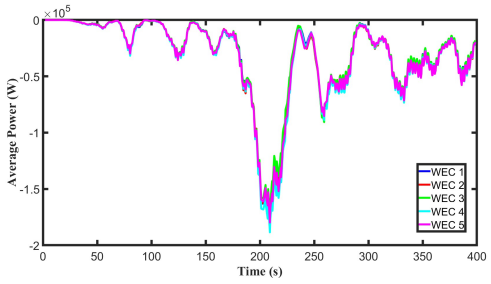

Figure 11. Power obtained for a five-device pentagon configuration in irregular waves

45, 60, 90, 135, 180, and 270 °. The maximum average power was obtained for an incident wave direction of 0 °, followed by 180 °, 30 °, then 45 °, 135 °, 60 °, 270 ° and lastly 90 °.

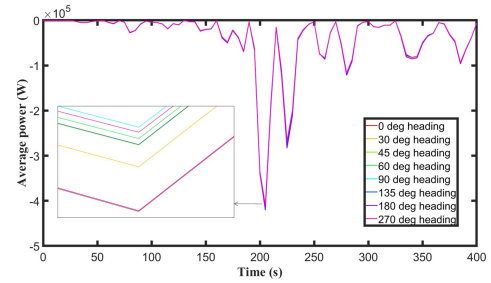

Figure 12. Power obtained for different wave directions for five-device triangular layout configuration

3.3. Effect of device spacing

Three device spacings were studied for the triangular configuration of 3 devices: 10 m, 20 m, and 30 m for regular wave conditions. From Figures 6, 13 and 14, it can be observed that the devices in the farm with 10 and 20 m spacing have varying power, with the device encountering the wave first having maximum power and subsequent devices having lesser power, whereas the farm with 30 m spacing all have the same power. Babarit [18] observed that for smaller arrays of smaller-diameter buoys, the separating distance should be 10 to 20 times the diameter to avoid any interference between the motion of the neighboring devices. If the spacing is less than this, the power produced from these interacting devices will be reduced.

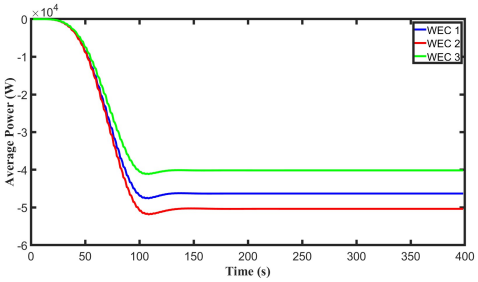

Figure 13. Power obtained for the farm of 10 m spacing for three-device triangular layout

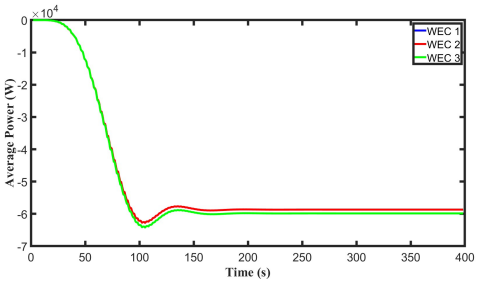

Figure 14. Power obtained for the farm of 30 m spacing for three-device triangular layout

4. CONCLUSION

The paper discusses the effect of layout, wave direction, and spacing between devices on the power produced by the wave farm. After obtaining the hydrodynamic coefficients in Ansys AQWA, the power produced was calculated using the time-domain simulation tool WEC-Sim. Only the heave direction was considered for power calculation. A 3- and 5-device farm was studied for both regular and irregular waves, where it was found that for the triangular layout, the power produced by the individual device was almost twice that of the individual device of the pentagon layout for both wave conditions. Also, for the triangular layout, the power produced by the individual devices in the 5-device configuration was more than the 3-device configuration. Consequently, the effect of incident wave direction was studied, and it was found that maximum power was obtained for a wave at 0 °. Lastly, varying the spacing between the devices, it was observed that a device spacing of the order of 10 times the diameter eliminated any destructive interference, whereas, for lesser device spacing of the order of 3 to 4 times the diameter of the device, the movement of one device affected that of the subsequent devices, reducing the power produced by them.

REFERENCES

[1] Budal, K., 1977, "Theory for absorption of wave power by a system of interacting bodies", *Journal of Ship Research*, Vol. 21 (04), pp. 248–254.

[2] Falnes, J., 1980, "Radiation impedance matrix and optimum power absorption for interacting oscillators in surface waves", *Applied Ocean Research*, Vol. 2 (2), pp. 75–80.

[3] Evans, D., 1981, "Maximum wave-power absorption under motion constraints", *Applied Ocean Research*, Vol. 3 (4), pp. 200–203.

[4] McIver, P., 1994, "Some hydrodynamic aspects of arrays of wave-energy devices", *Applied Ocean Research*, Vol. 16 (2), pp. 61–69.

[5] Fitzgerald, C., and Thomas, G., 2007, "A preliminary study on the optimal formation of an array of wave power devices", *Proceedings of the 7th European Wave and Tidal Energy Conference, Porto, Portugal*, pp. 11–14.

[6] Sannasiraj, S., and Sundar, V., 2016, "Assessment of wave energy potential and its harvesting approach along the Indian coast", *Renewable Energy*, Vol. 99, pp. 398–409.

[7] Patel, R. P., Nagababu, G., Kachhwaha, S. S., Surisetty, V. A. K., and Seemanth, M., 2023, "Techno-economic analysis of wave energy resource for India", *Journal of the Indian Society of Remote Sensing*, Vol. 51 (2), pp. 371–381.

[8] Amrutha, M., and Kumar, V. S., 2022, "Evaluation of a few wave energy converters for the Indian shelf seas based on available wave power", *Ocean Engineering*, Vol. 244, p. 110360.

[9] Amrutha, M. M., and Sanil Kumar, V., 2016, "Spatial and temporal variations of wave energy in the nearshore waters of the central west coast of India", *Annales Geophysicae*, Vol. 34 (12), pp. 1197–1208.

[10] Cruz, J., Sykes, R., Siddorn, P., and Taylor, R. E., 2009, "Wave farm design: preliminary studies on the influences of wave climate, array layout and farm control", *Proceedings of the 8th European Wave and Tidal Energy Conference, Uppsala, Sweden*.

[11] De Andrés, A., Guanche, R., Meneses, L., Vidal, C., and Losada, I., 2014, "Factors that influence array layout on wave energy farms", *Ocean Engineering*, Vol. 82, pp. 32–41.

[12] Ji, R., Sheng, Q., Wang, S., Zhang, Y., Zhang, X., and Zhang, L., 2019, "Array characteristics of oscillating-buoy two-floating-body wave-energy converter", *Journal of Marine Science and Application*, Vol. 18, pp. 325–333.

[13] Murai, M., Li, Q., and Funada, J., 2021, "Study on power generation of single Point Absorber Wave Energy Converters (PA-WECs) and arrays of PA-WECs", *Renewable Energy*, Vol. 164, pp. 1121–1132.

[14] Majumdar, A., Venkatesan, G., and Samad, A., 2024, "Numerical Analysis and Validation of Point Absorber Wave Energy Converters for the Indian Coast", *ISOPE Pacific/Asia Offshore Mechanics Symposium*, ISOPE, pp. ISOPE–P.

[15] Borgarino, B., Babarit, A., and Ferrant, P., 2012, "An implementation of the fast multipole algorithm for wave interaction problems on sparse arrays of floating bodies", *Journal of Engineering Mathematics*, Vol. 77, pp. 51–68.

[16] Engström, J., Eriksson, M., Isberg, J., and Leijon, M., 2009, "Wave energy converter with enhanced amplitude response at frequencies coinciding with Swedish west coast sea states by use of a supplementary submerged body", *Journal of Applied Physics*, Vol. 106 (6).

[17] Kumar, V. S., and Kumar, K. A., 2008, "Spectral characteristics of high shallow water waves", *Ocean Engineering*, Vol. 35 (8-9), pp. 900–911.

[18] Babarit, A., 2013, "On the park effect in arrays of oscillating wave energy converters", *Renewable Energy*, Vol. 58, pp. 68–78.

Conference on Modelling Fluid Flow (CMFF'25)
The 19th International Conference on Fluid Flow Technologies
Budapest, Hungary, August 26 - August 29, 2025

EXPERIMENTAL AND NUMERICAL INVESTIGATIONS OF NOZZLE SPACING EFFECTS ON FLOW CHARACTERISTICS OF TRIPLE RECTANGULAR FREE JETS

Koichi HAYASHIDA[1], Takahiro KIWATA[2], Peter OSHKAI[3]

[1] Corresponding Author. Graduate School of Natural Science and Technology, Kanazawa University. Kakuma-machi, Kanazawa-shi, Ishikawa, Japan. Tel.: +81 778 62 8309, E-mail: hayashida@fukui-nct.ac.jp
[2] School of Mechanical Engineering, Kanazawa University. E-mail: kiwata@se.kanazawa-u.ac.jp
[3] Department of Mechanical Engineering, University of Victoria. E-mail: poshkai@uvic.ca

ABSTRACT

The effect of nozzle spacing on the flow characteristics of triple rectangular free jets was studied experimentally and numerically. The nozzle spacing ratio S/d_e, where d_e is the equivalent diameter of a rectangular nozzle with an aspect ratio of 2, was varied from 2.06 to 4.13. The Reynolds number based on the nozzle exit velocity and the equivalent diameter was 1.5×10^4. The mean and fluctuating velocities were measured using a constant-temperature hot-wire anemometer with an X-type probe. Three-dimensional numerical simulations of triple rectangular free jets were also performed using Open FOAM 5.0, and the numerical results depicted the vortical structures in the jets. Triple rectangular free jets with a small nozzle spacing ratio, specifically S/d_e = 2.06, merge upstream. The mean velocity and the turbulent kinetic energy near the jet centerline become higher than those with a large nozzle spacing ratio. An axis-switching phenomenon occurs after the jets merge, and the whole cross-sectional shape of the triple rectangular free jets changes to an elliptical jet with a major axis in the z-direction. Farther downstream, the elliptical jet becomes round.

Keywords: flow measurement, hot-wire anemometry, nozzle spacing, OpenFOAM, rectangular jet, triple jets

NOMENCLATURE

B	[m]	width of rectangular nozzle
C	[m]	height of rectangular nozzle
C_s	[-]	Smagorinsky constant
d	[m]	diameter of circular nozzle
d_e	[m]	equivalent diameter of non-circular nozzle
k	[m^2/s^2]	turbulent kinetic energy
Q	[-]	second invariant iso-surface of velocity gradient tensor
Re	[-]	Reynolds number
S	[m]	nozzle spacing between the center of nozzles
u	[m/s]	x-axial velocity (streamwise velocity)
$\overline{u}$	[m/s]	mean x-axial velocity (streamwise mean velocity)
u'_{rms}	[m/s]	root-mean-square value of x-axial velocity fluctuation
$\overline{u}_{0cl}$	[m/s]	nozzle exit mean x-axial velocity at the center of nozzle
v	[m/s]	y-axial velocity
w	[m/s]	z-axial velocity
x	[m]	x-axial coordinate
x_c	[m]	potential core length
y	[m]	y-axial coordinate
z	[m]	z-axial coordinate
ν	[m^2/s]	kinematic viscosity

Subscripts

cl	on the jet centerline
cl,mid	on the jet centerline of the middle jet
cl,side	on the jet centerline of the side jet
sym	on the jet symmetry-line

1. INTRODUCTION

Multiple jets issuing from two or more nozzles are used in various applications, such as aircraft combustors, air ventilation systems, and chip removal systems in machine tools. The flow structures of twin jets, which issue from two nozzles arranged in parallel, have been reported by several researchers [1-3]. For example, the effects of nozzle spacing on the flow characteristics of twin circular jets were investigated by Okamoto et al. [1] and Laban et al. [2]. They reported that, for a small spacing ratio S/d, the twin circular jets merged at the

upstream side, and the streamwise mean velocity on the jet centerline increased due to the suppression of the entrainment with ambient flow in the inner shear layer.

A single non-circular jet provides higher mixing capabilities with the ambient fluid than those of a single circular jet due to the three-dimensional deformation of the vortex rings in the free shear layer. Therefore, the flow structure of multiple non-circular jets is expected to be more complex than that of multiple circular jets. Hayashida and Kiwata [4] experimentally studied the effects of the nozzle orientation and nozzle spacing on the flow characteristics of twin rectangular free jets with a nozzle aspect ratio of 2. They showed that, for a small nozzle spacing, the mean and fluctuating velocities of twin rectangular free jets become larger, after the combined point (CP) on the jet symmetry line, than those of a single circular jet. However, the nozzle orientation has little effect on the mean and fluctuating velocities.

Figure 1 shows a schematic diagram of the *x*-*y* cross-section of the flow field of the triple rectangular free jets described in the present paper. The flow field of the triple jets, which are lined up in a row, is divided into the converging, the merging, and the combined regions. The converging region ends at the plane corresponding to the merging point (MP), that is, $\overline{u}_{sym} \approx 0.015\overline{u}_{0cl}$. The combined region is formed downstream of the CP, where $\overline{u}_{cl,side} \approx \overline{u}_{sym}$. The region between these two regions is referred to as the merging region. The region between the middle jet and the side jets is defined as the inner mixing region, and the region between the side jets and the ambient fluid is defined as the outer mixing region. Thus, the shear layers in the outer mixing regions are defined as the outer shear layers. The shear layers in the inner mixing region are defined as the outside and inside inner shear layers, respectively. As shown in Fig. 1, the flow field of the triple jets is more complicated than that of the twin jets, because the middle jet is influenced by the adjacent jets. Morris et al. [5] investigated the effect of nozzle orientation on the flow characteristics of multiple non-circular jets with triple elliptic nozzles with an aspect ratio of 2, and a nozzle spacing of $4.1d_e$. They found that the triple elliptic jets with each nozzle oriented along the minor plane had a shorter potential core length and a closer MP location where the inner mixing region of the adjacent jets merge than the other orientations. However, they did not investigate the effect of nozzle spacing ratio.

The objective of the present research was to investigate the effect of nozzle spacing on the flow characteristics of triple rectangular free jets with each nozzle oriented along the major plane and having an aspect ratio of 2. This paper describes the distributions of velocity and turbulence intensity obtained experimentally using an X-type hot-wire probe, and large eddy simulation (LES) results obtained using the computational fluid dynamics (CFD) software OpenFOAM 5.0.

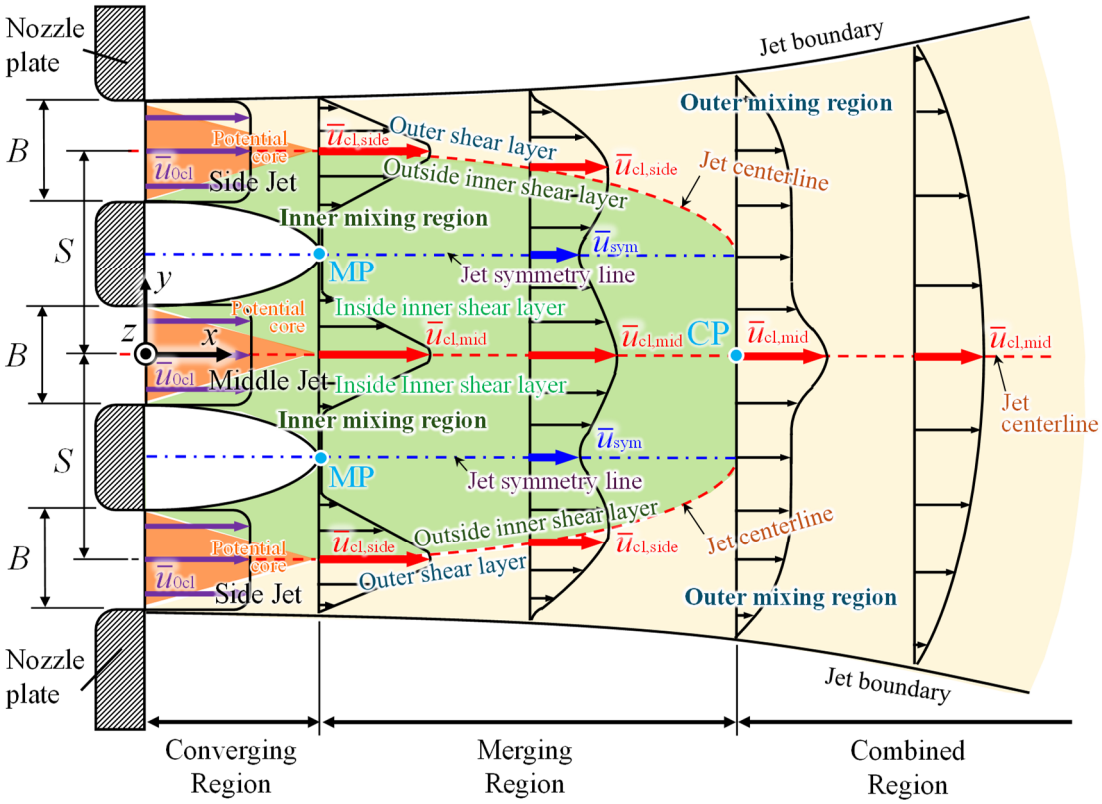

Figure 1. Schematic diagram of the flow field of triple rectangular free jets.

2. EXPERIMENTAL PROCEDURE AND NUMERICAL SETUP

2.1. Experimental apparatus and method

Figure 2 shows a schematic diagram of the experimental system [6]. Figure 3 shows a schematic diagram of an orifice plate with triple rectangular nozzles. The orifice plate was installed at the wind tunnel outlet to generate the rectangular free jets. The orifice plate was made of an acrylic resin 10 mm thick. Each rectangular nozzle had a height of $C = 10$ mm, a width of $B = 20$ mm, and a constriction formed by a circular shoulder with a radius $R = 4$ mm at the upstream edge of the orifice to prevent flow separation. The aspect ratio of the rectangular nozzle was $B/C = 2$, and the equivalent diameter of each nozzle was $d_e\,[= (4BC/\pi)^{1/2}] \approx 15.96$ mm. The nozzle spacing between the centers of the triple rectangular free jets was varied as $S = 33$ mm to 66 mm, specifically the four spacing ratios of $S/d_e = 2.06$ to 4.13. The nozzles were aligned with their major axes. The flow characteristics of a single rectangular free jet, a single circular free jet, and twin rectangular free jets were also investigated to compare with those of triple rectangular free jets. The results of the single rectangular free jet, twin rectangular free jet, and the single circular jet in the x-y cross-section on the major axis are referred to as "SingleMajor," "TwinMajor," and "SingleRound" configurations, respectively. The definition of the x, y, and z axes is shown in Figs. 1 and 2. The coordinate origin in the flow field of triple rectangular free jets was set to the center of the middle nozzle outlet. The flow direction was defined as x; the horizontal direction as y; the vertical direction as z; and velocity in each direction as u, v, and w, respectively.

The flow velocities were measured by an X-type hot-wire probe and constant-temperature hot-wire anemometers (CTA) with linearized output. The hot-wire probe could be moved three-dimensionally by a traverse unit. The output signals from the CTA were converted by a 16-bit analog/digital (A/D) converter at a sampling frequency of 6 kHz and 1.2×10^5 data points were recorded. The resulting digital signals were used to calculate the mean and the fluctuating velocities. Aleyasin and Tachie [3] found that, for Reynolds number $Re > 1.0 \times 10^4$, the velocity decay and the jet spread of twin circular jets are independent of the Reynolds number. Therefore, the Reynolds number was set to $Re = \bar{u}_{0cl}\, d_e/\nu = 1.5 \times 10^4$, where ν is the kinematic viscosity of air. The mean velocity at the center of the nozzle exit, that is, $x/d_e = 0.1875$, $y/d_e = 0$, and $z/d_e = 0$, was set to $\bar{u}_{0cl} \approx 14.2$ m/s. Further, the uncertainties of the mean velocity and the fluctuating velocity components measured using an X-type hot-wire probe were calculated, with reference to Nagano and Tagawa [7], to be less than 1.8% and 2.3%, respectively.

2.2. Numerical method

The three-dimensional numerical simulations of the triple rectangular free jets for a small nozzle spacing of $S/d_e = 2.06$ ($S = 33$ mm) and a large nozzle spacing of $S/d_e = 4.13$ ($S = 66$ mm) were performed by OpenFOAM 5.0 using a finite volume method. The flow field was assumed to be unsteady, viscous, incompressible, isothermal, and fully turbulent. The unsteady flow simulation used the Implicit-LES turbulence model, where the Smagorinsky constant of the Smagorinsky-subgrid-scale (SGS) model was set to $C_s = 0$ [8]. The convection terms of the governing equations were discretized using the second-order unbounded central differencing scheme. The second-order central differencing scheme was used for the diffusion terms, while the second-order implicit scheme was used for the time marching. The pressure-implicit with splitting of operators (PISO) method was used as the calculation algorithm for the pressure-velocity coupling.

Figure 4 shows the computational domain, the mesh, and the boundary conditions for $S/d_e = 2.06$ and 4.13. Nonuniform spacing and structured meshes were used in the computational domain. The streamwise, vertical, and spanwise lengths of the computational domain are 640 mm ($= 40d_e$), 320 mm ($= 20d_e$), and 320 mm ($= 20d_e$), respectively. The width and the height of each nozzle are $C = 20$ mm

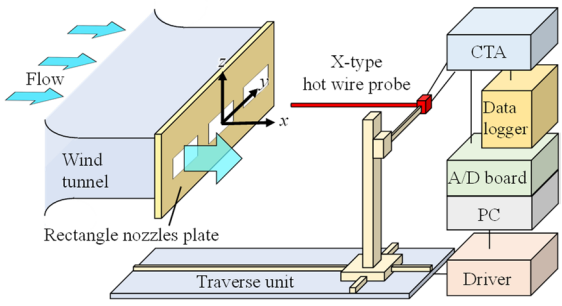

Figure 2. Schematic diagram of the experimental system.

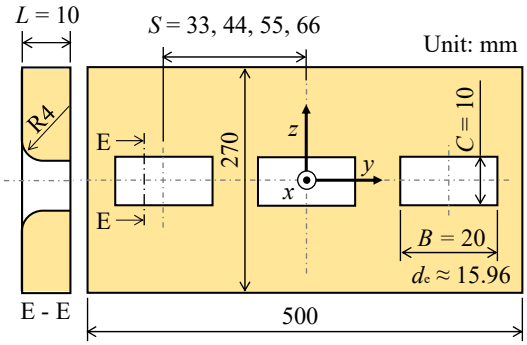

Figure 3. Schematic diagram of the orifice plate with triple rectangular nozzles.

and B = 10 mm, respectively. The effect of the number of grid points on the mean velocity profile was investigated for the triple rectangular jets with S/d_e =2.06. The numerical simulation was conducted with two numbers of grid points of approximately 1.3×10^7 and 6.5×10^6. The result for half the number of grid points deviated significantly from the experimental result. Therefore, the fine mesh was adopted for the numerical simulation, namely, the number of grid points was approximately 1.3×10^7 for S/d_e =2.06, and 1.8×10^7 for S/d_e = 4.13. The inlet boundary of the triple rectangular nozzles was set at a mean x-axial velocity of $\overline{u}$ = 14.2 m/s with x-direction velocity fluctuation of $u'_{rms}/\overline{u}$ = 0.02, the same as the experimental condition, and the gradient of zero was set for the pressure condition. The boundary condition of *pressureInletOutletVelocity* [9] was used at the top, bottom, outlet, and inlet surfaces of the computational domain. This boundary condition corresponds to a zero-gradient velocity everywhere on the boundary, except the inflow. When inflow occurred, a *fixedvalue* condition was applied to the tangential component. Furthermore, the pressure condition with the total pressure of 0 was set on each boundary of the computational domain. A time step size of 8×10^{-6} was used for the present simulation to satisfy the condition courant number CFL < 0.5.

3. RESILTS AND DISCUSSION

3.1. Comparison of experimental and numerical results

Figure 5 shows the profiles of the mean velocity $\overline{u}/\overline{u}_{0cl}$ along the x-axis in the x-y cross-section for nozzle spacing ratios of S/d_e = 2.06 and 4.13. The experimental profiles are in qualitative agreement with the simulation in both cases until the merging region. In particular, the agreement between the numerical simulations and the experimental results for S/d_e = 2.06 is good in the combined region of $x/d_e \geq 30$, and the agreement between the numerical simulations and the experimental results for S/d_e = 4.13 is also good at $x/d_e \geq 10$. In the following sections, the experimental results are discussed using the numerical simulation if necessary.

3.2. Mean velocity, and turbulent kinetic energy in the x-y cross section

Figure 6 shows contour plots of the mean x-axial velocity in the x-y cross-section, $\overline{u}/\overline{u}_{0cl}$, for triple rectangular free jets with S/d_e = 2.06, 4.13, and a single rectangular free jet of the SingleMajor case. The potential core region assumes a wedge shape due to the formation of the shear layer by mixing with the ambient fluid. The length of the potential core x_c is defined as the distance between the nozzle exit and

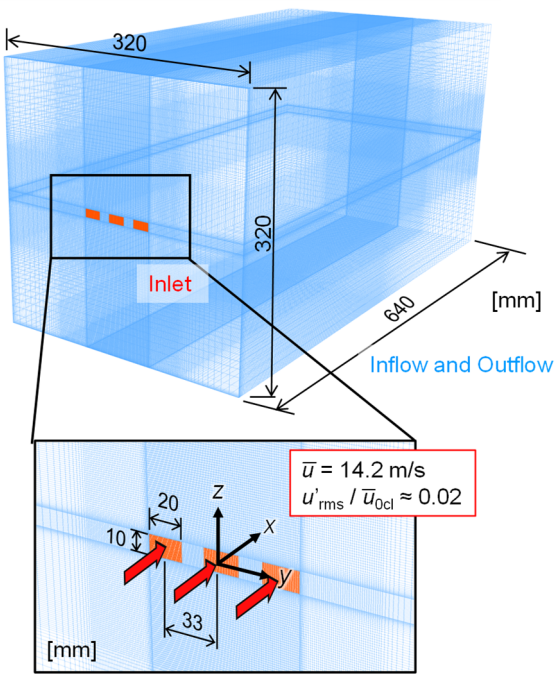

Figure 4. Computational domain, mesh and boundary conditions.

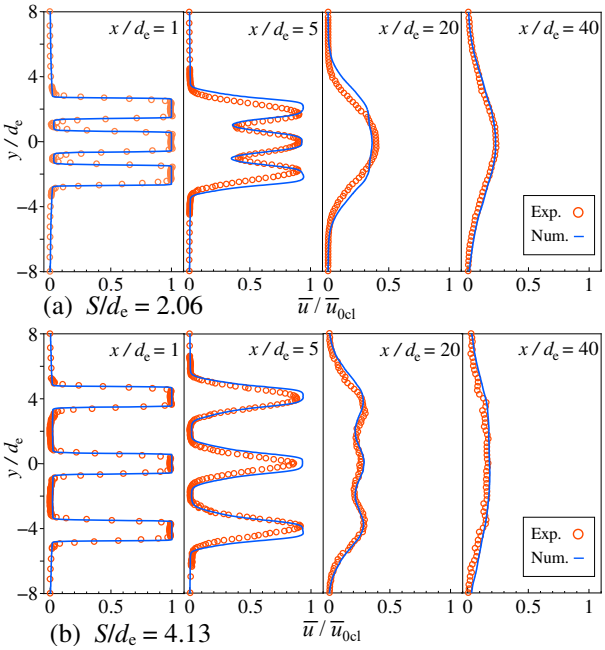

Figure 5. Profiles of mean velocity $\overline{u}/\overline{u}_{0cl}$ along x-axis in x-y cross section for (a) S/d_e = 2.06, and (b) S/d_e = 4.13 case.

the point at which $\overline{u}_{cl}/\overline{u}_{0cl}$ = 0.98 [2]. The length of the potential core of the rectangular jets is $x_c \approx 3d_e$ in all spacing ratios of triple rectangular jets and the SingleMajor case. The nozzle spacing has little effect on the length of the potential core. However, only for S/d_e = 2.06, it seems that the length of the wedge-shaped region of the middle jet becomes larger than that of the side jets. The middle jet does not cause the axis-switching phenomenon (discussed in Sec. 3.4). For a small spacing ratio S/d_e, the positions of the MP

and CP move upstream as compared with that for a large spacing ratio. In addition, the jet spread decreases in the downstream of CP due to the axis-switching phenomenon (discussed in Sec. 3.4). These results are consistent with those of Laban et al. [2], and Hayashida and Kiwata [4], who investigated the effect of nozzle spacing of twin round jets and twin rectangular free jets, respectively.

Figure 7 shows contour plots of the dimensionless turbulent kinetic energy in the x-y cross-section, $k/\overline{u}_{0cl}^2$ for triple rectangular free jets with $S/d_e = 2.06$, 4.13 and a single rectangular free jet of the SingleMajor case. At $0.5 \le x/d_e \le 5$, the turbulent kinetic energy increases in the inner and outer shear layers due to the Kelvin–Helmholtz instability. The y-direction position of the peak value of the turbulent kinetic energy of the side jets moves toward the middle jet. For $S/d_e = 2.06$, the turbulent kinetic energy ($k/\overline{u}_{0cl}^2 \ge 0.02$) in the outer shear layer of the side jets becomes larger than that in the outside inner shear layer of the side jets. At $5 \le x/d_e \le 10$, for a small spacing ratio of $S/d_e = 2.06$, the turbulent kinetic energy increases on the jet symmetry line because the larger mixing area in the middle jet does not expand in the x-direction. In the downstream region, the turbulent kinetic energy decreases gradually with the merging of the triple rectangular free jets. At $x/d_e \ge 20$, for $S/d_e = 2.06$, the turbulent kinetic energy increases more than that for the other spacing ratios due to the continuance of high velocity along the jet centerline as shown in Fig. 6. In contrast, the distribution of the turbulent kinetic energy of the triple rectangular free jets for $S/d_e = 4.13$ is not significantly different from that of the SingleMajor case. Thus, when the spacing ratio S/d_e is large, the flow characteristics of each jet in triple rectangular jets are similar to those of a single rectangular free jet.

3.3. Mean velocity and turbulent kinetic energy in the jet centerline and the jet symmetry line

Figure 8 shows the distributions of mean x-axial velocity on the middle jet centerline $\overline{u}_{cl,mid}/\overline{u}_{0cl}$, the side jets centerline $\overline{u}_{cl,side}/\overline{u}_{0cl}$, and the jet symmetry line $\overline{u}_{sym}/\overline{u}_{0cl}$. The results for twin rectangular jets with a spacing ratio of $S/d_e = 2.75$ [4], and the SingleMajor and the SingleRound cases are also shown in Fig. 8. the length of the potential cores, for the triple rectangular jets as described Sec. 3.2, and the TwinMajor and the SingleMajor jets are about $x_c \approx 3d_e$, respectively. This length of the potential core is smaller than that for the SingleRound case, that is, $x_c \approx 4d_e$. Commonly, the potential core length for a rectangular jet is shorter than that for a circular jet due to the three-dimensional deformation of the vortex rings in a non-circular jet [4]. From the end of the potential core region, the velocity on the jet centerline begins to decrease. The velocity on the jet centerline of a developed single circular jet and

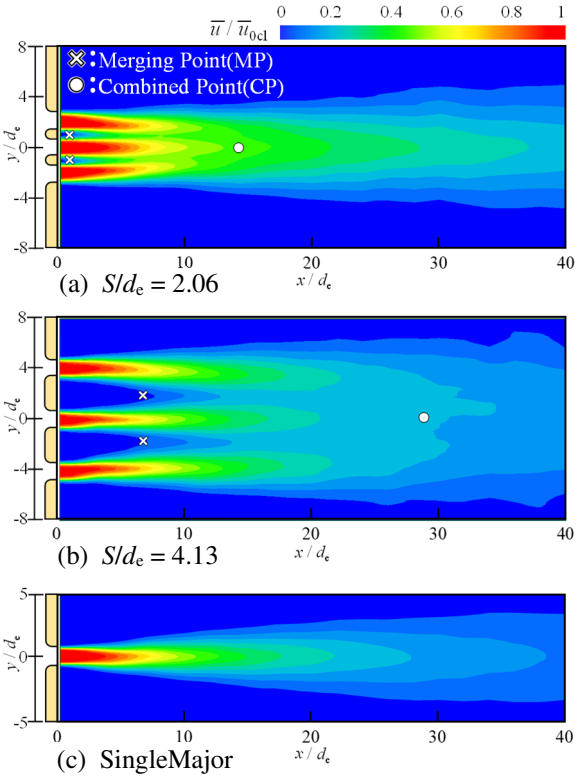

Figure 6. Contour plots of mean x-axial velocity in the x-y cross section for (a) $S/d_e = 2.06$, (b) $S/d_e = 4.13$ and (c) SingleMajor case.

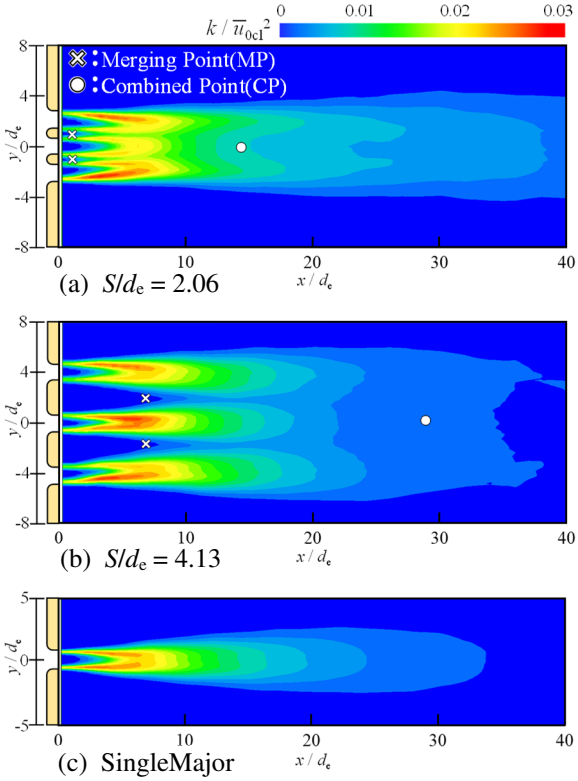

Figure 7. Contour plots of the turbulent kinetic energy in the x-y cross-section for (a) $S/d_e = 2.06$, (b) $S/d_e = 4.13$ and (c) SingleMajor case.

single rectangular jet, that is, SingleRound and SingleMajor, decays in proportion to x^{-1}. For S/d_e = 2.06, the velocity on the side jet centerline is lower than that on the middle jet centerline. However, for S/d_e = 4.13, the velocity on the side jet centerline is approximately the same as that on the middle jet centerline.

Figure 9 shows the second invariant iso-surfaces of the velocity gradient tensor Q from the numerical results for S/d_e = 2.06 and S/d_e = 4.13. For a small spacing ratio of S/d_e = 2.06, vortex rings at the nozzle exit are generated, and the middle and the side jets interfere between the outside and inside inner shear layers. From $x/d_e \approx 3$, longitudinal vortices are generated in the shear layer, and the vortices form a three-dimensional structure. As a result, the triple rectangular jets mix with the surrounding fluid, and a flow field develops. In contrast, for a large spacing ratio of S/d_e = 4.13, vortex rings at the nozzle exit are also generated. It seems that the interference between the outside and inside inner shear layers is weaker than that for a small spacing ratio of S/d_e = 2.06. The longitudinal vortex in the inner mixing region grows from about x/d_e = 5.

The distributions of the mean x-axial velocity, $\overline{u}_{sym}/\overline{u}_{0cl}$, on the jet symmetry line is also shown in Fig. 8. The MP, which is a point of the velocity deficit between the jets, is defined as the location where $\overline{u}_{sym} \approx 0.015\ \overline{u}_{0cl}$. The location of the MP is equal to $x/d_e \approx 1.1$, 2.8, 4.5, and 6.3 for S/d_e = 2.06, 2.75, 3.44, and 4.13, respectively. The location of the MP is close to the nozzle exit as the nozzle spacing ratio S/d_e decreases, similar to the case of the twin circular and twin rectangular jets [2, 4]. Downstream of the MP, the velocity of $\overline{u}_{sym}/\overline{u}_{0cl}$ on the jet symmetry line increases and has a peak value of 0.48, 0.3, 0.25, and 0.22 at $x/d_e \approx$ 9, 11, 15, and 17, respectively. Especially, for S/d_e = 2.06, the velocity $\overline{u}_{sym}/\overline{u}_{0cl}$ exhibits a high rate of increase because of the mixing between the middle and the side jets with the axis-switching phenomenon similar to that of the twin rectangular free jets [4].

The CP is defined as the location where $\overline{u}_{cl} \approx \overline{u}_{sym}$. The CP moves upstream with the decreasing nozzle spacing ratios, that is, $x/d_e \approx$ 14, 19, 24, and 29 for S/d_e = 2.06, 2.75, 3.44, and 4.13, respectively. The location of the CP is approximately proportional to the nozzle spacing ratio S/d_e, similar to the case of twin circular jets and twin rectangular jets [2, 4]. Downstream of the CP, the velocity $\overline{u}_{cl,mid}/\overline{u}_{0cl}$ on the jet centerline for a small spacing ratio of S/d_e = 2.06 is larger than that for a large spacing ratio S/d_e = 4.13. At x/d_e = 40, the velocity $\overline{u}_{cl,mid}/\overline{u}_{0cl}$ on the jet centerline for triple rectangular free jets of S/d_e =

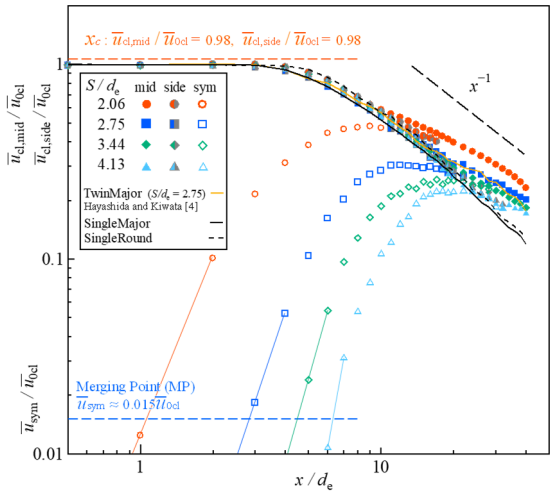

Figure 8. Distributions of the mean x-axial velocity on the jet centerline and the jet symmetry line along the x-axis.

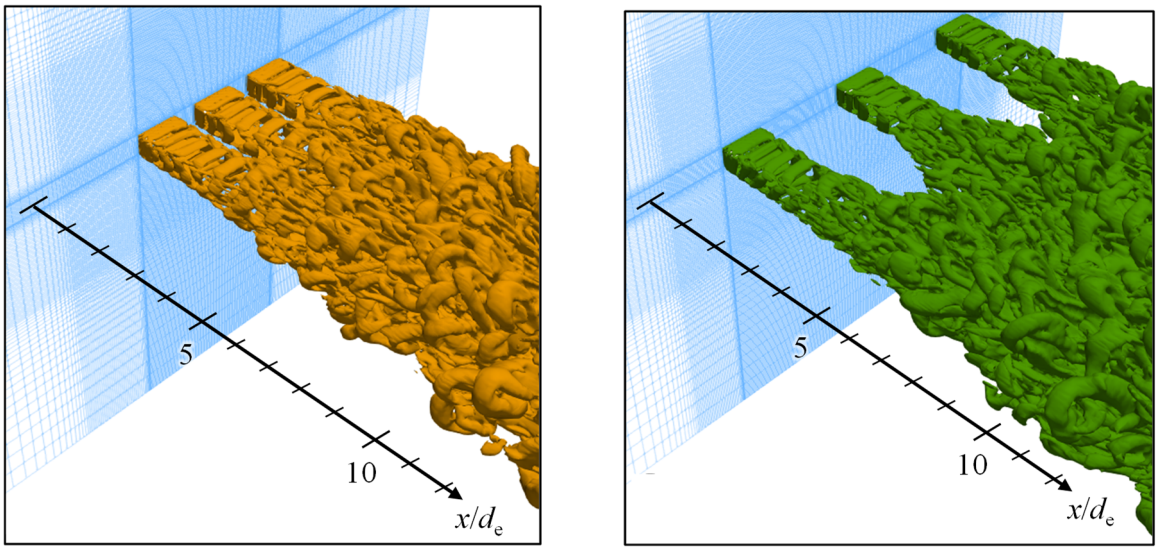

(a) S/d_e = 2.06 (b) S/d_e = 4.13

Figure 9. Second invariant iso-surfaces of the velocity gradient tensor Q for (a) S/d_e = 2.06 and (b) S/d_e = 4.13

2.75 is larger than that for twin rectangular free jets with the same spacing ratio. However, because the values are nearly identical at $x/d_e \leq 30$, the decrease in velocity of the twin rectangular jets at $x/d_e = 40$ is considered to be due to a difference in the flow rate of the jets.

3.4. Mean velocity in the y-z cross-section

Figure 10 shows contour plots of the mean x-axial velocity, $\overline{u}/\overline{u}_{0cl}$, in the y-z cross-section at x/d_e = 1, 5, 10, 20, 30, and 40 for triple rectangular free jets with S/d_e = 2.06, 2.75, and 4.13.

For S/d_e = 2.06, the cross-sectional shape of the side jets at x/d_e = 1 changes only at the corners on the side of the outer mixing region. Namely, these shapes change from rectangular to trapezoidal. From x/d_e = 5, the jets begin to merge. At x/d_e = 10, the triple rectangular free jets merge and form a horizontally long elliptic cross-sectional shape. At x/d_e = 20, the cross-section of merged triple rectangular free jets becomes round. At x/d_e = 40, this cross-section in the downstream region has a vertically long elliptic cross-sectional shape and retains a large area of mean velocity of $\overline{u}/\overline{u}_{0cl}$ = 0.18. Thus, the triple rectangular free jets for a small nozzle spacing ratio in the downstream exhibit an axis-switching phenomenon after jet merger. Specifically, at x/d_e < 5 for S/d_e = 2.06, the cross-sectional shape of the middle jet has a small elongation in the z-direction compared to the side jets, and the major axis of the cross-sectional shape is oriented in the y-direction. Thus, triple rectangular jets with a small nozzle spacing ratio may suppress the axis-switching phenomenon of the middle jet due to interference with the side jets.

For S/d_e = 2.75, the mixing development process for triple rectangular free jets shows a middle process between S/d_e = 2.06 and 4.13.

For S/d_e = 4.13 at x/d_e = 1, the cross-section of jets begins to deform, and the four corners of each rectangular jet each become round, that is, the axis-switching phenomenon starts. From x/d_e = 10, the merging of the whole jets begins. At x/d_e = 30, the merged jets have a horizontally long elliptic cross-sectional shape.

Downstream at x/d_e = 30 for S/d_e = 2.06 and 4.13, the contour plots of the velocity of the secondary flow and the velocity vector maps obtained from the numerical simulations are shown in Fig. 11. For S/d_e = 2.06, the vortices were generated on the four sides of the combined jet as they rolled up along the z-direction, suggesting that the axis-switching phenomenon occurred from x/d_e = 20 to 40 as shown in Fig. 10(a). In contrast, for S/d_e = 4.13, there was no roll-up to the z-direction, and the combined jet uniformly spread in the y- and z-directions.

5. CONCLUSIONS

The influence of nozzle spacing on the flow characteristics of triple rectangular jets with an aspect ratio of 2 was experimentally and numerically investigated at a Reynolds number of Re = 15,000. The results are summarized as follows:

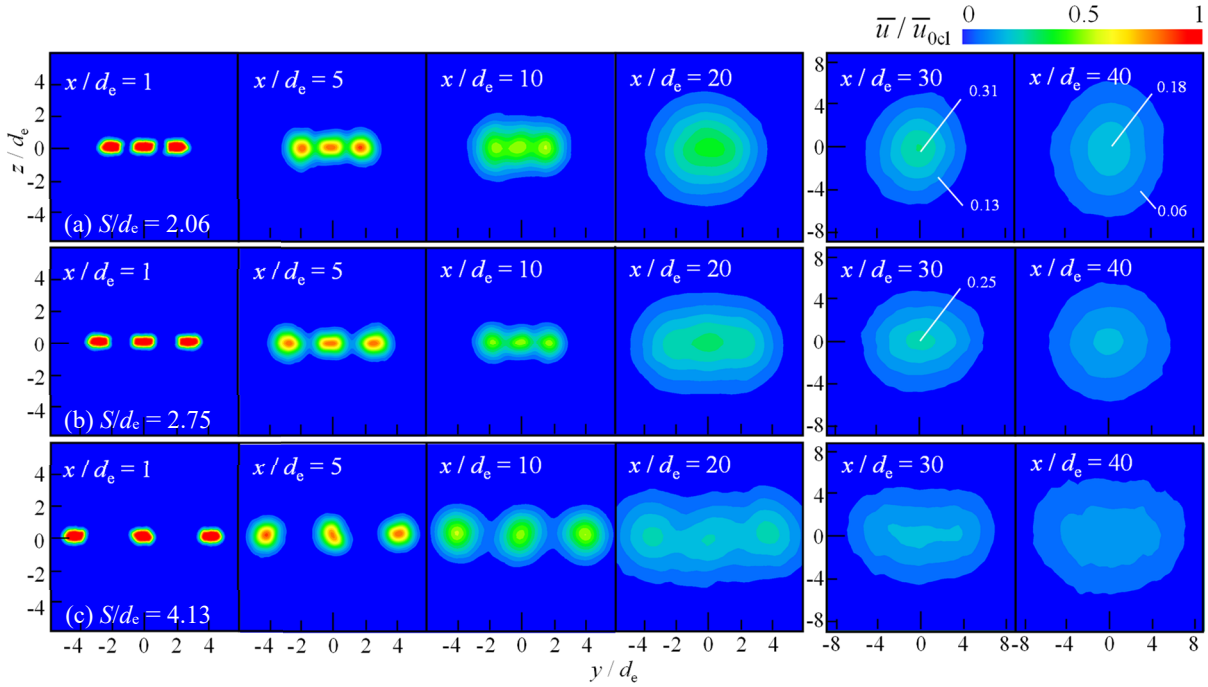

Figure 10. Contour plots of streamwise mean velocity in the y-z cross section for (a) S/d_e = 2.06, (b) S/d_e = 2.75, and (c) S/d_e = 4.13 case.

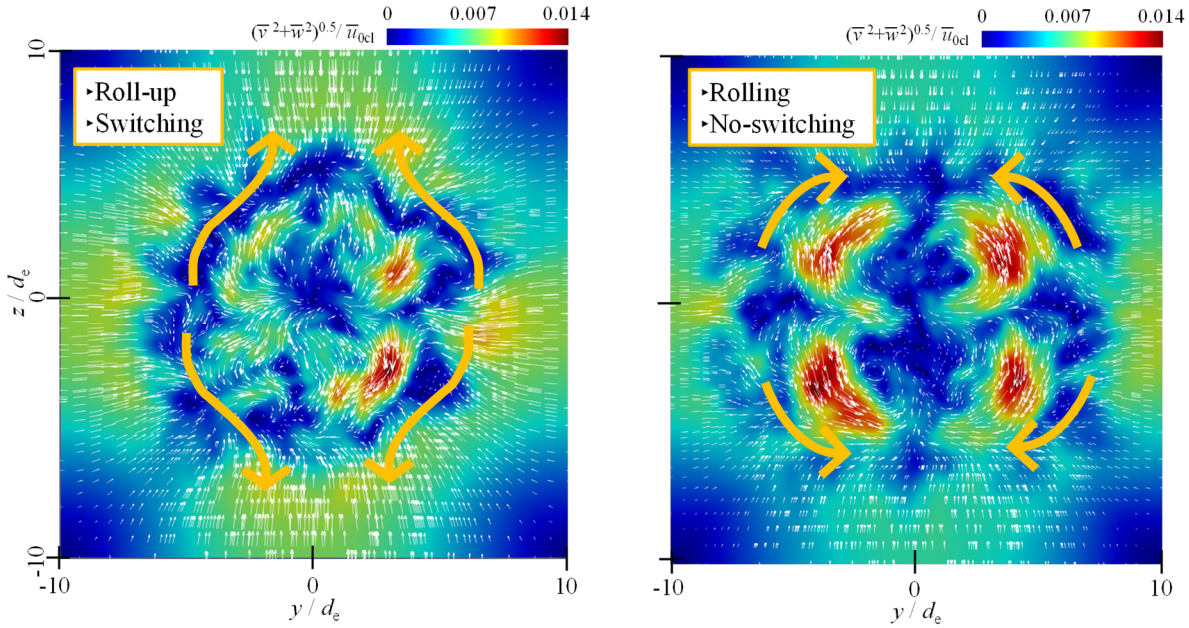

(a) $S/d_e = 2.06$ (b) $S/d_e = 4.13$

Figure 11. Contour plots of secondary flow and vector maps from numerical results at $x/d_e = 30$ for (a) $S/d_e = 2.06$, and (b) $S/d_e = 4.13$ case.

(1) For a small nozzle spacing ratio $S/d_e = 2.06$, the MP and CP move upstream, the mean velocity and turbulent kinetic energy increase on the jet symmetry line, and these increase on the jet centerline after the CP. Therefore, the triple rectangular jets with a small spacing ratio have a large mixing between the middle and side jets from upstream.

(2) For large nozzle spacing ratio, that is, $S/d_e = 4.13$, before the jets merge, the flow characteristics of the triple rectangular free jets were similar to that of the single rectangular free jet.

REFERENCES

[1] Okamoto, T., Yagita, M., Watanabe, A. and Kawamura, K., Interaction of twin circular jet, *Bulletin of JSME*, Vol. 28, No. 238(1985), pp. 617-622.

[2] Laban, A., Aleyasin, S. S., Tachie, M. F. and Koupriyanov, M., Experimental investigation of nozzle spacing effects on characteristics of round twin free jets, *Journal of Fluids Engineering*, Vol.141, No.7 (2019), pp.1-11.

[3] Aleyasin, S. S. and Tachie, M. F., Statistical properties and structural analysis of three-dimensional twin round jets due to variation in Reynolds number, *International Journal of Heat and Fluid Flow*, Vol.76 (2019), pp. 215-230.

[4] Hayashida, K. and Kiwata, T., Effects of nozzle orientation and spacing on flow characteristics of twin rectangular jets, *Transactions of the JSME*, Vol.89, No.927 (2023), Paper No.23-00193, pp.1-18 (in Japanese).

[5] Morris, E. M., Aleyasin, S. S. Biswas, N., and Tachie, M. F., Turbulent properties of triple elliptic free jets with various nozzle orientation, *Journal of Fluids Engineering*, Vol.142, No.3 (2020), pp.1-13.

[6] Teramoto, H., Kiwata, T. and Yajima, K., Influence of nozzle aspect ratio and orientation on flow characteristics of multiple elliptic jets, *Journal of Fluid Science and Technology*, Vol.15, No.2 (2020), Paper No.19-00579.

[7] Nagano, Y. and Tagawa, M., An error analysis of hot-wire measurements, Transactions of the *Japan Society of Mechanical Engineers*, Series B, Vol.54, No.503 (1988), pp.1642-1648 (in Japanese).

[8] Matsuyama, C., OK, LES. tell me the answer for turbulent planar jet, *Proceedings of Fluid Dynamics Conference / Aerospace Numerical Simulation Symposium 2020* (online) (2020), pp.83-91 (in Japanese).

[9] OpenCFD Ltd., OpenFOAM User Guide ver.12 (2024), pp. U-43.

[10] Harima, T., Fujita, S. and Osaka, H., Mixing and diffusion processes of twin circular free jets with various nozzle spacing, Proceedings of the JSME Annual Meeting' 2000 (2000), Paper No.1912 (in Japanese)

Conference on Modelling Fluid Flow (CMFF'25)
The 19th International Conference on Fluid Flow Technologies
Budapest, Hungary, August 26-August 29, 2025

An application of machine learning to compute thermochemistry of reactive flows: A Mixture of Experts Approach

Reza Namdar[1], Mohammad Norouzi[1], Fathollah Varnik[1]

[1] Interdisciplinary Centre for Advanced Materials Simulation (ICAMS), Ruhr-University Bochum, Bochum, 44801, Germany. E-mail: fathollah.varnik@rub.de

ABSTRACT

Accurate and efficient evaluation of chemical source terms is essential for high-fidelity simulations of reactive flows, particularly in large eddy simulation (LES) and direct numerical simulation (DNS). However, the stiffness and high dimensionality of detailed chemical kinetics render direct integration computationally expensive. To address this challenge, we propose a Mixture of Experts (MoE) neural network architecture that adaptively partitions the thermochemical space and models source terms using specialized subnetworks. These expert subnetworks are coordinated by a gating network that assigns input-dependent weights, allowing the model to capture complex, nonlinear reaction behavior across a wide range of conditions without manual zone definitions.

The MoE model is trained on data generated by detailed kinetic solvers and optimized using a mean squared error loss function. Once trained, it is integrated into our in house open source software OpenPhase Acadmic (`www.openphase.rub.de`), allowing for fully self-contained combustion simulations without the need for external libraries such as CANTERA. Comparative simulations show that the MoE model reproduces reaction rates and thermochemical trends with high accuracy, closely matching the CANTERA reference results. Beyond accuracy, the MoE approach is more convenient comparing to other recommended methods for the implementation and is inherently compatible with GPU-based inference. This enables fast, on-the-fly thermochemistry evaluation, making the method highly suitable for large-scale reactive flow simulations.

Keywords: Thermochemistry, Neural Network, Mixture of Experts, Reactive Flows

NOMENCLATURE

N	[−]	number of species
n	[−]	number of expert networks in the MoE model
$\mathcal{M}_k$	[−]	any property of species k
ν'	[−]	molar stoichiometric coefficient of reactants
ν''	[−]	molar stoichiometric coefficient of products
$\bar{W}$	[kg/mol]	mean molecular weight of the mixture
β_j	[−]	exponential temperature exponent for reaction j
$\dot{\omega}$	$[W/m^3]$	heat release rate
$\dot{\omega}_k$	$[mol/m^3 \cdot s]$	net production rate of species k
$\underline{\mathbf{X}}$	[−]	input vector to the neural network
$\underline{\mathbf{Y}}$	[−]	predicted output vector from neural network
ρ	$[kg/m^3]$	density
σ	[−]	standard deviation of prediction error
θ_g	[−]	trainable parameters of the gating network
θ_i	[−]	trainable parameters of the i-th expert network
A_j	[1/s]	pre-exponential factor for reaction j
$E_i(\underline{\mathbf{X}};\theta_i)$	[−]	output of the i-th expert network
E_j	[J/mol]	activation energy for reaction j
$g_i(\underline{\mathbf{X}})$	[−]	pre-activation output of gating network
$G_i(\underline{\mathbf{X}};\theta_g)$	[−]	gating coefficient for i-th expert
K_{fj}	[1/s]	rate constant of the forward reaction j
K_{rj}	[1/s]	rate constant of the reverse reaction j
p	[Pa]	thermodynamic pressure
R	[J/mol · K]	universal gas constant
T	[K]	temperature
T_w	[K]	wall temperature
T_{inlet}	[K]	inlet temperature
W_k	[kg/mol]	molecular weight of species k
Y_k	[−]	mass fraction of species k

$\mathcal{L}$	[−]	total loss function of the MoE model

Subscripts and Superscripts

f	forward reaction
inlet	inlet boundary
j	index of reaction
k	index of species
r	reverse reaction
w	wall

1. INTRODUCTION

Accurate and efficient modeling of chemical kinetics is essential for high-fidelity simulations of reactive flows, particularly in large eddy simulation (LES) and direct numerical simulation (DNS). These simulations depend on detailed chemical mechanisms to resolve flame structures and predict species evolution and heat release rates. However, the strong nonlinearity, stiffness, and high dimensionality of these mechanisms make direct integration of kinetic source terms prohibitively expensive in complex turbulent configurations. To reduce this cost, various surrogate modeling strategies have been explored, including mechanism reduction, manifold-based tabulation, and pre-trained neural networks [1, 2, 3, 4]. Among these, machine learning–based methods—particularly deep neural networks—have gained attention for their ability to approximate complex kinetics while significantly lowering computational expense.

One of the earliest applications of machine learning in combustion modeling employed dense feed-forward neural networks to emulate detailed chemical kinetics. These models are trained on high-fidelity datasets—typically generated from laminar flame simulations or precomputed manifolds—to learn mappings from input features such as species mass fractions and temperature to outputs like reaction rates or thermochemical source terms. Zhang et al. [5] demonstrated that deep neural networks can approximate complex reaction kinetics with high accuracy when trained on structured datasets and equipped with robust sampling strategies. Cheng et al. [4] further showed that such surrogates can be deployed in DNS to accelerate on-the-fly evaluation of chemical source terms, reducing overall simulation cost while preserving key flame characteristics. Despite their interpolation capabilities, these black-box models often lack physical consistency and may lose accuracy when extrapolating to regions of thermochemical space that are underrepresented in the training data [2].

To overcome the limitations of purely data-driven models, recent research has explored embedding physical laws into the training process through physics-informed neural networks (PINNs). Rather than relying solely on labeled data, PINNs incorporate domain knowledge—such as conservation of mass, element balance, and Arrhenius kinetics—into the loss function, enabling the network to satisfy governing equations during optimization. Zhang et al. [6] introduced a constrained reaction-kinetics PINN (CRK-PINN), which embeds both element conservation and kinetic rate expressions to improve prediction accuracy in laminar flames. Wu et al. [7] extended this approach with FlamePINN-1D, which enables both forward and inverse solutions of 1D reacting flow problems while maintaining thermodynamic consistency and reducing data requirements. By embedding physical structure into the training process, PINNs offer improved extrapolation performance and generalizability, particularly in low-data or multiscale environments.

Moving beyond loss-function constraints, Ji and Deng [8] introduced the Chemical Reaction Neural Network (CRNN), a neural architecture explicitly designed to reflect the structure of chemical kinetics. Rather than imposing physical laws through the loss function, the CRNN encodes them directly into the network architecture. Each layer and connection corresponds to a chemical species or reaction pathway, allowing the model to learn both reaction mechanisms and kinetic parameters from time-series data of species concentrations. This physics-structured design enforces thermodynamic consistency and mass-action kinetics by construction, while also enhancing interpretability. However, the fixed structure of CRNNs may limit their flexibility when adapting to mechanisms with different topologies or under varying flow conditions.

While structured and physics-informed networks have improved the fidelity of combustion surrogates, another effective strategy involves decomposing the domain—spatially or in thermochemical space—into distinct regimes, each modeled by a separate neural network. Cheng et al. [4] implemented this by dividing the flame domain into four zones—burned gas, reaction zone, preheated zone, and unburned gas—based on local thermochemical structure. A separate neural network was trained for each zone, allowing specialization in the dynamics and scales relevant to each region. This clustering-based method reduced local approximation error and improved robustness in DNS. However, its reliance on manually defined thresholds tied to specific fuels and flame conditions limits generalization. Cheng et al. acknowledged this drawback and suggested that future work could benefit from automated or unsupervised clustering strategies adaptable to different reaction mechanisms or combustion regimes.

A natural progression of the zone-based clustering idea is the Mixture of Experts (MoE) framework, where both the partitioning of thermochemical space and the specialization of subnetworks are learned automatically during training. Owoyele et al. [9] applied this concept to surrogate modeling of combustion manifolds by training multiple expert networks and a gating function to emulate species mass fractions from precomputed flamelet data. Their method

eliminated the need for *a priori* clustering while preserving interpretability through data-driven specialization.

Building on this principle, the present work employs a MoE architecture to directly learn chemical source terms—specifically, reaction rate outputs from detailed kinetics—based on local thermochemical states. The proposed surrogate is designed for on-the-fly evaluation within reactive flow solvers, enabling accurate and efficient replacement of stiff chemical source term calculations without relying on predefined zonal boundaries. The primary motivation for employing a neural network model is to enhance the flexibility and portability of the simulation framework. Unlike traditional libraries such as Cantera, which are not compatible with GPU-based computation using CUDA, a neural network can be deployed entirely on the GPU. This eliminates the need for external software to evaluate thermochemical properties and enables high-performance simulations on GPU-accelerated platforms.

2. MATHEMATICAL MODEL

For a mixture containing N chemical species, the reactions occur according to [10]:

$$\sum_{k=1}^{N} \nu'_{kj} \mathcal{M}_k \rightleftharpoons \sum_{k=1}^{N} \nu''_{kj} \mathcal{M}_k, \tag{1}$$

where $\mathcal{M}_k$ represents a property of species k involved in reaction j, and ν'_{kj} and ν''_{kj} are the molar stoichiometric coefficients of species k on the reactant and product sides, respectively.

Let Y_k, ρ, and $\dot{\omega}_k$ represent the mass fraction of species k, the mixture density, and the net production (or destruction) rate of species k due to chemical reactions. The governing equations are given by [10]:

$$\frac{\partial Y_k}{\partial t} = \frac{\dot{\omega}_k}{\rho}, \tag{2}$$

$$\dot{\omega}_k = W_k \sum_{j=1}^{N_r} \nu_{kj} \left(K_{fj} \prod_{k=1}^{N} [X_k]^{\nu'_{kj}} - K_{rj} \prod_{k=1}^{N} [X_k]^{\nu''_{kj}} \right), \tag{3}$$

$$\nu_{kj} = \nu''_{kj} - \nu'_{kj}, \tag{4}$$

$$[X_k] = \frac{\rho Y_k}{W_k}, \tag{5}$$

$$\rho = \frac{p \bar{W}}{RT}, \tag{6}$$

$$\frac{1}{\bar{W}} = \sum_{k=1}^{N} \frac{Y_k}{W_k}, \tag{7}$$

where W_k is the molecular weight of species k, and $[X_k]$ is its molar concentration. The terms $\bar{W}$, p, and T refer to the mean molecular weight, pressure, and temperature of the gas mixture, respectively. The universal gas constant is $R = 8.314\ \mathrm{J/(mol \cdot K)}$.

The reaction rate constants K_{fj} and K_{rj} for the forward and reverse directions of reaction j are typically modeled using the Arrhenius expression [10]:

$$K_j = A_j T^{\beta_j} \exp\left(-\frac{E_j}{RT}\right), \tag{8}$$

where A_j, β_j, and E_j are empirical parameters determined from experimental measurements. All these constants are evaluated separately for forward and reverse reaction.

3. DATA GENERATION

In this study, data required for training the machine learning models were generated through detailed numerical simulations of premixed methane/air combustion, using the BFER [11] chemical kinetics mechanism. This mechanism involves six species: $O_2, CH_4, H_2O, CO, CO_2, N_2$, participating in two global reaction steps,

$$CH_4 + 1.5\,O_2 \rightarrow CO + 2\,H_2O$$
$$CO + 0.5\,O_2 \leftrightarrow CO_2$$

For simplicity, the effect of pressure is neglected and fixed at 1 atm throughout all simulations.

To ensure comprehensive coverage of the thermochemical composition space encountered during practical simulations, a wall-flame interaction configuration was chosen as the test case. This configuration captures a wide range of flame behaviors and mixture conditions. The computational domain and boundary setup are shown in Figure 1. The key control parameters were the inlet temperature T_{inlet}, varied between 300 K and 800 K. The upper and the lower wall are kept at the same temperature, T_w. To cover a wide temperature range, T_w is varied from 300 K to 1200 K. These boundary conditions produce a wide variety of reactive flow states. To perform these simulations, OpenPhase Academic (`www.openphase.rub.de`) was used, which was coupled with CANTERA to model the thermodynamic properties and kinetic information. The simulations were conducted using a hybrid numerical solver that combines the Lattice Boltzmann Method (LBM) with the Finite Difference Method (FDM). In this approach, the flow field is resolved using a thermal compressible Lattice Boltzmann model, while the temperature and species transport equations are solved using finite difference techniques. The underlying mathematical model describes a mixture comprising N species under low Mach number conditions, as detailed in [12]. From these simulations, the local flow field—specifically, species mass fractions and temperature—was sampled and recorded as input features. As the next step in generating the dataset, for the sake of higher accuracy, the corresponding output quantities, namely the net production rates of chemical species, were calculated via CANTERA. These quantities exhibit complex, nonlinear, and stiff behavior, primarily due to their strong temperature dependence following the Arrhenius law. The net production rates span several orders of magnitude, reflecting the multi-scale nature of chemical kinetics

and presenting a significant challenge for data-driven modeling.

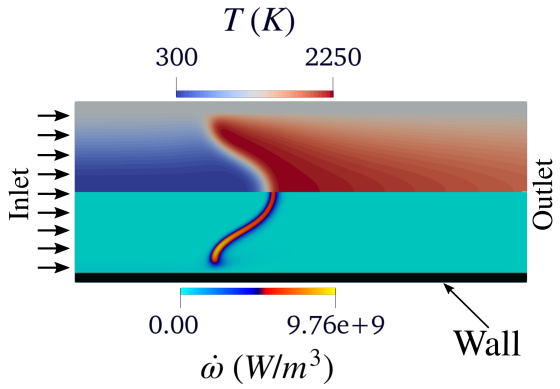

Figure 1. Schematic view of the simulation domain used to generate training data. The setup features a premixed methane/air flow interacting with two planar parallel walls at constant and equal temperature. By varying the inlet temperature (T_{inlet}) and wall temperature (T_w), a wide range of thermochemical states are obtained within the gas phase, which are used to train the neural network models. We use the symmetry of the problem with respect to the middle plane and show only half of the domain for the fields of temperature (upper half) and the rate of heat release (lower half).

4. NEURAL NETWORK ARCHITECTURE

Inspired by the approach of Chi et al. [13], who manually partitioned the reactive flow domain into sub-regions, we employ a neural network architecture that learns such partitions automatically from data. Manual domain decomposition often relies on problem-specific heuristics that may not generalize across different chemical mechanisms. To address this, we adopt a Mixture of Experts (MoE) framework, which enables the network to learn distinct functional regimes in a data-driven and adaptive manner.

The MoE model consists of multiple specialized subnetworks, known as *experts*, and a separate *gating network* that dynamically assigns soft weights to each expert based on the input. This design enhances the model's capacity to represent the complex, nonlinear behavior characteristic of detailed chemical kinetics.

4.1. Problem Formulation

Let the input vector $\underline{X} \in \mathbb{R}^d$ represent the local thermochemical state, consisting of the mass fractions of N chemical species and the temperature T:

$$\underline{X} = [Y_1, Y_2, \ldots, Y_N, T, 1/T]^\top . \tag{9}$$

To better capture Arrhenius-type behavior, the reciprocal of temperature ($1/T$) is included as an additional input. The output vector $\underline{Y} \in \mathbb{R}^N$ contains the net production rates of the species, as computed by a detailed chemical kinetics solver.

In the Mixture of Experts framework, the target function is approximated using K expert networks. The final output is computed as a weighted sum of the expert predictions:

$$\underline{Y} = \sum_{i=1}^{K} G_i(\underline{X};\theta_g) \cdot E_i(\underline{X};\theta_i), \tag{10}$$

where $E_i(\underline{X};\theta_i)$ is the output of the i-th expert, and $G_i(\underline{X};\theta_g)$ is the corresponding gating weight computed by the gating network. These weights are normalized using a softmax function:

$$G_i(\underline{X}) = \frac{\exp(g_i(\underline{X}))}{\sum_{j=1}^{K} \exp(g_j(\underline{X}))}, \quad i = 1, \ldots, K. \tag{11}$$

Each expert is encouraged to specialize in a particular thermochemical subdomain (e.g., high vs. low temperature, or fuel-lean vs. fuel-rich regions), while the gating network learns to interpolate between them smoothly.

4.2. Loss Function and Training Strategy

The model is trained end-to-end using supervised learning. The loss function is defined as the mean squared error (MSE) between the predicted and reference production rates:

$$\mathcal{L}(\theta_g, \theta_1, \ldots, \theta_K) = \left\| \underline{Y}_{\text{true}} - \sum_{i=1}^{K} G_i(\underline{X}) E_i(\underline{X}) \right\|^2 , \tag{12}$$

where $\underline{Y}_{\text{true}}$ denotes the reference production rates from detailed kinetics. The model is optimized using the Adam optimizer. The dataset is split into training, validation, and test subsets.

4.3. Architectural Illustration

Figure 2 illustrates the overall architecture. The input vector is fed into both the gating and expert networks. The gating network computes soft weights for each expert, and the final output is the weighted sum of the expert outputs.

4.4. Advantages for Reactive Flow Modeling

The MoE framework offers several advantages for modeling reactive flows. First, it is dynamically adaptive and can respond to varying chemical regimes. Second, it promotes functional specialization: Each expert learns to make accurate predictions within a specific subdomain. This does not lead to a division of the physical space among the experts. Rather, each expert becomes a good predictor for a part of the thermochemical data space spanned by the two sets of the input and output vari-

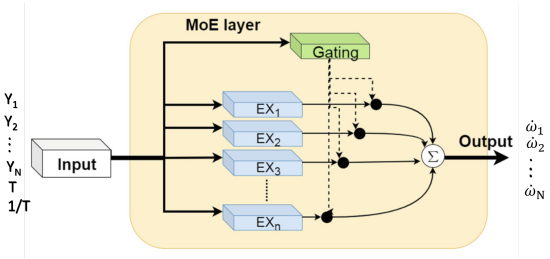

Figure 2. Schematic of the Mixture of Experts (MoE) model (adapted from [14]). The input vector X is processed by a gating network that produces a soft distribution over n experts. Each expert yields an independent output vector, and the final output Y is computed as their weighted sum.

ables—specifically the distribution of net production rates as a function of species concentrations and temperature. Third, the use of softmax-based weighting ensures a smooth transition between expert outputs, preserving numerical stability. Finally, the modular architecture is scalable and can accommodate additional species or features with minimal structural modifications.

4.5. Network Implementation Details

In our implementation, the input vector includes the mass fractions of five chemical species (excluding N_2), the temperature T, and its reciprocal $1/T$, for a total of seven input features. The output vector contains the net production rates of the same five species.

Prior to training, both input and output values are normalized using Min-Max scaling. The MoE model includes five expert networks and a single gating network. Each expert comprises three hidden layers with 16 ReLU units per layer, followed by a linear output layer with five neurons. The gating network consists of one hidden layer with 32 ReLU units, followed by a softmax-activated output layer with five neurons to produce the expert weights.The entire dataset is divided into three parts. First, 20% of the data is set aside and not used until the final testing phase. The remaining 80% is then further split: 80% of it is used for training the model, and the remaining 20% is used for cross-validation.

The model is trained using the Adam optimizer and a mean squared error loss. Figure 3 compares the outputs of the trained model against reference values computed using CANTERA. As shown, the model accurately predicts source terms for unseen test data.

5. RESULTS AND DISCUSSION

In this section, we present the results of numerical simulations performed with the neural network-based thermochemistry model integrated into the OpenPhase solver. All simulations are carried out using OpenPhase, with the thermochemical source terms computed either from the trained neural network (NN) or using detailed chemistry from Cantera

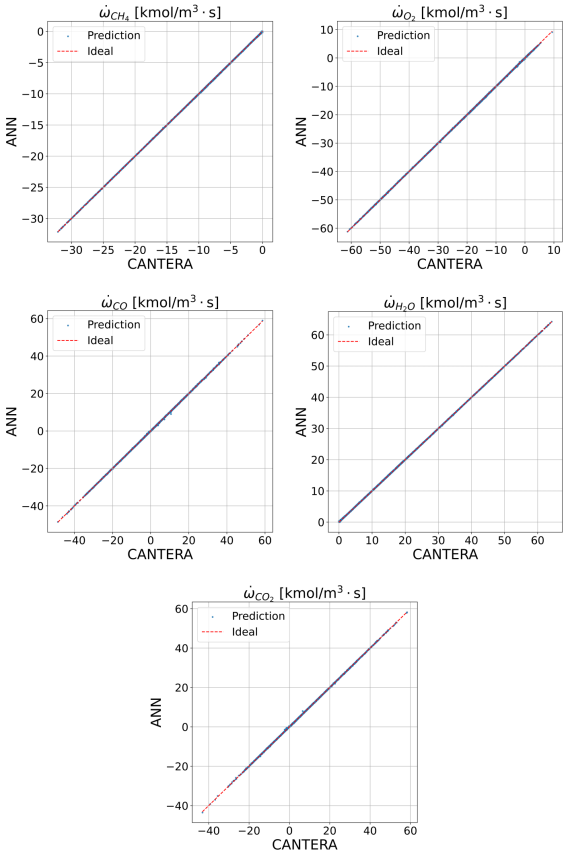

Figure 3. Comparison of net production rates of species obtained from model prediction versus reference source terms computed with CANTERA for the test set.

for comparison. In all test cases, the combustion of a premixed methane/air mixture is simulated under stoichiometric conditions. The chemical kinetics are modeled using the reduced BFER mechanism, which offers a simplified yet sufficiently accurate depiction of essential combustion phenomena. Although the BFER mechanism is relatively compact, the advantages of employing a neural network (NN) framework become even more pronounced when applied to more complex kinetic mechanisms, where the computational overhead of traditional solvers such as Cantera increases significantly, while a trained NN can evaluate source terms with greater computational efficiency.

To evaluate the performance of the NN-based model, we consider two test cases: (i) a one-dimensional freely propagating flame, and (ii) a flame propagating through a packed bed of solid cylinders.

5.1. One-Dimensional Flame Propagation

This test case simulates a freely propagating premixed flame in a one-dimensional domain. The initial setup consists of two regions: the left half contains a stoichiometric methane-air mixture, while the right half is filled with burnt combustion products.

An initial temperature perturbation is applied at the center to initiate ignition. The flame then propagates until a steady-state profile is achieved. The simulation parameters are summarized in Table 1.

Table 1. Simulation parameters for the one-dimensional freely propagating flame case

Parameter	Value
Inlet temperature	300 K
Pressure	1 atm
Equivalence ratio	1.0
Spatial resolution	1×10^{-5}m
Time step	2×10^{-8} s
Convective scheme	van Leer
Diffusion scheme	Central differencing
Fuel mixture	Methane/air
Chemical mechanism	BFER

Figure 4 shows the steady-state profiles of major species mass fractions obtained using the NN model and the detailed Cantera-based chemistry. Five key species are considered: CH_4, O_2, CO_2, H_2O, and CO. The results from both models are in close agreement, indicating accurate prediction of species consumption and product formation.

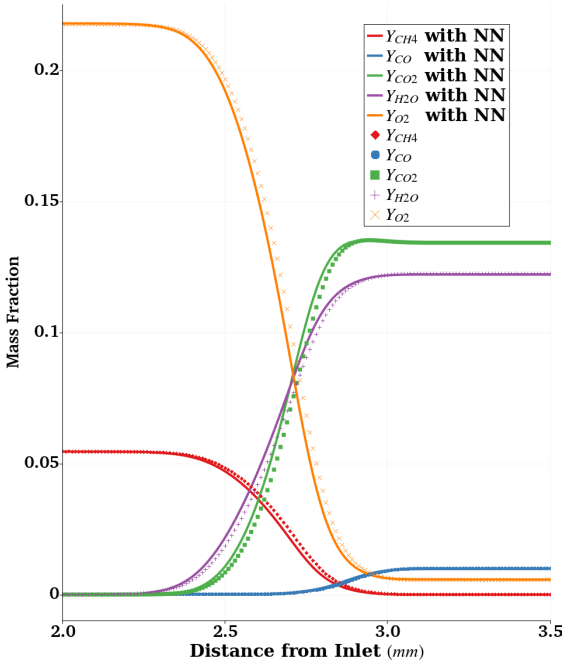

Figure 4. Comparison of species mass fraction profiles for the one-dimensional flame. Results from the NN model and Cantera are shown for CH_4, O_2, CO_2, H_2O, and CO.

In Figure 5, we compare the temperature profiles and heat release rate (HRR) for both models. The HRR peak location corresponds to the flame front and shows excellent agreement between the two approaches. The flame thickness and temperature rise are nearly identical, further confirming the NN model's accuracy in predicting the flame structure.

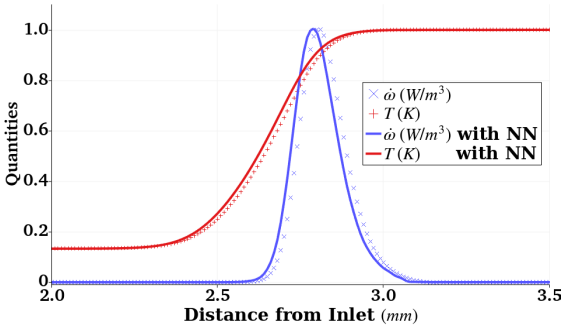

Figure 5. Comparison of temperature and heat release rate profiles for the one-dimensional flame. The peak of the HRR curve represents the flame front location.

5.2. Flame Propagation in a Packed Bed

The second test case models the propagation of a premixed flame through a two-dimensional domain filled with solid cylinders, representing a packed bed. The computational domain is initially divided into two parts: the lower region contains a stoichiometric methane-air mixture, while the upper region contains combustion products. A small velocity is imposed at the inlet to allow the flame to propagate upstream toward the boundary. The simulation setup is summarized in Table 2.

Table 2. Simulation parameters for the flame propagation in a packed bed

Parameter	Value
Inlet temperature	300 K
Equivalence ratio	1.0
Inlet boundary	Fixed velocity
Outlet boundary	pressure outlet
Solid wall condition	No-slip, adiabatic
Spatial resolution	2.5×10^{-5} m
Time step	2×10^{-7} s
Convective scheme	van Leer
Diffusion scheme	Central differencing
Fuel mixture	Methane/air
Chemical mechanism	BFER

Figure 6 presents a sequence of snapshots showing the temporal evolution of the flame as it propagates through the packed bed. The flame front interacts with the solid structures, leading to local curvature changes that affect propagation dynamics. The NN-based and Cantera-based results are compared side-by-side to highlight differences in flame behavior and methane consumption.

Overall, both test cases demonstrate that the neural network model captures key features of combustion dynamics with good fidelity compared to detailed chemistry. Although the BFER mechanism is relatively simple, the NN-based approach offers sig-

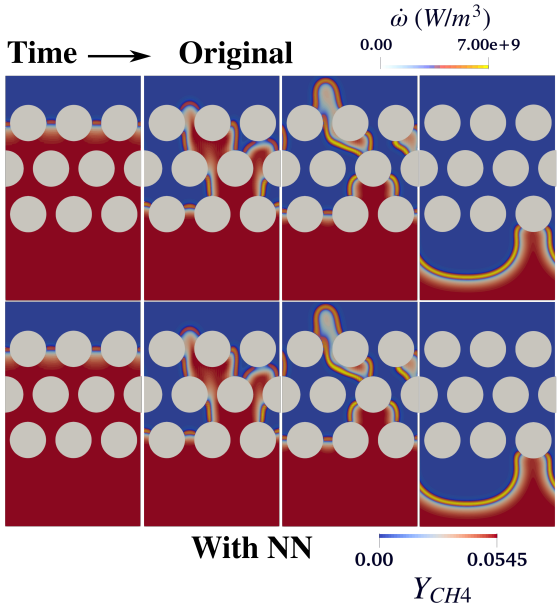

Figure 6. Temporal progression of the flame front and methane mass fraction within the packed bed domain. The simulation employs a low inlet velocity at the lower boundary, with a pressure outlet condition specified at the upper boundary. Periodic boundary conditions are enforced along the lateral boundaries. Results are presented for the Cantera-based model (top row) and the neural network (NN) model (bottom row).

nificant potential for scaling to larger mechanisms and for deployment on GPU architectures — a direction we plan to explore in future work.

6. CONCLUSION

This work introduces a Mixture of Experts (MoE) neural network framework for efficient and accurate prediction of chemical source terms in reactive flow simulations. By leveraging multiple specialized expert networks and a gating network that adaptively partitions the thermochemical space, the proposed model captures the complex, nonlinear behavior of chemical kinetics across a wide range of combustion regimes. This data-driven approach eliminates the need for rigid zone definitions and improves flexibility compared to traditional surrogate models.

Trained on high-fidelity data from detailed chemical solvers such as Cantera, the MoE model demonstrates strong agreement with reference results. In addition to maintaining high accuracy, the architecture can significantly reduce computational overhead for large and stiff reaction mechanisms. Unlike traditional libraries, which are not GPU-compatible, the neural network-based implementation enables efficient inference on CUDA-capable hardware. This makes the method well-suited for large-scale, high-fidelity simulations, such as those encountered in DNS and LES of turbulent combustion.

Future work will focus on extending this approach to more complex mechanisms, incorporating advanced clustering strategies for expert assignment, and applying the framework to multi-dimensional flow configurations. Overall, the MoE architecture represents a promising step toward scalable, GPU-accelerated reactive flow modeling that preserves the fidelity of detailed chemistry while enabling real-time performance.

ACKNOWLEDGEMENTS

Funded by the Deutsche Forschungsgemeinschaft (DFG, German Research Foundation) - Project-ID 422037413 - TRR 287.

REFERENCES

[1] Li, K., Rahnama, P., Novella, R., and Somers, B., 2023, “Combining flamelet-generated manifold and machine learning models in simulation of a non-premixed diffusion flame”, *Energy and AI*, Vol. 14, p. 100266.

[2] Readshaw, T., Franke, L. L., Jones, W., and Rigopoulos, S., 2023, “Simulation of turbulent premixed flames with machine learning - tabulated thermochemistry”, *Combustion and Flame*, Vol. 258, p. 113058.

[3] Luo, L., Liu, Q., Sun, J., and Huang, Y., 2025, “Exploring surface reaction mechanism using a surface reaction neural network framework”, *Chemical Engineering Science*, Vol. 306, p. 121307.

[4] Chi, C., Janiga, G., and Thévenin, D., 2021, “On-the-fly artificial neural network for chemical kinetics in direct numerical simulations of premixed combustion”, *Combustion and Flame*, Vol. 226, pp. 467–477.

[5] Zhang, T., Yi, Y., Xu, Y., Chen, Z. X., Zhang, Y., E, W., and Xu, Z.-Q. J., 2022, “A multi-scale sampling method for accurate and robust deep neural network to predict combustion chemical kinetics”, *Combustion and Flame*, Vol. 245, p. 112319.

[6] Zhang, S., Zhang, C., and Wang, B., 2024, “CRK-PINN: A physics-informed neural network for solving combustion reaction kinetics ordinary differential equations”, *Combustion and Flame*, Vol. 269, p. 113647.

[7] Wu, J., Zhang, S., Wu, Y., Zhang, G., Li, X., and Zhang, H., 2025, “FlamePINN-1D: Physics-informed neural networks to solve forward and inverse problems of 1D laminar flames”, *Combustion and Flame*, Vol. 273, p. 113964.

[8] Ji, W., and Deng, S., 2021, “Autonomous Discovery of Unknown Reaction Pathways from Data by Chemical Reaction Neural Network”,

The Journal of Physical Chemistry A, Vol. 125 (9), pp. 1990–1999.

[9] Owoyele, O., Kundu, P., and Pal, P., 2021, "Efficient bifurcation and tabulation of multi-dimensional combustion manifolds using deep mixture of experts: An a priori study", *Combustion and Flame*, Vol. 226, pp. 203–215.

[10] Poinsot, T., and Veynante, D., 2005, *Theoretical and numerical combustion*, RT Edwards, Inc.

[11] Franzelli, B. G., 2011, "Impact of the chemical description on direct numerical simulations and large eddy simulations of turbulent combustion in industrial aero-engines", Ph.D. thesis, INPT.

[12] Hosseini, S. A., Safari, H., Darabiha, N., Thévenin, D., and Krafczyk, M., 2019, "Hybrid lattice Boltzmann-finite difference model for low Mach number combustion simulation", *Combustion and Flame*, Vol. 209, pp. 394–404.

[13] Chi, C., Janiga, G., and Thévenin, D., 2021, "On-the-fly artificial neural network for chemical kinetics in direct numerical simulations of premixed combustion", *Combustion and Flame*, Vol. 226, pp. 467–477.

[14] Alazizi, A., Habrard, A., Jacquenet, F., He-Guelton, L., and Oblé, F., 2020, "Dual sequential variational autoencoders for fraud detection", *Advances in Intelligent Data Analysis XVIII: 18th International Symposium on Intelligent Data Analysis, IDA 2020, Konstanz, Germany, April 27–29, 2020, Proceedings 18*, Springer, pp. 14–26.

Conference on Modelling Fluid Flow (CMFF'25)
The 19th International Conference on Fluid Flow Technologies
Budapest, Hungary, August 26-August 29, 2025

COMBINING THE PARTIALLY STIRRED REACTOR WITH A DEM DESCRIPTION: THE PYROLYSIS OF BIOMASS

Davide MAPELLI[1], Don Dasun ATTANAYAKE[1], Berend VAN WACHEM[1], Fabian SEWERIN[1,*]

[1] Chair of Mechanical Process Engineering, Otto-von-Guericke-Universität Magdeburg, Universitätsplatz 2, 39106 Magdeburg, Germany
* Corresponding Author. E-mail: fabian.sewerin@ovgu.de

ABSTRACT

In DEM-CFD descriptions of granular assemblies, the thermochemical state of the interstitial gas is commonly assumed to vary on length scales that are comparable to the supplied spatial resolution. Since chemical reactions, gas-particle mass and heat exchanges and mixing limitations may, however, cause the gas composition to vary on much smaller scales, we present an amendment of the DEM-CFD formulation that is, conceptually, based on the likelihood for a particular gas composition to occur inside a CFD cell. Focussing on a single variable-size control volume at constant pressure, this probabilistic formulation leads to the notion of a partially stirred reactor (PaSR) that interacts with an assembly of DEM particles. The biomass particles we consider here feature a spherical porous structure and are enclosed by passive boundary layers that control the transfer of mass and heat towards the surrounding PaSR-atmosphere. For a fixed particle size, the species mass and gas-solid enthalpy balances representing intra-particle conversion and transport are discretised along the radial coordinate with a standard finite volume approach. The combined DEM-PaSR model can be solved using a statistical approach and, upon incorporation of solid and gas phase reaction mechanisms, provides a test bed for gauging the influence of small-scale thermochemical heterogeneity on the efficacy of the pyrolysis process.

Keywords: Biomass pyrolysis, Discrete element method, Partially stirred reactor, PDF method

ABBREVIATIONS

CFD	Computational fluid dynamics
DEM	Discrete element method
PaSR	Partially stirred reactor
PDF	Probability density function
SDE	Stochastic differential equation

1. INTRODUCTION

In the unresolved DEM-CFD approach for modelling of reactive granular assemblies, the flow field and the composition of the interstitial gas are described on length scales that exceed the particles' sizes. This is achieved with the aid of a spatial filtering operation that eliminates small-scale structures from the flow and composition fields, while referring the presence of particles and gas-particle boundaries to a void fraction and a surface density, respectively. Here, every spatial location is associated with a mean flow and a mean composition that are defined as weighted averages of the interstitial fields over the filter volume centred at the location. In the present article, our objective is to amend the unresolved DEM-CFD formulation by a description of small-scale variability in the gas phase composition as caused by intricate flow structures, thin reaction fronts, particle heating or mass transfer. The incorporation of small-scale compositional heterogeneity not only permits a closed-form treatment of gas phase chemical reactions, but also provides a pathway for including gas-particle mass and heat exchanges with a closure assumption that is less stringent than present hypotheses.

The gas phase composition is commonly expressed in terms of reactive scalars that uniquely define the gas' thermochemical state at low Mach numbers. Drawing on probabilistic methods that originated in the field of turbulent reacting flows [1, 2, 3], the values of the reactive scalars at any location inside the filter volume are conceived of as random variables and associated with a PDF [4]. Starting from the scalars' balance laws on the inter-particle void space and incorporating gas-particle mass and heat exchanges, we obtain an evolution equation for the one-point, one-time joint scalar PDF in which the effects of gas phase chemistry are naturally closed. Since spatial transport involves both two-point statistics and scalar-velocity correlations which cannot be evaluated based on the joint scalar

PDF, the transport terms in the PDF equation require phenomenological closure. For example, species diffusion and heat conduction promote a homogenisation on the smallest scales that is covered by a micromixing model. Additionally, small-scale advection causes reorganisations of the scalars' spatial distributions and is, in the presence of turbulence, often likened to large-scale diffusion. Finally, the incorporation of particles is rendered difficult by the presence of scalar-geometry correlations as well as the distinction between the scalars' distributions along the particle surfaces and their volume distribution. However, if the fluid elements are, at least conceptually, separated from the particle surface by a resistive boundary layer that controls the gas-particle mass and heat transfer, then it may be admissible to approximate the surface distributions in terms of the volume-related joint scalar PDF, a simplification we adopt here.

In the case of large-scale homogeneity, the PDF formulation reduces to the law of a PaSR [5]. This is a model flow system that may be viewed as a constant pressure, variable-volume vessel whose contained fluid elements differ in terms of their thermochemical composition. Physically, the compositional heterogeneity is driven by gas phase chemistry, inflow and outflow, while diffusion-induced micromixing acts in a converse way. In our case, the gas inside the PaSR additionally interacts with an assembly of spherical porous biomass particles through mass and heat transfer rates that are obtained from a passive boundary layer model. The chemical decomposition of the particles' solid skeleton is thermally activated and entails mass effluxes that yield pyrolysis gas and condensed phase oil as main products. The intra-particle transport and conversion are governed by balance laws for the species masses and the combined gas-solid enthalpy. The latter is evaluated based on the assumption that there is no temperature slip between the solid matrix and the intra-particle gas at any radial position. Upon spatial discretisation, the intra-particle balance laws turn into DEM equations that can be integrated in time alongside the PaSR equation.

Albeit idealised, the combined DEM-PaSR formulation we present constitutes a powerful computer-based tool for analysing the influence that the commonly disregarded small-scale variability of the gas composition has on the pyrolysis process. This, in turn, is a first step towards enriching the unresolved DEM-CFD approach by a description of small-scale variability and accommodating gas phase chemistry without intervening assumptions. As reference, Table 1 lists the modelling assumptions and simplifications we introduce in the following on part of the gas phase, the compositional heterogeneity and a single biomass particle.

The present article is organised as follows: After recalling the notion of a spatial filter, the closure challenges associated with small-scale interstitial transport, chemical reactions and gas-particle interactions are indicated and a transport equation for the joint scalar PDF is formulated (Section 2). This equation is coupled to the governing DEM equations through joint scalar statistics that represent the diversity of far-field compositions experienced by the DEM particles. Following a reduction to the PaSR (Section 3), we present a single particle model for biomass alongside the rates at which mass and enthalpy are emitted through a passive boundary layer (Section 4). The relevant numerical solution methods are briefly outlined (Section 5), before we conclude with a summary and an outlook (Section 6).

2. MODELLING FRAMEWORK

A granular assembly is a packed or slowly moving bed of centimetre-sized particles (Figure 1). In pyrolysis reactors, the bed is subjected to a high-temperature treatment by directing a hot inert gas through the bed's void space $\Omega_g(t)$. The interstitial gas behaves as a multicomponent ideal gas and is described in terms of the velocity $\mathbf{u}_g(\mathbf{x},t)$, the pressure $p_g(\mathbf{x},t)$ and the reactive scalars $\mathbf{\Phi} = (\mathbf{Y}_g, h_g)$ that encompass the species mass fractions $\mathbf{Y}_g(\mathbf{x},t) = (Y_{g,k}(\mathbf{x},t))_{k\in\mathcal{G}}$ and the gas enthalpy $h_g(\mathbf{x},t)$. The label set $\mathcal{G}$ that appears here contains the molecular formulas of all gas phase species. If the Mach number is small, then the thermodynamic pressure P is distinct from the mechanical pressure $p_g(\mathbf{x},t)$ and remains uniform across the flow domain. Consequently, the reactive scalars uniquely define the thermal state of the gas and both the gas temperature T and the gas density ρ_g may be computed in terms of $\mathbf{\Phi}$ at $(\mathbf{x},t)$ [6],

$$h_g = \sum_{k\in\mathcal{G}} Y_{g,k} h_k(T), \tag{1}$$

$$\rho_g = \frac{PW_g}{RT}. \tag{2}$$

Here, h_k denotes the specific enthalpy of species $k \in \mathcal{G}$ and R represents the universal gas constant. The gas' mean molecular weight W_g, moreover, is related to the species' molecular weights W_k according to $W_g = 1/\sum_{k\in\mathcal{G}}(Y_k/W_k)$.

On the void space $\Omega_g(t)$, the flow field $(\mathbf{u}_g, p_g)$ is governed by the variable-density Navier-Stokes equations [7, Chapter 1]. In the case of equal diffusivities $D(\mathbf{\Phi})$ and a Lewis number of unity ($Le = 1$), the reactive scalars Φ_k, moreover, obey the transport equations [7, Chapter 1]

$$\frac{\partial\rho_g\Phi_k}{\partial t} + \nabla_{\mathbf{x}}\cdot\left(\rho_g\mathbf{u}_g\Phi_k\right) = \nabla_{\mathbf{x}}\cdot\left(\rho_g D\nabla_{\mathbf{x}}\Phi_k\right) + \rho_g\dot{\omega}_k \tag{3}$$

with $k \in \mathcal{G}' = \mathcal{G}\cup\{h_g\}$. For $k\in\mathcal{G}$, $\dot{\omega}_k(\mathbf{\Phi})$ represents the rate (in $[\mathrm{kg}_k/(\mathrm{kg(g)\,s})]$) at which gas phase chemical reactions cause a species to form or vanish. The gas enthalpy, by contrast, is a conserved scalar and its associated source term $\dot{\omega}_{h_g}$ vanishes. Based on a Schmidt number Sc of 0.7, the common diffusivity $D(\mathbf{\Phi})$ in Eq. (3) is evaluated in terms

Table 1. Summary of the modelling assumptions we introduce in Sections 2 to 4. The properties of the gas phase listed in the first column also apply to the gas in the pore space and the boundary layer of a particle.

Gas phase	PDF formulation	Particle model
• Ideal gas law (Eq. (2)) • Equal diffusivities ($Sc = 0.7$) • $Le = 1$ • Low Mach number	• IEM model • $f_p^\rho = f^\rho$ • Large-scale homogeneity (PaSR)	• Spherical symmetry • Constant particle volume • No internal gas-solid temperature slip • Isolated and quasi-steady boundary layers with conductivities based on surface/far-field scalars • No gas phase chemistry

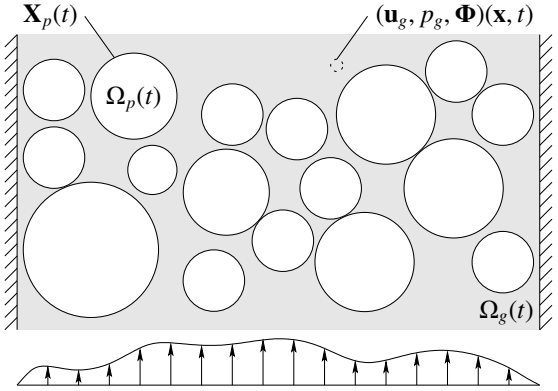

Figure 1. Illustration of a two-dimensional cut through a packed bed of spherical particles.

of the viscosity $\mu_g(\mathbf{\Phi})$ [8, Chapter 2] according to $D(\mathbf{\Phi}) = \mu_g(\mathbf{\Phi})/(\rho_g(\mathbf{\Phi})Sc)$ [9].

In order to reduce the spatial resolution requirements on the interstitial fields, Anderson and Jackson [10] introduced a spatial filtering operation based on a non-negative kernel $g(r)$ with $r \geq 0$. In particular, the spatially filtered counterpart $\langle Q(\mathbf{u}_g, \mathbf{\Phi})\rangle(\mathbf{x}, t)$ of an observable $Q(\mathbf{u}_g(\mathbf{x}, t), \mathbf{\Phi}(\mathbf{x}, t))$ on $\Omega_g(t)$ is defined as

$$\begin{aligned}&\varepsilon_g(\mathbf{x}, t)\langle Q(\mathbf{u}_g, \mathbf{\Phi})\rangle(\mathbf{x}, t)\\ &= \int_{\Omega_g(t)} g(\|\mathbf{x} - \mathbf{y}\|) Q(\mathbf{u}_g(\mathbf{y}, t), \mathbf{\Phi}(\mathbf{y}, t))\,\mathrm{d}\mathbf{y},\end{aligned} \tag{4}$$

where $\varepsilon_g(\mathbf{x}, t)$ denotes the void fraction. Within the scope of the unresolved DEM-CFD approach, the characteristic length scale associated with the filter kernel g is chosen much larger than the particles' sizes. Since the advective terms in the filtered continuity equation are naturally closed if the filtered velocity is amended by density-weighting, we further define the density-weighted average

$$\langle Q(\mathbf{u}_g, \mathbf{\Phi})\rangle_\rho = \frac{\langle \rho_g(\mathbf{\Phi}) Q(\mathbf{u}_g, \mathbf{\Phi})\rangle}{\langle \rho_g(\mathbf{\Phi})\rangle}. \tag{5}$$

In a similar way as in Eqs. (4) and (5), the spatial average $\{\cdot\}_p$ along the surface $\partial\Omega_p(t)$ of particle p [11, Chapter 8] and its density-weighted counterpart $\{\cdot\}_p^\rho$ are introduced. Here, the role of ε_g is taken on by the particle surface density $\xi_p = \{1\}_p$. In the following, we additionally employ the variable $\mathbf{X}_p(t)$ to indicate the degrees of freedom that define the current state of particle p.

By applying the filtering operation $\langle\cdot\rangle$ to Eq. (3), substituting the definitions of the density-weighted volume and surface averages and incorporating the mass and enthalpy fluxes $\rho_g(\mathbf{\Phi})\dot{s}_k(\mathbf{\Phi}, \mathbf{X}_p)$ across the particle boundaries, we obtain [3, 12]

$$\begin{aligned}&\frac{\partial \varepsilon_g \langle\rho_g\rangle\langle\Phi_k\rangle_\rho}{\partial t} + \nabla_{\mathbf{x}} \cdot \left(\varepsilon_g \langle\rho_g\rangle\langle\mathbf{u}_g\Phi_k\rangle_\rho\right)\\ &= \nabla_{\mathbf{x}} \cdot \left(\varepsilon_g \langle\rho_g\rangle\langle D\nabla_{\mathbf{x}}\Phi_k\rangle_\rho\right) + \varepsilon_g\langle\rho_g\rangle\langle\dot{\omega}_k\rangle_\rho\\ &\quad + \sum_p \xi_p \{\rho_g\}_p \{\dot{s}_k\}_p^\rho\,.\end{aligned} \tag{6}$$

Apart from the accumulation term on the left hand side of Eq. (6), all transport, reaction and gas-particle transfer processes remain unclosed in terms of $\langle\mathbf{u}_g\rangle_\rho$ and $\langle\mathbf{\Phi}\rangle_\rho$. In particular, the spatial advection and diffusion terms involve $\mathbf{u}_g$-$\mathbf{\Phi}$-correlations and spatial gradients, respectively, whereas the rates $\dot{\boldsymbol{\omega}}$ and $\dot{\mathbf{s}}(\cdot, \mathbf{X}_p)$ are, generally, nonlinear in $\mathbf{\Phi}$ and the gas-particle fluxes involve surface instead of volume averages. Indeed, the filtered fields $\langle\mathbf{u}_g\rangle_\rho$ and $\langle\mathbf{\Phi}\rangle_\rho$ do not include any information on the small-scale interdependency of $\mathbf{u}_g$ and $\mathbf{\Phi}$ or on their spatial distributions inside the filter's support. For the gas phase chemistry, a common closure hypothesis is the assumption of small-scale homogeneity that permits an evaluation of the filtered reaction rates in terms of the filtered composition, $\langle\dot{\boldsymbol{\omega}}(\mathbf{\Phi})\rangle_\rho = \dot{\boldsymbol{\omega}}(\langle\mathbf{\Phi}\rangle_\rho)$ [13]. In the context of unresolved DEM-CFD formulations for reactive granular assemblies, however, this assumption is not met if interstitial reaction fronts develop, mixing limitations persist or heterogeneities in the particles' mass or heat releases occur.

In order to augment the physical description of the interstitial gas by information on the values that the reactive scalars attain throughout the volume of a filter centred at $\mathbf{x}$, we adopt a technique that has originally been developed in the context of turbulent reacting flows [3, 4]. Here, the density-weighted PDF $f^\rho(\boldsymbol{\phi}, \mathbf{x}, t) = \langle\delta(\boldsymbol{\phi} - \mathbf{\Phi})\rangle_\rho(\mathbf{x}, t)$ is considered as a large-scale descriptor of the gas phase composition in place of the filtered scalars $\langle\mathbf{\Phi}\rangle_\rho(\mathbf{x}, t)$. The argument $\boldsymbol{\phi}$ of $f^\rho(\boldsymbol{\phi}, \mathbf{x}, t)$ is referred to as the sample space variable and ranges over all possible composi-

tion vectors. In the absence of density-weighting, the probability $f(\boldsymbol{\phi}, \mathbf{x}, t)\,\mathrm{d}\boldsymbol{\phi}$ with

$$f(\boldsymbol{\phi}, \mathbf{x}, t) = \frac{\langle \rho_g(\boldsymbol{\Phi})\rangle(\mathbf{x}, t) f^\rho(\boldsymbol{\phi}, \mathbf{x}, t)}{\rho_g(\boldsymbol{\phi})} \tag{7}$$

may be interpreted as the fraction of fluid elements near $\mathbf{x}$ that possess a composition $\boldsymbol{\Phi}$ in $[\boldsymbol{\phi}, \boldsymbol{\phi} + \mathrm{d}\boldsymbol{\phi})$. By taking the time derivative of $\varepsilon_g \langle \rho_g \rangle \langle \delta(\boldsymbol{\phi} - \boldsymbol{\Phi}) \rangle_\rho$ and substituting Eq. (3) alongside the mass balance equation and the flux boundary conditions at the particle surfaces, the following evolution equation for f^ρ is obtained,

$$\begin{aligned} &\frac{\partial \varepsilon_g \langle \rho_g \rangle f^\rho}{\partial t} + \nabla_{\mathbf{x}} \cdot \left(\varepsilon_g \langle \rho_g \rangle f^\rho \left\langle \mathbf{u}_g + \frac{\nabla_{\mathbf{x}} (\rho_g D)}{\rho_g} \middle| \boldsymbol{\phi} \right\rangle \right. \\ &\left. + \sum_p \xi_p \{\rho_g\}_p f_p^\rho D(\boldsymbol{\phi}) \{\mathbf{n}|\boldsymbol{\phi}\}_p \right) \\ &= \nabla_{\mathbf{x}} \cdot \left[D(\boldsymbol{\phi}) \nabla_{\mathbf{x}} \left(\varepsilon_g \langle \rho_g \rangle f^\rho \right) \right] \\ &\quad - \nabla_{\boldsymbol{\phi}} \cdot \left(\varepsilon_g \langle \rho_g \rangle f^\rho \dot{\omega}(\boldsymbol{\phi}) \right) + \mathcal{M} f^\rho + \sum_p \mathcal{S}_p f_p^\rho, \end{aligned} \tag{8}$$

where $\mathbf{n}(\mathbf{x}, t)$ denotes the unit normal vector on the surface of a particle and the particle-specific operator $\mathcal{S}_p$ is given by

$$\begin{aligned} \mathcal{S}_p f_p^\rho &= \xi_p \{\rho_g\}_p f_p^\rho \sum_{k \in \mathcal{G}} \dot{s}_k(\boldsymbol{\phi}, \mathbf{X}_p) \\ &- \nabla_{\boldsymbol{\phi}} \cdot \left[\xi_p \{\rho_g\}_p f_p^\rho \left(\dot{\mathbf{s}}(\boldsymbol{\phi}, \mathbf{X}_p) - \boldsymbol{\phi} \sum_{k \in \mathcal{G}} \dot{s}_k(\boldsymbol{\phi}, \mathbf{X}_p) \right) \right]. \end{aligned} \tag{9}$$

In Eq. (8), the influence of gas phase chemistry on the temporal evolution of f^ρ is naturally closed, while the contributions by the particles involve the unknown density-weighted surface PDFs $f_p^\rho(\boldsymbol{\phi}, \mathbf{x}, t) = \{\delta(\boldsymbol{\phi} - \boldsymbol{\Phi})\}_p^\rho(\mathbf{x}, t)$. Because the gas is separated from the particle surface by a boundary layer (Section 4) and since insights into the relation of f_p^ρ and f^ρ are yet absent, we adopt the simplifying closure hypothesis that the PDF f^ρ associated with the filter volume about $\mathbf{x}$ is representative also of the scalars' distribution f_p^ρ along the surface of particle p, $f_p^\rho = f^\rho$. The operator $\mathcal{M}$ in Eq. (8) represents micromixing and reads

$$\begin{aligned} \mathcal{M} f^\rho = -\varepsilon_g \langle \rho_g \rangle \sum_{k,l \in \mathcal{G}'} \frac{\partial^2}{\partial \phi_l \partial \phi_k} \Big(D(\boldsymbol{\phi}) \\ \times f^\rho \langle \nabla_{\mathbf{x}} \Phi_l \cdot \nabla_{\mathbf{x}} \Phi_k | \boldsymbol{\phi} \rangle \Big). \end{aligned} \tag{10}$$

Like the large-scale advection term on the left hand side of Eq. (8), this term involves conditional expectations and, hence, remains unclosed in terms of f^ρ. Since f^ρ does not include any information on the spatial arrangement of the fluid elements throughout the filter volume or on their velocities, neither filtered gradients nor $\mathbf{n}$-$\boldsymbol{\Phi}$- or $\mathbf{u}_g$-$\boldsymbol{\Phi}$-correlations can be evaluated based on f^ρ. On the positive side, f^ρ permits the direct evaluation of filtered $\boldsymbol{\Phi}$-dependent functions. For example, the filtered reaction rates are obtained as

$$\langle \dot{\omega} \rangle = \langle \rho_g \rangle \int \frac{\dot{\omega}}{\rho_g} f^\rho \, \mathrm{d}\boldsymbol{\phi}. \tag{11}$$

In order to close the micromixing contribution $\mathcal{M} f^\rho$ in terms of f^ρ, we employ the IEM (Interaction by Exchange with the Mean) model [5, 9]. This model is based on the idea that f^ρ relaxes towards the perfectly mixed state $\delta(\boldsymbol{\phi} - \langle \boldsymbol{\Phi} \rangle_\rho)$ over the time scale τ_{mix},

$$\mathcal{M} f^\rho = \frac{\varepsilon_g \langle \rho_g \rangle}{\tau_{\mathrm{mix}}} \nabla_{\boldsymbol{\phi}} \cdot \left[\left(\boldsymbol{\phi} - \langle \boldsymbol{\Phi} \rangle_\rho \right) f^\rho \right]. \tag{12}$$

Despite its shortcomings, the IEM model has the merit of conceptual and formal simplicity; it may be admissible if our objective is to assess in a qualitative, indicative way how small-scale heterogeneity affects process-level predictables.

Within the scope of DEM models of granular assemblies, temporal changes in the degrees of freedom $\mathbf{X}_p(t)$ of particle p are brought about by intra-particle conversion as well as momentum, heat and mass exchanges between the particle, the interstitial gas and the neighbouring particles. Excluding direct particle-particle interactions, the evolution laws of the DEM degrees of freedom can often be cast into a system of differential algebraic equations,

$$\mathbf{M}(\mathbf{X}_p(t)) \frac{\mathrm{d}\mathbf{X}_p(t)}{\mathrm{d}t} = \left\langle \dot{\mathbf{h}}(\langle \mathbf{u}_g \rangle|_p, \boldsymbol{\Phi}(t), \mathbf{X}_p(t)) \right\rangle \tag{13}$$

for $p = 1, 2, \ldots$. Here, $\mathbf{M}(\mathbf{X}_p(t))$ is a mass matrix that may be singular, $\langle \mathbf{u}_g \rangle|_p$ represents the filtered gas velocity experienced by particle p and $\dot{\mathbf{h}}(\langle \mathbf{u}_g \rangle|_p, \boldsymbol{\Phi}(t), \mathbf{X}_p(t))$ encompasses the rates associated with intra-particle processes and gas-particle interactions.

In summary, the combined DEM-PDF framework is based on Eq. (13) as well as modelled forms of Eq. (8) and the filtered gas phase momentum equation. Note that the filtered continuity equation follows as a consequence of Eq. (8) and that the filtered gas density $\langle \rho_g \rangle$ may be obtained from f^ρ by substituting unity for $\dot{\omega}$ in Eq. (11) [3],

$$\langle \rho_g \rangle = \left\langle \frac{1}{\rho_g} \right\rangle_\rho^{-1} = \left(\int \frac{f^\rho}{\rho_g} \, \mathrm{d}\boldsymbol{\phi} \right)^{-1}. \tag{14}$$

In order to circumvent the closure challenge associated with large-scale advection while maintaining a detailed description of small-scale compositional heterogeneity, the DEM-PDF approach is simplified to the case of large-scale homogeneity. This reduction gives rise to the concept of a PaSR that exchanges mass and heat with a granular assembly.

3. REDUCTION TO THE PARTIALLY STIRRED REACTOR

The PaSR is a simplified flow model in which the physical descriptors of the reactive gas are assumed to be uniform across the reactor domain (Fig-

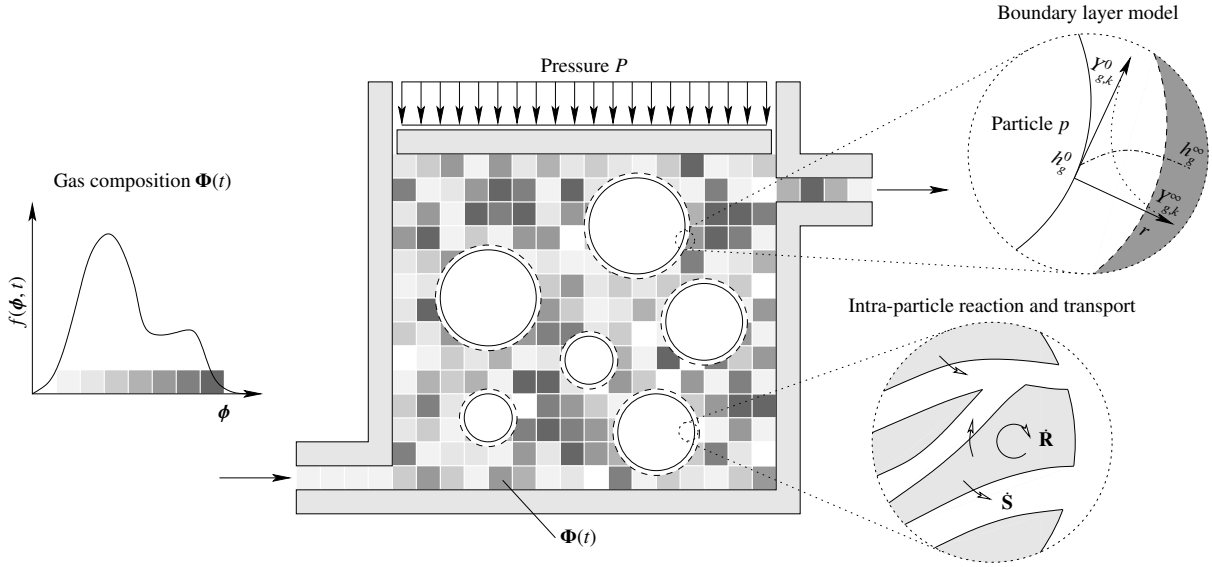

Figure 2. Schematic illustration of a constant pressure PaSR containing an assembly of spherical biomass particles (white disks) with modelled boundary layers (dashed circles). The grey patches indicate individual fluid elements whose thermochemical states $\mathbf{\Phi}(t)$ are distributed according to $f(\cdot, t) = \langle \rho_g(\mathbf{\Phi}) \rangle(t) f^\rho(\cdot, t)/\rho_g(\cdot)$. Note that, in slight departure from the graphical depiction, the fluid elements' individual extents are vanishingly small and that every fluid element inside the PaSR yields a far-field composition $\mathbf{\Phi}(t) = (\mathbf{Y}_g^\infty, h_g^\infty)$ with which a DEM particle interacts.

ure 2). If the thermodynamic pressure P remains constant, then the volume of the reactor changes commensurate with the temporal changes in the mean gas density $\langle \rho_g \rangle$. The distinguishing feature of the PaSR is that the thermochemical composition $\mathbf{\Phi}(t)$ of the gas inside the reactor is a vector-valued random variable with associated PDF $f(\cdot, t) = \langle \rho_g(\mathbf{\Phi}) \rangle(t) f^\rho(\cdot, t)/\rho_g(\cdot)$. If we interpret $\mathbf{\Phi}(t)$ as the composition of a single fluid element chosen uniformly randomly from within the reactor, then the PDF $f(\cdot, t)$ quantifies the compositional variability among the fluid elements. In Figure 2, the fluid elements are depicted as white-bordered squares and the shadings reflect the compositions they carry. While fluid elements are infinitely small, the finite extent of the squares is merely an aid to the graphical illustration. In particular, we emphasise that the white border lines do not correspond to a grid.

From Eqs. (8) and (12), the evolution law governing f^ρ is obtained by integrating over the reactor domain $\Omega(t)$ and substituting the filtered mass balance [5],

$$\begin{aligned} &\frac{\partial f^\rho}{\partial t} + \frac{f^\rho - f_{\text{in}}^\rho}{\tau_{\text{res}}} \\ &= f^\rho \sum_p \frac{\xi_p}{\varepsilon_g} \sum_{k \in \mathcal{G}} \Big(\dot{s}_k(\boldsymbol{\phi}, \mathbf{X}_p) - \langle \dot{s}_k(\mathbf{\Phi}, \mathbf{X}_p) \rangle_\rho \Big) \\ &\quad - \nabla_{\boldsymbol{\phi}} \cdot \Bigg\{ f^\rho \Bigg[\dot{\omega}(\boldsymbol{\phi}) - \frac{1}{\tau_{\text{mix}}} \Big(\boldsymbol{\phi} - \langle \mathbf{\Phi} \rangle_\rho \Big) \\ &\quad + \sum_p \frac{\xi_p}{\varepsilon_g} \Big(\dot{\mathbf{s}}(\boldsymbol{\phi}, \mathbf{X}_p) - \boldsymbol{\phi} \sum_{l \in \mathcal{G}} \dot{s}_l(\boldsymbol{\phi}, \mathbf{X}_p) \Big) \Bigg] \Bigg\}. \end{aligned} \tag{15}$$

Here, τ_{res} represents the mean residence time of the fluid elements inside the reactor and f_{in}^ρ is the joint scalar PDF associated with the gas flowing into the PaSR. In view of our closure assumption $f_p^\rho = f^\rho$, the density-weighted surface mean $\{\dot{s}_k(\mathbf{\Phi}, \mathbf{X}_p)\}_p^\rho$ associated with particle p has been approximated in terms of $\langle \dot{s}_k(\mathbf{\Phi}, \mathbf{X}_p) \rangle_\rho$ in Eq. (15).

Although we turn to a specific particle model in the following, the DEM-PaSR formulation is not restricted to this model (or, indeed, the process of biomass pyrolysis). Formally, the main conditions on the single particle model and the enveloping boundary layer are that the particle's degrees of freedom $\mathbf{X}_p$ obey Eq. (13) and that rate expressions for the mass and enthalpy fluxes $\rho_g(\mathbf{\Phi}) \dot{s}_k(\mathbf{\Phi}, \mathbf{X}_p)$, $k \in \mathcal{G}'$, crossing into the bulk gas are available.

4. MODEL FOR THE CONVERSION OF A BIOMASS PARTICLE

Considering a spherically symmetrical particle, we present a spatially one-dimensional model for the decomposition of biomass that captures both internal heat and mass transfer limitations and the transfer resistance imparted by the boundary layer surrounding the particle. While temperature inhomogeneities in thermally thick biomass particles have been accounted for in past DEM formulations [14, 15, 16], mass transport limitations associated with the gas flow through the particle's pore space or the gas-particle boundary layer have not yet been included to our awareness [17].

Since biomass particles naturally exhibit a complicated porous structure [18], we consider a single

particle with radius R as the union of a solid matrix with porosity $\psi(r,t)$, $r \in [0,R]$, and a pore space gas. As the particle's pyrolysis commences, the intra-particle solid matrix decomposes into solid and gaseous products [19]. The solid products are thought to remain attached to the matrix, while the gas products are released to the immediate pore space and migrate through the pore structure towards the ambient gas. Because of the short intra-particle gas retention times [20], gas phase chemical reactions inside the pore space are omitted. The chemical composition of the solid phase is described in terms of the mass fractions $\mathbf{Y}_s(r,t) = (Y_{s,i}(r,t))_{i\in\mathcal{S}}$ of the solid species whose labels i are aggregated into the set $\mathcal{S}$. Owing to pyrolysis reactions, the mass density of the solid species $i \in \mathcal{S}$ changes in time according to

$$\frac{\partial \rho_s Y_{s,i}}{\partial t} = \dot{R}_i, \tag{16}$$

where ρ_s is the constant mass density of the solid matrix and $\dot{R}_i(\mathbf{Y}_s, T)$ (in $[\mathrm{kg}_i/(\mathrm{s\,m^3(s)})]$) is the net mass production rate of solid species i due to pyrolysis. Since we assume the combined gas-solid volume of the particle to remain unchanged during its conversion, the porosity ψ changes only as a consequence of the production or consumption of the solid species' masses,

$$\frac{\partial \psi}{\partial t} = -\frac{(1-\psi)}{\rho_s}\sum_{i\in\mathcal{S}} \dot{R}_i. \tag{17}$$

Similar to the gas in the inter-particle void space of a particle assembly, the chemical make-up of the gas inside the particle's pore space is determined by the species mass fractions $\mathbf{Y}_g(r,t)$. Denoting by $\dot{S}_k(\mathbf{Y}_s, T)$ (in $[\mathrm{kg}_k/(\mathrm{s\,m^3(s)})]$) the rate at which species $k \in \mathcal{G}$ is released during the solid matrix's decomposition, the species-specific mass balance reads in spherical coordinates

$$\begin{aligned}&\frac{\partial \rho_g \psi Y_{g,k}}{\partial t} + \frac{1}{r^2}\frac{\partial}{\partial r}\left(r^2 \rho_g \psi u_g Y_{g,k}\right)\\ &= \frac{1}{r^2}\frac{\partial}{\partial r}\left(r^2 \rho_g \psi D \frac{\partial Y_{g,k}}{\partial r}\right) + (1-\psi)\dot{S}_k,\end{aligned} \tag{18}$$

where $u_g(r,t)$ represents the radial gas velocity. Upon summation over all species $k \in \mathcal{G}$, Eq. (18) yields the local mass balance

$$\frac{\partial \rho_g \psi}{\partial t} + \frac{1}{r^2}\frac{\partial}{\partial r}\left(r^2 \rho_g \psi u_g\right) = (1-\psi)\sum_{k\in\mathcal{G}} \dot{S}_k. \tag{19}$$

At every radial location, the solid matrix and the gas inside the particle's pore space are assumed to be thermally equilibrated. Consequently, the joint gas-solid enthalpy balance is given by [21]

$$\begin{aligned}&\frac{\partial \rho h}{\partial t} + \frac{1}{r^2}\frac{\partial}{\partial r}\left(r^2 \rho_g \psi u_g \sum_{k\in\mathcal{G}} Y_{g,k} h_k\right)\\ &= \frac{1}{r^2}\frac{\partial}{\partial r}\left(r^2 \rho_g \psi D \sum_{k\in\mathcal{G}} \frac{\partial Y_{g,k}}{\partial r} h_k + r^2 \lambda \frac{\partial T}{\partial r}\right).\end{aligned} \tag{20}$$

This balance law is formulated in terms of the total specific enthalpy $h(r,t)$ (in [J/kg]) associated with both phases. With reference to the local volume-averaged particle density $\rho = \rho_g\psi + \rho_s(1-\psi)$, h is defined according to

$$\begin{aligned}\rho h = {}& \rho_g \psi \sum_{k\in\mathcal{G}} Y_{g,k} h_k(T)\\ &+ \rho_s(1-\psi)\sum_{i\in\mathcal{S}} Y_{s,i} h_i(T).\end{aligned} \tag{21}$$

If the intra-particle gas and solid phases conduct heat radially in a parallel fashion, then the thermal conductivity λ in Eq. (20) coincides with the volume average of the conductivities λ_g and λ_s of the two phases,

$$\lambda = \psi\lambda_g + (1-\psi)\lambda_s. \tag{22}$$

In view of the ideal behaviour of the pyrolysis gas and the low Mach number of the intra-particle flow, the gas density ρ_g is linked to the species mass fractions $\mathbf{Y}_g$ and the temperature T by Eq. (2).

Since the flow around the biomass particle is not spatially resolved, we employ a boundary layer treatment to evaluate the rates at which mass and enthalpy are emitted from the particle surface towards the far-field gas. As in the particle's interior, gas phase chemical reactions are neglected. Following the formulation of Spalding [22], the mass and thermal boundary layers coincide ($Le = 1$) and behave in a quasi-steady way [23, Chapters 3 and 10]. For a given boundary layer conductivity $\overline{\rho_g D} = \overline{\mu_g}/Sc$, the conservation laws for the species masses ($k \in \mathcal{G}$) and the gas enthalpy may be integrated analytically across the boundary layer [24, p. 56] to yield the flow rates

$$\dot{m}_{g,k} = 2\pi R \overline{\rho_g D} Sh \left(Y^0_{g,k} - Y^\infty_{g,k}\right), \tag{23}$$

$$\dot{h}_g = 2\pi R \overline{\rho_g D} Nu \left(h^0_g - h^\infty_g\right) \tag{24}$$

in the case $\dot{m}_g = 0$ and

$$\dot{m}_{g,k} = \dot{m}_g \frac{Y^0_{g,k} - Y^\infty_{g,k}\exp\left(-\frac{\dot{m}_g}{2\pi R\overline{\rho_g D} Sh}\right)}{1-\exp\left(-\frac{\dot{m}_g}{2\pi R\overline{\rho_g D} Sh}\right)}, \tag{25}$$

$$\dot{h}_g = \dot{m}_g \frac{h^0_g - h^\infty_g\exp\left(-\frac{\dot{m}_g}{2\pi R\overline{\rho_g D} Nu}\right)}{1-\exp\left(-\frac{\dot{m}_g}{2\pi R\overline{\rho_g D} Nu}\right)} \tag{26}$$

otherwise. The flow rate $\dot{m}_g$ of the gas emanating from the biomass particle, moreover, is computed from

$$\dot{m}_g = 4\pi R^2 \left(\rho_g \psi u_g\right)\Big|_{r=R}. \tag{27}$$

The surface velocity $u_g(R,t)$ that appears here is, in turn, obtained from Eq. (19) and the boundary condition $u_g(0,t) = 0$. In Eqs. (23) to (26), the superscripts 0 and ∞ indicate values at the particle surface and in the far-field, respectively. Note that, for a particle contained in a PaSR with volume $V(t) = \mathrm{vol}\,\Omega(t)$,

the far-field scalars $(\mathbf{Y}_g^\infty, h_g^\infty) = \mathbf{\Phi}(t)$ are random variables that are distributed according to the PDF $f(\cdot, t)$ (Section 3), while $\dot{m}_{g,k}/V(t)$ and $\dot{h}_g/V(t)$ yield the sources $\xi_p(t)\rho_g(\mathbf{\Phi}(t))\dot{s}_k(\mathbf{\Phi}(t), \mathbf{X}_p(t))$ in Eq. (15). Since the Lewis number is unity, the Nußelt and Sherwood numbers Nu and Sh in Eqs. (23) to (26) are equal; they may be evaluated using the Ranz-Marshall correlation [25] which has been calibrated for a particle Reynolds number Re_p in the range $0 \leq Re_p \leq 200$. Following Abramzon and Sirignano [26], the viscosity $\overline{\mu_g}$ across the boundary layer is computed from the surface mass fractions and temperature as well as their far-field counterparts using the 1/3-rule. Because there is no efflux of solid phase enthalpy from the particle, Eqs. (23) through (27) jointly provide the boundary conditions at $r = R$ of Eqs. (18) and (20). At the particle centre, by contrast, symmetry boundary conditions apply.

In order to convert the balance laws in Eqs. (16) to (20) into the form of Eq. (13), we apply a radial finite volume discretisation with staggered variable arrangement. In particular, the degrees of freedom associated with the distributed solid masses $\rho_s Y_{s,i}(1 - \psi)4\pi r^2$, $i \in \mathcal{S}$, the gas' mass fractions $Y_{g,k}$, $k \in \mathcal{G}$, and the temperature T are stored at the cell centres, while the degrees of freedom parameterising the radial intra-particle gas velocity u_g live at the cell faces. Since the radial profile of u_g responds on an instantaneous basis to gas release and temporal changes in the gas density and particle porosity, the semi-discrete counterpart of the mass balance in Eq. (19) yields an algebraic relation that renders the mass matrix $\mathbf{M}$ in Eq. (13) singular.

5. NUMERICAL SOLUTION METHODS

The evolution equation governing $f^\rho(\boldsymbol{\phi}, t)$ (Eq. (15)) corresponds to a differential Chapman-Kolmogorov equation with vanishing diffusion matrix and may, therefore, be associated with a stochastic jump-drift process [27, Chapter 3]. Within the scope of a Monte Carlo solver, different realisations of this process are computed by solving the corresponding SDE for independent random drivers. Since the SDE is kinetically linked to the particles' degrees of freedom $\mathbf{X}_p(t)$ with $p = 1, 2, \ldots$, the deterministic DEM equations (Eq. (13)) are integrated concurrently. Over the course of a time step, the SDE is decomposed into fractional steps using a first order scheme [2, Section 6]. Consequently, physical and chemical effects that occur simultaneously can be treated in a sequential way, thus permitting the application of a dedicated time integration scheme in each fractional step.

6. CONCLUSIONS

In this contribution, we summarised the formal basis of a combined DEM-PaSR model for the pyrolysis of an assembly of spherical biomass particles. Here, the reactive scalars parameterising the gas' thermochemical state are conceived of as random variables whose associated PDF changes in time owing to mass and heat exchanges with the biomass particles, gas phase chemical reactions, micromixing and flow-through. By construction, this statistical description covers small-scale heterogeneity of the gas composition and allows for a closed-form treatment of gas phase chemical reactions. In order to accommodate gas-particle mass and heat exchanges, we argued that the separation of the DEM particles from the bulk gas by a resistive boundary layer permits the approximation of the particle surface-specific joint scalar PDFs in terms of the volume-based PDF that defines the state of the PaSR. Small-scale diffusion and heat conduction, moreover, are accounted for by a micromixing model. The DEM description of a biomass particle is based on a finite volume discretisation of the intra-particle balance laws for the solid species' masses, the masses of the gaseous species, the total gas mass and the combined gas-solid enthalpy. Additionally, the biomass particle is surrounded by a passive boundary layer that restricts the transfer of mass and heat towards the compositionally heterogeneous gas in the far-field.

By design, the PaSR permits a systematic analysis of how large-scale predictables, for example, the pyrolysis duration, the amount of energy consumed and the composition of the pyrolysis gas, are influenced by small-scale heterogeneity in the gas composition. In the near future, we plan to apply the DEM-PaSR model to the pyrolysis of cellulose, the main constituent of woody biomass, and quantify the impact of micromixing limitations.

ACKNOWLEDGEMENTS

This project was funded by the Deutsche Forschungsgemeinschaft (DFG, German Research Foundation) within the scope of the Collaborative Research Centre/Transregio 287 (Project number 422037413).

REFERENCES

[1] O'Brien, E. E., 1980, "The probability density function (pdf) approach to reacting turbulent flows", P. A. Libby, and F. A. Williams (eds.), *Turbulent Reacting Flows*, Springer, Berlin, Heidelberg, Vol. 44 of *Topics in Applied Physics*, pp. 185–218.

[2] Pope, S. B., 1985, "PDF methods for turbulent reactive flows", *Progress in Energy and Combustion Science*, Vol. 11 (2), pp. 119–192.

[3] Haworth, D. C., 2010, "Progress in probability density function methods for turbulent reacting flows", *Progress in Energy and Combustion Science*, Vol. 36 (2), pp. 168–259.

[4] Pope, S. B., 1991, "Computations of turbulent combustion: Progress and challenges", *Symposium (International) on Combustion*, Vol. 23 (1), pp. 591–612.

[5] Chen, J.-Y., 1997, "Stochastic modeling of partially stirred reactors", *Combustion Science and Technology*, Vol. 122 (1–6), pp. 63–94.

[6] Kee, R. J., Rupley, F. M., and Miller, J. A., 1989, "CHEMKIN–II: A FORTRAN chemical kinetics package for the analysis of gas-phase chemical kinetics", *Tech. Rep. SAND89-8009*, Sandia National Laboratories, Livermore, CA.

[7] Poinsot, T., and Veynante, D., 2011, *Theoretical and Numerical Combustion*, Aquaprint, Bordeaux, 3rd edn.

[8] Kee, R. J., Coltrin, M. E., Glarborg, P., and Zhu, H., 2017, *Chemically Reacting Flow: Theory, Modeling, and Simulation*, Wiley, Hoboken, NJ, 2nd edn.

[9] Jones, W. P., and Prasad, V. N., 2010, "Large eddy simulation of the Sandia flame series (D–F) using the Eulerian stochastic field method", *Combustion and Flame*, Vol. 157 (9), pp. 1621–1636.

[10] Anderson, T. B., and Jackson, R., 1967, "A fluid mechanical description of fluidized beds. Equations of motion", *Industrial and Engineering Chemistry Fundamentals*, Vol. 6 (4), pp. 527–539.

[11] Kuo, K. K., 1986, *Principles of Combustion*, Wiley, New York, Chichester.

[12] Capecelatro, J., and Desjardins, O., 2013, "An Euler–Lagrange strategy for simulating particle-laden flows", *Journal of Computational Physics*, Vol. 238, pp. 1–31.

[13] Golshan, S., Sotudeh-Gharebagh, R., Zarghami, R., Mostoufi, N., Blais, B., and Kuipers, J. A. M., 2020, "Review and implementation of CFD-DEM applied to chemical process systems", *Chemical Engineering Science*, Vol. 221, p. 115646.

[14] Mahmoudi, A. H., Hoffmann, F., and Peters, B., 2014, "Detailed numerical modeling of pyrolysis in a heterogeneous packed bed using XDEM", *Journal of Analytical and Applied Pyrolysis*, Vol. 106, pp. 9–20.

[15] Wang, W., Lu, Y., Xu, K., Wu, K., Zhang, Z., and Duan, J., 2021, "Experimental and simulated study on fluidization characteristics of particle shrinkage in a multi-chamber fluidized bed for biomass fast pyrolysis", *Fuel Processing Technology*, Vol. 216, p. 106799.

[16] Lu, L., Gao, X., Shahnam, M., and Rogers, W. A., 2021, "Simulations of biomass pyrolysis using glued-sphere CFD-DEM with 3-D intra-particle models", *Chemical Engineering Journal*, Vol. 419, p. 129564.

[17] Luo, H., Wang, X., Liu, X., Wu, X., Shi, X., and Xiong, Q., 2022, "A review on CFD simulation of biomass pyrolysis in fluidized bed reactors with emphasis on particle-scale models", *Journal of Analytical and Applied Pyrolysis*, Vol. 162, p. 105433.

[18] Crowley, M. F., Sitaraman, H., Klinger, J., Usseglio-Viretta, F., Thornburg, N. E., Brunhart-Lupo, N., Pecha, M. B., Dooley, J. H., Xia, Y., and Ciesielski, P. N., 2022, "Measurement of transport properties of woody biomass feedstock particles before and after pyrolysis by numerical analysis of X-ray tomographic reconstructions", *Frontiers in Energy Research*, Vol. 10, p. 850630.

[19] Papari, S., and Hawboldt, K., 2015, "A review on the pyrolysis of woody biomass to bio-oil: Focus on kinetic models", *Renewable and Sustainable Energy Reviews*, Vol. 52, pp. 1580–1595.

[20] Rabinovich, O. S., Korban, V. V., Pal'chenok, G. I., and Khorol'skaya, O. P., 2009, "Modeling of fast pyrolysis of a single biomass particle in an inert boiling bed", *Journal of Engineering Physics and Thermophysics*, Vol. 82 (4), pp. 611–622.

[21] Finke, J., and Sewerin, F., 2024, "A population balance approach for predicting the size distribution of oxide smoke near a burning aluminum particle", *Combustion and Flame*, Vol. 265, p. 113464.

[22] Spalding, D. B., 1953, "The combustion of liquid fuels", *Symposium (International) on Combustion*, Vol. 4 (1), pp. 847–864.

[23] Turns, S. R., 2012, *An Introduction to Combustion: Concepts and Applications*, McGraw-Hill Series in Mechanical Engineering, McGraw-Hill, New York, 3rd edn.

[24] Williams, F. A., 1985, *Combustion Theory*, Combustion Science and Engineering Series, Addison-Wesley, Reading, Menlo Park, 2nd edn.

[25] Ranz, W. E., and Marshall, W. R., 1952, "Evaporation from drops: Part I", *Chemical Engineering Progress*, Vol. 48 (3), pp. 141–146.

[26] Abramzon, B., and Sirignano, W. A., 1998, "Droplet vaporization model for spray combustion calculations", *AIAA 26th Aerospace Sciences Meeting*, Reno, NV, USA.

[27] Gardiner, C., 2009, *Stochastic Methods: A Handbook for the Natural and Social Sciences*, Springer Series in Synergetics, Springer, Berlin, Heidelberg, 4th edn.

Conference on Modelling Fluid Flow (CMFF'25)
The 19th International Conference on Fluid Flow Technologies
Budapest, Hungary, August 26 - August 29, 2025

USING JACOBI METHOD TO SOLVE THE TWO-EQUATION TURBULENCE MODEL FOR PARALLELIZATION ON GPU COMPUTING SYSTEM

Ivan TOMANOVIĆ[1], Srdjan BELOŠEVIĆ[2], Nenad CRNOMARKOVIĆ[3], Aleksandar MILIĆEVIĆ[4]

[1] Corresponding Author. Department of Thermal Engineering and Energy, "VINČA" Institute of Nuclear Sciences – National Institute of the Republic of Serbia, University of Belgrade, Mike Petrovića Alasa 12–14, 11351 Vinča, PO Box 522, Belgrade, 11001 Serbia. Tel.: +381 11 3408551, E-mail: ivan.tomanovic@vin.bg.ac.rs
[2] Department of Thermal Engineering and Energy, "VINČA" Institute of Nuclear Sciences – National Institute of the Republic of Serbia, University of Belgrade, Mike Petrovića Alasa 12–14, 11351 Vinča, PO Box 522, Belgrade, 11001 Serbia. E-mail: v1belose@vin.bg.ac.rs
[3] Department of Thermal Engineering and Energy, "VINČA" Institute of Nuclear Sciences – National Institute of the Republic of Serbia, University of Belgrade, Mike Petrovića Alasa 12–14, 11351 Vinča, PO Box 522, Belgrade, 11001 Serbia. E-mail: ncrni@vin.bg.ac.rs
[4] Department of Thermal Engineering and Energy, "VINČA" Institute of Nuclear Sciences – National Institute of the Republic of Serbia, University of Belgrade, Mike Petrovića Alasa 12–14, 11351 Vinča, PO Box 522, Belgrade, 11001 Serbia. E-mail: amilicevic@vin.bg.ac.rs

ABSTRACT

The advancement in computer development in recent years saw introduction of powerful graphics processing units (GPUs) intended as general-purpose computation units, beside their core purpose. To better accommodate the existing computational fluid dynamics (CFD) code with a k-ε turbulence model to be able to run on an upcoming generation of GPUs, the existing computer codes must undergo modifications due to very different nature of GPU architecture, compared to that of a central processing unit (CPU). Due to this, a Jacobi method is used instead of Gauss-Seidel based solvers. Application of Jacobi on a CPU predictably leads to a slower execution of code, due to its slower convergence rate. However, its highly parallel nature makes it very suitable for execution on modern GPU. The subroutines both for kinetic energy and its dissipation rate originally use Gauss-seidel based tridiagonal matrix algorithm (TDMA) solver, highly optimized to run on a single computational thread. While it can be modified to run on multiple computational threads, it scales poorly with their number increase. On the other hand, Jacobi offers full parallelism, and simple code implementation, regardless of the problem scale, avoiding conflicting memory operations at the same time, but at the cost of double memory consumption. The code itself is ported to GPU using OpenACC directives in compute unified device architecture (CUDA) FORTRAN. The 2D monophase turbulence flow test-case is solved on an orthogonal structured grid, and the parallel nature of Jacobi gives us the ability to solve equations in each control volume individually between the iteration steps, without dependencies on neighbouring cells, leading to a significant number of operations that can be executed in parallel. Due to initial memory operations overhead cost in time, the model must solve sufficiently large problem to be able to outperform fast CPU.

Keywords: CFD, GPU, Jacobi method, OpenACC, parallelization, turbulence

NOMENCLATURE

CLK	[*Hz*]	single processing unit clock speed
E	[-]	per core efficiency
n	[-]	input size of problem
p	[-]	number of processing units
S	[-]	speedup of the parallel algorithm
T(n)	[-]	total operations count
t	[*s*]	execution time

Subscripts and Superscripts

b, base	base (reference) case/value
overhead	overhead time or operations
parallel	executed in parallel
rw	real-world conditions
serial	executed in serial

1. INTRODUCTION

Application of turbulence models in CFD research demands a significant amount of high-performance computational resources. Past century brought us vast number of models specifically created and well optimized to run on single core processing units. Together with those codes less frequently were developed models intended to run on proprietary super computers, often closed to public. Development of computer graphics lead to creation of powerful GPU devices that could readily perform

operations beyond their intended purpose, and found their place in scientific computing. Understanding the potential of GPUs as very new and promising accelerators that can be used in computational research is essential, as they are being developed at high pace, and thus it is of great importance to create highly efficient computer codes that would follow.

The historical development of CFD codes and more importantly, the equation solvers in them followed the development of both personal and HPC computers, starting with the single core codes implementing the tridiagonal matrix algorithm (TDMA) e.g. [1] and Stone's SIP algorithm [2], as well as the parallel implementations of those on multicore CPUs: [3, 4]. Other solvers that include domain decompositions [5, 6], Cyclic Reduction (CR) and Parallel Cyclic Reduction (PCR) [7], Multi-Grid (MG), Colour Checkerboarding (CC) [8], Alternating-Direction Implicit (ADI) [9], and others followed the increase in core count on personal computers, and the early versions of GPUs as well, providing mixed results and success, but often fast solvers that have their own limitations.

The languages initially developed for GPUs, such as OpenCL and CUDA C, provided users with access to their capabilities, but at a cost of a very long learning curve in order to provide good working and well optimized codes. An easier tool that would move burden of sometimes difficult code writing and memory management from the user to the machine was needed, and it came in the form of OpenACC, providing wider audience with access to GPU device performance, while maintaining simplicity in code writing. A good example of difficulties that had to be overcome when writing codes from scratch can be found in work of Cohen and Molemaker [10] who created a massively parallel GPU implementation of fast CFD code for simulation of Rayleigh-Bérnard convection. Creation of such a code in native GPU language, such as CUDA C, is labour intensive task. On the other hand, OpenACC implementations of code nowadays can provide similar performance gains without requiring the user to tackle difficult tasks, including the load distribution and memory management. One of such implementations is by Xia et al. [11] who discussed the conversion of legacy CFD solvers to new hardware, and also presented a model of compressible CFD code implemented on unstructured grid using OpenACC.

Our own implementation is based off TEACH-T CFD code [12], converting and modifying it to allow massive parallelisation of all parts of the code. The turbulence in code is modelled using a well-known k-ε two equation model, and the implementation is done so that the turbulent kinetic energy equation is solved first, due to internal dependencies in the model itself. The entire CFD solver is ported to the GPU to avoid massive overhead times caused by data movements through the PCI-E lanes.

Amongst other changes to the code structure, one of the most important changes in this code is the inclusion of Jacobi based solver for equations, allowing future massive parallelization of code as the GPU computational cores number grows, and at the same time providing noticeable gains at current architecture. While the Jacobi implementation does have its own disadvantages on real-world parallel machines, most important the double memory consumption, and potentially slower convergence on machines with finite number of cores, it can still be the best choice for the newer machines that often have core count proportional to the size of problem solved, as these machines are moving closer to ideal parallel machines. This is also supported by findings of Tsitsiklis [13] who proves that parallel Jacobi iterations are no slower than any parallel Gauss-Seidel variant of that iteration, confirming the almost certain superiority of Jacobi algorithm over Gauss-Seidel [14]. On GPUs with lower computational core counts and low amount of available memory a good compromise could be the use of Red-Black checkerboarding in one or more directions, which is a version of Colour Checkerboarding algorithm, but is not considered as part of this work.

In this work we put our focus on determining the number of computational operations in subroutine for turbulent kinetic energy, setting aside other subroutines, and we use this information to determine potential for speedup of parallel code based on theoretical background set by Amdahl [15] and Gustafson [16]. Tasks in this work are separated to determination of total number of operations in serial code, grouping them in sections that can be parallelized, determining potential sections of code that can be asynchronously executed, upon which we can determine total number of steps on ideal parallel machine. Once these tasks are complete, we turn towards determination of the computational core number-based operation count, which is informative, but insufficient to provide real-world performance benchmarks. To gain insights into the code behaviour on real hardware, we set a base case that should be used as a ground-line benchmark for performance estimation over several grid sizes. We use running time as a reference and convert the operation count criteria into a running time criteria to provide a fair comparison between different platforms. This approach takes into account real-world overhead times, which, as shown, are significant for GPU-based CFD simulation platforms.

2. CODE IMPLEMENTATION

In order to accommodate CFD code with a k-ε turbulence model to run on GPU, an existing code is modified due to different nature of GPU architecture compared to CPU. A 2D monophase turbulence flow test case is solved on an orthogonal structured grid. Instead of Gauss-Seidel the Jacobi method is used,

enabling solving the equations in each control volume with no influence of neighbouring cells, thus offers parallelization potential. The code is ported to GPU by OpenACC directives in CUDA FORTRAN.

Parallelisation of this 2D code opens direct pathway towards creation of parallel 3D codes. Major change to a code would be an introduction of subroutine that would solve the third component of the velocity. Also, given that there are three dimensions it would lead to addition of k loop in most cases, and increased number of operations where new terms and variables are introduced in equations.

A code structure extracted from subroutine used for calculation of turbulent kinetic energy is given in Table 1, accompanied by the number of computational and memory access operations at every group of lines. The number of operations here is determined based on total arithmetic operations at the line/segment of code, as well as the memory read and write operations that took place. It can be noticed that many operations are enclosed in loops, thus increasing the number of operations depending on the loop size. The total number of operations, as can be noticed, depends on the problem size, but it can be estimated roughly for known size of computational domain. For example, the first loop over interior grid has in single pass total of 113 computational operations, that needed 109 memory reads, and wrote to the memory total of 29 times, but this is repeated (nj-2)·(ni-2) times in total. Sample number of operations for different grid sizes is given in Table 2. In all cases number of swipes (nswp), which tells us how many times Jacobi solver loop is repeated in each iteration step, is assumed 30.

Table 1. Number of computational and memory operations in subroutine for turbulent energy

Pseudo code	calculation	memory	
		read	write
loop over interior grid			
for j = 2 **to** nj – 1			
for i = 2 **to** ni – 1			
calculate areas	3	6	3
calculate volume	2	3	1
calculate conv. coef.	16	16	4
calculate diff. coef.	20	20	4
calculate source terms	61	59	11
update source terms	11	15	6
end			
end			
in total: **(nj – 2)·(ni – 2)·**	**113**	**109**	**29**
wall conditions: top wall			
initial ops	**1**	**3**	**2**
for i = 2 **to** ni – 1			
calculate y^+	7	9	3
update source terms	31	34	3
end			
in total: **(ni – 2)·**	**38**	**43**	**6**
: side wall			
for j = jstp **to** nj – 1			
calculate y^+	7	9	3
update source terms	31	34	3
end			
in total: **(nj – jstp)·**	**38**	**43**	**6**
: symmetry axis			
for i = 2 **to** ni – 1			
calculate source terms	15	22	9
update source terms	2	3	2
end			
in total: **(ni – 2)·**	**17**	**25**	**11**
res. and under-relaxation			
for j = 2 **to** nj – 1			
for i = 2 **to** ni – 1			
calculate $a_{p,te}$	4	5	1
calculate residual	10	11	1
calculate under-relax.	4	6	1
end			
end			
in total: **(nj – 2)·(ni – 2)·**	**18**	**22**	**3**
iterative solver loop			
for swipe = 1 **to** nswp			
for j = 2 **to** nj – 1			
for i = 2 **to** ni – 1			
calculate te_{new}	13	13	1
update residual	3	4	2
end			
end			
for j = 2 **to** nj – 1			
for i = 2 **to** ni – 1			
calculate te_{new}	0	1	1
end			
end			
in total: **n· (nj – 2)·(ni – 2)·**	**16**	**18**	**4**

Table 2. Estimated number of serial operations $T_{serial}(n)$ for different grid sizes

Grid	calculation	Memory access	
		read	write
32×16	$2.6 \cdot 10^5$	$2.8 \cdot 10^5$	$6.4 \cdot 10^5$
64×32	$1.1 \cdot 10^6$	$1.3 \cdot 10^6$	$2.8 \cdot 10^5$
128×64	$4.8 \cdot 10^6$	$5.3 \cdot 10^6$	$1.2 \cdot 10^6$
256×128	$2.0 \cdot 10^7$	$2.1 \cdot 10^7$	$4.9 \cdot 10^6$
512×256	$7.9 \cdot 10^7$	$8.7 \cdot 10^7$	$2.0 \cdot 10^7$
1024×512	$3.2 \cdot 10^8$	$3.5 \cdot 10^8$	$7.9 \cdot 10^7$
2048×1024	$1.3 \cdot 10^9$	$1.4 \cdot 10^9$	$3.2 \cdot 10^8$
4096×2048	$5.1 \cdot 10^9$	$5.6 \cdot 10^9$	$1.3 \cdot 10^9$

From this table we can see that the number of calculation operations grows from $2.6 \cdot 10^5$ all the way to $5.1 \cdot 10^9$ as the grid size grows from 32×16=512 elements to 4096×2048=$8.4 \cdot 10^6$ elements. Most of these operations are contained in loops that can be readily parallelised, and as such contribute to significant reduction in number of operations when the parallelisation is introduced. The rough estimation of number of parallel operations on an ideal parallel machine is $T_{parallel}(n)$ = 106 (due to

some parts of loops, or entire loops being able to execute asynchronously (i.e. parallel one to another), taking into account 16 successive parallel operations that include massive arrays inside the loops that can be executed in parallel, 3 operations on arrays that execute in series, 30 times each, as well as internal dependencies that enforce us to wait for computation of some variables before we are able to compute others.

3. CODE SPEEDUP AND EFFICIENCY

In theory, a proper way to estimate algorithm speedup and efficiency is to define the number of operations $T(n)$ executed to solve the problem of given size n. From here we can estimate the number of parallel operations necessary to reach the same solution under ideal conditions, with finite number of computational units, based on considerations brought by Amdahl [15]:

$$T_{parallel}(n) = \frac{T_{serial}(n)}{p} \tag{1}$$

This is true for each and every loop found in the problem we solve if it is readily parallelizable, and if we consider execution on an ideal parallel machine.

As an example, we will apply Eq. (1) to the calculation operations from Table 2, and compare data between the parallel CPU (Intel Xeon E5-1620 v3) with 8 threads against the GPU (NVIDIA Quadro RTX 4000) with 2304 cores. The $T_{parallel}(n)$ for both is given in Table 3, but it must be noted that this value reflects purely theoretical performance and it ignores overhead times necessary for load distribution, memory transfer times when simulations are done on GPU, other operational overheads, as well as the individual core performance (core speed, amount of available cache, bandwidth, etc.).

Table 3. Estimated number of computational operations $T_{parallel}(n)$ for different accelerators

Grid size	p = 8 (CPU)	p = 2304 (GPU)
32×16	$3.2 \cdot 10^4$	$1.1 \cdot 10^2$
64×32	$1.4 \cdot 10^5$	$5.0 \cdot 10^2$
128×64	$6.0 \cdot 10^5$	$2.1 \cdot 10^3$
256×128	$2.4 \cdot 10^6$	$8.5 \cdot 10^3$
512×256	$9.9 \cdot 10^6$	$3.4 \cdot 10^4$
1024×512	$4.0 \cdot 10^7$	$1.4 \cdot 10^5$
2048×1024	$1.6 \cdot 10^8$	$5.5 \cdot 10^5$
4096×2048	$6.4 \cdot 10^8$	$2.2 \cdot 10^6$

Given that both parallel CPUs and GPUs are not the ideal machines, they need additional resources to communicate, distribute and balance the load over their respective computational cores. This leads to the introduction of additional overhead operations, caused by additional communication and memory management, especially if we take into account memory transfers that are unavoidable in CPU-GPU communication in real-world runs, as an expansion of Amdahl's law by Gustafson [16], Eq. (2):

$$T_{parallel,rw}(n) = \frac{T_{serial}(n)}{p} + T_{overhead} \tag{2}$$

As the complexity of code structure increases it becomes more difficult to accurately estimate the number of operations. Also, in Eqs. (1) and (2) it is noticeable that if the $T(n)$ is less or equal to the number of processing units we can get the number of parallel operations smaller than 1, which is impossible, and such cases rather tend to have smallest, but finite number of operations that should be determined by estimating the number of parallel computation steps. While the total number of operations remain the same between serial and parallel codes, the number of execution steps is usually reduced as the parallelism is introduced, virtually converting a large number of steps found in parts of serial code to a single step on massively parallel machine. However, we still have to follow some execution thread, given that prior to executing some operations others must complete, creating a new kind of overhead that adds to previous, and a new issue in operation counting to overcome these issues, it would be easier to measure execution time, instead of operation counts in real life codes.

Furthermore, the physical differences in performance of different accelerators include additional challenges when estimating the performance originating from individual processing unit and memory speed. Those could be partially addressed by expressing the $T_{parallel,rw}(n)$ as a function of those variables, by expressing performance per normalised processing unit speed:

$$T_{parallel,rw}(n) = \frac{T_{serial}(n)}{p} \cdot \frac{CLK_{base}}{CLK} + T_{overhead} \tag{3}$$

On the other hand, the execution time as a measurable output, takes into account all overheads, without focusing on them individually, as well as the hardware constraints that include clock and memory speeds, limitations in bandwidth, and all other influences that occur, thus making it an indicator that is easier to measure. We can in a similar manner estimate the execution time that should be expected from an ideal parallel machine, based on its number of processors:

$$t_{parallel}(n) = \frac{t_{serial}(n)}{p} \tag{4}$$

Also, in the similar manner we can include overhead time to this equation:

$$t_{parallel,rw}(n) = \frac{t_{serial}(n)}{p} + t_{overhead} \tag{5}$$

It is important to note that, the parallel execution time expressed in this manner is the time per processing unit found in accelerator (parallel CPU or GPU), and as such has similar limitations as the number of operations from Eq. (3).

The overhead time, as a difference between real-world and ideal runs, can be determined by

comparing the actual measured execution time in real world runs to that obtained from Eq. (4), giving us the following:

$$t_{overhead} = t_{parallel,rw}(n) - t_{parallel}(n) \quad (6)$$

To effectively estimate both the speedup and efficiency of parallel execution on parallel CPU and GPU we need a solid baseline case that will serve as a reference. To this end we will utilize a code compiled for a single threaded run with same Jacobi algorithm, with all compiler optimizations applied. This will give us an insight into an actual execution time which we will denote as $t_{serial,CPU}(n)$ in analysis. From this $t(n)$ we will determine $t_{parallel,CPU}(n)$ and $t_{parallel,GPU}(n)$ using the Eq. (4). The number of processing units/threads p for CPU and GPU used in simulations is 8 and 2304, respectively.

The speedup of the parallel algorithm, both theoretical and real-world, can be determined by comparing it to its serial counterpart, per Eqs. (7) and (8):

$$S(p) = \frac{t_{serial,b}(n)}{t_{parallel}(n)} \quad (7)$$

$$S_{rw}(p) = \frac{t_{serial,b}(n)}{t_{parallel,rw}(n)} \quad (8)$$

Expressing the speedup over the available number of processing units provides us with an insight into the efficiency of parallelization, Eqs. (9) and (10), where values $E \approx 1$ indicate highly efficient parallelization, while the values of $E \ll 1$ indicate significant slowdowns due to overhead or insufficient utilization of individual processing units, this is in relation to the findings of Hill and Marty [17] who shown that locally inefficient core design can be globally efficient at large scale.

$$E(p) = \frac{S(p)}{p} \quad (9)$$

$$E_{rw}(p) = \frac{S_{rw}(p)}{p} \quad (10)$$

Results for simulations of turbulent flow model in 2D channel on parallel CPU and GPU, using Jacobi model to solve equations are given in Tables (4) and (5). Test cases are named after the accelerator used and number of cells in simulation grid for that case. All test case times are given for 20 000 iterations with double precision floating point numbers on numerical grids consisting of 8192 (8k), 23768 (32k), 131072 (131k), 524288 (524k), 2097152 (2M), and 8388608 (8M) elements. From the Table 4 it is noticeable that there is significant growth in overhead execution time for the parallel CPU execution. The growth in the overhead time with the grid size for the GPU is significantly lower, but it makes nearly entire difference between real-world and ideal parallel execution.

From these results, we notice that expected parallel execution times, using above Eqs. are significantly lower than the real-world performance. This is something that can't be avoided, but can be reduced by proper hardware selection and different solver choices depending on the scale of the problem.

Table 4. Simulation times and overhead times

CASE	$t_{serial,b}$	$t_{parallel}$	$t_{parallel,rw}$	$t_{overhead}$
Eq.		(4)		(6)
CPU8k	25.8	3.22	11.41	8.19
CPU32k	152.4	19.05	57.37	38.32
CPU131k	722.5	90.32	301.45	211.13
CPU524k	5860.5	732.56	4197.20	3464.63
CPU2M	25327.4	3165.93	23675.66	20509.73
CPU8M	120473.7	15059.21	82879.52	67820.31
GPU8k	25.8	0.011	92.50	92.49
GPU32k	152.4	0.066	125.73	125.66
GPU131k	722.5	0.313	158.14	157.82
GPU524k	5860.5	2.544	413.59	411.05
GPU2M	25327.4	10.993	1410.14	1399.15
GPU8M	120473.7	52.289	5366.13	5313.84

Following the results from the Table 4 speedup and computational efficiency of each test case is calculated. Results provided in Table 5 indicate that at larger grid sizes GPU can provide significant speedup in real-world conditions, providing real world benefits to the user. However, efficiency of the parallelisation from the same table indicates a very high overhead on GPU.

Table 5. Speedup and per core efficiency

CASE	$S(p)$	$S_{rw}(p)$	$E(p)$	$E_{rw}(p)$
Eq.	(7)	(8)	(9)	(10)
CPU8k	8	2.26	1	0.28
CPU32k	"	2.66	"	0.33
CPU131k	"	2.40	"	0.30
CPU524k	"	1.40	"	0.17
CPU2M	"	1.07	"	0.13
CPU8M	"	1.45	"	0.18
GPU8k	2304	0.28	"	0.000121
GPU32k	"	1.21	"	0.000526
GPU131k	"	4.57	"	0.001983
GPU524k	"	14.17	"	0.006150
GPU2M	"	17.96	"	0.007796
GPU8M	"	22.45	"	0,009744

It can be seen that the increase of grid size significantly reduces computational capabilities of parallel CPU, leading to a lower speedup performance over the base case after certain grid size, as well as to a drop in per core efficiency at the same time. However, on the GPU, the speedup is generally increasing with the grid size, and it should follow that trend until the physical limitations of the hardware are met. At the same time, we can notice significant rise in per core efficiency, even though its value remains very low, indicating the underutilization of computational resources and the existence of a significant overhead.

4. SUMMARY

A CFD code with a two-equation turbulence model was modified to run on GPU architecture. Monophase 2D turbulence flow test case was solved on an orthogonal structured grid, while the Jacobi solver is used for efficient parallelization. The code speedup and computational efficiency were analysed over the grid size and compared between parallel and serial execution of the code, both on CPU and GPU.

A significant disparity between results that can be expected in theory, and the ones obtained by solving the real-world problems that include turbulence modelling on parallel machines was observable. While the majority of the work executed can be readily parallelized, and the number of operations can in theory drop to a value close to 106 (for ideal parallel machine), in reality different kinds of overhead become an issue for performance, and as such significantly overload accelerators leading to slower than expected execution of programs.

Even though the existing accelerators do suffer from issues caused by different overheads, real-world performance improvements are noticeable, and they outperform each other at different problem sizes.

The use of Jacobi solver has potential on both current and upcoming GPU and similarly structured accelerators/platforms, due to its low number of operations, even though it is the slowest to converge to a solution, and takes double memory space. An alternative to it would be the implementation of red-black Gauss-Seidel algorithm, using less space, but operating only on one half of the problem per dimension of array, to avoid recursive dependencies that would prevent the parallelization.

Considering the implementation from the aspect of speedup and per core computational efficiency, it is noticeable that both parallel CPU and GPU outperform single core CPU by a significant amount. However, the speedup factor for parallel CPU slowly drops as the problem size increases. On the other hand, the speedup factor of GPU grows with the problem size at larger scales, and should keep growing until it meets hardware limitations. Efficiency-wise this parallel CPU shown highest value in cases CPU32k and CPU131k with a value over 0.30. Above those cases efficiency slowly drops. On the other hand, GPU efficiency per core is very low, in range of 10^{-3}, but it constantly grows, and we must keep in mind that these computational nodes (CPU and GPU cores) use significantly different amounts of power.

An average CPU core consumption is around 5-15W, or even high as 20-30W per core depending on its purpose and generation, while the GPU cores stay around 10-30mW power per core, leading to values for our devices that would fit range of 80-120W for CPU (total power 140W) and 45-70W for GPU for all CUDA cores (total power 160W). From this a power consumption per run in case CPU524k would be around 0.163 kWh, and similar case GPU524k will be in the range of 0.018 kWh on a GPU based accelerator.

The real-world performance of GPU depends on its characteristics. While the available number of computational cores is significant factor, major problems and performance losses come from the architecture of Streaming Multiprocessors and different Compute Capability versions, with significant differences in ability to manage memory, schedule tasks, locally store data, or utilize some other special functions. Even though improper coding for targeted family of GPUs leads to performance penalties, noticeable issues come from the outside parameters – PCIe lane size, causing the very slow data movements between CPU and GPU.

As said, current CPU-GPU architecture is very limited considering the data movements between CPU and GPU, creating inevitable overhead delays. These problems should be overcome as the new architectures and improvements to the existing ones are introduced, as well as their availability and affordability grows on the market. Some of promising current/future platforms/architectures for development of highly parallel CFD applications such as NVIDIA's Grace Hopper and Grace Blackwell, or the recently announced AMD CPUs with NPU Ryzen AI Max+ 395 should reach wider market in the following years. OpenACC expansion to those accelerators should follow, providing smooth and practical transition of existing codes to these new platforms with higher memory bandwidth, capacity and raw computational power.

ACKNOWLEDGEMENTS

This work has been supported by the Ministry of Science, Technological Development and Innovation of the Republic of Serbia (Contract Annex: 451-03-136/2025-03/ 200017).

REFERENCES

[1] Ferziger, J. H., Perić, M., and Street, R. L., 2020, *Computational Methods for Fluid Dynamics* (4th ed.), Springer International Publishing, Cham.

[2] Stone, H. L., 1968, "Iterative Solution of Implicit Approximations of Multidimensional Partial Differential Equations", *SIAM J Numer Anal*, Vol. 5, pp. 530–558.

[3] Reeve, J. S., Scurr, A. D., and Merlin, J. H., 2001, "Parallel versions of Stone's strongly implicit algorithm", *Concurr Comput*, Vol. 13, pp. 1049–1062.

[4] Chathalingath, A., and Manoharan, A., 2019, "Performance Optimization of Tridiagonal Matrix Algorithm [TDMA] on Multicore Architectures", *International Journal of Grid*

and High Performance Computing, Vol. 11, pp. 1–12.

[5] Ahmadi, A., Manganiello, F., Khademi, A., and Smith, M. C., 2021, "A Parallel Jacobi-Embedded Gauss-Seidel Method", *IEEE Transactions on Parallel and Distributed Systems*, Vol. 32, pp. 1452–1464.

[6] Amritkar, A., Tafti, D., Liu, R., Kufrin, R., and Chapman, B., 2012, "OpenMP parallelism for fluid and fluid-particulate systems", *Parallel Comput*, Vol. 38, pp. 501–517.

[7] Souri, M., Akbarzadeh, P., and Mahmoodi Darian, H., 2020, "Parallel Thomas approach development for solving tridiagonal systems in GPU programming − steady and unsteady flow simulation", *Mechanics & Industry*, Vol. 21, p. 303.

[8] Parker, J. T., Hill, P. A., Dickinson, D., and Dudson, B. D., 2022, "Parallel tridiagonal matrix inversion with a hybrid multigrid-Thomas algorithm method", *J Comput Appl Math*, Vol. 399, p. 113706.

[9] Wei, Z., Jang, B., Zhang, Y., and Jia, Y., 2013, "Parallelizing Alternating Direction Implicit Solver on GPUs", *Procedia Comput Sci*, Vol. 18, pp. 389–398.

[10] Cohen, J. M., and Molemaker, J., 2009, "A Fast Double Precision CFD Code using CUDA", *J Physical Soc Japan*, Vol. 1, pp. 237–341.

[11] Xia, Y., Lou, J., Luo, H., Edwards, J., and Mueller, F., 2015, "OpenACC acceleration of an unstructured CFD solver based on a reconstructed discontinuous Galerkin method for compressible flows", *Int J Numer Methods Fluids*, Vol. 78, pp. 123–139.

[12] Tomanović, I., Belošević, S., Milićević, A., Crnomarković, N., Stojanović, A., Deng, L., and Che, D., 2024, "CFD Code Parallelization on GPU and the Code Portability", *Adv Theory Simul*, p. 2400629.

[13] Tsitsiklis, J. N., 1989, "A Comparison of Jacobi and Gauss-Seidel Parallel Iterations", *Appl Math Left*, Vol. 2, pp. 167–170.

[14] Smart, D., and White, J., 1988, "*Reducing the Parallel Solution Time of Sparse Circuit Matrices Using Reordered Gaussian Elimination and Relaxation*", VLSI Memo No. 88-440, Massachusetts Institute of Technology.

[15] Gene, D. R., and Amdahl, M., n.d."Validity of the single processor approach to achieving large scale computing capabilities", *Spring Joint Computer Conference*, Atlantic City, New Jersey., 483–485.

[16] Gustafson, J. L., n.d."REEVALUATING AMDAHL'S LAW", *Commun ACM*, Vol. 31, pp. 532–533.

[17] Hill, M. D., and Marty, M. R., 2007, "Amdahl's Law in the Multicore Era", Technical Report #1593, University of Wisconsin-Madison.

Conference on Modelling Fluid Flow (CMFF'25)
The 19th International Conference on Fluid Flow Technologies
Budapest, Hungary, August 26 - August 29, 2025

EXPERIMENTAL AND NUMERICAL INVESTIGATION OF THE TURBULENT SWIRLING FLOW IN PIPE BEHIND THE AXIAL FAN IMPELLER

Milan BULAJIĆ, Novica JANKOVIĆ, Lazar LEČIĆ

[1] Corresponding Author. Department for Hydraulic Machinery and Energy Systems, Faculty of Mechanical Engineering, University of Belgrade. Kraljice Marije 16, 11000 Belgrade, Serbia. Tel.: +381 60 585 20 04, E-mail: mbulajic@mas.bg.ac.rs

ABSTRACT (STYLE: ABSTRACT TITLE)

Experimental and numerical research of the turbulent swirling flow in pipe behind the axial fan impeller, which generates solid body profile of the circumferential velocity, is presented in this paper. This is a phenomenon relevant to numerous industrial applications, where axial fans are still inbuilt without the guide vanes. The experimental investigation was carried out using stereo PIV, LDA, and original classical probes. However, in this research are discussed three velocity components measured subsequently by use of the one-component LDA system.

The applied numerical approach involved solving the Navier-Stokes equations under appropriate turbulence modeling conditions, ensuring a high level of accuracy in predicting the swirl intensity and velocity distribution in the pipe. The combination of the unstructured mesh in the inlet and the runner section and structured mesh in the outlet section with the application of the SST and k-ε turbulence models led to the final results. Average velocity profiles, determined in this numerical simulation, are compared with the experimentally obtained data and differences are quantified. These experimentally validated numerical results enable good physical interpretation of the development of the average velocity profiles of the generated turbulent swirling flow in the entire domain.

Keywords: axial fans, CFD, swirling flow, turbulence

Nomenclature

D	[mm]	inner diameter of the pipe
R	[mm]	radial coordinate in the polar cylindrical coordinate system
w	[m/s]	circumferential component of velocity
u	[m/s]	axial component of velocity
z	[mm]	axial coordinate in the polar cylindrical coordinate system
ε	[%]	relative difference between experimental and simulated results

Subscripts and Superscripts

1	section 1 plane
2	section 2 plane

1. INTRODUCTION

This paper presents a computational fluid dynamics (CFD) analysis of turbulent swirl flow generated behind the impeller of an axial fan operating without guide vanes at the outlet. The presence of swirl flow in industrial ventilation and fluid transport systems can significantly impact the overall performance of the system by increasing pressure losses within the pipeline. This, in turn, leads to higher energy consumption and a reduction in system efficiency. Due to these challenges, special attention must be given to the design of axial fan blades when the fan operates without outlet guide vanes, with the goal of minimizing vortex formation and turbulence in the downstream sections. An optimized blade design can help suppress unwanted swirl effects, improving the stability and efficiency of the fluid flow. [1-4]

Previous experimental studies have confirmed the development of swirl flow in the pipelines at the fan outlet. The persistence of this swirl can negatively affect downstream components, leading to vibrations, noise, and potential mechanical fatigue in the ducting system. Understanding the behavior of such flows is essential for optimizing fan performance in various industrial applications, including HVAC systems, cooling systems, and

aeration processes. The numerical investigation presented in this paper aims to complement experimental findings by providing detailed insight into the velocity field, pressure distribution, and turbulence characteristics of the swirling flow.

The investigated axial fan was tested according to the standard ISO 5801, case B, which features a free inlet and a ducted outlet configuration. The fan in question is the W30 model, which corresponds to the industrial fan model AP 400, manufactured by Minel, Serbia. It consists of seven blades with an outer diameter of 0.397 m. One of the notable features of this fan is its ability to adjust the blade angle, allowing for variations in flow characteristics based on operational requirements. In this study, the blade angle is set to 30° at the outer diameter to simulate a typical industrial setup. The outlet duct consists of a straight pipe with a length of $27.74 \cdot D$, where the duct diameter D is rounded to 400 mm. This setup ensures that the development of the swirling flow can be accurately captured in both the experimental and numerical analyses.

The experimental investigation was conducted at the Laboratory for Hydraulic Machinery and Energy Systems at the University of Belgrade – Faculty of Mechanical Engineering. A dedicated test rig was constructed to measure flow characteristics using a one-component laser Doppler anemometry (LDA) system. This advanced optical measurement technique provides high-resolution velocity data, which is critical for validating CFD simulations. The experimental setup included two measurement sections placed at z/D = 3.35 and z/D = 26.31 downstream of the fan outlet, ensuring a comprehensive assessment of flow evolution over a significant length of the duct. [1-3]

The fan was tested across a range of rotational speeds, allowing for an evaluation of its performance under different operating conditions. However, in this study, numerical and experimental results are compared specifically for a rotational speed of 2500 rpm, which corresponds to a Reynolds number of Re = 423,350. This flow regime falls within the range of highly turbulent conditions, making it an excellent test case for assessing turbulence models and swirl flow behavior in CFD simulations. [1]

The numerical simulation in this work aims to replicate the experimental conditions and provide a detailed analysis of the flow field, including velocity profiles, pressure variations, and turbulence intensity. The results obtained through CFD are compared with experimental measurements to evaluate the accuracy of the computational approach and its potential application in optimizing axial fan designs for industrial use.

2. EXPERIMENTAL RESEARCH AND FAN IMPELLER CAD PREPARATIONS

The test rig is presented in Figure 1, and is explained in detail in [1]. Measurements were conducted using LDA 1 component system Flow Explorer Mini LDA from Dantec, with smoke fluid EFOG, Density Fluid, Invision, which was freely sucked in the installation. Velocity components were measured subsequently.

A necessary step in the analysis was the 3D scanning of the impeller, allowing for an accurate digital representation to be transferred into CAD software for further modifications and simulations. This process ensured that the geometry of the impeller was precisely captured, enabling a more realistic computational study.

During the CAD modeling phase, certain non-essential components were intentionally excluded to simplify the model without compromising the accuracy of the results. Elements such as the shaft and electromotor were omitted, as their inclusion would have increased the complexity of the numerical analysis while providing little to no improvement in the precision of the simulation. By focusing solely on the impeller and the main flow path, the computational model remained efficient and manageable while still capturing the key aerodynamic characteristics of the fan.

Additionally, the exact geometry of the outlet duct was not fully replicated in the CAD model. Instead, it was assumed that the duct was a perfect cylindrical tube with a diameter of 400 mm. However, in reality, the physical duct contained surface imperfections, creases, and minor irregularities that could influence the flow characteristics. These discrepancies between the idealized model and the actual experimental setup may contribute to differences between the numerical and measured results. Such deviations are common in CFD studies and must be considered when analyzing the accuracy of the computational predictions.

By leveraging 3D scanning technology and CAD modeling, the study aimed to create a well-optimized numerical model that balances accuracy and computational efficiency. The assumptions made in the modeling process are carefully evaluated when comparing the simulation results with experimental data, ensuring a thorough understanding of the potential sources of error.

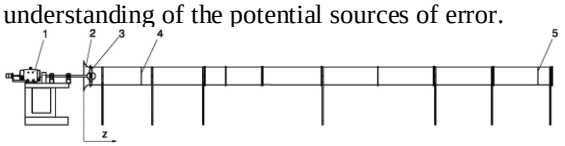

Figure 1 Experimental test rig: 1 - DC motor with electrical power 5 kW, 2 – profiled free bell-mouth inlet, 3- axial fan (swirl generator), 4 – measuring section 1, 5 – measuring section 3. [1]

Figure 2 Axial fan (W30), outside of its test rig [1]

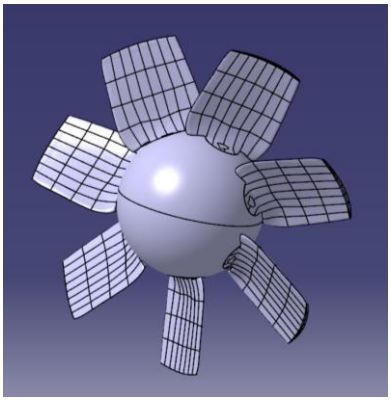

Figure 3 3D scan of the fan

The 3D-scanned impeller was not ideal for direct mesh generation, as it contained a large number of surfaces, which negatively affected the quality of the computational grid. The excessive surface detail resulted in a highly complex and irregular mesh, potentially leading to numerical instabilities and increased computational costs. To address this issue, the model was refined using cutting planes, simplifying its geometry while preserving the critical aerodynamic features of the impeller. This modification improved the mesh quality and ensured better computational performance without compromising the accuracy of the simulation.

3. CFD CALCULATIONS

In the computational domain, the entire air volume surrounding the fan was included to capture the full aerodynamic behavior. The mesh was generated using ANSYS Mesh, resulting in an unstructured numerical grid. While unstructured meshes offer flexibility in handling complex geometries, they are generally of lower quality compared to structured grids. To improve accuracy, the Contact Match method was applied, ensuring perfect alignment of the mesh nodes in the regions upstream and downstream of the fan. This technique significantly enhanced numerical stability by preventing interpolation errors at the interfaces between different flow regions. The final geometry is illustrated in Figure 3.

The outlet domain was carefully structured to facilitate the node-matching operation while simultaneously ensuring high mesh quality in the downstream region. This was particularly important because the research focused on two key measurement planes within the outlet domain. However, the Contact Match function does not support different mesh types or inflation layers within certain sectors. As a result, achieving a high-quality grid in the outlet region required careful adjustments to the meshing strategy.

One notable limitation arising from this approach was the absence of an inflation layer around the fan blades. Inflation layers are typically used to accurately resolve boundary layer effects, especially in turbulent flows. To compensate for this, the cell size in the blade region was reduced, allowing for a finer resolution of near-wall flow structures. The total computational grid consisted of 9.984 million cells, with 4.109 million cells dedicated to the structured outlet domain.

To overcome the problems of boundary conditions at the inlet of the fan, a large dome is created that incorporates the profiled free bell-mouth inlet. The outer perimeter of the dome represents the area where the total pressure is equal to the atmospheric pressure and where the velocity is equal to zero. The boundary conditions used are presented in Table 1.

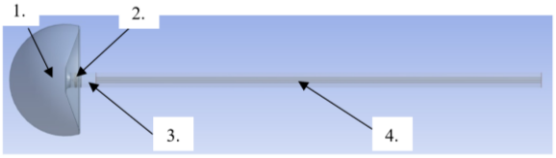

Figure 4 CAD model used for the simulation. 1 - inlet section, 2 - runner, 3 - non-structure mesh section outlet duct, 4 - structured mesh section outlet duct

Table 1. Boundary conditions

Surface	Boundary conditions	Input
Inlets	Total relative pressure	0 [Pa]
Outlets	Static relative pressure	0 [Pa]

For the simulation, the Shear Stress Transport (SST) turbulence model was chosen due to its favorable balance between computational cost and accuracy. The SST model effectively combines the k-ω model for near-wall regions and the k-ε model for free-stream turbulence, making it well-suited for complex aerodynamic flows such as those encountered in axial fan applications. While Large Eddy Simulation (LES) could potentially yield even more accurate results by resolving finer turbulence

structures, its significantly higher computational cost makes it impractical for the current study. However, LES is being considered for future research to further improve the accuracy of the numerical predictions.

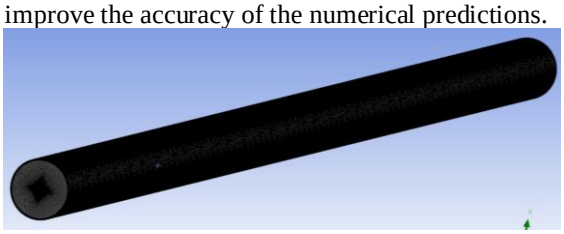

Figure 5 Mesh of the outlet pipe

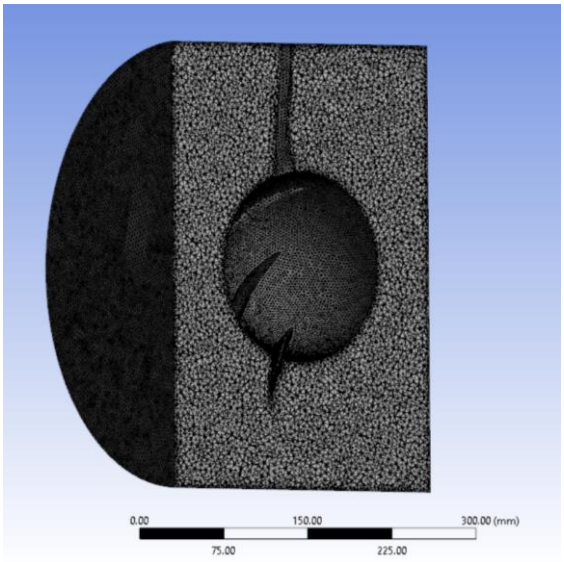

Figure 6 Mesh of the blade section

4. RESULTS AND DISCUSSION

The results obtained from the CFD simulation are compared with the experimental data acquired using a single-component Laser Doppler Anemometry (LDA) system which are obtained from Čantrak (2012)[1]. One of the primary advantages of CFD is its ability to provide detailed flow field analysis at any location within the simulation domain. However, for the sake of consistency and validation, the focus is placed on the same measurement planes that were analyzed during the experiments. These planes are located at z/D = 3.35 (referred to as Section 1) and z/D = 26.31 (referred to as Section 2) downstream of the fan outlet. These sections were chosen to capture both the near-field and far-field development of the swirling flow. [2]

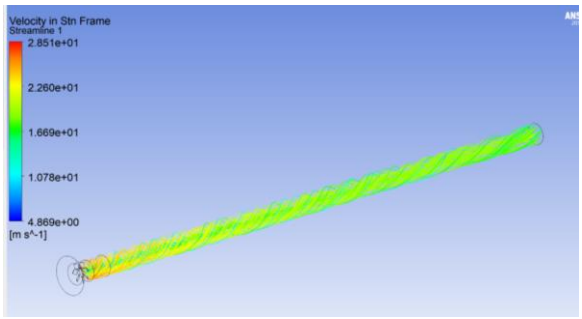

Figure 7 Representation of the streamlines starting from the outlet plane of the runner section until the end of the outlet

During the experimental measurements, all three velocity components were recorded in a polar-cylindrical coordinate system—the axial, radial, and circumferential velocity components. However, for this study, only the axial and circumferential velocity components are considered for comparison, as they are the most relevant in assessing the development of swirl flow and its impact on overall system performance. The circumferential velocity component plays a crucial role in influencing the axial velocity profile, as the presence of strong vortex structures alters the uniformity and distribution of axial flow. These vortex structures are clearly observed in the velocity contours obtained from the CFD simulation.

While the simulation successfully captures the general trend of the flow phenomena, discrepancies are observed in the magnitude of the velocity values when compared to experimental results. These differences can be attributed to multiple factors, including assumptions made in the numerical model, the idealized representation of the outlet duct, and the absence of certain geometric irregularities present in the experimental setup. Additionally, turbulence modeling limitations, such as the use of the SST model instead of LES, could contribute to minor deviations in predicted velocity distributions.

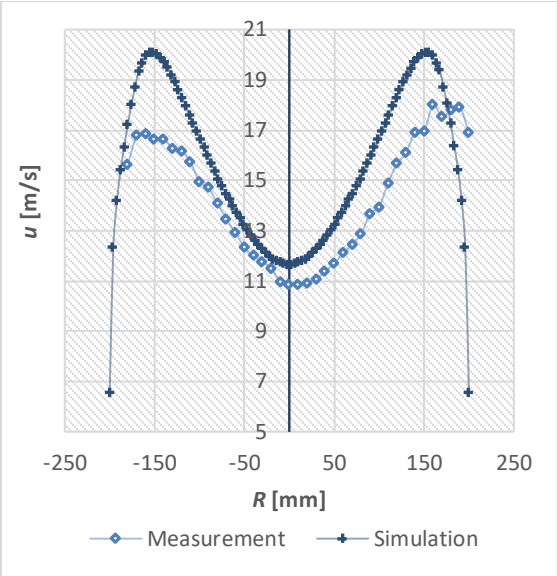

Figure 8 Axial velocity component in the section 1 plane [1]

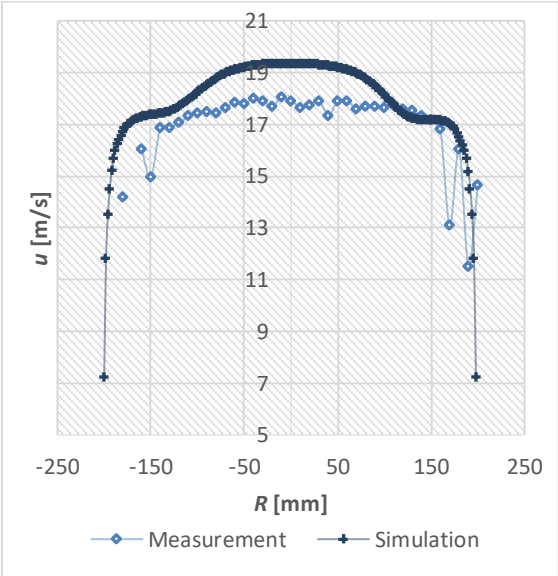

Figure 9 Axial velocity component in the section 2 plane [1]

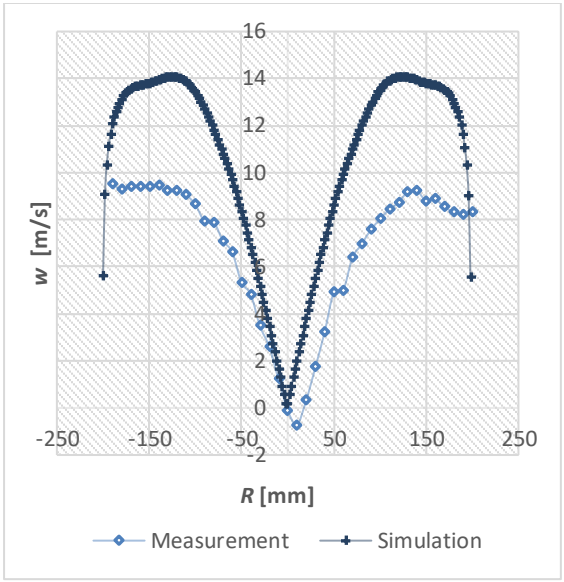

Figure 10 Circumferential velocity component in section 1 plane [1]

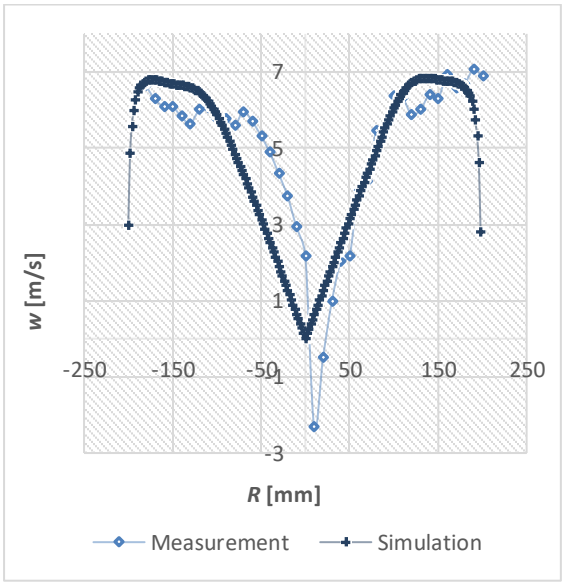

Figure 11 Circumferential velocity component in section 2 plane [1]

The simulation results indicate that the calculated velocity fields closely follow the trends observed in the experimental flow fields at both measurement sections. However, the agreement is more pronounced in Section 2 than in Section 1, suggesting that the numerical model better captures the flow characteristics further downstream.

One key observation is that the simulation treats the flow as nearly axisymmetric, whereas the experimental measurements reveal the opposite. In reality, the vortex core exhibited continuous shifts in position, indicating a more irregular, asymmetric behavior. This effect can be attributed to the presence of a significant radial velocity component, which the simulation does not fully capture. The shifting vortex core suggests the existence of complex secondary

flow structures that are difficult to resolve using RANS-based turbulence models and may require more advanced modeling techniques, such as Large Eddy Simulation (LES) or Detached Eddy Simulation (DES), for a more accurate representation.

Apart from the symmetry discrepancy, differences in velocity magnitudes are also evident. The circumferential velocity component in Section 1 shows the highest deviations between the simulation and the measurements. This suggests that the near-field region of the swirling flow is not fully resolved in the numerical model, possibly due to mesh limitations or turbulence model assumptions. On the other hand, the smallest discrepancies in velocity magnitude are also observed in the circumferential component, but in Section 2, where only a slight radial shift is noted. This indicates that the swirl intensity diminishes further downstream, a trend that was also confirmed through experimental measurements.

Another notable difference between the simulation and the experimental results is the volumetric flow rate. The CFD simulation predicts a 10% higher flow rate compared to the measurements. This discrepancy leads to a general increase in axial velocity across all analyzed sections, as well as throughout the entire computational domain. The most likely cause of this overestimation is the assumption that the outlet duct is a perfect cylinder. In reality, the experimental test rig was constructed using commercially available components, which inherently contain manufacturing imperfections, creases, and slight misalignments. These irregularities introduce additional pressure losses and flow disturbances, ultimately reducing the measured flow rate in comparison to the idealized numerical model.

Figure 12 does not optimally illustrate the relationship between the experimentally measured velocity profiles and the simulated results. The most significant discrepancies between the two are observed near the vortex core, particularly in the circumferential velocity component. In this region, the simulation and experimental results diverge the most, indicating that the numerical model does not fully capture the local flow dynamics at the core of the swirling motion.

A consistent difference is also present in the axial velocity component, which suggests a discrepancy in the overall flow rate between the simulation and the experiment. As previously discussed, the CFD model predicts a higher volumetric flow rate, which directly influences the axial velocity distribution throughout the domain. This overestimation in axial velocity affects the overall agreement between the computational and experimental results.

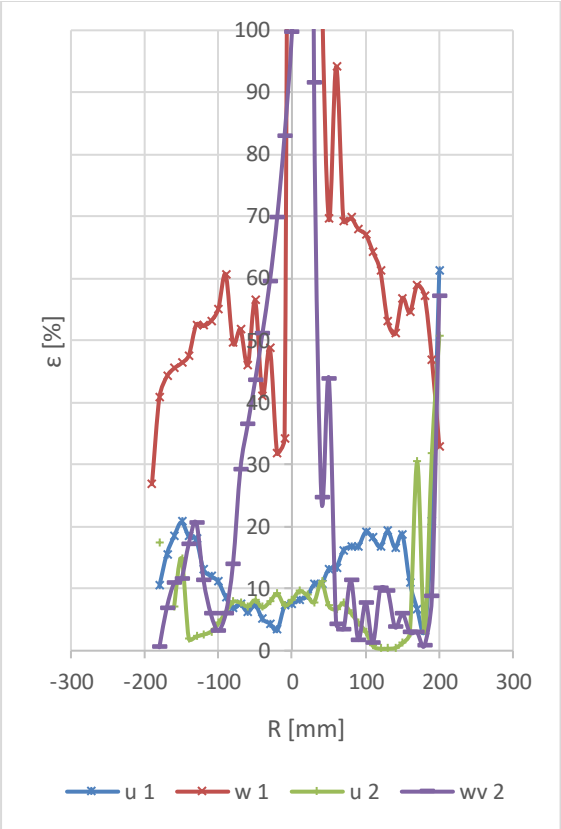

Figure 12 Relative difference between the simulated values and the experimental. Where u stands for axial, w for circumferential component of velocity, and 1 and 2 indicate the sections [1]

The relative difference in the circumferential velocity component near the vortex center can largely be attributed to the radial displacement of the vortex core. In the simulation, the vortex is treated as more stable and axisymmetric, while in the experiment, the vortex core exhibits continuous movement and shifting due to additional flow instabilities and secondary flow effects. If a correction method were applied to account for this radial displacement—such as realigning the vortex core locations between the simulation and the experiment—the resulting profiles would likely show better agreement.

5. SUMMARY

This paper presents a numerical comparison with a previously conducted experimental investigation on the flow characteristics in the ducted outlet of an axial fan without guide vanes. The study aims to evaluate the accuracy of computational fluid dynamics (CFD) simulations in replicating the complex flow structures observed in the experiment.

The results indicate a strong correlation in the general flow phenomena between the measured and simulated data, particularly in the solid-body circumferential velocity profiles. However, discrepancies in velocity magnitudes are evident, especially in the flow rate predictions. These

differences are primarily attributed to the idealized representation of the flow field in the numerical model, which eliminates geometrical imperfections and surface irregularities present in the real experimental setup. The test rig components, including the duct and fan housing, contain minor manufacturing defects, creases, and misalignments, which introduce additional losses and distortions in the measured flow field—elements that are inherently absent in the simulation.

Given the complexity of both the flow dynamics and the geometric configuration, this study serves as an initial step toward a more comprehensive understanding of the intricate flow behavior downstream of the fan. Future research efforts could focus on expanding the computational domain, incorporating a more detailed representation of the fan, duct, and outlet section to better capture real-world effects.

Furthermore, enhancements in numerical modeling could lead to improved accuracy. Refining the computational mesh, particularly in regions of high velocity gradients, would help resolve finer flow structures. Additionally, exploring alternative turbulence models—such as Detached Eddy Simulation (DES) or Large Eddy Simulation (LES)—or modifying the existing turbulence approach could provide a more precise depiction of the unsteady vortex structures and turbulence intensities present in the flow.

By implementing these improvements, future studies can achieve higher accuracy and reliability in CFD predictions, ultimately contributing to a more detailed and practical understanding of swirl flow in axial fan systems.

ACKNOWLEDGEMENTS

This research was funded by the Ministry of Science, Technological Development and Innovation of the Republic of Serbia under the Agreement on financing the scientific research work of teaching staff at accredited higher education institutions in 2025, No. 451-03-137/2025-03/200105, and under the Agreement on financing Scientific research institutions in 2025, No. 451-03-136/2025-03/200105.

REFERENCES

[1] Čantrak Đ., 2012, “Analysis of the Vortex Core and Turbulence Structure Behind Fans in a Straight Pipe Using PIV, LDA and HWA Methods”, Ph.D. thesis, Univ. Belgrade, Fac. Mech. Eng., Belgrade.

[2] Čantrak Đ., Janković N., Ilić D., 2015, “Investigation of the Turbulent Swirl Flow in Pipe Generated by Axial Fans Using PIV and LDA Methods”, Theoretical and Applied Mechanics, Vol. 42, Iss. 3, pp. 211-222.

[3] Ilić D., Svorcan J., Čantrak Đ., Janković N., 2025, “Experimental and Numerical Research of Swirl Flow in Straight Conical Diffuser”, Processes, Vol .13, 182.

[4] Benišek M., 1979, “Investigation of the turbulent swirling flows in straight pipes, Ph.D. thesis, Univ. Belgrade, Fac. Mech. Eng., Belgrade.

Conference on Modelling Fluid Flow (CMFF'25)
The 19th International Conference on Fluid Flow Technologies
Budapest, Hungary, August 26-August 29, 2025

A New Viscosity Formulation for Improved Turbulence Modeling in Kolmogorov Flow

Gergely Kristóf[2], Kinga Andrea Kovács[1], Tamás Kalmár-Nagy[2], Miklós Balogh[2]

[1] Corresponding Author. Department of Fluid Mechanics, Faculty of Mechanical Engineering, Budapest University of Technology and Economics, Műegyetem rkp. 3, Budapest, 1111, Hungary, Telephone: +36-1-463-2546, E-mail: kingaandrea.kovacs@edu.bme.hu
[2] Department of Fluid Mechanics, Faculty of Mechanical Engineering, Budapest University of Technology and Economics, Műegyetem rkp. 3, Budapest, 1111, Hungary, E-mail addresses: kristof.gergely@gpk.bme.hu, kalmar.nagy.tamas@gpk.bme.hu, balogh.miklos@gpk.bme.hu.

ABSTRACT

The Kolmogorov flow, a shear flow driven by a constant inhomogeneous body force in a periodic domain, has not been widely used for turbulence modeling despite its potential benefits. Commonly used Reynolds-averaged turbulence models (e.g., standard $k-\varepsilon$, RNG $k-\varepsilon$, standard $k-\omega$, $k-\omega$ SST, GEKO) give incorrect results for this flow. Similar issues arise in applications with sustained turbulence in a closed container, like pump shut-off head modeling. In the current paper a novel eddy viscosity model, the geometry-informed (GI) model, is proposed, which constrains the turbulent length scale by accounting for wall distance, even in dissipative flow regimes. The GI model is implemented in Ansys Fluent as a user-defined formula for the standard $k-\varepsilon$ model, and it is validated against Direct Numerical Simulation (DNS) and experimental data. In addition, the results are compared with the $k-\omega$ SST model. The test cases encompass channel flow, flow over a backward-facing step (BFS), and Kolmogorov flow. Results show that the GI model better predicts the near-wall peak of turbulent kinetic energy compared to $k-\omega$ SST in channel flow, and offers improved reattachment length predictions for high Reynolds number flow over a BFS. In Kolmogorov flow, the GI model produces qualitatively correct results, but with lower velocity amplitudes than DNS due to the shortcomings of the ε transport equation. Further improvements to the turbulent kinetic energy dissipation equation are planned.

Keywords: CFD, DNS, Kolmogorov flow, RANS, turbulence modeling, turbulent viscosity

NOMENCLATURE

Re	[-]	Reynolds number
Re_Δ	[-]	filter size-based Reynolds number
H	[m]	step size
P	$[\mathrm{m}^2\cdot\mathrm{s}^{-3}]$	turbulent production
S	$[\mathrm{s}^{-1}]$	shear modulus
U	$[\mathrm{m}\cdot\mathrm{s}^{-1}]$	x-wise velocity
U_τ	$[\mathrm{m}\cdot\mathrm{s}^{-1}]$	friction velocity
$\hat{f}$	$[\mathrm{m}\cdot\mathrm{s}^{-2}]$	force amplitude
f	$[\mathrm{m}\cdot\mathrm{s}^{-2}]$	driving force
k	$[\mathrm{m}^2\cdot\mathrm{s}^{-2}]$	turbulent kinetic energy
t	[s]	time
y^+	[-]	dimensionless wall distance
y_w	[m]	distance from the wall
Δ	[m]	filter size
κ_1	$[\mathrm{m}^{-1}]$	fundamental wave number
ν	$[\mathrm{m}^2\cdot\mathrm{s}^{-1}]$	kinematic viscosity
ν_t	$[\mathrm{m}^2\cdot\mathrm{s}^{-1}]$	turbulent viscosity
ω	$[\mathrm{s}^{-1}]$	eddy frequency
ε	$[\mathrm{m}^2\cdot\mathrm{s}^{-3}]$	turbulent dissipation

1. INTRODUCTION

The main aim of the current study is to develop better models near production-dissipation equilibrium using results from DNS models of Kolmogorov flow and channel flow. The most widely used eddy viscosity formula – Stress and Production (SP) model – was introduced by Jones and Launder [1] as an element of the model, currently known as the standard $k-\varepsilon$ turbulence model:

$$\nu_{t,\varepsilon} = C_\mu \frac{k^2}{\varepsilon}, \tag{1}$$

where k is the turbulent kinetic energy, ε is the turbulent dissipation, and $C_\mu = 0.09$ is an empiric constant.

Eq. (1) assumes a time step proportional to the k/ε ratio at all points in the flow field. However, it can be suspected that at locations where turbulent production exceeds dissipation (i.e., k increases along the trajectory of the fluid particle), the turbulent time scale relevant to eddy viscosity is determined by the large scales associated with production rather than the small scales associated with dissipation, and therefore Eq. (2) may be a reasonable alternative to Eq. (1):

$$\nu_t = C_\mu \frac{k^2}{P}, \tag{2}$$

where P is the turbulent production. The turbulent production can be determined with the following equation:

$$P = \nu_t S^2, \tag{3}$$

where S is the shear modulus of the bulk flow. Based on these equations a production-based eddy viscosity formula can be constructed as follows:

$$\nu_{t,P} = \sqrt{C_\mu}\frac{k}{S}. \tag{4}$$

Eq. (4) – first proposed by Chou [2] – seems to be consistent with Bradshaw's observation that the primary turbulent stress is proportional to the turbulent kinetic energy at the outer boundary layer. The obvious drawback of Eq. (4) is that it results in a turbulent viscosity approaching infinity, where S approaches zero. The need to combine the turbulent viscosity formulae – Eqs. (1) and (4) – was recognized by Menter [3]. In his $k-\omega$ SST model the following eddy viscosity formula was proposed:

$$\nu_{t,\mathrm{SST}} = \frac{a_1 k}{\max\left(a_1\omega, S F_2\right)}, \tag{5}$$

where $a_1 = 0.31$ is a constant, ω is the eddy frequency, and F_2 is given by (F_2 is a function that is one for boundary layer flows and zero for free shear layers):

$$F_2 = \tanh\left(\Phi_2^2\right), \tag{6}$$

where:

$$\Phi_2 = \max\left(2\frac{\sqrt{k}}{0.09\omega y_w}, \frac{500\nu}{y_w^2\omega}\right), \tag{7}$$

where y_w is the distance from the wall.

The eddy frequency can be expressed as:

$$\omega = \frac{\varepsilon}{C_\mu k}. \tag{8}$$

By substituting Eq. (8) into Eq. (5), and utilizing that $a_1 \cong \sqrt{C_\mu}$ one can obtain the following formula:

$$\nu_{t,\mathrm{SST}} = \min\left(\frac{k^2 C_\mu}{\varepsilon}, \frac{\sqrt{C_\mu}k}{S F_2}\right). \tag{9}$$

Based on Eq. (9) it can be seen that the $k-\omega$ SST model basically chooses the smaller value from Eqs. (1) and (4). A possible physical explanation is that the eddy viscosity can be considered as proportional to the turbulent kinetic energy multiplied by a time scale (k/ε or $\sqrt{C_\mu}/S$), and that the smaller time scale, which is characteristic of the faster process, dominates among the possible time scales. The model described by Eqs. (5)-(7) thus distinguishes two main regimes, production and dissipation regimes, based on time scales.

The $k-\omega$ SST model also constrains the dissipation-based formula for low (essentially less than 100) turbulent viscosity ratios using the viscosity ratio, and the production-based formula near the wall using the wall distance. The model does not use the wall distance to constrain the turbulent length scale in the dissipation regime. The $k-\omega$ SST model therefore describes the eddy viscosity as a five-variable function: $\nu_{t,\mathrm{SST}}(S, k, \omega, \nu, y_w)$.

Out of the widely used eddy viscosity models, the realizable $k-\varepsilon$ model of Shih et al. [4] assumes a C_μ value dependent on the ratio of the time scales of turbulence and the main flow, which leads to more accurate results for free jets and boundary layer separation. However, this model is not compatible with models involving rotating coordinate systems or rotating numerical grids [5]. Overall, the development of turbulent viscosity formulae has received relatively little attention in the last three decades.

2. INVESTIGATIONAL METHOD

2.1. Kolmogorov flow

The Kolmogorov flow is a flow induced by a sinusoidally varying force field in space in a periodic flow domain. The driving force can be written in the following way:

$$f = -\hat{f}\cos(\kappa_1 y), \tag{10}$$

where $\hat{f}$ is the force amplitude, and κ_1 is the wave number.

The driving force can be seen in Figure 1, where 2Δ is the side length of the cube corresponding to the simulation domain:

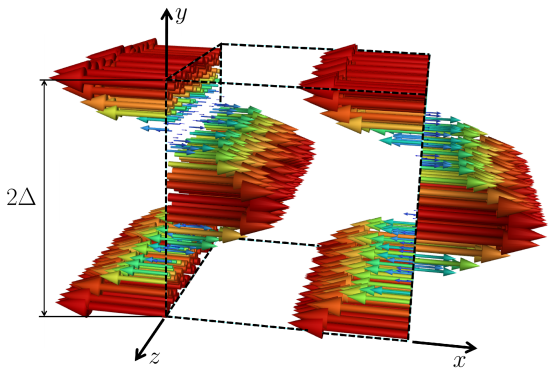

Figure 1. Spatial distribution of the driving force.

The x-wise velocity averaged in the $x-z$ planes varies with t and y as shown in Figure 2.

The Δ half side length (filter size) of the domain determines the wavenumber of the fundamental mode of the velocity field in turbulent flows, for instance, flow excited in the first mode: $\kappa_1 = \pi/\Delta$.

The reference velocity can be defined as the maximum value of the friction velocity:

$$U_\tau = \sqrt{\frac{\hat{f}}{\kappa_1}}, \tag{11}$$

and the Reynolds number being characteristic of the flow is defined in terms of the filter size:

$$\mathrm{Re}_\Delta = \frac{U_\tau \Delta}{\nu}. \tag{12}$$

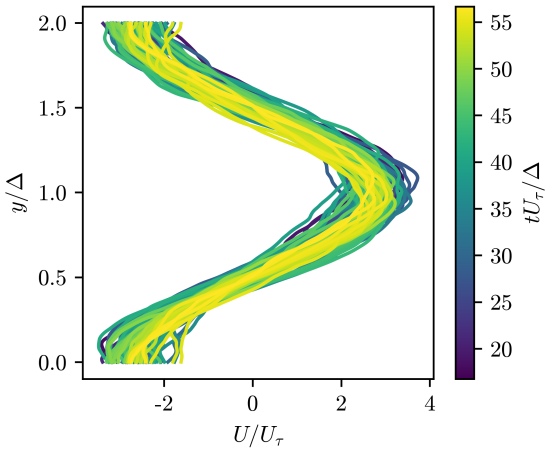

Figure 2. Dimensionless x-wise velocity profiles of the time-varying main flow. The different lines correspond to the different time steps.

Based on these equations the reference length and time are Δ and Δ/U_τ. We observed that for the quasi-stationary Kolmogorov flow, the various extensively applied Reynolds-averaged turbulence models (standard $k-\varepsilon$, RNG $k-\varepsilon$, standard $k-\omega$, $k-\omega$ SST, GEKO) lead to qualitatively incorrect results: the flow velocity amplitude decreases in time, resulting in a decrease in the spatial averages of hydraulic power, production and dissipation. On the other hand, the average value of the turbulent kinetic energy is close to the DNS results. A decreasing ε at a nearly constant k leads to an increasing turbulent viscosity, which supports the decrease in velocity amplitude at constant driving force. During this process, the turbulent length scale increases indefinitely, and this will be called herein as *turbulent inflation*.

2.2. DNS database

For the development of the eddy viscosity model, DNS model results for channel flow and Kolmogorov flow are used, which are the authors' own results in the latter case, and published data from the Johns Hopkins Turbulent Database (JHTDB) in the case of channel flow [6].

The spatially averaged characteristics of the Kolmogorov flow are strongly time-varying: Coefficient of Variation (COV) values of around 15% for S and around 20% for k are observed over the range of Reynolds numbers considered, which allows the authors to obtain data on the time variation of turbulence.

Both flow types have a layered symmetry, and therefore turbulent characteristics are derived from layer averages. The periodic lengths of the layers are $2\Delta\times2\Delta$ for Kolmogorov flow, and $8\pi\Delta_{max}\times3\pi\Delta_{max}$ for channel flow, where Δ_{max} is the distance of the channel midplane from the solid wall (y-wise distance). The Reynolds averages of the physical characteristics are approximated by the two-step averaging procedure detailed below.

The value of the characteristics averaged over the x and z coordinates varies as a function of the y coordinate and time t. In the case of Kolmogorov flow, the time variation of the layer-averaged velocity results in a significant variance, which, according to the authors' interpretation, is not part of turbulence. The transient main flow forms an energy storage between the hydraulic power and the turbulent production, so there is no need for an instantaneous equilibrium between them. Although layer averaging in a periodic domain occurs in planes of infinite size, the limited period length of the domain means that the instantaneous energy spectrum of the layer averages can differ significantly from the time-averaged turbulent spectrum. Therefore, the results of models based on simplified descriptions of the turbulence state (e.g., parameters k and ε only) are subject to significant noise. The noise in the turbulent characteristics and eddy viscosity model results can be reduced by a secondary averaging. Secondary averaging can be performed t-wise or y-wise, resulting in y-direction profiles or time series. The accuracy of the different eddy viscosity models can thus be tested in either spatial or temporal projection, which is an advantage for model fitting compared to classical time-averaged methods. In the case of channel flow, only time-averaged y-dependent characteristics were determined because the large size of the model domain meant that the layer averages did not show significant temporal variation.

2.3. The method of model fitting

In the case of isotropic turbulence, the maximum wavelength of turbulent structures corresponds to the height of the model domain, which is 2Δ for Kolmogorov flow, and $2\Delta_{max}$ for channel flow. For Kolmogorov flow, the filter size Δ is independent of the y coordinate. For channel flow, the turbulent length scale is proportional to the wall distance y_w, which is Δ_{max} in the median plane of the channel, so the filter size Δ for channel flow is taken to be equal to the wall distance, i.e., $y_w = \Delta$. By generalizing the notion of filter size, the optimal eddy viscosity model can be searched for in a wall bounded domain, and in a periodic domain open in the y direction as a function of the same physical parameters. Thus, a common platform can be used to fit the model parameters, and a common optimum can be found for both wall boundary layer and free shear flow. From this it follows that the filter size can be determined in the case of more complex geometries as well.

3. DISCUSSION OF THE RESULTS

3.1. Geometry-informed (GI) model

In order to control the turbulent inflation in Kolmogorov flow, it is useful to consider the geometric constraints in the dissipation regime, and therefore the optimal eddy viscosity model is sought in the

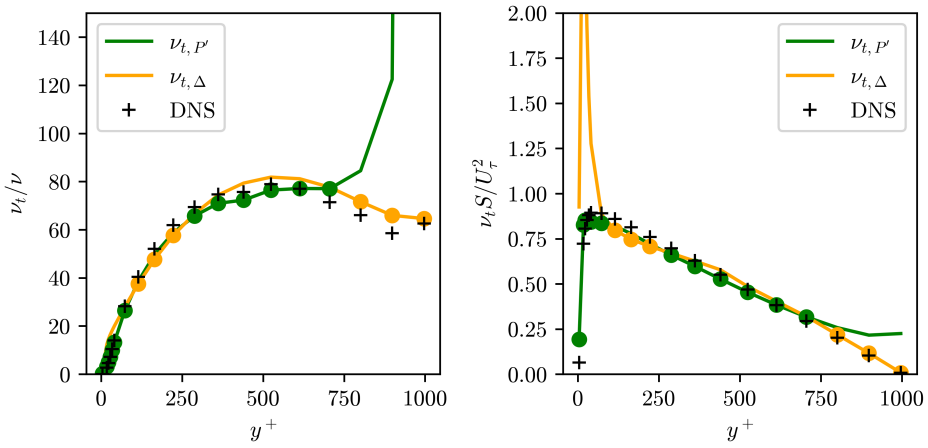

Figure 3. Comparison of dimensionless eddy viscosity (left) and turbulent shear stress (right) obtained from the proposed GI model with the DNS reference data for channel flow. The GI model uses the minimum of formulae $\nu_{t,P'}$ (green), and $\nu_{t,\Delta}$ (orange) indicated by the circular symbols.

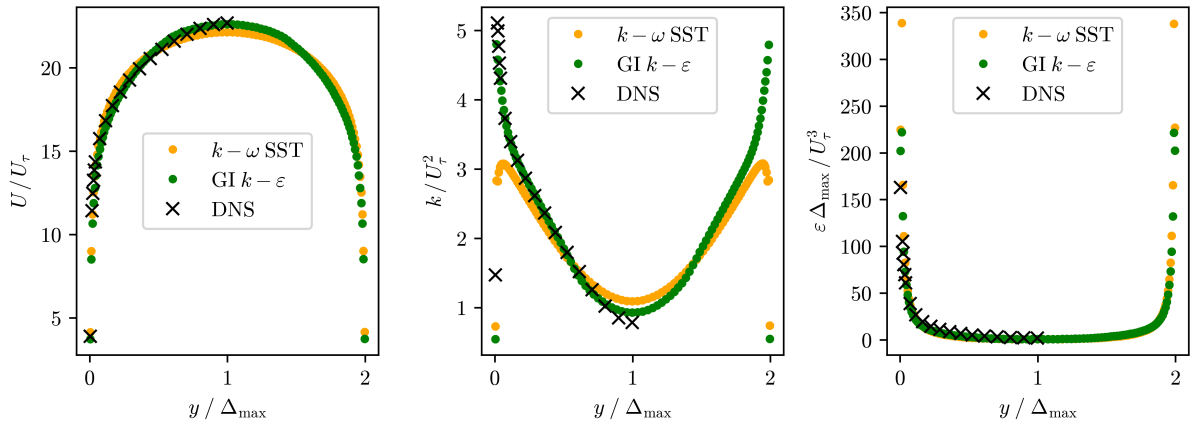

Figure 4. Streamwise velocity component (left), turbulent kinetic energy (middle), and turbulent kinetic energy dissipation (right) profiles in steady-state channel flow.

following form:

$$\nu_{t,\mathrm{GI}} = \min(\nu_{t,P'}, \nu_{t,\Delta}), \tag{13}$$

where:

$$\nu_{t,P'} = C_1 \frac{k}{S} \frac{1}{1 + e^{\left(-C_3 \frac{\sqrt{k}\Delta}{\nu}\right)}}, \tag{14}$$

and:

$$\nu_{t,\Delta} = C_2 \frac{k^{5/4}\sqrt{\Delta}}{\sqrt{\varepsilon}}. \tag{15}$$

The model constants were optimized based on channel flow, and quasi-stationary and decaying Kolmogorov flows. The minimum fitting error was observed for parameters $C_1 = 0.2535$, $C_2 = 0.1118$, and $C_3 = 0.0147$.

Figure 3 shows the GI model in equilibrium channel flow as a function of the y^+ dimensionless wall distance. It can be seen that only the production-based formula gives realistic results in the near-wall buffer layer and only the filter-based formula gives realistic results in the centerline of the channel (near $y^+ = 1000$). In the large part of the wall boundary layer the two formulae give nearly identical results. The GI model, which selects the smaller value out of the two alternative formulae, shows good agreement with the DNS reference data over the entire profile.

3.2. Implementation of the GI model

The in-situ testing of the GI model was performed in the ANSYS Fluent 2023 R1 software, using the standard $k-\varepsilon$ model. The model was implemented as a user-defined function (UDF). The eddy viscosity formula of the standard $k-\varepsilon$ turbulence model was replaced by the GI model, and the model constant value of $C_{1\varepsilon}$ was changed from the standard 1.44 to 1.55 to better fit the boundary layer flow. In other aspects, the standard model parameters were used,

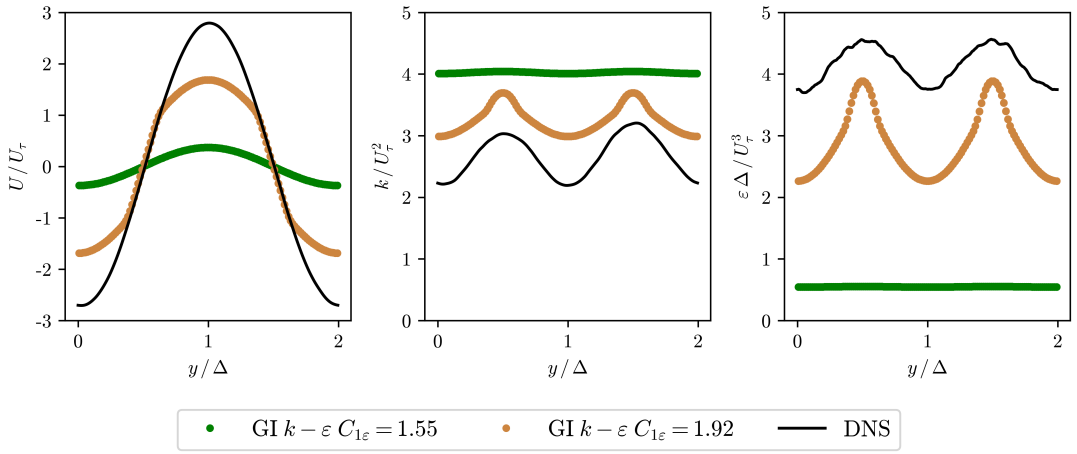

Figure 5. Streamwise velocity component (left), turbulent kinetic energy (middle), and turbulent kinetic energy dissipation (right) profiles in Kolmogorov flow.

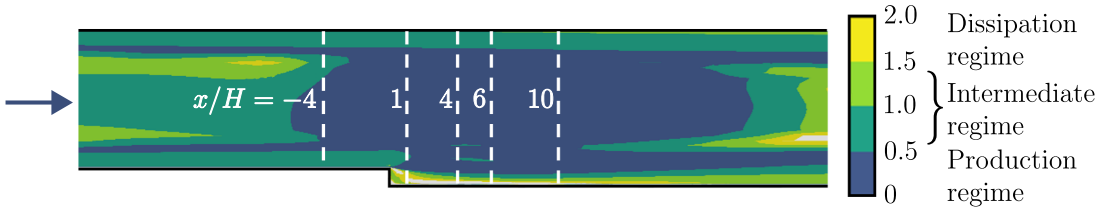

Figure 6. The value of the $\nu_{t,P'}/\nu_{t,\Delta}$ ratio calculated with the GI $k-\varepsilon$ model in the flow above a BFS. Dashed line: position of the tested profiles, and H denotes the step size.

i.e., $C_{2\varepsilon}=1.92$, and the turbulent Prandtl coefficients of $\sigma_k=1$, and $\sigma_\varepsilon=1.3$ were utilized. Therefore, the constructed model is referred to as the GI $k-\varepsilon$ model herein.

3.3. Validation of the GI $k-\varepsilon$ model

Thanks to the good fit of the GI $k-\varepsilon$ eddy viscosity formula, the new turbulence model can be integrated in the turbulent boundary layer without the use of a wall function, and in addition, it can be used with a wall function if the y^+ value necessitates it.

In the case of channel flow, the mesh consisted of 1040 quadrilateral elements, with refined mesh near the wall, and a wall resolution of $y^+=4.3$. Periodic boundary conditions were set for the inlet, and the outlet boundaries, and the boundaries in the y-direction were specified as stationary walls. Coupled pressure-velocity coupling was used, and the following spatial discretization schemes were applied: second order for pressure, second order upwind for momentum, first order upwind for turbulent kinetic energy, and first order upwind for turbulent dissipation rate. Figure 4 shows the simulation results for the channel flow corresponding to the JHTDB test case ($\mathrm{Re}=40\,000, \mathrm{Re}_\Delta=1000$). It can be seen that for steady-state channel flow, the GI $k-\varepsilon$ model provides more accurate results for the near-wall peak value of the turbulent kinetic energy than the $k-\omega$ SST model.

In the case of Kolmogorov flow, the mesh consisted of 512 hexahedral elements, and periodic boundary conditions were applied. The body force was applied as an x momentum source term. The applied numerical schemes were the same as in the case of the channel flow. Figure 5 shows the simulation results of the $\mathrm{Re}_\Delta=997$ quasi-stationary Kolmogorov flow which was excited in the first mode. The turbulent inflation observed for the known Reynolds averaged models (these could not even be fitted into Fig. 5) did not occur for the GI $k-\varepsilon$ model, so the model leads to a qualitatively different result: a convergent solution satisfying the turbulent energy balance and the discrete base equations is obtained. The model results show a high sensitivity to the value of the parameter $C_{1\varepsilon}$. With an optimal $C_{1\varepsilon}=1.55$ setting for the channel flow, the Kolmogorov flow yields a velocity amplitude one order of magnitude lower than the DNS reference data. Based on the analysis of the DNS data, it was observed that the transport equation for dissipation only correctly describes the Kolmogorov flow around $C_{1\varepsilon}=C_{2\varepsilon}$. For the choice of $C_{1\varepsilon}$ with the same value as $C_{2\varepsilon}$, the results of the GI $k-\varepsilon$ model are remarkably closer to the DNS reference data than with the parametrization optimized for channel flow. The adaptation of the transport equation for dissipation requires further investigation.

The results of the GI $k-\varepsilon$ model ($C_{1\varepsilon}=1.55$, $C_{2\varepsilon}=1.92$) were tested against measurement data [7] and against the widely used $k-\omega$ SST model

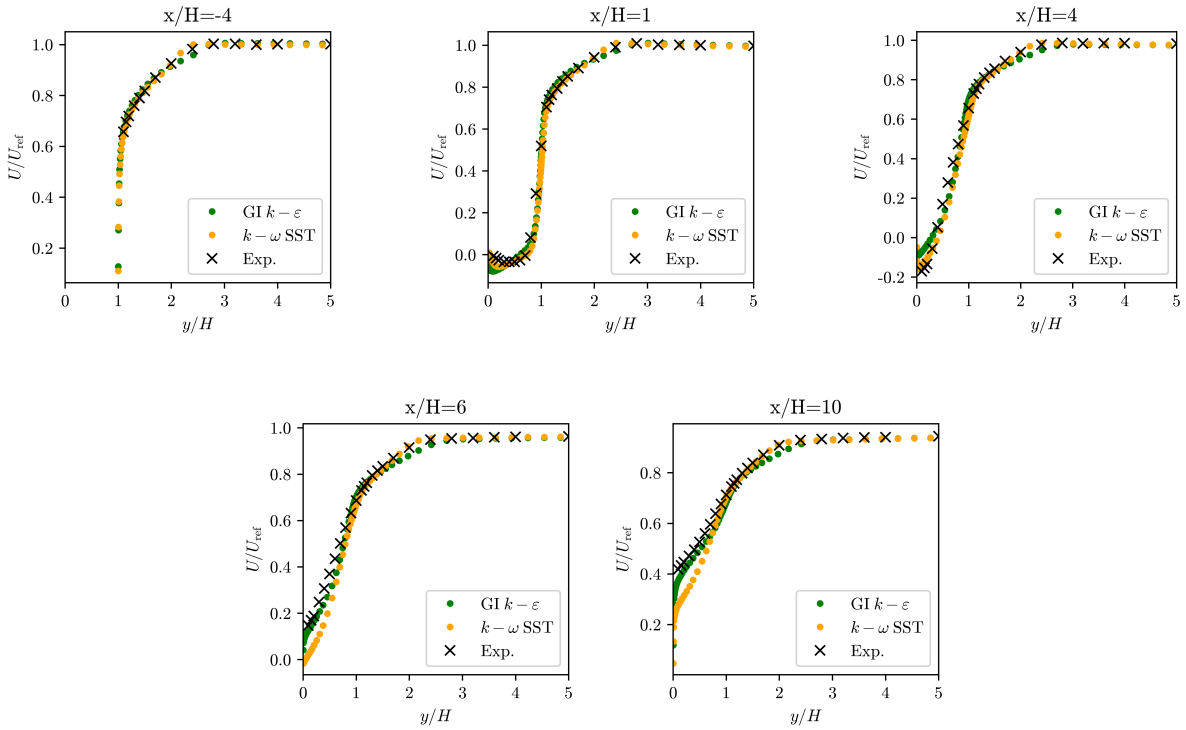

Figure 7. Normalized velocity profiles calculated from the GI $k-\varepsilon$ model (blue) compared to $k-\omega$ SST model results (orange) and measurement data (black) in flow over a BFS along different x/H profiles.

for a backward-facing step (BFS) flow. In the model domain shown in Figure 6, the fluid flows from left to right. At the edge of the step, the boundary layer separates and then reattaches to the bottom surface of the channel. The simulations were performed using a non-equidistant structured mesh with 76 180 hexahedral cells, and the grid had a $y^+ = 3$ wall resolution. For the inlet and the outlet, a velocity inlet (based on [7]) and a pressure outlet boundary condition were prescribed, respectively. For the lower and upper boundaries, wall boundary conditions were prescribed, and for the other boundaries a symmetry boundary condition was set. Coupled pressure-velocity coupling was used, and second order numerical schemes were utilized.

In Figure 6 the coloring shows the value of the $\nu_{t,P'}/\nu_{t,\Delta}$ ratio. For values less than 1 the GI $k-\varepsilon$ model applies the production-based formula ($\nu_{t,P'}$) and for values greater than 1 the filter-based formula ($\nu_{t,\Delta}$). In the intermediate (green) regions, local production and dissipation are approximately in equilibrium, therefore the two formulae give similar results. Figures 7 and 8 (Re = 36 000) show that the velocity and turbulent stress profiles calculated with the GI $k-\varepsilon$ model show a good overall agreement with the measurement data, similar to the $k-\omega$ SST model. In the boundary layer before the step ($x/H = -4$), the results of the $k-\omega$ SST model are in perfect agreement with the measurement results, while the GI $k-\varepsilon$ model produces a slightly thicker boundary layer with stronger turbulence. The GI $k-\varepsilon$ model, however, more accurately produces velocity profiles near the wall in the $x/H = 6$ and $x/H = 10$ sections – which defines the boundary layer reattachment length – as well as peak turbulent stresses in the first two sections after the step.

4. CONCLUSION

Although the Kolmogorov flow has been known for more than 70 years and has beneficial properties for the development of turbulence models, it has not been widely used in such areas. Several known Reynolds-averaged turbulence models (e.g., standard $k-\varepsilon$, RNG $k-\varepsilon$, standard $k-\omega$, $k-\omega$ SST, GEKO) lead to qualitatively incorrect results for Kolmogorov flow. The numerical solution leads to increasing turbulent length scale and decreasing flow velocity at nearly constant Reynolds stress. In the current study, it was proposed to eliminate this anomaly by modifying the eddy viscosity formula used in the turbulence model.

The maximum wavelength of the turbulent structures, that can be interpreted in a given model domain, is limited by the size of the domain and the distance from walls. These are taken into account in the models under study by a generalized Δ geometric filter size. The proposed GI eddy viscosity model approximates the eddy viscosity in the dissipation domain by a power function proportional to the square root of the filter size. The dependence of the model on the filter size makes it suitable for avoiding turbulent inflation in Kolmogorov flow.

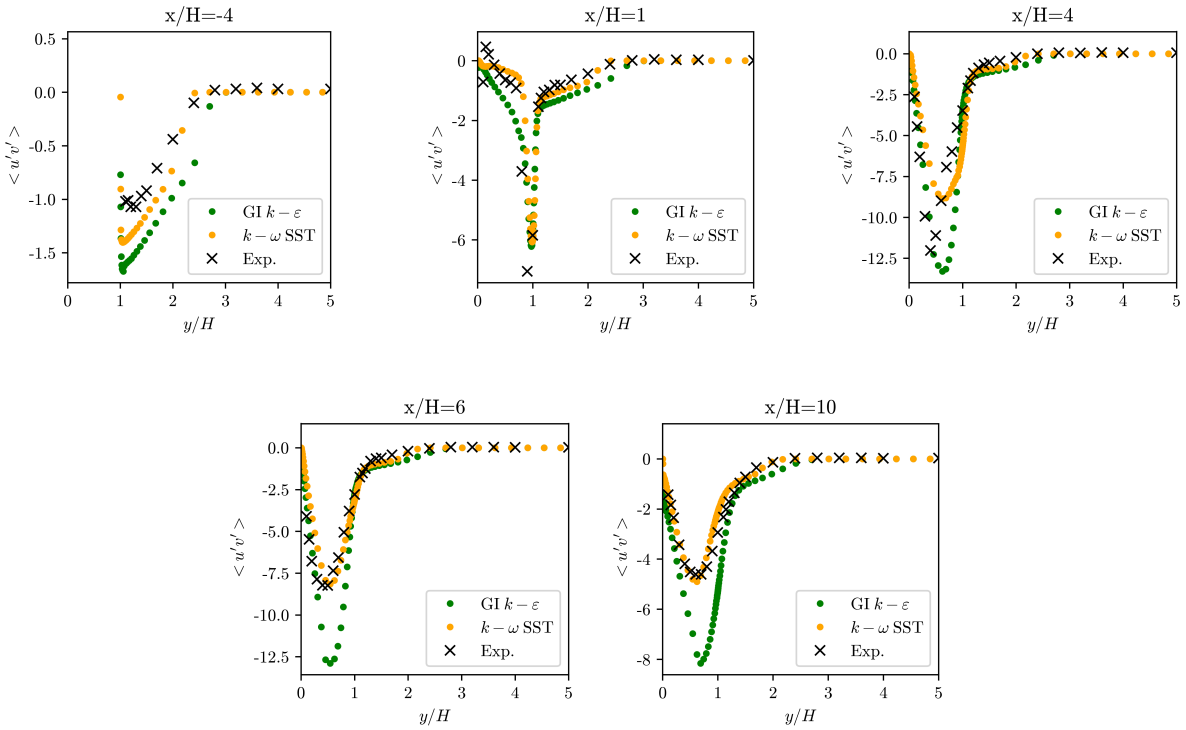

Figure 8. Principal Reynolds stresses calculated from the GI $k-\varepsilon$ model (blue) compared to $k-\omega$ SST model results (orange) and measurement data (black) in flow over a BFS along different x/H profiles.

The GI eddy viscosity model was tested in-situ coupled to the standard $k-\varepsilon$ transport equation in three different flows. In the transport equation of ε, $C_{1\varepsilon}$ was modified from the standard 1.44 to 1.55, to better fit the steady-state channel flow. All other model constants were chosen based on the standard $k-\varepsilon$ model. The resulting GI $k-\varepsilon$ model at $\mathrm{Re}_\Delta = 1000$ channel flow showed excellent agreement with the DNS data and reproduced the peak turbulent kinetic energy near the wall more accurately than the $k-\omega$ SST model.

In Kolmogorov flow, the GI $k-\varepsilon$ model did not exhibit the turbulent inflation typical of known RANS models, but the model produced velocity amplitudes significantly lower than the DNS results. From the DNS analysis of the Kolmogorov flow it was found that the transport equation of ε is consistent with the DNS data when the parameter $C_{1\varepsilon}$ is close to the parameter $C_{2\varepsilon}$. With $C_{1\varepsilon} = C_{2\varepsilon}$ the GI $k-\varepsilon$ model produced results close to the DNS results.

In the high Reynolds number (Re = 36 000) flow above the BFS, the GI $k-\varepsilon$ model showed similar agreement with the $k-\omega$ SST model. A more accurate agreement with the measurement data was observed for the length of the separation bubble.

The further validation of the GI $k-\varepsilon$ model, the addition of Kolmogorov flows excited by time-varying driving force to the DNS database, and the search for models to describe equilibrium shear flow are the planned future directions of the current research.

ACKNOWLEDGEMENT

Project no. TKP-6-6/PALY-2021 has been implemented with the support provided by the Ministry of Culture and Innovation of Hungary from the National Research, Development and Innovation Fund, financed under the TKP2021-NVA funding scheme.

The research reported in this paper is part of project no. **146158**, implemented with the support provided by the Ministry of Innovation and Technology of Hungary from the National Research, Development and Innovation Fund, financed under the **OTKA K 23** funding scheme.

Supported by the **EKÖP-24-3-BME-194** University Research Scholarship Program of the Ministry for Culture and Innovation from the source of the National Research, Development, and Innovation Fund.

REFERENCES

[1] Jones, W. P., and Launder, B. E., 1972, "The prediction of laminarization with a two-equation model of turbulence", *International journal of heat and mass transfer*, Vol. 15 (2), pp. 301–314.

[2] Chou, P.-Y., 1945, "On velocity correlations and the solutions of the equations of turbulent fluctuation", *Quarterly of applied mathematics*, Vol. 3 (1), pp. 38–54.

[3] Menter, F. R., 1994, "Two-equation eddy-viscosity turbulence models for engineering applications", *AIAA journal*, Vol. 32 (8), pp. 1598–1605.

[4] Shih, T.-H., Liou, W. W., Shabbir, A., Yang, Z., and Zhu, J., 1995, "A new k-ε eddy viscosity model for high reynolds number turbulent flows", *Computers and fluids*, Vol. 24 (3), pp. 227–238.

[5] Ansys Fluent Documentation, "Realizable k-ε Model", URL `https://www.afs.enea.it/project/neptunius/docs/fluent/html/th/node60.htm`.

[6] Johns Hopkins Turbulence Database, "Channel Flow Simulation Data", URL `https://turbulence.pha.jhu.edu/Channel_Flow.aspx`.

[7] Driver, D. M., and Seegmiller, H. L., 1985, "Features of a reattaching turbulent shear layer in divergent channel flow", *AIAA journal*, Vol. 23 (2), pp. 163–171.

Conference on Modelling Fluid Flow (CMFF'25)
The 19th International Conference on Fluid Flow Technologies
Budapest, Hungary, August 26 - August 29, 2025

INVESTIGATION OF LAMINAR STEADY AND UNSTEADY FLOWS IN GYROID TPMS STRUCTURES

Kasimhussen Vhora[1,2,3], Dominique Thévenin[3], Kai Sundmacher[2], Gábor Janiga[3]

[1] Corresponding Author. Laboratory of Fluid Dynamics and Technical Flows, Otto von Guericke University, Universitätspl. 2, 39106 Magdeburg, Germany. Tel.: +49 391 67-52324, E-mail: vhora@mpi-magdeburg.mpg.de
[2] Process Systems Engineering, Max Planck Institute for Dynamics of Complex Technical Systems Magdeburg, Germany. E-mail: sundmacher@mpi-magdeburg.mpg.de
[3] Laboratory of Fluid Dynamics and Technical Flows, Otto von Guericke University Magdeburg, Germany. E-mail: thevenin@ovgu.de; janiga@ovgu.de

ABSTRACT

This study presents an extensive computational fluid dynamics (CFD) investigation of the airflow behavior within Gyroid Triply Periodic Minimal Surface (TPMS) structures, focusing on both laminar steady and unsteady flow conditions. Using representative elementary volume (REV)-scale simulations, the pressure drop characteristics across these porous structures are examined. Three porosity levels of 50%, 60%, and 70% are analyzed to understand the effect of porosity on flow behavior and pressure drop. The results demonstrate that increased porosity significantly influences the hydraulic Reynolds number. For the 50% porosity structure, steady laminar flow is maintained at hydraulic Reynolds numbers up to 70, while the 70% porosity structure allows steady laminar flow at Reynolds numbers as high as 210. Additionally, flow fluctuation intensity within the Gyroid structure is quantified by measuring velocity fluctuations in the flow direction. These findings offer critical insights into the design and optimization of Gyroid TPMS structures for engineering applications.

Keywords: Gyroid, REV scale, Pressure drop, Laminar flows

NOMENCLATURE

ΔP	[Pa]	pressure drop
D_h	[m]	hydraulic diameter
ϕ	[-]	porosity
V	[m^3]	total volume
A	[m^2]	wetted surface area
ρ	[kg/m^3]	fluid density
u_s	[m/s]	superficial velocity
μ	[$Pa \cdot s$]	dynamic viscosity
$\mathrm{Re_h}$	[-]	hydraulic Reynolds number
I	[-]	flow fluctuation intensity
u'_{rms}	[m/s]	root-mean-square of fluctuations
$\bar{u}$	[m/s]	mean velocity

1. INTRODUCTION

Triply Periodic Minimal Surface (TPMS) structures, particularly the gyroid structure, are mathematically-defined surfaces that exhibit three-dimensional periodicity while maintaining zero mean curvature. Triple periodicity in a gyroid TPMS structure refers to its repeating pattern in three independent spatial directions, meaning it extends infinitely and uniformly along the x, y, and z axes. This creates a continuous, interconnected, and periodic minimal surface without boundaries or edges. A key advantage of gyroid structures is their high surface-area-to-volume ratio, making them highly suitable for applications such as heat exchangers [1], catalysis [2], and membrane reactors [3], where efficient mass and heat transfer are essential. Understanding the flow characteristics within gyroid structures is crucial for optimizing their performance in various engineering applications, as flow characteristics directly influence pressure drop, transport phenomena, and overall system efficiency. In applications such as fluid mixing, filtration, and energy conversion, precise knowledge of the flow dynamics enables better design and operational control, ensuring enhanced performance and durability. For instance, in energy conversion systems, gyroid structures are increasingly explored for their role in fuel cells and batteries [4] where their topology enhances reactant distribution, improves electrochemical performance, and facilitates effective heat dissipation. This study presents an investigation of laminar airflow behavior within a gyroid structure, providing insights into its hydrodynamic characteristics and potential engineering applications.

In our prior research, we conducted a computational fluid dynamics (CFD) study to

examine the air flow dynamics within Schwarz-D triply periodic minimal surface (TPMS) structures. The investigation primarily focused on evaluating pressure drop characteristics at both the full-scale and representative elementary volume (REV) scale. The findings revealed a good correlation between the simulated pressure drops and experimental measurements. Furthermore, the REV-scale simulations exhibited close agreement with both experimental data from the literature and full-scale CFD predictions, demonstrating their reliability in capturing fluid dynamic behavior within TPMS structures [5], [6].

Building on these findings, the present study extends the investigation of airflow within a Gyroid TPMS structure, utilizing only REV scale simulations. Through single-phase CFD simulations under both laminar steady and unsteady flow conditions, this work aims to predict pressure drop and analyze the influence of porosity on fluid flow characteristics. Unlike prior study, for laminar unsteady simulations, flow fluctuation intensity is calculated within the Gyroid structure's flow domain by measuring air velocity fluctuations in main flow direction at ten probes placed at different locations in the domain. These analyses provide a deeper understanding of airflow behavior in Gyroid TPMS structures, offering valuable insights into their fluid dynamic performance under varying flow conditions. This paper aims to explore the significance of gyroid structures and their potential in optimizing performance in the field of chemical engineering.

2. METHODOLOGY

The flow characteristics within Gyroid TPMS structures were analyzed using CFD simulations. The Gyroid TPMS structures were generated in Autodesk Fusion 360 and exported as STL files, which were then imported into STAR-CCM+ for CFD analysis. Three distinct Gyroid TPMS structures with porosities of 50%, 60%, and 70% were selected for investigation, allowing for a systematic study of how increasing porosity affects the flow characteristics such as pressure drop, velocity distribution, and flow fluctuations. To ensure geometric consistency and isolate the effect of porosity, the unit cell size (UCZ) was kept at a constant value of 3 mm across all cases.

The CFD simulations were conducted using air as the working fluid under both steady and unsteady laminar flow conditions to capture air flow behavior relevant to low-Reynolds number regimes. The simulations were performed at the REV scale, utilizing a computational domain composed of two repeating unit cells. Periodic boundary conditions were applied on the 4 sides to emulate an infinitely repeating Gyroid structure. This CFD simulation approach significantly reduces computational cost and resource requirements compared to full-scale CFD simulations, while still capturing the essential transport phenomena within the porous structure. By focusing on the REV scale, the analysis remains physically representative and computationally efficient, making it particularly suitable for parametric studies of flow behavior in complex geometries such as Gyroid TPMS structures.

First, the Reynolds number threshold beyond which a steady laminar flow model is no longer applicable was identified. Then, laminar unsteady CFD simulations were conducted to evaluate the unsteady flow within the flow domain. To confirm the onset of transition, flow fluctuation intensity was computed based on velocity fluctuations along the flow direction. This analysis was carried out using 10 probes placed at different locations within the flow domain to capture localized variations and assess early-stage flow fluctuation intensity.

2.1. CFD Simulation Setup

The REV-scale simulation setup for single-phase flow through the Gyroid TPMS structure with 50% porosity and a UCZ of 3 mm is depicted in Figure 1. The computational domain was created as a rectangular box, with a length six times the UCZ and a width equal to the UCZ, as shown in Figure 1. To define the flow region for the CFD simulation, the Gyroid structure was subtracted from the rectangular domain.

As illustrated in Figure 1, periodic boundary conditions were applied on all four lateral walls in the REV setup, while velocity inlet and pressure outlet boundary conditions were assigned at the inlet and outlet, respectively. The simulations were conducted using air with a constant density, flowing through the Gyroid TPMS structure under both steady and unsteady laminar conditions. A laminar, segregated flow model was employed for all CFD simulations.

To assess the pressure drop after the CFD simulation, two plane surfaces, P1 and P2, were positioned 3 mm apart, as shown in Figure 1. For steady laminar flow, the pressure drop ($\Delta P = P1 - P2$) was obtained by computing surface-averaged pressure reports at these planes during post-processing. For unsteady laminar flow, the pressure drop was measured as the temporal evolution of the space- and time-averaged pressure drop at the same plane surfaces, P1 and P2. This simulation framework was implemented for all cases with 50%, 60%, and 70% porosity.

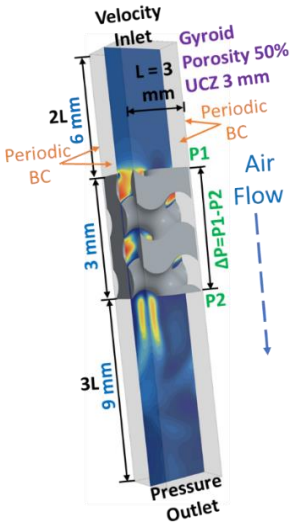

Figure 1. CFD setup for Representative Elementary Volume (REV) scale simulation.

2.2. Meshing

As depicted in Figure 2, the polyhedral mesh was generated using the automated meshing tool of STAR-CCM+ after defining the flow domain. A global base mesh size of 0.36 mm was chosen to ensure adequate resolution for capturing essential flow characteristics. To accurately model boundary layer effects and resolve near-wall regions, nine prism layers were incorporated, with a total thickness equivalent to 20% of the base size. A volume growth rate of 1.2 was applied to maintain a smooth cell size transition and ensure high mesh quality across the flow domain. Furthermore, a volumetric control mesh was introduced around the Gyroid Structure, with a base size set to 10% of the global mesh size, improving the mesh resolution to accurately capture the air flow within the structure. The final mesh contained approximately 2.5 million polyhedral cells for the simulation case with 50% porosity.

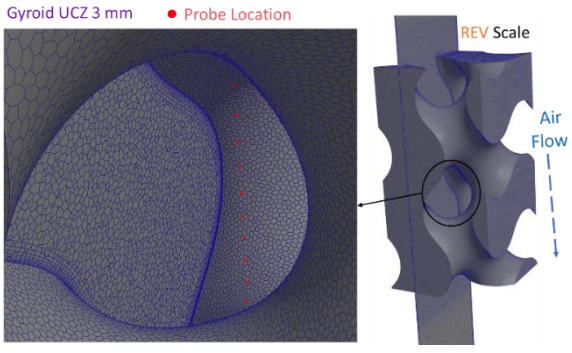

Figure 2. REV-scale polyhedral mesh with prism layers and designated probe locations for flow fluctuation intensity measurement.

As shown in Figure 2, ten probe locations were placed within the computational domain to measure velocity over time during the laminar unsteady simulations. At each probe location, the velocity component in the main flow direction (z-direction) was recorded at each time step. The velocity values at each probe location were then averaged over the simulation time to obtain a representative mean velocity for each specific location. This averaged velocity data was subsequently used to calculate the flow fluctuation intensity, which serves as a key indicator for assessing the presence of flow fluctuations within the domain. By analyzing the flow fluctuation intensity, this study was able to confirm whether the flow remained steady or exhibited unsteady behavior across the Gyroid TPMS structures.

Pre-processing, simulation, and post-processing were performed with Simcenter STAR-CCM+ (version 2302, Siemens Product Lifecycle Management Software Inc., Plano, TX, USA). The numerical simulations were run on a parallel computing system at the Max Planck Research Institute in Magdeburg, which featured 11th Gen. Intel Core i7-11700 processors operating at 2.50 GHz, each equipped with 64 GB of RAM.

2.3. Flow Properties

The hydraulic diameter is a generalized measure of length scale, independent of specific geometric details. It is calculated from the total surface area and the porosity of the structure.

$$D_h = \frac{4\phi V}{A}$$

where D_h is the hydraulic diameter, ϕ is the porosity, V is the total volume and A is the wetted surface area. The Reynolds number ($\mathrm{Re_h}$) is defined using the hydraulic diameter D_h as:

$$\mathrm{Re_h} = \frac{\rho u_s D_h}{\mu \phi},$$

where $\mathrm{Re_h}$ is the Reynolds number based on hydraulic diameter, ρ is the fluid density, u_s is the superficial velocity and μ is the dynamic viscosity.

Flow fluctuation intensity is one of the most straightforward and widely used methods for quantifying the magnitude of temporal velocity variations relative to the mean flow velocity in fluid dynamics. It serves as a non-dimensional indicator that reflects the degree of unsteadiness or turbulence in the flow field. In the context of laminar unsteady simulations, where the flow may exhibit periodic or aperiodic fluctuations even in the absence of turbulence, flow fluctuation intensity provides a clear and quantifiable measure of how much the instantaneous velocity deviates from its time-averaged value. This metric is particularly useful in

characterizing transitional or turbulent behaviors that are not captured by steady-state simulations.

Mathematically, the flow fluctuation intensity is computed by taking the root mean square of the fluctuating component of the velocity defined as the difference between the instantaneous velocity and the mean velocity and dividing it by the mean velocity itself, typically expressed as:

$$I = \frac{u'_{rms}}{\bar{u}}, \qquad u'_{rms} = \sqrt{\frac{1}{N}\sum_{i=1}^{N}(u'_i)^2}$$

where u'_{rms} is the root-mean-square of the fluctuations and $\bar{u}$ is the mean velocity.

3. RESULT AND DISCUSSION

In the CFD simulation of airflow through Gyroid TPMS structures, the behavior of the flow was initially evaluated using a laminar steady-state model. For the structure with 50% porosity, the simulations demonstrated good convergence characteristics, with continuity residuals falling below the threshold of 10^{-6} for hydraulic Reynolds numbers up to 70. However, when the hydraulic Reynolds number exceeded this limit, the steady-state model failed to converge, and oscillatory residual patterns began to emerge, indicating the breakdown of the steady flow assumption and the onset of unsteady flow behavior. This transition suggests that beyond the hydraulic Reynolds number of 70, the flow becomes time-dependent, necessitating the use of a laminar unsteady model to accurately resolve the evolving flow field.

Similarly, for the Gyroid structure with 60% porosity, the laminar steady model remained effective and well-converged, maintaining residuals below 10^{-6} up to a hydraulic Reynolds number of approximately 120. A comparable trend was observed for the 70% porosity Gyroid structure, where steady-state simulations remained stable and continuity residual converged below 10^{-6} up to the hydraulic Reynolds number of 210. Beyond these limits, oscillatory residuals emerge, signifying the transition to unsteady flow.

To appropriately capture the unsteady characteristics of the flow in these regimes, laminar unsteady simulations were carried out. Specifically, for the 50% porosity structure, unsteady simulations were performed for hydraulic Reynolds numbers ranging from 80 to 100. For the 60% and 70% porosity structures, the unsteady simulations covered hydraulic Reynolds number ranges of 130 to 150 and 220 to 240, respectively. These simulations enabled the resolution of transient flow phenomena that could not be captured under steady assumptions. Furthermore, the presence of unsteady airflow was validated through the quantification of flow fluctuation intensity, confirming the necessity of time-dependent model to accurately characterize the fluid dynamics within the TPMS structures at relatively high hydraulic Reynolds numbers.

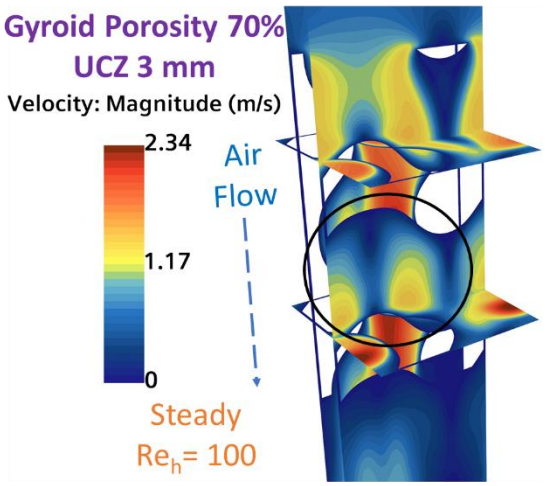

Figure 3(a). Velocity profile for steady laminar CFD simulations at Re_h =100.

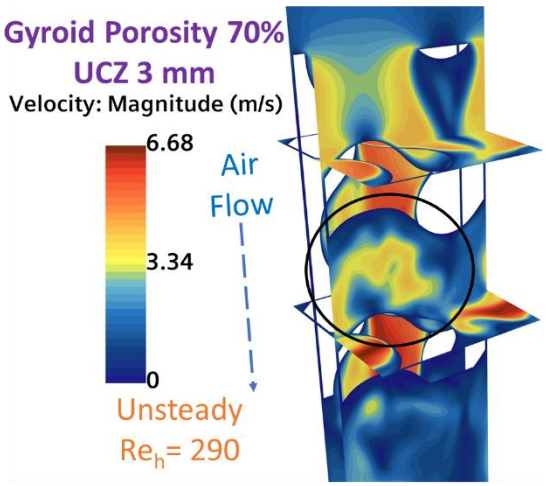

Figure 3(b). Velocity profile for unsteady laminar CFD simulations at Re_h = 290.

Figure 3 presents a comparative analysis of the velocity magnitude within a gyroid triply periodic minimal surface structure at different hydraulic Reynolds numbers: 100 (steady flow) and 290 (unsteady flow). At the lower hydraulic Reynolds number (top) the flow exhibits a quite uniform velocity profile throughout the structure, with relatively low maximum velocities. In contrast, at the higher hydraulic Reynolds number (bottom), the flow becomes fluctuating. Notably, within the black circled region, representing a specific section of the gyroid unit cell, the velocity magnitude increases substantially under unsteady flow conditions. This suggests the onset of inertial effects and potentially

localized flow acceleration within the Gyroid geometry as the Reynolds number rises, leading to a more dynamic airflow behavior compared to the lower Reynolds number.

Figure 4 shows the variation in pressure drop as a function of the hydraulic Reynolds number (Re_h) for a gyroid structure at different porosities (ϕ), considering either steady or unsteady laminar flow conditions. The results indicate a clear dependence of pressure drop on both porosity and hydraulic Reynolds number. At a given Re_h, a decrease in porosity leads to a significant increase in pressure drop due to the reduced flow passage and enhanced flow resistance. As a consequence, the structure with ϕ=50% exhibits the highest pressure drop, followed by ϕ=60% and ϕ=70%, in both steady and unsteady flow cases. Moreover, as Re_h increases, the pressure drop rises non-linearly due to the increasing inertial effects, which intensify the flow resistance through the porous Gyroid structure.

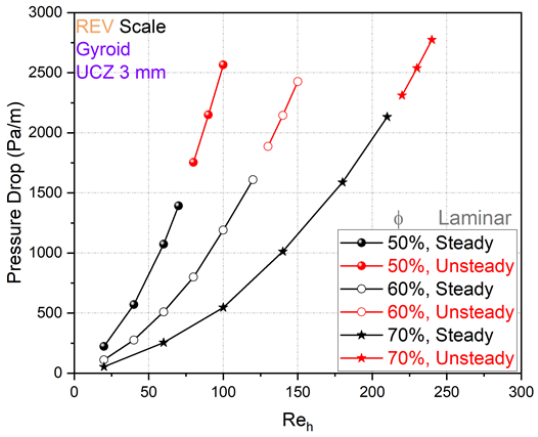

Figure 4. Pressure drop comparisons in gyroid structures (50–70% porosity) for steady or unsteady laminar CFD simulations.

The onset of unsteadiness occurs at progressively lower Re_h as porosity decreases, indicating a stronger influence of structural confinement on flow stability. These findings emphasize the critical role of porosity in controlling pressure drop characteristics and the transition between steady and unsteady laminar airflows in porous Gyroid structures.

Figure 5 presents the variation in flow fluctuation intensity (%) with the hydraulic Reynolds number for structures with different porosities (50%, 60%, and 70%). The results indicate that flow fluctuation intensity generally increases with increasing Reynolds number, marking the transition from laminar steady flow to unsteady flow. At lower Re_h, the intensity remains minimal, suggesting a stable laminar flow. However, as Re_h increases, a significant rise in flow fluctuation intensity is observed, indicating the onset of transitional flow.

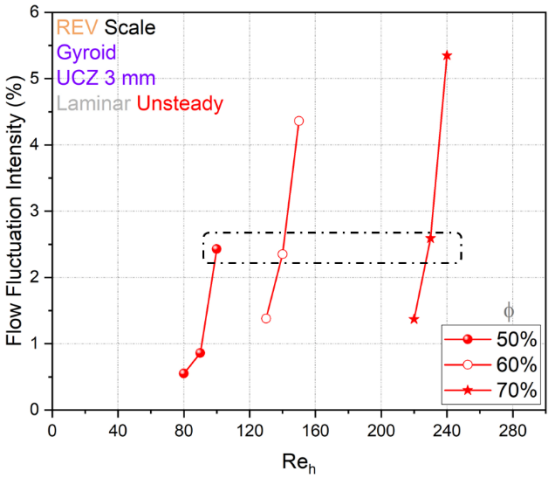

Figure 5. Flow fluctuation intensity vs. hydraulic Reynolds number for various structural porosities, with a rectangular dotted line indicating nearly identical values across different Reynolds numbers.

For instance, in the 50% porosity case, the flow fluctuation intensity is 0.5% at a hydraulic Reynolds number of 80, whereas at 100, it increases sharply to 2.5%. This steep rise in flow fluctuation intensity within the Re_h range of 80–100 clearly signifies the transition from a steady to an unsteady airflow state. Additionally, porosity plays a crucial role in shaping flow fluctuation characteristics. A higher porosity (70%) leads to a greater increase in flow fluctuation intensity within a hydraulic Reynolds number increment of just 20, compared to lower porosities (50% and 60%). This is because a more open structure enhances flow interactions and promotes flow instability.

The dotted-line rectangular box in the figure highlights an interesting phenomenon where different Reynolds numbers exhibit nearly identical flow fluctuation intensity values. This suggests that variations in porosity can shift the transition points between laminar and unsteady flow. Such findings imply that porosity modifications can be strategically employed to control the flow regime based on different engineering application requirements. Thus, by optimizing porosity and unit cell size, this structure could be specifically tailored for target applications, such as filtration, heat exchangers, and chemical reactors, where a precise control over the flow regime is essential.

4. CONCLUSIONS

This study conducted a comprehensive CFD analysis of fluid flow through Gyroid TPMS structures under laminar steady and unsteady flow conditions, focusing on pressure drop and flow fluctuation intensity in REV scale configurations. The results demonstrate that while the laminar steady model provides accurate predictions of pressure drop for Reynolds numbers up to approximately 70 in the 50% porosity case, this threshold extends to 210 for

the 70% porosity case, highlighting the influence of structural porosity on flow resistance.

The evaluation of flow fluctuation intensity under laminar unsteady conditions reveals a similar increase with hydraulic Reynolds number, indicating the transition from laminar steady to unsteady flow. For the 50% porosity case, a sharp rise in flow fluctuation intensity within the range of Re_h=80–100 marks the onset of flow instability. These findings provide valuable insights for the design and optimization of TPMS-based porous structures in engineering applications where pressure drop, permeability, and flow stability must be carefully balanced. The study underscores the importance of porosity selection in tailoring flow characteristics, contributing to improved performance and efficiency in industrial and scientific applications involving porous media.

ACKNOWLEDGEMENTS

This research is supported by the European Regional Development Fund (ERDF) and the International Max Planck Research School for Advanced Methods in Process and Systems Engineering (IMPRS ProEng), Magdeburg, Germany.

REFERENCES

[1] M. Beer and R. Rybár, “Optimisation of Heat Exchanger Performance Using Modified Gyroid-Based TPMS Structures,” Processes, vol. 12, no. 12, 2024.

[2] C.-F. Cheng et al., “Nanoporous gyroid platinum with high catalytic activity from block copolymer templates via electroless plating,” NPG Asia Materials, vol. 7, no. 4, pp. e170–e170, 2015.

[3] L. Li, L. Schulte, L. D. Clausen, K. M. Hansen, G. E. Jonsson, and S. Ndoni, “Gyroid Nanoporous Membranes with Tunable Permeability,” ACS Nano, vol. 5, no. 10, pp. 7754–7766, 2011.

[4] S. Choudhury et al., “Nanoporous Cathodes for High-Energy Li–S Batteries from Gyroid Block Copolymer Templates,” ACS Nano, vol. 9, no. 6, pp. 6147–6157, 2015.

[5] K. Vhora, T. Neeraj, D. Thévenin, G. Janiga, and K. Sundmacher, “Investigating Fluid Flow Dynamics in Triply Periodic Minimal Surfaces (TPMS) Structures Using CFD Simulation,” Computer Aided Chemical Engineering, vol. 53, 2024, pp. 709–714, 2024.

[6] K. Vhora, D. Thévenin, G. Janiga, and K. Sundmacher, “CFD Analysis of the Flow in Schwarz-D TPMS Structures for Engineering Applications,” Chemie Ingenieur Technik, vol. 96, no. 12, pp. 1683–1696, 2024.

Conference on Modelling Fluid Flow (CMFF'25)
The 19th International Conference on Fluid Flow Technologies
Budapest, Hungary, August 26 - August 29, 2025

DETAILED CHARACTERISATION OF PORE STRUCTURE AND TRANSPORT PROPERTIES OF BIOMASS PARTICLES DURING PYROLYSIS

N. Zhan[1,3], E. Liu[1], A. Dernbecher[2], N. Vorhauer-Huget[1], R. Wu[3], A. Dieguez-Alonso[2], A. Kharaghani[1*]

[1]Chair of Thermal Process Engineering, University Magdeburg, Universitätsplatz 2, 39106 Magdeburg, Germany. E-Mail: reza.kharaghani@ovgu.de
[2]Laboratory of Transport Processes, Faculty Biochemical and Chemical Engineering, TU Dortmund University, Emil-Figge-Str. 68, 44227 Dortmund, Germany
[3]School of Mechanical Engineering, Shanghai Jiao Tong University, Shanghai 200240, China

ABSTRACT

This study presents an advanced investigation into the dynamic evolution of pore structures in woody biomass during pyrolysis, focusing on the critical roles of structural heterogeneity and anisotropy. Building on earlier work that used X-ray micro-computed tomography (μ-CT) to analyse beech wood particles pyrolysed at various temperatures, we extended the analysis to track how structure and transport properties evolve throughout the pyrolysis process. Using the μ-CT images, we developed an equivalent pore network model (PNM) to simulate changes in permeability and gas flow behaviour over time. By segmenting the biomass into representative elementary volumes (REVs), the model accurately captured localised variations in porosity and permeability across the entire particle. Simulation results show that as the pyrolysis temperature increases, the anisotropic transport properties first decrease and then rise sharply, primarily due to directional pore expansion and the evolution of connectivity patterns. This integrated modelling framework offers deeper insights into structure-property relationships during biomass pyrolysis and supports the design and optimisation of gas transport processes in thermochemically evolving, thermally-thick porous particles.

Keywords: Anisotropic pores, biomass, heterogeneous pore structure, pyrolysis, pore morphology evolution, pore network modelling

NOMENCLATURE

φ	[°]	azimuth angle
θ	[°]	elevation angle
K	[m^2]	local permeability
ε	[-]	local porosity
r	[m]	radial distance
L_r	[-]	radial layer

Abbreviations

PNM	pore network model
OED	Omnidirectional Euclidean Distance
REV	representative elementary volume
μ-CT	X-ray micro-computed tomography

1. INTRODUCTION

Biomass pyrolysis, a promising thermochemical conversion process, has gained considerable attention for its potential to produce renewable fuels, valuable chemicals, and biochar [1]. Among the various biomass resources, woody biomass is particularly favoured due to its abundant availability, carbon-neutral profile, and relatively high energy density [2]. However, predicting pyrolysis behaviour remains challenging due to structural heterogeneity and anisotropy inherent in woody biomass. These complexities are further compounded in thermally-thick particles, where internal temperature and transport gradients significantly influence conversion pathways.

During pyrolysis, complex physicochemical transformations drive the decomposition of biomass components and the concurrent evolution of a porous structure within the particle. These transformations critically affect heat and mass transfer processes. Conventional models often oversimplify biomass as a homogeneous porous medium, neglecting the anisotropic nature of wood and the dynamic evolution of its pore network [3]. Consequently, there is a growing demand for advanced modelling frameworks that can capture the large-scale, heterogeneous, and dynamic characteristics of biomass pyrolysis.

Pore network modelling (PNM) has emerged as an effective tool to simulate transport phenomena in

complex pore structures [4,5]. In PNM, the biomass structure is abstracted into a discrete network of pores (nodes) and throats (bonds), where large voids are considered pore bodies, and the narrow connections between them are throats. Accurate construction of such networks requires high-fidelity imaging data. Advances in X-ray micro-computed tomography (μ-CT) have enabled the acquisition of high-resolution 3D images of biomass at various stages of pyrolysis, providing the structural basis for extracting realistic pore networks [6,7]. These images allow detailed characterisation of pore morphology, connectivity, and their evolution under thermal stresses.

In pyrolysing woody biomass, structural anisotropy significantly influences transport properties. However, extracting anisotropic pore structures with high fidelity remains a key challenge. To address this, we previously developed the Omnidirectional Euclidean Distance-based (OED-based) method, a pore-network extraction algorithm developed to accurately capture elongated and directionally aligned pores [8,9]. Incorporating such anisotropy into PNMs significantly improves the predictive capability of the model, especially when validated against experimental μ-CT data.

A critical aspect of pyrolysis is the dynamic evolution of pore connectivity, which governs intra-particle gas flow and the release of volatile compounds. As temperature increases, pores expand, elongate, or collapse, leading to significant changes in local permeability. These morphological changes often occur preferentially along specific directions, giving rise to anisotropic transport behaviour. This directional permeability is especially relevant in thermally-thick particles, where heterogenous temperature profiles and reaction rates drive localised structural changes. However, accurately modelling these effects is challenging due to the interplay between pore network dynamics and reactive gas flow. One major challenge in modelling biomass pyrolysis is accounting for the anisotropic transport properties resulting from the irregular and evolving pore network. Anisotropy in biomass is inherently linked to its hierarchical structure, where different wood components (e.g., vessels, fibres, and rays) contribute differently to permeability and thermal conductivity [10]. During pyrolysis, the decomposition of these components further modifies the pore network, leading to dynamic changes in anisotropic behaviour.

In addition to anisotropy, biomass heterogeneity further complicates pyrolysis modelling. Variability in pore size, orientation, and connectivity introduces localised differences in gas permeability and thermal diffusivity [11]. This is particularly evident in the outer layers of particles, which experience more rapid thermal and structural evolution. The resulting pressure gradients and flow pathways can significantly affect char yield and volatile escape.

Despite recent advances in PNM-based modelling, limitations remain in capturing the full temporal evolution of pore networks during pyrolysis. Since the decomposition of biomass components occurs at varying rates and temperatures, it is essential to update of the pore network dynamically to reflect ongoing structural changes. Additionally, accurately modelling the feedback between evolving structure and transport properties, particularly pressure-driven gas flow, requires a meticulous integration of experimental data with simulation frameworks.

This study aims to bridge the gap between pore-scale dynamics and macro-scale pyrolysis modelling by constructing deformable pore network models based on high-resolution μ-CT images of woody biomass. Focusing on thermally-thick particles, the model incorporates both anisotropic and heterogeneous features to capture the evolution of transport-relevant properties during pyrolysis. By segmenting particles into representative elementary volumes (REVs), we quantify local variations in porosity and permeability and explore how structural evolution governs gas transport characteristics. Ultimately, this work provides a comprehensive framework for understanding the structure-property-performance relationships in biomass pyrolysis and contributes to optimisation of thermal conversion technologies.

2. METHODS

2.1. Experiments and Characterisation

Beech wood spheres (10 mm diameter) were pyrolysed in a tubular reactor under a nitrogen (N_2) atmosphere (Fig. 1a). Preheated N_2 passed through an inert porous bed before contacting the particles. The heating rate was 10 °C/min, with final temperatures between 100 °C and 500 °C, held for about 30 minutes. Three spheres were pyrolysed simultaneously in a small basket hung from a scale for mass monitoring. Due to the small size of the particles relative to the reactor, heating conditions were considered uniform. One particle was drilled for internal temperature measurement, a second was used for μ-CT imaging, and the third for physic-chemical analysis. μ-CT imaging was performed on the same particle at different pyrolysis stages. After each treatment, the particle was cooled, analysed and reheated to the next temperature. Figure 1b presents photographs of wood particles at different pyrolysis stages. We selected four representative stages, corresponding to samples treated at 100°C, 300°C, 400°C, and 500°C, which are denoted as WP100, WP300, WP400, and WP500, respectively. Note that the sample treated at 200°C was excluded from this analysis, as its characteristics were observed to be largely similar to those of the 100°C sample.

The structural characterisation of wood and char samples treated at different temperatures was

performed using X-ray microcomputed tomography (μ-CT) with a Proton CT alpha system (Proton X-ray GmbH, Germany). The scans were conducted at 100 kV, 30 mA, and 2000 ms exposure time, with 1200 projections (3 radiographs per projection) and a voxel size of 5.9 μm. The sample-to-detector distance was 630 mm, allowing for a resolution sufficient to detect pores larger than 15 μm, thereby capturing only macropores. Similar resolution limits for μ-CT have been reported in the literature [12].

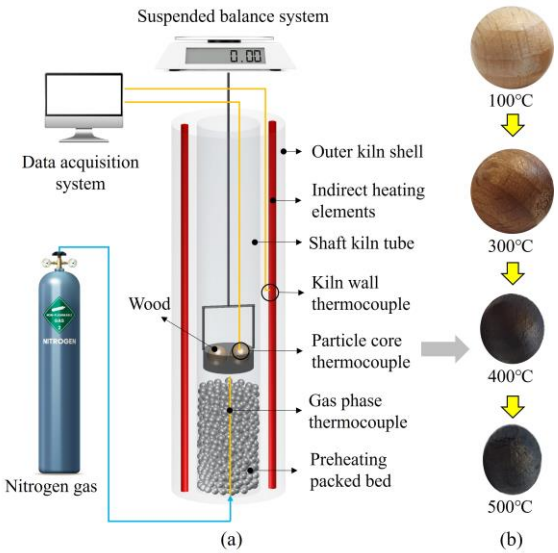

Fig. 1 Experimental setup: Tubular reactor used for pyrolysis of beech wood spheres at varying temperatures.

2.2. Pore Network Extraction

To accurately model the pore structure of beech wood particles, a PNM was constructed based on the extracted real pore geometry, capturing both the geometric and topological characteristics of the porous medium. This model not only preserves the anisotropic features of the pore structure but also accounts for the heterogeneous distribution of structural parameters and transport properties across the entire particle.

The pore network extraction was performed using the OED-based method, as described in our previous study [8,9]. The process involves identifying anchored void voxels on the boundary surfaces and calculating the OED for each void voxel to establish a hierarchical arrangement. Using the omnidirectional distance order homotopic thinning (ODOHT) algorithm, the medial axes (MAs) are extracted, and pore and throat positions are identified. The resulting pore network is represented as a graph where nodes correspond to pore and throat centres, and bonds capture the connectivity of the porous structure. To efficiently handle large-scale CT images (1936×1936×1383 voxels, see the left side of Fig. 2a), the domain was decomposed into subdomains, enabling parallel processing for network extraction. The partial MAs from each subdomain were then merged to reconstruct the complete pore network, maintaining both computational efficiency and accuracy. The extraction results of the entire wood particle are shown on the right side of Fig. 2a.

To characterise the anisotropy of the pore structure, ellipsoids were fitted to individual pores, with each pore's orientation defined by the semi-principal axes of the fitted ellipsoid. To visualise the directional distribution, the semi-major axis orientation was converted into elevation, θ_p, and azimuth, φ_p, angles (Fig. 2b). By calculating the angle between the semi-major axis and a reference direction, the frequency of orientation vectors within a 10° range was determined. This approach captures the inherent anisotropy of the wood pore structure effectively.

To evaluate heterogeneity, the entire particle was divided into multiple representative elementary volumes (REVs) based on a polar coordinate grid (Fig. 2c). For each REV, the sub pore networks were obtained and single-phase pressure field simulations were performed to calculate intrinsic permeability. The radial distribution of pressure was then calculated (Fig. 2c). This multi-scale approach ensures a comprehensive representation of both anisotropy and heterogeneity within the pore network model, facilitating the analysis of flow transport processes in porous wood structures.

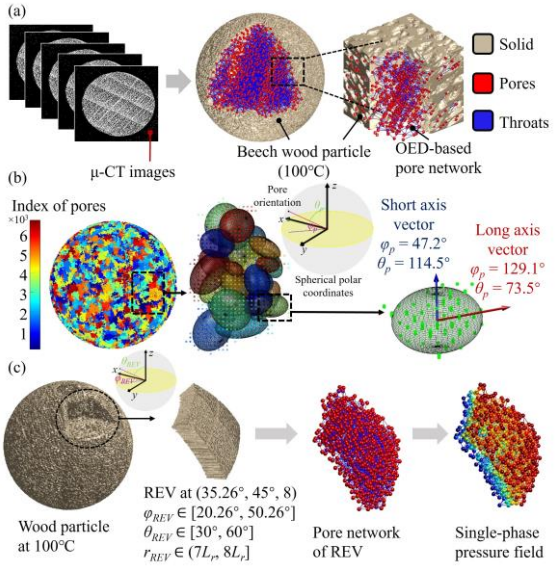

Fig. 2 (a) Large-scale pore network extraction from μ-CT images of beech wood particle. (b) Discretisation of pore bodies using point cloud data with ellipsoids fitted to represent the pore geometry. (c) The segmentation of wood particles into multiple REVs using a polar coordinate grid and the radial pressure distribution of the REV.

2.3. Pore Network Simulations

During pyrolysis, the evolution of the solid phase can be effectively represented using a

deformable pore network model. This model integrates the structural changes in the pore network as the wood particles undergo thermal decomposition. Specifically, pore bodies and throats are linked with adjacent solid elements, which gradually diminish as pyrolysis progresses, as shown in Fig. 3. As the solid elements on the pore surfaces reduce, the pore size increases until the solid elements at the surface completely vanish. At this stage, external pores and throats are removed, and new boundary pore-throat connections are identified, as illustrated in Fig. 3a. Figure 3b depicts the overall process by which the deformable pore network model captures the evolution of the solid phase.

To simulate the pyrolysis flow process, we construct deformable pore networks based on images obtained from wood particles at different temperatures during pyrolysis. It should be noted that the current deformable PNM does not incorporate the reaction kinetics of wood pyrolysis, which will be addressed in future work. In this study, the primary focus is on the structural evolution of biomass pore networks during pyrolysis, and all structural changes are derived directly from experimental CT image data. By quantifying the loss of solid mass, we calculate the gas flow rate generated during pyrolysis. This calculated flow rate is then incorporated into the deformable pore network model to simulate gas transport through the evolving porous structure. This approach enables an accurate representation of the dynamic changes occurring within the wood particle during pyrolysis, thereby enhancing the predictive accuracy of multiphase flow behaviour in the context of thermal decomposition.

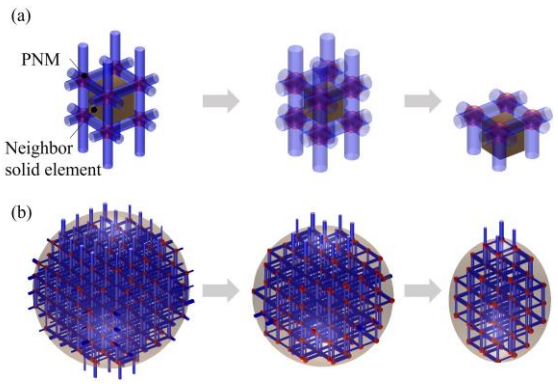

Fig. 3 Representation of the evolution of the solid phase during pyrolysis process within the framework of pore network modelling. (a) The reduction and disappearance of solid elements result in the expansion and eventual removal of neighbour pores and throats, (b) a deformable pore network captures the evolution of the pore structure throughout the pyrolysis process.

3. EVALUATION AND ANALYSIS

3.1. Structure Analysis and Anisotropy

The extraction algorithm described in Sec. 2.2 was applied to the original μ-CT images of wood particles obtained at different pyrolysis temperatures. This approach enabled the reconstruction of pore network models corresponding to each pyrolysis condition. The key structural parameters extracted from these PNMs are summarised in Table 1.

Table 1. Structural parameters of extracted PNMs of wood particles at different temperatures.

Sample	Domain (voxels × voxels × voxels)	Pore number	Throat number	porosity
WP100	(1384×1384×1384)	41803	227339	0.473
WP300	(1264×1000×1320)	30599	181296	0.456
WP400	(1040×960×1280)	21458	125892	0.545
WP500	(920×744×1080)	10362	63386	0.578

Figure 4 illustrates the evolution of wood pore structures at different pyrolysis temperatures: (a) 100°C, (b) 300°C, (c) 400°C and (d) 500°C. Each row in the figure has three parts. The first shows the OED maps of reconstructed wood structure based on image data and matches the actual structures shown in Fig. 1b. The second and third parts show the azimuth and elevation angles of the pores, based on fitted ellipsoids, as descripted in Fig. 2b.

From the first column, one can see that as the temperature rises, the amount of solid wood decreases (see also Fig. 1b). This is expected, as more material breaks down and volatile gases are released during pyrolysis. Even as the structure changes, the pores remain strongly oriented in one main direction – a clear sign of anisotropy. This effect is evident at all temperatures, especially at 500°C.

To quantitative analysis this pore structure anisotropy, we fitted ellipsoids to the pore bodies (as shown earlier in Fig. 2b). Each ellipsoid's major axis points in the direction of the largest pore dimension, helping us to define the main pore orientation. The azimuth and elevation angle distributions in the second and third columns show that pore orientations are strongly clustered rather than uniformly distributed. The clustering in the azimuthal distribution initially decreases with increasing pyrolysis temperature but then increases significantly, becoming particularly pronounced at 500°C. The elevation angle distribution also exhibits a concentrated pattern, further marking the anisotropic character of the pore network.

The alignment between the OED map and the orientation angle distributions demonstrates that the proposed ellipsoid fitting method accurately captures the anisotropic characteristics of the pore structure. This ability to quantitatively describe anisotropy isessential for understanding the relationship

between structural evolution and transport properties of the wood during pyrolysis. Since material transport properties are inherently influenced by structural orientation, the identified anisotropy directly affects gas flow and diffusion, which will be further analysed in subsequent sections.

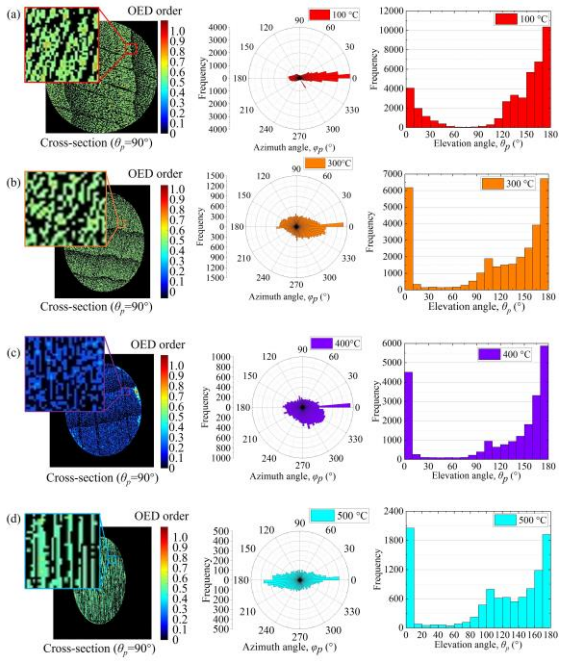

Fig. 4 Pore orientation analysis of wood particles at different temperatures: (a) 100°C, (b) 300°C, (c) 400°C, and (d) 500°C. The first column shows the sectional OED map; the second and third columns display the azimuth and elevation angle distributions of the fitted ellipsoids representing pore bodies, respectively.

3.2. Spatial Heterogeneity of Porosity and Permeability

To fully understand the structure of wood particles, two key aspects must be considered: anisotropy and heterogeneity. The previous section addressed anisotropy, highlighting the directional dependence of wood properties. In this section, the focus shifts to heterogeneity, which refers to spatial variations in material properties.

Wood is not a uniform substance. It consists of distinct components such as fibres and vessels that are unevenly distributed throughout the material. These structural differences cause complex variations at the microscopic level. Therefore, a comprehensive analysis must account for both the directional and spatial variability of wood. This section investigates how structural and transport properties vary across different regions of the particle.

To quantify heterogeneity, each wood particle is divided into representative elementary volumes (REVs) using a polar coordinate system (φ_{REV}, θ_{REV}, r_{REV}), as shown in Fig. 2c. Since the original wood particles are approximately spherical, the domain for heterogeneity analysis at all temperatures is based on the initial spherical particle region. The segmentation consists of 36 divisions in the azimuthal angle, φ_{REV}, 18 in the elevation angle, θ_{REV}, and 5 layers in radial distance, r_{REV}. As pyrolysis progresses, REVs where the solid phase disappears correspondingly increase porosity. If the remaining solid fraction in an REV becomes too low, its permeability will not be calculated. These details will be discussed further in the following sections. This framework allows for a detailed spatial analysis of heterogeneity across the entire particle.

From each REV, a sub-PNM is generated, and key local properties – such as porosity (ε_{REV}) and normalized permeability (K_{REV}) – are calculated. These are presented in Fig. 5 (ε_{REV}) and Fig. 6 (K_{REV}), which show the spatial distribution of these parameters within individual REVs in three-dimensional coordinates. The left columns of both figures show the full REV-level distributions, where part of the volume has been virtually removed to expose the internal radial layers. The right columns focus on radial layers 2 to 5, omitting layer 1 due to its irregular and non-representative patterns.

The porosity distributions under different thermal conditions reveal key insights. At 100°C, porosity remains relatively uniform throughout most of the particle, except in regions aligned with wood grain structures – dense, annular features show distinctly lower porosity values. At 300°C, highly porous zones with porosity values close to 1 begin to appear in the outermost radial layers (layers 4 and 5). These zones indicate complete pyrolysis within affected REVs, where solid matter has fully decomposed. In contrast, inner layers at this temperature retain porosity patterns similar to those observed at 100°C, though with a slight increase in average porosity.

By 400°C, the volume and continuity of fully pyrolysed regions grow substantially, forming larger and more connected high-porosity zones. At 500°C, the outer two radial layers become entirely pyrolysed, forming continuous, highly porous regions. This transformation marks a significant structural collapse, with a notable reduction in the overall particle volume due to extensive thermal degradation.

Permeability distributions were also analysed and are presented in Figs. 7 and 8. The values shown represent normalised permeability, defined as the single-phase intrinsic permeability of each REV normalised by the maximum permeability among all REVs. To ensure consistency and meaningful interpretation, REVs with porosity greater than 0.9 were excluded from the analysis, as these REVs are considered fully pyrolysed and no longer possess a well-defined porous structure that contributes to flow resistance.

Overall, regions with higher porosity tend to exhibit higher normalized permeability.

Additionally, permeability values are notably higher near both ends of the z-axis. This observation indicates that permeability is influenced not only by porosity but also by the directional organisation of the pore structure. The spatial distribution reflects the combined effects of porosity and anisotropy on fluid transport within the material.

These findings suggest that transport properties in pyrolysed wood particles are controlled by both the extent of thermal decomposition and the orientation of the internal pore structure. Quantitative retails of porosity and permeability distributions are provided in Fig. 7 and 8 for reference.

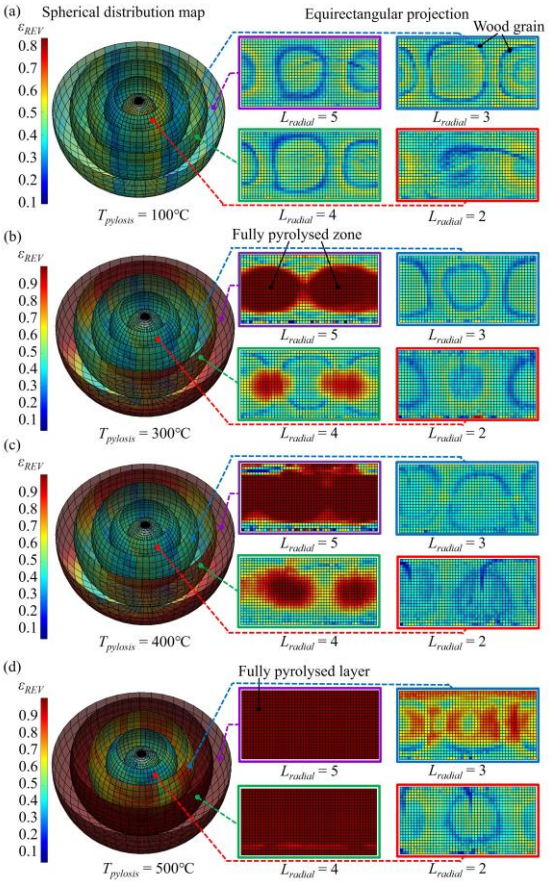

Fig. 5 Porosity distribution of wood particles at different temperatures: (a) 100°C, (b) 300°C, (c) 400°C and (d) 500°C.

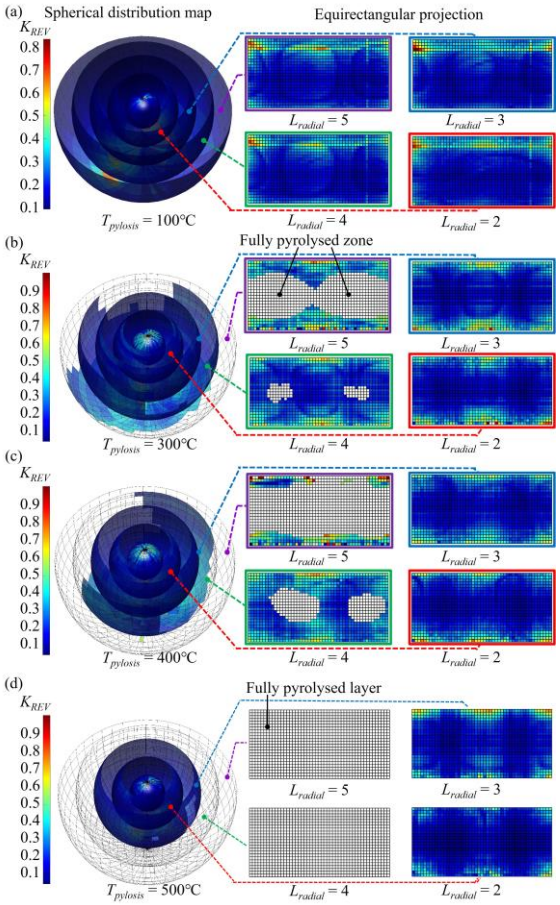

Fig. 6 Normalised permeability distribution of wood particles at different temperatures: (a) 100°C, (b) 300°C, (c) 400°C and (d) 500°C.

Figures 7 and 8 expand on this by showing the angular distributions of porosity and normalised permeability as a function of azimuth and elevation angles. Each curve represents the average value across all REVs within each angular segment, offering a directional perspective on the data. The porosity distribution shows lower values along the wood grain and near-complete voids in fully pyrolysed regions, consistent with earlier spatial observations. In contrast, the normalised permeability distribution exhibits a more complex, multimodal pattern, shaped by both porosity and the anisotropic organisation of the pore network.

These angular trends further underscore the strong directional dependence of transport behaviour in thermally decomposed wood.

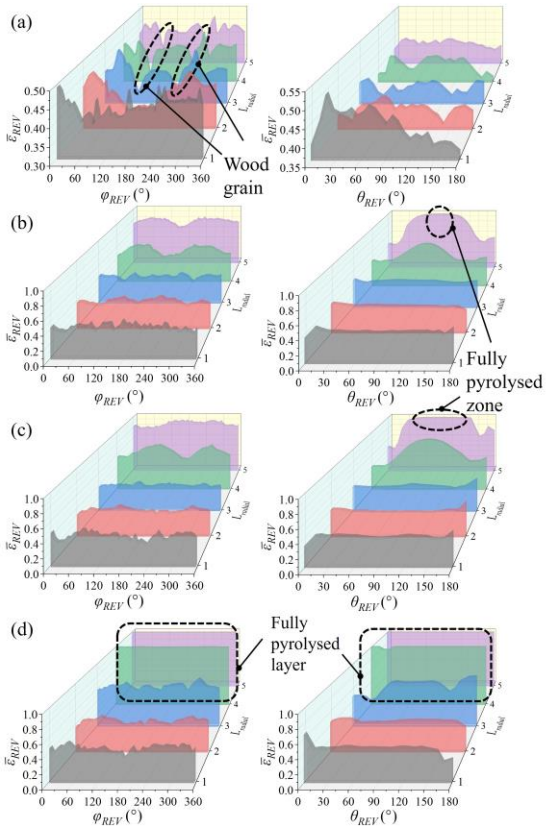

Fig. 7 Porosity distribution in φ_{REV} and θ_{REV} directions of wood particles at different temperatures: (a) 100°C, (b) 300°C, (c) 400°C and (d) 500°C.

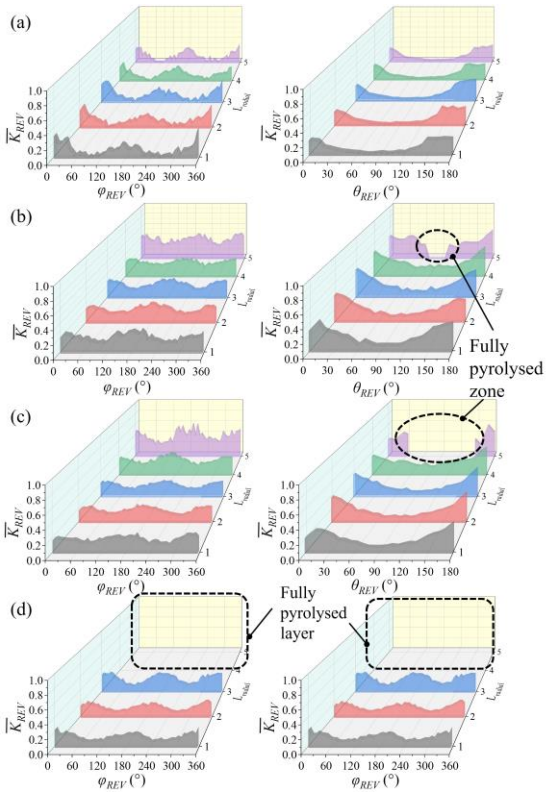

Fig. 8 Permeability distribution in φ_{REV} and θ_{REV} directions of wood particles at different temperatures: (a) 100°C, (b) 300°C, (c) 400°C and (d) 500°C.

3.3. Spatially Resolved Pressure Fields and Transport Behaviour during Pyrolysis

As pyrolysis progresses, the solid phase within the wood particles decomposes, resulting in gradual pore expansion. In the outermost regions, pores grow until they disappear and are replaced by newly formed pores further inward (Fig. 3a). This dynamic is modelled by converting solid mass loss into gas generation, followed by transport simulation throughout the pyrolysis process.

Figure 9 presents the simulated pressure fields at 100 ° C, 300 ° C, 400 ° C, and 500 ° C. Pressure propagates more efficiently along the x-direction than the y-direction, indicating strong anisotropy. This directional behaviour corresponds to the pore orientation (Fig. 4) and permeability distributions (Fig. 6). Areas with larger, better-aligned pores exhibit lower flow resistance and faster pressure transmission.

These findings are consistent with earlier studies on anisotropic porous media undergoing thermal decomposition, where directional pore growth and preferential gas flow were also observed. Our results further emphasize the need to accurately capture evolving pore structure in order to model transport processes in reactive porous materials.

In future work, we will compare REV-based simulation results with those obtained from homogenized models and full-scale pore network modelling. This comparison will include not only pressure distribution but also other key transport metrics, providing a more comprehensive evaluation of model performance and predictive capability.

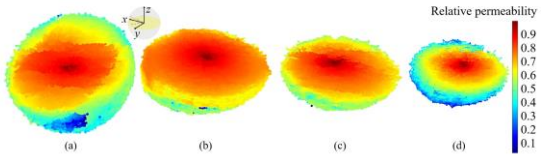

Fig. 9 Simulated pressure fields in the PNM model of wood particles at different pyrolysis temperatures: (a) 100°C, (b) 300°C, (c) 400°C, and (d) 500°C. The pressure distribution demonstrates increasing anisotropy with temperature, consistent with the evolving pore structure and permeability.

4. SUMMARY

Biomass pyrolysis is a critical thermochemical process for converting renewable feedstocks into fuels, chemicals, and biochar. Among biomass resources, woody biomass offers significant advantages due to its availability and carbon-neutral profile. However, accurately predicting pyrolysis behaviour remains challenging because of the

complex, evolving pore structures within the biomass during thermal decomposition.

This study investigates the structural and transport property evolution in beech wood particles under pyrolysis using PNM derived from high-resolution μ-CT images. The extracted networks at different temperatures capture key features such as pore growth, anisotropic expansion, and regional variation in porosity and permeability. Quantitative structural analysis based on fitted ellipsoids reveals that the pore orientation becomes increasingly anisotropic as temperature rises, especially at 500°C. The azimuthal and elevation angle distributions confirm strong directional clustering, indicating a consistent alignment of pores along preferred axes.

To assess spatial heterogeneity, each wood particle was segmented into representative elementary volumes (REVs) in a polar coordinate system. This allows for local evaluation of porosity and permeability. The results demonstrate clear radial and angular heterogeneity. Outer layers undergo full pyrolysis at higher temperatures, resulting in porosity values close to 1 and structural collapse. In contrast, inner layers retain partial solid structure. Permeability distributions are more complex, influenced by both porosity and pore orientation. Higher permeability is observed not only in high-porosity zones but also in directions aligned with major pore axes. Simulated pressure fields at multiple pyrolysis stages show increasing anisotropy in fluid transport. Pressure propagates more efficiently along the primary pore alignment, confirming the influence of both structural orientation and decomposition extent. These trends are consistent with earlier findings in thermally decomposing porous media.

Overall, this study provides a detailed spatially resolved analysis of pore structure and transport property evolution during wood pyrolysis. By combining local REV-based characterization with PNM simulation, we bridge the gap between microstructural changes and macroscopic transport behaviour. Future work will compare REV-based simulation outcomes with homogenized models and full-network computations. The evaluation will go beyond pressure fields to include comprehensive transport metrics, improving the accuracy and reliability of pyrolysis modelling frameworks for biomass conversion applications.

ACKNOWLEDGEMENTS

Funded by the Deutsche Forschungsgemeinschaft (DFG, German Research Foundation) – Project-ID 422037413 – TRR 287.

REFERENCES

[1] Lopez, G., Keiner, D., Fasihi, M., Koiranen, T., Breyer, C., 2023, " From fossil to green chemicals: sustainable pathways and new carbon feedstocks for the global chemical industry", *Energy & Environmental Science*, Vol. 16, pp. 2879-2909.

[2] Vilas-Boas, A. C. M., Tarelho, L. A. C., Oliveira, H. S. M., Silva, F. G. C. S., Pio, D. T., Matos, M. A. A., 2024, "Valorisation of residual biomass by pyrolysis: influence of process conditions on products", *Sustainable Energy & Fuels*, Vol. 8, pp. 379-396.

[3] Bermúdez, C. A., Porteiro, J., Varela, L. G., Chapela, S., Patiño, D., 2020, "Three-dimensional CFD simulation of a large-scale grate-fired biomass furnace", *Fuel Processing Technology*, Vol. 198, pp. 106219.

[4] Jiang, Z., Wu, K., Couples, G., Van Dijke, M. I. J., Sorbie, K. S., Ma, J., 2007, "Efficient extraction of networks from three‐dimensional porous media", *Water resources research*, Vol. 43, pp. 12.

[5] Gostick, J. T., 2017, "Versatile and efficient pore network extraction method using marker-based watershed segmentation", *Physical Review E*, Vol. 96, pp. 023307.

[6] Edeh, I. G., Masek, O., Fusseis, F., 2023, "4D structural changes and pore network model of biomass during pyrolysis", *Scientific Reports*, Vol. 13, pp. 22863.

[7] Srocke, F., Han, L., Dutilleul, P., Xiao, X., Smith, D. L., Mašek, O., 2021, "Synchrotron X-ray microtomography and multifractal analysis for the characterization of pore structure and distribution in softwood pellet biochar", *Biochar*, Vol. 96, pp. 671-686.

[8] Zhan, N., Wu, R., Tsotsas, E., Kharaghani, A., 2022, "Proposal for extraction of pore networks with pores of high aspect ratios", *Physical Review Fluids*, Vol. 7, pp. 014304.

[9] Zhan, N., Wang, Y., Lu, X., Wu, R., Kharaghani, A., 2024, "Pore-corner networks unveiled: Extraction and interactions in porous media", *Physical Review Fluids*, Vol. 9, pp. 014303.

[10] Yapici, F., Ozcifci, A., Esen, R., Kurt, S., 2011, "The effect of grain angle and species on thermal conductivity of some selected wood species", *BioResources*, Vol. 6, pp. 2757-2762.

[11] Pecha, M. B., Thornburg, N. E., Peterson, C. A., Crowley, M. F., Gao, X., Lu, L., Wiggins, G., Brown, R. C., Ciesielski, P. N., 2021, "Impacts of anisotropic porosity on heat transfer and off-gassing during biomass pyrolysis", *BioResources*, Vol. 35, pp. 20131-20141.

Conference on Modelling Fluid Flow (CMFF'25)
The 19th International Conference on Fluid Flow Technologies
Budapest, Hungary, August 26 - August 29, 2025

INVESTIGATING THE INFLUENCE OF PARTICLE SHAPE ON THE PYROLYSIS OF THERMALLY THICK PARTICLES IN DEM/CFD

Bo JAEGER[1,2], Rezvan ABDI[2], Enric ILLANA[2], Viktor SCHERER[2]

[1] Corresponding Author. Tel.: +49 234 32 23503. E-Mail: jaeger@leat.rub.de
[2] Institute of Energy Plant Technology, Ruhr-University Bochum, Universitätsstraße 150, 44780 Bochum, Germany.

ABSTRACT

Understanding how particle shape and packing arrangement affect heat transfer and flow dynamics is essential for accurately modeling pyrolysis in fixed particle beds. This study investigates the influence of particle geometry and bed structure on pyrolysis behavior, focusing on spherical, cylindrical, and cubical particles. As numerical tool, the coupling of Computational Fluid Dynamics (CFD) with the Discrete Element Method (DEM) is used incorporating a radiation model based on the Discrete Ordinates Method (DOM).

The results reveal that particle shape and spatial particle arrangement significantly influence local flow patterns, temperature gradients, and pyrolysis progression. While packings of spherical particles exhibit more uniform heating, beds of cylindrical and cubical particles demonstrate complex interactions between radiation and convection due to geometric shadowing of radiation and directional flow channels. In total, the pyrolysis progess of the bed is fastest for spheres, followed by cylinders and cubes.

Keywords: Blocked-Off, DEM/CFD, Particle shape, Pyrolysis

NOMENCLATURE

A	[m^2]	surface area
D_i	[m^2 s^{-1}]	diffusion coefficient
E	[W m^3 sr^{-1}]	emission
$\underline{F_i}$	[N]	force
I	[W m^3 sr^{-1}]	radiative intensity
$\underline{J}$	[kg m^2]	inertia of the body
$\underline{L}$	[kg m^2 s^{-1}]	angular momentum
$\underline{M_j}$	[Nm]	torque
N_i	[-]	number of i
$\underline{P}$	[kg m s^{-1}]	translational momentum
$\underline{s}$	[-]	radiation direction vector
S_E	[J m^{-3} s^{-1}]	enthalpy source term
S_{gas}	[kg m^{-3} s^{-1}]	mass source
S_i	[kg m^{-3}s^{-1}]	mass source of species i
S_M	[kg m^{-2} s^{-2}]	momentum source
T	[K]	temperature
Y_i	[-]	mass fraction
$\underline{g}$	[m s^{-2}]	gravitational acceleration
h_f	[J kg^{-1}]	specific enthalpy
k_f	[Wm^{-1} K^{-1}]	thermal conductivity
p_{rgh}	[N m^{-2}]	gauge pressure
$\underline{r_i}$	[m]	position vector
t	[s]	time
$\underline{u_f}$	[m s^{-1}]	velocity
$\underline{x}$	[m]	particle / cell position
ε	[-]	bed porosity
ρ_f	[kg m^{-3}]	density
τ_f	[Pa]	stress tensor
φ	[-]	surface area ratio
$\underline{\omega}$	[rad s^{-1}]	angular velocity

Subscripts and Superscripts

CV	control volume
f	fluid
p	particle
pf	particle face
$surf$	surface

1. INTRODUCTION

Pyrolysis is a thermochemical decomposition process in which organic materials are heated in the absence of oxygen, typically within a temperature range of 300 °C to 900 °C. This process is widely used in bioenergy applications, where it is a precursor step to combustion or where it enables the conversion of solid biomass into valuable fuels.

Although pyrolysis is a well-established process, achieving optimal efficiency and uniformity in fixed-bed pyrolysis reactors remains a significant challenge. The local arrangement of particles within the bed and their shape strongly influences flow fields, heat transfer, and ultimately, the rate and uniformity of thermal conversion. This paper aims to provide insight into this complex problem.

Pyrolysis of fixed beds of solid particles in DEM/CFD was already in the focus of previous studies. For example, Mahmoudi et al. simulated the pyrolysis of spherical particles in a small-scale packed bed [1]. The same reactor was also modeled by Gao et al. but with cubical particles instead of spheres [2]. Other authors combined the pyrolysis with a subsequent combustion process. Wiese et al. used DEM/CFD to model the pyrolysis (and combustion) of cylindrical particles [3] in a domestic pellet stove. Buss et al. [4] investigated the thermal conversion of (agitated) beds of straw pellet, representing the particles as sphero-cylinder.

However, these studies were restricted to only a single particle shape. Hence, the influence of particle shape and the corresponding bed morphology on the pyrolysis process could not be investigated.

To study the influence of particle shape in pyrolysis a numerical method is required that captures the details of the flow field in the void spaces among particles. In DEM/CFD this is typically realized by Immersed Boundary Methods (IBM) [5]. Boundaries of solid objects (walls, particles) are numerically embedded into the CFD domain and the underlying system of fluid conservation equations and their presence in the fluid flow is accounted for without meshing the actual shape. IBMs were used by several groups to model the fluid flow through packings with [6,7] and without [8, 9] heat transfer.

A simple version of an IBM, the so called Blocked-Off approach (BO) [10, 11], is used in this work. All simulations shown are based on an inhouse DEM code coupled with the FireFOAM solver of OpenFOAM [12].

Special emphasis is placed on analysing three distinct particle geometries—spheres, cylinders, and cubes—to systematically investigate their influence on thermal gradients, inter-particle heat transfer, and local flow phenomena within the bed. Particular attention is paid to the spatially heterogeneous heating behaviour observed in packings of non-spherical particles, where complex radiation shadowing effects and orientation-dependent exposure to radiation and flow lead to significant variation in particle temperature and pyrolysis rate—even among neighbouring particles.

The structure of the article is organized as follows: Section 2 outlines the mathematical framework and the governing equations. Section 3 introduces and details the test scenarios, which include a pyrolysis reactor filled either with cubes, spheres, or cylinders. In Section 4, the results are analyzed and discussed in depth, while Section 5 provides a summary of the key findings.

2. NUMERICAL MODELS

The numerical model used in this study combines the DEM/CFD method with the "Blocked-Off" (BO) approach, a simplified form of the Immersed Boundary Method (IBM)

While we describe the BO in short in chapter 2.2.1–2.2.3, we refer to [8, 11, 13] for more details about the method used.

2.1 Particle mechanics (DEM)

The Discrete Element Method (DEM) was employed to generate the initial packed bed configuration. The dynamics of the particles are governed by the momentum equation for translation ($\underline{P}$) and rotation ($\underline{L}$). The translational acceleration of a particle center of gravity is calculated based on the total contact forces $\underline{F_i}$ and gravitational force $m\underline{g}$. (Eq. 1). The angular acceleration (Eq. 2) is obtained from the torque due to contact forces $\underline{F_i}$ (both normal and tangential):

$$\frac{d\underline{P}}{dt} = m \cdot \frac{d^2\underline{x}}{dt^2} = \sum_{i=1}^{n} \underline{F_i} + m\underline{g} \tag{1}$$

$$\begin{aligned} \frac{d\underline{L}}{dt} = \underline{\omega} \times \underline{J} \cdot \underline{\omega} + \underline{J} \cdot \underline{\dot{\omega}} = \sum_{i=1}^{n} \underline{M_i} \\ = \sum_{i=1}^{n} \underline{r_i} \times \underline{F_i} \end{aligned} \tag{2}$$

where $\underline{x}$ is the particle position, m is the mass, t represents time, $\underline{\omega}$ the angular velocity and $\underline{J}$ is the inertia of the body. Contact forces were calculated with a linear spring-dashpot model and particles were modelles as polyhedrons.

2.2 Computational Fluid Dynamics (CFD)

The CFD solver ensures conservation of mass (Eq. 3), momentum (Eq. 4), and energy (Eq. 5) within the fluid phase by solving the corresponding transport equations.

$$\frac{\partial \rho_f}{\partial t} + \underline{\nabla} \cdot \left(\rho_f \underline{u}_f\right) = S_{gas} \tag{3}$$

$$\begin{aligned} \frac{\partial (\rho_f \underline{u}_f)}{\partial t} + \underline{\nabla} \cdot \left(\rho_f \underline{u}_f \underline{u}_f\right) \\ = -\underline{\nabla} p_{rgh} + \underline{\nabla} \cdot \tau_f \\ + \underline{g}\underline{x} \cdot \underline{\nabla}\rho + \underline{S_M} \end{aligned} \tag{4}$$

$$\begin{aligned} \frac{\partial (\rho_f h_f)}{\partial t} + \underline{\nabla} \cdot \left(\rho_f \underline{u}_f h_f\right) \\ = \underline{\nabla} \cdot \left(k_f \, \underline{\nabla} T\right) + S_E \end{aligned} \tag{5}$$

The behavior of the fluid phase is defined through parameters such as specific enthalpy (h_f), velocity ($\underline{u}_f$), and density (ρ_f). The term S_{gas} represents the mass transfer between the fluid and solid phases. Sources contributing to momentum include the gauge pressure gradient ($\underline{\nabla} p_{rgh}$), stress

tensor (τ_f) under the assumption of laminar flow, gravitational acceleration vector ($\underline{g}$) and momentum exchanged with the particles ($\underline{S_M}$). The vector field ($\underline{x}$) contains the cell centres.

In the context of energy transport, the fluid's ability to conduct heat is described by its thermal conductivity (k_f), and the enthalpy exchanged with the solid is expressed as S_E.

The transport equation for a chemical species i is expressed as:

$$\frac{\partial(\rho_f Y_\mathrm{i})}{\partial t} + \underline{\nabla}\cdot\left(\rho_f \underline{u}_f Y_\mathrm{i}\right) = \underline{\nabla}\cdot\left(\rho_f D_\mathrm{i}\,\underline{\nabla} Y_i\right) + S_\mathrm{i} \tag{6}$$

Where the source term S_i, and the term including the diffusion coefficient D_i, model the release and transport of i from the particles during the reaction, respectively.

2.2.1. Blocked-Off approach

The embedding of the particle surface within the CFD-domain is achieved by two means and is explained with Figure 1.: First, the CFD cells (CV) lying within the particle (core CV) and the cells containing the particle surface (surface CV) are determined. Cell faces belonging to both cell types are labeled as solid-fluid-interface. Scalar transport across these faces is turned off / blocked so that no fluid properties can penetrate the cell region occupied by a particle. Second, source terms S are calculated in the surface CVs and added to the fluid equations (Eqs. 3–5). The values of S depend on the local flow conditions and the properties of the discrete particle surface.

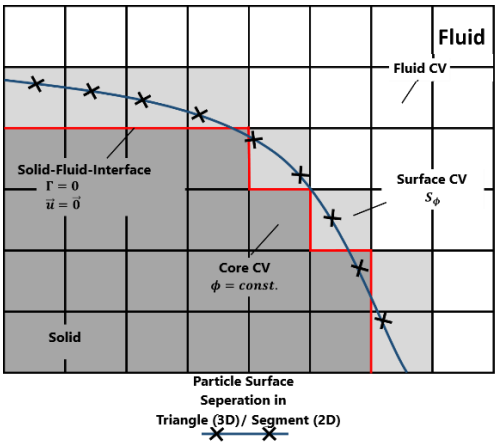

Figure 1. Schematic depiction of the BO-approach

By doing so, the fluid flow effectively evolves around the particle. The total domain was meshed with $4.6 \cdot 10^6$ fluid cells. The particle-to-cell size was $d_p/\Delta x_{BO} = 4.8 - 24$ (for cylinders) and $d_p/\Delta x_{BO} = 12$ (for spheres/cubes) CVs, which allows for an adequate representation of the particle shape.

2.2.2 Convective heat transfer fluid – particle

The rate of convective heat transfer, denoted as $S_{E,CV}$ [W], is expressed by the equation:

$$S_{E,CV} = \frac{1}{\varphi}\frac{k_{f,CV}}{L_{CV}}\left(T_{f,CV} - \bar{T}_{pf}\right)A_{CV} \tag{7}$$

φ is the ratio (A_P/A_{CFD}), where A_P is the actual particle surface area and A_{CFD} the enlarged particle area in CFD. L_{CV} is a charctersitic cell size, $T_{f,CV}$ is the fluid temperature in the cell, and $\bar{T}_{pf}$ represents the mean particle surface temperature associated with the cell. A_{CV} is the interfacial area in the cell. This source term S is also applied to the particle mesh as a boundary condition.

$$S_{pf} = \sum_{CV}^{CVs\in pf} \frac{S_{E,CV}}{N_{pf,CV}} \tag{8}$$

Whereby $N_{pf,CV}$ is the number of particle surfaces contained in the CV.

Please note that heat transfer through direct particle contact has been neglected, as convection, when present, dominates over contact heat transfer.

2.2.3 Radiative heat transfer

Radiative heat transfer between particle-particle and particle-wall is calculated with a Blocked-Off / Discrete-Ordinates-Model (BO/DO), described in more detail in [15]. This approach calculates the radiative transfer equations (RTE) on a cartesian grid, embedding the particle boundaries in the same manner as before. In its simplest form (no gas absorption), the RTEs are defined as:

$$\underline{\nabla}\cdot\left(I(\underline{s},\underline{r})\underline{s}\right) = \frac{E}{4\pi} \tag{9}$$

$I(\underline{s},\underline{r})$ is the radiative intensity at position $\underline{r}$ and for direction $\underline{s}$ and E is the emission due to the particle boundary. Particle surfaces are assumed to be gray and diffusive.

2.2.4 Pyrolysis Model

In this work, pyrolysis occurs in thermally thick particles, which means that particle internal transport must be resolved on a particle internal 3D mesh. The model used here is described in [11]. The model considers three components, which are reacting solid biomass (~80% of mass), solid char (~20% of mass) and gaseous volatiles (converted from biomass). Kinetic parameters (k, E_A) for conversion of

biomass→volatiles are 168.4 s^{-1} / 51,965 J $(mol\ K)^{-1}$ and 13.2 s^{-1} / 45,960 J $(mol\ K)^{-1}$ for biomass→char. Gaseous volatiles have a fixed mass composition of 4.46/0.82/11.1/83.62% (CH_4/CO/H_2/CO_2). Solid conductivity and heat capacity of biomass and char were modelled with temperature dependent. Solid and gaseous components are in thermal equilibrium. Anisotropy is considered and (temperature dependent) thermal conductivity along the fibre direction was twice as high as across the fibre for all particles. Enthalpy of pyrolysis was not considered here, as it is neglectable small compared to the external heat added to the particle. The diffusion coefficient was assumed to be isotropic ($3 \cdot 10^{-3}$ $m^2 s^{-1}$). All particles contained no water, so a drying phase prior to pyrolysis did not occur.

3. DEM/CFD SIMULATION SETUP

3.1 Individual Particles, Simulation Domain, and Boundary Conditions

Three different model bodies are investigated in the numerical simulations: spheres, cubes, and cylinders (Figure 2). The dimensions of the model bodies were chosen such that all bodies have the same surface-to-volume ratio of 0.6 mm^{-1}. This corresponds to a radius of 5 mm for a sphere, an edge length of 10 mm for a cube, and a length and radius of 20 mm and 4 mm, respectively, for a cylinder (see Table 1). The particles are made of beechwood, for which an average (atro) density of 700 kg/m^3 was specified. Their initial temperature is 298 K.

The thermochemical conversion of the particles takes place in a cylindrical reactor flushed by hot nitrogen at T = 973 K and $\underline{u_f}$ = 0.14 m/s ($\dot{m}$=1.16 g/s). The walls of the reactor were at 973 K as well; thus, the bed is heated additionally by radiation. A slightly larger cylindrical tube (not depicted) is placed above the reactor into which the released volatiles enter and may combust (not investigated here). The packed beds were generated by allowing for particles to fall from above into the reactor until a bed height of 50 mm was reached.

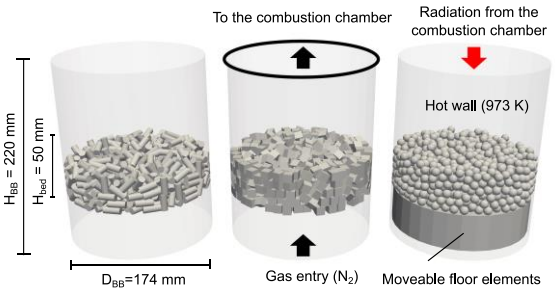

Figure 2. Pyrolysis reactor with movable base elements, stacked cylinders, cubes, spheres.

The bed was then mixed using movable floor elements, and more particles were added to restore the bed height to 50 mm. Due to the different volumes of the model bodies, this corresponds to different final number of particles and different bed porosities in the respective bed (left column). In the following, we refer the three packings simple as sphere, cube and cylinder bed, respectively.

4. RESULTS

4.1 Pyrolysis of single particles

Figure 3 shows the time evolution of the core temperature and the (dimensionless) particle mass for three (individual) particles of the respective shapes. Particles were placed into uniform radiation fields whose radiative intensities correspond to temperatures of T_{rad} = 700 C°, 800 C° and 900 °C. Convective heat transfer was not considered in these cases.

Table 1. Geometric properties of the three different particle shapes

Shape (N_P, ε_{bed})	Var. [mm]	A [10^{-4} m^2]	V [10^{-6} m^3]	m [10^{-4} kg]
Sphere (1278, 44%)	$r = 5$	3.14	0.52	3.2
Cylinder (636, 46%)	$r = 4$ $h = 20$	6.03	1.01	6.2
Cube (731, 39%)	$a, b, c = 10$	6.0	1.0	6.2

The core temperature rises faster with increasing T_{rad} and the thermochemical mass conversion (solid→gas) is completed earlier. It is noticeable that the core temperatures of the spheres and cylinders are very similar and increase faster than those of the cubes. For the cylinders, the distance between the shell surface and the core is the smallest (4 mm), which is why heat from the surface reaches the core faster than for the other two bodies. For spheres and cubes, the distance is 5 mm, whereby the distance from the surface to the core remains constant for the sphere but increases towards the corners for the cube. The heat flow in the cube is not exclusively in the direction of the core. Heat is also conducted in the direction of the corners/edges and is distributed there in the additional volume. Compared to the sphere, both the cylinder and the cube have about twice the surface area and about twice the volume and mass. More heat can therefore be exchanged over the surface of these two shapes, but more heat is required to heat the particles at the same time. After ~40 s, the

heating rate of the particles at 900 °C slightly decreases. This is because heat conductivity increases with temperature and more heat is required to further increase particle temperature. For 500°C and 700°C, although heat conductivity also increases, it is not enough to be reflected in the mean temperature curve.

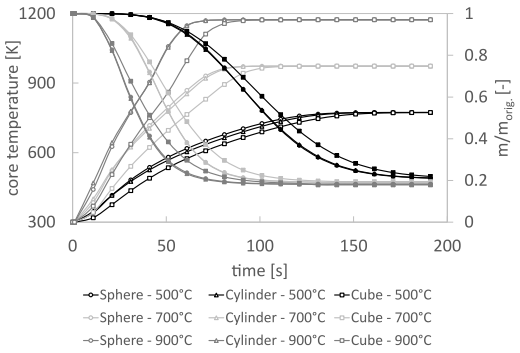

Figure 3. Core temperature and mass over time for the three particle shapes at 500 °C, 700 °C and 900 °C radiation temperature.

The mass conversion of solid biomass mainly depends on the temperature evolution within the particle and therefore, the mass evolution corresponds well to the core temperature evolution: Spheres and cylinders have almost identical mass evolution over time, whereas the mass of the cube decreases more slowly at the respective T_{rad}.

4.2 Total mass evolution within the bed

The temporal evolution of the (dimensionless) mass of the entire bed is presented in Figure 4. The sphere bed is converted the fastest, followed by the cylinder bed. The fixed cube bed is converted the slowest. This basically follows the trend that has already been observed for the individual particles, although the differences between the thermochemical conversion of the sphere and cylinder bed can be seen more clearly in the fixed bed.

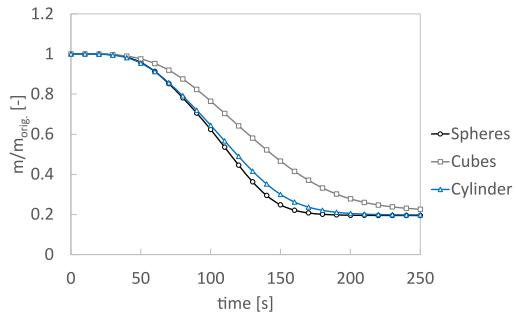

Figure 4. Dimensionless fixed bed mass of the sphere, cube and cylinder bed over time.

The complete conversion of biomass to char (approx. 20% by mass) takes place in around 180–250 seconds for spheres and cylinders, while for the cubes, pyrolysis is still not finally completed.

4.3 Flow field and convective heating within the packed bed

Snapshots of the fluid temperature field in the three packings as well as local velocity vectors are depicted slopes in Figure 5 in a cross-sectional view (t = 50 s). Based on the similar distribution and magnitude of the velocity vectors, it can be concluded that the flow within the sphere bed (top) is homogeneous, which can be attributed to its regular bulk morphology, i.e. homogeneously distributed void spaces / porosity.

The cube (middle) and cylinder (bottom) beds exhibit more complex flow conditions and larger local deviations. This is because the particles in the bed form more complex channel structures with larger statistical variation (heterogeneous porosity distribution).

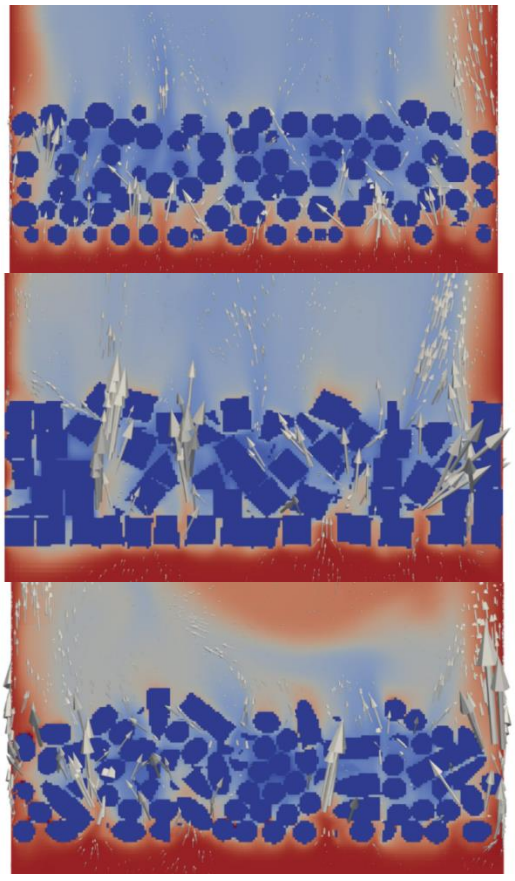

Figure 5. Cross-sectional snapshot of fluid temperature field in the three packings at t = 50 s. The arrows indicate magnitude and direction of the local fluid velocity.

This leads to locally constricted flow channels, which result in higher flow velocities (seen in the

larger arrows), e.g. in the case of cylinders near the walls where the local porosity approaches very small values. However, there are also differences between the cube and cylinder bed. In the case of cubes, the flow is predominantly axial with cross flows being suppressed, particularly near the walls, as there the cubes tend to stack directly on top of one another. In the case of the cylinder bed, the velocity vectors within the bulk have a larger horizontal component, indicating enhanced cross-mixing.

The immediate effect of these flow conditions on the temperature profile is also observable in Fig. 5. The temperature front (red color) penetrates the sphere bed homogeneously in axial direction. However, for the cube and cylinder bed, the penetration is more strand-like, which is for example seen around the lowest particle layers. The narrow channels, constructed by the particles, allow for an effective but straightened penetration of hot nitrogen into the bed.

In the cylinder bed particles, radial penetration near the wall is more pronounced due to the aforementioned cross flow conditions. The sphere bed exhibits a slightly weaker penetration near the wall, as approximately only one particle layer is enveloped by the hot fluid at this point in time. Radial penetration in the cube bed is negligible, as the flow is predominanteley axial and radial components are effectively blocked by the stacked cube arrangement.

In summary, the sphere bed particles exhibits homogeneous heating, whereas the beds of cylinders and cubes experience more heterogeneous heating due to differences in convective heat transfer

4.4 Radiative heating

Initially, only the particles in the outermost bed layers, which are visible to the hot walls, are heated by radiation. However, as soon as the particles are hot enough, they also emit radiative heat and heat up other visible particles. The effect of radiation in the beds is described with Figure 6, depicting the particle surface temperatures. The cross section was cut in half, with the middle axis indicated by a dashed line on the left and the wall shown on the right.

Penetration of radiation into the bed differs for the three beds. In the sphere bed (left), radiation reaches only a short distance due to the tight packing of the spheres (ε = 44%), which effectively blocks radiation from penetrating deeper layers. The thight packing, in combination with the homogeneous packing structure, prevents what we call partial shadowing. Partial shadowing occurs when one particle is partially visually obstructed by its immediate neighbours so that only fractions of far range radiation reach the particles surface. This leads to non-uniform particle heating with locally larger temperatures at the particles „visible" surface and colder surface areas at the visually blocked surfaces. As partial shadowing does not occur for the sphere bed, the surface temperatures depict only minimal temeprature gradients.

In the cube bed (middle), the stacked cubes adjacent to the wall initially block most of the wall-emitted radiation, preventing significant penetration into the bulk material. This face-to-face stacking near the wall results in locally low porosity. Although the packing becomes looser deeper in the bed, the overall porosity remains low at 39%. As the wall-adjacent particles heat up and particle-to-particle radiative transfer becomes more significant, radiation begins to penetrate further into the bed. Despite the more heterogeneous structure compared to the sphere bed, partial shadowing effects remain limited due to the dense stacking of the cubes.

The cylinder bed (right) exhibits the largest porosity (46%). While it is only slightly larger than for the sphere bed, the cylinder form larger void spaces between them due to their high aspect ratio (h/r = 5), leading to the highest particle-particle visibility. Wall radiation can penetrate further inside the bulk right from the beginning. Furthermore, a competing behaviour between convection and radiation exists: Particles are already heated from a distance by radiation and then receive less thermal energy from the fluid flow, once its temperature front reaches the particles. In addition, partial shadowing plays a major role due to the large aspect ratio of the cylinders. Both effects contribute to temperature gradients across the cylinder surfaces, visible in the right side of Fig. 6

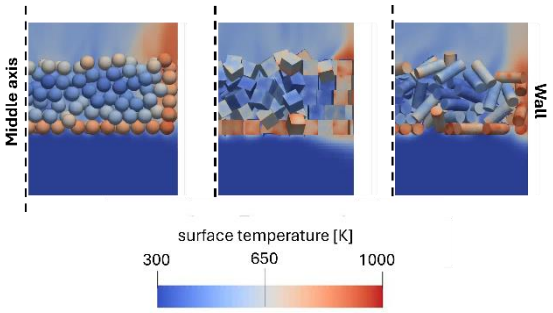

Figure 6. Comparison of particle surface temperatures.

4.5 Pyrolysis progress in the particle beds

Evolution of particle mass distribution is explained in conjunction with the concentration of CO_2 (as representative species for volatiles released) above the particle bed. Snapshots of the particle mass distribution at four different times (top to bottom) are shown in Figure 7 and CO_2 concentrations in the gas above the bed in Figure 8. After 50 s, particles in the outer layers of the beds have lost mass due to thermochemical conversion, induced by a) convective heat and b) radiative heat, both affecting the outer bed layers first. While differences in the mass distribution are not very distinct for the three

beds at this specific time, the CO_2 concentrations above the beds clearly show that particles pyrolyze differently, depending on their shape and the local packing. The CO_2 concentrations are the highest near the wall in all cases, as particles there pyrolyze first. For the cylinder bed, some eddies are visible in the flow field above the bed while the flow through the sphere / cube bed is straightened and therefore, no eddies are present above the bed.

After 100 s, one can distinguish two zones in the sphere bed (Fig. 7, left). A core zone, with mostly un-pyrolyzed particles and layers of pyrolyzed particles around this zone. The boundary between these two zones is clearly identifiable. However, for the cylinder bed, (Fig. 7, middle), such a distinct boundary is barely visible, and for the cube bed, no distinct boundary is visible, indicating a more heterogeneous progression of pyrolysis. While the conversion progress for cylinders in the outer layers is relatively uniform (m/m_0 = 0.2–0.3), those located in the core exhibit significantly greater variability in their conversion rates. Cubes in the inner and outer layers show a quite heterogeneous conversion progress, ranging from 0.3 to 1.

From Fig. 8 at 100 s, one can deduce that pyrolysis is now occurring in the whole particle bed and not just near the wall, as CO_2 covers the whole volume above the beds. CO_2 is distributed quite evenly above the sphere bed and the profile appears symmetric around the middle axis, indicating that thermal conversion of the solid material and subsequent release of gaseous volatiles occurs in a spatial homogeneous manner. Cubes near the wall still pyrolyze and, therefore, higher CO_2 concentrations are visible. Furthermore, elevated CO_2 concentrations are observed below the bed. This is attributed to the cubes obstructing the flow paths, causing minor backflow that also carries CO_2 in the reverse direction. CO_2 concentrations above and inside the cylinder bed appear most heterogeneous. This is due to: (a) the uneven progression of pyrolysis among the particles (see Fig. 7), and (b) the complex flow conditions within the cylinder bed resulting from irregular flow pathing.

At 150 seconds (Fig. 7), the appearance of the pyrolysis zones remain largely consistent with those observed at 100 seconds, i.e., symmetrical in the sphere bed, indicating homogeneous conversion, and asymmetrical in the beds of cubes and cylinders, reflecting heterogeneous conversion. The CO_2 concentrations at 150 s are quite different (Fig. 8) for the three beds. The sphere bed exhibits a candle flame-shaped distribution of CO_2. Particles in the outer layers are completely pyrolyzed and already released all volatiles. Pyrolysis in the cube bed is still ongoing in the whole bed and, therefore, the whole volume above the bed contains CO_2. Like the spheres, cylinders in the outer bed layers are already completely pyrolyzed and only the cylinder in the core region release volatiles. Again, due to the heterogeneous conversion and the flow pathing, the CO_2 distribution is spatially very heterogeneous.

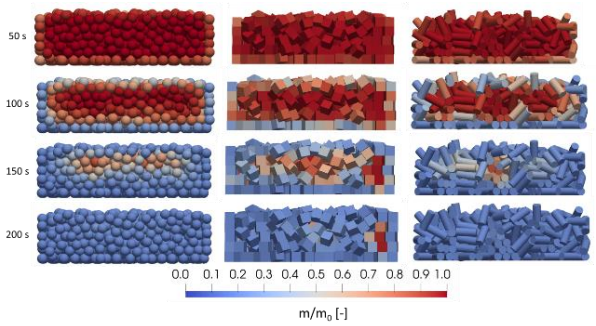

Figure 7. Cross-section of the three particle packings and colored representation of the dimensionless particle mass (t = 50 s, 100 s, 150 s and 200 s, from top to bottom).

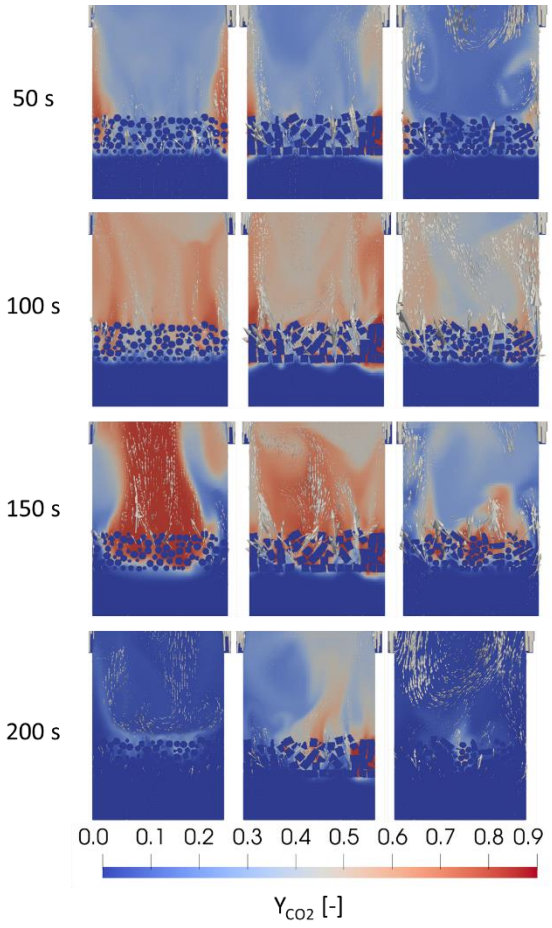

Figure 8. CO_2 mass fraction (cell values) in the gas phase in and above the bed (t = 50 s, 100 s, 150 s and 200 s, top to bottom) for spheres, cubes and cylinders, respectively (from left to right).

After 200 s, thermal conversion is largely completed. The sphere bed is nearly completely pyrolyzed and only little CO_2 remains in the gas phase. In contrast, the cube bed exhibits the slowest

conversion, with some particles in the core region still undergoing pyrolysis. The cylinder bed is also mostly converted, and similar to the sphere bed, only low concentrations of CO_2 remain.

5. SUMMARY

In this work, DEM/CFD simulations of the pyrolysis of particle beds containing thermally thick beechwood particles of three different shapes were conducted. Spheres, cubes and cylinders constituted the beds. The differences in the pyrolysis behaviour of the solid particles and in volatile gas concentrations were investigated.

The total conversion of the bed is fastest for the spheres, followed by the cylinders and then the cubes. Total bed conversion over time for spheres and cylinders is similar.

For the investigated shapes, local conversion of solid particles is spatially very different, as are the flow conditions in and above the beds.

Generally, the pyrolysis zone, where particles mainly undergo conversion, is spatially very homogeneous for the sphere bed but heterogeneous for the other two beds. This is attributed to the flow field and the radiative conditions within the bed, which depend on the packing structure. All beds pyrolyze from their outer layers towards their core. However, the pyrolysis front traveling into the bed is symmetric for the sphere bed with a distinct pyrolysis reaction front detectable. This is not the case for the beds of the other two bodies. Accordingly, volatiles in the sphere bed are distributed evenly in the gas phase, in and above the bed over the whole process duration. The beds of cubical and cylindrical particles exhibit locally larger volatile concentrations, depending on the local conversion progress and the flow conditions.

This paper demonstrates that DEM/CFD simulations representing particles as spheres—a common simplification used to reduce computational cost—may be highly misleading when the actual particles are non-spherical.

ACKNOWLEDGEMENTS

This work has been funded by the Deutsche Forschungsgemeinschaft (DFG, German Research Foundation) – Project-ID 422037413 – TRR 287.

REFERENCES

[1] A. H. Mahmoudi, F. Hoffmann, and B. Peters, “Detailed numerical modeling of pyrolysis in a heterogeneous packed bed using XDEM,” *Journal of Analytical and Applied Pyrolysis*, vol. 106, pp. 9–20, 2014.

[2] X. Gao, J. Yu, L. Lu, and W. A. Rogers, “Coupling particle scale model and SuperDEM-CFD for multiscale simulation of biomass pyrolysis in a packed bed pyrolyzer,” *AIChE Journal*, vol. 67, no. 4, p. 127654, 2021.

[3] J. Wiese, F. Wissing, D. Höhner, S. Wirtz, V. Scherer, U. Ley, and H. M. Behr, “DEM/CFD modeling of the fuel conversion in a pellet stove,” *Fuel Processing Technology*, vol. 152, no. 2, pp. 223–239, 2016.

[4] F. Buss, S. Wirtz, and V. Scherer, “Simulation of a reacting agitated bed of straw pellets by a resolved coupled DEM/CFD method using a blocked-off approach,” *International Journal of Thermal Sciences*, vol. 152, p. 106332, 2020.

[5] R. Mittal and G. Iaccarino, “Immersed Boundary Methods,” *Annu. Rev. Fluid Mech.*, vol. 37, no. 1, pp. 239–261, 2005.

[6] S. Das, N. G. Deen, and J. Kuipers, “Direct numerical simulation for flow and heat transfer through random open-cell solid foams: Development of an IBM based CFD model,” *Catalysis Today*, vol. 273, no. 1, pp. 140–150, 2016.

[7] S. Das, N. G. Deen, and J. Kuipers, “A DNS study of flow and heat transfer through slender fixed-bed reactors randomly packed with spherical particles,” *Chemical Engineering Science*, vol. 160, no. 15, pp. 1–19, 2017.

[8] C. Gorges, M. Brömmer, C. Velten, S. Wirtz, E. I. Mahiques, V. Scherer, K. Zähringer, and B. van Wachem, “Comparing two IBM implementations for the simulation of uniform packed beds,” *Particuology*, vol. 86, pp. 1–12, 2024.

[9] V. Chéron, F. Evrard, and B. van Wachem, “A hybrid immersed boundary method for dense particle-laden flows,” *Computers & Fluids*, vol. 259, p. 105892, 2023.

[10] E. Illana Mahiques, M. Brömmer, S. Wirtz, and V. Scherer, “Locally Resolved Simulation of Gas Mixing and Combustion Inside Static and Moving Particle Assemblies,” *Chem Eng & Technol*, vol. 46, no. 7, pp. 1362–1372, 2023.

[11] B. Jaeger, E. Illana Mahiques, S. Wirtz, and V. Scherer, “Pyrolysis of Spherical Wood Particles in a Packed Bed – Comparison between Resolved and Unresolved Discrete Element Method/Computational Fluid Dynamics,” *Chem Eng & Technol*, vol. 46, no. 10, pp. 2120–2132, 2023.

[12] OpenFOAM wiki, *FireFoam.* [Online]. Available: https://openfoamwiki.net/index.php/FireFoam (accessed: Aug. 22 2023).

[13] M. Brömmer, M. Scharnowski, E. Illana Mahiques, S. Wirtz, and V. Scherer, “Investigating the inflow into a granular bed using a locally resolved method,” *Particuology*, vol. 85, no. 1, pp. 89–101, 2024.

[14] B. Jaeger, M. Tyslik, S. Wirtz, and M. Schiemann, “Investigation of the radiative heating of cubic particles with DEM/CFD and the BO/DO approach,” *Powder Technology*, vol. 403, no. 6, p. 117424, 2022.

Conference on Modelling Fluid Flow (CMFF'25)
The 19th International Conference on Fluid Flow Technologies
Budapest, Hungary, August 26-August 29, 2025

NUMERICAL AND EXPERIMENTAL INVESTIGATION OF LOW REYNOLDS NUMBER FLOW IN A PACKED BED OF ROTATED BARS

Wojciech SADOWSKI[1,2], Christin VELTEN[3], Maximilian BRÖMMER[4], Hakan DEMIR[2], Francesca DI MARE[2], Katharina ZÄHRINGER[3], Viktor SCHERER[4]

[1] Corresponding Author, Email: wojciech.sadowski@rub.de
[2] Chair of Thermal Turbomachinery and Aero Engines, Ruhr University Bochum, UniversitätsstraSSe 150 D-44801 Bochum,
[3] The Laboratory of Fluid Dynamics and Technical Flows, Otto-von-Guericke-Universität Magdeburg.
[4] Institute of Energy Plant Technology, Ruhr University Bochum.

ABSTRACT

The present study focuses on the gas flow through an experiment-scale modular packed bed reactor consisting of square bars, arranged in layers. Each layer is rotated by 30^o resulting in a complex shape of the void spaces between the bars. Measurement results of the studied system are presented for particle-based Reynolds numbers $\mathrm{Re_p}$ of 100 and 200, and used as validation data for particle-resolved numerical simulations. The computations are performed for both $\mathrm{Re_p}$ using two different solid wall treatments: boundary conforming meshing and the blocked-off method. The flow inside the bed is largely independent of the Reynolds number and seems to be determined by the geometry of the void spaces. The flow in the freeboard is characterized by the presence of slowly dissipating jets downstream of the bed, which are characterized by unsteady oscillations for higher Reynolds number. The numerical results obtained with both boundary treatment approaches are in excellent agreement with the measurements inside the bed. In the freeboard, as a result of numerical properties of the current simulation approaches, some deviations between the simulation and measurements can be observed.

Keywords: packed bed, polyhedral particles, DNS, PIV, blocked-off method

NOMENCLATURE

$\mathrm{Re_p}$	$[-]$	particle Reynolds number
A	$[m^2]$	bed cross-section area
B	$[mm]$	bar size
Q	$[m^3/s]$	volumetric flow rate
T	$[s]$	time
$\langle w \rangle$	$[m/s]$	bulk velocity
u_ξ, w	$[m/s]$	velocity components
α	$[-]$	rotation angle
ϕ	$[-]$	porosity
ξ, z	$[m]$	coordinates

Subscripts and Superscripts

avg	averaging
i	initialization

1. INTRODUCTION

In packed-bed reactors, frequently used in chemical and process engineering, an assembly of particles is passed by a gas introducing reactants or facilitating processes, e.g., drying or coating. Hence, the flow characteristics (for example, dispersion of species, turbulence) influence the operation of packed-bed reactors to a large extent. At the same time, estimating these properties *a priori* is difficult, complicating design and leading to large error margins. A typical simplification in both analytical and numerical models is the assumption of spherical particles, which is often not appropriate when considering the randomly shaped polyhedra, or other industrially applied complex particle shapes [1]. At the same time, non-spherical geometry is known to influence the flow field to a large extent [2].

The use of Computational Fluid Dynamics (CFD) simulations, particularly the most accurate particle-resolved approach [3], can lead to valuable insight regarding the flow conditions, both in the packed beds and in the freeboard. The main drawback of the approach is its computational cost, resulting from the need to resolve the surface of each particle. Moreover, when a boundary conforming Finite Volume Method (FVM) is used, often a need to locally modify the geometry arises, to treat the regions of poor numerical stability near the contact points (surfaces) between individual particles [3].

Immersed boundary methods (IBM) are a common strategy to alleviate these issues, omitting the effort of boundary conforming mesh generation, treating contact points implicitly and avoiding expensive

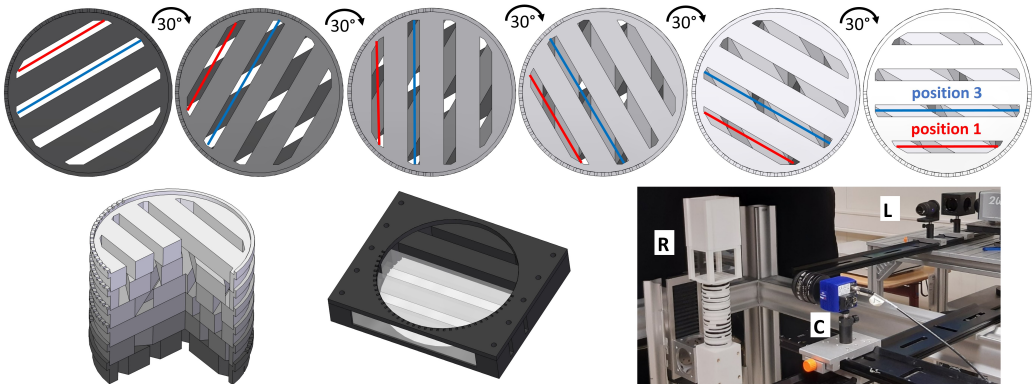

Figure 1. Schematic of the assembly process of a polyhedral packed bed assuming 30ř rotation between modules (upper line). The red and blue line mark the two measurement positions (P1 and P3) in different layers. The cut-out shows a complex structure of void spaces between the bars (lower left). To generate optical access an opaque standard module is replaced by a partially transparent optical module (lower centre). The PIV setup including the packed bed and measuring equipment is visible in the lower right part of the figure.

re-meshing in the case of moving objects. Numerous IBM approaches are available, among which the so-called *blocked-off method* introduced by Patankar [4] represents a simple variant of the method that does not involve complex interpolation schemes or surface reconstruction. It was recently validated against experimental measurements and smooth IBM for the simulations of packed beds [5]. Additionally, it was adopted to study the pressure drop over the bed of spherical particles [6] and used to construct a locally resolved flow model near the fuel lances of a reactor shaft [7]. A direct application of wall functions in case of higher Reynolds numbers and an easy integration into flow solvers are advantages of the present approach.

It is important to note that CFD-based predictions are of limited use without a proper validation using measurements of the flow properties, which are, however, rather scarce in packed bed reactors. Intrusive techniques Non-intrusive methods, which do not require optical access are typically limited to liquids [8] and their resolution is low compared to optical methods. For the latter, e.g., planar Particle Image Velocimetry (PIV) [9], the main difficulty lies in gaining an optical access to the interior of the packing. This is typically achieved via transparent packing material, which might require further post-processing.

Recently, Velten and Zähringer [10] used Particle Image Velocimetry (PIV) to measure both the flow in the interstices of a model packed bed with a BCC packing of spheres and the conditions above the bed. Although, the interstitial data was gathered only in a set of small, optically accessible regions, it enabled a detailed analysis of the flow field and validation of several methods and numerical codes [5, 11]. These applications highlight the synergies of combining experimental and numerical analyses for the study of flow conditions in packed beds.

Moving away from the typically assumed spherical particle geometry, in the present work, we investigate the flow in a packed bed, formed from the assembly of square bars. The configuration results in interstices with complex geometries with multiple inlets and outlets. The flow field is investigated experimentally, by the means of PIV, and numerically, by two different particle-resolved FVM-based simulation methods: the boundary-conforming, incompressible solver available in the OpenFOAM package and on the other side the blocked-off approach within the DEM/CFD framework of the Bulk-Reaction project also coupled with OpenFOAM. Two different Reynolds numbers are studied, and for each case, results are compared both within the bed and in the freeboard region.

2. PACKED BED GEOMETRY

The packed bed geometry is based on a modular design, in which each module consists of five parallel bars (square cross-section with size $B = 10\,mm$) spaced with a distance of $5\,mm$ inside dodecagon-shaped side walls. Additionally, the outer walls of the modules are circular (see fig. 1), allowing for each module to be rotated freely. This enables the study of various geometrical configurations at a constant porosity of $\phi = 0.332$, defined as a fraction of the void space volume to the volume of the module ($30\,cm^3$). In the current geometry, a total of 18 modules are combined, with the rotation angle of 30ř. This results in a bed height of $18B$, before the fluid enters into a rectangular outlet zone, where measurements are carried out above the bed. The flow is characterised by a particle Reynolds number based on bulk velocity $\langle w \rangle$ and the bar size $\mathrm{Re_p} = \rho \langle w \rangle B/\mu$. The velocity $\langle w \rangle$ is defined using the module cross-section area $A = 3000\,mm^2$ and the volumetric flow rate of the device $Q = A\phi\langle w \rangle$.

Table 1. Times used for collecting data in the experiments and each simulation: T_i start-up time, T_avg averaging time. The reference time scale is the flow through one module $T_B = B/\langle w \rangle$.

	exp.		b.-conf.		blocked-off
$\mathrm{Re_p}$	T_avg/T_B	T_i/T_B	T_avg/T_B	T_i/T_B	T_avg/T_B
100	755	12	88	75.5	226.5
200	1515	42	158	151.5	454.5

2.1. Experimental setup

To allow optical access inside the packed bed, a standard module is replaced by an optical one, where opaque bars are exchanged by transparent fused silica rods (fig. 1 lower center). The data has been gathered separately for the layers 15th to 17th and the freeboard region. For each module and the freeboard the data is gathered in two measurement planes (position 1 and 3, annotated with red and blue lines in fig. 1 and named P1 and P3 in the text), at the midspan of each void space between the bars. Flow data was averaged over 500 images, recorded with 10 Hz (50 s). In the current manuscript only the data from the 17th layer and the freeboard are discussed.

The full assembly of the packed-bed reactor (R) is presented in fig. 1 (lower right). Airflow is controlled by a Bronkhorst mass flow controller and seeded by Di-Ethyl-Hexyl-Sebacat (DEHS) tracer nebulized by a liquid nebulizer Type AGF 10.0 from Palas GmbH resulting in particle sizes below 10 μm. It enters into the packing through a diffuser filled with glass beads to homogenize the flow. The measurement region is illuminated by a double pulsed Quantel Q-smart Twins 850 Nd:YAG PIV-laser (L) and an Imager CX 12MP Camera (C) from LaVision GmbH records the PIV signal.

3. NUMERICAL MODEL

3.1. Simulations on the boundary-conforming mesh

The computations have been performed using OpenFOAM-12, using an unsteady solver, implementing the incompressible form of Navier–Stokes equations. The computational geometry is depicted in fig. 2. Based on the indications from our previous work, the flow conditions in the bed are influenced by the freeboard only in the topmost layers and are repeatable between layers [11]. Hence, to limit computational effort, only six top layers were realized in the simulation. The volume of fluid in the modules has been meshed with a boundary conforming hexahedral-dominant structured mesh (fig. 2). The initial mesh for the freeboard region has been generated in the same way, after which it was locally refined to allow for smooth transition in mesh resolution in both regions. The whole mesh, used for each simulation, consists of around 8.5M cells. The modules and the freeboard have been coupled using the Non-Conformal Coupling (NCC) interface. The uniform velocity profile with value $\langle w \rangle$ is prescribed at the inlet and the reference pressure value at the outlet. The rest of the boundaries are treated as no-slip walls.

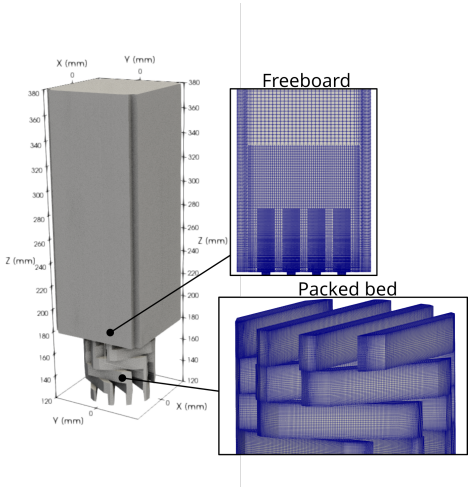

Figure 2. Domain used for the simulation with boundary-conforming mesh. Framed boxes illustrate the mesh used in the packed bed and the freeboard.

The time step of the simulation is adjusted to keep the Courant number under 0.6. Both spatial and temporal derivatives are computed using 2nd order schemes. PISO (Pressure-Implicit with Splitting of Operator) algorithm in the *consistent* variant is used to couple velocity and pressure, with 5 pressure corrector steps and 1 non-orthogonality correction step. To ensure that the flow is not influenced by initial conditions, sampling starts after an initial start-up time T_i which is presented along the sampling duration T_avg for all cases in table 1.

3.2. Simulations using the blocked-off method

The blocked-off method is based on creating an artificial boundary inside the computational grid. The current implementation is valid for particles of any shape and is described and validated in [5]. Flow variables in the cells obstructed by solid elements are set to the desired value which introduces a no-slip boundary condition at the solid-fluid interface. The original version by Patankar [4] involves the use of source terms. Here, we directly manipulate the coefficients in the system matrix to prevent complications in the calculation of residuals when solving the linear equation system. A general transport equation for a variable Φ, can be represented in algebraic form in any cell as $a_\mathrm{c}\Phi_\mathrm{C} + \sum_{N_\mathrm{c}} a_\mathrm{nb}\Phi_\mathrm{nb} = s_\Phi$, with a_c, a_nb and s_Φ denoting diagonal, non-diagonal matrix coefficients and source terms, respectively. Control volumes which are found to be in contact with a particle

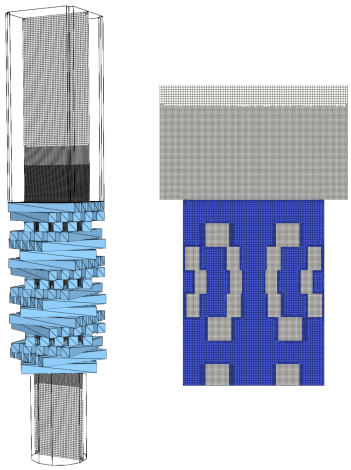

Figure 3. Particles and slice of mesh used in the blocked-off simulations. The right figure shows the mesh in the freeboard region with blocked fluid cells in blue.

are decoupled from the solution process by setting their non-diagonal contribution a_{nb} to zero and the diagonal coefficient a_{c} to one. Hence, inserting the desired value to the right-hand side results in specifying the cell value.

For the cells adjacent to these blocked volumes, the wall shear stresses are corrected to account for the case when particle faces are not aligned with the control volume faces. The stresses are estimated using tangential velocity and local distance from the particle surface, and used in a source term that replaces the viscous contribution at the solid-fluid interface in the momentum equation. Additionally, the Neumann boundary condition in the pressure equation at the solid-fluid interface is enforced by setting the matrix coefficient a_{nb} to a very low value.

The simulations using the blocked-off method are realized with the Bulk-Reaction DEM/CFD framework where a finite volume fluid solver based on *fireFoam* (OpenFOAM v2012) is utilized. The bars in the test rig are represented by cuboid particles which influence the fluid flow via the blocked-off methodology. Total of 90 cuboid particles are generated according to the bar dimensions and placed in the domain as in fig. 3. For the fluid flow computation, a cartesian grid fitted to the experimental rig is created. The dodecagon shape of the walls at the particle bed section is extended for the inlet. Mesh refinement is applied in the void spaces as well as up- and downstream of the particle region. In relation to the particle width, particles are discretised by $B/\Delta x = 20$ leading to a total number of 5.1M cells. The same mesh is used for all Reynolds numbers. The Courant number is kept between values of 0.1-0.3. The PISO algorithm is utilized to solve the evolution of the flow field with one non-orthogonal corrector step to account for the polyhedral cells at the walls of the test rig. In general, 2nd order schemes are applied in the discretisation of the transport equations, while for convection a 2nd order upwind scheme is employed to prevent pressure oscillations. Sampling times for averaging are reported in table 1.

4. RESULTS

4.1. Flow inside the bed

The flow inside the packed bed is visualised in detail in the figs. 4 and 5. In each of the figures, a coordinate system defined on the measurement plane is used, with ξ denoting the horizontal coordinate. Moreover, only the velocity components tangent to the measurement plane are plotted: w is the vertical velocity and u_ξ is the horizontal velocity along the measurement plane.

The velocity field is mainly determined by the adopted geometry and the connectivity between the void spaces in the layers. The P1 (position 1, see fig. 1) interstices have two inlets and two outlets, in a staggered arrangement due to the rotation of the module. The P3 interstice (position 3, see fig. 1) on the other hand have three inlets/outlets. In both P1 and P3 slits, the fluid is accelerated in the inlet and its further behaviour is determined by the positions of the outlets. In case of P1, the flow impinges on the top wall of the module and is forced to split into two outlets. This results in most of the flow converging from both inlets into the right outlet, while the rest is redirected into the left outlet, which has also a much smaller cross-section area. Inside P3, the outlets are much more closely aligned with the inlets, hence, a strong upwards flow can be observed. The regions positioned between the inlet/outlet pairs are characterised by a lateral flow, presumably driven by the pressure difference between these areas. This behaviour leads to the presence of recirculation regions, attached to the left side of the in-flowing streams.

Overall, the simulation results agree very well with the PIV measurements. The main differences can be observed in the far left and right areas of the measured regions. For example, for both Re, based on streamline visualisation, the PIV data indicates fluid crossing the boundary of the measured region on the left side of P1 and P3. This effect is observed due to the necessary modification of the geometry to enable the optical access to the interstices, which creates additional space on the left and right side (a standard module has a solid wall at these positions). Interestingly, this "outflow" is much stronger in P1 than P3, where the flow is directed more upwards near the left and right boundaries of the measurement region. It is probable that the impact of the modification of the geometry on the measured results is stronger in slits with stronger lateral flow.

On the other hand, simulation data suggests that the presence of the wall results in recirculation regions attached to the bottom left and top right corners of P1 region. The differences in the flow field

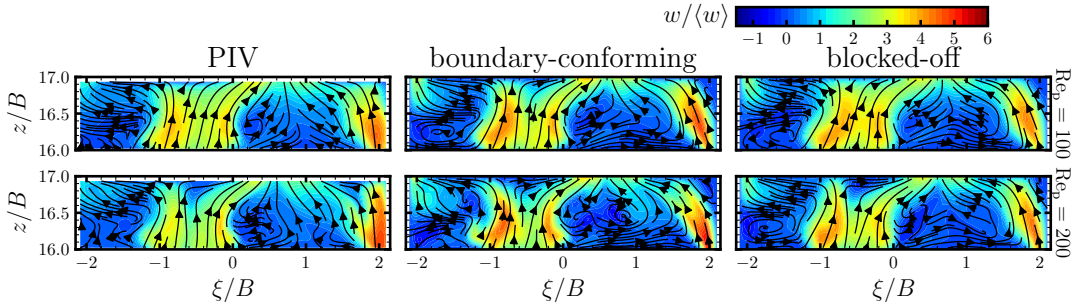

Figure 4. Velocity field at the measurement position 1 inside layer 17, visualised using streamlines. Color denotes the vertical component $w/\langle w\rangle$. Plotted data has been gathered using PIV and simulation approaches: boundary-conforming and blocked-off methods, at $\mathrm{Re_p} = 100$ (top) and 200 (bottom).

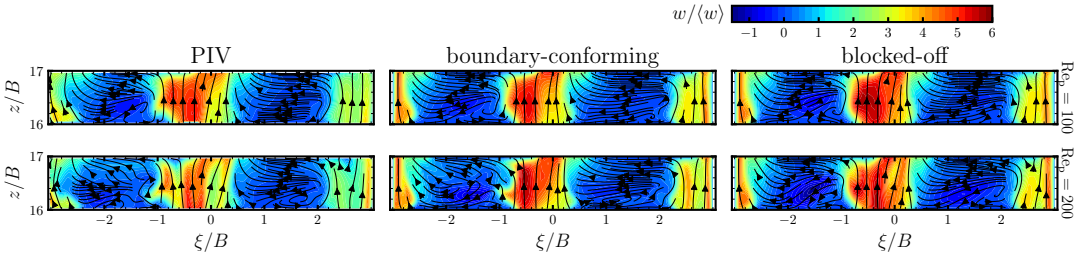

Figure 5. Velocity field at the measurement position 3 inside layer 17, visualised using streamlines. Colormap denotes the vertical component $w/\langle w\rangle$. Plotted data has been gathered using PIV and simulation approaches: boundary-conforming and blocked-off methods, at $\mathrm{Re_p} = 100$ (top) and 200 (bottom).

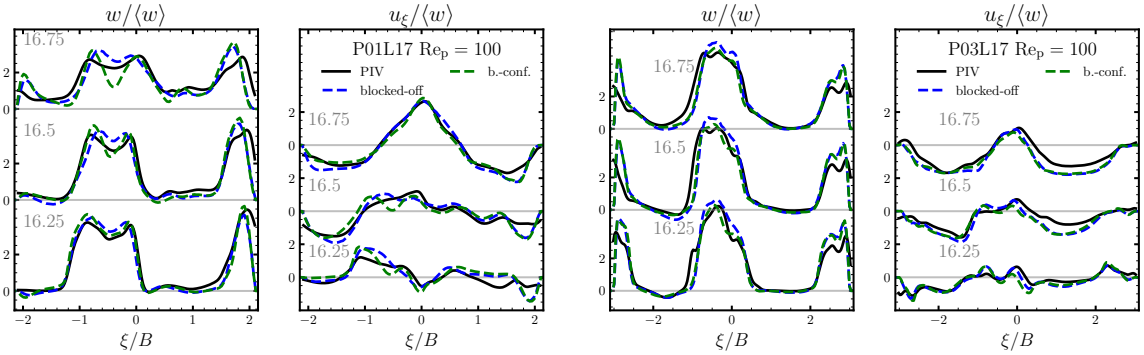

Figure 6. Velocity inside the bed for $\mathrm{Re_p} = 100$, plotted along the lines defined in planes P1 (left) and P3 (right) in the 17th layer. The gray numbers correspond to z/B coordinate.

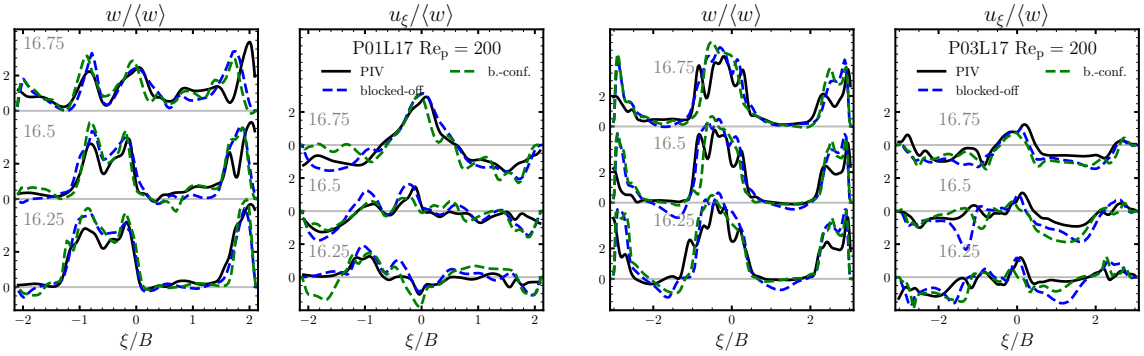

Figure 7. Velocity inside the bed for $\mathrm{Re_p} = 200$, plotted along the lines defined in planes P1 (left) and P3 (right) in the 17th layer. The gray numbers correspond to z/B coordinate.

near the side walls, can be observed in figs. 6 and 7. Both simulation approaches predict a different shape of boundary layer jets (P1 for large ξ and P3 for both sides of measurement region), with the simulations consistently overpredicting the maximum streamwise velocity in these regions. At the larger Reynolds number the differences between the measured and simulated flow fields grow larger. The differences between the numerical representations and real experimental setup have strong influence on the resulting flow field.

Although, the flow fields are largely similar across the two Reynolds numbers, the increase in the fluid's inertia influences the shapes and sizes of the separated flow regions. At P1, the increase of Reynolds number leads to a much more complex flow field between the two inlets, with recirculating flow appearing in the middle of the measurement section. At the other position, larger $\mathrm{Re_p}$ leads to increased separation on the right side of the measured region. On the left side, however, it seems that a faster reattachment can be observed. PIV data also indicates that the non-uniformity of the flow field is much stronger at larger $\mathrm{Re_p}$, although this effect is not fully represented in the simulation data.

Though the boundary-conforming and blocked-off approach yield different mesh refinements close to walls/particles (typical near-wall boundary layer refinement vs. equally spaced mesh), the line plots in figs. 6 and 7 show almost no difference in the prediction of the wall jets for $\mathrm{Re_p} = 100$ and slight differences for larger $\mathrm{Re_p}$. Especially in comparison to the deviation between simulations and experiment, these are negligible. Based on these results, the handling of the wall flow with the blocked-off approach seems to be appropriate for these Reynolds numbers. In general, the numerical methods align very well in the void space with only minor differences in height and shape of the jets. The strongest difference between the two simulation approaches are found for horizontal component u_ξ with $\mathrm{Re_p} = 200$ at P1 where a more pronounced horizontal motion in the recirculation region is predicted by the boundary-conforming method in contrast to the blocked-off approach and the experiment.

4.2. Freeboard

The flow field in the freeboard is visualised in fig. 8. It is dominated by jets issuing directly from the outlets of the last module. Hence, there are two and three jets present on planes P1 and P3, respectively. The resulting velocity field is quite complex with several recirculation regions present in between the jets and the walls of the model packed bed.

At lower $\mathrm{Re_p}$, in the P1 plane, the jets combine relatively quickly above the bed surface. At the sides of the measured region, the air is sucked into the freeboard from the outlet with relatively slow velocity, forming two large recirculation regions near the walls of the channel. As the Reynolds number increases, the momentum of the jets is redistributed laterally quicker by low-velocity vortical motions, resulting in a more uniform velocity in the middle of the outlet region. The interaction between both streams also results in a swirling flow between them, and smaller recirculation regions above the bed surface.

In the P3 plane, the effect of backflow into the freeboard from the outlet is much weaker, even at the lower Reynolds number. The leftmost jet impinges onto the downward moving air and is redirected, first, towards the bed surface, and into the middle jet. This phenomenon impacts the momentum distribution above the bed, and it could influence the scalar mixing in such systems as it reintroduces the gas which already left the reactor back into the bed. The increase of the inertial effects leads to more pronounced jets and, although, the left jet dissipates quicker then the other ones, much less of the ejected fluid is redirected into the middle one. Additionally, the unsteadiness at larger $\mathrm{Re_p}$ results in more diffusive behaviour of the jet downstream.

In general, a good agreement could be reached by the three methods especially for the low $\mathrm{Re_p}$ case. Figure 9 shows that the agreement is best in close distance to the bed surface. While excellent agreement of the boundary-conforming method is reached at $z/B = 19$, the blocked-off method predicts a too narrow jet on the left in P1 and a slight overshoot of the centre jet in P3 for the vertical velocity w, which also leads to a bigger discrepancy in the horizontal velocity component u_ξ.

As the distance from the bed surface increases, differences between simulations and the experiment get more pronounced. Here, the 3D interaction of the jets comes into play, causing small discrepancies in the jets to accumulate to larger deviations from experimental data. The errors in momentum prediction are probably caused by a limited resolution downstream of the bed surface diffusing and dampening the breakdown of the jets into smaller vortical structures. Alternatively, different conditions at the domain outlet (fixed pressure condition for simulations vs. small environmental interference in the experiment) may also contribute to different velocity fields above the bed.

Following the line plots of the higher Reynolds number in fig. 10, the agreement of the numerical data with the PIV data is again best close to the bed surface for P1. In the experiment and the blocked-off simulation the mean jets dissipate faster than in the body-conforming case. For P3, the outer jets are reproduced well but the centre jet shows a different flow structure with two velocity peaks in the numerical data for $z/B = 19$ and 21. Importantly, the accuracy of the simulation data might be limited by a relatively short averaging time (especially in case of the boundary-conforming method). Previous work [11] indicated that in such systems, exceedingly long averaging times are required to fully capture the dynamics of the freeboard. Although, the convergence

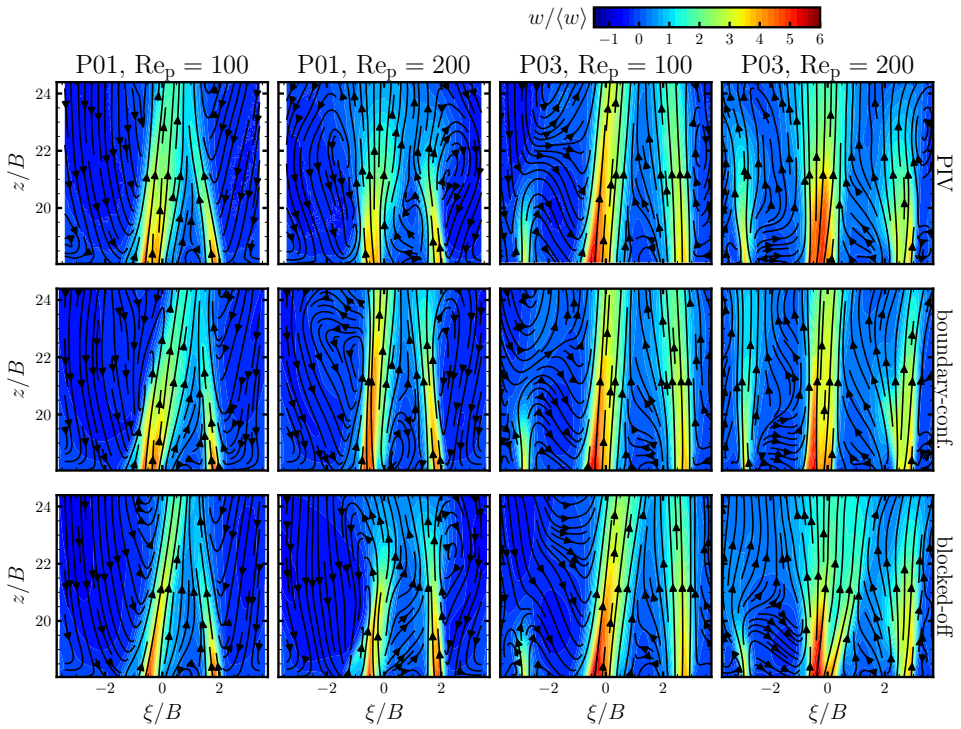

Figure 8. Velocity in the freeboard for $\mathrm{Re_p} = 100$, plotted along the lines defined in planes P1 (left) and P3 (right). The gray numbers correspond to z/B coordinate.

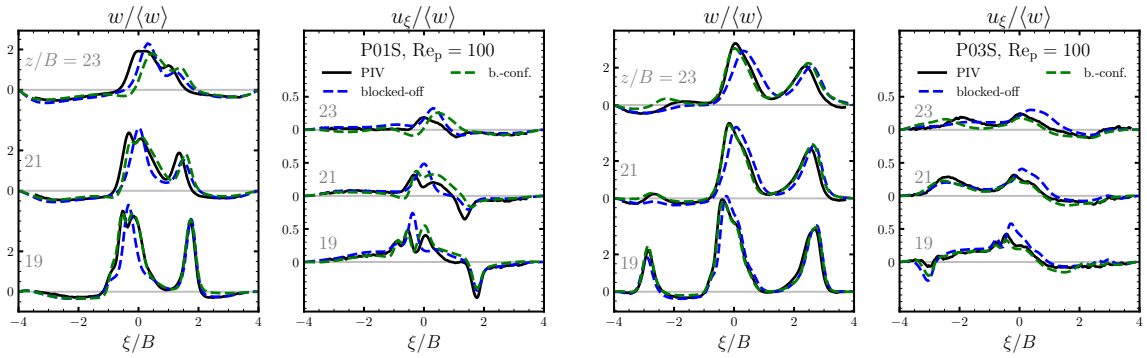

Figure 9. Velocity in the freeboard for $\mathrm{Re_p} = 100$, plotted along the lines defined in planes P1 (left) and P3 (right). The gray numbers correspond to z/B coordinate.

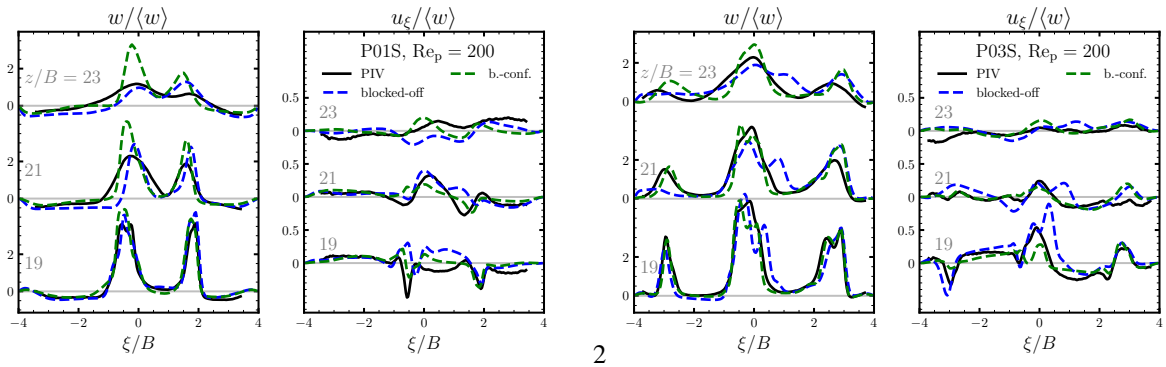

Figure 10. Velocity in the freeboard for $\mathrm{Re_p} = 200$, plotted along the lines defined in planes P1 (left) and P3 (right). The gray numbers correspond to z/B coordinate.

of statistics has to be further assessed the overall nature of the flow field is reproduced correctly by both simulation approaches.

5. CONCLUSIONS & OUTLOOK

In this contribution, the flow through a modular packed bed of bar-like particles and in the freeboard is examined by PIV measurements, and by conducting simulations with a boundary-conforming and a blocked-off approach. Two different Reynolds numbers are considered, Re_p = 100 and 200.

The flow inside the packed bed reveals good agreement between the experiment and simulations. Differences are majorly found due to geometry adjustments needed to measure the flow field between the particles. The increase of Reynolds number only slightly affects the flow features in the void spaces, which are determined to a large extent from the geometry and alignment of inlets/outlets in each interstice. While the simulation approaches do not show significant differences inside the bed, stronger deviations are found in the flow at the freeboard. The boundary-conforming simulations agree very well with experiments right at the bed surface while different rate of the dissipation of the jets issued into the freebord can be observed. Better agreement is found in the blocked-off cases but mismatches between the emerging jets are still visible, potentially due to an insufficient mesh refinement in the freeboard.

The blocked-off method has been found to capture adequately all flow features inside the bed, while allowing for minimisation of required mesh size and computational effort. The Non-Conformal Coupling interfaces coupling the modules in boundary conforming mesh, have resulted in stable and accurate solution, enabling the future studies of non-static packed beds with rotating modules. Further investigations of the current case are needed to fully assess the accuracy of the simulation approaches, concentrating on the fluctuations in the freeboard, the corresponding turbulent kinetic energy, and the influence of the averaging time on the results. Furthermore, higher Reynolds number cases would be of interest to get more knowledge about industrial packed beds' conditions.

ACKNOWLEDGEMENTS

This work was funded by the Deutsche Forschungsgemeinschaft (DFG, German Research Foundation) Project-ID 422037413 - TRR 287 and project number 279416000.

REFERENCES

[1] Rosseau, L. R., Middelkoop, V., Willemsen, H. A., Roghair, I., and van Sint Annaland, M., 2022, "Review on Additive Manufacturing of Catalysts and Sorbents and the Potential for Process Intensification", *Frontiers in Chemical Engineering*, Vol. 4.

[2] Moghaddam, E., Foumeny, E., Stankiewicz, A., and Padding, J., 2019, "Fixed bed reactors of non-spherical pellets: Importance of heterogeneities and inadequacy of azimuthal averaging", *Chemical Engineering Science: X*, Vol. 1, p. 100006.

[3] Jurtz, N., Kraume, M., and Wehinger, G. D., 2019, "Advances in Fixed-Bed Reactor Modeling Using Particle-Resolved Computational Fluid Dynamics (CFD)", *Reviews in Chemical Engineering*, Vol. 35 (2), pp. 139–190.

[4] Patankar, S., 1980, *Numerical Heat Transfer and Fluid Flow*, Hemisphere Publishing Company.

[5] Gorges, C., Brömmer, M., Velten, C., Wirtz, S., Mahiques, E. I., Scherer, V., Zähringer, K., and van Wachem, B., 2024, "Comparing two IBM implementations for the simulation of uniform packed beds", *Particuology*, Vol. 86, pp. 1–12.

[6] Brömmer, M., Scharnowski, M., Illana Mahiques, E., Wirtz, S., and Scherer, V., 2024, "Investigating the inflow into a granular bed using a locally resolved method", *Particuology*, Vol. 85, pp. 89–101.

[7] Illana Mahiques, E., Brömmer, M., Wirtz, S., and Scherer, V., 2023, "Locally Resolved Simulation of Gas Mixing and Combustion Inside Static and Moving Particle Assemblies", *Chemical Engineering & Technology*, p. ceat.202200622.

[8] Lovreglio, P., Das, S., Buist, K. A., Peters, E. A. J. F., Pel, L., and Kuipers, J. A. M., 2018, "Experimental and numerical investigation of structure and hydrodynamics in packed beds of spherical particles", *AIChE Journal*, Vol. 64 (5), pp. 1896–1907.

[9] Khayamyan, S., Lundström, T. S., Gren, P., Lycksam, H., and Hellström, J. G. I., 2017, "Transitional and Turbulent Flow in a Bed of Spheres as Measured with Stereoscopic Particle Image Velocimetry", *Transport in Porous Media*, Vol. 117 (1), pp. 45–67.

[10] Velten, C., and Zähringer, K., 2023, "Flow Field Characterisation of Gaseous Flow in a Packed Bed by Particle Image Velocimetry", *Transport in Porous Media*, Vol. 150, pp. 307–326.

[11] Sadowski, W., Sayyari, M., Di Mare, F., Velten, C., and Zähringer, K., 2024, "Particle-Resolved Simulations and Measurements of the Flow through a Uniform Packed Bed", *Physics of Fluids*, Vol. 36 (2), p. 023330.

Conference on Modelling Fluid Flow (CMFF'25)
The 19th International Conference on Fluid Flow Technologies
Budapest, Hungary, August 26-August 29, 2025

Enhancing DEM-CFD Simulations with Machine-Learning-Based Locally Resolved Nusselt Number Correlations

Ali Mjalled[1], Bo Jaeger[2], Reza Namdar[3], Lucas Mieg[1], Enric Illana[2], Fathollah Varnik[3], Viktor Scherer[2], Martin Mönnigmann[1]

[1] Automatic Control and Systems Theory, Ruhr-Universität Bochum. E-mails: {ali.mjalled, lucas.mieg, martin.moennigmann}@ruhr-uni-bochum.de
[2] Energy Plant Technology, Ruhr-Universität Bochum. E-mails: {jaeger, illana, scherer}@leat.ruhr-uni-bochum.de
[3] Interdisciplinary Centre for Advanced Materials Simulation. E-mails: {Reza.Namdarkedenji, fathollah.varnik}@ruhr-uni-bochum.de

ABSTRACT

Accurate prediction of heat transfer between solid particles and the surrounding gas is essential in discrete element method - computational fluid dynamics (DEM-CFD) simulations. Typically, these methods rely on empirical correlations of the Nusselt number (Nu) that provide only an averaged estimation of the heat transfer between the particles and the fluid. In light of this, we present in this paper a data-driven surrogate model that captures the local heat transfer on the particle surface and integrates it into the DEM-CFD simulation framework. The developed model is a Gaussian process (Nu-GP) that is trained using a database of 16 2D direct numerical simulations (DNS) of convective heat-transfer in air flow around an isolated circular particle with Reynolds numbers in the range $100 \leq \mathrm{Re} \leq 400$. The model uses the inlet Reynolds number and the local radial angle θ on the surface of the particle as inputs to predict the local Nusselt number. Comparisons to the DNS results demonstrate the ability of the Nu-GP to accurately predict the local Nusselt within the trained range. Furthermore, we show the Nu-GP model can be integrated into DEM-CFD and resolves the heat transfer on the particle surface with DNS accuracy with a negligible increase of computational cost compared to mean Nusselt correlations.

Keywords: DEM-CFD, Gaussian processes, lattice Boltzmann, Nusselt number

NOMENCLATURE

A	$[m^2]$	area
D	$[m]$	particle diameter
F	$[N]$	force
M_w	$[kg/mol]$	molecular weight
N_y, N_z	$[-]$	number of grid points
R	$[J/kg \cdot mol]$	universal gas constant
T	$[K]$	temperature
Nu	$[-]$	Nusselt number
Pr	$[-]$	Prandtl number
Re	$[-]$	Reynolds number
$\mathcal{D}$	$[-]$	training dataset
$\mathcal{K}$	$[-]$	GP covariance
$\mathcal{N}$	$[-]$	Gaussian distribution
c_p	$[J/kg \cdot K]$	specific heat capacity
l	$[m]$	length
p	$[-]$	probability
p_h	$[Pa]$	hydrodynamic pressure
p_t	$[Pa]$	thermodynamic pressure
$\underline{\underline{I}}$	$[-]$	identity matrix
$\underline{\underline{X}}$	$[-]$	training input matrix
$\underline{u}$	$[m/s]$	velocity
$\underline{x}$	$[-]$	training input vector
$\underline{y}$	$[-]$	training output vector
$\underline{\epsilon}$	$[-]$	noise
λ	$[W/m \cdot K]$	thermal conductivity
μ	$[Pa \cdot s]$	dynamic viscosity
ρ	$[kg/m^3]$	density
σ^2	$[-]$	variance
θ	$[^\circ]$	radial angle
$\underline{\phi}$	$[-]$	GP hyperparameters vector
$\underline{\underline{\tau}}$	$[Pa]$	viscous stress tensor
ε	$[-]$	porosity
ξ	$[-]$	GP mean

Subscripts and Superscripts

ref, surf	reference, surface
opt	optimal solution
b	body
t	time
$\bar{(\cdot)}$	spatial mean

1. INTRODUCTION

Particle-resolved direct numerical simulations (DNS) enable accurate predictions of heat transfer between solid particles and surrounding gas. These simulations require a finely resolved computational grid, at least an order of magnitude smaller than the (average) diameter of the particles. However, the substantial computational cost of DNS renders its application to flow fields in packed-bed configurations infeasible for many real-world scenarios. Instead, such systems are typically simulated using non-particle-resolved approaches, such as the discrete element method coupled with computational fluid dynamics (DEM-CFD) [1].

The computational cells in DEM-CFD are typically larger than the individual particles. Therefore, the heat transfer within the cell is approximated using spatially averaged values. To account for thermal effects, empirical correlations of the Nusselt (Nu) number are employed [2, 3]. While this approach enables faster simulations, it comes at the cost of reduced accuracy compared to DNS. To bridge this gap, the use of locally resolved Nusselt correlations in DEM-CFD has been proposed that provide more detailed thermal information within the computational cell [4]. Although many studies have investigated the local heat transfer at the particle surface [5, 6], relatively few have derived local models or correlations.

Notably, Haeri and Shrimpton [7] derived a correlation for the calculation of the local Nusselt number around a circular cylinder using trigonometric series with 13 coefficients. Each series is modelled as a 5th order polynomial in Reynolds (Re) and Prandtl (Pr) numbers within the ranges $10 \leq \mathrm{Re} \leq 250$ and $0.1 \leq \mathrm{Pr} \leq 40$. Similarly, Kravets and Kruggel-Emden [8] investigated local heat transfer and provided Nusselt correlations corresponding to $\mathrm{Pr} = 1$ for forced convection around an isolated sphere and random particle packings. Their correlations are applicable from low to moderate Reynolds numbers, i.e., $20 \leq \mathrm{Re} \leq 240$ for the single particle case, and $20 \leq \mathrm{Re} \leq 100$ for the packed-bed corresponding to porosity ε ranging from 0.6 and 1.0. To the best of our knowledge, no further local Nusselt number models or correlations for flow fields around solid bodies have been reported in the literature. Yet, we note that the local correlations have been developed in related applications, such as the local Nusselt correlations for circular impinging jet over a plate [9], and for nanofluids in circular horizontal tubes [10].

While the majority of heat transfer studies have relied on nonlinear regression to fit power-law Nusselt correlations, other machine learning methods have been also explored. For example, Urbina et al. [10] employed genetic programming to discover non-trivial local Nusselt correlations for nanofluids. Kahani et al. [11] used artifical neural networks and support vector machines to predict the average Nusselt number for TiO_2/water nanofluid flows. Similarly, Panda et al. [12] applied polynomial regression, random forest, and artifical neural networks to model average Nusselt values in heat exchanger with twisted tape inserts. More recently, Sanhueza et al. [13] utilized convolutional neural network to create detailed 2D maps of the local Nusselt number in turbulent flows over rough surfaces.

Despite recent advances, there remains a clear shortage in the literature regarding local Nusselt number correlations, especially for fluid flow around solid bodies. Accordingly, we aim in this work to develop a local Nusselt correlation using Gaussian processes (GP), which is, to the best of our knowledge, the first application of this machine learning method in this context. Specifically, we extend the Reynolds number range of the local correlations proposed by Haeri and Shrimpton [7] up to $\mathrm{Re} = 400$ with a fixed $\mathrm{Pr} = 0.7$. We aim to include our trained and validated GP within the DEM-CFD framework to obtain a locally resolved heat transfer on the particle surface in a non-particle-resolved framework.

The paper is organized as follows. Section 2 presents the DNS model. In Sec. 3, we derive the local and average Nusselt number correlations. Section 4 presents the DEM-CFD model with simulation results based on the derived local correlations. Conclusions and an outlook are stated in Sec. 5.

2. DNS SIMULATION SETUP AND DATA GENERATION

This section outlines the mathematical framework and numerical approach employed in the DNS, which are used to generate the database of the surrogate model. The simulations investigate convective heat transfer around a stationary circular particle, with air as the working fluid, over a range of Reynolds numbers.

2.1. Governing Equations

The flow and heat transfer are modeled using a thermal, compressible formulation under the low Mach number approximation. This allows for density variations driven by temperature changes, beyond the Boussinesq approximation. The governing equations include conservation of mass, momentum, and energy, and are given by

$$\partial_t \rho + \underline{\nabla} \cdot (\rho \underline{u}) = 0, \tag{1}$$

$$\partial_t (\rho \underline{u}) + \underline{\nabla} \cdot (\rho \underline{u} \otimes \underline{u}) = -\underline{\nabla} p_h + \underline{\nabla} \cdot \underline{\underline{\tau}} + \underline{F}_\mathrm{b}, \tag{2}$$

$$\rho c_p (\partial_t T + \underline{\nabla} \cdot \underline{u} T) = -\underline{\nabla} \cdot (\lambda \underline{\nabla} T) + \partial_t p_t, \tag{3}$$

$$\rho = \frac{p_t M_w}{RT}, \tag{4}$$

where, ρ, $\underline{u}$, p_h, $\underline{\underline{\tau}}$, and $\underline{F}_\mathrm{b}$ represent the gas density, velocity field, hydrodynamic pressure, viscous stress tensor, and body force per unit volume, respectively. T, c_p, λ, p_t, M_w, and R denote the temperature, specific heat at constant pressure, thermal conductivity, thermodynamic pressure, molecular weight, and the universal gas constant, respectively.

To capture the thermal expansion effects, the velocity divergence is computed from a combination of the continuity equation and the ideal gas law. Assuming a constant pressure, this yields

$$\underline{\nabla} \cdot \underline{u} = -\frac{1}{\rho}\frac{D\rho}{Dt} = \frac{1}{T}\frac{DT}{Dt}. \tag{5}$$

The dynamic viscosity is temperature-dependent and modeled using Sutherland's law

$$\mu(T) = \mu_{\text{ref}}\left(\frac{T}{T_{\text{ref}}}\right)^{3/2}\frac{T_{\text{ref}} + S}{T + S}, \tag{6}$$

where $\mu_{\text{ref}} = 1.68 \times 10^{-5} Pa \cdot s$, $T_{\text{ref}} = 273K$, and $S = 110.5K$ are reference values specific to air. With a fixed Prandtl number (Pr = 0.7), the thermal conductivity is computed as $\lambda = \mu c_p/\text{Pr}$. Local and average Nusselt numbers are defined as

$$\text{Nu}_i = \frac{D\,\lambda\,\frac{\partial T_i}{\partial n}\big|_{\text{surf}}}{\lambda_0(T_{\text{surf}} - T_{\text{inlet}})}, \tag{7}$$

$$\overline{\text{Nu}} = \frac{1}{A}\int_A \text{Nu}\, dA, \tag{8}$$

where λ and λ_0 are the gas thermal conductivities, respectively, calculated at surface temperature of cylinder and mean temperature $T_0 = (T_{\text{surf}} + T_{\text{inlet}})/2$. The symbol A represents the lateral surface area of the particle. In a discrete treatment, (8) can be approximated as $\overline{\text{Nu}} = \sum \text{Nu}_i/n_{\text{nodes}}$, where n_{nodes} denotes the total number of surface nodes and Nu_i the local Nusselt number. The temperature gradients (7) are approximated using a first-order-accurate finite-difference (FD) scheme, tuned to ensure that the total heat transfer matches the one computed between the inlet and outlet boundaries.

The above equations are solved using a hybrid numerical approach. Specifically, the lattice Boltzmann method (LBM) [14] is employed for solving the flow field, while the temperature field is evolved using a FD scheme. The reader is referred to Hosseini et al. [15] for more details related to the hybrid LBM-FD formulation.

2.2. Simulation setup

The simulations are conducted in a two-dimensional domain representing the flow of air around a stationary circular cylinder. The inlet boundary is subjected to a uniform velocity and temperature of $300K$, while the cylinder surface is held at a constant temperature of $301K$. Although the model is capable of accounting for thermal expansion effects, the temperature difference is deliberately kept small to suppress such influences and facilitate direct comparison with prior studies in the literature. No-slip boundary conditions are applied on the particle, with periodic boundaries along the lateral edges and a convective outflow condition at the outlet.

We consider Reynolds numbers in the range $\text{Re} \in [100, 400]$, defined based on the particle diameter D, inlet velocity, and inlet kinematic viscosity. Grid independence and time-step sensitivity analyses are performed to ensure accuracy. The convective and diffusive terms in the finite-difference method are discretized using a second-order central scheme, while the time integration employs a first-order explicit Euler scheme.

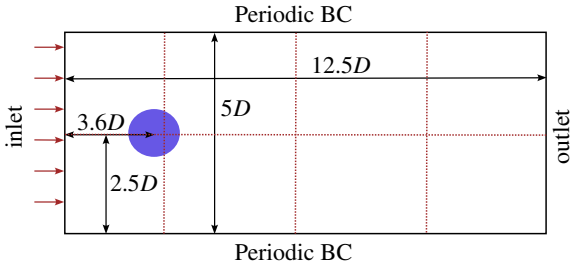

Figure 1. Schematic view of simulation setup. The red dashed lines denote the domain discretization used for the DEM-CFD simulation. D denotes the particle diameter.

After an initial transient period, the flow evolves into a repetitive pattern characterised by vortex shedding – commonly referred to as a Kármán vortex street. To avoid a bias from transient dynamics, the computation of the local Nusselt number is performed after the initial transient stage. These results on the local Nusselt number serve as the primary quantities of interest for thermal analysis and subsequent machine learning applications.

A sketch of the computational domain, including boundary conditions and geometric proportions, is shown in Figure 1. Additional details regarding the simulation parameters and flow properties are listed in Table 1, where N_y and N_z denote the total number of grid points along the lateral, y, and flow, z, directions, respectively (see Fig. 5 for the corresponding directions).

Table 1. Simulation parameters used in the study

Parameters	Values
Grid Size $[mm^2]$	0.0625
M_w $[kg/mol]$	0.02896
N_z, N_y	500, 200
c_p $[J/kg \cdot K]$	1005
Time Step $[s]$	4.0×10^{-4}

2.3. Model validation

In Fig. 2, we compare the local distribution of the Nusselt number with numerical benchmark results. Specifically, we compare our results to Kim & Choi [16] for Re = 120 and to Momose & Kimoto [17] and Zhang et al. [18] for Re = 218. The results show generally good agreement, with the LB-FD solver capturing the overall trend of the local Nusselt number distribution. However, minor discrepancies are observed, which can be attributed to the numerical model used. Specifically, LBM cannot achieve an orthogonal grid resolution with re-

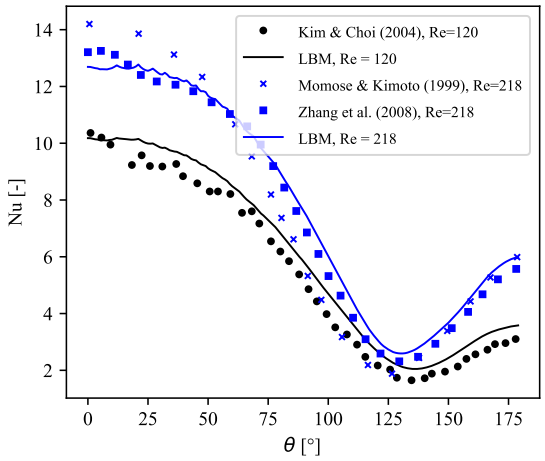

Figure 2. Validation of the model. The results are compared with Kim & Choi [16] for Re = 120 and Momose & Kimoto [17] and Zhang et al. [18] for Re = 218. The angle $\theta = 0°$ corresponds to the stagnation point of the flow.

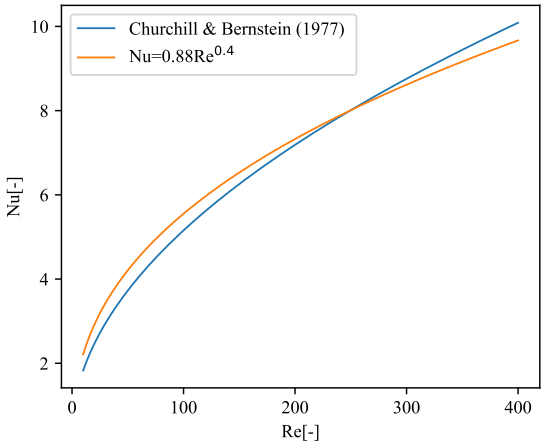

Figure 3. Comparison of steady-state average Nusselt values as function of the Reynolds number, based on (9) and Churchill & Bernstein's correlation (10).

spect to solid surfaces, requiring specialized treatments for curvature. In this study, a linear second-order bounce-back scheme is applied to approximate the exact position of the solid surface. While this approach yields reasonable results, some discrepancies may still arise due to the approximations in the representation of the boundary.

2.4. Average correlation

We fit an average steady-state Nusselt correlation using the available DNS database, in order to benchmark our results against established correlations from the literature. The resulting equation is given by

$$\overline{\mathrm{Nu}} = 0.88\mathrm{Re}^{0.4}. \tag{9}$$

Note that (9) does not depend on Pr number, as the training data are obtained from simulations with constant Pr = 0.7. We compare our results to Churchill & Bernstein's correlation for forced convection from gases and liquids to a circular cylinder in crossflow [19], which reads

$$\overline{\mathrm{Nu}} = 0.3 + \frac{0.62\,\mathrm{Re}_D^{1/2}\,\mathrm{Pr}^{1/3}}{\left[1 + (0.4/\mathrm{Pr})^{2/3}\right]^{1/4}} \times \left[1 + \left(\frac{\mathrm{Re}_D}{282\,000}\right)^{5/8}\right]^{4/5}. \tag{10}$$

The results are plotted in Fig. 3 for the range Re = [20, 400]. The two correlations show very good agreement, even in the range Re = [20, 100[that was not included during training. Overall, the maximum deviation is $\Delta\mathrm{Nu} \approx 0.48$ and occurs at Re = 40. This corresponds to a relative error of $\approx 14\%$.

3. LOCAL AND AVERAGE NUSSELT CORRELATIONS

3.1. Gaussian process regression

We consider a set of N training data points $\mathcal{D} = \{\underline{x}_i, \mathrm{Nu}_i\}_{i=1}^N$, where each $\underline{x} = [\mathrm{Re}, \theta]^T \in \mathcal{X} \subset \mathbb{R}^2$ denotes the input feature vector composed of the inlet Reynolds number and the local radial angle at the particle surface. The corresponding output Nu_i is obtained with (7). We note that the local Nusselt number values from each simulation are calculated by averaging the local values over all time steps after the transient phase. The start of this post-transient regime is identified by the appearance of the von Kármán vortex street in the wake of the cylinder.

We train a regression model $f : \mathcal{X} \to \mathbb{R}$ that maps the input feature vector $\underline{x}$ to the local Nusselt number on the particle surface for the configuration presented in Sec. 2. Since multiple regression functions may fit the data equally well, we adopt a Gaussian process (GP) prior over f, which provides distribution over functions and enables uncertainty quantification in the predictions. By definition, a GP is a collection of random variables, any finite number of which have a joint Gaussian distribution [20]. We assume that the prior of f is a GP and

$$f(\underline{x}) \sim \mathcal{GP}(\xi(\underline{x}), \mathcal{K}(\underline{x}, \underline{x}')), \tag{11}$$

where $\xi(\underline{x})$ is the mean function and $\mathcal{K}(\underline{x}, \underline{x}')$ is the covariance (or kernel) function describing the correlation between any pair of inputs $\underline{x}$ and $\underline{x}'$. The mean function $\xi(\underline{x})$ is chosen to be constant and equal to the mean of the training set. For the covariance function, we adopt a radial basis function (RBF) kernel, which is defined as

$$\mathcal{K}(\underline{x}, \underline{x}')) = \sigma_c^2 \exp\left(-\frac{(\mathrm{Re} - \mathrm{Re}')^2}{2l_{\mathrm{Re}}^2} - \frac{(\theta - \theta')^2}{2l_\theta^2}\right), \tag{12}$$

where σ_c^2 is the signal variance and $l_{(\cdot)}$ is the length scale of the corresponding input. These variables are treated as hyperparameters of the model.

Although our training data is generated from DNS, it is common in GPs to take measurement errors into consideration. Accordingly, we assume that the training outputs are corrupted by additive Gaussian noise $\epsilon \sim \mathcal{N}(0, \sigma_n^2)$, i.e.,

$$\mathrm{Nu}_i = f(\underline{x}_i) + \epsilon, \quad i = 1, \cdots, N, \tag{13}$$

where σ_n^2 is the noise variance and is considered as an additional hyperparameter.

Let $\mathcal{T} = \{\underline{x}_m^*\}_{m=1}^M$ be a collection of M test points, with each $\underline{x}_m^* = [\mathrm{Re}^*, \theta_m^*]^T$ comprising a new Reynolds number value, i.e., not used in the training dataset $\mathcal{D}$, and a local test angle θ_m^* on the particle surface. The goal is to predict the corresponding local Nusselt number at these test points. In GP regression, the joint distribution of the training outputs $\underline{y} = [\mathrm{Nu}_1, \cdots, \mathrm{Nu}_N]^T$ and the test outputs $\underline{y}^* = [\mathrm{Nu}_1^*, \cdots, \mathrm{Nu}_M^*]^T$ is a multivariate Gaussian. According to the conditional Gaussian theorem [21], the predictive distribution for $\underline{y}^*$, conditioned on the training data $(\underline{\underline{X}}, \underline{y})$ and test inputs $\underline{\underline{X}}^*$ is given by

$$p(\underline{y}^* | \underline{\underline{X}}, \underline{y}, \underline{\underline{X}}^*) = \mathcal{N}(\tilde{\xi}, \tilde{\mathcal{K}}), \tag{14}$$

where $\underline{\underline{X}}, \underline{\underline{X}}^*$ are the matrices of training and testing input features, respectively. Here, $\tilde{\xi}$ and $\tilde{\mathcal{K}}$ denote the mean and covariance of the posterior predictive distribution, and they are obtained using

$$\tilde{\xi} = \xi(\underline{\underline{X}}^*) + \mathcal{K}(\underline{\underline{X}}^*, \underline{\underline{X}}) \left(\mathcal{K}(\underline{\underline{X}}, \underline{\underline{X}}) + \sigma_n^2 \underline{\underline{I}} \right)^{-1} (\underline{y} - \xi(\underline{\underline{X}})), \tag{15}$$

$$\tilde{\mathcal{K}} = \mathcal{K}(\underline{\underline{X}}^*, \underline{\underline{X}}^*) - \mathcal{K}(\underline{\underline{X}}^*, \underline{\underline{X}}) \left(\mathcal{K}(\underline{\underline{X}}, \underline{\underline{X}}) + \sigma_n^2 \underline{\underline{I}} \right)^{-1} \mathcal{K}(\underline{\underline{X}}, \underline{\underline{X}}^*). \tag{16}$$

The hyperparameters of the GP, i.e., $\underline{\phi} = [\sigma_c^2, \sigma_n^2, l_{\mathrm{Re}}, l_\theta]^T$, have a strong influence on the prediction accuracy; therefore, they must be optimized. This is accomplished by maximizing the log-likelihood of training outputs $\underline{y}$ given the inputs $\underline{\underline{X}}$ and hyperparameters $\underline{\phi}$, i.e.,

$$\underline{\phi}_{\mathrm{opt}} = \underset{\underline{\phi}}{\mathrm{argmax}} \log(p(\underline{y} | \underline{\underline{X}}, \underline{\phi})), \tag{17}$$

where

$$\log(p(\underline{y} | \underline{\underline{X}}, \underline{\phi})) = -\frac{1}{2} \left(\underline{y} - \xi(\underline{\underline{X}}) \right)^T \left(\mathcal{K}(\underline{\underline{X}}, \underline{\underline{X}}) + \sigma_n^2 \underline{\underline{I}} \right)^{-1} \left(\underline{y} - \xi(\underline{\underline{X}}) \right) - \frac{1}{2} \log \left| \mathcal{K}(\underline{\underline{X}}, \underline{\underline{X}}) + \sigma_n^2 \underline{\underline{I}} \right| - \frac{N}{2} \log(2\pi). \tag{18}$$

The gradients of the log-likelihood with respect to every hyperparameter can be computed analytically. Therefore, the optimization problem shown in (17) can be efficiently solved using gradient-based optimization methods, e.g., L-BFGS [22] or conjugate gradient methods.

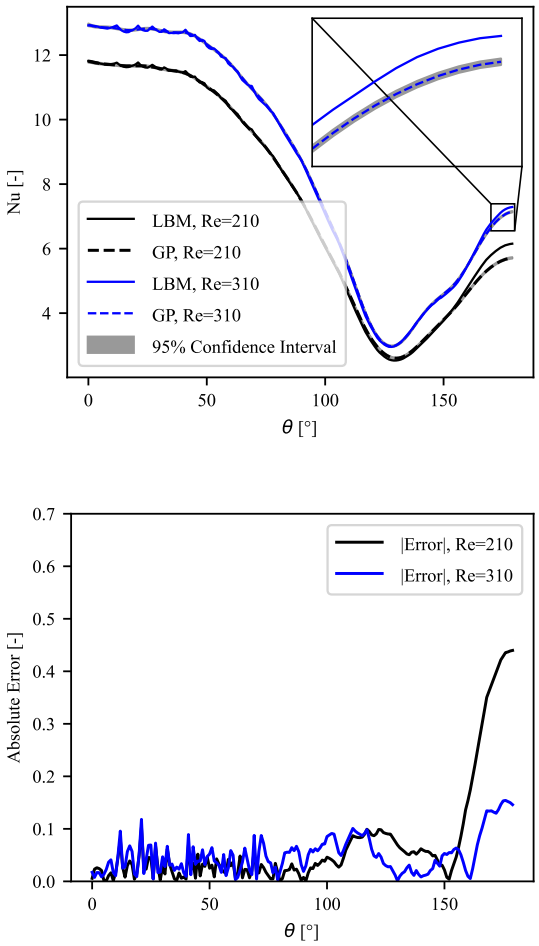

Figure 4. Top: GP evaluation for two test cases with Re = 210 and 310 with 95% confidence intervals. Bottom: Corresponding absolute prediction error. The angle $\theta = 0°$ corresponds to the stagnation point of the flow.

Once the hyperparameters have been optimized using $\mathcal{D}$, the GP model can be used for inference on an unseen test inputs by evaluating the posterior distribution according to Eqs. (14) to (16).

3.2. Training setup

Our training dataset $\mathcal{D}$ consists of 5760 training samples obtained by computing the local Nusselt number at every 1° increment along the particle surface, with 0° corresponding to the stagnation point. These values are extracted from 16 DNS simulations, each parameterized by a distinct inlet Reynolds number uniformly distributed in the range $[100, 400]$. In addition, we scale the input features of $\mathcal{D}$ between 0 and 1 to improve the numerical conditioning of the kernel matrix.

The hyperparameters $\underline{\phi}$ are optimized using the

L-BFGS algorithm provided by Scikit-learn [23]. We restart the optimization using 10 different initializations in the hyperparameter space to avoid poor local minima. The resulting optimal hyperparameter vector, identified using the scaled inputs, is $\underline{\phi} = [32.376, 1.71 \times 10^{-4}, 0.542, 0.01]^T$.

3.3. Gaussian Process model evaluation

We evaluate the accuracy of the model by comparing the local Nusselt values, predicted by the GP, to the ground truth values obtained from the DNS simulations for the test cases with Re = 210, 310. The corresponding root mean square errors (RMSE) are 0.14 and 0.09, respectively. Figure 4 shows the angular distribution of Nusselt number along the particle surface for the two considered test cases, along with the corresponding absolute prediction error. The results show that the GP is capable of accurately predicting the local Nusselt number values over the entire angular range, with near-perfect agreement except in the wake region behind the cylinder, where it slightly underestimates the Nusselt values. The reason for this discrepancy lies in the complex flow behavior in the wake region, where flow separation effects dominate. Specifically, the GP predicts temporally averaged local Nusselt values learned from the training data, which may not fully capture the influence of Reynolds number on the target values in this region. Moreover, the shaded gray region, which represents the 95% confidence interval, is extremely narrow, indicating high certainty in the predictions.

4. LOCALLY RESOLVED DEM-CFD SIMULATIONS

4.1. GP implementation in DEM-CFD framework

Gaussian Process DEM-CFD simulations for the setup described in Sec. 2.2 were carried out using the in-house DEM-CFD-code. We refer to [24, 25] for more details on the code. Here we focus on the integration of the GP into the DEM-CFD framework and highlight the benefits of using local Nusselt number model. First, to mimic the numerical conditions of unresolved 3D-DEM-CFD simulations, the fluid domain was deliberately meshed with a coarse grid consisting of (1x2x4) cells. This configuration ensures that the particle size remains much smaller than the CFD size $L_{\text{CFD, cell}}$, i.e., $L_{\text{CFD, cell}} \gg D$. Furthermore, only one cell constitutes the domain depth (x-direction) to enforce a quasi-2D flow configuration, which is comparable to the DNS setup. The grid of the fluid domain used is depicted in Fig. 1 with red dashed lines.

In the DEM approach, the particles are represented as polyhedra [26] with a discretized (triangulated) surface. This polyhedron representation has two advantages: First, any particle shape can be included and the local approach can later be easily translated to other particle shapes. Second, boundary conditions from the triangulated surface mesh can easily be translated to adjacent cells of an intra-particle tetrahedral mesh. The radial surface discretization of the circular particle is depicted in Fig. 5. We note that the particle depth is discretized using only one cell, analogous to the fluid domain.

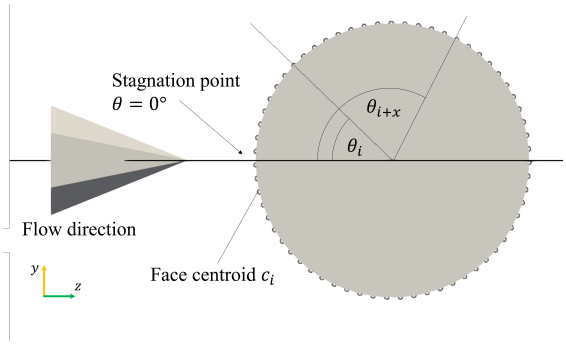

Figure 5. Radial discretization of the circular particle.

Our implementation of the GP within the DEM-CFD framework provides the Nu number distribution along the particle surface at every 1°, based on the inlet Reynolds number, which is readily available in the simulation. However, to project this distribution onto the particle faces in the DEM-CFD domain and assign the local Nusselt number Nu_θ, it is necessary to first identify the stagnation point on the particle surface ($\theta = 0°$). This is achieved by comparing the orientation of each particle face to the flow vector $\underline{u}$ obtained from the CFD solution. Once the stagnation point is known, the remaining θ_i are calculated during runtime from the face centroids c_i and the corresponding values of Nu_θ are assigned on the respective faces.

4.2. Results

The advantages of using the GP-Nu in DEM-CFD are obvious: While the simulation is unresolved ($L_{\text{CFD, cell}} \gg D$) and, therefore, local information of the fluid-solid heat transfer is not available, the GP provides Nu_θ on the particle surface with a DNS level of accuracy. This is particularly interesting if the external heat transfer is coupled to a resolved internal heat transport. An example of this is depicted in Fig. 6, which shows the temperature profiles of the disc for the locally resolved and mean case. It is evident from the temperature profiles that, due to the spatial resolution of Nusselt on the surface, the transient heat conduction inside the particle is more realistic than for a mean Nusselt value. As the Nusselt number at the stagnation point is the largest and drops to less than half its value on the back of the disc ($\theta > 90°$), the thermal front moving towards the disc core takes on a half-moon shape. Consequently, heat transfer in the particle is not uniformly directed towards the center of the particle as in the mean Nusselt case.

In Fig. 7, we compare the evolution of the mean

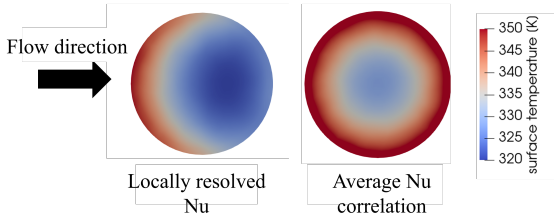

Figure 6. Temperature profiles at $t = 100s$, $T_{in} = 400K$ and Re = 100.

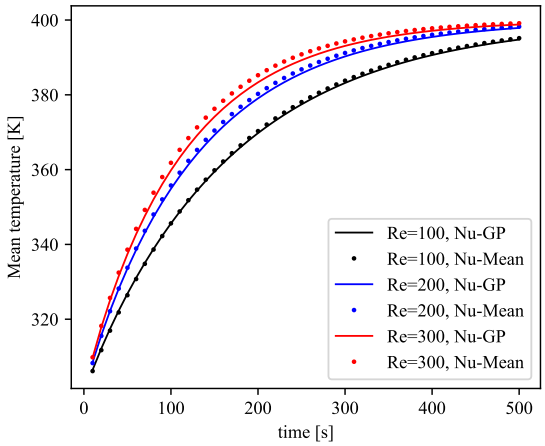

Figure 7. Temperature evolution for locally resolved GP DEM-CFD simulations and reference DEM-CFD for Re = 100, 200, 300.

particle temperature for the GP DEM-CFD model and the model that employs a mean Nusselt number for three different Reynolds numbers (Re = 100, 200, 300). As expected, the heating time of the particle is approximately the same for the two cases and the three respective Reynolds numbers, since the integral of Nu_θ (i.e. heat flux) in the GP case equals the mean Nusselt number value. Although mean temperatures are quite similar, temperature is not distributed radially uniform in the GP case, as shown before, and local surface temperature differences may lie in the range of $20 - 25K$ for the depicted cases.

Regarding the computational effort, the GP takes marginally more time to calculate the local Nu_θ, compared to using mean Nusselt values. This overhead is mainly attributed to computing a single Cholesky decomposition used for the matrix inversion given in Eqs. (15) and (16), which takes $\approx 3-4s$ to compute.

5. CONCLUSION

In this work, a local Gaussian process model for the Nusselt number (Nu-GP) has been presented. The GP was trained using a DNS database performed with the LBM to crossflow around an isolated circular cylinder, parameterized by Pr = 0.7 and $100 \leq \text{Re} \leq 400$. We first validated an LBM model against benchmark results from the literature, demonstrating good agreement with some deviations near the stagnation point. Subsequently, we trained a Gaussian Process to represent the LBM results at a low computational cost. The Gaussian Process achieves excellent accuracy on test cases when compared to the original LBM data, with a maximum RMSE of 0.14. Finally, we demonstrated that our GP-Nu can easily be integrated into a coupled DEM-CFD framework. We illustrated this integration with first GP-Nu DEM-CFD simulation results. Those show that GP-Nu models indeed provide locally resolved Nusselt numbers, while requiring only very little additional computational effort compared to mean Nusselt correlations.

The cylindrical particle case studied in this work constitutes a readily verifiable and thus essential step toward establishing a solid foundation for more complex particle geometries. This simplified scenario enables us to validate the approach before extending it to irregular shapes, which will require incorporating additional descriptors into the Gaussian Process model alongside Re and θ. In future work we aim to develop robust correlations that capture a broader spectrum of particle shapes and simulation setups, including cases involving denser particle packings.

ACKNOWLEDGEMENTS

Funded by the Deutsche Forschungsgemeinschaft (DFG, German Research Foundation) - Project-ID 422037413 - TRR 287.

REFERENCES

[1] Tsuji, Y., Kawaguchi, T., and Tanaka, T., 1993, "Discrete particle simulation of two-dimensional fluidized bed", *Powder Technology*, Vol. 77 (1), pp. 79–87.

[2] Gnielinski, V., 1976, "New equations for heat and mass transfer in turbulent pipe and channel flow", *International Chemical Engineering*, Vol. 16 (2), pp. 359–367.

[3] Wakao, N., and Kagei, S., 1982, *Heat and mass transfer in packed beds*, Vol. 1, Taylor & Francis.

[4] Sudbrock, F., Kruggel-Emden, H., Wirtz, S., and Scherer, V., 2015, "Convective drying of agitated silica gel and beech wood particle beds—experiments and transient DEM-CFD simulations", *Drying Technology*, Vol. 33 (15-16), pp. 1808–1820.

[5] Niazmand, H., and Renksizbulut, M., 2003, "Transient three-dimensional heat transfer from rotating spheres with surface blowing", *Chemical Engineering Science*, Vol. 58 (15), pp. 3535–3554.

[6] Kishore, N., and Ramteke, R. R., 2016, "Forced convective heat transfer from spheres to Newtonian fluids in steady axisymmetric flow regime

with velocity slip at fluid–solid interface", *International Journal of Thermal Sciences*, Vol. 105, pp. 206–217.

[7] Haeri, S., and Shrimpton, J., 2013, "A correlation for the calculation of the local Nusselt number around circular cylinders in the range $10 \leq \mathrm{Re} \leq 250$ and $0.1 \leq \mathrm{Pr} \leq 40$", *International Journal of Heat and Mass Transfer*, Vol. 59, pp. 219–229.

[8] Kravets, B., and Kruggel-Emden, H., 2017, "Investigation of local heat transfer in random particle packings by a fully resolved LBM-approach", *Powder Technology*, Vol. 318, pp. 293–305.

[9] Dhruw, L., Kothadia, H. B., and Rajagopal, A. K., 2023, "Local and area average Nusselt number correlation for a circular impinging jet over a flat plate", *Journal of Thermal Analysis and Calorimetry*, Vol. 148 (24), pp. 14031–14050.

[10] Guzman-Urbina, A., Fukushima, K., Ohno, H., and Fukushima, Y., 2023, "Deriving local Nusselt number correlations for heat transfer of nanofluids by genetic programming", *International Journal of Thermal Sciences*, Vol. 192, p. 108382.

[11] Kahani, M., Ahmadi, M. H., Tatar, A., and Sadeghzadeh, M., 2018, "Development of multilayer perceptron artificial neural network (MLP-ANN) and least square support vector machine (LSSVM) models to predict Nusselt number and pressure drop of TiO2/water nanofluid flows through non-straight pathways", *Numerical Heat Transfer, Part A: Applications*, Vol. 74 (4), pp. 1190–1206.

[12] Panda, J. P., Kumar, B., Patil, A. K., Kumar, M., and Kumar, R., 2023, "Machine learning assisted modeling of thermohydraulic correlations for heat exchangers with twisted tape inserts", *Acta Mechanica Sinica*, Vol. 39 (1), p. 322036.

[13] Sanhueza, R. D., Akkerman, I., and Peeters, J. W., 2023, "Machine learning for the prediction of the local skin friction factors and Nusselt numbers in turbulent flows past rough surfaces", *International Journal of Heat and Fluid Flow*, Vol. 103, p. 109204.

[14] Succi, S., 2001, *The lattice Boltzmann equation: for fluid dynamics and beyond*, Oxford University Press.

[15] Hosseini, S. A., Safari, H., Darabiha, N., Thévenin, D., and Krafczyk, M., 2019, "Hybrid lattice Boltzmann-finite difference model for low Mach number combustion simulation", *Combustion and Flame*, Vol. 209, pp. 394–404.

[16] Kim, J., and Choi, H., 2004, "An immersed-boundary finite-volume method for simulation of heat transfer in complex geometries", *KSME International Journal*, Vol. 18 (6), pp. 1026–1035.

[17] Momose, K., and Kimoto, H., 1999, "Forced convection heat transfer from a heated circular cylinder with arbitrary surface temperature distributions", *Heat Transfer—Asian Research: Co-sponsored by the Society of Chemical Engineers of Japan and the Heat Transfer Division of ASME*, Vol. 28 (6), pp. 484–499.

[18] Zhang, N., Zheng, Z., and Eckels, S., 2008, "Study of heat-transfer on the surface of a circular cylinder in flow using an immersed-boundary method", *International Journal of Heat and Fluid Flow*, Vol. 29 (6), pp. 1558–1566.

[19] Churchill, S. W., and Bernstein, M., 1977, "A correlating equation for forced convection from gases and liquids to a circular cylinder in cross-flow", *International Journal of Heat and Mass Transfer*.

[20] Williams, C. K., and Rasmussen, C. E., 2006, *Gaussian processes for machine learning*, Vol. 2, MIT Press Cambridge, MA.

[21] Murphy, K. P., 2012, *Machine learning: a probabilistic perspective*, MIT press.

[22] Liu, D. C., and Nocedal, J., 1989, "On the limited memory BFGS method for large scale optimization", *Mathematical Programming*, Vol. 45 (1), pp. 503–528.

[23] Pedregosa, F., Varoquaux, G., Gramfort, A., et al., 2011, "Scikit-learn: Machine Learning in Python", *Journal of Machine Learning Research*, Vol. 12, pp. 2825–2830.

[24] Illana Mahiques, E., Brömmer, M., Wirtz, S., and Scherer, V., 2023, "Locally Resolved Simulation of Gas Mixing and Combustion Inside Static and Moving Particle Assemblies", *Chemical Engineering & Technology*, Vol. 46 (7), pp. 1362–1372.

[25] Abdi, R., Jaeger, B., Illana, E., Wirtz, S., Schiemann, M., and Scherer, V., 2025, "Modelling of heat transfer in moving granular assemblies with a focus on radiation using the discrete ordinate method: A DEM-CFD approach", *Particuology*, Vol. 100, pp. 78–94.

[26] Höhner, D., Wirtz, S., and Scherer, V., 2012, "A numerical study on the influence of particle shape on hopper discharge within the polyhedral and multi-sphere discrete element method", *Powder Technology*, Vol. 226, pp. 16–28.

Conference on Modelling Fluid Flow (CMFF'25)
The 19th International Conference on Fluid Flow Technologies
Budapest, Hungary, August 26-August 29, 2025

An Open Workflow for Unsupervised Clustering of Fluid-Particle Flows into Compartments

Michael Mitterlindner[2], Daniel Berger[3], Maximilian Graber[3], Regina Kratzer[4], Markus Reichhartinger[3], Stefan Radl[1]

[1] Corresponding Author. Institute of Process and Particle Engineering, Graz University of Technology. Inffeldgasse 13/III, Graz, Austria. Tel.: +43 316 873 - 30412, E-mail: radl@tugraz.at
[2] Institute of Process and Particle Engineering, Graz University of Technology. Inffeldgasse 13/III, Graz, Austria. E-mail: mitterlindner@tugraz.at
[3] Institute of Automation and Control, Graz University of Technology. Inffeldgasse 21/B/I, Graz, Austria. E-mail: markus.reichhartinger@tugraz.at
[4] Institute of Biotechnology and Biochemical Engineering, Graz University of Technology. Petersgasse 10-12/I, Graz, Austria. E-mail: regina.kratzer@tugraz.at

ABSTRACT

We present a workflow for the unsupervised clustering of fluid–particle flows into distinct compartments based on open-source tools. Our aim is to enhance the understanding of complex multiphase flow systems - prevalent in many chemical and biochemical reactors - by using models consisting of such compartments. The proposed methodology integrates computational fluid dynamics (CFD) simulations with unsupervised machine learning (i.e., clustering algorithms) to identify coherent flow regions (i.e., compartments) without prior labelling. Our workflow is fully automated and designed for reproducibility, with a modular structure that allows for an easy adaptation to various flow systems. The results demonstrate that our approach can successfully capture essential flow features and partition the domain into meaningful compartments. This facilitates direct use in compartment models, which reduces computational costs in larger-scale simulations. Our findings suggest that unsupervised machine learning algorithms are mature enough to simplify complex multiphase systems in a largely automated fashion, making them a valuable tool for both academic research and industrial applications.

Keywords: CFD, multiphase, compartment modelling, bioreactor, clustering, unsupervised learning

NOMENCLATURE

C	$[-]$	cluster
Da	$[-]$	Damköhler number
H	$[m]$	channel height
J_C	$[-]$	clustering objective for the k-means algorithm
$J_{\dot{V}}$	$[-]$	optimization objective flow rate adaption
L	$[m]$	channel length
S	$[\frac{kmol}{m^3 s}]$	additional sources or sinks
V_R	$[m^3]$	volume of compartment
c	$[kmol/m^3]$	concentration of species
c^*	$[-]$	dimensionless concentration of species
k	$[s^{-1}]$	reaction rate constant
$k_L a$	$[s^{-1}]$	volumetric mass transfer coefficient
n_c	$[-]$	number of compartments
n_k	$[-]$	number of clusters
n_x	$[-]$	number of datapoints
$n_{cells,min}$	$[-]$	minimum number of CFD cells required per cluster
r	$[\frac{kmol}{m^3 s}]$	reaction rate
v_1	$[m/s]$	velocity of the moving top wall
$v_{\max}$	$[m/s]$	maximum velocity of the flow profile
$\dot{V}$	$[m^3/s]$	flow rate
$\underline{\underline{\dot{V}}}$	$[m^3/s]$	flow rate matrix
$\underline{\underline{\dot{V}}}'$	$[m^3/s]$	optimized flow rate matrix
$\underline{v}$	$[m/s]$	velocity vector with the components v_1 and v_2
$\underline{x}$	$[-]$	feature vector from data matrix
α	$[-]$	volume fraction
λ	$[-]$	regularization parameter
μ	$[-]$	cluster average
v_{thresh}	$[-]$	threshold for reassignment condition based on volume
τ_R	$[s]$	residence time
$\underline{\xi}_1^*$	$[-]$	dimensionless axial coordinate
$\underline{\xi}_2^*$	$[-]$	dimensionless transverse coordinate

C	[−]	set of clusters
C_i	[−]	cluster subset of $\mathcal{X}$
$\mathcal{X}$	[−]	data set

Subscripts and Superscripts

in	at the inlet
out	at the outlet
φ	for each phase

1. INTRODUCTION

Accurate prediction of large-scale multi-species gas-liquid bioreactor performance is essential for advancing biotechnological applications. For example, *Cupriavidus necator* bacteria within multiphase bioreactors may produce valuable products such as the polymer Polyhydroxybutyrate (PHB) [1], or food proteins. These systems often involve two-phase flows, in which the dissolution of key gases like O_2, CO_2, and H_2 significantly impacts reactor performance. However, the complexity of these systems requires advanced modelling techniques to capture the interplay between flow dynamics and chemical reactions.

Despite progress in computational fluid dynamics (CFD) and compartment modelling, several gaps in our scientific understanding of such reactors remain. Unsupervised machine learning algorithms can assist in finding patterns in the large datasets generated by CFD simulations. For instance, Laborda et al. [2] used unsupervised clustering on CFD and experimental data to identify flow regimes in bioreactors. While their custom k-means algorithm ensured spatial continuity and optimal compartment count, the study focused solely on regime identification without integrating chemical reaction networks (CRNs), or predicting reactor performance. Le Nepvou de Carfort et al. [3] proposed a fully automated CFD-based method for generating 3D compartment models using structured grids. Although their approach enabled real-time bioreactor simulations, it was constrained to Cartesian grids and lacked validation for non-ideal geometries. Savage et al. [4] combined CFD, high-dimensional design spaces, and Bayesian optimisation to improve reactor geometries with respect to flow behaviour and mixing characteristics. However, their work focused on the reactor design and did not address (bio-)chemical reaction kinetics, or propose a method to create to compartment models. Savarese et al. [5] developed a CRN generation method using unsupervised clustering and graph algorithms for combustion in CFD simulations. While effective for predicting NO_x emissions, their approach was limited to single-phase systems and consequently an application to multiphase bioreactors or biochemical reaction networks cannot be realized. Other studies, such as Tajsoleiman et al. [6] and Delafosse et al. [7], introduced automated CFD-based zoning and compartment models for stirred bioreactors. However, these methods were either geometry-specific, lacked spatial continuity enforcement, or did not integrate biochemical reactions or a fully automated zoning algorithm.

1.1. Goals of our Contribution

Given the limitations of CFD simulations in modelling detailed chemical reactions, our present study aims to identify meaningful compartments, and subsequently solve the equations that govern the resulting compartment model (CM). By leveraging analytical solutions, we validate the CM for flows between two infinite plates, including single-phase flow with reactions and two-phase flow with mass transfer.

Therefore, we utilise the codebase from Savarese et al. [5] and developing it further into our own tool box called CLARA (CLustering AlgoRithm Austria). To perform the clustering and compartment generation, simulation data is needed. We added two new simulation tool options from which the data can be read by CLARA. These tools are (i) OpenFOAM®, a classic open-source CFD tool, and (ii) SimVantage®, a commercial bioreactor CFD simulation tool developed by the SimVantage GmbH. The SimVantage® software uses the Lattice Boltzmann method (LBM) for simulating complex flows, including multi-phase and multi-component systems. With the integration of these tools, we have two powerful options for simulating complex flows in bioreactors, allowing us to accurately capture the dynamics of gas-liquid interactions therein. Our clustering and compartmentalization tool, CLARA, will soon be available as an open-source tool.

Our long-term vision is to develop a fast and reliable tool for optimising bioreactor reactor design, akin to the approach presented in [4], which showed that it is crucial to scan the design space and find the "best" geometrical design of a device. The tool will be useful for the process optimization of the gas-fermentation bioreactor as shown in [1]. Due to regulatory restrictions and safety issues, which arise due to the highly explosive medium (hydrogen and oxigen), it is vital to have an excellent understanding of transport phenomena in bioreactors to avoid explosive gas mixtures. A secondary vision is to develop a physics-informed model capable to be used for the design of model-based automatic control algorithms, and which can be exploited to optimise reactor performance during operation. This is particularly important for bioreactors, as they are complex systems with many variables that need to be controlled.

2. METHODS

In this section, we describe the methods used to achieve the goals outlined in the previous chapter. We begin by discussing the integration of OpenFOAM® and SimVantage®, followed by a detailed explanation of the clustering process, including feature selection and graph reassignment. We then present the compartment model equations and the optimisation process for inconsistent flow rates.

Specifically, the overall clustering process involves reading in field values, calculating volume flow rates over faces, and selecting relevant features for the core clustering step. Once the clustering is performed, graph reassignment ensures spatial continuity of the clusters. After the clustering is completed, we will call these clusters compartments as each represents a theoretical compartment in a reactor. The next step is to calculate the compartment attributes such as volume, flow rate matrix, temperature and, for multiphase systems, the volumetric mass transfer coefficient ($k_L a$). If mass balance inconsistencies are detected, an optimisation step is applied to correct them. Finally, boundary conditions for the compartment model (CM) are selected, including flow rates and concentrations, which are then passed to the CM solver. In order to ensure the quality of the code, analytical solutions are used to verify the results. Specifically, we test the performance of the CM with simple chemical reactions and mass transfer scenarios.

2.1. Integration of OpenFOAM® and SimVantage®

The integration of OpenFOAM® and SimVantage® with CLARA is achieved through a custom Python interface. This interface allows for seamless communication between the two software packages (i.e., OpenFOAM® or SimVantage® and CLARA), enabling the transfer of data and results. For the LBM method (which is used in SimVantage®), face fluxes must be calculated as a post processing step to obtain the volumetric flow rates as these are not used in a classical LBM-based simulation. This is especially critical for moving boundaries, such as the stirrer, where some cells are partly solid and partly fluid.

2.2. Clustering

To perform clustering, we must carefully select the features that represent the underlying physics of the system. These features are derived from CFD simulations and typically include flow-relevant quantities such as velocity, residence time, or turbulence intensity. It is recommended not to use concentration as a feature, since we simulate only until the flow reaches a quasi-steady state, long before the concentration field has fully evolved. This is particularly relevant in bioreactors, where bio-reactions involving bacteria often take several days to produce measurable outputs due to the inherently slow biological processes. Simulating such long timescales with CFD alone would be computationally prohibitive. Instead, we simulate the flow dynamics until a statistically steady state is reached and then use the compartment model (CM) to predict long-term concentration behaviour. This approach maintains accuracy while reducing computational cost. To enhance the clustering, it is also useful to include statistical measures such as the mean and standard deviation of time-dependent features, allowing the method to capture the unsteady or turbulent characteristics of the flow.

The core clustering step uses the k-means algorithm, which partitions the dataset into n_k distinct, non-overlapping clusters. The dataset consists of n_x feature vectors $\mathcal{X} = \{\underline{x}_1, \ldots, \underline{x}_{n_x}\}$. Each cluster $C_i \subseteq \mathcal{X}$, with $i = 1, \ldots, n_k$, is a subset of the data. The algorithm assigns each feature vector $\underline{x}_j$ to one of the clusters via the mapping $\underline{x}_j \mapsto C_i$. Each cluster has a centroid $\underline{\mu}_i$, defined as the mean of all feature vectors in that cluster $\underline{\mu}_i = \frac{1}{|C_i|} \sum_{\underline{x}_j \in C_i} \underline{x}_j$. where $|C_i|$ denotes the number of elements in C_i.

Each vector is then assigned to the cluster with the nearest centroid (in terms of Euclidean distance). The centroids are recalculated iteratively until the assignments no longer change, indicating convergence. The k-means algorithm minimizes the following objective function:

$$J_C = \sum_{i=1}^{n_k} \sum_{\underline{x}_j \in C_i} \|\underline{x}_j - \underline{\mu}_i\|^2. \tag{1}$$

To ensure cluster connectivity, a graph reassignment algorithm is applied. This algorithm checks each cluster for disconnected components and reassigns them based on a connectivity criteria (e.g. spatially next cluster). Additionally, thresholds can be defined to trigger reassignment. For example, a compartment must contain a minimum number of CFD cells (see Eq. 2) or a minimum volume (see Eq. 3). The reassignment conditions are:

$$\texttt{reassign}(C_i) \iff |C_i| < n_{cells,min} \tag{2}$$

$$\texttt{reassign}(C_i) \iff \sum_{\underline{x}_j \in C_i} V(\underline{x}_j) < \nu_{\text{thresh}} \cdot V_{\text{total}} \tag{3}$$

After clustering is completed, each cluster is converted into a compartment, as compartments can hold additional attributes. The number of clusters n_k is therefore equal to the number of compartments n_c.

2.2.1. Mass Conservation and Flow Balance

For a network of compartments, the flow rate matrix $\underline{\underline{\dot{V}}}$ represents the flow rates between the compartments via a two-dimensional matrix. These flow rates are derived by summing the volume flows extracted from the simulation data. Let $\underline{\dot{V}}_{\text{in}}$ and $\underline{\dot{V}}_{\text{out}}$ represent the external inflows and outflows, respectively, for each compartment. The system must satisfy mass conservation, which is expressed mathematically in Eq. 4:

$$\sum_{j=1}^{n_c} \dot{V}_{ij} - \sum_{j=1}^{n_c} \dot{V}_{ji} + \dot{V}_{\text{in}_i} - \dot{V}_{\text{out}_i} = 0 \quad \forall i \tag{4}$$

In this equation, $\dot{V}_{ij}$ represents the flow rate from compartment i to compartment j, while $\dot{V}_{ji}$ denotes

the flow rate from compartment j to compartment i. The terms $\dot{V}_{\text{in}_i}$ and $\dot{V}_{\text{out}_i}$ correspond to the external inflow and outflow rates for compartment i, respectively. Finally, n_c is the total number of clusters in the system. This equation ensures that the net flow into each compartment, considering both internal and external flows, is zero. It is important to note that for two-phase systems, achieving mass conservation can be challenging, as the mass transfer between the phases must be considered.

2.2.2. Optimisation of Flow Rates

To address inconsistencies in flow rates, an optimisation process is applied. The objective is to adjust the flow rate matrix $\underline{\underline{\dot{V}}}$ to minimise deviations from the initial values while ensuring mass conservation. The optimisation problem is defined by the objective function in Eq. 5:

$$J_{\dot{V}} = \sum_{i,j}^{n_c} (\dot{V}'_{ij} - \dot{V}_{ij})^2 + \lambda \sum_{i,j}^{n_c} \dot{V}'^2_{ij} \tag{5}$$

In this equation, $\dot{V}'_{ij}$ represents the optimised flow rates, which are adjusted to satisfy mass conservation while minimising deviations from the initial flow rates $\dot{V}_{ij}$. The parameter λ is a regularization term that penalizes large flow rates, thereby preventing excessive deviations and ensuring a more stable solution. A rule of thumb for estimating this regularization term is $\lambda \approx \frac{1}{||\underline{\underline{\dot{V}}}||^2}$. This approach ensures that the optimisation process maintains the integrity of the flow distribution across the clusters.

The optimisation is subject to the mass balance constraint, as shown in Eq. 6:

$$\sum_{j=1}^{n_c} \dot{V}'_{ij} - \sum_{j=1}^{n_c} \dot{V}'_{ji} + \dot{V}_{\text{in}_i} - \dot{V}_{\text{out}_i} = 0 \quad \forall i \tag{6}$$

This constraint ensures that the optimised flow rates satisfy mass conservation for each cluster. The terms in Eq. 6 are defined similarly to those in Eq. 4.

The optimisation problem is solved using Sequential Least Squares Quadratic Programming (SLSQP), an iterative method suitable for constrained optimisation. The solution is bounded to ensure positive flow rates. Additionally, flow rates which are under a certain threshold will be kept/set to zero, so that it is ensured that spatially not connected compartments remain not connected. This approach ensures minimal adjustments to the flow rates while maintaining the integrity of the flow distribution across the clusters.

2.3. Compartment attributes

The next step is to calculate the compartment attributes like volume, temperature, and also for a multiphase system the $k_L a$ value. For a two phase system the volume of the phase is used as the compartment volume ($\alpha_\varphi \cdot V$).

2.4. Compartment Model Equations

In the context of a bioreactor, k-Means can be used to cluster different regions based on certain characteristics, such as concentration or reaction rates, to form different compartments which can then be solved. This is very similar to a Chemical Reactor Network (CRN), or as we call it, the compartment model.

The compartment model (CM) simplifies a complex system by dividing it into compartments, each representing a distinct region or phase. The CM equations describe the mass balance of species within each compartment, accounting for inflows, outflows, reactions, and other processes. The governing equation for the liquid phase is given in Eq. 7:

$$\begin{aligned}\frac{dc_{\varphi,i,j}}{dt} =& \frac{\sum_k^{n_c} \dot{V}_{\varphi,i,k\to j} c_{\varphi,i,k} - \sum_k^{n_c} \dot{V}_{\varphi,i,j\to k} c_{\varphi,i,j}}{V_{R,\varphi,j}} \\ &+ \frac{\dot{V}_{\text{in}_{\varphi,i,j}} c_{\text{in}_{\varphi,i,j}} - \dot{V}_{\text{out}_{\varphi,i,j}} c_{\text{out}_{\varphi,i,j}}}{V_{R,\varphi,j}} + r_{\varphi,i,j} + S_{\varphi,i,j}\end{aligned} \tag{7}$$

In this equation, $c_{\varphi,i,j}$ represents the concentration of species i in compartment j. The terms $\dot{V}_{\varphi,i,k\to j}$ and $\dot{V}_{\varphi,i,j\to k}$ denote the flow rates of species i into and out of compartment j, respectively. These flow rates account for the transport of species between compartments. The external inflow and outflow rates of species i for compartment j are represented by $\dot{V}_{\text{in}_{\varphi,i,j}}$ and $\dot{V}_{\text{out}_{\varphi,i,j}}$, respectively. The volume of compartment j is denoted by $V_{R,\varphi,j}$, which is used to normalize the mass balance equation. The reaction rate of species i in compartment j is represented by $r_{\varphi,i,j}$, which accounts for the chemical reactions occurring within the compartment. Finally, S_φ represents additional sources or sinks, such as mass transfer from other phases. This term ensures that all external contributions to the species concentration are included in the model.

The CM equations are solved numerically using standard ODE solvers provided by the SciPy Python library. This approach allows for an accurate approximation of the system's dynamic behavior and supports efficient integration of the compartment model under various flow and reaction conditions.

2.5. Verification

To test the implementation and results of the compartment model, we verify it against an analytical solution. This analytical solution represents flow between two infinite plates with a simple first-order chemical reaction. The verification process ensures that the CM accurately predicts the concentration profiles and flow dynamics under controlled conditions.

The analytical solutions for plug flow, Couette flow, and Poiseuille flow provide benchmarks for evaluating the CM's performance. These solutions are derived based on non diffusive steady-state assumptions and specific velocity profiles. By com-

paring the CM results to these analytical solutions, we can assess the accuracy and reliability of the model. Additionally, the verification process helps to identify potential limitations or areas for improvement in the CM implementation.

2.5.1. Analytical Solution for Plug Flow

For a first-order chemical reaction in a plug flow between two infinite plates, the concentration profile can be derived under steady-state conditions. The velocity profile is uniform ($v_1 = v_{\max}, v_2 = 0$), and the concentration decreases exponentially along the flow direction. Specifically, the resulting concentration profile is given by:

$$c^*(\xi_1^*) = e^{-Da\xi_1^*} \tag{8}$$

where $Da = \frac{kL}{v_{\max}}$ is the Damköhler number, and $\xi_1^* = \frac{\xi_1}{L}$ is a dimensionless axial coordinate.

2.5.2. Analytical Solution for Couette Flow

In Couette flow, the velocity profile is linear and given by $v_1 = v_{\max}\frac{\xi_2}{L}, v_2 = 0$, where $v_{\max}$ is the velocity of the moving top wall, ξ_2 is the dimensionless transverse coordinate, and L is the characteristic length. The mean residence time can be approximated as $\tau_R = \frac{L}{\bar{v}}$, and for a linear velocity profile we get $\bar{v} = \frac{v_{\max}}{2}$. Substituting this, the mean residence time becomes $\tau_R = \frac{L}{2v_{\max}}$. Therefore, the Damköhler number is calculated as $Da = \frac{2kL}{v_{\max}}$. The concentration profile for a first-order reaction is expressed as:

$$c^*(\xi_1^*, \xi_2^*) = e^{-Da\frac{\xi_1^*}{\xi_2^*}} \tag{9}$$

where $\xi_1^* = \xi_1/L$ and $\xi_2^* = \xi_2/H$ are the dimensionless axial and transverse coordinate, respectively.

2.5.3. Analytical Solution for Poiseuille Flow

In a Poiseuille flow, the velocity profile is parabolic and given by $v_1 = v_{\max}\left(1 - \left(\frac{\xi_2}{H/2}\right)^2\right), v_2 = 0$, where $v_{\max}$ is the maximum velocity at the centerline, ξ_2 is the dimensionless transverse coordinate, and H is the channel height. The mean velocity for this profile is $v_1 = 2/3 v_{\max}$. Using this, the Damköhler number is evaluated as $Da = k\frac{3L}{2v_{\max}}$. The concentration profile for a first-order reaction is given by:

$$c^*(\xi_1^*, \xi_2^*) = e^{-Da\frac{\xi_1^*}{1-\xi_2^{*2}}} \tag{10}$$

where ξ_1^* and ξ_2^* are the dimensionless axial and transverse coordinate, respectively.

3. RESULTS

The results of this study demonstrate the capability of the compartment model (CM) to accurately reproduce the reaction dynamics of a simple tubular reactor. The Fig. 1 shows the concentration profile of a reactor with Poiseuille flow and a Darmköhler number of 1.

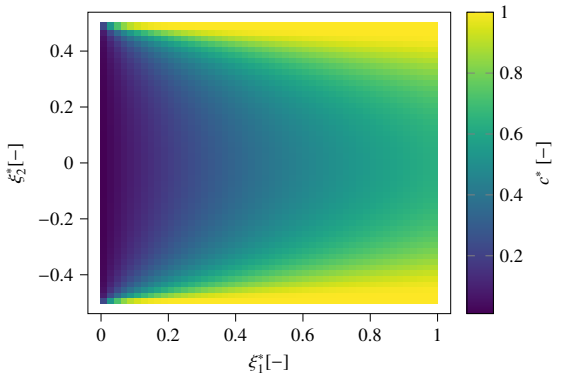

Figure 1. Analytical concentration profile for Poiseuille flow for a simple first-order chemical reaction.

3.1. Importance of Feature Selection

Feature selection plays a crucial role in the clustering process, as it directly determines how the compartments are formed and how well they capture the relevant dynamics of the system. To illustrate this, we compare two clustering results, each using six compartments: one based on concentration as the feature, see Fig. 2, and the other based on velocity, see Fig. 3. The clustering based on concentration yields a significantly lower error of 16% compared to 29% when using velocity, indicating that it provides a better representation of the system in this case. However, while the performance is better, concentration is very difficult to obtain from the simulation. In practical CFD setups, especially those limited to the flow field, the full concentration profile may not be available or may require prohibitively long simulation times to resolve accurately. This highlights a key trade-off: the most informative features may not be accessible in realistic scenarios. Moreover, in this

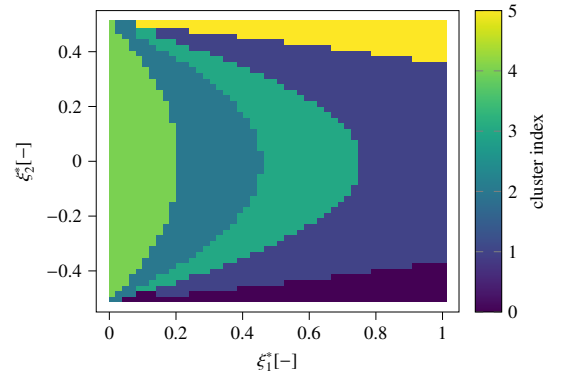

Figure 2. Clustering solution with six clusters and the concentration as feature vector.

simplified analytical test case, only a limited number of features are available, which further complicates the selection process. The lack of diverse or rich fea-

ture data restricts the clustering performance and the ability to tailor compartments to specific physical behaviours. Therefore, while the example shows that using concentration leads to better clustering quality, it also underlines the challenges in feature availability and extraction, particularly when applying this method to more complex or computationally expensive systems.

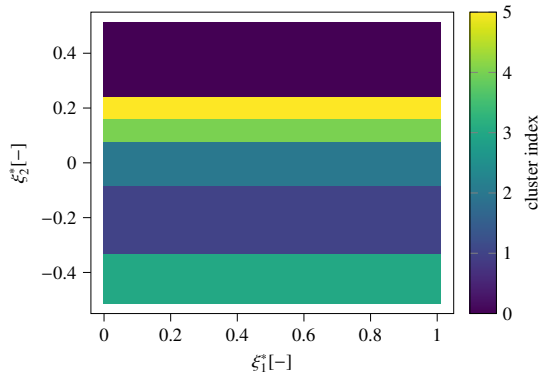

Figure 3. Clustering solution with six clusters and the velocity as feature vector.

3.2. Compartment Model Performance

Fig. 4 illustrates the absolute error of the predicted total mole flow compared to the analytical solutions for three different flow profiles: plug flow, Couette flow, and Poiseuille flow. These profiles serve as benchmarks for evaluating the CM's performance. For this comparison, the feature vectors used in the clustering included both the velocity and the concentration field.

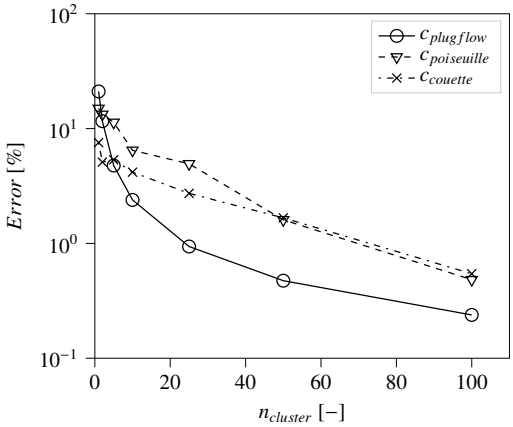

Figure 4. Absolute error of the CM solution compared to the analytical solution for plug flow, Couette flow, and Poiseuille flow.

The results show that as the number of compartments increases, the CM solution converges to the analytical solution, i.e., the error vanishes. This convergence highlights the ability of the CM to capture the essential flow and reaction characteristics of the system. For all three flow profiles, the error decreases significantly with an increasing number of compartments, demonstrating the robustness of the CM approach.

The plug flow results exhibit the lowest error, as the uniform velocity profile simplifies the flow dynamics. In contrast, the Couette and Poiseuille flows, which involve more complex velocity profiles, show slightly higher errors. These results were obtained without any advanced feature selection for clustering, meaning the compartments were generated based solely on basic flow properties. Despite this, the CM performed well, suggesting that even a straightforward clustering approach can yield meaningful results. Future work could explore the impact of incorporating additional features, such as turbulence intensity or residence time, to further enhance the accuracy and efficiency of the CM.

4. CONCLUSION

The results presented in our paper demonstrate the effectiveness of the compartment model (CM). We established a seamless, automated workflow by integrating the OpenFOAM® and SimVantage® flow solvers with our in-house tool called CLARA (CLustering AlgoRithm Austria). These CFD tools provide flow field data, which CLARA uses for unsupervised clustering via k-means and graph-based reassignment to identify spatially coherent compartments that mechanistically represent the reactor's flow characteristics. Based on these compartments, CLARA calculates compartment volumes, in- and outflows, and inter-compartment flow rates to generate the CM. An optimization step ensures mass conservation. This enables an efficient and mechanistic prediction of concentration fields and reactor behaviour using reduced-order models.

The verification of the CM against analytical solutions for plug flow, Couette flow, and Poiseuille flow confirmed its accuracy and reliability. The corresponding CMs successfully captured the concentration profiles and flow dynamics under various conditions, with errors below 1% for all flow profiles. These results highlight the potential of the CM as a fast and reliable tool for optimising reactor design and performance.

Future work will focus on extending the CM to handle more complex two phase system and complex chemical reactions. Additionally, efforts will be made to improve the feature selection with intelligent systems, enabling its application to larger-scale systems. The development of a physical-informed model for reactor control will also be explored, with the goal of optimising reactor performance under dynamic operating conditions.

ACKNOWLEDGEMENTS

This work is funded by Graz University of Technology through the lead project "DigiBioTech".

REFERENCES

[1] Lambauer, V., Permann, A., Petrášek, Z., Subotić, V., Hochenauer, C., Kratzer, R., and Reichhartinger, M., 2023, "Automatic Control of Chemolithotrophic Cultivation of Cupriavidus necator: Optimization of Oxygen Supply for Enhanced Bioplastic Production", *Fermentation*, Vol. 9 (7), p. 619, URL https://www.mdpi.com/2311-5637/9/7/619.

[2] Laborda, V. P. I., Puiman, L., Groves, T., Haringa, C., and Nielsen, L. K., 2025, "Unsupervised learning bioreactor regimes", *Computers & Chemical Engineering*, Vol. 194, p. 108891, URL https://linkinghub.elsevier.com/retrieve/pii/S0098135424003090.

[3] Le Nepvou De Carfort, J., Pinto, T., and Krühne, U., 2024, "An Automatic Method for Generation of CFD-Based 3D Compartment Models: Towards Real-Time Mixing Simulations", *Bioengineering*, Vol. 11 (2), p. 169, URL https://www.mdpi.com/2306-5354/11/2/169.

[4] Savage, T., Basha, N., McDonough, J., Krassowski, J., Matar, O., and Del Rio Chanona, E. A., 2024, "Machine learning-assisted discovery of flow reactor designs", *Nature Chemical Engineering*, Vol. 1 (8), pp. 522–531, URL https://www.nature.com/articles/s44286-024-00099-1.

[5] Savarese, M., Cuoci, A., De Paepe, W., and Parente, A., 2023, "Machine learning clustering algorithms for the automatic generation of chemical reactor networks from CFD simulations", *Fuel*, Vol. 343, p. 127945, URL https://linkinghub.elsevier.com/retrieve/pii/S0016236123005586.

[6] Tajsoleiman, T., Spann, R., Bach, C., Gernaey, K. V., Huusom, J. K., and Krühne, U., 2019, "A CFD based automatic method for compartment model development", *Computers & Chemical Engineering*, Vol. 123, pp. 236–245, URL https://linkinghub.elsevier.com/retrieve/pii/S0098135418308950.

[7] Delafosse, A., Collignon, M.-L., Calvo, S., Delvigne, F., Crine, M., Thonart, P., and Toye, D., 2014, "CFD-based compartment model for description of mixing in bioreactors", *Chemical Engineering Science*, Vol. 106, pp. 76–85, URL https://linkinghub.elsevier.com/retrieve/pii/S0009250913007690.

Conference on Modelling Fluid Flow (CMFF'25)
The 19th International Conference on Fluid Flow Technologies
Budapest, Hungary, August 26 - August 29, 2025

A COMPRESSIBLE TWO-FLUID MODEL FOR THE SIMULATION OF TRIBOELECTRIFICATION

Jürgen Abraham[2], Martin Gruber[3], Alexander Kospach[2], Mohammadsadegh Salehi[2], Stefan Radl[1]

[1] Corresponding Author. Institute of Process and Particle Engineering, Graz University of Technology. Inffeldgasse 13/III, Graz, Austria. Tel.: +43 316 873 - 30412, E-mail: radl@tugraz.at
[2] Virtual Vehicle Research GmbH, Inffeldgasse 21A, Graz, E-mail: Jürgen.Abraham@v2c2.at
[3] Institute of Process and Particle Engineering, Graz University of Technology. Inffeldgasse 13/III, Graz, Austria. E-mail: martin.gruber@tugraz.at

ABSTRACT

Electrostatic interactions in compressible particle-laden flows are relevant for applications ranging from lithium-ion batteries to industrial dust explosions. Currently, their simulation remains challenging because charge transport must be resolved alongside steep gas density gradients and turbulence. Our present contribution augments an existing compressible two-fluid framework in OpenFOAM® with a function object that predicts net particle charge. The model's fidelity is demonstrated in two unit tests: unit test 1 isolates diffusive and conductive terms in a planar channel, and shows good agreement with corresponding analytical solutions. Unit test 2 benchmarks the enhanced two-fluid solver against a single-phase reference solution in a converging-diverging nozzle. A showcase simulation then tracks charge build-up and electric-field hotspots in a turbulent particle plume.

The resulting function object enables predictive studies of potentially arc-triggering charge accumulation in relevant flow scenarios, e.g., during thermal runaway of batteries. Also, ignition risks in pneumatic powder transport, volcanic-ash electrification, or other safety-relevant configurations can be assessed with our tool.

Keywords: CFD, compressible flow, triboelectrification, two-fluid model, gas-particle flow

NOMENCLATURE

Latin symbols

d	$[m]$	diameter
E	$[\frac{kg\ m}{s^3\ A}]$	electric field
e	$[C = A \cdot s]$	electron charge
L	$[m]$	characteristic system length
m	$[kg]$	mass
M	$\left[\frac{kg}{kmol}\right]$	molar mass
n	$[-]$	inward normal of the wall
p	$[Pa]$	pressure
Q	$[A \cdot s]$	mean charge of particles
r	$[m]$	radius
R	$[\frac{J}{kmol\ K}]$	universal gas constant
T	$[K]$	temperature
t	$[s]$	time
u	$\left[\frac{m}{s}\right]$	velocity vector
V	$[m^3]$	volume
x	$[m]$	axial position

Greek symbols

α	[-]	volume fraction
δ	[m]	electron tunnelling distance
Δφ	$[eV]$	work function difference
ε_0	$\left[\frac{F}{m}\right]$	vacuum permittivity
θ	$\left[\frac{m^2}{s^2}\right]$	granular temperature
κ_p	$\left[\frac{m^2}{s}\right]$	thermal diffusivity
κ_q	$\left[\frac{1}{ms}\right]$	triboelectric diffusivity
ρ	$\left[\frac{kg}{m^3}\right]$	density
σ	$\left[\frac{S}{m}\right]$	triboelectric conductivity

Subscripts and Superscripts

c	contact point
e	exit (nozzle outlet)
g	gas phase
p	particle (solid) phase
q	triboelectric (charge-related)

t	total
w	wall
e	exit (nozzle outlet)
0	stagnation/total condition
*	(i) non-dimensionalised variable (e.g x^*,t^*) (ii) effective quantity (e.g r^*)

1 INTRODUCTION

Triboelectrification occurs in gas–particle systems when collisions and frictional contacts transfer charge between solid surfaces, resulting in additional cohesive forces and localized electric fields. When gas is released rapidly, these fields can initiate arcing events that damage equipment or ignite flammable mixtures [1], [2]. In addition, at speeds above Mach 0.3, the compressibility of the gas phase may lead to shock formation and rapid expansions that drive transient variations in density and enthalpy, amplify pressure and temperature peaks, and produce nonlinear wave interactions. Resolving these phenomena therefore requires considering the full compressible flow equations. Such charging behavior under high-speed, compressible conditions has been observed in lithium-ion battery venting [3], volcanic ash plumes [4], planetary dust storms [5], and pneumatic powder conveying [2], [6].

To predict net charge generation in these flows, particle-resolved CFD–DEM simulations resolve every contact. However, they are impractical for a high amount of particles due to the cost of collision resolution [7]. Continuum Euler–Euler two-fluid models address this limitation by treating gas and particles as interpenetrating continua, and simulate net particle charge transport with an additional scalar transport equation. This approach lowers the computational expense for large particle counts while retaining the essential coupling of flow dynamics, charge transport and cohesive forces [8].

Experimental efforts have quantified triboelectric charging under flow conditions using both single-particle rigs and bulk powder measurements. Xu and Grosshans measured peak net charges at intermediate humidity in a PMMA duct [9], Cruise et al. demonstrated that air breakdown limits surface-charge saturation in pressure-chamber tests [10], and Liu et al. employed a contact–separation triboelectric nanogenerator in high vacuum to isolate intrinsic surface-charge densities free of gas-phase losses [11].

Building on these findings, CFD–DEM frameworks now allow incorporating triboelectric contact models with turbulent powder flows. For example, Alfano et al. coupled DEM collision models to a compressible RANS solver in an aerodynamic powder disperser and confirmed material-specific charge-to-area ratios against experiments [12]. Grosshans applied four-way coupled Euler–Lagrange simulations to show that even weak electrostatic charges markedly enhance near-wall particle clustering in pneumatic conveying, with secondary vortices modulating rather than negating this effect [13].

More recently, Euler–Euler models have advanced continuum tribocharging modeling by including charge–momentum coupling, polydispersity, and compressible effects. For example, Zeybek and Grosshans proposed a DQMOM-based scheme that discretizes the joint size–velocity–charge distribution, closes wall-contact and particle-particle charge-transfer terms with kinetic theory-based models, and solves Poisson's equation for the volumetric charge field, reproducing the formation and diffusion of a sharp charge boundary layer whose characteristics depend on particle-size distribution and charge diffusivity [14]. Montilla et al. derived second-order moment equations for the charge–velocity covariance and charge variance, as well as demonstrated that including the covariance transport improves predictions of charge diffusion in unsteady flows [15]. Ray et al. developed mean-charge transport equations for bi-disperse systems and showed in one-dimensional simulations that size disparity alone can induce spontaneous bipolar charging for identical materials [16].

While recent advances in CFD–DEM and Euler–Euler models have enabled triboelectric simulations under turbulent and compressible conditions, critical gaps remain in the field of open-source, compressible two-fluid simulation frameworks: existing implementations often rely on in-house codes or lack integration with finite-volume solvers for reactive multiphase flows, limiting accessibility and scalability. Moreover, the interplay between compressibility effects (e.g., shocks, rapid expansions) and tribocharging dynamics – expected to be of key importance in applications like battery venting or volcanic plumes - has not been rigorously investigated with continuum-based solvers.

To address these challenges, we present a generalized charge transport function object for OpenFOAM®'s „reactingTwoPhaseEulerFoam" solver, verified for conductive/diffusive limits and in compressible nozzle flow. Also, we showcase the solver in a forward-facing step flow. Thereby, our work bridges the gap between high-fidelity triboelectric models and open-source multiphase CFD, enabling studies of charge-momentum coupling in industrially relevant geometries.

The remainder of our contribution is organised as follows: Section 2 details the governing equations, numerical implementation, and boundary conditions. Section 3 verifies the charge-transport with conductive and diffusive benchmarks, while in Section 4, a showcase is presented. Section 5 summarises the main conclusions and outlines future work.

2 METHODOLOGY

This section summarizes the governing compressible two-fluid and charge-transport equations, their implementation in OpenFOAM®, and the boundary-condition in this study. We note in passing that in our present study x^* and t^* denote non-dimensional variables, whereas r^* indicates the effective particle radius.

2.1 Flow

The Eulerian-Eulerian approach was applied in the present study to simulate a gas-particle flow system in OpenFOAM®. Two-Fluid Model (TFM) is also termed „Eulerian-Eulerian" approach since different phases are treated mathematically as interpenetrating continua. In this approach, conservation equations are solved for each phase, and these equations are linked by an interphase momentum transfer coefficient and the gas pressure. The interphase momentum exchange was modeled using the drag law proposed by Wen and Yu [17]. Besides this, the kinetic theory of granular flow, as well as a frictional model, was adopted to close the solid-phase stress tensor. Finally, the no-slip boundary condition was used for the gas phase, and the solid-phase transport equations are closed using the Johnson & Jackson boundary condition [18]. The full governing equations - including those for thermal energy – are standard, and will be shared by the authors upon reasonable request.

2.2 Charge transport equations

The following equation has been implemented in the form of a function object in the OpenFOAM® software environment to solve the charge transport equation:

$$\partial_t\left(\frac{\alpha_p}{V_p}Q_p\right)+\boldsymbol{\nabla}\cdot\left(\frac{\alpha_p}{V_p}Q_p\mathbf{u_p}\right)=-\sigma_q\frac{\alpha_pQ_p}{\varepsilon_0V_p}+\boldsymbol{\nabla}\cdot(\kappa_{total}\boldsymbol{\nabla}Q_p) \quad (1)$$

Here the following definitions have been used:

$$\sigma_q=\gamma_q2^{\frac{14}{5}}\frac{5\pi\sqrt{\pi}}{21}\varepsilon_0g_0d_p^3\left(\frac{\alpha_p}{V_p}\right)^2\cdot\Gamma\left(\frac{12}{5}\right)r^*\left(\frac{15m^*}{16Y^*\sqrt{r^*}}\right)^{\frac{2}{5}}\Theta_p^{\frac{9}{10}} \quad (2)$$

$$\kappa_{total}=\frac{d_p\sqrt{\Theta_\mathrm{p}}}{9\sqrt{\pi}g_0V_p}+\gamma_q2^{\frac{14}{5}}\frac{5\sqrt{\pi}}{21}g_0d_p^2\left(\frac{\alpha_p}{V_p}\right)^2\Gamma\left(\frac{12}{5}\right)r^*\left(\frac{15m^*}{16Y^*\sqrt{r^*}}\right)^{\frac{2}{5}}\Theta_p^{\frac{9}{10}} \quad (3)$$

2.3 Boundary Conditions for Charge

The boundary condition, as stated in [19], is given by

$$\sigma_{q,w}\left(\frac{\Delta\varphi}{\delta_ce}-\frac{2Q_p}{\pi\varepsilon_0d_p^2}\right)+\kappa_\mathrm{q}\mathbf{n}_\mathrm{w}\cdot\nabla Q_p-(\sigma_\mathrm{q}-\sigma_\mathrm{q,w})\mathrm{E}\cdot\mathbf{n}_\mathrm{w}=0 \quad (4)$$

The first term represents the role of the work function difference at the boundary. Additionally, the second and third terms stand for diffusion and conduction contribution. As reported by Kolehmainen et al. [19], the nature of the solution to this problem is determined by the ratio of two timescales, one associated with tribo-charging, τ_e, and the other representative of charge diffusion, τ_d:

$$\tau_e=\frac{\varepsilon_0}{\sigma_q} \quad (5)$$

$$\tau_d=\frac{\alpha_pL^2}{\kappa_qV_p} \quad (6)$$

In the above equations, L stands for a characteristic length of the system. If τ_e is much smaller than τ_d, the diffusion term can be neglected (as the latter effects will affect the charge distribution insignificantly).

3 RESULTS

3.1 Unit test 1: Tribocharging Solver Testing

The correctness of the implemented code was tested for fixed physical properties (i.e. particle density, volume, diameter, heat capacity and thermal conductivity), solid volume fraction (α_p) and granular temperature (Θ_p). Therefore, the coefficients for the charge transport equation can be considered as fixed (i.e. σ_q, κ_{total} are constant). With this assumption, one can rearrange Eqn. (1) as follows:

$$\frac{\alpha_p}{V_p}\partial_tQ_p+\frac{\alpha_p}{V_p}\nabla\cdot(Q_p\mathbf{u_p})=-\left(\sigma_q\frac{\alpha_pQ_p}{\varepsilon_0V_p}\right)+\kappa_{total}\Delta Q_p \quad (7)$$

The above equation contains a transient term and a convective term on the left-hand side, while the right-hand side comprises a conductive contribution caused by tribo-electrification and a diffusive contribution. To check the correctness of our implementation of this balance equation, we simulate two limiting cases: (i) pure conduction and (ii) pure diffusion inside a rectangular channel that spans $-96\,d_\mathrm{p} < x < 96\,d_\mathrm{p}$, $-6\,d_\mathrm{p} < y < 6\,d_\mathrm{p}$ and $-6\,d_\mathrm{p} < z < 6\,d_\mathrm{p}$. The channel is resolved by

a $50 \times 4 \times 4$ cartesian mesh and the equations are advanced with a constant time step of $\Delta t = 0.001\ s$. During all runs the granular temperature Θ_p, the solid volume fraction α_p and the particle material properties are kept constant. In the conductive case, convection is suppressed ($U_x = 0$), electrical conductivity is finite ($\sigma_q \neq 0$) and electrical diffusivity is set to zero ($\kappa_q = 0$). In the diffusive case the opposite holds ($\sigma_q = 0, \kappa_q \neq 0$). Both scenarios start from an identical step-wise initial charge distribution, $Q_p(t=0) = 10^{-14}\ C\ m^{-3}$ with -1 for $x < 0$ and $+1$ for $x \geq 0$.

The diffusive case can be also verified by considering charge diffusion in a semi-infinite medium whose surface is maintained at a constant charge (i.e. Q_0). The charge is initially zero in this medium. The analytical solution for this case is given in Eq. (3.13) of Crank [20].

Table 1. Physical properties of the particles.

Name	*Value*	*Unit*
Particle diam. (d_p)	250	[μm]
Particle density (ρ_p)	2500	$\left[\frac{kg}{m^3}\right]$
Granular temperature (Θ_p)	0.01	$\left[\frac{\mathrm{m}^2}{\mathrm{s}^2}\right]$
Volume frac. (α_p)	0.15	[−]

3.1.1 Conductive case

In this case we just consider the conductive contribution, meaning that electrical diffusivity is ignored (i.e. $\kappa_{total} = 0$) and no convection is present ($\mathbf{u_p} = 0$) We can hence simplify to:

$$\partial_t Q_p = -\left(\frac{\sigma_q}{\varepsilon_0} Q_p\right) \qquad (8)$$

With the analytical solution becoming:

$$Q_p(t,x) = Q_0(x) e^{-\frac{\sigma_q}{\varepsilon_0} t} \qquad (9)$$

Figure 1 shows that, for the pure-conduction benchmark, the dimensionless charge profile Q/Q_0 keeps its initial top-hat shape along the normalised coordinate x^* while its plateau levels decrease uniformly with time ($t^* = 10 - 60$). This is in line with the analytical solution of Eqn. (9) for a conduction-only process. Notably, the jump at $x^* = 0$ remains sharp and the plateaus do not spread, indicating that the solver adds virtually no numerical diffusion.

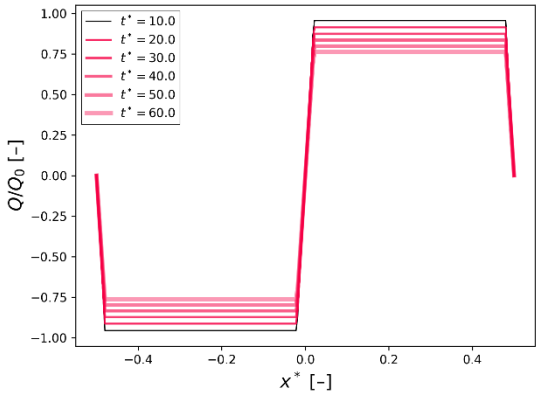

Figure 1 Dimensionless charge (Q/Q_0) for the case with σ_q calculated from physical properties from Table 1. The dimensionless time is defined as $t^* = t/\frac{L}{\sqrt{\theta}}$.

Figure 2 represents an extreme case in which the electrical conductivity σ_q was deliberately increased by three orders of magnitude. As a result, the characteristic relaxation time becomes much shorter than in the reference run, and the positive-and-negative charge plateaus level out almost immediately. While the charge step at $x^* = 0$ remains sharp, its amplitude collapses within a very brief period.

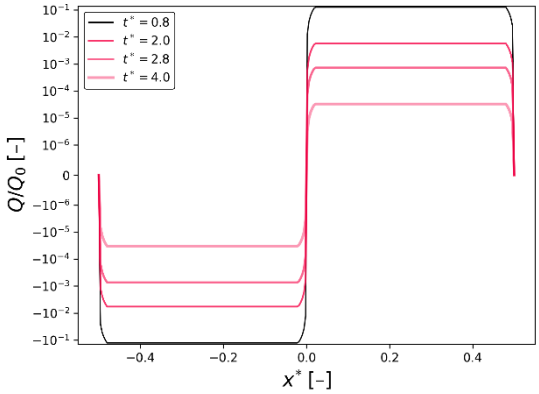

Figure 2. Dimensionless charge distribution (Q/Q_0) for the case with $1000\sigma_q$ (with σ_q calculated from the physical properties from Table 1). The dimensionless time is defined as $t^* = t/\frac{L}{\sqrt{\theta}}$.

3.1.2 Diffusive case

In this case, just the diffusion contribution is considered, meaning that the electrical conduction term is ignored (i.e. $\sigma_q = 0$) and no convection is considered (i.e,. $\mathbf{u_p} = 0$). In such circumstances, we can write:

$$\partial_t Q_p = \kappa_{total} \frac{V_p}{\alpha_p} \Delta Q_p \qquad (10)$$

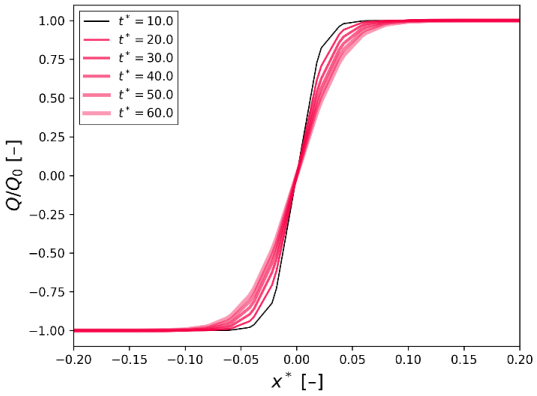

Figure 3. Dimensionless charge (Q/Q_0) for the case with κ_{total} calculated from physical properties of Table 1. The dimensionless time is defined as $t^* = t/\frac{L}{\sqrt{\theta}}$.

Figure 3 shows that, for the pure-diffusion benchmark, the dimensionless charge profile Q/Q_0 evolves as expected: starting from the same top-hat distribution as before, the plateau values remain essentially constant while the step at $x^* = 0$ spreads symmetrically with increasing time t^*producing the S-shaped curves that follow the error-function form expected for a diffusion-controlled process.

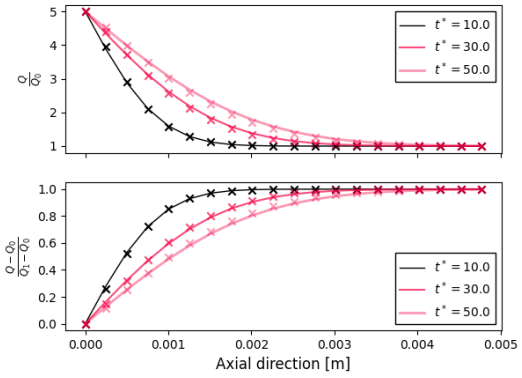

Figure 4. Comparison of dimensionless charge distribution to the analytical solution for initial charge $Q_0 = 10^{-14}$ and a fixed charge $Q_1 = 5e^{-15}$ at the left boundary in an semi-infinite box, The dimensionless time is defined as $t^* = t/\frac{L}{\sqrt{\theta}}$.

Figure 4 compares the simulated dimensionless charge profiles Q/Q_0 (symbols) with the analytical solution (solid lines) for the one–dimensional semi-infinite medium whose boundary at $x = 0$ is held at a constant charge Q_0. Results are shown for three dimensionless time coordinates. As can be seen, the diffusion front penetrates into the domain, and the simulation tracks the theoretical curves almost perfectly.

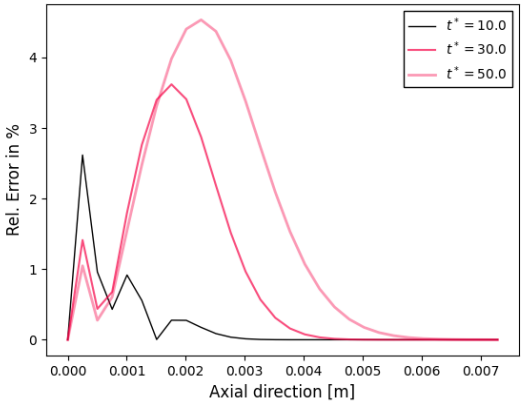

Figure 5. Relative error of dimensionless charge Q/Q_0 for the case of an semi-infinite half plane, The dimensionless time is defined as $t^* = t/\frac{L}{\sqrt{\theta}}$.

Figure 5 presents the corresponding relative error along the axial direction. The error peaks close to the charged wall, but decays rapidly with distance and time, falling below 1 % in the bulk of the domain. Together the two plots confirm that the solver reproduces the analytical solution with high accuracy.

3.2 Unit Test 2: Nozzle flow

Unit test 2 benchmarks the flow through a canonical converging–diverging nozzle (with geometric parameters $\Theta = 5.7\,°$, $D_b = 40\,mm$, $D_h = 28\,mm$, $D_e = 37.46\,mm$, and $L = 47.4\,mm$, as well as simulation parameters $\gamma = 1.4$, $R_s = 286.71\,{}^{J}/_{kg\,.\,K}$, and $p_t = 6e5\,Pa$) to compare the performance of two different OpenFOAM® solvers. Figure 6 contrasts the temperature and velocity fields generated by the single-phase compressible solver „rhoReactingBuoyantFoam" (upper row) with those from the „two-phase-capable reactingTwoPhaseEulerFoam" (bottom row).

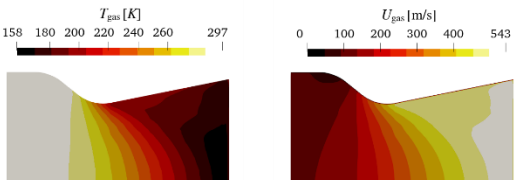

Figure 6. Simulated gas flow through a converging–diverging nozzle (flow direction is left to right). (a, c) gas temperature T_{gas} [K]; (b, d) gas velocity magnitude U_{gas} [$\frac{m}{s}$]. Results in the top row (a, b) were obtained with the compressible solver rhoReactingBuoyantFoam (RRBF), while the bottom row (c, d) employs the solver reactingTwoPhaseEulerFoam (RTPEF).

In both solutions predicted by the solvers the gas accelerates from sub-sonic conditions upstream of the throat to a supersonic jet at the exit: the colour maps show a smooth rise in velocity to about $543\ m/s$ for the solver RRBF and $533\ m/s$ for RTPEF. The core flow cools down to $158\ K$ for both cases. These outlet values match the one-dimensional analytical estimates listed in Table 2 within a few percent, while any discrepancies between the two numerical approaches are most likely confined to the wall regions. The unit test thus confirms that the „reactingTwoPhaseEulerFoam" reproduces compressible-flow behaviour with the same level of accuracy as the established single-phase solver, providing a reliable foundation for subsequent gas–particle simulations.

Table 2. Analytical results for nozzle flow according to the model of Kong et al. [21].

Name	*Unit*	*Value*
Gas temperature at the outlet $T_{g,e}$	$[K]$	161.6
Gas velocity at the outlet $U_{g,e}$	$\left[\frac{m}{s}\right]$	527.1

4 BENCHMARK: FORWARD-FACING STEP

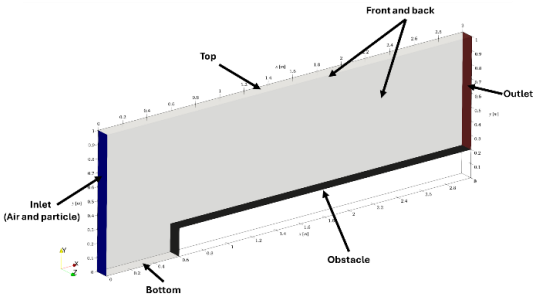

Figure 7. The geometry of the forward facing showcase.

We now shift our attention to a show case that illustrates the combined use of the flow and tribocharging solver. As shown in Figure 7, the air and particles would enter the domain from the inlet patch and would leave it via the outlet patch. The flow is confined by an obstacle which is defined as a wall. The top and bottom patches are symmetry planes, and the front and back faces were defined as "empty". The particles and the gas enter the domain with a fixed velocity of $(50,0,0)\ \frac{m}{s}$ with a volume fraction of $\alpha_p = 4.8 \cdot 10^{-4}$, as well as a temperature of $1000\ K$. The particle diameter is $d_p = 136\ \mu m$. The particle will get charged when hitting the obstacle surface with a work function difference of $1\ eV$. Figure 8 shows the results after a flowtime of $1\ s$. As it can be seen, the particles just above the obstacle's surface have a substantially higher-charge than the particles in other regions. However, the particle volume fraction in this high charge region is much smaller than at other locations. This can be explained by the flow condition affected by the obstacle's shape.

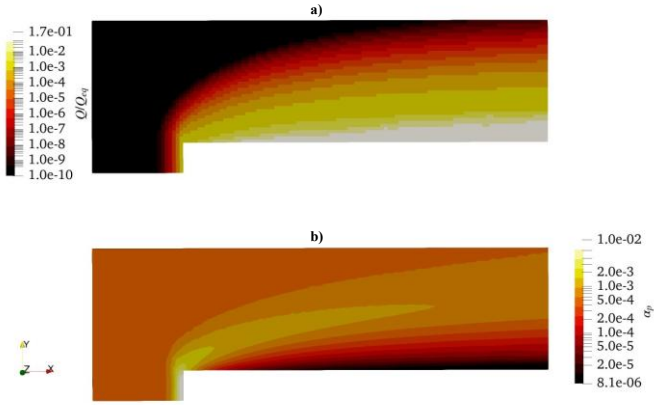

Figure 8. Results for the forward facing showcase: a) dimensionless charge, b) particle volume fraction contour plots.

5 CONCLUSIONS

We demonstrated the functionality of a newly implemented triboelectrification solver in the popular open-source environment OpenFOAM®. Also, appropriate boundary conditions were implemented. Specifically, this was done for two sets of unit test scenarios, as well as a showcase.

The latter case highlights a strongly heterogeneous net particle charge distribution. This may lead to the development of strong electric fields, and hence the danger of local arcing phenomena in practical applications.

For the unit test cases, a $k-\varepsilon$ turbulence model was applied to ensure robustness of the solver under weakly fluctuating conditions. In contrast, the nozzle-flow simulation employed a $k-\omega$ SST model, while the showcase simulation was conducted under laminar assumptions. In future studies, it would be potentially beneficial to apply high-fidelity turbulence-resolving approaches, such as Large Eddy Simulation (LES) or Direct Numerical Simulation (DNS), to better assess the interaction between turbulent fluctuations and triboelectric charge transport: the recent study of Croquer et al. [22] showed that LES does not offer advantages with repect to time averaged quantaties (compared to RANS data) for a similar flow situation. However, at turbulent fluctuations can be directly predicted by LES, which is not the case for RANS. Hence, using LES potentially is better suited to predict particle-wall collisions and hence triboelectrification.

Future work will (and has partially already) apply the solvers to relevant industry-scale problems in the field of battery venting channel design.

6 ACKNOWLEDGEMENTS

This work was financially supported by the Austrian Research Promotion Agency (FFG) through the projects "PREVENT+" and "Safe Sustain". PREVENT+ was funded under the program *"Mobilität der Zukunft"*, while SafeSustain was supported by the program *"Mobilitätstechnologie"* of the Austrian Federal Ministry for Innovation, Mobility and Infrastructure (BMIMI).

This publication was prepared at Virtual Vehicle Research GmbH in Graz and received partial funding within the COMET K2 Competence Centers for Excellent Technologies. The COMET program is funded by the Austrian Federal Ministry for Innovation, Mobility and Infrastructure (BMIMI), the Austrian Federal Ministry for Economy, Energy and Tourism (BMWET), the Province of Styria (Department 12), and the Styrian Business Promotion Agency (SFG). Programme management has been entrusted to the Austrian Research Promotion Agency (FFG).

For improving readability and language style, AI-based tools were utilized during manuscript preparation. The content and scientific arguments presented remain entirely the responsibility of the authors.

7 REFERENCES

[1] S. Matsusaka, H. Maruyama, T. Matsuyama, and M. Ghadiri, "Triboelectric charging of powders: A review," *Chemical Engineering Science*, vol. 65, no. 22, pp. 5781–5807, Nov. 2010, doi: 10.1016/j.ces.2010.07.005.

[2] S. Naik, R. Mukherjee, and B. Chaudhuri, "Triboelectrification: A review of experimental and mechanistic modeling approaches with a special focus on pharmaceutical powders," *International Journal of Pharmaceutics*, vol. 510, no. 1, pp. 375–385, Aug. 2016, doi: 10.1016/j.ijpharm.2016.06.031.

[3] Y. Zhang, P. Ping, X. Ren, W. Gao, D. Kong, and X. Yin, "Characteristics and generation mechanism of ejecta-induced arc for lithium-ion battery during thermal runaway," *eTransportation*, vol. 24, p. 100429, May 2025, doi: 10.1016/j.etran.2025.100429.

[4] C. Cimarelli and K. Genareau, "A review of volcanic electrification of the atmosphere and volcanic lightning," *Journal of Volcanology and Geothermal Research*, vol. 422, p. 107449, Feb. 2022, doi: 10.1016/j.jvolgeores.2021.107449.

[5] N. O. Renno *et al.*, "MATADOR 2002: A pilot field experiment on convective plumes and dust devils," *Journal of Geophysical Research: Planets*, vol. 109, no. E7, 2004, doi: 10.1029/2003JE002219.

[6] A. T. Ndama, P. Guigon, and K. Saleh, "A reproducible test to characterise the triboelectric charging of powders during their pneumatic transport," *Journal of Electrostatics*, vol. 69, no. 3, pp. 146–156, Jun. 2011, doi: 10.1016/j.elstat.2011.03.003.

[7] S. Golshan, R. Sotudeh-Gharebagh, R. Zarghami, N. Mostoufi, B. Blais, and J. A. M. Kuipers, "Review and implementation of CFD-DEM applied to chemical process systems," *Chemical Engineering Science*, vol. 221, p. 115646, Aug. 2020, doi: 10.1016/j.ces.2020.115646.

[8] J. Kolehmainen, A. Ozel, and S. Sundaresan, "Eulerian modelling of gas–solid flows with triboelectric charging," *J. Fluid Mech.*, vol. 848, pp. 340–369, Aug. 2018, doi: 10.1017/jfm.2018.361.

[9] W. Xu and H. Grosshans, "Experimental study of humidity influence on triboelectric charging of particle-laden duct flows," *Journal of Loss Prevention in the Process Industries*, vol. 81, p. 104970, Feb. 2023, doi: 10.1016/j.jlp.2022.104970.

[10] R. D. Cruise, S. O. Starr, K. Hadler, and J. J. Cilliers, "Triboelectric charge saturation on single and multiple insulating particles in air and vacuum," *Sci Rep*, vol. 13, no. 1, p. 15178, Sep. 2023, doi: 10.1038/s41598-023-42265-0.

[11] D. Liu *et al.*, "Standardized measurement of dielectric materials' intrinsic triboelectric charge density through the suppression of air breakdown," *Nat Commun*, vol. 13, no. 1, p. 6019, Oct. 2022, doi: 10.1038/s41467-022-33766-z.

[12] F. O. Alfano, A. Di Renzo, F. P. Di Maio, and M. Ghadiri, "Computational analysis of triboelectrification due to aerodynamic powder dispersion," *Powder Technology*, vol. 382, pp. 491–504, Apr. 2021, doi: 10.1016/j.powtec.2021.01.011.

[13] H. Grosshans, "Influence of weak electrostatic charges and secondary flows on pneumatic powder transport," *Can J Chem Eng*, vol. 101, no. 5, pp. 2347–2360, May 2023, doi: 10.1002/cjce.24824.

[14] M. Zeybek and H. Grosshans, "Eulerian formulation for the triboelectric charging of polydisperse powder flows," *Physics of Fluids*, vol. 33, no. 6, p. 063304, Jun. 2021, doi: 10.1063/5.0054374.

[15] C. Montilla, R. Ansart, and O. Simonin, "Charge–velocity correlation transport equations in gas–solid flow with triboelectric

effects," *J. Fluid Mech.*, vol. 955, p. A22, Jan. 2023, doi: 10.1017/jfm.2022.1054.
[16] M. Ray, F. Chowdhury, A. Sowinski, P. Mehrani, and A. Passalacqua, "Eulerian modeling of charge transport in bi-disperse particulate flows due to triboelectrification," *Physics of Fluids*, vol. 32, no. 2, p. 023302, Feb. 2020, doi: 10.1063/1.5140473.
[17] C. Y. Wen and Y. H. Yu, "Mechanics of fluidization," in *Fluid-Particle Technology*, vol. 62, in Chemical Engineering Progress Symposium Series, vol. 62. , New York: American Institute of Chemical Engineers, pp. 100–111.
[18] P. C. Johnson and R. Jackson, "Frictional–collisional constitutive relations for granular materials, with application to plane shearing," *Journal of Fluid Mechanics*, vol. 176, pp. 67–93, Mar. 1987, doi: 10.1017/S0022112087000570.
[19] J. Kolehmainen, L. Ceresiat, A. Ozel, and S. Sundaresan, "110th Anniversary: Effect of System Size on Boundary-Driven Contact Charging in Particulate Flows," *Ind. Eng. Chem. Res.*, vol. 58, no. 38, pp. 17980–17990, Sep. 2019, doi: 10.1021/acs.iecr.9b03437.
[20] J. Crank, *The mathematics of diffusion*, 2. ed., Reprint. Oxford: Clarendon Press, 1976.
[21] D. Kong, G. Wang, P. Ping, and J. Wen, "A coupled conjugate heat transfer and CFD model for the thermal runaway evolution and jet fire of 18650 lithium-ion battery under thermal abuse," *eTransportation*, vol. 12, p. 100157, May 2022, doi: 10.1016/j.etran.2022.100157.
[22] S. Croquer, O. Lamberts, S. Poncet, S. Moreau, and Y. Bartosiewicz, "Large Eddy Simulation of a supersonic air ejector," *Applied Thermal Engineering*, vol. 209, p. 118177, Jun. 2022, doi: 10.1016/j.applthermaleng.2022.118177.

Conference on Modelling Fluid Flow (CMFF'25)
The 19th International Conference on Fluid Flow Technologies
Budapest, Hungary, August 26 - August 29, 2025

INFLUENCE OF PACKING DENSITY ON THE CALCINATION PROCESS FOR LIME PRODUCTION: A DEM-CFD STUDY

Rezvan ABDI[1,2], Bo JAEGER[2], Torben BERGOLD[2], Enric ILLANA[2], Martin SCHIEMANN[2] and Viktor SCHERER[2]

[1]Corresponding Author. Tel.: +49 234 / 32-17986. E-mail: Abdi@leat.rub.de
[2]Institute of Energy Plant Technology, Ruhr-University Bochum, Universitätsstraße 150, 44780 Bochum, Germany.

ABSTRACT

To model the calcination of limestone in a moving particle bed, a radiation model based on the Discrete Ordinates Method (DOM) is incorporated into Computational Fluid Dynamics (CFD) and coupled with the Discrete Element Method (DEM). By accounting for local porosity, the radiation model adjusts the net radiative heat flux over the packing density accordingly.

The endothermic calcination reaction converts limestone ($CaCO_3$) into quicklime (CaO). The paper evaluates radiation penetration, temperature distributions, calcination degree, and CO_2 mass fraction in a system where limestone particles are heated by a gas in crossflow and a radiative enclosure. In addition to convection and radiation, conductive heat transfer among particles is accounted for. Three different packing conditions—dilute, moderate, and dense—are investigated.

Results highlight the significant role of radiation in driving the calcination process, as well as the dependence of radiation—and consequently calcination—on packing density. The study shows that the calcination degree decreases with increasing packing density. The simulation results yield average calcination degrees of 98%, 80%, and 60% for particles at the outlet in the dilute, moderate, and dense configurations, respectively.

Keywords: Lime Production, DEM, CFD, Calcination, DOM Radiation, AVM

NOMENCLATURE

a	[1 m^{-1}]	absorption coefficient
E_a	[kJ mol^{-1}]	activation energy
$k'_{r,s}$	[m s^{-1}]	reaction rate
I	[W m^{-2} sr^{-1}]	radiative intensity
rp_s	[-]	reaction progress
V_m	[m^3 mol^{-1}]	solid molar volumes
Y_{CO_2}	[-]	CO_2 mass fraction

Subscripts and Superscripts

CV	control volume
eff	effective
f	fluid
$Proj$	projected

1. INTRODUCTION

Quicklime (CaO) plays a crucial role in various industrial applications, including steel manufacturing, wastewater treatment and flue gas desulfurization. Its production is based on the thermal decomposition of limestone ($CaCO_3$) through calcination, which is commonly carried out in shaft kilns. Calcination is a thermally driven endothermic reaction, which requires 178 kJ/mol, that decomposes calcium carbonate into calcium oxide and carbon dioxide ($CaCO_3(s) \rightarrow CaO(s) + CO_2(g)$).

In recent years, significant research efforts have been dedicated to modelling and simulating the internal environment of lime shaft kilns to gain a clearer understanding of the complex mechanisms governing thermochemistry and material transport. Conventional methods often utilize one-dimensional (1D) heat and mass balance techniques or Computational Fluid Dynamics (CFD) models that tend to simplify the representation of solid particles. A more advanced approach integrates a particle-scale calcination model at a sub-grid resolution to offer deeper insights into shaft kiln behaviour [1].

To achieve a more realistic description of the calcination phenomena, researchers have investigated the application of the Discrete Element Method (DEM). This approach solves the motion and interactions among individual particles according to Newton's laws of motion [2]. DEM is a highly effective tool for studying the dynamics of particle-based systems due to its ability to easily access information at the individual particle level [3]. It enables a more precise description of the limestone bed's granular structure within the kiln. When

coupled with CFD, a comprehensive analysis of thermochemical processes by modelling both particle dynamics and gas-phase interactions is feasible. However, due to the computational challenges posed by the large number of particles in industrial-scale kilns, DEM-based simulations remain relatively scarce.

Several studies have successfully integrated DEM and CFD to investigate different kiln configurations, including single-shaft kilns [4-5] and regenerative two-shaft kilns [6]. Additionally, simulations of oxyfuel calcination have been conducted in [7].

Intra-particle heat and mass transfer adds another layer of complexity to kiln modelling. The particles in lime production are thermally thick and hence gradients of temperature and species must be resolved in the interior of the particle. In previous work [1], the particles are modelled as spheres and the calcination process is simulated using a shrinking core model, where the outer layer of the particle reacts first, gradually transitioning to the core as the reaction progresses. In another approach [6-7], thermally thick particles are modelled by discretizing the particle into concentric shells. Each shell is assumed to have a uniform temperature and heat conduction and mass transfer are solved radially through the particle. The same approach is used in this study.

A notable gap in current research is the absence of detailed 3D DEM-CFD studies for lime production that accurately incorporate radiation effects using the Discrete Ordinates Method (DOM). To the best of the authors' knowledge, this aspect has not been extensively explored in the literature. This study utilizes the DOM method, which is particularly effective for handling directional variability in radiation. This technique discretizes the radiation field into a set of fixed directions in the Cartesian system, solving the Radiative Transfer Equation (RTE) for each direction [8].

In DEM-CFD simulations involving large numbers of particles, the bulk can be efficiently represented within the Eulerian CFD framework using the Average Volume Method (AVM). Instead of individually resolving the particles and the voids between them [2], this method represents particles through a porosity field and all relevant properties are volume-averaged. The transfer of mass, energy, and species is computed for each particle and then distributed across the CFD domain accordingly. As a result, the precise shape of individual particles is not resolved during the CFD simulation.

In this study, to enable efficient computation, AVM is utilized by deriving a time-resolved porosity distribution from DEM. This strategy allows for multiple particles to be contained within a single CFD control volume, enabling the modelling of solid-fluid interactions at subgrid interfaces. The AVM model used here considers radiation shadowing between 'particle layers' in adjacent fluid cells [8].

A major contribution of this study is the detailed investigation of heat transfer mechanisms—including convection, contact conduction, and radiation—within a moving packed particle system. By adjusting absorption and emission coefficients in the DOM for varying packing densities, the study ensures accurate distribution of radiative heat in fluid cells. The accuracy of this adjustment is validated through comparison with experimental and numerical data, which were presented in our previous publication [8]. Additionally, for cases where only the overall effect of radiation shadowing is of interest, this approach may eliminate the necessity of particle-particle radiation modelling. This study is an extension of our previous work [8], in which calcination was not considered, and the results were obtained at much smaller particle residence times.

The proposed model has been integrated into an in-house DEM software, developed within the Bulk-Reaction research centre [9], supported by funding from the German Research Foundation. The DEM software is coupled with OpenFOAM [10] to solve for the energy, species, and mass transport in the gas phase. Section 2 introduces the calcination and radiation modelling approach, followed by a comparative analysis of scenarios with and without calcination in Section 3, and a summary of key findings in Section 4.

2. MODEL DESCRIPTION

2.1. Discrete Element Method (DEM)

Each particle is represented as an isotropic, homogeneous porous material. The motion of spherical limestone particles is tracked using the Discrete Element Method (DEM). For brevity, the details of the equations are referred to in [7].

2.2. Computational Fluid Dynamics (CFD)

The CFD component ensures mass, momentum and energy conservation in the fluid phase by solving the following transport equations:

$$\frac{\partial \phi \rho_f}{\partial t} + \nabla \cdot \left(\phi \rho_f \underline{u}_f\right) = S_{gas} \tag{1}$$

$$\frac{\partial (\phi \rho_f \underline{u}_f)}{\partial t} + \nabla \cdot \left(\phi \rho_f \underline{u}_f \underline{u}_f\right) = -\phi \nabla p + \phi \nabla \cdot \tau_f + \phi \rho_f \underline{g} + S_M \tag{2}$$

$$\frac{\partial (\phi \rho_f h_f)}{\partial t} + \nabla \cdot \left(\phi \rho_f \underline{u}_f h_f\right) = \nabla \cdot \left(\phi \, k_f \, \nabla T\right) + S_E \tag{3}$$

The fluid phase is characterized by its velocity $\underline{u_f}$, density ρ_f, porosity ϕ and specific enthalpy h_f. In these fluid equations, the local bed porosity (provided by the DEM model for each fluid cell) is used. S_{gas} is the mass (air and CO_2) exchanged with the solid phase. The momentum source terms include the pressure gradient ∇p, the stress tensor τ_f (assuming laminar flow), the gravitational acceleration $\underline{g}$ and the momentum exchanged with the particles S_M. In this formulation, S_M is determined using the Ergun equation [11]. Regarding the energy equation, the fluid's thermal conductivity is represented by k_f while the enthalpy exchange with the solid phase corresponds to S_E.

The transport equation for chemical species is expressed as:

$$\frac{\partial(\phi\rho_f Y_{CO_2})}{\partial t} + \nabla\cdot\left(\phi\rho_f \underline{u_f} Y_{CO_2}\right) = \nabla\cdot\left(\phi\rho_f D_{CO_2}\nabla Y_{CO_2}\right) + S_{CO_2} \quad (4)$$

The gas phase comprises the components H_2O, CO_2, N_2 and O_2. To simplify the modelling process, the species transport equation is solved only for the mass fraction Y_{CO_2}, as it significantly influences the calcination rate of lime particles. Additionally, the source term S_{CO_2} and the term including the diffusion coefficient D_{CO_2} model the release and transport of CO_2 from the particles during the calcination reaction, respectively.

2.3. Convective and Conductive Heat Transfer

The convective heat transferred, $\dot{Q}_{conv}$ [W], is given by:

$$\dot{Q}_{conv} = \alpha\, A_p \left(T_f - T_{p,surf}\right) \quad (5)$$

where T is the temperature, A_p represents the particle's surface area, and α denotes the convective heat transfer coefficient. Further details on the calculation of the α can be found in [7].

The contact heat transfer among particles is influenced by two main mechanisms: heat conduction through particle contact points and the gas layer in the vicinity of the contact points. Details of the equations can be found in Hilse et al. [12].

2.4. Radiation Model

Equation (6) provides a simplified form of the Radiative Transfer Equation (RTE), which characterizes the propagation of radiation along a specific direction $\underline{s}$ through a medium. The term $I_{(\underline{s},\underline{r})}$ denotes the radiation intensity [W/(m^{2}sr)] at position $\underline{r}$ and along direction $\underline{s}$. To determine $I_{(\underline{s},\underline{r})}$, the Discrete Ordinates Method (DOM) solves a predetermined set of RTEs. The radiation balance for an individual CFD cell results in the discretised formulation of the RTE (Eq. (7)). In addition, the net radiative heat flux to the particles within the system is expressed in Eq. (8).

$$(\nabla\cdot I)_{(\underline{s},\underline{r})}\cdot\underline{s} = -a_p\, I_{(\underline{s},\underline{r})} + \frac{E_p}{4\pi} \quad (6)$$

$$\sum_i^{N_{ray}}\sum_{face} I_{face,i}\,\underline{S_i}\,\underline{A_{face}} = -a_p\,\omega_i I_{cell,i} + \frac{E_p}{4\pi}\omega_i \quad (7)$$

$$\dot{Q}_{net\ rad.\ D-P} = \dot{Q}_{absorbed\ rad.\ p.} - \dot{Q}_{emitted\ rad.\ p.} = \epsilon_{rad,p}\phi A_p\left(\frac{G_{cell}}{4} - \sigma T_p^4\right) \quad (8)$$

where $\underline{S_i} = \underline{s_i}\omega_i$, ω_i is the discrete solid angle associated to a specific direction i, ϕ is the local bed porosity, $\epsilon_{rad,p}$ is the emissivity of the particle, G is incident radiation, σ is Stefan-Boltzmann constant. a_p is the particle absorption and E_p is the particle emission which is computed based on:

$$a_p = \frac{1}{V_{cell}}\phi\sum_{i=1}^{N}\epsilon_{rad,p}\,A_{Proj,i} \quad (9)$$

$$E_p = \frac{1}{V_{cell}}\phi\sum_{i=1}^{N}\epsilon_{rad,p}A_{p,i}\sigma\,T_{p,i}^4 \quad (10)$$

where V_{cell} is the CFD cell volume and $A_{Proj,i}$ denotes the area of the particle projected in the i-th direction.

As shown in the equations above, incorporating local bed porosity ϕ into the modelling of particle emission, absorption, and radiation propagation enables the model to account for the effects of varying packing densities. Further details on the DOM model, and its validation are available in our earlier publication [8].

2.5. Model for Intraparticle Calcination

A radially resolved model is used to track the conversion of limestone to quicklime. By discretizing a spherical particle into 40 radial control volumes (shells), the internal temperature distribution and reaction kinetics are solved. The particle's outer diameter remains constant, which is a reasonable assumption for limestone. The calcination degree is the ratio of the CO_2 released to the initial amount of CO_2 bound in $CaCO_3$.

$$D_{calcination,p} = \frac{m_{CaCO_3} - m(t)}{m_{CaCO_3} - m_{CaO}} \quad (11)$$

where m_{CaCO_3} is the initial mass of $CaCO_3$, $m(t)$ is the time-varying particle mass and m_{CaO} is the mass of CaO corresponding to fully calcined particles. The porosity of each shell, ε_s, is determined by considering the solid molar volumes V_m, the initial porosity of the limestone ε_{CaCO_3}, and reaction progress rp_s:

$$\varepsilon_s = \varepsilon_{CaCO_3} + \left(1 - \frac{V_{m,CaO}}{V_{m,CaCO_3}}\right)(1 - \varepsilon_{CaCO_3})\, rp_s \quad (12)$$

The reaction progress ranges from zero to one, indicating the extent of the calcination. It is mathematically defined as the ratio of the mass of calcium oxide ($m_{s,CaO}$) formed at any given stage to the total mass of calcium oxide that would be produced upon complete calcination:

$$rp_s = \frac{m_{s,CaO}}{(1-\varepsilon_{CaO})\, \rho_{CaO}\, V_s} \quad (13)$$

where V_s is the shell volume, ρ_{CaO} is the lime density and ε_{CaO} is the lime porosity. The porosity of lime (ε_{CaO}) is calculated from equation (13) by setting the reaction progress (rp_s) to 1, ensuring that it corresponds to the fully reacted state of the material.

At this stage, it is considered that the shell's solid temperature is in thermal equilibrium with the gas temperature within its pores, primarily due to the large surface area. It is also crucial to highlight that heat sources from convection, surface contact, and radiation are only applied to the outermost shell (control volume, CV).

$$V_s\, \rho_s c_{p,s} \frac{\partial T_s}{\partial t} = A_j k_j \nabla T_s + \dot{Q}_{conv} + \dot{Q}_{net\ rad\ D-P} + \dot{Q}_{contact} + \dot{Q}_{r,s} \quad (14)$$

Here, $c_{p,s}$ is the shell specific heat capacity, $\dot{Q}_{r,s}$ represents the heat generated by the reaction in each shell, and the subscript j denotes the boundary separating two adjacent control volumes (CVs), where interpolation based on CV values is utilized, with the exception of the area A_j. The rate of CO_2 release in each shell is obtained based on:

$$\frac{dn_{CO_2,s}}{dt} = A_{r,s}\, k'_{r,s}\left(c_{CO_2,s} - c_{CO_2,eq}\right) \quad (15)$$

where $A_{r,s}$ is the shell area of reaction and $k'_{r,s}$ is the reaction rate. The CO_2 concentration, $c_{CO_2,s}$, is:

$$c_{CO_2,s} = \frac{\rho_{gas,s} \cdot Y_{CO_2,s}}{M_{CO_2}} \quad (16)$$

The equilibrium CO_2 concentration, $c_{CO2,eq}$, is also temperature-dependent:

$$c_{CO_2,eq} = \frac{1}{R_m T_s}\left(101325 \cdot \exp\left(17.74 - 0.00108\, T_s + 0.332 \ln(T_s) - \frac{22020}{T_s}\right)\right) \quad (17)$$

where R_m is the universal gas constant. The associated reaction rate is defined by an Arrhenius-type expression:

$$k'_{r,s} = K_0\, T_s^{\,b}\, e^{-\frac{E_a}{R_m T_s}}\, K_{T,c} \quad (18)$$

where the activation energy is $E_a = 33.474$ [kJ/mol], the temperature exponent is $b = 1$ and the pre-exponential factor is $K_0 = 10^{-4}$ [$\frac{\mathrm{m}}{\mathrm{sK}}$]. The term $K_{T,c}$ represents a correction factor, as described in reference [7].

Hence, higher T accelerates reaction rate via the Arrhenius term and higher CO_2 concentrations slows down calcination by reducing the driving force for CO_2 to diffuse from within the particle and by shifting the equilibrium toward $CaCO_3$ formation.
Assuming that air and carbon dioxide are the only gaseous components present inside the particle, the transport equations, in their spatially discretized form are then expressed as:

$$\varepsilon_s\, V_s \frac{\partial \rho_{gas,s}}{\partial t} = -\sum(\rho_{gas,j}\ A_j\, \underline{v}'_j) + M_{CO_2} \frac{dn_{CO_2,s}}{dt} + S_{gas} \quad (19)$$

$$\varepsilon_s\, V_s \frac{\partial\left(\rho_{gas,s}\, Y_{CO_2,s}\right)}{\partial t} = -\sum\left(\varepsilon_s \rho_{gas,j}\, A_j \left(\underline{v}'_j\, Y_{CO_2,s} - D_{CO_2}\, \nabla Y_{CO_2,s}\right)\right) + M_{CO_2} \frac{dn_{CO_2,s}}{dt} + S_{CO_2} \quad (20)$$

where M_{CO_2} is the molecular weight of CO_2, $n_{CO_2,s}$ is the number of moles of CO_2 in shell s. The advection velocity $\underline{v}'_j$ is calculated based on Darcy's law for flow through porous media, as described in reference [7].

The diffusion term governs the transport of the generated CO_2 both inward and outward. The diffusion coefficient is evaluated at the interface between two adjacent shells, considering the effective diffusion coefficient $D_{eff,k}$ for the components $k = \{CaCO_3, CaO\}$ within the porous structure and the reaction progress [7].

The model has been validated in our previous paper [7] using experimental measurements for a single spherical particle.

2.6. DEM-CFD Coupling Routine

A one-way coupling approach is used for momentum exchange, meaning that while the particle bed influences the gas flow, the motion of the particles remains unaffected by drag or buoyancy forces. For the exchange of energy and species, a

two-way coupling method is applied, where fluid properties are transferred from the gas to the particles as boundary conditions and source terms are transferred from the solid phase to the fluid phase. More information on DEM-CFD coupling can be found in [13].

3. SIMULATION SETUP

The computational domain employed in this study is adapted from our previous work [8]. It consists of a box with dimensions 0.4 × 0.3 × 0.1 [m³], as illustrated in Figure 1, and is discretized into 6200 hexahedral elements. Mesh size in the bulk region is 0.02×0.02×0.02 [m³]. Finer mesh elements are applied in the upper section of the domain.

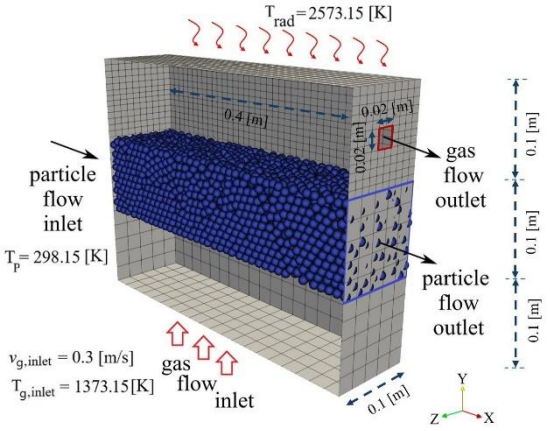

Figure 1. The meshed domain and boundary conditions. Reproduced from Abdi et al., 2025 [8], under CC BY 4.0

Air (comprising 23% O_2 and 77% N_2 by mass) enters the system through the bottom surface with a velocity of 0.3 m/s and temperature of 1373.15 K and exits via a small outlet (0.02 × 0.02 [m²], positioned at the top right boundary of the box), highlighted in red in Fig. 1. Particles flow through the left boundary (0.1 × 0.1 m) at 298.15 K and exit via the right outlet. The outlet boundary has a zero-gradient condition for both velocity and temperature, and the outlet pressure is set to atmospheric (zero relative gauge pressure). A no-slip condition is applied to all walls, which are assumed to be adiabatic with respect to convection. Additionally, the top wall is maintained at a fixed temperature of 2573.15 K (T_{rad}), while the remaining walls are kept at 298.15 K for radiation purposes. The absorption coefficient a_w and the emissivity of the top wall ε'_w are both 0.7, while for all other walls, the values are 1.

Three random particle arrangements—dilute (540-spheres), moderate (2560-spheres), and dense (5000-spheres)—were studied. The corresponding packing porosities within the particle zone (not for the entire box) are 93%, 66.5%, and 34.5% for the dilute, moderate, and dense cases, respectively. These values represent averages; in the fluid simulations, the local porosity in each computational cell is used.

The particle arrangements are created as follows: Initially, 5000 spheres are randomly introduced into the domain through a DEM simulation by dropping them from the top. To generate the moderate and dilute cases, approximately half and then another 2000 spheres are randomly removed, respectively. On average, each fluid cell contains 10, 5.12, and 1.08 spheres for the dense, moderate, and dilute cases.

Each case maintains similar particle velocities and residence times but differs in solid mass flow rates. For all cases, particles are assigned a constant velocity of 0.0002 m/s along the x-axis. Their trajectories are prescribed, meaning that the DEM mechanical motion equations are not solved—only the thermo-chemical behavior is computed. The residence time for a particle to travel from the left to the right boundary, $t_{residence}$, is 2000 seconds. The working fluid is air, with a thermal conductivity of 0.04 W/(m·K). Table 1 presents the general parameters used in the DEM-CFD simulations.

Table 1. Simulation parameters

parameter	unit	value
CFD time step	[s]	0.0002
DEM time step	[s]	0.001
gas absorption coefficient	[m^{-1}]	0
gas emissivity	[-]	0
gas inlet velocity	[m/s]	0.3
gas thermal conductivity	[W/m·K]	0.04
particle diameter	[mm]	10
particle emissivity	[-]	0.85
particle initial mass	[g]	1.413
particle Poisson's ratio	[-]	0.35
particles residence time	[s]	2000
particle velocity	[m/s]	0.0002
particle Young's modulus	[Pa]	1×10^9
$CaCO_3$ properties		
density (without pore)	[kg/m³]	2812
heat capacity	[J/kg K]	836.8
molar mass	[kg/mol]	0.1
porosity	[-]	0.04
solid conductivity	[W/mK]	2.26
specific surface area	[m²/ kg]	16000
tortuosity	[-]	1.4142
permeability	[m²]	5×10^{-15}
CaO properties		
density (without pore)	[kg/m³]	3310
heat capacity	[J/kg K]	753.1
molar mass	[kg/mol]	0.056
porosity	[-]	0.543
solid conductivity	[W/mK]	0.7
specific surface area	[m²/ kg]	7000
tortuosity	[-]	1.4142
permeability	[m²]	5×10^{-15}

4. RESULTS

4.1. Radiation Field

Figure 2 illustrates the distribution of incident radiation G within the domain in [W/m²]. Fig. 2a presents the results for cases without calcination, while Fig. 2b corresponds to cases with calcination.

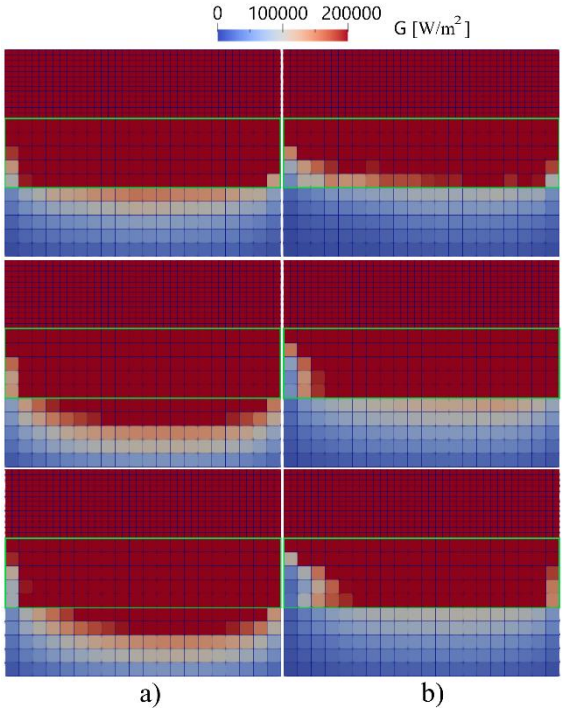

Figure 2: Incident radiation G [W/m²] contour in the case of 540 (top), 2560 (middle), and 5000 (bottom) spheres. a) without calcination. b) with calcination (G clipped above 200000 [W/m²]).

The local values of G indicate the extent to which radiation penetrates the particle bed. The particle-filled region is marked in green, so radiation reaches the lowest particle layer across all three packing densities. Notably, the radiation penetration depth is greater in the 2560- and 5000-sphere cases compared to the 540-sphere case. In the 2560 and 5000-sphere scenarios, the densely packed top layer absorbs more radiation from the upper wall. Over time, these top-layer particles emit more radiation toward the underlying layers, resulting in an increased radiation penetration depth.

As will be discussed in Figure 3, calcination causes a drop in particle temperature. Consequently, the top particle layers emit less radiation toward the lower layers, leading to a reduced radiation penetration depth. Therefore, the calcined cases exhibit lower values of G compared to the uncalcined cases.

4.2. Temperature Field

As the particles move through the system, they gradually absorb heat—primarily through convection from the bottom and radiation from the top. However, particles near the top layer, close to the outlet, are an exception—they are already heated due to high radiation absorption and lose heat via convection. Calcination begins as soon as the particle temperatures reach the threshold for this endothermic reaction which is around 800-900 °C.

According to Eqs. (15) and (18), the reaction rate of lime particles is governed by the local temperature and CO_2 mass fraction. In Fig. 3, the temperature field for both particles and fluid is shown for the two scenarios with and without consideration of calcination.

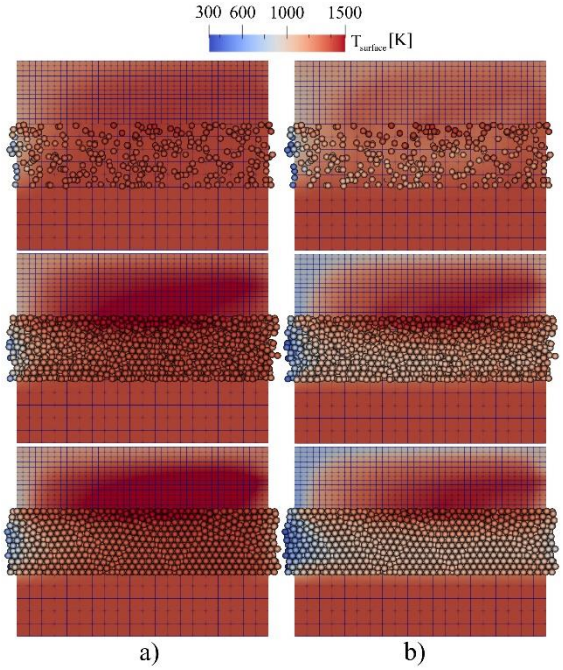

Figure 3: Surface temperature of particles in the case of 540 (top), 2560 (middle), and 5000 (bottom) spheres. a) without calcination. b) with calcination (clipped at 300 K and 1500 K).

The highest particle surface temperatures are observed in the upper region of the bulk, primarily due to radiation from the top. As expected, particle temperatures are slightly higher in the absence of calcination.

The maximum particle surface temperatures reach 1451 K, 1568 K, and 1568 K in the uncalcined cases. In the calcined cases, the maximum temperatures decrease to 1438 K, 1529 K, and 1503 K for the 540, 2560, and 5000 sphere cases, respectively. This difference is attributed to the temperature drop resulting from the endothermic nature of the calcination process. The temperature reduction occurs not only in regions with a high degree of calcination (see Figure 4a), but also

throughout the entire bulk region. This is because calcined particles at the top layers are colder than in the non-reacting case and therefore they emit less radiative heat to the lower layers.

Regarding the gas phase, the temperature above the bulk region is higher in the uncalcined case compared to the calcined cases. This is primarily because the hot particles at the top receive radiation heat from the top wall, and, without undergoing calcination, they retain more heat and transfer it to the gas through convection.

Radiation dominates heat transfer in all cases. In the calcined cases, average radiative transfer is 632 W, 3727 W, and 5922 W for the 540-, 2560-, and 5000-sphere cases, respectively, while convective transfer is lower at 360 W, 184 W, and 170 W. These are particle-averaged values; some particles gain heat by convection, others lose it.

4.3. Calcination Degree of the Lime Particles

Figure 4a shows the average calcination degree of lime particles across all radial shells for each case. The overall trends in the reacted particles are similar for all cases, with a high calcination degree observed near the upper section of the particle bed. This is primarily due to the radiation emitted by the hot top wall, which raises the particle temperatures significantly above the calcination threshold. Although the 540-particle case achieves a high overall calcination degree, some patches of uncalcined material remain, indicating non-uniform calcination. In fact, non-uniform calcination is observed across all three cases, with unreacted zones consistently appearing in the middle layers of the particle bed and near the particle inlet. This uneven calcination arises because particles in the middle layers receive neither sufficient radiation from the top wall nor adequate convective heat transfer from the bottom, preventing them from reaching the calcination temperature.

Notably, all three cases also show significant calcination at the lower part of the bed, attributed to the convective heat transfer from the incoming high temperature gas. Energy is transferred from the gas phase to supply the endothermic calcination reaction.

The key difference lies in the extent of the calcination zones: the 5000 case exhibits a smaller region with the highest calcination degree (red particles in Fig. 4a) compared to the 2560 case, which in turn shows a smaller high-calcination zone than the 540-sphere case. The simulation results yield average calcination degrees of 98%, 80%, and 60% for particles at the outlet in the dilute, moderate, and dense configurations, respectively, while the average calcination degrees for all particles are 65%, 48%, and 33%. These results demonstrate that the average calcination degree decreases with increasing packing density.

4.4. CO_2 Mass Fraction

Figure 4b illustrates the CO_2 mass fraction in both fluid and solid domain for each simulation case. Since the particles start with a uniform initial temperature of 298.15 K, there is no CO_2 production inside the particles at the inlet.

Particles gradually absorb heat, leading to the onset of calcination. Near the inlet, some top-layer particles appear red. As these particles move toward the outlet, they gradually change to orange and then blue as their internal CO_2 is released and transferred to the gas phase. Hence, the red top-layer particles in Fig. 4a have become orange (partially calcined particles) and blue (fully calcined particles with no remaining CO_2) in Fig. 4b.

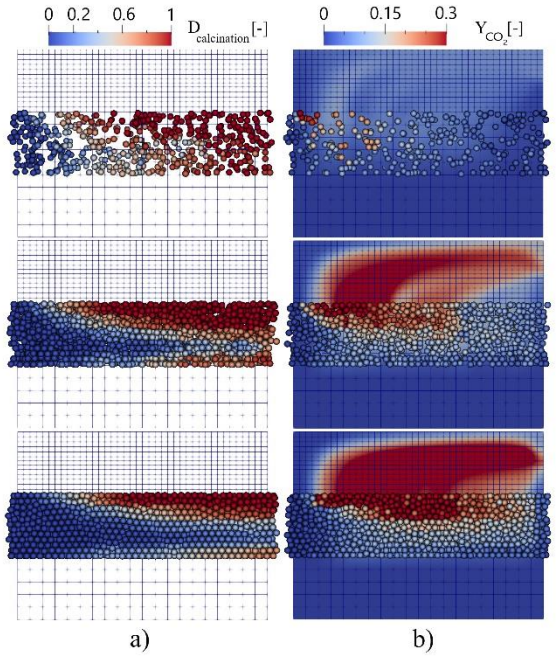

Figure 4: a) Calcination degree of lime particles b) Mass fraction of CO_2 (clipped to 0.3) in 540 (top), 2560 (middle), and 5000 (bottom) sphere cases.

Also, Fig. 4b shows the accumulation of CO_2 in the gas phase, resulting from the decomposition of limestone. Hence, the CO_2 concentration increases in alignment with the direction of the fluid flow. The amount of CO_2 in the fluid domain is highest in the 5000-sphere case due to the higher number of particles and, consequently, a greater amount of CO_2 released on the upper side of the bed. This is higher than in the 2560-sphere case, which in turn is higher than in the 540-sphere case. Therefore, although the overall calcination degree is lower in the 5000-sphere case, the influence of particle number is the dominant factor.

5. SUMMARY AND CONCLUSIONS

This study investigates the calcination behaviour of limestone particles, comparing results to cases where calcination is not considered. A Discrete Ordinates Method (DOM) is used in the coupled Discrete Element Method–Computational Fluid Dynamics (DEM-CFD) framework to model radiative heat transfer within systems of granular particles. The Averaged Volume Method was employed, introducing time-dependent source terms and a porosity field into the Navier-Stokes equations to account for the presence of particles. By incorporating local bed porosity in the modelling of particle emission and absorption, the effects of varying packing densities were captured.

A numerical test case has been simulated to analyse the interaction of heated walls, a moving particle bed with prescribed velocity, and a cross-flow of hot air. Spherical limestone particles were heated by a top wall at 2573.15 K and by cross-flowing air at 1373.15 K, with a constant inlet velocity of 0.3 m/s. Thermal conduction between particles has also been modelled. Three granular assemblies, with varying packing densities—dilute (93% porosity), moderate (66.5% porosity), and dense (34.5% porosity)—were considered, comprising 540, 2560, and 5000 particles, respectively. All scenarios shared the same residence time of 2000 seconds.

This work successfully demonstrates the influence of particle packing density and radiative heat transfer on the calcination process within moving particle beds. It was observed that as the particle number increased, the highest calcination degrees are concentrated in the upper and lower particle layers of the bed. Furthermore, the calcination degree distributions showed regions, particularly near the inlet and between densely packed lower and upper layers, where almost no calcination occurred. The average calcination degree decreases with increasing packing density. The simulation results yield average calcination degrees of 98%, 80%, and 60% for outlet particles in the dilute, moderate, and dense configurations, respectively.

Although the academic case studied here cannot be directly scaled to industrial kilns, the importance of granular packing, and radiation effects is highlighted.

ACKNOWLEDGEMENTS

This work has been funded by the Deutsche Forschungsgemeinschaft (DFG, German Research Foundation) – Project-ID 422037413 – TRR 287. Gefördert durch die Deutsche Forschungsgemeinschaft (DFG) – Projektnummer 422037413 – TRR 287.

REFERENCES

[1] Duan, S., Li, B., Rong, W. (2022a). Numerical simulation study of mixed particle size calcination processes in the calcination zone of a parallel flow regenerative lime kiln. *Materials*, 15(13), 4609.

[2] Abdi, R., Krzaczek, M., & Tejchman, J. (2023). Simulations of high-pressure fluid flow in a pre-cracked rock specimen composed of densely packed bonded spheres using a 3D CFD model and simplified 2D coupled CFD-DEM approach. *Powder Technol.*, 417, 118238.

[3] Abdi, R., Krzaczek, M., & Tejchman, J. (2022). Comparative study of high-pressure fluid flow in densely packed granules using a 3D CFD model in a continuous medium and a simplified 2D DEM-CFD approach. *Granul. Matter*, 24, 1-25.

[4] Krause, B., Liedmann, B., Wiese, J., Wirtz, S., & Scherer, V. (2015). Coupled three dimensional DEM-CFD simulation of a lime shaft kiln-calcination, particle movement and gas phase flow field. *Che. Eng. Sci.*, 134,834-849

[5] Kang, Z., et al. (2023). DEM-CFD coupled simulation of limestone calcination and fuel combustion in beam type lime shaft kiln. Applied Thermal Engineering, 231, 120935.

[6] Krause, B., & Liedmann, B., et al. (2017). 3d-dem-cfd simulation of heat and mass transfer, gas combustion and calcination in an intermittent operating lime shaft kiln. *Int. J. Therm. Sci.*, 117, 121-135

[7] Illana, E., Merten, H., et al. (2023). DEM/CFD simulations of a generic oxy-fuel kiln for lime production. *Therm. Sci. Eng. Prog.*, 45, 102076

[8] Abdi, R., Jaeger, B., et al. (2025). Modelling of heat transfer in moving granular assemblies with a focus on radiation using the discrete ordinate method: A DEM-CFD approach. *Particuology*, 100, 78-94.

[9]https://bulk-reaction.de/(accessed Apr. 11, 2025).

[10]https://www.openfoam.com/documentation/guides/v2012/doc/. (accessed Apr. 11, 2025).

[11] S. Ergun, A.A. Orning, Fluid flow through randomly packed columns and fluidized beds, *Ind. Eng. Chem*. 41 (6) (1949) 1179–1184.

[12] Hilse, N., Kriegeskorte, M., et al. (2023). Discrete Element Simulations of Contact Heat Transfer on a Batch-Operated Single Floor of a Multiple Hearth Furnace. *Processes*, 11(12), 3257.

[13] Illana Mahiques, et al. (2023). Locally resolved simulation of gas mixing and combustion inside static and moving particle assemblies. *Che. Eng. & Tech.*, 46(7), 1362-1372.

Conference on Modelling Fluid Flow (CMFF'25)
The 19th International Conference on Fluid Flow Technologies
Budapest, Hungary, August 26 - August 29, 2025

MULTISCALE COMPUTATIONS OF REACTIVE MULTIPHASE FLOWS

Xiaofei LI, Bingchen LI, Wei CHEN, Junjie LIN, Shuai WANG, Kun LUO*, Jianren FAN

* Corresponding Author. State Key Laboratory of Clean Energy Utilization, Zhejiang University, Hangzhou 310027, P. R. China, E-mail: zjulk@zju.edu.cn

ABSTRACT

Multiphase reactive flows are essential in energy, chemical, and environmental systems. This paper reviews and compares several multiscale modeling methods for simulating reactive multiphase flows, including particle-resolved direct numerical simulation (PR-DNS), computational fluid dynamics-discrete element method (CFD-DEM), coarse-grained CFD-DEM, multi-phase particle-in-cell (MP-PIC), and coarse-grained computational fluid dynamics -direct simulation Monte Carlo (CFD-DSMC). These methods are assessed for their accuracy, scalability, and computational efficiency in simulating dense gas-solid flows. The developed multiscale models are comprehensively validated against experimental measurements and applied across various scales: microscale simulations of char combustion, mesoscale simulations of particle clusters in coal gasification, macroscale simulations of biomass chemical looping gasification, and industrial-scale applications for coal pyrolysis and combustion staged conversion. This work emphasizes the importance of selecting appropriate modeling strategies for different scales and explores the potential integration of high-performance computing and artificial intelligence to enhance multiscale simulation tools.

Keywords: Multiphase flow, multiscale simulation, computational fluid dynamics, flow and reaction coupling

1. INTRODUCTION

The dense gas-solid reactive systems are widely present in energy, chemical, and environmental systems (e.g., combustors, gasifiers, reactors, etc.), where complex gas-solid flow, heat and mass transfer, and chemical reactions occur. With the rapid development of computer technology, computational fluid dynamics (CFD) has become an increasingly important complement to both theoretical analysis and experimental research. It effectively addresses the limitations of these two approaches and comprehensively and accurately reproduces the flow, heat transfer, and reactive characteristics of dense gas-solid flows. However, the complex multi-scale nature of dense gas-solid flows, both spatially and temporally, places stringent demands on numerical simulation and necessitates the adoption of appropriate multi-scale solving strategies[1–4].

Depending on the resolution and scale of interest, dense gas-solid reactive systems are commonly modeled by three classic approaches: particle-resolved direct numerical simulation (PR-DNS), computational fluid dynamics-discrete element method (CFD-DEM) under Euler-Lagrange framework, and two-fluid model (TFM) under Euler-Euler framework. In PR-DNS, every particle and the surrounding fluid field are fully resolved, so no closure models are needed to capture fluid motion; this yields outstanding accuracy but comes at the cost of extremely fine grids and correspondingly massive computational resources, which confines PR-DNS to small domains and modest particle counts [5,6]. The conventional CFD-DEM approach within the Euler-Lagrange framework alleviates this burden by allowing grid cells that are roughly three to five times larger than the particles they contain. [7–9]. The gas phase is solved within the Eulerian framework, while the solid-phase particle motion is solved in the Lagrangian framework. The reduction in grid quantity leads to a decrease in computational load. However, the accuracy of gas-phase motion predictions is slightly lower than that of PR-DNS. This method can track each particle individually, providing accurate particle-scale information, which is then interpolated and fed back into the gas-phase grid for further computations. This approach is constrained by particle collision models and grid size requirements and is still mainly applied in laboratory-scale simulations with a limited number of particles[10,11]. By contrast, the two-fluid model (TFM) under Euler-Euler framework adopts the continuous medium assumption, treating the solid phase as a fluid ("pseudo fluid") and solving its motion in the Eulerian framework. The key

challenge of this method lies in modeling the viscosity and pressure of the solid phase, often achieved through the kinetic theory of granular flow (KTGF) [12]. Generally speaking, the can significantly reduce computational load and has been widely used in predicting gas-solid flow within large-scale industrial equipment[13–15]. However, the Euler-Euler method has notable drawbacks: the accuracy of the solid-phase motion is limited to the computational grid scale, preventing the capture of rich particle-scale information. As a result, it is not well-suited for investigating the transport mechanisms of particles in fluidized bed equipment.

In the simulation of multiphase reactive flows, traditional single-scale methods often fail to effectively capture the complex interactions between fluids, particles, and reactions. Multi-scale simulation methods, by considering physical phenomena at different scales, can overcome the limitations of single-scale approaches, significantly improving prediction accuracy and computational efficiency. Specifically, multi-scale simulation methods not only focus on macroscopic flow characteristics but also allow for an in-depth exploration of microscopic particle behavior and chemical reaction mechanisms. This study comprehensively reviews and compares the applicability, accuracy, and scalability of the multiscale numerical simulation methods we have developed in recent years within the Euler-Lagrange framework for modeling multiphase reactive flows, providing essential tools for studying and optimizing these systems.

2. MODEL DESCRIPTION

2.1 Particle-resolved direct numerical simulation

In PR-DNS, the gas phase is solved within an Eulerian framework, while the solid phase is tracked using an Lagrangian framework. This approach requires enforcing no-penetration and no-slip boundary conditions on particle surfaces within the computational domain, along with the corresponding heat and mass transfer boundaries. The immersed boundary method with virtual points introduces the effect of particles without requiring mesh reconstruction, instead constructing a virtual embedded boundary through interpolation. The mass conservation equation, momentum conservation equation, energy conservation equation, and species conservation equation for the gas phase are expressed as follows:

$$\frac{\partial \rho}{\partial t} + \nabla \cdot (\rho \mathbf{u}) = 0 \tag{1}$$

$$\rho \frac{\partial \mathbf{u}}{\partial t} + \rho \mathbf{u} \cdot \nabla \mathbf{u} = -\nabla p + \nabla \cdot \tau \tag{2}$$

$$\rho \frac{\partial T}{\partial t} + \rho \mathbf{u} \cdot \nabla T = \sum_k (\dot{\omega}_k - \nabla \cdot \mathbb{J}_k)\left(\frac{TR}{c_y M_k} - \frac{h_k}{c_v}\right) - \frac{\rho TR}{c_v M} \nabla \cdot \mathbf{u} + \frac{\tau^2}{2\mu c_v} - \frac{\nabla \cdot \mathbf{q}}{c_v} \tag{3}$$

$$\rho \frac{\partial Y_k}{\partial t} + \rho \mathbf{u} \cdot \nabla Y_k = -\nabla \cdot \mathbb{J}_k + \dot{\omega}_k \tag{4}$$

where ρ_f, $\boldsymbol{u}_f$, and p_f represent the gas phase density, velocity, and pressure, respectively. τ_f denotes the viscous stress tensor. T represents temperature. c_v is the specific heat at constant volume. R denotes the universal gas constant. M is the molar mass of the gas mixture. h_k denotes the enthalpy of the individual species. Y_k denotes the mass fraction of species k. $\dot{\omega}_k$ represents the gas-phase reaction source term for species k, and $\mathbb{J}_k$ is the diffusion flux of species k.

The principle of the immersed boundary method with virtual points is to designate several layers of grid points near the particle boundary as virtual points (the number of layers is determined by the spatial discretization scheme; in this study, three layers are used). These virtual points are assigned values artificially through interpolation, ensuring that the fluid outside the particle satisfies the corresponding boundary conditions at the particle surface during spatial discretization. At each sub-time step, the assignment of values to the virtual points precedes the solution of the flow field. Mirror points symmetric to the virtual points across the boundary, along with additional auxiliary points on the same side of the interface, are selected to construct interpolation formulas for various boundary conditions, through which the values of the virtual points are determined. The construction of Dirichlet boundary conditions requires only a single mirror point, whereas Neumann and Robin boundary conditions necessitate, in addition to the mirror point, an auxiliary point. Depending on the dimensionality of the case study, the mirror and auxiliary points are obtained using bilinear or trilinear interpolation based on neighbouring grid points. Based on the boundary condition formulation, by specifying appropriate boundary conditions for species balance, velocity, and temperature, accurate simulation of particles can be achieved.

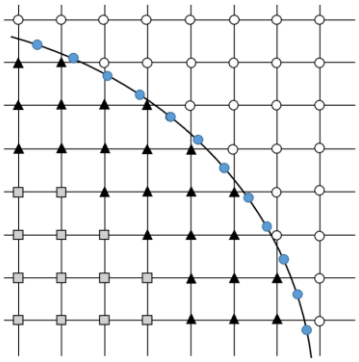

Figure 1. Schematic diagram of the immersed boundary method with virtual points.

2.2 Euler-Lagrange method

This section introduces the computational fluid dynamics-discrete element method (CFD-DEM) method, coarse-grained CFD-DEM method, the

multi-phase particle-in-cell method (MP-PIC) method, and the coarse-grained computational fluid dynamics-direct simulation Monte-Carlo (CFD-DSMC) method within the Euler-Lagrange framework, focusing on the governing equations for the gas phase and solid phase, as well as sub-models for particle collisions, heat and mass transfer, and chemical reactions.

2.2.1 Gas-phase control equations

The mass conservation equation and momentum conservation equation for the gas phase are expressed as follows:

$$\frac{\partial(\varepsilon_f \rho_f)}{\partial t} + \nabla \cdot (\varepsilon_f \rho_f \boldsymbol{u}_f) = R_f \tag{5}$$

$$\frac{\partial}{\partial t}(\varepsilon_f \rho_f \boldsymbol{u}_{f,i}) + \nabla \cdot (\varepsilon_f \rho_f \boldsymbol{u}_f \boldsymbol{u}_f) = -\varepsilon_f \nabla p + \rho_f \varepsilon_f g + \nabla \cdot (\varepsilon_f \tau_f) - I_{pf} \tag{6}$$

$$\frac{\partial(\varepsilon_f \rho_f C_{p,f} T_f)}{\partial t} + \nabla \cdot (\varepsilon_f \rho_f u_f C_{p,f} T_f) = \nabla \cdot [\varepsilon_f (\kappa_f + \frac{C_{p,f} v_{f,t}}{Pr_{T_{f,t}}}) \nabla T_f] - Q_{fp} - \Delta H_{rf} + \gamma_{Rf} (T_{Rf}^4 - T_f^4) \tag{7}$$

$$\frac{\partial(\varepsilon_f \rho_f X_n)}{\partial t} + \nabla \cdot (\varepsilon_f \rho_f u_f X_n) = \nabla \cdot (\varepsilon_f \rho_f D_n \nabla X_n) + R_{fn} \tag{8}$$

where ε_f represents the gas phase void fraction. R_f and I_{pf} correspond to the mass change source term due to chemical reactions and the interphase momentum exchange source term. $C_{p,f}$, T_f, κ_f, and $\mathrm{Pr}_{f,t}$ represent the specific heat capacity at constant pressure, temperature, thermal conductivity, and Prandtl number of the gas phase, respectively. Q_{fp} denotes the convective heat transfer between the gas and solid phases, ΔH_{rf} is the heat of reaction, γ_{Rf} is the radiative heat transfer coefficient, and T_{Rf} is the radiative temperature of the gas phase. X_n and D_n represent the mass fraction and diffusion coefficient of gas component n, respectively. R_{fn} denotes the mass change due to the chemical reactions involving component n.

2.2.2 Solid-phase control equations

In the Lagrangian framework, the motion of particles in the gas-solid flow is obtained by solving Newton's second law. The external forces acting on the particles in the flow field mainly include drag forces induced by fluid-particle interactions, pressure gradient forces, viscous forces, and other forces such as collision forces, viscous forces, and electrostatic forces arising from particle-particle and particle-wall interactions. These external forces allow the determination of particle position, velocity, acceleration, and other related quantities. The equation of motion for the particles can be expressed as:

$$m_p \frac{dv_p}{dt} = m_p g + F_{fp} + F_{drag} + F_c + F_{af} \tag{9}$$

$$I_p \frac{d\omega_p}{dt} = T_p \tag{10}$$

where m_p and v_p represent the particle mass and velocity, respectively, while m_pg, F_{fp}, F_{drag}, F_c, and F_{af} correspond to the gravitational force on the particle, pressure gradient force, drag force, collision force, and additional forces. I_p, ω_p, and T_p represent the particle moment of inertia, angular velocity, and torque, respectively. In the CFD-DEM and coarse-grained CFD-DEM method, the collision force can be resolved by decomposing it into the normal (F_{ij}^n) and tangential (F_{ij}^t) components. In the MP-PIC and CFD-DSMC methods, the collision force is not directly solved but rather modeled through a submodel. The particle collision models for the three methods will be discussed in detail in the following sections.

2.2.2.1 Interphase drag model

The drag force is primarily caused by the velocity difference between the particles and the fluid, and it is the main mechanism for momentum exchange between the particle and gas phases. Therefore, an accurate drag force model is crucial for predicting gas-solid flow processes. For a single particle within a particle group, the drag force it experiences can be calculated as:

$$F_{drag} = \frac{\beta V_p}{1 - \varepsilon_f}(u_f - v_p) \tag{11}$$

where β is the interphase momentum exchange coefficient, also known as the drag coefficient, and V_p represents the particle volume. Currently, commonly used drag force models can be broadly classified into the following categories: (i) experimental and empirical models such as the Gidaspow model[16] and the Syamlal-O'Brien model[17]; (ii) models derived from lattice-Boltzmann (LB) and direct numerical simulation (DNS) methods, such as the BVK drag model[18] and the Koch & Hill model[19]; (iii) models based on energy minimization multiscale (EMMS) theory, such as the EMMS drag model[20]. In this study, we primarily use the Gidaspow drag model, which applies to most fluidization calculations, the EMMS drag model that accounts for gas-solid flow heterogeneity, and the BVK drag model with particle size corrections.

2.2.2.2 Particle collision model

In gas-solid flow within a fluidized bed, frequent particle collisions significantly influence particle motion and the flow field distribution. Therefore, accurately calculating particle collisions in numerical simulations is crucial for predicting gas-solid flow behavior in the fluidized bed. Currently, depending on the method used to handle the interparticle interactions, collision models can be broadly classified into two main categories. The first is deterministic methods, which directly compute each particle collision in the computational domain during the simulation process, such as the soft sphere model used in the CFD-DEM and the coarse-grained CFD-DEM method. The second is stochastic methods, which do not directly calculate the particle collisions but instead introduce the concept of collision probability to model them, including the solid-phase stress model applied in the MP-PIC method and the DSMC method.

(1) Soft-sphere model for CFD-DEM and coarse-grained CFD-DEM

The soft-sphere model accounts for inter-particle forces during collisions and updates particle positions by computing acceleration, velocity, and displacement based on these forces. Interactions between particles are modeled by incorporating elasticity, damping, and tangential sliding mechanisms. Elasticity captures particle deformation during collisions, damping reflects energy dissipation, and sliding models tangential interactions. In the DEM, the contact force between particles is decomposed into a normal component (F_{ij}^{n}) and a tangential component (F_{ij}^{t}):

$$F_c = \sum_{j=1, j\neq i}^{N} \left(F_{ij}^{n} + F_{ij}^{t}\right) \tag{12}$$

$$F_{ij}^{n} = -(k_n \delta_n + \eta_n \dot{\delta}_n) n_{ij} \tag{13}$$

$$F_{ij}^{t} = \begin{cases} -(k_t \delta_t + \eta_t \dot{\delta}_t) t_{ij} & |F_{ij}^{t}| \leq \mu |F_{ij}^{n}| \\ -\mu |F_{ij}^{n}| t_{ij} & |F_{ij}^{t}| > \mu |F_{ij}^{n}| \end{cases} \tag{14}$$

where k, η, and δ represent the elastic stiffness, damping coefficient, and particle deformation displacement, respectively. The subscripts n and t denote the normal and tangential directions. The tangential contact force is constrained by the product of the particle-particle sliding friction coefficient μ and the normal contact force. If the tangential force exceeds this maximum static friction threshold, sliding occurs between the particles, and the tangential force is subsequently determined based on the sliding friction coefficient.

In traditional CFD-DEM methods, simulating large-scale fluidized bed is often challenging due to the large number of particles in the system, leading to excessive computational load and difficulties in solving the problem. To address this issue, the coarse-graining method is introduced to reduce the number of particles being computed. In the coarse-grained CFD-DEM method, multiple real particles with identical properties are grouped into a single computational particle with an equivalent coarse diameter, thereby reducing the number of particles in the computational domain by a factor of the cube, significantly lowering the computational complexity. The core framework of the coarse-grained CFD-DEM method is the same as that of the traditional CFD-DEM method, still using the soft-sphere model to directly solve the collision process between particles, but in the simulation, coarse particles are used to replace real particles for more efficient computation. The diameter of the coarse particle, d_{cgp}, is given by:

$$d_{cgp} = k d_p \tag{15}$$

where k is the coarse-graining coefficient, and d_{p} is the diameter of the real particles.

(2) Solid stress model for MP-PIC

In the MP-PIC method, a distribution function $f(\mathrm{x}_p, \mathrm{v}_p, m_p, T_p, t)$ is used to describe the distribution of particles in the flow field. This equation is a function of the particle's spatial position, velocity, mass, temperature, and time. The equation is expressed as follows:

$$\frac{\partial f}{\partial t} + \frac{\partial (f v_p)}{\partial t} + \frac{\partial (fA)}{\partial v_p} = \frac{f_D - f}{\tau_D} + \frac{f_G - f}{\tau_G} \tag{16}$$

where f_D and τ_D represent the particle distribution function and the particle collision relaxation time under local equilibrium conditions, respectively. After a collision, the particle velocity tends to follow an isotropic Gaussian distribution. In this state, τ_G and f_G denote the relaxation time and the particle distribution function, respectively. A is the particle acceleration, which is expressed as follows:

$$A = \frac{dv_p}{dt} = \beta(u_f - v_p) - \frac{\nabla p}{\rho_p} - \frac{\nabla \tau_p}{\rho_p \varepsilon_p} + g + \frac{\bar{v}_p - v_p}{2\tau_D} \tag{17}$$

where $\bar{\mathrm{v}}_p$ represents the local mass-averaged particle velocity, and τ_p is the solid-phase stress.

(3) Collision probability model for coarse-grained CFD-DSMC

The DSMC method, based on gas molecular kinetics[21], does not directly track the motion of each particle. Instead, it uses probabilistic methods to determine whether collisions occur between particles and employs a relatively small number of sampled particles to represent a large number of real particles. Over a time interval Δt_{p}, the collision probability P_{ij} between particle i and particle j within the same grid is given by[21,22]:

$$P_{ij} = \frac{w \pi g_0 (d_{p,i} + d_{p,j})^2 |G_{ij}| \Delta t_p}{4 V_c} \tag{18}$$

where w is the sampling coefficient; G_{ij} is the relative velocity between particle i and particle j; and g_0 is the equilibrium spherical radial distribution function at particle contact.

This study proposes the coarsed-grained CFD-DSMC method by coupling the coarse-grained model with the DSMC model. While using collision probability to model the collision process, the method also employs larger computational particles in terms of particle size to further reduce the number of simulated particles. Additionally, the collision probability is modified as follows:

$$P_{ij} = \frac{w \pi g_0 (d_{cgp,i} + d_{cgp,j})^2 |G_{ij}| \Delta t_p}{4 k^3 V_c} \tag{19}$$

2.2.2.3 Particle heat transfer model

Complex heat transfer between the gas and solid phases includes four types of heat transfer: particle-particle conduction, particle-fluid convective heat transfer, radiation heat transfer between particles and their surrounding environment, and the heat of reaction generated by chemical reactions. Particle-particle conduction primarily occurs in regions with high particle concentration and frequent collisions, and, compared to the other types of heat transfer, it accounts for a relatively small portion, often being neglected. Therefore, this study considers only particle-fluid convective heat transfer, radiation heat transfer between particles and their surrounding environment, and the heat of reaction generated by chemical reactions. Under these conditions, the

energy conservation equation for particle i is expressed as:

$$m_{p,i}C_{p,i}\frac{dT_{p,i}}{dt} = Q_{pf,i} + Q_{rad,i} - \Delta H_{r,i} \quad (20)$$

where $C_{p,i}$ is the specific heat capacity of particle i, $T_{p,i}$ is the temperature of particle i, $Q_{pf,i}$ and $Q_{rad,i}$ represent the convective heat transfer between the particle and the fluid, and the radiative heat transfer between the particle and its surrounding environment, respectively. $\Delta H_{r,i}$ is the heat of reaction.

2.2.2.4 Chemical reaction model

The heterogeneous reactions mainly include evaporation, pyrolysis, gasification, as well as carbonation and calcination reactions of adsorbents. For a specific computational particle, the mass conservation equation considering the mass changes caused by chemical reactions is given by:

$$\frac{dm_p}{dt} = \sum_{n=1}^{N_s} R_{sn} \quad (21)$$

where N_s is the total number of chemical components, and R_{sn} is the mass change rate of component n in the particle due to chemical reactions.

3. DISCUSSION AND RESULT

3.1 PR-DNS modeling of char combustion at the microscale

3.1.1 PR-DNS method validation

To verify the reliability of the PR-DNS method, we compared the drag coefficients of cold particles obtained from PR-DNS simulations with the empirical correlation proposed by Schiller and Naumann[16]. The simulation results show good agreement with the empirical formula in Figure 2 (a). Regarding char combustion, simulation results were validated against experimental data from Makino et al.[23] using their experimental configuration, as illustrated in Figure 2 (b). The simulations demonstrate satisfactory agreement with experimental measurements and notably reproduce the important phenomenon observed experimentally: As temperature increases, the dominant reaction shifts. When the CO_2-char reaction becomes predominant, it leads to a stepwise decrease in char consumption rate. In conclusion, the PR-DNS method achieves high precision in resolving forces, heat transfer, and mass transfer on particle surfaces, rendering it suitable for the full-scale particle direct numerical simulations conducted in this study.

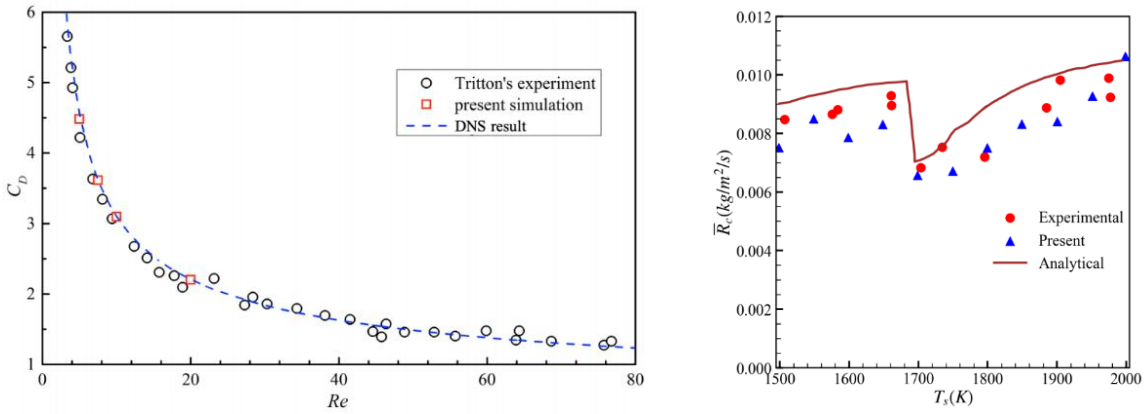

(a) (b)

Figure 2. PR-DNS method validation: (a) drag coefficient, (b) reaction rate.

3.1.2 PR-DNS on interaction during the combustion of two char particles

This subsection investigates the mechanistic effects of interactions between burning particles on reaction rates and drag forces. The interparticle interactions are decomposed into three components: wake effects, direct flame interactions between particles, and the nozzle effect arising from interparticle convective flow.

Figure 3 (a) shows the dimensionless drag force at different particle center distances and relative angles. This drag force is normalized by the drag on a single cold-flow particle. Overall, both cold and burning char particles show similar trends when influenced by neighboring particles. The nozzle effect becomes strong only when the line connecting the two particles is near 90 degrees to the flow direction. This causes the drag force to exceed that on a single isolated particle. Figure 3 (b) shows the char reaction rates at different angular positions. These are for center-to-center distances of l = 1.5, 2.0, and 3.0 particle diameters (D_p). The reaction rates are normalized by the single particle combustion rate. This normalization uses identical inflow conditions. In all cases except the side-by-side case at $l = 3.0D_p$, the carbon consumption rate is lower than for an isolated particle. As particle separation increases, the particles move from dense to sparse arrangements. During this process, the reaction rates gradually increase. Meanwhile, the

effects of wake flow and trailing flames progressively decrease.

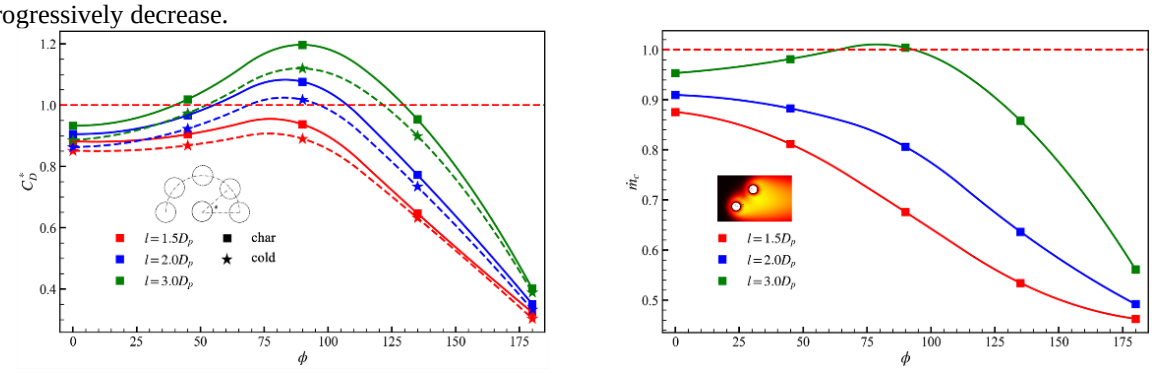

(a) (b)

Figure 3. The interaction during the combustion of two char particles: (a) drag coefficient distribution, (b) reaction rate distribution.

When studying how two-particle interactions affect reaction rates, we find that the nozzle effect has little influence on char reaction rates. Convection contributes almost nothing to species transport around particles. This is shown in Figure 4 and Figure 5. These figures display O_2 and CO transport budgets along the axis between side-by-side particles. Flame interaction is confined to boundary layers. Therefore, no direct flame interaction occurs when particle separation exceeds $2D_p$. The interactions between particles mainly affect forces through nozzle effects and wake flows. We also compared the drag coefficients of burning and cold-flow particles. This comparison shows that particle interaction effects on reaction rates cannot be directly applied to correct drag coefficients. Particle interactions remain dominant in controlling these forces.

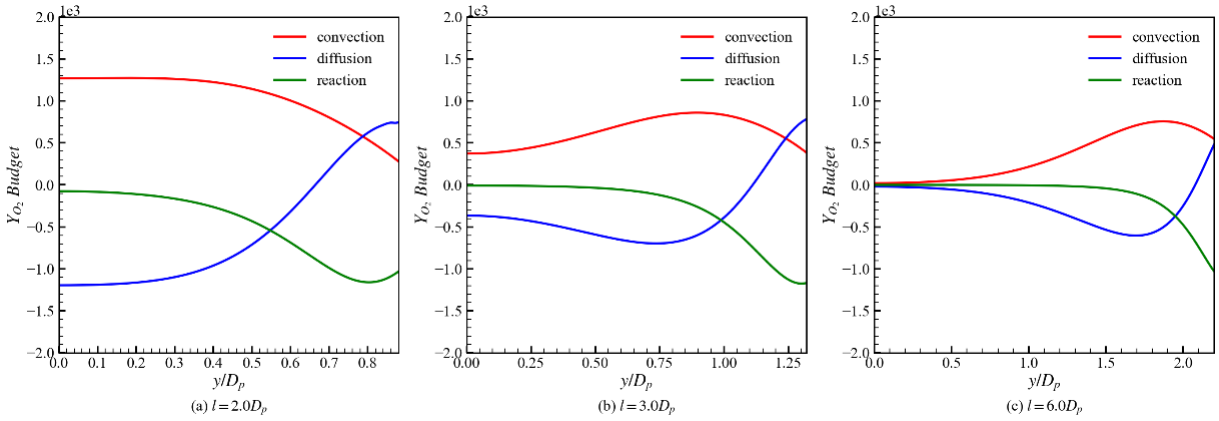

Figure 4. O_2 transport budget analysis between two char particles

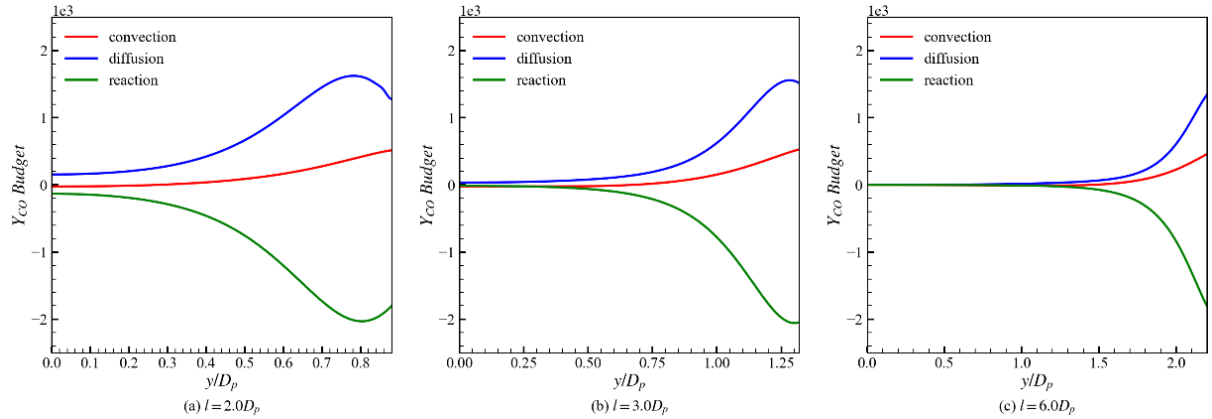

Figure 5. CO transport budget analysis between two char particles

3.2 CFD-DEM and coarse-grained CFD-DEM simulation of particle cluster behavior in coal gasification at the mesoscale

The presence of particle clusters in the riser of a circulating fluidized bed significantly affects the overall performance of the reactor. This study conducts in-depth investigations into the behavior of particle agglomerates in a riser adopting CFD-DEM and coarse-grained CFD-DEM simulations based on the Euler-Lagrange framework.

First, CFD-DEM simulations were performed on the characterization of particle clusters in laboratory-scale risers referring to Carlos Varas et al. [24] and compared with the longitudinal distribution curves of time-averaged particle concentrations, as shown in Figure 6 (a). The simulation results are in good agreement with the experimental data. It was observed that the overall particle concentration within the riser increases, and particles primarily accumulating in the lower region of the riser. Figure 6 (b) further compares the horizontal distribution of particle concentration at a gas velocity of 5.95 m/s, showing that the predicted results closely match the experimental values in both trends and magnitudes.

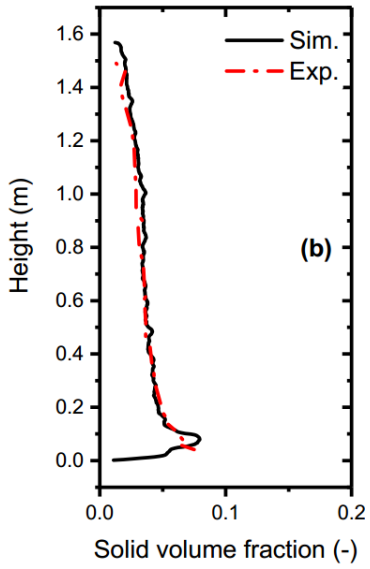

(a)

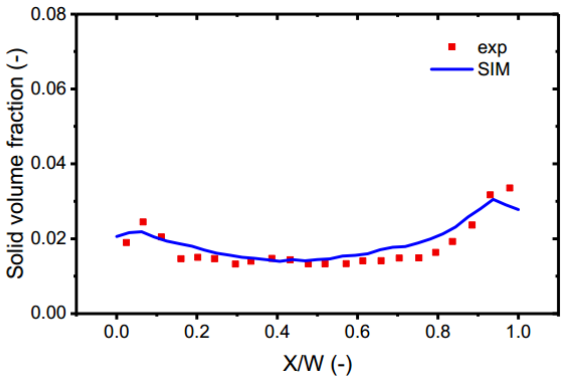

(b)

Figure 6. (a) Comparison between the predicted particle volume concentration and time-averaged measured values; (b) Horizontal distribution of particle volume concentration.

Furthermore, coarse-grained CFD-DEM is adopted to simulate a larger-scale fluidized bed reactor. The molar ratios of gas products at the riser outlet were statistically analyzed over 15s-30s, as shown in Figure 7 (a). It is observed that, although there are slight fluctuations in the CO to CO_2 ratio, the overall gasification product ratio remains relatively stable after 15s. Moreover, the outlet component data was time-averaged and compared with experimental data, as shown in Figure 7 (b). It was found that the particle size distribution of the bed material and fuel had relatively little impact on the component distribution at the outlet. Under all operating conditions, the simulated predictions closely match the experimental measurements, demonstrating that the coarse-grained CFD-DEM method can accurately predict the component distribution at the outlet.

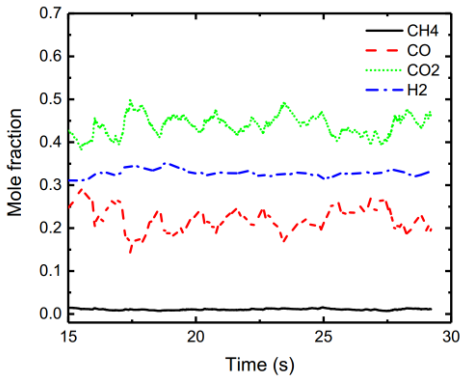

(a)

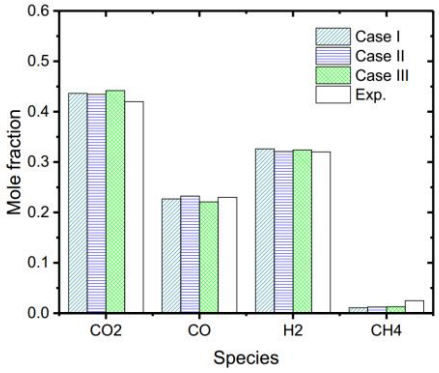

(b)

Figure 7. (a) Temporal variation of gas product ratios at the outlet; (b) Comparison of gas product ratios at the outlet under different operating conditions.

To gain a fundamental understanding of the fluidization characteristics within the riser, time-averaged results are presented in Figure 8. It is observed that the horizontal solid-phase concentration distribution within the bed exhibits a typical ring-core structure. In the vertical direction, as the height increases, the particle concentration decreases, and the high-concentration region near the wall accordingly shrinks.

Figure 8. Time-averaged gas-solid flow characteristics: (a) fluid voidage; (b) solid horizontal velocity; (c) solid vertical velocity; (d) solid velocity vector distribution.

Figure 9 provides a comprehensive summary of the intrinsic mechanisms underlying the temporal evolution of particle clusters. The analysis highlights the influence of the tail effect of the particle cluster on its formation. By tracking the dynamic evolution of a typical particle cluster, it was found that the characteristics of the cluster exhibit a quasi-periodic variation pattern. The changes in the properties of the particle cluster are primarily attributed to the interactions between the cluster and its surrounding environment. The competition and coordination between the growth and fragmentation mechanisms of the particle cluster lead to a strong correlation between its various characteristics (such as area, width, and falling velocity).

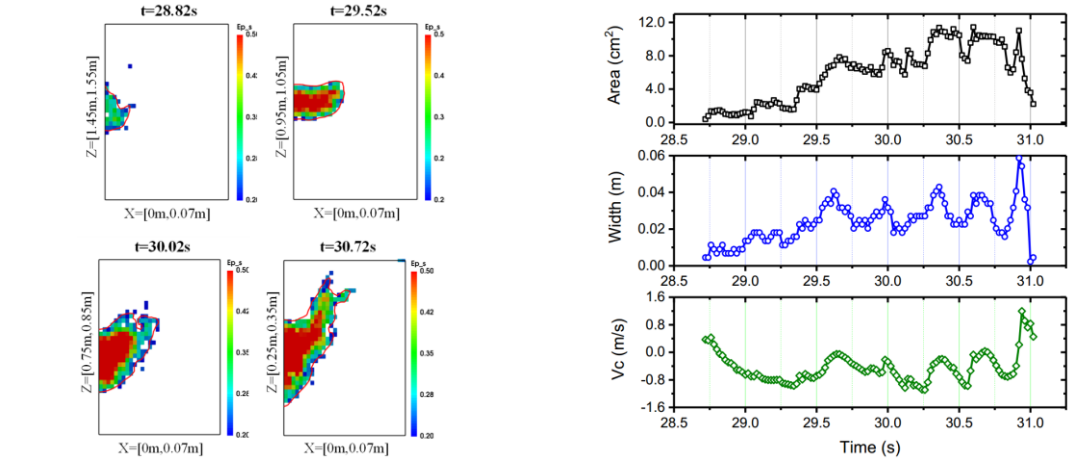

(a) (b)

Figure 9. Particle cluster behavior: (a) evolution of flow pattern; (b) temporal evolution curve.

3.3 Multiphase CFD-DSMC simulations of biomass chemical looping gasification at the macroscale

To simultaneously meet the requirements of both computational time and accuracy, a CG CFD-DSMC model was developed by coupling the coarse-graining method with the DSMC method. This model enhances computational efficiency while ensuring accuracy by employing collision probabilities and reducing the number of computational particles. The gasifier reactor from the dual-fluidized bed gasification system at Zhejiang University was selected as the simulation object. Figure 10 presents the gas product component concentrations at the gasifier outlet, as predicted by different simulation methods, alongside experimental results. It can be observed that CO and H_2 account for the majority of the gas composition at the gasifier outlet. The relative error between the simulated outlet gas concentrations and the experimental results is less than 20%, indicating that the errors in both methods are within an acceptable range. Compared to the MP-PIC method, the CG CFD-DSMC method demonstrates superior control of both the average and maximum errors in the prediction of gas component concentrations at the outlet.

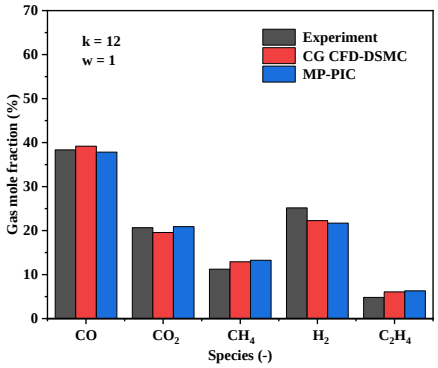

Figure 10. Concentration of gas product components at the outlet simulated by different methods.

Furthermore, based on the 1 MW_{th} pilot-scale BFB-CFB dual-fluidized bed system, a comparative simulation analysis of the biomass chemical-looping gasification process was conducted using the CG CFD-DSMC method proposed in this study and the traditional MP-PIC method. Figure 11 presents the average gas product component concentrations at the gasifier outlet. It can be observed that the computational accuracy and efficiency of the two models are approximately equivalent.

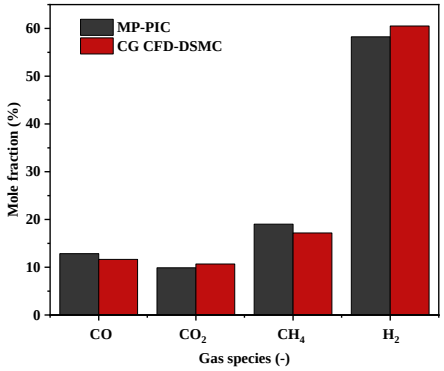

Figure 11. Gas product component concentrations at the gasifier outlet simulated by MP-PIC and CG CFD-DSMC method.

After ensuring the accuracy and efficiency of the model, a simulation study on the operational optimization of the structurally optimized biomass chemical-looping gasification system was conducted. Figure 12 presents the axial distribution characteristics of the biomass particle heat transfer coefficient (HTC) under different average particle sizes. The results indicate that the HTC of biomass particles is relatively high near the feed inlet and gradually decreases along the axial direction. This is primarily due to the continuous reduction in the temperature gradient between the biomass particles and the surrounding environment during the heat exchange process after the particles enter the gasifier. It is noteworthy that although the distribution trend of HTC is similar across different particle size conditions, the average absolute value of HTC decreases as the absorber's average particle size increases, suggesting a negative impact on the heat transfer process.

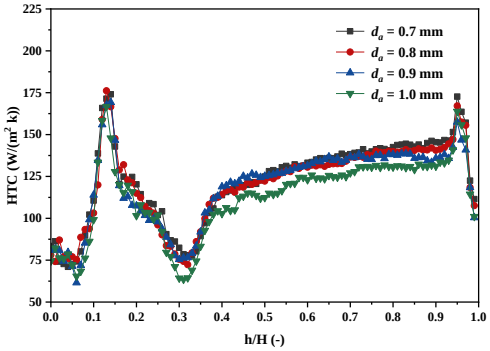

Figure 12. Effect of the average particle size on the heat transfer coefficient of biomass particles.

Figure 13 (a) illustrates the effect of biomass feed inlet height on the gas product composition. As the feed inlet height increases, the concentrations of CO and CO_2 in the outlet gas gradually increase, while the H_2 concentration significantly decreases. Simultaneously, the height of the gas-solid reaction zone increases with the feed inlet height, leading to reduced contact efficiency between CO_2 and bed material particles, thus affecting the carbonation reaction. After entering the gasifier, biomass particles undergo a series of physical and chemical transformations, causing a reduction in their mass. Some biomass particles are carried away by the gas flow after staying in the gasifier for a certain period. Therefore, a lower feed inlet height can extend the residence time of biomass particles in the gasifier, enhancing the gas-solid mixing effect and improving carbon conversion efficiency. Figure 13 (b) shows the effect of feed inlet height on LHV and CGC, where both LHV and CGC decrease as the feed inlet height increases, negatively impacting gasification efficiency.

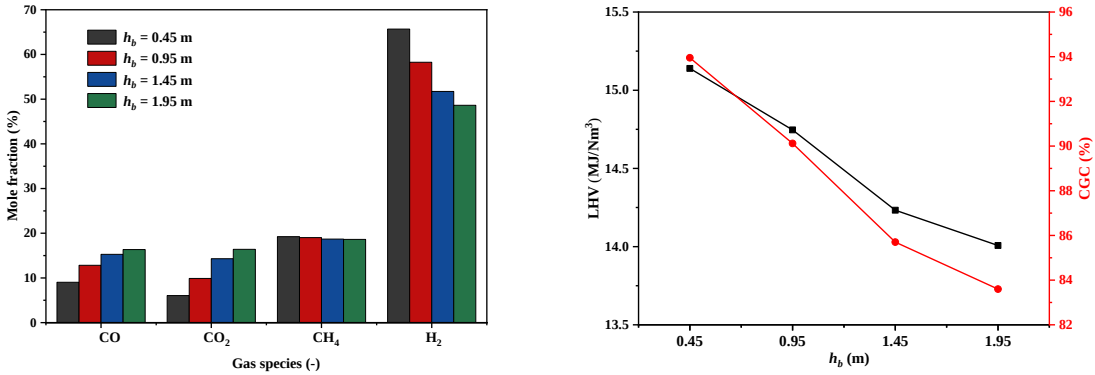

(a) (b)

Figure 13. Effect of biomass feed inlet height on gasification performance: (a) gas product components at the outlet; (b) LHV and CGC.

3.4 Industrial-scale MP-PIC simulation of coal pyrolysis and combustion staged conversion

The numerical model is extended to 150 MWe industrial-scale equipment and verifies the applicability of the model at industrial scale by simulating the cold and hot states of large existing equipment at Shanxi Power Plant. Figure 14 presents a comparison between the numerical simulation results and experimental data for the time-averaged normalized molar fractions of each gas component at the cyclone separator outlet of the pyrolysis furnace. The error between the simulation results and experimental data for CH_4 and H_2 is within 5%, while for CO_2, CO, and C_2H_6, the error is within 20%, which is acceptable in engineering applications.

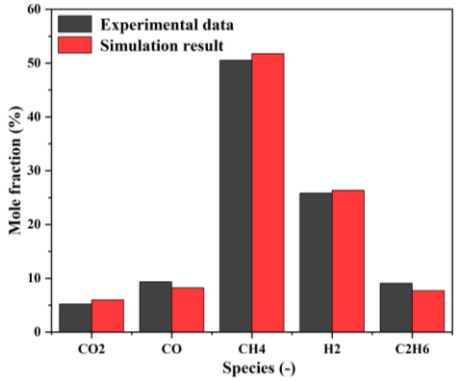

Figure 14. Comparison of simulated results and experimental data for the molar fractions of each gas component at the cyclone separator outlet of the pyrolysis furnace over time.

Figure 15 presents the simulation results, experimental data, and relative errors for the time-averaged syngas density at the cyclone separator outlet of the pyrolysis furnace at different operating temperatures. The trend of gas component content variation with temperature is consistent with engineering practice, and the simulation results closely match the experimental data. Monitoring the time-averaged syngas density at the pyrolysis furnace outlet and converting it to the density under standard conditions, the error in syngas density is within 3% at all temperatures. Overall, the model is reliable for predicting the flow regime and thermo-chemical properties of the circulating fluidized bed coal classification pyrolysis combustion integrated multi-product system.

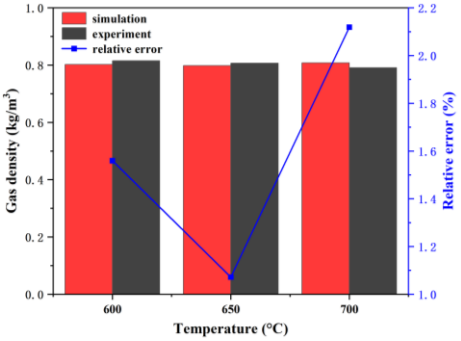

Figure 15. Comparison of time-averaged syngas density at the cyclone separator outlet of the pyrolysis furnace at different operating temperatures.

Based on the 150 MWe large-scale coal pyrolysis combustion classification conversion dual fluidized bed system at the Shanxi Pinglu Power Plant, the gas-solid flow field information inside the furnace was obtained using a cold-state model. Figure 16 shows the transient particle distribution in the system at different primary air velocities in the combustion furnace, with particle residence time represented by color. It can be observed that as the primary air velocity in the combustion furnace increases, the load on the four cyclone separators of the combustion furnace intensifies. Particularly at 15 m/s, a large number of particles clog the return feed pipes connecting the cyclone separators to the combustion furnace's bottom, which will impact the normal operation of the system. In contrast, the particle amount in the two small cyclone separators on the combustion furnace side connected to the pyrolysis furnace shows minimal variation. Therefore, changes in the primary air velocity of the

combustion furnace have a relatively small effect on the operation of the pyrolysis furnace side.

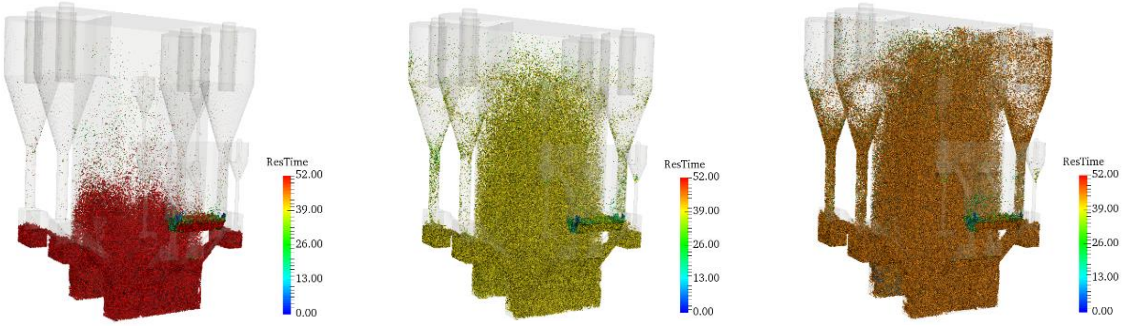

(a) (b) (c)

Figure 16. Transient particle distribution in the system at different primary air velocities in the combustion furnace: (a) 5 m/s; (b) 10 m/s; (c) 15 m/s.

Next, the temperature, gas composition, and particle distribution were obtained using a hot-state model to provide theoretical support for the system's design modifications. After the hot-state model reached dynamic stability, the distribution of particle volume fraction in the system was obtained, as shown in Figure 17 (a). It can be seen that the particle accumulation at the inclined surface of the feed leg, which was difficult to avoid in the cold-state model, has disappeared in the hot-state model, and the height of the high particle volume fraction area in the feed leg has decreased. The operation of the return feeders is stable, with sufficient particle accumulation effectively isolating the gas environments of the two furnaces, enabling material circulation between the furnaces while preventing gas backflow. The mass flow rates of syngas components at the pyrolysis furnace cyclone separator outlet were extracted, and the time-averaged molar fractions of the stable pyrolysis furnace circulating syngas components are shown in Figure 17 (b). The highest proportion is CH_4, close to 50%, followed by H_2 at about 25%, and then CO_2, CO, and C_2H_6 in decreasing order. Compared to the 1 MWth coal dual fluidized bed pyrolysis combustion classification conversion pilot plant, changes in the circulating syngas components were observed after the pyrolysis furnace stabilized. This suggests that compared to the pyrolysis furnace with single-sided coal feeding and sand as bed material, the system in this chapter involves some coal being fed directly from the combustion furnace and using coal particles generated ash as bed material, which led to significant changes in several characteristics.

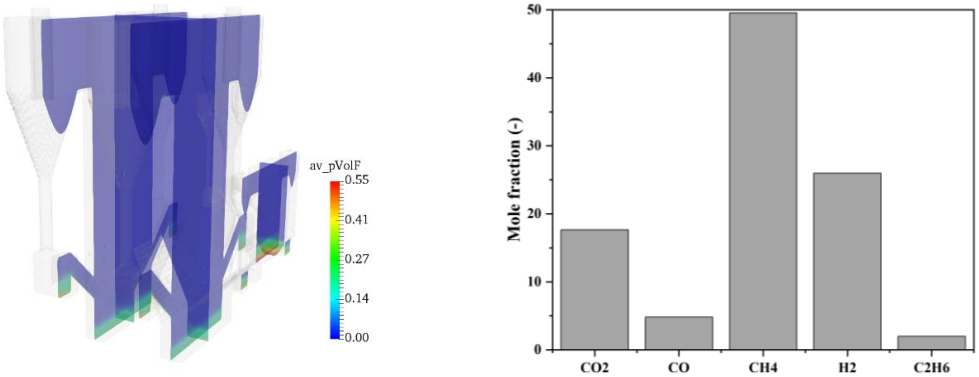

(a) (b)

Figure 17. (a) The distribution of the time-averaged particle volume fraction at each central cross-section; (b) the time-averaged molar fractions of each gas component at the cyclone separator outlet of the pyrolysis furnace.

4. CHALLENGES AND OUTLOOK

The various multiscale modeling methods reviewed in this paper each have distinct advantages and limitations depending on the scale and complexity of the system. At the microscale, the PR-DNS delivers unparalleled accuracy in resolving particle–fluid interactions and surface transport phenomena, yet its exorbitant mesh requirements confine it to small domains. Moreover, methods such as traditional CFD-DEM and its coarse-grained variant alleviate this burden by coupling continuum fluid solvers with discrete particle tracking, achieving reasonable precision while remaining

computationally tractable. For systems dominated by gas-phase transport, the coarse-grained CFD-DSMC and MP-PIC approaches scale efficiently to larger volumes, enabling practicale engineering simulations where computational efficiency becomes paramount.

A key challenge lies in the trade-off between model accuracy and computational efficiency. As the complexity of the simulations increases, the computational demand grows significantly. High-performance computing (HPC) and artificial intelligence (AI) integration offer great potential to accelerate multiscale simulations. AI can assist in optimizing models, improving computational strategies, and automating parameter adjustments. However, integrating AI with traditional physical models remains a challenge.

Looking ahead, a unified framework for multiscale coupling is essential. Such a framework would facilitate seamless integration across different scales, enhancing both accuracy and efficiency. Additionally, building a platform that combines data-driven approaches with physical modeling will be critical in advancing the next generation of simulation tools. This unified approach will offer more accurate, scalable, and efficient simulations, crucial for tackling complex engineering systems in the future.

ACKNOWLEDGEMENTS

We are grateful for the supports from the Fundamental Research Funds for the Central Universities (Grant No. 226-2024-00138), National Natural Science Foundation of China (Grant No. 588020-X42405), National Key Research and Development Plan of China (Grant No. 2024YFB4105902), Key Research and Development Program of Zhejiang Province (Grant No. 2025C01047), and Xplorer Prize.

REFERENCES

[1] Norouzi H R, Zarghami R, Sotudeh-Gharebagh R, et al. Coupled CFD-DEM modeling: formulation, implementation and application to multiphase flows[M]. John Wiley & Sons, 2016.

[2] Sundaresan S, Ozel A, Kolehmainen J. Toward Constitutive Models for Momentum, Species, and Energy Transport in Gas-Particle Flows[J]. Annual Review of Chemical and Biomolecular Engineering, 2018, 9: 61-81.

[3] Tenneti S, Subramaniam S. Particle-Resolved Direct Numerical Simulation for Gas-Solid Flow Model Development[J]. Annual Review of Fluid Mechanics, 2014, 46: 199-230.

[4] Van Der Hoef M A, Van Sint Annaland M, Deen N G, et al. Numerical simulation of dense gas-solid fluidized beds: a multiscale modeling strategy[J]. Annual Review of Fluid Mechanics, 2008, 40: 47-70.

[5] Luo K, Tan J, Wang Z, et al. Particle-resolved direct numerical simulation of gas-solid dynamics in experimental fluidized beds[J]. AIChE Journal, 2016, 62(6): 1917-1932.

[6] Tang Y, Lau Y M, Deen N G, et al. Direct numerical simulations and experiments of a pseudo-2D gas-fluidized bed[J]. Chemical Engineering Science, 2016, 143: 166-180.

[7] Clarke D A, Sederman A J, Gladden L F, et al. Investigation of Void Fraction Schemes for Use with CFD-DEM Simulations of Fluidized Beds[J]. Industrial & Engineering Chemistry Research, 2018, 57: 3002-3013.

[8] Freireich B, Kodam M, Wassgren C. An exact method for determining local solid fractions in discrete element method simulations[J]. Aiche Journal, 2010, 56: 3036-3048.

[9] Peng Z, Doroodchi E, Luo C, et al. Influence of void fraction calculation on fidelity of CFD-DEM simulation of gas-solid bubbling fluidized beds[J]. Aiche Journal, 2014, 60: 2000-2018.

[10] Li C, Eri Q. Comparison between two Eulerian-Lagrangian methods: CFD-DEM and MPPIC on the biomass gasification in a fluidized bed[J]. Biomass Conversion and Biorefinery, 2023, 13(5): 3819-3836.

[11] Singh R I, Brink A, Hupa M. CFD modeling to study fluidized bed combustion and gasification[J]. Applied Thermal Engineering, 2013, 52(2): 585-614.

[12] Gidaspow D. Multiphase flow and fluidization: continuum and kinetic theory descriptions[M]. Academic press, 1994.

[13] Adamczyk W P, Kozołub P, Kruczek G, et al. Numerical approach for modeling particle transport phenomena in a closed loop of a circulating fluidized bed[J]. Particuology, 2016, 29: 69-79.

[14] Hamidouche Z, Masi E, Fede P, et al. Unsteady three-dimensional theoretical model and numerical simulation of a 120-kW chemical looping combustion pilot plant[J]. Chemical Engineering Science, 2019, 193: 102-119.

[15] Lu B, Zhang N, Wang W, et al. 3-D full-loop simulation of an industrial-scale circulating fluidized-bed boiler[J]. Aiche Journal, 2013, 59: 1108-1117.

[16] Gidaspow D. Multiphase Flow and Fluidization: Continuum and Kinetic Theory Descriptions[M]. Academic Press, 1994.

[17] Syamlal M, O'Brien T J. The derivation of a drag coefficient formula from velocity-voidage correlations[J]. Technical Note, US Department of Energy, Office of Fossil Energy, NETL, 1987.

[18] Beetstra R, Van Der Hoef M A, Kuipers J. Drag force of intermediate Reynolds number flow past mono-and bidisperse arrays of spheres[J]. AIChE Journal, 2007, 53(2): 489-501.
[19] Hill R J, Koch D L, Ladd A J. Moderate-Reynolds-number flows in ordered and random arrays of spheres[J]. Journal of Fluid Mechanics, 2001, 448: 243-278.
[20] Li J, Cheng C, Zhang Z, et al. The EMMS model—its application, development and updated concepts[J]. Chemical Engineering Science, 1999, 54(22): 5409-5425.
[21] Bird G A. Molecular Gas Dynamics[M]. Oxford, 1976.
[22] Huilin L, Zhiheng S, Ding J, et al. Numerical simulation of bubble and particles motions in a bubbling fluidized bed using direct simulation Monte-Carlo method[J]. Powder Technology, 2006, 169(3): 159-171.
[23] Makino A, Namikiri T, Kimura K. Combustion rates of graphite rods in the forward stagnation field with high-temperature airflow[J]. Combustion and Flame, 2003, 132(4): 743-753.
[24] Kraft S, Kuba M, Kirnbauer F, et al. Optimization of a 50 MW bubbling fluidized bed biomass combustion chamber by means of computational particle fluid dynamics[J]. Biomass and Bioenergy, 2016.

Conference on Modelling Fluid Flow (CMFF'25)
The 19th International Conference on Fluid Flow Technologies
Budapest, Hungary, August 26 - August 29, 2025

OPTICAL THERMOMETRY COUPLED TO THE MEASUREMENT OF OTHER QUANTITIES (VELOCITY, PRESSURE)

Benoît FOND

[1] Department of Aerodynamics, Aeroelasticity and Acoustics (DAAA), ONERA, the French Aerospace Lab, Université Paris Saclay, benoit.fond@onera.fr

ABSTRACT

The visualization and quantification of thermal mixing in turbulent fluid flows is key to the development of accurate turbulence modelling. These models are needed to predict the behaviour of flows in industrially relevant applications as well as geophysical flows (ocean, atmosphere, earth's mantle, etc.). This talk will describe thermometry techniques based on luminescent tracer particles which can be combined with particle-based velocimetry to image both temperature and velocity in laboratory flows. The emphasis will be mostly on inorganic luminescent crystals, typically referred to as thermographic phosphors. These particles exhibit a wide range of luminescence properties and can be chosen to match the application needs, e.g., for use in cryogenic flows, at physiological temperatures, or up to 1000 K. There are also various implementations of this measurement concept. We can exploit the temperature dependence of the luminescence emission spectrum or the decay time of the particles to measure the temperature. The velocity can be measured simultaneously using temporally separated images of the particles using light scattering as in traditional Particle Image Velocimetry (PIV), using luminescence light or even single images of phosphorescence streaks caused by the motion of the particles during their luminescence decay.

Recent developments include high-resolution measurements in submillimeter boundary layers, a proof-of-concept study of 3D temperature and velocity measurements in gas flows, and 2D thermometry in water with sub-°C precision.

INTRODUCTION

The ubiquitous presence of thermometers in daily life is indicative of the significant influence temperature has on thermodynamical, thermomechanical and thermochemical variables. As examples, we can mention the diffusive properties of fluids, the chemical reactions rates, the saturation pressure of fluids or the solubility of gas such as oxygen in liquids. Common thermometers typically provide "absolute" temperature value, within a system: the human body, the oil in the pan or in a car engine, the water in the swimming pool because this value informs on the temperature-sensitive variables of interest, such as physiological activity, viscosity, decomposition rate. Properties are rarely insensitive to temperature, so a large part of temperature sensing applications are concerned with correcting the reading of other sensors, for example for pH, pressure, velocity, flow rates. In that case temperature accuracy is critical.

In fluid flow research, we are generally more interested in spatial or temporal derivatives of the temperature, which serve to detect the location and power density of heat sources, to estimate density variations resulting in buoyancy forces, or to quantify heat transfer. We can therefore tolerate larger error in the absolute temperature value that for the cases of the previous paragraph, as long as we can detect small relative temperature variations. Here we aim rather at achieving high spatial, temporal and temperature resolution (or precision), since they dictate together the uncertainty in spatial or temporal derivatives. Optical imaging techniques, can provide two- or sometimes three-dimensional information, and can rely on laser illumination to probe only a "thin" spatial or temporal slice of the flow.

Accurately predicting mass or heat transport in turbulent flows requires turbulence models with various levels of complexity. They necessitate calibration or validation step by "ground truth" reference data, either provided by direct numerical simulation (DNS) or experiments. As DNS is limited to low turbulent Reynolds number and/or small domain size, experiments remain necessary. An experimental data which would be crucial for turbulence model development are the so-called turbulent diffusion terms, which quantify the correlation between fluctuations of the velocity and

of a scalar quantity such as temperature, or concentration. Imaging of temperature alone is no longer sufficient, and velocity must be measured at the same location and at the same time. In this talk, we will cover optical techniques based on luminescent particles, which can act both as local thermometers and as flow tracers, therefore being able to provide correlated velocity and temperature information

PHOSPHOR PARTICLES

Phosphors are inorganic solid materials, which function is to convert light. They are generally in the form of polycrystalline ceramic particles. Note that most phosphors do not contain the element phosphorus, but phosphors and phosphorus share the property of luminescence, which is in their common greek root „phosphoros" – which means light bearer. Phosphor crystals are doped with luminescent ions, that means that a small fraction of the elements in the crystal are replaced with elements with specific electronic configurations. These dopants confer to the crystal its light absorbing and light converting properties. The light re-emission or luminescence, is as many physical processes sensitive to temperature. Unlike fluorescence, or phosphorescent molecules, the luminescence from phosphors is generally insensitive to the gas composition, in particular oxygen concentration and to the pressure. The ceramic nature of phosphors also provide their excellent thermochemical stability. Finally, various elements can be doped in a wide range of crystal phases, so that phosphor luminescent properties can be very varied, with emission from the UV to the mid-wave infrared, and temperature sensitive range which can be for example in the cryogenic range or around 1500 K.

Thermometry using these temperature sensitive particles, is refered to as phosphor thermometry. Often particles are applied onto a surface, using a binder material, to infer the surface temperature. This technique is often applied in combustion: on combustor wall, injector tip. It is then used to derive flame to wall heat transfer rates or to provide thermal boundary conditions for simulations of the fluid domain. However, there are also many other applications, e.g. to measure the surface of discharging batteries, that of rotating objects, or in biological media to name a few.

PHOSPHOR PARTICLES IN PRESSURE SENSITIVE PAINTS

As an example for the need of temperature measurements to correct another sensor, we mention here one of our recent study on pressure sensitive paints. These paints incorporate phosphorescent molecules, which emission can be extinguished by collision with oxygen molecules. When operating in wind tunnel with constant oxygen mole fraction, these paints which detect the oxygen partial pressure can be used as total static pressure measurements. Unfortunately, the luminescence is not only extinguished by oxygen molecules, but also by temperature. State of the art pressure sensitive paints, which are able to track pressure fluctuations at kHz rate over a wing model have very high temperature sensitivity on the order of 2%/°C, while their pressure sensitivity is below 1%/kPa. That means a variation of 1K in temperature, relates to at least a 2 kPa error. In wind tunnel experiments, the temperature continuously varies, sometimes by tens of degree, so that if not corrected for, temperature variations would lead to very wrong results. Correction is often done by integrating pressure taps to account for the temperature variations, but this is not possible for thin and/or rotating models. Since inorganic phosphors are insensitive to oxygen concentration, they can be integrated into a pressure sensitive paint to indicate the paint temperature without having to know the pressure. The temperature information can then be used to remove the contribution of the temperature variations on the pressure signal.

FLUID THERMOMETRY METHODS USING PHOSPHORS

To measure the fluid temperature, micron size particles are introduced into the flow. The approach relies on the assumption of thermal equilibrium between the fluid and the particle. Heat transfer for this size of particles is mainly by conduction. The particle thermal conductivity being large compared to that of the fluid, heat transfer is limited by thermal diffusion through the fluid and the particle temperature can be considered uniform. To derive temperature response times, we also consider that for gases, the thermal diffusivity of the fluid is high, leading to a very simple expression of a exponential decay response to a step-change variation in fluid temperature, with a time constant $\tau_T = {d_p}^2 \frac{\rho_p C_{pp}}{12 k_f}$.

Here d_p is the particle diameter, ρ_p the particle density, C_{pp} the particle heat capacity and k_f the thermal conductivity of the fluid. Phosphor particles are typically produced as micron size powder. Considering a 2 micron diameter particle, the thermal relaxation time constant is about 100 µs in air at 300 K. Across a flame front, the relaxation time constant gets significantly shorter, as the thermal conductivity increases.

The most obvious temperature sensitive response of luminescence sensors, is that of the emission intensity. Due to thermal quenching, when the temperature increases above a certain value (which greatly varies depending on the different dopant/host crystal phase combinations), the luminescence quenching rates become significant, which results in a drop in emission intensity. However this response cannot be exploited for reliable measurements, as the

detected signal intensity on a camera also scales with the particle concentration, and the distribution in excitation light. Those two quantities can vary significantly in time and space in a practical experiment due for example to light refraction at interfaces, or mixing of particle streams. Instead we exploit temporal or spectral variations of luminescence with temperature, to make the measurements independent of absolute light level. Either it is the persistence time or decay time of the luminescence after the end of the excitation, which is used as a measure of temperature, or the shift in emission spectrum or apparent colour.

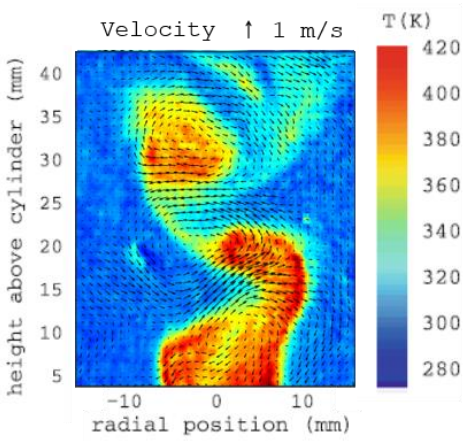

Fig. 1 Temperature and velocity field measured in the airflow in the wake of a heated cylinder [1]

To measure the velocity of the particles together with their temperature, we can simply exploit the shift in the particle position over time. In general we use lasers capable of delivery two shorts pulses of light during a short time, so that the particles only move by a few pixels between the two images. An example of combined temperature and velocity measurement obtained in the wake of a heated cylinder by this combined approach is shown in Fig. 1. Counter rotating eddies are alternatively shed from the cylinder on either side, and shear apart pockets of warm fluid which had formed near the rear stagnation point of the cylinder. This shearing process increase the surface area for heat exchange with the cooler surrounding fluid, leading to thin regions at intermediate temperatures between the two warm pockets.

While the spatial and temporal resolution is determined mainly by the laser and imaging system, the temperature range and temperature resolution is directly linked to the choice of phosphor and temperature sensitive response. We provide here two examples.

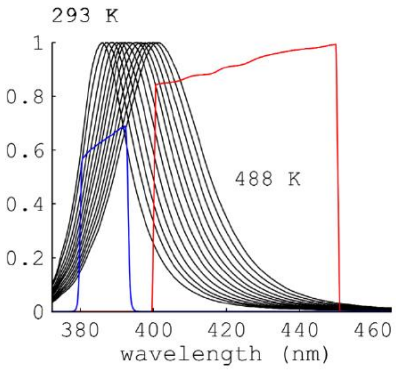

Fig. 2 ZnO emission spectrum and spectral filters [2]

The first is ZnO which can be used for a range of about 200 K with a precision in the order of 5 K. The range can start anywhere between 100 and 300 K. This depends on the choice of spectral filters used to detect with high sensitivity the change in emission colour. The ZnO emission spectrum in the range 20°C to 215°C is shown in Fig. 2. It is normalised to the emission maximum for each temperature. As the temperature increases, the emission band shifts towards higher wavelengths. Two filters are chosen, so that the area under the red curve increase with temperature and that area under the blue curve decreases. The ratio of the intensities collected by the two filters is therefore a monotonic function of temperature which can be calibrated against a reference sensor.

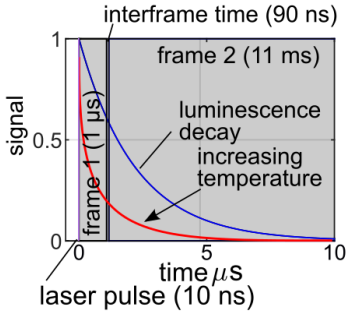

Fig. 3 Temporal diagram for rapid lifetime determination using a double frame camera and a pulse laser [3]

Instead of relying on emission spectrum changes, we can also image changes in the decay time. For this we can use a rapid lifetime determination approach with a double frame camera, as described in Fig. 3. Those cameras are able to take two exposure separated by only a short time delay (on the order of 100's of nanosecond), and are therefore used in PIV to capture the images of the particles during the two subsequent laser pulses. Here we place the excitation laser pulse during the first frame, so that the second exposure starts about 1 microsecond after the laser pulse. At the temperature increases, the decay time shortens so that the intensity collected by the second image relative to the first image is lower.

For this approach to work, the decay time of the phosphor needs to be sufficiently short, so that the particles do not move significantly during the second image, but also sufficiently long otherwise the second image is too late to detect any luminescence signal. An ideal range is 1-5 microseconds. For this approach to work, we need phoshors with decay time in that range, but that are also sensitive around the temperature of interest. Some phosphors such as $BaMgAl_{10}O_{17}:Eu^{2+}$, shows this behaviour but only at 500°C which is only of use to very specific applications. Many laboratory flows can study heat transfer around room temperature. We identified from some physics studies from the 70s, a material which has the right decay time and sensitivity. The composition is ScVO4:Bi, which has a short decay time of around 4 microseconds at 0°C and which rapidly changes with temperature around 20°C. The rate of change or temperature sensitivity is 2% per °C. We therefore synthesised, caracterised and applied this phosphor in a demonstration experiment shown in Fig. 4. Here the a cold liquid (30°C) is injected into a warm cuvette (50°C). Both hot and cold fluids are dispersion of water and phosphor particles. Based on a region unaffected by the jet, we can determine the temperature resolution of the approach as the standard deviation between pixels which are supposed to be at the same temperature. Here this single shot precision is 0.3 K.

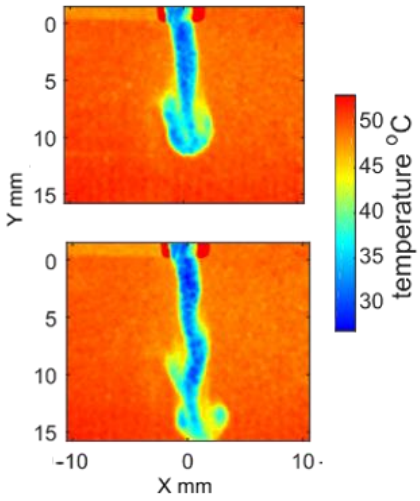

Fig. 4 Temperature fields in a water filled cuvette shortly after cold water injection [3]. Time separation (0.5 s)

3D MEASUREMENTS

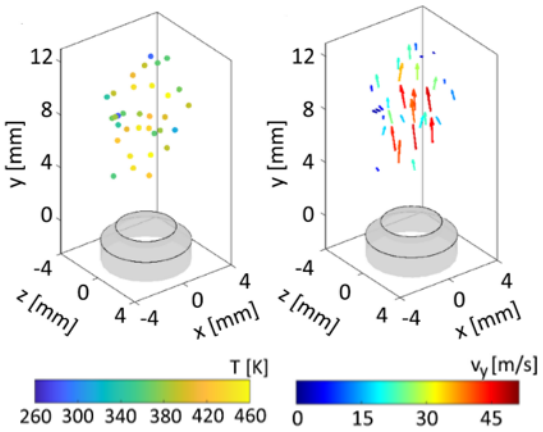

Fig. 5 Scatter plot of velocity and temperature data measured in a turbulent jet [4]

Using luminescent particle tracers, we showed that we can derive velocity and temperature information from the same particles. We can also exploit the fact the particles are distinct luminescence emitter in space, to make local temperature measurement in three dimensions. For this, we seed the particles in the flow, and take several views of the cameras to triangulate the position of each particle. We therefore imagined a system combining a 3D particle tracking velocimetry approach with a 2D two colour imaging approach. The 3D system determines the position of all the particles in the 3D space. The 2D two colour imaging approach capture luminescence particle image containing the temperature information for one view. If we isolate the signal from individual particles then the signal from that particle can be associated with its 3D position, and the ratio of luminescence intensity to its temperature. A demonstration of the concept is shown in Fig. 5, where one can see a scatter plot of velocity and temperature datapoints in the 3D space. Here particles are seeded in a turbulent heated jet surrounding by a coflowing stream. The aim is now to increase the density of temperature measurement using higher particle seeding concentration.

CONCLUSIONS

Luminescent particles make it possible to measure temperature and velocity simultaneously in a turbulent fluid flow using a single tracer. There are a variety of phosphors which can cover different temperature range, yet using the same instrumentation. The rapid lifetime system, which uses a single camera for temperature detection is particularly attractive for newcomers into the field.

ACKNOWLEDGEMENTS

I gratefully acknowledge the financial support of the French Research Agency (ANR), the German

Research Foundation (DFG), the National Research Council of Canada, the French Civil Aviation Authority (DGAC) and the Agence Innovation Defense (AID).
Many collaborators contributed to this work: Christopher Abram, Mohammadhassan Khodsiani, Guangtao Xuan, Joel Lopez Bonilla, Mohamed Elashry, Nammuni Chaturah, Luming Fan, Arwa Rashed, Encarnacion Arroyo, Georgios Kasapis, Orian Le Bourgeois, Fabio WA Martins, Frank Beyrau, Maria Klepikova, Yves Meheust, Patrizio Vena, Bruno Savard, Sergey Borisov, Gauthier Rousseau, François Nicolas, Guillaume Pilla, Nicolas Fdida, Cornelia Irimiea, Sylvain Petit.

REFERENCES

[1] C. Abram, B. Fond, A.L. Heyes, F. Beyrau, „High-speed planar thermometry and velocimetry using thermographic phosphor particles". *Appl. Phys. B,* Vol. 111, pp. 155–160 (2013).

[2] C. Abram, B. Fond and F. Beyrau "high precision fluid thermometry using ZnO tracer particles," *Opt. Express* 23, 19453-19468 (2015)

[3] C. Abram, I W. Panjikkaran, S N. Ogugua, and B. Fond, "$ScVO_4:Bi^{3+}$ thermographic phosphor particles for fluid temperature imaging with sub-°C precision," *Opt. Lett.,* Vol. 45, pp. 3893-3896 (2020),

[3] M. Stelter, F.W.A. Martins, F. Beyrau, B. Fond, „Thermographic 3D particle tracking velocimetry for turbulent gas flows", *Meas. Sci. Technol.* Vol. 34 p. 074008 (2023)

Conference on Modelling Fluid Flow (CMFF'25)
The 19th International Conference on Fluid Flow Technologies
Budapest, Hungary, August 26 - August 29, 2025

MACROSCOPIC AND MICROSCOPIC BLOOD FLOWS

Franck NICOUD[1,4], Salomé Bru[2], Pierre Pottier[2,3], Pierre Taraconat[3], Simon MENDEZ[2]

[1] Corresponding Author. Institut Montpeliérain Alexander Grothendieck, University of Montpellier, CNRS, Place Bataillon, 31095 Montpellier, France. Tel.: +33 6 730 55140, E-mail: franck.nicoud@umontpellier.fr
[2] Institut Montpeliérain Alexander Grothendieck, University of Montpellier, CNRS, Montpellier, France
[3] HORIBA Medical, 398 rue du Caducée - 34790 Grabels, France
[4] Institut Universitaire de France, Paris, France

ABSTRACT

This paper highlights some of the advancements enabled by computational physics in the field of cardiovascular biomechanics. We briefly introduce the numerical methods of the YALES2BIO platform before delving into two ongoing studies. The first study exemplifies macroscopic scenarios where blood is modelled as a continuous fluid. Specifically, we examine intracardiac hemodynamics, exploring how the design of the mitral valve can alter turbulent dissipation. This study demonstrates how such simulations can enhance a medical imaging technique used routinely in clinical settings. The second example addresses situations where the physical phenomena occur at such small scales that the suspension nature of blood must be considered. We discuss the results of a numerical pipeline designed to simulate the operation of an industrial blood cytometer, illustrating how computational physics can provide access to data that is experimentally unattainable and useful for improving system performance.

Keywords: cardiovascular biomechanics, computational physics, cardiac efficiency, red blood cells, cytometry

1. INTRODUCTION

The ability to predict blood flow characteristics could significantly enhance diagnostic and treatment capabilities, given that many cardiovascular diseases are related to blood flow features. In this respect, computational physics serves as a natural complement to theoretical, experimental, and medical imaging techniques used to address questions related to both microscopic and macroscopic blood flows.

Many medical questions related to blood flow pertain to the largest arteries and veins in the cardiovascular system. Typical length scales range from 1 mm to a few centimeters, and the Reynolds number can be as high as several thousand. At these scales, blood is often considered a homogeneous fluid with either constant viscosity (typically $\mu = 3 \times 10^{-3}$ Pa.s) or characterized by shear-thinning behavior. Key challenges include managing the highly complex and deformable geometry of the blood flow domain, the transitional nature of wall-bounded blood flow, interactions with thin and highly deformable membranes (e.g., valve leaflets), thrombus formation due to biomedical materials, and validation.

In reality, blood is not homogeneous but a dense suspension (volume fraction ranging from 20-50%) of particles sized from $2\,\mu m$ (platelets) to $20\,\mu m$ (white blood cells). Over 95% of the cells flowing in plasma are red blood cells, which are non-spherical particles (equivalent diameter of $6\,\mu m$). Given their reduced volume of only 0.65, red blood cells are highly deformable, with their dynamics resulting from the coupling between the inner fluid (cytosol), the cell membrane, and the outer fluid (plasma). In flow regimes typical of the microcirculation, hemodynamics is dominated by suspension-related phenomena, such as the non-inertial migration of red blood cells towards the center of vessels.

This paper outlines some of the accomplishments and ongoing modelling efforts utilizing the YALES2BIO solver (imag.umontpellier.fr/~yales2bio/), developed at Institut Montpelliérain Alexander Grothendieck (IMAG) in Montpellier, France. Section 2 provides a brief overview of the numerical strategy employed. Section 3 illustrates how macroscopic simulations of intracardiac flow can enhance a medical imaging technique, specifically echocardiography, and deepen the overall understanding of cardiac function. Section 4 presents the results of a numerical pipeline designed to simulate the dynamics of red blood cells flowing through a Coulter-based cytometer,

demonstrating its potential to improve the cytometer's performance.

2. NUMERICAL METHOD

YALES2BIO is a highly parallelized multiphysics solver, derived from the YALES2 solver developed at CORIA in Rouen, France. It is specifically designed for simulating blood flows at both macroscopic and microscopic scales. At its core, YALES2BIO solves the incompressible Navier-Stokes equations using a finite-volume approach with a fourth-order discretization scheme, suitable for unstructured meshes [1]. To maintain the divergence-free property of the velocity field, the solver employs the projection method introduced by Chorin [2]. Namely, the velocity field is first advanced in time using a low-storage, fourth-order Runge-Kutta scheme [3] during a prediction step. This predicted velocity field is then corrected by applying a pressure gradient, which is obtained by solving a Poisson equation for pressure. The Poisson equation is solved using the Deflated Preconditioned Conjugate Gradient algorithm [4]. For turbulence modeling, YALES2BIO performs large-eddy simulations using the sigma subgrid scale model [5, 6]. This model ensures that no eddy viscosity is applied in canonical laminar flows and is well-suited for wall-bounded and transitional flows [7, 8]. Additionally, the solver can handle computations with moving meshes by employing an Arbitrary Lagrangian-Eulerian formulation [9, 10].

YALES2BIO conducts various simulations involving fluid-structure interactions at both macroscopic [11] and microscopic scales [12-14]. For fluid-structure coupling, the solver utilizes Peskin's immersed boundary method (IBM) for massless structures [15]. In this approach, the fluid perceives the structure's action as a force density applied during the prediction step. The forced Navier-Stokes equations are then solved as previously described. Once the flow velocity is computed, the structure is convected by the flow after interpolating the fluid velocity onto the structure.

Since the deformed structure is massless, it remains in equilibrium, allowing for the calculation of forces at the nodes of the structure mesh. These forces are then regularized, or spread, over the fluid mesh. As YALES2BIO employs unstructured meshes, the original IBM, designed for Cartesian meshes, has been adapted using the Reproducing Kernel Particle Method. This method ensures that force regularization and velocity interpolation impose several mathematical moments of the regularization/interpolation function [16-18]. For red blood cells (RBCs), the membrane mechanics are modeled by combining different models that represent either the in-plane [19] or out-of-plane resistances of the membrane [20]. More details may be found in Mendez and Abkarian [14]. The method, initially developed for infinitely thin membranes, has also been extended to finite-size yet thin structures [11, 21].

Numerous validation test cases have been presented in both 2D [18] and 3D [21], particularly for fluid-structure interaction coupling. The remainder of this paper describes two ongoing applications to illustrate how computational physics can address academic, medical, or industrial questions relevant to either macroscopic (Section 3) or microscopic (Section 4) scales.

3. INTRACARDIAC BLOOD FLOW

Chnafa et al. utilized YALES2BIO to simulate intracardiac flow that aligns with the time-evolving geometry observed through computed tomography of an actual patient [9] or magnetic resonance imaging of a normal volunteer [10]. In both scenarios, the computational domain spans from the four pulmonary veins to the root of the aorta, encompassing the left atrium and ventricles, as well as simplified models of the mitral and aortic valves.

The simulations employed Large Eddy Simulations based on a subgrid scale model well-suited for representing wall-bounded transitional flows [5, 22], and were conducted over more than 50 cardiac cycles. The analysis revealed that turbulence is periodically generated in the left ventricle at the end of diastole and dissipates during systole [23]. Moreover, the large vortex observed from advanced medical imaging techniques [24] during late diastole is accurately captured in the phase-averaged computational results. This particular flow feature is of significant medical interest, as it is believed to aid in redirecting blood momentum towards the ventricle's outlet, thereby facilitating ejection. For cardiologists, the ability to characterize this feature using routine echocardiography would be highly beneficial.

To achieve this, it is essential to reconstruct the intraventricular velocity field based on the radial component measured in colour Doppler mode. The numerical database for intraventricular flow [9] has been instrumental in developing a reconstruction algorithm based on an optimization procedure [25]. As illustrated in Figure 1, the Computational Fluid Dynamics (CFD) recirculation zone is well retrieved by the so-called intraventricular Vector Flow Mapping (iVFM) technique. Several enhancements to the original algorithm have been proposed to better incorporate the divergence-free constraint [26] and to represent the three-dimensional structures of the flow more accurately [27]. Recently, a methodology based on machine learning has proven to be both robust and efficient in retrieving intraventricular flow features from echocardiography [28]; a physics-guided neural network was trained using a database produced at IMAG, which included a variety of sizes, heart rates, and mitral valve designs [29].

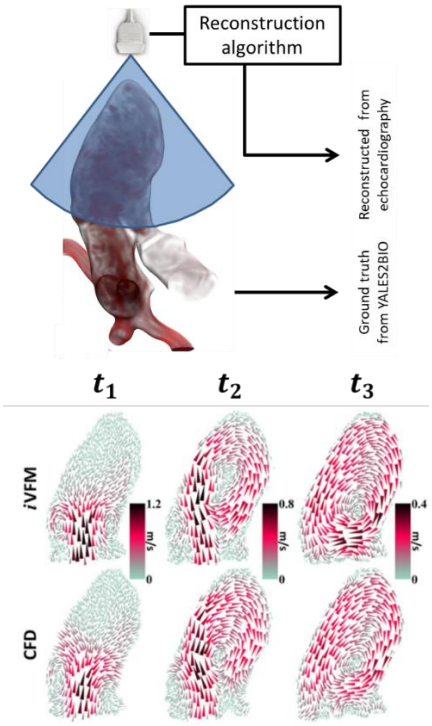

Figure 1. Top: A virtual echocardiography exam is performed on the numerical intracardiac flow. Bottom: The flow structure reconstructed from the virtual echocardiography image (top) is compared to the exact flow structure from the numerical database (bottom) at three different time points.

In addition to supporting the development of reconstruction methods for echocardiography, detailed simulations of intracardiac flow can enhance the overall understanding of heart function. As previously mentioned, the large vortex observed through advanced medical imaging techniques [24] during late diastole is of particular medical interest. It is believed to help redirect blood momentum toward the ventricle's outlet, thereby facilitating ejection [30]. This mechanism and its implications for the heart's pumping efficiency were recently studied computationally using simulations similar to those conducted by Chnafa et al. [9] enriched by a parameterized model, allowing for the investigation of the mitral valve shape's effect on intraventricular flow. Four cases considered are illustrated in Figure 2, which displays the vortical structure of the intraventricular flow at late diastole.

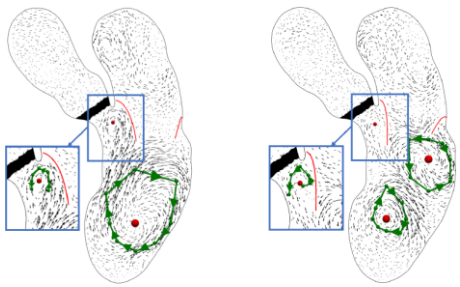

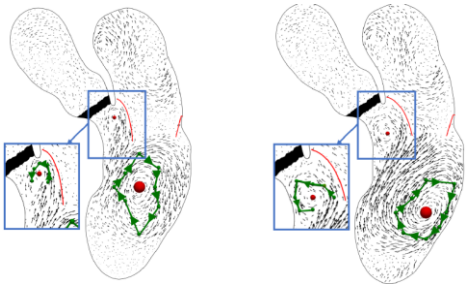

Figure 2. Phase-averaged velocity field at mid-diastole, the phase during which a large vortex, supposedly favourable for blood ejection through the aorta, is expected to be present. Green regions denote the different vortices within the ventricle, while red markers indicate their respective centres. The red lines depict the intersection between the mitral valve and the plane of view. Top left (C01): Physiological mitral valve with normal opening and orientation. Top right (C02): Normal opening with anterior orientation. Bottom left (C03): Normal orientation with wider opening. Bottom right (C04): Posterior orientation with smaller opening.

The expected large vortical structure is accurately captured in the reference case (top left), where the mitral valve opening and orientation are physiological. In cases where the valve opening is enlarged (bottom left) or reduced (bottom right), a vortical structure is still present, although its size and position are altered. The modifications are even more pronounced when the orientation of the mitral valve is changed (top right). In this scenario, the expected clockwise-rotating vortex (top left) is replaced by a pair of counter-rotating vortices. It is evident that the details of the mitral valve geometry significantly impact the flow organization within the ventricle.

To determine whether these modifications result in a significant change in cardiac pumping efficiency, the balance of ventricular kinetic energy has been recently studied [29]. This balance is obtained by integrating the kinetic energy equation over the time-dependent ventricular domain and applying the Reynolds transport theorem. The different contributions are displayed in Figure 3, which provides a physical interpretation of each term. In all the cases considered, the contributions sum up to approximately zero within a small fraction (approximately 3%) of the ventricle's power. This indicates that the simulations can be reliably used to further analyse the energy balance within the ventricle. As illustrated in Figure 4, this balance is dominated by the three pressure terms P_{AP}, P_{MP} and P_{muscle} (see Fig. 3), regardless of the specifics of the mitral valve.

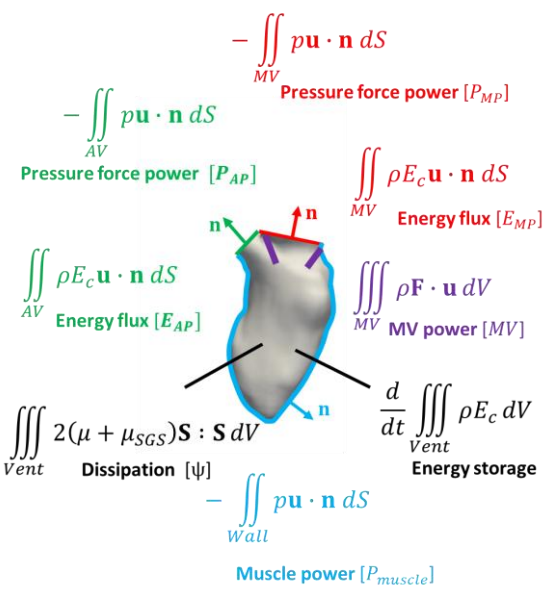

Figure 3. Main contributions to the balance of kinetic energy within the control volume defined by the cardiac muscle (blue) and two fixed planes located near the mitral annulus (red) and the aortic valve (green). In addition to energy storage (which cancels out after time integration due to time periodicity of the cardiac cycle), the two volume terms include the power of the mitral valve leaflets (violet) and the viscous dissipation (black). The latter accounts for turbulent effects through subgrid scale viscosity μ_{SGS}.

However, the dissipation term is highly dependent on the valve opening, reaching a value three times larger when the valve opens less (case C04) compared to the wider opening (case C03) — see Figure 4. Despite this variation, the amount of energy dissipated over one cardiac cycle remains a small fraction (1-2%) of the energy involved in pumping blood from the atrium to the aorta. From this perspective, the energy efficiency of the pumping mechanism remains very high (greater than 98%), independent of the mitral valve design and flow structure within the ventricle. Note that this conclusion may not hold in cases where valve leakage is present, causing some blood to flow back into the atrium during systole.

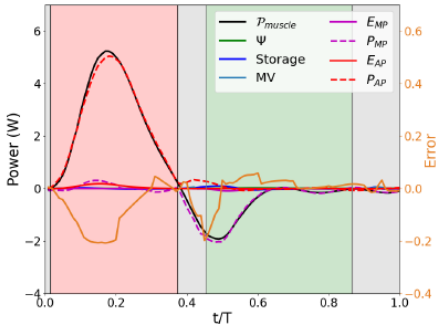

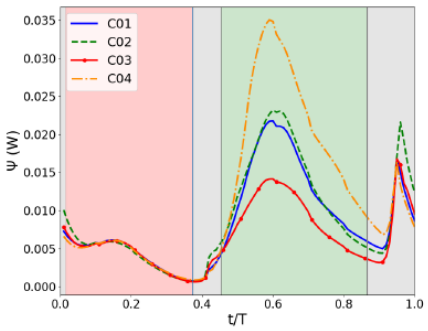

Figure 4. The top plot illustrates the time evolution of the main contributors to the kinetic energy balance for the normal case C01. The acronyms are defined in Figure 3. Very similar evolutions are obtained for the other cases displayed in Figure 2 (not shown). The bottom plot shows the time evolution of the dissipation term.

4. COMPUTATIONAL CYTOMETRY IMAGING

Taraconat et al. [31] examined the impedance measurement of red blood cells (RBCs) in an industrial hematology analyzer. The setup consists of a polarized micro-orifice through which red blood cells are aspirated one at a time, as illustrated in Figure 5. This constriction ensures a high electrical field in the aperture, such that the presence of an RBC increases the electrical resistance, detectable as a voltage pulse. Counting these electrical signals provides a tally of cells passing through the micro-orifice, and the amplitudes of these perturbations are assumed to be proportional to the particle sizes [32]. Commonly known as 'Coulter counter' [33], this system measures RBC volumes and concentrations. Although Coulter counters have been integral to blood analyzers for decades, some measurement artifacts remain poorly understood. Near the aperture walls, inhomogeneities in the electrical field and complex RBC dynamics lead to measurement errors. Investigating particle dynamics in the detection area to understand these edge effects is challenging due to accessibility issues in industrial systems. Consequently, numerical simulation was chosen as the preferred method for these investigations.

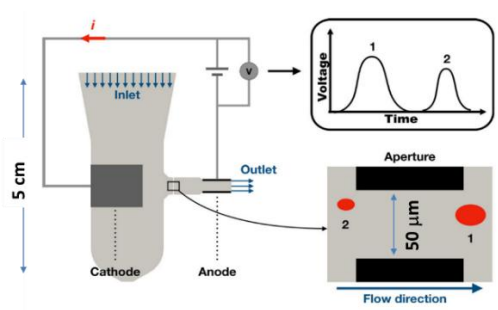

Figure 5. Principle of counting and sizing (red blood) cells using a Coulter counter. The diluted blood sample flows into the tank through the inlet, and each circulating cell generates an electrical perturbation, supposedly proportional to its volume, as it passes through the aperture. The cells then exit the system through the outlet. Note the significant separation of scales between the tank (cm) and the cell (μm) size.

Simulating deforming cells in a Coulter counter presents a multi-scale challenge that has been addressed through a specific sequence of simulations [31]. Essentially, the flow domain is conceptually divided into three distinct parts, each requiring a different type of simulation to accurately represent the physical phenomena occurring within them.

1. **Passive Transport Region**: In the largest part of the domain, red blood cells (RBCs) behave like passive tracers. They are transported by the flow without undergoing deformation.
2. **Stretching Region**: In an intermediate region, the RBCs continue to follow the streamlines of the baseline flow but begin to stretch as they move.
3. **Deformation and Rotation Region**: Finally, as the RBCs flow through the micro-orifice, they experience deformation and may rotate, thereby disturbing the electrical field.

The varying durations of these phases—on the order of 50 seconds, 20 milliseconds, and 20 microseconds, respectively—highlight the multi-scale complexity inherent in this type of analysis. The numerical simulation of the electrical pulse, which corresponds to the experimental measurements taken during each cell passage, is computed under static conditions. This involves solving the Laplace equation for the electrical potential across a series of cell positions and shapes.

The proposed simulation method was benchmarked against experimental data derived from both healthy blood samples and latex bead samples. Figure 6 demonstrates that the numerical results not only replicate the experimental findings but also offer deeper insights into the complex behaviors observed when particles traverse near the wall regions.

Specifically, the analysis reveals two distinct types of edge effects:

1. **Electrical Edge Effects**: These occur when particles pass through areas with highly non-uniform electrical fields, particularly near the corners of the aperture. This phenomenon is visually indicated by blue circles in Figure 6. The non-uniformity in the electrical field leads to variations in the electrical signals detected.
2. **Dynamical Edge Effects**: These involve the rotation of cells induced by significant velocity gradients near the aperture walls, as shown by black arrows in Figure 6. The shear forces in these regions cause the cells to rotate, which in turn affects their orientation and the resulting electrical signatures.

The simulations effectively distinguish between these two types of artifacts, providing a clearer understanding of their individual impacts on the electrical measurements. This separation is crucial for accurately interpreting the data obtained from Coulter counters and improving the precision of blood analysis techniques.

.

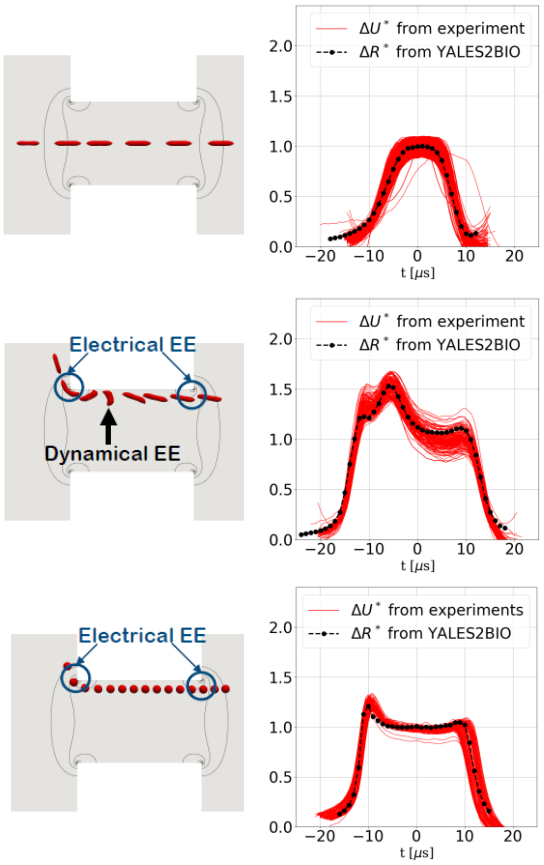

Figure 6. The left column illustrates the simulated dynamics of red blood cells (RBCs) in the micro-orifice, while the right column displays the associated electrical perturbations. In the right column, electrical pulses derived from simulations are superimposed with experimental observations. The top, middle, and bottom rows correspond to an RBC on a centred trajectory, an RBC on a near-wall trajectory, and a rigid sphere on a near-wall trajectory, respectively. Electrical field isolines are shown over the cut view of the fluid domain in the particle dynamics images of the left column. Electrical and dynamical edge effects (EE) are highlighted by blue circles and black arrows, respectively.

The cell rotation that occurs for cells flowing close to the wall of the aperture artificially increases the shape factor of the cell and thus the amplitude of the electrical perturbation [32]. This explains the right-skewed probability density function of the cells volume often observed in practice. Leveraging this knowledge and a numerical database built from the numerical pipeline developed in [31], two strategies were recently proposed [34] and patented [35] to correct the sizing error in Coulter-based cytometry. These strategies are based either on signal processing of the electrical pulse or on a neural network capable of detecting whether the cell has experienced rotation. Detecting and rejecting rotation-associated pulses have been shown to provide results comparable to hydrodynamic focusing [36], which forces cells to flow in the centre of the orifice, the gold standard implementation of the Coulter principle.

In the computational studies cited above, the membrane of red blood cells was modeled as purely hyperelastic, despite experimental evidence indicating viscoelastic behavior. Enhancing the physical description of membrane rheology [37] provides an even more accurate description of cell dynamics as they flow through the apparatus [38]. This improvement paves the way for Coulter-based detection of cellular pathologies.

5. DISCUSSION

Computational physics is now recognized as a complementary tool that, alongside experimental and theoretical approaches, can provide relevant answers to practical blood-related questions. This paper has discussed two examples, focusing on macroscopic intracardiac flow and the counting and sizing of red blood cells.

Over the past years, many other applications and scientific questions have been addressed at IMAG. On the macroscopic side, notable studies include the interaction between turbulent flow and aortic [21] or venous [39] valves, he robustness of computational representations of jet-like flows such as in the Food and Drug Administration cannula test case [40], and the modelling of intra-vascular medical devices like flow diverters or WEBs [41, 42]. Regarding the microscopic scales, successful studies have been conducted on the dynamics of a single red blood cell in shear flow [13], which have been compared to theoretical [43] and experimental [44] data, as well as the self-organization of cells in a microfluidic channel [45]. Modelling the thrombosis phenomenon requires both macroscopic [46, 47] and microscopic [48] computational capabilities, as well as a reliable and efficient description of the biochemical reactions involved in the coagulation cascade [49-51]. As a final note, let us mention a recent and active research topic at IMAG where computational physics is used to mimic the medical images obtained from actual Magnetic Resonance Imaging systems [52]. This aims to better understand the limitations and optimize the sequences used in clinical routines [53].

ACKNOWLEDGEMENTS

This work has been performed with the support of the MESO@LR computing centre at the University of Montpellier and resources from GENCI TGCC-IRENE (Grants No. A0100307194-A0180307194). This work was publicly funded through the French National Research Agency with the reference ANR-21-CE19-0034.

REFERENCES

[1] V. Moureau, P. Domingo, and L. Vervisch, “Design of a massively parallel CFD code for complex geometries,” *Comptes Rendus Mécanique*, vol. 339, no. 2–3, pp. 141–148, 2011, doi: 10.1016/j.crme.2010.12.001.

[2] A. Chorin, “Numerical solution of the Navier-Stokes equations,” *Math. Comput.*, vol. 22, pp. 745–762, 1968, doi: 10.2307/2004575.

[3] V. Moureau, P. Domingo, and L. Vervisch, “From Large-Eddy Simulation to Direct Numerical Simulation of a lean premixed swirl flame: Filtered laminar flame-PDF modeling,” *Combust. Flame*, vol. 158, no. 7, pp. 1340–1357, 2011, doi: 10.1016/j.combustflame.2010.12.004.

[4] M. Malandain, N. Maheu, and V. Moureau, “Optimization of the deflated Conjugate Gradient algorithm for the solving of elliptic equations on massively parallel machines,” *J. Comput. Phys.*, vol. 238, pp. 32–47, 2013, doi: 10.1016/j.jcp.2012.11.046.

[5] F. Nicoud, H. Baya Toda, O. Cabrit, S. Bose, and J. Lee, “Using singular values to build a subgrid-scale model for large eddy simulations,” *Phys. Fluids*, vol. 23, no. 8, p. 085106, 2011, doi: 10.1063/1.3623274.

[6] H. B. Toda, O. Cabrit, K. Truffin, G. Bruneaux, and F. Nicoud, “Assessment of subgrid-scale models with a large-eddy simulation-dedicated experimental database: The pulsatile impinging jet in turbulent cross-flow,” *Phys. Fluids*, vol. 26, no. 7, 2014, doi: 10.1063/1.4890855.

[7] F. Nicoud, C. Chnafa, J. Siguenza, V. Zmijanovic, and S. Mendez, “Large-Eddy simulation of turbulence in cardiovascular flows,” in *Lecture Notes in Applied and Computational Mechanics*, vol. 84, Peter Wriggers \& Thomas Lenarz, Ed., Springer, Cham, 2018, pp. 147–167. doi: 10.1007/978-3-319-59548-1_9.

[8] F. Nicoud, M. Garreau, and S. Mendez, “Turbulence modeling of blood flow,” in *Biomechanics of the Aorta*, C. Gasser, S. Avril, and J. Elefteriades, Eds., Academic Press, 2024, pp. 387–414. doi: 10.1016/B978-0-323-95484-6.00010-5.

[9] C. Chnafa, S. Mendez, and F. Nicoud, “Image-based large-eddy simulation in a realistic left heart,” *Comput. Fluids*, vol. 94, pp. 173–187, 2014, doi: 10.1016/j.compfluid.2014.01.030.
[10] C. Chnafa, S. Mendez, and F. Nicoud, “Image-Based Simulations Show Important Flow Fluctuations in a Normal Left Ventricle: What Could be the Implications?,” *Ann. Biomed. Eng.*, vol. 44, no. 11, pp. 3346–3358, 2016, doi: 10.1007/s10439-016-1614-6.
[11] J. Sigüenza *et al.*, “Validation of an immersed thick boundary method for simulating fluid–structure interactions of deformable membranes,” *J. Comput. Phys.*, vol. 322, pp. 723–746, 2016, doi: 10.1016/j.jcp.2016.06.041.
[12] L. Lanotte *et al.*, “Red cells’ dynamic morphologies govern blood shear thinning under microcirculatory flow conditions,” *Proc. Natl. Acad. Sci.*, vol. 113, no. 47, pp. 13289–13294, 2016, doi: 10.1073/pnas.1608074113.
[13] J. Mauer *et al.*, “Flow-Induced Transitions of Red Blood Cell Shapes under Shear,” *Phys. Rev. Lett.*, vol. 121, no. 118103, pp. 1–6, 2018, doi: 10.1103/PhysRevLett.121.118103.
[14] S. Mendez and M. Abkarian, “Single red blood cell dynamics in shear flow and its role in hemorheology,” in *Dynamics of Blood Cell Suspensions in Microflows*, Taylor and Francis Group, 6000 Broken Sound Parkway NW, Suite 300, Boca Raton, FL 33487-2742: CRC Press., 2019, pp. 125–182. doi: 10.1201/b21806-5.
[15] C. Peskin, “The immersed boundary method,” *Acta Numer.*, vol. 11, pp. 479–517, 2002, doi: 10.1017/S0962492902000077.
[16] W. K. Liu, S. Jun, and Y. F. Zhang, “Reproducing kernel particle methods,” *Int. J. Numer. Methods Fluids*, vol. 20, no. 8–9, pp. 1081–1106, Apr. 1995, doi: 10.1002/FLD.1650200824.
[17] A. Pinelli, I. Naqavi, U. Piomelli, and J. Favier, “Immersed-boundary methods for general finite-difference and finite-volume Navier-Stokes solvers,” *J. Comput. Phys.*, vol. 229, no. 24, pp. 9073–9091, 2010, doi: 10.1016/j.jcp.2010.08.021.
[18] S. Mendez, E. Gibaud, and F. Nicoud, “An unstructured solver for simulations of deformable particles in flows at arbitrary Reynolds numbers,” *J. Comput. Phys.*, vol. 256, pp. 465–483, 2014, doi: 10.1016/j.jcp.2013.08.061.
[19] R. Skalak, A. Tozeren, R. Zarda, and S. Chien, “Strain energy function of red blood cell membranes,” *Biophys. J.*, vol. 13, pp. 245–264, 1973, doi: 10.1016/S0006-3495(73)85983-1.
[20] W. Helfrich, “Elastic properties of lipid bilayers: Theory and possible experiments.,” *Z Naturforsch*, vol. 28, pp. 693–703, 1973, doi: 10.1515/znc-1973-11-1209.
[21] J. Sigüenza *et al.*, “Fluid-structure interaction of a pulsatile flow with an aortic valve model: A combined experimental and numerical study,” *Int. j. numer. method. biomed. eng.*, vol. 34, no. 4, pp. 1–19, 2018, doi: 10.1002/cnm.2945.
[22] H. Baya Toda, O. Cabrit, K. Truffin, G. Bruneaux, and F. Nicoud, “Assessment of subgrid-scale models with a large-eddy simulation-dedicated experimental database: The pulsatile impinging jet in turbulent cross-flow,” *Phys. Fluids*, vol. 26, no. 7, p. 075108, 2014, doi: 10.1063/1.4890855.
[23] C. Chnafa, S. Mendez, R. Moreno, and F. Nicoud, “Using image-based CFD to investigate the intracardiac turbulence,” in *Modeling the Heart and the Circulatory System. MS&A Vol. 14*, A. Quarteroni, Ed., New-York: Springer International Publishing, 2015, pp. 97–117. doi: 10.1007/978-3-319-05230-4_4.
[24] M. Markl, P. Kilner, and T. Ebbers, “Comprehensive 4D velocity mapping of the heart and great vessels by cardiovascular magnetic resonance.,” *J. Cardiovasc. Magn. Reson.*, vol. 13, no. 1, p. 7, 2011, doi: 10.1186/1532-429X-13-7.
[25] K. C. Assi *et al.*, “Intraventricular vector flow mapping - A Doppler-based regularized problem with automatic model selection,” *Phys. Med. Biol.*, vol. 62, no. 17, pp. 7131–7147, Aug. 2017, doi: 10.1088/1361-6560/aa7fe7.
[26] F. Vixege *et al.*, “Physics-constrained intraventricular vector flow mapping by color Doppler,” *Phys. Med. Biol.*, vol. 66, p. 245019, Dec. 2021, doi: 10.1088/1361-6560/ac3ffe.
[27] F. Vixege *et al.*, “Full-volume three-component intraventricular vector flow mapping by triplane color Doppler,” *Phys. Med. Biol.*, vol. 67, no. 9, 2022, doi: 10.1088/1361-6560/ac62fe.
[28] H. J. Ling *et al.*, “Physics-Guided Neural Networks for Intraventricular Vector Flow Mapping,” *IEEE Trans. Ultrason. Ferroelectr. Freq. Control*, vol. 71, no. 11, pp. 1377–1388, 2024, doi: 10.1109/TUFFC.2024.3411718.
[29] F. Nicoud, S. Bru, and S. Mendez, “Realistic intracardiac hemodynamics: A computational study,” in *12th FIMH conference – (Lyon, France)*, 2023.
[30] P. Kilner, G. Yang, J. Wilkes, R. Mohiaddin, D. Firmin, and M. Yacoub, “Asymmetric redirection of flow through the heart.,” *Nature*, vol. 404, no. 6779, pp. 759–761, 2000, doi: 10.1038/35008075.
[31] P. Taraconat, J.-P. Gineys, D. Isèbe, F. Nicoud, and S. Mendez, “Numerical simulation of deformable particles in a Coulter counter,” *Int. j. numer. method. biomed. eng.*, vol. 35, no. 11, p. e3243, 2019, doi: 10.1002/cnm.3243.
[32] V. Kachel, “Electrical resistance pulse sizing: Coulter sizing,” in *Flow cytometry and sorting*, 1990, pp. 45–80.
[33] W. H. Coulter, “Means for counting particles

suspended in a fluid," 1953
[34] P. Taraconat, J.-P. Gineys, D. Isèbe, F. Nicoud, and S. Mendez, "Detecting cells rotations for increasing the robustness of cell sizing by impedance measurements , with or without machine learning," *Cytometry*, vol. 99, no. 10, pp. 977–986, 2021, doi: 10.1002/cyto.a.24356.
[35] P. Taraconat, D. Isebe, F. Nicoud, and S. Mendez, "Focalisation numérique pour le tri des signaux d'impédance Coulter et l'amélioration de la volumétrie des cellules - Patent #FR1904410 - WO/2020/216952," FR1904410-WO/2020/216952, 2019
[36] L. Spielman, "Improving resolution in Coulter counting by hydrodynamic focusing," *J Colloid Interface Sci.*, vol. 26, pp. 175–182, 1968.
[37] P. Matteoli, F. Nicoud, and S. Mendez, "Impact of the membrane viscosity on the tank-treading behavior of red blood cells," *Phys. Rev. Fluids*, vol. 043602, pp. 1–21, 2021, doi: 10.1103/PhysRevFluids.6.043602.
[38] P. Pottier, P. Taraconat, J.-P. Gineys, D. Isèbe, F. Nicoud, and S. Mendez, "Key role of red blood cell membrane viscosity in Coulter counter signal understanding," in *12th International Conference on Multiphase Flow, Toulouse, France*, 2025.
[39] B. Thibaud, I. Soler, S. Mendez, and F. Nicoud, "Fluid-structure interaction modeling of deep vein valves," in *7th International Conference on Computational and Mathematical Biomedical Engineering*, Milan, 2022.
[40] V. Zmijanovic, S. Mendez, V. Moureau, and F. Nicoud, "About the Numerical Robustness of Biomedical Benchmark Cases: Interlaboratory FDA's Idealized Medical Device," *Int. j. numer. method. biomed. eng.*, vol. 33, no. 1, pp. 1-17 e02789, 2017, doi: 10.1002/cnm.2789.
[41] A. Bérod, C. Chnafa, S. Mendez, and F. Nicoud, "A Heterogeneous Model of Endovascular Devices for the Treatment of Intracranial Aneurysms," *Int. j. numer. method. biomed. eng.*, vol. 38, no. 2, p. e3552, 2021, doi: 10.1002/cnm.3552.
[42] A. Bérod, F. Mut, J. Cebral, C. Chnafa, and F. Nicoud, "Assessing a heterogeneous model for accounting for endovascular devices in hemodynamic simulations of cerebral aneurysms," *Int. j. numer. method. biomed. eng.*, no. June 2022, pp. 1–17, 2023, doi: 10.1002/cnm.3762.
[43] S. Mendez and M. Abkarian, "In-plane elasticity controls the full dynamics of red blood cells in shear flow," *Phys. Rev. Fluids*, vol. 3, no. 10, pp. 1–10, 2018, doi: 10.1103/PhysRevFluids.3.101101.
[44] L. Lanotte *et al.*, "Red cells' dynamic morphologies govern blood shear thinning under microcirculatory flow conditions," *Proc. Natl. Acad. Sci. U. S. A.*, vol. 113, no. 47, 2016, doi: 10.1073/pnas.1608074113.
[45] C. Iss *et al.*, "Self-organization of red blood cell suspensions under confined 2D flows," *Soft Matter*, vol. 15, pp. 2971–2980, 2019, doi: 10.1039/C8SM02571A.
[46] R. Méndez Rojano, S. Mendez, and F. Nicoud, "Introducing the pro-coagulant contact system in the numerical assessment of device-related thrombosis," *Biomech. Model. Mechanobiol.*, vol. 17, no. 3, pp. 815–826, 2018, doi: 10.1007/s10237-017-0994-3.
[47] R. Mendez Rojano *et al.*, "Kinetics of the coagulation cascade including the contact activation system : Sensitivity analysis and model reduction," *Biomech. Model. Mechanobiol.*, vol. 18, no. 4, pp. 1139–1153, 2019.
[48] C. Raveleau, S. Mendez, and F. Nicoud, "Impact of microstructured artificial surfaces on the dynamics of blood platelets," in *ESAO Congress, Enschede, The Netherlands*, 2025.
[49] F. Nicoud, "An adjoint-based method for the computation of gradients in coagulation schemes," *Int. j. numer. method. biomed. eng.*, vol. 39, no. 5, p. e3698, Mar. 2023, doi: 10.1002/cnm.3698.
[50] A. Ranc, S. Bru, S. Mendez, M. Giansily-Blaizot, F. Nicoud, and R. Mendez Rojano, "Critical evaluation of kinetic schemes for coagulation," *PLoS One*, vol. 18, no. 8, p. e0290531, 2023, doi: 10.1371/journal.pone.0290531.
[51] J. Chen, Q. Cazères, E. Riber, and F. Nicoud, "Multistep model reduction of coagulation schemes," *Biomech. Model. Mechanobiol.*, vol. 24, pp. 919–937, 2025, doi: 10.1007/s10237-025-01944-9.
[52] T. Puiseux, A. Sewonu, R. Moreno, S. Mendez, and F. Nicoud, "Numerical simulation of time-resolved 3D phase-contrast magnetic resonance imaging," *PLoS One*, vol. 16, no. 3, p. e0248816., 2021, doi: 10.1371/journal.pone.0248816.
[53] M. Garreau *et al.*, "Accelerated sequences of 4D flow MRI using GRAPPA and compressed sensing : A comparison against conventional MRI and computational fluid dynamics," *Magn. Reson. Imaging*, no. June, pp. 1–15, 2022, doi: 10.1002/mrm.29404.

Conference on Modelling Fluid Flow (CMFF'25)
The 19th International Conference on Fluid Flow Technologies
Budapest, Hungary, August 26 - August 29, 2025

A LOOK BACK ON 30 YEARS OF TURBOMACHINERY RESEARCH IN EUROPE.

Gérard BOIS[1]

[1] Corresponding Author. Emeritus Professor ENSAM. Fluid Mechanics Lab. Lille (LMFL).
University of Lille, CNRS, ONERA, Arts et Métiers Institute of Technology, Centrale Lille Institut, UMR 9014-LMFL - Kampé de Fériet, F-59000, Lille, France. E-mail: Gerard.bois@ensam.eu

ABSTRACT

This document aims to give a personal and therefore partial view of what has been learned, performed and achieved during the past 30 years in rotating machinery research fields and what are the possible new research targets in this specific domain. Numerical techniques will not be addressed here; the present paper comes from a CFD end-user and not from a CFD expert. This is the reason why physical aspects are rather highlighted here.

It does not claim to cover all aspects of the work carried out in all types of rotating machinery, but to look at specific research aspects that have contributed to a better understanding of turbomachinery aerodynamic features thanks to basic configuration studies, advanced experimental techniques and powerful data acquisition treatments.

At the end of the present document, the use of artificial intelligence to improve decision-making is put into perspective.

Keywords: experimental, numerical, research, turbomachinery.

PREFACE.

I would like to express my gratitude by dedicating some words to the memory of my former teachers and mentors from the von Karman Institute (VKI) and more particularly that of Claus Sieverding (passed on January 2024) that should have prepared this document with me on the kind invitation from Prof Janos Vad.

My respectful thoughts also go both to Prof. Franz Breugelmanns and Prof. Jacques Chauvin who founds the Turbomachinery Department of VKI.

Left: Claus SIEVERDING
Middle: Franz.A.E.BREUGELMANNS
Right: Jacques CHAUVIN

1. INTRODUCTION

It is obvious to say that the way turbomachinery's aerodynamic research has evolved during the past 30 years is strongly related to the emergence of improved numerical simulations starting from the 1980's and the development of advanced experimental techniques, data acquisition and reduction procedures.

The analysis procedure deduced from CFD flow capturing in single and multistage row configurations including unsteady behavior has been strongly transformed compared with steady 2D thinking that generally took place before the 90's.

With the development of high-performance computing resource and commercial or in house software, full 3D calculations in 2D straight and annular cascades, single stage and multistage configurations of increasingly complex architectures have been made possible both for ground and aerospace applications.

However, the use of numerical and experimental means has been carried out differently depending on the application and market needs. Single stage configurations like low-speed fans, hydraulic machines, wind and marine turbines, propellers have different design and mechanical requirements than

high speeds multistage compressors and turbines, turbochargers and space propulsion systems. Thus, different priority strategies and research targets have been set up for high-speed multistage machines (with high temperature and pressure levels with strong gradients, cooling systems and controls) and for hydraulic machineries subject to phase modification in stage components.

Nevertheless, similar attempts and achievements aiming at robust design concepts have been forced because of increasing end-users demands and expectations, manufacturing evolutions and political and economic constraints.

2. CONTEXT

Tasks chairing between those involved in fundamental research and those in applied research was significantly modified starting around the 1980's, a period for which people have essentially sought to obtain a good restitution of global or local performances from CFD without correctly check the validity and the limitations of their approaches or naturally preferred to only show their best results. Later, comparisons with experiments have made it possible to detect the importance of certain phenomena hitherto considered negligible in terms of their consequences. This was performed in association with extended close collaborations with research institutions, manufacturers and end-users, better CFD's accuracy and modelling re-enforced by new machine architectures and manufacturing techniques evolutions.

This was greatly facilitated by proactive actions of partnerships and exchanges promoted by the European Commission Research Programs including sustainable development policies. Competition between machine manufacturers was evolving towards closer collaboration in view of the increase in costs and the duration of research and development activities.

As emphasized by Cumpsty, [1]: "It *was an exceptional period of intellectual competition carried out with great openness and courtesy. Those involved recall it as a stimulating and enjoyable episode a quarter century later".*

3. TECHNICAL AND SCIENTIFIC PUBLICATIONS IN EUROPE

A rapid statistical overview on turbomachinery field publications per country, given on figure 1, can be seen as reflecting most of manufacturers' implantations in each European country. Significant differences can be noticed if scientific publications are classified into categories (figures 2a to 2f). These differences should be related to the energy policies and resources of each country as shown in figure 3.

Note. Publications for wind turbine are not involved in the present document (Main wind turbine manufacturers are in Denmark-Nordex SE and Vestas Wind Systems S/A and in Spain Siemens Gamesa Renewable Energy, S.A).

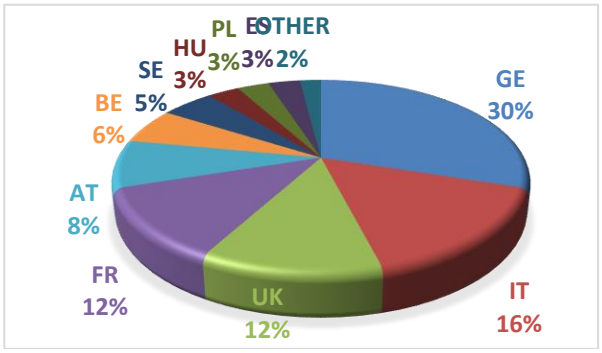

Figure 1. Turbomachinery aerodynamic publications' distribution per countries (1995-2025).

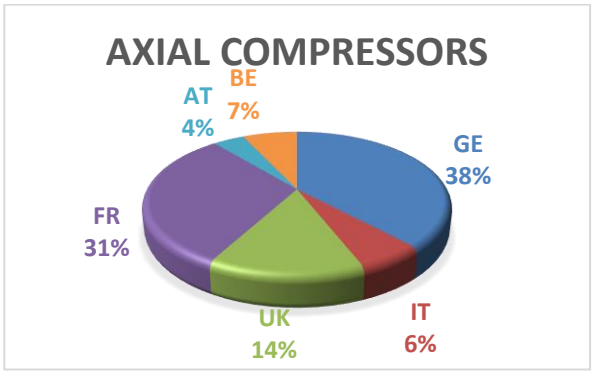

Figure 2a. Distribution for axial compressors

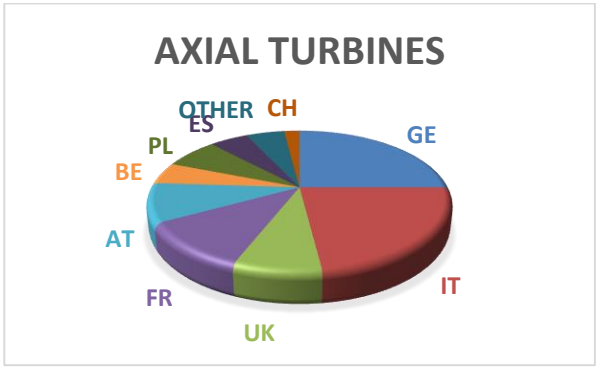

Figure 2b.Distribution for axial turbines.

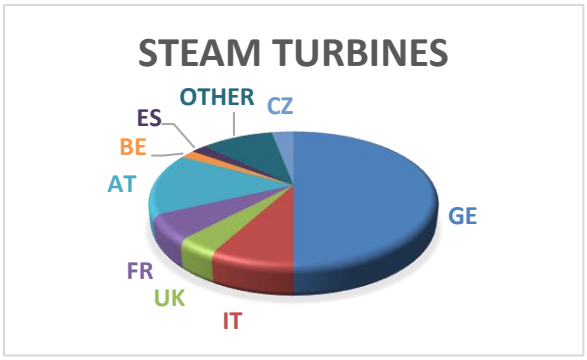

Figure 2c. Distribution for steam turbines

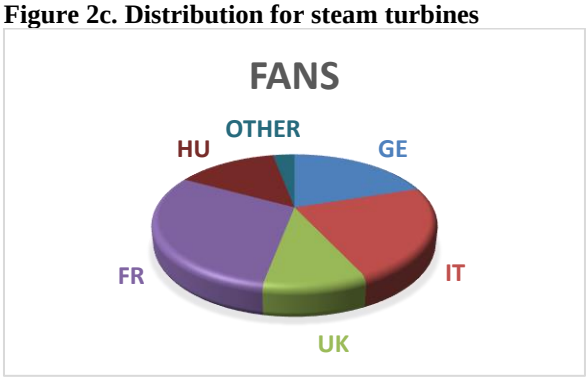

Figure 2d. Distribution for fans.

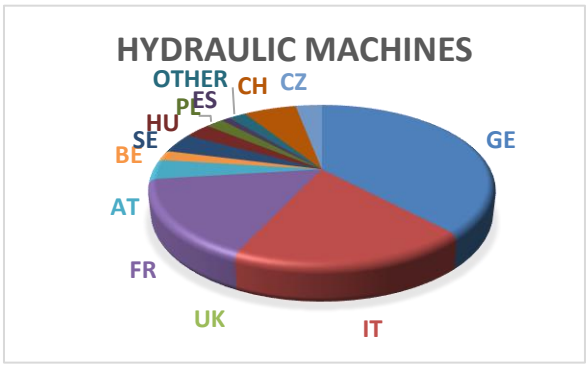

Figure 2e. Distribution for hydraulic machines

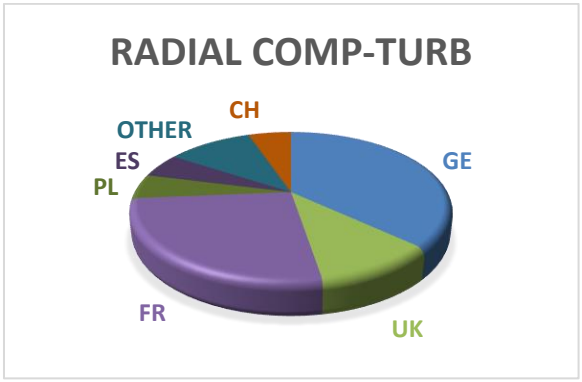

Figure 2f. Distribution for radial machines

Figures 2a to 2f. Research publications per topics.

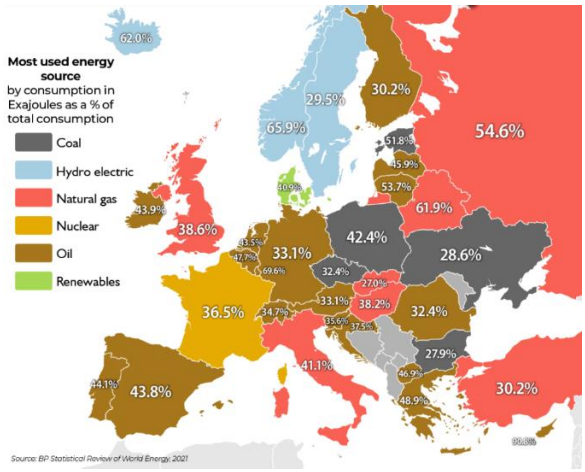

Figure 3. Main energy sources by country.

4. TURBOMACHINERY DESIGN PROCEDURE.

From the beginning, rotating machinery development is strongly based on a well-organized relationship between geometry definition, internal flow modelling, flow behavior understanding and performance analysis**.** Each step used models that can be classified according to the degree of complexity involved in the flow description. They can be divided into four distinct categories: statistical, one-dimensional (1D), two-dimensional (2D), and three-dimensional (3D) models.

During the last 25 years, thanks to larger computer resources and CFD improvements, inviscid and viscous approaches have been successfully used to analyse specific geometry components along with experimental validation both in 2D and 3D cases. One of the best way to analyse existing geometry concerns the pressure distribution in the blade to blade (tangential) and meridional directions either for single component designs and for the complete machine. Figure 4 shows the classical design chart for such purpose. The dates appearing on figures 4 and 5 indicate the most relevant CFD design steps associated to the accurate disposal of physical models related to turbomachinery aerodynamics research that are also recalled below:

a) Integrations of experimental results: up to the 70's

b) Model derivations: 1970-1990

c) Simulations

Up to 80's: 2D inviscid steady and Q3D
1990: 3D NS Steady multistage. Mixing plane assumption.
1995-2000: 3D Unsteady multistage.

d) Data science

2010: Optimization- Robust designs
2020: Artificial Intelligence (AI).

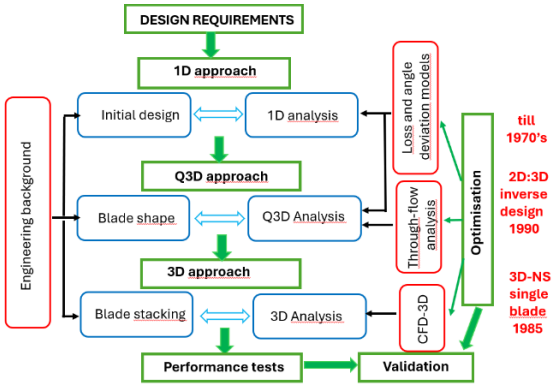

Figure 4. Turbomachinery design/analysis procedure

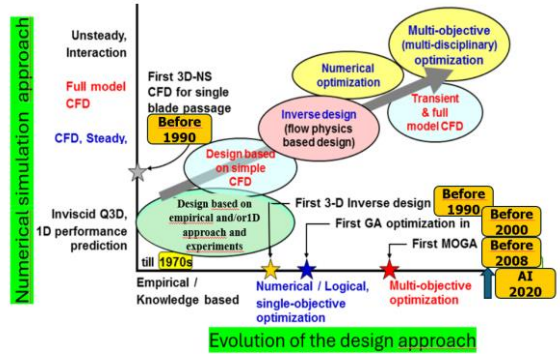

Figure 5. Design approach evolution along with increasing CFD modelling.

4.1. 3D flows in 2D cascades.

One of the most well-known phenomena that encountered numerous experimental and numerical studies, is related to what is commonly called "passage secondary flows" and "tip leakage flows" both for low-speed machines and transonic or supersonic ones. Basic research aiming at deep understanding on physical phenomena were initially performed in 2D cascades, then in annular cascades (see reference list [2] to [15)] for some contributions on this topic both for turbines and compressors.

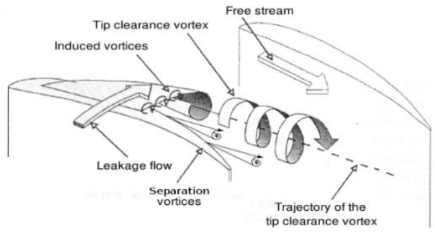

Tip leakage vortex

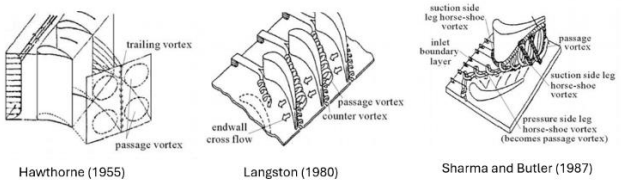

Reference [2]. Reference [3]. Reference [4].

Figure 6. 3D flow description in 2D cascades from different authors.

Starting with such an old story is directly linked to the fact that 2D blade-to blade surface remains relevant for the analysis for the turbomachinery community both in direct and inverse modes.

3D effects that were initially called "secondary flows" making some confusions about their real relative impact on what was supposed to be the main core flow in terms of pressure change and turning

- Secondary flows effects cannot be considered a kind of small perturbation for low aspect ratio for example.
- High loadings are responsible for greater interactions between main core flow and viscous flow developments.
- Vortex generation and development creates unsteady phenomena which strength and spreading are associated with specific frequencies (Strouhal number) and time-frequency patterns.
- Specific local flow features like, corner separation, corner stall and resulting mixing must be involved in design criteria and loading limitations.
- They can be affected by additional forced phenomena by adjacent steady or rotating components.

Several experimental and 3D numerical investigations continue to be performed in such basic 2D linear or annular cascades including passive and active flow control, vortex generators, tandem configuration, wall flow injection, film cooling, heat transfer measurements and so on….

4.2. Throughflow approach.

One must remember that, between 1970 and 1990, throughflow methods were currently used because they provide a reasonable trade-off between speed and accuracy. They remain still useful for performing parametric studies early in the

conceptual and preliminary design phases of multistage compressor and turbines.

The throughflow methods initially rely on the "quasi-three dimensional (Q3D) "simplification that solves azimuth-averaged flow in the meridional plane as first proposed by Wu in 1952 [16].

When steady state assumption is chosen, important flow aspects like the span-wise transport within the flow path (also called "radial mixing") is strongly under-predicted because of the circumferential averaging operation of flow properties at row interfaces (some aspects related to these effects are presented in section 7.2). The only way to correctly evaluate this key point is to perform an unsteady calculation. However, due to the high blade number and stages, such an approach has a computational cost not always suitable for industrial purposes. Currently, only the steady-state simulation can fit in a frequently used design chain. A "radial mixing" prediction, enhancing turbulent viscosity can promote span-wise diffusion and improve the radial mixing prediction of the steady approach. In this respect, large amount of modelling set-ups and improvements has been proposed by numerous researchers to recover part of the information that had been neglected and/or lost using the two-surfaces (meridional and blade-to-blade) coupling procedure. Some of the pioneers' work achievements are listed here after, mainly because their results can be still used to enrich data-based links for future analysis: Smith 1969 [17], Kerrebrock and Mikolajczak 1970 [18], Bosman and Marsh 1974 [19], Hirsch and Warzee 1976 [20], Denton 1978 [21], Denton and Singh 1979 [22], Adamczyk [23] 1985 and Jennions and Stow 1986 [24]

Extension to 3D simulations in rotor-stator and sub-systems components took place progressively, as shown on figure 7, when boundary conditions treatments and flow property transfers between single element, stages or sub-systems became more rigorous including unsteady effects that cannot be separated from turbomachinery applications (see section 7).

In case of multistage configurations, one the most challenging task for designers is to stick with stage matching or even between blade rows. This matching is based on corrected mass flow evaluation which depends on pressure rise and on blockage that are themselves depending on the 3D flow characteristics. This must be evaluated and modelled not only for design point, but for the whole flow range and rotational speeds when compressibility effects are important. This was clearly addressed by Dawes [25] and Cumpsty [1].

.

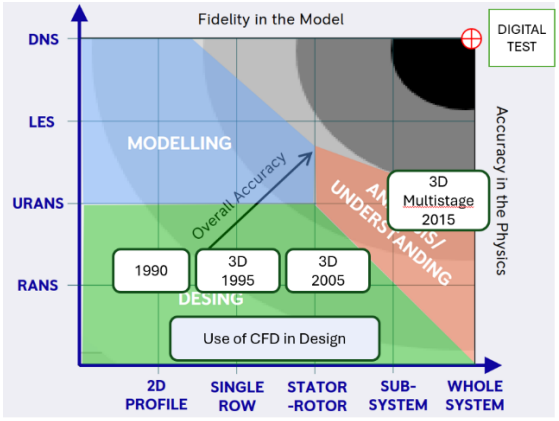

Figure 7. Numerical design and analysis evolutions.

Annulus gaps and corresponding leakage effects may strongly modify redial equilibrium, not only locally but in the entire radial flow path as demonstrated by Shabbir et al [26], in a high-speed rotor and Welborn et al. [27] for a shroud stator cavity. Their effects cannot be included just through a local mean additional flow rate or blockage coefficient but need to be studied by fully 3D calculation. Local geometrical mismatch can also make wrong experimental interpretation (see Escuret et al [28]). Because of increasing blade loading, strong radial gradients, increasing inlet temperatures and cooling effects, new engine architectures and so on, key points have been addressed by several authors like radial mixing evaluation (see [29] for a low aspect ratio rotor), tip clearances, leakages, wall boundary layer and interstage interactions (Adamczyk [30]). They have contributed to include more efficient methods by setting up tuning models, with the help of steady and unsteady simulation results starting from the early 80's. However, one must always be aware of errors that still may arise from different approximations as explained by Denton [31] because full 3D URANS calculations were too time consuming during this period.

Blade loading is a consequence of wall pressure distribution that depends on 3D effects which may be approached either by inviscid simplified hypothesis or viscous modelling. The control of the defined aerodynamic limitations was possible through the development of optimisation techniques that offers better capability to designers to:

- explore and determine the relative influence between several geometrical and flow parameters in single and multi-stage configurations.
- explore the effects and consequences due to leaning, bending and sweeping for the whole range of operation for single components

Some examples are given in the next section to illustrate how design procedures have evolved during this period.

5. EXAMPLES OF 2D/3D BASED APPROACH AND THEIR LIMITS.

These cases have been initially studied mainly based on inviscid considerations even before the 80's. The designs were then improved thanks to viscous steady analysis that took place in the 90's.

5.1. Example 1. 3D shaped of intake elbow and volute designs for pumps and compressors.

Early in1965, Pinckney, S. [32] tried to redesign both non-rotating intake volute to improve overall performances through a non symertic inlet fixed nose to overcome the swirling flow created by the elbow shape (see Figure 8a). Other ideas on the same topic were proposed by Neumann [33] for a tangential volute and by Flathers et al. [34] by introducing fixed non axisymmetric blades (see respectively Figures 8b and 8c).

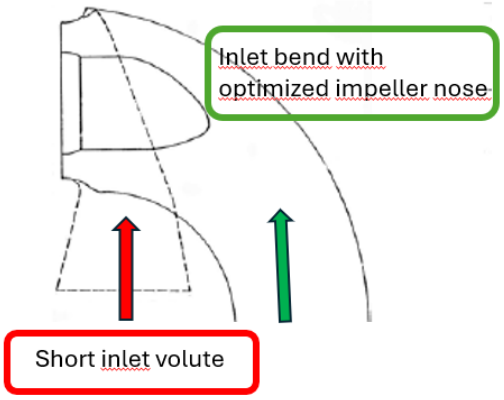

Figure 8a. Non axisymetric inlet with optimized impeller nose.

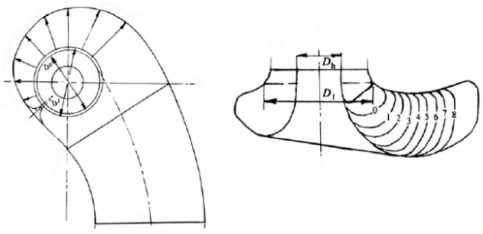

Figure 8b Bladeless tangential inler volute. Extracted from [33],

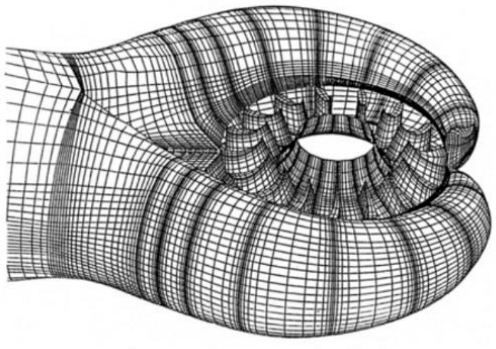

Figure 8c. Inlet volute with inlet guide vanes. Extracted from [34],

During the 90's and in early 2000's, specific analysis on flow in volutes were performed and published by Ayder and Van den Braembussche [35] to [37] and Van den braembussche et al. [38]. A complete revue on volute flow analysis can be also found from the same author in [39].

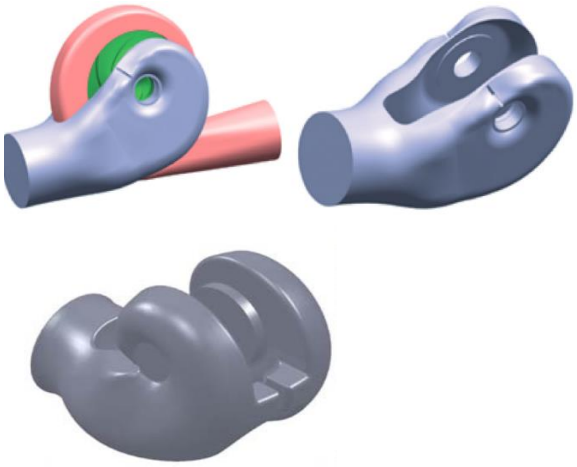

Figure 9. Examples of optimized geometries of inlet and outlet volutes and inlet chamber of a double suction pump..

Because inlet and outlet volute analysis cannot be dissociated from the rotating parts, inverse approach techniques were implemented both for fixed and rotating parts designs in mixed and centrifugal pumps and compressors by taking, for example, non uniform inlet conditions **(**Zangeneh [40], [41], [42] and Demeulenaere and Van den Braembussche [43]).

5.2. Example 2. Centrifugal Impeller blade lean effects.

This example concerns single stage centrifugal/ mixed flow configurations. The reason for such a choice is guided by the fact that, for a fairly long period, the research carried out on flows in radial machines was considered too difficult to handle compared with axial machines.

In 1960, Dean and Senoo [44] developed a loss model in the vaneless part downstream of a radial impeller coming from the development of low momentum flows transport along the span-wise meridional path that forms the so-called "jet and wake" structure. It has been first experimentally identified by Eckardt in 1976 [45] and numerically modelled by Moore and Moore [46] in 1980 assuming integral turbulent flow hypothesis. and later in 1993 by Hirsch et al [47-48] through a 3D Navier-Stokes simulation.

Before these 3D viscous simulations, in the 80's, it has been qualitatively demonstrated that blade leaning may have some effects on the wall boundary layer developments as examined by Van den Braembussche [49] simply performed on a 2D basic inviscid physical analysis as shown in figure 10.

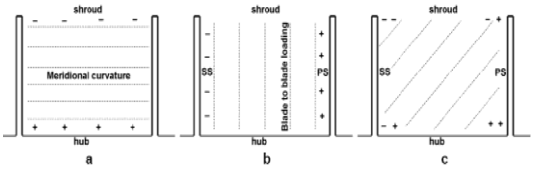

Pressure gradients in a crosswise plane with zero lean. Left: hub to shroud, middle: blade to blade, right: combined resulting effect.

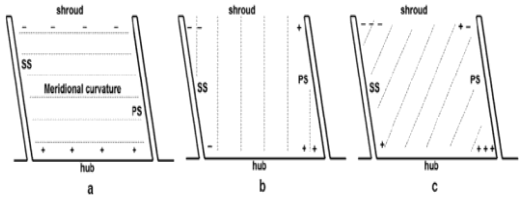

Influence of positive blade lean on pressure distribution

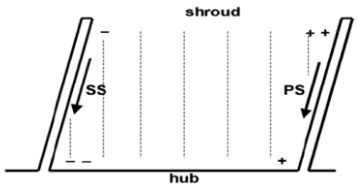

Influence of negative blade lean on pressure distribution

Figure 10. Qualitative effects of different leans on the blade-to-blade pressure gradients.

Around 2010, inverse technique results applied to an industrial mixed flow machine obtained by Goto et al. [50] based on previous Zangeneh's work [51] (see figure 11), quantitively gave what have been initially proposed to reduce the wake at the impeller outlet section.

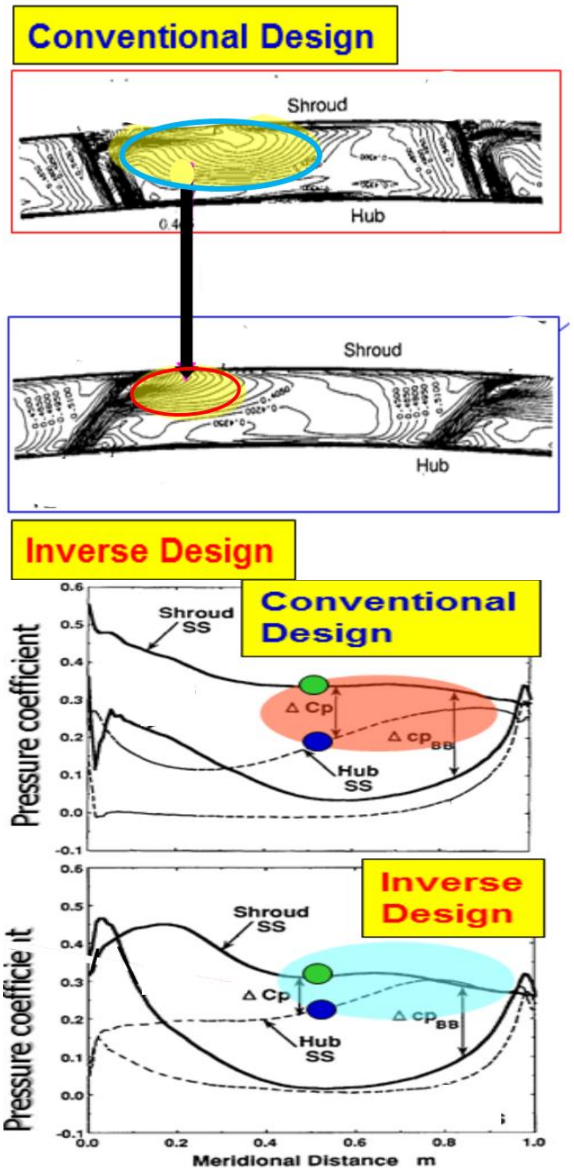

Figure 11. Results of an inverse design approach applied on a mixed-flow impeller pump at design conditions. Adapted from [50].

Recently, in 2019, Merli and Gaetani [52] proposed an extended study including vaneless diffuser performances for 3 different flow rates in a similar geometry including the consequences inside the vaneless diffuser. The study confirmed that negative lean is generally favourable to reduce losses in the complete stage.

5.3. Example 3: Non-axisymmetric turbine end wall profiling

In the early 2000's, end wall contouring attempts have been developed by D G Gregory-Smith et al. [53] in a two-dimensional linear turbine cascade. Spanwise secondary vorticity distribution was successfully improved but not loss coefficient.

P1

P2

The present concept was tested on a 2D cascade, based on inviscid blade-to-blade pressure gradient results. However, when applied to real cases as for a complete stage, overall results were not so good as expected because the rotor placed behind the modified stator was not redesigned. In other configurations, cooling effects coming from the hub platforms completely modify the initial flow inlet conditions entering the end wall region, destroying the initial beneficial effects.

With the implementation of inverse design techniques coupled with cooling injection effects in high pressure turbine stages as shown on figure 13, new end wall designs have been proposed by Burigana et al. [54], with an integration on local purge flow injection in low aspect ratio rotors.

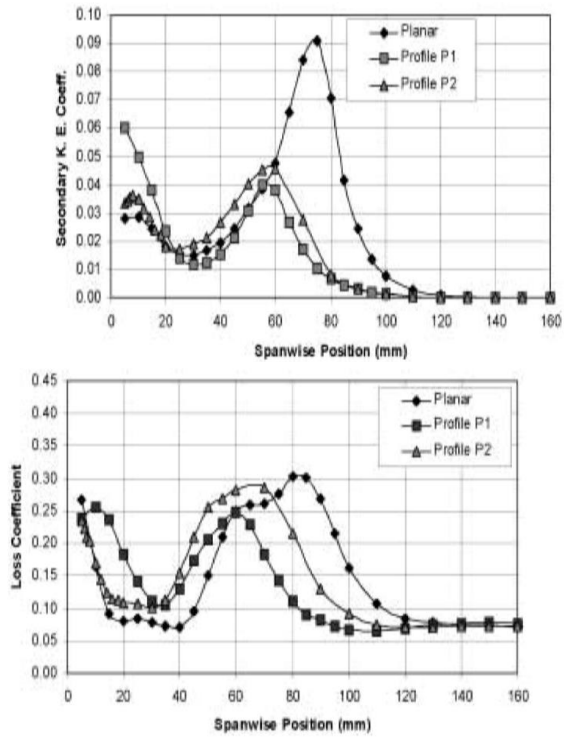

Figure 12. End-wall contouring applied in a turbine cascade. Adapted from [53].

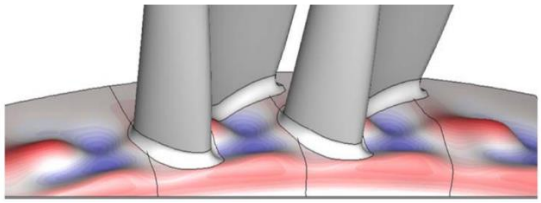

Figure 13. Inverse approach including non-axisymmetric end-wall designs. Adapted from ref. [54].

These last examples, taken for turbine blade rows, show that initial boundary conditions related to flow injection effects strongly modify the end wall design compared with 2D axisymetric inlet boundary layer. This is also the case for axial compressor components as can be seen below.

5.4 Example 4. Inlet leakage effects on performances.

A numerical sensitivity analysis of the hub leakage amount performed by Shabbir et al. [55] shows that induced local deviation angle and loss distribution differences strongly modify the whole

spanwise flow distribution especially when the inlet relative Mach number is higher than 1.

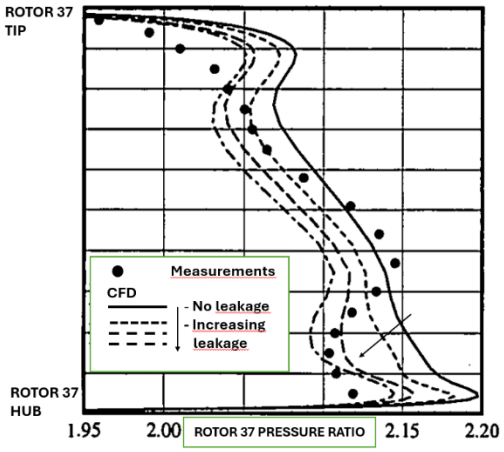

Figure 14. Effect of increasing hub leakage downstream of transonic rotor 37. Hub leakage flow cannot be considered axisymmetric along the blade channel. Adapted from [55].

5.5 Example 5. Cavitation onset and control.

Note: Only pump overall steady performances are here presented without hydraulic turbine cases that must be not forgotten. Unsteady cavitation problems will be discussed in section 7.3

Starting from the 60's up to the 90's, lots of experimental investigations have been carried out in Germany, Switzerland, Italy and France to analyze pumps performance variations under cavitation such as Barrand et al. [56] and Stoffel et al. using noise detection technique [57] among others. Numerical comparisons took place later with experimental comparisons such as Hofmann et al. et al. [58] in a radial pump and by Pelz et al. [59] in which erosion aspects have been introduced.

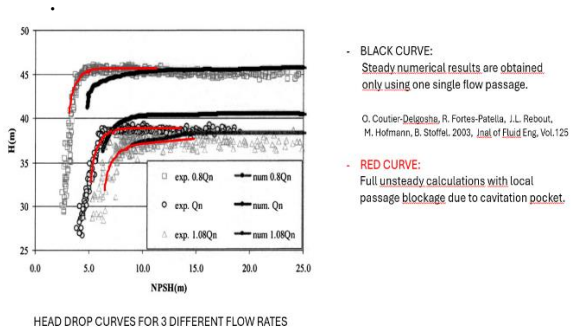

Figure 15. Numerical prediction of the head degradation due to cavitation. Adapted from [58]

Particular attention was also devoted to inducers' designs and performances. They are often used in front of centrifugal pumps to extend working operations when cavitation is present. In this respect, effects on cavitating performances have been also experimentally studied to enlarge single axial inducer performance in the early 2000's by Bakir et al. [60].

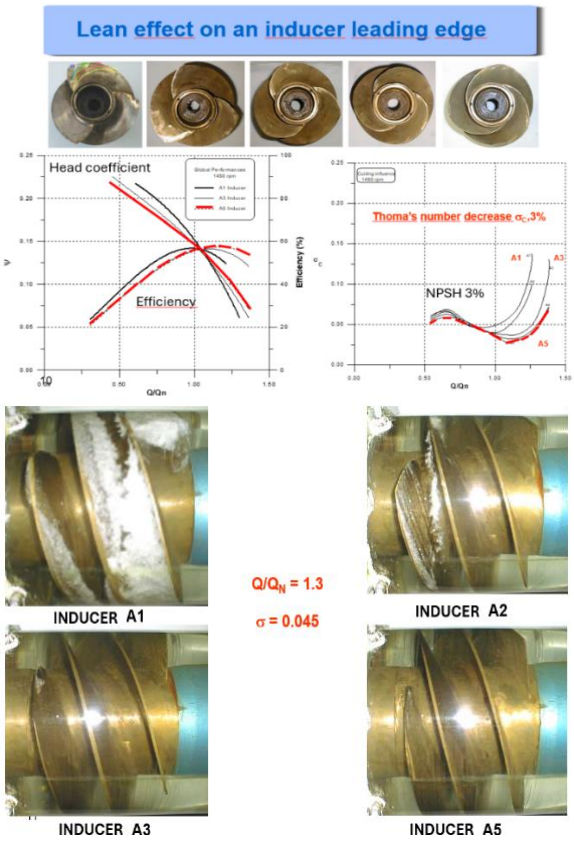

Figure 16. Cavitation visualisation for several inducer designs Adapted from [60].

More recently, an interesting investigation on performances including Inducer coupled with a radial impeller with contra-rotative shafts has been proposed by Dehnavi et al. [61].

These simplified approaches cannot reproduce the whole flow patterns and loss distributions. However, they can explain why quite efficient design improvements have been possible in the past. The implementation of complete 3D viscous softwares allowed to evaluate the relative importance of the missing terms between 2D and 3D inviscid approaches. This will lead to the implementation of multi-objective optimization techniques.

6. MULTIOBJECTIVES OPTIMIZATIONS.

Inverse design methods and optimization techniques brought important Improvements on flow pattern deliveries and, consequently on design improvements. They do help existing basic and acquired knowledge on flow physics, including noise level predictions, exploring large experimental databases and great deal of experience to free oneself from the lack of complete evaluation of several effects coming from technological aspects and other constraints.

However, this served as a basis for setting up a series of adequate design variables to speed up multi-objective optimization procedures including viscous effects that took place along with numerical technique improvements. Figure 17 illustrates how leading-edge modification can improve the cavitation onset in a centrifugal pump (Zhang et al. [62]). Other attempts applied in specific inducers' shape were also proposed like Parikh et al. [63] for example.

At the end, and for validation decision, one has be sure the chosen solution is well adapted to the related application or might be the best one not only for the design point but for the entire flow rate. For example, hydraulic low and medium specific speed machines that are used in land, sea and space applications are supposed to work within large flow rate operations, from shutt-off to high flow coefficients. These constraints lead to a trade-off decision as illustrated in figure 18.

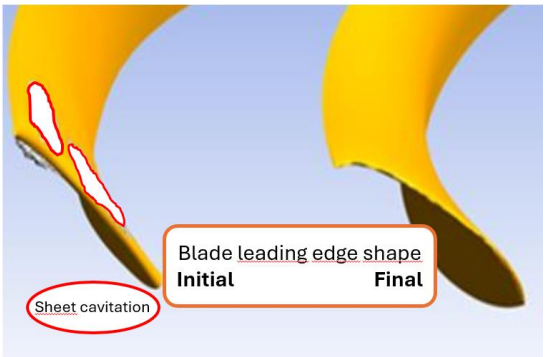

Figure 17. Multi-objectives optimisatio for inlet cavitation control. Adapted from [62].

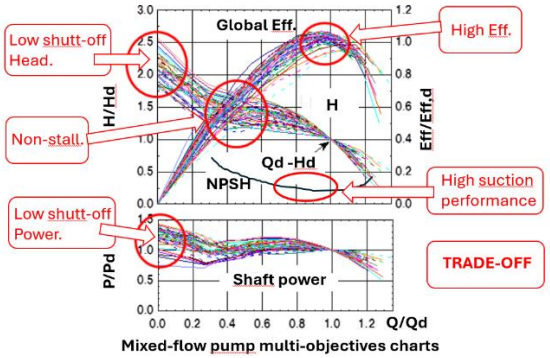

Figure 18. Multi-objectives achievements applied in a mixteflow pump. (Adapted from [50]).

In the same context, the case of high-speed machines has been strongly investigated with more variables due to high Mach numbers, thermal effects and multiple interactions. The choice of the adequate design space to perform efficient muti-objective optimisations becomes a crucial point.

Three separated examples, respectively published in 2001, 2013 and 2024, represent different design parametrisation that have been performed using 3D RANS approaches. The first and last ones are related to blade lean and sweep effects, respectively obtained for a stator blade downstream a high by-pass fan and for a single fan blade can be found in [64] and [65]; the second one concerns end wall and fillet optimisation attempts [66].

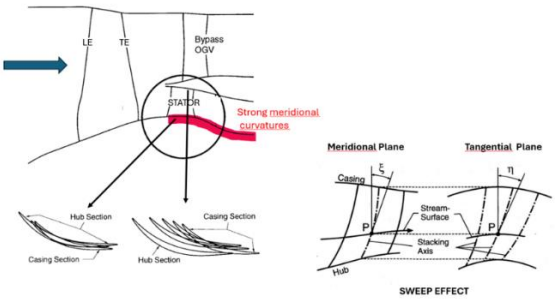

Figure 19. Sweep effects for a stator blade with strong meridional curvatures. Adapted from [64]

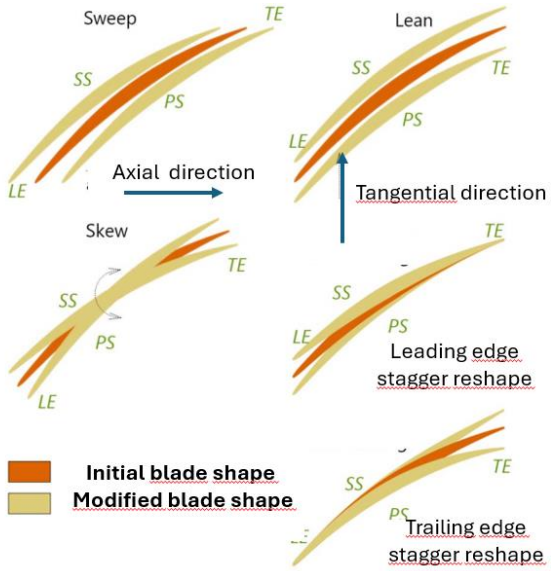

Figure 20. Representation of sweep, lean and skew in a compressor rotor. Adapted from [65]

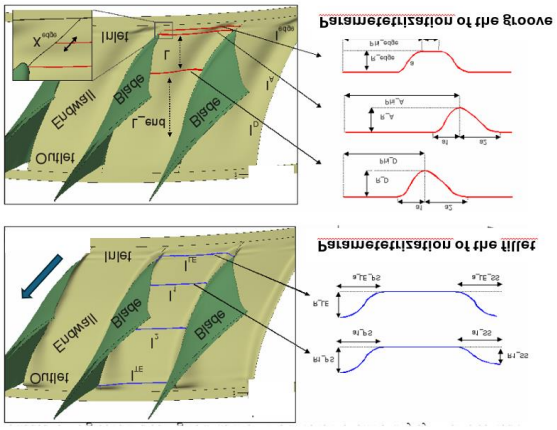

Figure 21. Parametrization of groove and fillet in a compressor blading. Extracted from [66].

More generally, robust designs techniques bring to enforce the following issues:

- check and found possible ultimate performance improvements in a specified design space,
- make possible innovative product development challenge by combining multi-objective and multi-disciplinary design aspects linked to real problems.
- allow to use physical aspects-based design optimization for flow control and systematize design knowledge, which possibly comprehends empirical design practice and /or know-how.
- the innovation design approach should be in close collaboration advance with manufacturing technology innovation. This is because numerically optimized shape can be very complex and difficult to manufacture accurately by conventional or innovative manufacturing technologies. Using fast 3-D printers for example, will expand design space and bring new possibility in product innovation.
- Visualization of multi-dimensional objective space is also important to make efficient trade-off design selection. Continuous challenges can be foreseen, employing numerical optimization, especially by young generations familiar with the digital engineering.

7. MULTI-STAGE UNSTEADY PHENOMENA.

7.1. Unsteady flow classification.

The deterministic and non-deterministic sources identification, listed from Leboeuf [67] (figure 22) and their consequences have been successfully treated when 3D URANS methods start to be used in the early 90's. They allow to perform more complete flow analysis avoiding the needs for additional models that are necessary to overcome the lost information coming from RANS hypothesis as pointed in the above paragraph.

- *Note: Unsteady sources evaluation also contribute to predict vibration, flutter and aerodynamic noise. For the last item, fast running, approximate analytical approaches and high-fidelity numerical simulations have now reached quite matured tools to meet the needs of the coming decades. These aspects are not treated in the present document. A complete review on turbomachinery noise can be found in the recent paper published by Moreau and Roger in 2024 [68], including key points related to blade passing frequency, vortex shedding and flow separation.*

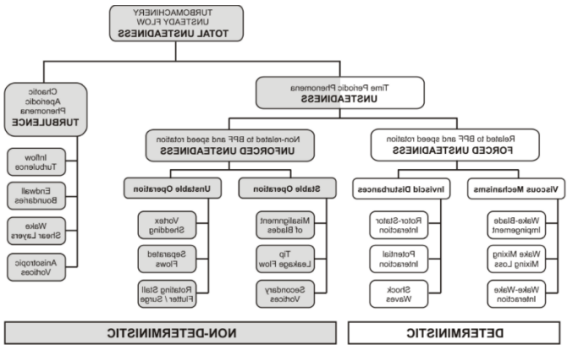

Figure 22. Unsteady flow classification. Extracted from Leboeuf [67].

7.2. Forced phenomena.

Gas turbines have numerous stages, low aspect ratio blades with large clearances especially in hot gas stages. Intense secondary flows enhance span-wise transport phenomena. These issues induce different mean flow blockage along the blade span that affects pressure recovery and can produce quite important misunderstanding and wrong data reduction analysis. Taking them at an early-stage design procedure through 3D RANS approach for example, ensure a correct evaluation and a good interstage matching through controlled circumferential flow averaging techniques especially for high-speed machines as already pointed just before.

Before 2000's, URANS methods were generally used both for in single stage configuration to evaluate the lost information coming from through flow methods. An example is given in Figure 23 about entropy contour differences using 2D steady approach and 3D unsteady one in a turbine stage [69]. When fully 3D URANS is performed as for the case of a multistage compressor, presented on Figure 24 which comes from Courtiade's PhD report [70].

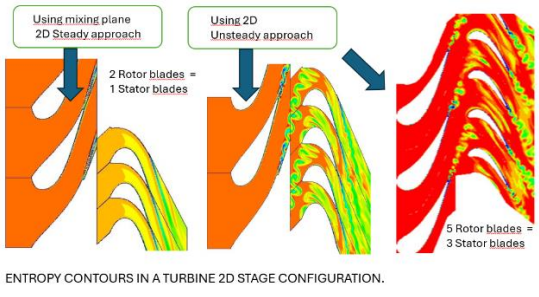

Figure 23. Differences on entropy contours resulting from steady and unsteady assumption. Adapted from [69].

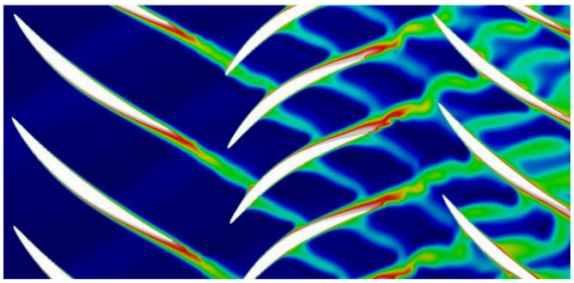

Figure 24. Mid-span wake (visualized from entropy values through fully unsteady calculation) in a 3.5 stage axial flow compressor CREATE. Extracted from [70].

The related major fluid mechanics issues that can be extracted from full 3D URANS results can be listed as follow:

a) Effects of spanwise and circumferential transport of wakes.

Three main phenomena are responsible for wakes' decay:

- Viscous mixing, which reduces the velocity deficit of the wakes regarding to the free stream. This is associated with dissipation due to the wake stretching when traversing the downstream rotating and/or fixed rows. In 1990, Poensgen and Gallus [71]. had already noticed that the presence of a downstream stator induced a decay of the wakes of a rotor twice faster than an isolated rotor configuration
- Circumferential redistribution involving interactions of incoming wakes on transitional or turbulent blade BL.
- Wake straining and wake recovery process due to blade passage transport. Different consequences for compressor (decelerating mean flow) and turbine (accelerating mean flow) cases have been explained and modelled.

The velocity deficit of the wake in comparison with the free stream, also called "negative jet". This produces a fluid accumulation on the pressure sides of the blades, as visible on Figure 25, extracted from Mailach *et al.* (2008, [72]). The velocity triangle at rotor inlet shows indeed that the local velocity deficit is responsible for the accumulation of the wakes on the pressure sides. Therefore, the wakes get locally thinner in the blade passages near suction side and thicker near pressure side which thickens the boundary layers on the blade pressure side. This is reinforced at tip sections when tip leakage flows are present.

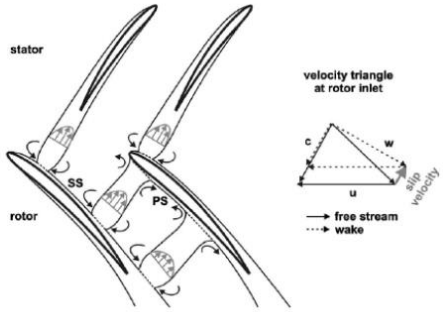

Figure 25a. Wake transport inside a rotor channel without tip leakage.Adapted from [72].

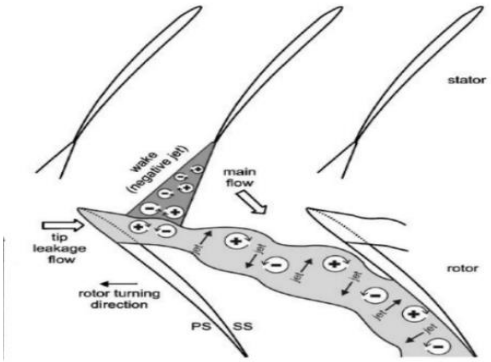

Figure 25b. Wake transport inside a rotor channel with tip leakage.Adapted from [72].

b) Misinterpretation of experimental results

- After a rotor, depending on the location of the measuring plane, interpretation of results may be confusing due to time and/or mass averages techniques and unsteady effects.

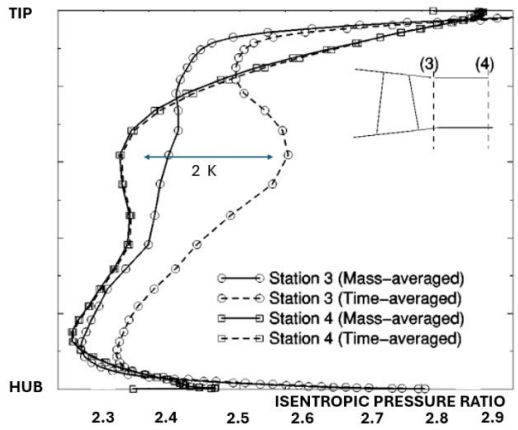

Figure 26. Axial evolution of the hub to shroud radial total temperature profile identified by Adamczyk [30].

c) Spanwise redistribution of total temperature and momentum that may produce hot spot temperature impacting turbine blade life.

d) Detection and identification of several modes that can be compared with fast response wall pressure transducers explained in the works performed by Ernst et al. [73] and Courtiade and Ottavy [74], both in 2011.

e) Unforced phenomena simulations as detailed below.

7.3. Unforced phenomena.

Throughout the last 30 years, several sources of unforced phenomena have been identified mainly from experimental investigations, long before the use of unsteady numerical tools.

Some particular phenomena are listed below:

- Wake instabilities as discussed before
- Vortex shedding. Vortex shedding effects on pressure loss (see Roberts and Denton [75]) and fluctuations behind turbine blades (see Cicatelli and Sieverding [76]).
- Aerodynamic interactions between core flow and shroud cavity as explored by Tanga et al. [77]. On figure 28, a clear peak at the blade passing frequency is detected, but the spectrum is dominated by several other peaks over a range at low frequencies between 0.35 and 0.8 times *BPFs*. Thus, the passing of the blades is not the only source of oscillations.
- Other coupling effects like blade flutter, shock instability, rotating stall and surge.

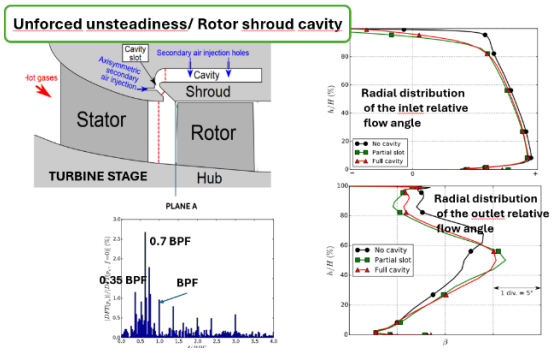

Figure 27. Unforced phenomena associated with a rotor should cavity in an axial turbine stage [77].

- Corner separation and corner stall. These flow features were studied by Schulz et al. in the 90's ([78], [79], [83]), followed by the attempt of Lei et al. [81], who propose an interesting simple 1D criteria for its onset.

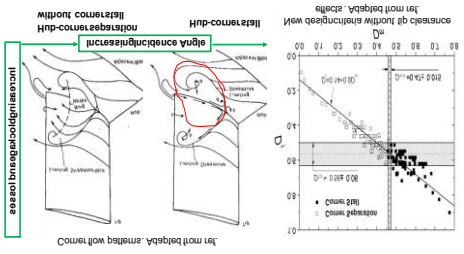

Figure 28. Flow topology of the corner separation and corner stall and the aerodynamic performance for the end wall corner flows. Adapted from [78] (Left) and from [81](Right).

7.3.1. Rotating stall.

In most cases, at low flow rates, the axisymmetric initial flow becomes unstable (Note that a non-axisymmetric flow can be highly stable). In the circumferential direction, the flow divides into regions of low flow rate called "stall cell patterns" and un-stalled regions in which the flow rate is larger than the mean flow rate just before critical stall point of operation.

This point has been an active research field, both in axial and radial machines, aiming to understand and predict its onset then try to control its effects.

Rotating stall onset arises in different ways in radial and axial machines and this is mainly due to different performance characteristics curves and different machine length-volume and mean velocity flow scales (time scales)

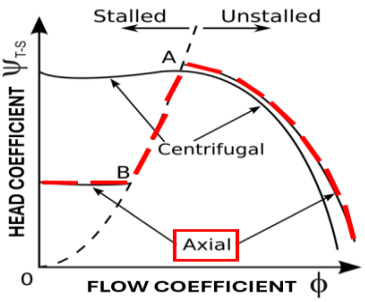

Figure 29. Typical curves of head coefficient versus flow coefficient in axial and centrifugal compressors.

a) Vaneless diffuser rotating stall.

This phenomenon was identified in the 60's by Jansen [83]. Many other experimental and numerical investigations were performed mainly after 1990, thanks to advanced experimental techniques like PIV and numerical simulation both in 2D and 3D approaches such as Fring and Van den Braembbusche [84](1985), Moore [85] (1989), Ferrara et al. [86] (2004) , Ljevar et al. [87] (2006) , Dazin et al. [88] [89] (2008 and 2011).

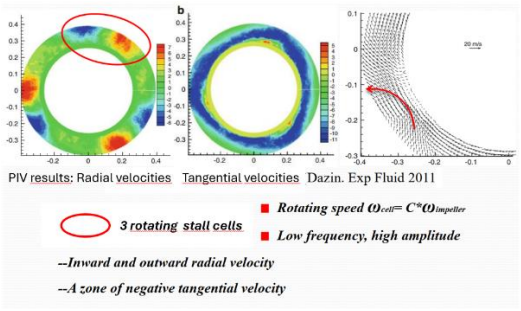

Figure 30. Rotating stall cells identification in a vaneless diffuser from PIV results. Adapted from [89].

b) Axial flow compressors.

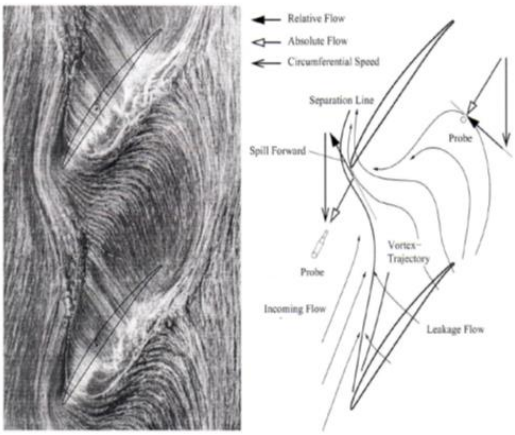

Figure 31. Secondary flow visualization in a 2D compressor cascade with tip leakage. Adapted from [9].

In axial flow machinery, it is generally recognised that transition to axial compressor rotating stall can develop in two different ways, the so-called spike type and modal type route to rotating stall. Figure 31 shows the visualisation of limiting streamlines that occur at high incidence angles in a 2D compressor rotor cascade including tip-leakage (from [9]).

An exhaustive review paper has been published by Day. [90] on this topic where only aerodynamic sources are present.

In some cases, acoustic resonance can trigger rotating stall or surge as detected by Hellmich and Seume [91].

More research insights are in progress about the combined effects of incidence, tip leakage and low momentum radial migration along the blades during the rotating stall route. Stall precursor detection for flow control activation is still an important topic to solve.

Recent works (Romano et al. [92]) looking at distinct type routes due to passive and active flow control and inlet distortions, brought new insights for better understanding on such phenomena.

In case of forced inlet inhomogeneities, an analysis of unsteady pressures measured at the casing shows that in the baseline case (with no injector and no grid), the transition to stall is of spike-type whereas, if the intensity of the inhomogeneity is increased, the stall can be of modal type or a mix between spike and modal.

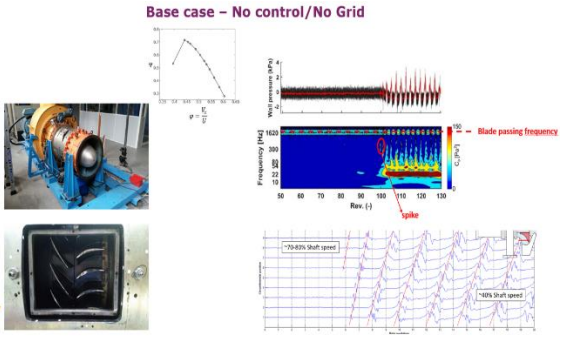

Figure 32. Time frequency charts in an axial flow compressor stage. Rotating stall inception for uniform axi-symetric inlet conditions.

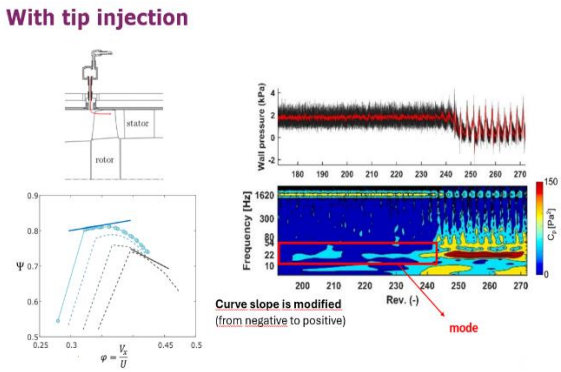

Figure 33. Time frequency charts in an axial flow compressor stage. Rotating stall inception for uniform axi-symetric inlet conditions with tip injection.

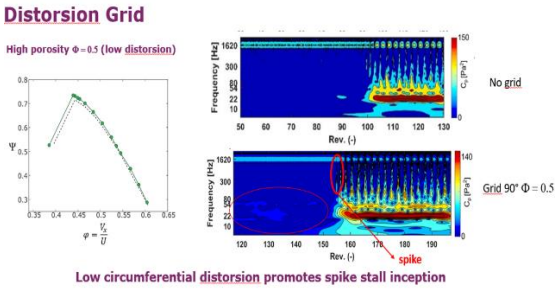

Figure 34. Time frequency charts in an axial flow compressor stage. Rotating stall inception for non-uniform inlet conditions.

7.3.2. Cavitation

Cavitation occurrence not only influences overall pump performances like already seen in section 5 (example 5) but can also produce unsteady phenomena especially in hydrofoils and axial pump inducers' parts.

Their designs are strongly related to the application since strong rotating pressure fluctuations at frequencies that can be coupled with the whole system (in the draft tube of Francis hydraulic turbine or POGO effects in cryogenic pump rocket propulsion systems for which an example is given on Figure 35a and 35b.

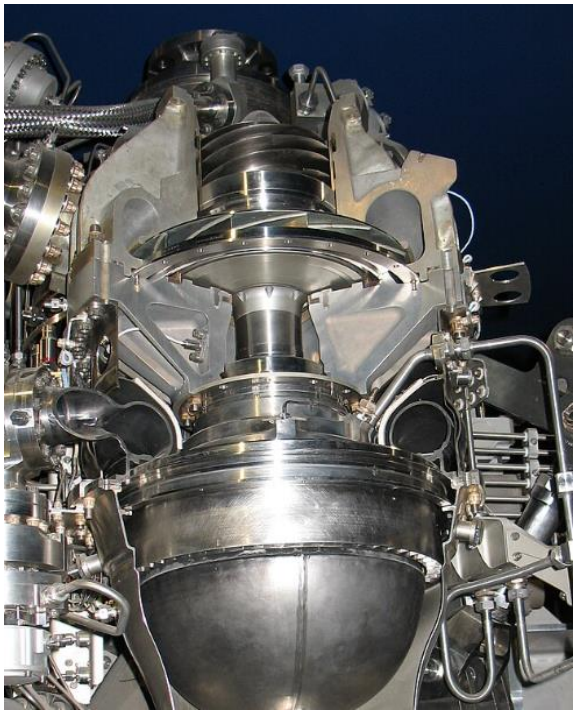

Figure 35a. Cryogenic pump for space application.

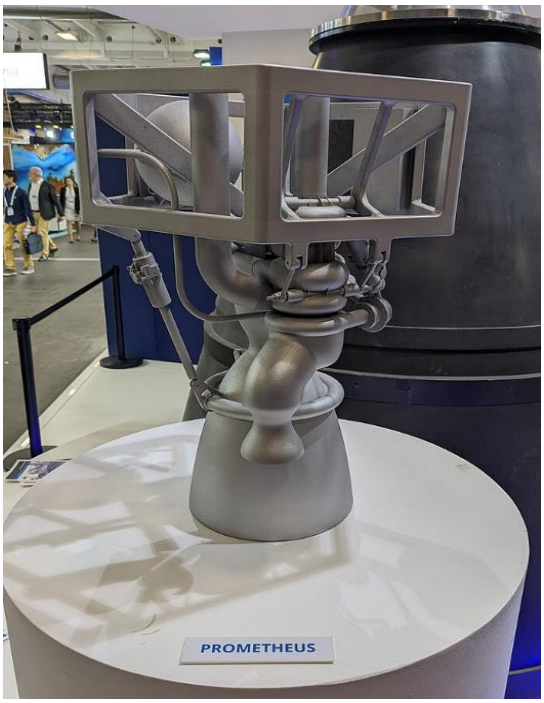

Figure 35b. New compact pump design.

It is so mandatory to improve existing flow unsteady models to better capture the re-entrant jet description which is strongly related to the local two-phase mixture density distribution. As pointed out in the published works referred in [93] to [97], it is responsible for unsteady pressure distribution along the blade chord related to the Strouhal number linked to the bubble detachment sequences that are transported in the main flow.

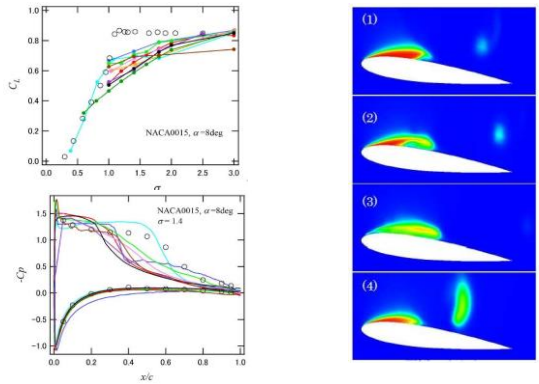

Figure 36. Blade pressure distribution with sheet cavitation (left). Unsteady sheet cavitation on the suction surface of a blade profile (right).

8. TOWARDS ROBUST DESIGN TOOLS. MACHINE LEARNING (ML).

During the last 20 years, more and more knowledge and strong experience has been acquired from basic experimental analysis to model derivations and numerical simulation packages. They have had strong consequences for better flow descriptions and design integrations and lead to important efforts to implement a robust design concept.

Robust design concept is based on good evaluation and calibration of performances for the whole range of operation whatever the accuracy of the model is, if it has been well calibrated according to the desired objectives. This should be inserted at an early stage in the design procedures

For this purpose, the need for detailed and well documented information on realistic test rigs is more and more recommended and even mandatory. There are still many existing experimental results that are available but with a lack of detailed information about inlet turbulent scales or inlet boundary layers for example.

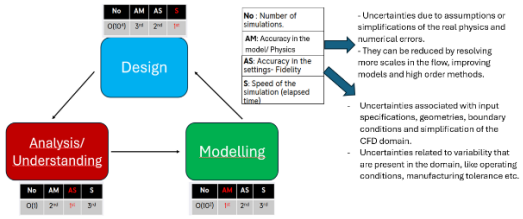

Figure 37. Design paradigm involving accuracy and simulation speed [98].

Robust design mainly depends on CFD overall accuracy that can be considered as a function of models and settings accuracy as shown on figure 37 extracted from Vasquez and Adami [98].

Reducing the sources of inaccuracies require precise information on:

1. Detailed geometry description: non-axisymmetric casings and blades, blade settings, hubs and shroud cavities and gaps, rotor tip clearance, stator hub clearance, geometry variations, buttons, blade fillet and surface finish, manufacturing tolerances,
2. Numerical errors due to mesh and/or finite difference approximations

3. Settings: geometry fidelity, real geometry discrepancy, impact of manufacturing variability on performances.

4. Models:

- trusting CFD's physics and mathematics according to the level of approximation,
- evaluate the aleatory uncertainty due to boundary conditions,
- inserting correct inflow and outflow boundary conditions: all leakage flows, bleed flow, purge and cooling flows (mainly for turbines)
- Steady flow assumption consequences.

Below, one can find 3 different examples that can illustrate different ways to evaluate existing empirical laws and built robust design tools depending on the level of approximation with an adequate design space choice. This corresponds to the so-called "machine learning" techniques that speed up prediction times, analyse and manage uncertainty and reconcile simulations with available data with better prediction accuracy. "Such techniques facilitate faster and more robust searches of the design space, with or without the help of optimization methods" as pointed out by the review paper proposed by Hammond et al. [99].

8.1. Example 1.

Even if it may seem paradoxical, it turns out that for some cases, a resumption of the analysis of isolated phenomena can enrich robust design approaches. The following research works from Raina et al. [100] [101] give some answers the two following questions:

- how to properly extract individual loss levels when strong interactions occur between vortices and wakes?
- to what extend is it possible to use independent loss models' assumption to predict overall losses?

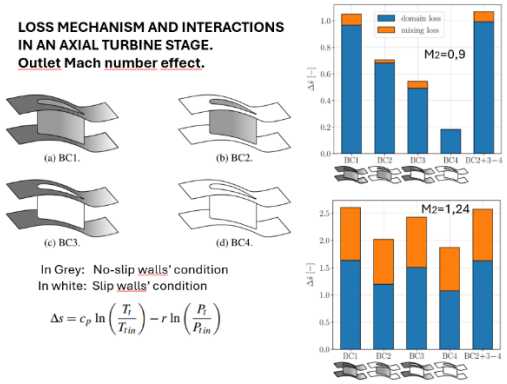

Figure 38. Evaluation of loss mechanism in an axial turbine stage. Outlet Mach number effect. Adapted from [100].

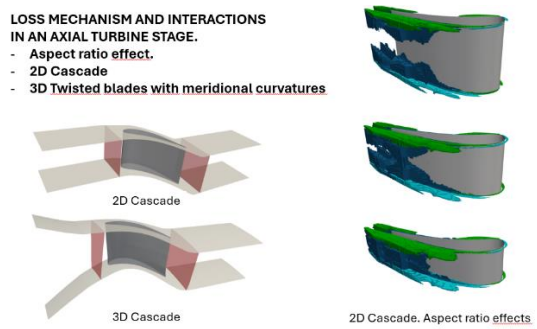

Figure 39. Evaluation of loss mechanism in an axial turbine stage. Aspect ratio effect. Adapted from [100].

8.2. Example 2.

How to use the differences between low and high-fidelity numerical simulations for a 2D case, under low Reynolds number like for high altitude flight conditions (see Bergmann et al. [102]).

- Uncertainties issued from RANS simulations do not produce constant offset of results compared with LES ones. They are flow dependant especially for off-design conditions.
- High fidelity scale-resolving simulations at low Reynolds number offer powerful tools for early design prediction processing at challenging operating points
- Evaluation and analysis on the differences between RANS and LES can enhance design reliability.

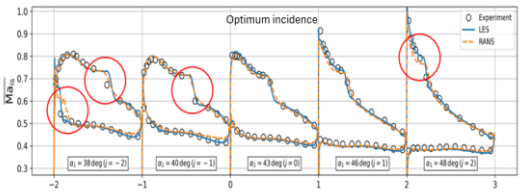

Figure 40. Comparison between RANS and LES in a compressor blade at low inlet Reynolds number condition. Adapted from [102].

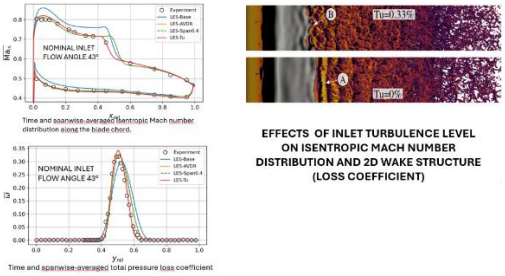

Figure 41. LES results in a compressor blade at low inlet Reynolds number condition. Effect of the inlet turbulence level. Adapted from [102].

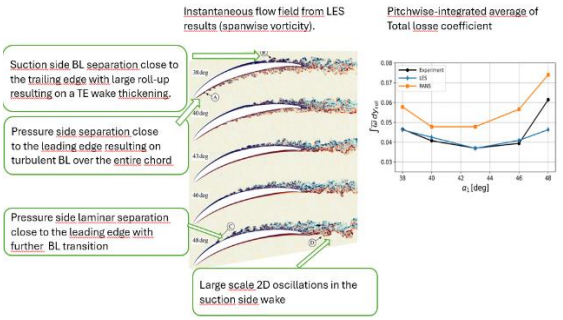

Figure 42. Comparison of total loss coefficient with incidence angle between RANS and LES in a compressor blade at low inlet Reynolds number condition. Adapted from [102].

8.3. Example 3.

What are the necessary conditions for the detection of pump sump submerged vortex onset? (Kato [103]).

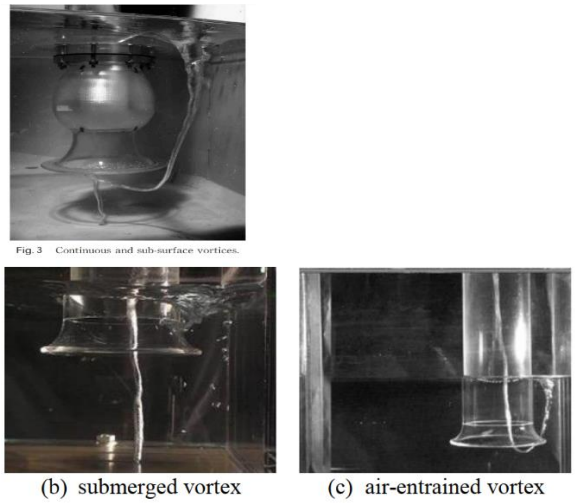

Figure 43. Experimental observation of submerged and air-entrained vortices.

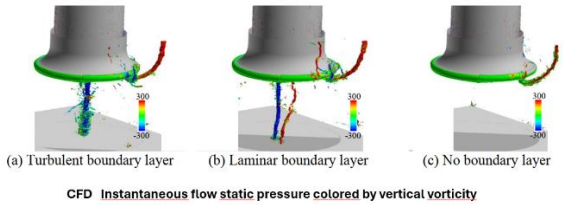

Figure 44. CFD LES results for vortex detection simulations in a pump sump. Adapted from [103].

One can observe that, in recent years, scale resolving simulations such as Large Eddy Simulation (LES) and Direct Numerical Simulation (DNS), as opposed to time-averaging methods like (U)RANS, are more frequently used for design aid. Figure 45 shows where each method lies on the trade-off between accuracy and computational expense and the correlation of these methods to the energy spectrum. Despite their undeniable superiority to (U)RANS, LES with appropriate grid resolution is still computationally prohibitive, while it is more common for the wall-bounded and statistically steady flows. Scale resolving simulations offer superior resolution allowing designers to determine not only *what* is happening in the fluid flow, but also *why* it is happening. They produce accurate numerical datasets to benchmark and improve (U)RANS models.

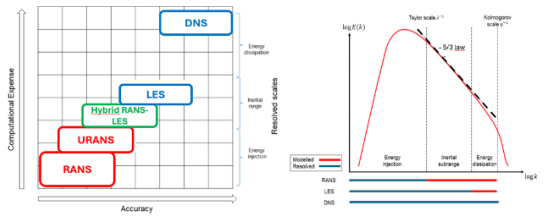

Figure 45. Computational expense against accuracy depending on the approach (left) and capability of each method to model or resolve energy spectrum (right).

9. ARTIFICIAL INTELLIGENGE (AI).

Artificial intelligence is asserting itself as a powerful tool for amplifying human decision-making capabilities and overcome difficult to solve problems in all aerodynamic fields.

Presently, the application of AI in turbomachinery field is at an early stage of exploration We are still far from fully mastering the extent and consequences of confrontation and mastery of this new paradigm.

Many investigations have still to be explored in several areas like real 3D inverse design, experimental testing, intelligent control systems and maintenance.

Take advantage of previous works and models to build improved and reliable rules extracted from experiments and CFD. This needs important background and clear knowledge of the relative importance of each isolated phenomena and interactions.

For any kind of turbomachinery applications, AI can be integrated into any step of the complete conception procedure, starting from the design step up to the validation and the maintenance.

AI can be employed for autonomous decision-making capability in aerodynamic optimization procedure and active flow control of turbomachines, generating optimal aerodynamic solutions and complex control strategies that surpass human capabilities.

AI uses machine learning data to perform most aerodynamic tasks whatever the level of approximation is.

An example of specific work devoted to centrifugal compressor families using AI-based fast design method can be found in [104].

It can be considered as an upgrade of up-to-date aerodynamic design systems allowing to replace the need for additional empirical expertise and numerical results.

It must allow to gather and share several kinds of data and information between the different fields of specialization, enforcing interactive 3D design optimization and real-time prognosis including in-situ control and global maintenance analysis.

For numerical simulations, AI can help to extracts knowledge from high-fidelity data in DNS simulations and experimental measurements to improve transition models for RANS and URANS simulations and consequently improve the simulation accuracy.

For experimental tests, AI can help to clean, complete, reconstitute or restore missing or incomplete or limited measuring data sets by incorporating physical constraints. AI could help to reconstruct overall flow fields from limited measurement data by physics-informed neural networks.

When validation is required, AI only acts as a supplement to classical methods that use numerical simulations and/or experimental tests.

The question is: what should be the researcher's involvement to produce results for AI data base mining?

10. CONCLUSIONS.

Whatever the evolution of future needs related to energy transition, drastic and rapid changes in demand are expected in many sectors, including the one for turbomachinery applications. In this context, new aerodynamic design processes exploiting the existing know-how and enriched by efficient multi-disciplinary techniques could quickly react to demand variations and ensure technical innovation and end-users' success.

Many of CFD approached are now mature and well advanced even if further improvements can be expected in near future as for laminar-transition evaluation accuracy and turbulence modelling. For such problems, machine learning have already a specific impact on CFD within the space of turbomachines specifically, where data from higher-fidelity simulations are used to train models issued from lower fidelity calculations.

Additionally, CFD assessments need extensive well documented experimental investigations and data base elaboration for a large multidisciplinary design space and in realistic geometries including all physical aspects including noise levels predictions

.

- For high-speed machines, there is still research needs to analyse 3D shock-structures interactions, coupled with deformation, blade flutter, vibration modes detection, off-design aspects including stall and surge, fast transient phenomena for safety problems in adiabatic and diabatic conditions, purge and leakage flow interactions with thermal effects, fouling and cleaning assessments. All these different aspects that involve different engineering fields must be integrated to

produce new architectures like the ones shown in figure 46 for air-breathing engines.

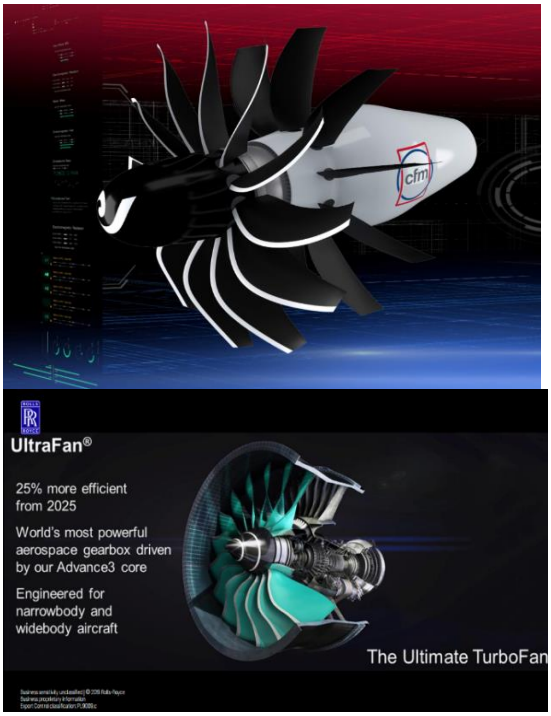

Figure 46. CFM-RISE Program (mid 2030). RR UltraFan (for narrow and wide body aircrafts)

- For hydraulic machines, extended estimation for high fluid viscosity and non-Newtonian behaviour should be foreseen, pump as turbine configurations should be more explored including better predictions on multiphase flow and cavitation instabilities.

A recent example of the open test case CATANA for a high-speed fan [105], provided by the Fluid Mechanics and Acoustic laboratory in Lyon illustrates what could be done for the whole turbomachinery community.

However, many flow and heat transfer processes cannot be easily tested. CFD provides the ability to theoretically simulate any physical conditions. It allows great control over the physical process and provides the ability to isolate specific phenomena that can be also tested experimentally for comparison and validation.

It may happen that, for some cases, initial and boundary conditions may be sufficient to run a computational simulation but does not guarantee agreement with measured data and design experience. Recent developments based on Physics-Informed Neural Networks (PINNs) offer a very interesting potential to combine all sources of available information in a single constrained optimisation network. Measured data, data from high-fidelity sources, theoretical physical laws and tried and tested empirical relationships can all be considered simultaneously by incorporating them in the loss function of a learning machine.

Today, producing a very good design for a turbomachinery component is not any more the main target. Compromise must be checked due to increasing technical constraints. For example, evolutions to new architectures, simplified geometries, compact designs, fast machining, long life targets, gain on weight and time of repairs, life duration, modelling of other fluids, new cycles, electric powering, energy distribution for safe operations and so on…. This will change the future to partially or completely solve each related task facing numerous multidisciplinary interactions.

Past knowledge cannot be ignored and must be stored for machine learning capability and efficient data base elaboration. In this respect, it is very important that a designer using CFD appreciates the underlying assumptions and limitations of the numerical techniques that are available to him. It is consequently very important to present all the predictions coming from future advanced developed models with uncertainty evaluations helping engineers for confidence in the results obtained and justify the design decisions taken as a result.

ACKNOWLEDGEMENTS

The author thanks the French ATTAG (Association Technique des Turbines à Gaz) for its support in collecting part of the information presented in this document.

REFERENCES

[1] Cumpsty N.A, 2010, “Some lessons learned”. ASME Jnal of Turbomachinery, vol. 132, October 2010.

[2] Hawthorne W.R., 1955, Rotational flow through cascades, Quart. J. Mech. Appl. Math., 8, 3, 266-279

[3] Horlock, B. Lakshminarayana and J. H. 1963. “Review : Secondary Flows and Losses in Cascades and axial - flow turbomachines.” Int. J.Mech.Sci. 5: 287–307.

[4] Horlock J.H., Lakshminarayana B., 1973, Secondary flows: theory, experiment, and application in turbomachinery aerodynamics, Ann. Rev. Fluid Mechanics, 5, 247-279 17.

[5] Lakshminarayana B., Horlock J.H., 1973, Generalised expressions for secondary vorticity

using intrinsic co-ordinates, J. Fluid Mech., 59, Part 1, 97-115

[6] Marchal Ph., Sieverding C.H., 1977, Secondary flows within turbomachinery bladings, Proc. AGARD-CP-24.

[7] Papailiou. K., Flot. R., Mathieu. J. Secondary flows in Compressor Bladings. ASME J. Eng. Power. Apr 1977, 99(2): 211-224 (14 pages). https://doi.org/10.1115/1.3446274

[8] Gallus, H.E. and Kummel, W. 1977. Secondary Flows and Annulus Wall Boundary Layers in Axial-Flow Compressor and Turbine Stages. AGARD CPP No. 214. Paper No. 4: 1–15.

[9] Langston, L.S. 1980. Crossflows in a Turbine Cascade Passage. *ASME Journal of Engineering for Power*. **102**: 866–874

[10] Sieverding, C.H. 1985. Recent Progress in the Understanding of Basic Aspects of Secondary
Flows in Turbine Blade Passages. *ASME Jour. of Turbomachinery*. **107**: 248–257.

[11] Sharma, O.P., and Butler, T.L. 1987. Predictions of Endwall Losses and Secondary Flows in Axial Flow Turbine Cascades. *ASME Jour. of Turbomachinery*. 109: 229–236.

[12] Hodson H.P., Dominy R.G., 1987, Three-dimensional flow in a low pressure turbine cascade at its design conditions, Trans. ASME, J. Turbomachinery, 109, 278-286

[13] Schulz, Gallus, Laksminarayana. Three-Dimensional Separated Flow Field in the Endwall Region of an Annular Compressor Cascade in the Presence of Rotor-Stator Interaction Journal of Turbomachinery OCTOBER 1990, Vol. 112, pp 669- 678)

[14] Kang S 1993 *Investigation on the Three-Dimensional Flow Within a Compressor Cascade with and without Tip Clearance* PhD Thesis, Dept. of Fluid Mech., Vrije Universiteit Brussels.

[15] Langston, L.S. 2006. "Secondary Flows in Axial Turbines-A Review." Annals of the New York Academy of Sciences.

[16] Wu, C. H.,1952, A General Theory of Three-Dimensional Flow in Subsonic or Supersonic Turbomachines of Axial, Radial and Mixed Flow Type, NACA TN 2604.

[17] Smith, L., H., Jr., 1969, Casing Boundary Layers in Multistage Compressors, Proc. Symp. Flow Research on Blading.

[18] Kerrebrock, J. L., and Mikolajczak, A. A., 1970, Intra-Stator Transport Of Rotor Wakes abd Its Effect on Compressor Performance, ASME Journal. Eng. Power, Vol. 92,p. 359
.
[19] Bosman C, and Marsh H., 1974, "An Improved Method for Calculating the Flow in Turbomachines, Including a Consistent Loss Model," *Journal of Mechanical Engineering Science*, Vol. 16, No. 1, pp. 25–31.

[20] Hirsch C., and Warzee , G., 1976, "A Finite-Element Method for Through-Flow Calculations in Turbomachines," *ASME Journal of Fluids Engineering*, Vol. 98, pp. 403–421
.
[21] Denton J. D., 1978, "Throughflow Calculations for Transonic Axial Flow Turbines," *ASME Journal of Engineering for Power*, Vol. 100, pp. 212–218.

[22] Denton, J. D., and Singh, U., K., 1979, Time Marching Methods for Turbomachinery Flows Calculations, VKI-Lecture Series, No . 7. VKI

[23] Adamczyk, J. J., 1985, "Model Equation for Simulating Flows in Multistage Turbomachinery," ASME Paper No. 85-GT-226.

[24] Jennions, I.K., and Stow, P., 1986, The importance of Circumferential Non-uniformities in a Passage-Averaged Quasi-Three-Dimensional Turbomachinery Design System, ASME Jnal Eng. Gas Turbine Power, Vol. 108, pp. 240-245.

[25] Dawes, W. N.,1990, Towards Improved Throughflow Capability: The Use of 3D Viscous Flow Solvers in a Multistage Environment, Paper 90-GT-18. Gas Turbine and Aeroengine Congress and Exposition—June 11-14, 1990—Brussels, Belgium**.**

[26] Shabbir, A., Celestina, M. L., Adamczyk, J. J., and Strazisar, A.,1997, The Effect of Hub Leakage Flow on Twi High Speed Axial Flow Compressor Rotors, ASME Paper No. 97-GT-346

[27] Wellborn, S. R., and Okiishi, T.H., 1998, The Influence of Shrouded Stator Cavity Flows on Multistage Compressor Performance, ASME Jnal of Turbomachinery, Vol. 121, pp. 486-497
.
[28] Escuret, J. F., and Veyssiere, P. H., Villain, M., Savarese, S., Bois, G., and Naviere, H., 1997, Effect of a Mismatch Between the Buttons of Variable Stator Vanes and the Flowpath in a Highly Loaded Transonic Compressor Stage, ASME Paper No. 97-GT-471.

[29] Adkins, Jr, G. G., Smith, Jr, L.H ,1982, Spanwise mixing in axial machines, Journal of Engineering and Power, Jan 1982, 104(1): 97-110 (14 pages). https://oi.org/10.1115/1.3227271

[30] Adamczyk, J. J., Aerodynamic Analysis of Multistage Turbomachinery Flows in Support of Aerodynamic Design, 1999, International Gas Turbine Institute Scholar Lecture, Journal nal of Turbomachinery, 2000, Vol. 122

[31] Denton, J. D. Some limitations of Turbomachinery CFD, Proceedings of the ASME Turbo Expo 2010: Power for Land, Sea and Air June 14-18, 2010, Paper GT2010-22540 Glasgow, UK.

[32] Pinckney, S. Optimized turning-vane design for an intake elbow of an axial-flow compressor. NASA Report TN D-3083, 1965.

[33] Neumann, B., The interaction between geometry and performance of a centrifugal pump. Mechanical Engineering Publications Ltd., London.

[34] Flathers, M., Bache, G., Rainsberger, R.: An experimental and computational investigation of flow in a radial inlet of an industrial pipeline centrifugal compressor. ASME Journal of Turbomachinery, Vol. 118, No 2, 1996, pp. 371-377

[35] Ayder, E., Van den Braembussche, R.A.: "Experimental Study of the Swirling Flow in the Internal Volute of a Centrifugal Compressor", ASME Paper 91-GT-7.

[36] Ayder, E., Van den Braembussche, R.A.: "Experimental and Theoretical Analysis of the Flow in a Centrifugal Compressor Volute", Trans. ASME, Journal of Turbomachinery, Vol 115, No. 3, July 1993, pp. 582-589.

[37] Ayder, E., Van den Braembussche, R.A.: "Numerical Analysis of the Three-Dimensional Swirling Flow in Centrifugal Compressor Volutes", Trans. ASME, Journal of Turbomachinery, Vol. 116, Nr. 3, July 1994, pp. 462-468

[38] Van den Braembussche**,** R. A., Ayder, E., Hagelstein, D., Rautenberg, M., Keiper, R., Improved model for the design and analysis of centrifugal compressor volutes, Proceedings of the 1998 International Gas Turbine & Aeroengine Congress & Exhibition - Stockholm, Sweden

[39] Van den Braembussche, R.A. [6] ((2006) Flow and Loss Mechanisms in Volutes of Centrifugal Pumps. In Design and Analysis of High Speed Pumps (pp. 12-1 – 12-26). Educational Notes RTO-EN-AVT-143, Paper 12. http://www.rto.nato.int/abstracts.asp.)

[40] Zangeneh, M., 1991, "A Compressible Three Dimensional Blade Design Method for Radial and Mixed Flow Turbo-machinery Blades," Int. J. Numerical Methods in Fluids, Vol. 13, pp. 599-624.

[41] Zangeneh M (1994) Inviscid-viscous interaction method for three-dimensional inverse design of centrifugal impellers. J Turbomach 116(2):280–290. https://doi.org/10.1115/1.2928362

[42] Zangeneh, M., Daneshkhah, K.2009, A Fast 3D Inverse Design Based Multi-Objective Optimization Strategy for Design of Pumps . Conference paper FEDSM, DOI:10.1115/FEDSM2009-78443

[43] Demeulenaere, A. and Van den Braembussche, R**.** Three-dimensional inverse design method for turbomachinery blading design. ASME paper 96-GT-39, 1996

[44] Dean, R.C., Jr.; Senoo, Y. Rotating Wakes in Vaneless Diffusers. *J. Basic Eng.* **1960**, *82*, 563–570

[45] Eckardt, D. Detailed Flow Investigations within a High-Speed Centrifugal Compressor Impeller. *J. Fluids Eng.* **1976**, *98*, 390–399

[46] Moore, J., Moore, J.G., 1983a. "Entropy production rates from viscous flow calculations. Part i A turbulent boundary layer flow," In: Proc. ASME International Gas Turbine Conference and Expo 1983 83-GT-70. Phoenix, AZ, USA.

[47] Hirsch Ch, Kang S and Pointet G 1996 *A Numerically Supported Investigation on the 3D Flow in Centrifugal Impellers. Part I: The Validation Base* ASME Paper 96-GT-151

[48] Hirsch Ch, Kang S and Pointet G 1996 *A Numerically Supported Investigation on the 3D Flow in Centrifugal Impellers. Part II: Secondary Flow Structure* ASME Paper 96-GT-152.

[49] Van den Braembussche, R., 1985, *Description of Secondary Flow in Radial Flow Machines* Published in Thermodynamics and Fluid Mechanics of Turbomachinery Volume II, Edited by Ucer A S, Stow P and Hirsch Ch, NATO ASI Series, pp. 665-684

[50] Agira GOTO, IJFMS Dec 2015, Historical perspective on fluid machinery flow Optimisation in an industry. Vol9, No 1, Jan- March 2016

[51] Zangeneh, M., Goto, A., Harada, H., [8] , 1998, "On the Design Criteria for Suppression of

Secondary Flows in Centrifugal and Mixed-Flow Impellers," ASME Journal of Turbomachinery, Vol.120, pp723-735

[52] Merli, F., and Gaetani. P., *NUMERICAL* INVESTIGATION OF THE LEAN EFFECTS IN CENTRIFUGAL COMPRESSORS, Proceedings of 13th European Conference on Turbomachinery Fluid dynamics & Thermodynamics ETC13, April 8-12, 2018; Paper ID: ETC2019-143 Lausanne, Switzerland

[53] Gregory-Smith, D.G., Jayaraman, G.P., Harvey, N. W. and Rose, M. G. End wall contouring Gregory Smith Secondary flow control. Proceedings of the Institution of Mechanical Engineers Part A Journal of Power and Energy · September 2001, DOI: 10.1243/095765001153902)

[54] Burigana. M., Verstraete. T., Lavagnoli. S. , Turbine End wall Contouring Through Advanced Optimization Techniques Turbine end wall contouring, ASME Jnal of Turbomachinery, August 2023 vol 145

[55] Shabbir, A., Adamczyk, J.J., Strazisar, A.J., and Celestina, M.L., 2007, The Effect of >Hub Leakage on Two High Speed Axial Flow Compressor Rotors, ASME Paper No. 97-GT-346.

[56] Barrand, J.P., Caignaert, G., Graeser, J.E., and Rieutord, E., Synthesis of the results of tests in air and water aimed at detecting the critical recirculating flow rates on the inlet and outlet of a centrifugal pump impeller. La Houille Blanche, N°5 (August 1985), pp. 405-420.
https://doi.org/10.1051/lhb/1985028

[57] Stoffel, B., and Schuller, W., Investigations in Respect to the Determination of Cavitation Intensity by the Means of Acoustic Signals La Houille Blanche, N°7-8 (Décembre 1992), pp. 601-604. htpps://doi.org/10.105(/lhb/1992064

[58] Pelz, P.F., Keil, T., Ludwig, G. (2014). On the Kinematics of Sheet and Cloud Cavitation and Related Erosion. In: Kim, KH., Chahine, G., Franc, JP., Karimi, A. (eds) Advanced Experimental and Numerical Techniques for Cavitation Erosion Prediction. Fluid Mechanics and Its Applications, vol 106. Springer, Dordrecht. https://doi.org/10.1007/978-94-017-8539-6_9

[59] Hofmann, H., Stoffel, B., Coutier-Delgosha, O., Fortes-Patella, R., Reboud, J.L., Experimental and numerical studies on a centrifugal pump with 2D-curved blades in cavitating condition, Conference CAV2001:sessionB7.005, June 2001.

[60] Bakir, F., Kouidri, S., Noguera, S., Rey. R., Experimental Analysis of an Axial Inducer Influence of the Shape of the Blade Leading Edge on the Performances in Cavitating Regime, *J. Fluids Eng*. Mar 2003, 125(2): 293-301, https://doi.org/10.1115/1.1539872

[61] Dehnavi; E., Danlos. A., Solis, M., Kebdani, M., Bakir, F., Cavitation Performance of a Pump with Independently Rotating Inducer and Impeller in Co-Rotation and Counter-Rotation Modes by Varying Rotor Speeds, Journal of Fluids Engineering, June 2025, Vol. 147 / 061203 (15 pages)

[62] Zhang, L., Davila, G., and Zangeneh, M., Multi-Objective Optimization of a High Specific Speed Centrifugal Volute Pump Using Three-Dimensional Inverse Design Coupled with Computational Fluid Dynamics Simulations, *J. Fluids Eng*. Feb 2021, 143(2): 021202 (12 pages) Paper No: FE-20-1286 https://doi.org/10.1115/1.4048292

[63] Parikh, T., Mansour, M., and Thevenin, D., 2021, Maximizing the Performance of Pump Inducers using CFD-based Multi-Objective Optimization, Structural and Multidisciplinary Optimization, 65.9, htpps://doi.org/10.1007/s00158-21-03108-6.

[64] Gümmer, V., , Wenger, U., and Kau, H. P Using Sweep and Dihedral to Control Three-Dimensional Flows in Transonic Stators of Axial Compressors, ASME Journal of Turbomachinery, Jan 2001, Vol 123.

[65] Lopez, I. L., Shisu, T., Kipouros, T., Shapar, S., and Wilson, M., Extending Highly Loaded Axial Fan Operability Range Through Novel Blade Design, ASME, Journal of Turbomachinery, Dec. 2022, Vol. 144 / 121009-1

[66] Reutter, O., Hervé, S., Nicke, E., 2013, AUTOMATED OPTIMIZATION OF THE NON-AXISYMMETRIC HUB ENDWALL OF THE ROTOR OF AN AXIAL COMPRESSOR Proceedings of 10th European Conference on Turbomachinery Fluid dynamics & Thermodynamics ETC10, April 15-19, 2013, Lappeenranta,

[67] Leboeuf, F., Unsteady flow analysis in transonic turbine and compressor stages, VKI Lecture Series on Recent Developments in

Numerical Methods for Turbomachinery Flows, 2002-01)

[68] Moreau, S. and Roger, M., 2024, Turbomachinery Noise Review, International Journal of Turbomachinery and Power, Vol. 9,11, htpps://doi.org/10.3390/ijtpp9010011.
[69] He, L. 2021, Averaging for High Fidelity Modelling-Toward Large Eddy Simulations in Multi-Passage Multi-Row Configurations, Journal of Turbomachinery, Feb. 2021, Vol. 143

[70] Courtiade, N., Experimental analysis of the unsteady flow and instabilities in a high-speed multistage compressor, PhD Thesis, LMFA, Ecole Centrale de Lyon, Novembre 2012.

[71] Poensgen, C., Gallus, H.E., Three-Dimensional Wake Decay Inside of a Compressor Cascade and Its Influence on the Downstream Unsteady Flow Field: Part I—Wake Decay Characteristics in the Flow Passage, Journal of Turbomachinery. 113 (1991) 180.

[72] Mailach, R., Lehmann, I., Vogeler, K., Periodical Unsteady Flow Within a Rotor Blade Row of an Axial Compressor: Part II — Wake–Tip Clearance Vortex Interaction, in: Montreal, Canada, 2007: p. 1587-1597

[73] Ernst, M., Michel, A., Jeschke, P., Analysis of Rotor-Stator-Interaction and Blade-to-Blade Measurements in a Two Stage Axial Flow Compressor, J. Turbomach. 133 (2011) 011027.

[74] Courtiade, N., Ottavy, X., Modal decomposition for the analysis of the rotor-stator interactions in a high-speed multistage compressor, Journal of Thermal Science. 21 (2011)

[75] Roberts, Q. and Denton, J. D. Loss production in the wake of a simulated turbine blade. ASME paper 96-GT-421,1996.

[76] Cicatelli, G. and Sieverding, C. H. The effect of vortex shedding on the unsteady pressure distribution around the trailing edge of a turbine blade. ASME paper 96-GT-359, 1996.

[77] Tanga. E., Trebinjac. I., Ngo Boumb. G., Philita. M., 2017, Aerodynamic Interactions between a High-Pressure Turbine Stage and a Shroud Cavity. Paper ID: ETC2017-176. Proceedings of 12th European Conference on Turbomachinery Fluid dynamics & Thermodynamics ETC12, April 3-7, 2017; Stockholm, Sweden.

[78] Schulz, H. D., and Gallus, H. E., 1988. "Experimental Investigations of the Three-Dimensional Flow in an Annular Compressor Cascade". Journal Turbomachinery, 110(3), pp. 467-478.

[79] Schulz, H. D., Gallus, H. E., and Lakshminarayana, B., 1990. "Three-Dimensional Separated Flow Field in the Endwall Region of an Annular Compressor Cascade in the Presence of Rotor-Stator Interaction. Part I. Quasi-Steady Flow Field and Comparison with Steady-State Data". Journal of Turbomachinery, 112(4), pp. 669-678.

[80] Schulz, H. D., Gallus, H. E., and Lakshminarayana, B., 1990. "Three-Dimensional Separated Flow Field in the Endwall Region of an Annular Compressor Cascade in the Presence of Rotor-Stator Interaction. Part Ii. Unsteady Flow and Pressure Field". Journal of Turbomachinery, 112(4), pp. 679-690.

[81] Lei, V. M., Spakovsky. Z.S., and Greitzer. E. M. 2008. “A Criterion for Axial Compressor Hub Corner Stall.” ASME Jnal of Turbomachinery, vol. 130, doi:10.1115/GT2006 91332.

[82] Xianjun Yu Baojie Liu, 2010 A Prediction Model for Corner Separation/Stall in Axial Compressors, Proceedings of ASME Turbo Expo 2010: Power for Land, Sea and Air GT2010, June 14-18, 2010, Glasgow, UK GT2010-22453.

[83] Jansen, W. (1964). Rotating stall in a radial vaneless diffuser. *Journal of Basic Engineering*, *86*, 750-758

[84] Fringe, P., & Van den Braembussche, R. (1985). A theoretical model for rotating stall in the vaneless diffuser of a centrifugal compressor. *Journal of Engineering for Gas Turbines and Power*, *107*(2), 507-513

[85] Moore, F. K. (1989). Weak rotating flow disturbances in a centrifugal compressor with a vaneless diffuser. *Journal of Turbomachinery*, *111*(4), 442-449

[86] Ferrara, G., Ferrari, L., & Baldassarre, L. (2004). Rotating stall in centrifugal compressor vaneless diffuser: experimental

analysis of geometrical parameters influence on phenomenon evolution. *International Jounal of Rotating Machinery*, *10*(6), 433-442. doi: 10.1080/10236210490503950.

[87] Ljevar, S., de Lange, H. C., & van Steenhoven, A. A. (2006). Two-dimensional rotating stall analysis in a wide vaneless diffuser. *International Journal of Rotating Machinery*, Article ID 56420, pp. 1-11. doi:10.115/IJRM/2006/56420

[88] Dazin, A., Coudert, S., Dupont, P., Caignaert, G., Bois, G. (2008). Rotating instability in the vaneless diffuser of a radial flow pump. *Journal of Thermal Science*, *17*(4), 368-374.

[89] Dazin, A., Cavazzini, G., Pavesi, G., Dupont, P., Coudert, S., Ardizzon, G., Caignaert, G., Bois, G. (2011). High-speed stereoscopic PIV study of rotating instabilities in a radial vaneless diffuser. *Experiments in Fluids*, *51*, 83-93.

[90] Day I.J. Stall, Surge, and 75 years of Research. Journal of Turbomachinery, January 2016, Vol 138.

[91] B. Hellmich, J.R. Seume, Causes of Acoustic Resonance in a High-Speed Axial Compressor, Journal of Turbomachinery. 130 (2008) 031003

[92] Francesco Romanò, Clemence Rannou, Alberto Baretter, Julien Marty, Pierric Joseph, Antoine Dazin, 2025, How inlet flow inhomogeneities can affect the transition to stall in an axial compressor?, Proceedings of the 16th European Turbomachinery Conference (ETC16) Turbomachinery, Fluid Dynamics and Thermodynamics, March 24-28, 2025, Hannover, Germany, Paper ID: ETC2025-304.

[93] Third International Symposium on Cavitation, April 1998, Grenoble, France TWO-PHASE FLOW STRUCTURE OF CAVITATION : EXPERIMENT AND MODELLING OF UNSTEADY EFFECTS Jean-Luc REBOUD, Benoit STUTZ*, Olivier COUTIER

[94] Callenaere, M., Franc, J.P., Michel, J.M., & Riondet, M. (2001). The cavitation instability induced by the development of a re-entrant jet. Journal of Fluid Mechanics, 444, 223–256.

[95] Leroux, J.B., Coutier-Delgosha, O., & Astolfi, J.A. (2005). A joint experimental and numerical study of mechanisms associated to instability of partial cavitation on two-dimensional hydrofoil. Physics of Fluids, 17, 052101.

[96] Schnerr, G.H., Sauer, J. (2001), Physical and numerical modelling of unsteady cavitation dynamics, Proc. of the Fourth International Conference on Multiphase Flow, New Orleans.

[97] R. Fortes-Patella, O. Coutier-Delgosha, J. Perrin and J.-L. Reboud, "A Numerical Model to Predict Unsteady Cavitating Flow Behavior in Inducer Blade Cascades," Journal of Fluid Engineering, Vol. 129, No. 2, 2007, pp. 128-135. doi:10.1115/1.2409320

[98] Vasquez, R., and Adami, P., 2019, Roles and Challenges on CFD in the Design of Gas Turbines, Private communication, Invited Lecture No.15 European Turbomachinery Conference, ETC 13.

[99] Hammond. J., Pepper. N., Montomoli. F., and Michelassi. V., Machine Learning Methods in CFD for Turbomachinery: A Review, International Journal of Turbomachinery Propulsion and Power · May 2022, DOI: 10.3390/ijtpp7020016

[100] Raina, G., Bousquet, Y., Luquet, Y., Lippinois, E., Binder, N., 2024, Loss Breakdown in Axial Turbines: A New Method for Vortex Loss and Wake Detection from 3D RANS Simulations, Paper GT2024-121181, Proceedings of ASME Turbo Expo 2024 Turbomachinery Technical Conference and Exposition GT2024 June 24-28, London, United Kingdom

[101] Raina, G., Bousquet, Y., Luquet, Y., Lippinois, E., Binder, N., 2025, Analysis of Interactions among loss-generating mechanisms in axial flow turbines. . Proceedings of the 16th European Turbomachinery Conference (ETC 16) Fluid Dynamics and Thermodynamics, March 24-28, 2025, Hannover , Germany, Paper OD: ETC2025-150

.

[102] Bergmann, M., Morsbach, C., Möller, F. M., Goinis, G., Klose, B., 2025, A comparative study of varying incidence angle effects on a low-Reynolds number compressor cascade based on experiments, low fidelity and high-fidelity numerical simulations. Proceedings of the 16th European Turbomachinery Conference (ETC 16) Fluid Dynamics and

Thermodynamics, March 24-28, 2025, Hannover, Germany, Paper ID: ETC2025-231

[103] Yamade, Y., Kato, C., Nagahara, T., and Matsui, J., 2019, Origin and formation process of a submerged vortex in a pump sump, IOP Conf. Ser.: Earth Environ. Sci. 240 032028

[104] Bicchi. M., Biliotti. D. , Marconcini. M., Toni. L. , Cangioli. F., and Arnone. A., 2022, An AI-Based Fast Design Method for New Centrifugal Compressor Families. MDPI *Machines* 2022, *10*, 458. https://doi.org/10.3390/machines10060458

[105] Ottavy, X., Brandstetter, C., Workshop-Open test case fan ECL5/CATANA, Introduction and Presentation of the tet case, . Proceedings of the 16th European Turbomachinery Conference (ETC 16) Fluid Dynamics and Thermodynamics, March 24-28, 2025, Hannover , Germany,

Sponsors and Partners:

The Japan Society of Mechanical Engineers
www.jsme.or.jp

The Visualization Society of Japan
www.vsj.jp

FLUID-LAB.HU Flow Technology Kft.
www.fluid-lab.hu

Chemical Engineering & Technology
onlinelibrary.wiley.com/journal/15214125

Department of Fluid Mechanics
www.ara.bme.hu

Szellőző Művek Kft.
www.szellozomuvek.hu

Hungaro-Ventilátor Kft.
www.hungaro-ventilator.hu

Knorr-Bremse,
Vasúti Jármű Rendszerek Hungária Kft.
rail.knorr-bremse.com/en/hu

LaVision GmbH
www.lavision.de

National Research, Development and Innovation Office, Hungary
nkfih.gov.hu

Euroturbo,
European Turbomachinery Society
www.euroturbo.eu

KNORR-BREMSE

JSME

LAVISION
FOCUS ON IMAGING

V.S.J.

Chemical & Engineering Technology

SZELLŐZŐ művek

HV-VENT
THE FAN FACTORY

EUROTURBO
european turbomachinery society

NATIONAL RESEARCH, DEVELOPMENT AND INNOVATION OFFICE
HUNGARY

PROGRAM
FINANCED FROM
THE NRDI FUND

Department of
Fluid Mechanics

FLUID-LAB.HU
FLOW TECHNOLOGY LTD

www.cmff.hu